Dongmei Zhang · Xin Huang *Editors*

Proceedings of GeoShanghai 2018 International Conference: Tunnelling and Underground Construction

Springer

Proceedings of GeoShanghai 2018 International Conference: Tunnelling and Underground Construction

Dongmei Zhang · Xin Huang
Editors

Proceedings of GeoShanghai 2018 International Conference: Tunnelling and Underground Construction

Springer

Editors
Dongmei Zhang
Department of Geotechnical Engineering
Tongji University
Shanghai
China

Xin Huang
Department of Geotechnical Engineering
Tongji University
Shanghai
China

ISBN 978-981-13-0016-5 ISBN 978-981-13-0017-2 (eBook)
https://doi.org/10.1007/978-981-13-0017-2

Library of Congress Control Number: 2018942167

© Springer Nature Singapore Pte Ltd. 2018
This work is subject to copyright. All rights are reserved by the Publisher, whether the whole or part of the material is concerned, specifically the rights of translation, reprinting, reuse of illustrations, recitation, broadcasting, reproduction on microfilms or in any other physical way, and transmission or information storage and retrieval, electronic adaptation, computer software, or by similar or dissimilar methodology now known or hereafter developed.
The use of general descriptive names, registered names, trademarks, service marks, etc. in this publication does not imply, even in the absence of a specific statement, that such names are exempt from the relevant protective laws and regulations and therefore free for general use.
The publisher, the authors and the editors are safe to assume that the advice and information in this book are believed to be true and accurate at the date of publication. Neither the publisher nor the authors or the editors give a warranty, express or implied, with respect to the material contained herein or for any errors or omissions that may have been made. The publisher remains neutral with regard to jurisdictional claims in published maps and institutional affiliations.

Printed on acid-free paper

This Springer imprint is published by the registered company Springer Nature Singapore Pte Ltd.
part of Springer Nature
The registered company address is: 152 Beach Road, #21-01/04 Gateway East, Singapore 189721, Singapore

Preface

The 4th GeoShanghai International Conference was held on May 27–30, 2018, in Shanghai, China. GeoShanghai is a series of international conferences on geotechnical engineering held in Shanghai every four years. The conference was inaugurated in 2006 and was successfully held in 2010 and 2014, with more than 1200 participants in total. The conference offers a platform of sharing recent developments of the state-of-the-art and state-of-the-practice in geotechnical and geoenvironmental engineering. It has been organized by Tongji University in cooperation with the ASCE Geo-Institute, Transportation Research Board, and other cooperating organizations.

The proceedings of the 4th GeoShanghai International Conference include eight volumes of over 560 papers; all were peer-reviewed by at least two reviewers. The proceedings include Volumes 1: Fundamentals of Soil Behavior edited by Dr. Annan Zhou, Dr. Junliang Tao, Dr. Xiaoqiang Gu, and Dr. Liangbo Hu; Volume 2: Multi-physics Processes in Soil Mechanics and Advances in Geotechnical Testing edited by Dr. Liangbo Hu, Dr. Xiaoqiang Gu, Dr. Junliang Tao, and Dr. Annan Zhou; Volume 3: Rock Mechanics and Rock Engineering edited by Dr. Lianyang Zhang, Dr. Bruno Goncalves da Silva, and Dr. Cheng Zhao; Volume 4: Transportation Geotechnics and Pavement Engineering edited by Dr. Xianming Shi, Dr. Zhen Liu, and Dr. Jenny Liu; Volume 5: Tunneling and Underground Construction edited by Dr. Dongmei Zhang and Dr. Xin Huang; Volume 6: Advances in Soil Dynamics and Foundation Engineering edited by Dr. Tong Qiu, Dr. Binod Tiwari, and Dr. Zhen Zhang; Volume 7: Geoenvironment and Geohazards edited by Dr. Arvin Farid and Dr. Hongxin Chen; and Volume 8: Ground Improvement and Geosynthetics edited by Dr. Lin Li, Dr. Bora Cetin, and Dr. Xiaoming Yang. The proceedings also include six keynote papers presented at the conference, including “Tensile Strains in Geomembrane Landfill Liners” by Prof. Kerry Rowe, “Constitutive Modeling of the Cyclic Loading Response of Low Plasticity Fine-Grained Soils” by Prof. Ross Boulanger, “Induced Seismicity and Permeability Evolution in Gas Shales, CO_2 Storage and Deep Geothermal Energy” by Prof. Derek Elsworth, “Effects of Tunneling on Underground Infrastructures” by Prof. Maosong Huang, “Geotechnical Data Visualization and Modeling of Civil

Infrastructure Projects" by Prof. Anand Puppala, and "Probabilistic Assessment and Mapping of Liquefaction Hazard: from Site-specific Analysis to Regional Mapping" by Prof. Hsein Juang. The Technical Committee Chairs, Prof. Wenqi Ding and Prof. Xiong Zhang, the Conference General Secretary, Dr. Xiaoqiang Gu, the 20 editors of the 8 volumes and 422 reviewers, and all the authors contributed to the value and quality of the publications.

The Conference Organizing Committee thanks the members of the host organizations, Tongji University, Chinese Institution of Soil Mechanics and Geotechnical Engineering, and Shanghai Society of Civil Engineering, for their hard work and the members of International Advisory Committee, Conference Steering Committee, Technical Committee, Organizing Committee, and Local Organizing Committee for their strong support. We hope the proceedings will be valuable references to the geotechnical engineering community.

Shijin Feng
Conference Chair
Ming Xiao
Conference Co-chair

Organization

International Advisory Committee

Herve di Benedetto	University of Lyon, France
Antonio Bobet	Purdue University, USA
Jean-Louis Briaud	Texas A&M University, USA
Patrick Fox	Penn State University, USA
Edward Kavazanjian	Arizona State University, USA
Dov Leshchinsky	University of Illinois, USA
Wenhao Liang	China Railway Construction Corporation Limited, China
Robert L. Lytton	Texas A&M University, USA
Louay Mohammad	Louisiana State University, USA
Manfred Partle	KTH Royal Institute of Technology, Switzerland
Anand Puppala	University of Texas at Arlington, USA
Mark Randolph	University of Western Australia, Australia
Kenneth H. Stokoe	University of Texas at Austin, USA
Gioacchino (Cino) Viggiani	Université Joseph Fourier, France
Dennis T. Bergado	Asian Institute of Technology, Thailand
Malcolm Bolton	Cambridge University, UK
Yunmin Chen	Zhejiang University, China
Zuyu Chen	Tsinghua University, China
Jincai Gu	PLA, China
Yaoru Lu	Tongji University, China
Herbert Mang	Vienna University of Technology, Austria
Paul Mayne	Georgia Institute of Technology, USA
Stan Pietruszczak	McMaster University, Canada
Tom Papagiannakis	Washington State University, USA
Jun Sun	Tongji University, China

Scott Sloan	University of Newcastle, Australia
Hywel R. Thomas	Cardiff University, UK
Atsashi Yashima	Gifu University, Japan

Conference Steering Committee

Jie Han	University of Kansas, USA
Baoshan Huang	University of Tennessee, USA
Maosong Huang	Tongji University, China
Yongsheng Li	Tongji University, China
Linbin Wang	Virginia Tech, USA
Lianyang Zhang	University of Arizona, USA
Hehua Zhu	Tongji University, China

Technical Committee

Wenqi Ding (Chair)	Tongji University, China
Charles Aubeny	Texas A&M University, USA
Rifat Bulut	Oklahoma State University, USA
Geoff Chao	Asian Institute of Technology, Thailand
Jian Chu	Nanyang Technological University, Singapore
Eric Drumm	University of Tennessee, USA
Wen Deng	Missouri University of Science and Technology, USA
Arvin Farid	Boise State University, Idaho, USA
Xiaoming Huang	Southeast University, China
Woody Ju	University of California, Los Angeles, USA
Ben Leshchinsky	Oregon State University, Oregon, USA
Robert Liang	University of Dayton, Ohio, USA
Hoe I. Ling	Columbia University, USA
Guowei Ma	Hebei University of Technology, China
Roger W. Meier	University of Memphis, USA
Catherine O’Sullivan	Imperial College London, UK
Massimo Losa	University of Pisa, Italy
Angel Palomino	University of Tennessee, USA
Krishna Reddy	University of Illinois at Chicago, USA
Zhenyu Yin	Tongji University, China
ZhongqiYue	University of Hong Kong, China
Jianfu Shao	Université des Sciences et Technologies de Lille 1, France
Jonathan Stewart	University of California, Los Angeles, USA

Wei Wu	University of Natural Resources and Life Sciences, Austria
Jianhua Yin	The Hong Kong Polytechnic University, China
Guoping Zhang	University of Massachusetts, USA
Jianmin Zhang	Tsinghua University, China
Xiong Zhang (Co-chair)	Missouri University of Science and Technology, USA
Yun Bai	Tongji University, China
Jinchun Chai	Saga University, Japan
Cheng Chen	San Francisco State University, USA
Shengli Chen	Louisiana State University, USA
Yujun Cui	École Nationale des Ponts et Chaussees (ENPC), France
Mohammed Gabr	North Carolina State University, USA
Haiying Huang	Georgia Institute of Technology, USA
Laureano R. Hoyos	University of Texas at Arlington, USA
Liangbo Hu	University of Toledo, USA
Yang Hong	University of Oklahoma, USA
Minjing Jiang	Tongji University, China
Richard Kim	North Carolina State University, USA
Juanyu Liu	University of Alaska Fairbanks, USA
Matthew Mauldon	Virginia Tech., USA
Jianming Ling	Tongji University, China
Jorge Prozzi	University of Texas at Austin, USA
Daichao Sheng	University of Newcastle, Australia
Joseph Wartman	University of Washington, USA
Zhong Wu	Louisiana State University, USA
Dimitrios Zekkos	University of Michigan, USA
Feng Zhang	Nagoya Institute of Technology, Japan
Limin Zhang	Hong Kong University of Science and Technology, China
Zhongjie Zhang	Louisiana State University, USA
Annan Zhou	RMIT University, Australia
Fengshou Zhang	Tongji University, China

Organizing Committee

Shijin Feng (Chair)	Tongji University, China
Xiaojqiang Gu (Secretary General)	Tongji University, China
Wenqi Ding	Tongji University, China
Xiongyao Xie	Tongji University, China

Yujun Cui	École Nationale des Ponts et Chaussees (ENPC), France
Daichao Sheng	University of Newcastle, Australia
Kenichi Soga	University of California, Berkeley, USA
Weidong Wang	Shanghai Xian Dai Architectural Design (Group) Co., Ltd., China
Feng Zhang	Nagoya Institute of Technology, Japan
Yong Yuan	Tongji University, China
Weimin Ye	Tongji University, China
Ming Xiao (Co-chair)	Penn State University, USA
Yu Huang	Tongji University, China
Xiaojun Li	Tongji University, China
Xiong Zhang	Missouri University of Science and Technology, USA
Guenther Meschke	Ruhr-Universität Bochum, Germany
Erol Tutumluer	University of Illinois, Urbana—Champaign, USA
Jianming Zhang	Tsinghua University, China
Jianming Ling	Tongji University, China
Guowei Ma	Hebei University of Technology, Australia
Hongwei Huang	Tongji University, China

Local Organizing Committee

Shijin Feng (Chair)	Tongji University, China
Zixin Zhang	Tongji University, China
Jiangu Qian	Tongji University, China
Jianfeng Chen	Tongji University, China
Bao Chen	Tongji University, China
Yongchang Cai	Tongji University, China
Qianwei Xu	Tongji University, China
Qingzhao Zhang	Tongji University, China
Zhongyin Guo	Tongji University, China
Xin Huang	Tongji University, China
Fang Liu	Tongji University, China
Xiaoying Zhuang	Tongji University, China
Zhenming Shi	Tongji University, China
Zhiguo Yan	Tongji University, China
Dongming Zhang	Tongji University, China
Jie Zhang	Tongji University, China
Zhiyan Zhou	Tongji University, China
Xiaoqiang Gu (Secretary)	Tongji University, China
Lin Cong	Tongji University, China
Hongduo Zhao	Tongji University, China

Fayun Liang	Tongji University, China
Bin Ye	Tongji University, China
Zhen Zhang	Tongji University, China
Yong Tan	Tongji University, China
Liping Xu	Tongji University, China
Mengxi Zhang	Tongji University, China
Haitao Yu	Tongji University, China
Xian Liu	Tongji University, China
Shuilong Shen	Tongji University, China
Dongmei Zhang	Tongji University, China
Cheng Zhao	Tongji University, China
Hongxin Chen	Tongji University, China
Xilin Lu	Tongji University, China
Jie Zhou	Tongji University, China

Contents

Effects of Tunneling on Underground Infrastructures 1
Maosong Huang, Jian Yu, Chenrong Zhang, Linlong Mu,
and C. F. Leung

Tunnelling-Induced Ground Response

Simulating Synchronous Grouting in Shield Tunnels with the Consideration of Evolution of Grouting Pressure 23
Yafei Qiao, Tianchi Zhao, and Wenqi Ding

The Behavior Analysis of a Cofferdam Constructed by Double Sheet Pile Wall Above Muck 32
Tianchi Zhao, Wenqi Ding, Lixin Wei, Weifeng Wu, and Yafei Qiao

Effects of Different Factors on the Mining of Extra-Thick Coal Seam 40
Naifei Liu, Zhu Zhang, Ning Li, Min Yang, and Yuanyang Ren

Explicit Analysis for the Ground Response Behavior Due to the Advancing Excavation of Tunnel Under Anisotropy Stress Field 54
Y. L. Lee and Y. X. Xin

Analysis of Large-section Tunnels with Small Spacing in Elastoplastic Stress-seepage-damage Model 63
Meng-fei Xu, An-nan Jiang, Gao Lin, Zhang Xue-liang,
and You-fu Wang

Parametric Study on Stability of Tunneling Excavation Face via Fluid-Solid Coupling Simulation 74
Jinlong Li, Zhijun Kang, and Yong Tan

Numerical Modeling on Localized Ground Subsidence Induced by the Tunneling in Sand 84
Min Zhou, Fei Wang, and Yan-Jun Du

Simplified Method for Calculating the Settlement of Existing Tunnel Induced by New Tunneling Based on Two Step Method 93
Junwei Jin, Jingyuan Zhan, Weikang Song, and Mingyu Li

Ground Surface Deformation Analysis of Quasi Rectangular EPB Shield Tunneling 103
Xi Jiang, Xuehui Zhang, Ang Chen, Jixiang Chen, and Yun Bai

Ground Penetrating Radar Inspection Experiment on a Shield Tunnel Segment and the Backfill Grouting 112
Tan Qin, Yonghui Zhao, Shufan Hu, Cong An, Nan Chen, Cheng Chen, and Yifan Chen

Numerical Analysis of Ground Displacement and Pile Response Due to Tunneling in Soft Soil Considering the Creep Behavior 121
Yu Pan, Jun-Jie Zheng, Lan Cui, and Rong-Jun Zhang

Defining a “shallow” Tunnel by Stability Analysis with Discontinuity Layout Optimization 131
Yiming Zhang and Xiaoying Zhuang

Three-Dimensional Seepage Flow Analysis of Slurry Shield with Permeable Filter Cake 136
Xinsheng Yin, Zhi Ding, Xinjiang Wei, and Gang Wei

Discrete Element Analysis of the Excavation Disturbance of Cross-River Twin-Tunnels on the Surroundings 156
Zhihua Zhang, Xiedong Zhang, Lin Wu, and Hang Zhang

An Arching Theory for Arch Tunnels Based on the Interaction Between the Lateral and Vertical Pressure in Good Ground 164
Xiaohu Cheng

Reliability Analysis of Ground Surface Settlement Given Multivariate Spatial Random Field in Shield Tunneling 181
Changhong Wang

The Surface Subsidence Prediction of Shield Construction Based on the Fuzzy Neural Network 190
Dong Han and Xiaojun Li

Analysis of Soil Disturbance Caused by DOT Excavation in Soft Soil Stratum 198
Xiao-Liang Chen and Xiao-Nan Gong

Study on Characteristics of Ground Motion in Karst Area Based on Viscoelastic Artificial Boundary 207
Mei-yan Bai, Hong-wei Wang, Chuan Shen, and Kai-zhong Xie

Research on Strength Characteristic Parameter of Sandy Pebble Soil Based on Different Density and Moisture Content. 215
Zhao Zhang, Junfu Lu, and Shenlin Ling

An Alternative Method for Soil Characterisation Using Pipe-Jacking Parameters and Spoil Characteristics 224
Wen-chieh Cheng, James C. Ni, and Louis Ge

Explorative Application of Peck Formula and Its Modifier Versions in Surface Subsidence Prediction Caused by Quasi-rectangular Tunnel Construction. 232
Jun Liu, Peinan Li, Xiaoyong Kou, and Dezhong Huang

Effects of Soil Cross-Anisotropy on the Wave-Induced Residual Liquefaction Around an Immersed Tunnel in the Liquefiable Seabed 241
Di Fang, Weiyun Chen, and Guoxing Chen

Numerical Analysis of Tunnelling in Sand - A Case Study of a Centrifuge Test 250
Bowen Yang and Alan Bloodworth

Mechanical Behavior of Tunnel Lining and Segmental Joints

A Prototype Load Test on Fracture and Damage Properties of Cracked Shield Tunnel Lining Segments 263
Longgang Tian, Qi Zhang, Xiao Wang, and Guangchao Zhang

A Multilayer Analytical Model and Experimental Verification for Tunnel Lining Segment Under Elevated Temperatures 273
Zhi-guo Yan, Yao Zhang, Yi Shen, and Hehua Zhu

Numerical Study on High Stiffness Segmental Joints of Shield Tunnels 282
Long Zhou, Zhi-guo Yan, He-hua Zhu, and Yi Shen

A New Form of Longitudinal Joint of Large Cross-section Segmental Tunnel Linings 292
Yifan Gong, Wenqi Ding, Chenjie Gong, and Yuelang Jin

Analytical Solution of Underneath Tunnelling-Induced Deformation of Existing Tunnel 300
Zhong-Kai Huang, Dong-Mei Zhang, Mao-Zhu Peng, and Xiang Zong

Influence of Pit Excavation on Deformation of Metro Tunnels Based on the Zone State Index 309
Feng-rui Zhang, An-nan Jiang, Shi-jie Zheng, Shu-xun Guo, Jin-man Wang, and Rui Yang

In-situ Experimental Analysis of Acceleration Response of Mountain Tunnel Lining to Rubblization-Induced Vibrations 319
Yong Zhao, Shi-Jin Feng, Mao-Zhu Peng, Dong-Mei Zhang, and Xiao-lei Zhang

Experimental and Numerical Study on Longitudinal Axial Force and Deformation of Shield Tunnel 329
Xiaojun Li, Xiaozhou Zhou, Bichen Hong, and Hehua Zhu

Theoretical Analysis and Model Testing of the Deformation Characteristics and Failure Mechanism of a Blocking Airbag System in a Tunnel Under External Pressure 339
Jing Chen, Shu-wang Yan, Li-qiang Sun, and Rui-qing Lang

Shearing Behavior of Segmental Joints of Large-Diameter Shield Tunnel 351
Dong-Mei Zhang and Jie Liu

Tunnel Roof Stability in Soft Rock with Tension Cutoff 361
Dowon Park and Radoslaw L. Michalowski

Mechanical Properties and Seismic Isolation Mechanism of Foamed Concrete Longitudinal Joints of Tunnel in Rock 369
Shaosen Ma and Weizhong Chen

Research on Seismic Response Characteristics of Long and Large Tunnel in Rock 376
Shaosen Ma and Weizhong Chen

Numerical Investigation on the Mechanical Characteristics of a Special-Shaped Shield Lining with a Large Cross-Section 384
Yeting Zhu, Zixin Zhang, Xin Huang, and Yanfei Zhu

Data Analysis of Shield Tunnel Deformation from Real-Time Monitoring with Wireless Sensing Network 392
Xin Xie, Dongming Zhang, and Hongwei Huang

An Analytical Solution for the Failure Process of a Shield Tunnel Segmental Joint with a Load-Transferring Gasket 402
Ting-jin Liu, Hong-hao Huang, Rao Xu, Xin-wei Tang, and Shan-yong Wang

Dynamic Response of Tunnel Lining to Resonance Rubblization Induced Vibration in Pavement Renewal 422
Mao-Zhu Peng, Dong-Mei Zhang, Yong Zhao, Xiao-Lei Zhang, and Zhong-Kai Huang

Analysis and Application Exploration of Smoothed Particle Hydrodynamics (SPH) for Non-circular Shield Tunneling 432
Peinan Li, Jun Liu, Yixin Zhai, and Wenqi Ding

Mechanical Analysis of a Super-large-diameter Shield Tailskin Under Deep Ground Load 442
Chen Zhou, Xuehui Zhang, and Yun Bai

Numerical Analysis of Influence of Ground Variation on Deformation and Internal Forces of Large Diameter Shield Tunnel 451
Jingkang Shi, Dongming Zhang, and Hongwei Huang

A Shield Tunnel Model Based on Generalized-Node Solid-Shell and Spacial Joint Element 460
Lin Yifeng

Numerical Validation of a New Testing Setup for Mechanical Test of Tunnel Lining Joints 468
Z. X. Zhang, W. Liu, X. Huang, and Q. W. Zhuang

Dynamic Response Analysis of Underground Station Under the Action of Falling Ground Vibration 477
Shan Ji, Jun Hu, and Wei-Ping Xie

Reliability-Based Analysis of Segmental Linings for Underwater Shield Tunnels 486
Youwen Wang, Zhe Luo, and Biao Hu

Three-Dimensional Transient Response of Deep Embedded Tunnels to Internal Explosions 496
F. Y. Liu, X. Wang, Y. Q. Cai, and C. J. Xu

A Coupled Hydro-Mechanical Modeling of Tunnel Leakage in Sand Layer 506
Jie Yang, Zhen-Yu Yin, Dong-Mei Zhang, Pierre-Yves Hicher, and Farid Laouafa

Tunnelling in Challenging Situations

Evolution of Frost Penetration and Ablation in the Surrounding Rock of Cold Region Tunnels 517
Zhitao Lv, Caichu Xia, Yu Zhou, Changling Han, and Yuesong Wang

TBMs: Capabilities, Limitations and Challenges 528
Yun Bai, Xi Jiang, Diana Diaz, Xuehui Zhang, and ZhuanZhuan Zhang

Progress of Research Advance on the Model Tests on the Interaction Between New Constructions and Adjacent Existing Buildings 536
Mingyu Li and Jibin Zhao

Studies on the Key Technologies for Underground Construction of High-Speed Rail Station Design 548
Chuanping Liu and Jian Jia

Centrifuge Investigation into the Effect of New Shield Tunneling on an Existing Overlying Large-Diameter Tunnel 559
Xiao-Guang Liu, Shou-Ji Du, and Peng Li

Study on Construction Control Measures of Shield Tunnel Overpassing Existing Tunnel in Sandy Silt 567
Yahui Wang, Yan Liu, Junyan Liu, and Liangliang Zhang

Research on the Shield Tunneling Construction Passing Through the Maglev Pile Foundations in Saturated Soft Soil Strata 576
Di Wu

Planning, Sustainability, Maintenance and Emergency Counter-Measures

Layout Patterns of Underground Space Comprehensive Utilization Around Metro Station for Urban Commercial Area 587
Jian Peng and Fang-Le Peng

Influence of Aspect Ratio of the Exhaust Opening on Smoke Propagation in a Large Cross-section Tunnel 597
Zhiguo Yan, Yuxin Zhang, and Hehua Zhu

Study on the Grade Evaluation of Highway Tunnel Cracks Based on PFC Simulation and BP Neural Network 605
Hao Ding, Ke Li, Yuyu Xiayang, and Jing Bi

Study on the Temperature Distribution and Thermal Damage of Concrete Lining in the Maximum Temperature Section of Tunnel Under Fire Condition 612
Baoping Xi, Yangchun Wu, Luhai Chen, Qinghua Guo, and Hehua Zhu

Fire Response Performance and Social Behavior in Tunnels Distinguishing from Buildings in Evacuation 625
Yuxin Zhang, Zhiguo Yan, Hehua Zhu, and Yi Shen

Natural Ventilating Behavior of Z-Shaped Pedestrian Underpass in Wuhan 633
Xiongwei Li, Yu Qin, and Yong Wang

Risk Assessment and Alignment Comparison Research on a Proposed Subsea Tunnel in Operation Periods 642
Lin Zhi and Chen Si

Ventilation Effect and Optimum Design of an Urban I-Shaped Pedestrian Underpass 652
Yong Wang, Xiongwei Li, Min Wang, Yanli Wang, and Jianbin Chen

Research Methods in Tunnel Fire Distinguishing from Buildings in Evacuation 666
Jingtao Dong, Zhiguo Yan, Yuxin Zhang, and Hehua Zhu

Cutter Ring Breakage Induced by Unbalanced Side Force in Circular Cutting Process 674
Dong-Jie Ren, Shui-Long Shen, Jin-Chun Chai, and Da-Jun Yuan

New Frontiers and Innovative Technologies

Large-Scale Mine Water Geothermal Applications with Abandoned Mines 685
Ting Bao, Zhen Liu, Jay Meldrum, and Christopher Green

Investigation on the Thermo-Mechanical Behavior of an Energy Pile and the Surrounding Soil by Model Test and 2D Finite Element-Finite Difference Method 696
X. H. Bao, Y. L. Xiong, H. Y. Mingi, H. Z. Cui, G. B. Liu, and R. Y. Zheng

Bearing Performance of Geothermal Energy Pile Subjected to Thermal Loading 710
Pengfei Fang, Abdelmalek Bouazza, Zhongjin Wang, and Xinyu Xie

Optimal Shock Absorption Layout of Lead Rubber Bearing in a Multi-story Underground Structure 718
Zhiyi Chen and Zhiqian Liu

Fuzzy Comprehensive Evaluation System of Tunnel Construction Method 728
Tianxiang Wu, Wenqi Ding, Shiding Cao, and Jun Li

Multi-time-Scale Analysis of Tunnel Temperature Field Based on Big Data 737
Zhiguo Yan, Jiangtao Liu, Hehua Zhu, and Jingtao Dong

A Summary of Precast Technology Application in Tunneling 749
Hong Jiang

Discussions About Key Problems in the Research and Development of Technology System for Rectangular Shield Tunnel 757
Yaohong Zhu, Zibo Dong, Peinan Li, and Junfu Lu

Research on Field Acquisition Geological Data Application in the Rock Tunnel Construction Phase Based on iS3 766
Chao Chen, Ziyang Chen, and Jin Lei

Author Index 775

About the Editors

Dongmei Zhang received her Ph.D. in Civil Engineering from Tongji University, China. She is now a Full Professor in the Department of Geotechnical Engineering of Tongji University, China.

Xin Huang graduated from a joint Ph.D. program in Geotechnical Engineering between the University of Hong Kong and Imperial College London. He is currently an Assistant Professor in the Department of Geotechnical Engineering of Tongji University, China.

Effects of Tunneling on Underground Infrastructures

Maosong Huang[1(✉)], Jian Yu[1,2], Chenrong Zhang[1], Linlong Mu[1],
and C. F. Leung[2]

[1] Tongji University, 1239 Siping Road, Shanghai, China
`mshuang@tongji.edu.cn`
[2] National University of Singapore, Singapore, Singapore

Abstract. In urban cities like Shanghai, the increasing need for urban tunnelling to serve the ever-growing population in space-constrained cities will result in part of the proposed tunnelling route running close or beneath infrastructures, such as pipelines and buildings founded on shallow or pile foundations. The ground volume losses due to the over-excavation of the tunnel result in ground, subsurface and lateral movements. These ground movements, result in additional stress and deformation on the existing infrastructures. Thus, a type of displacement control methods has been developed and widely applied to the risk assessment of the infrastructures subjected to tunneling. This paper will fully review the existing studies on the displacement control methods and their results to conclude critical responses of various infrastructures, provide effective methods of evaluating the responses for practical engineering.

Keywords: Tunnelling · Pipeline · Pile foundation · Raft foundation

1 Introduction

Land scarcity is a major concern in cities around the world. With the rapid development within build-up areas, building of infrastructure above ground becomes uneconomical due to the need for acquisition of valuable land. This is especially true for urban mass transit systems and waste water sewage. Hence, locating such infrastructure in underground spaces is an attractive alternative. However, it has always been a concern of whether such development will have detrimental effect on nearby infrastructures, such as pipelines and foundations of buildings. A possible solution is to locate such excavation away from existing foundations, but it is not always practical to align the tunnels for this purpose.

Soil disturbance is inevitable in the process of tunnel excavation. With advancement in technology such as the use of earth pressure balance shield and tail void grouting, disturbance is minimized but not completely eliminated. However, the original design of nearby infrastructures does not consider the additional stresses and deformations induced by soil movements due to tunneling. More importantly, different types of underground infrastructures have different sensitivities to various additional responses. Hence, it is of great interest to investigate their responses when subjected to tunneling activity in the vicinity.

© Springer Nature Singapore Pte Ltd. 2018
D. Zhang and X. Huang (Eds.): GSIC 2018, *Proceedings of GeoShanghai 2018 International Conference: Tunnelling and Underground Construction*, pp. 1–20, 2018.
https://doi.org/10.1007/978-981-13-0017-2_1

A general approach for solving the above problem is the finite element method (FEM) or finite difference method (FDM) by simulating actual tunnel excavation processes [1–3] and studying the effect on adjacent structures. The selection of soil constitutive models and determination of the model parameter have significant impacts on the predictions of the soil movements due to tunneling. More advanced models need more parameters, however, which are often missing for most practical sites. As a result, the reliability of the obtained responses of infrastructure behavior is doubtful.

To simplify the complex tunneling process, a more effective approach, displacement-controlled finite element method (DCFEM) is developed based on the concept of ground volume loss [4, 5]. In a tunnel excavation project, there is unloading of soil and even overcut as the tunnel boring machine advances. The overcut clearly reduces the soil volume. In addition, soil unloading takes the form of the release of earth pressure at the face of advancement, thereby causing the soil to expand into the excavation. These soil volume changes are given the term ground volume loss v_l and are generally normalised by the tunnel volume to give the term volume loss ratio ($v_s = 4v_l/\pi D_T^2$, where D_T is the tunnel diameter). In the DCFEM, the effect of tunneling is simulated by adding displacements to nodes around the tunnel rather than by modelling the detailed tunneling process. The proposed opening deformation mechanism is based on observations from centrifuge model tests and field cases. Previously, this convergence pattern around the tunnel boundary has been ideally assumed to be uniform in the analytical solutions proposed by Sagaseta [6]. However, it is expected that the tunnel convergence is highly non-uniform with more crown settlement and less invert heave. Centrifuge model tests by Hagiwara et al. [7] and field measurements at the Heathrow trial tunnel by Deane and Bassett [8] show that the area close to the tunnel invert experiences very little movement compared to the crown. Figure 1 shows the non-uniform convergence model on the tunnel boundary. The greenfield generated by such a convergence model has been validated by comparing with the reported field cases [9]. It is also employed to the adjacent structural responses, such as pipelines [10, 11], raft foundations [12, 13] and pile foundations [4, 5].

Additionally, the concept of displacement control has been further extended to a type of simplified methods. In these methods, affected infrastructures (such as pipelines, piles or raft foundations) are usually modelled as buried flexible beams and plates, while tunnel-induced soil movements at the positions of the infrastructures are used explicitly as the displacement boundary conditions to study the effects on the infrastructures. Therefore, these methods can also fall within the category of the displacement-based two-stage method [14]. The main difference between the various two-stage methods is the description of soil-structure interaction, such as Winkler model by simplifying soil as a series of independent springs and elastic continuum model by assuming soil having elastic behavior. They have been widely employed to study the effect of pipeline [15–18] and pile foundations [19, 20].

This review aims to compile and summarize the application of displacement-based method in the effect of tunneling on underground infrastructure.

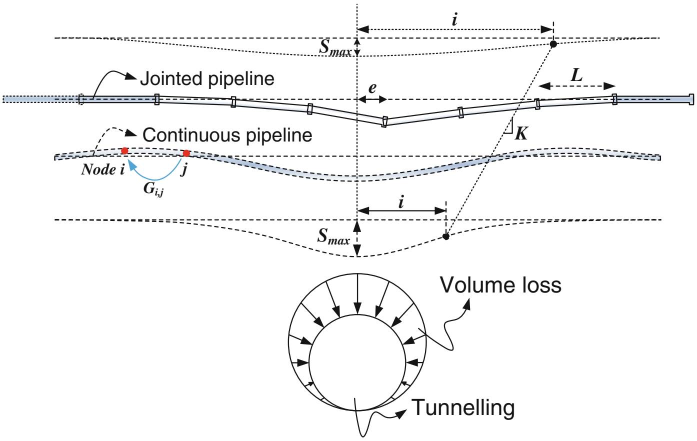

Fig. 1. Illustration of tunnel-pipeline interaction

2 Response of Pipeline Subjected to Tunneling

2.1 Illustration of Problem

Attewell et al. [15] indicated that, pipeline with welded, flanged, cement and turned-and-bored joints can be considered as continuous pipelines, as the bending stiffness of the joints have no obvious decrease compared that of the pipe sections. Therefore, the additional bending strain caused by tunnelling is the major concern. Pipelines with rubber gasket, push-in joints and bolted-gland joints, can be classified as discontinuous or jointed pipelines, as the joints allow relative rotation at the ends of the connected two pipe sections. Excessive angular rotation leads to the leakage at the joints. Clearly, the additional joint rotation is supposed as the critical concern in the evaluation of jointed pipelines subjected to tunnelling. Figure 1 illustrates the deformation characteristics of jointed and continuous pipelines.

2.2 Winkler Modelling of a Continuous Pipeline Subjected to Tunneling

The analysis process of the two-stage methods is as follows: (1) determining the free soil displacement at the pipeline position due to tunneling; (2) calculating the responses of the pipeline caused by the obtained free soil movement. Obviously, the green field soil movement is an important basis of this type of methods.

By investigating real life cases, Peck [21] indicated that the transverse settlement profile can be modelled using Gaussian distribution. The standard Gaussian curve follows the equation:

$$S_v(x) = S_{v,max}\, exp\left[\frac{-x^2}{2i^2}\right] \tag{1}$$

where x is the displacement from the tunnel centerline; i is the distance from the tunnel centre to the inflexion point, v_s is the ground volume loss ratio; $S_v(x)$ is the settlement at displacement x and $S_{v,max}$ is the maximum settlement, equaling to $v_s/\sqrt{2\pi i}$. Loganathan and Poulos [22] deduced an analytical solution for predicting the green field soil moment using the non-uniform convergence model shown in Fig. 1. Zhang et al. [9] further developed an analytical solution to predict soil displacement due to tunnelling in layered soils.

Considering the soil movement due to tunneling having a small magnitude, Klar et al. [16] indicated that the elastic continuum soil model is enough accurate to capture the behavior of pipe-soil interaction, in which the soil is represented by an elastic half-space. This model was first presented by Poulos and Davis [23] in the studies on responses of a pile subjected to axial and lateral loading. The equation for the rigorous elastic continuum solution [16] on the pipeline's response caused by tunnelling is expressed as follows;

$$\left[[\mathrm{S}] + [\mathrm{K}^*] + [\mathrm{K}^*]\left[\lambda_s^*\right][\mathrm{S}]\right]\{w\} = [\mathrm{K}^*]\{\mathrm{S}_v\} \tag{2}$$

where $[\mathrm{S}]$ is the stiffness matrix of the pipe composed of standard beam elements; $\{w\}$ is the pipe displacements; $[\mathrm{K}^*]$ is a local soil stiffness matrix, and is diagonal, ($[\mathrm{K}^*]_{i,i}$ equals to $1/G_{i,i}$, where $G_{i,j}$ is the elastic soil continuum displacement at point i due to unit loading at point j (see Fig. 1), and can be obtained from Mindlin's solution [24] for a uniform elastic half space.); $\{\mathrm{S}_v\}$ is the free soil displacement at the pipeline position and usually taken as a Gaussian curve; $\left[\lambda_s^*\right]_{i,j} = \left\{G_{i,j} for\, i \neq j; 0 for\, i = j\right\}$, the implication of which is that the soil reaction acting on the pipe is affected by the soil response at different locations along the pipe, namely that the transmission of stresses and the continuity of displacements in soil are considered.

In addition, Eq. (2) can also be reduced to a Winkler solution by taking $\left[\lambda_s^*\right]$ as a null matrix, which implies that the soil continuity is omitted. Instead, the soil behavior is simulated using a series of spring; therefore, the diagonal element $[\mathrm{K}^*]_{i,i}$ in the local soil stiffness matrix is replaced by the spring stiffness k (Winkler modulus), which is usually determined by means of the Vesic's expression [25].

The distributions of the normalized bending moments from the elastic continuum solutions are plotted in Fig. 2(a). Clearly, the pipe-soil relative stiffness $EI/E_s r_0^4$ (EI is the bending stiffness of pipe; E_s is the soil elastic modulus; r_0 is the pipe radius) has a significant impact on the normalized maximum moments. Figure 2(b) further shows the variation of the normalized maximum moments with $EI/E_s r_0^4$.

A comparison of the maximum moments between the elastic continuum solution and the Winkler solution with the Vesic's modulus is also shown in Fig. 2(b), which reveals that the Winkler one has a severe underestimation for the moments. Vesic's modulus [25] was deduced by allowing a beam on a Winkler foundation to exhibit similar displacements and moments to that of a beam on an elastic half-space when loaded with the same concentrated force. Attewell et al. [15] pointed out that this assumption is not suitable for the buried pipeline caused by soil movements due to construction of underground space. To solve the problem, Yu et al. [26] derived a

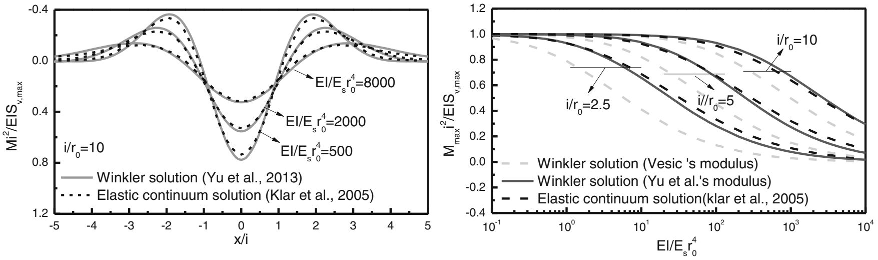

(a) (b)

Fig. 2. Comparison of normalized bending moments between elastic continuum solution and Winkler solution: (a) Effect of relative stiffness on bending moment distribution; (b) Maximum moments versus pipe-soil relative stiffness

Winkler subgrade modulus for the buried pipeline under the action of soil movements based on the elastic theory:

$$\begin{cases} k = \frac{3.08}{\delta}\frac{E_s}{1-v_s^2}\sqrt[8]{\frac{E_sD^4}{EI}} \\ \delta = \begin{cases} 2.18\, z/D \le 0.5 \\ 1 + \frac{1}{1.7z/D} z/D > 0.5 \end{cases} \end{cases} \tag{3}$$

where v_s is the Poisson's ratio; D is the pipe diameter; z is the buried depth of pipeline. The accuracy has been verified by compared with the moment distributions and maximum moments of the elastic continuum solution (see Fig. 2).

In addition, it should be noted that the Winkler model could not provide a better solution than the elastic continuum solution in the elastic range, but it does have a merit that it can be extended to nonlinear soil behavior easily. Furthermore, due to its simplicity, deduction of analytical expressions becomes possible. A closed-form Winkler solution was presented by Klar et al. [16], in which the bending moment M of the pipeline due to tunnelling is expressed as:

$$\mathrm{M}(x) = \int_{-\infty}^{+\infty} \frac{kS_v(t)}{4\lambda} exp(-\lambda|x-t|)[cos(\lambda|x-t|) - sin(\lambda|x-t|)]dt \tag{4}$$

where $\lambda = \sqrt{4k/4EI}$. Its application will be further given in the subsection with respect to jointed pipelines. When substituted Yu et al.'s Winkler modulus, Eq. (4) can provide a consistent prediction with the Winkler solution given in Fig. 2(b), which thus can be used to preliminary evaluate the maximum bending moment of a continuous pipeline due to tunneling.

2.3 Continuous Elastic Modelling of a Continuous Pipeline in Layered Soils Subjected to Tunneling

In the continuum elastic solution above, the soil behavior is simulated by the Mindlin's solution [24], which is the elastic solution for a concentrated force in a homogeneous elastic half space. In fact, Burmister [27] presented a similar solution for a concentrated force in two or three elastic layers with independent elastic parameters. Later, the Hankel transform and transfer matrix technique was employed to extend the Burmister solution to a layered elastic mass consisting of n parallel elastic isotropic layers, in which each layer has an independent elastic modulus E_{si}, Poisson ratio v_{si} and thickness ΔH_{i}.

According to the governing equations of elastic theory in axisymmetric conditions and the Hankel transform, the transfer matrix solution for one-layer soil become:

$$\{\bar{G}(\xi, z)\} = [\Phi(\xi, z)]\{\bar{G}(\xi, 0)\} \tag{5}$$

where $\{\bar{G}(\xi, z)\} = \{\bar{u}(\xi, z), \bar{w}(\xi, z), \bar{\tau}(\xi, z), \bar{\sigma}(\xi, z)\}$ are the displacement and stress components; $[\Phi(\xi, z)]$ is a 4 × 4 matrix. The details can be found in Ai et al. [28]. The soil is assumed as a layered elastic mass with a fixed displacement boundary condition at the bottom surface. As two neighboring layers are bonded together, the stresses and displacements satisfy the continuity condition at the interface without load. An additional interface has to be considered at the horizontal plane the point load is imposed on, at which the displacement is also continuous. By repeating Eq. (5) and the above continuous conditions, one can get:

$$\{\bar{G}(\xi, H_n^-)\} = [q]\{\bar{G}(\xi, 0)\} - [s]\{\mathrm{p}\} \tag{6}$$

where

$[q] = [\Phi(\xi, \Delta H_n)][\Phi(\xi, \Delta H_{n-1})] \cdots [\Phi(\xi, \Delta H_1)]$;

$[s] = [\Phi(\xi, \Delta H_n)][\Phi(\xi, \Delta H_{n-1})] \cdots [\Phi(\xi, \Delta H_{m2})]$;

$\{\mathrm{p}\} = [0, 0, 0, F/2\pi]$, $F/2\pi$ is the surface density distribution of the concentrated force at the depth of h_{m1}. ΔH_{m2} is the vertical distance between the concentrated force and the top of the next lower layer. Substituting the free and fixed boundary conditions at the surface and bottom into Eq. (6) respectively, all unknown variables at the top and bottom is determined. The stress and displacement $\{\bar{G}(\xi, z)\}$ in the Hankel transform domain at any position can be calculated in terms of the transfer matrix technique and the determined boundary variables. Finally, stresses and displacements in each layer can be obtained by using the inverse Hankel transform of the solution $\{\bar{G}(\xi, z)\}$.

Zhang et al. [29] utilized the solution to establish an elastic continuum solution for a pipeline buried in multi-layered soils. They further conducted a parametric study to examine the effects of soil layers on pipeline behaviour due to tunnelling. Figure 3(a) illustrates the three-layered sandwich soil model assumed with a weak or strong interlayer where a pipeline is buried, explaining the geometric configuration used for the parametric study of the influence of soil layers on the behaviour of the pipeline. The elastic modulus of the upper and bottom soil layer is E_{s1} and that of the intermediate soil layer is E_{s2}. The pipeline is buried in the middle soil layer with thickness $h_{\mathrm{m}} = 2r_0 + 2ar_0$. Figure 3(b) shows the strong interlayer with E_{s1}/E_{s2} of 1/10 lowers the maximum moment bending of the pipeline as compared with the results for homogeneous soil with E_{s1}/E_{s2} as 1. On the contrary, the weak interlayer would increase the moments. The effect can be ignored with the layer thickness increasing.

Based on the non-uniform convergence pattern on the tunnel boundary and the multi-layered elastic solution, Zhang and Huang [10] and Zhang et al. [11] presented a

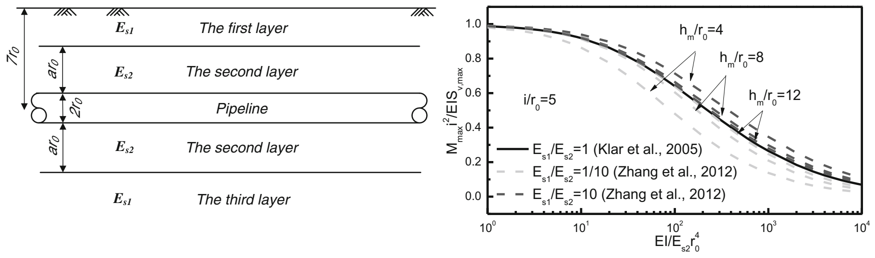

(a) (b)

Fig. 3. Schematic diagram of layered soil system and the pipeline: (a) Configuration of soil and pipeline; (b) Layered effect on maximum bending moment

displacement-controlled boundary element method (DCBFM) and DCBEM-FEM coupling method for response analysis of shield tunneling on adjacent existing pipelines in layered soils, respectively. Different from the two-staged method, the DCBEM-FEM considers the coupling effect of soil and pipeline movements, thereby providing the solutions with higher precision, but a complicated calculation process is inevitable.

2.4 Evaluation of a Jointed Pipeline in Layered Soils Subjected to Tunneling

In practical engineering, jointed pipelines are more common as compared with continuous pipelines. Therefore, Klar et al. [17] and Zhang et al. [29] presented elastic continuum solutions for jointed pipelines in nonhomogeneous and layered soil by introducing joint elements into the stiffness matrix [S] given in Eq. (2), respectively. Attewell et al. [15] established a bilinear model for the relationship between the joint rotation θ and the moment M. Klar et al. [17] defined $k_{jM} = M/\theta \ (N \cdot m/rad)$ as the joint elastic rotational stiffness. Typical values for k_{jM} of various joints can be found in Attewell et al. [15]. Also, Singhai [30] proposed an equation for calculating k_{jM} in terms of the joint characteristics.

It should be noted that, different from continuous pipelines, the response of jointed pipelines would be affected by the joint configuration relative to the tunnel center. As shown in Fig. 1, the closest distance of all joints to the tunnel center is termed as the eccentricity e. The value of the eccentricity ratio e/L (L is the length of pipe section) is in the range 0 to 0.5; where an e/L of 0 corresponds to “odd” and 0.5 corresponds to “even”. Klar et al. [17] and Zhang et al. [29] presented a series of normalized displacements $\frac{w}{S_{max}}$ and maximum joint rotation $\theta_{max} i/S_{max}$ varying with the relative pipe-soil bending stiffness $R = EI/E_S r_0 i^3$ and relative pipe-joint rotational stiffness $T = k_{jM} i/EI$, in which two symmetric configuration of the pipeline relative to the tunnel center (“odd” and “even”) were considered.

Figure 4(a) and (b) shows the displacements of the pipeline with the “odd” joint configuration and the corresponding design chart on the maximum joint varying with T. It is evident that, for the “odd” configuration, the maximum rotation occurs at the joint in the middle, and decreases with an increase in T. Figure 4(b) also shows the joint response of the pipeline buried in the three-layered sandwich soil model (see Fig. 3(a)). The similar finding with the continuous pipeline shown in Fig. 3(b) can be observed. More design charts on the different pipe section length L/i, T and R can be found in Klar et al. [17] and Zhang et al. [29].

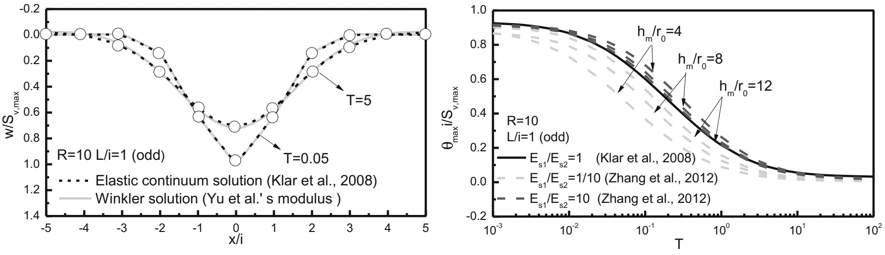

(a) (b)

Fig. 4. Comparison of normalized displacement and joint rotation between elastic continuum solution and Winkler solution: (a) Effect of relative rotation stiffness on displacement distribution; (b) Maximum joint rotations versus relative rotation stiffness

Analogous to continuous pipelines, the Winkler model can also be introduced to analyze the jointed response due to tunneling. A comparison between the elastic solution and the Winkler solution with Yu et al.'s modulus [13] is illustrated in Fig. 4(a), from which a good agreement can be found. To further validate the applicability of the Winkler model in jointed pipelines, it is also employed to predict the centrifuge tests conducted by Vorster [31]. Figure 5 reveals that the Winkler solution can provide reasonable predictions for the jointed pipelines with various volume loss ratios and joint configurations.

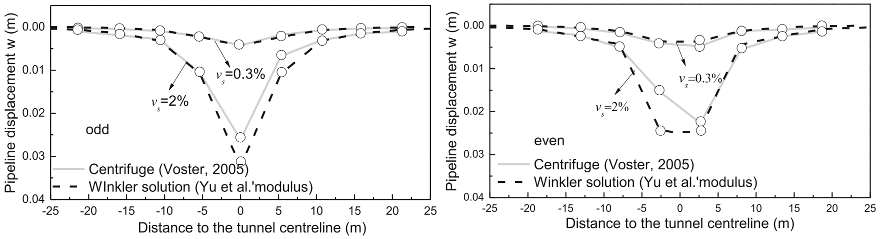

(a) (b)

Fig. 5. Displacement along the jointed pipeline: (a) Odd configuration; (b) Even configuration

Since the design charts above only considered two symmetric joint configurations, and L/i, T, R and e/L are independent variables affecting the design charts, a simpler design chart by relating the maximum joint moment M_{jmax} to the moment of the continuous pipelines with the same pipe-section bending stiffness is proposed. Figure 5(a) can be used to illustrate the establishment of the design chart, which shows the variation of the maximum joints moment M_{jmax} with the relative rotational stiffness T, in which M_{jmax} occur at the joint closest to the tunnel center. Based on this finding, a detailed parametric study is carried out to examine the effect of L/i, e/L, T, R and the shape of Gaussian curves on the position of M_{jmax}. The results reveal the finding above is true for a jointed pipeline with $L/i < 2$. Therefore, a modification factor MF is defined as follows:

$$MF = \frac{M_{jmax}}{M(x)} \tag{7}$$

where $M(x)$ is defined as the bending moment of a continuous pipeline, at a point whose horizontal distance to the tunnel center corresponds with that of M_{jmax} (see Fig. 6). Such a modification factor can partly consider the effect of the eccentricity on M_{jmax}, as $M(x)$ would vary with eccentricity.

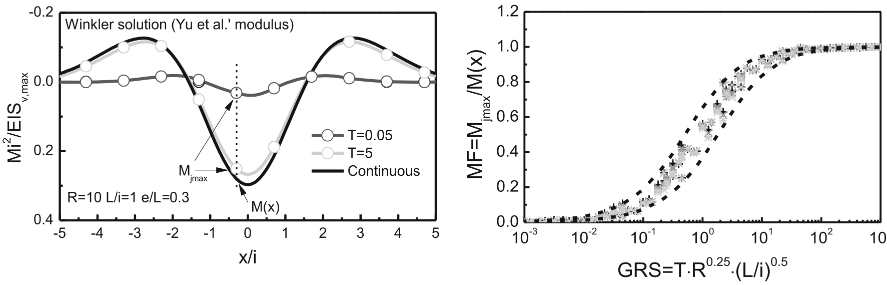

(a) (b)

Fig. 6. Normalized bending moments of jointed pipeline due to tunneling: (a) Effect of relative rotation stiffness on moment distribution; (b) Modification factor versus general relative stiffness

When all the modification factors MF calculated from the parametric study above are plotted against the general relative stiffness $GRS = T \cdot R^{0.25} \cdot (\mathrm{L}/i)^{0.5}$, all points fall into a narrow band. In practical engineering, once GRS is determined in terms of the parameters of the joint and pipe section, MF can be obtained from the upper break line in Fig. 6(b). Equation (4) can be used to calculate the moment $M(x)$ of a continuous pipeline at the position corresponding to the joint closet to the tunnel center, such that the maximum joint rotation can be preliminarily evaluated by $\theta_{max} = M_{jmax}/k_{jM} = MF \cdot M(x)/k_{jM}$.

3 Response of a Raft Foundation Subjected to Tunneling

3.1 Illustration of Problem

In Shanghai, the buildings built in earlier years was usually constructed to be supported on shallow foundations. Some are spread footings, and some are raft foundation.

When a tunnel plans to underpass a building with footings, a common protection strategy is to upgrade the foundation to a raft foundation to mitigate the settlement of the superstructure, in which the determination of the raft thickness is a major issue. In addition, for a building with a raft foundation, whether the raft has enough stiffness to resist the settlement due to tunneling is more concerned.

Therefore, risk assessment of existing building due to tunneling is important when new tunnels construct in urban environment. Burland and Worth [32] indicated that deflection ratio is the most critical in the risk assessment of potential building damage.

3.2 Introduction of Modification Factor Approach

A tunnel-foundation interaction model (see Fig. 7) was proposed by Potts and Addenbrooke [12] to investigate the difference of the deflection ratio between Greenfield and foundation deformations. By examining the shape of the Greenfield settlement trough, the concept of hogging and sagging deflection ratios (Fig. 7) was introduced as follows:

$$DR_{sag} = \frac{\Delta_{sag}}{L_{sag}} \quad DR_{hog} = \frac{\Delta_{hog}}{L_{hog}} \tag{8}$$

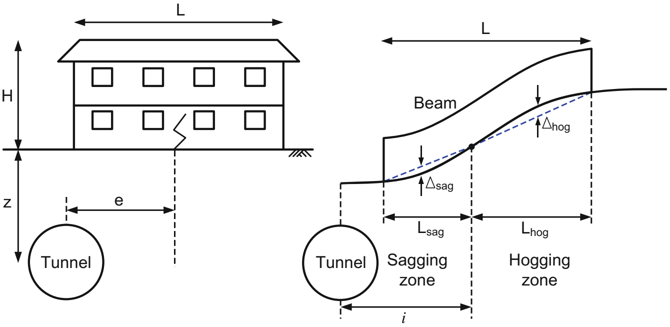

Fig. 7. Interaction diagram and definition of deflection ratios

where L_{sag} and L_{hog} were the lengths of the foundation in sagging and hogging respectively; Δ_{sag} and Δ_{hog} were the maximum differential settlements in the zones corresponding to L_{sag} and L_{hog} respectively. The building modification factors were defined as the ratio of the building deflection ratios to the green field conditions:

$$MF_{sag} = \frac{\Delta_{sag}/L_{sag}}{\Delta^{g}_{sag}/L^{g}_{sag}} \quad MF_{hog} = \frac{\Delta_{hog}/L_{hog}}{\Delta^{g}_{hog}/L^{g}_{hog}} \tag{9}$$

where the green field deflection ratios $\Delta^{g}_{sag}/L^{g}_{sag}$ and $\Delta^{g}_{hog}/L^{g}_{hog}$ were determined in terms of the building length and location in the green field settlement trough.

In their two-dimensional (2D) finite element (FE) study, a weightless elastic beam was employed to represent the building. By varying the building geometry and location in relation to the tunnel, a design chart of modification factors against building relative bending stiffness $EI/E_s(L/2)^4$ (EI is the building bending stiffness; E_s is the soil elastic modulus) was proposed. Later, 3D FE analyses were conducted by Franzius et al. [33] to extend the design chart to 3D. However, in these design charts, the eccentricity ratio e/L is an independent variable. Therefore, Goh and Mair [13] proposed a new relative bending stiffness as $EI/E_sL_{sag}^{g}{}^3$ or $EI/E_sL_{hog}^{g}{}^3$. Their 2D FE results demonstrated that such a definition could prompt the relationship between the modification factor and the relative bending stiffness to be fairly unique.

3.3 Continuous Elastic Modelling of a Raft Foundation Subjected to Tunneling

To study the effect of raft foundation dimension in the direction of the tunnel axis, a 3D elastic continuum solution is presented. The equation for the solution has the same form with that for pipelines (see Eq. (2)). The difference is that the plate elements is employed to represent a raft foundation, of which the bending stiffness is given by:

$$D_r = \frac{E}{12(1 - v^2)} \tag{10}$$

where v is the Poisson's ratio of plate. Different from the bending of a simple beam in 2D cases, the deformed plate would form a space surface. Along various directions, different deflection ratios can be obtained. Obviously, the maximum one of them represents the danger level of buildings; hence, it is defined as the principal deflection ratio (*PDR*). The 3D modification factors in sagging and hogging zones are defined as follows:

$$MF_{sag} = \frac{PDR_{sag}}{PDR_{sag}^{g}} \quad MF_{hog} = \frac{PDR_{hog}}{PDR_{hog}^{g}} \tag{11}$$

where PDR_{sag}^{G} and PDR_{hog}^{G} are calculated in the sagging and hogging zones corresponding to the building geometry and location using the Greenfield settlement trough. The 3D relative bending stiffness is proposed as $\rho_{sag} = D_r/E_sL_{sag}^{g}{}^3$ and $\rho_{hog} = D_r/E_sL_{hog}^{g}{}^3$ for the sagging and hogging zones respectively.

A series of parametric study is conducted to investigate the effect of the building location and the raft stiffness on the relationship between the modification factor and relative bending stiffness. Figure 8(a) illustrated the layout of a 3i-by-3i square raft foundation (it is close to the floor area of most single-family houses) and a tunnel, in which the lateral eccentricity e and rotational eccentricity θ are used to determine the building location relative to the tunnel.

Figure 8(b) illustrate the distribution of modification factors versus the relative bending stiffness when the lateral eccentricity e/i varies from vary from 0 to 3 and the rotational eccentricity θ varies from 0° to 45°. All data points fall into a narrow cluster.

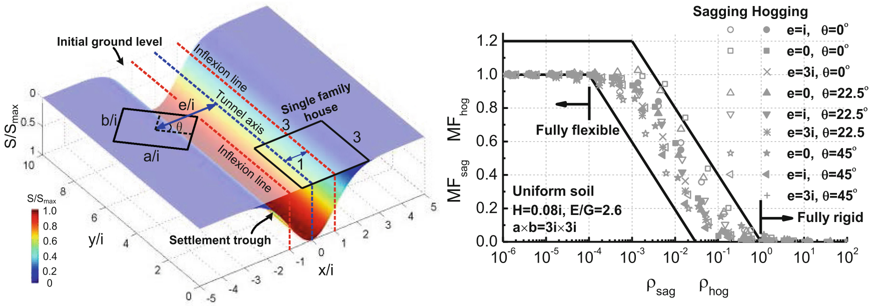

(a) (b)

Fig. 8. Establishment of design chart for 3D raft foundation: (a) Illustration of building location relative tunnel; (b) Modification factor versus relative bending stiffness

Analogous to the conclusion drawn from the jointed pipeline, the upper bound solid lines bounding the data points cluster can be used to determine the building maximum deflection ratios in sagging and hogging zones in terms of the greenfield condition.

4 Response of Pile Foundation Subjected to Tunneling

4.1 Illustration of Problem

In Shanghai, there remains a large number of high-rise buildings constructed three or four decades ago for residential use. To save engineering cost at that time, pile groups were designed with reinforcements for around one third of the pile length. It really becomes a challenge for maintenance of such old high-rise buildings when they are close to subway routes, since the lower plain concrete pile is obviously not an ideal structure to sustain passive loads. The illustration of the problem analyzed is shown in Fig. 9, where an existing pile group is situated adjacent to a tunnel construction. For the purpose of serviceability, the rational analysis of the pile foundation of a high-rise building under tunnel induced soil movements should consider the complete foundation system such as pile groups with or without cap or raft rather than only the individual piles. A Winkler analysis of a pile group and an elastic continuum analysis of a pile raft in layer soils is introduced below, which are verified by comparison with a two-stage boundary element method and a two-stage DCFEM method respectively.

4.2 Winkler Analysis of a Pile Group Subjected to Soil Movements

According to two stage methods, the tunnel-excavation induced free-field ground movements (both the vertical settlement and horizontal displacement) are applied as inputs for the analysis of a pile group nearby tunnel excavation. A pile group is analyzed following three phases: (1) behavior of a single pile, (2) pile-soil-pile interaction and (3) pile-group response to tunneling. In each phase, axial and lateral responses of the piles are analyzed separately [34].

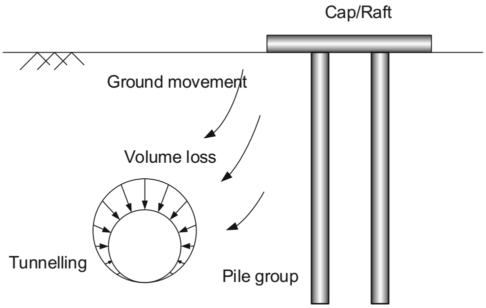

Fig. 9. Tunnel excavation induced soil movements on piles for high-rise buildings

Based on Winkler assumption of pile-soil interaction, the finite difference formulation for a single pile subjected to tunnel induced vertical and lateral free movements are given in matrix-vector form as:

$$\left[K_{pv}\right]\{w_v\} = [K_{sv}]\{S_v\} + \{F_v\} \tag{12}$$

$$\left[K_{ph}\right]\{w_h\} = [K_{sh}]\{S_h\} + \{F_h\} \tag{13}$$

in which, $\{w_v\}$ and $\{w_h\}$ are the vertical and horizontal displacement vector of the individual pile due to tunneling. $\{S_v\}$ and $\{S_h\}$ are the input of free-field vertical and lateral soil movement at the pile location due to excavation. $\left[K_{pv}\right]$ and $\left[K_{ph}\right]$ are the vertical and horizontal stiffness matrix of pile. $[K_{sv}]$ and $[K_{sh}]$ are the vertical and horizontal stiffness matrix of soil, related to the spring stiffness coefficient for Winkler foundation. $\{F_v\}$ and $\{F_h\}$ correspond to the boundary conditions of piles.

It is evident that a single pile doesn't follow exactly the free-field movements generated by tunneling at the pile location. Also the soil movement will reduce due to the shielding effect of pile. For two piles close to tunneling, if it is assumed that the tunnel excavation induced soil movement is only applied to pile 1, another pile 2 will also exhibit additional opposite displacement due to pile-soil-pile interaction, in which pile 2 can be treated as a new passive pile subjected to free soil movement by pile 1-soil interaction. If we assume the free shielding soil movement by pile 1 applied at the location of pile 2 as $\{\Delta \mathrm{S}_{v21}\}$ and $\{\Delta S_{h21}\}$, which can be obtained by theory of elasticity with a plain-strain model for the vertical response of the pile and the Mindlin's solution for the lateral response of the pile, the governing equation of pile 2 due to pile 1-soil-pile 2 interaction in the case of tunneling can be expressed as

$$\left[K_{pv}\right]\{w_{v21}\} = \psi_{21}[K_{sv}]\{\Delta S_{v21}\} \tag{14}$$

$$\left[K_{ph}\right]\{w_{h21}\} = \xi_{21}[K_{sh}]\{\Delta S_{h21}\} \tag{15}$$

where $\{w_{v21}\}$ and $\{w_{h21}\}$ are the additional displacement of pile due to pile-soil-pile interaction, ψ_{21} and ξ_{21} are displacement influence factor as functions of pile space s.

For a pile group with n identical piles, the total displacement of a single pile i could be obtained by superposition as the sum of a displacement due to the free-field soil movement caused by tunneling and a displacement due to shielding soil displacement by pile-soil-pile interaction (shielding effect), which are given as

$$\{w_{vi}\} = \left[K_{pv}\right]^{-1}([K_{sv}]\{S_{vi}\} + \{F_{vi}\}) + \sum\nolimits_{j=1,j\neq i}^{n} \left[K_{pv}\right]^{-1}[K_{sv}][K_{sv}][\psi_{ij}]\left\{\Delta S_{vij}\right\} \quad (16)$$

$$\{w_{hi}\} = \left[K_{ph}\right]^{-1}([K_{sh}]\{S_{hi}\} + \{F_{hi}\}) + \sum\nolimits_{j=1,j\neq i}^{n} \left[K_{ph}\right]^{-1}[K_{sh}][K_{sv}][\xi_{ij}]\left\{\Delta S_{hij}\right\} \quad (17)$$

Loganathan et al. [20] developed a displacement controlled two stage method to analyzed the elastic response of a 2 × 2 capped-pile group near a tunneling with ground loss ratio as 1%, in which a 3D boundary element program GEPAN was used to modeling pile groups–soil interaction. Figure 10 give calculations of "front" pile and "rear" pile by Winkler analysis and GEPAN, also the results for single pile without shielding effects. There is a general satisfactory agreement of the behavior of piles calculated by the two methods, although a slightly underestimation of axial force by the Winkler analysis and a variation of bending moments in pile-head due to different boundary condition. The maximum axial force estimated for a single pile is about 20% higher than "front" pile and about 50% for "rear" pile. Contrastingly, the difference of bending moment for the pile in pile group and the single pile is not obvious. This result agrees with the statement of Loganathan et al. [20] that the piles in a group can be treated as isolated single piles when the lateral behavior is investigated for piles nearby tunnel.

4.3 Elastic Continuum Analysis of a Pile Raft in Layer Soils Subjected to Multi-directional Active Loads and Soil Movements

To investigate the behavior of a pile raft in layered soils, the elastic displacement of a point in layered soils due to a point load inside the soil stratum considering the continuity condition at the interface of soil layers should be obtained first as a basic solution for the analysis of pile-soil interaction and pile-soil-pile interaction, which is introduced in Sect. 2.3. Assume a single pile with diameter, elastic modulus, moment of inertia as d, E_p, I_p, the response of a single pile in layered soils due to tunneling excavation can be expressed in matrix form as

$$\left([I] - \frac{E_p d^2}{4\delta^2}\left[I_{pv}\right][I_{sv}]\right)\{p_v\} = \{Y_v\} + \frac{dE_p}{4\delta^4}\left[I_{pv}\right]\{S_v\} \quad (18)$$

$$\left([I] + \frac{E_p I_p}{\delta^4}\left[I_{ph}\right][I_{sh}]\right)\{p_h\} = \{Y_h\} - \frac{E_p I_p}{\delta^4}\left[I_{ph}\right]\{S_h\} \quad (19)$$

where d is the diameter of the pile; E_p is the elastic modulus of the pile; I_p is the moment of inertia of the pile; $\{p_v\}$ and $\{p_h\}$ are the vertical and horizontal nodal soil resistance force vector of the pile; $[I]$ is unit matrix; $\left[I_{pv}\right]$ and $\left[I_{ph}\right]$ are the vertical and horizontal pile flexibility matrixes; $[I_{sv}]$ and $[I_{sh}]$ are the vertical and horizontal soil flexibility matrixs obtained by transfer matrix method based on the basic solution for a

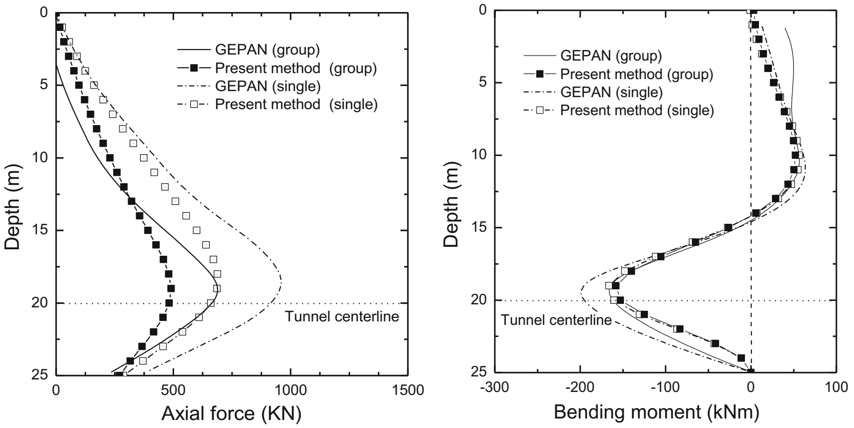

(a) axial force for front pile (b) bending moment for front pile

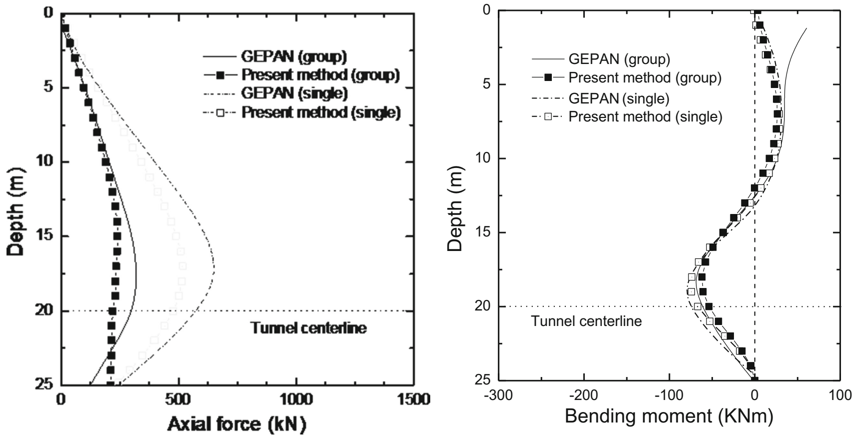

(c) axial force for rear pile (d) bending moment for rear pile

Fig. 10. Computed response of individual pile in 2 × 2 pile group

layer soil system; $\{S_v\}$ and $\{S_h\}$ are the vectors of the vertical and horizontal free-field soil deformation induced by tunneling.

For the pile-soil-pile analysis, as shown in Fig. 11, the pile deformation subjected to a load in a two-pile system would be smaller than that in a single pile system. In other words, pile 2 in the two-pile system would have a deformation even there is no load acting on the pile. The vertical and horizontal pile1-soil-pile 2 interaction can be solved by Eqs. (20) and (21) as below:

$$\begin{Bmatrix} [I^1] - a_1\left[I^1_{pv}\right]\left[I^{11}_{sv}\right] & -a_1\left[I^1_{pv}\right]\left[I^{12}_{sv}\right] \\ -a_2\left[I^2_{pv}\right]\left[I^{21}_{sv}\right] & [I^2] - a_2\left[I^2_{pv}\right]\left[I^{22}_{sv}\right] \end{Bmatrix} \begin{Bmatrix} p^1_v \\ p^2_v \end{Bmatrix} = \begin{Bmatrix} \left[Y^1_v\right] + a_1\left[I^1_{pv}\right]\left[S^1_v\right] \\ \left[Y^2_v\right] + a_2\left[I^2_{pv}\right]\left[S^2_v\right] \end{Bmatrix} \quad (20)$$

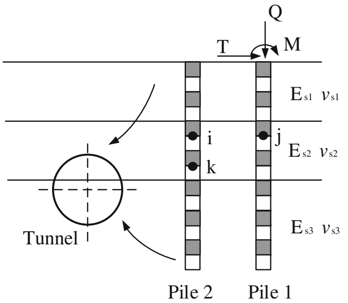

Fig. 11. Two pile-tunnel systems

$$\begin{Bmatrix} [I^1]-b_1\left[I^1_{ph}\right]\left[I^{11}_{sh}\right] & -b_1\left[I^1_{ph}\right]\left[I^{12}_{sh}\right] \\ -b_2\left[I^2_{ph}\right]\left[I^{21}_{sh}\right] & [I^2]-b_2\left[I^2_{ph}\right]\left[I^{22}_{sh}\right] \end{Bmatrix} \begin{Bmatrix} p^1_h \\ p^2_h \end{Bmatrix} = \begin{Bmatrix} \left[Y^1_h\right]+b_1\left[I^1_{ph}\right]\left[S^1_h\right] \\ \left[Y^2_h\right]+b_2\left[I^2_{ph}\right]\left[S^2_h\right] \end{Bmatrix} \tag{21}$$

where the superscripts 1 and 2 denote pile 1 and pile 2, $\left[I^{12}_{sv}\right]$ and $\left[I^{12}_{sh}\right]$ are the vertical and horizontal interaction matrix between pile 1 and pile 2. Similarly, the pile-soil interactions and the soil-soil interactions can also be obtained [35, 36].

For the analysis of a pile raft foundation subjected to tunnel excavation, the equilibrium condition and compatibility condition between the raft and the foundation can be summarized as follows: (1) the deformations of pile heads or of the soil surface elements are the same as the deformations of the corresponding elements of the raft and (2) the summations of the internal forces between the elements of the raft and the elements of the foundation, including piles and soil surface elements, are equal to the external loads acting on the raft, which is shown as:

$$\begin{Bmatrix} \mathbf{E}_{(m\times 1)} \\ \mathbf{F}_{(n\times 1)} \\ \mathbf{K}_{(3\times 1)} \end{Bmatrix} = \begin{bmatrix} \mathbf{A}_{(m\times m)} & \mathbf{B}_{(m\times n)} & -\mathbf{J}^T_{(m\times 1)} \\ \mathbf{C}_{(n\times m)} & \mathbf{D}_{(n\times n)} & \mathbf{R}_{(m\times 1)} \\ \mathbf{J}_{(1\times m)} & \mathbf{I}_{(1\times m)} & 0 \end{bmatrix} \begin{Bmatrix} \mathbf{P}_{(m\times 1)} \\ \mathbf{N}_{(n\times 1)} \\ \mathbf{EE}_{(3\times 1)} \end{Bmatrix} \tag{22}$$

where $\mathbf{E}_i$ and $\mathbf{F}_i$ are the deformation matrices on the pile element and the soil element induced by tunneling in pile group system, **K** is the matrix of the load acting on the raft, $\mathbf{P}_i$ and $\mathbf{N}_i$ are the matrices of the internal forces between the pile and the raft and those between the soil and the raft**,** **EE** is the matrix deformation on the top of pile 1 induced by the internal force**,** $\mathbf{A}_{ij}$, $\mathbf{B}_{ij}$, $\mathbf{C}_{ij}$, and $\mathbf{D}_{ij}$ are the pile-pile, pile-soil surface, soil surface-pile, and soil surface-soil surface interaction matrices, respectively. They can be obtained by analysis of pile-pile interactions, pile-soil interactions, soil-soil interactions based on layered elastic theory considering all the interactions between the nodes along the piles. Other matrices are the factors.

Both the finite-element analysis and the elastic continuum analysis were carried out to calculate the responses of a 2 × 2 pile group-raft foundation in the soil stratum with three layers and subjected to both multidirectional active and passive loads. For the DCFEM analysis, the active load applied on the pile-raft foundation was controlled by force magnitude, and the tunnel excavation was modelled by displacement controlled method with an exact ground-loss ratio. The comparisons of results from the DCFEM and the continuum analyses are shown in Fig. 12. It is encouraging that the two methods gives consistent results in the behavior of individual piles in the group, such as vertical and horizontal deformation along the pile length for front and rear pile, axial force and bending moment profile of the front and rear pile, which verified the suitability of the proposed method to calculate the coupled responses of a pile-raft foundation subjected to both multi-directional active and passive loads in layered soil.

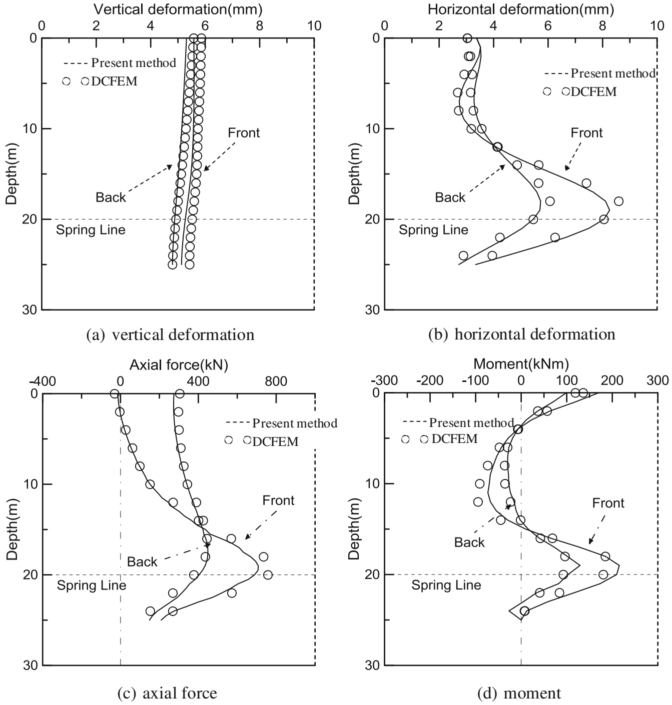

(a) vertical deformation

(b) horizontal deformation

(c) axial force

(d) moment

Fig. 12. Comparison with DCFEM

5 Conclusions

This paper has covered the problem of the effects of tunneling excavation on nearby infrastructures, for example buried pipelines, raft foundations and pile groups for high-rise buildings. The objective has been to review the ability of the displacement controlled two stage methods in analyzing the structures subjected to tunnel excavation-induced free soil movements.

Over the last decades, the underground excavation has moved from “strength design” to “displacement control”, with special attentions for nearby structures. This shift comes from the limited underground space in urban cities and the congested buildings with different foundations and underground structures. The advantage of the two stage methods lies in the emphasis on the analysis on the interaction of new tunnel on existing buildings and services, not the detailed construction measures for the tunnel excavation, which is able to give a direct and quantitative standard for practical engineers in the initial stage of tunnel design.

Design and construction for tunnel in Shanghai is extremely a challenge considering the sustainable development of underground space exploitation in these years. The future challenge includes simulating the notorious mechanical behavior of soft clay, the potential ageing of the buried structures saturated in the underground waters and the complex tunnel routes in large transportation exchange hubs.

Acknowledgements. The authors wish to express their gratitude to the National Key R&D Program of China (Grant No. 2016YFC0800200), the National Natural Science Foundation of China (Grant No. 51738010) and Singapore Housing and Development research grant on tunnel-foundation interaction (Grant No. R-302-000-086-490) for the financial support.

References

1. Mroueh, H., Shahrour, I.: Three-dimensional finite element analysis of the interaction between tunneling and pile foundations. Int. J. Numer. Anal. Meth. Geomech. **26**, 217–230 (2002)
2. Gordon, T.K., Ng, C.W.W.: Effects of advancing open face tunneling on an existing loaded pile. J. Geotech. Geoenviron. Eng. **131**(2), 193–201 (2005)
3. Zhang, Z., Huang, M.: Geotechnical influence on existing subway tunnels induced by multiline tunneling in Shanghai soft soil. Comput. Geotech. **56**, 121–132 (2014)
4. Cheng, C.Y., Dasari, G.R., Chow, Y.K., Leung, C.F.: Finite element analysis of tunnel-soil-pile interaction using displacement control model. Tunn. Undergr. Space Technol. **22**(4), 450–466 (2007)
5. Yang, C., Huang, M., Liu, M.: Three-dimensional numerical analysis of effect of tunnel construction on adjacent pile foundation. Chin. J. Rock Mech. Eng. **26**(s1), 2601–2607 (2007). (in Chinese)
6. Sagaseta, C.: Analysis of undrained soil deformation due to ground loss. Geotechnique **37** (3), 301–320 (1987)
7. Hagiwara, T., Grant, R.J., Calvello, M., Taylor, R.N.: The effect of overlying strata on the distribution of ground movements induced by tunneling in clay. Soils Found. **39**(3), 63–73 (1999)
8. Deane, A.P., Bassett, R.H.: The Heathrow express trial tunnel. Proc. Inst. Civil Eng. Geotech. Eng. **113**(3), 144–156 (1995)
9. Zhang, Z., Huang, M., Zhang, M.: Theoretical prediction of ground movements induced by tunnelling in multi-layered soils. Tunn. Undergr. Space Technol. **26**(2), 345–355 (2011)
10. Zhang, Z., Huang, M.: Boundary element model for analysis of the mechanical behavior of existing pipelines subjected to tunneling-induced deformations. Comput. Geotech. **46**, 93–103 (2012)
11. Zhang, Z., Huang, M., Zhang, M.: Deformation analysis of tunnel excavation below existing pipelines in multi-layered soils based on displacement controlled coupling numerical method. Int. J. Numer. Anal. Meth. Geomech. **36**(11), 1440–1460 (2012)

12. Potts, D.M., Addenbrooke, T.I.: A structures influence on tunneling induced ground movements. Proc. Inst. Civil Eng. Geotech. Eng. **125**(2), 109–125 (1997)
13. Goh, K.H., Mair, R.J.: Building damage assessment for deep excavations in singapore and the influence of building stiffness. Geotech. Eng. J. SEAGS AGSSEA **42**(3), 1–12 (2011)
14. Stewart, D.P., Jewell, R.J., Randolph, M.F.: Design of piled bridge abutments on soft clay for loading from lateral soil movements. Geotechnique **44**(2), 277–296 (1994)
15. Attewell, P.B., Yeates, J., Selby, A.R.: Soil Movements Induced by Tunneling and Their Effects on Pipelines and Structures. Blackie & Son Ltd, London (1986)
16. Klar, A., Voster, T.E.B., Soga, K., Mair, R.J.: Soil–pipe interaction due to tunneling: comparison between Winkler and elastic continuum solutions. Géotechnique **55**(6), 461–466 (2005)
17. Klar, A., Marshall, A.M., Soga, K., Mair, R.J.: Tunneling effects on jointed pipelines. Can. Geotech. J. **45**(1), 131–139 (2008)
18. Marshall, A.M., Elkayam, I., Klar, A.: Centrifuge and discrete element modelling of tunnelling effects on pipelines. In: 7th International Conference on Physical Modelling in Geotechnics, pp. 633–637. Taylor & Francis Group, London (2010)
19. Chen, L.T., Poulos, H.G., Loganathan, N.: Pile responses caused by tunneling. J. Geotech. Geoenviron. Eng. **125**(3), 207–215 (1999)
20. Loganathan, N., Poulos, H.G., Xu, K.J.: Ground and pile-group responses due to tunnelling. Soils Found. **41**(1), 57–67 (2001)
21. Peck, R.B.: Deep excavations and tunneling in soft ground. In: Proceedings of the 7th International Conference on Soil Mechanics and Foundation Engineering, Mexico, pp. 225–290 (1969)
22. Loganathan, N., Poulos, H.G.: Analytical prediction for tunneling-induced ground movements in clays. J. Geotech. Geoenviron. Eng. **124**(9), 846–856 (1998)
23. Poulos, H.G., Davis, E.H.: Pile Foundation Analysis and Design. John Wiley & Sons, New York (1980)
24. Mindlin, R.D.: Force at a point in the interior of a semi-infinite solid. Physics **7**(5), 195–202 (1936)
25. Vesic, A.B.: Bending of beams resting on isotropic elastic solids. J. Eng. Mech. Div. **87**, 35–53 (1961)
26. Yu, J., Zhang, C.R., Huang, M.S.: Soil–pipe interaction due to tunnelling: assessment of Winkler modulus for underground pipelines. Comput. Geotech. **50**, 17–28 (2013)
27. Burmister, D.M.: The general theory of stresses and displacements in layered soil systems (I, II, III). J. Appl. Phys. **6**(2), 89–96; **6**(3), 126–127; **6**(5), 296–302 (1945)
28. Ai, Z.Y., Yue, Z.Q., Tham, L.G., Yang, M.: Extended Sneddon and Muki solutions for multilayered elastic materials. Int. J. Eng. Sci. **40**, 1453–1483 (2002)
29. Zhang, C., Yu, J., Huang, M.S.: Effects of tunneling on existing pipelines in layered soils. Comput. Geotech. **43**(2), 12–25 (2012)
30. Singhai, A.C.: Behavior of jointed ductile iron pipelines. J. Transp. Eng. **110**(2), 235–250 (1984)
31. Vorster, T.E.B.: The effect of tunneling on buried pipes. Ph.d. thesis. University of Cambridge, UK (2005)
32. Burland, J.B., Wroth, C.P.: Settlement of buildings and associated damage. In: Conference on Settlement of Structures, pp. 611–654. Pentch Press, London (1974)
33. Franzius, J.N., Potts, D.M., Burland, J.B.: The response of surface structures to tunnel construction. Proc. Inst. Civil Eng. Geotech. Eng. **159**(1), 3–17 (2006)

34. Huang, M., Zhang, C., Li, Z.: A simplified analysis method for the influence of tunneling on grouped piles. Tunn. Undergr. Space Technol. **24**(4), 410–422 (2009)
35. Huang, M., Mu, L.: Vertical response of pile raft foundations subjected to tunneling-induced ground movements in layered soil. Int. J. Numer. Anal. Meth. Geomech. **36**(8), 977–1001 (2012)
36. Mu, L., Huang, M., Finno, R.J.: Tunnelling effects on lateral behavior of pile rafts in layered soil. Tunn. Undergr. Space Technol. **28**(28), 192–201 (2012)

Tunnelling-Induced Ground Response

Simulating Synchronous Grouting in Shield Tunnels with the Consideration of Evolution of Grouting Pressure

Yafei Qiao[1,2], Tianchi Zhao[1,2], and Wenqi Ding[1,2](✉)

[1] Department of Geotechnical Engineering, College of Civil Engineering, Tongji University, Shanghai, China
`dingwq@tongji.edu.cn`
[2] Key Laboratory of Geotechnical and Underground Engineering of the Ministry of Education, Tongji University, Shanghai, China

Abstract. Synchronous grouting is one key procedure to backfill the construction gap and control the ground subsidence. The grouting pressure and grout properties are key construction factors that dominate the consequence of synchronous grouting. To investigate the effect of these factors, a novel framework to simulate the process of synchronous grouting is proposed in this paper. The framework is formulated based on finite element theory and incorporates new developments, including (i) a detail evolution law of grouting pressure and its distribution in the cross section and (ii) an improved definition of the hardening law of grouts. The performance of the proposed framework is illustrated via a hypothetical simulation test. Both the upheaval at the initial synchronous grouting and the followed settlement could be clearly described.

Keywords: Simulation framework · Synchronous grouting · Deformation Hardening · Grouting pressure

1 Introduction

Lots of tunnels have been built by shield machines, especially in current days. This is because that the shield tunnel has a good ability to control the construction disturbance and can be applied to different geology conditions. Synchronous grouting is the one key procedure of shield tunneling to achieve these advantages. Therefore, many field observations and laboratory tests have been performed to investigate the process of synchronous grouting and its effects on adjacent soils and linings [1–3].

The grouting pressure is widely observed in the field to characterize the process of synchronous grouting and the evolution of grout with time [e.g. 1, 3]. The injection program during advancement dominates the grouting pressure distribution while the buoyancy forces and the bending moments of linings may influence the gradient of grouting pressure distribution [1]. The grouting pressure starts to increase after the tail and reaches its maximum value after a certain time. Then it decreases with the hardening of grout and finally stabilizes at a constant value. Many researchers have also proposed analytical solutions of the grouting pressure distribution in the cross section

© Springer Nature Singapore Pte Ltd. 2018
D. Zhang and X. Huang (Eds.): GSIC 2018, *Proceedings of GeoShanghai 2018 International Conference: Tunnelling and Underground Construction*, pp. 23–31, 2018.
https://doi.org/10.1007/978-981-13-0017-2_2

[e.g. 4]. In these formulations, the grout is assumed to be Newton or Bingham fluid and interactions between the grout and soil are neglected. Although with these simplifications, good agreements with field observations can be achieved by parameters sensitivity analysis.

Material and mechanical properties of grout affect its hardening process, its mass distribution and the final filling rate of construction gaps. Firstly, the grout should have good mobility to achieve the full filling of construction gaps. Secondly, the final Young's modulus of grout should be big enough to support the surrounding soil and control the surface settlement. In addition, the volume shrinkage of grout solidification should be limited. Finally, it should have good stability and low permeability.

Many simulation models have been proposed to have a general description of synchronous grouting and its effects on surface settlements. The empirical framework, such as the widely used Peck's formula [5], normally relates the settlement to the ground loss, which neglects all details of synchronous grouting. Assuming that soil mass is homogeneous and isotropic, the analytical framework adopts the cylindrical cavity expansion theory to simulate the synchronous grouting [e.g. 6]. The time effect of grouting pressure, grout properties and soil deformation are not considered. The FEM simulation framework was then proposed to overcome the above shortcomings. The solidification process is described by the increase of Young's modulus and the decrease of Poisson's ratio [e.g. 7]. The grouting pressure effect is neglected or simplified. Based on the author's knowledge, the evolution and distribution of grouting pressure was never considered in the literature.

In summary, the current simulation frameworks neglect some processes to simplify the simulation, resulting in a rough description of synchronous grouting and its effects. These frameworks worked well in past years while they may have limitations in analyzing current practical engineering. This is because that the high occupancy of underground space and the complex surface buildings require an extreme control of shield tunneling disturbance. As a consequence, an advanced detailed simulation of synchronous grouting is necessary to predict the tunneling induced settlement and optimize the construction factors.

Therefore, the aim of this paper is to propose an advanced simulation framework of synchronous grouting in shield tunnels that considers both the evolution of grouting pressure as well as the hardening process of grout. First, the key processes of synchronous grouting are analyzed in detail in Sect. 2 and the problems related to the simulation are identified. Second, the main assumptions and concepts to solve the problems are presented followed by a schematic summary of the proposed simulation framework. Finally, a hypothetical simulation test is carried out to illustrate the performance of the new proposed framework.

2 Problem Identification

2.1 Process of Synchronous Grouting

Two different ways of synchronous grouting have been used in shield tunnels. One is grouting through the injection pipes after the tail and the other is grouting through the injection holes in linings. With the development of grout materials, the first injection method is widely adopted nowadays. Therefore, this paper only focuses on the synchronous grouting through the injection pipes after the tail.

Figure 1 schematically illustrates the process of synchronous grouting and its distribution in the cross section and longitudinal section. At the beginning of grouting, the grout stays in the liquid condition and it flows from injection holes to fill the construction gaps. More grouts move downwards because of the weight effect (Fig. 1a). In addition, grouts also move in the longitudinal direction under the gradient of grouting pressure. After a certain time, the grout would fulfill the construction gaps.

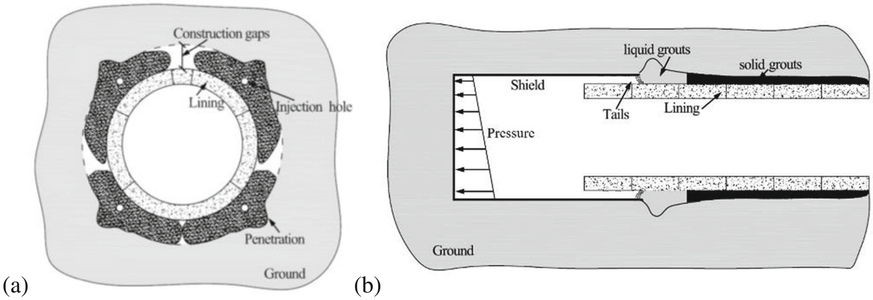

Fig. 1. Schematic illustration of synchronous grouting process: (a) cross section and (b) longitudinal section.

Owing to the high pressure at injection holes, the grout would press the adjacent soil and may penetrate into soils (Fig. 1). Moreover, this initial high pressure would result in the uplift of above soils. On the other hand, the grouting pressure at the bottom is higher than the grouting pressure at the crown, causing a float-up of the whole tunnel. The grouting pressure decreases with time, resulting in the deformation of adjacent soils.

As time goes, the grout starts to solidify, resulting in the increase of Young's modulus and the volume shrinkage. This would lead to the further deformation of soils above the tunnel (Fig. 1b). Finally, the grout becomes to be the solid condition and transfers the earth and water pressure to linings.

Considering the shrinkage of grout during its solidification and the leakage during the grouting process, the injection volume of grout is normally bigger than the volume of construction gaps. The injection ratio is in the range of 1.2 to 1.5 in soft soils.

2.2 Problem Analyzed

According to the presentation in Sect. 2.1, it is clear that both the grouting pressure and the material properties of grout dominate the process of synchronous grouting and its effects on adjacent soils. The grouting pressure is related to the injection pressure at injection pipes, the injection ratio, the mechanical and flow properties of adjacent soils, the hardening process of grout and others. The key grout properties affecting the deformation induced by tunneling are Young's modulus, Poisson's ratio and volume shrinkage ratio.

Therefore, to have a detailed simulation of synchronous grouting and its effect, the following problems have to be solved.

(1) The evolution of grouting pressure with time, in other words, the longitudinal distribution of grouting pressure along the tunnel axis;
(2) The distribution of grouting pressure in cross section;
(3) The hardening law of grout;

3 Simulation Framework

3.1 Evolution and Distribution of Grouting Pressure

In order to describe the evolution and distribution of grouting pressure during the tunneling process, the field observed data [1] was analyzed and some new formulas were proposed.

Sophia tunnel is a circle tunnel with a diameter of 9.5 m, which was built in Betuwe [1]. Many sensors were implemented during the construction and the observed grouting pressure at one section was illustrated in Fig. 2a. When the tail is passing, the observed grouting pressure increases owing to the compaction of shield tails. This value is not exactly the grouting pressure. After the passing of tails, the grouting pressure increases quickly because of the injection of fluid grouts. Then it starts to decrease after reaching its maximum value. With the advancement of shield, the observed grouting pressure shows a fluctuation. As the distance between the observed points and the injection pipes increases, this fluctuation fades (Fig. 2a). Finally, this grouting pressure would equal the local earth and water pressure. Neglecting this fluctuation effect, a function (Eq. 1) was proposed to describe the evolution of grouting pressure and its validation is illustrated in Fig. 2b. t_1 is the time when the grouting pressure reaches its maximum value.

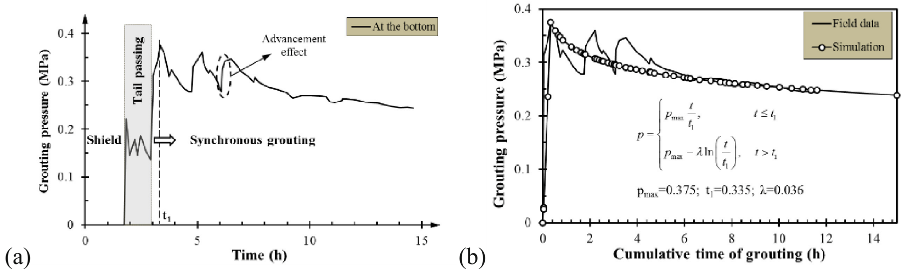

Fig. 2. The evolution of grouting pressure: (a) observed values and (b) simulation results.

$$p = \begin{cases} p_{\max}\frac{t}{t_1}, & t \le t_1 \\ p_{\max} - \lambda \ln\left(\frac{t}{t_1}\right), & t > t_1 \end{cases} \tag{1}$$

In addition, the grouting pressure is not evenly distributed in the cross section while it increases with the depth (Fig. 3). This is owing to the weight effect of grout. Therefore, the weight density of grout γ is assumed to be the increase slope of grouting pressure. Equation 2 is then adopted to describe the grouting pressure distribution in the cross section and its validation is shown in Fig. 3.

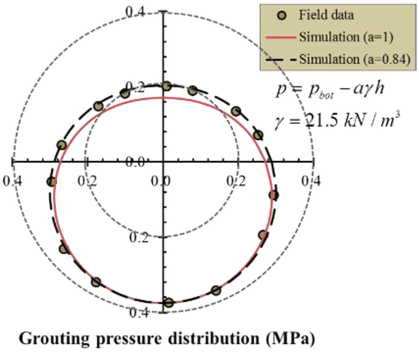

Fig. 3. The distribution of grouting pressure in the cross section

$$p = p_{bot} - a\gamma h \tag{2}$$

where p_{bot} is the grouting pressure at the bottom, and h is the vertical distance to the bottom. a is a fitting parameter that used to consider the solidification effect of grout. Normally a changes with time. However, this trend is not considered in this work to simplify the simulation.

3.2 Hardening Law of Grout

The injected grout solidifies with time, resulting in the increase of Young's modulus, the decrease of Poisson's ratio and permeability. This phenomenon has to be considered in the simulation. The data reported in [7] was analyzed and logarithm functions (Eq. 3) were proposed to back-fit these data (Fig. 4).

$$E = m\ \ln(t + 0.1) + n, \quad v = k\ \ln(t + 0.1) + l \tag{3}$$

3.3 Simulation Process

The simulation of tunneling process is performed in a step-by-step procedure. The advancement is simulated by deactivation of soil elements and activation of shield and

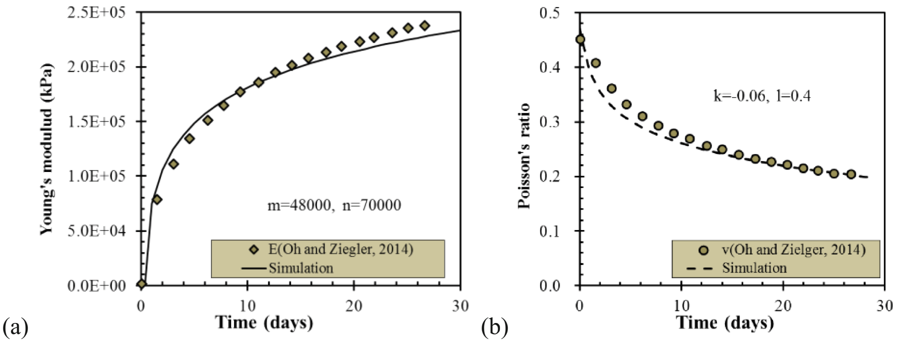

Fig. 4. The evolution of Young's modulus and Poisson's ratio of grouts.

lining elements. Then the new grout elements is activated with the application of grouting pressure that are described by Eqs. 1 and 2. The material properties of grout element also evolves with time as described by Eq. 3. The next advancement is simulated through the repeat of the steps above.

4 Performance of the Framework

4.1 FEM Model and Parameters

A hypothetical FEM model is formulated based on one practical metro project in Shanghai [8] and it is then used to investigate the performance of the proposed simulation framework of synchronous grouting presented in Sect. 3.

The model has a length of 100 m, a width of 150 m and a height of 60 m (Fig. 5). The diameter of tunnel is 6.3 m and the cover depth is 21 m. The lining has a thickness of 0.35 m and a width of 1.2 m. The thickness of grout layer is 35 mm and the maximum grouting pressure at the bottom is 0.4 MPa that evolves as described by Eqs. 1 and 2. The pressure at the excavation face is calculated by $k_0(\gamma_s z + p_s)$ (k_0 is the coefficient of earth pressure at rest; γ_s is weight density of soils; z is the depth and p_s is the overload at the surface).

The shield is modelled as shell elements, while soils, linings and grouts are all modelled as solid elements. The mechanical behavior of soils is described by HSS model and their core parameters are summarized in Table 1. The shield and linings are assumed to behave elastically. The Young's modulus of lining is 3.15×10^7 kN/m^2 while the Poisson's ratio is 0.2. The grouts have the behavior as shown in Fig. 4.

The full fixity is applied to the model base and two side boundaries, while roller supports for the two vertical boundaries at each end of the tunnel. Only the mechanical behavior is considered in this simulation. The step-by-step procedure presented in Sect. 3.3 is used to simulate the shield tunnel advancement.

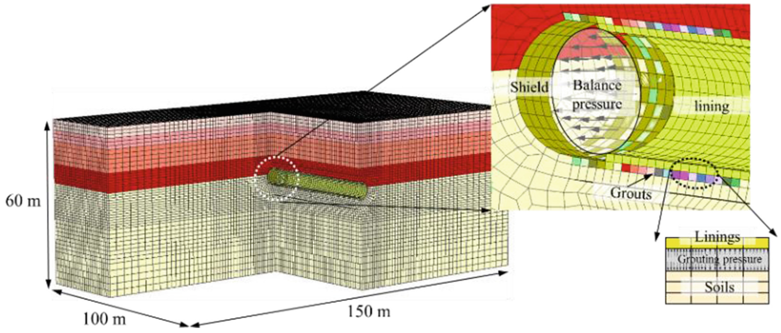

Fig. 5. The FEM model and simulation details.

Table 1. Mechanical parameters of soils used in HSS model (after [9]).

Layer	Fill	Clay-2	Silty clay	Soft clay	Clay-5
Thickness (m)	3.8	4.0	8.3	7	36.9
G_0 (MPa)	46.8	45	37.4	28.6	33.6
E_{50} (MPa)	4.5	4.7	3.0	3.9	6.4
E_{oed} (MPa)	3.3	3.7	2.5	3.6	5.9
E_{ur} (MPa)	22.5	38.8	33.9	36.6	42.4
$\gamma0.7$	2.5	2.49	2.42	2.53	2.69
Cohesion (kPa)	10	10.3	8.1	4.9	16.9
Friction angle (°)	15	29	34	27.3	34

4.2 Simulation Results and Discussions

The simulated settlements after the excavation of 40 rings are illustrated in Fig. 6. The maximum settlement at the surface is about 4.5 mm, occurring about 20 rings (24 m) after the shield tail. This is because of the solidification of grouts and the dissipation of grouting pressure. This simulated value is a little bit smaller than the observed field data, 6–10 mm [8], which is owing to the neglect of the building above the tunnel.

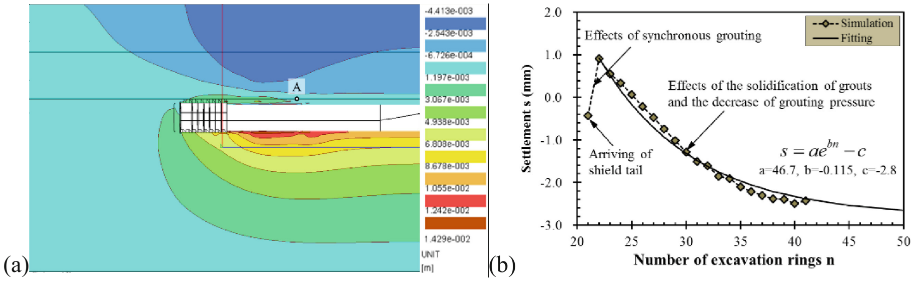

Fig. 6. The calculated settlements: (a) the section along the tunnel axis after the excavation of 40 rings and (b) the evolution trend at point A and fitting result by an exponential function.

To illustrate the synchronous grouting effect, the evolution of settlement at the point A (Fig. 6a) is plotted in Fig. 6b. At the arriving of the shield tail, a small settlement occurs owing to the unbalance pressure at the excavation surface, which can also be illustrated in Fig. 6a. At the beginning of synchronous grouting, the grouting pressure is bigger than the local earth pressure, resulting in an upheaval deformation (Fig. 6b). This upheaval reaches its maximum value at the time when the grouting pressure reaches its maximum value. However, this upheaval is not observed at the surface owing to the large depth of the tunnel (Fig. 6a). As times goes, the grouting pressure starts to decrease as described by Eq. 1. Meanwhile, the earth pressure starts to compress the grout although its Young's modulus increases. In addition, the decrease of Poisson's ratio would result in the shrinkage of grouts. Consequently, the settlement increases with time. Finally, the settlement stabilizes when the grouts become to solid state. The evolution of settlement at point A can be back-fitted using an exponential function (Fig. 6b), which agrees with the conclusions in [10].

All these results show the good performance of the proposed simulation framework to describe the effects of synchronous grouting on ground movement. Therefore, it could be used to analyze the problems that need the micro control of tunneling induced disturbance.

5 Conclusion

A new simulation framework of synchronous grouting in shield tunnels is presented. The step-by-step procedure is used to simulate the tunnel advancement with incorporating two new developments, including a logarithm evolution law of the grouting pressure and a detailed hardening law of grouts. The simulation results reveal that the grouting pressure dominates the upheaval at the beginning while the final settlement is a result of the decrease of grouting pressure as well as the solidification of grout.

Acknowledgement. This work was sponsored by the National Key R&D Program of China (2017YFC0806004), the National Natural Science Foundation of China (51378388), Shanghai Science and Technology Committee (16DZ1201701).

References

1. Bezuijen, A., Talmon, A.M., Kaalberg, F.J., Plugge, R.: Field measurements of grout pressures during tunneling of the Sophia rail tunnel. Soils Found. **44**(1), 39–48 (2004)
2. Kasper, T., Meschke, G.: A numerical study of the effect of soil and grout material properties and cover depth in shield tunnelling. Comput. Geotech. **33**(4), 234–247 (2006)
3. Ding, W.Q., Duan, C., Zhao, T.C., Tao, T., Li, P.N.: Experimental study on pressure distribution and influence of synchronous grouting of quasi-rectangular tunnels. Mod. Tunn. Technol. **53**(S1), 209–215 (2016)
4. Gou, Z.F., Ye, F., Zhang, J.L., Liu, Y.P.: Ring distribution model of filling pressure for shield tunnels under synchronous grouting. Chin. J. Geotech. Eng. **35**(3), 590–598 (2013)
5. Peck, R.B.: Deep excavations and tunneling in soft ground. In: Proceedings of 7th International Conference on Soil Mechanics and Foundation Engineering, Mexico City (1969)

6. Zou, J., Zuo, S.: Similarity solution for the synchronous grouting of shield tunnel under the vertical non-axisymmetric displacement boundary condition. Adv. Appl. Math. Mech. **9**(1), 205–232 (2016)
7. Oh, J.Y., Ziegler, M.: Investigation on influence of tail void grouting on the surface settlements during shield tunneling using a stress-pore pressure coupled analysis. Ksce J. Civil Eng. **18**(3), 803–811 (2014)
8. Qiao, Y., Ding, W., Xie, D., Song, W.: A 3D finite element model for shield tunnel undercrossing the historical building in soft ground. In: Proceeding of the 3rd International Conference on Computational Methods in Tunneling and Subsurface Engineering, pp. 855–862. Aedification Publishers, Bochun (2013)
9. Liang, F., Jia, Y., Ding, Y., Huang, M.: Experimental study on parameters of HSS model for soft soils in Shanghai. Chin. J. Geotech. Eng. **39**(2), 269–278 (2017)
10. Qiao, Y., Ding, W., Zhu, H., Guan, L., Wang, J.: Selection of prediction models for settlement induced by shield tunneling in soft soil area. In: Proceeding of the 7th China-Japan Conference on Shield Tunneling, pp. 304–310. China Communications Press, Xi’an (2013)

The Behavior Analysis of a Cofferdam Constructed by Double Sheet Pile Wall Above Muck

Tianchi Zhao[1,2], Wenqi Ding[1,2], Lixin Wei[3], Weifeng Wu[1,2],
and Yafei Qiao[1,2](✉)

[1] Department of Geotechnical Engineering, College of Civil Engineering,
Tongji University, Shanghai, China
tumuqiaoqi@126.com
[2] Key Laboratory of Geotechnical and Underground Engineering of the Ministry
of Education, Tongji University, Shanghai, China
[3] Guangzhou Municipal Engineering Design Research Institute,
Guangzhou, Guangdong, China

Abstract. This paper presents an investigation on the behavior of a cofferdam structure constructed by double sheet pile walls above the muck, which is used to construct the inner foundation for an immersed tube tunnel project in Guangzhou China. A detailed three-dimensional FEM model is formulated to simulate the whole processes, including the construction of the cofferdam and the excavation of the inner foundation. The strength reduction method is then adopted to calculate the safety factor of the cofferdam. In addition, the effects of the thickness of the filling sand is highlighted.

Keywords: Cofferdam · Double sheet pile wall · FEM model
Filling sand

1 Introduction

The cofferdam on the soft soil can be generally divided into two major types: gravity dam cofferdam and sheet pile cofferdam. Considering the stability and construction time, the later one is more suitable and convenient to use in practical projects. Moreover, the anti-seepage ability of the sheet pile is also better than others'. Double sheet pile wall, as one kind of the sheet pile, is widely used in cofferdam construction. However, the design specifications of double sheet pile wall are quite different all over the world, and most of them are still semi-empirical design method. Figure 1 presents the practical method which is widely used in China [1]. The double sheet pile wall is recognized as two cantilever beams, having the same deformation at the top of each sheet (two points connected by steel tie rods), and the soil and water pressure are acted on these two beams. The bending moment and shear force is then calculated through structure analysis.

Since the theoretical method is too complex to use in the design, the numerical simulation is always carried out to calculate the deformation and internal force of the

© Springer Nature Singapore Pte Ltd. 2018
D. Zhang and X. Huang (Eds.): GSIC 2018, *Proceedings of GeoShanghai 2018 International Conference: Tunnelling and Underground Construction*, pp. 32–39, 2018.
https://doi.org/10.1007/978-981-13-0017-2_3

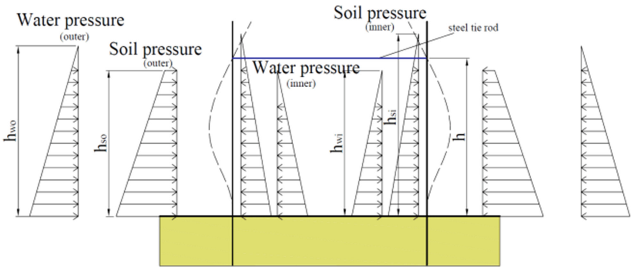

Fig. 1. Calculation scheme of double sheet pile wall

structure. Yong performed a FEM model of double-row steel sheet pile cofferdam system to calculate the static rigidity and intensity of the overall steel sheet pile [2]. Yu-wei made a numerical analysis on double-row steel sheet pile cofferdam for soft soil foundation, and the factors of cofferdam filling and water-lowering rate on the safety of the project was discussed [3]. Gui applied the numerical simulation to investigate the failure of a cofferdam caused by heavy rainfall [4]. Crawford used a numerical model for predicting the bending stresses and crimp forces in crimped pairs of Larssen piles that are used for the cofferdam [5].

The soil behavior has a remarkable effect on the performance of sheet piles. If the soil couldn't impose restrictions enough on the structure, the deformation of sheets increases and the internal force of cofferdam would exceed the capacity of steel sheets. Khan carried out a series of centrifuge model tests to investigate the different behavior of double sheet pile wall cofferdam on sand and clay [6, 7]. According to his result, the performance of double sheet pile wall constructed in the sand is better than the one in the clay. Therefore when the soil under the cofferdam has an adverse behavior, its impact on the responses of structure has to be investigated.

This paper mainly presents a numerical framework of a cofferdam constructed by double sheet pile wall above muck, which is based on a cofferdam project using for the construction of Ruyi Lane immersed tube tunnel in Guangzhou China. The FEM numerical model is applied to study the bearing capacity and stability of the structure, and to describe the characteristics of double sheet pile wall that is essential to the design of the cofferdam project. Contrast analysis about different thickness of filling sand and numbers of steel tie rods is also carried out to study their effect on the behavior of cofferdam. Overall, the influence of muck layer is highlighted.

2 Numerical Simulation

A 3D FEM model is presented in this section, which is used to simulate the intact construction of the double sheet pile wall cofferdam and the excavation of the inner foundation. The model is based on the connecting section of Ruyi Lane immersed tube tunnel, the joint of an immersed tube tunnel under the water and a cut-and-cover tunnel on the bank. The cofferdam includes double sheet pile walls, steel tie rods, filling sand and stone foundation. The inner foundation is constructed by concrete supports and steel pipe piles.

The simulation includes five procedures (Fig. 2): (a) applying the initial earth pressure, (b) construction of the double sheet pile wall, (c) back-filling the sand between the sheets and putting on the stone foundation, (d) construction of the support structure of the inner foundation, (e) excavation of the soil that is divided into four steps. According to the design, the excavation depth of each step is about 4 m. In addition, the strength reduction method is finally used to study the stability of the whole structure.

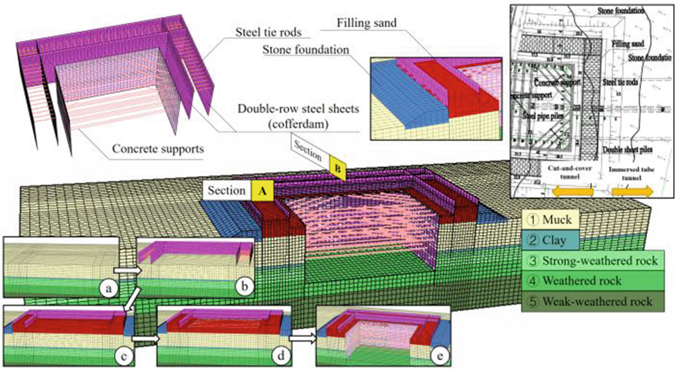
Steel tie rods
Filling sand
Stone foundation
Double-row steel sheets (cofferdam)
Concrete supports
Section B
Section A
Stone foundation
Filling sand
Stone foundation
Concrete support
Concrete support
Steel tie rods
Steel pipe piles
Double sheet piles
Cut-and-cover tunnel
Immersed tube tunnel
① Muck
② Clay
③ Strong-weathered rock
④ Weathered rock
⑤ Weak-weathered rock
a
b
c
d
e

Fig. 2. FEM model of the cofferdam constructed by double sheet pile wall

The Hardening Soil (HS) model [8] has been widely used in the model of foundation excavation because of its advantage on simulating the unloading process. Therefore it is adopted in this paper. The relevant parameters are summarized in Table 1. The other parts of this model are assumed to behave elastically. The values of unit weight, Poisson ratio, cohesive force and friction angel are obtained from the geological survey. According to relevant experience, the tangent modulus and secant modulus are defined to be equal to the compression modulus, while the rebound modulus is assumed to be 3 times of compression modulus.

Table 1. Material parameters of soil in the FEM model.

Soil layer	Unit weight kN/m^3	Poisson ratio	Cohesive force/kPa	Friction angel/°	Tangent modulus E_{oed}/kPa	Secant modulus E_{50}/kPa	Rebound modulus E_{ur}/kPa
Muck	16	0.4	6	4	2142	2142	7140
Clay	19.5	0.3	15	15	3600	3600	12000
Strong-weathered rock	20	0.3	30	30	45000	45000	150000
Weathered rock	20	0.35	550	30	90000	90000	300000
Weak-weathered rock	20	0.3	650	40	135000	135000	450000

3 Results

Two typical sections (Fig. 2) in different regions are chosen to illustrate the deformation, internal force and the stability behaviors of the structure. Apart from the result of each excavation step which is used to make a contrast study, the results of the step when the sand has been filled into the gap between two rows of sheets is also shown in this section.

3.1 Deformation of the Structure

The primary deformation is the settlement of filling sand and the lateral deflection of double sheet pile, which is related to the muck layer. As it has a low stiffness modulus and a high Poisson's ratio, it will be compressed and slip along the horizon direction when the weight of filling sand is applied. On the other hand, the stone foundation at the river side also contributes to the slip of soil because of the same reason. The maximum settlement of sand and lateral deflection of sheet piles are about 50 mm and 60 mm, respectively. According to the result from some analysis based on other double sheet piles projects, the lateral deformation is often larger than 100 mm, so the deflection of piles in this paper is acceptable and reasonable (Fig. 3).

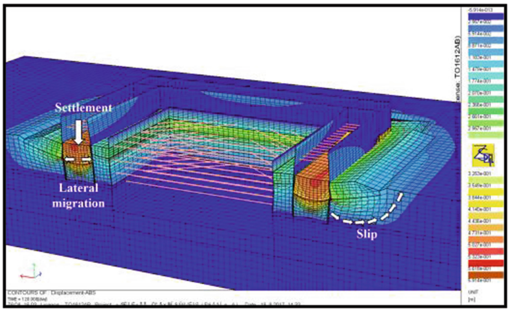

Fig. 3. The simulated displacement nephogram (Unit:m)

In terms of the double sheet pile wall, a similar behavior has been observed in both sections A and B (Fig. 2). Filling sand into the gap between two rows of sheets remarkably contributes to the lateral displacement of double sheet pile wall. As the structure is mainly constructed in the muck layer, the restriction of the displacement of sheets is not strong enough. Owing to the concrete support of the inner foundation, the excavation of the inner soil doesn't make an obvious influence on sheets at the river side, and only a little increase of deformation appears on sheets at the inner foundation side.

The bottom of sheets nearly has no lateral displacement because that it has been embedded into the rock layer. However, the restriction is not strong enough to eliminate the rotation of sheets as the insert depth of sheets is limited. As a result, the behavior of sheets shows a different behavior comparing to the cantilever beams. So the insert depth needs to be considered in the design (Fig. 4).

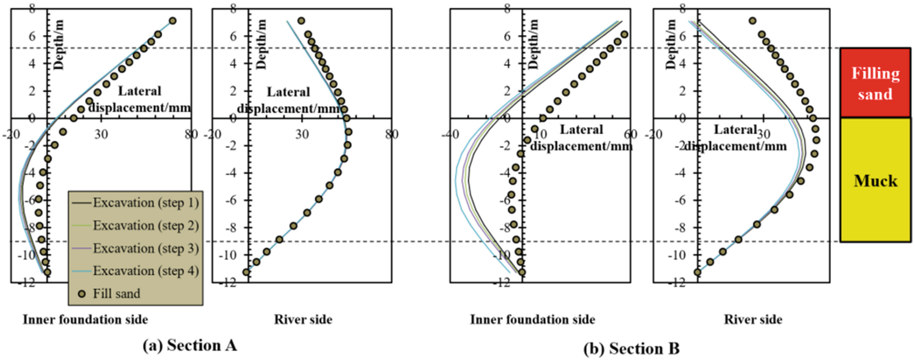

(a) Section A

(b) Section B

Fig. 4. Lateral displacement of the double-row sheets

3.2 Internal Force of Double Sheet Pile Wall

Since the internal force responses of double sheet pile wall in sections A and B are similar, only the results in the section A are analyzed hereafter. The maximum bending moment (about 300 kN·m) appears in the same region with the maximum deformation. In addition, only the bending moment of sheets at the inner foundation side increases with the excavation processes. The steel tie rods put a great constraint on two rows of sheets, decreasing the displacement as well as the bending moment. Therefore adding the rows of steel rods is an effective method to diminish the internal force of sheets. Additionally the range of the bending moment also reveals that the sheets in this model are not similar to cantilever beams but simply supported beams (Fig. 5).

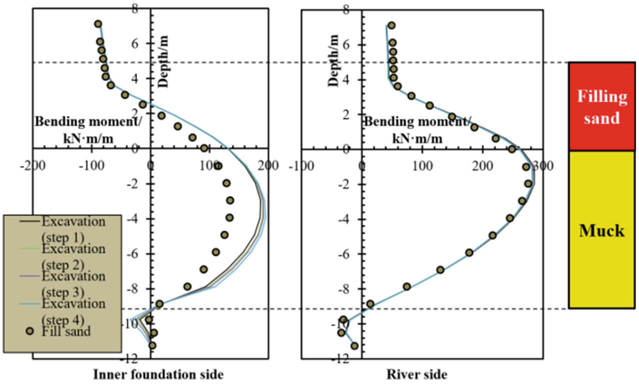

Fig. 5. Bending moment of the double-row sheets in Section A

3.3 Stability

The safety factor equals 1.9 according to the strength reduction calculation. The failure appears under the stone foundation. An intact slip surface has been observed in this region, which extends about 12 m away from the feet of the stone. It is obvious that the slippage only happens in the muck layer owing to the compression of stone. However, the double sheet pile wall still keeps stable without fall and topple. In other word, there is no slip surface forming under the bottom of double sheet piles. Overall, the stability of the cofferdam meets the requirement of the project (Fig. 6).

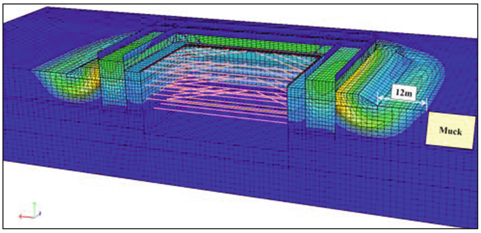

Fig. 6. Displacement nephogram (safety factor equals 1.9)

4 Discussion

4.1 Thickness of Filling Sand

When the support structure of inner foundation has enough bearing capacity, the filling sand is the most important factor to influence the behavior of the cofferdam. Most of the deformation and internal force of double sheet piles are caused by the compression of filling sand. A sensitivity analysis of the thickness of filling sand is carried out to highlight this effect. The considered thickness of filling sand are 3 m, 4 m, 5 m.

As the thickness of filling sand decreases, the lateral deflection comes down, while the range behavior doesn’t change. The maximum lateral deflection decreases about 30% when the thickness of sand changes 1 m (Fig. 7).

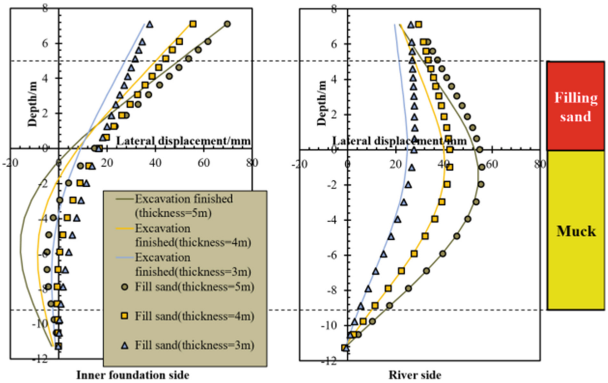

Fig. 7. Lateral deflection of the double-row sheets with different thickness of filling sand

The bending moment of sheets at the river side has an obvious decline when the thickness of sand decreases. When the thickness of filling sand comes down to 4 m, the direction of bending moment at the upper part of sheets would have a transform. This trend may cause the compression of the steel tie rods, which is adverse to the stability of the whole structure (Fig. 8).

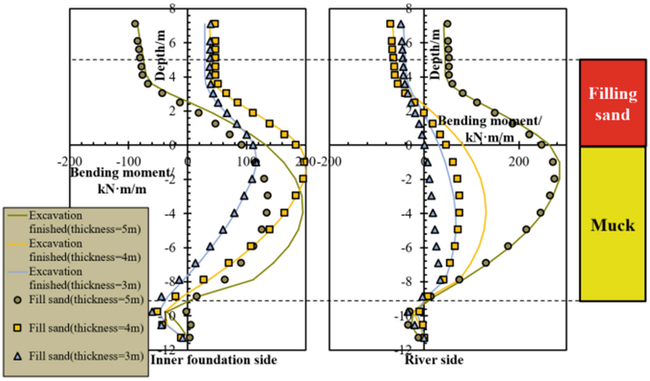

Fig. 8. Bending moment of the double-row sheets with different thickness of filling sand

4.2 Number of Steel Tie Rods

Three different designs (Fig. 9) are applied in the numerical simulation to investigate the effect of the number of steel tie rods. When the steel rod changes from single row to double rows, the bending moment of steel sheet pile is obviously reduced and the maximum value decreases about 40%. This value would continue to decrease about 20% when the number of steel tie rods increases to three. However, it should be noted that the axial force of the steel rod compared to the original program increases significantly. In addition, the deformation of cofferdam has been controlled and the settlement at the top of the sand is obviously reduced.

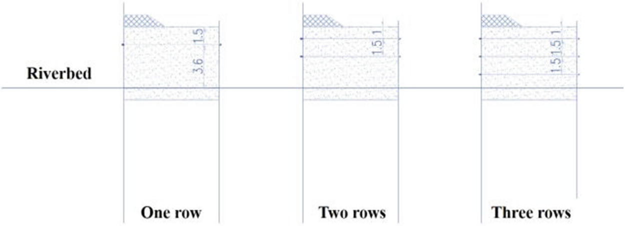

Fig. 9. Different kinds of design of steel tie rods

5 Conclusion

A detailed investigation of the behavior of double sheet pile wall working as the cofferdam is carried out. According to the simulation results, the following conclusions can be drawn:

(1) The lateral deflection of double sheet pile wall is mainly caused by the filling sand, and the excavation of inner foundation only contributes to a little increment of the sheet at the inner foundation side;
(2) The insert depth is a key design parameter for the double sheet pile wall, which has an obvious impact on the behavior of the structure. The sheet pile wall will act as simply supported beams when the insert depth is small;
(3) The stability of the whole structure is controlled by the soil layer under the stone foundation, and the stability of the cofferdam meets the requirement of the project;
(4) The displacement and bending moment of sheets decrease as the thickness of filling sand comes down. However, steel tie rods will suffer compression when the thickness of filling sand is too thin, which is adverse to the stability.
(5) Adding steel tie rods will decline the bending moment effectively, but it may weaken the restriction on the deformation of stone foundation;

Acknowledgement. This work was sponsored by the National Key R&D Program of China (2017YFC0806004), the project of Guangzhou Municipal Engineering Design & Research Institute (2017-018) and the National Natural Science Foundation of China (51378388).

References

1. COSTIND: Code for design of dry dock CB/T 8524–2011
2. Yong, H., Hao, Z., Xiao-xia, Y., Wei, C., et al.: Finite-element analysis on steel tie rod of double-row steel sheet pile cofferdam. J. Zhejiang Univ. Water Resour. Electric Power **28**(2), 58–63 (2016)
3. Li, Y.-W., Xie, M., Feng, T., Jiang, X., et al.: Numerical analysis double-row steel sheet pile cofferdam for soft soil foundation. Water Resour. Hydropower Eng. **46**(9), 40–44 (2015)
4. Gui, M.W., Han, K.K.: An investigation on a failed double-wall cofferdam during construction. Eng. Fail. Anal. **16**(1), 421–432 (2009)
5. Crawford, R.J., Byfield, M.P.: A numerical model for predicting the bending strength of Larssen steel sheet piles. J. Constr. Steel Res. **58**(10), 1361–1374 (2002)
6. Khan, M.R.A., Takemura, J., Fukushima, H., et al.: Behavior of double sheet pile wall cofferdam on sand observed in centrifuge tests. Int. J. Phys. Model. Geotech. **1**(4), 01–16 (2001)
7. Khan, M.R.A., Takemura, J., Kusakabe, O.: Centrifuge model tests on behavior of double sheet pile wall cofferdam on clay. Int. J. Phys. Model. Geotech. **6**(3), 01–23 (2006)
8. Schanz, T., Vermeer, P.A., Bonnier, P.G.: The harden soil model-formulation and verification. In: Beyond 2000 in Computational Geotechnics (1999)

Effects of Different Factors on the Mining of Extra-Thick Coal Seam

Naifei Liu[1,2(✉)], Zhu Zhang[2], Ning Li[2], Min Yang[2],
and Yuanyang Ren[2]

[1] Xi'an University of Architecture and Technology, Xi'an 710055, Shaanxi,
People's Republic of China
`liunaifei1985@126.com`
[2] Xi'an University of Technology, Xi'an 710048, Shaanxi,
People's Republic of China

Abstract. Based on the mining case of Dafosi Coal Mine in Shaanxi Province, which is a typical coal mine with extra-thick coal seam, the effects of mining width, buried depth and rock grade on the ground surface deformation and sur-rounding rock stress have been studied by numerical experiments. It is found that both of the ground Surface Settlement (SS) and Horizontal Displacement (HD) increased with the increase of the mining width, the weaken of the rock grade and the decrease of the buried depth. When the mining width increased form 10 m to 90 m, the SS and HD had a 180-fold and 15-fold increase, respectively. The mining width of 40 m is the starting point for the significant increase of surface deformation. When the buried depth increased form 100 m to 400 m, the SS and HD decreased by 38.2% and 63.4%, respectively. When the rock grade decreased from grade II to grade V, both the SS and HD increased by more than 10 times. Especially, when the rock grade is below II, it will appear different levels of collapse in the coal roof.

Keywords: Extra-thick coal seam · Influence factor · Ground surface deformation · Surrounding rock stress

1 Introduction

Coal plays an important role in the energy structure of China, which supporting the development of various industries (Wang 2006). However, the coal mining is extremely harmful to surface buildings and ecological environment, especially in the case of extra-thick coal seam (viz. coal seam with thickness greater than 8.0 m).

As early as 1920s–1930s, the United States, Britain and other countries have begun to pay attention to the influence of mining on the ground surface (Yacoub 1990; Berry and Sales 1961). Although this research starts late in China, a lot of meaningful achievements have been published. Zou (1998) proposed a probability integral method for deformation prediction of the ground surface. Huang (2007) analyzed the surface distortion rule of the mountain coal seam. Dai et al. (2013) proposed a prediction method for ground surface movement based on field data and similar model test. Sun et al. (2009) studied the effects of different width of working face on laneway stability

© Springer Nature Singapore Pte Ltd. 2018
D. Zhang and X. Huang (Eds.): GSIC 2018, *Proceedings of GeoShanghai 2018 International Conference: Tunnelling and Underground Construction*, pp. 40–53, 2018.
https://doi.org/10.1007/978-981-13-0017-2_4

by the method of numerical simulation. In addition, a large number of scholars carried out researches on the mining of thick and extra-thick coal seam. Wang (2013) has studied the key technologies of the Fully Mechanized Top Coal Caving Mining with Higher Mining Height (FMTCCMHMH) in extra-thick coal seam. Based on the theoretical analysis and numerical simulation, the reasonable machine mining height of FMTCCMHMH was studied by Wang et al. (2012). Yu and Duan (2014) have studied the control technology of hydraulic fracturing roof during high-strength mining of extra-thick coal seam. Wang (2013) and Wang et al. (2014) have studied the failure characteristics of surrounding rock and the failure mechanism of the tunnel roof, respectively. The above researches have greatly enriched the theory of coal mining in China and laid the foundation for the mining of extra-thick coal seam. However, the research on ground surface deformation and the distribution of surrounding rock stress of the coal seam caused by various factors (such as mining width, buried depth and rock grade) is rarely reported. Therefore, it is very necessary to carry out the research in this area.

Based on the Dafosi Coal Mine in Bin County, Shaanxi Province, the effects of mining width, buried depth and rock grade on mining of extra-thick coal seam are studied by the large-scale discrete element software (UDEC). The influence of various factors on the mining of the extra-thick coal seam is summarized by analyzing the ground surface settlement and horizontal displacement, the distribution of surrounding rock stress and deformation under different conditions, which could provide the theoretical basis for the design of support pattern and technical parameters for the extra-thick coal seam.

2 Numerical Model and Schemes

2.1 Numerical Model

The Dafosi Mine area is located in the mining boundary of Bin-Chang mining area. The mining area is about 15 km from east to west, with a width of 5.8 km from north to south and the production capacity is 5,000,000 t/a. The region is table-land-plain landscape and belongs to Ordos basin subregion of North China stratigraphic area. Mining way is the fully mechanized (long-wall) top coal caving of strip mining method. The depth of the coal-seam is 410 m and the average thickness is about 15 m.

In order to investigate the influence of mining width (MW), buried depth (BD) and rock grade (RG), the single-face mining method is adopted in the numerical model. The length of the model is 1000 m and vertical height is 500 m. The thickness of the coal-seam is 15 m with a buried depth of 400 m. The up-down step mining method (upper is 7 m, lower is 8 m) is adopted. The stratums of this model are T3h, coal seam and K11 from top to bottom.

In this paper, the influence of various factors on the mining of extra-thick coal seam is simulated by means of the UDEC software. The Mohr-Coulomb model is chosen for the rock block, and the Coulomb sliding model is chosen for the rock joint. The acceleration boundary condition is used in this study. The acceleration in the x direction of the left and right sides and the bottom is zero. The upper is the free boundary. This paper assumes that the calculation is balanced when the maximum unbalanced force is less than 10^{-5} N. The numerical model is shown in Fig. 1.

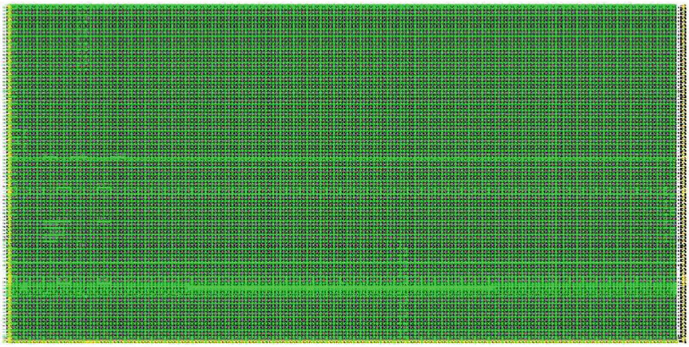

Fig. 1. The numerical model

2.2 Schemes

A total of 20 numeric simulation schemes are prepared to study the effects of various factors (MW, BD and RG) on the mining of extra-thick coal, as shown in Table 1.

Table 1. The numerical simulation schemes.

Various factors	Variation Range	Comment
Mining width (m)	10, 20, 30, 40, 50, 60, 70, 80, 90	BD = 400 m
Buried depth (m)	100, 150, 200, 250, 300, 350, 400	MW = 40 m
Rock grade	II, III, IV, V	MW = 40 m BD = 400 m

2.3 Parameters

The parameters of the three rock stratums obtained from the geological reports and the relevant tests of the Dafosi coal mine are shown in Table 2. The mechanical parameters of different rock grades are determined according to the “Standard for engineering classification of rock mass”, as shown in Table 3 (the data belong to rock parameters, and the parameters of rock joint refer to Table 2).

3 Effects of the Mining Width

3.1 Ground Surface Settlement

The ground surface settlement curves under different mining width are shown in Fig. 2.

As seen in Fig. 2, the ground surface settlement curves are approximately V-shaped and the medial axis of the mined-out area (goaf) is its symmetric axis. The closer the

Table 2. The mechanics parameters for different rock stratums.

Rock block	Bulk modulus (Gpa)	Shear modulus (Gpa)	Poisson ratio	Density (kg/m$^{3)}$	Cohesion (Mpa)	Friction angle (°)
K1l	1.18	0.36	0.36	2223	0.10	27.98
coal	0.41	0.26	0.24	1415	0.33	28.12
T3h	6.65	3.80	0.26	2350	1.45	38.56

Rock joint	Normal stiffness (Gpa)	Shear stiffness (Gpa)	Tensile strength (Mpa)	Cohesion (Mpa)	Friction angle (°)
K1l	0.5	0.5	70.0	25.0	18.0
coal	2.0	2.0	30.0	8.0	25.0
T3h	2.8	2.8	70.0	25.0	24.0

Table 3. The mechanics parameters for different rock grades.

Rock grade	Density (kg/m$^{3)}$	Bulk modulus (Gpa)	Shear modulus (Gpa)	Poisson ratio	Cohesion (Mpa)	Friction angle (°)
II	2500	5.56	4.17	0.20	1.50	45.00
III	2300	3.33	2.00	0.25	0.60	35.00
IV	2200	0.83	0.39	0.30	0.10	30.00
V	2000	0.33	0.11	0.35	0.05	20.00

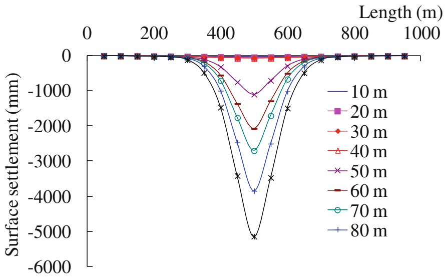

Fig. 2. The ground surface settlement

measuring points to the mining face, the greater ground surface settlement. The settling tank depth is increasing with the increase of mining width. The mining width has a significant impact on ground surface settlement. The maximal ground surface settlement is only 28.2 mm at a mining width of 10 m, however, the value increases to 5169 mm, which had a 180-fold increase when the mining width increased to 90 m. In addition, it can be observed that the ground surface settlement show dramatic increase when the mining width is greater than 40 m. In other words, the 40 m width is a turning point for the ground surface settlement.

3.2 Surface Horizontal Displacement

The surface horizontal displacement curves under different mining width are shown in Fig. 3. As seen in Fig. 3, there are two maximal values for the surface horizontal displacement curves, which are symmetrically distributed. The ground surface in both sides of mining area center moves towards each other, and the surface horizontal displacement at the center line is zero. The maximum value of the surface horizontal displacement appears at the place of 100 m away from the mining area center, which is increasing with the increase of the mining width. When the mining width is 10 m, the maximum horizontal displacement is about 9.10 mm, however, the value increased to 150.2 mm which has a 15-fold increase when the mining width increases to 90 m. The increment of horizontal displacement is much smaller than that of the ground surface settlement. The same as the ground surface settlement, the horizontal displacement also has a turning point with the increase of the mining width. when the mining width is greater than 40 m, the surface horizontal displacement begins to increase significantly.

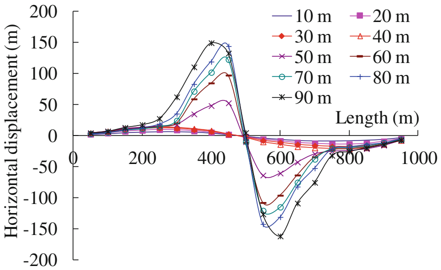

Fig. 3. The Surface horizontal displacement

3.3 Stress of Surrounding Rock

To save space, only the vertical stress contours of the surrounding rock under mining width of 10 m, 50 m and 90 m are presented, as shown in Fig. 4.

It is indicated that the surrounding rock stress released and adjusted as a result of the coal mining. The vertical stress contours are distributed as vertical shaft-shape. With the mining width increasing, the stress disturbed and concentration area increased as well. When the mining width is 10 m, the disturbed area is very small and the stress concentration area is almost negligible. However, when the value increased to 40 m, a significant stress concentration area occurred in the surrounding rock in both sides. When the value increased to 90 m, this range is further expanded up to the ground surface. It can be seen that the mining width of 40 m is the turning point of the stress field, which is consistent with ground surface deformation.

3.4 Displacement of Surrounding Rock

The vertical displacement cloud diagrams of the surrounding rock under mining width of 10 m, 50 m and 9 0 m are shown in Fig. 5.

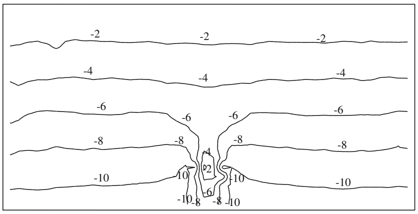

(a) MW = 10m (Unit: MPa)

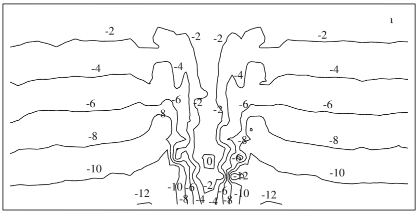

(b) MW = 50 m (Unit: MPa)

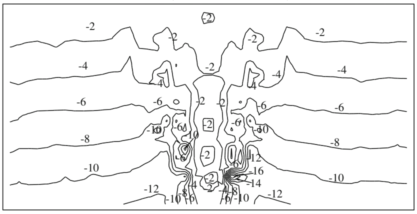

(c) MW = 90 m (Unit: MPa)

Fig. 4. The vertical stress field

As seen in Fig. 5, the distribution characteristic of the vertical displacement field is consistent with that of ground surface deformation and the vertical stress field. When the mining width is 10 m, the deformation of the surrounding rock is small, the roof settlement is about 20 cm and the uplift value of the floor is about 8 cm. When the mining width increased to 40 m, collapse occurred at the mining roof and its height is about 20 m. As the mining width further increasing, the collapse height and range significantly increased. When the mining width increased to 90 m, the collapse height increased to 40 m and the deformation field shown stratification phenomenon as well. As a result, the mining width of 40 m is the threshold value for the collapse of the mining roof.

4 Effects of the Buried Depth

4.1 Ground Surface Settlement

The ground surface settlement curves under different buried depth are shown in Fig. 6.

As seen in Fig. 6, the ground surface settlement curves are V-shaped. The settlement value decreased with the increase of buried depth and the biggest reductions for the surface settlement happened between the depth of 150 m to 250 m. When the

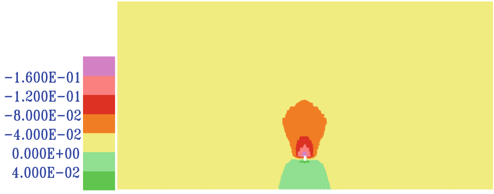
-1.600E-01
-1.200E-01
-8.000E-02
-4.000E-02
0.000E+00
4.000E-02

(a) MW = 10m (Unit: m)

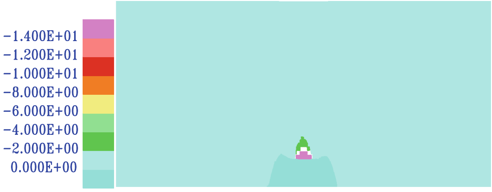
-1.400E+01
-1.200E+01
-1.000E+01
-8.000E+00
-6.000E+00
-4.000E+00
-2.000E+00
0.000E+00

(b) MW = 50 m (Unit: m)

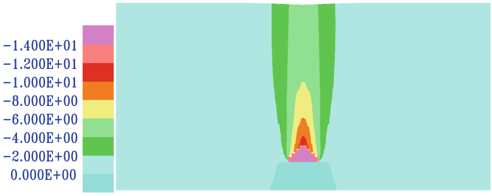
-1.400E+01
-1.200E+01
-1.000E+01
-8.000E+00
-6.000E+00
-4.000E+00
-2.000E+00
0.000E+00

(c) MW = 90 m (Unit: m)

Fig. 5. The vertical displacement field

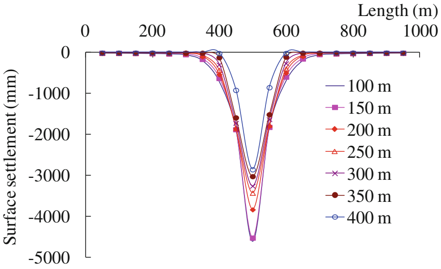

Fig. 6. The ground surface settlement

buried depth is 100 m, the maximal ground settlement is 4612 mm, however, the value decreased to 2851 mm which had a 38.2% decrease when the buried depth increased to 400 m. It shows that the buried depth has a significant effect on the ground surface settlement. So the supporting scheme should be determined according to the real buried depth during the mining process for the safety of surface buildings.

4.2 Surface Horizontal Displacement

The surface horizontal displacement curves under different buried depth are shown in Fig. 7.

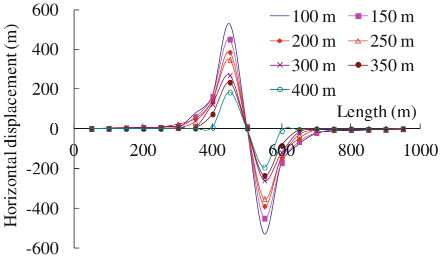

Fig. 7. The surface horizontal displacement

As seen in Fig. 7, the surface horizontal displacement curves are centrally symmetrical at different buried depths. The maximum appeared at 50 m away from the mining area centerline in both sides and the values are equal but in the opposite direction. With the increasing of buried depth, the surface horizontal displacement is decreasing. The biggest reductions for the horizontal displacement happened between the depth of 100 m to 300 m. This range is slightly larger than that of the ground surface settlement. When the buried depth is 100 m, the maximal horizontal displacement is 528.4 mm, however, the value decreased to 193.5 mm which had a 63.4% decrease when the buried depth increased to 400 m. It shows that the magnitude of the horizontal displacement is much smaller than that of the subsidence. The former is 1.5 times as the decreasing amplitude as the latter.

4.3 Stress of Surrounding Rock

The vertical stress contours of the surrounding rock under buried depth of 100 m, 250 m and 40 m are shown in Fig. 8.

As Fig. 8 shows, the distribution of surrounding rock stress under different buried depth and mining width is basically the same. The stress redistribution and concentration occurred during and after mining in both conditions. For the smaller buried depth (100 m), the stress disturbance area is relatively small and almost no stress concentration area appears as a result of the thinner overlying strata. With the increase of buried depth (250 m), the range of stress disturbance zone is expanding and the stress concentration area is increasing as well. When the buried depth increases to 400 m, the stress concentration area appears in both sides of the working face and floor. It shows that the development process of the stress field of the surrounding rock is consistent with that of the surface deformation.

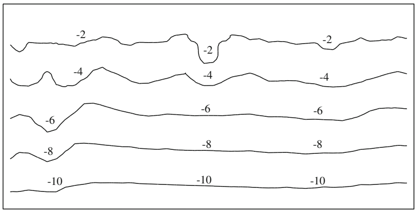

(a) BD = 100m (Unit: MPa)

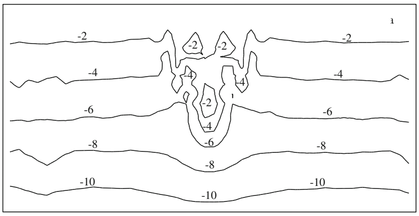

(b) BD = 250 m (Unit: MPa)

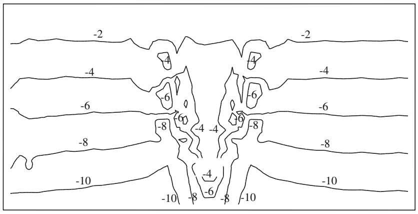

(c) BD = 400 m (Unit: MPa)

Fig. 8. The vertical stress field

4.4 Displacement of Surrounding Rock

The vertical displacement field of the surrounding rock under buried depth of 100 m, 250 m and 400 m are shown in Fig. 9.

As Fig. 9 shows, the distribution of displacement field under different buried depth and mining width is similar. With the increasing of buried depth, the deformed region caused by the mining is extending, but the deformation value is decreasing. when the buried depth is 100 m, the roof collapsed with a height of 20 m. When the buried depth increased to 150 m, just local collapse occurred in the roof. With the increasing of buried depth, the collapse range and height is decreasing and uplift deformation appeared in the floor. It shows that the distribution of the displacement field is in good agreement with that of the stress field.

5 Effects of the Rock Grade

5.1 Ground Surface Settlement

The ground surface settlement curves under different rock grade are shown in Fig. 10.

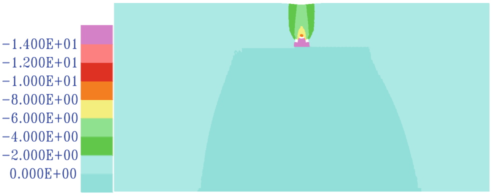
-1.400E+01
-1.200E+01
-1.000E+01
-8.000E+00
-6.000E+00
-4.000E+00
-2.000E+00
0.000E+00

(a) BD = 100m (Unit: m)

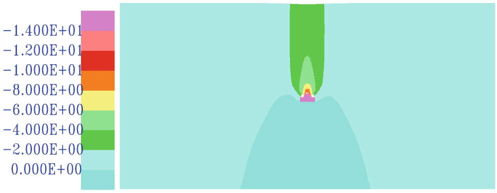
-1.400E+01
-1.200E+01
-1.000E+01
-8.000E+00
-6.000E+00
-4.000E+00
-2.000E+00
0.000E+00

(b) BD = 250 m (Unit: m)

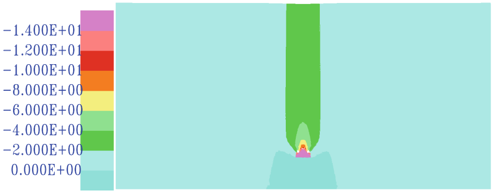
-1.400E+01
-1.200E+01
-1.000E+01
-8.000E+00
-6.000E+00
-4.000E+00
-2.000E+00
0.000E+00

(c) BD = 400 m (Unit: m)

Fig. 9. The vertical displacement field

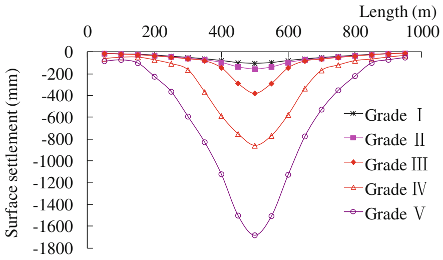

Fig. 10. The ground surface settlement

The surface subsidence curves are in wide V-shape under different rock grade as Fig. 10 shows. As the surrounding rock weaken, the ground surface settlement increases and its range extends. When the rock grade is better than II, the ground surface settlement is almost negligible at the current depth and width. Otherwise, the surface settlement will be very large. When the surrounding rock grade is II, the maximal surface settlement is only 155.3 mm, however, the value increases to 1692 mm, which had a 10-fold increase when the rock grade decreased to V. It shows that mining leads little effect on a better rock mass, but bring about a significant impact on a poor rock mass. Therefore, in order to ensure the safety of the surface buildings, the support scheme should be chosen according to the real rock grade.

5.2 Surface Horizontal Displacement

The surface horizontal displacement curves under different rock grade are shown in Fig. 11.

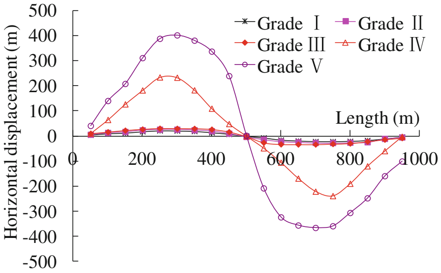

Fig. 11. The surface horizontal displacement

As seen in Fig. 11, the horizontal displacement curves are in horizontal S-shape under different rock grade. The maximum value appeared at both sides of mining area centerline, which are equal but in the opposite direction. With the rock grade weakening, horizontal displacement is increasing, which is similar to the ground surface settlement. When the rock grade is better than II, the horizontal displacement is really small. When the surrounding rock grade is II, the maximal surface settlement is only 27.7 mm, however, the value increases to 401.5 mm, which had a 13.5-fold increase when the rock grade decreased to V. It is also clear that mining has a remarkable influence on the poor surrounding rock.

5.3 Stress of Surrounding Rock

The vertical stress contours of the surrounding rock under rock grade III, IV and V are shown in Fig. 12.

As Fig. 12 shows, the vertical stress contours under different rock grade are in deep U-shape. Its distribution is similar to above-mentioned stress field under different mining conditions. When the rock mass is in high-quality, the range of disturbed surrounding rock is small, and the stress concentration occurs only in local area. With weaken of the rock grade, upper part of U-shaped further opened and the stress disturbance zone increased while the stress concentration area decreased. This is mainly due to the faster stress release and transfer in poor rock mass. Therefore, the support measures should be robust to prevent collapse.

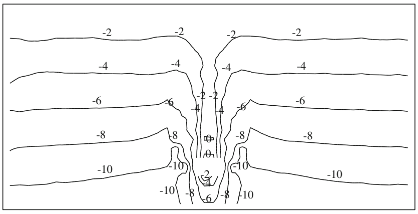

(a) RG = III (Unit: MPa)

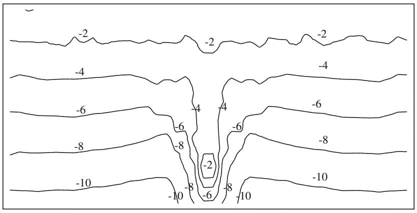

(b) RG = IV (Unit: MPa)

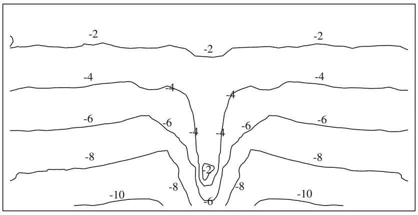

(c) RG = V (Unit: MPa)

Fig. 12. The vertical stress field

5.4 Displacement of Surrounding Rock

The vertical displacement cloud diagrams of the surrounding rock under rock grade III, IV and V are shown in Fig. 13.

As seen in Fig. 13, the roof is sinking and the floor is uplifting. The deformation range is extending and the value is increasing with the weaken of surrounding rock. When the surrounding rock is better than grade II, the floor is sinking with a maximum of 80 cm. With the further weakening of surrounding rock, the top of the coal seam collapsed. The collapse height for the surrounding rock of grade III is about 20 m, which is expanding with the lithology weakening.

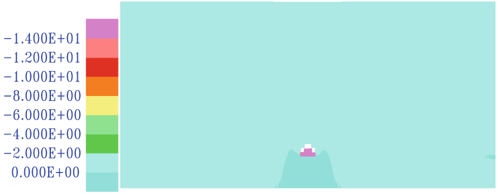

(a) RG = III (Unit: m)

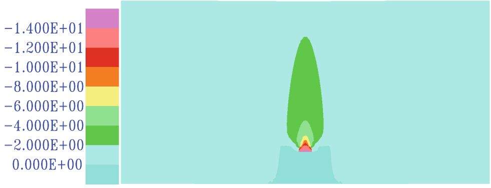

(b) RG = IV (Unit: m)

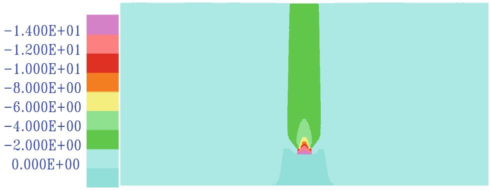

(c) RG = V (Unit: m)

Fig. 13. The vertical displacement field

6 Conclusion

Based on the Dafosi Coal Mine, the effects of various factors on the mining of extra-thick coal seam were studied in this paper by systematic numerical experiments. On the basis of the simulated results, the following conclusions can be drawn:

(1) Both the surface settlement and horizontal displacement increase with the weaken of rock grade, increase of mining width and decrease of buried depth.
(2) The surface settlement had a 180-fold increase and the horizontal displacement had a 15-fold increase when the mining width increased from 10 m to 90 m. The mining width of 40 m is the starting point for the significant increase of surface deformation. While the mining width exceeds this value, the roof will collapse.
(3) The surface settlement had a 38.2% decrease and the horizontal displacement had a 63.4% decrease when the buried depth increased from 100 m to 400 m. The collapse range of coal seam roof decreases and the stress concentration area increases with the increase of the buried depth.

(4) The surface settlement had a 10-fold increase and the horizontal displacement had a 13.5-fold increase when the rock grade decreased from II to V. The worse of rock grade, the larger stress disturbed area. The roof had different levels of collapse when the rock grade was worse than II.

Acknowledgements. The authors would like to express gratitude to the anonymous reviewers for their constructive comments and suggestions and Dr. Xiaogang Guo of Vienna University of agriculture and science for his help on English writing.

References

Berry, D., Sales, T.: An elastic treatment of ground movement due to mining. J. Mech. Phys. Solids **9**, 52–56 (1961)

Dai, H.Y., Yi, S.H., Guo, J.T.: Prediction method for surface movements and deformation induced by extra-thick steeply inclined coal seam horizontal slice mining. J. China Coal Sci. **38**(8), 1305–1311 (2013)

Huang, Z.Z.: Analysis of mountain surface subsidence. Coal Sci. Technol. **1**(1), 26–29 (2007)

Sun, G.Z., Wang, G.J., Guo, J.J.: Numerical simulation and analysis on stability of roadway group affected by mining action. Chin. J. Undergr. Space Eng. **5**(S1), 1412–1417 (2009)

Wang, J.H.: Present status and development tendency of fully mechanized coal mining technology and equipment with high cutting height in China. Coal Sci. Technol. **34**(1), 4–7 (2006)

Wang, J.H.: Key technology for fully-mechanized top coal caving with large mining height in extra-thick coal seam. J. China Coal Sci. **38**(12), 2089–2098 (2013)

Wang, G.F., Pang, Y.H., Liu, J.F.: Determination and influence of cutting height of coal by top coal caving method with great mining height in extra thick coal seam. J. China Coal Sci. **37** (11), 1777–1782 (2012)

Wang, Q., Wang, H.T., Li, S.C.: Upper bound limit analysis of roof collapse mechanism of large section roadway with thick top coal. Rock Soil Mech. **35**(3), 795–800 (2014)

Yu, B., Duan, H.F.: Study of roof control by hydraulic fracturing in full-mechanized caving mining with high strength in extra-thick coal layer. Chin. J. Rock Mech. Eng. **33**(4), 778–785 (2014)

Yacoub, M.: Constitutive modeling and finite element analysis of ground subsidence due to mining. University of OKlahoma, America (1990)

Zou, Y.F.: Strip mining of three-dimensional layered media theory and application research. J. Jiaozuo Inst. Technol. **17**(6), 414–419 (1998). Accessed 21 Nov 2016

Explicit Analysis for the Ground Response Behavior Due to the Advancing Excavation of Tunnel Under Anisotropy Stress Field

Y. L. Lee(✉) and Y. X. Xin

Department of Civil Engineering, Chung Hua University, Hsinchu, Taiwan,
rosalee@chu.edu.tw

Abstract. The purpose of this research is that the analytical solutions of non-linear behavior of ground in a deep circular tunnel under anisotropy stress field are derived, and the explicit analysis method (EAM) which bases on the convergence confinement method, the principle of confinement loss, and the simple calculation spreadsheet is particularly proposed. This study includes that introducing a incremental procedure of confinement loss into the analytical solutions derived under anisotropy stress field, establishing the direct calculation logic and flow chart, using a calculation spreadsheet to simply calculate and draw figures, considering the stress path and ground response curve at excavation face, and distribution of stress/displacement around tunnel. The results obtained by the explicit analysis and by the finite element analysis are approximately consistent in those curves described in the convergence-confinement method. The explicit analysis method proposed is easy and directly to simulate the ground response behavior due to the advancing excavation of tunnel.

Keywords: Tunnel advancing excavation · Anisotropy stress field
Convergence-Confinement method · Explicit analysis

1 Introduction

The convergence-confinement method (CCM) is a useful theoretical tool for designing support for underground excavations in rock. It consists of three fundamentals: the ground reaction curve (GRC), the support characteristic curve (SCC), and the longitudinal deformation profile (LDP). The ground reaction curve exhibits the increasing trends of radial displacement as the internal support pressure of the tunnel decreases; it plays an important role in determining when the supports are to be installed and how stiff the supports should be.

The idea of the ground reaction curve of the rock mass was first presented by Pacher [1] as a major design component behind the New Austrian tunneling method. The method was further improved by many researchers [2] and was proposed later by the French Association of Tunnel and Underground Space [3] for application in designs, becoming a useful preliminary tool in the rational design of tunnels.

Many researchers have been working on this method ever since, attempting to develop mathematical and empirical expressions for the ground reaction curve under

© Springer Nature Singapore Pte Ltd. 2018

D. Zhang and X. Huang (Eds.): GSIC 2018, *Proceedings of GeoShanghai 2018 International Conference: Tunnelling and Underground Construction*, pp. 54–62, 2018.
https://doi.org/10.1007/978-981-13-0017-2_5

different behavior hypotheses. However, only a few studies concerning tunnels excavated in anisotropy stress fields have been conducted [4, 5].

2 Analytical Solution for Stresses in the Elastic Region and the Plastic Region

2.1 Stresses in the Elastic Region

The convergence-confinement method is based on the analysis of the stress and strain state that develops in the rock around a tunnel. The stresses at the periphery of the tunnel are obviously altered due to the advance excavation of the tunnel face. Therefore, the variation of stresses can be mainly interpreted by the stress gradient which is a difference between far-field stress and near-field stress around a tunnel. By using the hypothesis of increments in the numerical analysis, the increment of stresses can be taken into account of the confinement loss λ as a fraction of the stress gradient. This is an important principal concept used by the convergence-confinement method [6]. The variables $k_1 = 1 + K_o$ and $k_2 = (1 - K_o)\cos 2\theta$, respectively.

$$\sigma_r = \frac{\sigma_v}{2}\left[k_1\left(1 - \lambda\frac{R^2}{r^2}\right) + k_2\left(1 - \lambda\left(4\frac{R^2}{r^2} - 3\frac{R^4}{r^4}\right)\right)\right] \tag{1}$$

$$\sigma_\theta = \frac{\sigma_v}{2}\left[k_1\left(1 + \lambda\frac{R^2}{r^2}\right) - k_2\left(1 + 3\lambda\frac{R^4}{r^4}\right)\right] \tag{2}$$

2.2 Stresses in the Plastic Region and Plastic Radius Around a Tunnel

In the more general case of rock with elastic-perfectly plastic behavior (as the Mohr-Coulomb failure criterion), the confinement loss in elastic limit situation λ_e appears when the elastic limit of the rock is reached, for a certain radial stress σ_r and with the decreasing of r, and when the stress state reaches the limit conditions defined by the strength criterion. Such a value of r is called the plastic radius R_p which is not only a function of the peak strength parameters of the rock mass, but also is a function of the confinement loss in elastic limit situation λ_e. When the confinement loss λ continuously increases, plastic radius R_p increases, but the radial stress decreases in the plastic region; therefore this radial stress is obviously a function of the plastic radius R_p $(R \le r \le R_p)$. For this reason, the radial and circumferential stresses in the plastic region can be shown as [7]

$$\sigma_r = \frac{\sigma_v}{K_p - 1}\left\{[(k_1 - k_2)\lambda_e - k_2]\left(\frac{r}{R_p}\right)^{K_p - 1} - 2N\right\} \tag{3}$$

$$\frac{\sigma_\theta}{\sigma_v} = \frac{1}{K_p - 1}\left\{[(k_1 - k_2)\lambda_e - k_2]K_p\left(\frac{r}{R_p}\right)^{K_p - 1} - 2N\right\} \tag{4}$$

Where the coefficient of passive lateral pressure K_p, the stability number N, the confinement loss in elastic limit situation λ_e and the plastic radius R_p can be expressed as

$$K_p = \tan^2\left(45^\circ + \frac{\varphi}{2}\right) N = \frac{\sigma_c}{2\sigma_v} \tag{5}$$

$$\lambda_e = \frac{(K_p - 1)k_1 + (K_p + 1)k_2 + 4N}{\left[(K_p + 1)k_1 + \left(4K_p - 3(K_p + 1)\left(\frac{R}{r}\right)^2\right)k_2\right]\left(\frac{R}{r}\right)^2} \tag{6}$$

$$\frac{R_p}{R} = \left[\frac{(k_1 - k_2)\lambda_e - k_2}{\frac{1}{2}\left[(K_p + 1)k_1 + (K_p - 3)k_2\right]\lambda_e - \frac{1}{2}(K_p - 1)(k_1 + k_2)\lambda - k_2}\right]^{\frac{1}{K_p - 1}} \tag{7}$$

where the R_p is the radius of the elastic-plastic interface, and is a function of the peak strength parameters of the rock mass (c,ϕ), the location of polar coordinates (r, θ), and the initial in-situ stress (σ_v, K_o). It is also dependent on the confinement loss λ which is an important key to simulate the effect of advance excavation of the tunnel face in the convergence-confinement method.

3 Analytical Solution for Displacements in the Elastic Region and the Plastic Region

3.1 Displacements in the Elastic Region

In the elastic region, the radial and circumferential displacements in the elastic region can be expressed as [7]

$$\frac{2G}{\sigma_v}\frac{u_r}{R} = \frac{\lambda}{2}\left(\frac{R}{r}\right)\left\{k_1 + k_2\left[4(1 - v) - \left(\frac{R}{r}\right)^2\right]\right\} \tag{8}$$

$$\frac{2G}{\sigma_v}\frac{u_\theta}{R} = \frac{\lambda}{2}\left(\frac{R}{r}\right)\left\{k_2\left[2(1 - 2v) + \left(\frac{R}{r}\right)^2\right]\tan 2\theta\right\} \tag{9}$$

3.2 Displacements in the Plastic Region

In the plastic region, the closed-form analytical solution for the radial displacement in the plastic region can be simplified as

$$\frac{2G}{\sigma_v}\frac{u_r}{R} = \lambda_e\left(\frac{r}{R}\right)\left[C_1 + C_2\left(\frac{r}{R_p}\right)^{K_p - 1} + C_3\left(\frac{R_p}{r}\right)^{K_\psi + 1}\right] \tag{10}$$

where

$$C_1 = -\frac{(1-2v)}{\left(K_p-1\right)}\left[\frac{\left(K_p+1\right)k_1+\left(K_p-3\right)k_2}{2}\right] \tag{11}$$

$$C_2 = \frac{1+K_\psi K_p - v\left(K_p+1\right)\left(K_\psi+1\right)}{\left(K_p-1\right)\left(K_\psi+K_p\right)}\left[(k_1-k_2)-\frac{k_2}{\lambda_e}\right] \tag{12}$$

$$\begin{aligned} C_3 = {} & \frac{(1-2v)}{K_p-1}\left[\frac{\left(K_p+1\right)k_1+\left(K_p-3\right)k_2}{2}\right] \\ & -\frac{1+K_\psi K_p - v\left(K_p+1\right)\left(K_\psi+1\right)}{\left(K_p-1\right)\left(K_\psi+K_p\right)}\left[(k_1-k_2)-\frac{k_2}{\lambda_e}\right]+\left[\frac{k_1+k_2(3-4v)}{2}\right] \end{aligned} \tag{13}$$

It should be noted that the consistency condition for the parameters C_1, C_2 and C_3 can be established by the following equation:

$$C_1 + C_2 + C_3 = \frac{k_1+k_2(3-4v)}{2} \tag{14}$$

4 Explicit Procedure (EAM)

The explicit procedure used by this study is also called an incremental procedure that can realize and transform the analytical solutions to an executable computation that can be directly calculated by using a simple calculation spreadsheet (e.g., the Microsoft Excel format).

The particular procedure proposed by this paper is called the explicit analysis method (EAM), which can deal with using the confinement loss as an incremental step to simulate the effect of advance excavation of the tunnel face, calculating the stresses and displacements in each step, and drawing the ground reaction curve, the stress path at the intrados of the tunnel, and the distribution of stresses/displacements on the cross-sections of a tunnel. The steps of calculation for the EAM are described by the following representations.

(1) Input data: This relates to the data of the initial is-situ stress, geometry of the tunnel, material properties, and unsupported distance.

(2) In order to estimate the confinement loss λ_z at a certain distance z from the tunnel working face, one can use a chosen advance effect function of tunnel excavation. Therefore, λ_z can be determined.

(3) Dividing the confinement loss λ_z by n segments, the incremental step of λ can be expressed as

$$\Delta\lambda = \frac{1}{n}(1-\lambda_z)\frac{(k_1+k_2)}{2} \tag{15}$$

(4) Calculating each step value of λ as

$$\left.\begin{array}{ll}\lambda_{i+1} = \lambda_z & i = 0 \\ \lambda_{i+1} = \lambda_i + i\Delta\lambda & i = 1 \sim (n-1)\end{array}\right\} \quad (16)$$

(5) Attaining the final value $\lambda_n = \lambda_{i+1}$

(6) According to the Eq. (6), to estimate the confinement loss in the elastic limit situation λ_e.

(7) If $\lambda_{i+1} < \lambda_e$, it means that the stress state is in the elastic region, and that the radial and circumferential stresses/displacements can be calculated with Eqs. (1), (2) and (8).

(8) If $\lambda_{i+1} \geq \lambda_e$, it means that the stress state is in the plastic region, and that the plastic radius R_p can be calculated with Eq. (7). Once one obtains this value R_p, the procedure automatically substitutes into Eqs. (3), (4), and (10) for the radial and circumferential stresses/displacements, respectively.

(9) Recording the calculated data, it relates to the ground reaction curve (u_r, σ_r), the stress path (σ_r, σ_θ) and the distribution of stresses/displacements (σ_r, r), (σ_θ, r), and (u_r, r).

(10) When $i < n-1$, repeat steps (5) through (10).

(11) When $i = n-1$, the process is not repeated, and the data from each step is recorded.

(12) Drawing the ground reaction curve, the stress path at the intrados of the tunnel, and the distribution of stresses/displacements on the cross-sections of the tunnel.

5 Comparison Between Explicit Analysis (EAM) and Numerical Analysis (FEM)

In order to investigate the results obtained by the analytical solutions which are realized by the explicit procedure (EAM), it is necessary to try to find the numerical analysis, or finite element method (FEM), which can provide rigorous results for comparison.

In this study, the mesh prepared of finite element analysis includes that the analysis boundary supported by rollers is twenty times the tunnel excavation radius, using three group elements (excavation, lining and rock mass), 658 elements (540 Q8 elements and 118 T6 elements) and 1971 total nodes; and these conditions are shown in Fig. 1. The input data of calculation considered the in-situ stress ratio, K_o = 0.8 and 1.2, is shown in Table 1. The comparison of results calculated by the EAM and FEM includes the stresses and displacements at the intrados of the tunnel and the distribution on the cross-sections of the tunnel.

5.1 Stresses/Displacements at Intrados of Tunnel

The comparison of GRCs in the elastic-perfectly plastic part is shown in Fig. 2, in which the observable appearance of the influence of in-situ stress ratio in this part of GRC are similar to those investigated in the elastic part. However, the radial

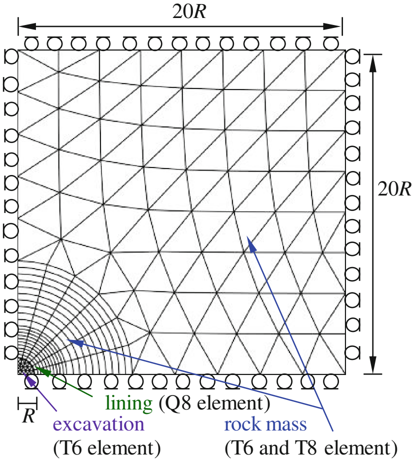

Fig. 1. Finite element mesh and boundary condition.

Table 1. Input data of calculation

Parameter	Value
In-situ stress ratio, K_o	0.8, 1.0, 1.2
Vertical stress, σ_v (MPa)	1.0
Tunnel radius, R (m)	5.0
Elastic modulus, E (MPa)	300
Unit weight, γ (MPa/m)	0.02
Poisson's ratio, v	0.25
Cohesion, c (MPa)	0.1
Friction angle, ϕ (°)	30
Dilation angle, ψ (°)	30

displacements obtained by the EAM and FEM are slightly different in terms of the maximum values, and the trends of GRCs simulated among these methods at different locations of the intrados of the tunnel are very consistent from $\lambda = 0$ to $\lambda = 1$.

In addition, for the stress path in the elastic-perfectly plastic part shown in Fig. 3, it displays very suitable trends for the stress path as simulated by the EAM and FEM. This stress path may follow along the line of Mohr-Coulomb failure criterion, finally attaining the last value of σ_c/σ_v.

Finally, it should be noted that the previously obtained results clearly give an important sign that the stresses/displacements at different locations of the intrados of the tunnel exhibit different characteristic trends (e.g. $\theta = 0°$, 45° and 90°); however, the stresses/displacements are caused with the same value of confinement loss which corresponds to a distance to tunnel working face.

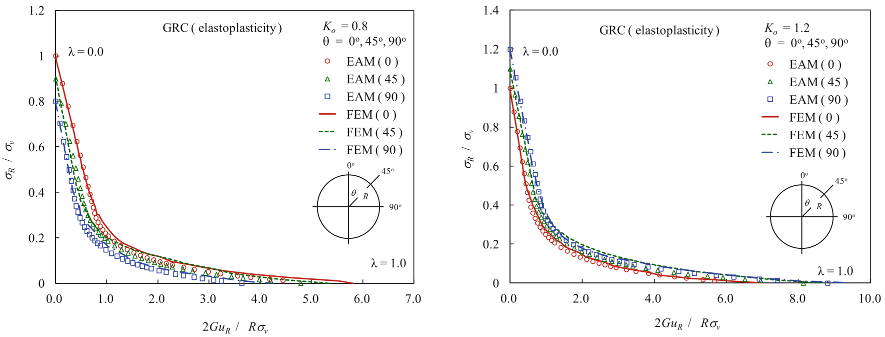

Fig. 2. Comparison of the ground reaction curves between the explicit analysis (EAM) and numerical analysis (FEM) in elastic-perfectly plastic media under anisotropy stress state conditions (a) $K_o = 0.8$ and (b) $K_o = 1.2$

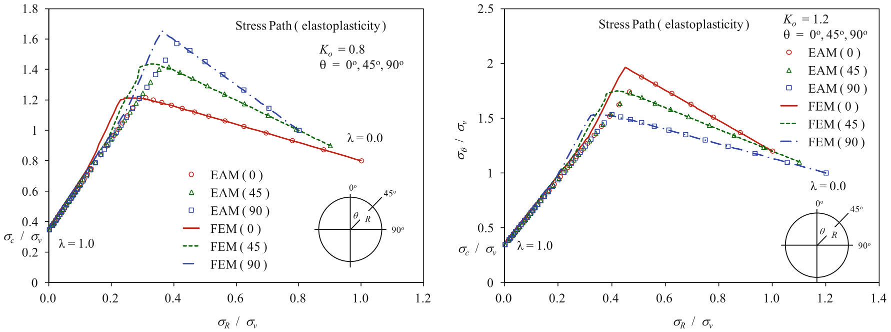

Fig. 3. Comparison of the stress paths at the intrados of the tunnel between the explicit analysis (EAM) and numerical analysis (FEM) in elastic-perfectly plastic media under anisotropy stress state conditions (a) $K_o = 0.8$ and (b) $K_o = 1.2$

5.2 Distribution of Stresses/Displacements on the Cross-Sections of Tunnel

Surrounding a circular tunnel excavation in an anisotropy stress state, one is interested in the distribution of stresses/displacements on the cross-sections of the tunnel.

From the point of view of continuity of stresses at the elastic-plastic interface, the stresses are proved and continuously connected in this interface. The comparison of the distribution of stresses between the EAM and FEM presents not only an approximate value, but also is consistent with the trends shown in Figs. 4 and 5.

In Fig. 4, the distribution of stresses at the crown in the cases of $K_o = 0.8$ and 1.2 is just contrary to each other. The radial displacement is also proved and continuously connected in this elastic-plastic interface. The comparison of the radial displacement distribution between the EAM and FEM is very consistent with the trends shown in Fig. 5.

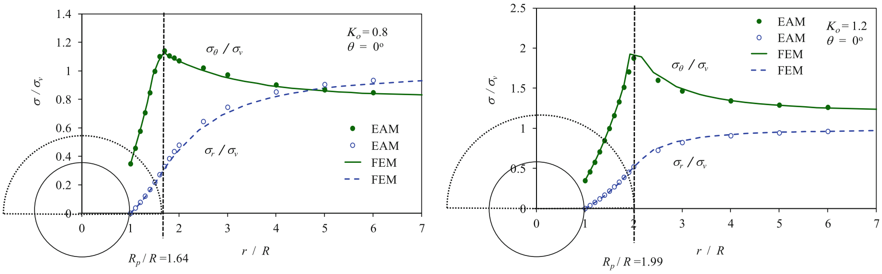

Fig. 4. Comparison of the distribution of stresses at the crown on the cross-sections of the tunnel between the explicit analysis (EAM) and numerical analysis (FEM) in elastic-perfectly plastic media under anisotropy stress state conditions (a) $K_o = 0.8$ and (b) $K_o = 1.2$

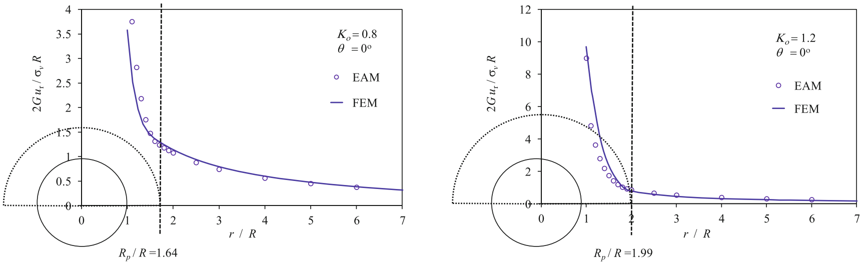

Fig. 5. Comparison of the distribution radial displacement at the crown on the cross-sections of the tunnel between the explicit analysis (EAM) and numerical analysis (FEM) in elastic-perfectly plastic media under anisotropy stress state conditions (a) $K_o = 0.8$ and (b) $K_o = 1.2$

6 Conclusion

The following main conclusions can be drawn from the present study: (1) A theoretically consistent closed-form analytical solution was derived for the elastic-perfectly plastic analysis of a circular tunnel in a rock mass governed by Mohr-Coulomb failure criterion and subject to an anisotrpic in-situ stress. (2) The procedure of the explicit analysis method (EAM) is particularly proposed to deal with using the confinement loss as an incremental step to simulate the effect of advance excavation of the tunnel face, calculating the stresses and displacements in each step. (3) The agreement between the finite element results and the proposed closed-form solutions with the explicit procedure was found to be excellent in elastic-perfectly plastic media.

References

1. Pacher, F.: Deformationsmessungen in Versuchsstollen als Mittel zur Erforschung des Gebirgsverhaltens und zur Bemessung des Ausbaues. Felsmechanik und Ingenieursgeologie Supplementum IV, pp. 149–161 (1964)

2. Panet, M.: Le Calcul des Tunnels par la Méthode de Convergence-Confinement. Presses de l'Ecole Nationale des Ponts et Chaussées, Paris (1995)
3. AFTES, Panet, M. et al.: Recommendations on the convergence-confinement method. Association Française des Tunnels et de l'Espace Souterrain, pp. 1–11 (2001)
4. Detournay, E., St. John, C.M.: Design charts for a deep circular tunnel under non-uniform loading. Rock Mech. Rock Eng. **21**, 119–137 (1988)
5. Ravandi, E.G., Rahmannejad, R.: Wall displacement prediction of circular, D shaped and modified horseshoe tunnels in anisotropy stress fields. Tunn. Undergr. Space Technol. **34**, 54–60 (2013)
6. Lee, Y.L.: Prise en compte des non-linéarité de comportement des sols et des roches dans la modélisation du creusement d'un tunnel. Thèse, École Nationale des Ponts et Chaussées (1994)
7. Lee, Y.L., Tsai, L.J., Lee, W.Y.: Explicit analysis for the ground response behavior due to the advancing excavation of tunnel under anisotropic stress field. J. Chin. Inst. Civil Hydraul. Eng. **25**(3), 231–240 (2013)

Analysis of Large-section Tunnels with Small Spacing in Elastoplastic Stress-seepage-damage Model

Meng-fei Xu[1(✉)], An-nan Jiang[1], Gao Lin[2], Zhang Xue-liang[2],
and You-fu Wang[2]

[1] Highway and Bridge Institute of Dalian Maritime University,
Dalian 116026, China
`824599159@qq.com`
[2] China Construction Eighth Engineering Division Corp. Ltd., Dalian Branch,
Dalian 116000, Liaoning, China

Abstract. Small spacing tunnels has the characteristics of large-section, lower flat-ratio and poor surrounding rock stability and its stability is significantly influenced by seepage field. The coupling effect of stress-seepage-damage on surrounding rock is obviously. According to this, the FEM calculation program based on elastoplastic stress-seepage-damage model of rock is established. Back analysis program is compiled on the basis of the principle of differential evolution algorithm in order to solve the problem that elastoplastic damage model involves many parameters and not so easy to determine. The calculating program is used to calculate the stability of Da-Dongshan tunnel which has large-section with small spacing. The parameters are identified by using back analysis program based on the displacement date from field monitoring. The stress distribution and seepage filed of the supporting structure are analyzed. The results show that the stability of surrounding rock is influenced by groundwater seepage which would increase the damage zone.

Keywords: Large section and small spacing tunnels
Elastoplastic stress-seepage-damage model · Damage zone of surrounding rock

1 Introduction

With the size of transportation infrastructure growing in China, more and more super highways construction which pass through mountains is needed especially. Two-lane tunnels have not meet the increasing traffic. The task to build more than three lanes of large cross section tunnel is getting heavier [1]. Meanwhile, due to the terrain or geological conditions, it is more difficult to tunnel line and cover areas so that small spacing tunnels also have been widely used.

Because of the particular and novelty of large-section tunnel with small spacing, its holes and middle rock pillars have obviously mutual influence during construction process. Furthermore, as the tunnels cross section is big, its flat rate is low and its stability of surrounding rock is poor. Therefore, the stress state of the structure is complicated in both design and construction view. Especially in areas where have rich

© Springer Nature Singapore Pte Ltd. 2018
D. Zhang and X. Huang (Eds.): GSIC 2018, *Proceedings of GeoShanghai 2018 International Conference: Tunnelling and Underground Construction*, pp. 63–73, 2018.
https://doi.org/10.1007/978-981-13-0017-2_6

underground water, seepage has important influence on actual rock engineering stability [2]. After excavation, mechanical properties and hydraulic characteristic of rock mass changes obviously. As the crack initiating, propagating and penetrating, rock permeability has changed greatly. Before rock damage, the permeability of rock is low, the stress-seepage coupling effect is insignificant. However the stress and water pressure induced new damage process. Along with expansion of the cracks, the mutual influence of stress-hydraulic-damage coupling effect becomes more obviously.

This paper established rock elastoplastic damage constitutive model based on Druker-Prager yield criterion. Implicit return mapping was adopted to implement elastoplastic, damage constitutive equation of numerical solution. Secondly, according to the rock coefficient of permeability dynamic evolution formula in elastoplastic state, the rock elastoplastic-hydraulic-damage model was established, the numerical iteration solution under the action of three field coupling which is implemented in C++ program. According to the monitoring data, the Differential Evolution method is used to confirm the damage coefficient. Finally, the stress and displacement state was calculated numerically in conditions of different water pressure. The result shows that fissure water aggravate the damage of surrounding which can provide theoretical basis for actual tunnel excavation.

2 Rock Elastoplastic-Hydraulic-Damage Model and Its Solve Program

According to elastoplastic mechanics, hydraulic mechanics, damage mechanics theory, the rock constitutive relation based on Druker-Prager yield criterion, the equivalent plastic strain damage variable and the coefficient of permeability evolution equation is used to establish the rock elastoplastic-hydraulic-damage coupling equation. The object-oriented finite element program is build which provide an effect method to solve the elastoplastic-hydraulic-damage coupling problem.

2.1 Rock Stress State Equation

For a micro cell body rocks, the stress components should satisfy the static equation. The balance differential equation in Cartesian coordinates is build as shown below.

$$\frac{\partial \sigma_{ij}}{\partial x_{ij}} + f_j = 0 \quad (i,j = 1,2,3) \tag{1}$$

Elastic-plastic boundary value problem is shown in Fig. 1.

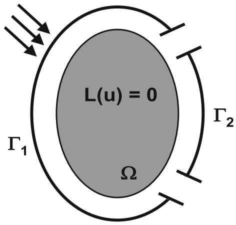

Fig. 1. Elastic-plastic boundary value problem

Boundary value problem consists of three components as Eq. 2.

$$\begin{aligned} &L(\mathbf{u}) = \sigma_{ij,i} + f_j = 0 \text{ on } \Omega \\ &\sigma_{ij} n_i = \bar{t}_j \quad \text{on } \Gamma_1 \\ &u_k \ = \overline{u_k} \qquad \text{on } \Gamma_2 \end{aligned} \tag{2}$$

where f_i is volume force. σ_{ij} is total stress tensor. Ω is problem solving domain. *ni* is the boundary normal cosine. t_j is known surface force on known surface. Γ_1 is known force boundary. Γ_2 is known displacement boundary.

The relation between stress and strain in different constitutive mode is also different. Constitutive equation is shown below.

$$\sigma_{ij} = f(\varepsilon_{ij}) \tag{3}$$

The geometric equations:

$$\varepsilon_{kl} = \frac{1}{2}\left(u_{k,l} + u_{l,k}\right) = u_{(k,l)} \tag{4}$$

where ε_{kl} is strain tensor. $u_{(kl)}$ is displacement vector.

The boundary value problem is transformed to the problem of solving displacement ***u.*** When the displacement ***u*** is solved out, stress and strain state can be get through geometric equation and constitutive equation.

The principle of effective stress in porous media is shown below.

$$\sigma'_{ij} = \sigma_{ij} - \delta_{ij}\alpha\, p \tag{5}$$

where σ'_{ij} is effective stress tensor (compression is positive, tension is negative); p is pore water pressure. α between 0 and 1 is coefficient of effective pore pressure. δ_{ij} is Kroneker symbol.

2.2 Seepage Equation

Seepage continuity equation without source unstable can be obtained based on Darcy's law assuming that water is impressible.

$$\frac{\partial}{\partial x}(k_x \frac{\partial h}{\partial x}) + \frac{\partial}{\partial y}(k_y \frac{\partial h}{\partial y}) + \frac{\partial}{\partial z}(k_z \frac{\partial h}{\partial z}) = S_s \frac{\partial h}{\partial t} \tag{6}$$

Substituting $h = (p/\gamma) + z$ into formula (6) can obtain:

$$\frac{\partial}{\partial x}(k_x \frac{\partial p}{\partial x}) + \frac{\partial}{\partial y}(k_y \frac{\partial p}{\partial y}) + \frac{\partial}{\partial z}(k_z \frac{\partial p}{\partial z}) = \gamma S_s \frac{\partial h}{\partial t} \tag{7}$$

where h is penetration head; x, y, z are space coordinates; t is time coordinate; k_x,k_y,k_z are the osmotic coefficients in x, y, z for principal axis direction; S_s is unit of storage capacity. γ is unit weight of water; p is pore water pressure.

The initial conditions for unsteady seepage free surface without pressure is shown below:

$$h|_{t=0} = h_0(x, y, z, 0) \tag{8}$$

Water head and flow initial condition:

$$\begin{aligned} &h|_{\mathrm{M}_1} = f_1(x, y, z, t) \\ &k_n \tfrac{\partial h}{\partial n}\Big|_{\mathrm{M}_2} = f_2(x, y, z, t) \end{aligned} \tag{9}$$

where M_1 is known water head, f_1 is known head, M_2 is the known flow boundary, f_2 is the known value of known boundary.

Differential equations of equilibrium can be obtained based on principle of effective stress according to the principle of effective stress formula (5) and equilibrium conditions (1).

2.3 Damage Variable and Its Evolution Equation

The equivalent plastic strain $\bar{\varepsilon}^p$ is used to represent evolution process of rock damage variable [3]. The experiment shows that the damage valuable grows as $\bar{\varepsilon}^p$ increases. Damage variable is the nonlinear function about $\bar{\varepsilon}^p$.

The equivalent plastic strain $\bar{\varepsilon}^p$ can be calculated as follows:

$$\bar{\varepsilon}^{\mathrm{p}} = \frac{\sqrt{2}}{3}\sqrt{(\varepsilon_{\mathrm{p1}} - \varepsilon_{\mathrm{p2}})^2 + (\varepsilon_{\mathrm{p2}} - \varepsilon_{\mathrm{p3}})^2 + (\varepsilon_{\mathrm{p3}} - \varepsilon_{\mathrm{p1}})^2} \tag{10}$$

where ε_1, ε_2, ε_3 are three principal plastic strain respectively.

The equivalent equation for damage $\boldsymbol{D}$ is:

$$D = 1 - \exp[-\kappa(\bar{\varepsilon}^p - \bar{\varepsilon}_0^p)] \tag{11}$$

where $\bar{\varepsilon}_0^p = 0$ is the threshold value of equivalent plastic strain which means the equivalent plastic strain produced damage evolution. κ is the normal number from experiment.

The formula (11) shows that damage evolves as the increase of cumulative plastic strain, and finally tends to be stable.

The simultaneous stress field Eq. (2), seepage differential equations Eq. (6), damage evolution Eq. (11), and the corresponding initial and boundary conditions (8) and (9) can be used to build the numerical model for stress-damage field and seepage field coupling. Water pressure and rock mass strain relation is used as a bridge to implement coupling interaction of meantime. For unsteady seepage flow, two equations talked above have double coupling effect which the first layer has the property of three dimensional Biot consolidation equations. It is the coupling effect of fluid pressure and rock stress; The second layer is that the rock stress or strain changes its permeability properties to affect the distribution of seepage field, and then reacts on rock stress filed. The seepage continuous equation of the right end is zero for unsteady seepage flow, coupling effect is reflected in the second floor above.

2.4 The Stress-seepage Coupling Equation

The permeability coefficient and strain (or stress) equation is necessary for seepage-stress coupling numerical analysis control equation. In this paper, the permeability coefficient is defined as function of stress and damage respectively based on different rock mass stress state to realize the different evolution law of the permeability coefficient of rock mass (K) in elastic and plastic stage. Under this circumstance, once the rock material yields, the rock permeability will be increased dramatically due to the original cracks extension, cut-through and a large number of new cracks generate. Therefore, some scholars introduce the concept of area reduction rate or sudden jump coefficient to simulate rock damage under seepage effect [4].

Relational expression between the rock mass coefficient of permeability and volume strain can be obtained based on in the elastic stage Kozeny-Carman formula:

$$K = K_0 \frac{[1 + \varepsilon_{\mathrm{v}}/n_0]^3}{1 + \varepsilon_v} \tag{12}$$

Where n_0 is the initial porosity.

The permeability coefficient of the rock in plastic phase using the following formula:

$$K = (1 - D)K^{\mathrm{M}} + DK^{\mathrm{D}}(1 + \varepsilon_{\mathrm{v}}^{\mathrm{pF}})^3 \tag{13}$$

Where K^M and K^D are permeability coefficient of the non-damage rock and fractured rock respectively; $\varepsilon_{\mathrm{v}}^{\mathrm{pF}} = D\varepsilon_{\mathrm{v}}^{\mathrm{p}}$ is defects of plastic volume strain.

2.5 Numerical Solving and Step Iteration Method for Coupling Model

Finite element method has been widely used as a numerical method applied to solve nonlinear. Based on solid and seepage finite element theory, the elastoplastic constitutive integration theory and fractional step iteration coupling method has been used to compile the program of elastic-plastic stress-seepage-damage model.

The finite element equations were obtained taking the displacement as unknown variables, its incremental form after discrete the formula (2)–(5) is shown below:

$$[K_m]\{u\} = \{f_m\} \text{ or } [K_m(\Delta u)]\{\Delta u\} = \{\Delta f_m\} \tag{14}$$

where $[K_m]$ is the total stiffness matrix of stress field; $\{u\}$ is the node displacement column vector; Δu is increment displacement; $\{\Delta f_m\}$ is nodal force vector that includes physical strength, surface strength and pore pressure of the equivalent load.

The overall stiffness matrix K is assembled with element stiffness matrix. $K_T^{(e)}$ is the function of consistent tangent modulus C as follows:

$$K_T^{(e)} = \int_{\Omega(e)} B^T C B dv \tag{15}$$

Drucker-Prager is widely adopted in rocks and other materials to describe the plastic stress and deformation characteristics. The damage effect on the plastic yield function showed as follows:

$$f^p(\sigma, \bar{\varepsilon}^p, D) = \sqrt{J_2(s(\sigma))} + \eta p(\sigma) - (1 - D)\xi c(\bar{\varepsilon}^p) \tag{16}$$

where $p = 1/3tr[\sigma]$; $J_2 = 1/2\ s{:}s$; s = $\sigma\text{-}p(\sigma)\boldsymbol{I}$, $I = \delta_{ij} e_j \otimes e_j, i, j = 1, 2, 3$; $c(\bar{\varepsilon}^p)$ is the cohesive under the damage; D is damage variable.

Displacement increment is obtained by formula (14) to calculate strain incremental by displacement. Each iteration step are calculated from a given strain increment stress increment, the solution of the stress associated with the selection of constitutive model. This paper adopts Drucker-Prager constitutive model to solve formula (16). Fully implicit return mapping algorithm is used as constitutive integration algorithm [5] (Fig. 2).

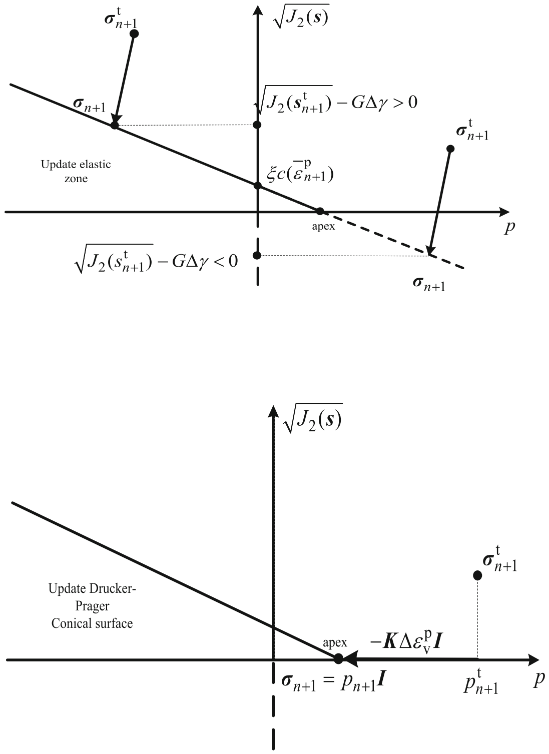
$\boldsymbol{\sigma}_{n+1}^{t}$
$\sqrt{J_2(\boldsymbol{s})}$
$\boldsymbol{\sigma}_{n+1}$
$\sqrt{J_2(\boldsymbol{s}_{n+1}^{t})} - G\Delta\gamma > 0$
$\boldsymbol{\sigma}_{n+1}^{t}$
Update elastic zone
$\xi c(\bar{\varepsilon}_{n+1}^{p})$
apex
p
$\sqrt{J_2(s_{n+1}^{t})} - G\Delta\gamma < 0$
$\boldsymbol{\sigma}_{n+1}$
$\sqrt{J_2(\boldsymbol{s})}$
$\boldsymbol{\sigma}_{n+1}^{t}$
Update Drucker-Prager Conical surface
apex
$-\boldsymbol{K}\Delta\varepsilon_{v}^{p}\boldsymbol{I}$
$\boldsymbol{\sigma}_{n+1} = p_{n+1}\boldsymbol{I}$
p_{n+1}^{t}
p

Fig. 2. Stress mapping method for D-P constitutive model

Disperse the seepage field into combinations of a finite number of units. Disperse the formula (6) to solve the seepage field in the hydraulic head function h of finite element basic equations, the formula as:

$$[K_s]\{h\} = \{f_s\} \tag{17}$$

where $[K_s]$ is seepage matrix; $\{h\}$ is hydraulic head column vector; $\{f_s\}$ is free term column vector. Thus the original solution of the partial differential equation is instead of by solving algebraic equations.

In this paper, fractional step iteration method is used to implement the elastic-plastic stress and damage-seepage coupling. Elastic-plastic stress-seepage-da-mage coupling process shows as in Fig. 3.

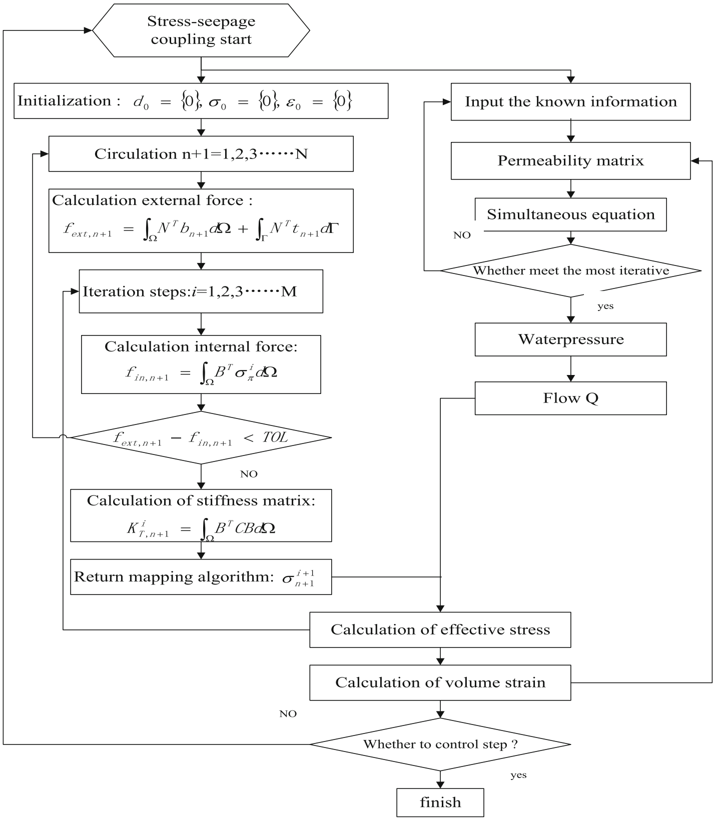
Stress-seepage coupling start
Initialization : $d_0 = \{0\}, \sigma_0 = \{0\}, \varepsilon_0 = \{0\}$
Circulation n+1=1,2,3······N
Calculation external force :
$f_{ext,n+1} = \int_\Omega N^T b_{n+1} d\Omega + \int_\Gamma N^T t_{n+1} d\Gamma$
Iteration steps:i=1,2,3······M
Calculation internal force:
$f_{in,n+1} = \int_\Omega B^T \sigma_\pi^i d\Omega$
$f_{ext,n+1} - f_{in,n+1} < TOL$
NO
Calculation of stiffness matrix:
$K_{T,n+1}^i = \int_\Omega B^T CB d\Omega$
Return mapping algorithm: σ_{n+1}^{i+1}
Input the known information
Permeability matrix
Simultaneous equation
NO
Whether meet the most iterative
yes
Waterpressure
Flow Q
Calculation of effective stress
Calculation of volume strain
NO
Whether to control step ?
yes
finish

Fig. 3. Elastic-plastic stress-seepage-damage coupling process

3 The Application for Elastoplastic Model

Da-dong tunnel is part of Bohai sea road engineering which is located in the north of Pulandian in Dalian. The tunnel construction is separated to eight lanes where the west line pile number is from K06 + 890 to K08 + 003.785 and its maximum thickness of its overlying soil is 134.7 m. East line pile number is from K06 + 894–K08 + 004.300 and its maximum thickness of overlying soil is 155 m. The width of tunnel construction architectural boundaries is 17.5 m and its height is 5 m. The width of contour line is 18.184 m and its height is 10.1 m. The total line belongs to small spacing tunnel.

During the investigation, there is groundwater development during control drilling depth which belongs to phreatic water that mainly occurrence in the bedrock fissure.

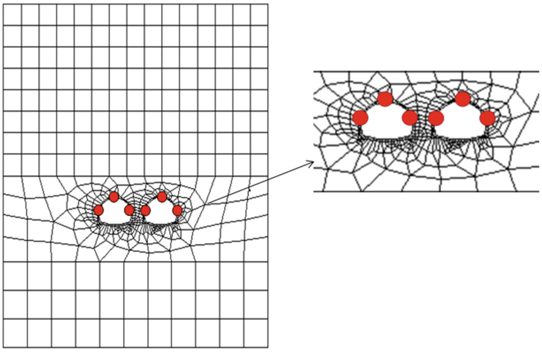

Fig. 4. Calculation model for Da-dong tunnel

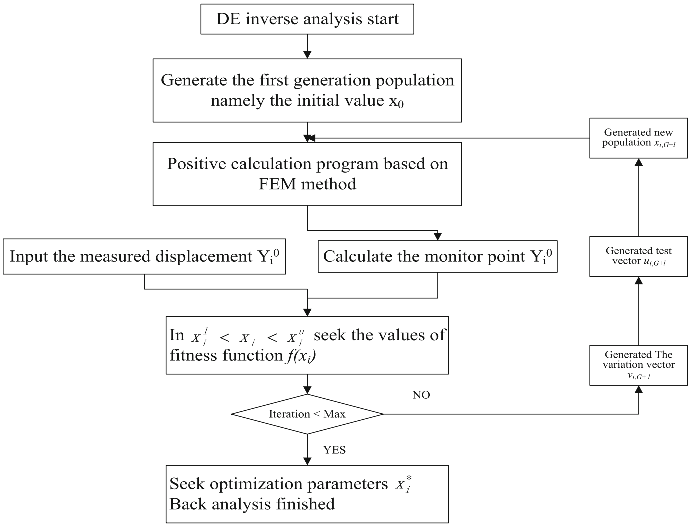
DE inverse analysis start
Generate the first generation population namely the initial value x_0
Positive calculation program based on FEM method
Input the measured displacement Y_i^0
Calculate the monitor point Y_i^0
In $x_i^l < x_i < x_i^u$ seek the values of fitness function $f(x_i)$
Iteration < Max
NO
YES
Seek optimization parameters x_i^* Back analysis finished
Generated The variation vector $v_{i,G+1}$
Generated test vector $u_{i,G+1}$
Generated new population $x_{i,G+1}$

Fig. 5. DE inversion analysis program process

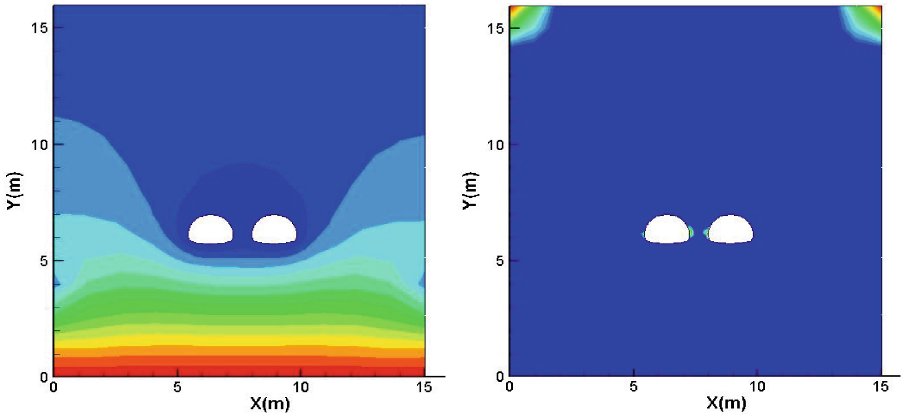

Water pressure

Damage zone

H=3m

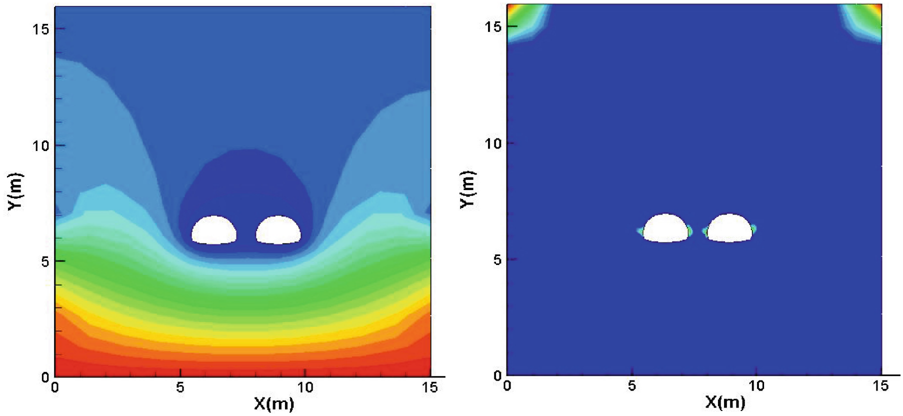

Water pressure

Damage zone

H=6m

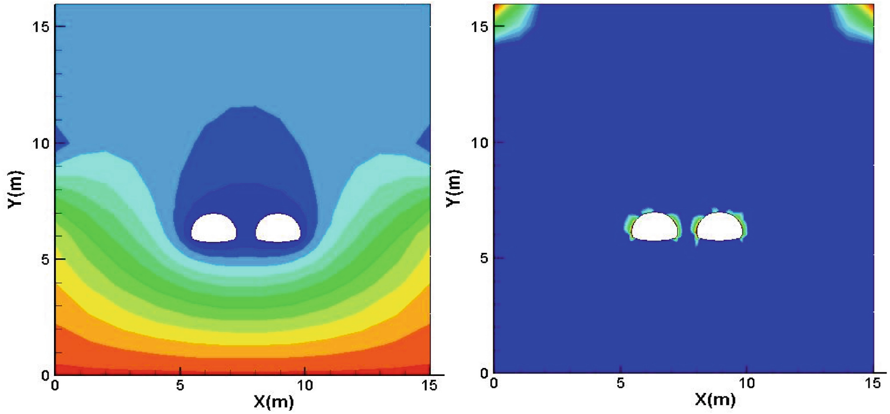

Water pressure

Damage zone

H=9m

Fig. 6. Contour map of water pressure and damage zone under different water height

Its mainly source is atmospheric precipitation and the mainly discharge way is evaporation and spring.

3.1 Damage Parameters Inversion Based on Differential Evolution Algorithm

In this paper, DK06 + 670 is selected as research object and generalized into a numerical model. Tunnel plane strain finite element model is established, calculation model range x-axis direction is 15 m wide and y-axis height is 17 m. Quadrilateral element is adopted to divide the surrounding rock, and the model is divided into 465 elements and 527 nodes.

The calculation model is established as Fig. 4 and the red circles is monitor points to inverse the rock damage parameters.

The differential evolution method is used to inverse the damage parameters c_r, η and κ. The program process is shown as follows [6] in Fig. 5.

According to the field monitoring data, inversion damage parameters of surrounding rock are calculated as follows: cohesive force of obvious damage c_r is 75 kPa, η is 0.7, damage parameter κ is 70.

3.2 Stress State Under Different Water Height

Based on the coupling calculation model built above, the efficient of underground water on the stability of surrounding rock is analysis. Different water height H is set and the result is shown as follows in Fig. 6.

According to Fig. 6, the damage zone increases as water height higher which means seepage field has an important influence on static stress state. Pore water aggravate the surrounding rock damage processing. The calculation result will be inaccurate if the pore water was not taken into consideration.

4 Conclusion

The rock stress-seepage-damage coupling model is established and the numerical calculation method is given.

The differential evaluation method was used to confirm the damage parameter. The coupling model was used to calculate the damage zone under different water height. The result shows that underground water has an important influence on surrounding rock stability.

For large-scale water conservancy and hydropower project, undersea tunnels and so on, the engineering safety problems need to consider the stress-hydraulic-damage coupling phenomenon of rock to make the numerical calculation more reality to guide the project construction.

Acknowledgement. This paper is supported by national nature science funds of China (51678101).

References

Zhang, D.L., Wang, M.-S., Jun, G., et al.: Construction technique of large-span- tunnel under condition of complicated surrounding rocks. Chin. J. Rock Mech. Eng. **22**(2), 290–296 (2003)

Li-yuan, Y., Shu-cai, L., Bang-shu, X., et al.: Study of solid-fluid coupling model test and numerical analysis of underwater tunnels. Chin. J. Rock Mech. Eng. **30**(7), 1467–1474 (2011)

Shan-po, J., Wei-zhong, C., Hong-dan, Y., et al.: Research on seepage-stress coupling damage model of boom clay during tunneling[J]. Rock Soil Mech. **30**(1), 19–26 (2009)

Qi-quan, R., Xiao-yun, G.: Coupling analysis of multiphase flow and stress for oil reservoir. Chin. J. Geotech. Eng. **20**(2), 69–73 (1998)

Jun-xiang, W., An-nan, J.: Elastoplastic damage constitutive model of rock considering the action of the pore water pressure and numerical algorithm. Rock Soil Mech. (in press)

Jun-xiang, W., An-nan, J., Song, Z.: Study of the coupling model of rock elastoplastic stress-seepage-damage (I): Modelling and its numerical solution procedure. Rock Soil Mech. **35**(2), 626–644 (2014)

Parametric Study on Stability of Tunneling Excavation Face via Fluid-Solid Coupling Simulation

Jinlong Li[1], Zhijun Kang[1,2], and Yong Tan[1](✉)

[1] Tongji University, Shanghai, China
tanyong21th@tongji.edu.cn
[2] Poly (CHENGDU) Holdings Company Limited, Chengdu 610000, China

Abstract. In case of shallow buried depth and high hydraulic pressure, it was very difficult to control excavation face stability during shield tunneling, frequently followed by catastrophic results (e.g., significant subsidence due to collapse of tunneling face). Based on three-dimensional (3D) numerical parametric analyses validated by centrifuge model test results, this study investigates the effect of supporting pressure on tunneling face stability, in terms of deformation of tunneling face and ground settlement and so on. To simulate the cases featuring high groundwater level, complete fluid-solid coupling calculation was taken into account in the numerical analyses. This was achieved by assuming that shield was in a shutdown state; meanwhile, by reducing excavation pressure gradually and setting the seepage time, the relationship between the stress-strain of the strata surrounding shield and supporting pressure of tunneling were explored.

Keywords: Fluid-solid coupling simulation · Stability of excavation face
Displacements of tunneling excavation face and ground · Supporting pressure

1 Introduction

With rapid urbanization in China, shield tunneling technology is widely used for utilization of underground space (e.g., subway tunnels, utility tunnels, and cross-river tunnels). Because of challenging geological and hydraulic conditions as well as congested urban environment, accidents associated with tunneling were frequently reported. One of them was instability of tunneling excavation face due to lack of excavation support pressure and associated excessive ground subsidence (e.g., Gao 2010). When shield tunneling was conducted underwater, water seepage would significantly affect stability of tunneling excavation face because of shallow overburdening soils and high water pressure. Many studies have been contributed to stability of excavation face under seepage conditions in recent years, in terms of analytical methods, centrifuge testing and numerical simulations. Using wedge model, Anagnostou and Kovári (1996) analyzed effect of seepage on stability of excavation surface. Schweiger et al. (1991) pointed out that seep-age force is an important part of the excavation face support pressure and its ratio in the total support force will increase with rising of water level.

© Springer Nature Singapore Pte Ltd. 2018
D. Zhang and X. Huang (Eds.): GSIC 2018, *Proceedings of GeoShanghai 2018 International Conference: Tunnelling and Underground Construction*, pp. 74–83, 2018.
https://doi.org/10.1007/978-981-13-0017-2_7

When studying influence of groundwater seepage on stability of tunneling excavation face in numerical simulation, it is often to calculate steady state seepage first, and the calculated seepage forces were treated as stress boundary to calculate the mechanical equilibrium (e.g., Qin 2005; Huang et al. 2006). The coupling effect between stress field and seepage field was not taken into account. In this study, numerical simulations, which considered fluid-solid coupling effect, were carried out to study stability of shield tunnel excavation subject to high water pressure.

2 Numerical Model of Simulated Excavation Face Instability

2.1 The Calculation Method

In this paper, it's assumed that the shield is in a shutdown state (e.g. Zhu 2010). The relationship between horizontal displacement of the excavation face and support pressure is considered by reducing the excavation face supporting pressure step by step and setting a certain seepage time to carry out the complete flow-solid coupling calculation (e.g. Wu 2007; Deng et al. 2016). To achieve the simulation purpose of flow-solid coupling, this paper calculates the deformation of soil element in FLAC3D mechanical equilibrium and then calculates the variety of pore water pressure caused by the deformation of soil element in fluid coupling so that the deformation of soil element can be calculated again by the change of effective stress. The horizontal displacement of the center point of the excavation face increases gradually with the decrease of the supporting pressure ratio.

When the horizontal displacement is increased sharply and the change of support pressure ratio is small, the damage of the excavation face occurs.

The supporting force of the central point of excavation face is used to represent the supporting force of the whole excavation face. The concept of support pressure ratio λ is introduced to characterize support pressure:

$$\sigma_s = \lambda \cdot \sigma_0 \tag{1}$$

Where σ_s stands for the support pressure value of center point of excavation face, σ_0 stands for the static earth pressure value of the original formation at the center point of excavation face.

The numerical calculation flow of the simulated excavation face is shown in the following Fig. 1:

2.2 Calculation Method Validation

In order to verify the rationality of the numerical calculation method of the simulated excavation face instability, this paper uses the result of centrifugal test model (Lü et al. 2016) to examine the numerical model. The comparison results are shown in Fig. 2. It can be seen that in the dry sand and saturated sand strata, the displacement curve of the numerical simulation and centrifugal test of the excavation face fits well, the ultimate support pressure is also similar.

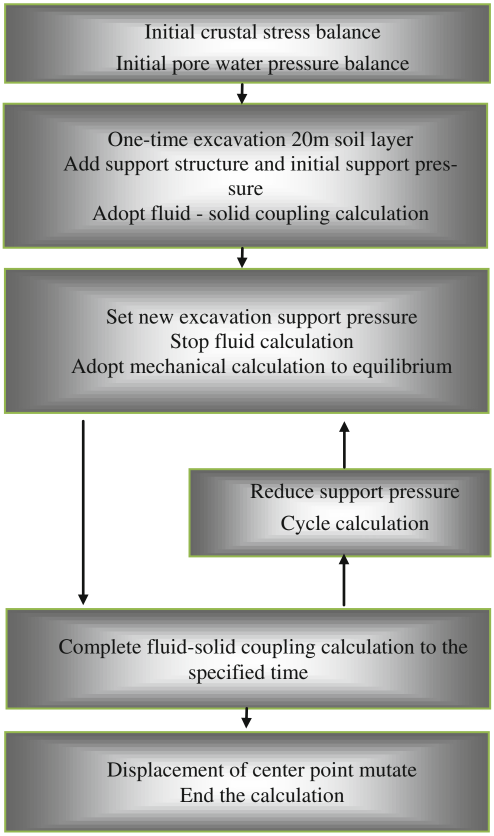
Initial crustal stress balance
Initial pore water pressure balance
One-time excavation 20m soil layer
Add support structure and initial support pressure
Adopt fluid - solid coupling calculation
Set new excavation support pressure
Stop fluid calculation
Adopt mechanical calculation to equilibrium
Reduce support pressure
Cycle calculation
Complete fluid-solid coupling calculation to the specified time
Displacement of center point mutate
End the calculation

Fig. 1. Flow chart of cycle calculation

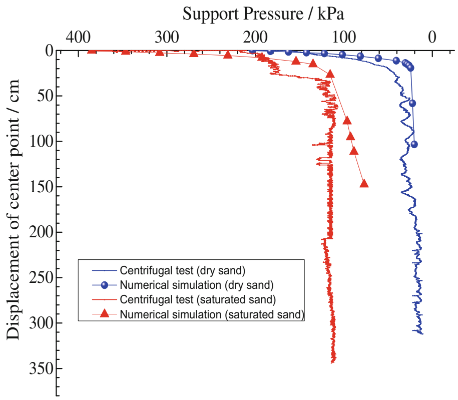

Fig. 2. Development curves of horizontal displacement at center of tunneling face

3 Numerical Model Establishment

3.1 Model Geometry and Boundary Conditions

In this paper, the tunnel diameter D is 10 m, the covering soil depth C is 10 m. The water line is located at the surface. In order to eliminate the influence of the boundary effect of the numerical model on the calculation results, set the vertical length of the model Lz = 50 m, the horizontal length Lx = 30 m, along the longitudinal length of the tunnel Ly = 50 m. The model grid is shown in Fig. 3.

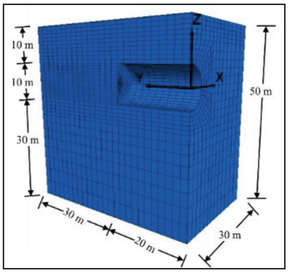

Fig. 3. Mesh of calculated model

Young's modulus E and Poisson's ratio need to be converted into bulk modulus K and shear modulus G by using Flac^{3D}, the conversion formula is as follows:

$$\mathrm{K} = \frac{E}{3(1-2v)} \tag{2}$$

$$\mathrm{G} = \frac{E}{2(1+\upsilon)} \tag{3}$$

3.2 Value of Numerical Model Parameters

The soil which its cohesion is 0 kPa and its internal friction angle is 25° is an ideal homogeneous elastic-plasticity body, also it is subject to Mohr-Coulomb yield criteria. The material of shield segments is C50 reinforced concrete material, which thickness is 0.35 m. SHELL unit is adopted in simulation. The mechanical parameters of soil and tube material are shown in Table 1. In the flow - solid coupling calculation, the soil parameters are measured by the effective stress index, the initial static level of soil pressure using water and soil classification algorithm, the formula is as follows:

$$\sigma_0 = \gamma_w \cdot h + K_0 \cdot \gamma' \cdot h \tag{4}$$

$$\gamma' = \gamma_s - \gamma_w \tag{5}$$

Table 1. Physical and mechanical parameters of soil and segments

Material	Dry weight density γ_d/(kN/m^3)	Saturation weight density γ_s/(kN/m^3)	Elastic modulus E/(MPa)	Poisson's ratio ν
Sand soil	18	23	20	0.35
Segment	24.5	24.5	3.45×10^4	0.17

Where h stands for the soil height, γ_w stands for water heavy, γ' stands for the soil floating weight density, γ_s stands for saturated soil weight density.

The fluid in the simulation is set as an isotropic model, and the flow time T in the flow - solid coupling calculation is 2 h. The parameters of seepage calculation are shown in Table 2.

Table 2. Parameters of seepage calculation

Material	Permeability coefficient k/(m/s)	Bulk modulus Kf/(MPa)	Porosity n	Saturation s	Seepage time T/(h)
Water	10^{-5}	2×10^3	0.5	1.0	2

4 Effect of Supporting Pressure on Tunneling Face Stability

The reduction of support pressure of the excavation face will cause the deformation of surrounding rock as stress releasing. First, the horizontal displacement of the soil near the excavation face occurs toward the shield pressure chamber. The relationship between horizontal displacement of center point of the tunneling face and the change of support pressure can be considered to denote that tunneling face is unstable when the horizontal displacement of center point of the excavation face increases sharply.

The following schematic diagram (Fig. 4) shows the deformation index collected in the numerical simulation:

Where δ_0 stands for the displacement of the center point, d stands for distance from the center point to measuring point, δ_h stands for the displacement of measuring point, δ_{vm} stands for maximum settlement of the longitudinal earth surface, δ_v stands for the settlement of measuring point.

4.1 Displacement of the Center Point of Excavation Face

In Fig. 5 it can be seen that when the support pressure ratio λ is in the range of 0.6–1.0, the horizontal displacement of the center point of the excavation face increases slowly with the decrease of λ. When λ reduces from 0.6 to 0.4, the slope of the curve increases to a certain extent; when λ is cut down to 0.3, the curve steeply declines: the displacement of center point suddenly increases from 9 cm to 91 cm. The buckling collapse of tunneling face has occurred. Figure 5 also shows simulation data that does not take into account the flow-solid coupling effect. The trend of the curve without

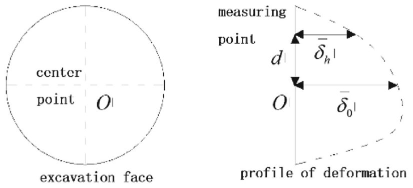
center
point
O
excavation face
measuring
point
d
$\bar{\delta}_h$
O
$\bar{\delta}_0$
profile of deformation

Excavation face deformation diagram

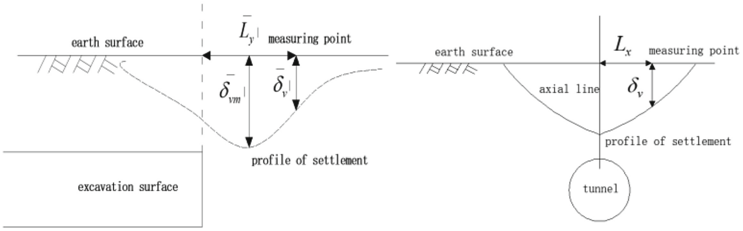
earth surface
$\bar{L}_y$
measuring point
$\bar{\delta}_{vm}$
$\bar{\delta}_v$
profile of settlement
excavation surface
earth surface
L_x
measuring point
axial line
δ_v
profile of settlement
tunnel

Longitudinal settlement diagramHorizontal settlement diagram

Fig. 4. Deformation index diagram

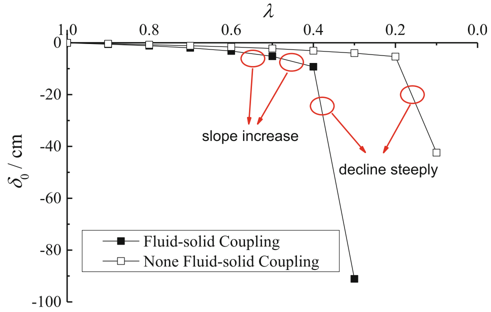

Fig. 5. Development curves of horizontal displacement at center of tunneling face

considering the flow-solid coupling is similar to that of the flow-solid coupling, but the ultimate λ is significantly smaller. When λ is cut down from 0.2 to 0.1, the displacement of the center point abruptly changes.

When λ is 0.6, the soil in front of the excavation face enters the plastic state. When λ is relatively close to 0.5 or 0.4, the plastic zone gradually diffuses into the soil before excavation. The soil plastic area is rapidly expanding and extending to the earth surface as λ is 0.3. The excavation face enters the stage of complete plastic deformation and buckling collapse happens (Fig. 6).

4.2 Deformation of Excavation Face

When λ = 1.0, the excavation face has a very minor horizontal displacement, indicating that in the shield construction process, if the support pressure could balance the soil and

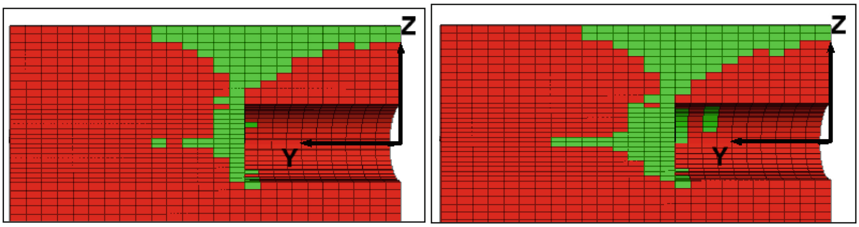

$\lambda = 0.6\lambda = 0.5$

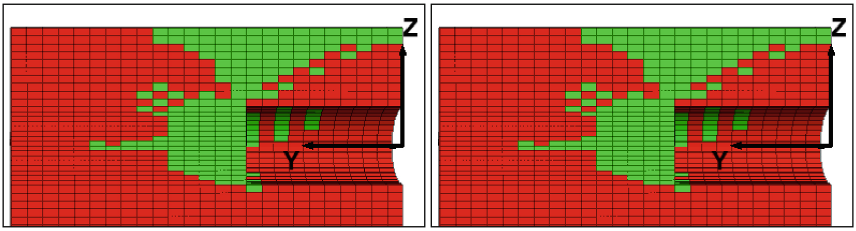

$\lambda = 0.4\lambda = 0.3$

Fig. 6. Development of soil plastic zone

water pressure in front of the excavation within a short time during shield shutdown state, the tunneling face can maintain a steady state. With λ decreases, the horizontal displacement of the excavation face progressively increases, and rate of displacement increases gradually, which is due to the diffusion of soil plastic zone. When λ is reduced to 0.3, because of the rapid diffusion of the plastic zone in the soil to the surface, the excavation face enters the stage of complete plastic deformation. The horizontal displacement of the lower soil of the excavation face is larger (Fig. 7).

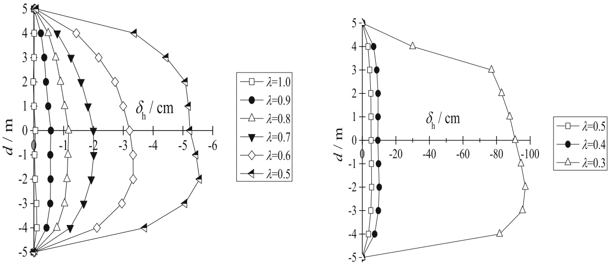

Without buckling collapseWith buckling collapse

Fig. 7. Horizontal displacement curve of excavation face

4.3 Ground Settlement

Longitudinal Ground Settlement

Figure 8 is the longitudinal ground settlement curve with different supporting pressure ratios, whose positive value denotes uplifting and negative value means settlement. It indicates that excavation face within 10 m range outside the surface occurs protrusion deformation. The earth surface in front of the excavation face occurs the settlement deformation like groove. The maximum settlement happens at the 5 m position in front of the excavation face, and the main settlement influence area is 20 m in front of the excavation face. When λ is greater than 0.5, the settlement increases slowly with the decrease of λ. When λ decreases from 0.4 to 0.3, the maximum settlement abruptly increases to 42 cm. The plastic zone of the soil spreads from the front of the excavation face to the surface, forming the soil sliding area, but the main settlement influence range does not spread to the farther area.

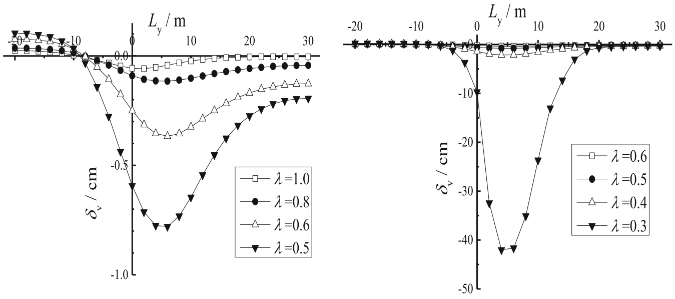

Without buckling collapseWith buckling collapse

Fig. 8. Longitudinal ground settlement curve

Horizontal Ground Settlement

The cross section of the surface has obvious groove settlement deformation, and the main settlement influence range is 15 m from the axis of the surface (1.5D). The trend of settlement with the vertical surface is similar: when λ is more than 0.5, the surface subsidence decreases slowly with the decrease of λ, and the form of the settlement becomes more apparent. When λ decreases from 0.4 to 0.3, the maximum ground settlement increases sharply to 42 cm, the surface produces significant subsidence collapse (Fig. 9).

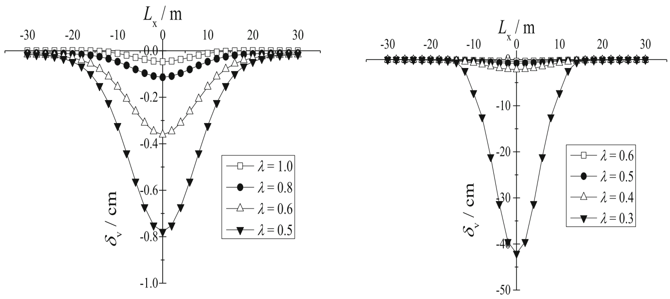

Without buckling collapseWith buckling collapse

Fig. 9. Horizontal ground settlement curve

5 Conclusion

In this paper, both numerical model and numerical calculation method are introduced first, followed by parametric study on influence of support pressure ratio on the stability of excavation face. The following major conclusions are drawn:

(i) When the support pressure is relatively large, the horizontal displacement of the center point of the excavation face increases slowly with decreasing of supporting pressure ratio. When support pressure ratio is reduced to 0.3, the horizontal displacement of the center point increases sharply to 90 cm. Meanwhile the soil of excavation face slid towards the excavation face and tunneling excavation face lost its stability.

(ii) The maximum ground subsidence occurs near the 5 m in front of the excavation face. There are obvious groove settlement deformations along the longitudinal surface of the tunnel axis. The main influencing area is 20 m in front of the excavation surface. The surface subsidence of cross section at 5 m in front of the excavation face is obviously groove type, and the main settlement area is 15 m from the axis of the surface.

(iii) Shield in a shutdown state mainly causes the displacement of the soil in front of the excavation face, and gradually spreads to the earth surface with the decrease of the supporting pressure ratio.

References

Gao, J.: Analysis of face instability of shield tunnels with consideration of groundwater seepage. Tianjin University (2010)

Anagnostou, G., Kovári, K.: Face stability conditions with earth-pressure-balanced shields. Tunn. Undergr. Space Technol. **11**(2), 165–173 (1996)

Schweiger, H.F., Pottler, R.K., Steiner, H.: Effect of seepage forces on the shotcrete lining of a large undersea cavern. In: International Conference on Computer Methods and Advances in Geomechanics, pp. 1503–1508. Balkema, Rotterdam (1991)

Qin, J.S.: Study on face deformation and collapse of earth pressure shield tunnel. Hohai University (2005)

Huang, Z.R., Zhu, W., Liang, J.H.: Study on limit supporting pressure and stabilization of excavation face for shallow shield tunnels in sand. Chin. J. Geotech. Eng. **11**, 2005–2009 (2006)

Zhu, J.: Face stability and deformation of shield tunneling in sand silt soil. Zhejiang University (2010)

Lü, X., Zhou, Y.C., Lee, F.D.: Centrifuge model test and numerical simulation of stability of excavation face of shield tunnel in silt sand. Rock Soil Mech. **37**(11), 3324–3328 (2016)

Wu, J.G.: A coupled fluid-mechanical study on seepage field of tunnels with high hydraulic pressure. Beijing Jiaotong University (2007)

Deng, S.Y., Yang, Q.X., Jiang, Y.J., et al.: Discussion on seepage model based on FLAC3D solid-fluid coupling. Tunn. Constr. **36**(02), 179–185 (2016)

Numerical Modeling on Localized Ground Subsidence Induced by the Tunneling in Sand

Min Zhou, Fei Wang(✉), and Yan-Jun Du

Institute of Geotechnical Engineering, Southeast University,
Nanjing 210096, China
feiwangseu@gmail.com

Abstract. Ground subsidence caused by tunneling is becoming a common problem in China due to rapid developing of underground space. Superstructures may crack and/or incline subjected to localized ground subsidence caused by tunneling. Ground subsidence would also induce breakage of buried pipelines which may even cause ground collapse due to pipe leakage. Mechanism of ground subsidence caused by tunneling in clay has been well understood. Volume of settlement troughs in clay are widely accepted as a constant along the depth, which is equal to ground volume loss in the ground. However, ground subsidence caused by tunneling in sand is still not clear considering the change of volume of settlement trough with depth, which has been observed in practice. Therefore, mechanism of ground subsidence caused tunneling in sand deserves in-depth investigation. In this study, ground subsidence caused by tunneling in three different types of sand with relative densities of 30% (i.e., loose sand), 50% (i.e., medium-dense sand), and 70% (i.e., dense sand), were adopted in finite element (FE) modeling. All soils were modeled using Mohr-Coulomb model. Gaussian-shape displacements were applied at bottom of FE models to simulate the tunneling effect. FE modeling results demonstrate that Gaussian functions can provide a good estimation of soil settlement trough at different depth. Trough width parameter decreased with the depth, while volume of soil settlement increased with the depth. It was also found that volume of settlement trough in the loose sand was greater than those in the medium-dense sand and dense sand, which may be attributed to contraction of the medium-dense and dense sand during the settlement propagating towards the ground surface. A modified empirical equation was proposed to calculate the settlement caused by tunneling in the sand at any depth with consideration of the effect of relative density of the sand. In the proposed method, the volume change of the settlement through was also incorporated.

Keywords: Ground subsidence · Tunneling · Sand · Finite element modeling

1 Introduction

Damage of underground facilities and superstructures caused by tunneling-induced ground subsidence is becoming a common problem in China due to rapid developing of subway tunnels. For example, on October 11th 2014, huge amount of water flew into an excavation of the Metro Line #1 in Nanchang city, which caused ground collapse and

© Springer Nature Singapore Pte Ltd. 2018
D. Zhang and X. Huang (Eds.): GSIC 2018, *Proceedings of GeoShanghai 2018 International Conference: Tunnelling and Underground Construction*, pp. 84–92, 2018.
https://doi.org/10.1007/978-981-13-0017-2_8

formed a hole with a diameter of 23 m and a depth of 4 m. Two workers injured and buried pipelines in the range of ground collapse were broken. Characteristics of ground subsidence caused by the tunneling have attracted wide research attention [1–3]. According to [4], Gaussian function can be employed to fit settlement trough at ground surface induced by tunneling. Gaussian function has been used successfully in the previous studies [5–8]. Mair et al. [7] investigated mechanism of settlement propagation caused by tunneling in clay based on their centrifuge tests results. They reported that volume of settlement troughs in clay could be treated as a constant along the depth, which is equal to the volume of ground loss in the ground. They also proposed an empirical method to predict the subsurface settlement at a given depth. Wang et al. [9] proposed a modified method for estimating the subsurface settlement caused by tunneling in sand with consideration of volume change of settlement trough based on lab-scale physical model tests. However, the relative density was not taken into account in Wang et al.'s method, which is essential for granular material and may influence the settlement propagation mechanism.

In this study, finite element (FE) modeling was conducted to investigate the effect of sand relative density on the mechanism of settlement propagation caused by tunneling in sand. Three different types of sand, namely, loose, medium-dense, and dense sand were used as the surrounding soil of tunnel, which was simulated using Mohr-Coulomb model. Gaussian-shape displacements were applied at the bottom of FE models to simulate tunneling effect. Finally, characteristics of subsurface settlement and ground subsidence were analyzed and a modified method was proposed to predict subsurface settlement caused by tunneling in sand.

2 Numerical Modeling

Finite element program ABAQUS® was employed for the numerical modeling in this study. Considering the symmetry of the numerical model, only half was calculated as shown in Fig. 1. Vertical boundaries were restrained against displacements in the horizontal direction. A Gaussian distribution displacement was applied at the bottom of the numerical model expressed as Eq. (1), where $S_{\max}$ and i were set as 0.3 and 2 m, respectively. Vertical displacements at upper boundary (i.e., the ground surface) were set as free.

$$S = S_{\max}(\exp(-0.5(x/i_{s})^{2})) \tag{1}$$

where $S_{\max}$ is maximum soil settlement (m); i_s is trough width parameter corresponding to distance from centerline of soil settlement trough to the point of inflection (m); and x is distance from the interested point to the centerline of ground subsidence zone (m).

Three different soils, namely, loose sand, medium sand, and dense sand, were used in the FE modeling. Elastic perfect plastic responses of soil to tunneling were characterized by using the Mohr-Coulomb failure criterion. Properties of soils in the numerical

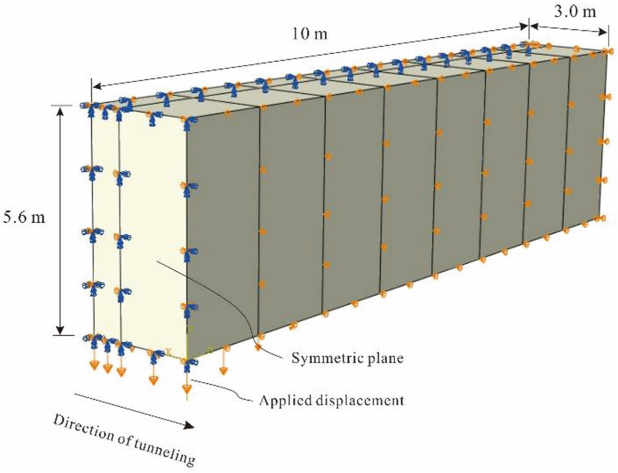

Fig. 1. Finite element model

Table 1. Properties of the sand used in FE modeling

Parameters	Loose sand	Medium sand	Dense sand
Elastic modulus (MPa)	20	40	80
Relative density (%)	30	50	70
Possion's ratio	0.3	0.3	0.3
Density (Mg/m^3)	1.8	2	2.1
Internal friction angle (°)	28	35	40
Dilation angle (°)	5	20	25
Cohesion (MPa)	0.001	0.001	0.001

Note: cohesion of sand was set as small values intentionally to avoid divergence convergence.

model were adopted from Balkaya and Moore (2013), as tabulated in Table 1. Soil materials were modeled as isotropic solids, employing C3D20 type twenty nodded (quadratic) brick elements. A finer FE mesh was used near the symmetric plan of the model, as shown in Fig. 2. The groundwater effect on the tunneling-induced ground subsidence was not considered in this study.

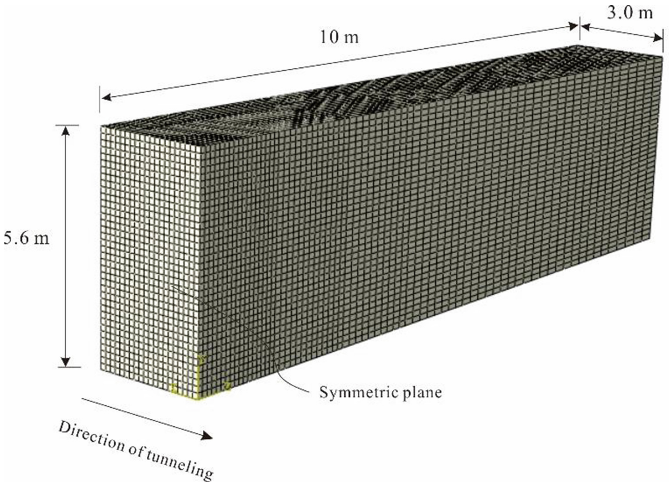

Fig. 2. Finite element mesh

3 Numerical Results Analysis

Figure 3 shows the variation of soil settlements obtained from FE models at selected depths of 0, 1.05, and 2.1 m for three cases. It is seen that the soil settlements increase with an increase of depth from the ground surface, which presents as Gaussian curves. Equation (1) was therefore employed to characterize the soil settlement troughs with values of coefficient of determination, R^2, greater than 0.95. The maximum settlement at a given depth decreased with an increase of the relative density.

Figure 4 shows the variation of trough width parameter (i_s) with the depth. It is seen that the i_s values increased with decrease of the depth. Width of settlement trough in sand can be calculated by the following expression (Wang et al. [9]),

$$i_s = -0.36(Z_0 - Z)/(Z_0 + 0.75)(Z_0 - Z) \tag{2}$$

where Z_0 is depth of the tunnel axis (m); Z is depth of the calculated settlement from ground surface (m).

Figure 5 shows the relationship between normalized width of settlement trough of the sand (i_s') obtained in this study by that calculated one by Eq. (2) (i_s'') and normalized relative density of the sand (D_r) in this study by that in Wang et al. [9] (i.e., 62%). The relationship between i_s/i_s' and $D_r/0.62$ was expressed as follows:

$$i_s'/i_s'' = 1.2 \tag{3}$$

Volume of soil settlement trough (denoted as V_s) was calculated by the following equation (Vorster [3]):

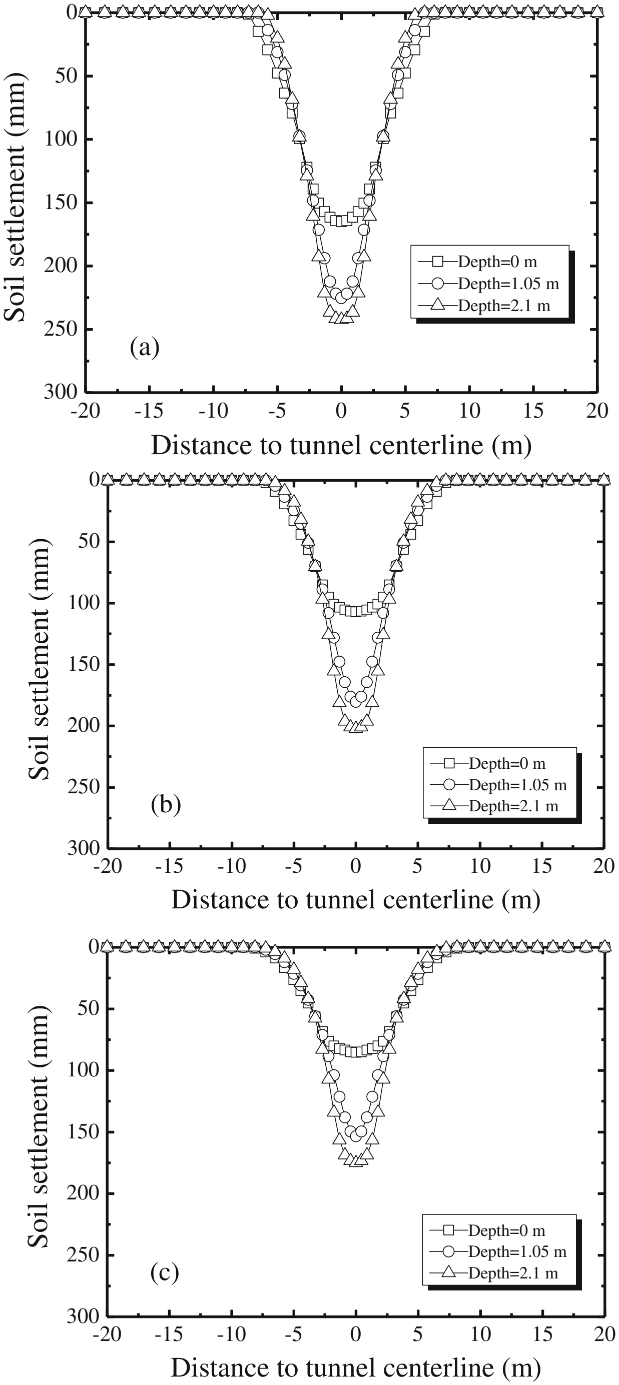

Fig. 3. Variation of soil settlement with the depth: (a) loose sand; (b) medium sand; and (c) dense sand

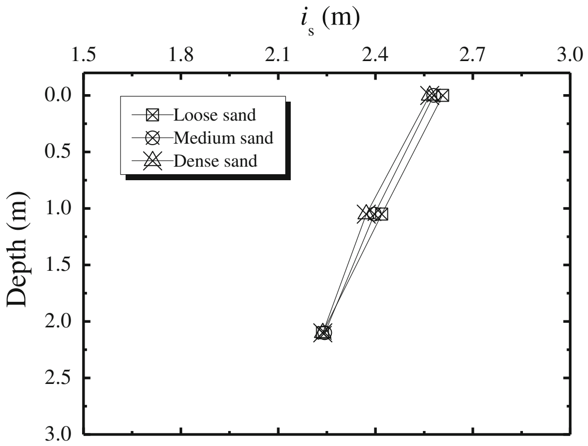

Fig. 4. Variation of settlement trough width parameter with the depth

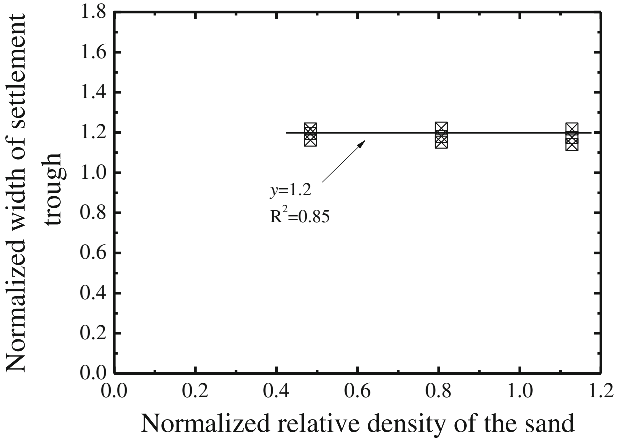

Fig. 5. Relationship between normalized relative density of the sand and normalized width of settlement trough

$$V_s = \sqrt{2\pi} S_{\max} i_s \tag{4}$$

where all parameters and their units were defined in Eq. (1).

Figure 6 shows the variation of volume of soil settlement trough (V_s) with the depth (Z). It is seen that the V_s values increased with an increase of Z with an order of $V_{\text{Loose sand}} > V_{\text{Medium sand}} > V_{\text{Dense sand}}$. Volume of the settlement trough of the sand can be also determined by (Wang et al. [9]),

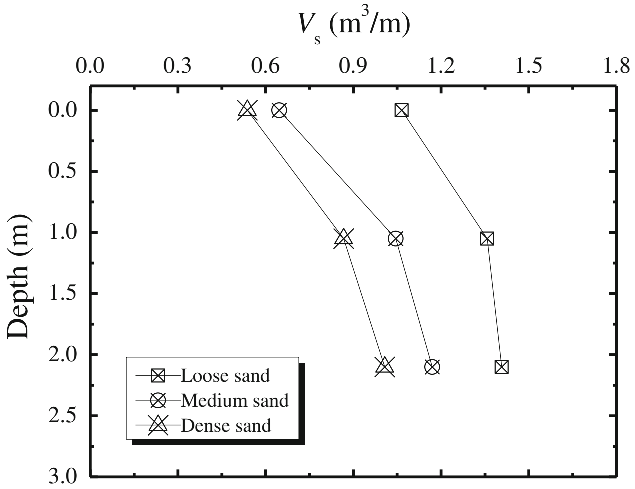

Fig. 6. Variation of volume of soil settlement trough with the depth

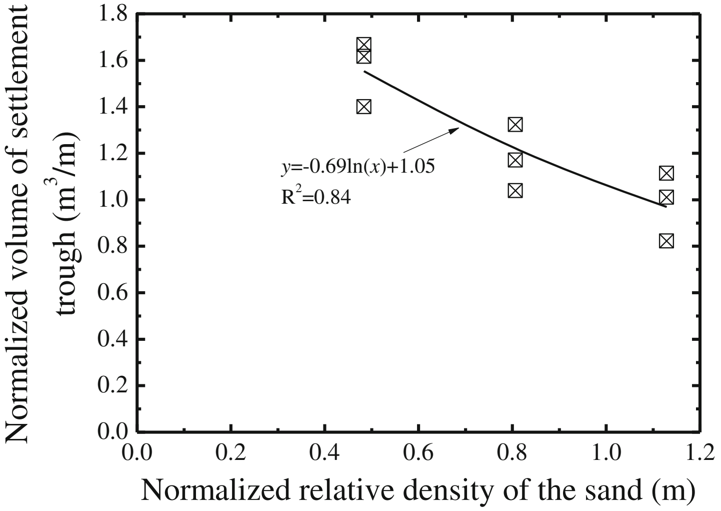

Fig. 7. Relationship between normalized relative density of the sand and normalized volume of settlement trough

$$V_s = V_L[1.82-(Z_0-Z)/Z_0]/1.85 \tag{5}$$

where V_L is volume of ground loss per unit length in tunnel (m^3/m); other parameters and their units were defined in Eq. (2).

Figure 7 shows the relationship between normalized volume of settlement trough of the sand (V_s') obtained in this study by the calculated one using Eq. (5) (V_s'') and normalized relative density of the sand (D_r) in this study by that in Wang et al. (2016) (i.e., 62%). A linear equation was derived using the least-square-root method to quantify the relationship between V_s/V_s' and $D_r/0.62$, as expressed by the following equation:

$$V_s'/V_s'' = -0.69\ln(D_r/0.62) + 1.05 \tag{6}$$

Substituting Eq. (2) through (6) into Eq. (1) can be used to calculate settlement caused by tunneling in sand with considering the effect of relative density of the sand:

$$s = \frac{(-0.69\ln(D_r/0.62) + 1.05)V_L(1.82-(Z_0-Z)/Z_0/1.85}{1.2\sqrt{2\pi}(-0.36(Z_0-Z)/Z_0 + 0.75)(Z_0-Z)} \exp\left(\frac{x}{1.2\sqrt{2}(-0.36(Z_0-Z)/Z_0 + 0.75)(Z_0-Z)}\right)^2 \tag{7}$$

4 Conclusions

Finite element modeling was conducted to investigate the characteristics of soil settlement trough caused by tunneling in sand. Three different types of sand, loose (D_r = 30%), medium (D_r = 50%), and dense sand (D_r = 70%), were used in this study. Gaussian function displacements were applied at the model bottom to simulate the tunneling effect. Based on the numerical results in this study, the following conclusions can be drawn:

(1) Maximum soil settlements caused by tunneling increased with an increase of the depth. Surface and subsurface settlement troughs are all fit for Gaussian curves.
(2) Trough width parameter increased with a decrease of the depth, while volume of soil settlement decreased with a decrease of the depth.
(3) Values of volume of settlement trough at a given depth increased with a decrease of the relative density of sand.
(4) A modified equation was proposed to calculate the settlement caused by tunneling in the sand at any depth with consideration of the effect of sand relative density on the settlement propagation mechanism.

References

1. Attewell, P.B., Yeates, J., Selby, A.R.: Soil Movements Induced by Tunneling and their Effects on Pipelines and Structures. Blackie and Son Ltd., London (1986)
2. Klar, A., Marshall, A.M.: Shell versus beam representation of pipes in the evaluation of tunneling effects on pipelines. Tunn. Undergr. Space Technol. **23**(4), 431–437 (2008)
3. Vorster, T.E.B.: The effects of tunnelling on buried pipes. Ph.D. thesis, Cambridge University, Cambridge, UK (2005)
4. Peck, B.: Deep excavations and tunneling in soft ground. In: Proceedings of 7th International Conference on Soil Mechanics and Foundation Engineering, Mexico city, pp. 225–290 (1969)

5. O’Reilly, M.P., New, B.M.: Settlement above tunnels in the United Kingdom – their magnitude and prediction. In: Tunnelling 1982, Proceedings of the Third International Symposium, pp. 173–18. Institution of Mining and Metallurgy, London (1982)
6. New, B.M., O’Reilly, M.P.: Tunneling induced ground movements: predicting their magnitudes and effects. In: Proceedings of the 4th International Conference on Ground Movements and Structures, pp. 671–697. Pentech Press, London (1991)
7. Mair, R.J., Taylor, R.N., Bracegirdle, A.: Subsurface settlement profiles above tunnels in clays. Géotechnique **43**(2), 315–320 (1993)
8. New, B.M., Bowers, K.H.: Ground movement model validation at the Heathrow Express trial tunnel. In: Tunnelling 1994, Proceedings of the 7th International Symposium, pp. 301–329. Chapman & Hall, London (1994)
9. Wang, F., Miao, L., Yang, X., Du, Y.J., Liang, F.Y.: The volume of settlement trough change with depth caused by tunneling in sands. KSCE J. Civil Eng. **20**(7), 2719–2724 (2016)

Simplified Method for Calculating the Settlement of Existing Tunnel Induced by New Tunneling Based on Two Step Method

Junwei Jin(✉), Jingyuan Zhan, Weikang Song, and Mingyu Li

School of Civil Engineering, Zhengzhou University, Zhengzhou, China
`jinjunwei2003@qq.com`

Abstract. Settlement induced by new tunneling is important in assessing the safety of existing tunnel. A simplified settlement calculation method for the existing tunnel was obtained based on the two-step method. Firstly, ground settlement induced by tunneling was calculated using experimental method and elastic method. Then the entire tunnel deformation can be calculated using elastic-foundation-beam model and the ground settlement obtained in the first step was applied on the existing tunnel as a passive settlement load. Finally, the simplified method was verified by the results from modal test. The results show that the simplified method is available for calculating settlement of existing tunnel induced by new tunneling. Parametric study also studied in the paper, it is found that the tunnel settlement induced by tunneling increases with the increasing ground loss and decreases with the increasing net distance between new tunnel and existing tunnel. The settlement of tunnel with larger depth and harder soil stiffness is larger than the one with lower depth and softer soil when the ground loss is same.

Keywords: Tunnel settlement · Two-step method · Elastic foundation beam
Tunnel-soil interaction

1 Introduction

With the rapid subway tunnel development, more and more new tunnel construct in urban area in China. It is becoming increasingly difficult to ignore the interaction between the new tunnel and the existing one. Methods for estimating the existing tunnel settlement due to tunneling is needed when assessing the safety of existing tunnel. Figure 1 shows a typical example of the related problem: an existing tunnel locates under a new tunnel under construction. Soil movement induced by tunneling tends to impose the downward movement of the existing tunnel. This problem has been analyzed through model test (Kim et al. 1998; Byun et al. 2006; Choi and Lee 2010), field observation (Kimmance et al. 1996; Fang et al. 2015), and Numerical simulation method (Addenbrooke and Potts 2001).

In this paper the analysis of this problem will be carried out in two stages as (Chen 1999) when solving a problem on the pile responses caused by tunneling. Firstly, it should obtain the soil settlement induced by new tunneling ignoring the existing tunnel. Secondly, impose the soil movement on the existing tunnel and calculate the tunnel settlement.

© Springer Nature Singapore Pte Ltd. 2018
D. Zhang and X. Huang (Eds.): GSIC 2018, *Proceedings of GeoShanghai 2018 International Conference: Tunnelling and Underground Construction*, pp. 93–102, 2018.
https://doi.org/10.1007/978-981-13-0017-2_9

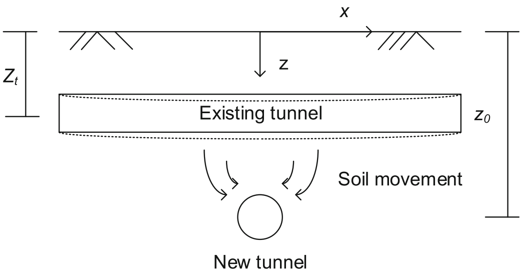

Fig. 1. Existing tunnel above tunneling

2 Method for Analysis

2.1 Analyses of Tunnel Response

In order to calculate the longitudinal settlement of tunnel, the following assumption are proposed: (1) Winkler elastic beam foundation modal is applicable in this condition; (2) tunnel (beam) and soil cannot separate with each other, satisfying the deformation coordination; (3) Tunnel axial force can be ignored during the analysis.

Simplify the tunnel as a beam of infinite length, the pressure p of any node on the beam only related with the foundation deformation s.

$$p = ks \tag{1}$$

where, k is coefficient of subgrade reaction, kN/m^3; p is the pressure, kPa; and s is the settlement of the point, m.

For one element of tunnel underground, as shown in Fig. 2. The length of the tunnel is dx, p is the axial force, M is the moment, v is the shear force, q is the distribution load, p is the soil resistance.

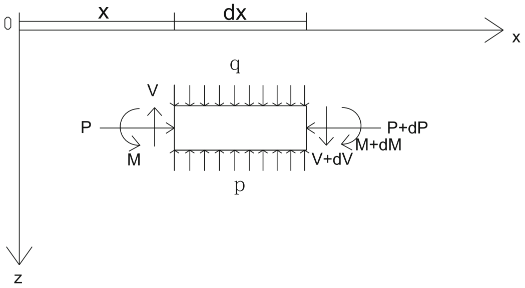

Fig. 2. Tunnel longitudinal calculate element force analysis

Ignoring the axial force of tunnel, based on the moment balance:

$$(M + dM) - M + Vdx - (q - p)dx\frac{dx}{2} = 0 \tag{2}$$

Simplify the Eq. 2 and ignoring the high order differential item, Eq. 3 can be obtained that,

$$\frac{d^2M}{dx^2} + \frac{dV}{dx} = 0 \tag{3}$$

Based on the material mechanics knowledge:

$$\frac{d^2M}{dx^2} = EI\frac{d^4z}{dx^4} \tag{4}$$

where *EI* is the flexural rigidity, z is the vertical settlement of tunnel.

Based on the force balance:

$$V + (p - q)dx - (V + dV) = 0 \tag{5}$$

It can be obtained that:

$$EI\frac{d^4z}{dx^4} + (p - q) = 0 \tag{6}$$

where q is the distribution load induce by soil, hence it can be seen as a part of the resistance force, the Eq. 7 can be obtained:

$$p - q = k(z - s) \tag{7}$$

where k is the Winkler subgrade reaction modulus. Z is the vertical settlement of tunnel, s is the soil settlement at the location of tunnel, (z-s) is the relative settlement between the soil and tunnel.

Hence,

$$EI\frac{d^4z}{dx^4} + kz = ks \tag{8}$$

Introducing the parameter λ,

$$\lambda = \sqrt{4}\frac{k}{4EI} \tag{9}$$

Equation 10 can be obtained:

$$\frac{d^4 z}{dx^4} + 4\lambda^4 z = 4\lambda^4 s \tag{10}$$

Both z and s are functions related with variable value x, hence the Eq. 10 can change to

$$\frac{d^4 z(x)}{dx^4} + 4\lambda^4 z(x) = 4\lambda^4 s(x) \tag{11}$$

Equation 11 is the governing equation used to calculate the tunnel settlement z induced by soil settlement.

3 Estimation of Soil Settlement

In recent years, many methods have been used to calculate the soil settlement induced by tunneling in free field. These methods can be classified into three categories: empirical methods (Peck 1969; Jacobsz 2002), numerical methods (Alsahly et al. 2016), and analytical methods (Loganathan 1998; Park 2005). This paper will focus on the empirical methods and analytical method, which can calculate effectively.

The ground settlement trough caused by tunneling is often estimated using the Gaussian equation as follows (Peck 1969):

$$S = S_{\max} \exp\left(-\frac{x^2}{2i^2}\right) \tag{12}$$

where $S_{\max}$ is the maximum settlement above the tunnel centerline; i is the distance from tunnel center line to the point of inflexion of the trough; x is distance from tunnel centerline to the calculate point location, as illustrated in Fig. 3.

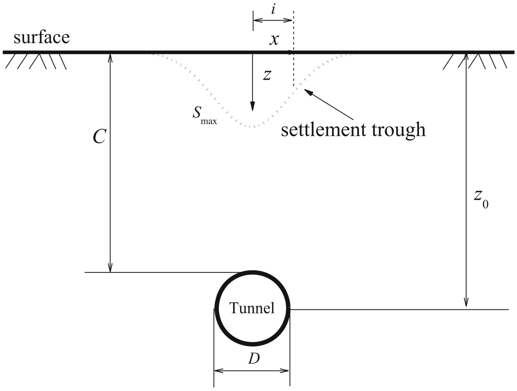

Fig. 3. Ground settlement induce by tunneling

Based on a series of geotechnical centrifuge tests, Jacobsz (2002) suggested that the surface settlement trough due to tunneling in sand can be written as follows:

$$S_z(x) = S_{\max} \exp\left[-\frac{1}{3}\left(\frac{|x|}{i}\right)^{1.5}\right] \tag{13}$$

When the Gaussian curve is used to estimate the subsurface settlement trough caused by tunneling, the key is to obtain the inflexion parameter *i*. Based on various tests results and practical data, the inflexion parameter *i* can be calculated as follows (Mair et al. 1993):

$$i = K(z_0 - z) \tag{14}$$

where K is parameter of settlement trough; z_0 is depth of tunnel center; z is depth of calculation point.

Based on the practical test data, Mair et al. (1993) found that the settlement trough parameter K in clay can be calculated by the following equation:

$$K = \frac{0.175 + 0.325(1 - z/z_0)}{(1 - z/z_0)} \tag{15}$$

From the results obtained from a series of geotechnical centrifuge tests tunneling in sand, Jacobsz (2002) remarked that the parameter K can be obtained as follows:

$$K = \frac{0.09 + 0.26(1 - z/z_0)}{1 - z/z_0} \tag{16}$$

When tunnel volume loss is less than 5% (for ground volume loss, it is about 2%), the relationship between V_{lt} and V_{ls} can be expressed as (Jin 2014):

$$V_{ls} = \left(a + be^{-[(V_{lt}-c)/d]^2}\right)\left[\frac{C}{D} - \alpha\frac{z}{D}\right]^{\beta} \tag{17}$$

Where $a = 2.0$, $b = -3.7$, $c = -2.8$, $d = 3.6$, $\alpha = 0.5$, $\beta = 0.5$.

$$S_{\max,z} = \frac{V_{ls,z}}{\int \exp\left[-\frac{1}{3}\left(\frac{|x|}{i_z}\right)^{1.5}\right]\mathrm{d}x} \tag{18}$$

By using elastic method (Park 2005), the soil displacement at the z depth can obtained by Eq. 19. The ground loss ratio can also calculated from Eq. 17.

$$S_z = -\frac{\mathrm{V}_{ls}D^2}{2}\left(-\frac{z - z_0}{x^2 + (z - z_0)^2} + \frac{z + z_0}{x^2 + (z + z_0)^2} - \frac{2z\left[x^2 - (z + z_0)^2\right]}{x^2 + (z + z_0)^2}\right) \tag{19}$$

4 Foundation Stiffness Coefficient

Combining with the moment equal condition, Klar et al. (2005) obtained the foundation stiffness coefficient by using the Winkler model and Elastic continuum theory,

$$k = \frac{6E_S d}{i} \tag{20}$$

In which, E_s is the elastic modulus of soil, d is the tunnel diameter, i is the wide factor of settlement trough of tunnel.

Biot (1922) proposed a solution for infinite beam under concentrated load in three dimension, and the stiffness coefficient is as follows:

$$k = \frac{0.95E_S}{1 - v_S^2}\left[\frac{D^4 E_S}{EI(1 - v_S^2)}\right]^{0.108} \tag{21}$$

In which, E_s is the elastic modulus of soil, v_s is the poison ratio of soil, D is the diameter of tunnel, EI is the bending stiffness of tunnel.

Based on the equations above, Vesic (1961) analyzed infinite beam under concentrate force and concentrate moment in the half space, and set the elastic foundation beam theory get the same degree with elastic continuum theory, the following relationship can be obtained:

$$k = \frac{0.65E_S}{1 - v_S^2}\left(\frac{D^4 E_S}{EI}\right)^{\frac{1}{12}} \tag{22}$$

In this paper, the modulus used for the ground reaction is calculated by Eq. 22.

5 Compared with Test

In order to test and verify the above equation, the advised method are used to compare with the geo-centrifuge test by Ng et al. (2013). The test is used to investigate the influence of new tunneling to existing tunnel, as shown in Figs. 4 and 5.

The prototype of the test is shown in Figs. 4 and 5. The acceleration is 60 g, the real diameter of the existing tunnel D is 6.0 m, cover depth C is 12.0 m, the diameter of the new tunnel is also 6.0 m, the net distance between the two tunnels are P = 3.0 m. The volume loss of soil is 2%, the prototype of the tunnel is made of aluminum alloy material, the elastic modulus is about 69 GPa, the thickness is about 180 mm. The sand used in the test is Toyoura sand, the average grain diameter $D_{50} = 0.17$ mm, the maximum and minimum void ratio are $e_{\max} = 0.977$ and $e_{\min} = 0.597$, separately. Relative density G_s is 2.46, critical friction angle $\varphi = 30°$. According to Zhang et al. (2013), the logarithm volume elastic modulus of Toyoura sand $\kappa$is 0.0064. The Young's modulus of soil can obtained through Eq. 15. The average density of sand is 1530 kg/m^3, and the elastic modulus of sand is 76 MPa.

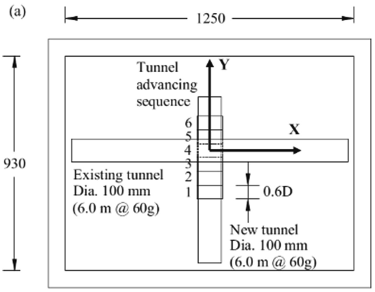
(a)
1250
930
Tunnel advancing sequence
Y
6
5
4
3
2
1
X
Existing tunnel
Dia. 100 mm
(6.0 m @ 60g)
0.6D
New tunnel
Dia. 100 mm
(6.0 m @ 60g)

Fig. 4. Geotechnical centrifuge test – plan view (Ng et al. 2013)

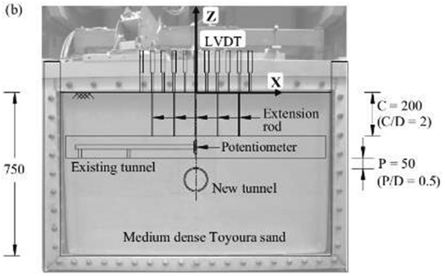
(b)
Z
LVDT
X
750
Extension rod
Potentiometer
Existing tunnel
New tunnel
Medium dense Toyoura sand
C = 200
(C/D = 2)
P = 50
(P/D = 0.5)

Fig. 5. Geotechnical centrifuge test profile (Ng et al. 2013)

$$E = \frac{3(1-2v)(1+e_0)p'}{\kappa} \tag{23}$$

Based on the settlement from ‘two-stage’ method, the tunnel vertical settlement can be calculated by using elastic method and empirical method, as shown in Fig. 6. The result show that the differences between both the analytical solution and empirical method and geo-centrifuge test result are not large. The maximum of elastic method is 18.5 mm and the empirical method is 16.0 mm, the test result is 17.1 mm. Hence it is reasonable to the two step method to calculate the tunnel settlement induced by new tunneling introduce in this paper. Figure 6 shows that the tunnel settlement at the existing tunnel location calculated by empirical method is narrower than the elastic method. Meanwhile, if the nonlinear relation is considered for elastic method (method 2), the maximum tunnel settlement reduced a little as the ground loss is less than tunnel loss ratio in this test.

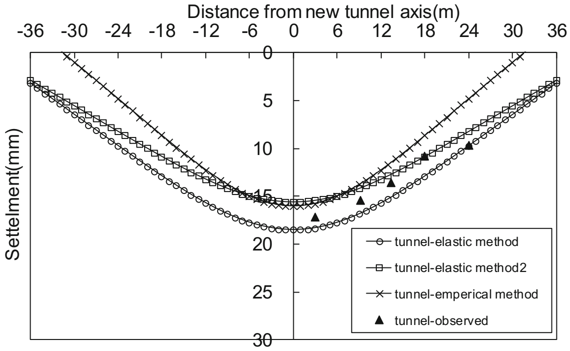

Fig. 6. Comparison of theatrical value and test value

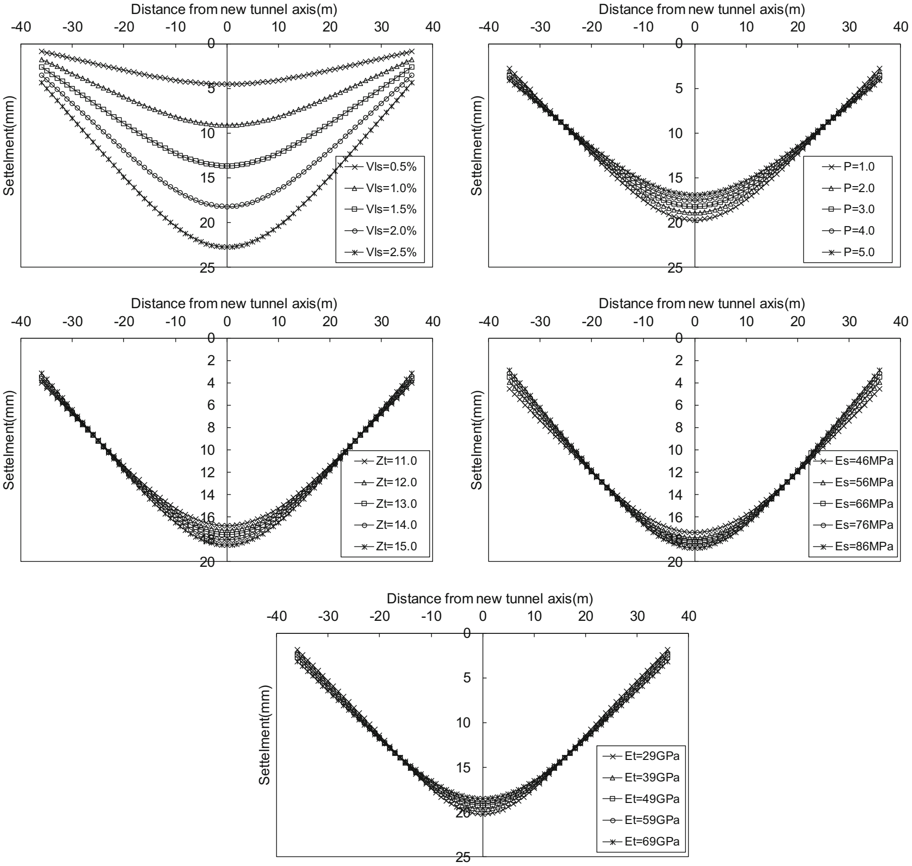

Fig. 7. Existing tunnel settlement induced by new tunneling with different V_{ls}, P, Z_t, E_s, E_t.

6 Discussion

Longitudinal settlement of existing tunnel induced by new tunneling based on two-step method is introduced in this paper. The tunnel settlement induced by new tunneling can be estimated by simplify the tunnel as an elastic ground beam. By adding the soil movement at the tunnel location on the elastic ground beam, settlement of existing tunnel is obtained. In this section, the tunnel settlement induced by new tunneling with different ground loss V_{ls}, net distance between new tunnel and existing tunnel P, existing tunnel depth Z_t, and elastic modulus of soil Es are analyzed. The standard model as described in the former geo-centrifuge test, with tunnel length $L_t = 72$ m, tunnel diameter $D_t = 6.0$ m, thickness of tunnel $t_t = 0.18$ m, elastic modulus of tunnel $E_t = 69$ GPa, existing tunnel depth $Z_t = 15$ m, new tunnel depth $Z_{t1} = 24$ m, tunnel volume loss ratio $V_{lt} = 2\%$, elastic modulus of soil $E_s = 76$ MPa.

As shown in Fig. 7 the tunnel settlement induced by new tunneling increases with the increase of ground loss V_{ls}, it is because large ground loss induces more ground settlement. The settlement of existing tunnel induced by tunneling decrease with the increase of net distance between new tunnel and existing tunnel *P*, for the reason that the largest ground settlement located near the new tunnel. For the same reason, the existing tunnel with large depth Z_t (which mean small *P*) has larger settlement than the one with small depth. Large soil stiffness E_s will case less ground loss, but with the same ground loss, the large soil stiffness make the relative settlement and soil compress small, causing the existing tunnel settlement increase. With the increase of elastic modulus of tunnel, the tunnel settlement reduced. Form the result of the five parameters in this section, it can be found that the most important parameter in this research is the tunnel volume loss, hence the tunnel volume loss should in controlled in practice.

Acknowledgements. The authors would like to acknowledge the financial support of the National Natural Science Foundation of China (No. 51509017) and the Education department of Henan Province, China (No. 17B560013).

References

Addenbrooke, T.I., Potts, D.M.: Twin tunnel interaction: surface and subsurface effects. Int. J. Geomech. **1**(2), 249–271 (2001)

Alsahly, A., Stascheit, J., Meschke, G.: Advanced finite element modeling of excavation and advancement processes in mechanized tunneling. Adv. Eng. Softw. **100**, 198–214 (2016)

Biot, M.A.: Bending of an infinite beam on an elastic foundation. Zeitschrift fiir Angewandte Maihematik und Mechanik **2**(3), 165–184 (1922)

Byun, G.W., Kim, D.G., Lee, S.D.: Behavior of the ground in rectangularly crossed area due to tunnel excavation under the existing tunnel. Tunn. Undergr. Space Technol. **21**(3–4), 361 (2006)

Choi, J.I., Lee, S.W.: Influence of existing tunnel on mechanical behavior of New tunnel. KSCE J. Civ. Eng. **14**(5), 773–783 (2010)

Chen, L., Poulos, H.G., Loganathan, N.: Pile responses caused by tunneling. J. Geotech. Geoenviron. Eng. **125**(3), 207–215 (1999)

Fang, Q., Zhang, D., Li, Q.Q., Wong, L.N.Y.: Effects of twin tunnels construction beneath existing shield-driven twin tunnels. Tunn. Undergr. Space Technol. **45**, 128–137 (2015)

Jin, J., Yang, M.: Ground subsidence caused by tunnel excavation in sand. In: Geo-Shanghai, pp. 174–183 (2014)

Jacobsz, S.W.: The Effects of Tunnelling on Piled Foundations. University of Cambridge, Cambridge (2002)

Kim, S.H., Burd, H.J., Milligan, G.W.E.: Model testing of closely spaced tunnels in clay. Géotechnique **48**(3), 375–388 (1998)

Kimmance, J.P., Lawrence, S., Hassan, O., Purchase, N.J., Tollinger, G.: Observations of deformations created in existing tunnels by adjacent and cross cutting excavations. In: Proceedings of the Geotechnical Aspects of Underground Construction in Soft Ground, pp. 707–712 (1996)

Klar, A., Vorster, T.E.B., Soga, K., Mair, R.J.: Soil-pipe interaction due to tunnelling: comparison between winkler and elastic continuum solutions. Géotechnique **55**(6), 461–466 (2005)

Loganathan, N., Poulos, H.G.: Analytical prediction for tunneling-induced ground movements in clays. J. Geotech. Geoenviron. Eng. **124**(9), 846–856 (1998)

Mair, R.J., Taylor, R.N., Bracegirdle, A.: Subsurface settlement profiles above tunnels in clays. Géotechnique **45**(2), 361–362 (1993)

Ng, C.W.W., Lu, H., Peng, S.Y.: Three-dimensional centrifuge modelling of the effects of twin tunnelling on an existing pile. Tunn. Undergr. Space Technol. **35**, 189–199 (2013)

Peck, R.B.: Deep excavations and tunnelling in soft ground. In: Proceedings of the International Conference on SMFE, pp. 225–290 (1969)

Park, K.H.: Analytical solution for tunnelling-induced ground movement in clays. Tunn. Undergr. Space Technol. Incorporating Trenchless Technol. Res. **20**(3), 249–261 (2005)

Vesic, A.B.: Bending of beams resting on isotropic elastic solid. J. Eng. Mech. Div. **87**(2), 35–54 (1961)

Zhang, F., Ye, B., Ye, G.: A unified description of Toyoura sand. In: Constitutive Modeling of Geomaterials, pp. 663–674 (2013)

Ground Surface Deformation Analysis of Quasi Rectangular EPB Shield Tunneling

Xi Jiang, Xuehui Zhang, Ang Chen, Jixiang Chen, and Yun Bai(✉)

Tongji University, Shanghai 200092, China
`baiyun1958@tongji.edu.com`

Abstract. The first quasi rectangular shield tunnel in China was developed during the construction of Ningbo Metro Line 3. Based on the Mindlin solution, this paper presents the computerized outcome of the ground surface deformation caused by the following three factors: the horizontal excess pressure at the excavation face, the friction between the shield skin and soil, and the grouting force outside the tailskin. The result shows: (1) Superposition of these three factors causes large surface heave near the tunneling area, with a maximum of 15 mm; (2) Grouting force plays an absolutely dominant role in ground surface deformation, which can cause a maximum 19 mm ground heave; (3) However, the total ground surface deformation induced by these three factors remains controllable. This study can be used for disturbance-control of future quasi rectangular shield tunneling.

Keywords: Surface deformation · Quasi rectangular shield · Excess pressure Friction · Grouting pressure

1 Introduction

Shield tunneling method has become the dominant method for tunnel construction in soft soil layer. Ground disturbance control is important in underground shield tunneling. However, construction processes, like cutterhead advance and synchronous grouting, will inevitably lead to soil disturbance, ground subsidence, etc. Many scholars have researched ground stress and deformation caused by circular shields, double circle shield (Double-O-Tube, DOT) and pipe jacking [1–4]. Most of the previous studies focus mainly on the circular and DOT shield, however, ground disturbance analysis results of the former circular shield or DOT shield tunneling, cannot be directly applied to the safety control of this new quasi rectangular shield.

Although quasi rectangular shield have absorbed the advantages of DOT and is technically promising in future, its impact on ground disturbance needs to be studied. This paper takes the first quasi rectangular shield tunnel - Ningbo Metro Line 3 tunnel as an example. To study the ground deformation by quasi rectangular shield tunneling, additional pressure on the excavation face, non-uniform skin friction between shell and soil, and synchronous grouting pressure are considered [5]. The results can provide theoretical basis for ground disturbance control of future quasi rectangular tunnel projects.

© Springer Nature Singapore Pte Ltd. 2018
D. Zhang and X. Huang (Eds.): GSIC 2018, *Proceedings of GeoShanghai 2018 International Conference: Tunnelling and Underground Construction*, pp. 103–111, 2018.
https://doi.org/10.1007/978-981-13-0017-2_10

2 Overview of Quasi Rectangular Shield

In 2015, the first quasi rectangular EPB shield in China was adopted in Ningbo Metro Line 3 project. The new shield machine has a dimension of 11.83 m * 7.267 m (maximum width * maximum height), as shown in Fig. 1.

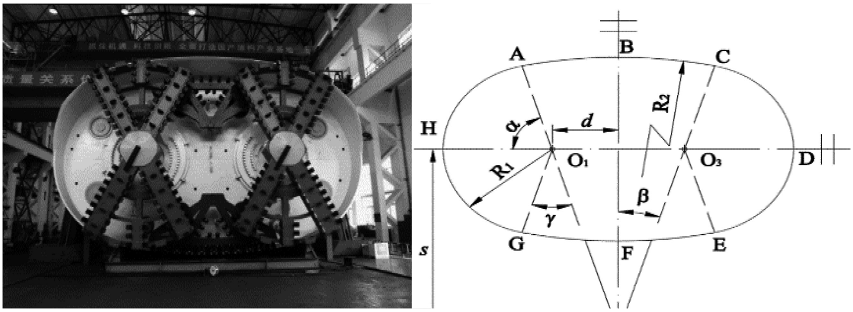

Fig. 1. Quasi rectangular shield & the cross section

As shown in Fig. 1, the cross section boundary of a rectangular shield is composed of two pairs of circular arcs with different radii. It is divided into two waists $\widehat{CDE}$、$\widehat{GHA}$, and upper and lower arches $\widehat{ABC}$、$\widehat{EFG}$. The centers of arc $\widehat{CDE}$ and $\widehat{GHA}$ are located respectively at O_1 and O_3 and they are symmetrical with the vertical axis of the cross section. The center of the arc $\widehat{ABC}$ is located at O_2 outside the shield section. Relevant parameters of the shield section are shown in Table 1.

Table 1. Geometry size of the quasi-rectangle shield

Length L/m	Radii R_1/m	Radii R_2/m	Center shift d/m	Center shift s/m	α/°	β/°	γ/°
11.61	3.37	15.61	2.55	11.97	78	12	24

3 The Model and Assumptions

The surface deformation analysis model (Fig. 2) is based on the following assumptions:

① The consolidation of soil and ground volume loss is not considered
② The longitudinal slope and deflection of the shield are not considered
③ The front additional thrust is evenly distributed along the excavation surface
④ The soil layer is homogeneous, linearly elastic semi infinite
⑤ The influence of cutter torque is not considered

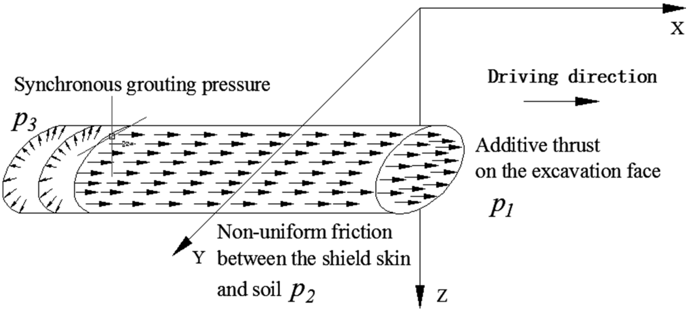

Fig. 2. Model of ground deformation induced by tunneling

3.1 Additive Thrust on the Excavation Face P_1

According to Wang [6], the value of the additional thrust is calculated using this formula,

$$P_1 = \frac{10.13(1-\mu)E_u\,\pi\,v(1-\xi)^2}{(1+\mu)(3-4\mu)Dkw} + \Delta p' \tag{1}$$

In the above formula:

μ: Soil poison ratio; E_u: Undrained modulus of elasticity of soil (MPa) [7]; $E_{s0.1\sim0.2}$: Modulus of compressibility of soil (MPa); v: Tunneling speed of shield machine (cm/min); ξ: Cutter opening ratio; D: Cutter diameter (m); k: Number of closed parts of cutterhead; w: Cutter speed of shield machine (r/min); $\Delta p'$: The extruding force produced by the incision entering the soil (10–25 kPa).

3.2 Non-uniform Friction Between the Shield Skin and Soil p_2

The softening effect of the frictional resistance between the shell and soil interface produced by the shield shell propulsion should be taken into account [8]. Based on the results of soil friction at the pile-soil interface, the expression of the friction resistance of the shield-soil interface is:

$$p_2 = \eta\sigma_\theta \tan\varphi \tag{2}$$

In the above formula:

η: Softening coefficient (0.83–0.94) [9]; σ_θ: Normal stress at θ; φ: Friction angle between shield shell and soil (6.5°–9°) [10].

3.3 Synchronous Grouting Pressure p_3

Shield grouting can fill the gap between the segment and the stratum in time to reduce the ground subsidence. The grouting pressure can cause a squeezing effect on the outer layer of the segment and cause the soil to deviate from the shield. Eight synchronous grouting pipes are set up in the quasi rectangular shield to ensure that the slurry can fill the gap between the segment and ground quickly and evenly [11]. This paper assumes that the grouting pressure is distributed uniformly along the outer side of the segment in the last two segments of the shield tail (L = 2.4 m). Its attenuation in longitudinal and radial directions is not considered. The horizontal component of the grouting pressure has little influence on the vertical displacement of formation, so this paper only takes the vertical component into consideration. According to the on-site working record, the grouting pressure is 250 kPa during the construction of Ningbo Metro Line 3.

4 Surface Deformation

4.1 Mindlin Stress Solution

According to coordinate transformation formula, the following relations can be deduced: $x' = x-1$; $y' = y-m$; $z' = z-n$. The vertical displacement caused by the horizontal and vertical concentrated force are obtained [9], see formula (3) and (4).

$$\omega_h = \frac{P_h(x-l)}{16\pi G(1-\mu)}\left\{\begin{array}{l} \frac{z-n-c}{R_1^3} + \frac{(3-4\mu)[z-n-c]}{R_2^3} \\ -\frac{6c(z-n)[z-n+c]}{R_2^5} \\ +\frac{4(1-\mu)(1-2\mu)}{R_2(R_2+z-n+c)} \end{array}\right\} = H(x,y,z) \tag{3}$$

$$\omega_v = \frac{P_v}{16\pi G(1-\mu)}\left\{\begin{array}{l} \frac{(3-4\mu)}{R_1} + \frac{8(1-\mu)^2-(3-4\mu)}{R_2} \\ +\frac{(z-n-c)^2}{R_1^3} \\ +\frac{(3-4\mu)(z-n+c)^2-2c(z-n)}{R_2^3} \\ +\frac{6c(z-n)(z-n+c)^2}{R_2^5} \end{array}\right\} = V(x,y,z) \tag{4}$$

In the above formula,

(x, y, z): The overall coordinates of the points to be calculated; c: The distance between horizontal concentrated force and the ground; P: Horizontal concentrated force; μ: Poisson's ratio; R_1, R_2 are the distances of action points of concentrated force and their symmetric points to the unknown stress points. In this paper, the uplift deformation is positive, and the settlement deformation is negative.

4.2 Surface Ground Deformation Caused by p_1

As shown in Fig. 3(a), the area of the excavation face is taken as $r\mathrm{d}r\mathrm{d}\theta$, so the load on it is $p_1 r\mathrm{d}r\mathrm{d}\theta$. Then integral over the entire excavation face, the additional stress caused by p_1 can be obtained.

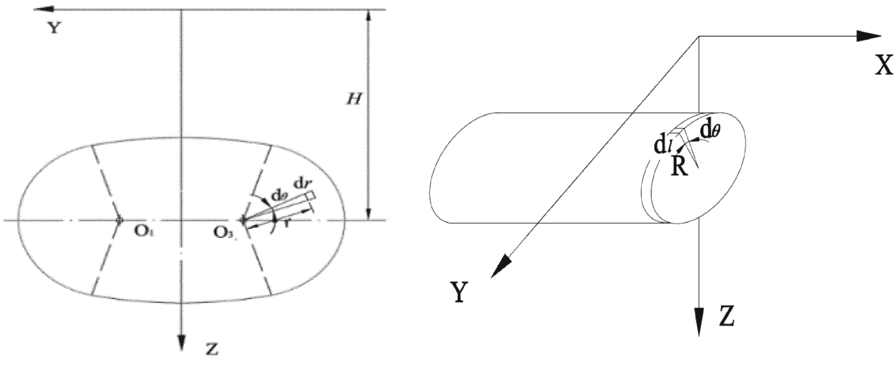

(a) (b)

Fig. 3. Analysis model of ground surface deformation induced by (a) excess pressure and (b) by friction force around skin

$$\omega_1 = \iint H(r, \theta) \mathrm{d}r \mathrm{d}\theta \tag{5}$$

4.3 Surface Ground Deformation Caused by p_2

As shown in Fig. 3(b), take the surface area of the shell as $R\mathrm{d}\theta \mathrm{d}l$, The load on the element is $P_2 R\mathrm{d}l\mathrm{d}\theta$. Then integral along the shell boundary and the shield length, the following formula can be obtained,

$$\omega_2 = \iint H(l, \theta) \mathrm{d}l \mathrm{d}\theta \tag{6}$$

4.4 Surface Ground Deformation Caused by p_3

Take the surface area of the segment as $R\mathrm{d}\theta \mathrm{d}s$, so the load on it is $p_3 R_1 \mathrm{d}s\mathrm{d}\theta$. The vertical component of the synchronous grouting pressure is taken as an integral to the segment boundary and the length of the two segments, see Fig. 4.

$$\omega_3 = \iint V(s, \theta) \mathrm{d}s \mathrm{d}\theta \tag{7}$$

Based on the above three factors, the surface ground deformation during the whole quasi rectangular shield construction can be obtained using this formula.

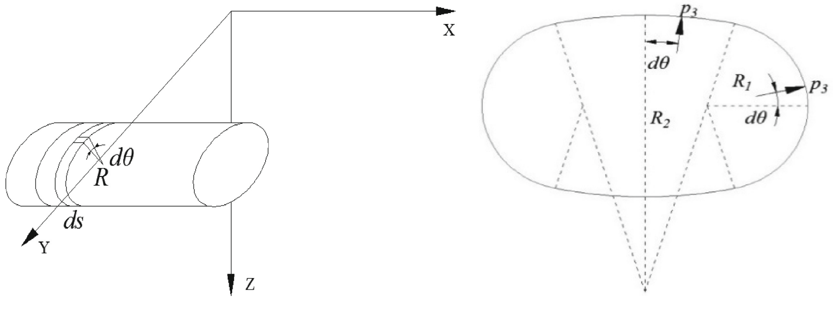

(a) (b)

Fig. 4. (a) Analysis model of ground surface deformation induced by tailskin grouting; (b) Pressure distribution along the tailskin perimeter

$$\omega = \omega_1 + \omega_2 + \omega_3 = \iint H(r,\theta)\mathrm{d}r\mathrm{d}\theta + \iint H(l,\theta)\mathrm{d}l\mathrm{d}\theta + \iint V(L,\theta)\mathrm{d}L\mathrm{d}\theta \tag{8}$$

5 Results of Analysis

5.1 The Parameter

The quasi rectangular shield test section of Ningbo Metro Line 3 starts with the reinforcing area of the starting well and the average buried depth of the tunnel axis is $H = 13.1$ m. The tunnel mainly passes through the silty clay layer and the mechanical parameters of the soil layer are shown in Table 2.

Table 2. Parameters of soil & quasi rectangular shield machine

Parameter index	Value	Reference source
Poisson's ratio μ (KN/m^3)	0.42	[7]
Average soil gravity	17.12	Project design document
Coefficient of lateral pressure at rest k_0	0.67	[7]
Modulus of compressibility $E_{s0.1\sim0.2}$(MPa)	2.18	[7]
modulus of deformation E_μ(MPa)	6.54	[7] & Project design document
Cutter opening ratio ξ(%)	80	Project design document
Cutter diameter D(m)	6.72	Project design document
Propulsion speed v(1.9 cm/min)	1.9	Project design document
The number of spokes in closed portion k	4	Project design document
Rotate speed of cutter w(r/min)	0.9	Project design document

5.2 The Distribution of Surface Deformation ω Along X and Y Direction

Figure 5(a) shows the surface deformation along the x direction. Along the shield driving direction, there is a large range of uplift and the maximum deformation is located at the central shield axis ($y = 0$). The maximum surface uplift is 15.4 mm, which occurs about 12 m behind the excavation face ($x = -12$ m). The uplift at the face ($x = 0$ m) is 2.9 mm. The maximum ground deformation is concentrated in the back grouting area of the shield tail ($-13\ \mathrm{m} < x < -11.4$ m), and this deformation is mainly caused by the synchronous grouting pressure p_3. From the analysis, the ground surface deformation along the central shield axis ($y = 0$ m) is the largest. Along the vertical range of $y = 12.66$ m ($y = d + 3R_1$) position, the surface deformation is from –1.5 mm to 2 mm, which means the impact shield construction is negligible. Along the shield driving direction, the surface deformation is less than 2 mm at 6 m ahead of the excavation face and 13 m behind the shield ($x > 6$ m or $x < -24$ m). Analytical results of this paper are in agreement with the on-site monitoring results.

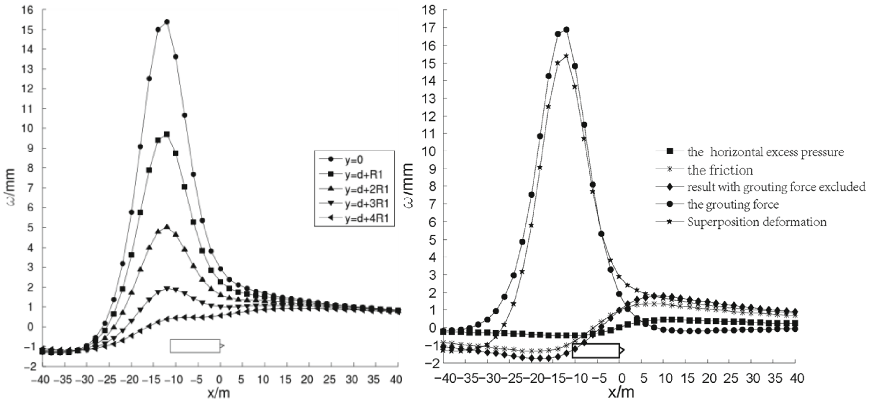

(a) (b)

Fig. 5. (a) Ground surface deformation along the X direction; (b) Comparison of effects of three factors on ground surface deformation

As for y direction, the surface deformation is symmetrical along the shield axis, and it decreases with the increasing distance ($x = 0/5/20$ m). The ground surface deformation is mainly concentrated within 12 m of both sides of the central shield axis (deformation value >2 mm). With the increase of the distance from the central axis, the ground deformation decreases gradually, and so does the disturbance of shield tunneling.

5.3 Comparison of Contributing Factors

To further analyze the characteristics of surface deformation under the three factors, surface deformation along the central axis ($y = 0$) was studied. p_1 has little effect on the surface deformation because the value of surface deformation caused by p_1 is between –0.5 mm–0.5 mm. The surface deformation induced by p_2 is bounded about 6 m behind the excavation face ($x = -6$ m). Surface deformation caused by the non-uniform friction p_1 is much larger than that caused by p_1. What's more, the surface deformation under the impact of p_1 and p_2 is antisymmetric in the shape of an 'S'.

It should be noted that surface uplift caused by the synchronous grouting pressure p_3 is very obvious, and the maximum uplift is 16.78 mm (at $x = -18$). What's more, p_3 strengthens the surface uplift caused by p_1 and p_2, but offsets the settlement behind the excavation face. Therefore, appropriate setting of the synchronous grouting pressure p_3 can assist the settlement control behind the excavation face.

6 Conclusions

Based on the quasi rectangular shield tunnel project at Ningbo Metro Line 3, the Mindlin solution in elastic mechanics was used to analyze the surface deformation caused by quasi rectangular shield tunneling. The analysis results show that:

(1) The maximum uplift caused by the construction of the quasi rectangular shield is 15.4 mm, and this is controllable (20 mm).
(2) Synchronous grouting pressure induces significant surface uplift, and it can enhance the surface uplift caused by excess pressure at the face and shell friction. However, it can also offset the surface settlement caused by those two factors.
(3) Surface deformation is sensitive to grouting pressure. Therefore the grouting pressure should be controlled so that it will not be too large during the construction.

References

1. Kashima, Y.: Development and application of the DPLEX shield method: results of experiments using shield and segment models and application of the method in tunnel construction. Tunn. Undergr. Space Technol. **11**(11), 45–50 (1996)
2. Zhou, W.: Construction technique of DOT shield. Modern Tunn. Technol. **04**, 22–32 (2004)
3. Zhang, D.: Additional stress analysis of subway shield tunneling. Undergr. Space **19**(5), 379–382 (1999)
4. Sun, T.: Analysis of additional stresses of soil disturbance induced by propulsion of double-O-tube shield. Rock Soil Mech. **19**(8), 2246–2251 (2008)
5. Lin, C.: Influences of tunnel slope on shield tunnelling-induced heave and subsidence of ground surface. Chin. J. Geotech. Eng. **36**(7), 1203–1212 (2014)
6. Wang, H.: Effect of cutterhead compressing the front soil and influence of head aperture ratio on contact pressure of EPB shield to the front soil. China Civil Eng. J. **42**(7), 113–118 (2009)
7. Yang, M., et al.: An approach for a single pile in layered soil. J. Tongji Univ. **04**, 421–428 (1992)
8. Qi, J.: Analysis of superimposed stress of surrounding soil due to shield tunneling. Rock Soil Mech. **29**(2), 528–529 (2008)

9. Liang, R., et al.: Analysis of ground surface displacement and horizontal movement of deep soils induced by shield advancing. Chin. J. Rock Mech. Eng. **34**(3), 583–593 (2015)
10. Potyondy, J.: Skin friction between various soils and construction materials. Geotechnique **11**(4), 339–353 (1961)
11. Fu, D.: Technical development and application of rectangular shield tunnelling in china. Shanghai Constr. Sci. Technol. **02**, 4–5 (2008)

Ground Penetrating Radar Inspection Experiment on a Shield Tunnel Segment and the Backfill Grouting

Tan Qin[1], Yonghui Zhao[1](✉), Shufan Hu[1], Cong An[1], Nan Chen[1], Cheng Chen[1], and Yifan Chen[2]

[1] School of Ocean and Earth Science, Tongji University, Shanghai, China
`zhaoyh@tongji.edu.cn`
[2] College of Civil Engineering, Tongji University, Shanghai, China

Abstract. Defects of the backfill grouting have a strong impact on the shield tunnel engineering and gotten more and more attention from the experts in recent years. To estimate the thickness of the grouting and the position of some objects behind a shield tunnel segment, we conducted a field experiment using Ground Penetrating Radar (GPR). In the paper, a segment was put vertically on the ground with half of its outer surface covered by a wooden box. We injected concrete grout into the box until 80% of the box was filled by it. SIR4000 pulse radar system made by GSSI (Geophysical Survey System Inc.) with 400 MHz center-frequency antenna was used in this experiment. First, static measurements show that the direct wave and the coupling wave were stacked together when the antenna was put on the internal surface of the segment. We, therefore, regard the peak point as the time zero of the signal. Then contrastive analysis reveals that Principal Component Analysis (PCA) performed better than Average Mean Removal (AMR) in eliminating the direct wave and highlighting the effective signals. From the processed radargram of dynamical measurement, we can see that it was easy to distinguish the inner structure and the interfaces of the segment, as well as the grouting and other objects in the back. After a week, we retested it again and found that the travel time of electromagnetic wave passing through the grouting became shorter than the previous one. It may be attributed to the loss of moisture in the solidification process of concrete, which means that the technique we proposed can monitor the change of the grouting layer and provide decision-maker with reliable information of the shield tunnel quality.

Keywords: GPR · Backfill grouting · Shield tunnel segment
Principal component analysis

1 Introduction

With the rapid development of urbanization in China, more and more underground space has been used for transportation. The shield tunnel plays a vital role in the underground construction. There is an annular region between the shield tunnel segments and the stratum, which is grouted synchronously in the process of tunnel construction so as to bed and stabilize the tunnel. However, some potential problems, such as cavities, water

© Springer Nature Singapore Pte Ltd. 2018
D. Zhang and X. Huang (Eds.): GSIC 2018, *Proceedings of GeoShanghai 2018 International Conference: Tunnelling and Underground Construction*, pp. 112–120, 2018.
https://doi.org/10.1007/978-981-13-0017-2_11

seepages, and cracks, might occur if the distribution of the grouting is heterogeneous. Those problems will shorten the expectancy service life of tunnel, threaten personal security and give rise to inestimable economic losses (Du 2006; Liu 2012). Therefore, it is necessary to detect the quality of the backfill grouting, in terms of the layer thickness and homogeneity of it, at the same time as the construction.

For a long time, engineers usually controlled the quality of the back grouting by monitoring the corresponding parameters, such as grouting volume and the pressure, and the properties and amount of the fluid cement grout. Those estimation methods are costly and blind and sometimes cannot give an accurate result (Xie 2016). Borehole coring provides the worker with direct evidence but it is destructive and only reveals regional features (Qi 2011). In recent years, Ground Penetrating Radar (GPR) has been used to determine the distribution of mortar and cavities in the grouting layer due to its benefits including safety, convenience, low-cost, quickness, high-accuracy and non-destruction for the testing object, and so on (Benedetto 2010). However, GPR is easily affected by the materials connected with shield tunnel segment, especially the bar-mat reinforcement, since that this technology is built on the theory of electromagnetic wave propagation. So the identification of the grouting layer interfaces in radar profiles would be hard unless appropriate methods are introduced to data processing stage. Furthermore, the solidification and the shrink of the grouting would bring about water loss and electrical characteristic variation with time goes by, which may alter the probing result. In this way, the radar reflection features in different time should be taken into consideration. it would be useful for the assessment of ground settlement and disengagement, and finally, help the engineer to make the decision whether the secondary grouting is implemented.

From what has been mentioned above, we can see that it is necessary to carry out a GPR experiment associated with the qualitative detection of the grouting layer behind the shield tunnel segment. In the paper, the fundamental principle of GPR is presented firstly. Then we conduct two static tests to ensure the penetrability of radar and the effectiveness of data processing methods. Finally, the responses from a shield tunnel segment and the backfill grouting in a series of the dynamical comparative trial are discussed.

2 The Principle of GPR

2.1 GPR System

In the study, we used SIR4000 pulse radar system made by GSSI (Geophysical Survey System Inc.) with 400 MHz center frequency antenna. Transmitter and receiver are packaged in a shielded antenna which keeps those two at a fixed position and focuses the transmitted electromagnetic waves mainly propagating in the forward direction. Figure 1a shows a 3000 × 1200 × 350 mm (mm) shield tunnel segment with a 6000-millimeter inner diameter and 6350-millimeter external diameter. It is put vertically on the ground and detected by a worker holding the antenna on the internal surface of it. The antenna transmits an electromagnetic wave into the segment and objects behind it such as grouting and stratum in practice. The signals then received by it represent the reflection from the interfaces with different electrical properties (e.g. dielectric permittivity, conductivity, and permeability). The information will be displayed as a real-time radar profile on the screen and be saved automatically. After a number of data processing, radargram finally shows the general distribution characteristics of the medium which offers interpreter precise and effective images associated with the invisible area behind the inner surface.

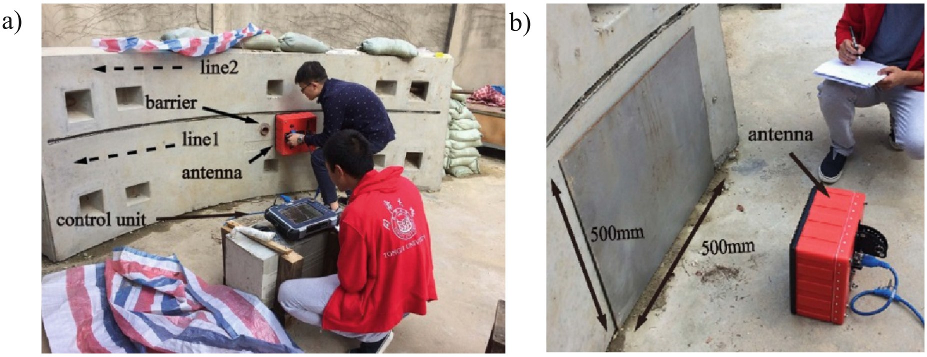

Fig. 1. GPR experiment site. (a) a shield tunnel segment and GPR equipment; (b) steel plate total reflection test using a 400 MHz antenna.

2.2 Zero Time: Steel Plate Testing

Zero time is the start point of effective signals and plays a vital role in time-depth conversion. The travel time of the direct wave reflected from the segment surface is regarded as the zero time in general. Whereas the coupling wave which transfers from the transmitter to receiver directly always obstructs the identification of direct wave because they may stack together in some cases. So we need to do several tests to find in which situation the coupling wave has the similar travel time as the direct wave and when they separate.

First, we put the shield antenna toward the air, at which situation no substance reflected the electromagnetic wave and the received signal was nothing but the coupling wave. As it is shown in Fig. 2a, the amplitude of the signal reached its peak at about 15 nanoseconds (ns) which means the first arrival of the coupling wave is about 15 ns. Second, we conducted an experiment of measuring the reflected wave from a steel plate (size 500 × 500 mm in Fig. 1b), namely the direct wave. Both the steel plate and the antenna were perpendicularly put on the ground. We kept the 400 MHz antenna at the position of 500 mm away from the steel plate for a moment and then changed it to 1000 mm, 1500 mm and 2000 mm respectively. Signals acquired can be seen in Fig. 2b–e, the original signal only consisted of antenna coupling wave and the direct wave. The coupling wave had stable waveform and the amplitude of it was much larger than the direct wave in different distance between the antenna and the steel plate. To see the direct wave clear, we matched the maximal amplitude of the original signal in Fig. 2a with Fig. 2b–e and subtracted the coupling wave from Fig. 2b–e severally. Unfortunately, the reflection from the plate surface was still very weak even after the elimination of antenna coupling wave. It was caused by the exponential attenuation of electromagnetic radiation, hence we added an exponential gain to the processed signals. In this way, the direct wave could be well-marked in the waveform (dotted line in Fig. 2b–e).

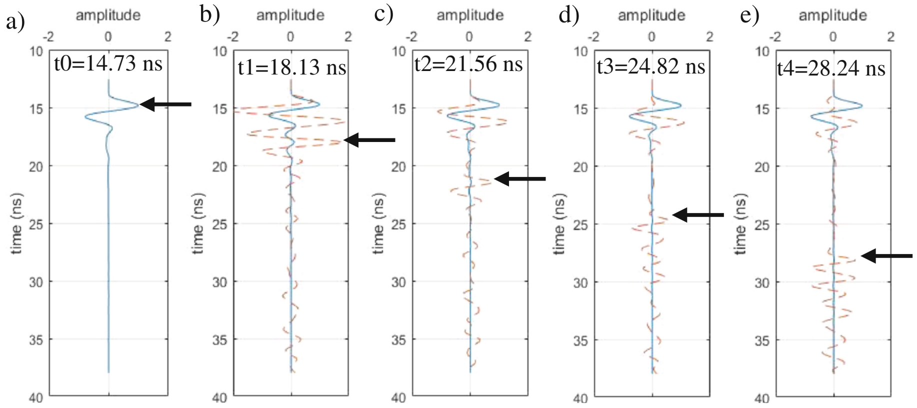

Fig. 2. GPR single trace signals. (a) the coupling wave; (b) (c) (d) (e) reflected signals from the steel plate surface, the distance between the antenna and the steel plate is (b) 50 cm; (c) 100 cm; (d) 150 cm; (e) 200 cm. the solid line means original signal, the dotted line means signal after the elimination of the coupling wave and the addition of exponential gain.

It is clear from Fig. 2b–e that travel time of the reflected wave from the steel plate is signified by black arrows at t1 = 18.13 ns, t2 = 21.56 ns, t3 = 24.82 ns and t4 = 28.34 ns respectively. We can then obtain the interval time $\mathrm{d}t = (\mathrm{t4} - \mathrm{t1})/3 = 3.403333\,\mathrm{ns}$, the speed of electromagnetic propagation in the air $v = 2\mathrm{dx}/\mathrm{dt} = 0.293829608\,\mathrm{m/ns}$ with the error rate 1.99% compared with the internationally acknowledged value c = 0.299792458 m/ns. Therefore we acquire the zero time $t0 = \mathrm{t1} - \mathrm{dt} = 14.73\,\mathrm{ns}$ when the antenna is positioned on the surface of the steel plate where the distance between them is zero. The zero time is coincident with the travel time of the coupling wave, which means that antenna coupling wave and direct wave share the same arrival time when we put the antenna on the inside surface of shield tunnel segment. So the first peak of the waveform can be considered to be the position of the surface.

2.3 Direct Wave Removal Methods: Man Movement Testing

After zero time adjusting, the coupling wave elimination and exponent gain, it can be observed from the processed radargram (Fig. 2b–e) that the direct wave has comparatively strong energy, especially when the distance between the antenna and the surface is very near. Thus we also need to remove direct wave so that the effective signals in segment detection can be visible. Average Mean Removal (AMR) is based on the fact that the travel time and the energy of the direct wave change a little no matter where the antenna moves on the internal surface of shield tunnel segment. For this reason the average of all trace in radar profile is supposed to be the direct wave. We eliminate the average from radargram and then the information reflected from interior structure emerges on the processed profile.

To test the feasibility of processing method and test the penetrability of radar when it is used for tunnel segment detection, we designed two kinds of human movement experiments with radar antenna keeping in a fixed place. Figure 3a and b shows that

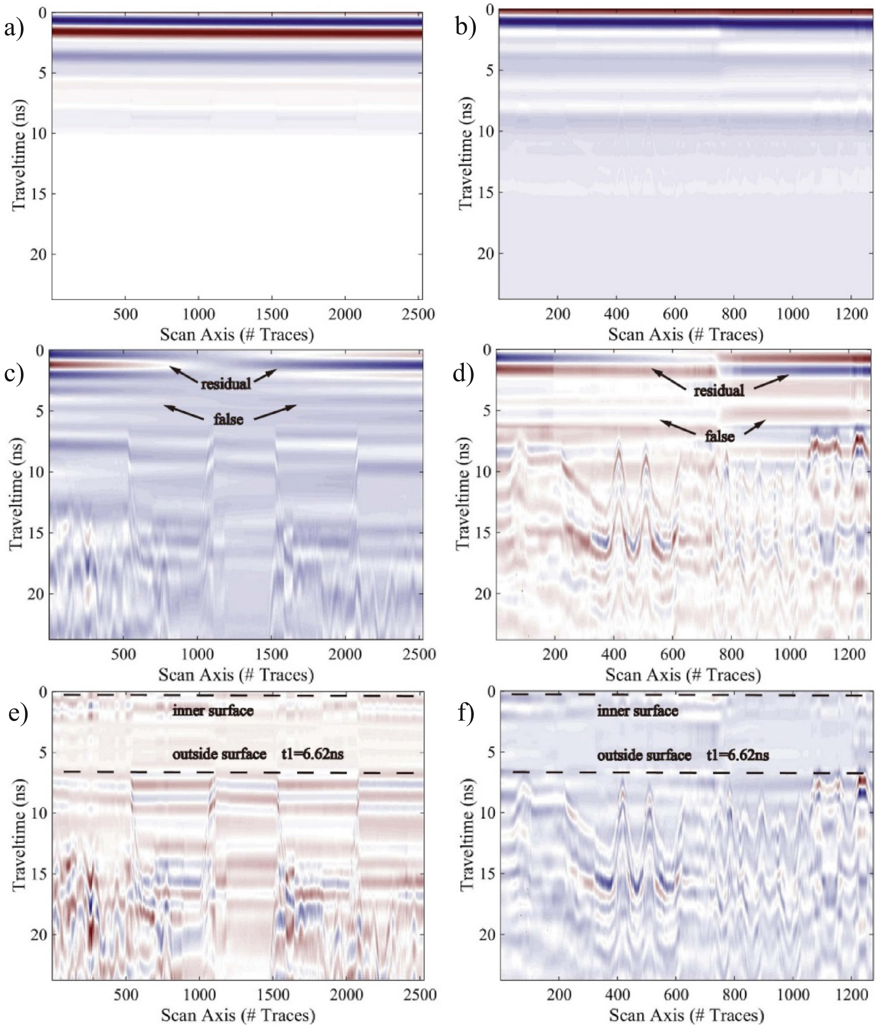

Fig. 3. Processed GPR profiles. (a) regular walking behind the segment (original data); (b) regular walking behind the segment (original data); (c) regular walking behind the segment (processed by AMR); (d) random walking behind the segment (processed by AMR); (e) regular walking behind the segment (processed by PCA); (f) random walking behind the segment (processed by PCA).

there was a man regularly and randomly walking behind the segment respectively. After processed by AMR we can see the personal movements occur (Fig. 3c–d). In Fig. 3c, we notice that he stayed at the place 0 mm against the outside surface of the segment during the period of 0–500 traces, as well as 1000–1500 and 2000–2500, and moved to the position of 1000 mm behind the segment in 500–1000 traces and 1500–2000 traces. Figure 3d illustrates that test taker did the random movement in the rear. However, the residual of the direct wave in Fig. 3c and d is still strong and the horizontal false which does not exist before the treatment of AMR occurs.

Principal Component Analysis (PCA), one of the well-known signal-processing methods, is a compression technique with minimum loss of information in time-domain GPR signals. PCA identifies similar patterns in data and reorganizes the data in such a way that the similarities and differences are highlighted. Mathematically, this is achieved by an orthogonalization of a matrix constructed by adding rows with traces of input data, so that these rows are not correlated with each other. It was used to estimate the depth and radius of buried tubes in a non-homogenous concrete structure and shown a great performance (Pantoja 2011). In our study, we introduced PCA to remove the direct wave. We can see from Fig. 3e and f that the residual of the direct wave has been cleared up and the horizontal false does not arise. In addition, the inner surface and outside surface (t1 = 6.62 ns) of shield tunnel segment are easy to be recognized and the human motion become clearer than Fig. 3c and d respectively. The thickness of the segment is h1 = 350 mm, so we can get the velocity of electromagnetic wave in segment is v1 = 2h1/t1 = 0.105740 m/ns, the relative dielectric constant $\varepsilon_1 = (v/v1)^2 = 8.584319$.

3 Back-Filled Grouting Testing

As it is shown in Fig. 4a and b, half of the outside surface of the shield tunnel segment was covered by a wooden box with a volume of 1500 × 1200 × 200 mm. The box consisted of three planks and was separated from the segment by a plastic film in advance. We grouted cement paste into the box until the height of 1000 mm leaving 200 mm empty (the thickness of the grouting is 200 mm). Then we moved the shield antenna from right side of the internal segment surface to the left among the direction of line1 in Fig. 1a. Rebars can be easily picked out from the segment in processed profile (Fig. 5a), which will generate distraction to the objects behind it to some extent (Zhao 2010; Xie 2014). The antenna goes through the area with back-filled grouting in the section of 0.5–2.0 meters (m), there is a continuous reflection in travel time t2 = 12.48 ns which is the boundary of the grouting and the board. The regions from 2.0 m to 3.0 m can only be observed with a strong reflection of the external surface of the segment and other disorder reflection from the objects behind the segment, such as a sandbag.

In Fig. 5b, we place a steel plate against the grouting (signed by a red solid line), compared with Fig. 5a, the reflection of the interface between the grouting layer and steel plate is stronger slightly, and the difference of plus-minus amplitude in the boundary become bigger. What is worth mentioning that there was a barrier in the middle part of the segment and the antenna had to be lifted up when it was moved to this area (see Fig. 1a). The vertical interference around 1.5 m in Fig. 5a–c is caused by this action.

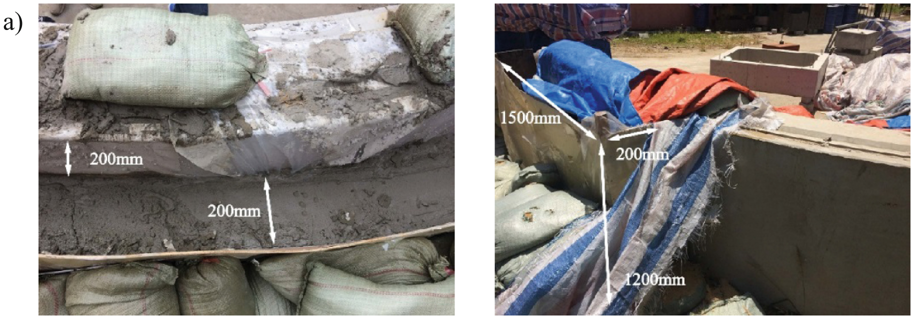

Fig. 4. Outside surface of the segment. (a) the grouting in the wooden box; (b) half of the outside surface is covered by the wooden box.

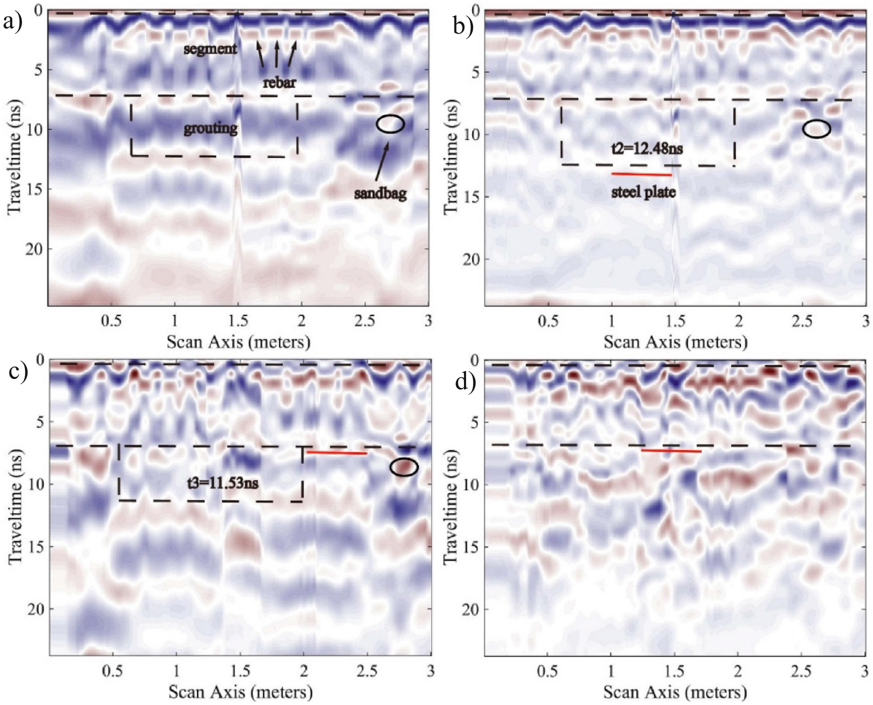

Fig. 5. GPR measurements of the segment with half of the outside surface covered by the wooden box and back-filled grouting. (a) no steel plate; (b) a steel plate is placed behind the grouting layer; (c) a steel plate is placed behind the segment, data measured 7 days after grouting; (d) a steel plate is placed behind the segment where no grouting fills.

When it comes to the Fig. 5c which obtained 7 days after the first measurement, we changed the steel plate to a position just beside the grouting. From the GPR profile, it can be seen that the reflection from the outside surface of the segment is stronger than it's in Fig. 5b. On the other hand, it should be noticed that the travel time of the interface between the grouting layer and the wooden box (t3 = 11.53 ns) is shorter than the previous one (t2 = 12.48 ns). with the comparative analysis of the relative dielectric coefficient of the segment in the first measurement $\varepsilon_2 = 18.533397$ and in the second measurement $\varepsilon_3 = 13.011363$, we conclude that the reduction of a relative dielectric constant in 7 days is the result of water loss in the solidification process of concrete (Li 2010). It proves that dynamic monitoring should be implemented in engineering practice for the sake of probing the compactness and thickness of grouting.

We conducted the measurement along with the line2 in Fig. 1a where no grouting filled in the wooden box in the height of 1000–1200 mm and the plate was put near the middle area behind the segment. As it is presented in Fig. 5d, reflection from the steel plate is strongest in the outside surface of the segment and the signal behind the steel plate is chaotic. While the diffraction generated by a metal border in both ends of the steel plate seriously influences the surrounding effective signals.

4 Conclusion

The result from research proves that the proposed technique is an effective and reliable technique in the tunnel grouting quality inspection. With the exact identification of time zero and elimination of coupling wave and direct wave, the grouting and other objects such as man and steel plate behind the shield tunnel segment can be distinguished easily from the GPR profiles. Moreover, solidification degree of grouting can be evaluated by the relative dielectric constant of radar detecting result which is a vital factor in judging the moisture content and its trend over time.

Further research will be conducted on the construction site where solum and another complicated medium will be taken into account.

Acknowledgement. This work is partially sponsored by National Natural Science Foundation of China No. 41774124 and No. 41374146. Authors wish to express gratitude to Prof. Xiongyao Xie and Mr. Biao Zhou who offered the technical guidance and experimental sites in College of Civil Engineering, Tongji University.

References

Benedetto, A., Blasiis, M.R.D.: Applications of ground penetrating radar to road pavement: state of the art and novelties. In: Geoshanghai International Conference, pp. 412–419 (2010)

Du, J., Huang, H.W., Xie, X.Y., et al.: Research on the effect of permittivity on the result of GPR detection of grouting material behind shield tunnel segment. In: American Society of Civil Engineers, pp. 120–127 (2006)

Li, C., Miao, L., Yue, J.: Research on detection to moisture content of flexible pavement by GPR. In: Geoshanghai International Conference, pp. 420–426 (2010)

Liu, H., Xie, X., Sato, M.: Accurate thickness estimation of a backfill grouting layer behind shield tunnel lining by CMP measurement using GPR. In: International Conference on Ground Penetrating Radar. IEEE, pp. 137–142 (2012)

Pantoja, M.F., Rodríguez, J.B., Bretones, A.R., et al.: Application of neural network and principal component analysis to GPR data. In: International Workshop on Advanced Ground Penetrating Radar. IEEE, pp. 1–4 (2011)

Qi, W., Tian, T.J., Wu, C.X.: Ground penetrating radar in tunnel backfill grouting quality evaluation research on the application. In: International Conference on Electric Technology and Civil Engineering. IEEE, pp. 6633–6636 (2011)

Xie, X.Y., Chen, Y.F., Zhou, B.: Data processing of backfill grouting detected by GPR in shield tunnel and research on equipment of GPR antenna. In: International Conference on Ground Penetrating Radar. IEEE, pp. 1–5 (2016)

Xie, X., Yao, R., Qin, H., et al.: Study on radargram characteristics of the backfill grouting quality evaluation of a shield tunnel using GPR. In: International Conference on Ground Penetrating Radar. IEEE, pp. 407–412 (2014)

Zhao, Y., Wu, J., Xie, X., et al.: Multiple suppression in GPR image for testing back-filled grouting within shield tunnel. In: International Conference on Ground Penetrating Radar. IEEE, pp. 1–6 (2010)

Numerical Analysis of Ground Displacement and Pile Response Due to Tunneling in Soft Soil Considering the Creep Behavior

Yu Pan, Jun-Jie Zheng(✉), Lan Cui, and Rong-Jun Zhang

Institute of Geotechnical and Underground Engineering,
Huazhong University of Science and Technology, Wuhan 430074, China
`zhengjj@hust.edu.cn`

Abstract. The additional pile response due to the creep behavior of the soil is disadvantageous to the safety of pile. However, in the current studies for considering the creep behavior of the soft soil, the pile response induced by the long-term settlement of soil is seldom investigated. This paper mainly discusses the pile response during the excavation and operation periods considering the creep behavior of soft soil. The finite difference software FLAC3D is utilized to simulate the excavation of tunnel and the creep behavior of soil based on the two-stage analysis method. In the first stage, the displacement controlled method (DCM) is applied to simulate the instantaneous settlement of soil during excavation period. In the second stage, the creep behavior of soft soil is considered to estimate the long-term settlement of soil during operation period. While the creep behavior of soil is not considered, the simulation results such as the shape of trough, pile response are compared with the results of existing studies, and the numerical model is verified to be acceptable. While the creep behavior of soil is considered during the operation period, the influence of the creep behavior on the pile response such as its deflection, settlement, axial force and bending moment of the long-term soil settlement are discussed. The effects of the four typical mechanical parameters in the creep model on soil deformation and pile response are investigated.

Keywords: Pile response · Tunneling · Creep behavior · Soft soil
Two-stage analysis method

1 Introduction

The urban underground rail transit has developed rapidly in recent decades. The complexity of soil and the negative impact on adjacent buildings induced by tunneling are gradually appearing to be a crucial problem to be solved in the excavation and operation periods. The problem caused by long-term settlement in soft clays was studied by several authors. Shirlaw [1] analyzed many data in practice and acknowledged that 30% to 90% of the total settlement of soft soil is due to the time-dependent settlement. Zhang [2] established a numerical model to investigate the effects of consolidation and lining in a long-term settlement based on stepped excavation method.

© Springer Nature Singapore Pte Ltd. 2018
D. Zhang and X. Huang (Eds.): GSIC 2018, *Proceedings of GeoShanghai 2018 International Conference: Tunnelling and Underground Construction*, pp. 121–130, 2018.
https://doi.org/10.1007/978-981-13-0017-2_12

The pile responses induced by tunneling were mainly evaluated by the experiment, the analytical and numerical methods. For the experiment method, Morton [3] implemented the laboratory test, Loganathan [4] carried out the centrifugal model tests, Meguid [5] presented a scale testing to investigate the process of excavation and the stresses were measured between the lining and the exited piles. For the analytical method, Loganathan [6] and Chen [7] proposed a two-stage method to analyze the pile responses, Huang [8] combined the method of Loganathan [6] and Winkler model to simplify the computation. For the numerical method, Han [9] adopted a two-stage method in numerical analysis of pile response. Liu [10] used the nonlinear coupled finite element analysis to evaluate the disturbance to piles induced by tunnelling. Zhang [11] compared the three-dimensional finite element analysis with the field data. Jongpradist [12] conducted a parameter analysis on the development of tunneling influence zones by numerical method. For simulations of creep behavior in tunneling, stepped method [2] is commonly used, however, the complexity in practice are not comprehensively considered, which may lead to inaccurate result. In the researches of pile response induced by tunneling [3, 4, 6], the main focus was the stress and deformation characteristics of pile, but the mechanism of how the soil deformation affects pile stress and deformation was seldom discussed.

This paper mainly simulates the excavation and operation period in two stages. In the first stage, the DCM (Displacement Controlled method) is applied in the excavation process, the result is verified with related researches and further analysis of the pile-soil interaction mechanism is implemented. In the second stage, the creep behavior is considered during the operation period, the effects of the four typical mechanical parameters in the creep model on soil deformation and pile response are discussed, and the comparison between creep model and Mohr-Coulomb (M-C) model is proposed to investigate the impact of creep behavior on pile responses.

2 Problem Statement

2.1 First Stage Analysis

Two methods have been presented by the current studies to simulate the excavation of a tunnel. The first one is the stepped excavation simulation that considers the elaborate construction steps. Another one is the one-step excavation simulation that excavates the tunnel in one step. In this analysis, as the long-term mechanical behavior of the soft soil is investigated, the one-step excavation simulation is applied based on the displacement control method, which has two merits: (1) it is simplified and efficient; (2) it fits well with a large amount of the measured data.

Rowe [13] proposed an oval-shaped displacement mode for the soil settlement after the excavation (see Fig. 1). The mode is observed to agree with the measured data. Hence, in the simulation, the displacement is controlled according to this mode. The numerical simulation is undertaken by the FLAC3D and it consists of three steps: (1) excavate the soil and fix the boundary; (2) determine the nodal displacement and add it to the excavation boundary (see Fig. 1); (3) calculate the model until the excavation tunnel boundary nodes reach to the convergence boundary.

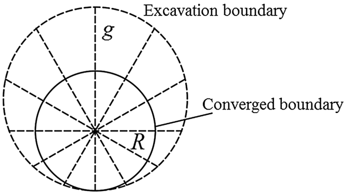

Fig. 1. Oval-shaped displacement mode

2.2 Second Stage Analysis

Based on the practical engineering, Shirlaw [1] pointed out that 30% to 90% of the total settlement of the soft soil corresponds to the time-dependent settlement. This implies that the creeping behavior of the soft soil cannot be neglected during the operation period. Herein, in the second stage, the impact of the creeping behavior of soft soil on the pile response is discussed.

Cvisc model in FLAC3D was adopted to model the time-dependent behavior of soft soil (see Fig. 2). It is characterized by a visco-elasto-plastic deviatoric behavior and an elasto–plastic volumetric behavior [14]. The visco-elasto-plastic constitutive law corresponds to a Burger model, and the plastic constitutive law corresponds to a Mohr-Coulomb model.

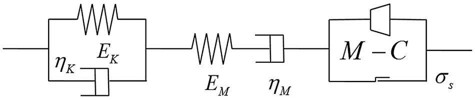

Fig. 2. Schematic graph of Cvisc model

3 Numerical Simulation

The gap parameter g of the numerical model can be solved by the following equations proposed by Loganathan [6]:

$$\varepsilon = \frac{\pi\left(R + \frac{g}{2}\right)^2 - \pi R^2}{\pi R^2} = \frac{4gR + g^2}{4R^2} \tag{1}$$

$$g = 2R\left(\sqrt{1+\varepsilon} - 1\right) \tag{2}$$

where R represents the radius of tunnel, and ε represents the equivalent ground loss ratio.

As shown in Fig. 3, the dimensions in the direction of x y and z is 110 m, 24.8 m, and 40 m. As shown in Fig. 4, the tunnel diameter and depth are 6 m and 20 m. A 2 × 2 pile group, with four identical piles of 0.8 m diameter and 25 m long, is located horizontally 4.5 m (front piles) and 6.9 m (rear piles) away from the tunnel centerline, and the pile spacing is 1.2 m.

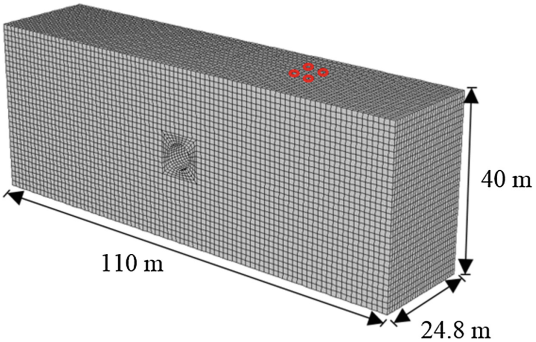

Fig. 3. Numerical model

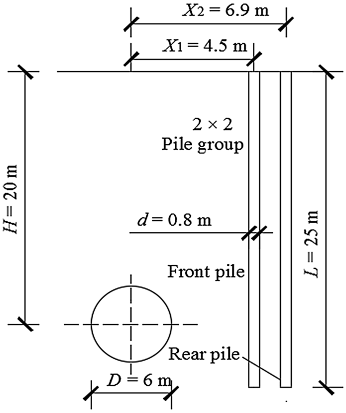

Fig. 4. Tunnel-pile group configuration

4 Verification

The proposed numerical simulation by FLAC3D is compared to the studies proposed by Loganathan [4] and the finite element solution of Xu and Poulos [8]. In the study by Xu and Poulos [15], the pile response induced by the tunneling is simulated by use of a finite program GEPAN, and analysis of multiple single piles which incorporate the effect of external soil movements due to tunnel excavation has been carried out. It is mentioned that both the analyses in [4, 15] adopted the DCM. For verification, the equivalent ground loss is set to be 1%. By substituting the equivalent ground loss in Eq. (2), the corresponding gap parameter g is 30 mm. The mechanical properties of soil and pile are listed in Table 1. In the FLAC3D model, pile is modeled as structural element and soil is regarded as elastic material.

Table 1. Properties of soil and pile.

Soil	Elastic model
Young's modulus	2.4×10^{7} N·m^{-2}
Poisson's ratio	0.495
Density	2000 kg·m^{-3}
Pile	Structure element
Young's modulus	30×10^{9} N·m^{-2}
Poisson's ratio	0.25
Stiffness of shear coupling	1.92×10^{10} N·m^{-2}
Cohesive strength of shear coupling	7.5×10^{4} N·m^{-2}
Friction of shear coupling	10°
Stiffness of normal coupling	1.6×10^{11} N·m^{-2}
Cohesive strength of normal coupling	7.5×10^{4} N·m^{-2}
Friction of normal coupling	0°

The reasonability of the FLAC3D model is verified by the program GEPAN. As shown in Fig. 5, the inflection points of the axial force, moment and deflection solved by the FLAC3D and GEPAN are almost located at the vicinity of tunnel centerline. Thus, the results of the inflection points mostly show a good agreement.

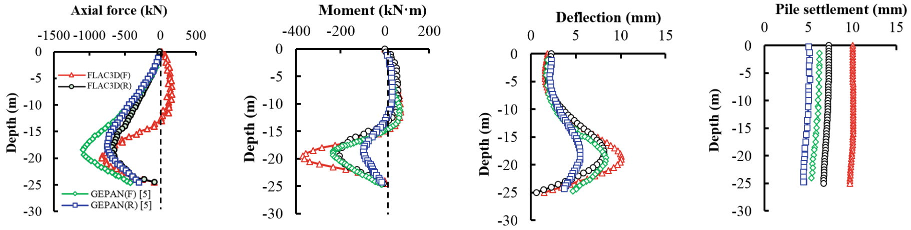

(a) Axial force (b) Moment (c) Deflection (d) Settlement

Fig. 5. Pile response due to excavation of elastic model (F denoting the front pile, R denoting the rear pile)

However, there is a significant difference above the inflection point of the front pile between the FLAC3D and GEPAN. The axial force of the FLAC3D appears to be positive above the depth of 13 m while GEPAN shows a negative axial force. What contributes to these opposite results is mainly the compressive stress inside the pile segment. As assumed, the compressive force generated by the compression deformation is positive and the pile shaft friction is negative, and the accumulated pile shaft friction is inferior to the compressive stress above the depth of 13 m.

Moreover, the results shown in Fig. 5(b) below the inflection point also reveal differences. First, the higher deflection and moment of the FLAC3D than the GEPAN are mainly due to the simplifications of GEPAN. The distributions of the stress at the pile-soil interface are assumed to be uniform over each element of GEPAN, actually the stress should varies around the pile interface, and the average value calculated at the center of GEPAN is definitely lower than the value at the edge of FLAC3D. Second, the pile settlement calculated by the FLAC3D is higher than the GEPAN program, because pile elements applied in FLAC3D have a better consideration of the frictional interaction, particularly the shear-directed friction, which may increase the pile settlement. As the settlement predicted by GEPAN is lower than that by FLAC3D, the relative settlement between the pile and soil, solved by GEPAN becomes higher. Since the pile shaft friction mainly affects to the axial force in the lower segment of pile, the axial force is consequently overestimated by GEPAN.

5 Discussion

5.1 Parameters During the Excavation and Operation Period

During the excavation period, the M-C model is applied. The soil properties are listed in Table 2. Han [9] suggested that the ground loss parameter ε varies from 0.5% to

Table 2. Soil Properties of Mohr-Coulomb model

Soil Properties	Mohr-Coulomb model
Young's modulus	2.4×10^7 N·m^{-2}
Poisson's ratio	0.3
Density	2000 kg·m^{-3}
Cohesion	3.0×10^4 N·m^{-2}
Angle of internal friction	20°
Tension limit	1.0×10^{10} N·m^{-2}

6.9%, herein, the ground loss parameter ε is selected to be 1.67%. By Eqs. (1) and (2), g is calculated as 50 mm. During the operation period, Cvisc model in FLAC3D is utilized to simulate the creep behavior of the soil mass. The related properties are listed in Table 3, the basic soil properties of Cvisc model are identical with the M-C model (i.e., Young's modulus, Poisson's ratio, density, cohesion, Angle of internal friction, Tension limit).

Table 3. Soil parameters of Cvisc model

Soil Parameters	Cvisc model
Maxwell shear modulus	576 MPa
Maxwell viscosity	57600 MPa·d
Kelvin shear modulus	576 MPa
Kelvin viscosity	576 MPa·d
Creep time	200 d

5.2 Sensitivity Analysis

The mechanical properties of the base case are listed in Table 3. The variable (i.e., $E_\text{M}, E_\text{K}, \eta_\text{M},$ and η_K) is represented by e, e_base indicates the value of e in the base case. s_base is the surface settlement above the tunnel center. $F_\text{base}, \text{M}_{\text{base},1},$ and $\text{M}_{\text{base},2}$ is the maximum axial force, positive moment and negative moment of pile for the base case.

As observed in Fig. 6, compared with η_K, the influences of η_M and E_M on the pile reaction and soil settlement are greater. η_K has trivial influence on all the results. It is interesting to note that the maximum axial force increases as the E_K increases (see Fig. 6(b)). The amount of pile shaft friction depends on the relative displacement of pile and soil, the pile shaft friction becomes higher with the increase of the relative displacement. While E_K decreases, the settlements of soil and pile all increases. However, the increase of the pile settlement is larger than that of the surrounding soil. Hence, as E_K decreases, the relative displacement of the soil and pile, and the pile shaft friction reduce.

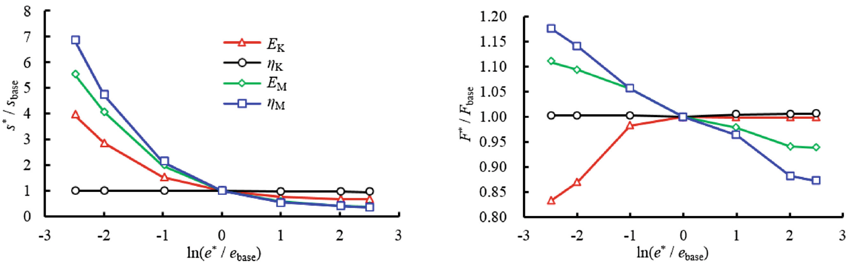

(a) Surface settlement above tunnel center (b) Maximum axial force

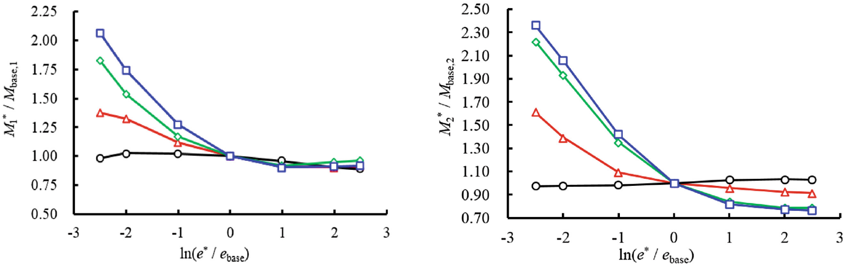

(c) Maximum positive moment (d) Maximum negative moment

Fig. 6. Sensitive analysis of E_M, E_K, η_M, and η_K

5.3 Comparison of Ground Settlement and Plastic Zone

A Gaussian distribution curve is proposed by Peck [16] to predict the transverse settlement profile based on the commonly observed profiles, and the result of his method is proved to be reasonable in practice, the settlement of any pinpoint on the ground can be estimated as shown in (3)

$$s = s_{\max} \exp(\frac{-y^2}{2i^2}) \tag{3}$$

where s represents the settlement of the pinpoint on the ground, $s_{\max}$ represents the maximum settlement on the ground, which occurs above the central point of the tunnel, y represents the spacing between the pinpoint to be computed and the central point, and i represents the spacing between the inflection point and the central point.

Figure 7 plots the curve of the transverse settlement of three constitutive models (i.e. elastic model, M-C model, creep model). It is found that the curve of the transverse settlement reveals the Gaussian distribution. While the distance is relatively far away from the excavation face, the settlement solved by the M-C model is close to that by the elastic model. However, while the distance is near the excavation face, the settlement solved by the M-C model is greater. This is due to the fact that M-C model leads to a great plastic zone near the tunnel face. When it considers the time dependent behavior of soil in creep model, the settlement of soil grows as expected.

5.4 Comparison of Pile Response

The deformation and force of the pile with the creep model and M-C model are compared here. The mechanical properties of the soil for the creep and M-C models can be found in Tables 2 and 3. The pile properties can be found in Table 1. As shown in Fig. 8(a), the axial force of the front pile by the M-C model is positive, which means the upper part of the pile is under compression during the excavation period.

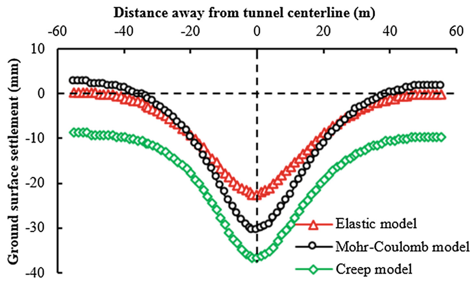

Fig. 7. Settlement curve of three constitutive model

It is noticed that the axial force of the front pile of the creep model is negative, and its magnitude is much greater than that of the M-C model. This implies that from the excavation period to the operation period, the positive axial force initially decreases to 0 but then changes to negative value, which increase to a higher value. The reason is, in the operation period, as time passes by, the long-term deformation around pile grows more rapidly due to the creep behavior, which leads to a higher pile shaft friction along the pile-soil interface. The sign of the pile shaft friction is opposite to that of the positive axial force. As a result, due to the increase of the pile shaft friction, the axial force changes the sign and increase to relatively great value. This implies, a safety factor for the bearing capacity of the pile during the operation period should be carefully considered. The divergence of deflection by the two model is noticed in the lower segment of front pile and rear pile. And the main reason accounts for this is, in this two models plastic zone develops. The upper soil tends to move to the excavation face, which squeezes the lower soil to move away from the tunnel (see Fig. 8(c)).

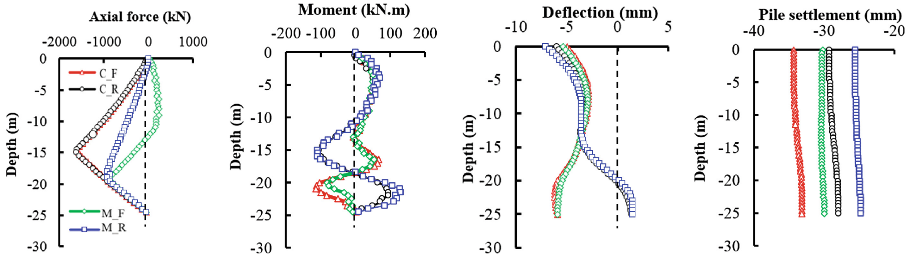

(a) Axial force (b) Moment (c) Deflection (d) Settlement

Fig. 8. Comparison of pile responses of M-C model and creep model (C denoting the creep model, M denoting the M-C model)

6 Conclusion

This paper mainly discusses the pile response due to tunneling considering creep behavior of soft soil. The following conclusions can be drawn from the analysis:

E_M and η_M have a greater impact on the long-term settlement and adjacent piles than the E_K, and η_K has rare influence on the results. In the comparison between creep model and M-C model, there are three points to be noticed. First, the axial force in the upper segment of front pile changes from negative value to positive value when considering creep behavior. Second, the divergence in the lower part of pile appears in both models, which is induced by the squeezing of upper soil. Third, for the creeping soft soil, it is required to consider the safety factor in engineering practice, especially in the design of pile bearing capacity.

References

1. Shirlaw, J.N.: Observed and calculated pore pressures and deformations induced by an earth balance shield: discussion. Can. Geotech. J. **32**(1), 181–189 (1995)
2. Zhang, D.M., Huang, H.W., Yang, J.: Influence of partial drainage of linings on long-term surface settlement over tunnels in soft soils. Chin. J. Geotechn. Eng. **27**(12), 1430–1436 (2005)
3. Morton, J.D., King, K.H.: Effects of tunnelling on the bearing capacity and settlement of piled foundations. In: Proceeding of the Tunnelling 1979, IMM, London, pp. 57–68 (1979)
4. Loganathan, N., Poulos, H.G., Stewart, D.P.: Centrifuge model testing of tunneling-induced ground and pile deformations. Géotechnique **50**(3), 283–294 (2000)
5. Meguid, M.A., Mattar, J.: Investigation of tunnel-soil-pile interaction in cohesive soils. J. Geotech. Geoenv. Eng. **135**(7), 973–979 (2009)
6. Loganathan, N., Poulos, H.G.: Analytical prediction for tunneling-induced ground movements in clays. J. Geotech. Geoenviron. Eng. **124**(9), 846–856 (1998)
7. Chen, L.T., Poulos, H.G., Loganathan, N.: Pile responses caused by tunneling. J. Geotech. Geoenv. Eng. **126**(6), 580–581 (1999)
8. Huang, M.S., Li, Z., Yang, C.: Analysis of the shielding effect of a pile group adjacent to tunneling. China Civ. Eng. J. **40**(40), 69–74 (2007)
9. Han, X., Li, N., Standing, J.R.: An adaptability study of Gaussian equation applied to predicting ground settlements induced by tunneling in China. Rock Soil Mech. **28**(1), 23–39 (2007)
10. Liu, C., Zhang, Z., Regueiro, R.A.: Pile and pile group response to tunnelling using a large diameter slurry shield – case study in Shanghai. Comput. Geotech. **59**(59), 21–43 (2014)
11. Zhang, Z.X., Liu, C., Huang, X., et al.: Three-dimensional finite-element analysis on ground responses during twin-tunnel construction using the URUP method. Tunn. Undergr. Space Technol. **58**, 133–146 (2016)
12. Jongpradist, P., Kaewsri, T., Sawatparnich, A., et al.: Development of tunneling influence zones for adjacent pile foundations by numerical analyses. Tunn. Undergr. Space Technol. **34**(1), 96–109 (2013)
13. Rowe, R.K., Kack, G.J.: A theoretical examination of the settlements induced by tunnelling: four case histories. Can. Geotech. J. **20**(2), 299–314 (1983)

14. Fahimifar, A., Tehrani, F.M., Hedayat, A., et al.: Analytical solution for the excavation of circular tunnels in a visco-elastic Burger's material under hydrostatic stress field. Tunn. Undergr. Space Technol. **25**(4), 297–304 (2010)
15. Xu, K.J., Poulos, H.G.: General elastic analysis of piles and pile groups. Int. J. Numer. Anal. Methods Geomech. **24**(15), 1109–1138 (1988)
16. Peck, R.B.: Deep excavation and tunneling in soft ground. In: Proceedings of the 7th International Conference on soil Mechanics and Foundation Engineering, Paper. Mexico, pp. 225–290 (1969)

Defining a “shallow” Tunnel by Stability Analysis with Discontinuity Layout Optimization

Yiming Zhang[2,3] and Xiaoying Zhuang[1,3](✉)

[1] Tongji University, Shanghai 200092, China
zhuang@ikm.uni-hannover.de
[2] Hebei University of Technology, Tianjin 300401, China
[3] Leibniz University of Hanover, 30167 Hanover, Germany

Abstract. During excavation of NATM tunnel in soft clays, stability problems could arise when the tunnel is too shallow, necessitating special treatment for the surrounding ground such as freezing and jet grouting. However, there is generally no specific rules to help the engineers to determine the critical depth of “shallow” tunnel, which is the dividing line between stably and unstable NATM tunnel design. When using factor of safety λ to quantify the stability of unlined shallow tunnel, λ can be considered as a function of tunnel depth D, height H, width W, cohesion, friction angle, and weight of the medium C, ϕ, and γ. In this paper, aiming at finding the relationship among D, W, C, ϕ, γ and λ of unlined shallow tunnel, we conduct parameters studies with an efficient numerical method for upper bound limit analysis: Discontinuity Layout Optimization. The results show it is possible to obtain λ only as a function of tunnel height and width when the other parameters are known, paving the way for quickly evaluate the stability of shallow tunnels for the researchers.

Keywords: Shallow tunnel · Stability of unlined tunnel
Discontinuity Layout Optimization (DLO) · Parameter studies

1 Introduction

The stability of tunnel depends on many factors including tunnel vertical depth. When shallow tunnels are more inclined to suffer from stability problems, the word “shallow” would correspond to different depth regarding different tunnel width, height and material properties of surrounding soils. In this work, we would like to present numerical studies helping to determine the critical depth for “shallow unlined tunnels” regarding different factors through a recently presented numerical approach—Discontinuity Layout Optimization (DLO).

Stability of tunnel structures can be quantified by factor of safety λ [1], with λ > 1 indicating high stability. In this work, we use the increasing factor of the load as λ, that λ is defined as the increasing factor of gravitational acceleration triggering the failure. If an unlined tunnel section holds λ > 1, the structure design can be considered as a relatively preferable design that the surrounding medium is theoretically self-supported.

© Springer Nature Singapore Pte Ltd. 2018
D. Zhang and X. Huang (Eds.): GSIC 2018, *Proceedings of GeoShanghai 2018 International Conference: Tunnelling and Underground Construction*, pp. 131–135, 2018.
https://doi.org/10.1007/978-981-13-0017-2_13

In our former work [2], we present a general numerical procedure for analyzing the stability of shotcrete supported shallow tunnels by applying a recently presented numerical method discontinuity layout optimization [3–7]. Our research reveals for shotcrete supported shallow tunnel, λ is a time-space-depended parameter, caused by the hydration processes of shotcrete and three dimensional effect. Regarding unlined tunnel in 2D condition, λ is considered to be time-independent, as a function of tunnel depth D, height H, width W, cohesion, friction angle, and weight of the medium C, ϕ, and γ, the relationship among which is the focus of this paper, which will be revealed by parameter studies.

2 Method and Model

2.1 Discontinuity Layout Optimization

As presented in [2], we use increasing factor of load for defining the factor of safety, that λ is a factor associating to the gravitational acceleration triggering the failure. Moreover, when considering the unified soil properties and the topology is independent of soil cohesion C. That our target function is to minimize(λ/C). And the constraints including:

- Compatibility constraint: $\mathbf{Bd} = \mathbf{0}$, where $\mathbf{B}$ is the compatibility matrix;
- Mohr-Coulomb associated flow rule constrain $\mathbf{N}[\mathbf{d}\ \mathbf{p}]^{\mathrm{T}} = \mathbf{0}$, where $\mathbf{N}$ is the flow rule matrix, as a function of the friction angle ϕ, and $\mathbf{p}$ is the plastic multiplier;
- Unit work constraint, which assumes that the total work done by the cohesive force is 1.

The detailed form of the target function and the constrains can be found in [2–5], which will not be recalled in this paper again.

The model considered in this paper is shown in Fig. 1, in which "n = 0" indicates the corresponding boundaries fixed along normal direction. The fully connected grid method is used for preprocessing. More specifically, a great number of nodes with spacing dp are prescribed into the model, then every two nodes are connected as a pair of potential discontinuity. When dp is small enough, great amount of potential discontinuities are introduced, leading to a reliable result. Benchmark tests have proved that the error between the results of DLO and analytical solutions will be less than 3% when the number of discontinuities is over millions [3, 6].

2.2 Parameters for Studies

Regarding the original geometric and material parameters used in the model, several dimensionless parameters are introduced the values and ranges of which are determined by considering normal soil materials, see Table 1. The spacing dp is taken as 0.25 m, which is a reliable value based on [2].

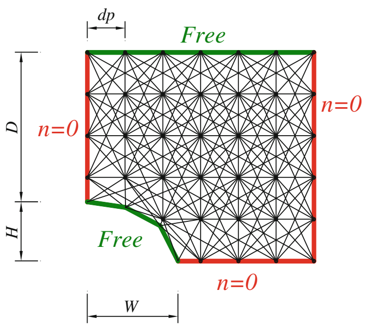

Fig. 1. The model of the unlined tunnel and the fully connected grid method for preprocessing (only a subset of the discontinuities are shown for the sake of clarity).

Table 1. The parameters for studies.

Basic parameter	Values
D	10 m
Γ	20 kPa/m
Φ	30°
Dimensionless parameter	Range
$\Pi_1 = H/D$	0.4–1.6
$\Pi_2 = H/W$	0.2–1.4

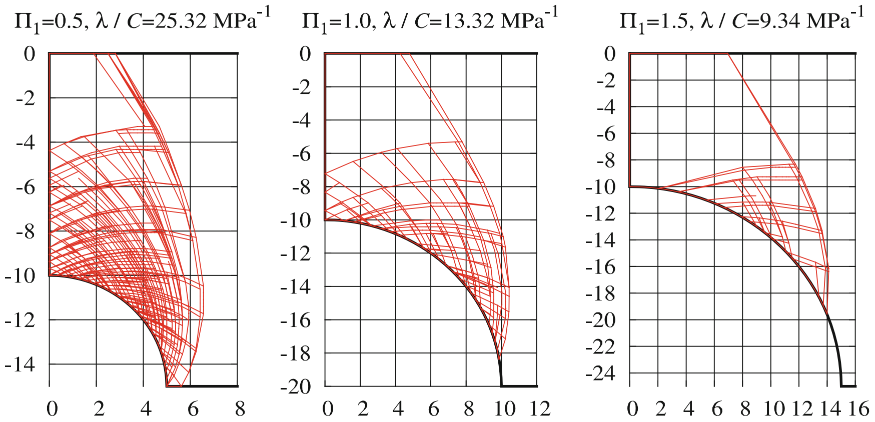

Fig. 2. The influence of Π_1 on (λ/C) with $\Pi_2 = 1$

3 Numerical Results

Figures 2 and 3 show the numerically obtained λ/C regarding changing Π_1 and Π_2, indicating general rules that deeper and narrower tunnels are more stable (or higher value of λ/C) than shallow and wide tunnels. Then Fig. 3 shows the shape of λ/C as a function of Π_1 and Π_2. Theoretically once C is known, base on this function it is possible to obtain the region λ bigger than 1 or a higher design value, assuring the design is preferable (Fig. 4).

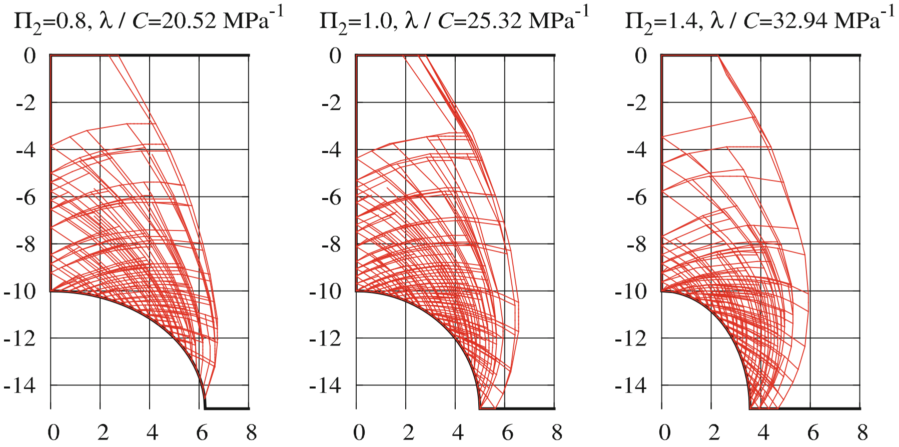

Fig. 3. The influence of Π_2 on (λ/C) with $\Pi_1 = 0.5$

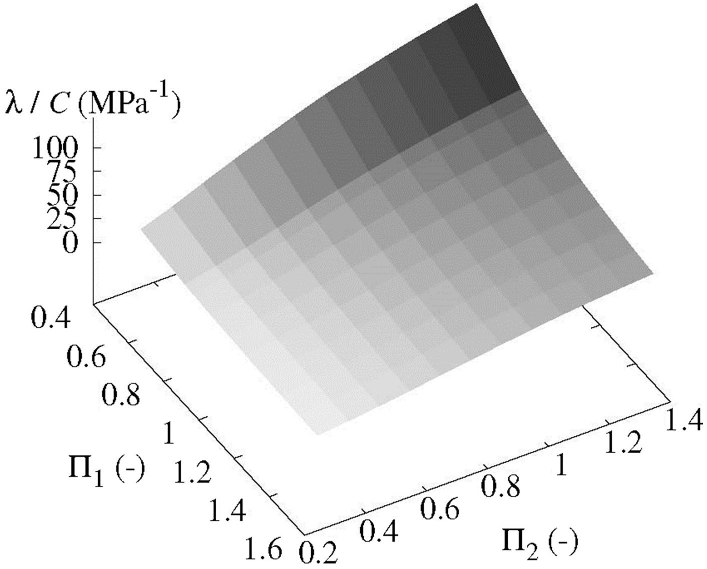

Fig. 4. Shape of (λ/C) as a function of Π_1 and Π_2

4 Conclusions

In this paper, we used an unlined tunnel model and applied discontinuity layout optimization for evaluating the factor of safety λ regarding different tunnel depth and width with parameter studies. The results prove that λ can be considered as a function of tunnel’s relative height and width when the other factors such as soil material properties are known. More parameter studies will be done in the future with the results of which the engineers are able to quickly evaluate λ regarding specific tunnel design.

References

1. Zheng, H., Tham, L., Liu, D.: On two definitions of the factor of safety commonly used in the finite element slope stability analysis. Comput. Geotech. **33**, 188–195 (2006)
2. Zhang, Y., Zhuang, X., Lackner, R.: Stability analysis of shotcrete supported crown of NATM tunnels with Discontinuity Layout Optimization (DLO). Int. J. Numer. Anal. Methods Geomech. (2017, under review). https://doi.org/10.1002/nag.2775
3. Smith, C.C., Gilbert, M.: Application of discontinuity layout optimization to plane plasticity problems. Proc. R. Soc. A **463**, 2461–2484 (2007)
4. Hawksbee, S., Smith, C.C., Gilbert, M.: Application of discontinuity layout optimization to three-dimensional plasticity problems. Proc. R. Soc. A **469**, 20130009 (2013)
5. Zhang, Y.: Multi-slicing strategy for the three-dimensional discontinuity layout optimization (3D DLO). Int. J. Numer. Anal. Methods Geomech. **41**, 488–507 (2017)
6. Smith, C.C., Gilbert, M.: Identification of rotational failure mechanisms in cohesive media using discontinuity layout optimisation. Geotechnique **63**, 1194–1208 (2013)
7. Smith, C.C., Cubrinovski, M.: Pseudo-static limit analysis by discontinuity layout optimization: application to seismic analysis of retaining walls. Soil Dyn. Earthq. Eng. **31**, 1311–1323 (2011)

Three-Dimensional Seepage Flow Analysis of Slurry Shield with Permeable Filter Cake

Xinsheng Yin, Zhi Ding(✉), Xinjiang Wei, and Gang Wei

Zhejiang University City College, Hangzhou 310015, China
dingz@zucc.edu.cn

Abstract. The filter cake on the tunnel face has a significant influence on the project of the slurry-driven shield. During the excavation, the only permeable filter cake is allowed to form because the rotating speed of cutter wheel is fast. Through the filter cake, the water of slurry will infiltrate into the soil. The water enhances the hydraulic head and the risk the failure of tunnel face. In order to determine the extent of hydraulic head, the analysis of seepage flow with the considering of the permeable filter should be conduct. A three-dimensional numerical model with the permeable filter cake was established for the analysis of seepage flow. Based on the numerical results, the hydraulic head field was obtained under different conditions. The hydraulic head field shows that the existence of filter cake seriously affects the hydraulic head field near the tunnel face. The hydraulic head tends to a hydrostatic head, at the points where is 2D in front of tunnel face, horizontal 1.5D to the lining of tunnel or soil surface. Three factors are simultaneously considered for assessing hydraulic head. The first is the excavation time, the second is the excess pressure and the third is the hydraulic conductivity. The excavation time and excess pressure have little influence on the distribution of normalized hydraulic head. When the hydraulic conductivity of soil increases, the hydraulic loss in filter cake increases from 0.16 to 0.5 the difference between slurry and hydrostatic pressure. On the contrary, the hydraulic loss in soil decreases when the hydraulic conductivity of soil increases.

Keywords: Bentonite slurry · Hydraulic conductivity · Hydraulic head
Seepage flow · Excess pressure

1 Introduction

The slurry shield has been widely used to construct the tunnels, especially for the tunnels under the river. The pressurized bentonite slurry is frequently used to stabilize the tunnel face in sandy soil. Under the pressure, the water of slurry infiltrates into the ground. Some of the small particles of slurry plug the pores on the tunnel face. And the large particles of slurry bridge the pores on the tunnel face. These particles form the filter cake, which becomes thicker with the increasing filtration time [1]. Some researchers [2, 3] presumed that filter cake is impermeable because the hydraulic conductivity of filter cake is far less than the hydraulic conductivity of soil [4, 5]. Based on the impermeable filter cake, a principle instructs the slurry pressure must be equal to the sum of three components (Fig. 1): the hydrostatic pressure at the center of the tunnel face,

© Springer Nature Singapore Pte Ltd. 2018
D. Zhang and X. Huang (Eds.): GSIC 2018, *Proceedings of GeoShanghai 2018 International Conference: Tunnelling and Underground Construction*, pp. 136–155, 2018.
https://doi.org/10.1007/978-981-13-0017-2_14

lateral effective stress at the tunnel axis and addition pressure (20 kPa) [6]. The density of the slurry is 1200 kg/m^3, the slurry pressure increases by 12 kPa when the height decreases by one meter. And the gradient of the earth pressure (including the hydrostatic pressure and lateral effective stress) is about 14–16 kPa/m. According to the principle above, the slurry pressure may be lower than the earth pressure. The probability of the tunnel face failure exists when the filter cake is presumed impermeable.

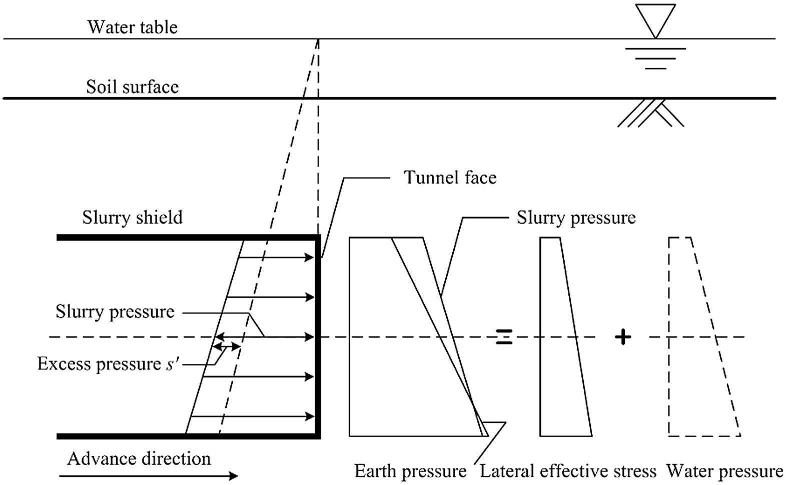

Fig. 1. Schematic diagram of slurry shield

However, the filter cake is permeable, because rotating cutter wheel removed the filter cake at a certain time interval (about 12 s) [7]. And only the permeable filter cake is formed in 12 s [8]. The permeable filter cake results in the rising hydraulic head in the soil. If the filter cake with a high hydraulic conductivity, the failure of tunnel face will occur. For instance, during the advance of a sewage gallery of 2.8 m diameter in Zurich, the bentonite slurry established only a low-quality filter cake, which led to various surface failures [9]. The failure will be prevented base on a better understanding of the seepage flow with the consideration of filter cake. Hence, the seepage flow analysis for slurry shields continues to be a major research topic.

Analytical and numerical methods were applied to analyze the seepage flow near the tunnel face of the slurry shield. Anagnostou and Kovári [10] assumed that the scope of seepage force is equal to the slurry penetration distance. And the seepage flow was considered based on the empirical equation. Broere and van Tol [11] ignored the filter cake and presumed that the penetration distance had an influence on the seepage flow. An analytical solution was suggested to calculate the pore pressure on the tunnel axis. However, this solution cannot deduce the three-dimension hydraulic head field. The omitting of the permeable filter cake may lead an insufficient result. Kim and Tonon [3] and Li et al. [2] used the numerical method to study the problem on the slurry shield. In the existed numerical model, the filter cake is supposed to be impermeable. The hydraulic head field from numerical result does not match the field measurement.

A three-dimension numerical model with the permeable filter cake should be established for calculating the hydraulic head field near tunnel face.

In this paper, the permeable filter cake on the tunnel face under transient-state groundwater flow conditions is considered and applied to the three-dimension numerical model. The analysis of seepage flow is performed based on the numerical results.

2 Numerical Modeling

In order to study the distribution of the hydraulic head around the tunnel face, the three-dimensional numerical modeling was performed by finite element program COMSOL. Figure 2 shows the typical model for a tunnel with the diameter *D* of 15 m located at *C/D* ratio equaling to 1, *C* is the overburden thickness. The model is 150 m long, 60 m high and 60 m wide. The size of the model is large enough to eliminate the boundary effect. The model is filled with soil except for the tunnel. A horizontal tunnel with a length of 45 m is located in the model and 30 m above the bottom. One end of the tunnel is connected to the model side wall. A rectangle tunnel cross-section (15 m × 5.89 m) is adopted for simplicity [12]. Due to the vertical symmetry plane, the computational domain consists of one-half of the system. The mesh was automatically generated by computer and the configuration is physics-controlled mesh with a normal element size. The size of automatically generated soil element is 1 to 3 m.

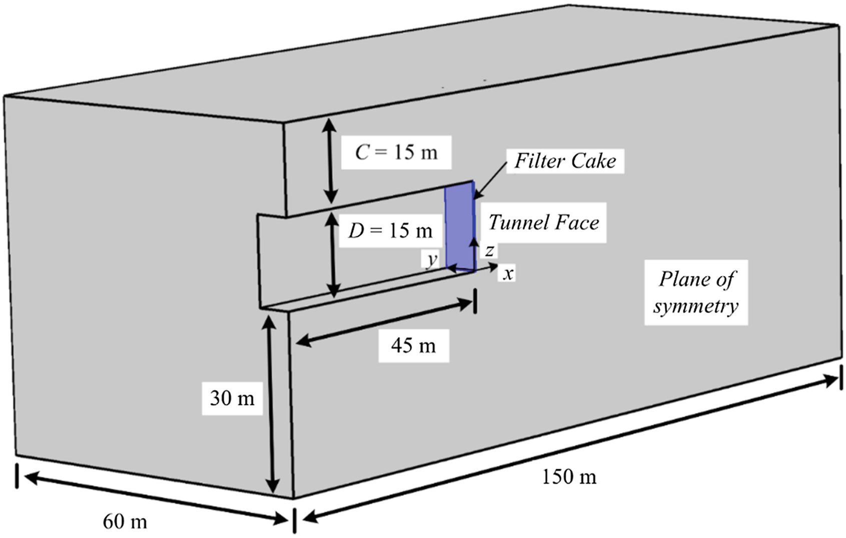

Fig. 2. Schematic view of the numerical model

In the model, a thin block attached to the tunnel face was created (Fig. 2). This block was used to simulate the filter cake of slurry shield. The width of the block is 5.89 m and the height of the block is 15 m. Since the shape of the block must be inconsistency with the tunnel face. The thickness of the block is different with the actual thickness of the filter cake. When filtration time is 60 min, a filter cake is formed in constant pressure (71–120 kPa) dead-end filtration, whose thickness is ranged from 3 to 5 mm [8]. If the thickness of the block is equal to the thickness of filter cake immediately, the FEM solutions will be not convergent. Since the maximum size of filter cake element is smaller than 5 mm, which is only 0.5% of the minimum size of the soil element. The FEM convergence is sensitive to the element size; the size difference between two adjacent elements must be controlled. After conducting a series of FEM analysis with different thicknesses of the block, the numerical result was reasonable when the thickness of the block was equal to 35 mm. Thus the 35-mm thin block was adopted to simulate the filter cake. The mesh of the filter cake was physics-controlled mesh with a normal element size. It resulted that tetrahedrons of filter cake element and soil element share the same side, at the boundary.

The no-flow boundary was prescribed to the tunnel lining, the vertical surfaces and bottom of the model. The boundary condition of hydraulic pressure was applied on the tunnel face to simulate the slurry pressure. The slurry pressure increases linearly with depth with a gradient of 12 kPa/m, because the unit weight of the slurry is 1.2 kN/m^3. The excess pressure s' is equal to the difference of the slurry pressure and the hydrostatic pressure at the center line of the tunnel. h_F is the hydraulic head at the center of tunnel face.

At the far-field boundary, the hydraulic head h_0 has no influence on the pore pressure when s' keeps constant. The seepage field only depends on the s' at tunnel face. The water table was taken equal to the initial elevation of the top surface of the ground. Assuming a sufficient groundwater discharge from the surface, the inflow effect of the tunnel does not cause the rise of the water level. It was taken into consideration by prescribing the height of the model to the water table.

3 Model Parameters

The filter cake is formed on the tunnel face when the pressurized slurry is applied. The filter cake is made from the slurry particles filtrated by the soil. Under slurry pressure, the porosity of the filter cake decreases. The hydraulic conductivity of filter cake is lower than the soil. Since the porosity of filter cake is small and the slurry particles are bentonite, which is a kind of clay. The low hydraulic conductivity of filter cake leads to a hydraulic loss in the filter cake. This hydraulic loss has a relationship with the seepage force on the tunnel face. Thus the hydraulic conductivity of filter cake is a significant parameter for seepage flows analysis.

On the tunnel face, hydraulic resistance R, the ratio between the thickness and hydraulic conductivity of filter cake, is varying dynamically when the cutter wheel is rotating. At a certain point on tunnel face, the filter cake grows with the time because the slurry particles accumulate during cake filtration. But the filter cake will be removed by cutter when spoke of the cutter wheel passes that point. The spoke passes that point at a certain time interval when the cutter wheel is rotating. The filter cake grows until being removed and this process occurs repeatedly. The time for filter cake growing t can be calculated with Eq. (1).

$$t = \frac{\alpha}{w} \tag{1}$$

α is the angle between the past spoke and the line between the certain point and center of the tunnel face; w is the angular velocity of the cutter wheel. The maximum time for filter cake growing depends on the w and the angle between two adjacent spokes. For example, a cutter wheel with five spokes rotating at 1 rpm, it means the angle between adjacent spokes is 72° and the time interval of each spoke passing is 12 s. Thus the maximum time for filter cake growing is 12 s. along the reverse direction of the rotation, the time for filter cake growing increases with the increasing α. For instance, $w = 60°/\text{s}$, when α increases one degree, the time for filter cake growing increases 0.167 s at this point.

In order to determine the hydraulic conductivity of filter cake during excavation, the relationship between R and time must be clarified. This relationship was investigated by a series of constant pressure (71–120 kPa) dead-end filtrations [8]. The result shows that R increases quickly from 175 m/s to about 3.5×10^4 m/s with the increasing time, in the first 5 s. Then R tends to a value between 1.8×10^6 m/s and 4.0×10^6 m/s in the following 295 s. If the thickness of filter cake is presumed to be constant and equal to 35 mm. When the slurry infiltration starts, the hydraulic conductivity of filter cake is decreases quickly from 2×10^{-4} m/s to about 1×10^{-6} m/s within first 5 s, then slowly decreases to a stable value between 8.8×10^{-9} m/s and 2×10^{-8} m/s in the following 295 s. An attention should be paid because the hydraulic conductivity of filter cake is an equivalent value when the thickness of filter cake is 35 mm. This value is not the actual hydraulic conductivity of filter cake.

The relationship between hydraulic conductivity and time is applied to analyze the hydraulic conductivity of filter cake on the tunnel face during excavation. For a cutter wheel with five spokes rotating at 1 rpm, the angle between adjacent spokes is 72°. Five spokes divide tunnel face into five sectors. In each sector, the hydraulic conductivity is ranged from 2×10^{-4} m/s to about 1×10^{-6} m/s. On the tunnel face, the hydraulic conductivity at a certain point changes dynamically, because the cutter wheel is rotating. It is assumed that the hydraulic conductivity of filter cake on the tunnel face has a mean value k_{fm}. k_{fm} is 1×10^{-6} m/s because the average hydraulic conductivity of filter cake keeps about 1×10^{-6} m/s in the first 12 s of filtration.

It was assumed that no particles in the slurry penetrate into the soil, the hydraulic conductivity of the ground k_s kept constant. Different k_s (5×10^{-5} m/s, 2×10^{-4} m/s, and 5×10^{-4} m/s) were considered to study the influence of k_s on the hydraulic head field. The other characteristic parameters are listed in Table 1.

Table 1. Soil parameters used in the finite element analysis

Parameter	Value
Young's modulus, E (kPa)	2.972×10^4
Poisson's ratio, v	0.35
Porosity, n	0.39
Density of grain, r (kg/m^3)	2650
Saturated density of soil, r_s (kg/m^3)	2000
Effective unit weight of soil, r' (kN/m^3)	10

4 Process of Analysis

The analysis started by setting the boundary condition on the tunnel face as a no-flow boundary. Then the steady-state calculation was conducted for initial hydrostatic pressure. The data resulted from this step was inherited for the next calculation. The boundary condition of hydraulic pressure on the tunnel face was enabled. After that, the transient-state calculation was conducted. The pore pressure increases with time during excavation. When the shield stops to assemble linings, the time is enough to form an impervious filter cake. The pore pressure dissipates during assembling linings because the inflow effect of the tunnel is disabled. It is assumed that all the excess pore pressure dissipates during this time. Thus the pore pressure reaches the peak when the shield halts. The time for transient-state calculation was equal to excavation time t. For an excavation speed of 5 cm/min and a lining length of 1.5 m, t is 30 min.

5 Numerical Results and Discussion

5.1 Typical Hydraulic Head Field

A typical hydraulic head field is analyzed in this section. In this case, the diameter of tunnel D is 15 m, C/D is 1, k_{fm} is 1×10^{-6} m/s, k_s is 2×10^{-4} m/s and t is 30 min. The typical contour lines of hydraulic head h based on the numerical results are shown in Fig. 3. h in the filter cake is higher than the initial hydraulic head h_0 (60 m) because the pressurized slurry on the tunnel face raises the pore pressure. At the center of tunnel face, h is equal to 65 m (Fig. 3(a)). A dramatic change of h occurs on the permeable filter cake. The difference of h between both sides of the filter cake is about 1.5 m. It leads to a strong seepage force on the tunnel face and its direction is along the tunnel axis. h in the soil around the tunnel face is increased. For example, h is 63 m at the tunnel axis and 1/3 D ahead of the tunnel face. This position has a lower h than the center of tunnel face. The loss of h causes a seepage force in the soil. The direction of the seepage force is from the tunnel face to the front soil surface, which can be judged from the contour lines of h (Fig. 3(a)). The seepage force in the soil and filter cake will improve the tunnel stability.

Figure 3(b) is the typical contour lines of h at $x = 0$. At the plane paralleled the tunnel cross-section, h increases around the tunnel face. For example, at the point where the horizontal distance to the tunnel lining is 0.5D and $x = 0$, h is about 61.5 m,

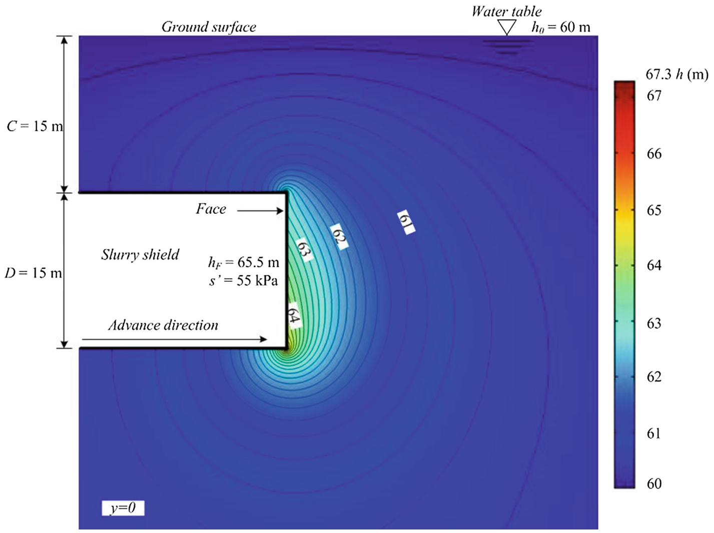

(a) $y = 0$

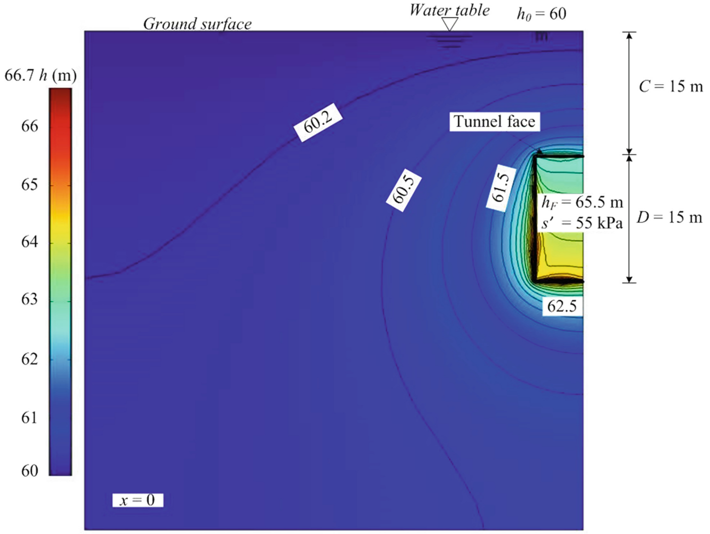

(b) $x = 0$

Fig. 3. Typical contour lines of the hydraulic head (numerical results for $s' = 55$ kPa, $C/D = 1$, $k_s = 2 \times 10^{-4}$ m/s, $k_{fm} = 1 \times 10^{-6}$ m/s; (a) $y = 0$, (b) $x = 0$, (c) $x = \mathrm{D}$ and (d) $x = \mathrm{D}$).

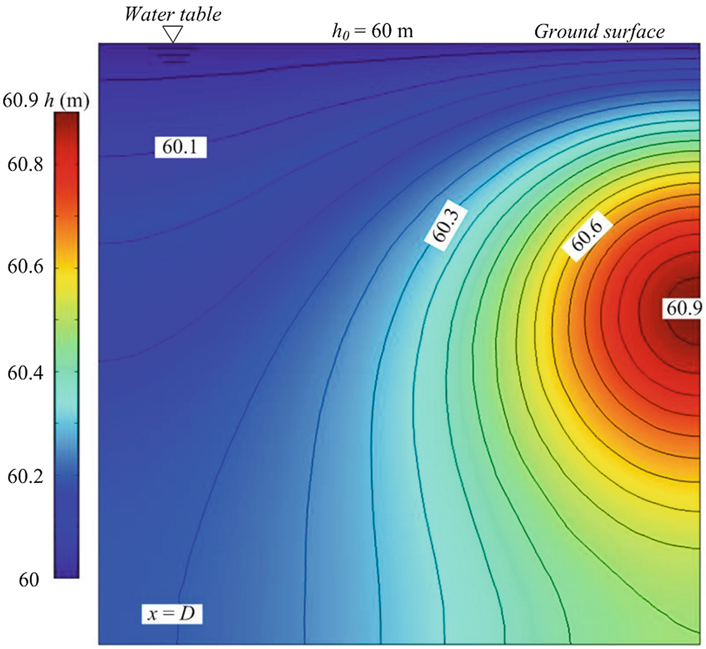

(c) $x = \mathrm{D}$

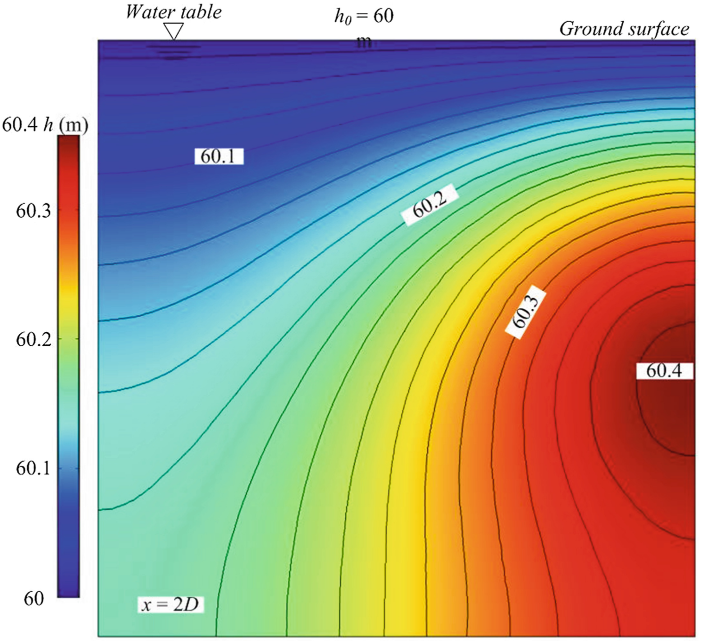

(d) $x = \mathrm{D}$

Fig. 3. (*continued*)

higher than h_0 (60 m). It implies that the pressurized slurry boosts the pore pressure along the plane paralleled the tunnel cross section. At $x = 0$, the influence zone where h increases can be determined from the Fig. 3(b). And the size of the zone is about $1.5D$. Since h is 60.5 m at the point where the horizontal distance to the tunnel lining is $1.5D$ and $x = 0$ and the difference between h and h_0 are only 10% of the difference between the hydraulic head at the center of tunnel face h_F and h_0. The difference of h causes the seepage force along the y-axis. However, due to the symmetry, this force has no effect on the tunnel stability.

Figure 3(c) and (d) are the typical contour lines of h at $x = D$ and $2D$. On the plane $x = D$, the maximum h is 60.9 m at the tunnel axis (Fig. 3(c)). It indicates that h still affected by the pressurized slurry where the distance from the tunnel face is D, although h has dropped substantially by comparing with h_F. On the plane $x = 2D$, the maximum h is 60.4 m and the location of maximum h is beneath the tunnel axis. The difference between h and h_0 is only 0.4 m, 8% of the difference between h_F and h_0. At $x = 2D$, h has little influence of the pressurized slurry. The size of influence zone is $2D$ along the tunnel axis.

5.2 Time Effect

The numerical result at different t (10, 20 and 30 min) is obtained to analyze the time effect. In this numerical model, D is 15 m, C/D is 1, s' is 55 kPa, k_{fm} is 1×10^{-6} m/s and k_s is 2×10^{-4} m/s. The contour lines of h at the plane $y = 0$ are shown as Fig. 4(a), (b) and (c). When the t is 10, 20 and 30 min, the maximum h is 67.3 m at the bottom of the tunnel face. And the minimum h is 67.3 m at the far field, such as the soil surface. At the point besides the tunnel face and soil surface, h improves slightly with the increasing t. It is reflected that the area enclosed by the contour line of $h = 61$ m is becoming larger with the increasing t. The time effect on the h around the tunnel face is limited. For example, at the point where horizontal distance from the center of tunnel face is D, h is 61.5 m when t is 10 min and h is 61.7 m when t is 30 min. h changes little at the same point when t is varying. The reason may be that the steady-state seepage is quickly reached in the soil with a high hydraulic conductivity.

5.3 Hydraulic Loss in Filter Cake and Soil

The normalized hydraulic head $(h - h_F)/(h_0 - h_F)$ is adopted for the quantitative analysis of the hydraulic loss. $(h - h_F)/(h_0 - h_F)$ is beneficial for comparing the hydraulic loss under different numerical cases. The influence of k_s and s' on the $(h - h_F)/(h_0 - h_F)$ are investigated based on the numerical computation. Two groups computation is conducted, $(h - h_F)/(h_0 - h_F)$ under varying k_s (5×10^{-5}, 2×10^{-4} and 5×10^{-4} m/s) are calculated in the first group. And different s' (55, 72, 88 and 105 kPa) are variables in the second group. The rest configuration of the numerical model is as follows: D is 15 m, C/D is 1 and k_{fm} is 1×10^{-6} m/s. in order to analyze the hydraulic loss in filter cake and soil, $(h - h_F)/(h_0 - h_F)$ at different locations of the model are obtained. On the plane $y = 0$, $(h - h_F)/(h_0 - h_F)$ at three horizontal axis ($z = 0$, $0.5D$ and D) is used to investigate the hydraulic loss in front of tunnel face, as line AB, CD, EF in Fig. 5. $(h - h_F)/(h_0 - h_F)$, at the line from tunnel top to the soil surface (line CG in Fig. 5), is obtained to research the hydraulic loss above the tunnel. $(h - h_F)/(h_0 - h_F)$ at line HI (as shown in Fig. 5) can be used to analyze the hydraulic loss nearby the tunnel.

Figure 6 shows the numerically computed distribution of the normalized hydraulic head $(h - h_F)/(h_0 - h_F)$ along three horizontal lines ahead of the face in the axial

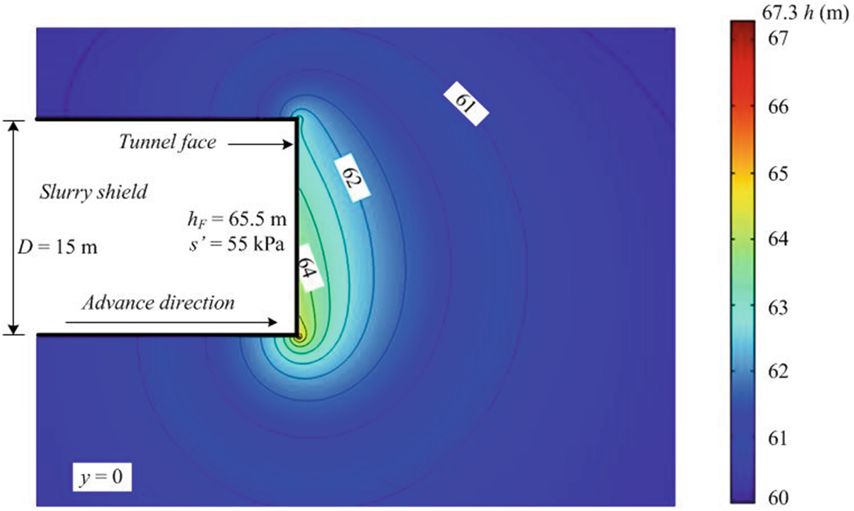

(a) $t = 10$ min

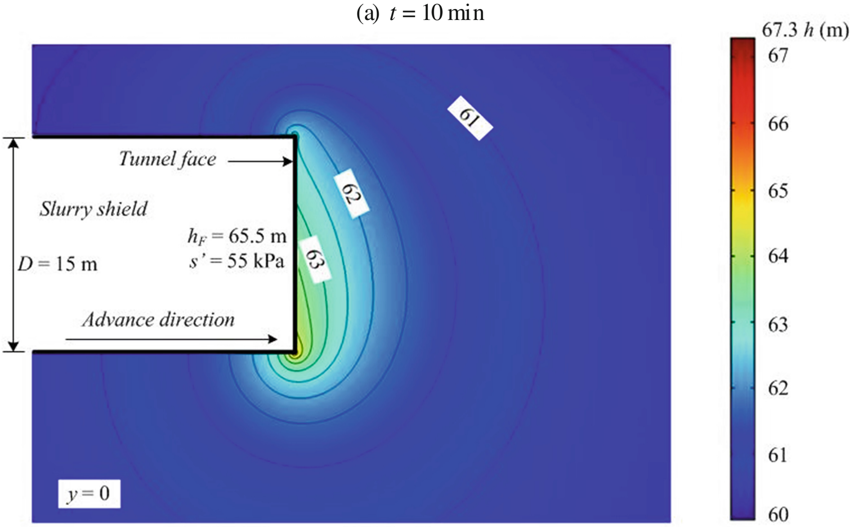

(b) $t = 20$ min

Fig. 4. Contour lines of the hydraulic head at different excavation time (numerical results for $s' = 55$ kPa, $C/D = 1$, $k_s = 2 \times 10^{-4}$ m/s, $k_{fm} = 1 \times 10^{-6}$ m/s; (a) $t = 10$ min, (b) $t = 20$ min and (c) $t = 30$ min).

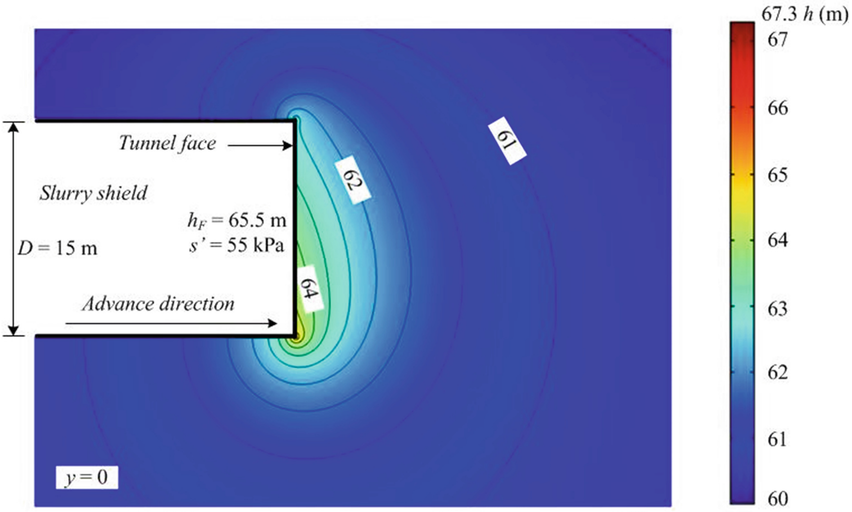

(c) $t = 30$ min

Fig. 4. (*continued*)

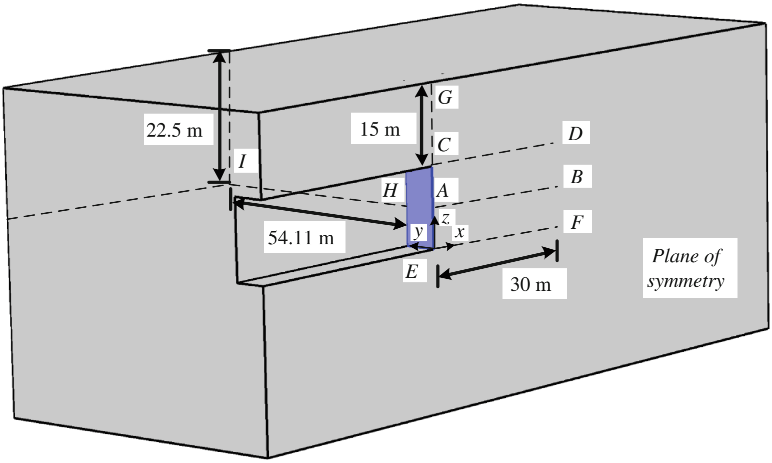

Fig. 5. Characteristic location in the numerical model

direction ($y = 0$, $z = 0$, $0.5D$ and D), along the vertical axis z above the tunnel and along the horizontal line HI ($z = 0.5D$, $x = 0$), for first group ($C/D = 1$, $k_{fm} = 1$ 10^{-6} m/s, $s' = 55$ kPa and $k_s = 5 \times 10^{-5}$, 2×10^{-4} and 5×10^{-4} m/s)). $(h - h_F)/(h_0 - h_F)$ increases substantially in the filter cake ($0 < x < 35$ mm) and tends to 1 at x = $2D$ (Fig. 6(a), (b) and (c)). In the line CD and EF, $(h - h_F)/(h_0 - h_F)$ is not zero, at $x = 0$. Since, the density of slurry is 1200 kg/m^3 and slurry pressure increases 12 N

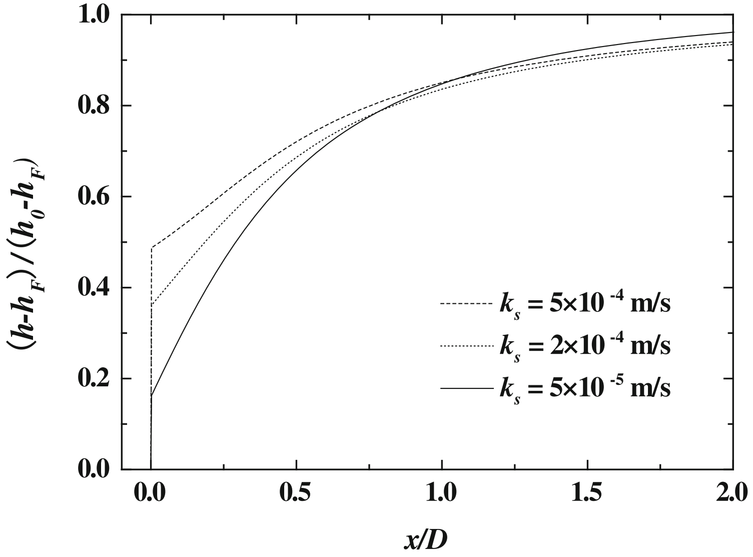

(a) Line AB ($y = 0$, $z = 0$)

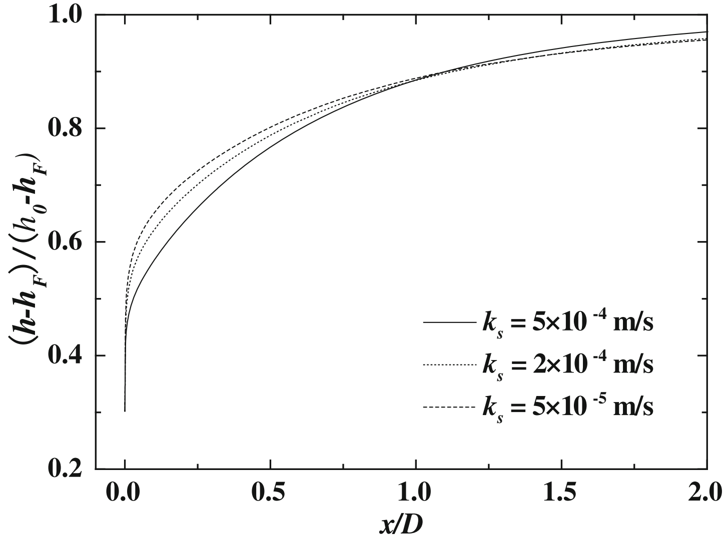

(b) Line CD ($y = 0$, $z = 0.5D$)

Fig. 6. Distribution of normalized hydraulic head $(h - h_F)/(h_0 - h_F)$ under different hydraulic conductivity k_s ($C/D = 1$, $s' = 55$ kPa and $k_{fm} = 1 \times 10^{-6}$ m/s; (a) Line AB, (b) Line CD, (c) Line EF, (d) Line CG and (e) Line HI).

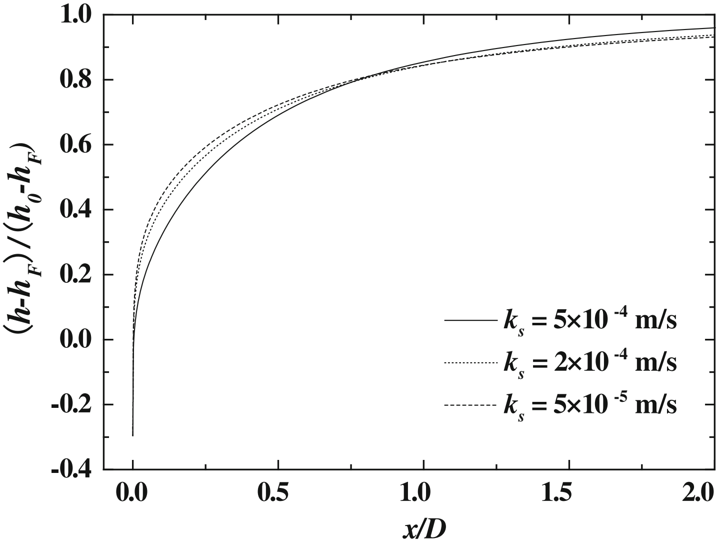

(c) Line EF($y = 0$, $z = D$)

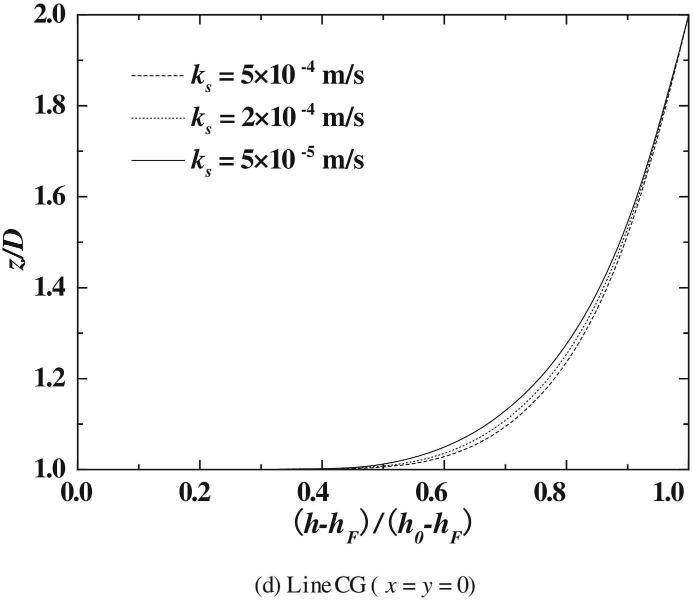

(d) Line CG ($x = y = 0$)

Fig. 6. (*continued*)

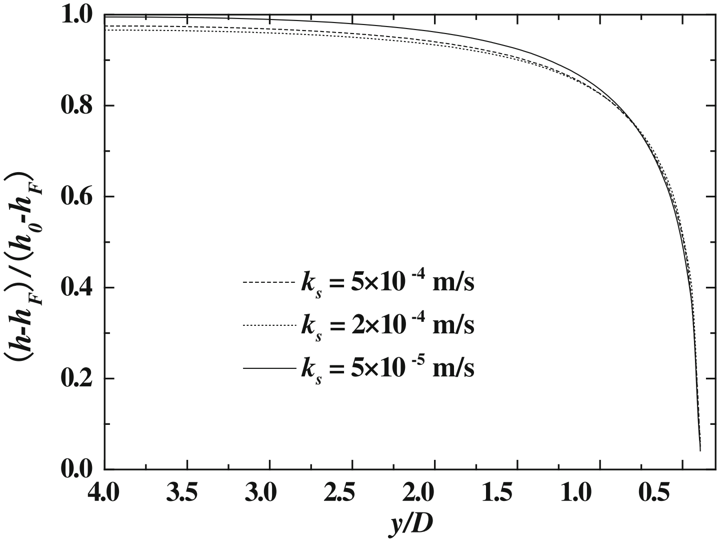

(e) Line HI ($x = 0$, $z = 0.5D$)

Fig. 6. (*continued*)

when z decreases one m. h at the top of tunnel face is smaller than h_F and h at the bottom is larger than h_F. The hydraulic loss in the filter cake depends on the k_s: the smaller k_s, the less hydraulic loss will be. This phenomenon is most obvious at tunnel axis ($y = 0$, $z = 0.5D$). For example, at $x = 35$ mm, $(h - h_F)/(h_0 - h_F)$ is 0.49 for $k_s = 5 \times 10^{-4}$ m/s, $(h - h_F)/(h_0 - h_F)$ is 0.36 for $k_s = 2 \times 10^{-4}$ m/s and $(h - h_F)/(h_0 - h_F)$ is 0.16 for $k_s = 5 \times 10^{-5}$ m/s. On the contrary, the hydraulic loss in the soil increases with the decreasing k_s. For example, hydraulic loss in soil is 0.51 $(h_F - h_0)$ for $k_s = 5 \times 10^{-4}$ m/s and hydraulic loss is equal to 0.84 $(h_F - h_0)$ for $k_s = 5 \times 10^{-5}$ m/s. For the hydraulic loss in the filter cake and soil in front of the tunnel face, k_s is a key factor.

Along the vertical axis z above the tunnel, $(h - h_F)/(h_0 - h_F)$ increases with the increasing z and tends to 1 at the soil surface. The distribution of $(h - h_F)/(h_0 - h_F)$ along the axis z depends slightly on the k_s (Fig. 6(d)): the smaller k_s, the lower $(h - h_F)/(h_0 - h_F)$ will be. Along the horizontal line HI ($z = 0.5D$, $x = 0$), $(h - h_F)/(h_0 - h_F)$ increases with the increasing y (Fig. 6(e)). $(h - h_F)/(h_0 - h_F)$ is larger than 0.9 at y = 1.5D and tends to 1 at the model boundary. At the same position, $(h - h_F)/(h_0 - h_F)$ increases slightly with the decreasing k_s. In the soil above tunnel and nearby tunnel, k_s has little influence on the hydraulic loss.

Figure 7 shows the numerically computed distribution of the normalized hydraulic head $(h - h_F)/(h_0 - h_F)$ along three horizontal lines ahead of the face in the axial direction ($y = 0$, $z = 0, 0.5D$ and D), along the vertical axis z above the tunnel and along the horizontal line HI ($z = 0.5D$, $x = 0$), for second group ($C/D = 1$, $k_{fm} = 1 \times 10^{-6}$ m/s, $k_s = 2 \times 10^{-4}$ m/s and $s' = 55, 72, 88$ and 105 kPa). $(h - h_F)/(h_0 - h_F)$ increases

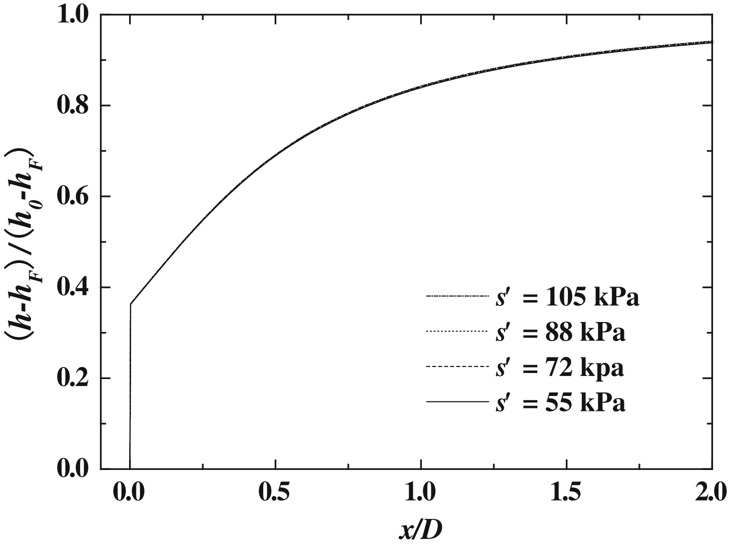

(a) Line AB ($y = 0, z = D$)

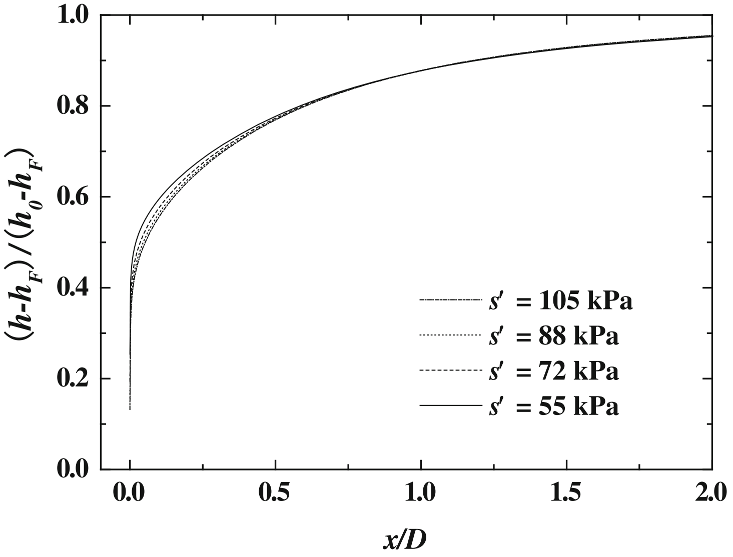

(b) Line CD ($y = 0,\ z = 0.5\,D$)

Fig. 7. Distribution of the normalized hydraulic head $(h - h_F)/(h_0 - h_F)$ under different excess pressure s' (C/D = 1, $k_s = 2 \times 10^{-4}$ m/s and $k_{fm} = 1 \times 10^{-6}$ m/s; (a) Line AB, (b) Line CD, (c) Line EF, (d) Line CG and (e) Line HI).

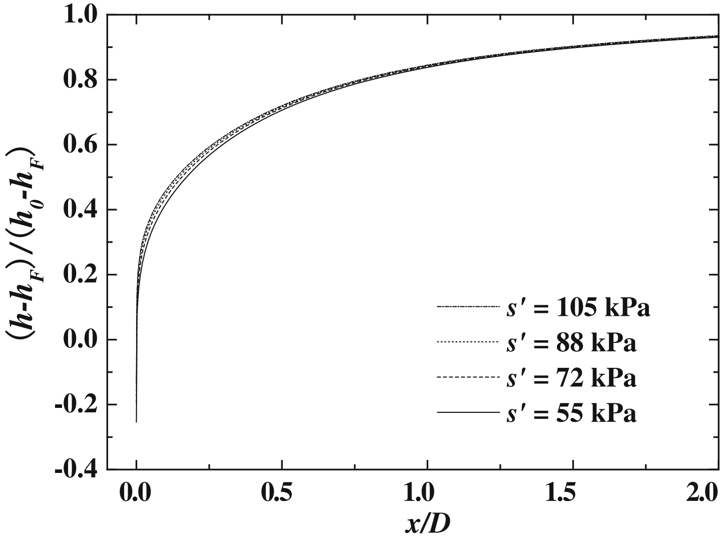

(c) Line EF ($y = 0$, $z = 0$)

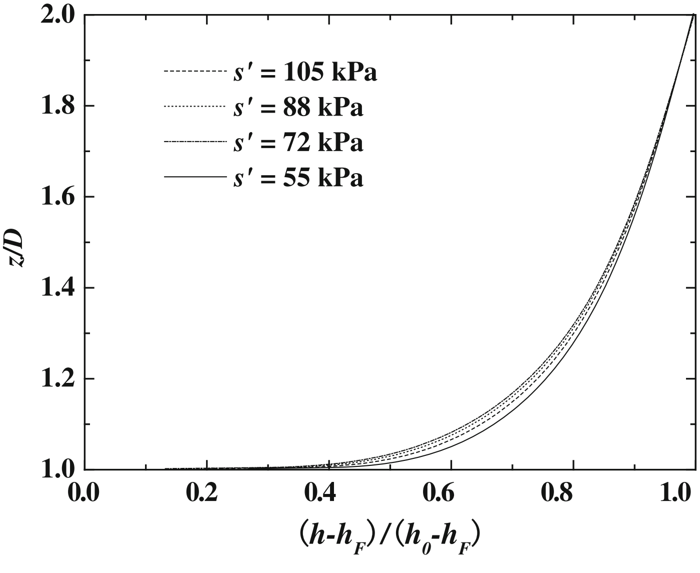

(d) Line CG ($x = y = 0$)

Fig. 7. (*continued*)

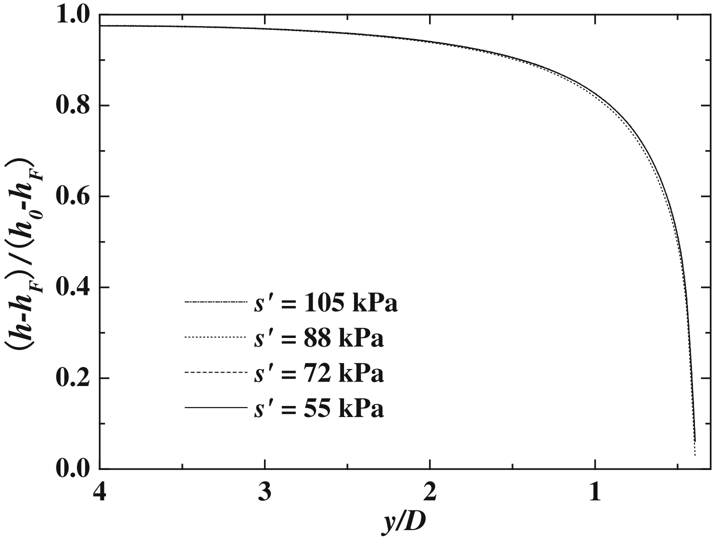

(e) Line HI ($x = 0$, $z = 0.5D$)

Fig. 7. (*continued*)

substantially in the filter cake ($0 < x < 35$ mm) and tends to 1 at x = $2D$ (Fig. 6(a), (b) and (c)). The hydraulic loss in the filter cake is analogous under different s'. This phenomenon is most obvious at tunnel axis ($y = 0$, $z = 0.5D$). For example, at $x = 35$ mm, $(h - h_F)/(h_0 - h_F)$ is 0.36 for $s' = 55$, 72, 88 and 105 kPa (Fig. 6(b)). On the contrary, the hydraulic loss in the soil is about 0.64 ($h_F - h_0$) when s' is varying, at the tunnel axis. s' has little effect on the ratio between hydraulic loss and ($h_F - h_0$), in the filter cake and soil.

Along the vertical axis z above the tunnel, $(h - h_F)/(h_0 - h_F)$ increases with the increasing z and tends to 1 at the soil surface. The distribution of $(h - h_F)/(h_0 - h_F)$ along the axis z depends slightly on the s': the smaller s', the higher the hydraulic head will be (Fig. 5(d)). Along the horizontal line HI ($z = 0.5D$, $x = 0$), $(h - h_F)/(h_0 - h_F)$ increases with the increasing y (Fig. 6(e)). $(h - h_F)/(h_0 - h_F)$ is larger than 0.9 at y = $1.5D$ and tends to 1 at the model boundary. At the same position, $(h - h_F)/(h_0 - h_F)$ is similar to different s'. In the soil above tunnel and nearby tunnel, the ratio between hydraulic loss and ($h_F - h_0$) changes slightly when s' is varying.

5.4 Comparison with Field Case

$(h - h_F)/(h_0 - h_F)$ calculated by the numerical model is compared with the field measurement. The field case is the project of Second Heinenoord Tunnel [7]. The tunnel has a diameter of 8.55. This tunnel was constructed in the sand; the hydraulic conductivity of sand is 2×10^{-4} m/s. The tunnel is covered by 12-meter-thick clay; the hydraulic conductivity of clay is 5×10^{-5} m/s. The water table is on the soil surface. s' on the tunnel face is. The yield strength of slurry is 5 Pa, the k_{fm} is presumed

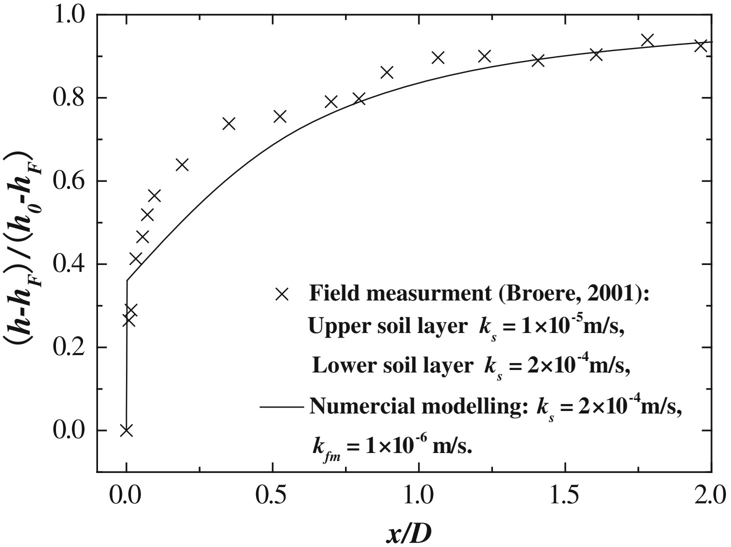

Fig. 8. Field measured $(h - h_F)/(h_0 - h_F)$ compared with numerical calculated $(h - h_F)/(h_0 - h_F)$

to be 1×10^{-6} m/s. $(h - h_F)/(h_0 - h_F)$ is calculated from the pore pressure at the tunnel axis. $(h - h_F)/(h_0 - h_F)$ of field measurement increases with the increasing *x/D*; $(h - h_F)/(h_0 - h_F)$ boosts rapidly in the filter cake and tends to 1 at *x* = 2*D* (crosses in the Fig. 8). The configuration of the compared numerical model for comparison is as followed: *D* = 15 m *C/D* = 1, $k_{fm} = 1 \times 10^{-6}\,\text{m/s}$, $k_s = 2 \times 10^{-4}\,\text{m/s}$ and s' = 55 kPa. $(h - h_F)/(h_0 - h_F)$ at tunnel axis is obtained from the numerical result, as the solid line shown in Fig. 8. The numerical result is slightly smaller than the field measured data. The reason may be the heterogeneous soil in field case. The numerical modeling is capable simulating the real hydraulic head field.

6 Conclusions

In this study, the hydraulic head field near the tunnel face of the slurry shield was studied using the numerical analysis. A finite element analysis program, COMSOL, was used to establish the three-dimensional numerical model. In the model, A block, its thickness is 35 mm and hydraulic conductivity is 1×10^{-6} m/s, was adopted to simulate the filter cake on tunnel face. Based on the numerical results, the seepage flow analysis was conducted. To verify the calculated results of the numerical analysis, a comparison with the field measurement was performed. The results of the numerical study on the hydraulic head field with the consideration of filter cake on tunnel face lead to the following conclusions.

(1) The existence of filter cake seriously affects the hydraulic head field near the tunnel face. In the front of tunnel face, the hydraulic head decreases dramatically in the filter cake. At the tunnel axis, the hydraulic head decreases by 0.39 $(h_F - h_0)$ from tunnel face to the outer side of the filter cake. In the soil, the hydraulic head decreases with the increasing distance to the tunnel face. The hydraulic head tends to the hydrostatic head, at the points where is $2D$ in front of tunnel face, horizontal $1.5D$ to the lining of tunnel or soil surface.

(2) The results of transient-state seepage flow analysis show that the maximum and minimum hydraulic head remains the same when the excavation time is 10, 20 or 30 min. In the soil, the hydraulic head increases slightly when excavation time increases. When the excavation time is longer than 10 min, it has little effect on the hydraulic head.

(3) The hydraulic loss in filter cake increases with the increasing hydraulic conductivity of the soil. On the contrary, the hydraulic loss in soil decreases when the hydraulic conductivity of soil increases. For s' is 55 kPa, $C/D = 1$, hydraulic conductivity of filter cake is 1×10^{-6} m/s, hydraulic loss increases from 0.16 $(h_0 - h_F)$ to $0.5(h_0 - h_F)$ when hydraulic conductivity of soil increases from 5×10^{-5} to 2×10^{-4} m/s, at the tunnel axis.

(4) s' has little influence on $(h - h_F)/(h_0 - h_F)$. When s' increases from 55 to 105 kPa, distribution of $(h - h_F)/(h_0 - h_F)$ keeps constant in the soil and filter cake.

References

1. Tien, C.: Principles of Filtration. Elsevier, Amsterdam (2012)
2. Li, Y., Emeriault, F., Kastner, R., Zhang, Z.: Stability analysis of large slurry shield-driven tunnel in soft clay. Tunn. Undergr. Space Technol. **24**(4), 472–481 (2009)
3. Kim, S., Tonon, F.: Face stability and required support pressure for TBM driven tunnels with ideal face membrane–drained case. Tunn. Undergr. Space Technol. **25**(5), 526–542 (2010)
4. Yeo, S., Shackelford, C., Evans, J.: Consolidation and hydraulic conductivity of nine model soil-bentonite backfills. J. Geotech. Geoenvironmental **131**(10), 1189–1198 (2005)
5. Chung, J., Daniel, D.: Modified fluid loss test as an improved measure of hydraulic conductivity for bentonite. Geotech. Test. J. **31**(3), 1–10 (2008)
6. Zhang, F., Zhu, H., Fu, D.: Shield Tunnelling Method. China Communication Press, Beijing (2004). (in Chinese)
7. Broere, W.: Tunnel face stability & new CPT application. Ph.D. thesis, Delft University of Technology, Delft, Netherlands (2001)
8. Yin, X., Chen, R., Li, Y., Qi, S.: A column system for modeling bentonite slurry infiltration in sands. J. Zhejiang Univ. Sci. **17**(10), 818–827 (2016)
9. Fritz, P., Stengele, R., Heinz, A.: Modified bentonite slurries for slurry shields in highly permeable soils. In: 4th International Symposium Geotechnical Aspects of Underground Construction in Soft Ground, Toulouse, France (2002)
10. Anagnostou, G., Kovári, K.: The face stability of slurry-shield-driven tunnels. Tunn. Undergr. Space Technol. **9**(2), 165–174 (1994)

11. Broere, W., van Tol, A.F.: Influence of infiltration and groundwater flow on tunnel face stability. In: Geotechnical Aspects of Underground Construction in Soft Ground, pp. 339–344. CRC Press, Tokyo (2000)
12. Perazzelli, P., Leone, T., Anagnostou, G.: Tunnel face stability under seepage flow conditions. Tunn. Undergr. Space Technol. **43**, 459–469 (2014)

Discrete Element Analysis of the Excavation Disturbance of Cross-River Twin-Tunnels on the Surroundings

Zhihua Zhang(✉), Xiedong Zhang, Lin Wu, and Hang Zhang

School of Transportation, Wuhan University of Technology,
Wuhan 430063, Hubei, China
zzh@whut.edu.cn, carnation_hust@163.com

Abstract. The increasing number of twin-tunnels constructed in river-crossing subway traffic compels the designers to explore its dynamics performance in the excavation progress. The characteristics of particle accelerations of the granular medium in the surroundings are the important factors to reflect the excavation disturbance. In the construction process of the twin-tunnels, the excavation of the second tunnel (named tunnel_2) will be conducted when the first tunnel (named tunnel_1) is stable. In this paper, a three-dimensional scale model of the cross-river twin-tunnels is established utilizing the discrete element method (DEM) with PFC3D, the model aims to investigate the influence of the twin-tunnels construction on the surroundings. The numerical results show that the accelerations of the particles in the surroundings around tunnel_2 are larger than those around tunnel_1 both in horizontal and vertical directions. Kinetic energy transfers as a transverse wave and is dissipated by the friction resistance and the damping effect as the transmission distance increasing in the surroundings.

Keywords: Twin-tunnels · Excavation disturbance · Particle acceleration
Discrete element method

1 Introduction

With the traffic development in large cities, twin or multi-tunnels are increasingly constructed under the ground in urban area. The complicated geology and the hard-controlled construction process result in high risk for tunnel construction, especially in case of the cross-river tunnel with high water pressure. The excavation influence of the tunnels on the surroundings has been the crucial problem which should be paid more attention.

The study of the construction of twin-tunnels had been started in recent years. Mohammad [1] carried out a series of dynamic centrifuge tests to analyze the seismic behavior of buried box tunnels that an underground tunnel could have either positive or negative effect on the ground surface acceleration. Chehade [2] concluded the construction of the tunnels induced movement of soil and strain action in the lining. Li [3] presented the deformation of twin-tunnels construction with the diameter of 6 m below twin-deck tunnels with a distance of 13.6 m and evaluated the effects of the shield tunneling on adjacent existing tunnels. Ng [4] investigated the response of an existing

© Springer Nature Singapore Pte Ltd. 2018
D. Zhang and X. Huang (Eds.): GSIC 2018, *Proceedings of GeoShanghai 2018 International Conference: Tunnelling and Underground Construction*, pp. 156–163, 2018.
https://doi.org/10.1007/978-981-13-0017-2_15

tunnel in sand to the excavation of a new tunnel which was located perpendicularly below it by using three-dimensional centrifuge tests and numerical modelling. For a cross-river tunnel, the water pressure and soft ground are more sensitive as a case study when the tunnel is constructed. The deformation, macro-micro mechanism of an existing tunnel during the excavation of an adjacent new one should be analyzed. However, little has been published on this subject.

In this paper, a three-dimensional model of the cross-river twin-tunnels is proposed based on discrete element method (DEM), this model aims to investigate the disturbance of the excavation process on the surroundings around the existing tunnel (e.g. tunnel_1) and a new one (e.g. tunnel_2). The purpose of this study is to obtain the dynamic response of the surroundings in horizontal and vertical direction during the excavation process. The results provide a deeper understanding of how the surroundings is affected by the construction of the twin-tunnels.

2 Model Setup

2.1 Project Overview

The Metro Line 2 is one of the largest passenger transportation lines in the Wuhan Metro Transit system. Figure 1 depicts a partial view of the main geological strata of the Yangtze River. The cross-river tunnel passes mainly through sand layers, including mud rock, fine sand, and coarse sand, with high permeability and low clay content [5]. The subsurface soil under the river consists of silty clay, coarse sand, and mud rock. The cross-section marked in Fig. 1 is used for the numerical simulation.

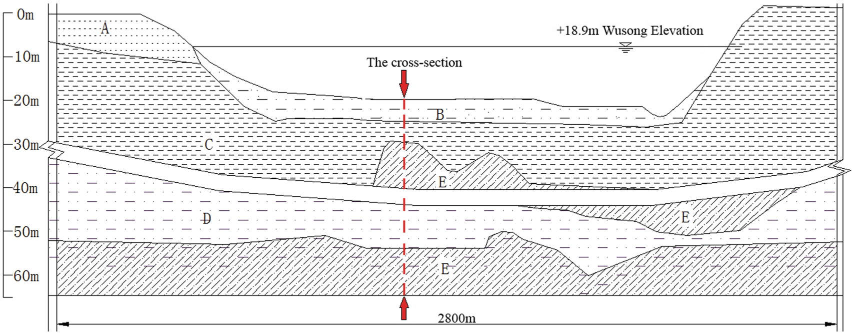

Fig. 1. The soil profile of twin-tunnels underlying the river of Wuhan metro.

For coarse sand containing some gravel and cobble represented by layers C and D, respectively, the micro parameter calibrations had been conducted by Lu [6] from triaxial tests using DEM in numerical simulation. Referring to Zhang [7], the parameter calibration of the silty clay has been finished and the micro parameters of soft rock [8] are shown in Tables 1 and 3.

Table 1. Basic parameters of each stratum in the cross-river twin-tunnels of Wuhan metro.

Symbol	Thickness (m)	γ (kN/m^3)	Φ (°)	C (kPa)	e	E_c (MPa)	λ	W (%)
(B)	7	1670	10.5	14	0.4	2.17	0.2	49.5
(C)	8	2010	42	5.4	0.44	35.4	0.2	16.1
(E)	7	2780	40	10	0.40	80	0.2	
(D)	8	2070	40	6.2	0.51	38.1	0.2	18.0

Note: B is the silty clay; C is the sandstone (contained with some gravel); D is the sandstone (contained with some cobble); E is the soft rock; γ is the density; Φ is frictional angle; c is the cohesion strength; e is porosity; E_j is modulus of compression; λ is Poisson's ratio; w is moisture content.

2.2 The Ratio of Scale Model Similitude

The scale model test should satisfy a series of similarity requirements with corresponding prototype in terms of geometry, physical-mechanical properties, boundary conditions and initial stress conditions. Rocha [9] systematically described the principle of similitude in soil mechanics. The similarity ratio [10] of several parameters between the prototype and the scale model are shown in Table 2.

Table 2. The similarity ratio of several parameters in the scale model.

Category	Value	Category	Value
The similarity ratio of geometry size	20	The similarity ratio of frictional angle	1
The similarity ratio of gravity	1	The similarity ratio of modulus	20
The similarity ratio of cycles	$\sqrt{20}$	The similarity ratio of stress	20
The similarity ratio of Poisson's ratio	1	The similarity ratio of displacement	20
The similarity ratio of strain	1	The similarity ratio of cohesion	20
The similarity ratio of acceleration	1		

2.3 Numerical Test Programme

The construction stages of the numerical twin-tunnels model are defined as follows:

Step 1. A cubic box composed of six walls with the size of 1.8 × 0.06 × 1.5 m (Length × Width × Height) is created and the small particles inside it are generated with the expansion method.

Step 2. The assembly with the calculated constant water pressure (2.94×10^5 Pa) is consolidated by the servo-system [11], then the gravity and buoyancy for each particle are applied.

Step 3. Micro parameters of each stratum are set which are shown in Table 3, and several cycles for reaching a quasi-static state are executed.

Step 4. Several measurement spheres in the model are arranged and the tunnel_1 is excavated by reducing the stiffness and cohesive bond of particles in the excavation area with a diameter of 6.52 m. Then the concrete lining is installed by setting a ring with the properties of C60 and a thickness of 0.51 m.

Table 3. Micro-macro parameters in the twin-tunnels model

Parameters (unit)	Silty clay	Coarse sand (C)	Coarse sand (D)	Soft rock	Concrete lining
d (m)	0.007–0.012	0.007–0.012	0.007–0.012	0.007–0.012	0.003
k_n (N/m)	1.45×10^4	2.34×10^5	2.5×10^5	5.36×10^5	9×10^8
k_s (N/m)	5.8×10^3	9.36×10^4	1×10^5	2.144×10^5	9×10^8
μ	0.185	0.9	0.84	0.84	1.98
σ_n (Pa)	–	–	–	–	1×10^8
σ_s (Pa)	–	–	–	–	1×10^8
k_{n_p} (N/m)	–	–	–	–	1.8×10^{11}
k_{s_p} (N/m)	–	–	–	–	7.2×10^{10}
ς	–	–	–	–	1.0

Note: d is the diameter; k_n is the normal stiffness; k_s is the shear stiffness; μ is the friction coefficient; σ_n is the normal strength of parallel bond; σ_s is the shear strength of parallel bond; k_{n_p} is the normal stiffness of parallel bond; k_{s_p} is the shear stiffness of parallel bond; ς is the parallel bond radius multiplier.

Step 5. The model is consolidated until a stable condition is obtained when there is no deformation of the surroundings around the tunnel_1, then the tunnel_2 is excavated with the same method mentioned in step 4. The DEM model and the measurement spheres are shown in Fig. 2.

3 Numerical Results

In order to analyze the excavation disturbance induced by the tunnel construction, particle acceleration as a sensitive parameter in four directions of the right, vault, left, and the foot (e.g. 0°, 90°, 180° and 270°, respectively) around the tunnel in the surroundings have been measured.

3.1 The Lateral Sides of the Tunnel

The particle accelerations in vertical and horizontal directions around the twin-tunnels are considered which have been depicted in Figs. 3 and 4, respectively.

The peak accelerations of particles in the surroundings can reflect the disturbance level of the tunnel excavation. As shown in Fig. 3(a), 32 measurement spheres are arranged into the model with different distances from the outer edge of the lining. The peak vertical accelerations of the particles in the two lateral sides of the twin-tunnels are shown in Fig. 3(b). As shown in Fig. 3(b), the peak vertical accelerations decrease with the distance from the out edge of the lining increase. It is suitable for explaining this phenomenon that the kinetic energy induced by the excavation is dissipated by the friction resistance and the damping effect [7]. The peak vertical accelerations of the particles in the surroundings around the twin-tunnels should be consistent theoretically (same values) due to the same excavation process and the uniform geology, however, some differences occur. After the construction of tunnel_1, the stress distribution of the

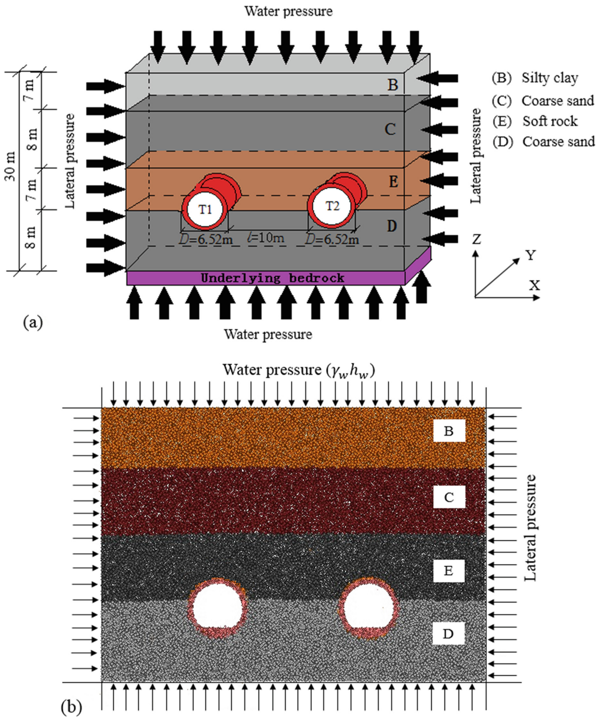
Water pressure
B
C
E
D
T1
T2
D=6.52m
l=10m
D=6.52m
Underlying bedrock
7 m
8 m
7 m
8 m
30 m
Lateral pressure
Lateral pressure
(B) Silty clay
(C) Coarse sand
(E) Soft rock
(D) Coarse sand
Z
Y
X
(a)
Water pressure
Water pressure ($\gamma_w h_w$)
B
C
E
D
Lateral pressure
(b)

Fig. 2. (a) Schematic diagram; (b) DEM model of the cross-river twin tunnels scale model, T1 is the tunnel_1, T2 is the tunnel_2.

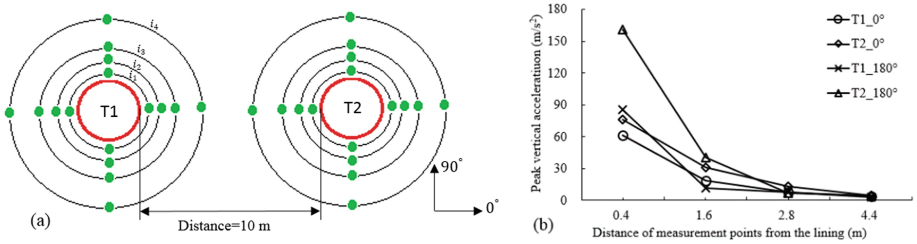

Fig. 3. (a) The distribution of the measurement spheres, $i_1 = 0.4$ m, $i_2 = 1.6$ m, $i_3 = 2.8$ m and $i_4 = 4.4$ m; (b) The peak vertical accelerations of particles with different distances from the lining.

surroundings around the tunnel_2 has been influenced by the excavation of the tunnel_1. As depicted in Fig. 3(b), the peak vertical accelerations of the surroundings around tunnel_2 are larger than those around the tunnel_1. The reason may be that after the excavation of tunnel_1, the surroundings around the tunnel_2 are densified that the kinetic energy being dissipated is associated with the compactness of the material [7].

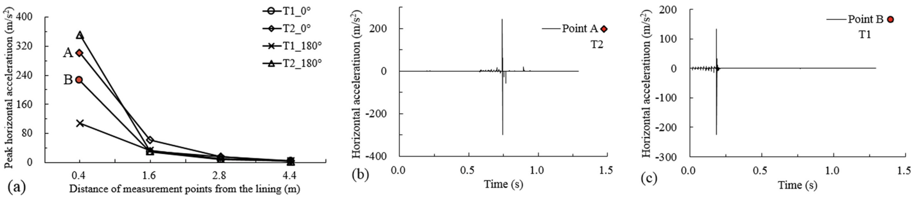

Fig. 4. (a) Peak horizontal acceleration with the different distances from the lining; (b–c) Variation of the horizontal acceleration of measurement spheres A and B during excavation process, respectively.

As shown in Fig. 4(a), the peak horizontal accelerations of the particles decrease with the increase of the distance, which has the same tendency of the peak vertical acceleration shown in Fig. 3(b). The peak horizontal accelerations of the surroundings at the distance of 0.4 m around the tunnel_2 in the two lateral sides of 0° and 180° are larger than those around the tunnel_1, which are also consistent with those of peak vertical acceleration that the surrounding material is densified induced by the excavation of the tunnel_1. Comparison between peak vertical and horizontal accelerations has been made that the values of the peak horizontal accelerations are much larger than those of the horizontal. It demonstrates that the excavation disturbance, represented by the kinetic energy, mainly transferring in horizontal way. The variation of the horizontal accelerations of the particles around the twin-tunnels at the distance from the out edge of the concrete lining of 0.4 m are illustrated in Fig. 4(b–c). The particular and sudden acceleration variations occur when the time approximates 0.75 s and 0.2 s shown in Figs. 4(b) and (c), respectively, which are the time nodes when the excavations of the tunnel_1 and tunnel_2 are finished, respectively. When the concrete lining is constructed, the continuous deformation of the surroundings is terminated which results in large accelerations based on the inertial law. As shown in Fig. 4(b–c), the surrounding material at the distance of 0.4 m is mainly influenced by the own tunnelling rather than the adjacent one.

3.2 The Vault and Bottom of the Tunnel

The disturbance at the vault and bottom of the surroundings around the twin-tunnels are measured as well which considers the peak horizontal and vertical accelerations. As shown in Fig. 5(a), the peak horizontal accelerations of the particles in the surroundings at the distance of 0.4 m is the maximum. The peak horizontal accelerations at the vault of the tunnel are larger than those at the bottom. The reason may be that the deformation of the surroundings at the vault of the tunnel is larger than that at the bottom which has been studied by Chehade [2]. As shown in Fig. 5(b), the peak vertical accelerations of the particles in the surroundings decrease with the increase of the distance. The values of the peak vertical accelerations at the vault of the tunnel are much larger than those at the bottom, and the comparison has been made between the peak vertical and horizontal accelerations that the vertical accelerations are much larger than the horizontal accelerations. It shows that the kinetic energy induced by the excavation process in the vertical direction is transferring in horizontal way.

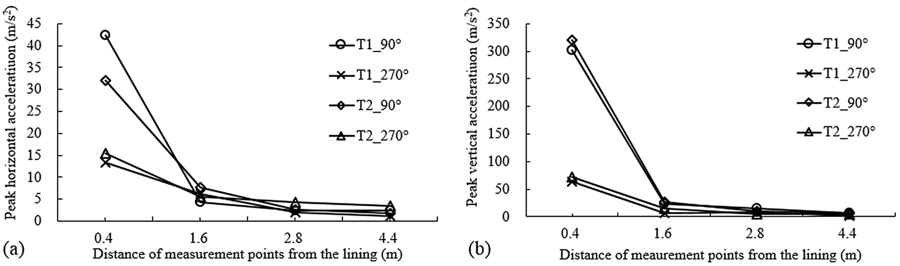

Fig. 5. Peak accelerations of the measurement points at the different distances from the lining in (a) horizontal; (b) vertical.

Combining with the results of the lateral sides of the tunnel, the kinetic energy transfers in the surroundings as a transverse wave.

4 Conclusions

To investigate the excavation disturbance of the cross-river twin-tunnels on the surroundings, a three-dimensional model is proposed with discrete element method. The horizontal and vertical accelerations of the particles in the surroundings during the excavation process have been evaluated, the following conclusions can be drawn:

(1) The peak horizontal accelerations of the particles in the surroundings at the lateral sides of the twin-tunnels are distributed asymmetrically that the surrounding material around the tunnel_2 is densified which is influenced by the excavation of the tunnel_1. The kinetic energy is dissipated by the friction resistance and the damping effect as the transferring distance increasing.

(2) At the lateral sides of the twin-tunnels, the values of the peak horizontal accelerations are much larger than those of the peak vertical accelerations, while at the vault and bottom, the opposite result occurs that the peak horizontal accelerations are much smaller that the vertical accelerations. It is concluded that the kinetic energy is transferred as a transverse wave in the surroundings.

Acknowledgement. The project was financially supported by the National Natural Science Foundation of China (No. 51408450) and the Fundamental Research Funds for the Central Universities (WUT: 2017-YB-014; 2017IVB079).

References

1. Mohammad, H.B., Masoud, R.M., Kim, D.S., Yun, W.C.: Effect of underground tunnel on the ground surface acceleration. Tunn. Undergr. Space Technol. **44**(1), 10–22 (2014)
2. Chehade, F.H., Shahrour, I.: Numerical analysis of the interaction between twin-tunnels: influence of the relative position and construction procedure. Tunn. Undergr. Space Technol. **23**(1), 210–214 (2008)

3. Li, X., Yuan, D.: Response of a double-decked metro tunnel to shield driving of twin closely under-crossing tunnels. Tunn. Undergr. Space Technol. **28**(1), 18–30 (2012)
4. Ng, C.W.W., Boonyarak, T., Mašín, D.: Three-dimensional centrifuge and numerical modeling of the interaction between perpendicularly crossing tunnels. Can. Geotech. J. **50** (9), 935–946 (2013)
5. Xiong, C.: Technical characteristics and innovation of the cross-Yangtze river tunnel of Wuhan subway line No. 2. Railw. Surv. Des. **3**, 1–7 (2014). (in Chinese)
6. Lu, J., Zhang, C., Jian, P.: Meso-structure parameters of discrete element method of sand pebble surrounding rock particles in different dense degrees. In: Proceedings of the 7th International Conference on Discrete Element Methods, vol. 188, pp. 871–879. Springer, Singapore (2016)
7. Zhang, Z., Zhang, X., Tang, Y., Cui, Y.: Discrete element analysis of a cross-river tunnel under random vibration levels induced by trains operating during the flood season. J. Zhejiang Univ. Sci. A. https://doi.org/10.1631/jzus.a1700002
8. Min, F., Zhu, W., Lin, C., Guo, X.: Opening the excavation chamber of the large-diameter size slurry shield: a case study in Nanjing Yangtze River Tunnel in China. Tunn. Undergr. Space Technol. **46**, 18–27 (2015)
9. Rocha, M.: The possibility of solving soil mechanics problems by use of models. In: Proceedings of the 4th International Conference on Soil Mechanics and Foundation Engineering, London, England, vol. 1, pp. 83–88 (1957)
10. Fang, Y., Xu, C., Cui, G., Kenneally, B.: Scale model test of highway tunnel construction underlying mined-out thin coal seam. Tunn. Undergr. Space Technol. **56**, 105–116 (2016)
11. Itasca Consulting Group Inc.: PFC2D, Version 4.0. Itasca, Minneapolis (2008)

An Arching Theory for Arch Tunnels Based on the Interaction Between the Lateral and Vertical Pressure in Good Ground

Xiaohu Cheng(✉)

CCCC Railway Consultants Group Co., Limited, Beijing 100088, China
821876441@qq.com

Abstract. Terzaghi's theory illustrates the arching effect phenomenon by which the vertical pressure on a flat plate will be reduced as the flat plate moves downward, but without considering the effect of the inclined sliding surfaces below tunnel roofs and roof shapes. Based on Terzaghi's theory, this paper presents a practical arching theory for two-dimensional arch tunnels in good ground. One concise formula for the vertical pressure on arch tunnels is developed considering the inclined sliding surfaces below the tunnel roof. The shape effect of the tunnel roof on earth pressure is also considered by adopting the empirical values of the total lateral pressure coefficient λ_t, which is closely related to the shape of tunnels for the flexible lining. This proposed formula is verified by the upper bound theory while the formula is simpler and more suitable for engineering applications than the upper bound theory. The vertical pressure on arch tunnels calculated by the proposed formula is significantly smaller than that calculated by Terzaghi's formula. This formula also reveals that there is an interaction between the lateral and vertical pressure on arch tunnels in good ground. The interaction mechanism is discussed and models for soil arches near tunnels are proposed. Finally, the proposed theory provides a good explanation for the experimental results in good ground. The theory is not only suitable for shallow tunnels but also for deep tunnels, and it broadens the understanding of the arching effect from a flat plate to a two-dimensional arch tunnel.

Keywords: Arch tunnel · Arching effect · Earth pressure
Lateral pressure coefficient · Inclined sliding surfaces

1 Introduction

Due to the arching effect, which is a fundamental phenomenon in tunnel construction, the vertical and lateral pressure on a tunnel lining will be reduced from the over-burden weight in soil. Many researchers have studied the arching phenomenon and proposed some classical theories including Marston theory (1930), Terzaghi's theory (1943), Ground arch (dome) approach (Whitman et al. 1962, 1963). The first systematic study of the arching mechanism was performed by Terzaghi using trapdoor experiments (Moradi and Abbasnejad 2013). Terzaghi then proposed the theoretical formula of active arching and defined arching as the pressure transfer from a yielding mass of soil onto adjoining stationary parts (Terzaghi 1943). Obviously, the pressure transfer is

© Springer Nature Singapore Pte Ltd. 2018
D. Zhang and X. Huang (Eds.): GSIC 2018, *Proceedings of GeoShanghai 2018 International Conference: Tunnelling and Underground Construction*, pp. 164–180, 2018.
https://doi.org/10.1007/978-981-13-0017-2_16

through sliding surfaces where the shear resistance acts. The trapdoor test has become a classical method to investigate the arching effect, and many researchers have performed the trapdoor test (Ladanyi and Hoyaux 1969; Vardoulakis et al. 1981; Evans 1983; Adachi et al. 1997, 2003; Dewoolkar et al. 2007; Chevalier et al. 2009; Costa et al. 2009; Sadrekarimi and Abbasnejad 2010; Iglesia et al. 2014; Pardo and Sáez 2014). However, the field-measured pressure on arch tunnels in good ground is much smaller than Terzaghi's theoretical value (Koyama et al. 1995, 2003; Mashimo and Ishimura 2003), which should be the minimum loads in limit state. In fact, Terzaghi's theory and the trapdoor experiments considered only the role of sliding surfaces above the tunnel roof for the arching effect, and not the inclined sliding surfaces below the tunnel roof.

The roof shape of tunnels is another important factor, and Terzaghi's theory did not consider the geometric configuration (Luscher and Höeg 1964a). Some researchers proposed a structural analogy or ground arch (dome) approach for the arching effect (Whitman et al. 1963; Nielson 1966; Getzler et al. 1968). Getzler conducted experiments with structures having various roof shapes (Getzler et al. 1968), concluding that buried structures with peaked roofs of triangular or arch shape would experience greater load reduction than structures with flat roofs. Getzler proposed a soil arch sitting on the soil bodies at the sides of the structure. Similar experimental results were obtained by Whitman et al. (1963). (Luscher and Höeg 1964b) pointed out that the restraint against tunnel deformations causes stresses to redistribute to a more uniform configuration as the tunnel crown deflects vertically and the spring lines horizontally. The ground arch approach provides an explanation for the arching effect of tunnels roof shapes, but no theoretical formulation has been developed.

This study presents a practical arching theory for two-dimensional arch tunnels (including circular tunnels) in good ground (such as very dense sand and hard clay ground). First, considering the inclined sliding surfaces below the tunnel roof, a formula for the vertical pressure on arch tunnels is derived through the ultimate equilibrium method based on Terzaghi's theory. The shape effect of the tunnel roof is also considered by adopting empirical values for the total lateral pressure coefficient. The formula is then compared with the upper bound theory and Terzaghi's theory. An interaction between the lateral and vertical pressure on the tunnel lining is discussed, and the interaction mechanism is further explained. Finally, the theory is compared with experimental results in good ground.

2 The Pressure on a Flat Plate According to Terzaghi's Theory

Based on the trapdoor tests, Terzaghi (1943) proposed a theoretical approach for the arching problems under a plane strain condition. It was assumed that the normal stress is uniform across the horizontal section. The pressure on a flat plate like the trapdoor is equal to the difference between the weight of the soil above the trap door and the shear resistance along the vertical sliding surfaces. According to Terzaghi's formula, the pressure p on a flat plate is

$$p = \frac{(\gamma a_1 - c)}{K \tan \varphi}\left(1 - e^{(-K \tan \varphi H/a_1)}\right) + p_1 e^{(-K \tan \varphi H/a_1)}, \tag{1}$$

where c is the coefficient of cohesion, φ is the internal friction angle of the soil, p_1 is the surcharge pressure, a_1 is half the trapdoor width B (i.e., $B = 2a_1$), γ is the density of the soil, K is the lateral pressure coefficient (Terzaghi suggested K = 1.0 based on tests), and H is the depth of overburden.

Terzaghi applied the above theory to tunnel design. The stress state in the soil above a tunnel roof is similar to that above the trapdoor.

In essence, Terzaghi's formula illustrates an arching effect induced only by a flat plate like a trapdoor, not by two-dimensional arch tunnels.

3 Solution of the Vertical Pressure on Arch Tunnels in Limit State

3.1 Assumptions

Two assumptions of Terzaghi's theory are adopted for arch tunnels (as shown in Fig. 1). (1) Soil mass below the tunnel roof slides along surfaces AB and A′B′ in limit state, and the angle of inclination with the vertical direction is α (α = 45°−φ/2). (2) Sliding surfaces above the tunnel roof are assumed to be vertical (BC and B′C′), although real sliding surfaces are sometimes curved.

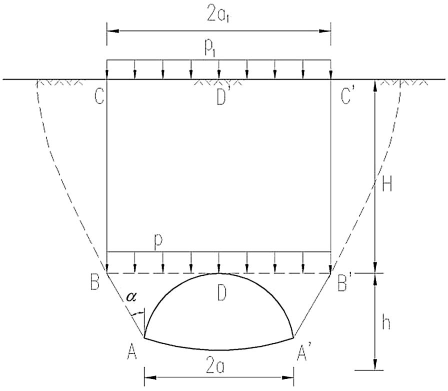

Fig. 1. Calculation diagram of arch tunnel in soil ground

3.2 Theoretical Derivation

The sliding surfaces (*BC* and *B′C′*) above the tunnel roof are similar to those above the trapdoor. The pressure transfer through the inclined sliding surfaces (*AB* and *A′B′*) is also considered in this paper.

In good ground such as very dense sand and hard clay ground, soil above the tunnel crown will sink first when excavating, and then soil on both sides is wedged to form a solid arch (*ABCC'B'A'*) as a whole, which is different in loose sand and soft clay ground. Soil mass *ABCD'D*-1/2 of the symmetrical arch body is selected to carry out the loading analysis, as seen in Fig. 2. Shear stress on the mid-arch section is equal to zero because of symmetry.

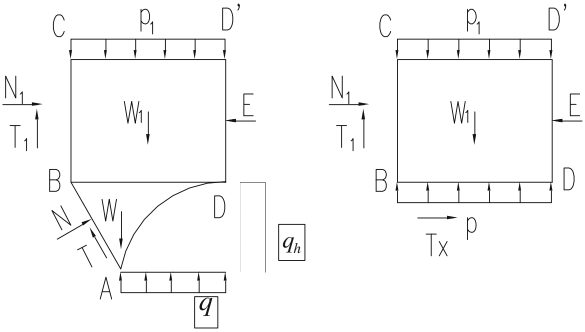

Fig. 2. Force analysis diagram of elements

Vertical pressure q (kPa) acting on curved surface *AD* is equivalent to a uniform load. Lateral pressure q_h (kPa) is also simplified to a uniform force considering the good ground and the convenience of analysis. And q_h can be calculated as

$$q_h = \lambda_t q, \tag{2}$$

where λ_t is the total lateral pressure coefficient.

According to vertical and horizontal force equilibrium, the following equations can be derived from *ABCD'D*:

$$p_1 a_1 + W_1 + W = qa + T\cos\alpha + N\sin\alpha + T_1 \tag{3}$$

$$E + q_h h = N\cos\alpha - T\sin\alpha + N_1, \tag{4}$$

where p_1 (kPa) is ground overload acting on *CC'*; W (kN) and W_1 (kN) are the soil weights of *ABD* and *BCD'D*, respectively; and normal pressure N (kN) and tangential resistance T (kN) act on sliding surface *AB*. Normal pressure N_1 (kN) and tangential resistance T_1 (kN) act on sliding surface *BC*. Normal pressure E (kN) acts on mid-arch section *DD'*. a is half the width of the tunnel and h is the height of the tunnel.

Applying the Mohr-Coulomb strength criterion to sliding surfaces *AB* and *BC*, we can obtain the following equations:

$$T = \frac{ch}{\cos\alpha} + N\tan\varphi \tag{5}$$

$$T_1 = cH + N_1\tan\varphi, \tag{6}$$

where c is the coefficient of cohesion, φ is the internal friction angle of the soil, and H is the depth of overburden.

Horizontal stress of the mid-arch section is greatest in the height range of *BCD′ D* due to the arching effect. Therefore, $E > N_1$, and frictional resistance T_x on *BD* has the same direction as N_1. On the basis of horizontal and vertical force equilibrium of *CD′DB*, we can get:

$$N_1 = E - T_x \tag{7}$$

$$p_1 a_1 + W_1 = p a_1 + T_1, \tag{8}$$

where *p* (kPa) is the vertical stress at the level of tunnel crown BB′, which is equivalent to a uniform pressure on a flat plate according to Terzaghi's theory, although the distribution is not uniform.

According to Eqs. (3)–(8), the variable N can be separated as follows:

$$N = (pa_1 + W - qa)\sin\alpha + T_x\cos\alpha + \lambda_t qh\cos\alpha. \tag{9}$$

Then the vertical pressure on arch tunnels can be deduced:

$$q = \frac{\xi(pa_1 + W) - ch\sec^2\alpha - T_x(\tan\alpha + \tan\varphi)}{\lambda_t h(\tan\varphi + \tan\alpha) + \xi a}, \tag{10}$$

where $\xi = 1 - \tan\alpha\tan\varphi$ and $a_1 = a + h\tan\alpha$.

Frictional resistance T_x does not act on sliding surfaces and its value varies with the difference between *E* and N_1. In addition, the value of *E* is between active and passive earth pressure, which is difficult to confirm. Therefore, it is hard to obtain a closed solution for T_x. But the safer vertical pressure can be obtained if T_x is ignored in Eq. (10). Therefore, an approximate solution for vertical pressure *q* can be obtained as follows:

$$q \approx \frac{\xi(pa_1 + W) - ch\sec^2\alpha}{\lambda_t h(\tan\varphi + \tan\alpha) + \xi a}. \tag{11}$$

In case the cohesion of soil is low, T_x may be roughly calculated by taking the part of the cohesive strength as ca_1. Equation (10) can also be expressed as

$$q = \frac{\xi(pa_1 + W) - ch\sec^2\alpha - ca_1(\tan\alpha + \tan\varphi)}{\lambda_t h(\tan\varphi + \tan\alpha) + \xi a}. \tag{12}$$

The cohesion (c) is equal to zero for cohesive soil under long-term operation and sandy soil. Then Eq. (11) can be simplified with trigonometric function transformations as follows:

$$q \approx \frac{pa_1 + W}{\lambda_t h\tan(\alpha + \varphi) + a}. \tag{13}$$

Equation (11) is also suitable for circular tunnels, a special form of arch tunnels. In this case, the sliding surfaces below the tunnel roof are tangential to the circle as usual.

For circular tunnels, the soil weight of ABD can be expressed as

$$W = \frac{\gamma}{2}\left[(a + a_1)h - R^2\left(\frac{\pi}{2} + \alpha\right) - R^2 \sin\alpha\cos\alpha\right], \tag{14}$$

where

$$a_1 = R\cot\left(\frac{\pi}{8} + \frac{\varphi}{4}\right)$$

$$a = R\cos\alpha,$$

γ is the unit weight of soil (kN/m^3) and R is the radius of the circular tunnel (m).

It's necessary to note that Eq. (11) can be derived directly based on element *ABD,* as shown in Fig. 3. Therefore, Eq. (11) is suitable for not only shallow tunnels but also deep tunnels. Here, the vertical stress p can also be calculated by Protodyakonov's theory in deep tunnels. The above indirect derivation is to correct the general comprehension that the vertical pressure q is not smaller than the vertical stress p, but this does not consider the effect of the inclined sliding surfaces below the tunnel roof in good ground.

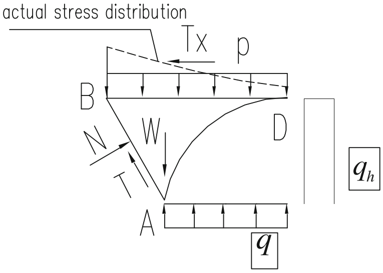

Fig. 3. Force analysis diagram of element ABD

4 Lateral Pressure on Arch Tunnels

It should be noted that the lateral pressure on arch tunnels contains not only active earth pressure but also deformation pressure on enclosed structures. Unlike Rankine's retaining wall, the sidewall of an arch tunnel does not satisfy the assumption that the retaining wall is upright, rigid, and frictionless, and more importantly, the major principal stress is not vertical and the overload on the side wall is greater than the vertical pressure on the tunnel roof due to the arching effect (as shown later in this paper).

So, the lateral pressure on an arch tunnel lining, which is an enclosed structure, is remarkably different from that on Rankine's retaining wall, and the total lateral pressure coefficient λ_t is introduced to calculate the lateral pressure on arch tunnels. The coefficient λ_t is expressed as

$$\lambda_t = \frac{q_h}{q}, \tag{15}$$

where q_h (kPa) is the lateral pressure on arch tunnels and q (kPa) is the vertical pressure on arch tunnels.

Unlike the coefficient of active earth pressure, the total lateral pressure coefficient λ_t reflects the adaptive ability of enclosed structures to the surrounding ground. The ability is related to the relative stiffness between the lining and surrounding soil, and it is closely related to the tunnel shape for the flexible lining. For example, circular tunnels can transfer greater loads from the roof to both sides than ordinary arch tunnels, and it brings about greater lateral deformation pressure than the latter. A tunnel with curved walls has greater lateral deformation pressure than a tunnel with straight walls. Therefore, under the same conditions, the coefficient λ_t of circular tunnels is larger than that of arch tunnels with curved walls, and the coefficient of the latter is larger than that of arch tunnels with straight walls.

Considering the change of earth pressure on tunnels in working condition, it is more meaningful to carry out the envelope design using the approximate range of the coefficient λ_t than to determine the specific value of the coefficient λ_t. Lin (1982) summarized the measured data of earth pressure on railway tunnels (mainly arch tunnels with curved and straight walls) in soil and rock ground, and indicated that the measured coefficient λ_t is usually between 0.6–1.0. Many field measurements also show that λ_t of circular shield tunnels is close to 1.0 in hard clay and dense sand ground (Koyama 2003; Nishizawa et al. 1996; Hashimoto et al. 2009) (as shown in Fig. 4). Therefore, for a flexible lining in homogeneous ground, empirical values of λ_t are suggested to refer to Table 1 when the span of the tunnel is approximately equal to the height. In the other case, a conservative approximation of the coefficient λ_t can be obtained according to FEM results of the traditional load-structure model.

Except that the restraint against tunnel deformations causes stress to redistribute to a more uniform configuration (Luscher and Höeg 1964), the interaction between the lateral and vertical pressure will also lead to a more uniform distribution of pressure on arch tunnels (as shown later in this paper), especially on a circular tunnel. Therefore,

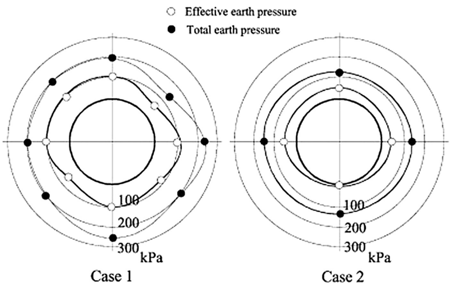

Fig. 4. Distribution of earth pressure in sandy diluvium (Nishizawa et al. 1996)

Table 1. Empirical values of the total lateral pressure coefficient λ_t

Tunnel type	λ_t
Circular tunnel	about 0.8–1.0
Arch tunnel with curved wall	about 0.7–0.9
Arch tunnel with straight wall	about 0.6–0.8

the coefficient λ_t is much larger than the coefficient of active earth pressure, and this is a feature of two-dimensional arch tunnels that is different from the trapdoor.

5 Comparison with the Upper Bound Theory of Limit Analysis

The upper bound theory of limit analysis is an effective method to analyze the stability of shallow tunnels. The model test results matched the upper solutions very well (Atkinson et al. 1975). The upper bound solution is the supporting pressure at the critical state of failure. A circular tunnel may be transformed to a square tunnel.

According to the principle of virtual power, the vertical pressure q on a tunnel can be obtained as (Yang and Yang 2008; Yang et al. 2013)

$$q = \frac{P_\gamma - P_\mathrm{c}}{\lambda_t h \tan(\alpha_n + \varphi) v_n + b v_0}, \tag{16}$$

where P_γ is the power of the soil weight, P_c is the power of dissipation, b is the half-width of the tunnel, α_n is the angle variable in the velocity field, and v_0 and v_n are the velocities of the rigid blocks.

Comparing Eq. (11) or (13) and the upper bound solution (16), we find that they have similar mathematical forms, which reflects that they have some common mechanical principles. The upper bound solution also considers the contribution of the inclined sliding surfaces below the tunnel roof to the arching effect.

A circular tunnel with $R = 5$ m, $\gamma = 20$ kN/m^3, $c = 10$ kPa, $\varphi = 18°$, and $H = 20$ m is selected to carry out a comparative analysis. The normalized pressure is defined as the ratio of the vertical pressure (q) to the overburden stress (γH). Figure 5 shows that the vertical pressure calculated by the proposed Eq. (11) is 8%–11% larger than values of the upper bound solution with different values of λ_t.

The solution of the upper bound theory is complicated and difficult in engineering applications. The proposed theory is simpler and more suitable for engineering applications, and the result is slightly safer.

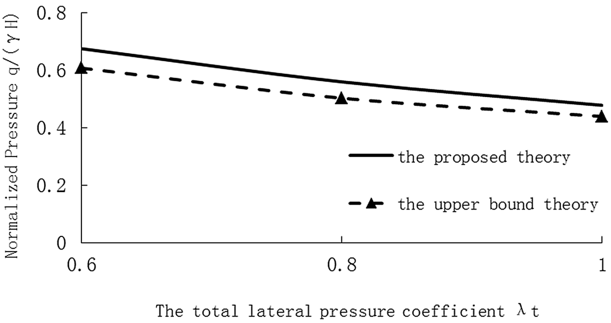

Fig. 5. Comparison between the proposed theory and the upper bound theory

6 Comparison with Terzaghi's Theory

6.1 Interaction Between the Lateral and Vertical Pressure on the Tunnel

According to Eq. (11), there are three distinct characteristics that differ from Terzaghi's theory.

(1) The vertical pressure on tunnels calculated by the proposed formula is significantly smaller than that calculated by Terzaghi's formula (as shown in Fig. 6, R = 3 m, γ = 20 kN/m^3, c = 20 kPa, φ = 30°, H = 15 m). The former is 50% smaller than the latter in some cases. The gap between them increases with the increase of the total lateral pressure coefficient λ_t.

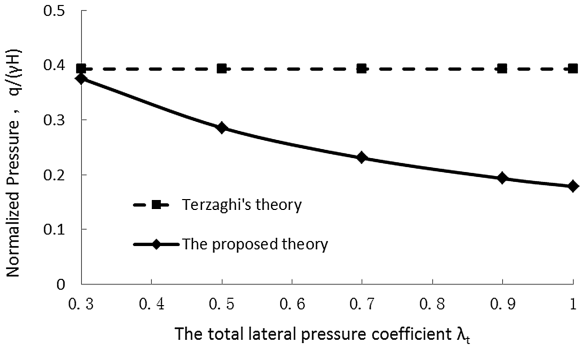

Fig. 6. Comparison between the proposed theory and Terzaghi's theory with different λ_t

(2) The vertical pressure on tunnels decreases with the increase of lateral pressure and the total lateral pressure coefficient λ_t in the limit state (as shown in Figs. 6 and 7). The lateral pressure has an effect on the vertical pressure, but the vertical pressure is independent of the lateral pressure according to Terzaghi's theory.

(3) In the limit state, the lateral pressure decreases with increasing vertical pressure (as shown in Fig. 7). But Terzaghi's theory regards the vertical pressure on tunnels as overloads of the retaining wall, and the lateral pressure increases with increasing vertical pressure.

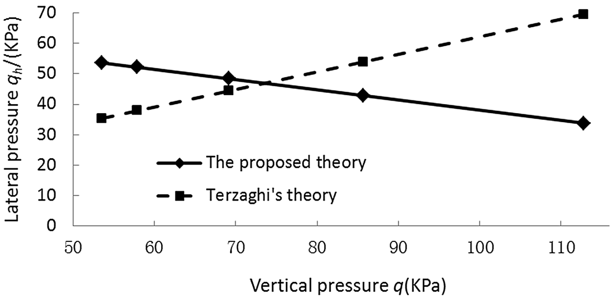

Fig. 7. Relationship between the lateral pressure and vertical pressure

Points 2 and 3 above reveal an interaction between the lateral pressure and the vertical pressure on arch tunnels in well strata. The interaction causes the vertical pressure on tunnels to decrease and the total lateral pressure coefficient λ_t to increase. The law reflects the distribution mechanism of the earth pressure and the inherent relationship between the lateral and vertical pressure on arch tunnels in the limit state.

6.2 Reasons for Differences from Terzaghi's Theory

There are three main reasons for differences between the proposed theory and Terzaghi's theory.

First, the proposed theory considers the role of the inclined sliding surface below the tunnel roof. Because of stress concentration, there is very large stress along the inclined sliding surfaces, which transfers tremendous pressure from the yielding mass of soil onto adjoining stationary parts. As a result, the loads on tunnels are remarkably reduced.

Second, the model for calculating lateral pressure (Rankine's retaining wall) is separated from Terzaghi's trapdoor model concerning the vertical pressure. Actually, the lateral and vertical pressures act on the tunnel lining simultaneously and influence each other.

Third, at the elevation of the tunnel crown, the vertical stress above the tunnel roof is smaller than that beside the tunnel roof (dashed line in Fig. 3). Along with the increase of lateral pressure, the vertical stress beside the tunnel roof increases, and the vertical stress above the tunnel roof decreases accordingly because total vertical stress is equal in the limit state. The vertical stress distribution at the elevation of the tunnel crown agrees with the numerical simulation results of an arch tunnel in well strata (Lin et al. 2007).

6.3 The Importance of Resistance on the Inclined Sliding Surfaces Below the Tunnel Roof

Unlike the vertical sliding surfaces above the tunnel roof, vertical resistance below the tunnel roof includes not only the component of the shear resistance ($T \cos \alpha$) but also the component of normal pressure ($N \sin \alpha$) on the inclined sliding surfaces (as shown in Eq. (3)).

To understand the importance of resistance on the inclined sliding surfaces below the tunnel roof, a circular tunnel (R = 3 m, γ = 20 kN/m^3, c = 0 kPa, λ_t = 1.0) is selected to carry out calculations. Figure 8 shows that the lower the buried depth of the tunnel is, the greater the proportion of vertical resistance below the tunnel roof to the total resistance on the whole sliding surface will be. This proportion is more than 50–60% in shallow tunnels and about 20–30% in deep tunnels in well strata. It also shows that the proportion of vertical resistance below the tunnel roof increases with the decrease of internal friction angles. So, the proportion of resistance on the inclined sliding surface is very large and cannot be ignored as in Terzaghi's theory.

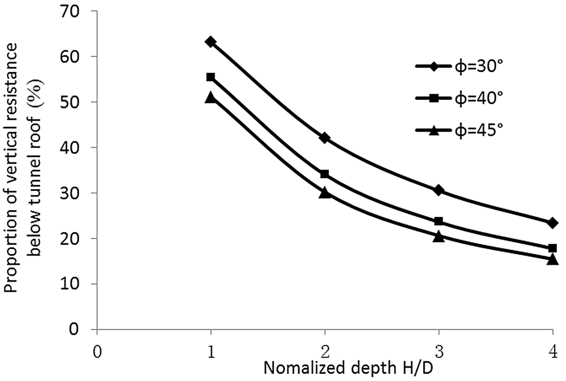

Fig. 8. Proportion of vertical resistance below tunnel roof to total resistance under different depths

7 Mechanism of Interaction Between Lateral and Vertical Pressure on Tunnels

7.1 Vertical Pressure Transfer and Models for Soil Arches Near Tunnel

Major principal stress and major principal strain rate around a tunnel coincides in direction. Figure 9(a) shows the direction of the major principal strain rate for model tunnel experiments in dense sand by Atkinson et al. (1977). Based on major principal stress, we propose a soil arch supporting on the inclined sliding surfaces below the tunnel roof in well strata (as shown in Fig. 10(a)). The arch model shows that the soil arch transfers loads from the tunnel roof to the inclined sliding surfaces. As a result, the vertical pressure on the tunnel roof decreases and the lateral pressure increases because the inclined sliding surfaces cannot bear all the shifted loads. The total lateral pressure coefficient increases correspondingly. It also shows that the inclined sliding surfaces below the tunnel roof play an important role for load-transfer that is different from a trapdoor.

Stress transfer can also explain interaction between the lateral and vertical pressure on arch tunnels (as shown in Fig. 10(b)). Figure 9(b) shows that there are interior sliding surfaces in the yielding zone (Lee et al. 2004), in which soil mass sustains bigger displacement than adjoining parts. So, friction on interior sliding surfaces transfers loads above the tunnel roof to adjoining relatively stationary parts in the

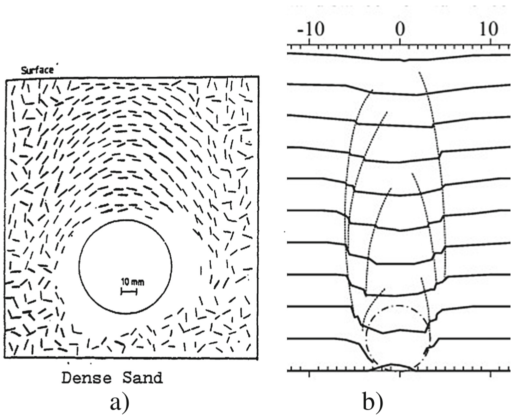
Surface
10 mm
Dense Sand
-10
0
10
a)
b)

Fig. 9. (a) Direction of major principal strain rate (from Atkinson et al. 1977). (b) Exterior and interior sliding surfaces in experiments (Lee et al. 2004)

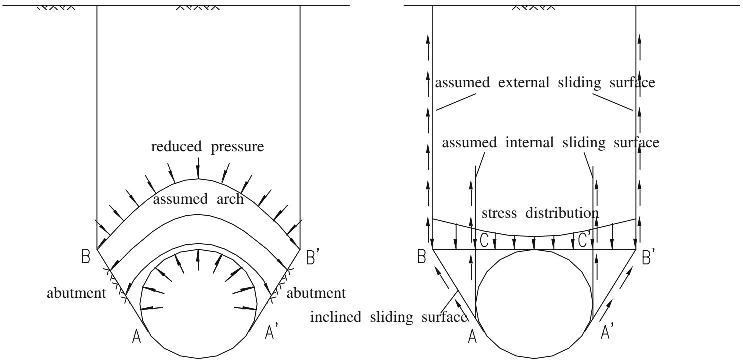
reduced pressure
assumed arch
B
B'
abutment
abutment
A
A'
assumed external sliding surface
assumed internal sliding surface
stress distribution
C
C'
B
B'
inclined sliding surface
A
A'

a) Structural analogy model b) Stress transfer model

Fig. 10. Simplified models for soil arches near tunnel

yielding zone. As a result, the vertical pressure on the tunnel roof decreases and the lateral pressure increases. It also shows that at the elevation of the tunnel crown, the vertical stress above the tunnel roof is smaller than that beside the roof (as shown in Fig. 10(b)).

Luscher and Höeg (1964) concluded that a thrust-ring formed around the tube when deflection occurred. The proposed model in this paper shows that the assumed soil arch is only a part of the thrust-ring (Fig. 10(a)).

7.2 Counteractive of the Lateral Pressure at Vertical Pressure

Counteractive of the lateral pressure at vertical pressure is caused by the deformation of arch tunnels. Because the initial vertical pressure on arch tunnels is greater than the lateral earth pressure, deformation of the tunnel expands horizontally and the deformation will cause lateral reaction of surrounding soil, i.e., the lateral pressure increases due to ground-structure interaction (as shown in Fig. 11). The other way round, the increase of the lateral pressure results in the reduction of the vertical pressure on the tunnel roof according to Eq. (11). As mentioned above, this interaction leads to a more uniform earth pressure distribution around the tunnel, and the total lateral pressure coefficient λ_t rises noticeably.

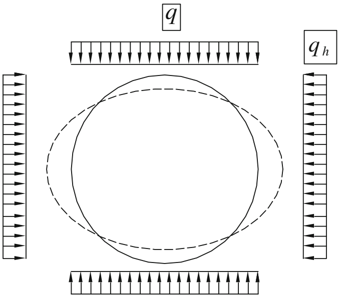

Fig. 11. Lateral deformation pressure on circular tunnels

When designing a shield tunnel, there is the peripheral spring model in which the subgrade reaction is modeled by linear elastic springs (Mashimo and Ishimura 2003), but the tensile spring located at the tunnel roof does not agree with the nature of the soil. In this case, Eq. (11) can explain the reduction of vertical pressure on the tunnel roof, and it is more reasonable to be applied in good ground.

8 Comparison with the Experimental Results

Atkinson et al. (1975) studied the stability of shallow tunnels using pressurized air bags under 1 g conditions. A rubber membrane was used as a flexible circular tunnel lining supported by the applied air pressure. The test was conducted by reducing the tunnel pressure in stages until collapse occurred. The pressure in final equilibrium was recorded in each test. The comparison between the theoretical values and experimental results is shown in Fig. 12 (c = 0 kPa, $\varphi = 35°$). Considering that air pressure in the tunnel is equal in different directions, we have $\lambda_t = 1$. Values according to the proposed theory are about 4%–14% greater than the experimental results, but values according to Terzaghi's theory are about 53%–114% higher than experimental results. The proposed theory is basically consistent with the upper bound analysis used by Atkinson.

Lee et al. (2004) conducted a series of model tunnel tests in a centrifuge with pressurized air bags embedded in sandy soil below the groundwater table (as shown in Fig. 9(b)). The diameter of the simulated circular tunnel was 6 m, and the internal friction angle φ of sandy soil was 38°. Values according to the proposed theory are about 9%–15% greater than the experimental results in both shallow and deep tunnels,

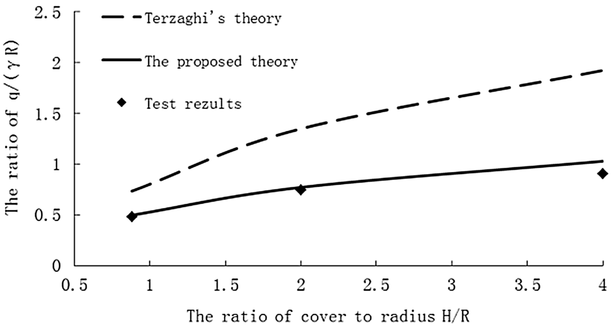

Fig. 12. Comparison with test results from Atkinson et al. (1975)

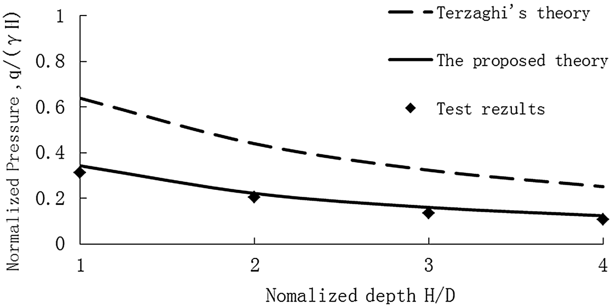

Fig. 13. Comparison with test results from Lee et al. (2004)

while values under Terzaghi's theory are about 104%–141% higher than the results (as shown in Fig. 13).

Compared with model test results, it is shown that the proposed theory is feasible to calculate the support pressure on arch tunnels. It is not only suitable for shallow tunnels but also for deep tunnels.

9 Conclusions

Based on Terzaghi's theory, this study presents a practical arching theory for two-dimensional arch tunnels (including circular tunnels) in good ground (such as very dense sand and hard clay ground). The main results obtained from the study are as follows.

(1) One concise formula for the vertical pressure on arch tunnels is developed considering the inclined sliding surfaces below the tunnel roof. This formula is verified by the upper bound theory, while this formula is simpler and more suitable for engineering applications than the upper bound theory. The vertical pressure on tunnels calculated by the proposed formula is significantly smaller than that calculated by Terzaghi's formula.

(2) The total lateral pressure coefficient λ_t is introduced to calculate lateral pressure. The coefficient λ_t reflects the ability of enclosed structures to adapt to the surrounding ground. It is closely related to the shape of tunnels for the flexible lining. The shape effect of the tunnel roof is considered by adopting empirical values of λ_t.

(3) The proposed formula reveals that there is an interaction between the lateral pressure and the vertical pressure on arch tunnels in good ground. The vertical pressure on tunnels decreases with the increase of lateral pressure and the total lateral pressure coefficient, and the lateral pressure on tunnels increases with the decrease of the vertical pressure on tunnels in the limit state. The interaction mechanism is also discussed, and models for soil arches near tunnels are proposed.

(4) Finally, the theory provides a good explanation for experimental results in good ground. It is found that the proposed theory is not only suitable for shallow tunnels but also for deep tunnels.

The proposed theory broadens the understanding of the arching effect from the flat plate like a trapdoor to a two-dimensional arch tunnel.

Acknowledgement. The author thanks LetPub and Dr. Lin Fang for its linguistic assistance during the preparation of this manuscript.

References

Atkinson, J.H., Potts, D.M., Schofield, A.N.: Centrifugal model tests on shallow tunnels in sand. Tunn. Tunn. **9**, 59–62 (1977)

Atkinson, J.H., Brown, E.T., Potts, M.: Collapse of shallow unlined tunnels in dense sand. Tunn. Tunn. **3**, 81–87 (1975)

Adachi, T., Kimura, M., Kishida, K.: Experimental study on the distribution of earth pressure and surface settlement through three-dimensional trapdoor tests. Tunn. Undergr. Space Technol. **18**, 171–183 (2003)

Adachi, T., Kimura, M., Nishimura, T., Koya, N., Kosaka, K.: Trap door experiment under centrifugal conditions. In: Asaoka, A., Adachi, T., Oka, F. (eds.) Deformation and Progressive Failure in Geomechanics, pp. 725–730. Pergamon, New York (1997)

Chevalier, B., Combe, G., Villard, P.: Experimental and numerical study of the response of granular layer in the trap-door problem. In: Nakagawa, M., Luding, S. (eds.) Proceedings of the 6th International Conference on the Micromechanics of Granular Media, Powders and Grains 2009. American Institute of Physics, Melville, pp. 649–652 (2009)

Costa, Y.D., Zornberg, J.G., Bueno, B.S., Costa, C.L.: Failure mechanisms in sand over a deep active trapdoor. J. Geotech. Geoenviron. Eng. **135**, 1741–1753 (2009). https://doi.org/10.1061/(asce)gt.1943-5606.0000134

Dewoolkar, M.M., Santichaianant, K., Ko, H.-Y.: Centrifuge modeling of granular soil response over active circular trapdoors. Soils Found. **47**(5), 931–945 (2007)

Evans, C.H.: An examination of arching in granular soils. S.M. thesis, Department of Civil Engineering. MIT, Cambridge, MA (1983)

Getzler, Z., Komornik, A., Mazurik, A.: Model study on arching above buried structures. J. Soil Mech. Found. Div. **94**(SM5), 1123–1141 (1968)

Hashimoto, T., Ye, G.L., et al.: Study on earth pressure acting upon shield tunnel lining in clayey and sandy grounds based on field monitoring. In: Ng, C.W.W., Huang, H.W., Liu, G.B. (eds.) Geotechnical Aspects of Underground Construction in Soft Ground, London, pp. 307–312 (2009)

Iglesia, G.R., Einstein, H.H., Whitman, R.V.: Investigation of soil arching with centrifuge tests. J. Geotech. Geoenviron. Eng. (2014). https://doi.org/10.1061/(asce)gt.1943-5606.0000998

Koyama, Y., Okano, N., Shimizu, M., Fujiki, I., Yoneshima, K.: In-situ measurement and consideration on shield tunnel in diluvium deposit. Proc. Tunn. Eng. JSCE **7**, 385–390 (1995)

Koyama, Y.: Present status and technology of shield tunneling method in Japan. Tunn. Undergr. Space Technol. **18**(2), 145–159 (2003)

Luscher, U., Höeg, K.: The action of soil around buried tubes. In: Proceedings of Sixth International Conference on Soil Mechanics and Foundation Engineering, Montreal, Canada, vol. 2, pp. 396–400 (1964a)

Luscher, U., Höeg, K.: The beneficial action of the surrounding soil on the load-carrying capacity of buried tubes. In: Proceedings of the Symposium on Soil-Structure Interaction, University of Arizona, Tucson, Arizona, pp. 393–402 (1964b)

Lee, C.J., Chiang, K.H., Kuo, C.M.: Ground movement and tunnel stability when tunneling in sandy ground. J. Chin. Inst. Eng. **27**(7), 1021–1032 (2004)

Ladanyi, B., Hoyaux, B.: A study of the trap-door problem in a granular mass. Can. Geotech. J. **6** (1), 1–15 (1969)

Lin, L., Liu, H., Liu, H.: Stress analysis method for pressure of surrounding rocks on tunnels. China Civ. Eng. J. **40**(8), 85–89 (2007). (in Chinese)

Lin, P.: On the lateral pressure of tunnel linings. China Civ. Eng. J. **15**(1), 54–62 (1982). (in Chinese)

Marston, A.: The Theory of External Loads on Closed Conduits in the Light of the Latest Experiments. Bulletin 96, Iowa Engineering Experiment Station, Ames, Iowa (1930)

Mashimo, H., Ishimura, T.: Evaluation of the load on shield tunnel lining in gravel. Tunn. Undergr. Space Technol. **18**, 233–241 (2003)

Moradi, G., Abbasnejad, A.: The state of the art report on arching effect. J. Civ. Eng. Res. **3**(5), 148–161 (2013)

Nielson, F.D.: Soil structure arching analysis of buried flexible structures. Ph.D. thesis, University of Arizona, Faculty of Civil Engineering (1966)

Nishizawa, K., Shiotani, T., Tsutiya, K., Mima, K., Hashimoto, T., Nagaya, J.: The field measurement of the earth pressure on the segments in the stiff clay (in Japanese). In: Proceedings of the 31st Japan National Conference on Geotechnical Engineering, pp. 2289–2290. The Japan Geotechnical Society (1996)

Pardo, G.S., Sáez, E.: Experimental and numerical study of arching soil effect in coarse sand. Comput. Geotech. **57**, 75–84 (2014)

Sadrekarimi, J., Abbasnejad, A.: Arching effect in fine sand due to base yielding. Can. Geotech. J. **47**(3), 366–374 (2010)

Terzaghi, K.: Theoretical Soil Mechanics, pp. 66–76. Wiley, New York (1943)

Vardoulakis, I., Graf, B., Gudehus, G.: Trap-door problem with dry sand: a statical approach based upon model test kinematics. Int. J. Numer. Anal. Methods Geomech. **5**(1), 57–78 (1981)

Whitman, R.V., Getzler, Z., Hoeg, K.: Static tests upon thin domes buried in sand. MIT Research Project Report No. R62-41, December 1962

Whitman, R.V., Getzler, Z., Hoeg, K.: Tests upon thin domes buried in sand. J. Boston Soc. Civ. Eng. **50**, 1–22 (1963)

Yang, F., Yang, J.S.: Limit analysis method for determination of earth pressure on shallow tunnel. Eng. Mech. **25**(7), 179–184 (2008). (in Chinese)

Yang, X.L., Yang, Z.H., Li, Y.X., Li, S.C.: Upper bound solution for supporting pressure acting on shallow tunnel based on modified tangential technique. J. Cent. South Univ. **20**, 3676–3682 (2013)

Reliability Analysis of Ground Surface Settlement Given Multivariate Spatial Random Field in Shield Tunneling

Changhong Wang(✉)

Shanghai University, Shanghai 200444, China
changhong.wangsir@gmail.com

Abstract. It is well known that geotechnical parameters impact dramatically soil-tunneling mechanics. Random field theory has been widely used for a single geotechnical parameter, including aleatory uncertainty, spatial variability and local singularity. Current challenge is focused on analyzing the spatially correlated soil layers. Coefficient of cohesion, internal friction angle, and Young's modulus are accounted in reliability analysis of ground surface settlement due to shallow-buried shield tunneling. At first, convert multiple non-stationary soil layers into stationary field using a local detrending method, and define the geostatistical parameters. Then, assume spatial variability of geotechnical parameters into aleatory randomness, and classical response surface method is utilized into reliability analysis. Furthermore, Co-sequential Gaussian discretization is conceived for multivariate spatial random field, in which failure probability of ground surface settlement is calculated directly by subset Monte-Carlo simulation. This approach is applied into the paralleling zone of four shield tunnels of the 5th and 6th metro lines linking to Huanhu W Rd station, Tianjin China. Results prove that reliability index of considering geotechnical parameters as random variables is lower than the assumption of multivariate spatial random field, which would support substantially to construction control and design optimization in complex shallow-buried shield tunneling projects.

Keywords: Geotechnical parameter · Spatial variability · Stochastic simulation
Multivariate · Reliability index

1 Introduction

In design & construction of geotechnical engineering, stability analysis of shallow-buried tunneling is conducted to evaluate the ground surface settlement due to input variables. In the past several decades, a great deal of researches has been studied by the deterministic approaches (Loganathan and Poulos 1998; Pinto and Whittle 2014). Reliability analysis of tunneling is relatively reasonable since it enables engineers to consider aleatory uncertainty of geotechnical parameters (Mollon et al. 2009; Zhang et al. 2015). In fact, spatial variability study is more practical due to complex geological activities. This led to move advanced geostatistics forward into the hotspot. In engineering practice, uncertainties come from multiple soil layers, which could not be inferred separately. The noteworthy is the Monte-Carlo (MC) simulation, and its

© Springer Nature Singapore Pte Ltd. 2018
D. Zhang and X. Huang (Eds.): GSIC 2018, *Proceedings of GeoShanghai 2018 International Conference: Tunnelling and Underground Construction*, pp. 181–189, 2018.
https://doi.org/10.1007/978-981-13-0017-2_17

drawback focusing on that spatial variability of geotechnical parameters is usually assumed to be independent, which may result in risks and conservation.

It is remarked that the previous studies did not take multiple soil layers and cross-correlated geotechnical parameters into account. Multivariate spatial random field is much reasonable due to the advantages namely, (1) it could transform non-stationary soil layers into stationary field using a local detrending method; (2) it modifies cross discretization according to sequential Gaussian algorithm; and (3) it improves subset acceleration to classical Monte-Carlo simulation.

2 Engineering Background

Metro Lines 5 and 6 linking to Huanhu W Rd Station owns total four shield tunnels in Tianjin, China. Central lines twist and overlap with each other in a narrow underground space. There is a traffic artery and densely packed resident buildings in the subway zone. Therefore, quantitative settlement analysis of soil mass would prevent constructing risks effectively, and support scientific decision.

According to the 62 geotechnical boreholes of site investigation, we got 84 strength parameters from the consolidated-undrained triaxial tests, and obtained 607 groups of the Young's modulus transformed from the in-situ cone penetration test. Key values of the multiple soil layers are listed in Table 1.

Table 1. Key geotechnical parameters of the multiple soil layers

Soil layer	H (m)	ρ (kg/m^3)	c (kPa)	φ (°)	E (MPa)
①$_1$ Land fill	2.2	1800	4.0	7.0	16.0
④$_1$ Silty clay	3.5	1970	8.0	9.0	30.4
⑥$_1$ Silty clay	5.8	1900	11.0	15.0	28.4
⑥$_4$ Silty clay	3.1	1950	15.0	14.0	29.2
⑦Silty clay	1.6	1990	15.0	13.0	26.8
⑧$_1$ Silty clay	5.8	1990	12.0	12.0	44.4
⑨$_1$ Silt	9.0	2010	16.0	28.0	98.4
⑩$_1$ Silty clay	2.0	2020	19.0	17.0	33.2
⑪$_1$ Silt	3.0	2000	16.0	33.0	114.4

Three-dimensional numerical analysis of the soil-structure system (as shown in Fig. 1) is executed in the finite difference code FLAC^{3D}. Length of the central axis direction is 2 m. In order to reduce the potentially boundary impacts, width and depth of the geometry is adopted 80 m and 36 m, respectively. Excavation sequence follows the sequence from the bottom to the top, and the left to the right.

According to the mechanical properties of the soil layers, constitutive model is assumed to comply with theoretical elastic-plastic model with Mohr-Coulomb failure criterion. Concrete segment and shield machine skin belong to linear elastic material. Detailed values are listed in Table 2.

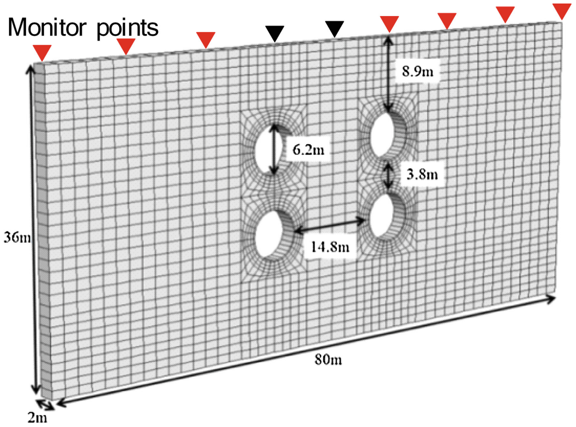

Fig. 1. Three-dimensional mechanical soil-structure system.

Table 2. Mechanical parameters of segment and shield enclosure

Elastic material	ρ /(kg/m^3)	v	E /(MPa)
Shield segment	2450	0.17	2.1×10^4
Shield machine skin	8000	0.22	2.06×10^5

Taking the tunnel unloading effects into account, excavation process is divided into four phases: soil removing, shield enclosing, shield tail separating and segment liner supporting. Step Drills forward 2. 0 m at each time, unfilled gaps of the shield tail are assumed as 20%, and to be circular homogenous void.

3 Response Surface Method (RSM)

Hasofer-Lind formula (Hasofer and Lind 1974) is widely used in reliability analysis of geotechnical engineering.

$$\beta_{\mathrm{HL}} = \min_{\boldsymbol{Z} \in G} \sqrt{(\boldsymbol{Z} - \boldsymbol{\mu}_Z)^T \boldsymbol{C}^{-1} (\boldsymbol{Z} - \boldsymbol{\mu}_Z)} \tag{1}$$

where, bold letter $\boldsymbol{\mu}_Z$ denotes the mean values vector. $\boldsymbol{C}$ is the covariance matrix of input variables. $\boldsymbol{Z}$ represents the design points of limit state function G. β_{HL} represents the absolute quantile value of $G \leq 0$ on the standard normal distribution.

$$P_f = \Phi[-\beta_{\mathrm{HL}}] \tag{2}$$

where, P_f denotes the failure probability, $\Phi[\cdot]$ is the statistical operator of standard normal distribution.

Limit state function G of maximal ground surface settlement is denoted as follows.

$$G = v_{\max} - v \tag{3}$$

where, v represents the theoretically maximal value of ground surface settlement, and $v_{\max}$ denotes the actual threshold. A quadratic polynomial is designed as response surface for limit state function (Tandjiria et al. 2000).

$$G(\mathbf{Z}) = g_0 + \sum_{i=1}^{n} a_i Z_i + \sum_{i=1}^{n} b_i Z_i^2 \tag{4}$$

where, g_0 and a_i, b_i, $i = 1, \ldots, n$ are the unknown coefficients.

4 Multivariate Spatial Random Field

Classical statistics simplified spatial variability of geotechnical parameters into aleatory uncertainty. However, geostatistics theory could not only take the randomness into account, but also emphasize the structural characteristics of discrete samples. It offsets the shortage of the former one that ignoring spatial variability. Especially, multivariate spatial random field would depict completely the cross-correlated variables in reliability analysis.

4.1 Stationary Process

Detrending analysis is a common method to obtain stationary field, and a geotechnical parameter could be expressed as follows.

$$Z(x) = \mu(x) + \varepsilon(x) \tag{5}$$

where, $\mu(x)$ denotes drift, and $\varepsilon(x)$ represents residual uncertainty. Local detrending method would build a stepped mean curve for multiple similar soil layers along one direction.

Table 1 gives out the stepped mean values $m(x_i), i = 1, \ldots, N$ of coefficient of cohesion c, internal friction angle φ and Young's modulus E in the vertical direction. Variance of spatial random field could adopt the thickness-weighted mean values of multiple soil layers.

$$\sigma^2 = \frac{\sum_{i=1}^{N} \sigma^2(x_i) \cdot H_i}{\sum_{i=1}^{N} H_i} \tag{6}$$

where, N is the number of multiple soil layers. H_i is the corresponding thickness, and σ^2 represents the weighted variance of spatial random field.

It assumes $Z(x_i)$, $i = 1, \ldots, n$ as direct observations, and experimental variogram (Matheron and Armstrong 1963) could be calculated as follows.

$$\gamma^*(h) = \frac{1}{2N_h} \sum_{i=1}^{N_h} [Z(x_i + h) - Z(x_i)]^2 \tag{7}$$

where, h is the lag distance. N_h denotes the data set number in interval $(x_i + h, x_i)$ to calculate experimental variogram.

Theoretically spherical has been applying widely in auto-variogram and cross-variogram.

$$\gamma(h) = \begin{cases} C_0 + C_1[1.5(h/a) - 0.5(h/a)^3] & 0 \le h \le a \\ C_0 + C_1, & h > a \end{cases} \tag{8}$$

where, C_0 defines the nugget, $C_0 + C_1$ equals the sill (i.e., σ^2), and a denotes the range (or correlated distance). Regression algorithms in R language (Pebesma 2004) would derive the unknown coefficients from experimental variogram.

Three-dimensional heterogeneity of a geotechnical parameter would be taken into account by the weighted lag distance h.

$$h = \sqrt{\left(\frac{h_1}{\eta_1}\right)^2 + \left(\frac{h_2}{\eta_2}\right)^2 + \left(\frac{h_3}{\eta_3}\right)^2} \tag{9}$$

where, η_1 equals to 1.0 constantly, η_2, η_3 are the ratios of the second, third ranges divided by the main range a_1.

4.2 Co-sequential Gaussian Discretization

Let's assume the spatially correlated bivariate $Z_1(x)$, $Z_2(x)$ subjecting to Gaussian distribution through the local detrending (e.g., three variables are in similarity). Known quantities include stepped mean curves $\mu_1(x)$ and $\mu_2(x)$, variogram $r_{11}(h)$ and $r_{22}(h)$, as well as cross-variogram $r_{12}(h)$. As similar as Co-Kriging equations (Eldeiry and Garcia 2010), correlated discretization is proposed in this paper. There are K grid nodes in the space A. Therefore, $Z(x)$ would be a linear multivariate of K variables $\{Z(x_k), x \in A, k = 1, 2, \ldots, K\}$,

$$Z(x) = \sum_{k=1}^{K} \lambda_k Z(x_k), \tag{10}$$

the corresponding K multivariate joint cumulative distribution is,

$$F_K(Z_1, Z_2, \ldots, Z_K | k) = \mathrm{Prob}\{Z_i < z_i, i = 1, 2, \ldots, K | k\} \tag{11}$$

In order to obtain a sample of the K multivariate, sequential simulation consists of K steps, and each one denotes a realization from the joint probabilistic distribution. Samples would become the conditional observations in a new round simulation.

(1) Define a random path in the spatially discrete domain A, if and only if each grid node could be traversed once a time, conditional data consists of the original site observation $z_a, a = 1, 2, \ldots, n$ and the simulated data $z(x_1), \ldots, z(x_{i-1})$ at grid nodes.
(2) Predict the mean value $Z_1(x_k)$, $Z_2(x_k)$ and variance σ_1^2, σ_2^2 for the grid node x_k given conditional data z_a, variogram $r_{11}(h)$ and $r_{22}(h)$, cross-variogram $r_{12}(h)$.
(3) Build two normal distributions $N[Z_1(x_k), \sigma_1^2]$ and $N[Z_2(x_k), \sigma_2^2]$ at the grid node x_k, with which sampling randomly to get one realization, respectively. Of course, they also become the conditional data for the next grid nodes.
(4) Move to the next grid node x_{k+1}, repeat the above steps 2–3, until iterate over-all K grid nodes.
(5) Finish one realization of multivariate spatial random field.

4.3 Subset Monte-Carlo (SMC) Simulation

For the reason to accelerate sampling efficiency of multivariate spatial random field, subset Markova chain (Papaioannou and Straub 2012) is employed. In a probabilistic space, systemic failure event F could be denoted by a continuous cascade multiplication of M failure events.

$$F = \bigcap_{i=1}^{M} F_i \tag{12}$$

furthermore, joint probability of a systemic failure event is,

$$P_f\left(\bigcap_{i=1}^{M} F_i\right) = P_f(F_1) \prod_{i=2}^{M} P_f(F_i | F_{i-1}) \tag{13}$$

Systemic failure event could be denoted by $G \leq 0$, and cascade failure events are defined as $F_i = \{G \leq c_i\}$, $i = 1, \ldots, m$, $c_1 > \ldots > c_i > \ldots > c_m = 0$. c_i equals to the limit state function G_0 value corresponding to the failure ratio p_0 of subset Monte-Carlo algorithm. It is worth mentioning that initial failure probability $P_f(F_1)$ is calculated directly by the classical Monte-Carlo simulation. Algorithm is organized as follows.

5 Results and Discussion

According to the geotechnical investigation of the background project, spatially correlated variables include the coefficient of cohesion c, internal friction angle φ and Young's modulus E. Classical statistical and geostatistical would analyze the reliability index of ground surface settlement due to shield tunneling respectively, and calibrating the results with field measurements.

5.1 Characteristics of Spatial Random Field

First-order statistical moment of the spatial random field is the local mean value curve, and the second-order moment could adopt the thickness-weighted average variance of the similarly multiple soil layers.

According to the large amount of on-site and off-site works, Geostatistical characteristics of the geotechnical parameters are tabulated in Table 3.

Table 3. Geostatistical characteristics of the multivariate spatial random field

Geotechnical parameter	$\mu(x)$	σ^2	a_3/(m)	η_3	Correlation coefficient r		
					c/(kPa)	φ/(°)	E_s/(MPa)
c/(kPa)	$\mu_c(x_3)$	1.3^2	2.0	0.1	1.0	–0.5	–0.4
φ/(°)	$\mu_\varphi(x_3)$	2.0^2	2.0	0.1	–0.5	1.0	0.4
E/(MPa)	$\mu_E(x_3)$	6.0^2	2.0	0.1	–0.4	0.4	1.0

5.2 Stochastic Analysis Results

According to local engineering practice and taking mechanical model bias into account, threshold of ground surface settlement is kept into $v_{\max}^{(1)} = 15$ mm in terms of one shield tunneling, and it increases to $v_{\max}^{(4)} = 30$ mm after the fourth tunnel excavation.

Figure 2(a) demonstrates the reliability index calculated by RSM, MC and SMC in the first shield tunnel excavation. It is obvious that β_{SMC} is bigger than β_{RSM}, and classical statistics is a special case of geostatistics when the range becomes long enough. In the classical statistics, β_{MC} varies less than 10% comparing with β_{RSM}. According to Chinese specification of structural reliability, the index needs to be greater than 2.70, that means the classical statistics is partial to conservation. Figure 2(b) gave out the field measurements of ground surface settlements, which displayed the good superposition by side-by-side and overlapped excavations. And the magnitudes of the settlements are closer to the thresholds, which support substantially to the aforementioned reliability analysis.

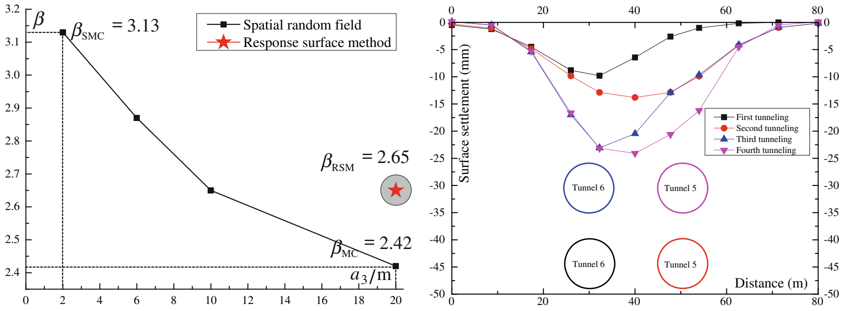

(a) (b)

Fig. 2. Reliability index and field measurements of maximal ground surface settlement. (a) Reliability index calculated by RSM, MC and SMC method in the first tunneling; (b) Field measurements of ground surface settlements due to shield tunnel excavation.

Classical Monte-Carlo algorithm needs 100,000 simulations to calculate the failure probability at $P_f = 1 \times 10^{-3}$. Subset Monte-Carlo algorithm adopts subset parameters $P_0 = 0.1$, $N = 500$ in numerical simulation. There are total 1,850 stochastic calculations, which only consumes 2% time of the classical algorithm did. Table 4 compared the results of response surface method and subset Monte-Carlo algorithm.

Table 4. Reliability index of ground surface settlement by different statistical assumptions

Threshold	Reliability index	Classical statistics	Geostatistics
$v_{\max}^{(1)} = 15$ mm	β	2.65	3.13
	P_f	4.0‰	0.9‰
$v_{\max}^{(4)} = 30$ mm	β	2.15	2.81
	P_f	15.8‰	2.5‰

6 Conclusions

Classical statistics and geostatistics are applied into ground surface settlement analysis of multiple shield tunneling. (1) Local trending method could establish stationary field for multiple similar soil layers. And the anisotropic variogram would fully depict the spatial variability of geotechnical parameters. (2) Co-sequential Gaussian algorithm is conceived to divide multivariate spatial random field into finite points. (3) Subset simulation would improve efficiently for classical Monte-Carlo algorithm. (4) Reliability index is more accurate according to spatial random field than random variable assumption.

References

Eldeiry, A., Garcia, L.: Comparison of ordinary kriging, regression kriging, and cokriging techniques to estimate soil salinity using LANDSAT images. J. Irrigation Drain. Eng. **136**(6), 355–364 (2010)

Hasofer, A., Lind, N.: Exact and invariant second-moment code format. J. Eng. Mech. Div. **100** (1), 111–121 (1974)

Loganathan, N., Poulos, H.: Analytical prediction for tunneling-induced ground movements in clays. J. Geotech. Geoenviron. Eng. **124**(9), 846–856 (1998)

Matheron, G., Armstrong, M.: Principles of geostatistics. Econ. Geol. **58**(8), 1246–1266 (1963)

Mollon, G., Dias, D., Soubra, A.: Probabilistic analysis of circular tunnels in homogeneous soil using response surface methodology. J. Geotech. Geoenviron. Eng. **135**(9), 1314–1325 (2009)

Papaioannou, I., Straub, D.: Reliability updating in geotechnical engineering including spatial variability of soil. Comput. Geotech. **42**, 44–51 (2012)

Pebesma, E.: Multivariable geostatistics in S: the gstat package. Comput. Geosci. **30**(7), 683–691 (2004)

Pinto, F., Whittle, A.J.: Ground movements due to shallow tunnels in soft ground. I: analytical solutions. J. Geotech. Geoenvironmental Eng. **140**(4), 1–43 (2014)

Tandjiria, V., Teh, C., Low, B.: Reliability analysis of laterally loaded piles using response surface methods. Struct. Saf. **22**, 335–355 (2000)

Zhang, J., Chen, H., Huang, H., Luo, Z.: Efficient response surface method for practical geotechnical reliability analysis. Comput. Geotech. **69**, 496–505 (2015)

The Surface Subsidence Prediction of Shield Construction Based on the Fuzzy Neural Network

Dong Han[1,2](✉) and Xiaojun Li[1,2]

[1] Department of Geotechnical Engineering, Tongji University,
1239 Siping Road, Shanghai 200092, China
18817312390@163.com
[2] Key Laboratory of Geotechnical and Underground Engineering of the Ministry of Education, Tongji University, 1239 Siping Road, Shanghai 200092, China

Abstract. There are many factors that influence the surface subsidence caused by shield construction, which make it difficult to predict the subsidence using the mechanical models. The fuzzy neural network proves to be good at dealing with nonlinear and fuzzy problems and can well establish the nonlinear relationship between influence factors and surface subsidence. In order to improve predicting the tunneling-induced surface settlement, the fuzzy neural network is adopted. The model gives a consideration to the tunneling boring machine (TBM) geometric size, stratum mechanical properties and construction parameters. Compared with the predicted results of BP neural network in Nanchang subway, Adaptive Network-based Fuzzy Inference System (ANFIS) has a higher accuracy in the prediction. The model of ANFIS can be applied to the similar projects to guide the construction of tunnel and guarantee the safety of surface constructions.

Keywords: Upper-soft lower-hard stratum · Prediction of surface subsidence
Tunneling-induced subsidence · ANFIS

1 Introduction

Artificial neural network possesses a strong ability to learn rules and adapt to rules independently [1], but it looks like a black box, and is not transparent to the users. Fuzzy system does not possess a good adaptive ability, which leads to limitation in application. The Adaptive Network-based Fuzzy Inference System combines the advantage of artificial neural network system and fuzzy system, and it has great advantage in dealing with nonlinear and fuzzy problems [2]. In this paper, the tunneling boring machine (TBM) geometric size, stratum mechanical properties, construction parameters and the surface subsidence are used as training samples. The relational model between the three factors and settlement is established in the article. The adaptive fuzzy neural network theory provides a solution to this problem. It is more accurate than BP neural network in prediction.

© Springer Nature Singapore Pte Ltd. 2018
D. Zhang and X. Huang (Eds.): GSIC 2018, *Proceedings of GeoShanghai 2018 International Conference: Tunnelling and Underground Construction*, pp. 190–197, 2018.
https://doi.org/10.1007/978-981-13-0017-2_18

2 Establishment of Surface Subsidence Prediction Model Based on ANFIS

2.1 Design of the Input Layer and Output Layer

According to deformation mechanism of the surface subsidence, the input layer variables of this model are geometric parameters of tunnel boring machine and stratum, stratum parameters and construction parameters. The output variable is surface subsidence. The structure of the input and output layers is shown in Fig. 1.

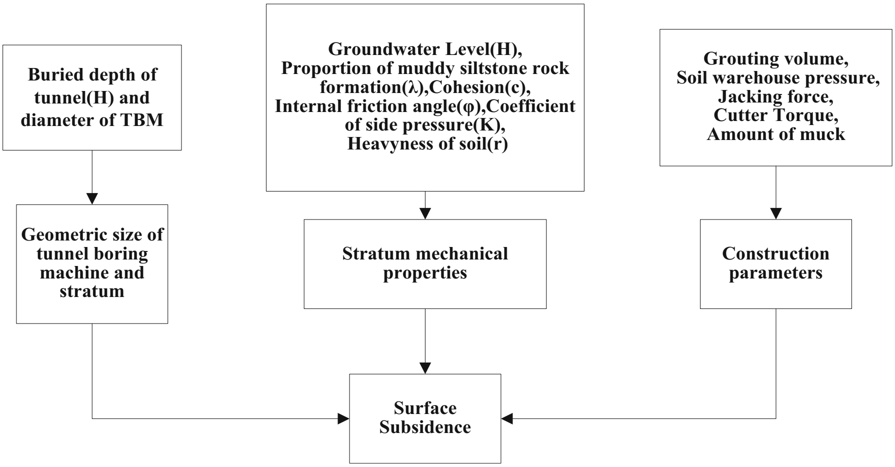
Buried depth of tunnel(H) and diameter of TBM
Groundwater Level(H), Proportion of muddy siltstone rock formation(λ),Cohesion(c), Internal friction angle(φ),Coefficient of side pressure(K), Heavyness of soil(r)
Grouting volume, Soil warehouse pressure, Jacking force, Cutter Torque, Amount of muck
Geometric size of tunnel boring machine and stratum
Stratum mechanical properties
Construction parameters
Surface Subsidence

Fig. 1. Relationship between influence factors and surface subsidence.

2.2 Data Preprocessing

The size of sample is 16 × 13, that is, 16 samples, 13 observing objects in each sample. The difference between the samples is show in Table 2. From 90 ring to 165 ring, the parameters, such as H, λ, φ and r, are gradually increasing and the parameters, such as L, c, K, are gradually decressing. In order to speed up the convergence of ANFIS, the original data need to be normalized.

2.3 Principle of Adaptive Network-Based Fuzzy Inference Systems

The typical two-input ANFIS is shown in Fig. 2, where each node of the same layer has a similar function (where $Q_{1,i}$ represents the output of the i-th node of the first layer) [3].

(1) The first layer: the choice of input parameters and fuzzification.

$$\begin{aligned} Q_{1,i} &= u_{Ai}(x_1), i = 1, 2 \\ Q_{2,i} &= u_{Bi}(x_2), i = 1, 2 \end{aligned} \tag{1}$$

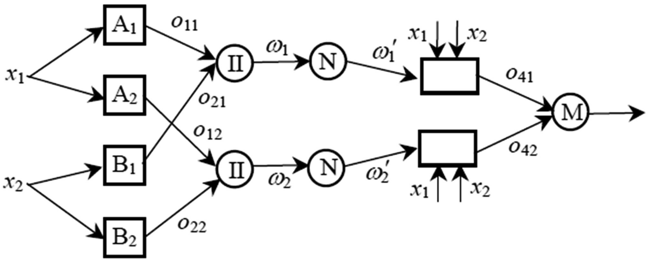

Fig. 2. The structure of ANFIS.

Where x_i is the input of node i; A_i or B_i is the fuzzy variable associated with the node; $Q_{1,i}$ and $Q_{2,i}$ are the membership functions of fuzzy sets A_i and B_i, respectively.

(2) The second layer:calculating excitation intensity of the fuzzy rule, the multiplication of input signal and output of its results.

$$Q_{2,i} = \omega_i = u_{Ai}(x_1)u_{Bi}(x_2), i = 1, 2 \tag{2}$$

(3) The third layer: the normalization of excitation intensity

$$Q_{3,i} = \omega' = \omega_i/\omega_1 + \omega_2, i = 1, 2 \tag{3}$$

(4) The fourth layer: each node of the layer is the self-adaptive node, the output result is:

$$Q_{4,i} = \omega_i'(p_i x_1 + q_i x_2 + r_i), i = 1, 2 \tag{4}$$

(5) The fifth layer: Calculating the total output result of all input signals.

$$Q_{5,i} = \sum_i \omega_i' f_i = \left(\sum_i \omega_i f_i\right) \Big/ \left(\sum_i \omega_i\right), i = 1, 2 \tag{5}$$

The structure of ANFIS is a multilayer feedforward network. The weights between layers can be adjusted adaptively by the given samples. It adopts mixed learning algorithm and the mixed learning algorithm can greatly improve the training speed of the parameters.

3 Case Study

3.1 The Project Overview

Earth pressure balance shield construction is used in Nanchang Metro Line 1. The diameter of the tunnel boring machine is 6.28 m. The groundwater level in the stratum is about 10 m below the surface, and the stratum surrounding the tunnel boring

Table 1. Indexes of physical and mechanical properties of the shield interval.

Stratum	ρ/(g/cm^{-3})	c/kPa	φ	K	μ	e
Silty clay	1.80	16	12	0.42	0.45	0.68
Silver sand	1.93	0	36	0.33	0.33	0.70
Gravelly sand	2.00	0	38	0.30	0.30	0.65
Intense weathered argilaceous siltstone	2.20	/	/	0.30	/	/
Moderately weathered argilaceous siltstone	2.25	58	39	0.28	/	/

tunneling machine is typical upper-soft lower-hard stratum. The upper soft soil consists of fine sand and gravel, and the lower hard soil is muddy siltstone. The indexes of physical and mechanical properties of the shield interval are shown in Table 1. The samples are mainly from monitoring section data in the downline of interval [4].

3.2 Selection of Samples and Training of Network

The influence factors and surface subsidence values of 16 monitoring sections are selected as training data (Table 2) to establish relational model. The training results are shown in Fig. 3.

Table 2. Network training samples.

Ring number	Geometric size	Stratum mechanical properties					
	H/D	L/m	λ	c/KPa	φ	K	r/(kN/m^3)
90	2.75	10.09	0.43	8.78	20.94	0.5	13.07
95	2.75	10.02	0.43	8.78	20.94	0.5	13.36
100	2.76	10.1	0.45	8.57	21.38	0.49	13.34
105	2.78	10.18	0.45	8.47	21.59	0.49	13.31
110	2.79	10.27	0.47	8.17	22.2	0.49	13.27
115	2.81	10.35	0.47	8.27	22	0.49	13.18
120	2.82	10.42	0.49	8.01	22.55	0.48	13.08
125	2.83	10.48	0.5	7.76	23.07	0.48	12.99
130	2.82	10.52	0.53	7.3	24.02	0.47	13.01
135	2.82	10.57	0.55	7.07	24.49	0.47	13.09
140	2.82	10.6	0.55	7.11	24.42	0.47	13.18
145	2.82	10.63	0.57	6.85	24.96	0.46	13.22
150	2.83	10.73	0.62	6.09	26.53	0.45	13.56
155	2.85	10.85	0.6	6.3	26.1	0.46	13.57
160	2.86	10.97	0.64	5.82	27.1	0.45	13.49
165	2.86	11.08	0.64	5.81	27.12	0.45	13.32

(*continued*)

Table 2. (*continued*)

Ring number	Construction parameters					Maximum settlement value/mm
	Grouting volume/m^3	Soil warehouse pressure/bar	Jacking force/kN	Cutter Torque/(kN·m)	Amount of muck/m^3	
90	4.5	0.75	14000	2500	51.43	−25.8
95	6	0.93	16500	3010	47.58	−23.13
100	4	0.8	16600	3000	45.49	−23.79
105	3	1	15000	3000	47.88	−27.52
110	3	1	16500	3000	48.16	−26.51
115	2.5	0.7	15600	3000	49.02	−31.29
120	5	0.8	18500	3500	50.69	−38.23
125	5	0.8	15500	3000	41.71	−30.17
130	5	0.8	16000	3300	45.39	−28.96
135	8.5	0.9	14000	3200	51.94	−28.94
140	6	0.8	14000	3000	46.04	−27.44
145	5	0.75	14500	3000	45.16	−25.88
150	6	0.8	18000	3500	47.57	−29.12
155	4	0.9	16000	3000	45.43	−27.28
160	5	0.9	18000	3000	48.5	−21.62
165	4	1	18000	3200	49.38	−18.6

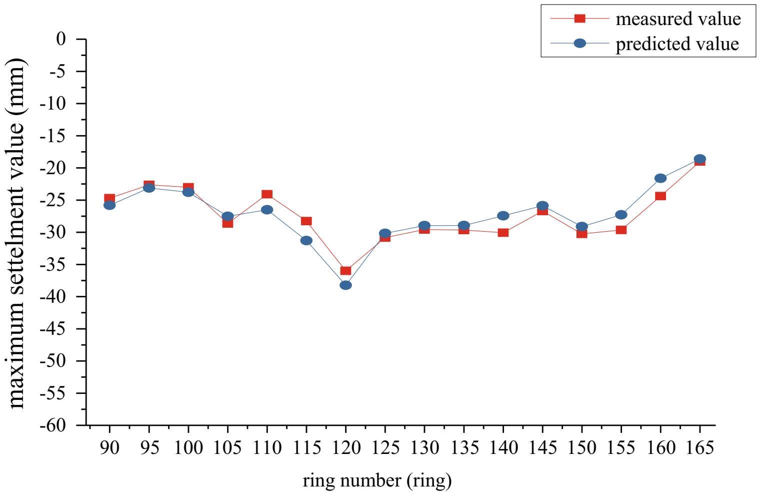

Fig. 3. The result of training.

Table 3. Data used to predicted.

Ring number	Geometric size	Stratum mechanical properties					
	H/D	L/m	λ	c/KPa	φ	K	r/(kN/m^3)
170	2.88	11.19	0.67	5.34	28.77	0.44	13.18
175	2.91	11.3	0.67	5.34	28.77	0.44	13.19
180	2.9	11.39	0.68	5.19	29.08	0.44	13.22
185	2.92	11.47	0.7	4.91	29.7	0.43	13.34
190	2.91	11.55	0.67	4.76	30.01	0.43	13.47

Ring number	Construction parameters				
	Grouting volume/m^3	Soil warehouse pressure/bar	Jacking force/kN	Cutter Torque/(kN·m)	Amount of muck/m^3
170	3	0.8	18000	3700	53.06
175	6	1	17000	2900	54.19
180	7	1	18000	3000	51.99
185	6	1.2	18000	3000	49.55
190	6	0.8	17000	3200	55.23

3.3 Analysis of Prediced Results

Based on the data in Table 2, the model between the three factors and the maximum settlement of the surface is established. Through training of fuzzy neural network, residuals are slighter and network is more and more stable. Data of Table 3 are used for predicting surface subsidence. The maximum settlement value of the predicted results and residual analysis at the 5 monitored section are shown in Fig. 4.

As is shown in Fig. 4 that the predicted values of surface subsidence by ANFIS for the five sections at the 170–190 ring are −19.80 mm, −22.72 mm, −21.00 mm, −19.14 mm and −17.01 mm respectively, the predicted values by BP neural network are −18.68 mm, −19.8 mm, −22.84 mm, −22.86 mm and −19.05 mm. Based on analysis, surface subsidence values are within 30 mm, and it can be seen from forecast results that the maximun predicted value of surface subsidence does not exceed the warning value.

By comparison, the maximum residual rate of the predicted results by ANFIS is 12.32% and the mean residual rate by ANFIS is 7.61%; the maximum residual rate of predicted results by BP neural network is 24.65% and the mean residual rate by BP neural network is 16.24%. Consequently, it can be concluded that ANFIS is more superior to BP neural network in predicting surface subsidence and the predicted results by ANFIS are more accurate.

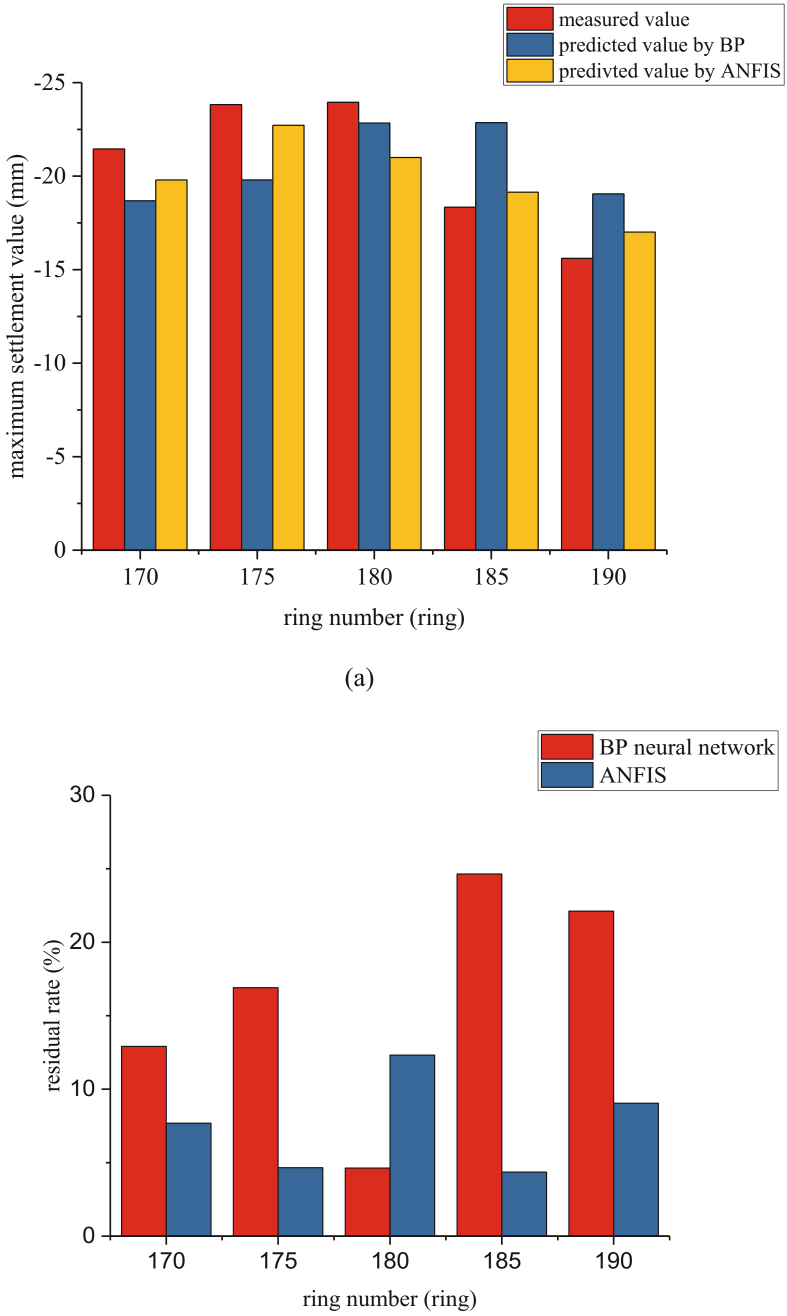

(a)

(b)

Fig. 4. Comparison of surface subsidence prediction by BP neural network and ANFIS.

4 Conclusion

(1) The ANFIS is built on the geometric size of tunnel boring machine, stratum mechanical properties and construction parameters and is used in Nanchang Metro Line 1. The result shows that the residuals between measured settlement and predicted settlement are small, with the maximum residual rate of 12.32% and the mean residual rate of 7.61%. It proves that the ANFIS is more precise than BP neural network since it can preferably establish the nonlinear and fuzzy model between the influence factors of surface subsidence.

(2) Adaptive Network-based Fuzzy Inference System is used to predict the tunneling-induced surface subsidence. It not only has the advantages of short learning period and high accuracy, but also can overcome the problem that the single neural network is not easy to converge.

(3) ANFIS combines the advantages of artificial neural network and fuzzy system to predict surface subsidence accurately. It is very significant for practical shield tunnel construction.

References

1. Qin, B., Mao, Y.: Application of adaptive network-based fuzzy inference system for load forecasting. Comput. Inf. **25**(2–3), 194–196 (2009)
2. Zhang, M.X., Zhou, H., Tu, M.: Prediction of surface settlement of shield tunneling based on fuzzy neural network. In: The Second National Conference on Geotechnical Engineering, Wuhan, China, pp. 290–295 (2006)
3. Liu, H.B., Wang, L.G., Zhang, L.H., Dai, B.B., Jing, Y.B.: Prediction of tunneling-induced surface settlement based on artificial neural network technology. Min. Res. Dev. **27**(2), 26–29 (2007)
4. Zhou, C.Z., Yang, J.S., Mou, Y.T., Wang, S.Y.: Prediction of tunneling-induced surface settlement in upper-soft lower-hard stratum in Nanchang. J. Disaster Prev. Mitig. Eng. **35**(8), 556–562 (2015)

Analysis of Soil Disturbance Caused by DOT Excavation in Soft Soil Stratum

Xiao-Liang Chen(✉) and Xiao-Nan Gong

Research Center of Coastal and Urban Geotechnical Engineering,
Zhejiang University, Hangzhou 310058, China
`543739851@qq.com`, `xngong@zgtm.com`

Abstract. DOT has the characteristics of special section and relatively large area of excavation face. Its propulsion will cause large formation disturbance. But too much soil disturbance usually leads to a series of environmental diseases. 3D elastoplastic FDM model was applied to analysis the dynamic construction process relying on a DOT project in Shanghai. Surface displacement field and the distribution of the stress field caused by the double circle shield tunneling were calculated and analyzed. And the numerical model calculation results and field monitoring data are compared and verified comprehensively. The results show that the transverse distribution of surface deformation caused by the double circle shield construction is basically in line with the normal distribution. And the influence area is mainly concentrated in the 2 times of the width of the shield on both sides of the axis. At the time of the incision, the surface of the earth was raised, while the surface of the earth was sinking after the shield tail left. The vertical settlement of the ground surface is stabilized gradually from 20 rings. The influence of shield tunneling on the lower soil is relatively small, and the earth pressure at the bottom of the shield is the least, and the earth pressure increment is maximum in the upper part of the shield. The research results can provide some theoretical basis and prophase guidance for similar projects in the future.

Keywords: Soft soil stratum · Double-Tube · Surface subsidence
Earth pressure distribution · Finite difference method

1 Introduction

With the rapid development of rail transit construction in large and medium cities in China, the underground space resources of the city become more and more tense. Double circular tunnel (DOT) to optimize the cross section form, reduce the section area, the resources of underground are more rational used. As a result, it is widely used in the construction of underground rail transportation in large and medium cities in china. Compared with single round tunnel, double circle tunnel can pass through the narrow underground space, reduce the influence on the ground structure, but also avoid the contact passage and avoid construction risk. According to statistics, the double ring shield tunneling can reduce the project cost by about 15% and reduce the excavation area by 10% compared to the two individual circular tunnels [1].

© Springer Nature Singapore Pte Ltd. 2018
D. Zhang and X. Huang (Eds.): GSIC 2018, *Proceedings of GeoShanghai 2018 International Conference: Tunnelling and Underground Construction*, pp. 198–206, 2018.
https://doi.org/10.1007/978-981-13-0017-2_19

Because of the particularity of the double circular cross-sectional shape, higher requirements are put forward to prevent back soil and erector, influence of shield construction on Soil and the surrounding environment compared with the single circle shield there are certain differences, the construction land subsidence by soil conditions, soil depth and other factors. At present, domestic and foreign scholars on the shield construction caused the disturbance of the environment is mostly studied [2–7], and achieved fruitful results, while the double circular shield tunnel construction is a new construction technology, since 1989 in Japan since the advent of Hiroshima, used only in Japan and Chinese more than 10 engineering, Europe and the United States this research is almost blank. The world related research reports on ground settlement and earth pressure induced by Double-O-Tube shield is rare, mainly in the China and Japan, the main research methods are summarized in Japan only focused on the statistical data of construction projects have been built [8, 9]. At this stage, the study of land subsidence law is also obtained through construction experience. Zhou Wenbo and Gu Chunhua analyzed the deformation of the actual formation, especially the settlement of the shield and the settlement of the back of the shield. It is the characteristic position of the settlement [10]. Other researchers have done some regression and Analysis on the data of double circle shield tunnel construction [11–13]. It can be said that, at this stage, the construction of double circle shield in the soft soil layer is not perfect, and the corresponding project is relatively small, the lack of regularity of construction disturbance summary.

Therefore, based on a double round Shanghai subway tunnel engineering, construction of three-dimensional elastoplastic finite difference model, calculation and analysis of the double circular shield tunneling induced ground displacement field and soil stress distribution, and verify the accuracy of the calculation results of the model and field monitoring data, summed up the double shield construction in the silt clay medium disturbance influence, has practical significance to research on the reasonable design of soft soil stratum Double-O-Tube shield tunnel and construction.

2 General Situation of Engineering

Shanghai double circle subway tunnel engineering, the head of wells from Binzhou station south along the road down line from north to south to promote the earth pressure balance shield, through Qihe Road, Tang Jiabang, Chang Li, arrived at the station into a mountain north end shaft, outer diameter 6340 mm, tunnel diameter 6200 mm, consists of 6 pieces of pipe plate assembly, segment thickness 350 mm, length 1200 mm, width of ring 1.6 m, the total length of the tunnel excavation 2599 m. The maximum slope of the project is 20 per thousand, and the top soil of the tunnel is about 5.7–15 m.

The soil layer through the shield construction is as follows: ③$_2$ gray clay powder, ③$_3$ grey silt silty clay, ④$_1$ gray silt clay, ⑤$_{1-1}$ gray clay and ⑤$_{1-2}$ gray silty clay (shown in Fig. 1).

In this paper, the construction of monitoring section is mainly considered, and the physical and mechanical parameters of the double circle shield crossing the soil layer are shown in Table 1.

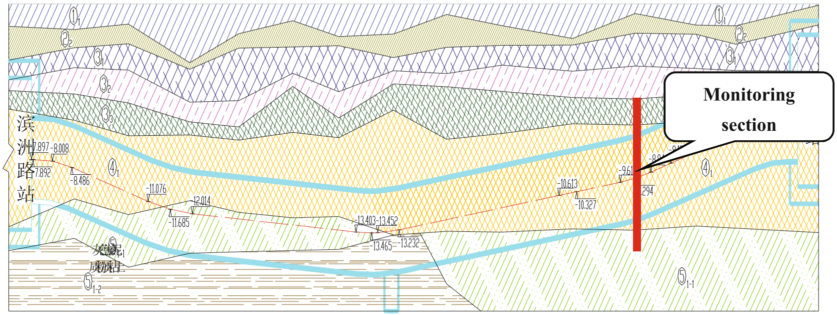

Fig. 1. Geological profile of tunnel section

Table 1. Parameters of soil

Type	μ	E/MPa	$r^{'}$/kN·m^{-3}	c/kPa	φ/(°)	K_0/kN/m^3
③$_2$	0.26	9.03	18.4	5	20.5	0.44
③$_3$	0.25	2.65	17.2	9	12.0	0.56
④$_1$	0.25	1.98	16.8	9	8.0	0.62

Where μ is Poisson ratio, E is modulus of elasticity, $r^{'}$ is bulk density, c is cohesion, φ is internal friction angle, and K_0 is Permeability coefficient.

3 Numerical Simulation of Double Circle Shield Construction

3.1 Numerical Model Building

According to the actual situation based on double circular tunnel, shield construction of three-dimensional dynamic numerical model of FLAC^{3D} software is constructed by finite difference, X direction (horizontal surface direction) width 36 m, Y direction (150 excavation direction) ring width of 150 × 1.2 m = 180 m, Z direction (severe soil depth of 60 m, the model of direction) size: X × Y × Z = 36 m × 180 m × 60 m. The lining of the tunnel is made of reinforced concrete lining, which is a universal ring wedge segment. The strength of the segment concrete is C55, the concrete impermeability grade is S12, the Poisson's ratio is 0.22, and the elastic modulus is 30.200 GPa. In reference to the synchronous grouting action and formation loss in shield construction are replaced by equal layers, and the thickness is 0.105 m. Assuming that the soil depth at the top of the tunnel is 8 m, there are 51994 solid units in the whole numerical model (shown in Fig. 2).

In numerical model, the basic parameters of the soil are chosen the same as the actual conditions, and the parameters of the equal layer are selected as shown in Table 2.

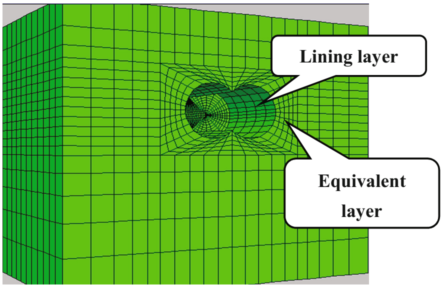

Fig. 2. Finite difference method grid of DOT

Table 2. Parameters of equivalent circle zone

Equivalent layer	Step1	Step2	Step3
E/MPa	0.2	2.0	18.0
K/m·s^{-1}	1.1×10^{-8}	0.6×10^{-8}	0.2×10^{-8}

3.2 Layout of Measuring Points

As compared with the measured data, the monitoring points selected in numerical simulation and field test point arrangement is consistent, namely in the right circle at 1 m above the upper back, tunnel buried depth is 7 m, right round the waist position at the tunnel bottom and the bottom of the back and right circular pre embedding 5 miniature earth pressure the box, with additional monitoring when the soil excavation 5 location of the stress changes as shown in Fig. 3. The location of the transverse surface subsidence is the deformation at the surface above the loop.

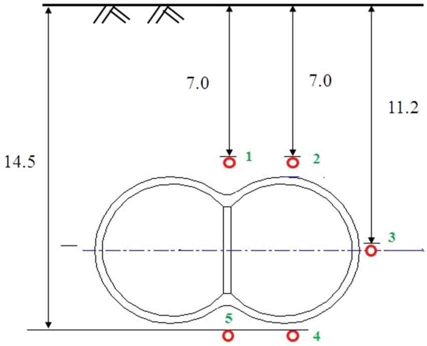

Fig. 3. Location of soil pressure monitoring points in DOT (unit: m)

4 Result Analysis and Comparison Verification

As a comprehensive and systematic understanding of the soft soil layer of double circle shield the disturbance of soil around the tunnel, the numerical results from the analysis of seventy-fifth rings above the lateral surface settlement, vertical surface settlement, vertical ground settlement and soil pressure distribution around tunnel results, and the numerical calculation results and field monitoring results were verified.

4.1 Lateral Surface Subsidence

Figure 4 is a lateral surface deformation curve at the top of the 75 ring caused by the double circle shield driving. Figure 4 shows that the numerical results, when the shield incision arrived, the ring above the surface uplift trend appears, at this time because of the effects of shield machine thrust, the earth pressure on the excavation face of occurrence of imbalance, caused by shield front soil extrusion to move forward; when the shield tail detachment (tail before the 1 ring to shield tail after 4 rings), due to the construction process of building space, shield tail through observation points when the settlement is the shield tail void shield support or lose soil grouting behind segment in soil due to the stress release caused by the shield tail; after the surface settlement continues to increase, the increase of deformation is due to subsequent disturbance deformation elastic aging on the surrounding soil caused by shield tunneling.

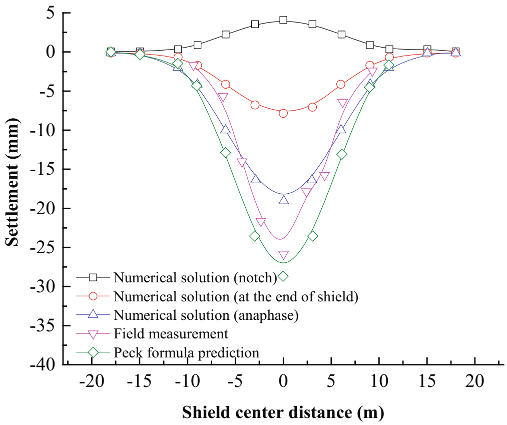

Fig. 4. Lateral deformation of the 75th ring driven by DOT

Through numerical calculation and field monitoring data analysis, the surface caused by shield construction deformation of transverse distribution accords with the normal distribution, and the calculation results and measured results, and is consistent with the empirical formula of Peck, the position of the inflection point of the settlement trough roughly in place of $\sqrt{3}i$. The influence of ground deformation caused by double circle shield construction is mainly concentrated in the width of 2 times of shield width on both sides of the axis, and that part of the settlement accounts for about 95% of the total settlement.

4.2 Longitudinal Ground Settlement

Figure 5 is the vertical settlement curve of the double circle shield when it is pushed to the 75 ring (coordinate axis 0 m position). From the different stages of construction, the settlement of the settlement of the numerical solution before the arrival of the cut is somewhat deviation from the actual situation when the earth pressure is larger, and the value is slightly larger than the measured value. In the excavation face after when the DOT shield machine back soil caused by the shield through the surface uplift, the deformation is very different from the single circular tunnel, but also impact on the settlement prediction of shield tail prolapse, greater than the measured value of surface subsidence prediction of the shield tail from the. When the tail of the shield is left, the soil behind the excavation surface has been subsiding, and the vertical settlement of the ground surface is gradually stabilized when it is separated from the 20 ring.

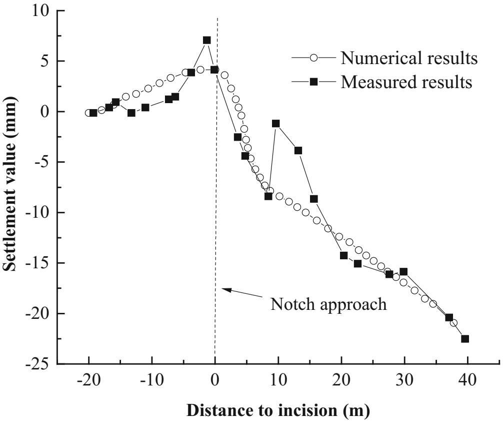

Fig. 5. Vertical settlement curve of 75th ring

4.3 Deep Settlement

Figure 6 is the soil displacement curve above the central axis of the double circle shield. As can be seen from Fig. 6, with the further advance of the shield machine to the distance around the measuring point about 2 rings, the obvious settlement of the soil above the shield, with the further approaching of the incision, the settlement value has gradually increased. When the incision arrives, the settlement of the soil at 1 m

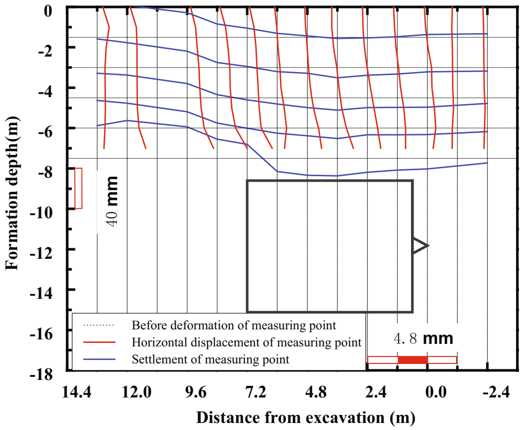

Fig. 6. Displacement of soil above center axis of DOT

above the shield is about −5.3 mm, and the settlement at the top of the shield 3.5 m is −2 mm. In the process of passing through the measuring point, the settlement continues to increase, and the maximum settlement reaches about −17.6 mm. When the shield tail is out of grouting, the soil is uplifted again, and the value is about 0.78 mm.

4.4 Distribution of Soil Pressure Around Tunnel

Figure 7 is the dynamic change of the measured values of 5 earth pressure boxes around the 75 ring in the double circle shield tunneling. From the following diagrams (a, b, c, d), it can be seen that the numerical simulation results are in good agreement with the field measurement, and the maximum error is about 19%. With the gradual advance of the shield, the horizontal earth pressure in the front soil is gradually increasing. Figure 7 Comparison (a) and Fig. 7 (b) shows that the upper part of double circle shield center axis exist concave covering 1 measuring points measured earth pressure value is measured at 2 smaller; compare Fig. 7 (c) and 7 (d) shows that the lower position of the center axis because of double circle shield the existence of “convex” type of soil, and soil caused by shield construction of additional stress in this location is measured at point 4.

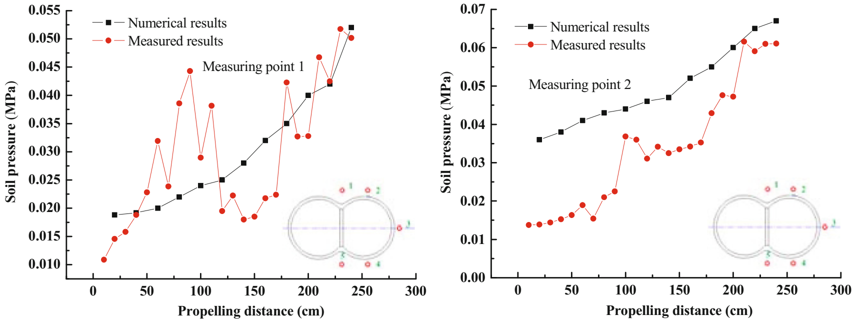

(a) Measuring point 1 (b) Measuring point 2

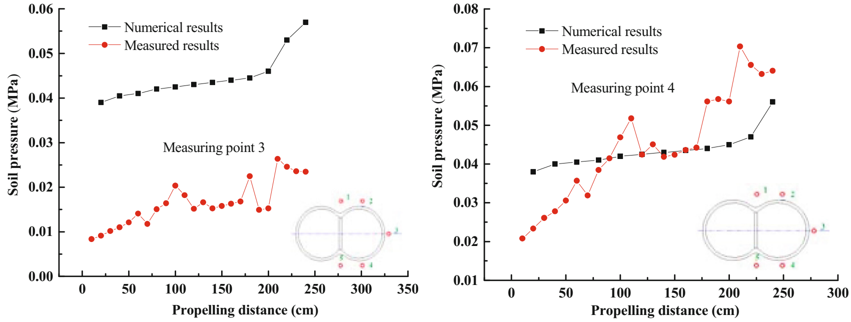

(c) Measuring point 3 (d) Measuring point 4

Fig. 7. Comparison of measured and calculated values of earth pressure around 75th ring

5 Conclusion

(1) The lateral surface deformation induced by Double-O-Tube shield construction to conform to normal distribution, The surface deformation affected zone concentrated on opposite sides of the axis of shield 2 times width range caused by shield construction, accounting for about 95% of the total settlement.

(2) When the double circle shield cut arrives, the predicted surface subsidence is greater than the measured value when the shield tail is pulled out. After the shield tail leaves, the rear soil body produces the subsidence, leaves the 20 annulus, the surface longitudinal subsidence gradually tends to be stable.

(3) The influence of the shield on the lower soil mass during tunneling is relatively small. The earth pressure measured on the panel is much higher than that in the front soil, which is close to the vertical earth pressure value.

References

1. Wei, G., Chen, W.J., Wei, X.: Prediction of surface settlement induced by Double-O-Tube shield tunnel excavation. Rock Soil Mech. **32**(4), 991–996 (2011)
2. Yu, N., Zhu, H.H.: Analysis of earth deformation caused by shield tunnel construction and 3D-FEM simulation. Rock Soil Mech. **25**(8), 1330–1334 (2002)
3. Sun, J., Yuan, J.R.: Soil disturbance and ground movement under shield tunneling and intelligent prediction by using ANN technology. Chin. J. Geotech. Eng. **23**(3), 261–267 (2001)
4. Zhang, Y., Yin, Z.-Z., Xu, Y.-F.: Analysis on three-dimensional ground surface deformations due to shield tunnel. Chin. J. Rock Mech. Eng. **28**(3), 261–267 (2002)
5. Chapman, D.N., Ahn, S.K., Hunt, D.V.L.: Investigating ground movements caused by the construction of multiple tunnels in soft ground using laboratory model tests. Can. Geotech. J. **44**(6), 631–643 (2007)
6. Addenbrooke, T.I., Potts, D.M.: Twin tunnel interaction: surface and subsurface effects. Int. J. Geomech. **1**(2), 249–271 (2001)
7. Wei, G.: Prediction of surface settlement induced by ground loss during shield tunneling construction. Rock Soil Mech. **28**(11), 2375–2379 (2007)
8. Yamaguehi, I., Yamazaki, I., Kiritani, Y.: Study of ground-tunnel ineractions of four shield driven in close proximity in relation to design and construction of parallel shield tunnels. Tunn. Undergr. Space Technol. **13**(3), 289–304 (1998)
9. Zhou, W.-B., Gu, C.: Construction technique of DOT shield. Mod. Tunn. Technol. **41**(4), 22–32 (2004)
10. Sun, T.-L., Zhang, Q.-H., Hu, X.-D., et al.: Numerical simulation of ground settlement induced by Double-O-Tube(DOT) shield construction. J. Tongji Univ. Nat. Sci. **36**(4), 466–471 (2004)
11. Bob, C.: Double-O-Tube shield tunneling technology in the shanghai rail transit project. Tunn. Undergr. Space Technol. **21**(6), 594–601 (2006)
12. Wei, G., Zhu, K., Chen, W.-J.: Ground settlement induced by Double-O-Tube shield tunneling under different construction conditions. Chin. J. Geotech. Eng. **33**(3), 477–482 (2011)
13. Fang, M., Zhou, C.-Y., Liu, Z.: Influence of construction parameters and cross angle on existing tunnel settlement during undercrossing shield tunneling construction. Eng. Mech. **28** (12), 133–138 (2011)

Study on Characteristics of Ground Motion in Karst Area Based on Viscoelastic Artificial Boundary

Mei-yan Bai[1], Hong-wei Wang[1](✉), Chuan Shen[1],
and Kai-zhong Xie[1,2,3]

[1] College of Civil Engineering and Architecture, Guangxi University,
Nanning 530004, China
779348631@qq.com
[2] Key Laboratory of Ministry Education of Engineering Disaster Prevention
and Structural Safety, Guangxi University, Nanning 530004, China
[3] Guangxi Key Laboratory of Engineering Disaster Prevention and Structural
Safety, Guangxi University, Nanning 530004, China

Abstract. Karst is a common geological condition in engineering construction. In order to study the influence of karst cave and boundary condition on the analysis of free field ground motion in karst area, viscoelastic artificial boundary was studied in free field ground motion analysis of karst region, a three-dimensional finite element model whose dimension is 1000 m × 1000 m × 500 m was set up, characteristics of ground motion in karst region were studied on the basis of viscoelastic artificial boundary, as well as the influence of karst cave on displacement, velocity and acceleration were considered. The results show that, natural frequencies of free field were decreased at different degrees after viscoelastic artificial boundary was adopted. Compared with the response of free field without karst cave, the variation trend of maximum displacement, maximum velocity and maximum acceleration were all spread around the karst cave, the biggest change of maximum displacement, maximum velocity and maximum acceleration appeared on the top of karst cave. Compared with spectrum curve of free field without karst cave, the amplitude difference of free field with karst cave was significant in low order frequency, and was opposite in high order frequency, the influence of karst cave on vertical direction is bigger than horizontal direction, which can provide reference for construction of karst region.

Keywords: Karst area · Vibration analysis · Karst cave
Viscoelastic artificial boundary

1 Introduction

The karst areas in the south of China are mainly composed of soluble carbonate rocks. Under the action of dissolution, weathered, denuded and red soil, the karst area is formed with various terrain. The representative soil layers or strata in karst areas are: carbonate rock layer, calcareous mud stone layer and red clay layer, the geological structure of karst area determines the activity and its nature of earthquake [1, 2], for some small magnitude

© Springer Nature Singapore Pte Ltd. 2018
D. Zhang and X. Huang (Eds.): GSIC 2018, *Proceedings of GeoShanghai 2018 International Conference: Tunnelling and Underground Construction*, pp. 207–214, 2018.
https://doi.org/10.1007/978-981-13-0017-2_20

earthquake can cause considerable damage in karst area, As a result, free vibration analysis is really essential in karst area. So far, among the study on the influence of karst cave in karst area, boundary is often simplified as a fixed end constraint, viscoelastic artificial boundary was seldom used. In order to study the influence of karst cave and boundary condition on free field vibration analysis in karst area, a three-dimensional karst area finite element model of 1000 m × 1000 m × 500 m was established by ANSYS finite element software, and the effects of fixed end constraint and artificial boundary constraint on natural vibration frequency of karst free field were studied, the influence of karst cave on the displacement, velocity and acceleration of free field, as well as the influence of karst cave on spectral curve of center node on surface of free field was researched, which can provide reference for engineering construction in karst area.

2 Artificial Boundary of Karst Foundation

The purpose of artificial boundary is to convert an infinite model into a finite model which is easy for implementation [3]. At present, the widely used artificial boundary in engineering mainly includes viscous boundary, transmission boundary and viscoelastic boundary [4, 5]. The earliest adhesion boundary aims to set up the damper on the artificial boundary to absorb the external wave whose concept is simple and easy to implement. However, it ignores the resilience of elastic boundaries. The transmission boundary proposed by the academician Liao Zhenpeng is the process of using artificial boundary to simulate the boundary crossing, and it establishes the inner point to simulate the displacement of the boundary node at the edge of the boundary at the same time, however, when the input time is long and the waveform is highly irregular, the seismic wave will cause instability [6].

The viscoelastic boundary is the spring unit which is set up in parallel with the damping element on the viscous boundary, which possesses a good stability [7]. It is a local artificial boundary to use the viscoelastic boundary for the boundary effect of the distance simulation of karst foundation. It overcomes the low frequency drift caused by the viscous boundary, as well as it can simulate the elastic recovery performance of the outer half of the artificial boundary and can be excellently combined with the finite element software to meet engineering requirements [8]. The viscoelastic boundary is the stress boundary, and the elastic boundary element parameter is on the principle of dissipating energy by using viscous dampers, i.e. the vibration energy is dissipated by the viscous damping force produced by the damper which is set up at the boundary. In this paper, we adopt the concentrated viscoelastic artificial boundary. The specific parameters are as follows:

$$\text{The normal elastic stiffness is: } K_N = \alpha_N \frac{G}{R} \sum_{i=1}^{n} A_i \tag{1}$$

$$\text{The tangential elastic stiffness is: } K_T = \alpha_T \frac{G}{R} \sum_{i=1}^{n} A_i \tag{2}$$

$$\text{The normal damping coefficient is: } C_N = \rho c_p \sum_{i=1}^{n} A_i \tag{3}$$

$$\text{The tangential damping coefficient is: } C_T = \rho c_s \sum_{i=1}^{n} A_i \tag{4}$$

R: distance from source to artificial boundary, c_p and c_s: wave velocity of P wave and S wave, G: shear modulus of the foundation, ρ: mass density of foundation, α_N and α_T: correction coefficients of spring stiffness for normal and tangential in viscoelastic artificial boundary, based on parameter robustness and a large number of literatures [9–11], correction factor can be set as 1.33 and 0.67, formulas of wave velocity were shown as follows:

$$c_p = \sqrt{\frac{\lambda + 2G}{\rho}} = \sqrt{\frac{(1-\upsilon)E}{(1+\upsilon)(1-2\upsilon)\rho}} \tag{5}$$

$$c_s = \sqrt{\frac{G}{\rho}} = \sqrt{\frac{E}{2(1+\upsilon)\rho}} \tag{6}$$

$$m = \rho r,\ c = \rho c_p,\ k = \frac{4G}{r} \tag{7}$$

The viscoelastic boundary is a stress boundary, which is the actual state of infinite domain, it is a function associated with the acceleration, velocity and displacement of boundary nodes. The force on the artificial boundary node is applied to the free space according to the equilibrium of the boundary node force:

Normal node force: $R_N = K_N \cdot w_N + C \cdot \dot{w}_N + f_N$

Tangential force: $R_T = K_T \cdot w_T + C \cdot \dot{w}_T + f_T$

These parameters are obtained by an infinite domain linear elastic medium:

$$f_N = -A\sigma = A\rho c_p \dot{w}_N \tag{8}$$

$$f_T = -A\tau = A\rho c_s \dot{w}_T \tag{9}$$

3 Overview of Karst Free Field Finite Model

In order to analyze the vibration of free field in karst area, a three-dimensional finite element model of free site in karst area was established by ANSYS finite element software. The model size is 1000 m × 1000 m × 500 m, the field length direction was set as X axis direction, the width direction was set as Y axis direction, and the vertical direction was set as Z axis direction. Solid 45 element was used to simulate soil, element grid size is 25 m × 25 m × 25 m, whose precision meets engineering requirements, viscoelastic artificial boundary condition was simulated by Combin14 unit. For the shape of actual cave is complicated and various, it was simplified as a cube of 50 m × 50 m × 25 m, which was located at 37.5 m below the surface of free ground in karst area. Sketch map of cave position with a red mark is shown in Fig. 1. Sketch map of viscoelastic artificial boundary condition is shown in Fig. 2.

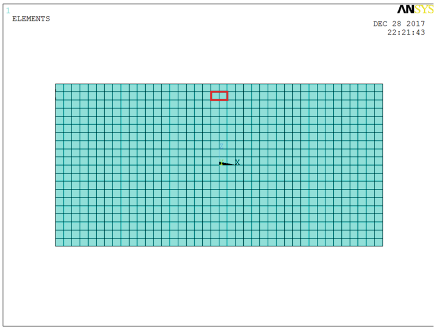

Fig. 1. Sketch map of karst cave position

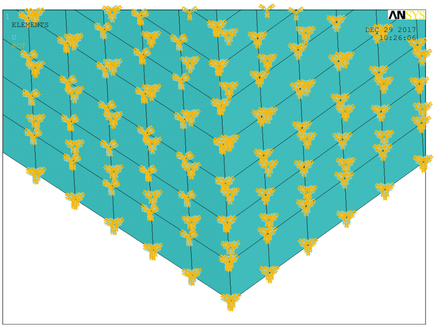

Fig. 2. Sketch map of viscoelastic artificial boundary condition

Material characteristics were as follows, elasticity modulus: 8000 MPa, deformation modulus: 4000 MPa, density: 2680 kg/m^3, Poisson's ratio: 0.25, damping ratio: 0.05, Longitudinal wave velocity: 0.60 m/s, Shear wavevelocity: 11937500 m/s.

4 The Influence of Boundary Condition on Natural Vibration Characteristics of Free Field

In order to study the influence of boundary condition on natural vibration characteristics of free field in karst area, the boundary condition of finite model was divided into three kinds: the first kind of boundary condition refers to only applying fixed end constraint at the bottom of finite element model, the second kind of boundary condition refers to applying fixed end constraint at the bottom and four sides of finite element model, the third boundary condition refers to the application of viscoelastic artificial boundary condition at the bottom and four sides of finite element model. Finite element model of the three boundary conditions was analyzed respectively, the results were shown in Table 1.

Table 1. Influence of boundary conditions on natural vibration characteristics of free field.

Order number	1	2	3	4
The 1st boundary condition (Hz)	0.4594	0.5128	0.7533	0.8166
The 2nd boundary condition (Hz)	1.1044	1.1662	1.3248	1.3605
The 3rd boundary condition (Hz)	0.3279	0.3287	0.3358	0.3362

Table 1 shows that, for free field model, compared with the 1st and the 2nd boundary condition, after viscoelastic artificial boundary condition was applied in finite element model, natural frequencies of free field model in karst area were reduced at different degrees, and vibration modes were also changed, which is more consistent with actual situation.

5 The Influence of Karst Cave on Displacement, Velocity and Acceleration of Karst Free Field

In order to study the influence of karst cave on the displacement, velocity and acceleration of karst free field. Viscoelastic artificial boundary condition was adopted in the finite element, EI Centro seismic wave was applied in the finite element, finite element model with karst cave and without karst cave were both analyzed. The maximum displacement, maximum speed and maximum acceleration of each node between free field with karst cave and free filed without karst cave were subtracted. The difference contour line of maximum displacement, maximum velocity maximum acceleration on each node was shown in Figs. 3, 4 and 5 respectively.

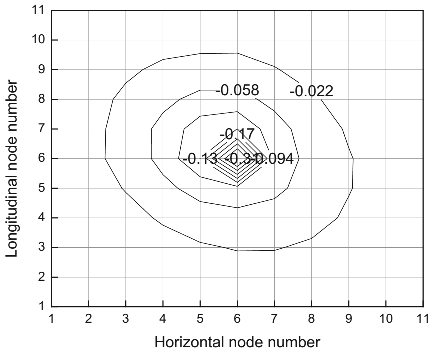

Fig. 3. Difference contour line between the maximum displacement of each node (m)

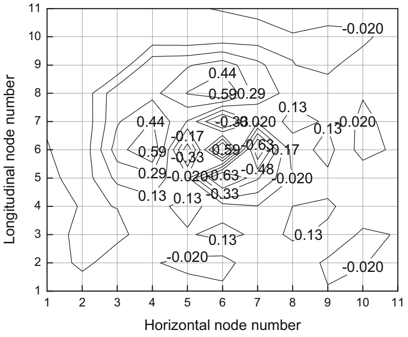

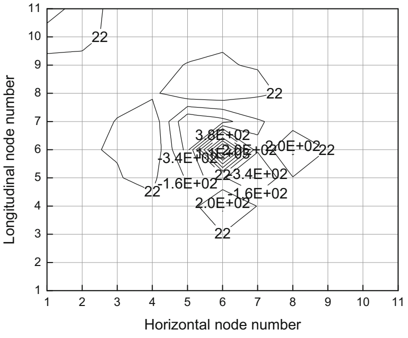

Fig. 4. Difference contour line between the maximum speed of each node (m/s)

Fig. 5. Difference contour line between the maximum acceleration of each node (m/s^2)

Based on Figs. 3, 4 and 5, after viscoelastic artificial boundary was adopted in finite element and EI Centro earthquake wave was applied in finite element, the response of the maximum displacement, the maximum velocity and the maximum acceleration in the free field with karst cave in karst area compared with them of free filed without karst cave were spread around the karst cave, and the significant change of the maximum value of the displacement, velocity and the acceleration appeared at the top of karst cave.

6 Influence of Karst Cave on Spectrum Curve for Surface Center of Free Field

In order to study the influence of karst cave on the spectral curve of the center surface in free field, free field finite element model was divided into two working conditions: free field with karst cave and free field without karst cave, at the same time viscoelastic artificial boundary conditions and EI Centro seismic wave were applied in the finite element. Then the acceleration epoch curve was extracted from the center of earth surface in free field finite element model, and Fourier transform was carried out. In karst area, the variation trend of spectrum curve for the center node of earth surface was consistent, peak frequency were mainly located between 0 Hz and 5 Hz. In order to study the influence of karst cave on karst field better, the spectral curve values for center node of earth surface in free field with karst cave were subtracted by them without karst cave, the results were shown in Fig. 6.

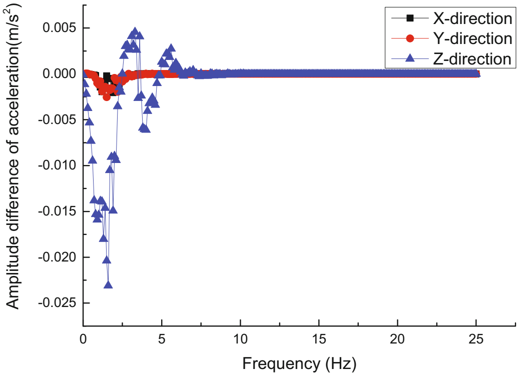

Fig. 6. Amplitude difference of acceleration for free field with and without karst cave

It can be seen from Fig. 6 that, for the surface center node of karst free field, the amplitude difference of acceleration between free field with karst and free field without karst is significant in low order frequency, while it is the opposite in high order frequency, and the influence of karst cave on vertical direction is bigger than horizontal direction.

7 Conclusions

In this paper, a three-dimensional finite element model of free field in karst area was established, and the influence of boundary condition and karst cave on the analysis of free field vibration in karst area was studied respectively. Main results and conclusions are as follows:

(1) For the free field finite element model in karst area, compared with the fixed boundary condition, the natural frequency of karst free field model was reduced to a certain extent by using viscoelastic artificial boundary condition.
(2) After artificial boundary was used in the free field finite element model in karst areas and EI Centro earthquake wave was applied in free field finite element, compared with the response of free field without karst cave, the change trend of maximum displacement, maximum velocity and maximum acceleration were spread around the karst cave, and the change of maximum displacement, maximum velocity and maximum acceleration is the biggest on the top of karst cave.
(3) After artificial boundary was used in free field finite element model in karst areas and EI Centro earthquake wave was applied in free field finite element, compared with spectrum curve of free field without karst cave, the amplitude difference between free field with karst and free field without karst is significant in low order frequency, while it is the opposite in high order frequency, and the influence of karst cave on vertical direction is bigger than horizontal direction, which can provide reference for construction of karst region.

Acknowledgement. This work was supported by National Natural Science Foundation of China (Grant No. 51068001 and 51368005), the Systematic Project of Guangxi Key Laboratory of Disaster Prevention and Structural Safety (2012ZDX04), and the Scientific Research Foundation of Guangxi University (Grant No. XBZ100762).

References

1. Yang, S., He, S., Meng, L., et al.: Research on earthquake-induced geological disasters in the karst area in Guangxi and methods for engineering-site preparation. China Earthq. Eng. J. **36** (04), 790–796 (2014)
2. Yang, S., Meng, L., Wang, Y.: Research of acceleration change in karst area by earthquake. World Earthq. Eng. **31**(03), 85–92 (2015)
3. Liu, J., Wang, Z.: 3D finite element analysis of large dynamic machine foundation considering soil-structure interaction. Eng. Mech. **19**(3), 34–38 (2002)
4. Zhang, X., Li, X., Chen, G., et al.: An improved method of the calculation of equivalent nodal forces in viscous-elastic artificial boundary. Chin. J. Theor. Appl. Mech. **05**, 1126–1135 (2016)
5. Du, X., Zhao, M., Wang, J.: A stress artificial boundary in fea for near-field wave problem. Chin. J. Theor. Appl. Mech. **38**(1), 49–56 (2006)
6. Liao, Z., Liu, J.: Finite element simulation of wave motion-basic problems and conceptual aspects. Earthq. Eng. Eng. Vib. **9**(4), 1–14 (1989)

7. Liu, J., Huan, Y., Li, J.: Application of artificial boundary and seismic input in general finite element software. Chin. J. Undergr. Space Eng. **7**(2), 1774–1779 (2011)
8. Liu, J., Lu, Y.: A direct method for analysis of dynamic soil-structure interaction. China Civil Eng. J. **31**(3), 55–64 (1998)
9. Gu, Y., Liu, J., Du, Y.: 3D consistent viscous-spring artificial boundary and viscous-spring boundary element. Eng. Mech. **24**(12), 31–37 (2007)
10. Liu, J., Wang, Z., Du, X., et al.: Three-dimensional visco-elastic artificial boundaries in time domain for wave motion problems. Eng. Mech. **22**(06), 46–51 (2005)
11. Zhao, R., Zhang, J., Liu, Z., et al.: Analysis of seismic wave problem based on visco-elastic artificial boundary under the ladder terrain. World Earthq. Eng. **31**(03), 220–227 (2015)

Research on Strength Characteristic Parameter of Sandy Pebble Soil Based on Different Density and Moisture Content

Zhao Zhang, Junfu Lu(✉), and Shenlin Ling

State Key Laboratory of Geohazard Prevention and Geoenvironment Protection,
Chengdu University of Technology, Chengdu 610059, Sichuan, China
Lujunfu@126.com

Abstract. Sandy pebble soil is widely distributed in our country. Lots of studies show that sandy pebble soil makes dynamic behavior not clear due to typical discreteness of gravels and random geometrical distribution. This paper quantitatively analyzes the law of the strength characteristics of sandy pebble tunnel surrounding rock under different density and moisture content conditions through large-scale triaxial tests in laboratory. The Results show that: Initial modulus of sandy pebble soil increases with the accretion of consolidation ratio; When the moisture content of sandy pebble soil stays the same, the larger the density is, the higher the stress peak is; when density of sandy pebble soil stays the same, the stress peak of moisture content in natural state is the maximal; When the moisture content of sandy pebble soil stays the same, with the increase of density, angle of internal friction is greater; With the change of moisture content, angles of internal friction and cohesion force of sandy pebble soil have a mutational phenomenon.

Keywords: Tunnel surrounding rock · Sandy pebble · Moisture content
Strength characteristic

1 Introduction

With the continuous increase of urban population and the excessive use of above-ground space, some cities start to strengthen the development of underground space and accelerate the planning and construction of underground channels, during which some complicated stratum and geological conditions are usually met during construction. For example, in Chengdu located at Grade-I terrace of Minjiang River system in Chuanxi Plain, a large quantity of pebbles or sandy articles deposit resulting from the scouring and transportation of river water, and thus form sandy pebble soil body, seriously influencing the design and construction safety of Chengdu underground channel [1–3]. In sandy pebble soil body, skeleton particles (generally referred to as particles with a grain size larger than 5 mm) typically account for 60%–70%; the pores between coarse particles are mostly filled with medium and fine sands; coarse and fine particles are arranged in various and complicated forms, mostly being medium compact [4]. Sandy pebble soil in different areas are typically different in such aspects as

© Springer Nature Singapore Pte Ltd. 2018
D. Zhang and X. Huang (Eds.): GSIC 2018, *Proceedings of GeoShanghai 2018 International Conference: Tunnelling and Underground Construction*, pp. 215–223, 2018.
https://doi.org/10.1007/978-981-13-0017-2_21

density, grading and moisture content. In addition to Chengdu, sandy pebble soil is also widely distributed in other areas of China [5].

Over the past years, researches on the strength, mechanics and deformation characteristics of sandy pebble soil by Chinese and overseas scholars were mainly conducted by means of indoor triaxial test, and some ground-breaking conclusions have been made. By means of indoor large-scale axial test, Hardin and Kalinski tested the relationship between the shear modulus and shear strain of given sandy pebble soil and estimated its shear elasticity modulus under the condition of small deformation [6]. Likewise, relying on indoor axial test, Zhang and other scholars researched the change laws and mechanical strength characteristics of the stress-strain curve of coarse-grained soil, improved Duncan Model and proposed a n expression formula applicable to the strength characteristics of coarse-grained soil [7]; Jiang mainly discussed the strength characteristics and of rheological behavior of pebble soil by means of creep tests on sandy pebble soil [8, 9];. Through a large-scale triaxial test research on sandy pebble soil based on different density and moisture content conducted under in a unconsolidated-undrained way, the paper analyzed the shear strength laws of sandy pebble soil under different physical states for the purpose of supplying some references for researches on the strength characteristics of sandy pebble soil.

2 Large-Scale Triaxial Test on Sandy Pebble Soil

2.1 Test Instruments

The instrument adopted for the axial test is YLSZ30-3 stress-type large-scale axial tester, as is shown in Fig. 1. The set of equipment can automatically control axial stress, strain and confining pressure by means of electro-hydraulic servo valve and it measures volume change during the test by the method of drain-pipe micro-differential pressure. For samples adopted for the test, the specification is $\varphi 300 \times 600$ mm, the maximum axial stress is 21 MPa, the maximum perpendicular load is 1500 kN, the maximum confining pressure is 3.0 MPa and the maximum axial stroke is 300 mm.

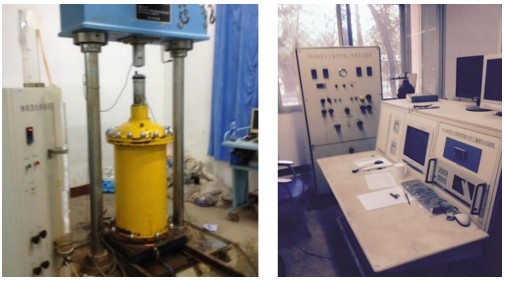

Fig. 1. Triaxial test instrument

2.2 Test Methods and Samples

The method of isotropic unconsolidated-undrained (UU) shear was adopted for the test, during which the saturation was ensured by means of air exhaust and hydraulic head, strain control room was adopted to exert confining pressure of 100 kPa, 200 kPa and 300 kPa successively for each group of test samples, and shear was conducted by an axial strain rate of 1.5 mm/min, and finally, when axial strain reaches 20%, the test was terminated. See Fig. 2 for sample preparation process.

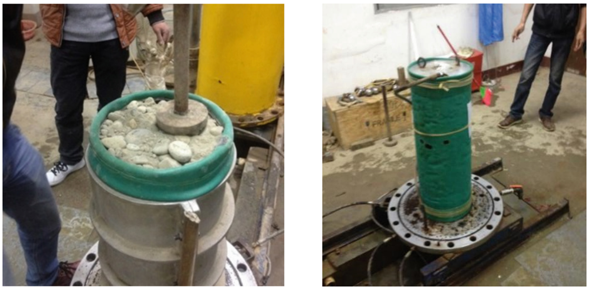

Fig. 2. Sample preparation process in the triaxial test

Soil samples selected originate from Chengdu. 17 groups of pebble soil were sampled through drilling and the arithmetic method for grain grading was adopted to figure out the values of the finest, coarsest and average grain grading. See Fig. 3 for grading curve.

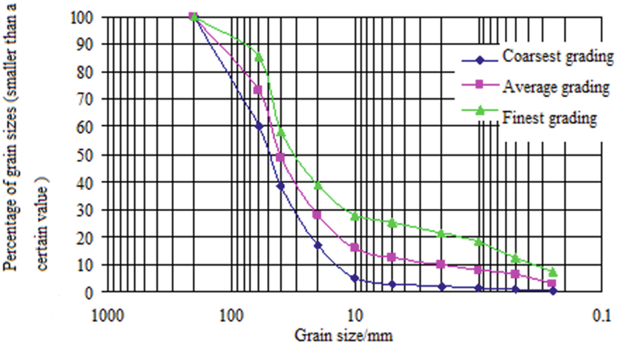

Fig. 3. Grading curve of sandy pebble soil

The average grading was adopted for sampling for the research on the strength characteristics of sandy pebble soil based on different density and moisture content in the test. See Table 1 for sample preparation required.

Table 1. List of samples for the triaxial test on sandy pebble soil

Natural state (moisture content 1.5%)	Compact (2.1 g/cm^3)
	Medium compact (2.0 g/cm^3)
Moisture content 4%	Compact
	Medium compact
Moisture content 6%	Compact
	Medium compact
Saturated state (moisture content 8.5%)	Compact
	Medium compact

3 Test Achievements and Analyses

3.1 Stress and Strain Characteristics Curves of Sandy Pebble Soil Based on Different Density and Moisture Content

The stress and strain curves of sandy pebble soil under different density and moisture conditions have been acquired through the test, as is shown in Figs. 4, 5 and 6.

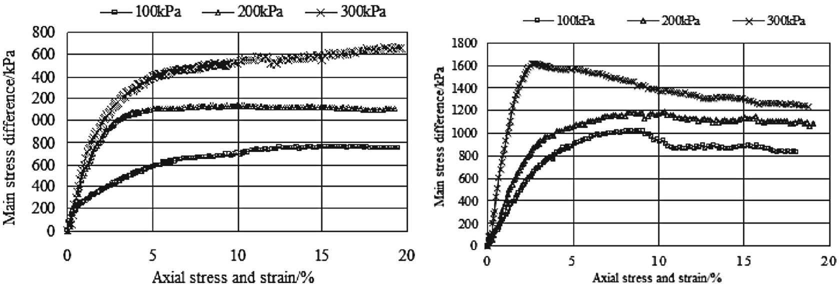

(a) Under saturated state

(b) Moisture content is 6%

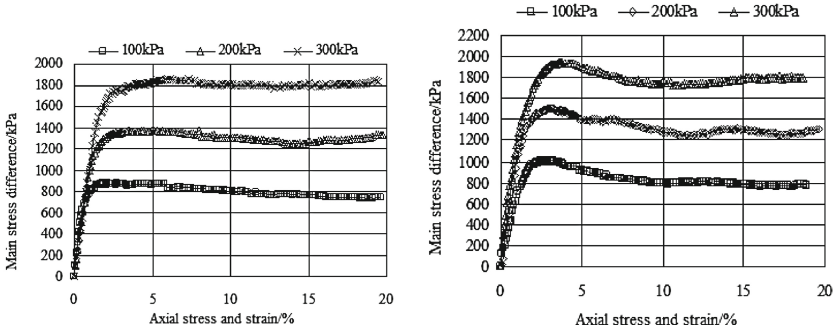

(c) Moisture content is 4%

(d) Under natural state

Fig. 4. Stress and strain curves differing in moisture content under compact state

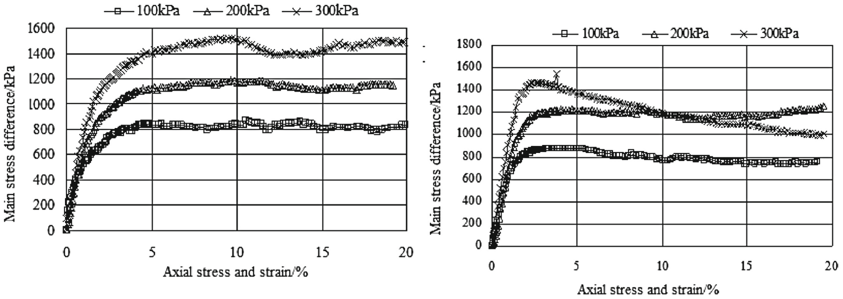

(a) Under saturated state (b) Moisture content is 6%

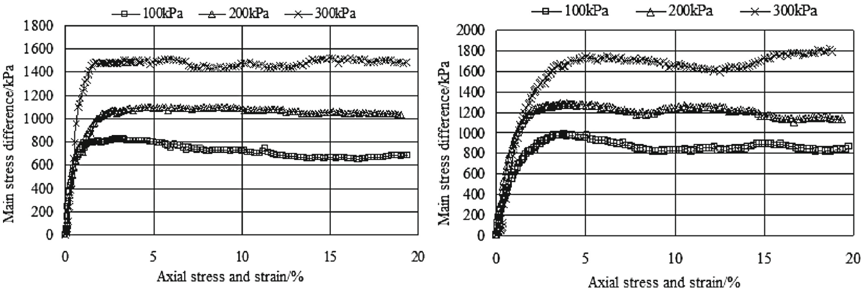

(c) moisture content is 4% (d) Under natural state

Fig. 5. Stress and strain curves differing in moisture content under medium compact state

(1) $(\sigma_1\text{–}\sigma_3)$—ε curves differing in moisture content under compact state
(2) $(\sigma_1\text{–}\sigma_3)$—ε curves differing in moisture content under medium compact state:

The following conclusions can be made from Figs. 4 and 5:

(1) Both the peak stress and initial modulus of sandy pebble soil increase with the increase of confining pressure.
(2) When the moisture content of sandy pebble soil remains unchanged, its stress peak increases with the increase of density; when the density of sandy pebble soil remains unchanged, its stress peak reaches the maximum value under natural state.
(3) None of the stress and strain curves of sandy pebble soil above is completely smooth, because the triaxial shear test is dominated by point contacts, and it is common to see stress concentration in contact points, owing to which the stress is stronger than the shear strength in certain areas, thus making pebble particles broken and the deformation curve fluctuated to some degree.
(4) Sandy pebble soil starts to break when the axial strain is 3.5%, which is different form other fine-grained soil, as the later typically breaks when the strain is 15%. Besides, being larger in density than other fine-grained soil, sandy pebble soil will not experience obvious strain softening, and thus can still bear a certain amount of load even it reaches its strength peak.

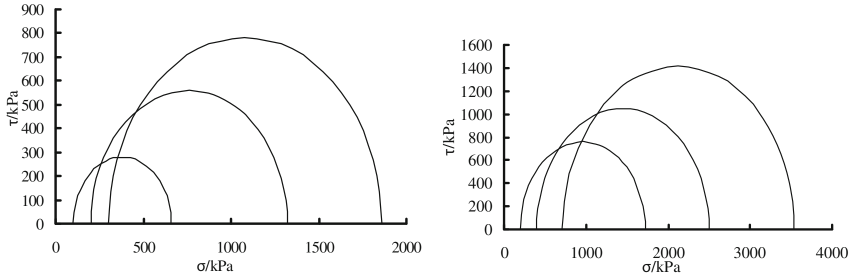

(a) Mohr’s stress under saturated state

(b) Mohr’s stress under 6% moisture content

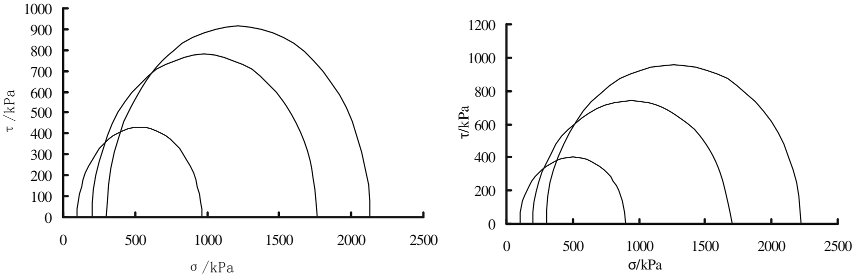

(c) Mohr’s stress circle under 4% moisture content

(d) Mohr’s stress circle under natural state

Fig. 6. Mohr’s stress circle acquired in times of failure of sandy pebble soil under compact state

3.2 Strength Characteristics of Sandy Pebble Soil Based on Different Density and Moisture Content

Mohr’s Stress Circle Acquired in Times of Sample Failure. Mohr’s stress circles in times of sample failure under different density and moisture conditions have been acquired through the test, as is shown in Figs. 6 and 7.

(1) Mohr’s stress circle acquired in times of sample failure under compact state:
(2) Mohr’s stress circle acquired in times of sample failure under medium compact state:

The strength parameters of test samples can be acquired according to Mohr’s stress circles above, as is shown in Table 2 as follows:

It can be seen from Table 2 that when the moisture content of sandy pebble soil remains unchanged, its internal friction angle enlarges with the increase of density, which is mainly due to the fact that at the beginning of the shear, there is no relative displacement between the particles of sandy pebble soil with larger density, whose main deformation form is elasticity deformation, while with the continuation of the shear, the relative position between particles changes, which incurs the necessity of overcoming the occlusion force between them, thus resulting in the dense arrangement of particles, making internal friction angle larger.

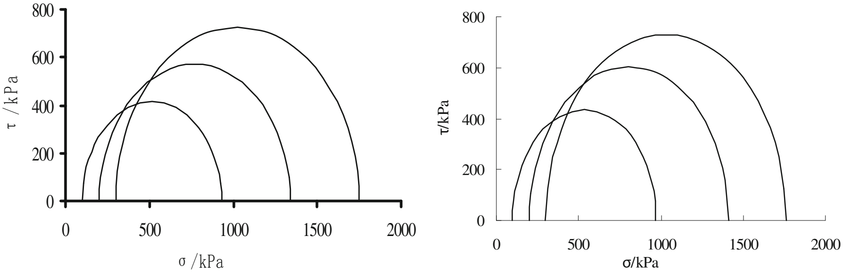

(a) Mohr's stress under saturated state

(b) Mohr's stress under 6% moisture content

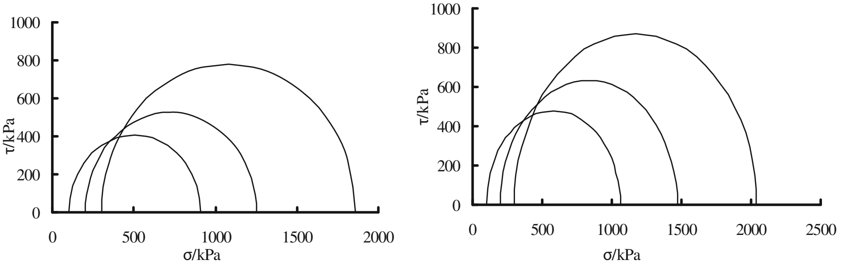

(c) Mohr's stress circle under 4% moisture content

(d) Mohr's stress circle under natural state

Fig. 7. Mohr's stress circle acquired in times of failure of sandy pebble soil under medium compact state

Table 2. Strength parameters of sandy pebble soil

Compact state	Moisture content (%)	Internal friction angle φ (°)	cohesion force c (kPa)
Compact	Saturated state	37.1	90.8
	6% moisture content	35.1	118.5
	4% moisture content	41.5	80.3
	Natural state	44.6	85.8
Medium compact	Saturated state	32.3	140.4
	6% moisture content	31.4	163.4
	4% moisture content	33.7	120.8
	Natural state	35.9	143.9

When density remains unchanged, there is no obvious law for the change of internal friction angle and cohesion force of sandy pebble soil with the increase of moisture content. When the moisture content is 6%, the internal friction angle of sandy pebble soil is the smallest while the cohesion force is the largest. The research on the law for the change of strength parameters of sandy pebble soil with the change of moisture content should be deepen.

Strength Characteristic Law of Sandy Pebble Soil Based on Different Density and Moisture Content. The relation between the change of internal friction angle and cohesion force of sandy pebble soil and the change of moisture content is as follows:

It can be seen from Figs. 8 and 9 that under various density states, when moisture content is 1.5% (natural state), the internal friction angle becomes the largest; both the internal friction angle and cohesion force of sandy pebble soil experience sudden changes with the change of moisture content: when moisture content is lower than 6%, the internal friction angle becomes smaller with the increase of moisture content, while when moisture content is larger than 6%, the internal friction angle becomes larger with the increase of moisture content.

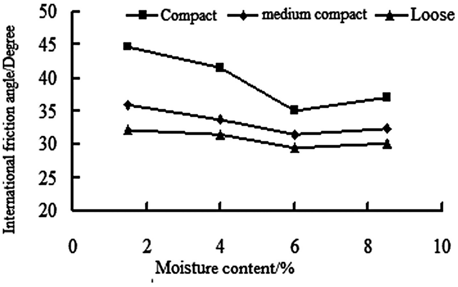

Fig. 8. Relation between moisture content and internal friction angle

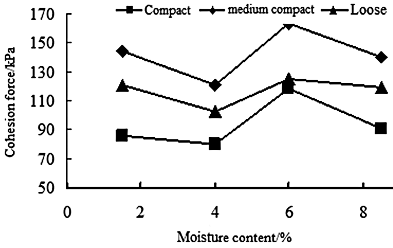

Fig. 9. Relation between moisture content and cohesion force

4 Conclusions

Based on a large-scale indoor triaxial test, the paper researched the strength characteristics of sandy pebble soil based on different density and moisture content, and conclusions are as follows:

(1) Both the peak stress and initial modulus of sandy pebble soil increase with the increase of confining pressure.
(2) When the moisture content of sandy pebble soil remains unchanged, its stress peak increases with the increase of density; when the density of sandy pebble soil remains unchanged, its stress peak reaches the maximum value under natural state.
(3) When the moisture content of sandy pebble soil remains unchanged, its international friction angle increases with the increase of density.
(4) Both the internal friction angle and cohesion force of sandy pebble soil experience sudden changes with the change of moisture content: when moisture content is lower than 6%, the internal friction angle becomes smaller with the increase of moisture content, while when moisture content is larger than 6%, the internal friction angle becomes larger with the increase of moisture content.

References

1. Yuan, J., Zhan, B., Chen, S., et al.: Effects of water content and compaction degree on mechanical characteristics of roadbed. J. Water Resour. Archit. Eng. **11**(2), 98–102 (2013)
2. Jin, J., Zhang, L., Wu, H., et al.: Study on the relationship between soil strength and water content and density. Sci. Technol. Eng. (22), 6148–6152 (2008)
3. Gan, L., Yuan, G.: High pressure large triaxial tests and strength characteristics of coarse-grained soil. Dam Obs. Geo Tech. Tests **21**(3), 9–12 (1997)
4. Editing Committee of Manual for Geological Engineering. Manual for Geological Engineering, 2nd edn., pp. 926–928. China Architecture and Building Press, Beijing (1982)
5. Guo, Q.: The Engineering Properties and Application of Coarse Grained Soil. Yellow River Water Conservancy Press, Zhengzhou (1998)
6. Hardin, B.O., Kalinski, M.E.: Estimating the shear modulus of gravelly soils. J. Geotech. Geoenviron. Eng. **131**(7), 867–875 (2015)
7. Zhang, Q., Si, H.: Strength and stress strain behaviour of large triaxial compression tests on coarse granular materials. J. Hydraul. Eng. (9), 22–31 (1982)
8. Jiang, P., Yang, S.: Experimental study on rheologic behavior and long term strength of gravel in Chengdu area. J. Geol. Hazards Environ. Preserv. **9**(1), 38–42 (1998)
9. Shi, Z., Zhao, X., Peng, M.: Review of studies on large scale triaxial tests of coarse–grained soils. J. Eng. Geol. **22**(5), 792–796 (2014)

An Alternative Method for Soil Characterisation Using Pipe-Jacking Parameters and Spoil Characteristics

Wen-chieh Cheng[1(✉)], James C. Ni[2], and Louis Ge[3]

[1] Institute of Tunnel and Underground Structure Engineering,
School of Civil Engineering, Xi'an University of Architecture and Technology,
Shaanxi 710055, China
s2428030@gmail.com, w-c.cheng@xauat.edu.cn
[2] Department of Civil Engineering, National Taipei University of Technology,
Taipei 10608, Taiwan
[3] Department of Civil Engineering, National Taiwan University,
Taipei 10617, Taiwan

Abstract. As only a few boreholes are present along a tunnel design alignment, geological understanding of the worksite may not be adequate and the ability to optimise the tunnelling parameters is thus limited. Since this lack of boreholes will cause a significant potential of geo-hazards for tunnelling works. This study proposes an alternative method to determine the major and other proportions of ground. The variation of the torque of the cutter wheel and sieve residue can be utilised to determine the major ground proportion, whereas the flow rate of the supply line and pressure in the supply and discharge lines, as well as the density of bentonite slurry can be utilised to determine other proportions. The validity of the proposed method is verified by a case study. The proposed method provides an opportunity to better understand the geological structure of worksite, refining the design tunnelling parameters and minimising the potential of geo-hazards.

Keywords: Torque of cutter wheel · Flow rate of supply line
Slurry density

1 Introduction

Significant variations in the jacking force can not only eat up the jacking capacity, but can also cause damage to the pipe itself [1–3] as well as to adjoining properties, despite jet grouting techniques being available for building protection purposes [4, 5]. Mitigation of the impacts on the jacking capacity can be better achieved by a comprehensive understanding of the geological conditions [6, 7]. However, the number of geological boreholes along a design alignment is usually limited, due to project budget constraints. Barla et al. [8] summarised on a microtunnelling project in Italy, where the boring machine got stuck during the jacking of a 760 mm diameter pipe in a limestone formation. Since there is currently no published guidance on the excavatability of Irish rock for microtunnelling applications, Sheil et al. [9] established useful relationships between the excavatability index and the uniaxial compressive strength and brittleness

© Springer Nature Singapore Pte Ltd. 2018
D. Zhang and X. Huang (Eds.): GSIC 2018, *Proceedings of GeoShanghai 2018 International Conference: Tunnelling and Underground Construction*, pp. 224–231, 2018.
https://doi.org/10.1007/978-981-13-0017-2_22

index of rocks, based upon the results of microtunnelling through rock at five Irish sites. Alzabeebee et al. [10] carried out a study to verify a simple equation which has been adopted for estimating the soil pressure on a buried pipe under traffic loads, for the current design practice in the United Kingdom. The results indicated that there are significant issues with the maximum soil pressure equation. Despite some wireless sensor network systems being available [11], they are not ultimately intended for absolute-pressure measurements, but for the monitoring of relative pressure changes in pipes. Thus, an alternative method to determine the major and other ground proportions that closely relate to jacking loads is shown to be essential to prevent running out of the jacking capacity and damage of pipe.

The objectives of this study are: (1) to determine the major proportion of ground by investigating the variation in the current of the cutter wheel and the tunnelling spoil characteristics when tunnelling between various soils, (2) to determine other proportions of ground, by analysing the relationship between the flow rate of the supply line and the cutter wheel current, the pressure in the supply and discharge lines, and the density of bentonite slurry in circulation, and (3) to verify the validity of the proposed method through a case study.

2 Proposed Method

In this paper, an alternative method to determine the major and other proportions of ground was proposed by considering five parameters; that is, (1) torque of cutter wheel, (2) tunnelling spoil characteristics, (3) flow rate of supply line, (4) pressure in the supply and discharge lines, and (5) density of bentonite slurry. The first two parameters are to determine the major proportion of ground. While the other three parameters are to determine other proportions.

2.1 Torque of Cutter Wheel

The variation in the torque of the cutter wheel is closely correlated to the type of soil encountered during tunnelling operations, so that it may vary from one soil type to another. The variation in the torque of the cutter wheel is directly related to the measured current of cutter wheel. A greater variation in the current of the cutter wheel is likely when there are soil particles present that are greater than 4.76 mm in diameter (e.g., gravel), while a smaller variation corresponds to soil particles present that are less than 4.76 mm in diameter (e.g., sand, silt, and clay). It is thus evident that the variation in the torque of cutter wheel provides an important clue to determining the major proportion of ground.

2.2 Tunnelling Spoil Characteristics

Tunnelling spoils retained on sieves mounted on shaker decks are to further verify the deduced major proportion of ground. Gravels are broken into smaller particles of 10–30 mm in diameter after passing through the cone section of shield. The more the particles retained on sieve #1 (opening = 2 mm), the larger the proportion of gravels.

Otherwise, the ground comprises a major sand proportions with a particle size larger than 0.3 mm although small proportions of sands retained on sieve #1 or passed through sieve #2 (opening = 0.3 mm) could be noted. In the event there are only a few particles retained on both the sieves, the ground primarily contains silts of smaller than 0.075 mm in diameter. As for plastic clays, due to their electrical double layer structure, they are consisted of individual clay particles surrounded by a film of water, thereby leading to the clays to be present together with gravels only on the sieve #1.

2.3 Slurry Line Flow Rate and Pressure Responses

Three out of the five proposed parameters are adopted in the method for determining other ground proportions. Silts and/or clays could significantly reduce the spoil carrying ability of slurry, leading to some difficulties in maintaining an effective slurry circulation. Manipulating the flow rates of supply and discharge lines have often been adopted to tackle this problem in practice. Generally, increasing the flow rate of the supply line could effectively scrape sands and/or silts off the cutting face resulting in a decline in the current of the cutter wheel. However, it may not be effective in scraping off gravels and/or clays from the cutting face and the current of the cutter wheel thus remains nearly constant while tunnelling. As slurry circulation proceeds, the pressure in the supply and discharge lines could be largely increased when the slurry carries an excessive amount of clays and/or silts. In short, the decreasing current of the cutter wheel due to the increasing flow rate of the supply line reveals sands and/or silts, whereas the increasing pressure in the supply and discharge lines corresponds to fine-grained soil proportions.

2.4 Density of Bentonite Slurry

The more the clays carried, the higher the slurry density. Since the slurry density can largely affect its spoil carrying ability, it should be maintained at an appropriate value to ensuring an effective slurry circulation during tunnel construction. In this study, the threshold slurry density; that is, 12.8 kN/m^3, was derived through a series of preliminary field measurements. In the event that the slurry density exceeds 12.8 kN/m^3, the ground may contain some proportions of clay. Otherwise, the ground may comprise of sands and/or silts, with the slurry density being smaller than the threshold value.

Procedures associated with the proposed method for soil characterisation are shown in Fig. 1 and summarised as follows. Firstly, the variation in the current of the cutter wheel will determine the major proportion of ground. The greater the variation in the current of the cutter wheel, the larger the proportion of soil particles larger than 4.76 mm diameter. Secondly, the tunnelling spoils retained on sieves will verify the deduced major ground proportion. When the particles retained are more on sieve #1 than on sieve #2, the ground primarily comprises gravels; otherwise the ground mainly comprises of sands. As there are very few particles retained on both the sieves, the ground principally comprises of silts. Thirdly, the flow rate of the supply line and the pressure in the supply and discharge lines during slurry circulation can be used to determine other ground proportions. In the case the reducing current of the cutter wheel is associated with the increasing flow rate of the supply line, the ground should include some sands and/or silts. Fourthly, during slurry circulation, the increasing pressure in the supply and discharge lines corresponds to fine-grained soil proportions. Lastly, the slurry density will further clarify whether the ground contains clays.

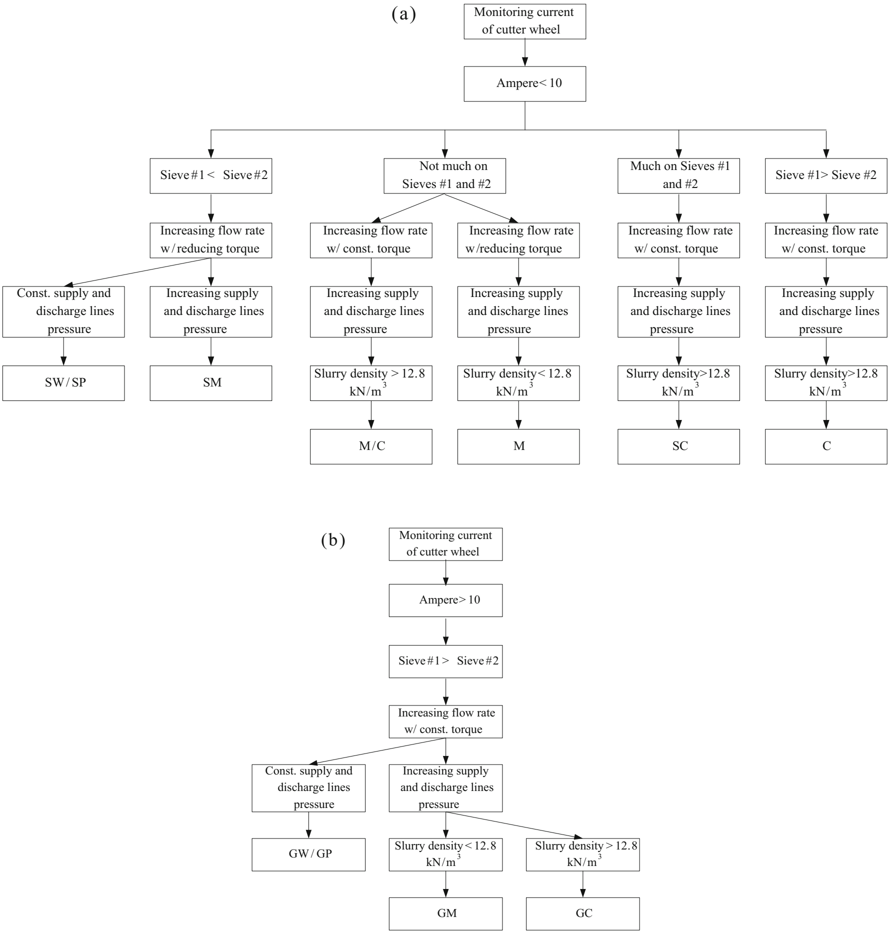
(a)
Monitoring current of cutter wheel
Ampere< 10
Sieve#1< Sieve#2
Not much on Sieves #1 and #2
Much on Sieves #1 and #2
Sieve #1> Sieve #2
Increasing flow rate w/reducing torque
Increasing flow rate w/ const. torque
Increasing flow rate w/reducing torque
Increasing flow rate w/ const. torque
Increasing flow rate w/ const. torque
Const. supply and discharge lines pressure
Increasing supply and discharge lines pressure
Increasing supply and discharge lines pressure
Increasing supply and discharge lines pressure
Increasing supply and discharge lines pressure
Increasing supply and discharge lines pressure
SW/SP
SM
Slurry density > 12.8 kN/m3
Slurry density< 12.8 kN/m3
Slurry density>12.8 kN/m3
Slurry density>12.8 kN/m3
M/C
M
SC
C
(b)
Monitoring current of cutter wheel
Ampere> 10
Sieve#1> Sieve#2
Increasing flow rate w/ const. torque
Const. supply and discharge lines pressure
Increasing supply and discharge lines pressure
GW/GP
Slurry density< 12.8 kN/m3
Slurry density > 12.8 kN/m3
GM
GC

Fig. 1. Procedures associated with the proposed alternative method for soil classification: (a) Measured current of cutter wheel < 10 A (for sands and fine-grained soils); (b) Measured current of cutter wheel > 10 A (for gravels).

3 Project Description

3.1 Pipe-Jacking Project

The pipe-jacking project was located in the Shulin district in Taipei County, Taiwan, at depths varying from 10.3 to 10.8 m below the surface [12–14]. Five geological boreholes drilled from a backfill layer, through a silty sand layer into a dense to very dense, poorly-graded to well graded sand and gravel layer were constructed close to the design tunnel alignment [15–17]. The piezometric level was at a depth of 4.8 m.

3.2 Pipe-Jacking Works

The tunnel bore was excavated using a 1500-mm diameter cutter wheel. A 1-m long, 1200-mm internal diameter reinforced concrete pipe, with a thickness of 120 mm, was adopted in this project. This led to an overcut annulus of 30 mm, in which a special bentonite lubricant with 2% polymer was injected, not only to reduce the friction resistance, but to mitigate impacts due to its loss on the total jacking load during tunnelling in gravel formations. Additionally, a bentonite slurry with a unit weight varying from 10.3 to 10.5 kN/m^3 was utilised to maintain the stability of the cutting face and also to transport tunnelling spoils to decantation chambers which would remove coarse particles from the tunnelling spoils through a slurry circulation system.

4 Analysis and Discussions

4.1 Pipe-Jacking Drive

The flow rate of the supply line, jacking speed, and current of cutter wheel activities for a pipe-jacking drive are plotted in Fig. 2. As evident, the variation in the current of the cutter wheel due to jacking in sands or fine-grained soils was reduced in the 17–22 m, 39–48 m, and 81–99 m sections. While jacking, there were more residue presented on sieve #2 for the 17–22 m and 81–99 m sections, which indicated a major sand proportions. The reduced current of the cutter wheel in the 17–22 m section was associated with the increasing flow rate of supply line, which corresponded a certain silt proportions. Whereas in the 81–99 m section, as there were no records of flow rate available, determining other ground proportions relied upon the pressure and density measurements. The flow rates of supply and discharge lines, the associated pressures, and the slurry density activities at this pipe-jacking drive are plotted in Fig. 3. The pressure buildup along with the increasing jacking distance for the 81–99 m section represented a poor slurry circulation caused by carrying more fine-grained soils. As the densities measured right after refreshing the slurry from the 81–99 m section were greater than 12.8 kN/m^3, the ground should include some clay proportions. Since slurry refreshing was not carried out in the 17–22 m section, the ground due to the presence of a few residue left on sieve #1 was likely to include gravels, rather than clays (Fig. 3). As to the 39–48 m section, the major ground proportion was changed from silt for the first 5 m section to sand for the later 4 m section, according to sieve residue records. The pressure buildup along with the increasing jacking distance indicated that the ground included fine-grained soils, as shown in Fig. 3. Because there were no density records available in the 39–48 m section, the ground was inferred to include some silts although the densities due to no slurry refreshing undertaken were likely to exceed 12.8 kN/m^3. Thus, the ground comprised a majority of sands, with some silts and small gravels in the 17–22 m section, as labelled by “S/M/G” in Figs. 2 and 3, and a major sand proportion with some clays in the 81–99 m section, as labelled by “SC” in Figs. 2 and 3. Whereas the ground included principally silts in the 39–44 m section, as labelled by “M” in Figs. 2 and 3, and sands with some silts in the 44–48 m section, as labelled by “SM” in Figs. 2 and 3.

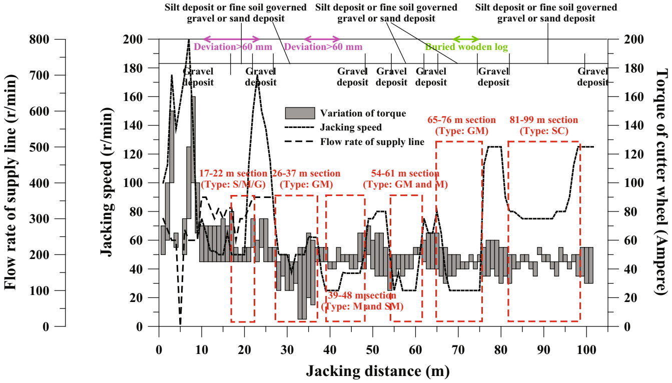

Fig. 2. Variations of flow rates of feed line, jacking speed, and torque of cutter wheel during pipe-jacking works at this drive.

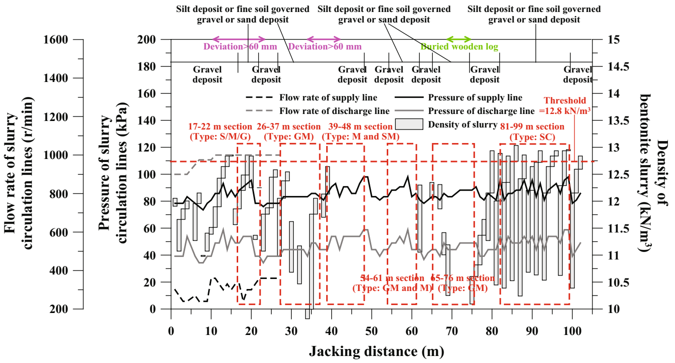

Fig. 3. Variations of flow rates of feed and discharge lines, associated pressures, and slurry density during pipe-jacking works at this drive.

Compared to the 17–22 m, 39–48 m, and 81–99 m sections, the variation in the current of the cutter wheel in the 26–37 m, 54–61 m, and 65–76 m sections was much more significant. However, for the last 3 m of the 54–61 m section, the reducing current of cutter wheel and the sieve residue less on both the sieves were most likely due to tunnelling in silts (Fig. 2). Thus, the ground in the aforesaid three sections principally contained gravels, with the exception of the 59–61 m section, in which silt soils were included. Similarly, there were no records of flow rate available for the 26–37 m, 54–61 m, and 65–76 m sections and determining other proportions of ground relied upon the pressure and density measurements. The pressure buildups along with the increasing jacking distance and slurry densities below 12.8 kN/m^3 from the aforesaid three sections suggested that the ground should include few silt soils. In summary, the ground in the 26–37 m and 65–76 m sections was primarily comprised of gravels with some silt soils, whereas the ground principally comprised gravels with some silts in the 54–59 m section and silts in the 59–61 m section. The seven other sections due to their tunnelling and spoil characteristics opposite to the fine soil governed gravel or sand deposits should include gravels with some sands (their labels "G/S" are not particularly highlighted in Figs. 2 and 3).

4.2 Limitations of the Proposed Method

While tunnelling, in-situ materials encountered at the cutting face are initially crushed by cutter discs and then by the cone section of shield machine. The drill cuttings are then transported to the shaker decks to segregate coarser spoils from the bentonite slurry. Thus, the ability to determine whether the ground soils are poorly-graded or well graded through the drill cuttings or sieve residue by the proposed method is limited. Additionally, the plasticity of clays is related to the morphology of the plate-like clay mineral particles that slide over the others when water is added and can be quantified using the liquid limit (LL) and the plasticity index (PI). As the values of LL and PI can only be evaluated by the Atterberg limits tests, the ability to determine whether the ground soils are of high plasticity by the proposed method is also limited.

5 Conclusions

Based upon the results of an application of the proposed method and discussions made, the following conclusions can be drawn:

(1) The proposed method adopted two parameters; that is, the current of the cutter wheel and the tunnelling spoil characteristics, to determine the major proportion of ground. The more gravels that are present at the cutting face, the greater the variation in the current of cutter wheel, and the more the residue retained on sieve #1. The variation in the current of the cutter wheel was less significant with more residue presented on sieve #2 in the event of jacking in sands. In the case that the residue was less retained on both the sieves, the ground should include primarily silts.

(2) The pressure in the supply and discharge lines, the flow rate of supply line, and the slurry density were adopted in the proposed method for determining other proportions. The higher slurry viscosity due to some proportions of clay and/or silt led to an increase in the pressure of supply and discharge lines, which also indicated an ineffective slurry circulation. In the event that the reduced current of the cutter wheel was associated with the increasing flow rate of supply line, which indicated some silt and/or sand proportions. The density of slurry could exceed the value of 12.8 kN/m^3 as it carried clays.

(3) Since the geological understanding of the worksite was limited because only a few boreholes were available along the tunnel alignment, the application of the proposed method provided an opportunity of establishing a more comprehensive geological structure for refining the design tunnelling parameters.

References

1. Bergeson, W.: Review of long drive microtunneling technology for use on large scale projects. Tunn. Undergr. Space Technol. **39**, 66–72 (2014)
2. Zhen, L., Chen, J.J., Qiao, P., Wang, J.H.: Analysis and remedial treatment of a steel pipe-jacking accident in complex underground environment. Eng. Struct. **59**, 210–219 (2014)
3. Shen, S.L., Cui, Q.L., Ho, C.E., Xu, Y.S.: Ground response to multiple parallel microtunneling operations in cemented silty clay and sand. J. Geotech. Geoenviron. Eng. **142**(5), 04016001 (2016)
4. Shen, S.L., Wang, Z.F., Yang, J., Ho, E.C.: Generalized approach for prediction of jet grout column diameter. J. Geotech. Geoenviron. Eng. **139**(12), 2060–2069 (2013)
5. Shen, S.L., Wang, Z.F., Cheng, W.C.: Estimation of lateral displacement induced by jet grouting in clayey soils. Geotech. ICE **67**(7), 621–630 (2017)
6. Ni, J.C., Cheng, W.C.: Characterising the failure pattern of a station box of Taipei Rapid Transit System (TRTS) and its rehabilitation. Tunn. Undergr. Space Technol. **32**, 260–272 (2012)
7. Ni, J.C., Cheng, W.C.: Quality control of double fluid jet grouting below groundwater table: case history. Soils Found. **54**(6), 1039–1053 (2014)
8. Barla, M., Camusso, M., Aiassa, S.: Analysis of jacking forces during microtunnelling in limestone. Tunn. Undergr. Space Technol. **21**(6), 668–683 (2006)
9. Sheil, B.B., Curran, B.G., McCabe, B.A.: Experiences of utility microtunnelling in Irish limestone, mudstone and sandstone rock. Tunn. Undergr. Space Technol. **51**, 326–337 (2016)
10. Alzabeebee, S., Chapman, D., Jefferson, I., Faramarzi, A.: The response of buried pipes to UK standard traffic loading. Geotech. Eng. ICE Proc. **170**(GE1), 38–50 (2017)
11. Sadeghioon, A.M., Walton, R., Chapman, D., Metje, N., Anthony, C., Ward, M.: Design and development of a nonintrusive pressure measurement system for pipeline monitoring. J. Pipeline Syst. Eng. Pract. **5**(3), 04014001 (2014)
12. Cheng, W.C., Ni, J.C., Shen, S.L., Huang, H.W.: Investigation of factors affecting jacking force: a case study. Geotech. Eng. ICE Proc. **170**(GE4), 322–334 (2017)
13. Cheng, W.C., Ni, J.C., Arulrajah, A., Huang, H.W.: A simple approach for characterising tunnel bore conditions based upon pipe-jacking data. Tunn. Undergr. Space Technol. **71**, 494–504 (2018)
14. Cheng, W.C., Ni, J.C., Cheng, Y.H.: Alternative shoring for mitigation of pier foundation excavation disturbance to existing freeway. J. Perform. Constr. Facil. **31**(5), 04017072 (2017)
15. Ni, J.C., Cheng, W.C.: Shield machine disassembly in grouted soils outside the ventilation shaft: a case history in Taipei Rapid Transit System (TRTS). Tunn. Undergr. Space Technol. **26**(2), 435–443 (2011)
16. Ni, J.C., Cheng, W.C., Ge, L.: A case history of field pumping tests in a deep gravel formation in the Taipei Basin Taiwan. Eng. Geol. **117**(1–2), 17–28 (2011)
17. Ni, J.C., Cheng, W.C., Ge, L.: A simple data reduction method for pumping tests with tidal, partial penetration, and storage effects. Soils Found. **53**(6), 894–902 (2013)

Explorative Application of Peck Formula and Its Modifier Versions in Surface Subsidence Prediction Caused by Quasi-rectangular Tunnel Construction

Jun Liu[1(✉)], Peinan Li[2,3], Xiaoyong Kou[3], and Dezhong Huang[3]

[1] College of Urban Rail Transportation, Shanghai University of Engineering Science, Shanghai 201620, China
junliurs@163.com
[2] College of Civil Engineering, Tongji University, Shanghai 200092, China
[3] Shanghai Tunnel Engineering Co. Ltd., Shanghai 200232, China

Abstract. Surface subsidence is one of the key control indexes of tunnel construction. Peck formula is generally adopted to estimate the settlement of the soft ground induced by shallow tunneling work, which is suggested by Professor Peck in 1969. Verification work is necessary to be done before the formula is applied in engineering. At present, the application experience of Peck formula in Quasi-rectangular tunnel construction is relatively lack, resulting in the limited application in engineering. Based on Peck formula and modified double circular formula, the paper suggested a method to calculate the settlement of soft ground in Quasi-rectangular tunnel, which contributes to estimate the surface subsidence before the construction of shield tunnel.

Keywords: Peck formula · Quasi-rectangular · Shield tunnel
Surface subsidence · Settlement estimation

1 Introduction

Shield excavation will inevitably cause disturbance to the surrounding soft soils, causing surface subsidence, which in turn results in safe risk to the surface buildings and underground pipelines. In order to take specific protective measures, it is necessary to obtain the characteristics and size of the formation settlement. The calculation methods of settlement caused by shield construction mainly include empirical formula, theoretical analysis and numerical analysis [1, 2]. Peck formula suggested by Peck in 1969 is one of the most popular empirical formulas. Since the derivation of Peck formula is based on critical parameters collected around engineering site, the verification work of applicability of Peck formula needs to be done [3].

Round section is mostly adopted since the development of shield technology. Due to the highly intensive development of urban, underground engineering begins to face more and more restrictions. With the continuous development and utilization of urban underground space, the tunnels cross each other and the underground structures overlap, which results in the construction space to be limited. Shield technology tends

© Springer Nature Singapore Pte Ltd. 2018
D. Zhang and X. Huang (Eds.): GSIC 2018, *Proceedings of GeoShanghai 2018 International Conference: Tunnelling and Underground Construction*, pp. 232–240, 2018.
https://doi.org/10.1007/978-981-13-0017-2_23

to be large depth, rapid curve, long distance and large dimension. Presently, a large number of new profiled section shields come to spring up in foreign countries, which are mainly divided into two types: complex circular shield and non-circular shield.

Double circular shield tunnel has a great advantage in terms of construction efficiency, surface subsidence influence, tunnel section and underground space utilization ratio. The vault "seagull block" may cause earthquakes and aggravate stratum disturbances, which increases the difficulty of controlling the deformation of ground soil and limits the application of double circular shield. On the basis of preserving the original advantages of the double circular shield, Quasi Rectangular Tunnel properly arch the vault and arch bottom. On the one hand, it can improve the arching effect of the segment and the mechanical performance of the segment can also be improved. On the other hand, the excavation curve of the vault is more moderate, which can slow the effect of the back soil and is conducive to the control of the surface subsidence.

So far, there are few examples of rectangular tunnels in China. The calculation of surface soil settlement is still blank. Based on Peck formula and modified double circular formula, the paper suggested a method to calculate the settlement of soft ground in Quasi-rectangular tunnel, which will contributes to estimate the surface subsidence before the construction of shield tunnel.

2 Project Profile

The total length of line 3 project in Ningbo is about 25.71 km. The length of rectangular shield section tunnel is 390.3 m. The thickness of the soil above tunnel is 2.5–10.46 m. The largest vertical slope is 3.5% and the minimum plane radius is 400 m. The excavation size of Quasi-rectangular tunnel is 11830 mm × 7267 mm and the external dimension of segment is 11500 mm × 6937 mm. The excavation area of tunnel is 71.98 m^2.

3 Peck Formula and Modified Formula

3.1 Peck Formula

Based on a large number of detected data, Peck proposed that the soil settlement curve conforms to the normal distribution in 1969, who think of the surface subsidence is caused by soil damage. The settlement during construction is in the condition of un-drainage. It is assumed that the volume of sedimentation curve is equal to soil loss. However, the soil loss volume is related to the shield type, construction method, soil conditions, surface environment and construction management [4].

For homogenous mucous strata, the settlement value caused by shield construction can be calculated in the following formula (1),

$$S(x) = \frac{V_S}{\sqrt{2\pi} \times i} \times \exp\left(-\frac{x^2}{2i^2}\right) \tag{1}$$

$$S_{\max} = \frac{V_S}{\sqrt{2\pi} \times i} \tag{2}$$

where,

$S(x)$ – the surface settlement of the point, the horizontal distance to the centerline of the tunnel is x, m
$S_{\max}$ – the maximum settlement value of the surface, m
i – width coefficient of settlement curve, m
V_S – the soil loss volume per unit length, m^3/m.

3.2 Circular Tunnel Modified Peck Formula

Peck conducted a large number of analysis on soil settlement caused by shield construction. He suggested that the volume of sedimentation curve is equal to soil loss and the settlement curve conforms to the normal distribution. Based on the monitoring data of line 8 and line 6 in Shanghai, the Peck formula has been modified. And the modified formula is applied to the calculation of the soil settlement of double circular shield construction [5, 6].

$$S(x) = \frac{V_S}{\sqrt{2\pi} \times i} \times \exp\left(-\frac{(x+2.3)^2}{2i^2}\right) + \frac{V_S}{\sqrt{2\pi} \times i} \times \exp\left(-\frac{(x-2.3)^2}{2i^2}\right) \tag{3}$$

$$S_{max} = \frac{2V_S}{\sqrt{2\pi} \times i} \times \exp\left(-\frac{2.3^2}{2i^2}\right) \tag{4}$$

where,

$S(x)$ – the surface settlement of the point, the horizontal distance to the centerline of the tunnel is x, m
$S_{\max}$ – the maximum settlement value of the surface, m
i – width coefficient of settlement curve, m
V_S – the soil loss volume per unit length, m^3/m.

4 Settlement Calculation of Quasi-rectangular Tunnel

4.1 Quasi Rectangular Shield Tunnel Settlement Simulate

In this paper, the Plaxis software is used to simulate the surface subsidence caused by single circular, double circular and rectangular tunnel construction. In the case, the calculated points are respectively 1.5D and 3.0D meter to the tunnel axis. The numerical model is 100 m long and 50 m deep. According to the geological data, soil is built and groundwater level is located in the soil surface. The effect of tunnel construction on the stratum is simulated through the stratum loss. The dimension of rectangular tunnel is based on actual engineering conditions, while the size of single and double circular tunnel is set by the principle of area equivalent. The stratum loss is 5% in all cases. The numerical results are shown in Fig. 1. The surface settlement value is plotted for analyzing.

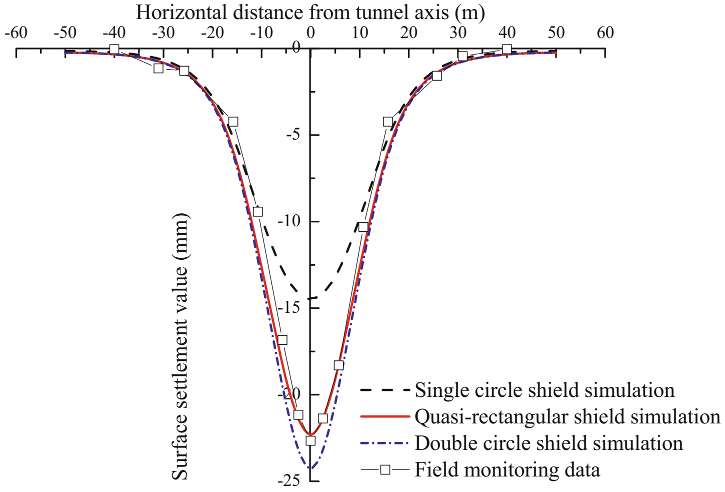

(a) Depth of tunnel axis 1.5D

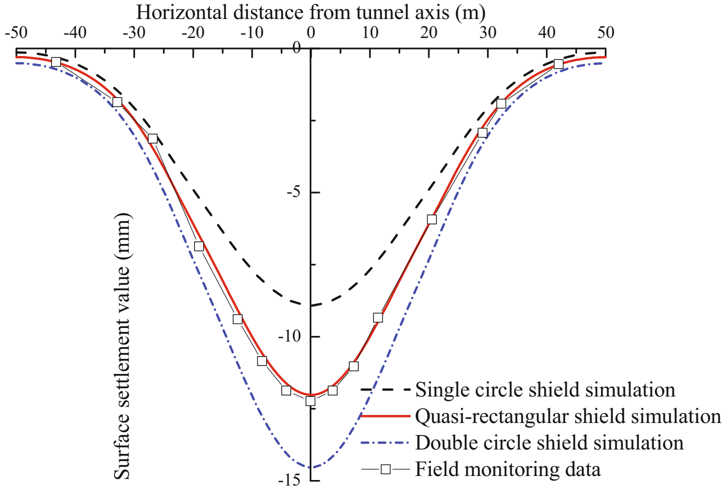

(b) Depth of tunnel axis 3D

Fig. 1. Surface settlement curve caused by shield tunnel construction

Figure 1 shows that the settlement caused by rectangular tunnel is similar to the single and double circular tunnel. Meanwhile, the settlement value is larger than single circular tunnel and smaller than double circular tunnel. The field monitoring data are consistent with the results by numerical simulation.

4.2 Rectangular Tunnel Settlement Simulation

According to the numerical results, the settlement value of rectangular tunnel is larger than single circular and smaller than double circular tunnel if the design factors, environmental factors, and construction conditions are the same. The results can be expressed in the formula, $S_S(x) < S_R(x) < S_D(x)$. In the absence of reliable numerical results, the surface subsidence value can be estimated through the single and double circular tunnel in the same condition.

The width coefficient can be obtained through the following formula (5),

$$i = R \times \left(\frac{z}{2R}\right)^{0.8} \tag{5}$$

where,

i – the width coefficient, m

R – the excavation radius of tunnel, m. $R = \sqrt{W/\pi}$

where,

W – the excavation area of tunnel, m^2

Z – the depth of tunnel axis, m

According to design criteria, the surface settlement value of the axial depth 1D and 2D should be less than 1% or 30 mm. The settlement value is calculated through formulas (1) and (3) and the simulation cases are shown in Table 1. The settlement value is plotted in Fig. 2.

Table 1. Simulation cases

Calculation method	Burial depth of axis	
	1D	2D
Single circular Peck formula	Case 1	Case 2
Double circular modified Peck formula	Case 3	Case 4

Figure 2 suggests that the surface settlement value of single circular Peck formula is similar to the results of double circular modified Peck formula. With the loss rate of the formation controlled at 1% and in case 1 & 3, the maximum settlement value of single circular Peck and double circular modified circular are respectively 76.6 mm and 128.3 mm. While the maximum settlement value of rectangular tunnel is in the range of 76.6 mm to 1283.3 mm. In case 2 & 4, the value of rectangular tunnel is in the range of

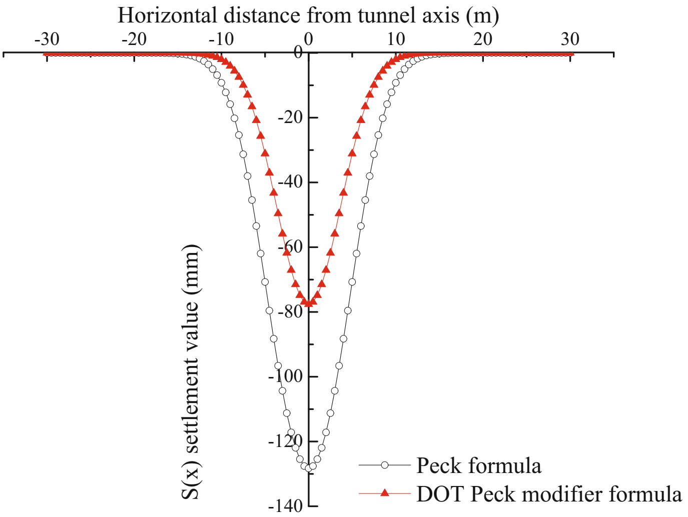

(a) Depth of tunnel axis 1D

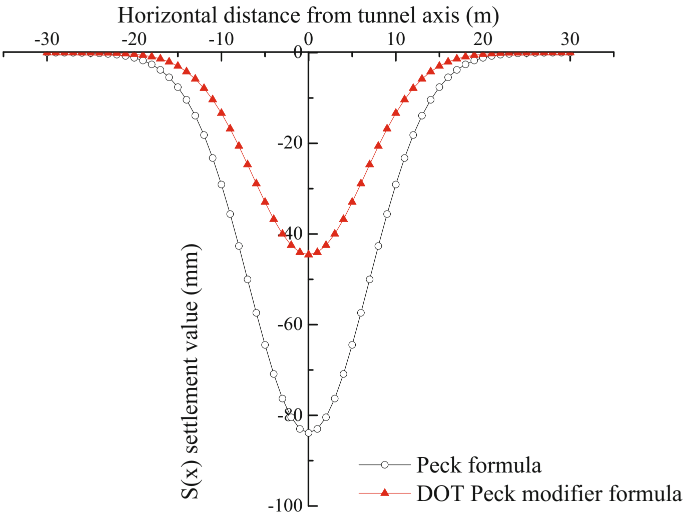

(b) Depth of tunnel axis 2D

Fig. 2. Surface settlement curve of different tunnel depth

44.6 mm to 83.9 mm. It can be considered that for 1D–2D buried depth, the maximum settlement value is difficult to meet the limit requirement of 30 mm.

With different buried depth of tunnel, the stratum loss corresponding to the maximum settlement value of the soil surface can be obtained through formula (1) and (3).

In the construction, the stratum loss rate corresponding to the control index S_{max}^{k} is called as the critical stratum loss rate δ.

With 30 mm as the maximum settlement value of the control index, the critical stratum loss of single and double circular tunnel under different burial depth can be calculated through formula (6) and (7) respectively.

$$\delta_1 = (S_{max}^{k} \times \sqrt{2\pi} \times i)/V \tag{6}$$

$$\delta_2 = (S_{max}^{k} \times \sqrt{2\pi} \times i \times \exp\left(\frac{2.3^2}{2i^2}\right))/2V \tag{7}$$

The results are shown in Table 2 and plotted in Fig. 3. The maximum settlement value of rectangular tunnel can be controlled less than 30 mm with the stratum loss under the critical value δ.

Table 2. Critical loss ratio of different burial depth

Burial depth Z/m	Width coefficient i/m	Stratum loss ratio δ_1/‰	Critical stratum loss ratio δ_2/‰
6	3.29	3.44	1.94
7	3.73	3.89	2.14
8	4.15	4.33	2.33
9	4.56	4.76	2.53
10	4.96	5.18	2.73
11	5.35	5.59	2.92
12	5.73	5.99	3.11
13	6.11	6.39	3.30
14	6.49	6.78	3.49
15	6.86	7.16	3.67

Figure 3 suggests that the critical stratum loss rate tended to increase with the increase of burial depth. The increase of δ_1 in Peck formula is much faster than that of double circular modified Peck formula. Based on the above numerical results, the critical stratum loss δ should be in the range of δ_1 to δ_2. The two critical stratum loss rate line δ_1 and δ_2 in Fig. 3 divided the coordinate space into three parts, I, II and III. For a rectangular tunnel with a given buried depth, if the stratum loss rate δ is controlled in the part I zone, the control index of the surface settlement can be satisfied. If δ is distributed in part II, the settlement cannot meet the settlement control criterion. When distributed in part III, it is uncertain whether the control index is satisfied.

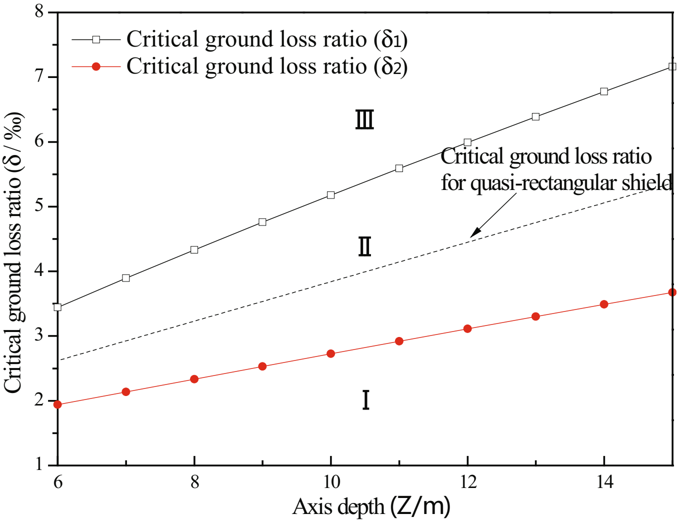

Fig. 3. Critical stratum loss ratio versus different burial tunnel depth

5 Conclusions and Suggestions

This paper presented a method to simulate the surface settlement of rectangular shield tunneling. Without any other effective calculated methods, the surface settlement value can be estimated before construction by using this method. The main conclusions are shown as follows.

(1) Under the same conditions of design factors (tunnel buried depth, excavation area, etc.), environmental factors (engineering hydrogeological conditions, along the construction of buildings, etc.) and construction factors (construction parameters, technical measures, etc.), the surface settlement caused by rectangular shield tunnel construction should be less than the double circle tunnel and larger than the single circular tunnel.

(2) The lower limit of the maximum settlement of rectangular tunnel can be calculated by the Peck formula while the upper limit can be calculated by double circular modified Peck formula. In this way, the maximum settlement value of rectangular tunnel can be estimated indirectly.

(3) When the burial depth of the tunnel is 7 m, the stratum loss rate δ should be controlled below 0.214% to meet the surface settlement criterion. When the buried depth of tunnel depth is 14 m, the loss rate should be controlled below 0.349%.

References

1. Peck, R.B.: Deep excavations and tunneling in soft ground. In: Proceedings of the 7th International Conference on SMFE, pp. 225–290. State of the Art Volume, Mexico City (1969)
2. Han, X., Li, N., Standing, R.: An Adaptability study of Gaussian equation applied to predicting ground settlements induced by tunneling in China. Rock Soil Mech. **28**(1), 23–28 (2007)
3. Zhang, Y., Ying, Z., Xu, Y.: Analysis on three-dimensional ground surface deformations due to shield tunnel. Chin. J. Rock Mech. Eng. **21**(3), 388–392 (2002). Author, F., Author, S., Author, T.: Book Title, 2nd edn. Publisher, Location (1999)
4. Jianxiu, W., Huixian, F., Yanfei, Z., Yiqun, T., Ping, Y.: Advance in calculation of subsidence caused by shield tunnel based on strata loss. Chin. J. Undergr. Space Eng. **6**(1), 112–117 (2010)
5. Zheng, Y.: On-site monitoring of surroundings disturbed by double-o-tube tunnel construction. Chin. J. Undergr. Space Eng. **S1**, 1349–1353 (2007)
6. Weng, C., Zhang, Q., Zhu, J., et al.: Analysis on surface subsidence resulting from DOT tunneling in soft ground. Chin. J. Undergr. Space Eng. **2**(1), 124–127 (2006)

Effects of Soil Cross-Anisotropy on the Wave-Induced Residual Liquefaction Around an Immersed Tunnel in the Liquefiable Seabed

Di Fang[1], Weiyun Chen[1,2(✉)], and Guoxing Chen[1]

[1] Institute of Geotechnical Engineering,
Nanjing Tech University, Nanjing 210009, China
`fangdi66@126.com`, `zjucwy@gmail.com`
[2] Griffith School of Engineering,
Griffith University, Southport, QLD 4222, Australia

Abstract. Immersed tunnel is already a major underwater construction and the stability analysis of immersed tunnel is of great significance in marine engineering. Most previous investigations of the immersed tunnel are about seismic response and did not consider soil anisotropy. In this paper, we developed a 2D model to discuss the effects of soil cross-anisotropy on the residual liquefaction around an immersed tunnel in the liquefiable seabed. The effect of gravitational force including the body of the tunnel is pre-estimated. We use Biot's consolidation theory on the soil-wave interaction and consider the seabed a porous medium. The tunnel is considered as a single phase and behaves under the linear elastic law. We validate the numerical model by comparing with the experimental data. Parametric studies reveal that soil cross-anisotropy affects the pore pressure around immersed tunnel a lot and should not be negligible.

Keywords: Residual liquefaction · Cross-anisotropic soil · Pore pressure
Immersed tunnel

1 Introduction

When ocean wave spreads over seabed, they produce periodic oscillation as dynamic pressure in the seabed and then generate pore pressure. Part of the ocean floor may become unstable or even liquefied due to the decrease of effective stress and the increase of pore pressure. Based on laboratory experiment [1], we can divide the wave-induced liquefaction mechanisms to two types. The oscillatory liquefaction occurs under troughs in unsaturated seafloor. The residual liquefaction is caused by buildup of excess pore pressure [2]. In addition, immersed tunnels are usually embedded in a loose surface ground layer, they are also particularly sensitive to tensile and compressive deformations. The unit weight of immersed tunnel is much lighter than that of liquefied soil [3], so the immersed tunnel may be affected by an upward buoyancy. Therefore, the evaluation of the seabed around the tunnel is important for geotechnical engineers.

© Springer Nature Singapore Pte Ltd. 2018
D. Zhang and X. Huang (Eds.): GSIC 2018, *Proceedings of GeoShanghai 2018 International Conference: Tunnelling and Underground Construction*, pp. 241–249, 2018.
https://doi.org/10.1007/978-981-13-0017-2_24

Seed and Rahman [4] set out a theory to check for residual liquefaction. McDougal [5] studied the analytical solutions of wave-induced pore-pressure cumulation in homogeneous soil. Jeng [6] re-examined the wave-induced residual soil response.

Conventional investigations only considered the isotropic soil behavior of porous seabed. Few investigations for anisotropic soil have been carried out [7–11]. However, researches of wave-induced response around immersed tunnel are quite rare [12]. This paper aims to examine the effects of soil cross-anisotropy on the wave-induced liquefaction around an immersed tunnel.

2 Theoretical Formulation

The spreading of ocean waves will generate excess pore pressure in the seabed. The pore pressure development can be expressed as $p = \tilde{p} + \bar{p}$, where p is wave-induced dynamic pore pressure, $\tilde{p}$ is the oscillatory pore pressure. $\bar{p}$ represents the residual pore pressure [2, 13].

2.1 Oscillatory Mechanism

Based on Biot's consolidation equation, the inertial terms are ignored in flow and deformation formulation and the governing equation can be

$$\mathrm{k_s}\nabla^2\tilde{\mathrm{p}} - \gamma_\mathrm{w}\mathrm{n_s}\beta_\mathrm{s}\frac{\partial\tilde{\mathrm{p}}}{\partial \mathrm{t}} = \gamma_\mathrm{w}\frac{\partial \in_\mathrm{e}}{\partial \mathrm{t}} \tag{1}$$

$$\frac{\partial\sigma'_{\mathrm{xx}}}{\partial \mathrm{x}} + \frac{\partial\tau_{\mathrm{xz}}}{\partial \mathrm{z}} = \frac{\partial\tilde{\mathrm{p}}}{\partial \mathrm{x}} \tag{2}$$

$$\frac{\partial\tau_{\mathrm{xz}}}{\partial \mathrm{x}} + \frac{\partial\sigma'_{\mathrm{zz}}}{\partial \mathrm{z}} + \rho\mathrm{g} = \frac{\partial\tilde{\mathrm{p}}}{\partial \mathrm{z}} \tag{3}$$

Where n_s is the soil porosity, k_s is Darcy's permeability coefficient, ∇^2 is the Laplace operator, τ_{xz} is the shear stress, σ'_{xx} and σ'_{zz} are the effective normal stress in the direction of x and z. The pore fluid compressibility can be

$$\beta_s = \frac{1}{k_f} = \frac{1}{k_w} + \frac{1-s_r}{p_0} \tag{4}$$

where k_w is the water bulk modulus, s_r is the degree of saturation.

Considering the bedding and backfilling as isotropic, based on the pore-elastic theory, relationships between displacements and effective stresses become

$$\sigma'_{xx} = \frac{2G_s}{1-2v_s}\left[(1-v_s)\frac{\partial u_s}{\partial x} + v_s\frac{\partial w_s}{\partial z}\right] \tag{5}$$

$$\sigma'_{zz} = \frac{2G_s}{1-2v_s}\left[(1-v_s)\frac{\partial w_s}{\partial z} + v_s\frac{\partial u_s}{\partial x}\right] \tag{6}$$

$$\tau_{xz} = \tau_{zx} = G_s\left(\frac{\partial w_s}{\partial x} + \frac{\partial u_s}{\partial z}\right) \tag{7}$$

Where Poisson's ratio and Young's modulus are related to shear modulus G_s as $G_s = E_s/2(1+v_s)$. And μ_{xz} and G_x can be inter-related as [15]

$$\frac{\mu_{xz}}{\mu_{zx}} = \frac{E_x}{E_z} = M, G_x = \frac{E_x}{2(1+\mu_{xx})} \tag{8}$$

where E_x and E_z are Young's modulus in the directions of horizontal and vertical, the modulus of shear deformation G_z is

$$G_z = NE_z \tag{9}$$

in which N is the anisotropic constant. M is equal to 1 for an isotropic soil, N is equal to $1/2(1+\mu)$. Based on the poro-elastic theory, relationships between displacements and effective stresses can be

$$\sigma'_{xx} = C_{11}\frac{\partial u_x}{\partial x} + C_{13}\frac{\partial u_z}{\partial z} \tag{10}$$

$$\sigma'_{zz} = C_{13}\frac{\partial u_x}{\partial x} + C_{33}\frac{\partial u_z}{\partial z} \tag{11}$$

$$\tau_{xz} = G_z\left[\frac{\partial u_z}{\partial x} + \frac{\partial u_x}{\partial z}\right] \tag{12}$$

where $C_{11} = E_z(1-\mu_{xz}\mu_{zx})/\Delta$, $C_{13} = E_x\mu_{xz}(1+\mu_{xx})/\Delta$, $C_{33} = E_z(1-\mu_{xx}^2)/\Delta$, $\Delta = (1+\mu_{xx})(1-\mu_{xx}-2\mu_{xz}\mu_{zx})$.

2.2 Residual Mechanism

Considering the bedding sand and backfilling as hydraulically isotropic, the 2-D residual soil response model becomes [14]

$$\frac{\partial \bar{p}}{\partial t} = C_v\left(\frac{\partial^2\bar{p}}{\partial z^2} + \frac{\partial^2\bar{p}}{\partial z^2}\right) + f(x,z,t) \tag{13}$$

C_v is the consolidation coefficient and can be expressed as

$$C_v = \frac{G_s k_f}{(1-2v_s)\rho_f g} \tag{14}$$

$f(x, z, t)$ is defined as a function of both space and time

$$f(x, z, t) = \frac{\sigma_0'}{T}\left[\frac{|\tau_{xz}(x, z, t)|}{\alpha_r \sigma_0'}\right]^{-\frac{1}{\beta_r}} \tag{15}$$

where $\tau_{xz}(x, z, t)$ means phase-resolved oscillatory shear stress, σ_0' means the initial effective stress, α_r and β_r are two empirical constants can be written as

$$\alpha_r = 0.34D_r + 0.084, \beta_r = 0.37D_r - 0.46 \tag{16}$$

The initial stress status in the seabed is determined through an elastic consolidation process. Then, the distribution of initial stress can be expressed as:

$$\sigma_0' = \frac{1 + \nu_s}{3}\left(\sigma_{xx0}' + \sigma_{zz0}'\right) \tag{17}$$

where σ_{xx0}' and σ_{zz0}' are effective stresses of x and z directions after consolidation.

The elastic volumetric strain increment cross-anisotropic soil increment can be

$$\mathrm{d}\varepsilon = \frac{C_{13} - C_{33}}{C_{13}C_{13} - C_{11}C_{33}}\frac{\partial \sigma_{xx}'}{\partial t} + \frac{C_{13} - C_{11}}{C_{13}C_{13} - C_{11}C_{33}}\frac{\partial \sigma_{zz}'}{\partial t} \tag{18}$$

The storage equation of deformable soil is

$$\frac{\partial \varepsilon}{\partial t} = -\frac{1}{\gamma_w}\left(k_s\frac{\partial^2 p}{\partial x^2} + k_s\frac{\partial^2 p}{\partial z^2}\right) \tag{19}$$

$$-\frac{k_s}{\gamma_w}\left(\frac{\partial^2 p}{\partial x^2} + \frac{\partial^2 p}{\partial z^2}\right) = \frac{C_{13} - C_{33}}{C_{13}C_{13} - C_{11}C_{33}}\left(\frac{\partial \sigma_{xx}'}{\partial t} - \frac{\partial p}{\partial t}\right) + \frac{C_{13} - C_{11}}{C_{13}C_{13} - C_{11}C_{33}}\left(\frac{\partial \sigma_{zz}'}{\partial t} - \frac{\partial p}{\partial t}\right) \tag{20}$$

The time averages of $\Delta\sigma_x$, $\Delta\sigma_z$, $\Delta\tilde{p}$ can be zero, the residual component can be expressed by

$$\frac{\partial \bar{p}}{\partial t} = \frac{k_v k_s}{\gamma_w}\left(\frac{\partial^2 \bar{p}}{\partial z^2} + \frac{\partial^2 \bar{p}}{\partial z^2}\right) + f(x, z, t) \tag{21}$$

where $k_v = (C_{13}C_{13} - C_{11}C_{33})/(2C_{13} - C_{33} - C_{11})$ stands for the bulk modulus of cross-anisotropic soil of 2D problem.

2.3 Governing Equations for Tunnel

In this paper, the immersed tunnel is considered to be impermeable elastic medium with large stiffness. The governing equation can be

$$G_t\left(\frac{\partial^2 u_t}{\partial x^2}+\frac{\partial^2 u_t}{\partial z^2}\right)+\frac{G_t}{1-2\nu_t}\frac{\partial}{\partial x}\left(\frac{\partial u_t}{\partial x}+\frac{\partial w_t}{\partial z}\right)=0 \tag{22}$$

$$G_t\left(\frac{\partial^2 w_t}{\partial x^2}+\frac{\partial^2 w_t}{\partial z^2}\right)+\frac{G_t}{1-2\nu_t}\frac{\partial}{\partial z}\left(\frac{\partial u_t}{\partial x}+\frac{\partial w_t}{\partial z}\right)+\rho_t g=0 \tag{23}$$

where u_t and w_t means the displacements of x and z directions, ρ_t is density of tunnel, G_t and ν_t donate the shear modulus and Poisson's ratio of the tunnel.

2.4 Boundary Conditions

In this study, we consider ocean waves spread on a porous seabed with limited thickness above a rigid impermeable bottom (see Fig. 1). And no relative displacement occurs on the outer surface of tunnel, the pore pressure of the seabed, bedding, backfill is continuous. There are no vertical shear stress and effective stress on the surface of seabed and the residual pore pressure is considered as zero: $\sigma'_{zz}=\tau_{xz}=0$, $\bar{p}=0$, $p=p_b$. There are no vertical flow and displacement for soils of lateral boundaries and impermeable rigid bottom: $u_s=w_s=0$, $\frac{\partial\bar{p}}{\partial z}=\frac{\partial\tilde{p}}{\partial z}=0$. The inner surface of tunnel is free of stress while the outer surface of the tunnel is considered impermeable without pore pressure: $\frac{\partial\bar{p}}{\partial z}=\frac{\partial\tilde{p}}{\partial z}=0$.

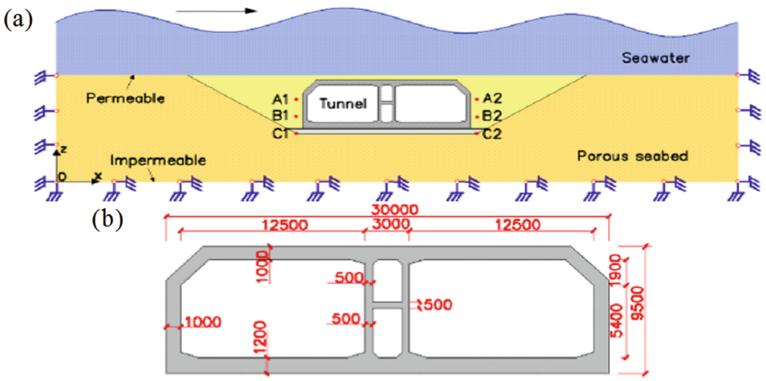

Fig. 1. (a) Schematic of the model, (b) main dimensions of immersed tunnel (Unit: mm).

3 Numerical Results and Discussion

Model configuration of the immersed tunnel buried in seabed in this paper is 200 m × 30.5 m and input data are provided in Table 1.

Table 1. Input data of numerical study.

Wave parameters		Seabed parameters		Tunnel parameters	
Wave height	5 m	Soil porosity	0.42	Young's modulus	35 GPa
Wave period	8 s	Saturation degree	1	Burial depth	1 m
Water depth	16 m	Soil permeability	10^{-5} (m/s)	Poisson's ratio	0.18
Wave length	83.4 m	N	0.33–0.5	Density	2700 (kg/m^3)
		M	0.6–1.0		

3.1 Validation of the Present Model

So far lots of investigations of marine structures such as pipelines have been carried out. However, available data related to immersed tunnel are quite limited. So the present model is simplified without tunnel to compare with experimental data [15]. The initial mean effective stress without structure is $\sigma_0' = (1+2K_0)(\rho - \rho_f)gz/3$. The parameters for the comparison are: $T = 1.6\,s$, $H = 0.18\,m$, $h = 0.4\,m$, $k_f = 1.5 \times 10^{-5}\,m/s$, $\rho_s = 2650\,kg/m^3$, $n = 0.51$, $G_s = 1.92\,MPa$, $v_s = 0.29$, $D_r = 0.28$, $S_r = 1.0$, $K_0 = 0.42$. The time variations of the period-averaged residual pore pressure calculated by this model is compared with experiment date (see Fig. 2). The consistency of the results from present model and experimental data shows that the present model can predict the oscillatory mechanism reliably.

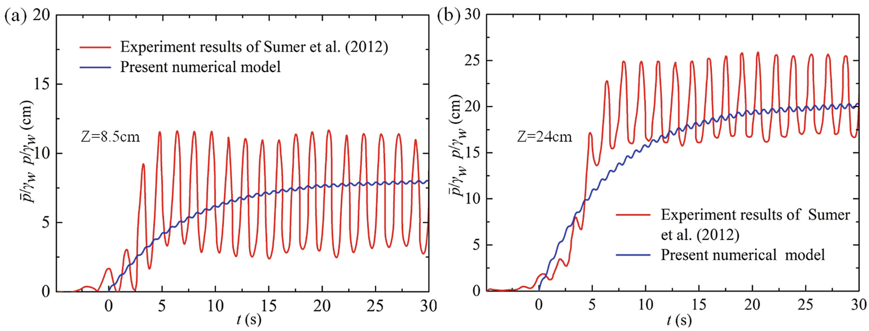

Fig. 2. Comparison of residual pore pressure with experimental data.

3.2 Wave-Induced Residual Liquefaction of Seabed

The criterion to identify the residual liquefaction zone can be expressed as $\frac{\bar{p}(x,z,t)}{\sigma_0'(x,z)} \geq 1$.

In this study, six locations are selected to investigate the development of residual pore pressure (see Fig. 3). It can be observed that liquefaction occurs first closer to the seabed surface. Ocean waves are considered to propagate from the left side of tunnel to the right, then liquefaction first occurs in soils outside the right side of the tunnel. Which may result in uneven liquefaction distribution in the seabed at the tunnel's base. Then development of liquefaction area with different wave cycle is investigated (see Fig. 4).

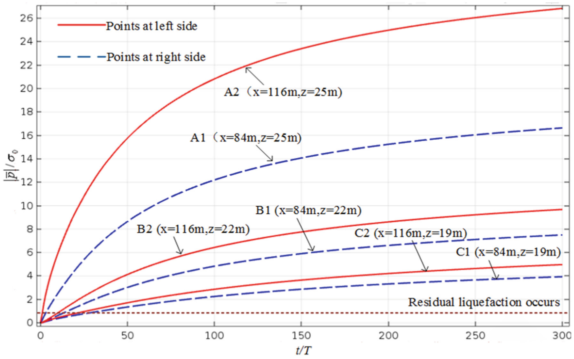

Fig. 3. Development of the residual pore pressure $\left(|\bar{p}|/\sigma_0'\right)$ versus time (t/T) for 6 points

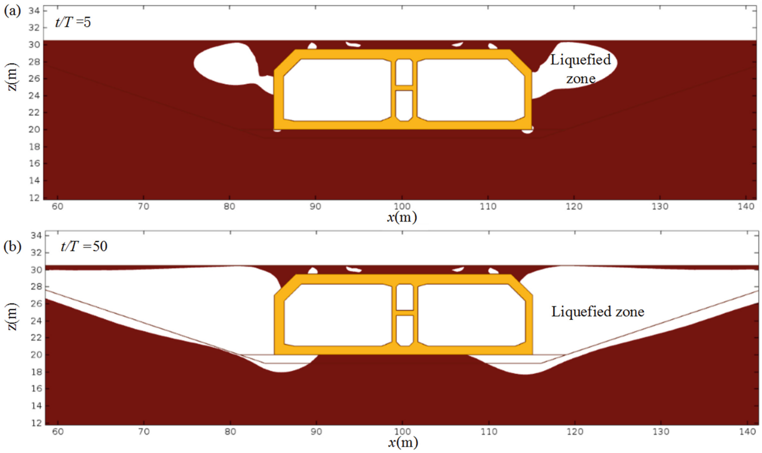
(a)
t/T =5
Liquefied zone
z(m)
x(m)
(b)
t/T =50
Liquefied zone
z(m)
x(m)
34
32
30
28
26
24
22
20
18
16
14
12
60
70
80
90
100
110
120
130
140

Fig. 4. Liquefaction zone with different wave cycle (*t*/*T*)

Liquefaction occurs in the seabed near the external parts of tunnel with irregular shape and then develops outward.

3.3 Comparison Between Soil Cross-anisotropy and Isotropy

To discuss on the effects of the soil cross-anisotropy behaviors, the effects of the anisotropic constants M and N are investigated. The development of liquefaction potential near the tunnel with various M is shown in Fig. 5. It is found that the anisotropic constant M significantly affects the liquefaction potential around an immersed tunnel. The development of liquefaction area with various N is also investigated. It can be found that the liquefaction area develops deeper as N increases (see Fig. 6).

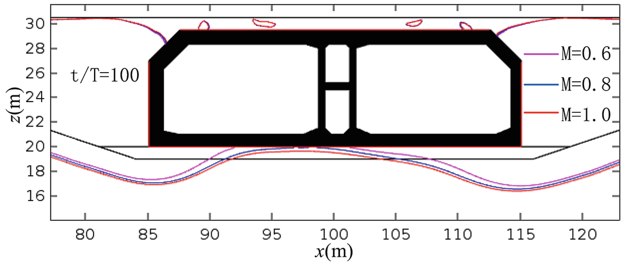

Fig. 5. Liquefaction potential with different M.

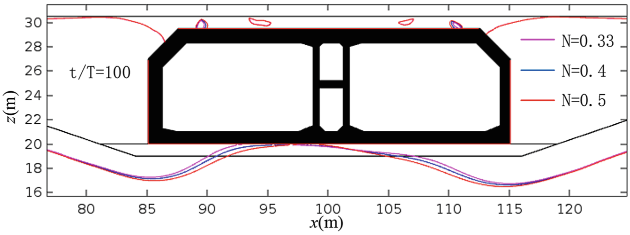

Fig. 6. Liquefaction potential with different N.

4 Conclusions

In this study, we developed a numerical model to investigate the problem of wave-seabed-tunnel interaction with soil cross-anisotropy behaviors. Based on the numerical results presented, the following conclusions can be draw:

(1) The validation shows that the model can predict the buildup of residual pore pressure around the immersed tunnel reliably.
(2) The development of liquefaction area is asymmetric naturally which could result in the uneven liquefaction deformation.
(3) Compared with isotropic soil, the pore pressure can accumulate to a larger value in the cross-anisotropic soil, so the liquefaction is more likely to occur.
(4) M and N can significantly affect the maximum depth of residual liquefaction. The liquefaction potential around the tunnel is more likely to occur as N and M increase.

Acknowledgements. The authors are grateful for the support provided by the National Natural Science Foundation of China (No. 41502285), Natural Science Foundation of Jiangsu Province (No. BK20150952), and Postgraduate Research & Practice Innovation Program of Jiangsu Province (No. SJCX17_0279). China Scholarship Council is also acknowledged by the second author for supporting him during his visiting in the Griffith University.

References

1. Zen, K., Yamazaki, H.: Oscillatory pore pressure and liquefaction in seabed induced by ocean waves. Soils Found. **30**(4), 147–161 (1990)
2. Sumer, B.M., Fredsøe, J.: The Mechanism of Scour in the Marine Environment. World Scientific Publishing Co. Pte Ltd., Singapore (2002)
3. Kiyomiya, O.: Earthquake-resistant design features of immersed tunnels in Japan. Tunn. Undergr. Sp. Tech. **10**(4), 463–475 (1995)
4. Seed, H.B., Rahman, M.S.: Wave-induced pore pressure in relation to ocean floor stability of cohesionless soils. Mar. Geotechnol. **3**(2), 123–150 (1978)
5. McDougal, W.G., Tsai, Y.T., Liu, P.L.F., Clukey, E.C.: Wave-induced pore water pressure accumulation in marine soils. J. Offshore Mech. Arct. Eng. **111**(1), 1–11 (1989)
6. Jeng, D.S., Seymour, B.R., Li, J.: A new approximation for pore pressure accumulation in marine sediment due to water wave. Int. J. Numer. Anal. Methods Geomech. **31**(1), 53–69 (2007)
7. Gatmiri, B.: Response of cross-anisotropic seabed to ocean waves. J. Geotech. Geoenviron. **118**(9), 1295–1314 (1992)
8. Wang, X., Jeng, D.S., Lin, Y.S.: Effects of a cover layer on wave-induced pore pressure around a buried pipe in an anisotropic seabed. Ocean Eng. **27**, 823–839 (2000)
9. Jeng, D.S., Lin, Y.S.: Poroelastic analysis of the wave-seabed interaction problem. Comput. Geotech. **26**, 43–64 (2000)
10. Gao, F.P., Jeng, D.S., Sekiguchi, H.: Numerical study on the interaction between non-linear wave, buried pipeline and non-homogenous porous seabed. Comput. Geotech. **30**, 535–547 (2003)
11. Hua, L.N., Yu, X.P.: Element-free Galerkin method for response of stratified seabed under wave action. J. Hydrodyn. **21**(4), 550–556 (2009)
12. Kasper, T., Steenfelt, J.S., Pedersen, L.M., Jackson, P.G., Heijmans, R.W.M.G.: Stability of an immersed tunnel in offshore conditions under deep water wave impact. Coastal Eng. **55** (9), 753–760 (2008)
13. Sassa, S., Sekiguchi, H.: Analysis of wave-induced liquefaction of sand beds. Géotechnique **51**(2), 115–126 (2001)
14. Jeng, D.S., Zhao, H.Y.: Two-dimensional model for accumulation of pore pressure in marine sediments. J. Offshore Mech. Arct. Eng. **141**(3), 04014042 (2014)
15. Sumer, B.M., Ozgur Kirca, V.S., Fredsøe, J.: Experimental validation of a mathematical model for seabed liquefaction under waves. Int. J. Offshore Polar Eng. **22**(2), 133–141 (2012)

Numerical Analysis of Tunnelling in Sand - A Case Study of a Centrifuge Test

Bowen Yang(✉) and Alan Bloodworth

The University of Warwick, Coventry CV4 7AL, UK
B.Yang.2@warwick.ac.uk

Abstract. Ground movement induced by TBM tunnelling in sand has been the subject of much discussion in recent years. It is commonly agreed that prediction of the ground movement trough in cohesionless soil is not easy. The main cause of ground movement in TBM projects is the tunnel volume loss induced by shield over-cutting and the dimensional difference between the shield and the lining. Numerical modelling could be a useful tool for ground movement prediction especially when dealing with projects where complex underground structures and strata distributions are involved. This paper employs the commercial FEM software Plaxis 3D in simulating of a centrifuge TBM tunnelling prototype using the constitutive model suggested by the software in analyzing behaviour of sands. Some popular empirical and analytical approaches of predicting ground movements are also adapted for the purpose of comparing with the numerical results.

Keywords: Tunnelling in sands · Numerical modelling · Analytical solution

1 Background

With the use of the finite element method, [1] noticed that with a simple linear elasto-plastic constitutive model, the predicted settlement trough is wider than the observed trough in sandy soil. Non-linear elasto-plastic behaviour (non-linear elastic pre-yield behaviour; plastic deformation based on plastic potential after initial yield surface reached) with Mohr-Coulomb yield surface (e.g. the hardening soil model used in this report) sometimes with anisotropy considerations forms the basis of current popular constitutive models for soft ground. With the use of these elasto-plastic constitutive models, numerous researchers have analyzed soft ground tunnelling cases [2, 3]. Some recent studies have considered more complex problems, such as subsurface/surface structure ground interaction [4, 5] and 3D effects [3, 6] which aim to analyze both longitudinal and transverse ground movements. In this paper, the hardening soil model is used. The basic idea of the hardening soil model [7] is as follows:

$$\begin{aligned} \varepsilon_1 &= \frac{1.11q_f}{2E_{50}} \frac{(\sigma_1 - \sigma_3)}{1.11q_f - (\sigma_1 - \sigma_3)} \quad \mathit{for}\ q < q_f \\ E_{50} &= E_{50}^{ref} \left(\frac{\sigma_3 + c\ \cot\phi}{\sigma^{ref} + c\ \cot\phi} \right)^m \end{aligned} \tag{1}$$

© Springer Nature Singapore Pte Ltd. 2018
D. Zhang and X. Huang (Eds.): GSIC 2018, *Proceedings of GeoShanghai 2018 International Conference: Tunnelling and Underground Construction*, pp. 250–259, 2018.
https://doi.org/10.1007/978-981-13-0017-2_25

Where ε_1 is the axial strain; q is the deviatoric stress; the confining stress dependent stiffness modulus is expressed as E_{50}; E_{50}^{ref} is the reference modulus dependent on the reference stress; q_f is the ultimate deviatoric stress.

Of particular relevance to this study is the set of centrifuge tests performed by [8]. The size of the model tunnel is 62 mm in diameter with its axis level at a depth of 180 mm. With a centrifuge scaling factor N of 75, the centrifuge model represents a 4.65 m diameter tunnel with axis depth of 13.65 m. The centrifuge test considers the particular situation in TBM tunnelling where the majority of the ground deformation occurs above the tunnel crown, by using a fixed brass cylinder inside the latex tunnel model.

The current study uses a finite element surface contraction model to simulate the centrifuge tests. The tunnel profile is defined as a contractive surface in the FEM model. The area of the tunnel section will uniformly contract by a pre-set value before the calculation proceeds. The aim of the current preliminary study is to explore the capability of the hardening soil model and the surface contraction model to predict the ground settlement in sand, and to compare the results with the analytical approaches.

2 The Model

The geometry of the FEM model (Fig. 1) is consistent with the centrifuge model used by [8]. The larger cylinder representing the latex membrane is free to move in all directions. The smaller cylinder of plate elements representing the brass cylinder is prescribed as zero deformation in all three directions. As suggested by the Plaxis 3D manual [9], both ‘Hardening soil model’ and ‘Hardening soil model with small strain stiffness’ can provide reasonable results when simulating sand behaviour. Most tunnel projects involve quite large shear strains ($1e^{-3}$–$1e^{-2}$) [10]. Therefore, this FEM model will use the Hardening soil model for FEM calculation.

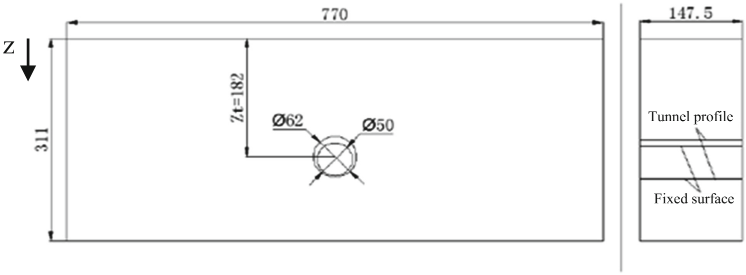

Fig. 1. Geometry of FEM model (all dimensions in mm).

The box was filled with dry Leighton Buzzard Fraction E silica sand. Many researchers have used this type of soil for laboratory tests and have provided useful parameters. This sand has an initial void ratio of 0.68 in the strong box before testing [11] and maximum and minimum void ratios of 0.97 and 0.63, respectively [12], therefore, the dilatancy cut-off option in Plaxis 3D parameter setting should be activated so that the maximum void ratio is not exceeded. The initial unit weight of the soil was 16.0 kN/m^3 [13]. With the consideration of the scaling factor N of 75, the unit weight of the soil is taken as 1200 kN/m^3 in this FEM model as shown in Table 1. Therefore, the mean effective stress p0 at tunnel level will be 214 kPa. According to [13], with p_0 = 210 kPa, the friction angle φ is taken as 41° and Young's modulus E is taken as 300 MPa. Based on the Plaxis 3D manual, for sands, the cohesion c and dilatancy angle ψ are set as 0 kN/m^3 and 10° respectively. The dry silica sand was poured in layers using an automatic sand pourer in the centrifuge tests and no over-consolidation is applied, thus K_0 is 1 − sinφ in this FEM model, which equals 0.34.

Table 1. Soil parameters.

Parameter		Value	Unit
Unit weight	γ	1200	kNm^3
Young's modulus	E	30	Mpa
Ratio of horizontal effective stress	K_0	0.34	
Cohesion	c	0	kN/m^2
Friction angle	φ	41	°
Dilatancy angle	ψ	10	°
Initial void ratio	e_{ini}	0.68	
Minimum void ratio	e_{min}	0.63	
Maximum void ratio	e_{max}	0.97	

In the centrifuge test, $V_{l,t}$ was controlled by extracting the liquid between the latex tunnel and the brass cylinder. It is straightforward that the volume of the extracted fluid becomes the tunnel volume loss $V_{l,t}$ of the prototype tunnel. The extraction of the fluid is controlled by an electric powered piston system. To achieve stable tunnel deformation, the rate of tunnel volume loss (rate of extracting fluid) is set to 3 %/min thus the movement of the piston is set as 0.64 mm/min [8]. To replicate this procedure in the FEM model, plate elements are defined around the tunnel profile. Then a uniform contraction of these tunnel plate elements is prescribed before calculation. The FEM model ready for calculation is shown in Fig. 2. The deformed tunnel profile in Fig. 3 illustrates that the deformation pattern of the tunnel model matches the desired pattern observed in the centrifuge test.

3 The Model

3.1 Settlement Troughs

The settlement trough profiles at the surface (z = 0 mm), z = −70 mm (z/z_t = 0.38) and z = −120 mm (z/z_t = 0.66) are plotted in Fig. 4. As illustrated in Fig. 4(a), the surface settlement troughs predicted by the FEM model are well consistent with the centrifuge data when the tunnel volume loss is very low ($V_{l,t}$ = 0.5%). As $V_{l,t}$ increases,

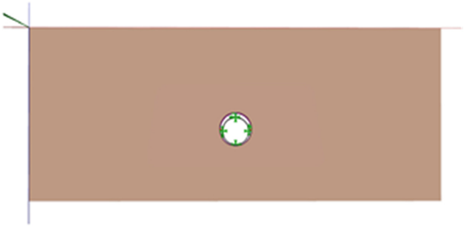

Fig. 2. The FEM model.

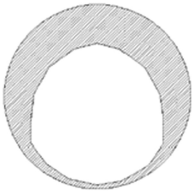

Fig. 3. Deformed tunnel when $V_{l,t} = 5.0\%$ in FEM.

both the magnitude and the width of the surface settlement troughs are underestimated by the FEM model for medium tunnel volume loss ($V_{l,t} = 1.0\%$ and $V_{l,t} = 2.5\%$). This scenario may suggest that the surface settlement predicted by the surface contraction model becomes less conservative when the tunnel volume loss is increasing. However, when $V_{l,t}$ increases to 5.0% the maximum settlement value predicted by the surface contraction model surprisingly is in good agreement with the centrifuge data, although the predicted trough is generally narrower than the centrifuge data.

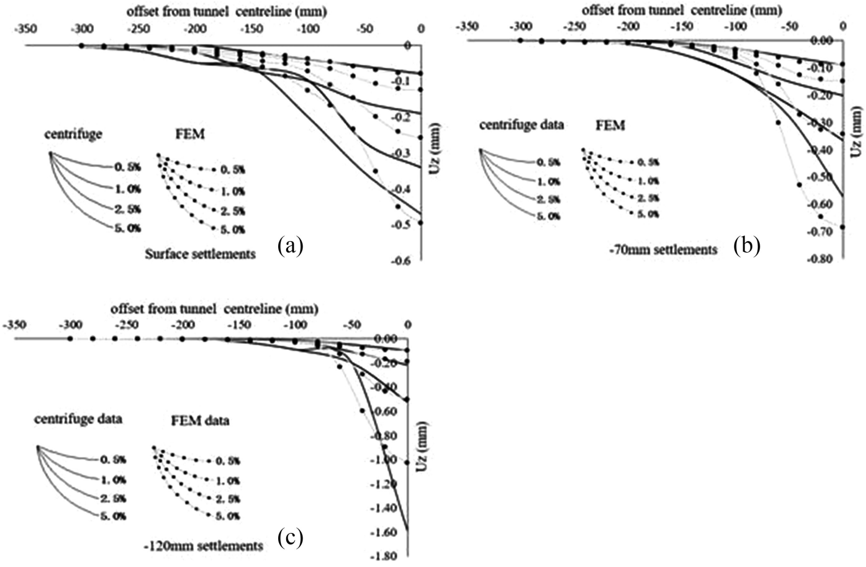

Fig. 4. Settlement troughs

In terms of the predicted troughs at z = −70 mm and z = −120 mm, the numerical results are generally good when $V_{l,t} = 0.5\%$. According to Fig. 4(b) and (c), when $V_{l,t}$ increases, the numerical results either give shallower troughs or over-estimated deeper troughs. Interestingly, sometimes (e.g. $V_{l,t}$ = 1.0% and 2.5% at −120 mm depth) the numerical results match the centrifuge data well. When it comes to numerical modelling in clay, people can at least say the numerical results are always wider and shallower compared to field data [14]. However, it seems like there is no common defect of the numerical results of modelling problems in sand.

The reason causing the oscillation of the accuracy of the numerical results could be the contracting/dilating behaviour of sand. In an undrained soil, from surface to tunnel level, the soil volume loss is consistent with the tunnel volume loss [15] whereas for drained soils such as sand and gravels, shearing causes contraction and dilation which lead to an inconsistent $V_{l,s}$:$V_{l,t}$ ratio [11, 15].

3.2 Dilation and Contraction

For all tunnel volume loss ranges, in both centrifuge test and numerical modelling, the ground movement becomes negligible when the offset to tunnel centerline is larger than 300 mm. Therefore, the soil volume loss is calculated by integrating the settlement curves within 300 mm offset to tunnel centerline. Soil volume loss ratio to tunnel volume loss ratio is plotted in Fig. 5. According to [13]'s triaxial compression test data for the Leighton Buzzard Fraction E silica sand, when the confining pressure is 200 kPa (the effective stress at tunnel level in the FEM model is 214 kPa), the soil shows a contraction tendency when the shear strain is less than 0.3%, and a dilation tendency when the shear strain is larger than 0.3%. This soil contracting/dilating phenomenon can be seen in Fig. 5, where the slope of tangent of the $V_{l,s}$:$V_{l,t}$ curve > 1 illustrates the soil is in contracting behaviour; the slope of tangent < 1 means the soil is in dilating behaviour.

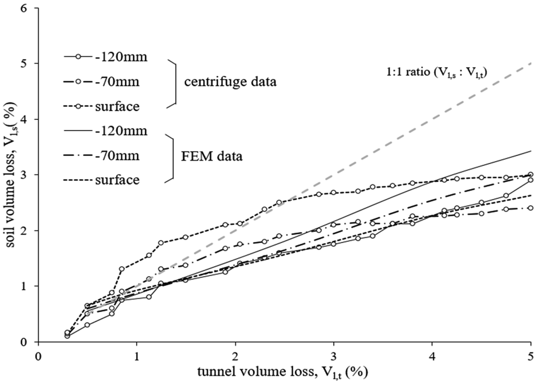

Fig. 5. Soil volume loss to tunnel volume loss ratio.

Overall, for small values of tunnel volume loss, the FEM surface contraction model can give relatively accurate simulation results from the surface to 120 mm depth. From

$V_{l,t}$ = 1.0% upwards, the FEM data either underestimate or exaggerate the ground vertical displacement and sometimes by chance gives an accurate S_{max} value:

(a) At surface, when $V_{l,t}$ = 1.0% and 2.5%, as the soil is characterized by contracting behaviour and the surface volume loss is greater than the tunnel volume loss, the actual ground settlement is larger than the FEM data. When $V_{l,t}$ = 5.0%, the dilating soil slows down the ground settlement, this causes the S_{max} predicted by the FEM model to match the centrifuge data in Fig. 4(a), even though the FEM model has failed to model the contracting-dilating behaviour. (b) Soil at −70 mm level experiences a dilatant behaviour from around $V_{l,t}$ = 2.0% to $V_{l,t}$ = 5.0% which lead to a predicted S_{max} much larger than the centrifuge data when $V_{l,t}$ = 5.0%. (c) The FEM data at z = −120 mm level are generally good when $V_{l,t}$ = 0.5% to 2.5% (soil dilating). When the stabilized area of volumetric strain area is generated above the tunnel crown and reaches z = −120 mm level as $V_{l,t}$ reaches 5.0%, the FEM data become conservative.

Therefore, the key reason for the irregular oscillation of the accuracy of the FEM prediction is that the hardening soil model is unable to simulate the contracting and dilating behaviour of sand during shearing.

3.3 Comparison with DEM

[16] used a discrete element method (DEM) line-sink model to predict the shape of the surface settlement trough induced by volume loss in sandy soil. The tunnelling process was simulated by removing soil particles successively. For the purpose of comparing with the FEM results, only the shape of the settlement troughs will be analyzed here, thus the values of $V_{l,t}$ and S_{max_surf} are of less importance. Comparison of the FEM surface contraction method, DEM line sink method and centrifuge settlement trough shape is shown in Fig. 6, where the settlement troughs at different $V_{l,t}$ values are normalized by their maximum vertical displacements. Regardless of the S_{max_surf} value (maximum settlement at the surface), the DEM and FEM models can predict a relatively good settlement trough shape. However the troughs predicted by the two

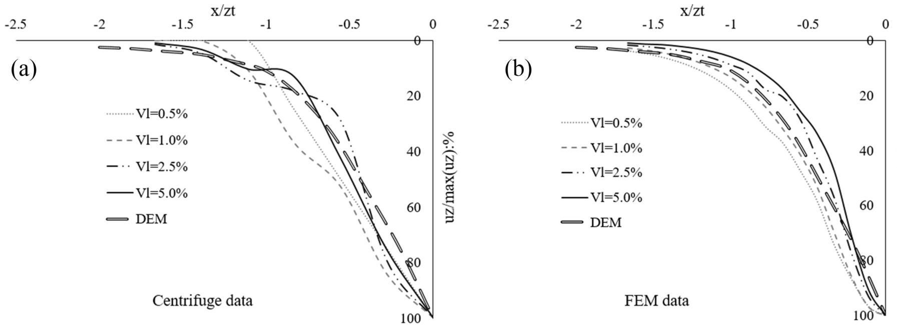

Fig. 6. Fitting the shape of surface settlement troughs to the DEM data. u_z is the vertical displacement. $max(u_z)$ is the maximum vertical displacement.

numerical methods are both very smooth curves which is not consistent with the 'chimney' settlement mechanism observed from the centrifuge data resulting in platform patterns in the settlement trough.

According to Fig. 6(a), a small platform can be identified on the settlement curve when $V_{l,t}$ = 1.0%, 2.5% and 5.0%. This is due to the two near vertical shear bands generated from the tunnel shoulder and below the tunnel to the surface. The platform just located between the two shear bands as soil between shear bands moves downwards as a rigid body [8] within which there is no large vertical relative displacement. Obviously, none of the two numerical methods is able to simulate the effects induced by the two pairs of shear bands.

3.4 Comparison with Empirical and Analytical Methods

The empirical Gaussian curve [17] has been widely used in predicting the surface settlement trough in undrained soil. It gives the surface settlement as

$$S_{v,x} = S_{\max} \exp\left(-x^2/2i^2\right) \tag{2}$$

where $S_{v,x}$ stands for vertical settlement, $S_{\max}$ is the vertical settlement value at the tunnel centerline, x is the horizontal offset from the tunnel centerline, and i is the horizontal distance from the tunnel centerline to the inflexion point of the settlement trough where the curve transforms from hogging to sagging. For drained soil like sands, however, the Gaussian curve does not always provide a reasonable fit [18, 19]. The surface settlement trough is found to be generally narrower than the Gaussian curve [11, 20, 21]. In addition, with larger $S_{\max}$, settlement tends to cause narrower trough width due to the 'chimney' mechanism in sand. To obtain better fit to the settlement data in sand, [11] provided a modified Gaussian curve of the following form:

$$\begin{aligned} S_{v,x} &= \frac{n \cdot S_{\max}}{(n-1) + \exp\left[\alpha(x/i)^2\right]} \\ n &= e^{\alpha} \cdot \frac{2\alpha - 1}{2\alpha + 1} + 1 \end{aligned} \tag{3}$$

where n is a function parameter which controls the width of the curve; and α is the parameter that ensure i remains the distance to the inflection point from the tunnel central line.

Apart from the two popular empirical methods, some researchers have developed analytical methods to predict the volume loss induced ground movement. [23] extended [22]'s linear elastic assumption when predicting volume loss induced ground deformation by considering soil compression and tunnel ovalization. The shape of the predicted trough is highly depend on the ratio ε/δ. ε and δ here are calculated according to the $V_{l,t}$ value and the deformed tunnel profile in the FEM model. [23]'s method may not always to be accurate when considering TBM tunnelling in sand, as most tunnels built in sand use TBMs for which most of the ground movement is concentrated around the tunnel crown [14]. Therefore, [24, 25] state that the actual ground deformation for a sand mass forms a non-concentric elliptical ring. [24] modified [23]'s method by incorporating the gap parameter g representing the space between the final position of the tunnel lining crown and the original position of the remaining ground after excavation. As there is currently no knowledge about how much g should be for a similar TBM tunnel, g is set to 0.00327 so that the calculated S_{max_surf} matches the centrifuge data. The solution proposed by [24] is as follow:

$$\begin{aligned} u_x &= -R^2 x\left[\frac{1}{x^2+(H-z)^2}+\frac{3-4v}{x^2+(H+z)^2}-\frac{4z(z+H)}{x^2+(H+z)^2}\right] \\ &\cdot \frac{4gR+g^2}{4R^2}\exp\left\{-\left[\frac{1.38x^2}{(H+R)^2}+\frac{0.69z^2}{H^2}\right]\right\} \\ u_z &= R^2\left\{-\frac{z-H}{x^2+(z-H)^2}+(3-4v)\frac{z+H}{x^2+(z+H)^2}-\frac{2z\left[x^2-(z+H)^2\right]}{\left[x^2+(z+H)^2\right]^2}\right\} \\ &\cdot \frac{4Rg+g^2}{4R^2}\exp\left\{-\left[\frac{1.38x^2}{(H+R)^2}+\frac{0.69z^2}{H^2}\right]\right\} \end{aligned} \tag{4}$$

where u_x and u_z are the horizontal and vertical deformations respectively; R is the radius of the tunnel; H is the vertical distance from the surface to the tunnel axis; and g is the gap parameter.

Comparison of the surface settlement at $V_{l,t}$ = 5.0% predicted by numerical, analytical and empirical methods is shown in Fig. 7. The goodness of fit can be identified according to the coefficient of determination, R^2. R^2 closer to 1 indicating a better data fit. The calculated R^2 are shown in Table 2. Overall, the empirical methods show better agreement with the centrifuge data than the FEM model and the analytical methods.

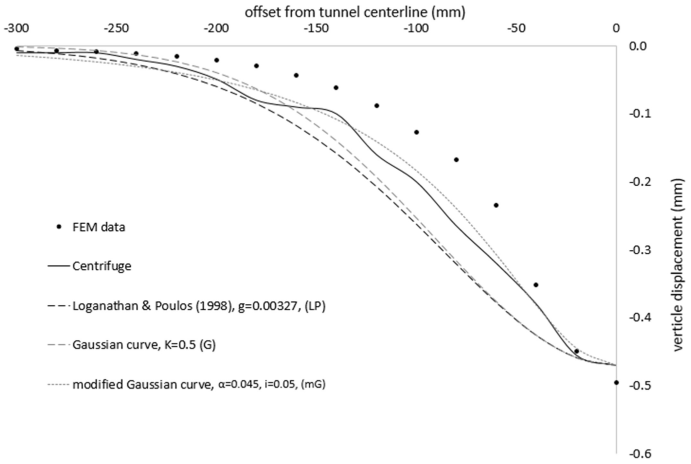

Fig. 7. Comparison of predicted surface settlement troughs.

Table 2. Values of R^2

Gaussian	Modified Gaussian	[24]	FEM
0.970	0.994	0.955	0.912

4 Conclusions

Although the numerical modelling of tunnelling has been utilized for many years, the numerical modelling of sandy ground issues has been limited. Generally, the FEM surface contraction model using the hardening soil model can give an acceptable prediction when the tunnel volume loss is relatively low. As $V_{l,t}$ increasing, the predicted results becomes less accurate due to the FEM mode is unable to simulate the soil contracting/dilating behaviour in sandy ground.

The finite element surface contraction model and the discrete-element line-sink model can give a general good surface and subsurface settlement trough shape. However none of them is able to consider the effect of the shear bands and the ‘chimney’ like mechanism. For green field condition, the FEM surface contraction model, [24]’s method and the two empirical methods mentioned above can both predict the surface settlement well ($R^2 > 0.9$). The modified Gaussian curve proposed by [11] is still the best tool to predict surface settlement induced by tunnelling in sandy ground.

Overall, this study suggest that the FEM method can give acceptable results when $V_{l,t}$ is relatively low. Further work is required to develop a new simulation model or constitutive soil model which is able to tackle the shear bands and soil contracting/dilating issues.

References

1. Manouchehr, K.: Modelling and finite element analysis of soil behavior. University of Illinois (1979)
2. Addenbrooke, T.I., Potts, D.M., Puzrin, A.M.: The influence of pre-failure soil stiffness on the numerical analysis of tunnel construction. Geotechnique **57**(3), 693–712 (1997)
3. Franzius, J.N., Potts, D.M., Burland, J.B.: The influence of soil anisotropy and K0 on ground surface movements resulting from tunnel excavation. Géotechnique **3**, 189–199 (2005)
4. Potts, D.M., Addenbrooke, T.I.: A structure’s influence on tunnelling-induced ground movements. Proc. ICE - Geotech. Eng. **125**, 109–125 (1997)
5. Burd, H.J., Houlsby, G.T.: Modelling tunnelling-induced settlement of masonry buildings. Proc. ICE - Geotech. Eng. **143**, 17–29 (2000)
6. Mroueh, H., Shahrour, I.: A simplified 3D model for tunnel construction using tunnel boring machines. Tunn. Undergr. Space Technol. **23**(1), 38–45 (2008)
7. Schanz, T., Vermeer, P., Bonnier, P.: The hardening soil model: formulation and verification. In: Beyond 2000 Computational Geotechnics, pp. 1–16 (1999)
8. Marshall, A.M.: Tunnelling in sand and its effect on pipelines and piles. University of Cambridge (2009)
9. Brinkgreve, R.B., Engin, E., Swolfs, W.: PLAXIS Material Models Manual 2013. Plaxis bv, Delft (2013)

10. Atkinson, J., Sallfors, G.: Experimental determination of stress-strain-time characteristics in laboratory and in situ tests. In: Proceedings of the 10th European Conference on Soil Mechanics and Foundation Engineering, vol. 3, pp. 915–956 (1991)
11. Vorster, T.E.B., Klar, A., Soga, K., Mair, R.J.: Estimating the effects of tunneling on existing pipelines. J. Geotech. Geoenviron. Eng. **131**, 1399–1410 (2005)
12. Lee, S.: The effects of compensation injections on tunnels. Cambridge University (2001)
13. Zhao, Y.: In situ soil testing for foundation performance prediction. University of Cambridge (2008)
14. Rowe, R.K., Kack, G.J.: A theoretical examination of the settlements induced by tunnelling: four case histories. Can. Geotech. J. **20**(2), 299–314 (1983)
15. Marshall, A.M., Farrell, R., Klar, A., Mair, R.: Tunnels in sands: the effect of size, depth and volume loss on greenfield displacements. Geotechnique **5**, 385–399 (2012)
16. Bym, T., Marketos, G., Burland, J.B., O'Sullivan, C.: Use of a two-dimensional discrete-element line-sink model to gain insight into tunnelling-induced deformations. Géotechnique **63**(9), 791–795 (2012)
17. Peck, R.B.: Deep excavations and tunnelling in soft ground. In: Proceedings of 7th International Conference on SMFE, pp. 226–290 (1969)
18. O'Reilly, M.P., New, B.M.: Settlement above tunnels in the United Kingdom-their magnitude and prediction. Tunnelling 1982 papers presented at the third international symposium, pp. 173–181 (1982)
19. Celestino, T.B., Gomes, R.A.M.P., Bortolucci, A.A.: Errors in Ground Distortions Due to settlement trough adjustment. Tunn. Undergr. Space Technol. **15**(1), 97–100 (2000)
20. Mair, R.J., Taylor, R.N.: Theme lecture: bored tunnelling in the urban environment. In: The 14th International Conference on Soil Mechanics and Foundation Engineering, pp. 2353–2385 (1997)
21. Jacobsz, S.W., Standing, J.R., Mair, R.J.: Centrifuge modelling of tunnelling near driven piles. Soils Found. **44**(1), 49–56 (2004)
22. Sagaseta, C.: Analysis of undraind soil deformation due to ground loss. Geotechnique **37**(3), 301–320 (1987)
23. Verruijt, A., Booker, J.R.: Surface settlements due to deformation of a tunnel in an elastic half plane. Geotechnique **46**(4), 4–7 (1996)
24. Loganathan, N., Poulos, H.G.: Analytical prediction for tunneling-induced ground movements in clays. J. Geotech. Geoenviron. Eng. **124**, 846–856 (1998)
25. Park, K.H.: Analytical solution for tunnelling-induced ground movement in clays. Tunn. Undergr. Space Technol. **20**(3), 249–261 (2005)

Mechanical Behavior of Tunnel Lining and Segmental Joints

A Prototype Load Test on Fracture and Damage Properties of Cracked Shield Tunnel Lining Segments

Longgang Tian[1,2](✉), Qi Zhang[1,2], Xiao Wang[2],
and Guangchao Zhang[3]

[1] Key Laboratory of Concrete and Prestressed Concrete Structures of Ministry of Education, Southeast University, Nanjing 210096, China
`lgtian@seu.edu.cn`
[2] Institute of Future Underground Space,
Southeast University, Nanjing 210096, China
[3] Department of Geotechnical Engineering,
Tongji University, Shanghai 200092, China

Abstract. In this paper, a prototype load test on cracked shield tunnel lining segment was conducted to study fracture properties of the segment with initial crack. Principle and process of the test were introduced, and test phenomena were detailedly depicted. Experimental results reveal that lining segment with initial crack finally shows the I-type fracture property, and the failure mode is dominated by the initial crack. Deformation and damage of the specimen show obvious phases, which consist of initial crack, cracking stage, steady crack propagation, unsteady crack propagation and eventual failure. Fracture energy of the specimen is also estimated through the measured load-displacement curve.

Keywords: Prototype load test · Shield tunnel · Lining segment
Fracture property

1 Introduction

With the progress of construction technology in underground engineering, shield tunnel has gradually become the main form of urban metro tunnel. The supporting structure of shield tunnel is precast reinforced concrete lining segment, which may contain various flaws in the pouring of concrete or the assembling of lining ring. These flaws reduce the effective force-bearing area of the lining segment, thus deteriorate the safety of the shield tunnel. In the worst situation, it may cause failure of the shield tunnel.

As one of the most effective methods to study mechanical behavior of the shield tunnel, load test has aroused the interests of many researchers in this research field. Huang et al. [1] conducted prototype load test on the lining segment of Qingcaosha water-conveyance tunnel in Shanghai, and studied the deformation law of the segment joints. Xia [2] studied the mechanical behavior of lining segments in Shiziyang Tunnel in Guangzhou, and obtained failure mode of the lining segments by load test. Guo and He [3] conducted three prototype shear tests on lining segment joints of the Nanjing

© Springer Nature Singapore Pte Ltd. 2018
D. Zhang and X. Huang (Eds.): GSIC 2018, *Proceedings of GeoShanghai 2018 International Conference: Tunnelling and Underground Construction*, pp. 263–272, 2018.
https://doi.org/10.1007/978-981-13-0017-2_26

yangtze river tunnel, and studied the deformation and failure mode of segment joints under shear force. Bi and Liu [4] studied the bearing capacity of shield tunnel by static load test, and analyzed the lining deformation, segment cracking and failure process of the lining structure. Zhou [5] explored the ultimate bearing capacity of shield tunnel lining segment, and analyzed the influences of loading mode and reinforcement ratio on ultimate bearing capacity and failure mechanism of the lining segment. Also, they obtained the practical formula for calculation of eccentric compression bearing capacity of the segment. Zhang [6] studied the ultimate bearing capacity and failure mode of composite lining segments, and established finite element analysis method for composite lining segment based on the experimental results. Wang [7, 8] conducted a systematic research on underwater shield tunnel by model test, not only about damage of the material, but also included macro local failure of the structure, and finally reached the progressive failure of the entire structure.

Joint is the weakness of the shield tunnel lining structure, which has a confidential influence on lining's bearing capacity, and cracks often initiate besides the joints. Huang [9] proposed vulnerability analysis and assessment methods of segment joints in shield tunnel, considering bending moment, shear force and penetrability. Feng and He [10] took Shiziyang Tunnel of the high-speed railway between Guangzhou and Hong Kong as an example, and conducted prototype test on the flexural behavior and failure characteristics of the complex segment joints under high axial press. Yang [11] combined model test and numerical simulation to simulate the reactions of tunnel lining and surrounding strata, and analyzed the inner stress distribution of the lining under different loads. Yang and Xie [12] explored the fracture mechanism of shield tunnel lining segment based on fracture mechanics. Their study revealed that the simplified continuum joint model could sufficiently simulate mechanical behavior of the joints when load is small, however, when the applied load is large, this model could not produce good simulation of joint fracture and concrete cracking. Yang [13] conducted large-scale model test of fatigue failure for shield tunnel under dynamic loads, and proposed fatigue law of the lining segment based on the first and second phase of the concrete damage.

The present research on shield tunnel lining segment is mainly focused on macro mechanical parameters and the computational model, little is about the ultimate condition and failure mode of lining segment. Current load tests mainly aim at intact lining segments, so researches on segment's mechanical behavior and propagation law of initial defects are not sufficient and thorough. In this paper, a prototype load test on cracked shield tunnel lining segment is conducted to study mechanical behavior, developing law of initial crack and final failure mode of the specimen. The aims are to reveal fracture and damage properties of the lining segments, and provide benchmark and guidance of disease prevention and repairing for shield tunnels in the future.

2 A Brief Introduction of the Test

2.1 Specimen Design

This prototype load test is based on the shield tunnel of Shanghai Metro Line 12. Supporting structure of the tunnel is reinforced concrete lining ring, which has an outer radius of 3.1 m, inner radius of 2.75 m, and width of 1.2 m. Concrete strength grade is C55. The configuration of reinforced bar in the lining segment is shown in Fig. 1, which is the standard case as in practical engineering. The initial crack is generated by cutting a straight crack using a small cutting machine, as shown in Fig. 2, which is 50 mm in depth, 2 mm in width and runs through the entire lining segment. Specimen with initial crack is shown in Fig. 3.

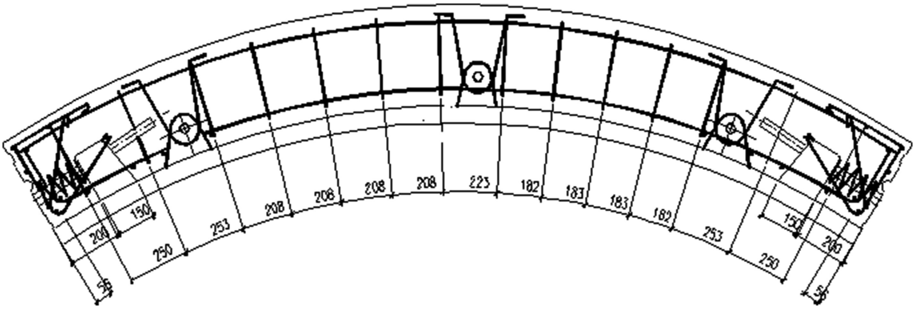

Fig. 1. Configuration of reinforced bar in the lining segment

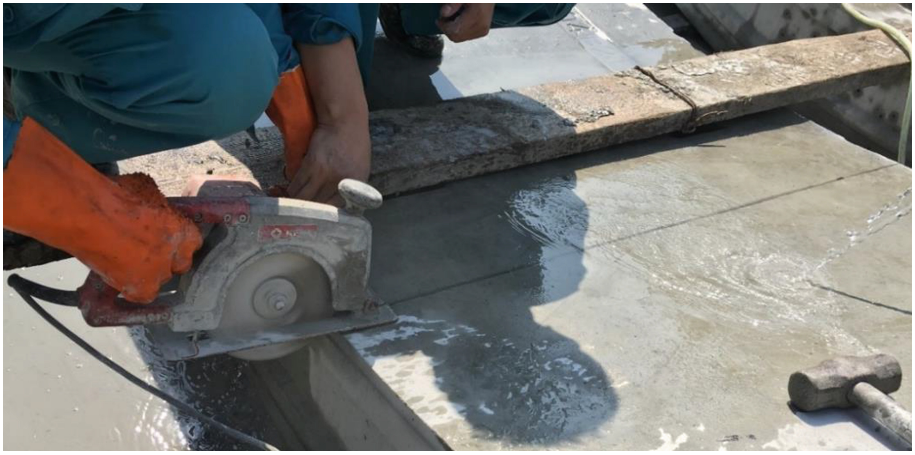

Fig. 2. Initial crack is generated using a small cutting machine

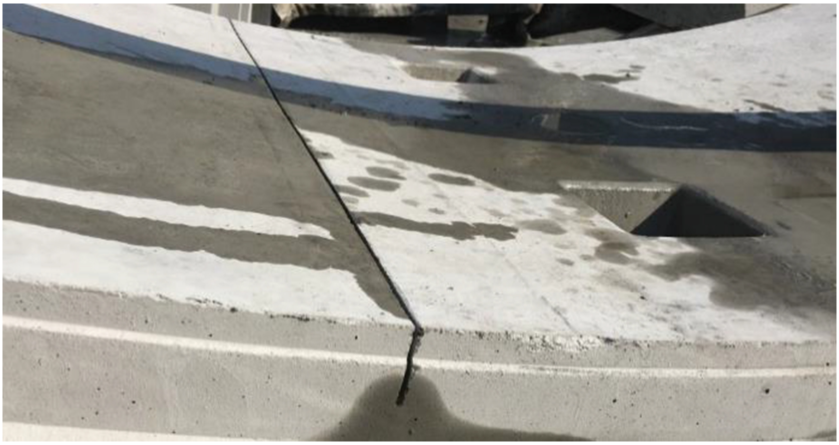

Fig. 3. Specimen of the shield tunnel lining segment with initial crack

2.2 Loading Device and Scheme

As shown in Fig. 4, the TJGPJ-2000 shield tunnel loading device is employed to conduct this test. The specimen is loaded in the four-point bending way, and the eccentricity is 0.24 m. As shown in Fig. 5, P stands for vertical load, N stands for axial load, the dimensions and initial crack are also depicted in Fig. 5.

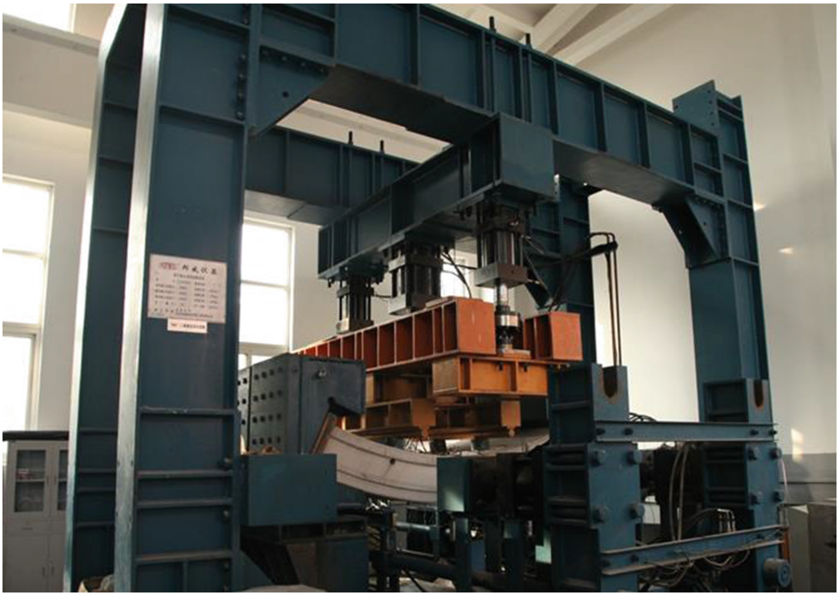

Fig. 4. Loading system of the experiment

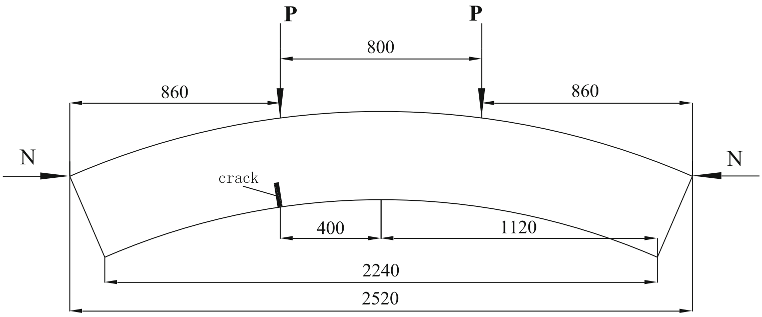
P
P
800
860
860
N
N
crack
400
1120
2240
2520

Fig. 5. Schematic diagram of the loaded specimen (unit: mm)

Because the specimen is symmetrically loaded, only half of it is used to make force analysis. As shown in Fig. 6, the moment at the centroid of the cross-section is:

$$M = (P + W)L_1 - PL_2 - WL_3 - Nh_1 \tag{1}$$

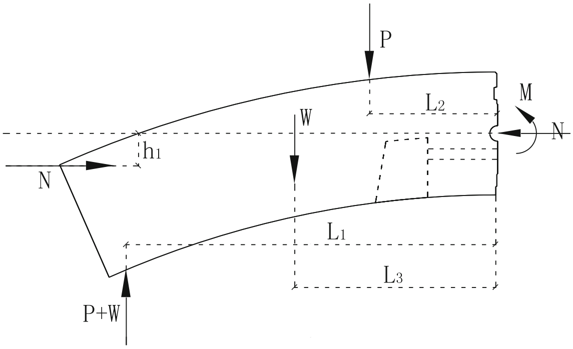
P
M
L2
W
N
h1
N
L1
L3
P+W

Fig. 6. Force analysis of the loaded specimen

The eccentricity of load is defined as:

$$e = \frac{M}{N} \tag{2}$$

The vertical load can be derived from Eqs. (1) and (2) as:

$$P = \frac{N(e + h_1) - W(L_1 - L_3)}{(L_1 - L_2)}. \tag{3}$$

2.3 Measurement of the Test

The items to be measured in this test include load, displacement, Crack Mouth Opening Displacement (CMOD), surface strain of the concrete. Load can be read by the device, displacement and CMOD are measured by displacement meter, and the surface strain of concrete is measured by resistance strain gauge. Figures 7 and 8 show measurement of the items in the test.

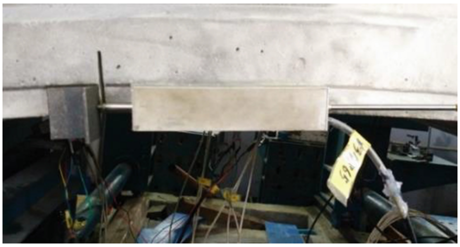

Fig. 7. Measuring CMOD by displacement meter

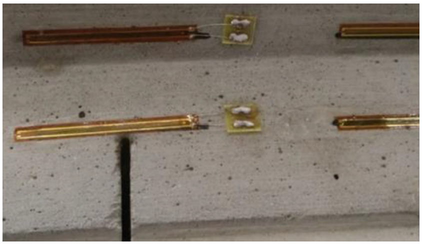

Fig. 8. Measuring the strain of concrete using resistance strain gauge

3 Experiment Phenomena

For the lining segment with initial crack in this load test, its inner surface is subjected to tension while the outer surface is subjected to compression. The initial crack opens as is subjected to tension, which shows the I-type fracture characteristics. High-resolution camera is used to capture the deformation of the specimen during loading process. Based on the deformation characteristics, cracking stages of the specimen are identified as different phases, which consist of: (a) initial crack, (b) cracking stage, (c) steady crack propagation, (d) unsteady crack propagation, (e) eventual failure. Figure 9 shows the deformation process and final failure mode of the specimen.

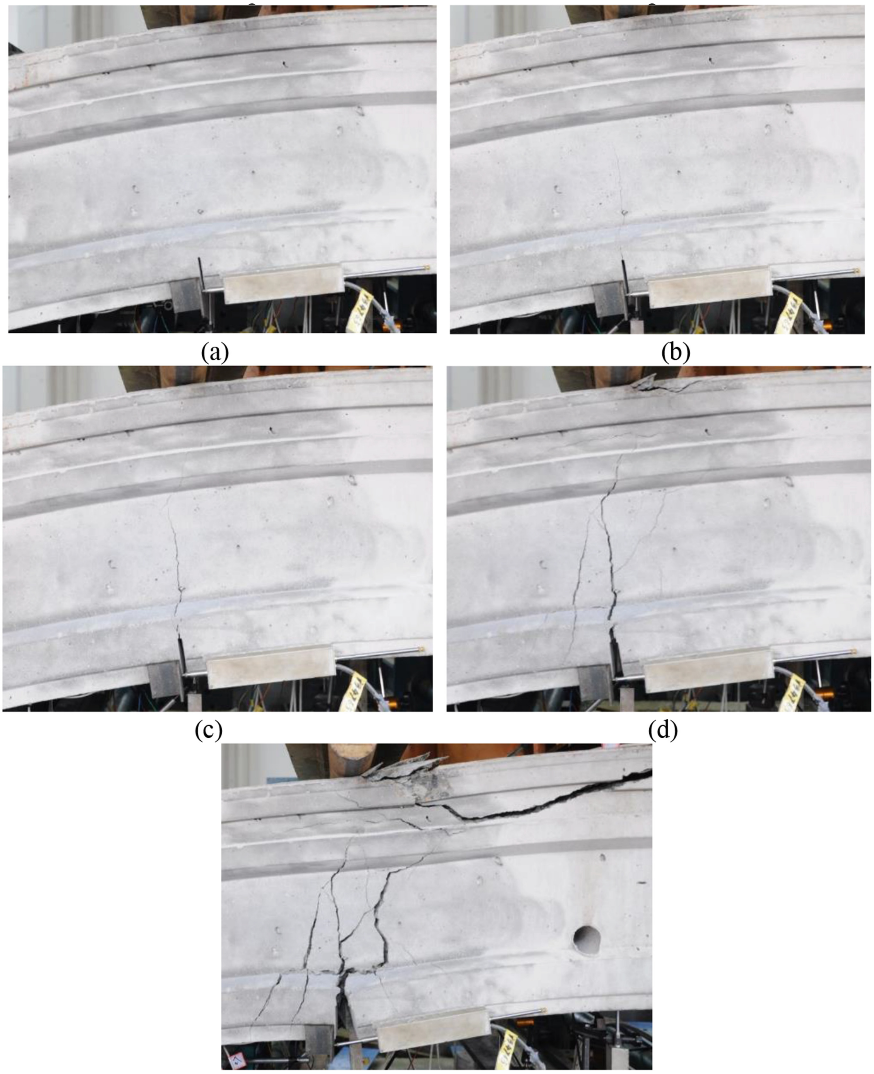
(a) (b) (c) (d) (e)

Fig. 9. The fracture and damage process of the cracked lining segment

4 Experiment Result Analysis

4.1 Bearing Capacity of the Specimen

Here, cracking load of the specimen is defined as the load that makes initial crack start to grow. Ultimate load is defined as the largest load that the specimen can bear. Figure 10 shows the variation of CMOD and vertical displacement at the loading point during the loading process. Figure 11 demonstrates the variation of load versus strain at the crack tip during the load test. The turning point in Fig. 10 is at which CMOD starts to grow, which represents the cracking load. In Fig. 11 the turning point is more obvious, which also stands for the cracking load.

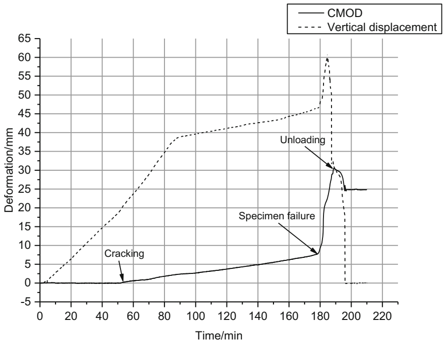

Fig. 10. Variation of CMOD and vertical displacement vs. time

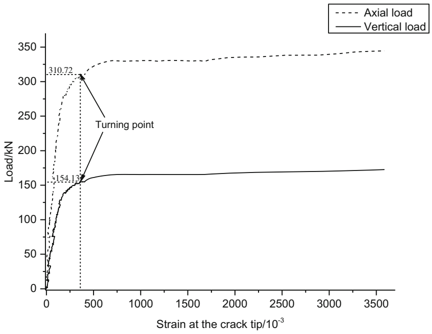

Fig. 11. Variation of load vs. strain at the crack tip

The measured cracking loads of the specimen are listed in Table 1 based on the above-mentioned methods. As can be seen, the results show good agreement with each other.

Table 1. Measured cracking load of the specimen

Method	Cracking load of the specimen	
	Axial load/kN	Vertical load/kN
Load-Strain curve	310.72	154.13
CMOD-Time curve	310.08	154.88
Error	0.21%	0.49%

In this prototype load test, the real lining segment of Shanghai Metro Line 12 is used as the specimen. The loads are increased gradually until the specimen is broken. The measured ultimate vertical load is about 767.1 kN.

4.2 Fracture Energy of the Specimen

Fracture Energy is a very important parameter for the study of concrete fracture mechanics. The definition of fracture energy is the energy consumed to form new crack surface with unit area, which is represented with the symbol G_F. Since prototype lining segment is used as the specimen in this test, the load device is not as rigid as to capture the descending stage of the load-displacement curve. Estimation of the fracture energy is based on the following Fig. 12, which shows the variation of vertical load versus displacement at the loading point.

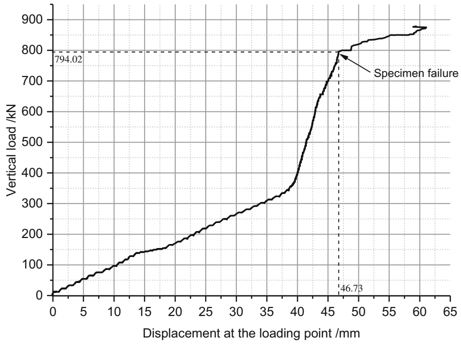

Fig. 12. Variation of vertical load vs. displacement at the loading point

When the specimen is broken, the corresponding vertical load is 794.02 kN, and displacement at the loading point is 46.73 mm. Based on the definition, the following equation can be employed to estimate fracture energy of the specimen.

$$G_F(a) = \frac{1}{(D - a_0)H} \int P d\delta \tag{4}$$

In the above equation, a_0 is the depth of the initial crack, D is the thickness of the segment, H is the width of the segment, and P is the vertical load. The area of load-displacement curve in Fig. 12 is estimated at 11.292 kN*m. Finally, fracture energy of the specimen is estimated at 31.37 kN/m.

5 Conclusions

To study the bearing capacity and fracture properties of shield tunnel lining segment with initial crack, a prototype load test is conducted. The following conclusions can be drawn:

(1) Deformation and damage of the lining segment show obvious phases, which consist of initial crack, cracking stage, steady crack propagation, unsteady crack propagation and eventual failure.
(2) The lining segment with initial crack finally shows the I-type fracture property, and its failure mode is dominated by the initial crack.
(3) Estimated fracture energy of the segment is 31.37 kN/m based on the load-displacement curve.

Acknowledgements. The authors gratefully acknowledge the support of National Natural Science Foundation of China (No. 41602300), Natural Science Foundation of Jiangsu Province (No. BK20170670), and the Fundamental Research Funds for the Central Universities (No. 3205007810).

References

1. Huang, F., Zhu, H., Ding, W., et al.: Test on mechanical behavior of segment circumferential joint of water conveyance tunnel. J. Archit. Civ. Eng. **29**(4), 38–43 (2012)
2. Xia, S.: Proto-type test of lining structure of segment rings with straight joints for Shiziyang tunnel. Southwest Jiaotong University, Chengdu (2010)
3. Guo, R., He, C., Su, Z., et al.: Study on the shear performance of segment joints in shield tunnel. Mod. Tunn. Technol. **48**(4), 72–77 (2011)
4. Bi, X., Liu, X., Wang, X., et al.: Experimental investigation on the ultimate bearing capacity of continuous-jointed segmental tunnel linings. China Civ. Eng. J. **47**(10), 117–127 (2014)
5. Zhou, H., Li, L., Chen, T., et al.: Experiments and calculation method for bearing capacity of the lining segment of metro shield tunneling. J. Shandong Univ. (Eng. Sci.) **40**(4), 84–87 (2010)
6. Zhang, W., Koizumi, A.: Behavior of composite segment for shield tunnel. Tunn. Undergr. Space Technol. **25**(4), 325–332 (2010)
7. Wang, S., Yu, Q., Peng, B., et al.: A model test for the progressive failure mechanism of lining segment structure of underwater shield tunnels. China Civ. Eng. J. **49**(4), 111–120 (2016)
8. Wang, S., Yu, Q., Peng, B., et al.: Model tests on influences of cavity defects on mechanical characteristics and failure laws of segment linings of shield tunnels. Chin. J. Geotech. Eng. **39**(1), 89–98 (2017)
9. Huang, H., Shen, X., Wang, F., et al.: Vulnerability analysis and assessment of segment joints in shield tunnel. J. Tongji Univ. (Nat. Sci.) **44**(2), 198–206 (2016)
10. Feng, K., He, C., Xiao, M.: Bending tests of segment joint with complex interface for shield tunnel under high axial pressure. China Civ. Eng. J. **49**(8), 99–110 (2016)
11. Yang, W., Xu, Z., Chen, Z., et al.: Research on influence of segment joints on dynamic response of shield tunnel and surrounding soft soil due to train induced vibration. Chin. J. Rock Mech. Eng. **36**(1), 1–12 (2017)
12. Yang, Y., Xie, X.: Breaking mechanism of segmented lining in shield tunnel based on fracture mechanics. Chin. J. Rock Mech. Eng. **34**(10), 2114–2124 (2015)
13. Yang, S.: Research on the fatigue design of large-scale model test for shield tunnel structure dynamic loads caused by high-speed train. Southwest Jiaotong University, Chengdu (2016)

A Multilayer Analytical Model and Experimental Verification for Tunnel Lining Segment Under Elevated Temperatures

Zhi-guo Yan[1,2,3], Yao Zhang[2,3], Yi Shen[4(✉)], and Hehua Zhu[1,2,3]

[1] State Key Laboratory of Disaster Reduction in Civil Engineering,
Tongji University, 1239 Siping Road, Shanghai 200092, China
[2] Department of Geotechnical Engineering, Tongji University,
1239 Siping Road, Shanghai 200092, China
[3] Key Laboratory of Geotechnical and Underground Engineering of the Ministry of Education, Tongji University, 1239 Siping Road, Shanghai 200092, China
[4] Shanghai Municipal Engineering Design
Institute (Group) Co. Ltd., Shanghai 200092, China
shenyi@smedi.com

Abstract. The thermal-mechanical behavior of tunnel lining segment plays a key role in governing its fire protection design. Existing models are mainly developed for the analysis nonlinear and non-elastic behavior of segment under fire, however the complexity of the model impede their application in engineering. In this study, a multilayer analytical model is proposed to describe the behavior of segment under elevated temperature. The temperature distribution on the cross section can be described by a piecewise function. The contributions of the concrete, and bolt are equivalent to a set of spring in the model. Based on the plane cross-section assumption, the strain distribution on the section is derived. Further, it can lead to the radial and tangential displacements of the tunnel lining segment in general restrictions with 9 integration constants in accordance with geometric relation of displacement and strain. Combination of continuity and equilibrium of forces conditions, equations are established to solve 12 basic unknown parameters. Some special examples with various boundary conditions, such as statically determinate structure, statically indeterminate structure with two hinged ends and fixed ends structure, are analyzed. To verify the feasibility of the model, four points bending tests are conducted with reduced-scale specimens. Test results indicate that this multilayer model well predicts the response of the tunnel lining segment under or after elevated temperature and can be utilized with corresponding design codes in the fire protection design of the tunnel lining segment.

Keywords: Tunnel lining segment · Elevated temperature · Multilayer model
Experimental verification

© Springer Nature Singapore Pte Ltd. 2018
D. Zhang and X. Huang (Eds.): GSIC 2018, *Proceedings of GeoShanghai 2018 International Conference: Tunnelling and Underground Construction*, pp. 273–281, 2018.
https://doi.org/10.1007/978-981-13-0017-2_27

1 Introduction

The models for tunnel segmental lining design can be classified as indirect model and direct model. The indirect model assumes that tunnel lining is a ring with uniform rigidity. A reduction factor is introduced to correct the effect of joints on the bending stiffness of the tunnel lining. In the direct model, the segments and joints are simplified as a group of springs with equivalent bending stiffness, axial stiffness and shear stiffness [1, 2]. Several tests showed that the stiffness at joint exhibited a bilinear behavior when it gradually lost contact, which was fully characterized by a progressive model [1, 3–5]. Many other models were formulated to analyze the mechanical behavior of tunnel lining segment in three dimensional space [6–9]. These studies mainly focus on the mechanical analysis of tunnel lining segment under ambient temperature. Owing to limit of experimental condition, numerical analysis has been one of the most popular methods to investigate the mechanical performance of tunnel lining segment at elevated temperature [10]. Corresponding accurate analytical model to predict the behavior of tunnel lining segment under elevated temperature, has so been little reported.

Therefore, we focus on developing analytical and progressive thermal-damage model of tunnel lining segment on basis of the combination of curved beam theory and fiber model. The present study deal with derivation of thermal-mechanical model for the reinforced concrete tunnel lining segment in the given fire scenario. Moreover, this study lays down the foundation for further investigation on the design of tunnel fire protection and assessment of structural safety after exposure to fire.

2 Theoretical Development

2.1 Sectional Analysis

The following assumptions have been adopted to facilitate the multilayer model development of tunnel lining segment under fire.

(1) Material is isotropic and the damage caused by temperature is also isotropic at each layer.
(2) The bolt and corresponding bolt hole contact closely, so that non-elastic deformation caused this factor can be negligible.
(3) Small deformation is assumed. So the deformation of tunnel lining segment has a small impact the internal force distribution.

Tunnel lining segment cross section subjected to bending moment as well as axial thrust can be divided multi layers according to the distribution of mechanical and thermal properties on the section. As pointed out by Shen, three layers (see Fig. 1) might be feasible to be used to analyze the response of tunnel lining segment under

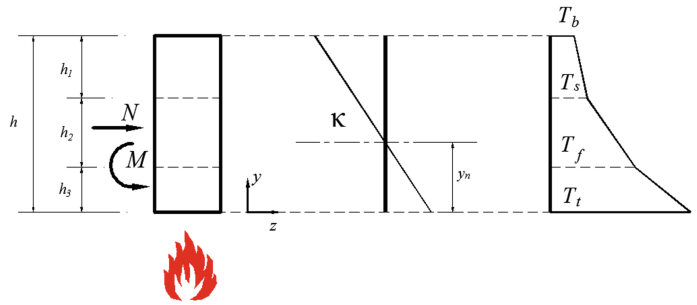

Fig. 1. The strain and temperature distribution on the cross section of tunnel lining segment.

elevated temperature. Plane cross-section assumption is made to derive the stress on the cross section. Thus strain on this section can be expressed as:

$$\varepsilon_t = (y - y_n)\kappa \tag{1}$$

κ is the curvature and y_n is the height of compressive zone and it ranges from 0 to h. Meanwhile, thermal strain can be written as:

$$\varepsilon_{\theta\alpha} = \lambda_\alpha T_\alpha(y) \quad (\alpha = 1, 2, 3) \tag{2}$$

where λ_α is the thermal conductivity of α layer; $T_\alpha(y)$ is the thermal distribution function of α layer. At a fixed time point, $T_\alpha(y)$ is known. Three-layer method can avoid unintegrable problem due to complex thermal distribution function. And the strain and temperature distribution on the cross section of tunnel lining segment are as shown in Fig. 1.

$T_\alpha(y)$ can be expressed as follows:

$$T_\alpha(y) = T_t + y\nabla_\alpha + \widetilde{\nabla}_\alpha \quad (\alpha = 1, 2, 3) \tag{3}$$

$$\nabla_1 = \frac{T_f - T_t}{h_1}, \nabla_2 = \frac{T_s - T_f}{h_2}, \nabla_3 = \frac{T_b - T_s}{h_3}, \ \widetilde{\nabla}_\alpha = \sum_{1}^{\alpha} h_{\alpha-1}\nabla_{\alpha-1} \tag{4}$$

Elastic strain ε_e can be defined as strain that the total strain ε_t removes the thermal strain ε_θ.

$$\varepsilon_e = \varepsilon_t - \varepsilon_\theta \tag{5}$$

The strain caused by temperature gradient can be noted as ε_c:

$$\varepsilon_c = \lambda_\alpha(T_t + \widetilde{\nabla}_\alpha) \tag{6}$$

Thus we can obtain normal stress on the section:

$$\sigma_\alpha = E_T(y)\varepsilon_e = E_T(y)\cdot(-\varepsilon_c - y_n\kappa + y(\kappa - \lambda_\alpha\nabla_\alpha)) \tag{7}$$

$E_T(y)$ corresponds to the Young's modulus at y where the temperature is T. Further, the axial thrust can be obtained through integration.

$$N_\alpha = \int_{A_\alpha}\sigma_\alpha dA_\alpha = -(\varepsilon_c + y_n\kappa)\overline{EA_\alpha} + (\kappa - \lambda_\alpha\nabla_\alpha)\overline{EB_\alpha} \quad (\alpha = 1,2,3) \tag{8}$$

Where $\overline{EA_\alpha} = \int_{A_\alpha} E_\alpha(y)dA_\alpha$, $\overline{EB_\alpha} = \int_{A_\alpha} yE_\alpha(y)dA_\alpha$. And E_α and A_α are respectively Young's modulus and area of α layer.

In a similar way, bending moment can be given by:

$$M_\alpha = \int_A \sigma_\alpha y dA_\alpha = -(\varepsilon_c + y_n\kappa)\overline{EB_\alpha} + (\kappa - \lambda_\alpha\nabla_\alpha)\overline{EI_\alpha} \quad (\alpha = 1,2,3) \tag{9}$$

Where flexural stiffness is defined as $\overline{EI_\alpha} = \int_{A_\alpha} y^2E_\alpha(y)dA_\alpha$.

According to the compatibility of Eqs. (8) and (9), the curvature can be derived as follows:

$$\kappa = \frac{\sum\limits_{\alpha=1}^{3}\overline{EA_\alpha}}{\left(\sum\limits_{\alpha=1}^{3}\overline{EA_\alpha}\right)\left(\sum\limits_{\alpha=1}^{3}\overline{EI_\alpha}\right) - \left(\sum\limits_{\alpha=1}^{3}\overline{EB_\alpha}\right)^2}\left[M_{\text{int}} + M_\Pi - \frac{\sum\limits_{\alpha=1}^{3}\overline{EB_\alpha}}{\sum\limits_{\alpha=1}^{3}\overline{EA_\alpha}}(N_{\text{int}} + N_\Pi)\right] \tag{10}$$

Where $N_{\text{int}} = \sum\limits_{\alpha=1}^{3} N_\alpha$, and $N_\Pi = \sum\limits_{\alpha=1}^{3}(\lambda_\alpha\nabla_\alpha\overline{EB_\alpha} + \varepsilon_c\overline{EA_\alpha})$. N_Π refers to coupling axial thrust. $M_{\text{int}} = \sum\limits_{\alpha=1}^{3} M_\alpha$, $M_\Pi = \sum\limits_{\alpha=1}^{3}(\lambda_\alpha\nabla_\alpha\overline{EI_\alpha} + \varepsilon_c\overline{EB_\alpha})$. M_Π refers to coupling bending moment.

2.2 Analysis of Tunnel Lining Segment Under General Boundary Conditions

In order to facilitate the verification of this multilayer model through data acquired in test, symmetrical concentrated loads are adopted in this section, as shown in Fig. 2. To simulate the contribution of bolt and connected lining segments to stiffness of the segments' ends, horizontal, vertical and rotational springs with equivalent stiffness are adopted. k_{0h}, k_{0v} and k_{0r} are horizontal, vertical and bending stiffness at the left end, respectively. While k_{Lh}, k_{Lv} and k_{Lr} are corresponding stiffness on the other end (See Fig. 2). $k_{0h}(k_{Lh})$, $k_{0v}(k_{Lv})$ stand for the force per unit length required to cause a unit length in corresponding directions. Meanwhile, k_{0r} and k_{Lr} are the bending moment per length required to induce a unit rotation angle at the joints.

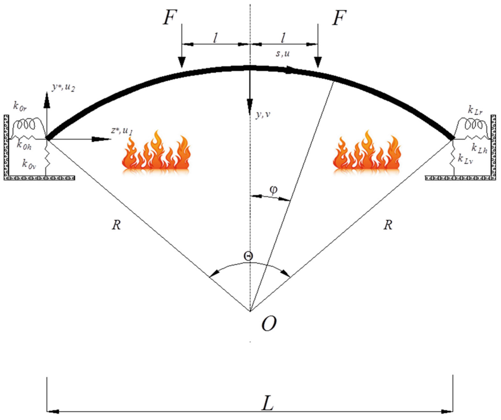

Fig. 2. The tunnel lining segment with general restrictions.

2.3 Displacement Derivation

The relation between curvature κ, bend angle θ and radial displacement v is recapitulated as follows:

$$\kappa = \frac{d\theta}{ds} = \frac{d^2 v}{ds^2} \tag{11}$$

Based on the theory of Bradford [11], the geometric relation between strain and tangential displacement u of the curved beam section can be given by

$$\varepsilon_t = \frac{du}{ds} + \frac{1}{2}\left(\frac{dv}{ds}\right)^2 - \frac{v}{R} - y\left(\frac{d^2 v}{ds^2}\right) \tag{12}$$

And the tangential displacement can be derived if Eq. (12) equals Eq. (1) at y = 0.

$$u(s) = \int \left[-y_n \kappa - \frac{1}{2}\left(\frac{dv}{ds}\right)^2 + \frac{v}{R}\right] ds + C_{e3} \quad e = 1, 2, 3 \tag{13}$$

Substitution of expressions of displacement (u, v) and bend angle (θ), as derived above, into continuity requirements i.e. Eqs. (14) and (15) then leads to six equations, which involve nine unknowns: C_{11}, C_{12}, C_{13}, C_{21}, C_{22}, C_{23}, C_{31}, C_{32}, and C_{33}.

$$\left\{ \theta\Big|_{z^*=\left(\frac{L}{2}-l\right)^-} = \theta\Big|_{z^*=\left(\frac{L}{2}-l\right)^+},\ v\Big|_{z^*=\left(\frac{L}{2}-l\right)^-} = v\Big|_{z^*=\left(\frac{L}{2}-l\right)^+},\ u\Big|_{z^*=\left(\frac{L}{2}-l\right)^-} = u\Big|_{z^*=\left(\frac{L}{2}-l\right)^+} \right. \tag{14}$$

$$\left\{ \theta\Big|_{z^*=\left(\frac{L}{2}+l\right)^-} = \theta\Big|_{z^*=\left(\frac{L}{2}+l\right)^+},\ v\Big|_{z^*=\left(\frac{L}{2}+l\right)^-} = v\Big|_{z^*=\left(\frac{L}{2}+l\right)^+},\ u\Big|_{z^*=\left(\frac{L}{2}+l\right)^-} = u\Big|_{z^*=\left(\frac{L}{2}+l\right)^+} \right. \tag{15}$$

As for the tunnel lining segment, the reaction should satisfy the equilibrium of forces at the support. Thus it can lead to

$$H_0 = H_L,\ V_0 + V_L = 2F,\ M_0 = M_L + V_L L - FL \tag{16}$$

Use of simultaneous equations above, it can be solved to obtain these 12 unknowns: C_{11}, C_{12}, C_{13}, C_{21}, C_{22}, C_{23}, C_{31}, C_{32}, C_{33}, H_0, V_0, and M_0. Because of the number of unknowns and coupling between them, it is tedious to solve these equations directly. Adjusting the sequence of solution can facilitate uncoupling between unknowns. After observation of these equations, it can be easily found that C_{11}, C_{12}, C_{13}, C_{21}, C_{22}, C_{23}, C_{31}, C_{32} and C_{33} should be solved first, which are followed by C_{21}, C_{22}, and C_{23}; then are H_0, V_0, and M_0. When these unknowns are solved, the displacements and bending angle can be obtained directly with substitution of solutions into corresponding expressions.

3 Case Study

In practical tunnel engineering, symmetric design is widely adopted due to its briefness. When the stiffness at both ends are the same or the difference can be overlooked, the boundary conditions can be simplified as follows:

(1) Continuity condition:

$$\left\{ \theta\Big|_{z^*=\left(\frac{L}{2}-l\right)^-} = \theta\Big|_{z^*=\left(\frac{L}{2}-l\right)^+},\ v\Big|_{z^*=\left(\frac{L}{2}-l\right)^-} = v\Big|_{z^*=\left(\frac{L}{2}-l\right)^+},\ u\Big|_{z^*=\left(\frac{L}{2}-l\right)^-} = u\Big|_{z^*=\left(\frac{L}{2}-l\right)^+} \right. \tag{17}$$

(2) Boundary conditions at the end:

$$\left\{ \begin{aligned} H_0 &= -k_{0h}(u\cos\varphi + v\sin\varphi)|_{s=-R\Theta/2} \\ V_0 &= -k_{0v}(u\cos\varphi - v\sin\varphi)|_{s=-R\Theta/2} \\ M_0 &= k_{0r}\theta|_{s=-R\Theta/2} \end{aligned} \right. \quad \varphi = -\Theta/2, z^* = 0 \tag{18}$$

(3) Boundary conditions at the mid span:

$$\theta\Big|_{z^*=\frac{L}{2}} = 0,\ u\Big|_{z^*=\frac{L}{2}} = 0,\ V_{\text{int}}|_{z^*=\frac{L}{2}} = 0\ \varphi = 0, z^* = \frac{L}{2} \tag{19}$$

Substitution of these boundary conditions into corresponding equation, several unknowns can be rewritten as explicit expressions. Then the unknowns have been solve with the given symmetric boundary conditions. Some special examples, e.g. statically determinate structure with two hinged ends or with two fixed ends can also be simplified analyzed as reference for the fire-resistant design of tunnel lining segment.

4 Model Validation

Several experimental tests about tunnel lining segment with various boundary condition were conducted to validate this multilayer model. The size of specimens utilized in the test were a third of the actual size in the engineering. And they were all 300 mm wide and 120 mm thick with an average radius 990 mm. To avoid the scaling effect, the size of the specimens was determined to allow the composition of the materials in the actual construction to be maintained. In a companion paper [12], the details of the test were presented specifically.

Table 1 lists the detail information about the load condition adopted in this present study, as well as corresponding boundary conditions. Two load cases were considered in this study, namely:

(1) Loading Case1 (LC-1): In this case, the test segments were first loaded mechanically to a prescribed initial (service) load level, and then subjected to a complete heating, following the standard Eurocode HC curve, and cooling period. After complete cooling, the specimens were loaded to onset of visible concrete cracking, by increasing the vertical load, to investigate the mechanical behavior after exposure to elevated temperature. One specimen was tested with LC-1 (RC4 under BC2).

(2) Loading Case2 (LC-2): The specimens were heated following the standard Eurocode HC curve, without any initial loads. After approximately 40 min of heating, the specimens were mechanically loaded to onset of visible concrete cracking to investigate the response under elevated temperature. One specimen was subjected to LC-2 test (RC1 under BC1).

Table 1. Summary of specimens and load condition.

No.	Age (day)	BC[a]	LC[b]	Fire load
RC1	226	BC1	LC-2	HC(60 min)
RC4	540	BC2	LC-1	HC(60 min)

[a] BC-Boundary conditions, i.e. horizontal constraints (BC1-free slide; BC2-restrained).
[b] LC-Load case.

Based on the model predicted results and test results, it can be seen that prediction meet well with the test results, which indicate that this model can be used to calculate the response of the tunnel lining segment (Fig. 3).

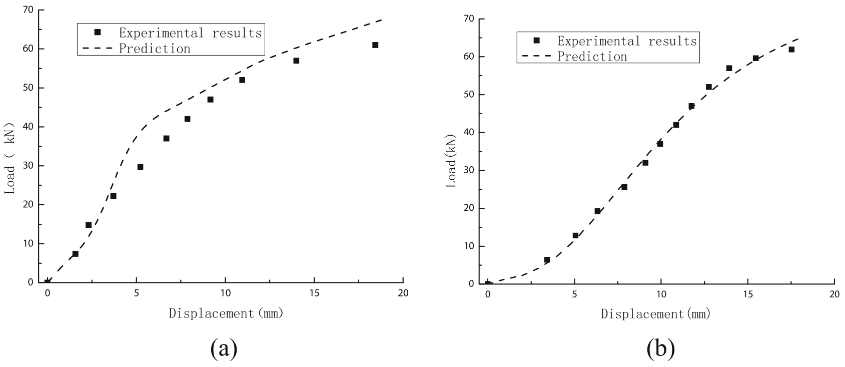

(a) (b)

Fig. 3. The experimental and predicted displacement at the mid span of (a) RC1 and (b) RC4.

5 Conclusions

In this study, a multilayer model of tunnel lining segment under fire is systematically developed on the basis of the distribution of mechanical properties of the cross section. In the proposed model, the basic unknowns are the tangential and radial displacement of tunnel lining segment. The cross section is divided into multi layers (three layers as an example in this paper). Based on the plane cross-section assumption, the strain distribution on the section is derived. Further, it can lead to the radial and tangential displacements of the tunnel lining segment in general restrictions with 9 integration constants in accordance with geometric relation of displacement and strain. Combination of continuity and equilibrium of forces conditions, equations are established to solve 12 basic unknown parameters. Some special examples, such as statically determinate structure, statically indeterminate structure with two hinged ends and fixed ends structure, are displayed to exhibit the feasibility of this multilayer model. The model is nearly linear elastic. In order to illustrate its accuracy, predictions from the proposed model are compared with experimental results from four points bending tests under or after fire. The model is nearly linear elastic. Test results indicate this model can be utilized to analyze the response of tunnel lining segment under non-uniform transverse temperature field when the temperature distribution is uniform in longitudinal direction.

References

1. Li, X., Yan, Z., Wang, Z., Zhu, H.: A progressive model to simulate the full mechanical behavior of concrete segmental lining longitudinal joints. Eng. Struct. **93**, 97–113 (2015)
2. Blom, C.B.M.: Design philosophy of concrete linings for tunnels in soft soils. Delft University Press (2002)
3. Koyama, Y.: Present status and technology of shield tunneling method in Japan. Tunn. Undergr. Space Technol. **18**(2), 145–159 (2003)
4. Klappers, C., Grübl, F., Ostermeier, B.: Structural analyses of segmental lining - coupled beam and spring analyses versus 3D-FEM calculations with shell elements. Tunn. Undergr. Space Technol. **21**(3–4), 254–255 (2006)

5. Zhu, H.H.: Designs and analysis on underground structures. Geo-Research Institute Report, Osaka, Japan (1995)
6. Molins, C., Arnau, O.: Experimental and analytical study of the structural response of segmental tunnel linings based on an in situ, loading test.: Part 1: test configuration and execution. Tunn. Undergr. Space Technol. **26**(6), 764–777 (2011)
7. Liu, X., Bai, Y., Yuan, Y., Mang, H.A.: Experimental investigation of the ultimate bearing capacity of continuously jointed segmental tunnel linings. Struct. Infrastruct. Eng. **12**(10), 1–16 (2014)
8. Huang, Z.R., Zhu, W., Liang, J.H., Lin, J., Jia, R.: Three-dimensional numerical modelling of shield tunnel lining. Tunn. Undergr. Space Technol. **21**(3), 434 (2006)
9. Zhu, H.H., Yan, Z.G., Liao, S.M., Liu, F.J., Zeng, L.J.: Numerical analysis and field test on performance of steel fibre reinforced concrete segment in subway tunnel. In: Geoshanghai International Conference, Shanghai, pp. 248–255 (2006)
10. Choi, S.-W., Lee, J., Chang, S.-H.: A holistic numerical approach to simulating the thermal and mechanical behaviour of a tunnel lining subject to fire. Tunn. Undergr. Space Technol. (incorporating Trenchless Technology Research) **35**(35), 122–134 (2013)
11. Bradford, M.A.: In-plane nonlinear behaviour of circular pinned arches with elastic restraints under thermal loading. Int. J. Struct. Stab. Dyn. **06**(2), 163–177 (2011)
12. Yan, Z.G., Shen, Y., Zhu, H.H., Li, X.J., Lu, Y.: Experimental investigation of reinforced concrete and hybrid fibre reinforced concrete shield tunnel segments subjected to elevated temperature. Fire Saf. J. **71**(3), 86–99 (2015)

Numerical Study on High Stiffness Segmental Joints of Shield Tunnels

Long Zhou[1], Zhi-guo Yan[1(✉)], He-hua Zhu[1], and Yi Shen[2]

[1] Department of Geotechnical Engineering, Tongji University, Shanghai, China
yanzguo@tongji.edu.cn
[2] Shanghai Municipal Engineering Design Institute (Group) Co. Ltd.,
Shanghai, China

Abstract. Deep buried drainage shield tunnels have the characteristics of large buried depth and high inner water pressure. The load effect of high inner water pressure and large earth pressure causes the increase of bending moment and decrease of axial force in the joint section. To meet the requirements of bearing capacity and deformation of lining structures, high stiffness segmental joints (HSSJs) with complicated structural styles and high bearing capacity are put forward to use for deep buried drainage shield tunnels. The three-dimensional finite element method is applied to study the mechanical characteristics and failure modes of the HSSJs. On the basis of numerical simulation results, the optimization method for HSSJs is proposed, which could provide references to the design and construction of similar projects.

Keywords: High stiffness segmental joint · Shield tunnel
Mechanical characteristic · Failure mode

1 Introduction

With the accelerated urbanization process, a lot of buildings and concrete and bituminous pavement appear in urban area, which causes permeability degradation in urban underlying surface. When rainstorms occur, the occurrence possibility of urban waterlogging greatly increases (Rose and Peters 2001; White and Greer 2006; Leopold et al. 2012; Luo 2016). Waterlogging disasters occurred in 637 cities in China between 2008 and 2012. Drawing lessons from developed countries and regions applying deep tunnel drainage systems to improve drainage ability and solve waterlogging problems (Scalise and Fitzpatrick 2012; Wu et al. 2016), Shanghai puts forward to construct deep buried tunnels to regulate rainwater and reduce the occurrence of waterlogging. Considering the geology condition of Shanghai and construction environment of deep underground space, shield-driven method is one of the main methods suitable for the construction of deep drainage tunnels. Unlike subway and road shield tunnels, deep buried drainage shield tunnels bear larger external earth pressure and higher inner water pressure. High inner water pressure changes the stress state of segmental joints, which causes the increase of bending moment and decrease of axial force in the joint sections. To meet the requirements of bearing capacity and opening of segmental joints, high stiffness segmental joints (HSSJs) should be used for the concrete linings of deep

© Springer Nature Singapore Pte Ltd. 2018
D. Zhang and X. Huang (Eds.): GSIC 2018, *Proceedings of GeoShanghai 2018 International Conference: Tunnelling and Underground Construction*, pp. 282–291, 2018.
https://doi.org/10.1007/978-981-13-0017-2_28

buried drainage shield tunnels. Ductile iron joint panels (DIJPs) are generally mounted in HSSJs of shield tunnels via anchor bars, and shield segments are connected by tightening bolts which act on the DIJPs (Koyama 2003). Current research has primarily covered segmental joints with low bearing capacity and without DIJPs (Blom 2002; Teachavorasinskun and Chub-Uppakarn 2010; Li et al. 2015; Yan et al. 2016). For segmental joints having high bearing capacity with DIJPs which are suitable for deep buried drainage shield tunnels, the studies are relative less and the bearing characteristics and failure modes are not revealed. Therefore, the numerical analysis method is applied to study the behavior of HSSJs with different structural styles of DIJPs in this paper. Based on the numerical results, a reasonable design model of HSSJs suitable for deep buried drainage tunnels is proposed.

2 Numerical Analysis Models

The finite-element software package ABAQUS was used to establish the three-dimensional finite element models of the HSSJs. According to previous research, an arc segmental joint can be replaced by a straight segmental joint to simplify experiments or numerical analysis models when evaluating the flexural behavior of segmental joints (Zhang and Koizumi 2010; Ding et al. 2011). Considering the complicated structural styles of HSSJs, numerical models of straight segment joints without regard to waterproof materials and groove gaps are adopted.

2.1 Ductile Iron Joint Panel

Three types of DIJPs are selected in the numerical analysis models (see Fig. 1). The DIJP of Type 1 has a sidewall with a thickness of 1.5 cm and a height equaling to half of the height of the hand hole. The DIJP of Type 2 has a sidewall with a thickness of 1.5 cm and a height equaling to the height of the hand hole. The DIJP of Type 3 has a sidewall with a thickness of 1.5 cm and a height equaling to the height of the hand hole, and a baseplate with a thickness of 1 cm. The panel thicknesses of the three DIJPs are all 5 cm. The material of these DIJPs is QT500-7 ductile cast iron with an elasticity modulus of 210 GPa, a Poisson's ratio of 0.3 and a yield strength of 500 MPa. The DIJPs are modeled as solid elements and the element types are C3D6 elements.

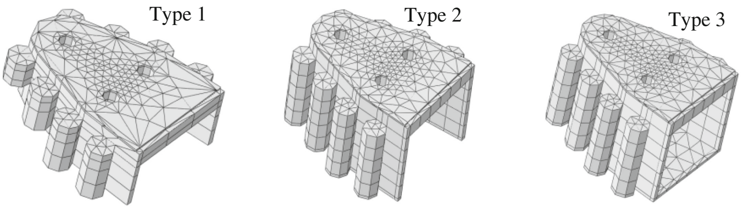

Fig. 1. Three different types of DIJPs

2.2 Reinforcing Bar

The arrangement of the longitudinal reinforcing bars with a diameter of 32 mm and the stirrups with a diameter of 10 mm in the straight joint models is shown in Fig. 2(a). The DIJPs are mounted in the joint via anchor bars with a diameter of 32 mm, and the arrangement of the anchor bars is shown in Fig. 2(b). The strength grade of longitudinal reinforcing bars and anchor bars and that of stirrups is HRB 400 and HRB 335, respectively. The elasticity modulus of all the reinforcing bars is 210 GPa and the Poisson's ratio is 0.3. The reinforcing bars are modeled as truss elements and the element types are T3D2 elements. In the straight joint models, the longitudinal reinforcing bars and stirrups are embedded in the concrete; the anchor bars are embedded in the concrete and the anchor zones of the DIJPs (ABAQUS Inc. 2011).

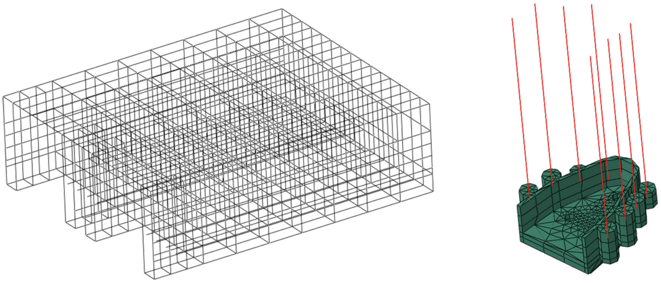
(a) Reinforcement cage of straight joint models (b) Anchor bars of DIJPs

Fig. 2. Reinforcing bars of straight joint models

2.3 Bolt

The M39 straight bolts of Grade 10.9 are applied in the numerical models; and they are prestressed with a pretightening force of 120 kN. The elasticity modulus of the bolts is 210 GPa, the Poisson's ratio is 0.3, and the yield stress is 904 MPa. The bolts are modeled as solid elements and the element types are C3D8R elements. The interaction between the DIJPs and bolts and that between the DIJPs and concrete are modeled as surface-to-surface contact (see Fig. 3), in which the normal contact is "hard contact" and the tangential friction coefficient is 0.5.

2.4 Concrete

The strength grade of the concrete in the straight joint models is C60 (compressive strength of 38.5 MPa and tensile strength of 2.85 MPa). The elasticity modulus of the concrete is 36 GPa and the Poisson's ratio is 0.2. The concrete is modeled as solid elements and the element types are C3D6 elements. The contact between the joints is modeled as surface-to-surface contact (see Fig. 3), in which the normal contact is "hard contact" and the tangential friction coefficient is 0.5. There are 3 straight joint models in the numerical analysis: Model T1, Model T2 and Model T3, representing the straight

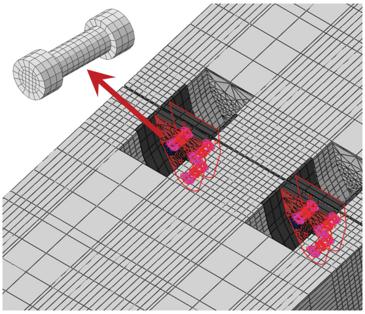

Fig. 3. Contact between different parts

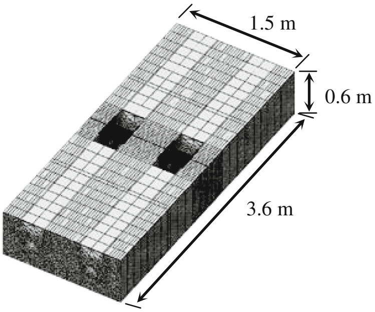

Fig. 4. Model dimensions

model with the DIJP of Type 1, Type 2 and Type 3, respectively. The dimensions of the models are 3.6 m × 1.5 m × 0.6 m (see Fig. 4).

2.5 Boundary Condition

The load and displacement boundary conditions of the numerical models are shown in Fig. 5.

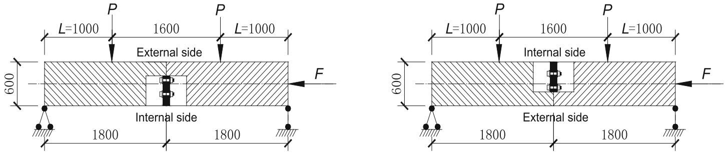

(a) Positive bending moment case (b) Negative bending moment case

Fig. 5. Load and displacement boundary conditions (Unit: mm)

The boundary conditions in Fig. 5 show that the models are simply supported, and the bending moment and axial force in the joint sections are applied by applying the vertical load *P* and lateral load *F* on the models: the axial force *N* equals to *F* and the bending moment *M* equals to $P \cdot L$ (Zhang and Koizumi 2010; Zhu et al. 2014). The bearing characteristics of HSSJs when the lining structure is subjected to the earth pressure resulting from the soil depth of 50 m and inner water pressure of 0.6 MPa, are analyzed. For the positive bending moment case (corresponding to the joint opening at the internal side), the bending moment is 909 kN·m and the axial force is 1893 kN; for the negative bending moment case (corresponding to the joint opening at the external side), the bending moment is −834 kN·m and the axial force is 3234 kN. In the loading process, the axial force is firstly increased to the target value, then the axial force is kept unchanged and the bending moment is increased to the target value. After both the axial force and bending moment reach the target values, the axial force is kept unchanged and the bending moment is increased, to study the failure modes of the HSSJs.

3 Behavior of High Stiffness Segmental Joints

3.1 Stress and Deformation of Ductile Iron Joint Panels

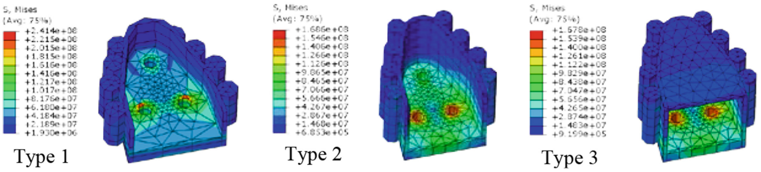
S, Mises
(Avg: 75%)
+2.414e+08
+2.215e+08
+2.015e+08
+1.815e+08
+1.616e+08
+1.416e+08
+1.217e+08
+1.017e+08
+8.176e+07
+6.180e+07
+4.184e+07
+2.189e+07
+1.930e+06
Type 1
S, Mises
(Avg: 75%)
+1.686e+08
+1.546e+08
+1.406e+08
+1.266e+08
+1.126e+08
+9.865e+07
+8.465e+07
+7.066e+07
+5.666e+07
+4.267e+07
+2.867e+07
+1.468e+07
+6.853e+05
Type 2
S, Mises
(Avg: 75%)
+1.678e+08
+1.539e+08
+1.400e+08
+1.261e+08
+1.122e+08
+9.829e+07
+8.438e+07
+7.047e+07
+5.656e+07
+4.265e+07
+2.874e+07
+1.483e+07
+9.199e+05
Type 3

Fig. 6. Mises stress distribution of DIJPs for positive bending moment case (Unit: Pa)

The Mises stress distribution of the DIJPs in different straight joint models for the positive bending moment case (bending moment of 909 kN·m and axial force of 1893 kN) is shown in Fig. 6.

As shown in Fig. 6, the maximum Mises stresses of the DIJPs in Model T1, T2 and T3 are 241.4 MPa, 168.6 MPa and 167.8 MPa, respectively, which means the DIJP stress decreases with the increase of sidewall height of the DIJP whereas adding a baseplate for the DIJP has little impact on the decrease of DIJP stress for the positive bending moment case.

The opening of the straight joint for the positive bending moment case is shown in Fig. 7(a). For HSSJs, the opening of the joints is not in conformity with the plane cross-section assumption: the joint opening near the hand holes is smaller due to the restriction effect from the bolts and high stiffness of the DIJPs while the joint opening

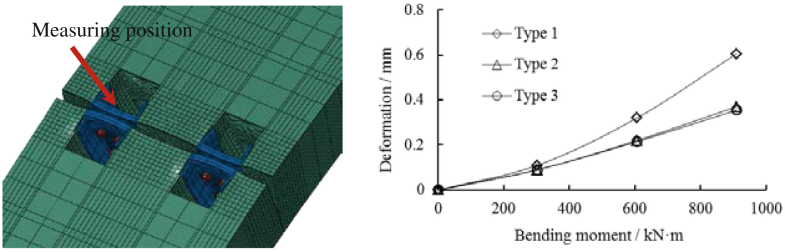

(a) Joint opening (Deformation magnification: 50 times) (b) DIJP deformations

Fig. 7. Joint opening for positive bending moment case

away from the hand holes is larger, i.e., the joint opening is non-uniform. The DIJP deformations in the straight joint models for the positive bending moment case are shown in Fig. 7(b) (the measuring position is shown in Fig. 7(a)).

As shown in Fig. 7(b), the DIJP deformation in Model T1 is larger than that in Model T2 and T3 and the DIJP deformations in Model T2 and T3 are basically the same for the positive bending moment case, which means that enlarging the sidewall height of the DIJP can decrease the DIJP deformation whereas adding a baseplate for the DIJP has little impact on the decrease of DIJP deformation.

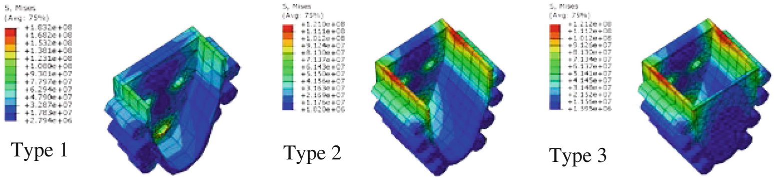

Fig. 8. Mises stress distribution of DIJPs for negative bending moment case (Unit: Pa)

The Mises stress distribution of the DIJPs in different straight joint models for the negative bending moment case (bending moment of −834 kN·m and axial force of 3234 kN) is shown in Fig. 8.

As shown in Fig. 8, the maximum Mises stresses of the DIJPs of Type 1, Type 2 and Type 3 are 183.2 MPa, 121.0 MPa and 121.2 MPa, respectively, which means the DIJP stress decreases with the increase of sidewall height of the DIJP whereas adding a baseplate for the DIJP has little impact on the decrease of DIJP stress for the negative bending moment case.

3.2 Concrete Stress

The distribution of concrete stresses in different straight joint models for the positive bending moment case (bending moment of 909 kN·m and axial force of 1893 kN) is shown in Fig. 9.

As shown in Fig. 9, the maximum compressive stresses of the concrete in the compressive zone of Model T1, T2 and T3 are 38.2 MPa, 34.3 MPa and 34.1 MPa, respectively, which means the concrete stress in the compressive zone decreases with

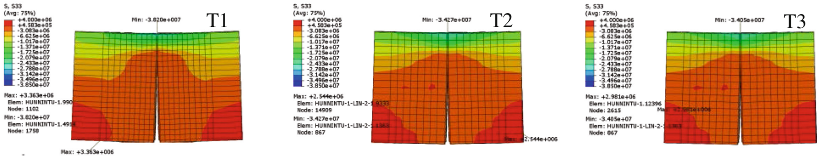

Fig. 9. Distribution of concrete stresses for positive bending moment case (Deformation magnification: 20 times; unit: Pa)

the height increase of the DIJP sidewall whereas adding a baseplate for the DIJP has little impact on the decrease of the concrete stress in the compressive zone for the positive bending moment case.

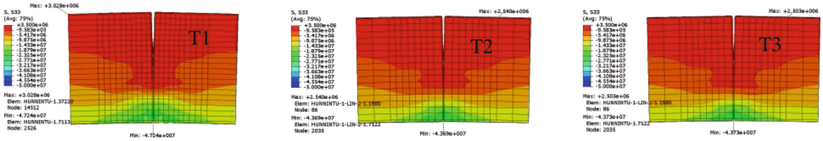

Fig. 10. Distribution of concrete stresses for negative bending moment case (Deformation magnification: 20 times; unit: Pa)

The distribution of concrete stresses in different straight joint models for the negative bending moment case (bending moment of −834 kN·m and axial force of 3234 kN) is shown in Fig. 10.

As shown in Fig. 10, the maximum compressive stresses of the concrete in the compressive zone of Model T1, T2 and T3 are 47.2 MPa, 43.7 MPa and 43.7 MPa, respectively, which means the concrete stress in the compressive zone decreases with the height increase of the DIJP sidewall whereas adding a baseplate for the DIJP has little impact on the decrease of the concrete stress in the compressive zone for the negative bending moment case.

For HSSJs subjected to negative bending moment, the compressive stresses of the concrete in compressive zones exceed 38.5 MPa (the design value of the compressive strength of C60 concrete); if the hand holes are filled with cement, the compressive stresses of the concrete in compressive zones significantly decrease below 38.5 MPa (see Fig. 11). The main reason of that is the sectional area of concrete in the compressive zone increases after the filling of hand holes when the joint is subjected to

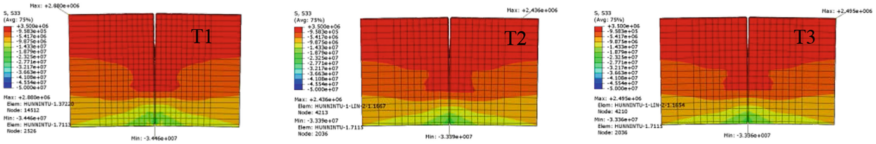

Fig. 11. Distribution of concrete stresses for negative bending moment case after filling of hand holes (Deformation magnification: 20 times; unit: Pa)

negative bending moment. Therefore, in the design of HSSJs, the dimension of the hand hole should be reduced as far as possible to increase the sectional area of concrete in the compressive zone on the premise that the bolts can be tightened conveniently.

The distribution of concrete stresses in the hand holes of different straight joint models for the negative bending moment case (bending moment of −834 kN·m and axial force of 3234 kN) is shown in Fig. 12.

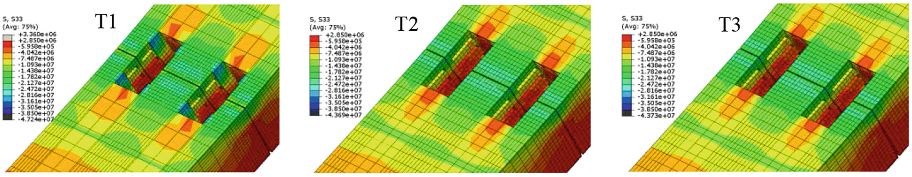

Fig. 12. Distribution of concrete stresses in hand holes for negative bending moment case (Deformation magnification: 20 times; unit: Pa)

As shown in Fig. 12, the maximum compressive stresses of the concrete in the hand holes of Model T1, T2 and T3 are 37.6 MPa, 21.6 MPa and 21.7 MPa, respectively, which means the compressive stress of the concrete in the hand holes decreases with the height increase of the DIJP sidewall whereas adding a baseplate for the DIJP has little impact on the decrease of the compressive stress of the concrete in the hand holes for the negative bending moment case. The maximum compressive stress of the concrete in the hand holes for the segmental joints with the DIJP of Type 1 is larger than that with the DIJP of Type 2 and Type 3. The main reason is that the DIJP of Type 1 will compress the concrete sidewall of the hand holes when the joints are subjected to negative bending moment.

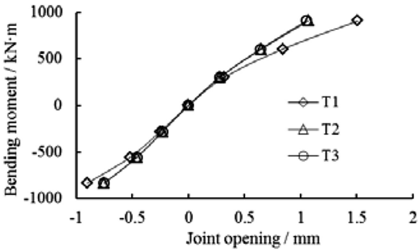

Fig. 13. Joint Opening (Positive values indicate that the joint opens at the internal sides and negative values indicate that the joint opens at the internal sides)

3.3 Joint Opening

The joint opening of the straight joint models for both the positive and negative bending moment case is shown in Fig. 13.

As shown in Fig. 13, the joint opening of Model T1 is larger than that of Model T2 and T3, and the joint openings of Model T2 and T3 are basically the same for both the positive and negative bending moment case, which means that enlarging the sidewall height of the DIJP can decrease the joint opening whereas adding a baseplate for the DIJP has little impact on the decrease of joint opening.

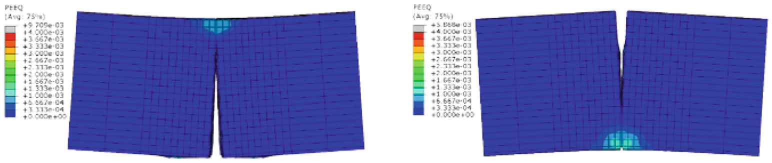

(a) Positive bending moment case (b) Negative bending moment case

Fig. 14. Plastic zone distribution of the concrete in ultimate capacity state (Deformation magnification: 20 times)

3.4 Failure Mode

The plastic zone distribution of the concrete in different straight joint models for ultimate capacity state in positive bending moment case (bending moment of 1212 kN·m and axial force of 1893 kN) and that in negative bending moment case (bending moment of −1118 kN·m and axial force of 3234 kN) is shown in Fig. 14.

As shown in Fig. 14, for HSSJs, the penetrating plastic zones appear in the concrete, and the bolt tension in ultimate capacity state is shown in Table 1. For the M39 bolts of Grade 10.9 with a yield stress of 904 MPa, the yield load is 1079 kN. Considering the distribution of concrete plastic zones and that the bolts are not yielded, the failure of HSSJs is determined to be caused by the appearance of penetrating plastic zones in the concrete.

Table 1. Bolt tension

Model	Positive moment loading		Negative moment loading	
	Bolt close to the external side (kN)	Bolt close to the internal side (kN)	Bolt close to the external side (kN)	Bolt close to the internal side (kN)
T1	207	437	543	123
T2	203	429	553	125
T3	199	432	552	125

4 Conclusions

The three-dimensional finite element models of the HSSJs are established to study the bearing characteristics and failure modes of HSSJs subjected to large earth pressure and high inner water pressure in this paper. The primary conclusions are as follows:

(1) Increasing the sidewall height of the DIJP can effectively improve the bearing capacity of HSSJs for both the positive and negative bending moment case, including the decrease of DIJP stress and deformation, compressive stress of concrete in compressive zones and hand holes, and joint opening; however, adding a baseplate for the DIJP has little impact on the improvement of bearing capacity.
(2) For HSSJs in ultimate capacity state of both the positive and negative bending moment case, the penetrating plastic zones appear in the concrete and the bolts are

not yielded, which means the failure of HSSJs is caused by the appearance of penetrating plastic zones in the concrete.

(3) Considering the bearing characteristics and failure modes of HSSJs, the DIJP having a sidewall with a height equaling to the height of the hand hole is optimal and suitable for deep buried drainage shield tunnels. At the same time, the dimension of the hand holes should be reduced as far as possible to increase the sectional area of the concrete in the compressive zone and decrease the compressive stress of concrete for the negative bending moment case on the premise that the bolts can be tightened conveniently.

Acknowledgements. This research was supported by the Scientific and Technological Project of the Shanghai Science and Technology Commission (16DZ1202200).

References

ABAQUS Inc.: Abaqus Analysis User's Manual (Version 6.11) (2011)

Blom, C.B.M.: Design philosophy of concrete linings for tunnels in soft soils. Delft University of Technology, Delft (2002)

Ding, Y.N., Liu, H.K., Pacheco-Torgal, F., et al.: Experimental investigation on the mechanical behaviour of the fiber reinforced high-performance concrete tunnel segment. Compos. Struct. **93**(4), 1284–1289 (2011)

Koyama, Y.: Present status and technology of shield tunneling method in Japan. Tunn. Undergr. Space Technol. **18**(2), 145–159 (2003)

Leopold, L.B., Wolman, M.G., Miller, J.P.: Fluvial Processes in Geomorphology. Courier Corporation, Mineola (2012)

Li, X.J., Yan, Z.G., Wang, Z., et al.: Experimental and analytical study on longitudinal joint opening of concrete segmental lining. Tunn. Undergr. Space Technol. **46**, 52–63 (2015)

Luo, H.: Research on source control technology of urban rainstorm waterlogging. Southwest Jiaotong University, Chengdu (2016)

Rose, S., Peters, N.E.: Effects of urbanization on streamflow in the Atlanta area (Georgia, USA): a comparative hydrological approach. Hydrol. Process. **15**(8), 1441–1457 (2001)

Scalise, C., Fitzpatrick, K.: Chicago deep tunnel design and construction. In: Structures Congress (2012)

Teachavorasinskun, S., Chub-Uppakarn, T.: Influence of segmental joints on tunnel lining. Tunn. Undergr. Space Technol. **25**(4), 490–494 (2010)

White, M.D., Greer, K.A.: The effects of watershed urbanization on the stream hydrology and riparian vegetation of Los Peñasquitos Creek, California. Landscape Urban Plan. **74**(2), 125–138 (2006)

Wu, H., Huang, G., Meng, Q., et al.: Deep tunnel for regulating combined sewer overflow pollution and flood disaster: a case study in Guangzhou City, China. Water **8**, 329 (2016)

Yan, Z.G., Shen, Y., Zhu, H.H., et al.: Experimental study of tunnel segmental joints subjected to elevated temperature. Tunn. Undergr. Space Technol. **53**, 46–60 (2016)

Zhang, W.J., Koizumi, A.: Behavior of composite segment for shield tunnel. Tunn. Undergr. Space Technol. **25**(4), 325–332 (2010)

Zhu, H.H., Huang, B.Q., Li, X.J., et al.: Unified model for internal force and deformation of shield segment joints and experimental analysis. Chin. J. Geotech. Eng. **36**(12), 2153–2160 (2014)

A New Form of Longitudinal Joint of Large Cross-section Segmental Tunnel Linings

Yifan Gong[1,2], Wenqi Ding[1,2], Chenjie Gong[1,2](✉),
and Yuelang Jin[1,2]

[1] Department of Geotechnical Engineering, College of Civil Engineering,
Tongji University, Shanghai, China
08gongcj@tongji.edu.cn
[2] Key Laboratory of Geotechnical and Underground Engineering,
Ministry of Education, Tongji University, Shanghai, China

Abstract. The resistance of longitudinal joint is a crucial design parameter on the mechanical properties and structural behavior of precast tunnel segmental linings constructed by the Tunnel Boring Machine (TBM). Recently, with the increased dimensions and functions of the shield tunnel, the traditional bolted connection forms (e.g., straight bolts, inclined bolts, curved bolts) for segmental joints may not meet the requirement of safety or usage. This study tries an effort to propose an optimized form of bolted joint, which is a combination of both straight bolts and incline bolts, on the basis of a detailed three-dimensional (3D) finite element (FE) model. The developed FE model is first validated against the full-scale joint mechanical experimental results in terms of the joint failure mode and bearing capacity. The computed results agree well with physical observations at low bending moment and bearing capacity. An optimal study on the design parameters of bolted joints is then undertaken using the validated FE model. According to the test results, the bearing capacity of the optimized joint under the positive and negative moment case is approximately 70% and 200% of the short straight bolts joint, respectively. As the practical outcome of this study, a series of FE analyses are performed to investigate the joint behavior with different bolt parameters. Based on the numerical results, it is suggested that the proposed new form of joint is applicable to design cases where the axial force is moderate, especially for negative moment cases, for example, water-conveyance tunnel under internal load.

Keywords: Large cross-section segmental tunnel · Longitudinal bolted joints
New form · Parameter optimization · Finite element modelling

1 Introduction

Recent years, shield tunneling method has been widely adopted for designing and constructing urban underground tunnels in soft grounds. Increasing dimensions and functions of the shield tunnel calls for better structure performance. For example, a water-conveyance tunnel (Fig. 1) is not only exposed to high ground water pressure, but also to high internal water pressures, which in turn necessitates high capacity in

© Springer Nature Singapore Pte Ltd. 2018
D. Zhang and X. Huang (Eds.): GSIC 2018, *Proceedings of GeoShanghai 2018 International Conference: Tunnelling and Underground Construction*, pp. 292–299, 2018.
https://doi.org/10.1007/978-981-13-0017-2_29

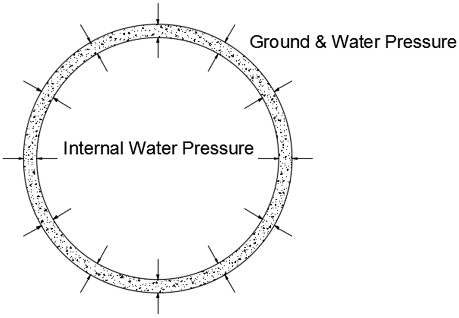

Fig. 1. Water-conveyance tunnel

negative moment cases. In this regard, optimizing the behavior of segmental lining joint is an important issue from both structural design and cost control standpoints.

In this study, an optimized form of bolted joint combined both straight bolts and incline bolts was developed based on a fined 3D numerical model for segmental contact locations. First, the formulation of the model will be given. Then, a full-scale experimental test was conducted on straight bolt segmental joints will be presented to emphasize the relevance of the model in reproducing the segment joints failure modes and bearing capacity. Experiment result shows that the ultimate bearing capacity under positive moment was significant larger than that under negative moment. Finally, to solve this problem, the mentioned optimized form of joint was suggested. Moreover, model predictions were investigated at the optimized bolted joint to figure out the behaviors of the new form of joint.

2 Optimized Segmental Joint Design

The optimized joint was a composite one combined both straight bolts and incline bolts (Fig. 2). Straight bolts were arranged on the inner arc surface of the segment to resist the positive bending moment, incline bolts were arranged on the upper part of the straight bolts and inserted into the outer arc surface of the segment to resist the negative bending moment. By this way, structure resistance subjected to positive and negative bending moment is more balanced, and the size of hand hole can be obviously reduced relative to straight bolt.

As is shown in Fig. 2, reasonable arch axis theory was used to optimize the structure stress state of the hand hole. To some extent, stress caused by bolt tension could be counteracted by the compression on the hand hole. At the junction of the hand hole and the segment fillet was designed to ensure the insertion of the incline bolt, which is convenient for construction. Moreover, steel plate was set to disperse the concentrated force acted on concrete.

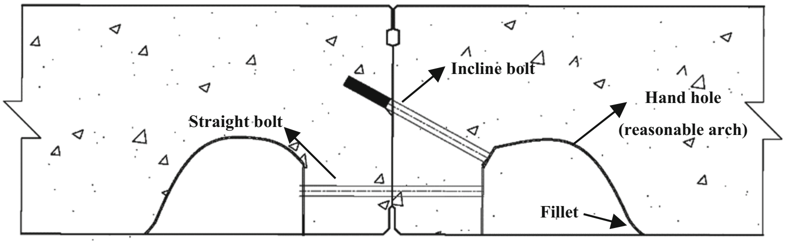

Fig. 2. Optimized joint

3 Finite Element Modelling

The algorithm used in the present study is three-dimensional finite element method (FEM). The FE models took intact parts such as grooves, bolts, and cast iron panels as well as interaction among contact surface to simulate the segmental joint behavior as realistically as possible. All developments and simulations described in this paper have been implemented into ABAQUS (version 6.14).

3.1 Constitutive Law

For small deformations, concrete exhibits a linear elastic response characteristic, and then, with increasing stress, plastic performance appears. In the interest of computational cost, bi-linear model proposed by Zhang et al. (2003) [2] was used for reinforced concrete tunnel segment in the present FEM model, whilst the steel supports at the ends of the tunnel segments were modeled as linear elastic material. Moreover, the linear elastic-perfectly plastic stress-strain relationship was also adopted to model the bolt and cast iron panels. The input parameters and adopted stress-strain relationships for concrete, cast iron, bolts, and steel were summarized in Table 1.

Table 1. Input parameters for the FEM models according to Chinese code

Model part	Young's modulus E (MPa)	Poisson's ratio μ (−)	Yield stress σ (MPa)
Concrete	3.5×10^4	0.167	38.5
Bolt	2.0×10^5	0.3	640
Cast iron	1.6×10^5	0.275	320
Steel support	2.0×10^5	0.3	− (Elastic)

3.2 Modelling Contacts Interfaces

Strength and deformational features of a segmental joint strongly depend on properties of the connections. It is thus essential to accurately describe the interactions between intact parts interfaces. In the present simulation, "hard contact" (ABAQUS, 2014) was used to define the interaction between two reinforced concrete segments and cast iron panels. In normal direction, this "hard contact" prevents two components from penetrating into each other when compression, while allowing them to separate when subjected to tension [3, 4].

Tangential deformation of contact surface was controlled Coulomb laws and can be split into two parts, the adhesion and sliding. The shear interaction force is linear using a constant slope, defined as friction coefficient. The friction coefficient of concrete was set to 0.4 and the maximum value was set as 1 MPa [5, 6]. After the shear force reaches its maximum value, the friction coefficient was set to zero.

The proposed FEM modeling has been employed in several segmental joint studies, such as determination of non-linear behavior of segmental joints [7], failure mechanism segmental joints under uneven longitudinal ground settlement [8], and the shear behavior [1]. However, this approach and input parameters have not been rigorously compared with actual experiments and further improvement and validation are still required.

4 Model Validation

The aim of this section is to explore the ability of FEM modelling to reproduce actual values of bearing capacity and failure mode of segmental joint recorded in laboratory bending capacity testing conducted on the CPJ-2000 triaxial loading equipment developed by Tongji University (Fig. 3), which has been extensively employed to conduct similar joint full-scale tests [9–11]. In order to calibrate the FEM model, numerical bending capacity testing are undertaken and the simulation results under an axial force of 1000 kN are compared with the data of laboratory test.

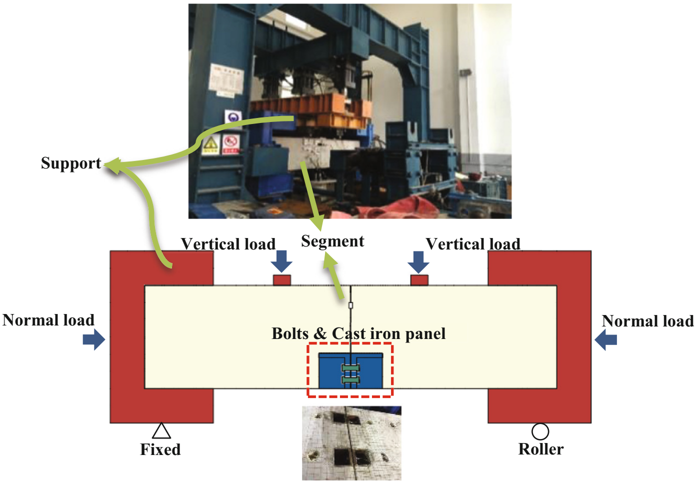

Fig. 3. Experiment setup & numerical model

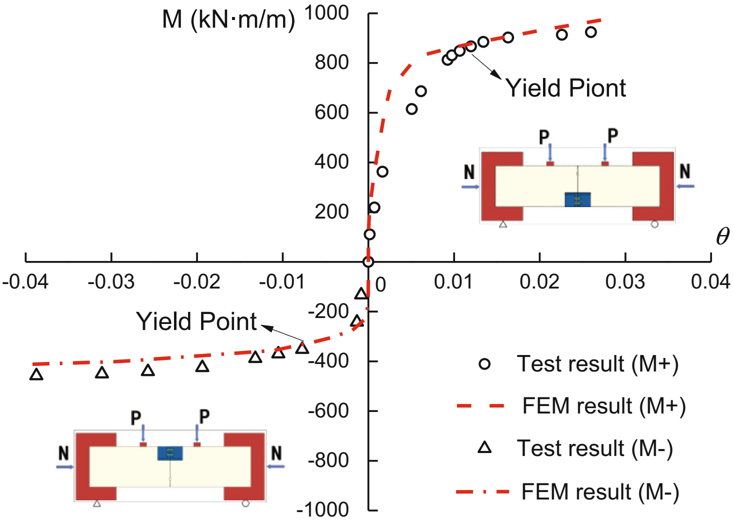

Fig. 4. $M - \theta$ curves of the FEM model simulation and experimental tests

Comparison of test and FE results are present in Fig. 4 in the form of bending moment (M) and the rotational angle at joint section (θ). As displayed in Fig. 4, the bending moment increase fast in the initial, then keep almost constant values in the rest of bending. Base on this feature, variation of bending moment and rotational angle for both samples subjected to positive/negative moment can be divided into two stages.

Stage I: Before the yield point, variation of bending moment and rotational angle was approximately linear and the average slope of the line represented the rotation stiffness, k_θ. It is noted that the simulation result diverges from test results in the bending moment range of 400–800 kN·m. These difference between test and simulation showed an overestimated intact segment by numerical simulation that adopt the linear elastic-perfectly plastic mechanics properties. As a heterogeneous material in reality, there are always defects existing in the intact segment, which may lead to reduction of the strength and elastic modules of concrete materials. When bending moment increasing, this phenomenon became more obvious.

Stage II: When the applied moment was larger than the yield moment, the joint stiffness decreased sharply with the increasing plastic strain in the concrete in the compression zone of the joint section. In contrast to Stage I, the ultimate bearing capacity of FEM model have a good compatibility with experimental result. That can be explained by the similar failure definition of the material in both FEM model and test.

It's noted that the bearing capacity for positive and negative moment were 812 kN·m/(m·Rad) and 370 kN·m/(m·Rad) respectively, with a difference of 54.4%. As is known to us all, the segmental joint bears both positive and negative moment and for large cross-section segmental tunnel linings, the larger section height resulted in the lower acting point of joint bolt. This difference may cause waste in joint subject to positive moment but safety problem in those subject to negative moment. The problem will be discussed in Sect. 4.

5 Optimized Evaluation of Segmental Joint

As mentioned before, a validation study has been undertaken to investigate the ability of the 3D numerical modelling to reproduce segment joints failure modes and bearing capacity as determined by bending capacity testing (joint with short straight bolts) in laboratory. It is indicated that the numerical analyses agree well with physical experimentation at low bending moment and bearing capacity. The difference shown in ultimate bearing capacity under positive and negative moment was recorded. As explained in Sect. 3, for large cross-section segmental tunnel linings, the lower ultimate bearing capacity of joint under negative bending moment may cause excessive opening or even damage.

In the next section, an optimized form of bolted joint was developed based on a 3D FEM model for segmenting contact locations (as explained in Sects. 2 and 3) to solve the problem mentioned before. Moreover, model predictions were investigated at the optimized bolted joint figure out the behaviors of the new form of joint.

5.1 Optimized Segmental Joint Evaluation

Since the numerical simulation approach in this study had been confirmed through the comparison with the test results, it allowed us to conduct numerical study on the optimized joint, in order to evaluate the behavior of the joints.

A study of optimized bolted joint was conduct on a similar 3D model explained in Sects. 2 and 3. To make a comparison of its behavior to the short straight bolt in Sect. 3, the normal load was set as 1000 kN. The resulting Mises stress contours of the segments at the joint section under both positive and negative moment were presented in Fig. 5. As is illustrated in Fig. 5, the maximum Mises stress appeared in the compression zone of concrete. In the negative bending moment cases, the existence of large size hand holes impedes the stress transfer in compression zone concrete, which to some degree, leads to the weakening of the whole cross section. Moreover, in both cases, stress concentration was detected near hand hole, however, under low axial force the weakening effect of the big hand hole is not obvious.

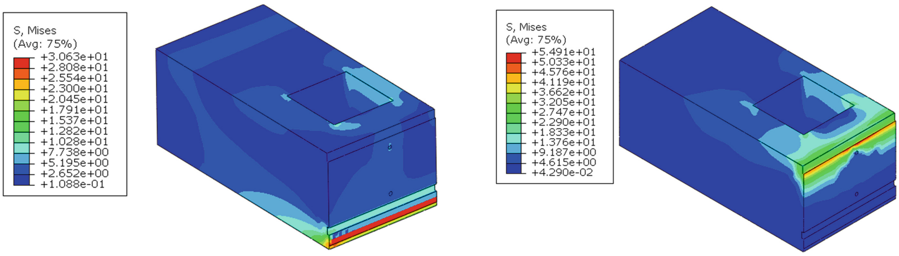

(a) (b)

Fig. 5. Mises stress contours near the segmental joints (MPa). (a) M (+), (b) M (−)

5.2 Optimized Segmental Joint Discussion

To fully evaluate the behavior of the optimized segmental joint, a comparison of its behavior to the short straight bolt in Sect. 3 was carried out, the normal load was set as 1000 kN. The corresponding M $-\ \theta$ was shown in Fig. 6.

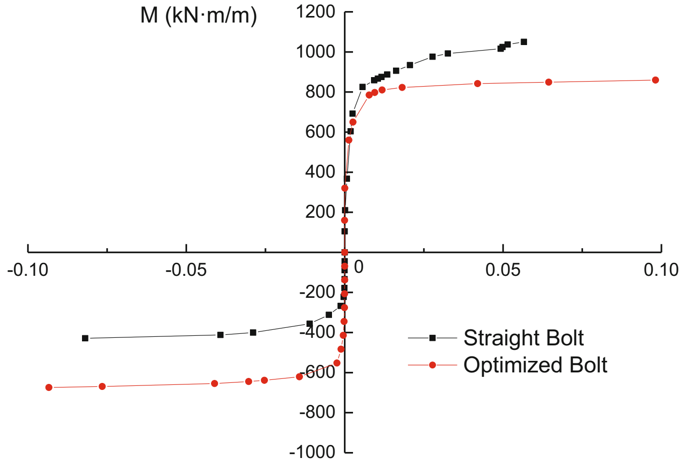

Fig. 6. $M - \theta$ curves of the straight bolt joint and the optimized joint

As is illustrated in Figs. 5 and 6, under the given load (N = 1000 kN), the new joint exhibited good mechanical properties subject to both positive and negative bending moment. According to the simulation results, the bearing capacity of the optimized joint under the positive is approximately 70% the short straight bolts joint. The reason for the decline is weakening effect of large size hand holes. However, the bearing capacity of the optimized joint under the negative moment case is approximately 200% of the short straight bolts joint. This can be explained by the incline bolt insert deeply into the outer surface of the segments, which can better control the outer opening of the joint. It is suggested that the new form joint has good applicability in the negative bending moment joint with low axial force.

6 Conclusion

The present paper developed an optimized form of bolted joint combined both straight bolts and incline bolts based on a validated 3D numerical model for segmenting contact locations. The mechanical behavior of this new joint was examined. The conclusions derived from the FE results and the comparison with the experimental data are summarized as follows:

(1) The presented numerical analyses agree well with physical experimentation at low bending moment and bearing capacity. However, the computed result diverges

from test results in the end of stage I. This can be explained by defects existing in the intact segment.

(2) Compared to the straight joint bolt joints, positive bending bearing capacity of the new joint decreased slightly (about 90% of the latter), and negative bending bearing capacity has a significant increase (about 200%), which suggested that the new joint in the positive and negative moment conditions have good bearing capacity.

(3) The new form of joint can be well used in cases where the axial force is moderate, especially those joints bearing negative moment. Moreover, model predictions were investigated at the optimized bolted joint in different cases and the behaviors of the new form of joint were evaluated.

Acknowledgments. This work was funded by the Shanghai Committee of Science and Technology, China (NO. 16DZ1201701, NO. 15DZ1204003), and the National Natural Science Foundation of China (No. 51378388). All of the sponsoring the programs are gratefully acknowledged. The first author would also like to express his gratitude to Dr. Yafei Qiao from Tongji University for his help.

References

1. Salemi, A., Esmaeili, M., Sereshki, F.: Normal and shear resistance of longitudinal contact surfaces of segmental tunnel lining. Int. J. Rock Mech. Min. Sci. **77**, 328–338 (2015)
2. Zhang, H., Zhang, Z., Wang, J.: 3-D FEM analysis on prefabricated segment joints of shield tunnel. J. Shanghai Jiaotong Univ. **37**(4), 566–569 (2003)
3. Li, Z., Soga, K., Wright, P.: Behaviour of cast-iron bolted tunnels and their modelling. Tunn. Undergr. Space Technol. **50**, 250–269 (2015)
4. Li, Z., Soga, K., Wright, P.: Long-term performance of cast-iron tunnel cross-passage in London clay. Tunn. Undergr. Space Technol. **50**, 152–170 (2015)
5. ASCE: Building code requirements for structural concrete and commentary (ACI 318-95). J. Archit. Eng. (2011)
6. Li, Z., Soga, K., Wang, F., Wright, P., Tsuno, K.: Behaviour of cast-iron tunnel segmental joint from the 3D FE analyses and development of a new bolt-spring model. Tunn. Undergr. Space Technol. **41**, 176–192 (2014)
7. Ding, W.Q., Jin, Y.L., Yan, Z.G., Soga, K., Li, Z.L.: Experimental investigation of the nonlinear behavior of segmental joints in a water-conveyance tunnel. Tunn. Undergr. Space Technol. **68**, 153–166 (2017)
8. Wang, Z., Wang, L., Li, J., Wang, J.: Failure mechanism of tunnel lining joints and bolts with uneven longitudinal ground settlement. Tunn. Undergr. Space Technol. **40**, 300–308 (2014)
9. Ding, W.Q., Peng, Y.C., Yan, Z.G., Shen, B.W., Zhu, H.H., Wei, X.X.: Full-scale testing and modeling of the mechanical behavior of shield TBM tunnel joints. Struct. Eng. Mech. **45** (45), 337–354 (2013)
10. Ding, W.Q., Gong, C.J., Mosalam, K.M., Soga, K.: Development and application of the integrated sealant test apparatus for sealing gaskets in tunnel segmental joints. Tunn. Undergr. Space Technol. **63**, 54–68 (2017)
11. Gong, C.J., Ding, W.Q., Mosalam, K.M., Günay, S., Soga, K.: Comparison of the structural behavior of reinforced concrete and steel fiber reinforced concrete tunnel segmental joints. Tunn. Undergr. Space Technol. **68**, 38–57 (2017)

Analytical Solution of Underneath Tunnelling-Induced Deformation of Existing Tunnel

Zhong-Kai Huang[1], Dong-Mei Zhang[1,2](✉), Mao-Zhu Peng[1,2],
and Xiang Zong[1]

[1] Department of Geotechnical Engineering, Tongji University, Shanghai, China
{5huangzhongkai,dmzhang}@tongji.edu.cn
[2] Key Laboratory of Geotechnical and Underground Engineering of Ministry
of Education, Shanghai, China

Abstract. Tunnelling underneath the existing tunnels are very common these days. It is obvious that the under-crossing tunnelling will affect and even damage the existing tunnels. An analytical method is proposed in this paper to better understand the effects of the under-crossing tunnelling on the existing tunnel. The existing tunnel is modeled as a Timoshenko beam lying on a Kerr foundation. The validity of the analytical solution is verified by a series of centrifuge tests. The parametric study is then carried out to well understand the effect of under-crossing tunneling on the deformation of existing tunnel. The results indicate that the pattern and the magnitude of the deformation of the existing tunnel dependent on the longitudinal shear stiffness, volume loss and the vertical clearance between newly built and existing tunnels.

Keywords: Analytical solution · Timoshenko beam · Kerr foundation
Existing tunnel

1 Introduction

With the rapid urbanization of China, more and more tunnels are constructed to facilitate different needs (Zhang et al. 2017). Consequently, tunnelling underneath the existing tunnels is very common, which will inevitably induce adverse effects on the existing tunnels due to the ground loss. In order to ensure the safety and serviceability of the existing tunnels, there is an urgent need to obtain a comprehensive understanding of their responses. Up to date, various approaches have been adopted to study the impacts of underneath tunnelling on existing tunnels or pipelines, namely, physical model experiments (Marshall 2010), numerical analyses (Karl and Marshall 2008) and analytical methods (Klar et al. 2007). Compared with the other methods, the analytical approaches provide a relative simple way for assessing the interactions between the new tunnel and the existing tunnel. Hence, it is adopted herein to study the underneath tunnelling-induced deformation of existed tunnel.

Moreover, the previous analytical solutions modeled the existing tunnel as an Euler–Bernoulli beam, ignoring the effect of shear deformation of the existing tunnel.

© Springer Nature Singapore Pte Ltd. 2018
D. Zhang and X. Huang (Eds.): GSIC 2018, *Proceedings of GeoShanghai 2018 International Conference: Tunnelling and Underground Construction*, pp. 300–308, 2018.
https://doi.org/10.1007/978-981-13-0017-2_30

In this paper, the Timoshenko beam model is used to model the existing tunnel considering the effect of shear deformation. The applicability of the proposed method is verified by a series of centrifuge tests. Parametric analyses are also performed to study the influences of various factors on the tunnel response.

2 Formulation

Figure 1 presents a schematic diagram of the studied problem. The response of exiting tunnel caused by under-crossing tunnelling is normally investigated using a two-stage method. (Liang et al. 2016). Firstly, the under-tunnelling induced loading is estimated, and secondly, the response of existing tunnel are computed. Some assumptions are made for simplification: (1) Soil is homogeneous and isotropic; (2) The existing tunnel is an elastic and infinite long beam; (3) The existing tunnel remains in contact with the soil; (4) The under-tunnelling construction is not affected by the existing tunnel; (5) The tunnelling-induced ground movement is described using a Gaussian curve.

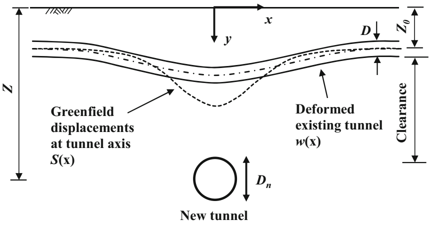
x
y
D
Z_0
Z
Clearance
Greenfield displacements at tunnel axis S(x)
Deformed existing tunnel w(x)
D_n
New tunnel

Fig. 1. Schematic representation of the studied problem

The simplified calculation model of existing tunnel due to under-tunnelling is illustrated in the Fig. 2. The existing tunnel is modeled as a Timoshenko beam lying on a Kerr foundation.

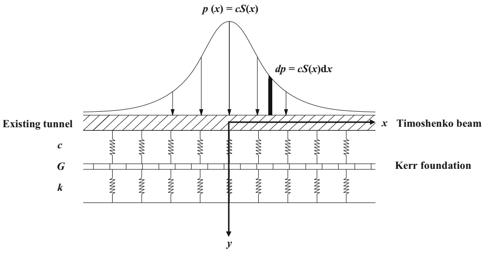
$p(x) = cS(x)$
$dp = cS(x)\mathrm{d}x$
Existing tunnel
x
Timoshenko beam
c
G
k
Kerr foundation
y

Fig. 2. Mechanical representation of the problem

2.1 Tunnelling-Induced Ground Movement

To compute the applied loading on the existing tunnel, the green field displacement at the level of the existing tunnel axis, $S(x)$, should be determined firstly. The commonly adopted Gaussian curve is used to describe the tunnelling-induced ground movement, as shown in Fig. 2 (Klar et al. 2007).

$$S(x) = S_{max} \exp(-0.5x^2/i^2) \tag{1}$$

Where $S(x)$ is the green field displacement at the existing tunnel level, x is the horizontal distance from the new tunnel centerline, S_{max} is the maximum settlement; and i is the trough width parameter.

Considering the green field displacement at the level of the existing tunnel axis can be calculated. The applied loading, $p(x)$, on the existing tunnel can be estimated as:

$$p(x) = cS(x) \tag{2}$$

Where c is the subgrade modulus, i.e., the Young's Modulus of upper spring layer of Kerr foundation and $S(x)$ is the green field displacement at the existing tunnel axis.

2.2 Subgrade Ground Foundation

In order to consider the compression and shear of soil, Kerr foundation is adopted to model the interaction of tunnel and soil, as shown in Fig. 2. In this paper, considering the continuity of soil deformation, three parameters of Kerr foundation are determined by Eq. (3) based on the method proposed by Karl et al.:

$$c = 1.9k; k = 4E/3H; G = 2EH/9(1 + \upsilon) \tag{3}$$

Where E and v is the Young's Modulus and Poisson's ratio respectively, and H is the depth of foundation model.

2.3 Analytical Solution

Following these assumptions, calculation model can be formed and analytical solution can be derived. The existing tunnel is modeled by an infinite Timoshenko beam lying on Kerr foundation. The applied loading on the beam is supposed to be $p(x)$, the corresponding deformation of beam can be expressed as:

$$w(x) = w_1(x) + w_2(x) \tag{4}$$

Where w_1 and w_2 are the deformation of upper spring and bottom spring, respectively.

Let q_1 and q_2 denote the force acting on the bottom of beam and shear layer respectively, then:

$$q_1(x) = cw_1 = c(w - w_2) \tag{5}$$

$$q_2(x) = kw_2 \tag{6}$$

For the shear layer, we have:

$$q_1(x) = -G\frac{d^2w_2}{dx^2} + kw_2 \tag{7}$$

Combining Eqs. (5) and (7), the relationship between w and w_2 can be established as Eq. (8):

$$w = (1 + \frac{k}{c})w_2 - \frac{G}{c}\frac{d^2w_2}{dx^2} \tag{8}$$

When the shear stiffness of the beam is considered, the curvature of beam can be expressed by Eq. (9):

$$\frac{d^2w}{dx^2} = -\frac{M}{EI} - \frac{(p(x) - q_1(x))D}{\Phi} \tag{9}$$

Where arbitrary $p(x)$ is point load, EI is the equivalent longitudinal flexural stiffness, D is the diameter of the existing tunnel and Φ is the shear stiffness of beam.

Based the material's law, the following equation can be derived:

$$\frac{d^2M}{dx^2} = -(p(x) - q_1(x))D \tag{10}$$

Then, subject Eq. (10) to the second order differential equation of Eq. (9):

$$\frac{d^4w}{dx^4} = \frac{(p(x) - q_1(x))D}{EI} - \frac{1}{\Phi}\frac{d^2(p(x) - q_1(x))D}{dx^2} \tag{11}$$

Combining Eqs. (5), (6), (7) and (11), the governing equation of the beam is obtained:

$$\frac{d^6w_2}{dx^6} - (\frac{c+k}{G} + \frac{Dc}{\Phi})\frac{d^4w_2}{dx^4} + (\frac{Dc}{EI} + \frac{Dck}{\Phi G})\frac{d^2w_2}{dx^2} - \frac{Dck}{EIG}w_2 = -\frac{Dc}{EIG}p + \frac{Dc}{\Phi G}\frac{d^2p}{dx^2} \tag{12}$$

It is noted that when the shear stiffness Φ is removed from the aforementioned equation (when Φ is great enough), the equation presented above will degenerate into the equation of the Euler–Bernoulli beam:

$$\frac{d^6w_2}{dx^6} - \frac{c+k}{G}\frac{d^4w_2}{dx^4} + \frac{Dc}{EI}\frac{d^2w_2}{dx^2} - \frac{Dck}{EIG}w_2 = -\frac{Dc}{EIG}p \tag{13}$$

Which is given by Huang et al. (2012) to describe the behavior of an Euler–Bernoulli beam resting on a Kerr foundation.

In order to obtain the solution of Eq. (12), firstly, the general solution of Eq. (12) should be derived. Assuming p equals to 0, so the Eq. (12) is changed into:

$$\frac{d^6 w_2}{dx^6} - (\frac{c+k}{G} + \frac{Dc}{\Phi})\frac{d^4 w_2}{dx^4} + (\frac{Dc}{EI} + \frac{Dck}{\Phi G})\frac{d^2 w_2}{dx^2} - \frac{Dck}{EIG} w_2 = 0 \tag{14}$$

Based on the above analysis, the general equation of the governing equation is:

$$w_2(x) = A_1 e^{-\rho x} + A_2 e^{\rho x} + e^{-Rx}(A_3 \cos Tx + A_4 \sin Tx) + e^{Rx}(A_5 \cos Tx + A_6 \sin Tx) \tag{15}$$

Where A_i (i = 1, 2, 3, 4, 5, 6) are constants and can be calculated from the boundary conditions, and compatibility conditions.

Through the boundary conditions, the solution of w_2 can be obtained, then, the solution of w can be derived based on the Eq. (8):

$$w(x) = B_1 e^{-\rho x} + e^{-Rx}(B_2 \cos Tx + B_3 \sin Tx) \tag{16}$$

Where B_i (i = 1, 2, 3) are integration constants and can be calculated from the boundary conditions.

Assuming the additional load induced by the under-crossing tunnelling on arbitrary location ξ is $q(\xi)d\xi$, the settlement of arbitrary location x of the tunnel axial caused by this load can be expressed as:

$$dw(x) = B_1 e^{-\rho|x-\xi|} d\xi + e^{-R|x-\xi|}(B_2 cos\,\mathrm{T}|x-\xi| + B_3 \sin \mathrm{T}|x-\xi|)d\xi \tag{17}$$

Considering the distribution range of the additional load on the beam and through the integrals of the Eq. (17), the settlement of the existing tunnel caused by the under-crossing tunnelling can be derived as follows:

$$w(x) = \int_{-\infty}^{+\infty} dw(x) \tag{18}$$

3 Verification

The centrifuge tests conducted by Marshall et al. (2010) are adopted to demonstrate the proposed analytical solution. The tests represent a 4.65 m diameter tunnel buried with its axis at a depth of 13.65 m with an existing tunnel buried with its axis at a depth of 5.6 m. The existing tunnel has a diameter of 2.6 m with a lining thickness of 20 mm, then the longitudinal bending stiffness is 2.56×10^{10} N·m^2. The soil adopted is Leighton Buzzard Fraction E dry silica sand, which has an elastic modulus of 19.52 MPa and a Possion's ratio of 0.4. More details can be found in a paper by Marshall et al. (2010). The comparisons of the existing tunnel displacement calculated by the proposed solutions and the centrifuge measured data are shown in Fig. 3. The trends of the vertical tunnel displacements predicted using the proposed analytical solutions are in reasonable agreement with the centrifuge measured data, though when V_l equals to 2.5%, little discrepancy was found in the location where $|x|$ was larger than 15 m, which was possibly due to the simplification of the analytical methods, ignoring the nonlinear soil behavior. From the comparisons, it is indicated that the proposed analytical solutions can be used to predict the deformation of existing tunnel when subjected to under-crossing tunnelling.

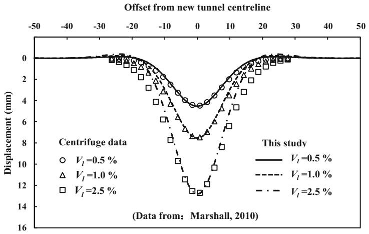

Fig. 3. Comparison of analytical solution with centrifuge test data

4 Parametric Study

Longitudinal shear stiffness, the volume loss and the vertical clearance between the new and existing tunnel influence the behavior of the existing tunnel. A reference case illustrated herein involves a new shield-driven tunnel buried with its axis at a depth of 20.1 m with an existing tunnel buried with its axis at a depth of 9.1 m in Shanghai, China. Both two tunnels have a typical diameter of 6.2 m with a lining thickness of 0.35 m. The segments of existing tunnel are composed of C60 concrete with a Young's modulus of 34.5 GPa. Considering the effect of the segmental ring and the joint, the equivalent longitudinal flexural stiffness $(EI)_{eq}$ is equal to 1.59×10^{10} Nm^2 calculated using the method proposed by Liao et al. (2008), and the longitudinal shear stiffness Φ is equal to 4.44×10^{10} N/m calculated using the proposed method by Wu et al. (2015). The Young's modulus and Possion's ratio of the soil are 16.49 MPa and 0.3, respectively.

4.1 Longitudinal Shear Stiffness

A modified factor ξ is introduced in this study to consider different longitudinal shear stiffness. The equivalent modified shear stiffness $(\Phi)_{eq}$ can be further expressed as: $(\Phi)_{eq} = \xi\Phi$. For the Euler–Bernoulli beam model, it ignores the effect of shear stiffness. For the Timoshenko model, the equivalent shear stiffness, $(\Phi)_{eq}$ is equal to 4.44×10^{11} N/m with different modified factors, ξ = 10, 1, 0.5, 0.2, and 0.1. Figure 4 shows the calculated deformation of tunnel based on the Euler–Bernoulli model and Timoshenko model, and displacements of the tunnel calculated by Timoshenko model are generally larger than that obtained from the Euler–Bernoulli model. For the Euler–Bernoulli model, the width of settlement trough is largest among these curves, and the maximum displacement is 6.02 mm, located in the bottom of the settlement trough. For the Timoshenko model, with a decrease of the shear stiffness, the displacement along the tunnel is increased gradually. If the modified factor of the shear stiffness reaches 10, the curves of the Timoshenko model are close to those of the Euler–Bernoulli model.

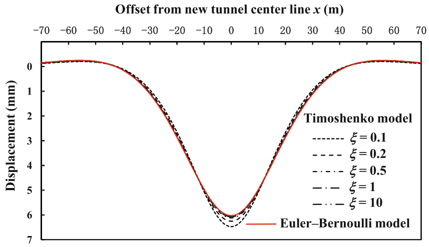

Fig. 4. Displacements of existing tunnel for different longitudinal shear stiffness

4.2 Volume Loss

A series of volume losses are involved in the analysis herein, including V_l = 0.2%, 0.4%, 0.6%, 0.8% and 1.0%. Figure 5 presents the computed vertical displacement curves of the existing tunnel with different volume losses. The vertical displacement of the existing tunnel develops obviously from $x = -40$ to $x = 40$ m, and as $|x|$ gets larger, the vertical displacement is close to zero.

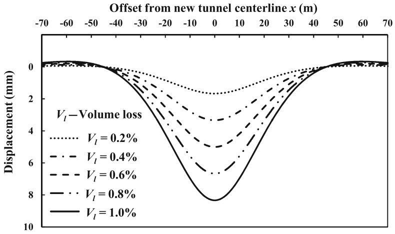

Fig. 5. Displacements of existing tunnel for different volume losses

Figure 6 presents the variation of the vertical displacements for different location with the volume loss increasing. A positive linear correlation is appeared between the vertical displacement and the volume loss. As it can be seen from the results as presented in Fig. 6, the values of the vertical displacement at $x = 0$ m are 1.66, 3.33, 5.00, 6.67, and 8.34 mm, corresponding to volume losses of 0.2%, 0.4%, 0.6%, 0.8%, and 1.0%, respectively. Furthermore, with the increase of x, it is observed that the variation rate of displacement for different volume losses is decreased gradually.

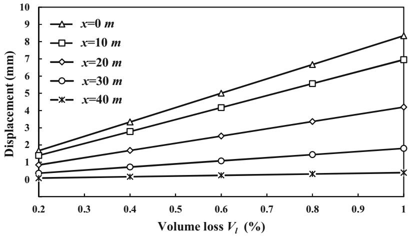

Fig. 6. Displacement versus volume loss

4.3 Vertical Clearance Between Newly Built and Existing Tunnels

A series of different clearance distances are involved in the analysis, including $d = 0.5D$, D, $1.5D$, $2D$ and $2.5D$. The variation of tunnel displacement curves are illustrated in Fig. 7. It is shown that the maximum displacement of the existing tunnel increases and the displacement curve becomes wider as the clearance distance decreases. The displacement sharply decreases within the range of $x = -18$ m to $x = 18$ m, which is the most significant affected region. While within the range from $|x| = 18$ to $|x| = 50$ m, the displacement of the existing tunnel increases with the increase of vertical clearance.

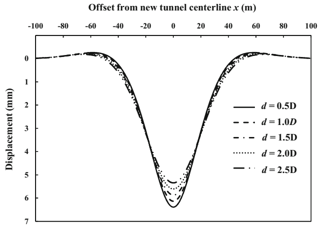

Fig. 7. Displacements of existing tunnel for different vertical clearances

5 Conclusion

In this paper, an analytical solution for evaluating the effects caused by under-crossing tunnelling on existing tunnels is proposed. The main findings are summarized as follows.

(1) The effect of longitudinal shear stiffness of existing tunnel is significant for evaluating under-crossing tunnelling effects on existing tunnels based on the Timoshenko model. Moreover, the Euler-Bernoulli model, which ignores the shear stiffness of lining, underestimates the vertical displacements compared with the Timoshenko model.

(2) The results reveal that the volume loss has prominent effects on the magnitude and the pattern of the displacement curves of the existing tunnel. The maximum vertical displacement rise linearly with volume loss increases.

(3) With the increase of vertical clearance between two tunnels, the maximum vertical displacements decreases obviously, and the width of the displacement curve becomes larger.

Acknowledgement. This study is financially supported by the Key Laboratory of land subsidence monitoring and prevention, Ministry of Land and Resources of the People's Republic of China (KLLSMP201501), National Natural Science Foundation of China (Grants No. 41772 295 and No. 51478344), Shanghai Science and Technology Committee Project (Grant No. 16DZ 1200403) and Science and Technology Project for Transportation and Construction in West of China (2013318J11300). The support is acknowledged.

References

Zhang, D.M., Huang, Z.K., Yin, Z.Y., Ran, L.Z., Huang, H.W.: Predicting the grouting effect on leakage-induced tunnels and ground response in saturated soils. Tunn. Undergr. Space Technol. **65**, 76–90 (2017)

Marshall, A.M., Klar, A., Mair, R.J.: Tunnelling beneath buried pipes: view of soil strain and its effect on pipeline behavior. J. Geotech. Geoenvironmental Eng. **136**(12), 1664–1672 (2010)

Klar, A., Marshall, A.M.: Shell versus beam representation of pipes in the evaluation of tunnelling effects on pipelines. Tunn. Undergr. Space Technol. **23**(4), 431–437 (2008)

Klar, A., Vorster, T.E., Soga, K., Mair, R.J.: Elastoplastic solution for soil-pipe-tunnel interaction. J. Geotech. Geoenvironmental Eng. **133**(7), 782–792 (2007)

Liang, R., Xia, T., Hong, Y., Yu, F.: Effects of above-crossing tunnelling on the existing shield tunnels. Tunn. Undergr. Space Technol. **58**, 159–176 (2016)

Huang, X., Huang, H.W., Zhang, D.M.: Longitudinal deflection of existing shield tunnels due to deep excavation. Chin. J. Geotech. Eng. **34**(7), 1241–1249 (2012). (in Chinese)

Liao, S.M., Peng, F.L., Shen, S.L.: Analysis of shearing effect on tunnel induced by load transfer along longitudinal direction. Tunn. Undergr. Space Technol. **23**(4), 421–430 (2008)

Wu, H.N., Shen, S.L., Liao, S.M., Yin, Z.Y.: Longitudinal structural modelling of shield tunnels considering shearing dislocation between segmental rings. Tunn. Undergr. Space Technol. **50**, 317–323 (2015)

Influence of Pit Excavation on Deformation of Metro Tunnels Based on the Zone State Index

Feng-rui Zhang[1(✉)], An-nan Jiang[1], Shi-jie Zheng[2], Shu-xun Guo[2],
Jin-man Wang[2], and Rui Yang[2]

[1] Highway and Bridge Institute of Dalian Maritime University, Dalian, China
26975290l@qq.com
[2] CCCC Tunnel Engineering Co., Ltd., Beijing, China

Abstract. Excavation of foundation pit can cause surface subsidence and ground movement, further influencing the force and deformation of adjacent tunnel, threatening the safety of tunnel. ZSI is a kind of safety evaluation method based on Mohr-Coulomb yield criterion. It can evaluate the safety and risk of rock and soil mass according to different stress and strain state of the unit, which is an effective way to study local progressive failure of rock and soil mass. Taking the deep foundation pit of Dalian as an engineering example, analyze of the influence of foundation pit excavation on adjacent metro tunnels based on ZSI. In the construction process, the foundation pit and tunnel have been monitored dynamically, and are compared with the numerical simulation results. The results indicate that numerical simulation and field monitoring are basically the same, the overall tendency of settlement curve is also consistent. The achievements may provide references for design and construction of similar projects.

Keywords: Excavation of foundation pit · Metro tunnel · Zone safety index FLAC^{3D} · Stability analysis

1 Introduction

In recent years with development of urban underground space utilization, underground construction is increasing. Most of the foundation pit engineering are located in built-up areas, adjacent to existing tunnels. Excavation of foundation pit can cause surface subsidence and ground movement, further influencing the force and deformation of adjacent tunnel, threatening the safety of tunnel. Therefore, it is very important to study the influence of foundation pit excavation on the existing tunnel.

This paper is supported by the National Natural Science Foundation of China (project number: 51678101).

© Springer Nature Singapore Pte Ltd. 2018

D. Zhang and X. Huang (Eds.): GSIC 2018, *Proceedings of GeoShanghai 2018 International Conference: Tunnelling and Underground Construction*, pp. 309–318, 2018.
https://doi.org/10.1007/978-981-13-0017-2_31

Domestic and foreign scholars have studied the influence of foundation pit excavation on the subway tunnel [1–8]. The ZSI (Zone State Index index) is a kind of safety evaluation method based on Mohr-Coulomb yield criterion. It can evaluate the safety and risk of rock and soil mass according to different stress and strain state of the unit, which is an effective way to study local progressive failure of rock and soil mass. Taking the deep foundation pit of Dalian as an engineering example, analyze of the influence of foundation pit excavation on adjacent metro tunnels based on ZSI. In the construction process, the foundation pit and tunnel have been monitored dynamically, and are compared with the numerical simulation results.

2 Evaluation Method of Unit Safety Index

The symbol of the principal stress is consistent with the symbol of Material Mechanics, tensile stress is positive, compressive stress is negative, $\sigma_1 > \sigma_3$. The expression of ZSI is derived as follows

(1) Elastic stage $(\varepsilon^{ps} = 0, \varepsilon^{pt} = 0))$

The plastic strain of the unit is 0, the safety index of the material unit is calculated according to the stress state. The stress state, as shown in Fig. 1. The Mohr-Coulomb criterion yield surface in the main stress space is an irregular hexagonal section of the pyramid surface. θ_σ is Rhodes angle of Stress.

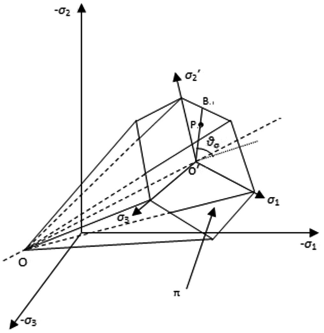

Fig. 1. Stress state

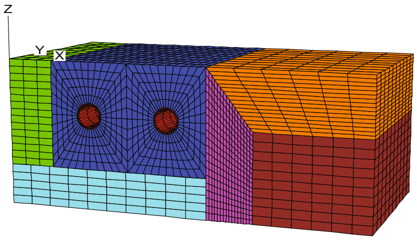

Fig. 2. The finite element model

When $\sigma_1 \leq 0$, there is no tensile stress, the unit in the state of elastic shear. In Fig. 1, P is the actual stress state of the unit, O′ on the isoclinic line is in the same π plane as the P, and O′ is the safest reference point at this stress level. Connect O′P and extend the EFG plane to the B, the ZSI can be expressed as: the ratio of the distance of the safest reference point along the Rhodes angle to the yield surface to the distance between this point and the stress point. When the material is in the safest state, the stress point should be on the isoclinic line. The length of O′B is τ'_π, the length of O′Pis τ_π, B satisfies the yield function, therefore:

$$\begin{aligned} F &= \frac{I_1 \sin\varphi}{3} + (\cos\theta_\sigma - \frac{1}{\sqrt{3}}\sin\theta_\sigma \sin\varphi)\sqrt{J'_2} - c\cos\varphi \\ &= \frac{I_1 \sin\varphi}{3} + \beta(\theta_\sigma)\tau'_\pi - c\cos\varphi \\ &= 0 \end{aligned} \tag{1}$$

$$\beta(\theta_\sigma) = \frac{\cos\theta_\sigma - \sin\theta_\sigma \sin\varphi/\sqrt{3}}{\sqrt{2}} \tag{2}$$

$$\tau'_\pi = \frac{c\cos\varphi - \frac{I_1\sin\varphi}{3}}{\beta(\theta_\sigma)},\ \tau_\pi = \sqrt{2J_2} \tag{3}$$

$$ZSI = \frac{O'B}{O'P} = \frac{\tau'_\pi}{\tau_\pi} = \frac{\frac{I_1\sin\varphi}{3} - c\cos\varphi}{(\frac{1}{\sqrt{3}}\sin\ \theta_\sigma \sin\ \varphi - \cos\theta_\sigma)\sqrt{J_2}} \tag{4}$$

When $\sigma_1 > 0$, consider the tension state of the unit, the tensile strength of the rock material is weak, so the tensile failure needs to be considered in the safety evaluation, ZSI = σ_t/σ_1.

When σ_1 goes to zero, the tension state is the safest state, ZSI = +∞, the shear failure may not be ignored. ZSI is a smaller value in the shear and tension.

In the elastic stage, the ZSI can be expressed as follows:

$$ZSI = \begin{cases} \frac{\frac{I_1\sin\varphi}{3} - c\cos\varphi}{(\frac{1}{\sqrt{3}}\sin\theta_\sigma\sin\varphi - \cos\theta_\sigma)\sqrt{J_2}} & \sigma_1 \le 0 \\ \min\left(\frac{\frac{I_1\sin\varphi}{3} - c\cos\varphi}{(\frac{1}{\sqrt{3}}\sin\theta_\sigma\sin\varphi - \cos\theta_\sigma)\sqrt{J_2}}, \frac{\sigma_t}{\sigma_1}\right) & \sigma_1 > 0 \end{cases} \tag{5}$$

When the ZSI > 1, the unit is in the elastic stage, the larger the ZSI value, the higher the security. When ZSI = 1, the unit begins to enter the yield stage.

(2) Yield stage ($0 < \varepsilon^{ps} \le \bar{\varepsilon}^{ps}$, $\varepsilon^{pt} = 0$; $\varepsilon^{ps} = 0$, $0 < \varepsilon^{pt} \le \bar{\varepsilon}^{pt}$; $0 < \varepsilon^{ps} \le \bar{\varepsilon}^{ps}$, $0 < \varepsilon^{pt} \le \bar{\varepsilon}^{pt}$)

When stress more than the yield stress, the rock is the state of plastic softening, the equivalent plastic strain is greater than 0.

$0 < \varepsilon^{ps} \le \bar{\varepsilon}^{ps}$, $\varepsilon^{pt} = 0$ expresses that the unit is in shear yield state; $\varepsilon^{ps} = 0$, $0 < \varepsilon^{pt} \le \bar{\varepsilon}^{pt}$ expresses that the unit is in tensile yield state; $0 < \varepsilon^{ps} \le \bar{\varepsilon}^{ps}$, $0 < \varepsilon^{pt} \le \bar{\varepsilon}^{pt}$ expresses that two states reach the yielded state; $\varepsilon^{ps}/\bar{\varepsilon}^{ps}$ expresses that the distance between the shear yield surface and the failure surface, when the rock is in shear yield state, the formula of ZSI is as follows:

$$ZSI = 1 - \frac{\varepsilon^{ps}}{\overline{\varepsilon}^{ps}} \tag{6}$$

Similarly, when the material is in the tensile yield state, the formula of ZSI is as follows:

$$ZSI = 1 - \frac{\varepsilon^{pt}}{\overline{\varepsilon}^{pt}} \tag{7}$$

$0 < \varepsilon^{ps} \leq \overline{\varepsilon}^{ps}$, $0 < \varepsilon^{pt} \leq \overline{\varepsilon}^{pt}$ expresses that the shear and tensile states of the unit have reached the yielded state, ZSI takes the smaller value in both cases. The formula of ZSI is as follows:

$$ZSI = \min(1 - \frac{\varepsilon^{ps}}{\overline{\varepsilon}^{ps}}, 1 - \frac{\varepsilon^{pt}}{\overline{\varepsilon}^{pt}}) \tag{8}$$

(3) Failure stage ($\varepsilon^{ps} > \overline{\varepsilon}^{ps}$ 或 $\varepsilon^{pt} > \overline{\varepsilon}^{pt}$)

When the equivalent plastic strain more than the limit equivalent plastic strain, the rock is in failure state. $\varepsilon^{ps} > \overline{\varepsilon}^{ps}$ expresses that the unit occurs shear failure, $\varepsilon^{pt} > \overline{\varepsilon}^{pt}$ expresses that the unit occurs tensile failure. The expression of ZSI is the same as formula (13). The ZSI decreases with the increase of the equivalent plastic strain. ZSI $\in (-\infty, 0)$, the smaller the ZSI is, the higher the degree of damage.

3 Influence of Foundation Pit Excavation on Subway Tunnel

3.1 General Situation of Engineering

The foundation pit project is located on the west side of the second line of dalian subway tunnel. It's an irregular trapezoid. The foundation pit covers an area of about 48,000 m^2, the excavation depth of the foundation pit is about 22.1 m–26.8 m, and the excavation width of the foundation pit is 29.95 m–43.76 m. The minimum distance from the outer edge of the tunnel structure is 11.6 m. The tunnel spacing is 15 m, the height is 6.41 m, and the width is 6.2 m. The tunnel with composite lining, the thickness of initial lining is 25 cm, the thickness of secondary lining is 30 cm.

3.2 Numerical Simulating Model

Based on the general situation of the project, the numerical model is established by FLAC3D. The width of the tunnel is 6 m, and the height of the tunnel is 6 m. The thickness of concrete lining is 0.5 m, the spacing of two tunnels is 15 m. The excavation width of foundation pit is 31 m–43.5 m, and the depth of foundation pit is 16 m, the minimum distance from the outer edge of the tunnel structure is 11.6 m.

The model can be divided into 5 layers from top to bottom: the first layer is plain fill, with a thickness of 2 m; the second layer is silty clay, with a thickness of 5 m; the three layer is completely weathered slate, with a thickness of 3 m; the four layer is strongly weathered slate, with a thickness of 4 m; the five layer is strongly moderately weathered slate, with a thickness of 16 m. The finite element model as shown in Fig. 2.

3.3 Calculation Parameters and Excavation Steps

A strain softening model is used in numerical calculation, the reduction coefficient of the residual strength after the peak stage c, $\varphi = 1.5$. The depth of the foundation pit is 16 m, which is excavated 8 times and each excavation is 2 m. The bolt support is set on the slope during each excavation, the length of bolt is 15 m, the spacing is 1.3 m. The parameters of soil layer and concrete lining as shown in Table 1. The parameters of bolt and cement slurry as shown in Table 2.

Table 1. The parameters of soil layer and concrete lining

Stratum	Elastic modulus (GPa)	Poisson ratio	Thickness (m)	Density (kg/m^3)	Internal friction angle (°)	Cohesion (kPa)
Plain fill	0.05	0.47	2	1800	9	15
Silty clay	0.1	0.35	5	1950	12	12
Completely weathered slate	0.15	0.43	3	2000	15	30
Strongly weathered slate	0.24	0.32	4	2050	20	36
Moderately weathered slate	0.8	0.30	16	2200	26	45
Concrete lining	1.8	0.28	0.5	2600	23	500

Table 2. The parameters of bolt and cement slurry

Elastic modulus/GPa	Cross sectional area/m^2	Tensile strength/N	Stiffness of cement slurry/Pa	Adhesion of cement slurry/N	External angle/°
45	1.6e−3	120 kN	1.8e7	2.0e6	15

4 Analysis of Numerical Results

4.1 Influence of Foundation Pit Excavation on Tunnel Deformation

The results (Fig. 3 and Table 3) show that the displacement of foundation pit and tunnel increase gradually with the increase of excavation depth. When the foundation pit is excavated to the bottom, the displacement of the slope is the largest, the maximum horizontal displacement is 2.07 mm, and the maximum vertical displacement is

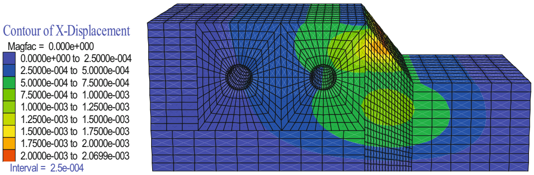
Contour of X-Displacement
Magfac = 0.000e+000
0.0000e+000 to 2.5000e-004
2.5000e-004 to 5.0000e-004
5.0000e-004 to 7.5000e-004
7.5000e-004 to 1.0000e-003
1.0000e-003 to 1.2500e-003
1.2500e-003 to 1.5000e-003
1.5000e-003 to 1.7500e-003
1.7500e-003 to 2.0000e-003
2.0000e-003 to 2.0699e-003
Interval = 2.5e-004

（a）Horizontal displacement of the foundation pit

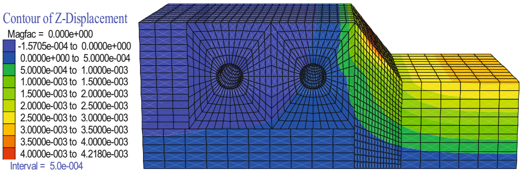
Contour of Z-Displacement
Magfac = 0.000e+000
-1.5705e-004 to 0.0000e+000
0.0000e+000 to 5.0000e-004
5.0000e-004 to 1.0000e-003
1.0000e-003 to 1.5000e-003
1.5000e-003 to 2.0000e-003
2.0000e-003 to 2.5000e-003
2.5000e-003 to 3.0000e-003
3.0000e-003 to 3.5000e-003
3.5000e-003 to 4.0000e-003
4.0000e-003 to 4.2180e-003
Interval = 5.0e-004

（b）Vertical displacement of the foundation pit

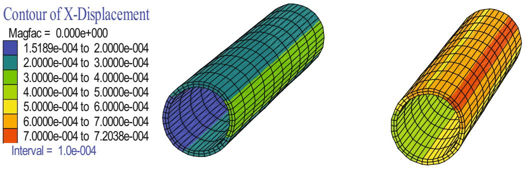
Contour of X-Displacement
Magfac = 0.000e+000
1.5189e-004 to 2.0000e-004
2.0000e-004 to 3.0000e-004
3.0000e-004 to 4.0000e-004
4.0000e-004 to 5.0000e-004
5.0000e-004 to 6.0000e-004
6.0000e-004 to 7.0000e-004
7.0000e-004 to 7.2038e-004
Interval = 1.0e-004

（c）Horizontal displacement of the tunnel

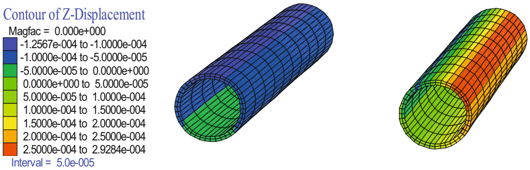
Contour of Z-Displacement
Magfac = 0.000e+000
-1.2567e-004 to -1.0000e-004
-1.0000e-004 to -5.0000e-005
-5.0000e-005 to 0.0000e+000
0.0000e+000 to 5.0000e-005
5.0000e-005 to 1.0000e-004
1.0000e-004 to 1.5000e-004
1.5000e-004 to 2.0000e-004
2.0000e-004 to 2.5000e-004
2.5000e-004 to 2.9284e-004
Interval = 5.0e-005

（d）Vertical displacement of the tunnel

Fig. 3. The change of displacement after completion of excavation

Table 3. The displacement of the foundation pit and tunnel at different excavation depth

Excavation depth/m	Horizontal displacement of the foundation pit/m	Vertical displacement of the foundation pit/m	Horizontal displacement of the tunnel/m	Vertical displacement of the tunnel/m
2	0.6	2.84	0.2	0.12
6	1.3	3.45	0.45	0.18
12	1.87	3.87	0.65	0.23
16	2.07	4.2	0.72	0.29

4.22 mm. The excavation of foundation pit has an effect on the deformation of adjacent tunnel, the most obviously changed area is about 45° away from the crown of arch of the right tunnel, the maximum horizontal displacement is 0.72 mm, and the maximum vertical displacement is 0.29 mm.

4.2 Analysis of Unit State Index

In Fig. 4, $ZSI < 0$ is the damage area of the tunnel. The damage area of the tunnel is concentrated near the arch waist of the tunnel. The minimum of ZSI is −6, and the maximum of ZSI is 4. With the increase of excavation depth, the destruction rate of the tunnel increases, moreover, the yield area increases gradually, and the overall stability of the tunnel decreases gradually.

Dangerous degree of the unit cannot be obtained directly from the results of displacement or stress, ZSI can be more intuitionistic to express the dangerous degree of the unit. ZSI can still express safety degree of the area where the plastic zone cannot be displayed, and also can be applied to the dynamic destruction process of the model.

As can be seen from the Fig. 5, with the increase of the excavation steps of the foundation pit, ZSI decreases sharply at first, and then slowly. The arch waist of tunnel is close to the foundation pit, the failure state is reached in fourth step of foundation pit excavation, $ZSI < 0$. The vault is in a yield state in fifth step of foundation pit excavation, $0 < ZSI < 1$. The arch foot of tunnel is far from the foundation pit, although the ZSI decreases with the increase of the excavation steps, the unit is always in the elastic state.

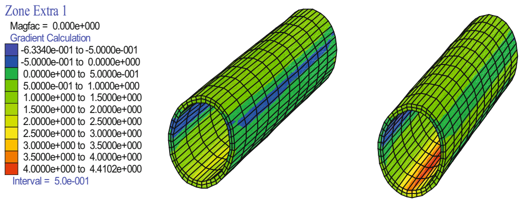
Zone Extra 1
Magfac = 0.000e+000
Gradient Calculation
-6.3340e-001 to -5.0000e-001
-5.0000e-001 to 0.0000e+000
0.0000e+000 to 5.0000e-001
5.0000e-001 to 1.0000e+000
1.0000e+000 to 1.5000e+000
1.5000e+000 to 2.0000e+000
2.0000e+000 to 2.5000e+000
2.5000e+000 to 3.0000e+000
3.0000e+000 to 3.5000e+000
3.5000e+000 to 4.0000e+000
4.0000e+000 to 4.4102e+000
Interval = 5.0e-001

（a）Excavation 2m

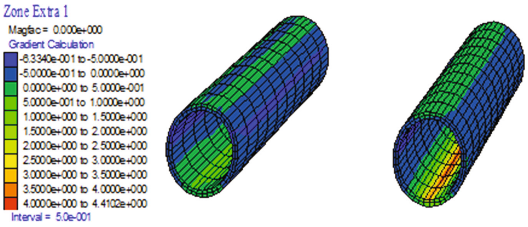
Zone Extra 1
Magfac = 0.000e+000
Gradient Calculation
-6.3340e-001 to -5.0000e-001
-5.0000e-001 to 0.0000e+000
0.0000e+000 to 5.0000e-001
5.0000e-001 to 1.0000e+000
1.0000e+000 to 1.5000e+000
1.5000e+000 to 2.0000e+000
2.0000e+000 to 2.5000e+000
2.5000e+000 to 3.0000e+000
3.0000e+000 to 3.5000e+000
3.5000e+000 to 4.0000e+000
4.0000e+000 to 4.4102e+000
Interval = 5.0e-001

（b）Excavation 6m

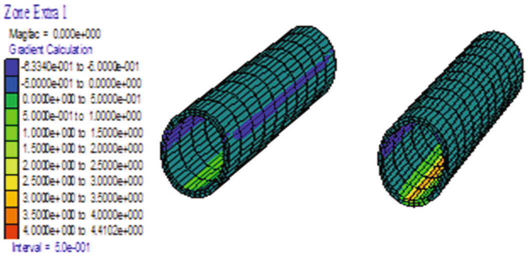
Zone Extra 1
Magfac = 0.000e+000
Gradient Calculation
-6.3340e-001 to -5.0000e-001
-5.0000e-001 to 0.0000e+000
0.0000e+000 to 5.0000e-001
5.0000e-001 to 1.0000e+000
1.0000e+000 to 1.5000e+000
1.5000e+000 to 2.0000e+000
2.0000e+000 to 2.5000e+000
2.5000e+000 to 3.0000e+000
3.0000e+000 to 3.5000e+000
3.5000e+000 to 4.0000e+000
4.0000e+000 to 4.4102e+000
Interval = 5.0e-001

（c）Excavation 12m

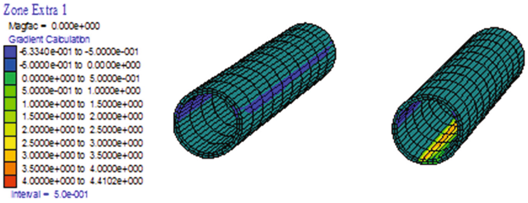
Zone Extra 1
Magfac = 0.000e+000
Gradient Calculation
-6.3340e-001 to -5.0000e-001
-5.0000e-001 to 0.0000e+000
0.0000e+000 to 5.0000e-001
5.0000e-001 to 1.0000e+000
1.0000e+000 to 1.5000e+000
1.5000e+000 to 2.0000e+000
2.0000e+000 to 2.5000e+000
2.5000e+000 to 3.0000e+000
3.0000e+000 to 3.5000e+000
3.5000e+000 to 4.0000e+000
4.0000e+000 to 4.4102e+000
Interval = 5.0e-001

（d）Excavation 16m

Fig. 4. The ZSI contour lines of the tunnel under different excavation depth

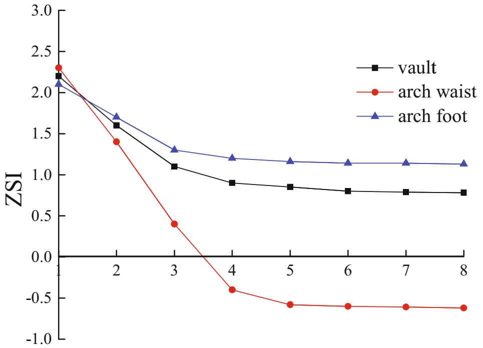

Fig. 5. The changing curve of ZSI of the middle section of the right tunnel

5 Comparative Analysis

To ensure the safety of the tunnel, the vertical displacement of tunnel is monitored by Static Force Level, the horizontal displacement of the tunnel is measured by Total Station. The results of four subsidence monitoring points in tunnel are compared with the numerical simulation results.

It can be seen from the Fig. 6, numerical simulation and field monitoring are basically the same, the overall tendency of settlement curve is also consistent, so the accuracy of numerical simulation is verified.

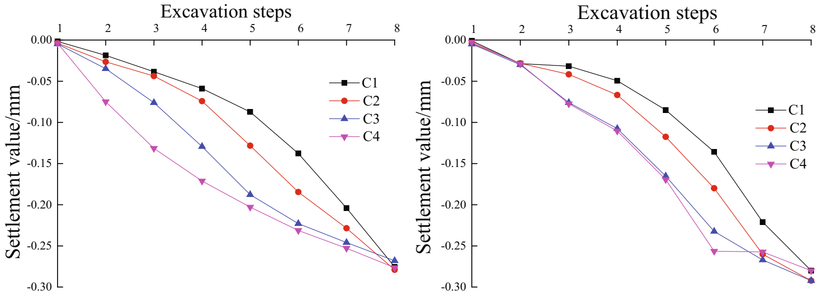

Numerical simulation

Field monitoring

Fig. 6. The settlement value of numerical simulation and field monitoring

6 Conclusion

(1) The ZSI (Zone State Index index) is a kind of safety evaluation method based on Mohr-Coulomb yield criterion. It can evaluate the safety and risk of rock and soil mass according to different stress and strain state of the unit, which is an effective way to study local progressive failure of rock and soil mass.

(2) The displacement of foundation pit and tunnel increase gradually with the increase of excavation depth. When the foundation pit is excavated to the bottom, the displacement of the slope is the largest, the maximum horizontal displacement is 2.07 mm, and the maximum vertical displacement is 4.22 mm. The excavation of foundation pit has an effect on the deformation of adjacent tunnel, the most obviously changed area is about 45° away from the crown of arch of the right tunnel, the maximum horizontal displacement is 0.72 mm, and the maximum vertical displacement is 0.29 mm.

(3) The damage area of the tunnel is concentrated near the arch waist of the tunnel. The minimum of ZSI is −6, and the maximum of ZSI is 4. With the increase of excavation depth, ZSI decreases sharply at first, and then slowly, the overall stability of the tunnel decreases gradually.

(4) Numerical simulation and field monitoring are basically the same, the overall tendency of settlement curve is also consistent, so the accuracy of numerical simulation is verified.

References

1. Sharma, J.S., Hefny, A.M., Zhao, J.: Effect of large excavation on deformation of adjacent MRT tunnels. Tunn. Undergr. Space Technol. **16**, 93–98 (2001)
2. Dolezalova, M.: Tunnel complex unloaded by a deep excavation. Comput. Geotech. **28**(6–7), 469–493 (2001)
3. Boscardin, M.D., Cording, E.J.: Building response to excavation-induced settlement. J. Geotech. Eng. **115**(1), 1–21 (1989)
4. Blackburn, J.T.: Automated Remote Sensing and Three Dimensional Analysis of Internally Braced Excavations, pp. 50–80. Northwestern University, Illinois, USA (2005)
5. Cao, Q., Li, Q., Xiang, W., et al.: Automatic monitoring of effects of excavation of group foundation pits on existing adjacent metro tunnels. Chin. J. Geotech. Eng. **34**(Sup1), 552–556 (2012)
6. Zhang, J., Wang, J., Chen, J., et al.: 3-D FEM back-analysis of an over size and deep excavation. J. Shanghai Jiaotong Univ. **46**(1), 42–46 (2012)
7. Zhang, M.Y., Yang, X.P., Liu, T.J.: Comparative analysis of construction schemes for foundation pit excavation adjacent to subway tunnel. Chin. J. Undergr. Space Eng. **7**(6), 1203–1208 (2011)
8. Zheng, G., Liu, Q.-C., Deng, X., et al.: Field measurement and analysis of effect of excavation on existing tunnel boxes of underlying metro tunnel in operating. Rock Soil Mech. **34**(5), 1459–1468 (2013)

In-situ Experimental Analysis of Acceleration Response of Mountain Tunnel Lining to Rubblization-Induced Vibrations

Yong Zhao(✉), Shi-Jin Feng, Mao-Zhu Peng, Dong-Mei Zhang,
and Xiao-lei Zhang

Department of Geotechnical Engineering, Tongji University,
Shanghai 200092, China
1530775@tongji.edu.cn

Abstract. Resonant rubblization technology is often utilized to rehabilitate deteriorated concrete pavements. Vibrations induced by a resonant breaker would produce detrimental effects on lining structures in tunnel during rubblization construction. The in-situ experiments were carried out in Yangjiao Mountain Tunnel in Zhejiang Province, China. First, the characteristics of rubblization-induced vibration are analyzed in time and frequency domains. Then effects of different testing points and pavement breaking positions on lining dynamic response in several frequency bands are taken into consideration to investigate vibration propagation rules. Later, the amplitudes of acceleration, vibration acceleration level (Val) and velocity in the examined cross section are presented to evaluate the dynamic response of lining structure in the procedure of resonant rubblization. The results show that the acceleration peak (3.52 g) appears on the lining arch foot while the maximum of Val (132.6 dB) and velocity (17.2 mm/s) show on the arch side. The presented data and results can be useful for design and safety assessment of resonant rubblization construction in mountain tunnel.

Keywords: Rubblization-induced vibration · Lining dynamic response
Experimental analysis

1 Introduction

Resonant rubblization technology was utilized to rehabilitate the deteriorated pavements of Maoliling Highway Tunnels in Taizhou, Zhejiang Province and no similar case has been reported in China. Rubblization is an efficient and unique means of rehabilitating concrete pavements by in-place conversion of the old concrete pavement into a useable base [1]. A Resonant Pavement Breaker (RPB), which employs a low amplitude, high frequency breaking shoe to strike the surface of the pavement, can break the concrete in place and leave pieces small enough to significantly reduce reflection cracking in the hot-mixed asphalt overlays. Researches on resonant rubblization technology can be divided into two parts. Some researchers focus on the rubblization construction design and quality evaluation [2, 3], the other specialize in characteristic analysis of fractured slab after rubblization [4, 5]. Reports concentrated

© Springer Nature Singapore Pte Ltd. 2018
D. Zhang and X. Huang (Eds.): GSIC 2018, *Proceedings of GeoShanghai 2018 International Conference: Tunnelling and Underground Construction*, pp. 319–328, 2018.
https://doi.org/10.1007/978-981-13-0017-2_32

on surrounding impact of rubblization construction have rarely been found. Different from rubblizing in open field, rubblization performing inside a tunnel would produce detrimental effects on surrounding structures. Vibrations induced by a resonant pavement breaker transfer and superpose through the tunnel, threatening the safety of lining structures. Previous researchers analyzed dynamic response of lining structures to vibration mostly induced by train [6], vehicle [7] or blast [8]. The performance of lining structures under rubblization-induced dynamic load has never been studied before.

Based on pavement rehabilitation construction in Yangjiao Mountain Tunnel, one of Maoliling Highway Tunnels in Taizhou, Zhejiang Province, in-situ monitoring was carried out on the acceleration response of tunnel lining sections effected by resonant rubblization. In this paper, characteristics of dynamic load induced by rubblization construction are described and the rules of acceleration transmission in lining sections are investigated. The vibration of lining structures under rubblization construction load is also evaluated by the peak of vibration velocity.

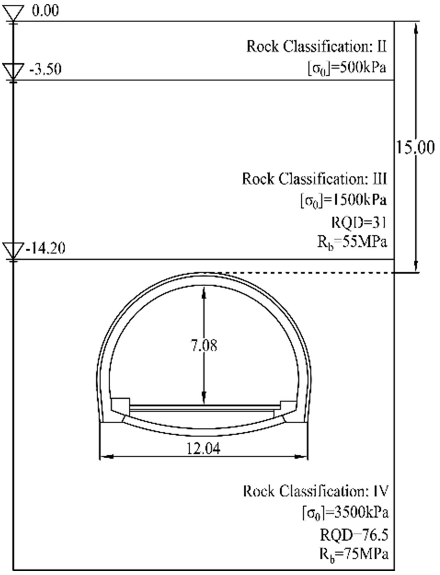
0.00
-3.50
-14.20
Rock Classification: II
$[\sigma_0]$=500kPa
15.00
Rock Classification: III
$[\sigma_0]$=1500kPa
RQD=31
R_b=55MPa
7.08
12.04
Rock Classification: IV
$[\sigma_0]$=3500kPa
RQD=76.5
R_b=75MPa

Fig. 1. Parameters of the surrounding rock.

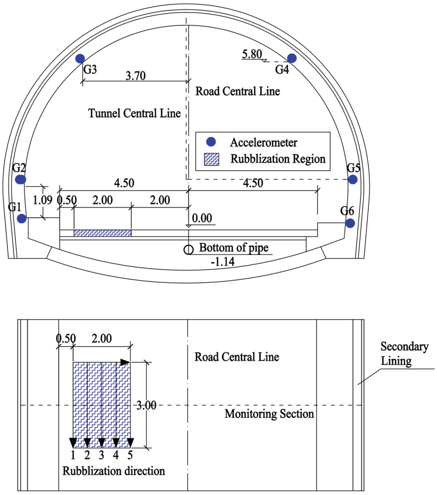
G3
3.70
5.80
G4
Road Central Line
Tunnel Central Line
Accelerometer
Rubblization Region
G2
G5
4.50
4.50
G1
1.09
0.50
2.00
2.00
G6
0.00
Bottom of pipe
-1.14
0.50
2.00
Road Central Line
Secondary Lining
3.00
Monitoring Section
1 2 3 4 5
Rubblization direction

Fig. 2. Monitoring layout.

2 In-situ Experiment

2.1 Characterization of the Tunnel

The in-situ experiment was performed in Yangjiao Mountain Tunnel (Wenzhou direction), located in Taizhou, Zhejiang Province, China. This tunnel, with the maximum burial depth of 45 m, is part of the Ningbo-taizhou-wenzhou Expressway and its survey mark ranges from K19+735 to K19+910. In the experiment, four typical cross sections of the tunnel were examined. This paper mainly discusses the K19+880 monitoring section, which was buried at the depth of 15 m from the ground to the arch crown. The section bedrock, consist mainly of intermediate-fine grain moyite, is classified into Rock Grade III for its poor stability according to the Chinese Code for Design of Road Tunnel (JTJ 026-90). More relevant parameters of the surrounding rock can be seen in Fig. 1. By the positive step method, this part of tunnel was excavated and its supports were designed following the New Austrian Tunneling Method (NATM). C20 shotcrete was used to build tunnel initial supports and C25 concrete was for secondary lining and invert. The material of the tunnel slab is C40 concrete and the space between the pavement and the invert is filled with C15 rubble concrete.

2.2 Experimental Set-up

Employing several accelerometers, signal acquisition boxes, data cables and a laptop, the acceleration of the examined lining section was recorded during the rubblization construction. Parameters of main test equipment can be found in Table 1. Six accelerometers(G1–G6) were set in radial direction on the monitoring lining surface at the position of arch foot, arch side and arch crown respectively (Figs. 2 and 3).

Table 1. Parameters of main test equipment.

Signal acquisition box	Parameter	Type	Sampling frequency		Channel number
	Value	NI cDAQ9191	1000 Hz/Channel		4
Unidirectional accelerometer	Parameter	Type	Sensitivity	Measurement range	Frequency range
	Value	LC0155	700 mV/g	7 g	0.1–4000 Hz

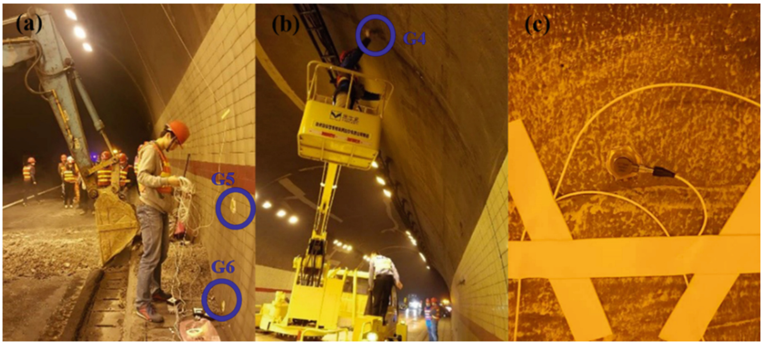

Fig. 3. Accelerometer installation

2.3 Rubblization Construction

Employing a GPJ3X-600 Resonant Pavement Breaker (RPB), the rubblization construction was conducted. RPB is a self-propelled device that utilizes high frequency, low amplitude impacts with a foot force of 2,000 lbs [9]. The foot is located at the end of a pedestal that is attached to a beam and counter weight. The force applied to the pavement is achieved by vibrating the large steel beam connected to the foot. The foot is moved along the concrete surface at the front of the machine. Operation performance parameters of the RPB are expatiated in Table 2.

Table 2. Parameters of the RPB

Parameters	Value
Type	GPJ3X-600
Size (length × width × height)	7.65 × 2.65 × 3 m
Weight	$\leq$ 30000 kg
Power	448 kW
Foot width	100–200 mm
Operating frequency	45–70 Hz
Amplitude	8–16 mm
Construction efficiency	4000 m^2/day (8 h)
Speed	0–14 km/h

One 3 m × 2 m region of the tunnel pavement, marked in Fig. 2, was chosen to initiate the test. During rubblization construction, the RPB drove towards one direction. Every time the breaking foot reached the end edge of the rubblization region, the RPB drove back to the beginning edge. It took 11 times to complete the construction and each breaking area is 3000 mm in length and 150–200 mm in width.

3 Results

3.1 Characteristics of Vibration Acceleration

During rubblization construction process, lining acceleration data was recorded separately each time the RPB finished one breaking line. Figure 4a shows typical time history variations of G1–G6 during one time of rubblization. It can be seen that this process of construction last for 20 s and no sharp peak is recorded. Higher vibration intensity is observed at positions of G1 and G2 than the other test points of lining structure. The acceleration peak, appearing in the 18th seconds at position G1, is 2.6 g. Then acceleration data is analyzed in frequency spectrum (Fig. 4b) using Fast Fourier Transform (FFT). It can be seen that frequency contents of 25–350 Hz are relatively strong. The acceleration amplitude of all frequency at position G2, slightly larger than that at G1, is significantly higher than G3. Similar intensity relationship of corresponding positions (G6–G4) can be detected on the other half of lining structure, although their vibration strength is at a low level. Conclusions can be drawn that vibration induced by rubblization construction propagates along the slab to both sides of arch foot and then to the arch crown. The predominant frequencies of lining vibration are observed at 58 Hz, 87 Hz and 103 Hz. Since the operating frequency of the RPB is 45–70 Hz, the vibration excitation frequency is 58 Hz.

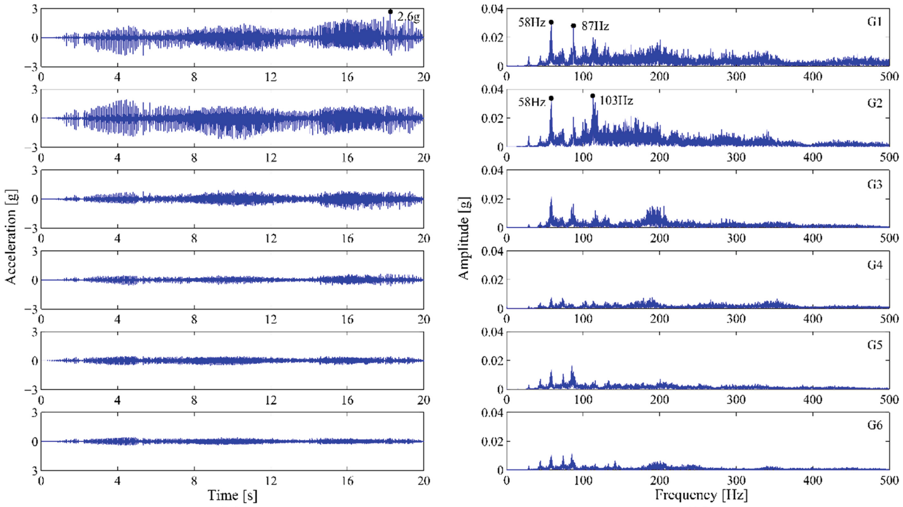

(a) (b)

Fig. 4. (a) Time domain; (b) Frequency domain

Analyzing the characteristics of lining acceleration response above, vibrations induced by rubblization construction is different from that by train or blast. Blast-induced lining dynamic response, featured in large intensity, short duration and quick attenuation, is transient free vibration [10]. Train-induced lining dynamic response, of which acceleration peak would be no more than 0.1 g, is close to steady forced vibration. Periodism could be found in time domain and one or two remarkable peak could be observed in frequency domain [11]. Lining dynamic response induced by rubblization construction is also one kind of steady forced vibration. Considering the features of large vibration acceleration, wide frequency domain and regular distribution of predominant frequency, the regularity of rubblization-induced vibration propagation is a topic worth studying.

3.2 Regularity of Vibration Propagation

According to Chinese Code: Measurement Method of Environmental Vibration of Urban Area (GB10071-88), vibration acceleration is converted into vibration acceleration level (Val) using Eq. (1) to describe the vibration intensity.

$$\mathrm{Val} = 20\lg\frac{a'}{a_0}(dB) \tag{1}$$

Where Val is acceleration level in decibels; a′ is virtual value of acceleration (m/s^2); a_0 is reference acceleration equal to 10^{-6} m/s^2.

Fixed Vibration Source. More significant impact by rubblization construction is noticed at testing points G1–G3 than G4–G6 in Fig. 4. Therefore, acceleration data of

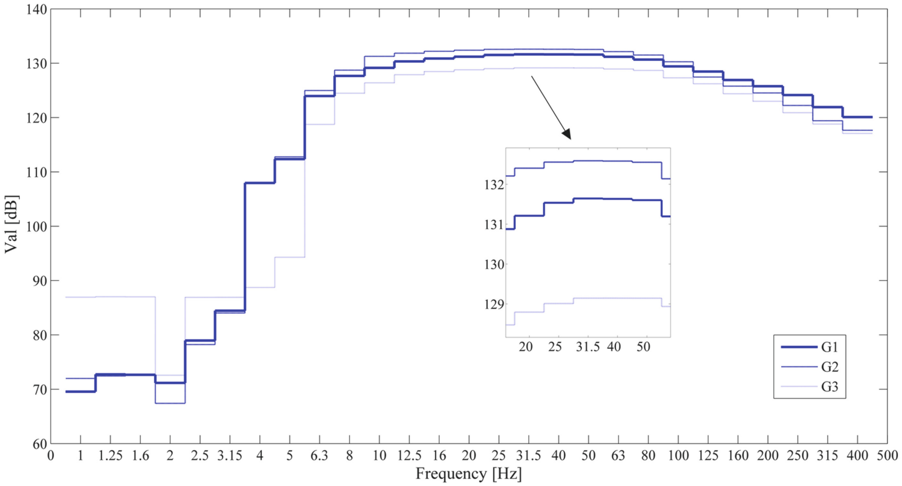

Fig. 5. 1/3 octave frequency at G1, G2 and G3

G1 to G3, recorded when rubblization line is closest to the curb, is analyzed in 1/3 octave frequency (Fig. 5).

It can be seen from Fig. 5 that Val in 1/3 octave frequency at G2 is at the top level. Similar distribution of Val is found at G1 and G2: vibration energy of frequency band 0–4 Hz is of small value; Val increases sharply in center frequency from 4 Hz to 10 Hz and then reaches the maximum; A smooth drop-down trend takes place in vibration energy with the increase of center frequency after 80 Hz. Val of low frequency components (0–4 Hz) at G3 is of a comparatively high value comparing to that at G1 and G2.

According to the descriptions above, vibrations of frequency band 20–80 Hz play a dominant role in lining dynamic response induced by rubblization. And based on previous research, buildings and precise instruments fall under great influence of low frequency vibration (0–10 Hz). Employing the band-pass filter, variations of vibration acceleration level of 0–500 Hz, 0–10 Hz and 20–80 Hz between G1, G2 and G3 are plot in Fig. 6a.

Figure 6a shows that the value and distribution regularity of Val of 20–80 Hz frequency band are approximate to that of 0–500 Hz. Similar conclusions can be drawn as from Fig. 5 that the main frequency content of vibration induced by rubblization is 20–80 Hz. Though 0–10 Hz vibration could exercise negative influence on buildings, it may not dominate lining dynamic response due to low value of Val. Vibration intensity of 20–80 Hz increases slightly at G2 and drops at G3, while that of 0–10 Hz is in the rising trend from G1 to G3. It can be account to that vibration of 20–80 Hz, possessing relatively shorter wavelength, attenuates quickly along the distance from vibration source to G3. However, considering the features of slow attenuation, vibration of 0–10 Hz propagates to both sides of lining and superposes at the position of G3.

Moving Vibration Source. During the progress of rubblization construction, the breaking line that the RPB drives along moves from the curb to the road central line.

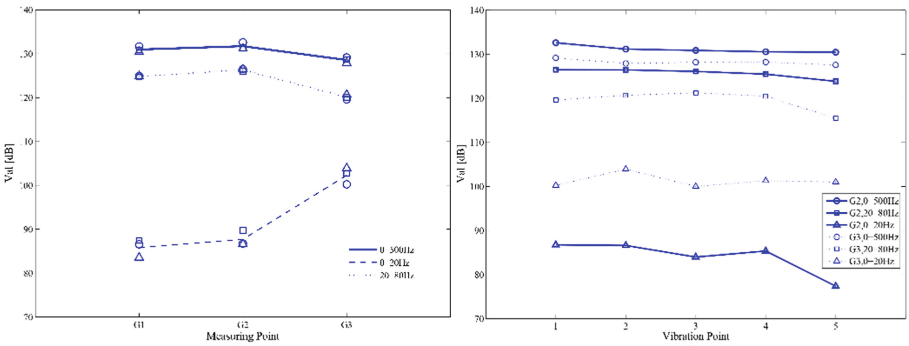

(a) (b)

Fig. 6. Vibration acceleration level: (a) variation with measuring point; (b) variation with vibration point

Acceleration data from G2 and G3 at 5 different rubblization position, as shown in Fig. 2, is analyzed in Val and compared in frequency band of 0–500 Hz, 0–10 Hz and 20–80 Hz in Fig. 6b. Data from G1 is not presented in Fig. 6b due to similar regulation from G2.

In Fig. 6b, Val of 0–500 Hz frequency at position G2 and G3 declines slowly with vibration source moving towards the road central line. It is because the longer distance between vibration source and testing point becomes as the RPB moving away from the curb, the more vibration attenuates. Val of 20–80 Hz frequency from G2 follows the same trend. However, 20–80 Hz Val from G3 increases at the first three vibration positions and then decreases. More measuring work is in need to verify this phenomenon. Variation energy of 0–20 Hz at position G2 declines rapidly as the distance between vibration source and testing point G2 grows while at position G3 basically maintains a constant value. The relatively high Val at G3 can also be contribute to the superposition of vibration propagating from both side of lining. Wherever the vibration source, the sum of distance from both sides between vibration source and position G3 remains constant, thus causing a stable Val at position G3. As for G2, due to the long propagation path from the other side, attenuation increases and superimposed effect weakens. More testing data and analytic theory are needed to support the explanation.

3.3 Vibration Evaluation of Lining Structure

On account of a close relationship with structure damage, variation velocity and frequency are often used to evaluate dynamic response of structure. Vibration velocity is converted from measuring acceleration data using Eq. (2), which can be derived from basic sinusoidal vibration expression. The peak of acceleration, variation acceleration level and velocity of the testing points in measured lining cross section is presented in Table 3.

$$\mathrm{v} = \frac{a}{2\pi f} \tag{2}$$

Where v is velocity (m/s); a is acceleration (m/s^2); f is frequency (Hz).

Table 3. Peak of lining dynamic response index

Measuring point	Acceleration (g)	Val (dB)	Velocity (mm/s)
G1	3.52	131.65	14.5
G2	3.14	132.60	17.2
G3	1.51	129.15	12.5

The acceleration peak appears at position G1 while the maximum of Val and velocity are present at position G2. Acceleration peak shows instantaneously but Val, representing one period of vibration, is more objective to describe vibration intensity. From Table 3 and Sect. 3.2, it comes to conclusions that lining arch side (G2) suffers the most intense vibration during rubblization construction. Peng et al. (2005) reported the similar results when analyzing dynamic response of lining induced by blast [12].

As for vibration assessment of lining structure during rubblizaiton construction, no codes can be consult in China at present. According to the Swiss Standard SN640312a-1992, vibration evaluation of tunnel lining structure is performed. Vibration velocity peak of lining structure induced by resonant rubblization construction in Yangjiao Mountain Tunnel is 17.2 mm/s. The maximum of vibration velocity in frequency contents of 10–30 Hz and 30–60 Hz is 2.3 mm/s and 10.3 mm/s, which are lower than standard values in Table 4. Nevertheless, vibration of frequency above 60 Hz also plays an important role in lining dynamic response. Further researches deserves to be done in estimating tunnel lining safety during rubblization construction.

Table 4. SN640312a-1992 Permissible value of vibration velocity

Structure type	Vibration source M		Vibration source S	
	Frequency (Hz)	Velocity (mm/s)	Frequency (Hz)	Velocity (mm/s)
Reinforced concrete structures, underground structures	10–30	12	10–60	30
	30–60	12–18	60–90	30–40

Vibration source S: Impact load; Vibration source M: Mechanic, vehicle, construction equipment etc.

4 Conclusions

Acceleration measurements relative to rubblization-induced vibration on the lining structure in Yangjiao Mountain Tunnel in Taizhou, Zhejiang Province, China have been presented. The aim is to fully understand the characteristics and propagation law of rubblization-induced vibration in lining structure and to access the lining vibration during resonant rubblization construction eventually. Conclusions can be drawn as follows.

(1) Lining dynamic response induced by rubblization construction, characterized in large vibration acceleration, wide frequency domain and regular distribution of predominant frequency is one kind of steady forced vibration. The vibration excitation frequency is 58 Hz.
(2) Rubblization-induced vibration propagates along the slab to both sides of arch foot and then to the arch crown. The most intense vibration take place in the lining arch side close to the vibration source during rubblization construction. The main frequency content of Rubblization-induced vibration is 20–80 Hz.
(3) Val of 20–80 Hz frequency increases then decreases from G1 to G3 and declines as the vibration source moving towards road central line. Val of 0–10 Hz frequency follows a different trend with the variation of testing points and vibration positions. More experiments and theory need to be investigate to support and explain this phenomenon.
(4) Vibration velocity peak of lining structure induced by resonant rubblization construction in Yangjiao Mountain Tunnel is 17.2 mm/s. The maximum of vibration velocity in frequency contents of 10–30 Hz and 30–60 Hz is 2.3 mm/s and 10.3 mm/s. More work needs to be done to assess lining safety in the process of resonant rubblization.

Regulation and data this paper reported can be consult in design and assessment of pavement rehabilitation by resonant rubblization in tunnel. 3D numerical simulation of rubblization construction and detailed analysis of lining vibration mode will be done in future work.

References

1. Chen, D.H., Huang, Q., Ling, J.: Shanghai's experience on utilizing the rubblization for jointed concrete pavement rehabilitation. J. Perform. Constructed Facil. **22**(6), 398–407 (2008)
2. Boyer, R., Jones, W.: State-of-the-Practice: rubblization of heavy load concrete airfield pavements. In: Airfield Pavements Specialty Conference, pp. 424–435 (2004)
3. Wienrank, C.J., Lippert, D.L.: Illinois performance study of pavement rubblization. Transportation Research E-Circular (2006)
4. Xu, Z.J., Ling, J., Huang, Q., et al.: Analysis of modulus of rubblized concrete pavement based on resonant technique. J. Tongji Univ. **36**(9), 1195–1198 (2008)
5. Qiu, X., Ling, J., Wang, F.: Concrete pavement rehabilitation procedure using resonant rubblization technology and mechanical–empirical based overlay design. Can. J. Civil Eng. **41**(1), 32–39 (2014)
6. Real, T., Zamorano, C., Ribes, F., et al.: Train-induced vibration prediction in tunnels using 2D and 3D FEM models in time domain. Tunneling Undergr. Space Technol. **49**, 376–383 (2015)
7. Li, Y.J., Wang, M.R., Song, G.X., et al: Influence study on the mining tunnel line cracks by vibration of metro train. China Civil Eng. J. (s1), 346–350 (2015)
8. Jiang, N., Zhou, C.: Blasting vibration safety criterion for a tunnel liner structure. Tunn. Undergr. Space Technol. Incorporating Trenchless Technol. Res. **32**(6), 52–57 (2012)
9. Decker, D.S., Hansen, K.R.: Design and construction of HMA overlays on rubblized PCC pavements: state of the practice. Transportation Research E-Circular (2006)

10. Shin, J.H., Moon, H.G., Chae, S.E.: Effect of blast-induced vibration on existing tunnels in soft rocks. Tunn. Undergr. Space Technol. Incorporating Trenchless Technol. Res. **26**(1), 51–61 (2011)
11. He, W., Xie, W.P., Liu, L.S.: Experimental investigation of vibration induced by subway train loading in tunnel. J. Huazhong Univ. Sci. Technol. (Nat. Sci. Edn.) **44**(4), 85–89 (2016)
12. Peng, D.F., Li, Z.X., Yang, N.H., et al.: Vibration effect on the working tunnel induced by an adjacent blasting. China Railway Sci. **26**(4), 73–76 (2005)

Experimental and Numerical Study on Longitudinal Axial Force and Deformation of Shield Tunnel

Xiaojun Li, Xiaozhou Zhou(✉), Bichen Hong, and Hehua Zhu

Tongji University, 1239 Siping Road, Shanghai 200092, China
zxz646@tongji.edu.cn

Abstract. Dislocation between adjacent rings and opening of conferential joints are two typical distress of shield tunnel due to longitudinal uneven settlement. However, most existing analysis methods only considered one distress. In this study, a longitudinal deformation model of shield tunnel is proposed based on the longitudinal deformation mechanism, which takes both bending deformation and shear deformation of the lining structure into consideration. With a three-dimensional numerical simulation, the longitudinal deformation of shield tunnel under typical settlement load, the influences of longitudinal axial force and ground spring stiffness are investigated. The results show that the longitudinal deformation of shield tunnel is significantly influenced by axial force and load transmission mechanism between rings. Generally, the longitudinal deformation is dominated by shear deformation when axial force is small. As the axial force increases, bending deformation takes larger and larger weights gradually.

Keywords: Shield tunnel · Longitudinal deformation
Dislocation between adjacent rings · Opening of conferential joints

1 Introduction

Shield-driven tunnels are widely adopted in the construction of urban underground space for transportation and utility networks in soft soil. However, the distress of tunnel lining caused by differential settlement is increasing rapidly in recent years, which induced serious damage to urban underground transportation [1–3]. The settlement of tunnel is influenced by a lot of factors, mainly the longitudinal design which is one of the critical problems in the design of tunnel [3–5].

As the lining segment rings is discontinuous, the distress caused by differential settlement, which include adjacent rings dislocation and conferential joints opening, occurs mainly in the conferential joints [6]. According to the deformation theory of beams, the dislocation of adjacent rings and conferential joints opening is due to the shear deformation of rings and bending deformation of tunnels, respectively. Now there are two hypotheses on the contribution of these two deformation modes to the overall deformation. One hypothesis is that the overall deformation is dominated by conferential joints opening. For instance, Zheng and Zhou established the numerical

© Springer Nature Singapore Pte Ltd. 2018
D. Zhang and X. Huang (Eds.): GSIC 2018, *Proceedings of GeoShanghai 2018 International Conference: Tunnelling and Underground Construction*, pp. 329–338, 2018.
https://doi.org/10.1007/978-981-13-0017-2_33

relationship between the longitudinal deformation curvature and joints opening amount [7, 8]. Moreover, Zhong and Li studied the longitudinal bending stiffness of the tunnel and put forward an analytical solution of the longitudinal structure response based on the elastic foundation beam theory [9–11]. Another hypothesis is that the longitudinal overall deformation is dominated by adjacent rings dislocation, the experimental study was proposed by Wang and Li [6, 12, 13]. However, most of the studies neglected the influence of longitudinal axial force, which actually exists in the tunnel due to the lifting jack force. Also the longitudinal axial force is an important factor to ensure the integrity of the tunnel structure [12, 13].

In this study, a longitudinal deformation model of shield tunnel is proposed based on the longitudinal deformation mechanism, which takes both bending deformation and shear deformation of the lining structure into consideration. With a three-dimensional numerical simulation, the longitudinal deformation of shield tunnel under typical settlement load, the influences of longitudinal axial force and ground spring stiffness are investigated.

2 Three Dimensional Shell - Spring Model of Lining

2.1 A Simplified Transverse Continuous Shell - Spring Model

To simulate the mechanics behavior of tunnel segments, a three-dimensional shell-spring model is established, in which the longitudinal joints and circumferential joints are simulated by non-linear spring [14, 15]. Based on the load-structure method or the stratum-structure method, the transverse and longitudinal deformation distributions of the structure are calculated.

Since our research is focused on the longitudinal deformation of the structure, a simplified shell-spring model is adopted in this paper. In fact, the definition of EI shows that its value is only varied with the material properties and cross-section of the moment of inertia, the transverse discontinuity will not directly lead to the change of material properties and cross-section moment of inertia. Therefore, on the basis of the hypothesis of small deformation, the tunnel could be approximately considered as an one dimension uniform structure [16]. It should be noted that, due to that the changes in material parameters also cause the changes in the vertical stiffness, our calculation does not consider the impact of lateral stiffness efficiency.

Based on the above analysis, a transverse continuum-spring model is used to simulate the longitudinal mechanical behavior of the lining structure without considering the discontinuity of longitudinal joints.

In order to investigate the characteristic of longitudinal deformation of the structure, a 200 m (100 rings) lining structure model was established based on the Hongmei South Road tunnel with the FEM software Abaqus. As the differential settlement caused by different factors could be equivalent to the load difference between the upper and lower of the tunnel, and this settlement will descend from the middle of tunnel to both sides along the tunnel axis, an inverted triangular form of load is applied on the middle section to simulate longitudinal non-uniform settlement. Figure 1 shows the three-dimensional numerical model of the lining structure.

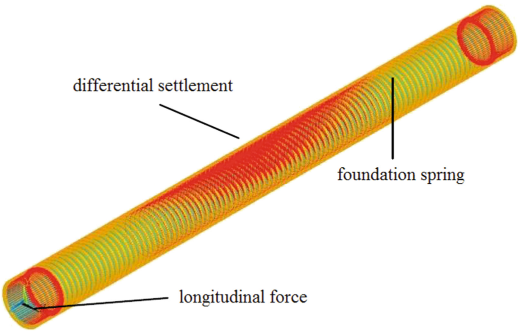

Fig. 1. Three-dimensional numerical model of the lining structure

2.2 Circumferential Joint Unit

Because the performance of the tunnel longitudinal bending deformation could be tension or compression at different part, the shield tunnel circumferential joint deformation include shear mode and tension & compression mode.

The simplified shear force-displacement curves are shown in Eqs. (1) to (3) and Fig. 2(a), where the initial frictional stiffness is supposed to be infinite,

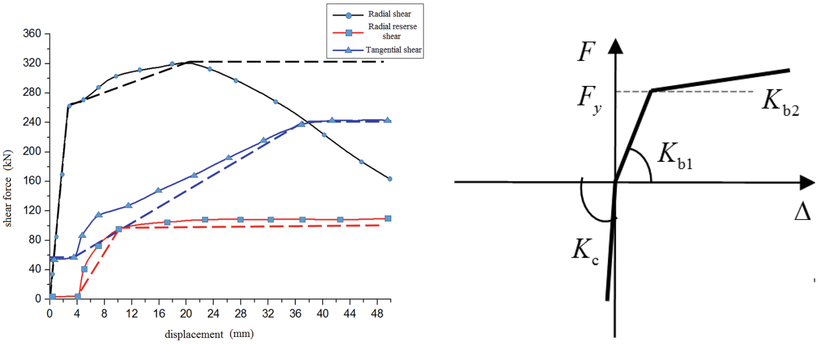

Fig. 2. Force-deformation curve of spring at circumferential joint. (a) shear (b) tension and compression

Radial shear:

$$Q = \begin{cases} 10 \times Pfx & 0 \le x < 0.1\,\text{mm} \\ Pf + 107(x - 0.1) & 0.1\,\text{mm} \le x < 2.6\,\text{mm} \\ Pf + 3.3(x - 2.6) + 263 & 2.6\,\text{mm} \le x < 20\,\text{mm} \\ Pf + 321 & x \ge 20\,\text{mm} \end{cases} \tag{1}$$

Radial reverse shear:

$$Q = \begin{cases} 10 \times Pfx & 0 \le x < 0.1\,\text{mm} \\ Pf & 0.1 \le x < 4\,\text{mm} \\ Pf + 16.1(x - 5) & 4\,\text{mm} \le x < 11\,\text{mm} \\ Pf + 96 & x \ge 11\,\text{mm} \end{cases} \tag{2}$$

Tangential shear:

$$Q = \begin{cases} 10 \times Pfx & 0 \le x < 0.1\,\text{mm} \\ Pf & 0.1 \le x < 4\,\text{mm} \\ Pf + 19(x - 4) & 4\,\text{mm} \le x < 7\,\text{mm} \\ Pf + 3.8(x - 7) + 75 & 7\,\text{mm} \le x < 37\,\text{mm} \\ Pf + 237 & x \ge 37\,\text{mm} \end{cases} \tag{3}$$

where P is longitudinal axial force, f is friction coefficient between the segments, which can be taken as 0.6, Q is shear force between the segments, the unit is kN, x is the tangential displacement, the unit is mm.

The tension and compression force-deformation curve of circumferential joint is shown in Eq. 4 and Fig. 2(b).

$$K_b = \begin{cases} K_{b1} = \frac{\pi d^2 E_s}{4 l_b} \\ K_{b2} \\ K_c \end{cases} \tag{4}$$

where K_{b1} and K_{b2} are tensile spring stiffness before and after yield, respectively, K_c is compression spring stiffness, d is bolt diameter, E_s is bolt elastic modulus, l_b is bolt length.

Figure 3 shows the distribution of circumferential joint units, K_s represents the shearing spring and K_b represents the tension spring.

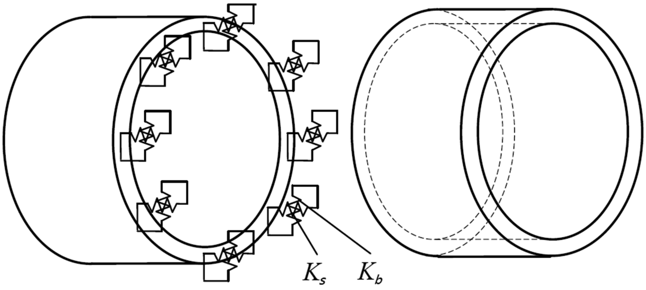

Fig. 3. Diagram of circumferential joint model

2.3 The Value of Foundation Spring Stiffness

Muir Wood [17] presented a analytic solution of the stiffness of foundation spring considering the influence of tunnel radius in 1975:

$$k = \frac{3E}{(1+v)(5-6v)R_0} \tag{5}$$

where, k is the foundation spring stiffness, E is the elastic modulus of the foundation, v is the Poisson's ratio and R_0 is the tunnel outer radius.

According to the geological survey report, the elastic modulus of the soil layer is 15 MPa and the static pressure coefficient is 0.5 (the corresponding Poisson's ratio is 0.33). The foundation spring is compression only, the stiffness is about 1500 kN/m3 and the rigidity of foundation spring is 2000 kN/m3 when considered the surrounding soil after slip casting, and the influence of the value of foundation stiffness in the range of 2000 kN/m3 to 6000 kN/m3 is discussed in this paper.

In addition, since the whole longitudinal deformation of the structure is considered in this paper, the tangential ground spring mainly affects the local deformation of the structure, therefore, we do not consider the influence of tangential spring.

According to the above model and structural parameters, the inverted triangle load peak value is 100 kPa–400 kPa, and the maximum annular gap calculated at 400 kPa is more than 6 mm, which is assumed as the maximum of serviceability limit.

3 Results and Discussion

3.1 Structural Deformation Modes Under Different Longitudinal Forces

Figure 4 shows the additional differential settlement under different vertical forces and vertical loads. It can be found from Fig. 4 that the maximum additional settlement of the tunnel increases linearly with the increase of the vertical load at the same longitudinal axial force. Under the same vertical load, the inter-annular shear transfer is enhanced with the increase of longitudinal axial force, the structural integral type is promoted and the maximum additional settlement is gradually reduced. The maximum settlement of the tunnel decreases from –0.14 m at 0 MN to –0.105 m at 80 MN when the vertical load is 300 kPa, which is approximately 29% less.

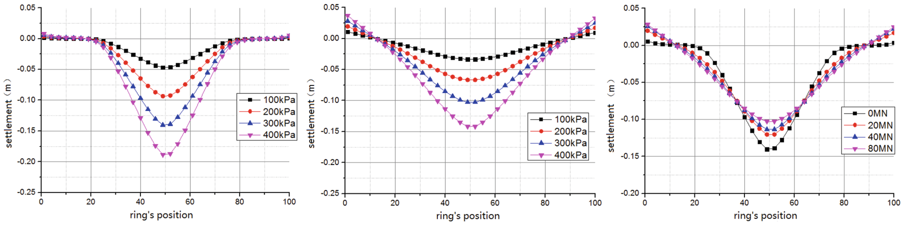

Fig. 4. Settlement structural deformation under different axial force and load (a) 0 MN (b) 80 MN (c) 300 kPa.

Figure 5 shows the curve of circumferential opening at different horizontal longitudinal axial forces and different vertical loads. The positive opening represents the top opening of the tunnel, whereas the negative opening represents the bottom. Figures 5(a) and (b) shows that, at the same longitudinal axial force level, with the increase of vertical load, the growth mode of tunnel inter-opening is different: when the longitudinal axial force is small (0 MN), all the different levels of vertical load cause the gap open. When the longitudinal axial force is very large (80 MN), no circumferential opening appears at 100 kPa and 200 kPa vertical load but 300 kPa. When the vertical load increases to 400 kPa, the bolts under the positive bending moment becomes yielding and the circumferential opening increases rapidly.

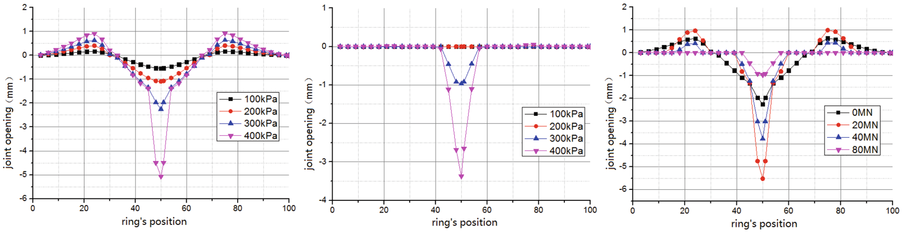

Fig. 5. Longitudinal joint opening under different axial force and load (a) 0 MN (b) 80 MN (c) 300 kPa.

Figure 6 is the dislocation curve under different load. From Fig. 6(a) and (b), when the vertical axial force is the same, the vertical displacement increases linearly with the increase of the vertical load. From Fig. 6(c), there is a large difference of the magnitude of dislocation under different axial forces. When the longitudinal axial force is 0 MN, the maximum dislocation is 3.5 mm. This is because when the longitudinal axial force is 0 MN, there is no initial static friction force between the tunnel rings. However, when the longitudinal axial force increase to 80 MN, there is a very large static friction between the tunnel rings. As a result, if we suppose the friction coefficient is 0.3 and the longitundinal axial force is only 20 MN, 6 MN friction force must be overcome to achieve the same shear deformation at longitudinal axial force 0 MN.

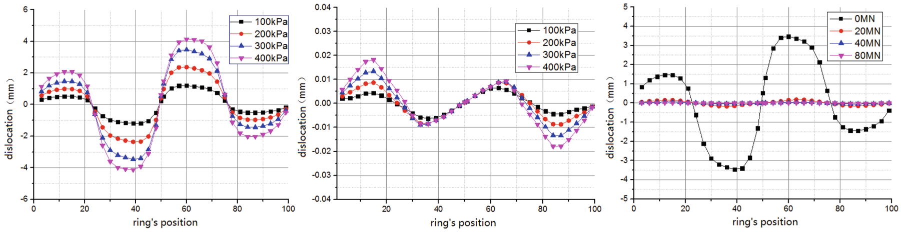

Fig. 6. Dislocation under different axial force and load (a) 0 MN (b) 80 MN (c) 300 kPa.

3.2 The Ratio of Shear Deformation Under Different Longitudinal Axial Forces

In order to describe the ratio of shear deformation of the shield tunnel to the total settlement deformation, firstly we define the cumulative dislocation δ, which is the sum of the dislocation between adjacent rings, as shown in Fig. 7.

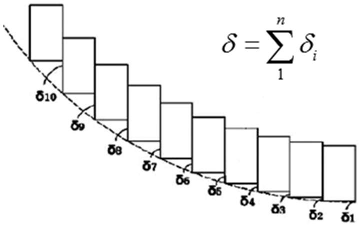

Fig. 7. Cumulative dislocation between rings

In our calculation model, n is taken as 50, and Fig. 8 shows the cumulative dislocation under different longitudinal axial loads and vertical loads. It can be found that under different longitudinal axial forces, the cumulative deformation of the dislocation increases linearly with the increased vertical load, but the increased amount becomes larger and larger. In the case of large longitudinal axial force, the shear deformation is very small due to the large static friction between the rings, which is almost negligible compared to the value at 0 MN.

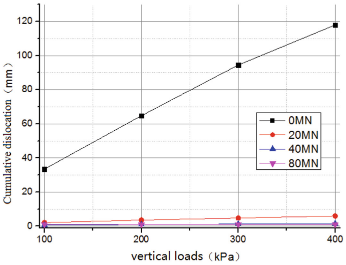

Fig. 8. Cumulative dislocation under different axial force and load

The cumulative shear deformation is divided by the maximum non-uniform additional settlement to obtain the proportion of shear deformation, as shown in Fig. 9.

From Fig. 9, it can be found that, similar to the above analysis results, the ratio of tunnel shear deformation decreases rapidly from 56% at 0 N to 0.4% at 80 MN as the longitudinal axial force increases. And under the same longitudinal axial force, the shear deformation ratio changes little with the change of vertical load.

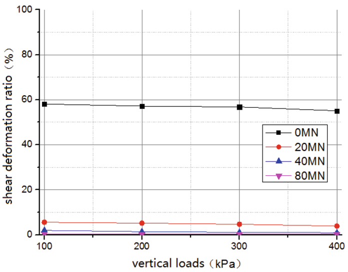

Fig. 9. Shear deformation ratio under different axial force and load

3.3 Influence of Foundation Stiffness on Calculation Results

In order to investigate the influence of different foundation spring stiffness values on the calculation results, the stiffness of foundation is 2000 kN/m3, 4000 kN/m3 and 6000 kN/m3 respectively. The vertical axial load is 20 MN and the vertical load is 300 kPa in Fig. 10.

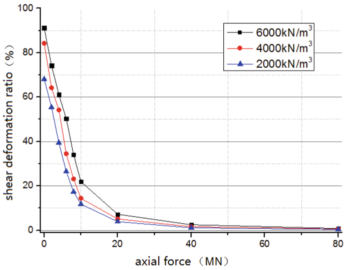

Fig. 10. The influence of the ground reaction coefficient on the calculation results

It is found from the Fig. 10 that the larger the stiffness of the foundation, the greater the ratio of shear deformation under the same longitudinal axial force and vertical load is obtained. When the longitudinal axial force is 0, the shear deformation ratio is 56.2% and 73.1% under the foundation stiffness of 2000 kN/m3 and 6000 kN/m3, respectively, where is an increase of about 20%. However, with the increase of longitudinal axial force, the calculated results of different foundation stiffness decreases gradually. When the longitudinal axial force is 20 MN, the shear deformation ratio is less than 10% under the three kinds of foundation stiffness. Therefore, it can be considered that when the longitudinal axial force is greater than 20 MN, the tunnel deformation is dominated by bending deformation.

4 Conclusion

In this paper, the longitudinal and axial forces are calculated with the transverse continuous three-dimensional shell-spring lining model based on the Shanghai Hongmei South Road tunnel project. The main conclusions are as follows:

(1) Through the establishment of three-dimensional finite element model of rings, it is found that the shear capacity of radial shearing is the largest, tangential shear is the second, and radial shearing is the smallest.

(2) The calculation results of the three-dimensional lining model of shell-joint based on transverse continuum show that with the increase of the longitudinal force, the transmission capability of inter-ring interaction is enhanced, and the structure will gradually change from shear deformation mode to bending deformation mode. When the longitudinal force reaches 20 MN, the longitudinal shear deformation of the structure has decreased to less than 10% of the total deformation, which is mainly the bending deformation mode.

References

1. Huang, H., Zang, X.: Research and analysis on longitudinal deformation characteristics of shield tunnel. Undergr. Space **22**(3), 244–251 (2002)
2. Lin, Y., Liao, S., Liu, G.: A discussion of the factors effecting on longitudinal deformation of subway tunnel. Undergr. Space **20**(4), 264–267 (2000)
3. Huang, X., Huang, H., Zhang, D.: Longitudinal deflection of existing shield tunnels due to deep excavation. Chin. J. Geotech. Eng. **34**(7), 1241–1249 (2012)
4. Liao, S., Hou, X., Peng, F.: Longitudinal shear transfer of tunnel and its 1D analytical solution]. Chin. J. Rock Mechan. Eng. **24**(7), 1110–1116 (2005)
5. Huang, X., Huang, H., Zhang, J.: Flattening of jointed shield-driven tunnel induced by longitudinal differential settlements. Tunn. Undergr. Space Technol. **31**, 20–32 (2012)
6. Wang, R.: Factors influencing deformation of shanghai soft soil metro tunnel and deformation analysis. Undergr. Eng. Tunnels **1**, 1–6 (2009)
7. Zhou, N., Yuan, Y.: Correlation of cross-river shield tunnel between longitudinal deformation curvature and segment leakage. J. Tongji Univ. (Nat. Sci.) **37**(11), 1446–1451 (2009)
8. Zheng, Y., Han, W., Tong, Q.: Study on longitudinal crack of sheild tunnel segment joint due to asymmetric settlement in soft soil. Chin. J. Rock Mechan. Eng. **24**(24), 4552–4558 (2005)
9. Zhong, X., Zhang, J., Qin, J.: Simplified calculation model for longitudinal equivalent bending stiffness of shield tunnel and its influence factors' analysis. Rock Soil Mech. **32**(1), 132–136 (2011)
10. Li, X., Liu, G., Yang, X.: Deformation and stress of tunnel structures based on modified longitudinal equivalent continuous model. Chin. J. Geotech. Eng. **36**(4), 662–670 (2014)
11. Liao, S., Bai, T., Peng, F.: Longitudinal settlement forms and structural response of shield tunnel. Chin. J. Undergr. Space Eng. **2**(4), 566–570+595 (2006)
12. Atsushi, K.: Shield Tunnel Design-From Allowable Stress Design Method to Limit State Design Method. (Translated by GUAN Linxin). China Building Industry Press, Beijing (2012)

13. Cao, W., Shen, W.: Large and Particularly Long Shield Tunnel Design - Design of Shanghai Yangtze River Tunnel. China Building Industry Press, Beijing (2010)
14. Su, S., He, C.: Shell-spring-contact model for load and structure interaction. J. SE Jiaotong Univ. **42**(3), 288–292 (2007)
15. Zhu, W., Huang, Z., Liang, J.: Studies on shell-spring model for segment of shield tunnels. Chin. J. Geotech. Eng. **28**(8), 940–947 (2006)
16. Ye, F., He, C., Zhu, H.: Longitudinal equivalent rigidity analysis of shield tunnel considering transverse characteristics. Chin. J. Geotech. Eng. **33**(12), 1870–1876 (2011)
17. Muir Wood, A.M.: The circular tunnel in elastic ground. Geotechnique **25**(1), 115–127 (1975)

Theoretical Analysis and Model Testing of the Deformation Characteristics and Failure Mechanism of a Blocking Airbag System in a Tunnel Under External Pressure

Jing Chen, Shu-wang Yan, Li-qiang Sun(✉), and Rui-qing Lang

State Key Laboratory of Hydraulic Engineering Simulation and Safety,
Tianjin University, Tianjin 300072, China
`chen_jing@tju.edu.cn`, `409436591@qq.com`

Abstract. With the development and utilization of underground spaces, subways and tunnels are often located in poor underground environments subject to problems with water and mud bursts. To reduce project losses, areas of gushing water must be isolated as soon as possible to enable repairs. To accomplish this isolation, the installation of a rubber airbag in a tunnel as a temporary retaining structure is proposed. An airbag is a membrane structure, which differs from a conventional structure. As a result, the force and deformation under the external pressure directly affect an airbag's slip failure mode. In this study, by combining the boundary conditions and stress conditions of an airbag in a tunnel, the rules governing the deformation of the airbag under uniform loading and the control conditions of the failure limit state are obtained. Model tests are conducted using airbags of two different diameters to block the external pressure, and the test results agree well with the theory. To improve the static friction resistance of the airbag and enable convenient and easy construction, a double airbag system is proposed. The deformation characteristics and failure mechanism of the double-airbag system are obtained from a force analysis. The double-airbag system blocks external pressure better and each of the airbags weighs less and easy to handling.

Keywords: Plugging tunnel · Single airbag and double-airbag system
Uniform load · Failure mode · Model testing

1 Introduction

In recent years, with the development and utilization of underground spaces, the safety of tunnel construction and operation has become increasingly important. Threats such as groundwater leakage, sudden floods, and toxic gases can cause great harm. In 1992, the Chicago flood drowned the downtown tunnel freight system. Because of the failure to block the flood in time, the flood spread rapidly [1] and forced the evacuation of 250,000 people [2, 3]. Tianjin, Shanghai and other regions also face safety problems caused by groundwater seepage during subway construction [4, 5]. The use of an airbag as a temporary retaining structure may be effective. The method has the advantages of a lightweight structure, low cost, high efficiency, and convenient installation. The

© Springer Nature Singapore Pte Ltd. 2018
D. Zhang and X. Huang (Eds.): GSIC 2018, *Proceedings of GeoShanghai 2018 International Conference: Tunnelling and Underground Construction*, pp. 339–350, 2018.
https://doi.org/10.1007/978-981-13-0017-2_34

principle of the method is to increase the pressure inside the airbag such that the airbag contacts the tunnel wall and the friction between the wall and the airbag stops water leakage at one end of the airbag [6].

Some scholars have proposed that airbags can be used as a safety device for partitioning a tunnel. Martinez [7] used protection airbag devices mounted to the top of a tunnel. In the event of danger, the airbag can be inflated quickly. Sosa [8] conducted a test for the friction coefficient between airbag material and concrete in dry and wet states and conducted a model test. The airbag will slip in the case of insufficient friction resistance. Sosa and Thompson [9] conducted field trials with an airbag mounted in a tunnel above a travelator. Because of an irregular tunnel shape, the airbag was not completely tight against the tunnel wall, and leakage occurred in a corner. Sosa and Wong [10] used the finite element method to simulate the deployment of airbags, including the expansion of the corners of the airbag. Zeng [11] introduced the basic principle of airbag plugging, the construction characteristics of the equipment and the application methods; the airbag plugging approach achieved good results in a pipeline project. Li [12] concluded that a large-diameter airbag requires a material of great tensile strength.

These scholars did not consider force analysis or the deformation characteristics and plug failure mode of the airbag under external pressure. An airbag is a membrane structure surrounded by the tunnel wall with positive force constraints. The external pressure that an airbag can resist depends on the friction resistance and on the airbag's shape. Thus, studies of the deformation of airbags under external pressure and the slip control conditions are necessary. The airbag must be long to ensure sufficient frictional resistance, substantially increasing the weight of the airbag. However, the airbag is a temporary emergency plugging device, and its low weight and convenient handling are key features that may allow for its widespread use. The airbag system can not only significantly improve the ability to resist external pressure but also facilitate handling and installation, which have important impacts on the popularization and application of airbag plugs.

In this study, combined with the boundary conditions, a force analysis of an airbag under a uniform load in a tunnel is conducted, and the shape of the critical state of the airbag failure is determined. The theoretical results are validated by two airbag model tests with different friction resistances. To allow for sufficient friction, a double airbag system is proposed, and the deformation characteristics of the double airbag system are obtained by analysing the force and failure mechanism to provide a theoretical basis for engineering applications.

2 Theoretical Analysis of a Single Airbag

2.1 Basic Assumptions

To study the changes in the force and shape of the airbag under loading, the following basic assumptions are made: (1) the tunnel has a circular cross section; (2) the airbag is subjected to a uniform external load; (3) the airbag is made of a homogeneous material whose stiffness and ductility are very small and can be ignored; and (4) the internal gas obeys the ideal gas equation under external pressure.

2.2 Initial State of the Single Airbag

The airbag is inflated under internal pressure and is close to the tunnel wall. The right and left ends (regions I and III) are hemispherical, and the middle portion (region II) is a cylinder. A cross section along the central axis is shown in Fig. 1. The diameter of the tunnel is D, and the length of the cylindrical region is L.

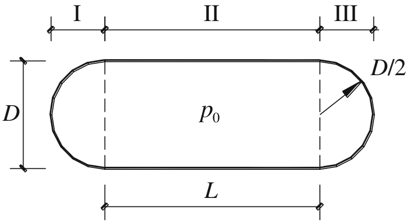

Fig. 1. Initial shape profile of the airbag

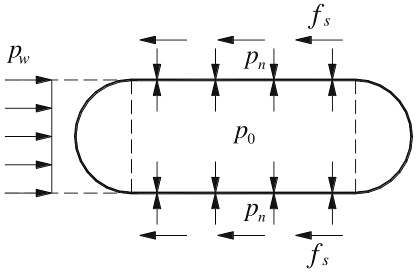

Fig. 2. Force analysis of the airbag under a uniform load

2.3 Force and Deformation Analysis of a Single Airbag Under a Uniform Load

When the left end of the airbag is subjected to a uniform load, it is necessary to determine whether the maximum static friction resistance between the airbag and the tunnel wall is sufficient to resist the external force. Assuming sufficient friction resistance, the deformation characteristics and failure mechanism of the airbag were studied.

Force Analysis of the Airbag. The forces on the airbag are shown in Fig. 2. These forces include a uniform external pressure p_{w}, an internal gas pressure p_0, a support force p_{n} and friction f_{s}. Figure 2 shows that in the vertical direction, the external pressure, F_{wy}, is zero. The horizontal external force F_{wx} is given by Formula (1).

$$F_{wy} = 0 \quad ; \quad F_{w\mathrm{x}} = 0.25 p_w \pi D^2 \tag{1}$$

Before the shape of the airbag changes, the maximum static friction resistance is given by Formula (2), where μ is the friction coefficient. The support pressure p_{n} is equal to the difference between the internal pressure p_0 and p_{a}; p_{a} is the internal pressure required for the airbag to expand to the tunnel wall. If the diameter of the airbag is slightly greater than or equal to the diameter of the tunnel, even if the internal pressure is zero, then the airbag can make full contact with the tunnel wall. When the inside of the airbag is pressurized, the support force of the tunnel wall is equal to the internal pressure of the airbag at this time, and p_{a} is zero. If the airbag diameter is less than the diameter of the tunnel, then p_{a} is greater than zero.

$$F_s = \mu p_n L \pi D \;\; ; \;\; p_n = p_0 - p_a \tag{2}$$

According to the force analysis, if the maximum static friction resistance exceeds the external force, then the airbag will not undergo overall slip failure. The deformation of the airbag under this condition was studied.

Deformation Analysis of the Airbag. When the airbag is loaded by the external pressure p_w, the shape of the curve at any point r(x) is determined using Formula (3). The difference between the internal and external pressures is the same at each point, and the tensions are also the same; thus, the curve is a circular arc segment with a radius of R, and $R > D/2$, the central angle is θ, and the arc length l_y is $R\ \theta$. Initially, region I consists of a semicircle with an arc length of l_y and a straight segment of length n, as shown in Fig. 3. When the external pressure increases, the airbag shape parameters n and θ change.

$$r(x) = T_{1l}/(p_1 - p_w) \tag{3}$$

Because the airbag is a membrane structure, the tension should be greater than zero, i.e., $T_{1l} > 0$. As formula (3) shows, when the external force p_w is less than the internal pressure of the airbag p_1, the radius of curvature of the arc is positive, and the airbag can retain its convex shape. In contrast, when p_w exceeds p_1, the airbag cannot retain its shape and will slip. Therefore, an important control condition for the airbag to function properly is that the external pressure must be less than the internal pressure. When the external pressure is equal to the internal pressure, the airbag reaches a limit state infinitesimally near the left end of the straight portion, as shown in Fig. 4.

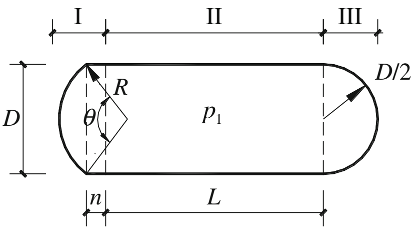

Fig. 3. Profile of the airbag under a uniform load

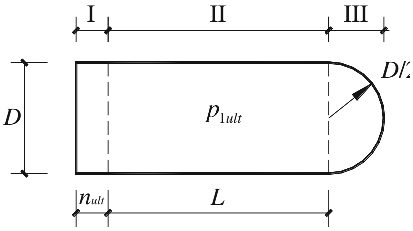

Fig. 4. Limit profile of the airbag

To determine the shape parameters n and θ and the internal pressure p_1 after deformation, equations are used to define each of the following three conditions: (1) the total surface area of the airbag is equal before and after deformation, (2) ideal gas conditions, and (3) the functional principle.

$$\frac{1}{2}\pi D^2 = \pi D^2 \Big/ 2\sin\frac{\theta}{2}\left(1\Big/\sin\frac{\theta}{2} - \cot\frac{\theta}{2}\right) + \pi D\mathrm{n} \tag{4}$$

$$\frac{\mathrm{p}_0}{p_1} = \frac{V_b}{\mathrm{V}_a} = \frac{D\left(\frac{1}{\sin\frac{\theta}{2}} - \cot\frac{\theta}{2}\right)\left[\frac{3}{4} + \left(\frac{0.5}{\sin\frac{\theta}{2}} - 0.5\cot\frac{\theta}{2}\right)^2\right] + 3\mathrm{n} + 3L + D}{2D + 3L} \tag{5}$$

$$(V_a - V_b)\,p_1 = \frac{1}{3}p_w \times \frac{1}{4}\pi D^2\left(0.5D - n - 0.5D\Big/\sin\frac{\theta}{2} + 0.5D\cot\frac{\theta}{2}\right) \tag{6}$$

V_a and V_b are the total volumes (m^3) before and after the deformation, respectively.

According to Eqs. (4), (5) and (6), the shape parameters n and θ and the internal pressure p_1 can be obtained under any external pressure p_w.

Failure Mode of Single Airbag. There are two failure modes of the single airbag under a uniform load. In the first mode, the friction is sufficient, and the airbag failure mechanism is caused by the external pressure exceeding the internal pressure such that the airbag cannot maintain its shape. In the second mode, the friction is insufficient, and the failure mechanism is caused by the external force exceeding the maximum static friction resistance of the airbag, causing the airbag to slip.

2.4 Single Airbag Model Test

To verify the changes in airbag shape and the failure control conditions for the different failure modes, two different airbags were used to conduct model tests to verify the correctness of the theoretical analysis: one group of tests is used to study the condition with sufficient friction; the other group is used to study the condition without adequate friction.

Test Apparatus. (1) Model tunnel, shown in Fig. 5①. Tunnel walls are generally made of concrete, but the deformation of an airbag in a model tunnel made of concrete cannot be observed. Concrete and plexiglass differ only in terms of their friction coefficients, which does not affect the deformation characteristics. The model plexiglass tunnel is 2 m long, its inner diameter is 0.4 m, and the left end is closed. The coefficient of friction μ between the airbag material and Plexiglas is 0.31. (2) The airbag (Fig. 5②). Two airbags with different diameters were installed. When they are filled to the same internal pressure, the contact area with the pipe wall differs; thus, the static friction resistance differs. Airbag No. 1 is in close contact with the tunnel wall when the inner pressure is zero, whereas airbag No. 2 is in close contact with the tunnel wall when the internal pressure reaches a certain value. Its straight segment consists of two parts: a 0–0.8 m part and a 0.8–1.1 m part. The circumferences of the two parts differ and require different internal pressures to fit against the wall, so it produces different maximum static friction resistance under the same internal pressures. The sizes of the airbags and the required internal pressures are listed in Table 1.

Table 1. Sizes and required internal pressures of the two airbags

Number	Length of straight segment L, m		Section perimeter, cm	Internal pressure required to fit the wall p_a, kPa
1	1.0		126.7	0
2	1.1	0–0.8	119.2	35
		0.8–1.1	124.3	4.8

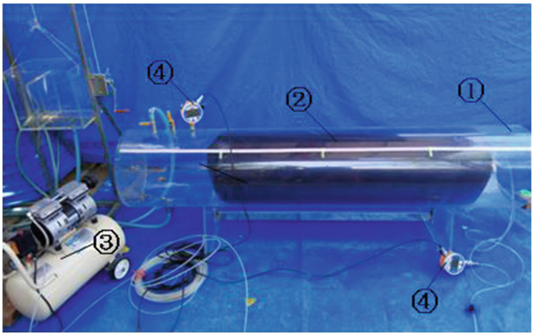

Fig. 5. Apparatus for testing the capacity of the airbag for blocking air pressure

(3) Pressure pump (Fig. 5③). A pressure pump is used to provide the internal pressure and the external distributed pressure. (4) Pressure gauge and collector (Fig. 5④). A pressure gauge is used to measure the internal and external pressures in real time and is connected to a logger to record the pressure changes.

Test Procedure. As the external pressure is increased, changes in the shape and internal pressure are recorded until the airbag fails. The initial internal pressure is changed, and the above steps are repeated several times to observe patterns in the changes in shape and failure of the airbag.

Test Results. *Sufficient friction* (*airbag No. 1*). (1) Test phenomenon and deformation of the airbag. The internal pressure of airbag No. 1 is raised to 10 kPa. At this time, the airbag fits the wall well, consistent with theoretical assumptions of the initial shape, as shown in Fig. 6, state ①. The external pressure increases, and the left side of the airbag gradually flattens (state ②). When the external pressure increases to nearly the internal pressure, the left end of the airbag flattens (state ③ is critical). When the external pressure continues to increase, air will flow around the airbag and will cause airbag dislocation, as shown in state ④. The initial internal pressure of the airbag was changed, and the same phenomena were observed.

The test values and theoretical values of the shape parameters (n, θ) and the internal pressure p_1 of the airbag during the test are compared with those in Table 2. The values in the table indicate that in the initial state of the test, region I is not a standard semicircle; that is, the value of n' is not zero, and the value of θ' is not π. As the external pressure increases, the internal pressure p_1 gradually increases, and the shape

Table 2. Changes in the shape and internal pressure of the airbag with changing external pressure

p_w, kPa	Theoretical p_1, kPa	Experimental p'_1, kPa	Theoretical n, m	Experimental n', m	Theoretical θ	Experimental θ'
0	9.80	9.80	0	0.021	3.141	2.932
3	9.81	9.83	0.052	0.048	2.426	2.530
6	9.86	9.88	0.084	0.081	1.492	1.692
10.01	10.06	10.10	0.099	0.092	0.017	0.087

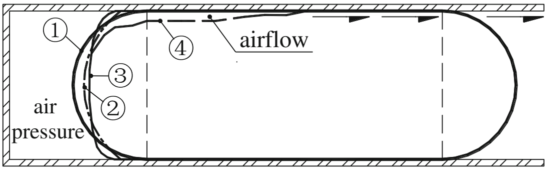

Fig. 6. Deformation of airbag No. 1 under external pressure

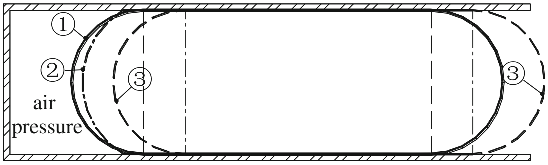

Fig. 7. Deformation of airbag No. 2 under external pressure

parameter *n*' of region I gradually increases while the central angle *θ*' gradually decreases. The experimental values and theoretical calculations are in good agreement, which supports the applicability of the theoretical derivation.

(2) Analysis of airbag failure mode. The external and internal pressures are obtained from the tests when the airbag is in the critical state. Thus, the maximum static friction force and the external force can be calculated. These data are summarized in Table 3. In the critical state of failure, the external force is much smaller than the maximum static friction between the airbag and the pipe wall; thus, the failure is not caused by a lack of friction. At this time, the external pressure is equal to the internal pressure; this condition is the first failure mode.

Table 3. Internal and external pressures on airbag No. 1 at the limit state under air pressure

Measurement	p_w, kPa	p_1, kPa	p_w/p_1	P_w, kN	F_s, kN	P_w/F_s
1	10.0	10.1	0.990	1.26	3.93	0.319
2	17.9	18.0	0.994	2.25	7.01	0.321
3	20.0	20.1	0.995	2.51	7.83	0.321
4	31.5	31.6	0.997	3.96	12.31	0.322

Insufficient friction (airbag No. 2). (1) Test phenomenon. The internal pressure of airbag No. 2 is increased to 10 kPa. The data in Table 2 indicate that only in the range of 0.8–1.1 m is the airbag affixed to the wall, as shown in Fig. 7, state ①. As the external pressure increases, the left end of the airbag deforms slightly (state ②). When the external pressure reaches a certain value, the airbag moves as a whole, resulting in a large displacement relative to the tunnel (state ③). Airbag No. 2 was not very flat during the deformation because the outer pressure was far lower than the internal pressure. (2) Failure mode analysis of the airbag. The statistical results from numerous experiments reveal that when airbag No. 2 is in the sliding failure mode, the ratio between the external pressure and the internal pressure ranges from 0.5 to 0.75. These values can be substituted into formulas to calculate the external forces and friction resistance. Because the left side in the range of 0–0.8 m is not attached to the wall and the range of 0.8–1.1 m is attached when the internal pressure is 4.8 kPa, the adhering length L is 0.3 m, and p_a is 4.8 kPa. A plot of the calculated maximum static friction resistance and the external force is shown in Fig. 8. Figure 8 shows that the external force on the airbag is equal to the maximum static friction resistance in the sliding critical state, which indicates that the airbag failure is a result of insufficient friction. Thus, this condition is the second failure mode.

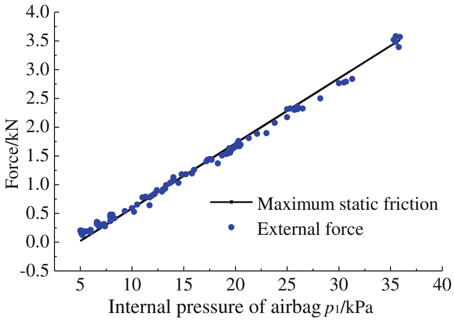

Fig. 8. Maximum friction and external force on the airbag in the sliding critical state under air pressure

3 Theoretical Analysis of the Double-Airbag System

To solve the problem of insufficient friction resistance of the airbag and thereby avoid occurrence of the second failure mode, the static friction resistance should be increased. As the length of the airbag increases, the weight and volume of the single airbag also increase, thus making it difficult to transport and install, particularly when construction time pressures are great. To solve this problem, a double-airbag system for plugging the tunnel is proposed. After the first airbag is installed, another airbag is added; the two airbags together provide enough friction resistance to maintain the stability of the airbags and ensure that the overall airbag friction resistance is adequate. In addition, this approach is convenient during construction.

3.1 Basic Assumptions

To study the forces and shape of the double-airbag system, the following basic assumptions are used: (1) The friction is sufficient when the two airbags work together. (2) The initial internal pressures of the two airbags are equal. The internal pressures of the two airbags during deformation are nearly equal.

3.2 Initial State of the Double-Airbag System

A cross section showing the initial state of the two airbags is presented in Fig. 9. The diameter of each airbag is D, the initial lengths of the two straight segments are L_1 and L_2, and $L_1 = L_2 < L$. There is no interaction between the two airbags. The shape of each airbag is the same as that of the individual airbag in its initial state.

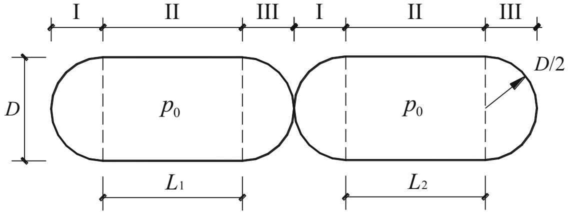

Fig. 9. Initial shape profile of double airbag in the tunnel

3.3 Force and Deformation Analysis of the Double-Airbag System Under a Uniform Load

Force Analysis of the Double-Airbag System. When the external force is less than the maximum static friction between the first airbag and the wall, the first airbag does not slip and has no contact with the second airbag and conforms to the deformation law described above. When the external force exceeds the maximum static friction resistance, the first airbag slides and makes contact with the second airbag, thereby transmitting force to the second airbag to form a system that balances the external forces with a combined friction force to stabilize the airbags. The horizontal forces in the double-airbag system are shown in Fig. 10.

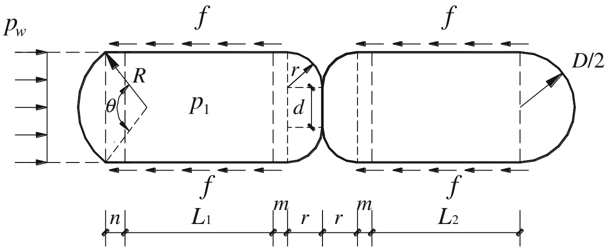

Fig. 10. Force analysis of the double-airbag under a uniform load

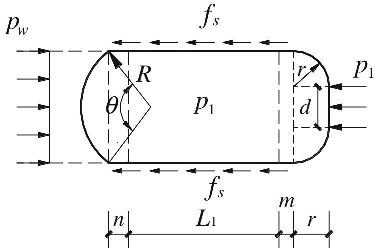

Fig. 11. Force analysis of the first airbag

Deformation Analysis of the Double-Airbag System. The force analysis of the first airbag is shown in Fig. 11. Its deformation follows the deformation rule of a single airbag. When the first airbag is in contact with the second airbag, because the internal pressures of the two airbags are nearly equal, it can be assumed that the contact between the airbags is linear, and the length of this line segment is d. The curved part of region III of the first airbag is a quarter circle of radius r. Thus, the deformation of region III of the first airbag forms two quarter-circle arcs, a straight segment of length d, and two adhering portions of length m. With increasing external pressure, d increases gradually, m increases gradually, and r decreases gradually.

To determine the shape and internal pressure of the first airbag under any external pressure, including the shape parameters θ, n, r, m, and p_1, equations describing the following five conditions are required: (1–2) the surface areas of the left and right sides of the airbag are equal before and after the deformation; (3) ideal gas conditions; (4) the first airbag is balanced horizontally; and (5) the functional principle.

$$\frac{1}{2}\pi D^2 = \frac{\pi D^2}{2\sin\frac{\theta}{2}}\left(\frac{1}{\sin\frac{\theta}{2}} - \cot\frac{\theta}{2}\right) + \pi D n \tag{7}$$

$$\frac{1}{2}\pi D^2 = \pi D m + 2\pi r^2 + \frac{1}{2}\pi^2 d r + \frac{1}{4}\pi d^2 \tag{8}$$

$$\begin{gathered} V_{\mathrm{b}} = \frac{\pi}{6}\left(\frac{D}{2\sin\frac{\theta}{2}} - \frac{D}{2}\cot\frac{\theta}{2}\right)\left[\frac{3}{4}D^2 + \left(\frac{D}{2\sin\frac{\theta}{2}} - \frac{D}{2}\cot\frac{\theta}{2}\right)^2\right] + \frac{1}{4}\pi D^2 n + \frac{1}{4}\pi D^2 L_1 + \frac{1}{4}\pi D^2 \mathrm{m} + \pi\left(\frac{2}{3}r^3 + \frac{1}{4}d^2 r + \frac{1}{4}\pi d r^2\right) \\ V_a = \frac{1}{6}\pi D^3 + \frac{1}{4}\pi D^2 L_1 \quad ; \quad p_0 V_a = p_1 V_b \end{gathered} \tag{9}$$

$$p_w \frac{1}{4}\pi D^2 = p_1 \frac{1}{4}\pi d^2 + \mu p_1 \pi D(m + n + L_1) \tag{10}$$

$$(V_{\mathrm{a}} - V_b)p_1 = \frac{1}{3}p_{\mathrm{w}}\frac{1}{4}\pi D^2 \delta_1\left(0.5D - n - 0.5D\Big/\sin\frac{\theta}{2} + 0.5D\cot\frac{\theta}{2}\right) + \frac{1}{3}p_1\frac{1}{4}\pi d^2(0.5D - m - r) \tag{11}$$

The shape parameters (n, θ, m, and r) and internal pressure p_1 of the loaded airbag can be obtained using the five formulas simultaneously.

When the diameter D of the airbag is 5.5 m, the length L_1 of the straight portion is 2 m, the initial internal pressure p_0 is 50 kPa, and the friction coefficient μ is 0.25. The changes in the internal pressure and the shape parameters with changes in external pressure are listed in Table 4. As indicated in Table 4, the arc angle θ of the left side of the airbag gradually decreases, and the adhering length n gradually increases. The adhering region m of the right side of the airbag gradually increases, the radius r of the arc gradually decreases, and the internal pressure gradually increases.

Table 4. Shape and internal pressure of the left side of the airbag under external pressure

External pressure p_w, kPa	n, m	θ	m, m	R, m	Internal pressure p_1, kPa
30	1.14	1.57	0.08	2.56	50.83
35	1.20	1.36	0.28	2.13	51.23
40	1.27	1.09	0.40	1.86	51.83
45	1.32	0.79	0.50	1.65	52.62

Because the internal pressures of the two airbags are nearly equal, the deformation of the second airbag on the left side is similar to that of the right side of the first airbag, and their shapes are symmetrical. Thus, the maximum static friction resistance is provided by the two airbags acting together:

$$F_{\mathrm{st}} = \mu p_1 \pi D(2m + n + L_1 + L_2) \tag{12}$$

Failure Modes and Design Calculation of the Double-Airbag System. The double-airbag system also has two failure modes: the first failure mode occurs when the friction is sufficient, and the external pressure gradually approaches the internal pressure, which causes shape instability and failure. The second failure mode occurs when the external force exceeds the maximum static friction resistance provided by two airbags, thereby causing slip failure of the entire airbag system. The double-airbag system can withstand a larger external pressure than a single airbag. When designing the double-airbag system, if the external pressure p_{w} is known, then one first ensures that the internal pressure p_1 is greater than the external pressure. Next, the total length (L_1 + L_2) of the double-airbag system is calculated using formula (12).

4 Conclusions

Based on the boundary conditions of the airbag in the tunnel, the force and deformation analysis of the single airbag under a uniform pressure were studied, and the theoretical results were verified in two airbag model tests involving different amounts of static friction resistance. The double-airbag occlusion system was proposed, and a force analysis and deformation study were conducted under a uniform pressure. The main conclusions obtained from these tests are as follows:

(1) On the basis of the force analysis of the single airbag under a uniform load and the state equation, the deformation characteristics and internal pressure of the single

airbag under an external load were obtained. Region I of the single airbag was found to gradually flatten under the external pressure, and the internal pressure gradually increased.

(2) The single airbag undergoes two failure modes under external pressure: one failure mode in which the airbag changes shape due to the external pressure exceeding the internal pressure, and a second failure mode in which overall slip failure is caused by the external force exceeding the maximum static friction. The model tests showed that airbag No. 1 fails in the first failure mode and that airbag No. 2 fails in the second failure mode. The deformation characteristics of the two airbags under pressure were found to be consistent with the theoretical results.

(3) Force analysis of the double airbag system was conducted, and the deformation characteristics and failure mechanism of the double airbag system were obtained. The double-airbag system can withstand larger external pressures than the single airbag.

References

1. Menkus, B.: The lessons of the Great Chicago flood of 1992. Comput. Secur. **11**, 417–420 (1992)
2. Inouye, R.R., Jacobazzi, J.D.: Great Chicago flood of 1992. Civil Eng. (ASCE) **62**(11), 52–55 (1992)
3. Transportation Security. Federal Transportation Administration. TCRP report 86(12) and NCHRP report 525(12), pp. 37–39 (2006)
4. Zheng, Y.-L., Li, M.-L., Wang, M.-Y., et al.: Study on influence of seepage of metro tunnels in soft soil on the settlements of tunnels and ground. Chin. J. Geotech. Eng. **27**(2), 243–247 (2005)
5. Liu, K.-L., Wen, B.-L., Liu, C.-B., et al.: Integrated leak treatment for tunnel of Tianjin subway existing line. China waterproof plugging insulation technology Summit Forum (2006)
6. Jiang, Q.-H.: Construction technology of airbag blocking for underground pipeline construction and dredging maintenance. Heilongjiang Sci. Technol. Inf. **2013**(22), 258 (2013)
7. Martinez, X., Davalos, J., Barbero, E.J., Sosa, E.M., Huebsch, W., Means, K., Banta, L., Thompson, G.J.: Inflatable plug for threat mitigation in transportation tunnels. In: Proceedings of the Society for the Advancement of Material and Process Engineering Conference, Baltimore, MD, 21–24 May 2012
8. Sosa, E.M., Thompson, G.J., Barbero, E.J., et al.: Friction characteristics of confined inflatable structures. Friction **2**(4), 365–390 (2014)
9. Sosa, E.M., Thompson, G.J., Barbero, E.J.: Testing of full-scale inflatable plug for flood mitigation in tunnels. Transp. Res. Rec. J Transp. Res. Board **2407**(–1), 59–67 (2014)
10. Sosa, E.M., Wong, J.C.-S., Adumitroaie, A., et al.: Finite element simulation of deployment of large-scale confined. Thin-Walled Struct. **104**, 152–167 (2016)
11. Zeng, Q.: Application of pipeline plugging airbag in pipeline maintenance. Water Conservancy Construction Manage. **35**(9), 76–77 (2015)
12. Li, M.: Application of plugging gasbag in large diameter pipeline. GD Sci. Technol. **3**, 108–109 (2012)

Shearing Behavior of Segmental Joints of Large-Diameter Shield Tunnel

Dong-Mei Zhang[1,2](✉) and Jie Liu[1]

[1] Department of Geotechnical Engineering, Tongji University,
Shanghai 200092, China
dmzhang@tongji.edu.cn
[2] Key Laboratory of Geotechnical and Underground Engineering
of Ministry of Education, Tongji University, Shanghai 200092, China

Abstract. Segments floating is often encountered during the large-diameter shield tunneling. Shearing resistance of circumferential joints is of great importance for resisting the tunnel floating. The shearing resistance in terms of circumferential joint dislocation is studied using 3D numerical simulation. The influences of bolt types, gaskets, transmission cushions, and longitude bolt pre-force on the shearing resistance are investigated, respectively. The simulation results indicate that the dislocation process of circumferential joint can be divided into three stages, and the friction force between transmission cushion and concrete mainly determines the shear resistance of segment joint in the first stage, then in the last two stages, bolts contact the bolt holes and perform shear ability which varies from the bolt type. Based on the results, the safety and durability of circumferential joint are discussed. Some suggestions of shearing resistance design of lining structure are presented.

Keywords: Circumferential joints · Numerical method · Structure
Shearing resistance

1 Introduction

Large diameter shield tunnel construction has made great breakthrough in recent years to meet the urgent transportation requirement in urban area. However, segments floating is very often encountered especially for shallow-buried tunnel. The segmental floating can result in segment staggering, cracks or even axes deflection [1]. It is usually caused by unloading of tunnel excavation and the buoyancy of ground water and grouting [2]. The physical gap caused by the clearance of the tunnel external diameter and shield machine as well as excessive excavation produces the space for upward movement [3]. Many solutions have been proposed to optimize the shield driving and grouting technology [4]. Actually, improving the shearing resistance of circumferential joints of the tunnel is an effective way to decrease the tunnel floating.

In general, the structure of the joint is composed of connectors, tenons, transmission cushions, waterproof gaskets and caulking. Connectors can improve the joint stiffness significantly, and bolts are often used for large-diameter tunnel segments, mainly including straight bolts, curved bolts, oblique bolts. Tenons are mainly for

© Springer Nature Singapore Pte Ltd. 2018
D. Zhang and X. Huang (Eds.): GSIC 2018, *Proceedings of GeoShanghai 2018 International Conference: Tunnelling and Underground Construction*, pp. 351–360, 2018.
https://doi.org/10.1007/978-981-13-0017-2_35

positioning, improving waterproof capacity and increasing shear strength, and they tend to be designed in circumference joint instead of longitude joint [5]. Transmission cushions can prevent stress concentration, but they would slide and be destroyed easily under the high load, and what's more, they can reduce the friction force between the adjacent ring segments and the joint bending stiffness [6, 7]. Gaskets are the key of shield tunnel waterproofing, but they decrease the shear stiffness slightly [8]. The caulking on the inner and outer edges of segment has little influence on the joint stiffness, leading to uneven stress distribution on the joints.

Many researches have been performed to investigate the behavior of circumferential joints. Huang et al. [9] obtained the shearing stiffness parameters between tunnel rings in beam-spring model using small scale model tests. Wang et al. [10] determined the interactions between the lining tenons, bolts and their holes by numerical method based on uneven longitudinal ground settlement. Chen et al. [11] studied the floating problem and analyzed the floating laws, the circumferential joints deformation and the bolts force changing. Several field tests were also taken to study the joints shearing process and failure mechanism, then presented the calculation model and the relevant stiffness parameters [12–14]. However, the influence of joint components on joint shearing resistance and their action mechanism are not well understood. Furthermore, the anti-floating design of circumferential joints is lack of guidance.

This paper is to study the circumferential joint dislocation, and to analyze the involved parameters as well as their influence on shearing resistance systematically. For this purpose, 3D numerical segment joint models are finely established, and the boundary conditions and loads are applied according to the practical cases. The complex interactions between joint components are also considered. Influences of blot types, gaskets, transmission cushions and bolt pre-force on shearing resistance are studied successively. Based on the simulation results, the circumferential joints shear behavior is revealed and the joint designation guidance is concluded.

2 Numerical Simulation

2.1 Simulation Model of the Segmental Joint

This paper focuses on the circumferential joint shearing behavior. To figure out the structure components' influence more clearly, the two curved lining segments connected by three bolts are deliberately simplified as rectangular ones (Fig. 1(a)). Three types of bolt are considered to study the influence of bolt types on shearing resistance, including straight bolt, curved bolt and oblique bolt. The length of bolt is 0.6 m, the diameter is 36 mm, and the bolt hole is 42 mm in diameter for fitting allowance. The section of gasket is simplified as rectangle of 12 mm × 40 mm without inner structure, and the pre-field stress is applied to the gaskets to simulate the compression. The thickness of cushion is 2 mm. The segment concrete and bolt steel are assumed to be elastoplastic as shown in Fig. 2, and the possible cracking and material yield can be estimated by stress concentration. And other materials are assumed to be linear elasticity. The numerical model parameters and relevant values are listed in Table 1. The dimensions of segments and three kinds of joint are labeled in Fig. 1.

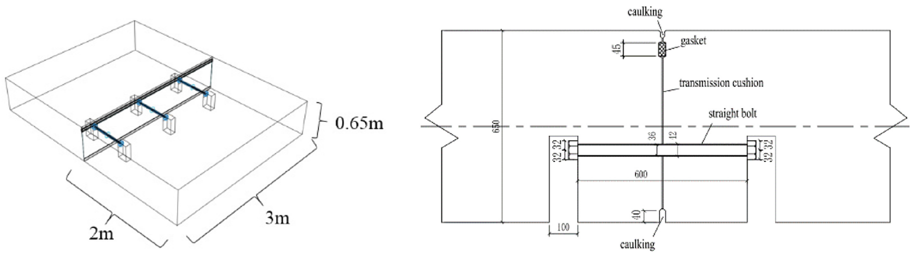
0.65m
3m
2m
caulking
gasket
45
transmission cushion
straight bolt
650
36
12
32 32
32 32
600
40
100
caulking

(a) Segment connection (b) Straight bolt joint

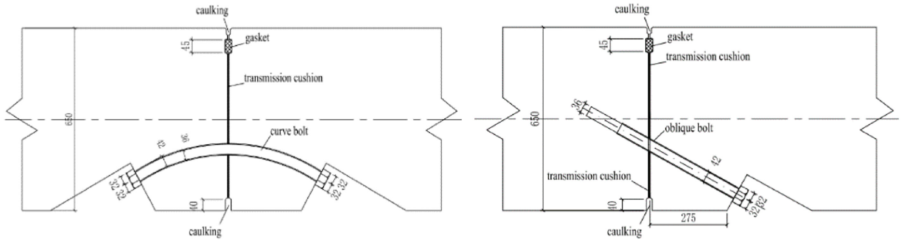
caulking
gasket
45
transmission cushion
650
curve bolt
42
36
32 32
32 32
40
caulking
caulking
gasket
45
transmission cushion
650
36
oblique bolt
42
transmission cushion
40
275
32 32
caulking

(c) Curved bolt joint (d) Oblique bolt joint

Fig. 1. Sketch of lining segment model.

Table 1. Materials and parameters.

Component	Material	Young's modulus (MPa)	Poisson's ratio	Constitutive model	Element type
Segment	Concrete (C60)	3.60×10^4	0.167	Broken line	C3D8R
Bolt	Steel (M8.8)	2.06×10^5	0.30	Bilinear	C3D8R
Gasket	Rubber (EPDM)	7	0.30	Linear elasticity	C3D8
Cushion	Rubber	250	0.35	Linear elasticity	C3D8
Nut washer	Steel	2.00×10^6	0.30	Elastoplastic	S4R

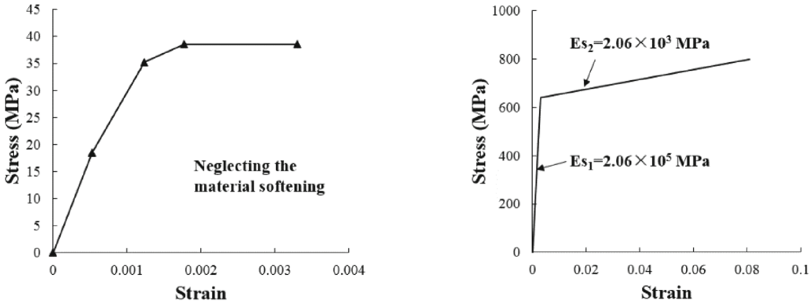

(a) Segment concrete (C60) (b) Bolt steel (M8.8)

Fig. 2. Stress-strain curves of segment concrete (a) and bolt steel (b).

2.2 Circumferential Joint Interactions

The interactions of circumferential joints are simulated by contact method. The normal contact behavior is simulated by hard contact, and the penalty function is utilized to simulate the tangential contact behavior. The oblique bolt nuts are embedded in the concrete (Fig. 1(d)), thus the tie constraint is used. While the frictional contact is used for the nuts of straight and curved bolts, and the nut washers are simulated to reduce the stress concentration at hand holes. The circumferential joint interaction parameters are listed in Table 2. The frictional coefficient between cushion and segment is 0.7 theoretically, but it varies largely in practical cases, which is studied as an important factor in the third part. And the other frictional coefficients are presented in Table 2.

Table 2. Interaction parameters

Contact pair	Nut to segment	Bolt to bolt hole	Gasket to segment	Gasket to gasket	Cushion to concrete	Segment to segment
Friction coefficient	0.3	0	0.7	0.55	0.7	0.4

2.3 Loading Process

The segment rings floating raises different shearing orientations relating to segment position. The segment blocks at the crown and invert experience ordinal shearing and reverse shearing, respectively, and the blocks at the side behave tangential shearing, while the blocks at other position behave the combination of the three shearing orientations. Therefore, three shearing models of straight bolt joint, named ordinal shearing model, reverse shearing model and tangential shearing model, are suggested as shown in Fig. 3(a). A simplified half model (Fig. 3(b), e.g. straight bolt joint, ordinal

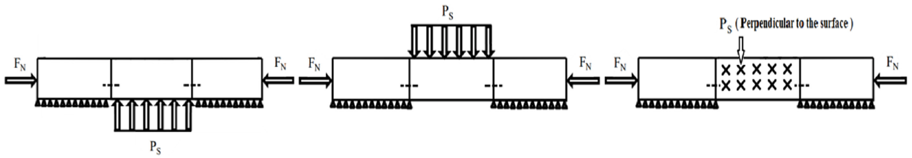

(a) Ordinal shearing model (left), reverse shearing model (middle) and tangential shearing model (right)

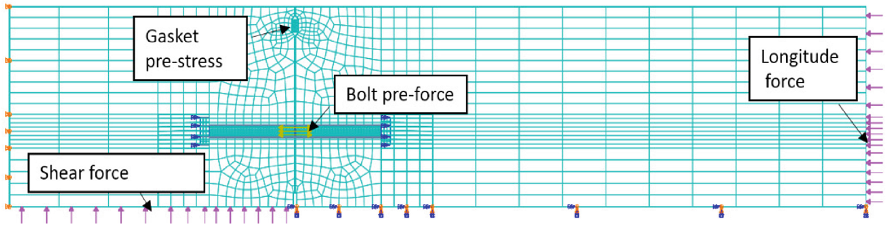

(b) Simplified numerical model

Fig. 3. Sketch of boundary condition and load application (e.g. straight bolt joint).

shearing) is accepted in this paper to improve calculation efficiency. Calculation models of different bolt types and shear orientations are all based on the example shown in Fig. 3.

The loading process is divided into three steps, and the loads are gained according to the design guides and practical cases. Step 1, the bolt pre-force (200 kN) and gasket pre-stress (3.2 MPa) are applied to establish contacts and simulate assembling; Step 2, the longitude force (8 MPa) is applied to simulate the jacks force; Step 3, the shear force is applied to simulate shear dislocate process.

3 Simulation Results

3.1 Influence of Bolt Types on Shearing Resistance

The relationships of relative dislocation and shear force of three types of bolt are shown in Fig. 4. The dislocation process can be divided into three stages: in the first stage, the dislocation can nearly be ignored, and the shear strength depends on the friction before the dislocation reaches approximately 0.8 mm; in the second stages, the dislocation develops rapidly between 0.8 mm and 6 mm and the shear stiffness decreases significantly; in the third stage, the bolts contact the bolt holes completely and perform shear ability so that the shear resistance increases, but it's not obvious as the material yielding. As shown in Fig. 4, the second and third stages are difficult to be distinguished, and it's because that the shearing capacity of the two stages is far less than that of the first stage. Actually, for straight bolt joint, the third stage's shearing stiffness is about 10 times larger than the second stage's, while, for curved and oblique bolt joint, the shearing stiffness of the third stage is only half of that of the second stage.

In addition, when the dislocation reaches about 10 mm, the segment concrete cracks occur around the hand hole and bolt hole, and the bolts get yielding (Fig. 5, e.g. straight bolt joint, ordinal shearing). Thus, the concrete plastic zone develops rapidly and joint has already been in failure state when the dislocation exceeds 10 mm. And linear fitting can be used at each stage to obtain a simplified computational model.

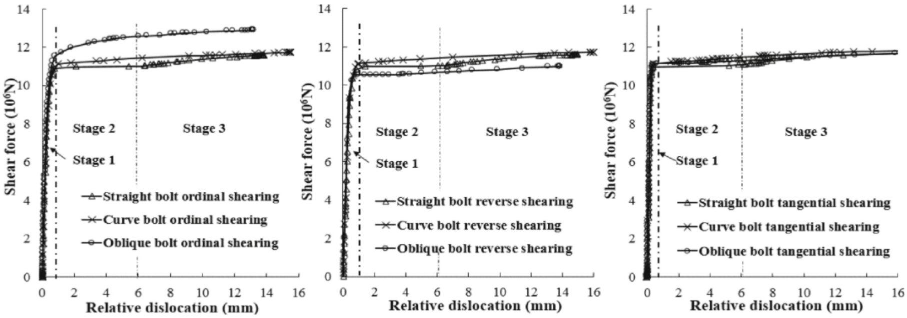

(a) Ordinal shearing (b) Reverse shearing (c) Tangential shearing

Fig. 4. Development of dislocation of circumferential joint with shearing force.

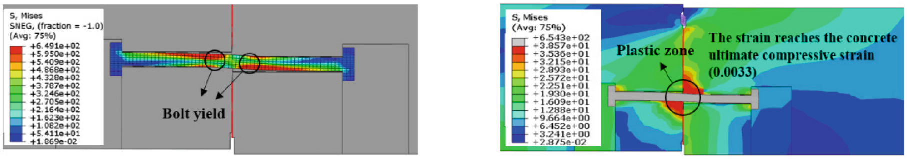
S, Mises
SNEG, (fraction = -1.0)
(Avg: 75%)
+6.491e+02
+5.950e+02
+5.409e+02
+4.868e+02
+4.328e+02
+3.787e+02
+3.246e+02
+2.705e+02
+2.164e+02
+1.623e+02
+1.082e+02
+5.411e+01
+1.869e-02
Bolt yield
S, Mises
(Avg: 75%)
+6.543e+02
+3.857e+01
+3.536e+01
+3.215e+01
+2.893e+01
+2.572e+01
+2.251e+01
+1.930e+01
+1.609e+01
+1.288e+01
+9.664e+00
+6.452e+00
+3.241e+00
+2.875e-02
Plastic zone
The strain reaches the concrete ultimate compressive strain (0.0033)

(a) Straight bolt (b) Bolt hole concrete

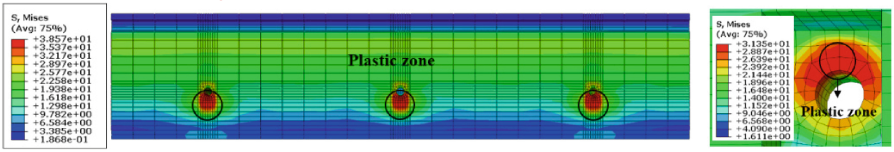
S, Mises
(Avg: 75%)
+3.857e+01
+3.537e+01
+3.217e+01
+2.897e+01
+2.577e+01
+2.258e+01
+1.938e+01
+1.618e+01
+1.298e+01
+9.782e+00
+6.584e+00
+3.385e+00
+1.868e-01
Plastic zone
S, Mises
(Avg: 75%)
+3.135e+01
+2.887e+01
+2.639e+01
+2.392e+01
+2.144e+01
+1.896e+01
+1.648e+01
+1.400e+01
+1.152e+01
+9.046e+00
+6.568e+00
+4.090e+00
+1.611e+00
Plastic zone

(c) Joint surface concrete (d) Hand hole concrete

Fig. 5. Stress contours of segment and bolt (e.g. straight bolt joint, dislocation 10 mm).

The bolt's shear ability is associated with the stress level and deformation characteristics. Straight bolt mainly undertakes shearing deformation, and the shear behaviors of three orientations are similar. Curved bolt mainly undertakes bending deformation (even torsion deformation when tangential shearing), so its' shear resistance is most significant when reverse shearing or tangential shearing happens. Oblique bolt mainly undertakes tensile deformation and the shear resistance is most significant when ordinal shearing, while at other two orientations mainly undertakes shearing deformation. What's more, the nuts separate the segment when reverse shearing occur so that the shear resistance is lowest.

3.2 Influence of Gaskets on Shearing Resistance

Gaskets are important for tunnel waterproofing. Based on the ordinal shearing model with straight bolt shown in Fig. 3(b), two models without and with gaskets are compared to figure out the influence of gaskets on shearing resistance.

As shown in Fig. 6(a), generally, the effect of gaskets on shearing resistance is not notable. When the dislocation is smaller than 6 mm, the gaskets don't exhibit any

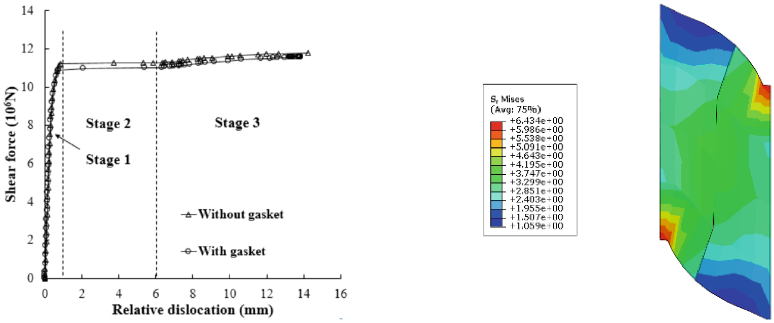

(a) Difference in dislocation without and with gasket (b) Deformation pattern of gasket

Fig. 6. Simulated results of joint shearing behavior without and with gasket.

influence on shear resistance. The shear strength of the joint with gaskets is lower than the one without gaskets after the first stage. When the dislocation reaches 14 mm, the normal force and shear force of the gasket contact face are 3.3×10^5 N (which can ensure the waterproof ability) and 7.5×10^3 N, respectively, and the ratio is 0.023, far less than the preset friction coefficient. The gaskets deform in terms of distortion (Fig. 6(b)) and nearly don't bear shear force, and share part of the longitudinal force and bolt pre-force to ensure their own compression, thus the joint shear resistance decreases.

3.3 Influence of Cushions on Shearing Resistance

The cushions can release the stress concentration, and the effect is proportion to the cushion thickness. Actually, the cushion material property and joint contact condition will change the friction coefficient between cushions and segment greatly. Based on the model in Fig. 3(b), the influence of cushion thickness and friction coefficient on shearing resistance are studied.

The dislocation of the first stage increases with the cushion thickness, and the shear stiffness decreases accordingly (Fig. 7(a)). And the compression deformation of the cushions increases, making bolt pre-force loosen and joint shear resistance decrease slightly. When there is no cushion, shear resistance decreases greatly and the dislocation is only 0.12 mm in the first stage. Cushion thickness mainly determines the dislocation of first stage and nearly doesn't influence the shear resistance of later stages.

The friction coefficient has significant influence on the shear resistance, showing linear relationship (Fig. 7(b)). As the friction coefficient increasing, the dislocation of the first stage increases slightly and the nonlinear character becomes clearer. Comparing to the model without cushions, the friction coefficient between cushion and segment should be kept above 0.55 (the friction coefficient between concrete), and the cushion shearing failure should also be avoided.

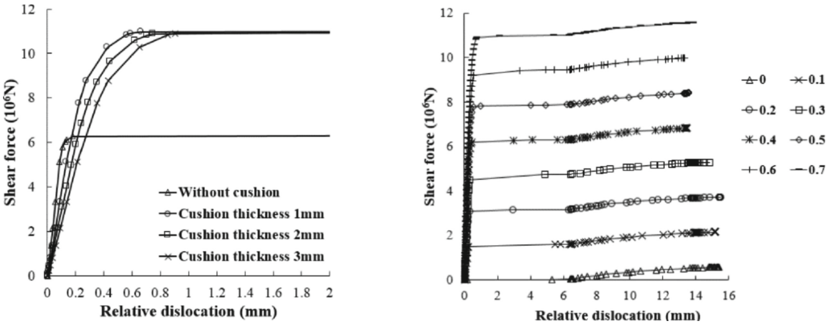

(a) Cushion thickness (b) Friction coefficient

Fig. 7. The dislocation curves varying with cushion parameters.

3.4 Influence of Bolt Pre-force on Shearing Resistance

The bolt force will loosen during tunneling, thus the influence of bolt pre-force is studied using straight bolt joint and oblique bolt joint under ordinal shearing models. As for curved bolt joint, the influence is indistinguishable for its' complex stress condition which is not considered in this part.

For straight bolt joint, the increase of the bolt pre-force leads to obvious increase of shear strength, and shows the linear relation at every stage (Fig. 8(a)). The shear stiffness of the third stage decreases as the bolt pre-force increasing, while the shear stiffness is nearly the same in the previous stages.

For oblique bolt joint, the increase of bolt pre-force enhances the first stage's shear resistance but not significant (Fig. 7(b)). It can be seen that the curves coincide when the dislocation exceeds 6.2 mm, and the shear strength decreases with the bolt pre-force increasing. This is because the bolt's stress reaches yield stress as the result of bolt pre-force increase, and the plastic zone increases with the bolt pre-force as shown in Fig. 9.

Above all, pre-force of bolts can effectively improve the shear stiffness and bearing capacity at the early stages of joint shearing, but decreases the following stage's bearing capacity. The stress concentration at hand holes is more serious as the pre-force increases. Consequently, the option of reasonably pre-force of bolt is very important.

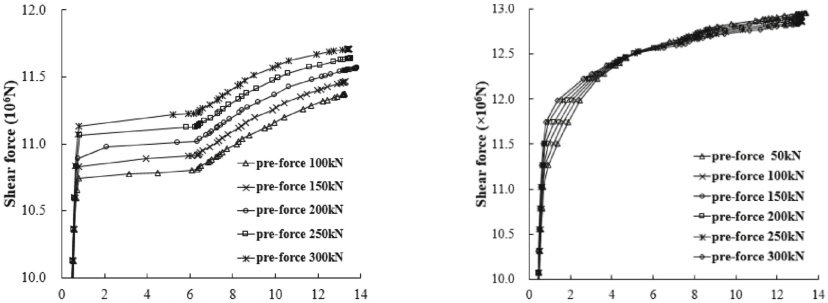

(a) Straight bolt (b) Oblique bolt

Fig. 8. The dislocation curves varying from bolt pre-force (partial).

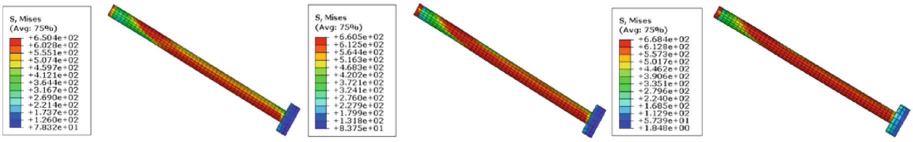
S, Mises
(Avg: 75%)
+6.504e+02
+6.028e+02
+5.551e+02
+5.074e+02
+4.597e+02
+4.121e+02
+3.644e+02
+3.167e+02
+2.690e+02
+2.214e+02
+1.737e+02
+1.260e+02
+7.832e+01
S, Mises
(Avg: 75%)
+6.605e+02
+6.125e+02
+5.644e+02
+5.163e+02
+4.683e+02
+4.202e+02
+3.721e+02
+3.241e+02
+2.760e+02
+2.279e+02
+1.799e+02
+1.318e+02
+8.375e+01
S, Mises
(Avg: 75%)
+6.684e+02
+6.128e+02
+5.573e+02
+5.017e+02
+4.462e+02
+3.906e+02
+3.351e+02
+2.796e+02
+2.240e+02
+1.685e+02
+1.129e+02
+5.739e+01
+1.848e+00

(a) Bolt pre-force 100kN (b) Bolt pre-force 200kN (c) Bolt pre-force 300kN

Fig. 9. Stress contours of oblique bolt when the joint dislocation is 6.2 mm.

4 Discussion

Based on the numerical simulation results, the effects of structure components on shearing resistance of circumferential joints are well understood. The high joint shear stiffness can improve the shear resistance but increase the segment crack possibility. And the joint durability and safety are of the equal importance to shear resistance.

The straight bolt structure is simple and easy for construction, but the hand hole weakens the cross section significantly. The shear strength of curved bolts is optimum, however, the stress condition of tunnel joint during shearing is complex, which brings the risk of cracks for the segment concrete. The shearing strength of oblique bolts under ordinal shearing mode is largest, but it's weak in reverse shearing. Therefore, to cross install the oblique bolts in a crossed way or combine with the tenons is beneficial to improve the joint shearing resistance and guarantee structure safety.

The pre-force of bolt improve the joint shear resistance slightly. However, the overlarge pre-force cause the material yielding advance and stress concentration at hand holes, which will damage the joint durability. The setting of bolt pre-force and quantity should also be reasonable to ensure the compression of gaskets.

Gaskets can reduce the shear capacity of tunnel circumferential joints. A combination of non-expansion gaskets and water expansion gaskets can reduce initial compression and improve the shear resistance, and it's beneficial to the long-term durability.

The friction coefficient has a significant influence on the shear capacity of circumferential joints. Keeping the joint in good contact condition can improve the shear resistance obviously, but the shear failure and sliding of cushions aroused by high load should be avoided.

The joint shear behavior closely depends on the joint structure. Special attention should be considered for the segment safety and durability when the measures are adopted to improve the shearing resistance.

5 Conclusion

In this paper, the shearing behavior and shear capacity of circumferential joint of large-diameter tunnel is studied considering the effect of blot types, gasket, transmission cushion and bolt pre-force. The findings are summarized as follows:

(1) The joint's shear dislocation process can be divided into three stages. Linear fitting can be used at each stage to obtain the simplified calculation model.
(2) The shearing resistance of bolts is associated with the stress level and deformation characteristics of joints. To install the oblique bolts in a crossed way and combine with the tenons are suggested.
(3) The gaskets are the key of joint waterproofing, but it decreases the joint's shear resistance slightly. And the composite gasket can make up this shortage.
(4) The transmission cushions can reduce the segment stress concentration and effect the first stage's dislocation greatly. The friction coefficient between segment and cushion showing linear relationship with shear resistance.

(5) The pre-force of bolts can effectively improve the shear stiffness and bearing capacity of the early stages, but decreases the following stage's shear bearing capacity. Thus, the magnitude of pre-force of bolts should be considered reasonably.

Acknowledgement. This study is financially supported by the National Natural Science Foundation of China (Grants No. 41772295 and No. 51478344), Shanghai Science and Technology Committee Project (Grant No. 16DZ1200403). The support is gratefully acknowledged.

References

1. Ye, F., Zhu, H., Ding, W., et al.: Analysis on anti-buoyancy calculation in excavation of big cross-section shield tunnel. Chin. J. Undergr. Space Eng. **3**(5), 849–853 (2007)
2. Xiao, M., Sun, W., Han, X.: Research on upward moving of segments of shield tunnel. Rock Soil Mech. **30**(4), 1041–1996 (2009)
3. Shen, Z.: Analysis and Control of the upward moving of tunnel segments in the process of shield excavation. Mod. Tunneling Technol. **41**(6), 51–56 (2004)
4. Dong, S., Yang, P., Jiana, C., et al.: Analysis of mechanism and controls of segment floating of shield tunnels. Chin. J. Undergr. Space Eng. **12**(1), 49–54 (2016)
5. Yan, J.: Research on the Behavior of the Segment Joint in Shield Tunnel. Tongji University (2007)
6. Du, C., Wang, K.: Analysis on uplift and dislocation of segment in tunnel bored by large-diameter slurry shield in water-rich soft ground. Tunnel Constr. **31**(2), 171–174 (2011)
7. Zhong, X., Zhu, W., Huang, Z., et al.: Effect of joint structure on joint stiffness for shield tunnel lining. Tunneling Undergr. Space Technol. **21**(3), 407–408 (2006)
8. Salemi, A., Esmaeili, M., Sereshki, F.: Normal and shear resistance of longitudinal contact surfaces of segmental tunnel linings. Int. J. Rock Mech. Min. Sci. **77**, 328–338 (2015)
9. Huang, Z., Liao, S., Hou, X.: Research on shear model of ring joint bolts in stagger-jointed segmental linings. Chin. J. Rock Mech. Eng. **23**(6), 952–958 (2004)
10. Wang, Z., Wang, L., Li, L., et al.: Failure mechanism of tunnel lining joints and bolts with uneven longitudinal ground settlement. Tunneling Undergr. Space Technol. **40**(1), 300–308 (2014)
11. Chen, R., Liu, Y., Liu, S., et al.: Characteristics of upward moving for lining during shield tunneling construction. J. Zhejiang Univ. **48**(6), 1068–1074 (2014)
12. Guo, R., He, C., Su, Z., et al.: Study of shearing mechanical properties of segment joints of shield tunnels. Mod. Tunneling Technol. **48**(4), 72–77 (2011)
13. Yan, Z., Peng, Y., Ding, W., et al.: Load tests on segment joints of single lining structure of shield tunnel in Qingcaosha water conveyance project. Chin. J. Geotech. Eng. **33**(9), 1385–1390 (2011)
14. Zhu, H., Huang, B., Li, X., et al.: Unified model for internal force and deformation of shield segment joints and experimental analysis. Chin. J. Geotech. Eng. **36**(12), 2153–2160 (2014)

Tunnel Roof Stability in Soft Rock with Tension Cutoff

Dowon Park[1] and Radoslaw L. Michalowski[2](✉)

[1] University of Michigan, Ann Arbor, MI 48109, USA
[2] University of Michigan, 2028 G.G. Brown Bldg., 2350 Hayward,
Ann Arbor, MI 48109, USA
rlmich@umich.edu

Abstract. Underground structures are exposed to stability issues associated with roof collapse, both during their construction and operation. A major source of uncertainties in tunnels' roof stability come from the behavior of rock or soil. The Hoek-Brown yield criterion is typically used in analyses when tunnels are constructed in rocks, but in soils and soft rocks the Mohr-Coulomb criterion is more often utilized. However, the tensile strength following from the Mohr-Coulomb criterion may be unrealistic. For that reason, a tension cutoff is proposed, which truncates the yield surface in tensile regime. An analysis of tunnel roof stability in geomaterial with tension cutoff is described in this paper. The kinematic approach of limit analysis is used. Introducing tensile strength cutoff produces nonlinearity in the strength envelope, promoting a multiplicity of admissible roof failure patterns. Stability numbers for an unsupported roof are calculated and support stress is derived that assures stability.

Keywords: Tunnel roof stability · Tension cutoff · Limit analysis

1 Introduction

Roof stability in tunnels is a major concern in tunneling operations. The uncertainties in assessment of roof stability come from several sources, with the behavior of the rock or soil being one of them. In stability analyses involving rocks, the Hoek-Brown (H-B) yield criterion is typically used, but in soils, the Mohr-Coulomb (M-C) criterion is more often utilized. The latter is also used for soft rocks, but the tensile strength following from the M-C criterion may be unrealistic. While limitation of the tensile strength is part of the H-B non-linear strength envelope, a tension cutoff feature is introduced in the M-C envelope to limit the tensile strength.

Tunnel roof stability analyses are often categorized as shallow and deep tunnel analyses [2, 12]. The former includes a tunnel failure that propagates to the ground surface. The latter includes mechanisms propagating into the space above the roof, but not reaching the surface; these have been extensively considered using the kinematic approach of limit analysis since the early 1970s [6]. Recent literature on the subject [3, 13] is typically associated with the Hoek-Brown strength criterion [4], because the traditional Mohr-Coulomb criterion does not correspond to the true behavior of rocks (or bonded geomaterials), particularly in the low-stress regime, and thus it does not

© Springer Nature Singapore Pte Ltd. 2018
D. Zhang and X. Huang (Eds.): GSIC 2018, *Proceedings of GeoShanghai 2018 International Conference: Tunnelling and Underground Construction*, pp. 361–368, 2018.
https://doi.org/10.1007/978-981-13-0017-2_36

correspond to the actual collapse mechanisms. An attempt is made in this paper at a deep tunnel roof stability analysis utilizing analysis with a modified Mohr-Coulomb failure envelope with limited tensile strength. By introducing a tension cutoff [1, 7, 10], the yield surface adheres better to the true behavior of rocks, and the failure mechanisms of roof collapse become more realistic.

2 Problem Statement

A tunnel of circular cross-section is considered in geomaterial with strength described by the Mohr-Coulomb yield condition with tensile strength cutoff. The tunnel is deep enough not to cause a failure propagating to the surface (H > C), Fig. 1.

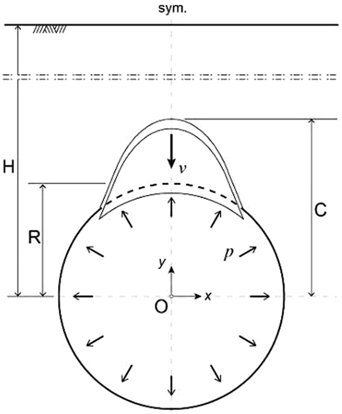

Fig. 1. Problem statement

A solution to supporting pressure p distributed on the interior surface of the tunnel is sought, which is needed to maintain tunnel stability. Alternatively, the strength of the rock will be sought, needed to maintain stability of unsupported tunnels. The tunnel is long, and plane-strain solutions will be sought.

The kinematic approach of limit analysis will be used, with collapsing block moving downward with velocity v, as shown in Fig. 1. The unit weight of the soil/rock is γ, and the relevant strength parameters in the strength criterion are described in the next section.

3 Tensile Strength Cut-off

3.1 The Yield Condition

The yield surface in the principal stress space is illustrated in Fig. 2(a). This is essentially the Mohr-Coulomb surface with a limitation imposed in the tensile regime that follows the Rankine tensile strength criterion [5]. Such a limitation on tensile strength was suggested by Paul [10] in order to account for the fracture mode or rock "yielding", though the tension cutoff in the strength envelope for soils was introduced earlier by Drucker and Prager [1]. More recently, such criterion was used in an analysis of slopes with cracks and intact slopes [8, 9]. Transformed into the Mohr plane, Fig. 2(b), this surface represents a strength envelope encasing all admissible stress states; the envelope is tangent to all of the limit state stress circles.

As the normality flow rule is enforced in limit analysis, the strain rate vector $\dot{\varepsilon}_{ij}$ in Fig. 2(a) and the velocity jump vector on kinematic discontinuities **v** in Fig. 2(b) are perpendicular to the yield surface and to the strength envelope, respectively.

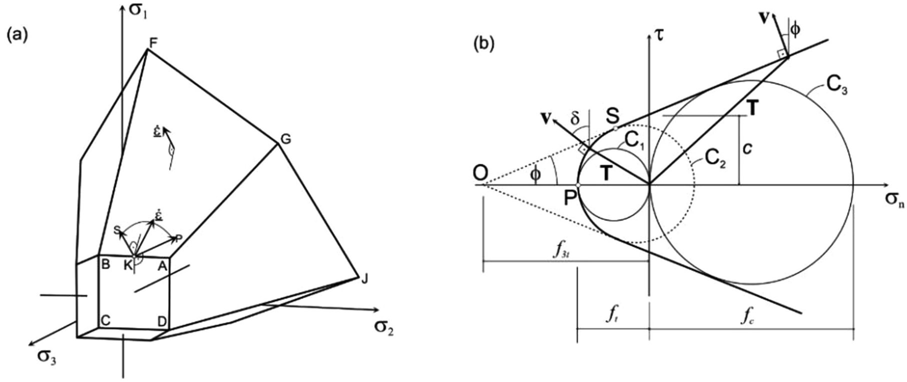

Fig. 2. (a) Yield surface with tension cutoff, and (b) strength envelope

The consequence of the normality flow rule is that the dilatancy angle equals the internal friction angle. However, along section SP of the strength envelope, Fig. 2(b), angle δ starts increasing from ϕ to $\pi/2$. This angle can no longer be interpreted as a dilatancy angle in Reynolds [11] sense, as it is associated with a large separation component typical of fracturing rather than continual strain. This angle might be more appropriately called a *rupture angle*.

3.2 Internal Work During Failure

The uniaxial tensile strength associated with the Mohr-Coulomb yield function is equal to $2c\cos\phi/(1+\sin\phi)$, and the tensile strength modified by the strength cutoff is defined here as

$$f_t = \xi \frac{2c\cos\phi}{1+\sin\phi} \tag{1}$$

where ξ is the coefficient that can vary from 0 (no tensile strength) to 1. The expression for the work rate dissipation d per unit area of the rupture surface, associated with tension cutoff was derived as a dot product of stress vector **T** and the velocity discontinuity vector **v** in Fig. 2(b) (see [9])

$$d = cv\left(\cos\,\phi\frac{1-\sin\delta}{1-\sin\phi} + 2\xi\frac{\sin\delta - \sin\phi}{\cos\phi}\right) \tag{2}$$

where velocity v is the magnitude of vector $\mathbf{v}$. In general, c is not *cohesion*, but an intercept of the linear portion of the strength envelope with axis τ on the Mohr plane.

4 Mechanism of Tunnel Roof Failure

4.1 Collapse Pattern and Method of Solution

The roof collapse mechanism is depicted in Fig. 3 (plane strain analysis). The collapsing block moves downward with velocity v, but the block is divided into smaller triangular sections to allow for changing rupture angle along the rupture surface. However, all sections move with one velocity v. The kinematic theorem of limit analysis states that the rate of internal work (dissipated) is not smaller than the work rate of true external forces in any kinematically admissible mechanism. Hence, the following inequality can be written for an unsupported tunnel, $p = 0$ (symmetric mechanism)

$$c\,v\sum_{i=1}^{n}\left(\cos\phi\frac{1-\sin\delta_i}{1-\sin\phi} + 2\xi\frac{\sin\delta_i - \sin\phi}{\cos\phi}\right)L_i \geq \gamma v\left[\sum_{i=1}^{n}A_\mathrm{i} - \left(\frac{\pi}{2} - \beta\right)R^2\right] \tag{3}$$

where L_i is the length of segment i of the rupture surface (CD in Fig. 3), and A_i is the area of section i (shaded area in Fig. 3). Consequently, one can calculate the lower bound on the dimensionless group $c/\gamma R$ as

$$\frac{c}{\gamma R} = \frac{\sum\limits_{i=1}^{n}A_i - \left(\frac{\pi}{2} - \beta\right)R^2}{R\sum\limits_{i=1}^{n}\left(\cos\phi\frac{1-\sin\delta_i}{1-\sin\phi} + 2\xi\frac{\sin\delta_i - \sin\phi}{\cos\phi}\right)L_i} \tag{4}$$

The maximized value of the dimensionless group $c/\gamma R$ will be referred to as the *stability number*. The process of optimization involves a search for the geometry of the collapsing block that maximizes the value of $c/\gamma R$ in Eq. (4). The failure surface is a piece-wise linear curve with n sections. The geometry of the falling block is fully described by $2n$ parameters (angles): n angles α_i and n angles η_i (identified in Fig. 3). Angle δ in the first block is $\delta_1 = 90° - \alpha_1$ and it is equal to or higher than the internal friction angle, whereas angle δ_n (in the last block) is equal to or lower than 90°; this is the consequence of the normality flow rule.

The best lower bound on the stability number is obtained by maximizing $c/\gamma R$ in Eq. (4), with the geometry of the falling block being varied.

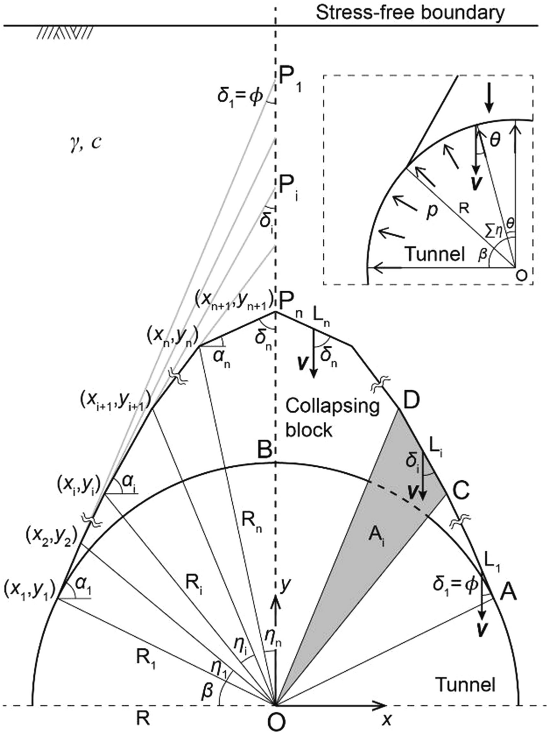
Stress-free boundary
γ, c
P_1
$\delta_1=\phi$
P_i
δ_i
(x_{n+1},y_{n+1})
P_n
L_n
δ_n
(x_n,y_n)
α_n
δ_n
V
Collapsing block
D
(x_{i+1},y_{i+1})
B
L_i
δ_i
V
C
(x_i,y_i)
α_i
R_n
A_i
(x_2,y_2)
L_1
(x_1,y_1)
α_1
R_i
y
$\delta_1=\phi$
A
V
η_i
η_n
R_1
η_1
β
Tunnel
R
O
x
θ
V
p
R
$\Sigma\eta$
θ
Tunnel
β
O

Fig. 3. Roof failure mechanism

4.2 Supporting Pressure

If the strength of soil/rock above the tunnel is not large enough, a supporting structure will be necessary to maintain the required safety margin against the roof failure. The supporting structure is simulated here with supporting pressure p (see insert in Fig. 3), which is assumed uniformly distributed and perpendicular to the interior surface of the tunnel. In order to account for pressure p in the analysis, an additional term needs to be included on the right-hand side of inequality (4). This term includes the work rate of pressure p on the moving boundary of the collapsing block (see insert in Fig. 3 for angle θ)

$$W_p = -\int_0^{\frac{\pi}{2}-\beta} pvR\cos\theta d\theta = -pvR\cos\beta \tag{5}$$

Consequently, the lower bound on the supporting pressure p needed to maintain stability is derived as

$$\frac{p}{\gamma R} = \frac{1}{R\cos\beta}\left[\frac{1}{R}\left\{\sum_{i=1}^{n} A_i - \left(\frac{\pi}{2}-\beta\right)R^2\right\} - \frac{c}{\gamma R}\sum_{i=1}^{n}\left(\cos\phi\frac{1-\sin\delta_i}{1-\sin\phi} + 2\xi\frac{\sin\delta_i-\sin\phi}{\cos\phi}\right)L_i\right] \tag{6}$$

The dimensionless group $c/\gamma R$ in Eq. (6) is now the true combination of the parameters for a given tunnel and not the stability number. The best lower bound on pressure p is obtained by maximizing $p/\gamma R$ in Eq. (6), with the geometry of the collapsing block being varied.

5 Results and Discussions

The supporting pressure required for stability and the stability number for unsupported tunnels were calculated using the kinematic approach of limit analysis. Calculations were performed using a maximization scheme based on sequential incremental change of variable angles (n angles α_i, and n angles η_i), with the initial increments of 0.1° and final increments of 0.001°. Computations were carried out for internal friction angle ϕ in the range of 20° to 60°. The number of segments n in the analysis was 10 (in one symmetric half of the mechanism), but the difference between the results calculated with 10 and 50 segments was only about 0.15%.

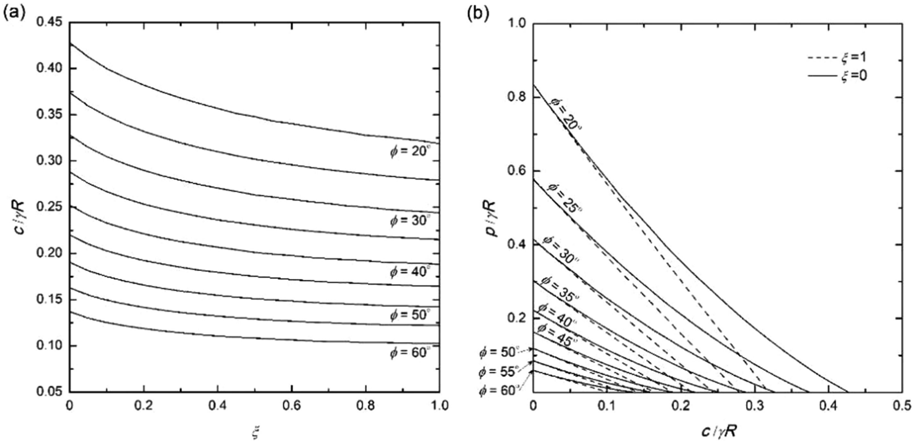

Fig. 4. (a) Stability number as a function of the tensile strength coefficient ξ, and (b) required supporting pressure as a function of the strength of the geomaterial

Figure 4(a) presents the numerical results of the stability number in Eq. (4) as a function of the coefficient ξ representing the uniaxial tensile strength, Eq. (1). The stability number decreases with an increase in the uniaxial tensile strength defined by coefficient ξ, and this decrease is more prominent for small internal friction angle ϕ.

Figure 4(b) shows the calculated supporting pressure, Eq. (6), necessary to maintain stability of the roof for given intercept c ($c/\gamma R$) and internal friction angle ϕ. As expected, the supporting pressure decreases with an increase in the material strength (increase in $c/\gamma R$ and ϕ). Calculation results for both $\xi = 0$ and $\xi = 1$ (dashed line) are shown in Fig. 4(b). It is interesting to notice that the tunnel roof can be stable even if the material has no uniaxial tensile strength, but it must have uniaxial compressive strength.

The geometry of falling blocks for unsupported tunnels is illustrated in Fig. 5. The straight-line segments of the failure surfaces correspond to the linear portion of the strength envelope in Fig. 2(b), whereas the curvilinear segments are governed by the tension cutoff in Fig. 2(b), with rupture angle δ. It is interesting to see the influence of the internal friction angle (ϕ) and the uniaxial tensile strength (ξ) on the shape of the falling block, but the conclusions from Fig. 5 are not straightforward, because every failure surface in the figure is associated with a different stability number.

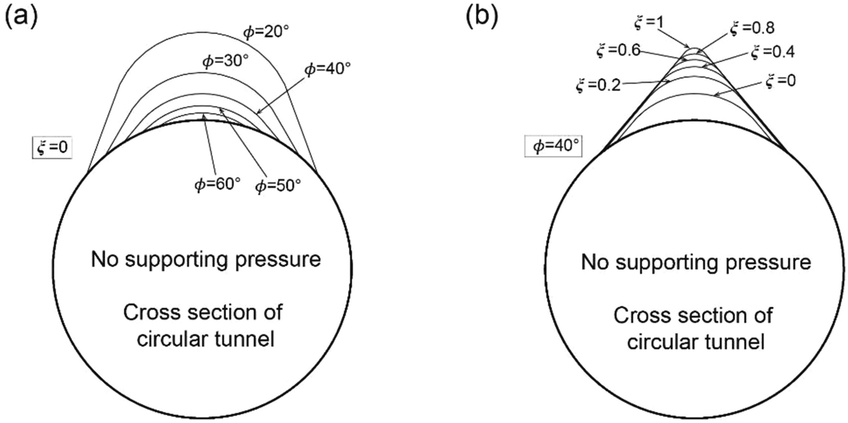

Fig. 5. Geometry of a collapsing block without supporting pressure: (a) effect of internal friction angle (ξ = 0), and (b) influence of the tensile strength

Further studies are needed, including failures of supported tunnels, in order to uncover the causes behind the optimized mechanisms developed in this study. A comparison to the solutions using the Hoek-Brown strength envelope may yield additional insight into whether or not the tension cutoff strength formulation is a viable alternative to the Hoek-Brown criterion when analyzing roof stability.

6 Conclusions

The Mohr-Coulomb yield condition is often used in stability analyses involving soils. The tensile strength predicted by the M-C condition for bonded materials, however, is usually the result of extrapolation of the test results in compressive regime. Application of such a description to rocks or ‘hard soil’ might be risky, as the tensile strength is known to depend on the state of rock (e.g., the degree to which it was weathered). In general, the Hoek-Brown yield condition is used in rock analyses, but a linear strength criterion with tension cutoff might be a viable alternative in some cases.

Tension cutoff superimposed on the Mohr-Coulomb yield condition introduces nonlinearity into the strength envelope, and allows describing the failure modes with rupture of geomaterial characterized by large separation velocity components. Such strength description was used in this paper in the analysis of roof stability in a circular tunnel. The outcome of the analysis appears to be reasonable, but further studies are needed to justify the model as an alternative to the Hoek-Brown criterion for ‘hard soils’ and ‘soft rocks’ when analyzing tunnel roof stability.

References

1. Drucker, D.C., Prager, W.: Soil mechanics and plastic analysis or limit design. Quart. Appl. Math. **10**(1), 157–165 (1952)
2. Fraldi, M., Guarracino, F.: Analytical solutions for collapse mechanisms in tunnels with arbitrary cross sections. Int. J. Solids Struct. **47**(2), 216–223 (2010)
3. Fraldi, M., Guarracino, F.: Evaluation of impending collapse in circular tunnels by analytical and numerical approaches. Tunneling Undergr. Space Technol. **26**(4), 507–516 (2011)
4. Hoek, E., Carranza-Torres, C., Corkum, B.: Hoek-Brown failure criterion – 2002 Edition. In: Hammah, R., Bawden, W., Curran, J., Telesnicki, M. (eds.) Proceedings of the Fifth North American Rock Mechanics Symposium (NARMS-TAC), vol. 1, pp. 267–273. University of Toronto Press, Toronto (2002)
5. Lagioia, R., Panteghini, A., Puzrin, A.M.: The ‘I3’ generalization of the Galileo–Rankine tension criterion. Proc. Roy. Soc. A **470**(2172) (2014). Article Number: 20140568. http://dx.doi.org/10.1098/rspa.2014.0568
6. Lippmann, H.: Plasticity in rock mechanics. Int. J. Mech. Sci. **13**, 291–297 (1971)
7. Michalowski, R.L.: Limit analysis of quasi-static pyramidal indentation of rock. Int. J. Rock Mech. Min. Sci. **22**(1), 31–38 (1985)
8. Michalowski, R.L.: Stability assessment of slopes with cracks using limit analysis. Can. Geotech. J. **50**(10), 1011–1021 (2013)
9. Michalowski, R.L.: Stability of intact slopes with tensile strength cut-off. Géotechnique **67** (8), 720–727 (2017). https://doi.org/10.1680/jgeot.16.P.037
10. Paul, B.: A modification of the Coulomb-Mohr theory of fracture. J. Appl. Mech. **28**(2), 259–268 (1961)
11. Reynolds, O.: On the dilatancy of media composed of rigid particles in contact With experimental illustrations. Phil. Mag. **20**, 469–482 (1885)
12. Sloan, S.W., Assadi, A.: The stability of tunnels in soft ground. In: Houlsby, G.T. (ed.) Proceedings of the Wroth Memorial Symposium on Predictive Soil Mechanics, Oxford, UK, 27–29 July 1992, pp. 644–663. Thomas Telford Ltd., London (1992)
13. Yang, X.L., Huang, F.: Three-dimensional failure mechanism of a rectangular cavity in a Hoek-Brown rock medium. Int. J. Rock Mech. Min. Sci. **61**, 189–195 (2013)

Mechanical Properties and Seismic Isolation Mechanism of Foamed Concrete Longitudinal Joints of Tunnel in Rock

Shaosen Ma(✉) and Weizhong Chen

Research Center of Geotechnical and Structural Engineering,
Shandong University, Jinan 250061, Shandong, China
mashaosenll09@gmail.com

Abstract. Foamed concrete has excellent shock absorption properties, so it can be used as one type of seismic isolation material for tunnels. The objective of this study is to investigate the mechanical properties and seismic isolation mechanism of foamed concrete longitudinal joints. In this paper, under the moderate strain rates (10^{-5} s^{-1}–10^{-2} s^{-1}), a series of uniaxial and triaxial compression tests were conducted to study the effects of density, confining pressure and strain rate on the mechanical properties of foamed concrete. The test results showed that the strength of foamed concrete grows with the increase of the density. Besides, the foamed concrete has the high volumetric compressibility and rate dependence properties: (1) as the confining pressure increases, its strength increases; (2) as the strain rate increases, its strength increases logarithmically. Then, based on the test results, a rate-dependent constitutive model of foamed concrete was chosen and the fitting parameters involved the model were obtained. Finally various parametric studies were performed to study the influence of density, thickness and spacing on the seismic isolation effect of tunnel joints. It found that the seismic isolation effect would be better when the density is lower, the thickness is thicker and the spacing is smaller.

Keywords: Tunnel · Foamed concrete · Longitudinal joints
Seismic isolation mechanism

1 Introduction

In highly seismic areas, earthquakes occur frequently and simultaneously pose hazards to tunnels and underground structures, as the evidence of many seismic damage investigations [1–5]. Thus the seismic isolation design must be taken into consideration.

Seismic isolation materials mainly contain the asphalt, silicone, foamed concrete and other hyper-elastic or foam materials [6, 7]. Among these, foamed concrete is regarded as the desirable material, which has good energy absorption properties and construction performance [8]. Currently, its mix proportion, mechanical properties, physical and chemical characteristics have been explored much [9, 10]. Furthermore, setting the tunnel with some longitudinal foamed concrete joints is an effective seismic isolation method. Compared with the costly circumferential tunnel layer [11, 12], it saves much.

© Springer Nature Singapore Pte Ltd. 2018
D. Zhang and X. Huang (Eds.): GSIC 2018, *Proceedings of GeoShanghai 2018 International Conference: Tunnelling and Underground Construction*, pp. 369–375, 2018.
https://doi.org/10.1007/978-981-13-0017-2_37

In this paper, a series of uniaxial and triaxial compression tests were conducted to investigate the mechanical properties of foamed concrete. On the other hand, based on the numerical simulation, various parametric studies were performed to study the influence of density, thickness and spacing on the seismic isolation effect of tunnel joints.

2 Experimental Research on the Mechanical Properties of Foamed Concrete

2.1 Specimen Preparation and Test Procedure

Three basic constituents (cement, water, foaming agent) were taken and four densities (300, 450, 600 and 800 kg/m^3) of foamed concrete were made, as shown in Table 1.

Table 1. Mix proportions of foamed concrete.

Mix code	Target density (kg/m^3)	Cement (kg)	Water (kg)	Foaming agent (kg)
M1	300	250.00	125.00	1.41
M2	450	375.00	168.75	1.26
M3	600	500.00	225.00	1.09
M4	800	666.67	300.00	0.86

Several cylindrical specimens were shaped to the standard samples (with a diameter of 50 mm and a length of 100 mm) and then compressed on a RMT-150 system. During the tests, four different densities (300, 450, 600, 800 kg/m^3) and four different strain rates (10^{-5} (pseudo-static), 10^{-4}, 10^{-3}, 10^{-2} s^{-1}) were applied [13]. Besides, there were three levels of confining pressure respectively employed. In particular, 0, 0.25, 0.5 MPa were applied to the specimens whose densities were 300 and 450 kg/m^3, and 0, 0.5, 1.0 MPa were loaded to the ones whose densities were 600 and 800 kg/m^3.

2.2 Effect of Confining Pressure on the Strength of Foamed Concrete

The average strength of foamed concrete in the static compression tests are presented in Table 2. It can be observed that the compressive strength of foamed concrete continuously grows with the increasing confining pressure. This is because the foamed

Table 2. Average strength of foamed concrete in the static compression tests.

Confining pressure (MPa)	Density (kg/m^3)			
	300	450	600	800
0	0.43	1.25	2.38	4.94
0.25	0.99	2.68	–	–
0.5	1.54	3.83	4.76	7.87
1	–	–	6.29	9.68

concrete has the volumetric compressibility properties, and thus the confining pressure can circumferentially compress the specimen and then increase the proportion of aggregate skeleton, which would result in a strength enhancement of foamed concrete.

2.3 Effect of Density on the Strength of Foamed Concrete

From Table 2, it can be seen that the compressive strength of foamed concrete improves dramatically with the increasing density. This is because the foamed concrete strength is mainly determined by its aggregate skeleton, as the density increases, the aggregate skeleton accounts for a greater proportion and then the strength enhances.

2.4 Effect of Strain Rate on the Strength of Foamed Concrete

The average strength of foamed concrete in the dynamic compression tests are shown in Table 3. To be specific, with the increase of the strain rate, the compressive strength of foamed concrete increases logarithmically.

Table 3. Average strength of foamed concrete in the dynamic compression tests.

Confining pressure: 0 MPa				
Strain rate (s^{-1})	Density (kg/m^3)			
	300	450	600	800
1.E–05	0.43	1.25	2.38	4.94
1.E–04	0.43	1.28	2.45	5.09
1.E–03	0.44	1.30	2.50	5.28
1.E–02	0.44	1.33	2.58	5.43
Confining pressure: 0.5 MPa				
Strain rate (s^{-1})	Density (kg/m^3)			
	300	450	600	800
1.E–05	1.54	3.83	4.76	7.87
1.E–04	1.66	4.40	5.66	9.53
1.E–03	1.75	4.98	6.43	11.18
1.E–02	1.85	5.44	7.19	12.65

3 Constitutive Modeling and Fitting Parameters in the Numerical Simulation

Due to the high volume compressibility and rate dependence properties of the foamed concrete, the crushable foam model [14] was chosen in ABAQUS software. And based on the given test results, the mechanical and fitting parameters were obtained, as shown in Table 4.

Table 4. Mechanical and fitting parameters in the crushable foam modeling.

Density (kg/m^3)	Uniaxial compressive strength (MPa)	Elastic modulus (MPa)	Poisson's ratio	k_t	k	m	n
300	0.43	44.72	0.14	0.027	0.37	0.011	1.055
450	1.25	183.21	0.16	0.008	0.31	0.031	1.134
600	2.38	318.60	0.18	0.003	0.18	0.032	1.139
800	4.94	916.34	0.20	0.001	0.09	0.036	1.159

As listed in Table 4, the k and k_t can be defined as follows:

$$\begin{aligned} k &= \frac{\sigma_c^0}{p_c^0} \\ k_t &= \frac{p_t}{p_c^0} \end{aligned} \tag{1}$$

where σ_c^0 is the initial yield stress under uniaxial compression; p_c^0 is the initial yield stress under hydrostatic pressure; p_t is the uniform tensile yield stress.

The m and n can be considered as the fitting parameters, as follows:

$$\frac{\sigma_c(\dot{\varepsilon})}{\sigma_c(\dot{\varepsilon}_0)} = m \lg(\frac{\dot{\varepsilon}}{\dot{\varepsilon}_0}) + n \tag{2}$$

where σ_c is the uniaxial compressive strength; $\dot{\varepsilon}$ is the target strain rate; $\dot{\varepsilon}_0$ is the strain rate as reference; m and n are the fitting parameters.

4 Parametric Studies on the Seismic Isolation Mechanism of Tunnel Joints

4.1 Computational Model

A three-dimensional computational model was established using ABAQUS software, as shown in Fig. 1.

In this model, the length, width and height in total are 40 m, 80 m and 60 m respectively. The tunnel buried depth is 30 m and the lining thickness is 60 cm. Solid elements (hexahedrons) were taken and their average size is 1/8 of the length of seismic wave. Besides, the infinite elements were set up at the boundary of the model.

Furthermore, the mechanical parameters of surrounding rock and tunnel lining are given in Table 5.

The acceleration wave was provided by the Tibet Seismological Bureau, whose peak ground acceleration (the probability of exceeding this is 10% in 50 years) is 0.3 g. Then the wave was vertically inputted at the bottom of the model. In addition, the transverse section which is 10 m away from the portal was chosen and the two locations (vault and left-side arch springing) were monitored.

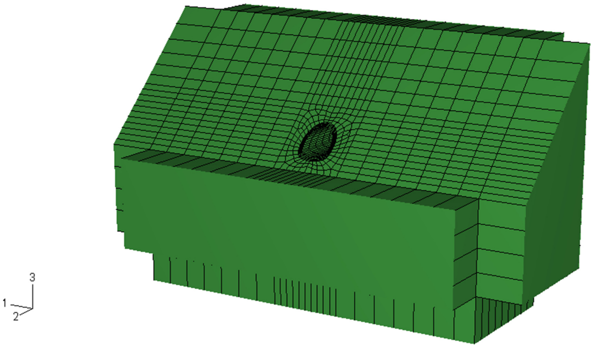

Fig. 1. The computational model

Table 5. Mechanical parameters of surrounding rock and tunnel lining.

Material	Elastic modulus (GPa)	Poisson's ratio	Cohesion (MPa)	Friction angle	Density (kg/m^3)
Surrounding rock	2.0	0.3	0.30	35.0	2300
Lining	25.2	0.2	0.96	51.0	2500

4.2 Case Setting

In the parametric studies, nine cases were set up in total. Four different densities (300, 450, 600, 800 kg/m^3), three different thicknesses (10, 15, 20 cm), three different types of spacing (4, 8, 12 m) were respectively taken into consideration.

4.3 Results and Discussions

From Figs. 2, 3 and 4, it can be seen that the variation laws of maximum principal stress in different situations. To be specific, with the increase of thickness, or with the

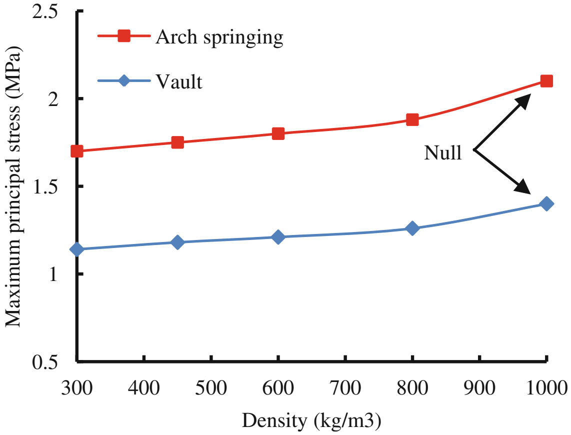

Fig. 2. Maximum principal stress of vault and arch springing under different density

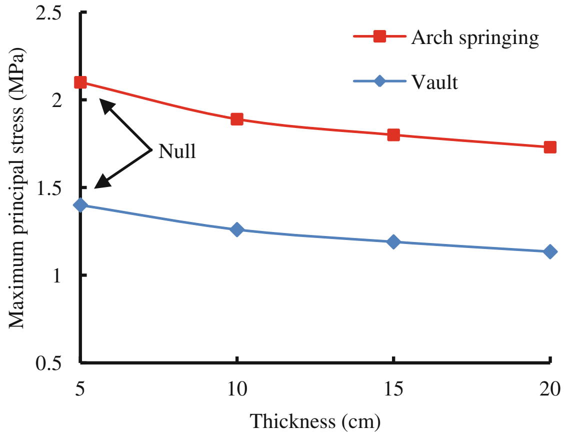

Fig. 3. Maximum principal stress of vault and arch springing under different thickness

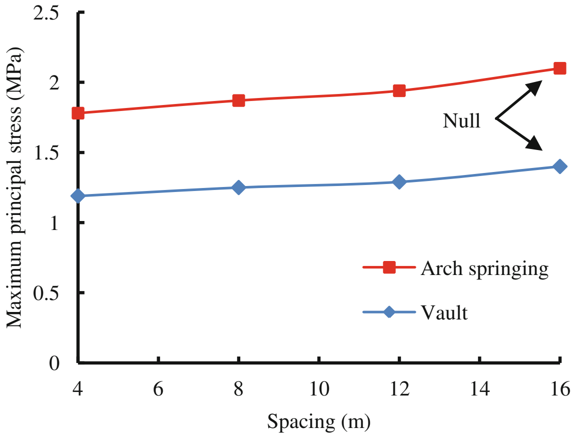

Fig. 4. Maximum principal stress of vault and arch springing under different spacing

decrease of density and spacing, the maximum principal stresses on both vault and arch springing are alleviated obviously. And among them, the influence of joint thickness appears to be more significant. Furthermore, it found that the tunnels with the foamed concrete joints are subjected to the slighter maximum principal stresses than those without the joints, and it is also tested that the foamed concrete longitudinal joints are effective in the seismic isolation of tunnels.

5 Conclusions

The main conclusions in this paper are presented as follows:

(1) Foamed concrete has the high volumetric compressibility and rate dependence properties, and it is also highly influenced by the density. To be specific, (1) with

the increase of the density, the strength of foamed concrete grows; (2) as the confining pressure increases, its strength increases; (3) as the strain rate increases, its strength increases logarithmically.

(2) The crushable foam model in ABAQUS software can well characterize the mechanical properties of foamed concrete, especially the high volumetric compressibility and rate dependence properties.

(3) Seismic isolation mechanism of foamed concrete longitudinal joints can be evaluated in the three aspects: density, thickness and spacing. It found that the seismic isolation effect would be better when the density is lower, the thickness is thicker and the spacing is smaller. Among them, the influence of joint thickness tends to be more significant.

References

1. Huo, H., Bobet, A., Fernández, G., et al.: Load transfer mechanisms between underground structure and surrounding ground: evaluation of the failure of the Daikai station. J. Geotech. Geoenviron. Eng. **131**(12), 1522–1533 (2005)
2. Kontoe, S., Zdravkovic, L., Potts, M., et al.: Case study on seismic tunnel response. Can. Geotech. J. **45**(12), 1743–1764 (2008)
3. Wang, L., Wang, T., Su, J., et al.: Assessment of damage in mountain tunnels due to the Taiwan Chi-Chi earthquake. Tunnelling Undergr. Space Technol. **16**(3), 133–150 (2001)
4. Hashash, A., Hook, J., Schmidt, B., et al.: Seismic design and analysis of underground structures. Tunnelling Undergr. Space Technol. **16**(4), 247–293 (2001)
5. Li, T.: Damage to mountain tunnels related to the Wenchuan earthquake and some suggestions for aseismic tunnel construction. Bull. Eng. Geol. Environ. **71**(2), 297–308 (2012)
6. Zhao, W., Chen, W., Tan, X., et al.: Study on foamed concrete used as seismic isolation material for tunnels in rock. Mater. Res. Innovations **17**(7), 465–472 (2013)
7. Takeuchi, M., Kameda, S., Misawa, T., et al.: The characteristics of asphalt-based material for the seismic isolation applied to the underground structure. Doboku Gakkai Ronbunshu **658**, 93–106 (2000). (in Japanese)
8. Ramamurthy, K., Nambiar, K., Ranjani, S.: A classification of studies on properties of foam concrete. Cement Concr. Compos. **31**(6), 388–396 (2009)
9. Hamad, J.: Materials, production, properties and application of aerated lightweight concrete: review. Int. J. Mater. Sci. Eng. **2**(2), 152–157 (2014)
10. Amran, M., Farzadnia, N., Ali, A.: Properties and applications of foamed concrete; a review. Constr. Build. Mater. **101**, 990–1005 (2015)
11. Wang, S., Gao, B.: Damping mechanism and shaking table test on mountain tunnel linings with buffer layers. Chin. J. Rock Mech. Eng. **35**(3), 592–603 (2016). (in Chinese)
12. Wang, S., Gao, B., Sui, C., et al.: Mechanism of shock absorption layer and shaking table tests on shaking absorption technology of tunnel across fault. Chin. J. Geotech. Eng. **37**(6), 1086–1092 (2015). (in Chinese)
13. Xiao, S., Lin, G., Wang, Z., et al.: Effects of strain rate on dynamic behavior of concrete in tension. J. Dalian Univ. Technol. **41**(6), 721–725 (2001). (in Chinese)
14. Dassault Systèmes: Abaqus analysis user's manual. Simulia Corp. Providence, RI, USA (2007)

Research on Seismic Response Characteristics of Long and Large Tunnel in Rock

Shaosen Ma(✉) and Weizhong Chen

Research Center of Geotechnical and Structural Engineering,
Shandong University, Jinan 250061, Shandong, China
mashaosen1109@gmail.com

Abstract. Tunnels and underground structures in highly seismic areas may suffer severe seismic damage under earthquakes. The objective of this study is to investigate the seismic response characteristics of long and large tunnel in rock. A three-dimensional finite element modeling was established using ABAQUS software and a case study of Galongla tunnel was made to examine the effects of wave intensity, frequency, duration, incidence direction as well as tunnel lining stiffness on the seismic response characteristics. The results showed that the seismic wave with higher intensity, lower frequency and longer duration would result in the greater displacement and cumulative damage of tunnel. And as the incidence direction increases within the range of 0–90°, the displacement has an overall upward trend accompanying with a temporary reduction at 45°. In addition, it revealed that the greater the tunnel lining stiffness is, the stronger the seismic response becomes. At last, an aseismic design for tunnel lining was proposed.

Keywords: Tunnel · Seismic wave · Seismic response characteristics
Seismic damage

1 Introduction

In highly seismic areas, earthquakes occur frequently and they would pose huge hazards to tunnels and underground structures, as the evidence of the existing seismic damage investigations [1–5]. Thus the tunnel seismic response analysis and aseismic design must be taken into consideration.

Finite element method (FEM) is a popular approach to study the tunnel seismic response. Its superiority lies in at least three aspects. First, it could meticulously simulate the complex structures of the long, large, linear tunnels [6]. Second, it is easy to change the features of seismic waves, including the intensity, frequency, duration and incidence direction [7, 8]. Third, it could rapidly adjust the properties of surrounding rock [9]. Based on the abovementioned advantages, it could provide the cogent results of nonlinear seismic response analysis and the reasonable suggestions for anti-seismic measures [10, 11].

Displacement and cumulative damage of tunnel are regulated by the seismic wave characteristics, surrounding rock properties and tunnel structure features. In this paper, a three-dimensional finite element modeling was established using ABAQUS software

© Springer Nature Singapore Pte Ltd. 2018
D. Zhang and X. Huang (Eds.): GSIC 2018, *Proceedings of GeoShanghai 2018 International Conference: Tunnelling and Underground Construction*, pp. 376–383, 2018.
https://doi.org/10.1007/978-981-13-0017-2_38

and a case study was made to investigate the seismic response characteristics of Galongla tunnel.

2 Computational Model

Based on the geological and geotechnical conditions surrounding the Galongla tunnel, a three-dimensional finite element model was established using ABAQUS software, as shown in Fig. 1.

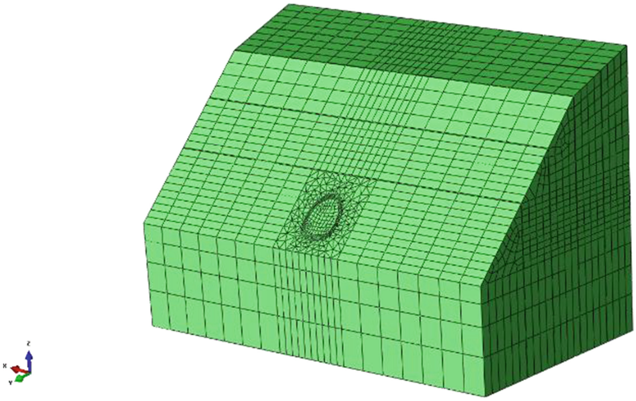

Fig. 1. The computational modeling

In this model, the length, width and height in total are 50 m, 80 m and 80 m respectively. The tunnel buried depth is 40 m and the lining thickness is 60 cm. Solid elements (hexahedrons) were taken and their average size is 1/8 of the length of seismic wave. Besides, the infinite elements were set up at the boundary of the model.

The tunnel lining was built by C20 sprayed concrete and the surrounding rock was judged to be grade V according to the China standard. The behavior of the surrounding rock and tunnel lining were assumed to be elastic-perfectly plastic and they would obey the Mohr-Coulomb failure criterion [12]. And the mechanical parameters of the surrounding rock and tunnel lining are given in Table 1.

Table 1. Mechanical parameters of surrounding rock and tunnel lining.

Material	Elastic modulus (GPa)	Poisson's ratio	Cohesion (MPa)	Friction angle	Density (kg/m^3)
Surrounding rock	2.0	0.3	0.30	35.0	2300
Lining	25.2	0.2	0.96	51.0	2500

The sine shear wave was taken and vertically inputted at the bottom of the model. Its velocity time-history is represented as follows:

$$V_S = \lambda \sin\left(\frac{2\pi}{T} t\right) \tag{1}$$

where λ and T are the amplitude and period of the seismic wave respectively.

The transverse section which is 20 m away from the portal was selected where three locations (vault, intrados and hance) were monitored, as shown in Fig. 2.

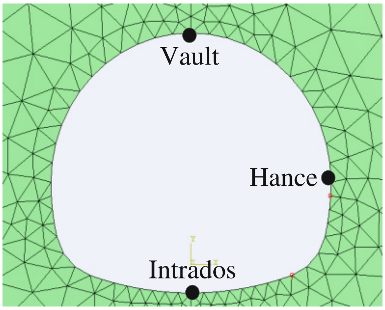

Fig. 2. Schematic of monitoring locations

3 Computational Procedure

For the given seismic wave, the initial parameters were pre-set, the intensity, duration, frequency and incidence direction are 0.25 m/s (peak velocity), 5 s, 1 Hz and 90° respectively.

To investigate the effect of wave intensity on the seismic response characteristics, four levels of peak velocity were taken, they are 0.031, 0.062, 0.130 and 0.250 m/s. When examining the effect of wave duration, the durations were selected as 1, 2, 5, 10 and 15 s. To study the influence of wave frequency, the frequencies were taken as 0.5, 1, 2, 10 and 20 Hz. In order to explore the effect of wave incidence direction, the incidence directions were chosen as 0, 30, 45, 60 and 90°.

Moreover, in order to examine the effect of tunnel lining stiffness on the seismic response characteristics, the lining stiffness was individually chosen as 240, 380, 480, 960 and 1440 MPa*m^4. Meanwhile, for the input seismic wave, its intensity, duration, frequency and incidence direction were respectively adjusted to be 0.130 m/s, 1 s, 1 Hz and 90°.

4 Results and Discussions

4.1 Effect of Wave Intensity on the Seismic Response Characteristics

Figure 3 shows the displacement laws of vault and intrados with the peak velocity.

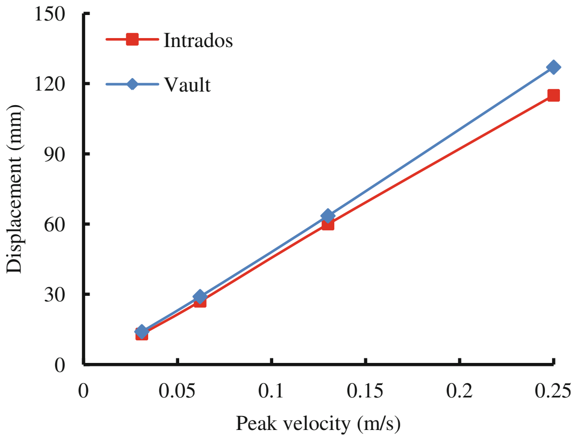

Fig. 3. Displacement of vault and intrados under different peak velocity

It can be observed that as the wave intensity (peak velocity) increases, the tunnel displacement tends to grow in an approximately linear way, and the response of vault is slightly greater than that of intrados.

4.2 Effect of Wave Duration on the Seismic Response Characteristics

Figure 4 represents the displacement laws of vault and intrados with the duration.

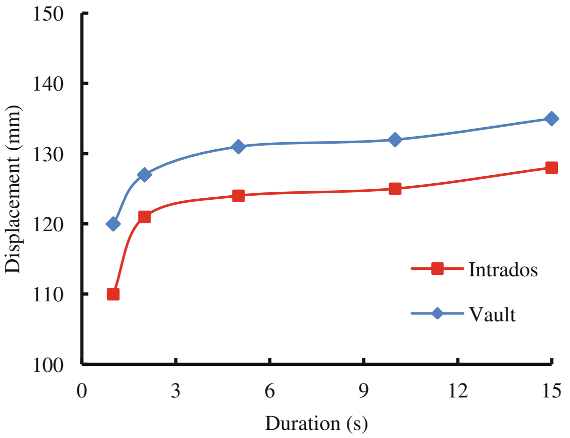

Fig. 4. Displacement of vault and intrados under different durations

As we can see, the displacement is significantly influenced by the duration, which grows with the increase of duration. It indicates that as the input ground motion energy continues to grow, the tunnel damage also continues to accumulate.

4.3 Effect of Wave Frequency on the Seismic Response Characteristics

Figure 5 demonstrates the displacement laws of vault and intrados with the frequency.

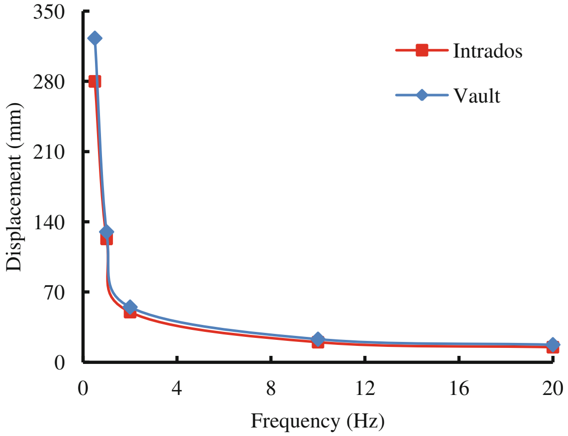

Fig. 5. Displacement of vault and intrados under different frequencies

Generally, as the frequency increases, the tunnel displacement tends to decline, especially when the frequency is less than 10 Hz, the displacement decreases obviously. On the other hand, the displacement changes less when the frequency exceeds 10 Hz. It shows that the tunnel displacement under low frequency seismic waves is obviously greater than that under higher frequency earthquakes.

4.4 Effect of Wave Incidence Direction on the Seismic Response Characteristics

Figure 6 indicates that the displacement laws of vault and intrados with the incidence direction. It can be seen that, as the incidence angle of seismic wave increases from 0° (horizontal direction) to 90° (vertical direction), the tunnel displacement expands at first, then decreases slightly when the angle approaches to 45°, afterwards gradually increases again, and finally reaches the maximum value.

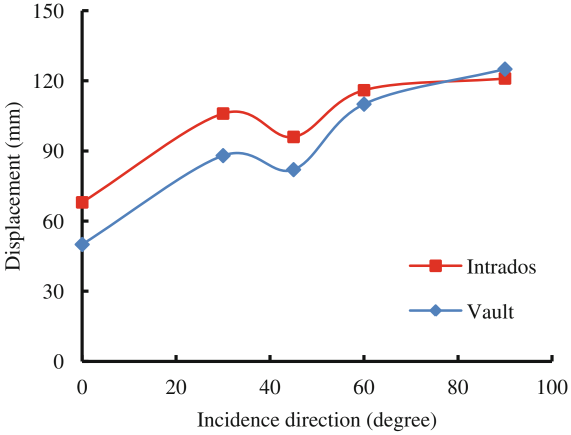

Fig. 6. Displacement of vault and intrados under different incidence directions

4.5 Effect of Tunnel Lining Stiffness on the Seismic Response Characteristics

Figures 7 and 8 respectively suggest the displacement laws and the stress amplification coefficient (the stress on lining divided by the stress on surrounding rock) variation laws of vault and hance with the tunnel lining stiffness.

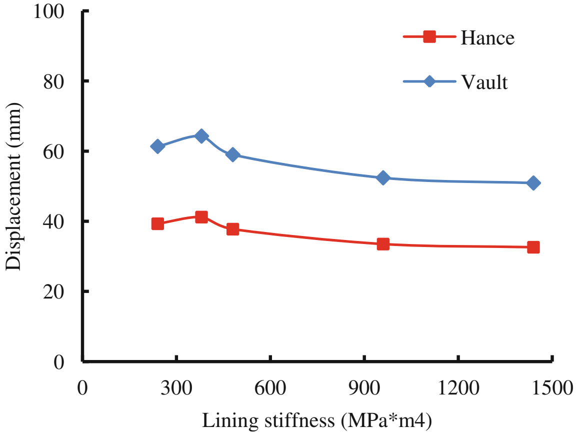

Fig. 7. Displacement of vault and hance under different tunnel lining stiffness

As shown in Fig. 7, when the lining stiffness increases, the tunnel displacement declines slightly, especially when the stiffness increases to two and three times the initial value, the displacement of vault becomes respectively 0.9 and 0.85 times the original value, which is also similar to that of hance.

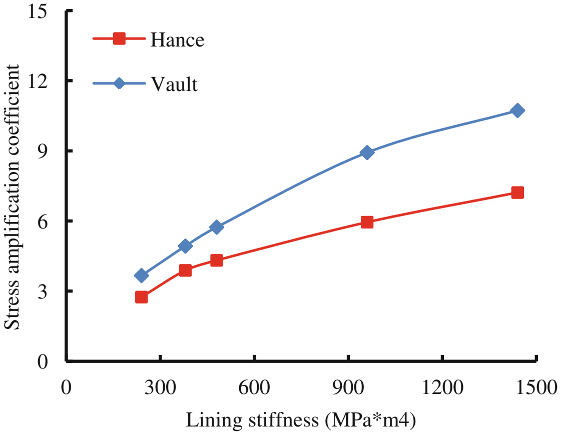

Fig. 8. Stress amplification coefficient on vault and hance under different tunnel lining stiffness

On the other hand, from Fig. 8, we can see that under the same level of in-situ stress, the increase of lining stiffness can lead to a growth of stress amplification coefficient on vault, which is dramatically higher than that on hance. When the lining stiffness doubles, the stress amplification coefficients on both positions are all about 1.4 times the original values; when the stiffness triples, 1.7 times. When the stress amplification coefficient rises and the stress difference between lining and surrounding rock widens, the lining would be loaded greater and subjected to more damage. Thus, appropriately lowering the tunnel lining stiffness is a proposed aseismic design.

At last, there is one technical issue worth being concerned. Only when the validation of the adopted tunnel modeling is verified, the results from such parametric studies would be more reliable and convincing. Exactly, some acceleration transducers have been installed at the three transverse sections of the Galongla tunnel (respectively 20, 40, 60 m away from the portal) and a large amount of field data have been collected. By processing these data, it found that their variation trends are, to some extent, similar to those from the abovementioned parametric studies based on the adopted numerical model. If possible, the detailed evaluation related to this will be presented in the prospective full length paper.

5 Conclusions

Based on the parametric studies, the seismic response characteristics of long and large tunnel in rock were examined using a three-dimensional finite element modeling. The main conclusions are as follows:

(1) The seismic response characteristics of tunnel are highly influenced by the wave intensity, duration and frequency. To be specific, when the seismic intensity increases, the tunnel displacement augments; and as the seismic duration increases, so do the tunnel displacement and accumulative damage. Moreover, the

displacement increases with the decrease of frequency and its amplification caused by low frequency seismic waves is obviously greater than that caused by high frequency earthquakes, which is more dangerous.

(2) As the incidence angle of seismic wave increases (from horizontal incidence to vertical incidence), the tunnel displacement expands at first, then decreases slightly when the angle approaches to 45°, afterwards gradually increases again. As a whole, the displacement arrives at the maximum value when the direction is vertical, and 90° is the most dangerous incidence angle.

(3) Greater lining stiffness can result in a slight reduction in tunnel displacement, but simultaneously enlarge the stress amplification coefficient, widen the stress difference between lining and surrounding rock, and finally cause the lining to be loaded greater and subjected to more damage.

(4) For the tunnel buried in weak surrounding rock masses, appropriately lowering the lining stiffness is a feasible aseismic approach to reduce tunnel damage.

References

1. Huo, H., Bobet, A., Fernández, G., et al.: Load transfer mechanisms between underground structure and surrounding ground: evaluation of the failure of the Daikai station. J. Geotech. Geoenviron. Eng. **131**(12), 1522–1533 (2005)
2. Kontoe, S., Zdravkovic, L., Potts, M., et al.: Case study on seismic tunnel response. Can. Geotech. J. **45**(12), 1743–1764 (2008)
3. Wang, L., Wang, T., Su, J., et al.: Assessment of damage in mountain tunnels due to the Taiwan Chi-Chi earthquake. Tunn. Undergr. Space Technol. **16**(3), 133–150 (2001)
4. Hashash, A., Hook, J., Schmidt, B., et al.: Seismic design and analysis of underground structures. Tunn. Undergr. Space Technol. **16**(4), 247–293 (2001)
5. Li, T.: Damage to mountain tunnels related to the Wenchuan earthquake and some suggestions for aseismic tunnel construction. Bull. Eng. Geol. Env. **71**(2), 297–308 (2012)
6. Huang, S., Chen, W., Yang, J., et al.: Research on earthquake-induced dynamic responses and aseismic measures for underground engineering. Chin. J. Rock Mechan. Eng. **28**(3), 483–490 (2009). (in Chinese)
7. Zhao, W., Chen, W.: Effect of near-fault ground motions with long-period pulses on the tunnel. J. Vibroeng. **17**(2), 841–858 (2015)
8. Huang, J., Du, X., Zhao, M., et al.: Impact of incident angles of earthquake shear (S) waves on 3-D non-linear seismic responses of long lined tunnels. Eng. Geol. **222**, 168–185 (2017)
9. Bao, X., Xia, Z., Ye, G., et al.: Numerical analysis on the seismic behavior of a large metro subway tunnel in liquefiable ground. Tunn. Undergr. Space Technol. **66**, 91–106 (2017)
10. Kim, S., Konagai, K.: Seismic isolation effect of a tunnel covered with coating material. Tunn. Undergr. Space Technol. **15**(4), 437–443 (2000)
11. Konagai, K., Kim, S.: Simple evaluation of the effect of seismic isolation by covering a tunnel with a thin flexible material. Soil Dyn. Earthq. Eng. **21**(4), 287–295 (2001)
12. Systèmes, D.: Abaqus Analysis User's Manual. Simulia Corporation, Providence (2007)

Numerical Investigation on the Mechanical Characteristics of a Special-Shaped Shield Lining with a Large Cross-Section

Yeting Zhu[1,2](✉), Zixin Zhang[1], Xin Huang[1], and Yanfei Zhu[2]

[1] Department of Geotechnical Engineering, Tongji University,
Shanghai 200092, China
1210278theronzhu@tongji.edu.cn
[2] Shanghai Tunnel Engineering Co. Ltd., Shanghai 200233, China

Abstract. A shell-spring finite element model of a special-shaped tunnel was established to investigate the distribution of internal forces and deformation mode of the lining at the designed buried depth. The numerical results were compared with prototype loading test results and uniform beam model, which showed that the shell-spring model can be an optimal model to calibrate the 3D distribution of the internal forces and deformations of the special-shaped tunnel. Finally, the internal forces in the design condition were given. Furthermore, the economy and mechanical property of a special-shaped tunnel were compared with circular and rectangular tunnels with the same dimension and joint parameters. Results showed that the proposed special-shaped tunnel was more suitable for shallow overburden ground.

Keywords: Special-shaped shield · Prototype test · Shell-spring model
Mechanical characteristic

1 Introduction

Generally, the shield tunnel is considered to be in a plane-strain state along the longitudinal direction at the design stage, and the internal forces can be calculated based on the elastic homogeneous ring with free-form deformation. The early and the most widely-used model is the modified routine method [1]. Later, the beam-spring model [2, 3] was employed to check the results calculated from the modified routine method through setting the rotational stiffness of the circumferential joints to values acquired from prototype loading tests on joints [4]. However, the actual mechanical behavior of the lining structure in a staggered-jointed state does not follow the plane hypothesis, especially for the lining deformation caused by the longitudinal joint rotation and the relative displacements between the segments or rings. The three-dimensional mechanical properties can be investigated via a full-ring prototype loading test [5, 6], but it is expensive and could only be loaded with limited times. Therefore, it is more reasonable to develop a three-dimensional calculation model to determine the distribution of internal forces and deformation modes under complex loading conditions for the special-shaped tunnels. The shell-spring model is a convenient option.

© Springer Nature Singapore Pte Ltd. 2018
D. Zhang and X. Huang (Eds.): GSIC 2018, *Proceedings of GeoShanghai 2018 International Conference: Tunnelling and Underground Construction*, pp. 384–391, 2018.
https://doi.org/10.1007/978-981-13-0017-2_39

For a shell-spring model, its segment can be simulated by shell elements connected by joint springs to simulate the axial tension, radial shear, axial shear and rotation properties of the circumferential and longitudinal joints. Typically, Zhang et al. [7] analyzed the internal force distributions of a segment lining structure with different segment widths and different ring joint shear stiffnesses for Wuhan Yangtze River tunnel. Teachavorasinskun and Chub-Uppakarn [8] established a simplified shell-spring model to analyze the influences of the joints, the number of segments and the modulus of soils on the mechanical properties of a segmental structure. Arnau and Molins [9] studied the mechanical coupling effect between the segments and joints and identified the main influencing factors. Do et al. [10] revealed the significant influence of the joints on the internal forces of the successive rings along the tunnel axis in a staggered segmental lining.

In this paper, a full-ring shell-spring model was established to compare the simulation results with the prototype loading test results to validate the reliability of the suggested shell-spring model. Then, the economy and mechanical property of a special-shaped tunnel were compared with circular and rectangular tunnels with the same dimension and joint parameters.

2 Testing Segments

The special-shaped segments with the municipal universal function, which could be applied in projects of subway stations, underpasses, highway or railway tunnels, etc. in the future, were designed based on the No. 4 stratum (silt clay soil) of Shanghai in the operation period. The main design parameters were as follows: design depth = 10 m; underground water level = −0.5 m; unit weight of soil = 18.0 kN/m^3; static lateral pressure coefficient = 0.6; coefficient of subgrade reaction = 6000 kN/m^3; ground overload = 20 kPa.

The cross section of the special-shaped shield tunnel was composed of eight arcs (see Fig. 1) including top and bottom arcs, left and right arcs and four angle arcs. A full ring was assembled by six blocks: one seal roof block (F), two adjacent blocks (L1 and L2) and three standard blocks (B1, B2 and B3). Each ring casted by CF50 steel fiber reinforced concrete has an inner dimension of 10.2 m × 7.7 m with a thickness of 0.5 m and a width of 1.2 m. The segments were fabricated by the staggered-jointed assembling method to enhance the longitudinal rigidity. The six segmental blocks were hinged by four M30 straight bolts circumferentially, and the neighboring rings were connected by 26 M33 bent bolts in the longitudinal direction. The detailed introduction of the prototype loading tests can be referred to Zhu [11].

3 Numerical Simulation Methods

A shell-spring model was established using the finite element software, ABAQUS. In detail, S4R shell elements were adopted to simulate the solid segment; Spring 2 was used to simulate the characteristics of the axial tension, radial shear, axial shear and rotation of the circumferential and longitudinal joints. The interaction between the lining and the elastic rubber bearings during the prototype loading test of Zhu [11] was simulated by Elastic Foundation. Finally, the calculation model was shown in Fig. 2, and the calculation parameters were given as follows: the radial shear and tangential shear stiffness of the longitudinal seams were 2.4 × 10^5 kN/m; the radial shear and axial shear stiffness of the circumferential seams were 3.0 × 10^5 kN/m; and the axial tension and compression stiffness of both the longitudinal and circumferential seams were 2.0 × 10^7 kN/m, which were obtained from the prototype joint loading tests. The joint rotational stiffness was also provided by the full-ring prototype loading tests [11].

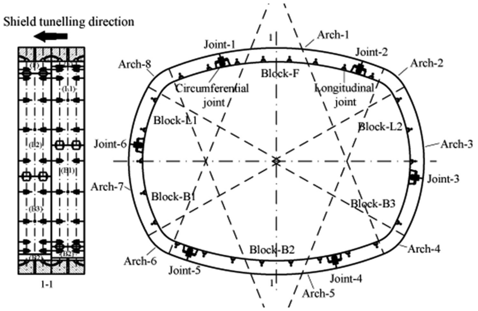
Shield tunelling direction
Joint-1
1
Arch-1
Joint-2
Arch-8
Arch-2
Block-F
Circumferential joint
Longitudinal joint
Block-L1
Block-L2
Joint-6
Arch-3
Joint-3
Arch-7
Block-B1
Block-B3
Block-B2
Arch-4
Arch-6
Joint-5
1
Joint-4
Arch-5
1-1

Fig. 1. Segment layout of a shield tunnel lining with a special-shaped cross-section

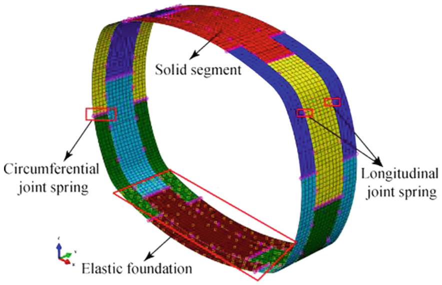
Solid segment
Circumferential joint spring
Longitudinal joint spring
Elastic foundation

Fig. 2. Shell-spring model

4 Comparison Between Testing and Numerical Results

The comparison of the internal forces in the design condition among the prototype test results, shell-spring model (the coefficient of subgrade reaction 9.45 × 10^4 kN/m^3 and 6 × 10^3 kN/m^3) and uniform beam model (effective stiffness ratio $\eta = 0.7$) were illustrated in Fig. 3. Note that among these models, the last one was adopted to design the lining structure at the design stage.

As shown in Fig. 3, the distribution of the internal forces of the four datasets were basically consistent. Specifically, the roof and the bottom of the lining were the positive moment regions, while both of two sides were subjected to negative moment. Four zero moment regions were identified in the arch shoulders and arch feet. Moreover, the vault

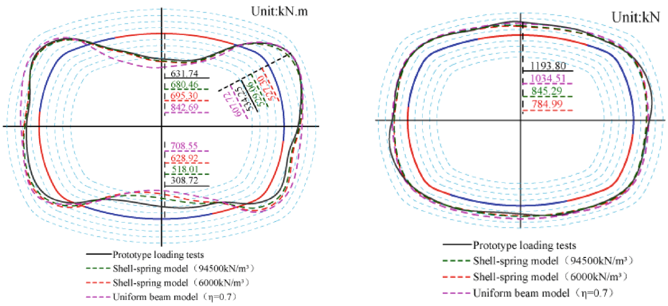

(a) Bending moments (b) Axial forces

Fig. 3. Comparison of the internal forces from the tests and numerical results

experienced the maximum positive bending moment with a small axial force, which was determined to be the most dangerous section as well as the control section of whole lining structure, where the cracks would firstly initiate on the inner surface at the ultimate state.

While the axial forces were almost the same, the calculated moments of the modified routine method were obviously larger than others, which could be explained that the modified routine method considered the segmental lining to be in a plane-strain state, assuming the stiffness of the lining and that of joint to be same, thus exaggerating the enhancement effect of the staggered-jointed assembling on the lining structure in the longitudinal direction. Therefore, additional internal forces were induced to the structure. In fact, during deformation under external loading the lining structure will exhibit unloading characteristics.

The actual internal force distribution of the special-shaped shield lining in the design state was given with the subgrade reaction coefficient of 6000 kN/m^3. Except at the bottom, the moments of the rest parts for the special-shaped shield lining had little difference.

The overall deformation of the special-shaped tunnel under the prototype loads in the designed buried depth was shown in Fig. 4a, and the comparison of the deformations between the loading tests and numerical calculation were given in Fig. 4b.

Both of the testing and numerical results showed that the special-shaped segmental lining deformed in a pattern of ‘expansion in the horizontal direction and closure in the vertical direction’ (see Fig. 4a), which could be explained that the horizontal dimension was larger than that in the vertical direction, and the lateral pressure was not large enough to confine the lateral deformation. Taking the relative displacement between the vault and the bottom in the vertical symmetry axis was taken as the vertical closure, and the relative displacement between two sides in the horizontal symmetry axis as the horizontal expansion, it can be seen from Fig. 4b that the deformation results of the shell-spring model were close to the prototype test, and the linear feature also proved the advantage of the shell-spring model in predicting the segmental deformation, since the elastic characteristic of whole lining structure was revealed in the range of the designed buried depth. Furthermore, the shell-spring model was recommended to be

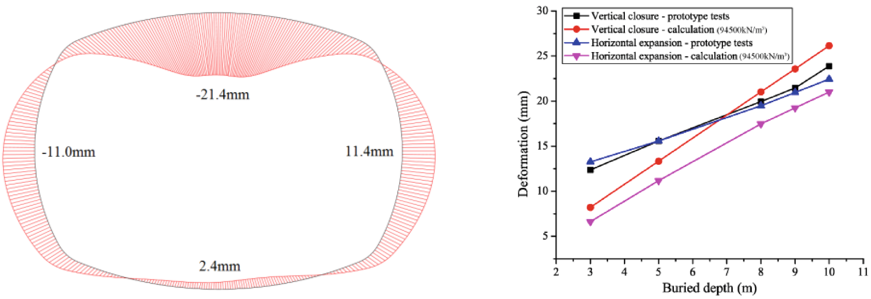

(a) Deformation mode of the designed depth in the prototype loading state

(b) Variation of the deformations with the buried depths

Fig. 4. Deformation of the special-shaped lining

the optimal model to determine the 3D distribution of the internal forces and deformations for the special-shaped tunnel lining.

5 Comparison of the Economy and Mechanical Characteristics Among Three Kinds of Tunnel Sections

In order to explore the difference in the aspects of economy and mechanical characteristics among the special-shaped, rectangular and circular shield tunnels thoroughly, other two tunnel sections were created with the same outer dimension and same segment division. The excavation section area of the special-shaped tunnel was 74.47 m^2, and the corresponding values of the circular and rectangular tunnels were 89.97 m^2 and 87.74 m^2, which are respectively about 20.81% and 17.81% higher than the special-shaped tunnel. The torus areas of the segmental lining of the special-shaped, circular and rectangular tunnels were 14.86 m^2, 16.01 m^2 and 17.9 m^2, respectively, which indicated that the usage of concrete per meter length of the circular and rectangular tunnels were more than 7.7% and 20.5% larger than special-shaped tunnel, respectively. The horizontal and vertical displacement vectors of all three tunnels were shown in Fig. 5.

Seen from Fig. 5, all three tunnels deformed differently under the designed depth of 10 m. Specifically, the special-shaped tunnel deformed in a pattern of ‘expansion in the horizontal direction and closure in the vertical direction’, the circular tunnel ‘expansion in the vertical direction and closure in the horizontal direction’, and the rectangular tunnel ‘closure in the vertical direction, expansion in the upper 1/4 part, closure in the middle 1/2 part in the horizontal direction’. More specifically, the vertical and horizontal deformation values were 26.13 and 17.02 mm for the special-shaped tunnel, 5.54 and 8.75 mm for the circular tunnel, and 37.54 and 4.02 mm for the rectangular tunnel. It is noted that circular tunnel exhibited absolute advantages in the resistance to the structural deformation than the special-shaped tunnel. However, the deformation values of the rectangular tunnel had greatly exceeded the requirement of the national

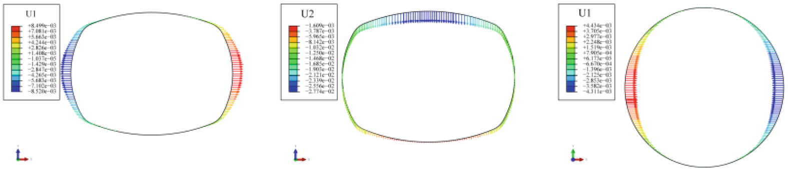

(a) Horizontal displacement of the special-shaped lining

(b) Vertical displacement of the special-shaped lining

(c) Horizontal displacement of the circular lining

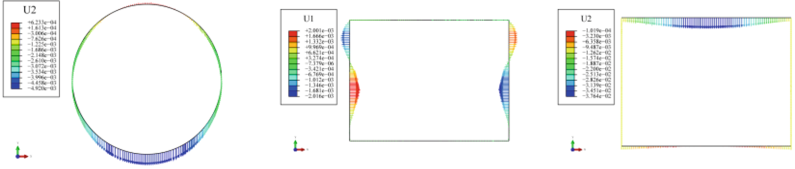

(d) Vertical displacement of the circular lining

(e) Horizontal displacement of the rectangular lining

(f) Vertical displacement of the rectangular lining

Fig. 5. Displacement vectors of three kinds of lining structures under design depth

code [12], and the further local reinforcement measures must be done to control the deformation before applied to the real projects.

The distribution of the moments and shear forces of the afore-mentioned three tunnels were shown in Fig. 6, with the location of maximum values sketched in the figures. It can be seen that the maximum positive moment of the special-shaped tunnel was 680.46 kN · m, located in the vault with an axial force of 845.26 kN which led to a theoretical crack width of the inner surface of 0.1268 mm close to the national damage standard of 0.2 mm. The maximum negative moment located in the right arch shoulder with the value of −529.06 kN · m, the axial force was 1316.0 kN, yielding a theoretical crack width of the outer surface of 0.0600 mm.

The maximum positive moment of the circular tunnel positioned at the left arch foot was 130.3 kN · m with the corresponding axial force being 1266.2 kN and a theoretical crack width of the inner surface being only 0.0040 mm; and the maximum negative moment was −244.4 kN · m with the axis force being 1180.3 kN, (corresponding to a crack width of 0.0077 mm), occurring in the left arch waist. The data showed that there was still much space for the circular tunnel to resist extra loads.

The maximum positive moment of the rectangular tunnel was located in the vault with ta value of 1142.1 kN · m, and the maximum negative moment was −1698.0 kN · m in the right arch shoulder. Both two crack widths exceeded the limit value too much, and great stress concentration was shown at the four corners.

The maximum shearing force was located at the roof close to the right arch shoulder (671.8 kN) for the special-shaped tunnel, was 401.2 kN for the circular tunnel in the right arch foot, and was 1407.0 kN for the rectangular tunnel in the roof close to the right arch shoulder. Apparently, the two arch shoulders of the rectangular tunnel must be further optimized and strengthened so as to improve the shear-bearing capacity.

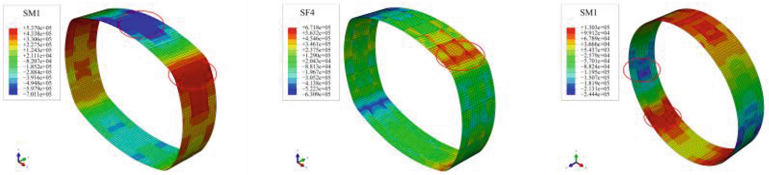

(a) Moments of the special-shaped lining (b) Shear forces of the special-shaped lining (c) Moments of the circular lining

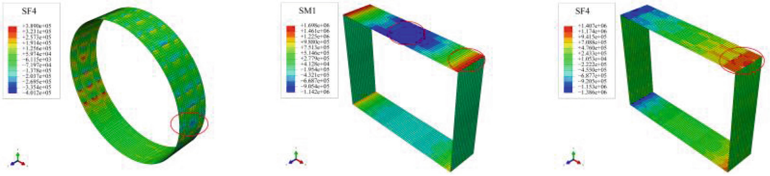

(d) Shear forces of the circular lining (e) Moments of the rectangular lining (f) Shear forces of the rectangular lining

Fig. 6. Distribution of inner forces under design depth for three kinds of tunnels

In summary, for a shallow shield-driven tunnel, the circular tunnel which showed the obvious advantages of resisting external loads, is not economical compared with the special-shaped tunnel. The rectangular tunnel was also proved to be not beneficial for force transmission and needed to be further reinforced at the shoulder corners.

6 Conclusions

A shell-spring model for the special-shaped tunnel was established. The simulation results were compared with the prototype loading tests and uniform beam model. The internal forces and deformation modes of the lining structure at the designed buried were revealed, and the shell-spring model was proved to be the optimal model to determine the 3D distribution of the internal forces and deformations. The economy and mechanical properties of the special-shaped, circular and rectangular tunnels were compared, and the advantages of the special-shaped tunnel when applied to shallow overburden ground were explained in detail.

Acknowledgement. The research was funded by State-owned Assets Supervision and Administration Commission of Shanghai, China (Grant No. 2013017).

References

1. Takano, Y.H.: Guidelines for the design of shield tunnel lining - working group no. 2, international tunnelling association. Tunn. Undergr. Space Technol. **15**(3), 303–331 (2000)
2. Do, N.A., Dias, D., Oreste, P., et al.: 2D numerical investigation of segmental tunnel lining behavior. Tunn. Undergr. Space Technol. **37**(6), 115–127 (2013)

3. Guo, R., He, C., Feng, K.: Bending stiffness of segment joint and its effects on segment internal force for underwater shield tunnel with large cross section. China Railway Sci. **34** (5), 46–53 (2013)
4. Li, X., Yan, Z., Wang, Z., et al.: Experimental and analytical study on longitudinal joint opening of concrete segmental lining. Tunn. Undergr. Space Technol. Inc. Trenchless Technol. Res. **46**(46), 52–63 (2015)
5. Nakamura, H., Kubota, T., Furukawa, M., et al.: Unified construction of running track tunnel and crossover tunnel for subway by rectangular shape double track cross-section shield machine. Tunn. Undergr. Space Technol. **18**(2), 253–262 (2003)
6. Liu, X., Dong, Z.B., Bai, Y., et al.: Investigation of the structural effect induced by stagger joints in segmental tunnel linings: first results from full-scale ring tests. Tunn. Undergr. Space Technol. **66**(1), 1–18 (2017)
7. Zhang, J.G., He, C., Yang, Z.: Analysis of 3D internal forces distribution of wide segment lining for large-section shield tunnel. Rock Soil Mech. **30**(7), 2058–2062 (2009)
8. Teachavorasinskun, S., Chub-Uppakarn, T.: Influence of segmental joints on tunnel lining. Tunn. Undergr. Space Technol. **25**(4), 490–494 (2010)
9. Arnau, O., Molins, C.: Three dimensional structural response of segmental tunnel linings. Eng. Struct. **44**(6), 210–221 (2012)
10. Do, N.A., Dias, D., Oreste, P., et al.: Three-dimensional numerical simulation for mechanized tunnelling in soft ground: the influence of the joint pattern. Acta Geotech. **9**(4), 673–694 (2013)
11. Zhu, Y.T.: Study on the mechanical behavior of special-shaped shield lining structure with a large cross-section. Doctoral dissertation, Tongji University, Shanghai (2017)
12. GB50157-2013 Code for Design of Metro. China Architecture & Building Press, Beijing (2013)

Data Analysis of Shield Tunnel Deformation from Real-Time Monitoring with Wireless Sensing Network

Xin Xie(✉), Dongming Zhang, and Hongwei Huang

Tongji University, Shanghai, China
Xiexin1989@tongji.edu.cn

Abstract. As an important part of critical infrastructure, shield tunnel is widely used in urban area of China recent years. The safety of shield tunnel during construction and operation has drawn more and more attention. In the operational period, real time deformation monitoring is an effective way to help us to reveal the long-term deformation mechanism and control the lifetime safety of shield tunnel. Tilt sensors were installed in one interval shield tunnel in Shanghai Metro 2. From Oct 2015 to Feb 2017, monitoring data of inclination and temperature about nearly 500 days were collected at 20 min per acquisition. Kalman Filter has been used to reduce impact of temperature and vibration on the inclinations. The long-term measurement was stable and reliable. It should be noted that the long term deformation of shield tunnel is asymmetrical around the tunnel perimeter and related to the different leakage positions of tunnel segment. The influence of excavation caused by nearby construction can also be recognized by the real-time monitoring. In summary, the advantage of the monitoring system is its ability of real-time dynamic monitoring which may help us understand the long-term deformation mechanism and make a dynamic safety control.

Keywords: Shield tunnel · Real-time monitoring · Kalman Filter
Tilt sensor

1 Introduction

Operated metro tunnel is influenced by sophisticated geology and surrounding construction activities. Adjacent project construction such as excavation of foundation pit and soil surcharging can have a distinct change in both the deformation and the internal force distribution of the tunnel structure [1–4]. As a result, serious consequences such as large deformation, leakage and crack of concrete may happen due to the long term tunnel deformation. The impact of construction on the operated tunnel may also be investigated by advanced monitoring technology in order to protect the tunnel and environmental system. Therefore, real time monitoring is necessary to reduce the risks related to the near construction process. Monitoring of tunnel convergences have been commonly used as a primary method of evaluation the health of tunnel [5–7]. For timely diagnosis of structural damage, real time monitoring method with sufficient deformation data obtained from field measurements are required [8, 9]. However,

© Springer Nature Singapore Pte Ltd. 2018
D. Zhang and X. Huang (Eds.): GSIC 2018, *Proceedings of GeoShanghai 2018 International Conference: Tunnelling and Underground Construction*, pp. 392–401, 2018.
https://doi.org/10.1007/978-981-13-0017-2_40

because of the interference of surrounding environment factors especially air temperature and train vibration, these monitoring data are not always quite accurate. Data fusion method such as Kalman filter would be useful to reduce the uncertainty of field observations [10, 11]. The real mechanical response of the tunnel under the external construction process can be presented. And actual deformation form of a tunnel under different kind of external load will be recognized more clearly.

The paper showed the method for real-time monitoring of horizontal convergence. Then, the impacts of temperature and train vibration have been studied and extended Kalman filter was used to alleviate these impacts. Finally, long-term variation trend of tunnel lining and the influence of construction were studied.

2 Site Information

The present case is an interval tunnel of east extension of Shanghai metro line 2, which is located in Pudong District. The alignment of the internal tunnel goes from north-eastern to southern, with a length of about 1800 m. The tunnel is surrounded by a multi-layered formation which is typical in Shanghai. The multi-layer stratum is composed of soft clays, muddy silty clay and muddy clay from top to down respectively.

The segmental lining of Shanghai Metro line 2 was excavated by an earth pressure balance (EPB) shield machine. A typical ring of the tunnel in Shanghai consists 6 concrete segments, denoted as segment F, L1, L2, B1, B2 and D as shown in Fig. 1. Adjoining segments were connected using 2 steel bolts each with a diameter of 30 mm. A rubber sealer and a rubber packer were installed in the longitudinal joint for the sake of waterproof.

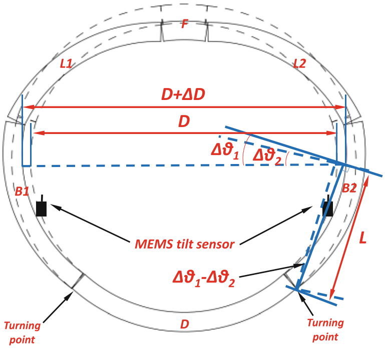

Fig. 1. Calculating model of convergence

In order to measure the convergence of the tunnel, 27 pairs of tilt sensors have been installed in the lower line with a distance of about 36 m or 60 m. Real time data such as time, temperature and tilt have been collected every 20 min from October 3rd 2015 to February 15th 2017. And nearly 35,000 sets of data have been recorded.

3 Real Time Monitoring of Metro Tunnel Convergence

3.1 Basic Information of Tilt Sensor

TJ-UWIS is a series of wireless tilt sensors developed by Tongji University. It can measure the inclination change of the segments in real time. The approximate shape of shield tunnel and layout position of tilt sensors are shown in Fig. 2. Assuming that the segments are perfectly rigid and ignoring the dislocation of the segment, horizontal convergence of the tunnel can be calculated by Eq. 1 using the inclination data of both sides.

$$\Delta D = L \cdot (\Delta\theta_1 - \Delta\theta_2) \cdot \cos\omega \tag{1}$$

where ΔD was the change of horizontal convergence. Δθ1 and Δθ2 were the changes of inclination of the standard segments. L is the distance from the turning point of the segment to inner surface at the center point level. ω is the angle between diameter at X and the horizontal line.

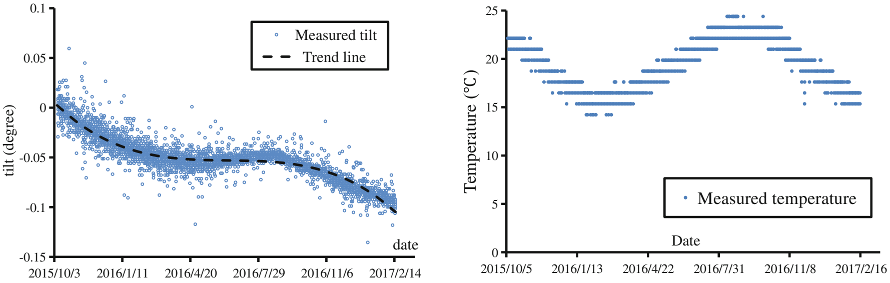

(a) Measured tilt (b) Measured temperature

Fig. 2. Measured and compensated tilt

However, bias drift of the MEMS (short for Micro Electro Mechanical System) should be taken into consideration for the sake of getting the accurate real-time monitoring data. Bias drift is a common phenomenon of electronic sensors which is usually related to time, temperature and stochastic factors [12]. Researchers categorize the bias drift into two main types: slowly changing long-term drift and rapidly changing short-term random drift [13]. Temperature is the important factor of long-term drift of MEMS and it will be discussed in the next subsection. The short-term bias is mainly caused by train induced vibration of tunnel and it will be discussed in Subsect. 3.3.

3.2 Impact of Temperature

Due to the fact that MEMS sensors are fabricated with silicon which is a high temperature-sensitive material, the measurement will be apparently influenced by environmental temperature [14]. Moreover, the impact of temperature may be even more obvious for the long-term monitoring especially for those monitoring for a time longer than 1 year.

According to the temperature measured in the tunnel as shown in Fig. 2(b), the annual temperature difference in the tunnel is about 10–20 °C. That means the temperature change will cause an annual bias drift of convergence more than 1 mm based on one of the temperature calibration functions. So temperature calibration and compensation are quite important for the accuracy of real time monitoring.

Using the temperature compensation method, the measurement of MEMS can be improved significantly [13]. The common temperature compensation method is to subtract the temperature bias which can be calibrated in the laboratory test and fitted using a polynomial. However, it can be seen from Fig. 2(b) that the temperature measurement is discrete. To some extent, it reflects the measurement errors of temperature. Therefore, this paper proposed a method based on data fusion to alleviate the uncertainty caused by temperature measurement. The detail calculation process of temperature compensation will be introduced in Sect. 4.

3.3 Impact of Temperature Change

With the development of urban railway, train-induced vibration of environments and buildings is a popular direction. Field monitoring and numerical research of train-induced vibration have been conducted by many researchers these years [15–18]. All these studies indicate that train load can induce apparently vibration of surrounding ground and buildings.

The monitoring data also can reflect the train-induced vibration to some degree. Figure 3(a) is the filed tilt monitoring data from 0:00 AM to 2:00 AM every day in a year, and Fig. 3(b) is the data from 7:00 AM to 9:00 AM. It can be seen that the data of non-operating time (Fig. 3(a)) is much more stable than that of operating time (Fig. 3(b)). The most important difference of the tunnel load condition is the train load which only exists in the operating time. Considering that the tilt sensors installed in metro line 2 measured every 20 min, train-reduced vibration may be captured by the tilt sensor and it will mislead our judgment of tunnel safety. Fortunately, this kind of short-term bias can be

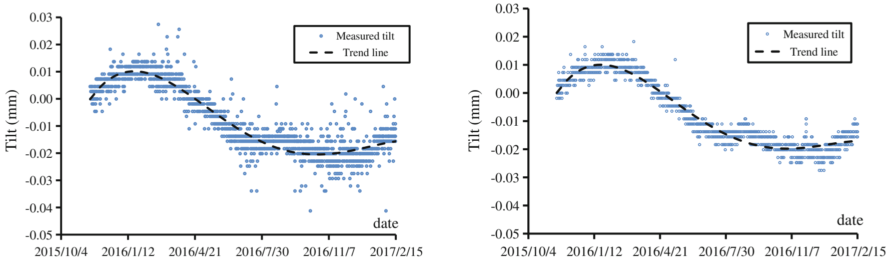

(a) (b)

Fig. 3. Measured and compensated tilt of different time of day: (a) Measured tilt from AM 7:00 to AM 9:00 everyday (b) Measured tilt from AM 0:00 to AM 2:00 everyday

alleviated by Kalman Filter [13]. In the next chapter, we'll propose a method that can alleviate the drift induced by vibration and compensate for temperature in the same time.

4 Data Estimation Using Extended Kalman Filter

4.1 Extended Kalman Filter

Kalman Filter is a mathematical method for state variable estimation using observed measurements which contain noise and other inaccuracies. By constantly predicting and updating, Kalman Filter can eliminate the interference effectively [11]. The operation of the Kalman Filter is summarized in Fig. 4.

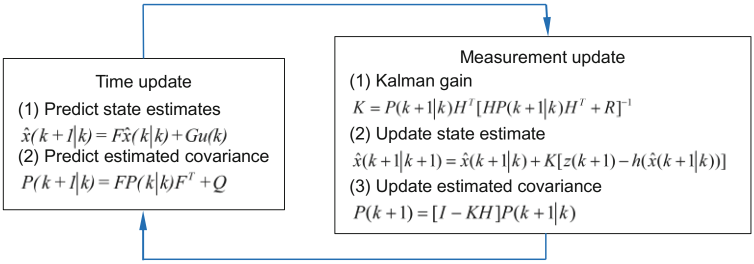
Time update
(1) Predict state estimates
$\hat{x}(k+1|k) = F\hat{x}(k|k) + Gu(k)$
(2) Predict estimated covariance
$P(k+1|k) = FP(k|k)F^T + Q$
Measurement update
(1) Kalman gain
$K = P(k+1|k)H^T[HP(k+1|k)H^T + R]^{-1}$
(2) Update state estimate
$\hat{x}(k+1|k+1) = \hat{x}(k+1|k) + K[z(k+1) - h(\hat{x}(k+1|k))]$
(3) Update estimated covariance
$P(k+1) = [I - KH]P(k+1|k)$

Fig. 4. The operation of Kalman Filter

Extended Kalman Filter (EKF) is a modified method of Kalman Filter which is proposed by Sunahara et al. in [19]. The main idea of EKF is to approximate the nonlinear system to the linear system using the Taylor series expansion method.

4.2 Data Processing Using EKF

The temperature measurement accuracy of the tilt sensors is about 1 °C, which may cause a bias of 0.1 mm. Kalman filter is an efficient way to estimate and alleviate the effect of measurement error. However, the relationship between temperature and thermal bias is not a single linear relation and it usually conforms to a polynomial function. Due to the fact that Kalman Filter method is only applicable for variable estimation of linear system, Extended Kalman filter should be used to solve the nonlinear relationship between temperature and thermal bias.

Tilt of the segment and environmental temperature were measured in the real time monitoring project. As mentioned before, the observed tilt was also influenced by the environmental temperature in the form of the temperature bias [20]. So the observed tilt (z1) was composed of three parts: real tilt of segments (x1), temperature bias (f(x2)) and observation error (v1). Temperature bias can be calibrated by laboratory test and fitted using a polynomial f(x2). The observed environmental temperature was composed of two parts: real environmental temperature (x2) and observation error (v2). The typical formula is shown as follows:

$$\begin{bmatrix} z_1(k)\\ z_2(k)\end{bmatrix} = \begin{bmatrix} h_1(x_1(k),x_2(k))\\ h_2(x_1(k),x_2(k))\end{bmatrix} + \begin{bmatrix} v_1(k)\\ v_2(k)\end{bmatrix} = \begin{bmatrix} 1 & \frac{\partial f}{\partial x_2(k-1)}\\ 0 & 1\end{bmatrix}\begin{bmatrix} x_1(k)\\ x_2(k)\end{bmatrix} + \begin{bmatrix} v_1(k)\\ v_2(k)\end{bmatrix} \tag{2}$$

4.3 Estimated Data Using EKF

Real time tilt of segment (x2) can be estimated using data fusion method above mentioned. The comparison of compensated tilt and estimated tilt using EKF of the right side sensor located in ring 490 are shown in Fig. 5(a). It can be seen that the estimated data is more stable after the process of EKF. Because this sensor was installed in the right side of tunnel, the data indicates that the segment has rotated clockwise with change rate of −0.05739 degree per year (moving away from the center axis of tunnel).

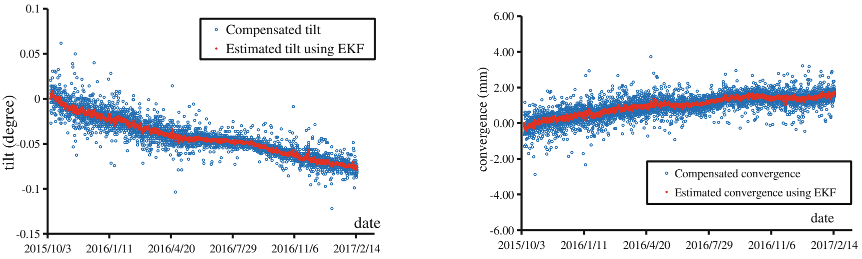

(a) Tilt (b) Convergence

Fig. 5. The comparison of compensated tilt and tilt estimated by EKF

Horizontal convergence of the tunnel section 490 can be calculated by Eq. 1. The comparison of compensated convergence and the convergence estimated by EKF is shown in Fig. 5(b). It can be seen that the horizontal diameter of the tunnel was growing steadily with velocity of 1.268 mm per year.

5 Result of Real-Time Convergence Monitoring in Metro Line 2

As mentioned before, the influence of environmental temperature and train vibration can be alleviated using the data fusion method. According to the real-time monitoring data recorded over 1 year, changes of horizontal deformation can be divided into two categories. The first kind of section whose tilts and convergences of most sections changed with a stable rate took up the majority. Only 3 sections which were affected by the nearby construction have abnormal convergence changes in the early June of 2016. We will analyze these two kinds of deformation changes in next section respectively.

Tilt data have been recorded from Oct 18th 2015 to Feb 15th 2017 about for 500 days, and were calculated into convergence. In view of the overall situation, convergences of 17 sections have stable and linear growth trend with an average growth rate of about 1 mm per year. However, some sections have different changing rate of convergence due to the effect of nearby construction process and the difference of hydrological conditions.

5.1 Normal Deformation Variation

As above mentioned, convergences of most sections (17 sections from the whole 27 sections) grew steadily. The changing rate approximately subjected to linear variation with an average growth rate of 1 mm per year.

It should be noted that the right side segments which are far from the upper line sections rotated around the lower joint clockwise. According to the monitoring data of the tilt sensor, it can be seen that the rotation of the right standard block (far from the upper line) is larger than that of left side (close to the upper line). According to the annual defect inspection of tunnel, tunnel leakage is mainly distributed in the left side. According to many researches about the effect of leakage on the tunnel deformation, joint leakage will cause the asymmetrical stress distribution on the tunnel. Integral transverse deformation of the tunnel may be influenced by this kind of stress distribution. Moreover, left side segment with an opposite displacement direction (clockwise) also existed according to the monitoring. Based on the rotation direction of the left side segment, all the normal monitoring sections can be divided into two forms.

The First Deformation Form

For the first kind of deformation mode as shown in Fig. 6(a), the left standard block (B1 block) rotates counterclockwise around the lower joint. It indicated that the outside joint opening of the left side tunnel was becoming larger and larger. Due to the fact that the standard segments of both sides moved outward, the horizontal diameter of the tunnel was growing rapidly. The average changing rate of convergence was 1.385 mm per year, which was higher than other sections. Combining with the spatial relative location, this kind of sections is mainly distributed at the bank of river and the position of transverse passageway.

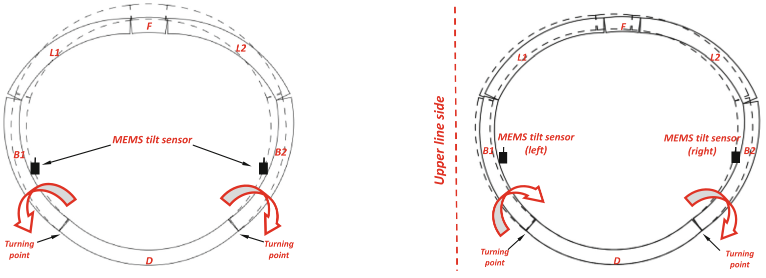

(a) (b)

Fig. 6. Two kinds of section deformation forms: (a) the first form (b) the second forms

The Second Deformation Form

For the second deformation mode, left segments rotate around the lower joint clockwise (the same rotation direction as the right segment). According to the recorded data, the rotation rate of the right segment is similar to the first mode. Because the rotation directions of left segments present a recovery of ovalization to some degree, the total convergences of the second mode are much smaller than the first kind of sections. As shown in Fig. 6(b), although the total convergence is only relatively smaller than that of the first mode, the rotation angle of the right segment reached degree. The second mode indicates that we should draw more attention on the specific changing mode not only the convergence.

5.2 The Effect of Nearby Construction Process

As shown in Fig. 7, ring 280, 311, 340 are neighboring monitoring sections. All the 3 rings proved a rapid short-term fall in convergence from June 9th to June 10th. Consulted nearby construction record, we found that soil mass about 1.5 m thickness has been unloaded in those days. Although happened suddenly and accidently, soil unloading was helpful to the long-term stability of the tunnel. As an example, the variation of convergence of ring 311 is shown in Fig. 8. It can be seen that there is a

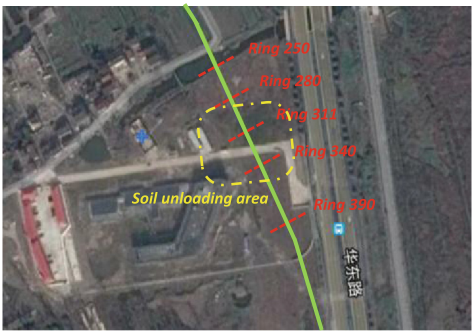

Fig. 7. Relative position of the affected area

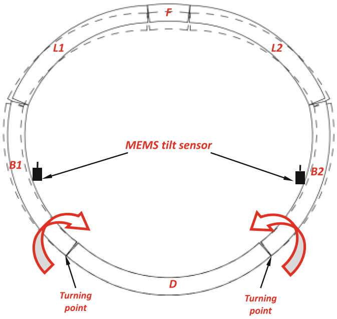

Fig. 8. Inclination of sections affected by the construction

rapid change about 1.25 mm and the inclination changes of the left standard block and right standard block are 0.01° and 0.015° respectively.

6 Conclusion

According to the real-time monitoring data using tilt sensors, several conclusions can be drawn as follows:

(1) Temperature and train vibration may cause measurement bias in the real time monitoring, and safety evaluation may be influenced by these two kinds of factors.
(2) Kalman filter is an effect way to alleviate the interference of measurement bias such as temperature and train vibration. However, extended Kalman filter should be taken into use in order to solve the nonlinear problems.
(3) According to the real time monitoring data, normal sections should be divided into two groups with different deformation modes. To some extent, tilt changes may be a more useful index than the convergence for the safety evaluation of tunnel.

Acknowledgements. This study is substantially supported by the Natural Science Foundation Committee Program (No. 51608380, 51538009), by Shanghai Rising-Star Program (17QC1400300) and by Shanghai Science and Technology Committee Project (17DZ1204205). Hereby, the authors are grateful to these programs.

References

1. Sharma, J.S., Hefny, A.M., Zhao, J., Chan, C.W.: Effect of large excavation on deformation of adjacent MRT tunnels. Tunn. Undergr. Space Technol. Inc. Trenchless Technol. Res. **16**(2), 93–98 (2001)
2. Zhang, Z., Huang, M., Wang, W.: Evaluation of deformation response for adjacent tunnels due to soil unloading in excavation engineering. Tunn. Undergr. Space Technol. **38**(3), 244–253 (2013)
3. Chang, C.T., Sun, C.W., Duann, S.W., Hwang, R.N.: Response of a Taipei Rapid Transit System (TRTS) tunnel to adjacent excavation. Tunn. Undergr. Space Technol. Inc. Trenchless Technol. Res. **16**(3), 151–158 (2001)
4. Huang, H.W., Shao, H., Zhang, D., Wang, F.: Deformational responses of operated shield tunnel to extreme surcharge: a case study. Struct. Infrastruct. Eng. **13**(3), 345–360 (2017)
5. Ye, Y.D.: Research on deformation and method of health diagnose of operational subway structures in soft soil. Tongji University (2007)
6. Wang, R.: Structural safety analysis of Shanghai rail transit tunnel. Undergr. Eng. Tunn. **4**, 37–43 (2011)
7. Ye, Y.D., Zhu, H.H., Wang, R.L.: Analysis on the current status of metro operating tunnel damage in soft ground and its causes. Chin. J. Undergr. Space Eng. **3**(1), 157–160 (2007)
8. Bennett, P.J., Kobayashi, Y., Soga, K., Wright, P.: Wireless sensor network for monitoring transport tunnels. Geotech. Eng. **163**(3), 147–156 (2010)
9. Xie, X.Y., Feng, L.: Real-time health monitoring system for power tunnel. In: GeoCongress 2012, pp. 3099–3108 (2012)

10. Jin, C., Jang, S., Sun, X., Li, J., Christenson, R.: Damage detection of a highway bridge under severe temperature changes using extended Kalman filter trained neural network. J. Civil Struct. Health Monit. **6**(3), 1–16 (2016)
11. Kalman, R.E.: A new approach to linear filtering and prediction problems. J. Basic Eng. Trans. **82**, 35–45 (1960)
12. Gulmammadov, F.: Analysis modeling and compensation of bias drift in MEMS inertial sensors. In: International Conference on Recent Advances in Space Technologies, vol. 36, no. 4, pp. 591–596 (2009)
13. Shiau, J.K.: Noise characteristics of MEMS gyro's null drift and temperature compensation. J. Appl. Sci. Eng. **15**(3), 239–246 (2012)
14. Fontanella, R., Accardo, D., Caricati, E., Cimmino, S., Simone, D.D.: An extensive analysis for the use of back propagation neural networks to perform the calibration of MEMS gyro bias thermal drift. In: Position, Location and Navigation Symposium, pp. 672–680 (2016)
15. Gupta, S., Berghe, H.V.D., Lombaert, G., Degrande, G.: Numerical modelling of vibrations from a Thalys high speed train in the Groene Hart tunnel. Soil Dyn. Earthq. Eng. **30**(3), 82–97 (2010)
16. Kwak, C.W., Park, I.J., Park, J.B.: A numerical study on the effect of train-induced vibration in shield tunnel. J. Korean Soc. Civil Eng. **6**(2), 261–267 (2014)
17. Nejati, H.R., Ahmadi, M., Hashemolhosseini, H.: Numerical analysis of ground surface vibration induced by underground train movement. Tunn. Undergr. Space Technol. Inc. Trenchless Technol. Res. **29**(5), 1–9 (2012)
18. Yang, N., Guo, T., Sun, G.Z.: Train-induced vibration on elevated railway station. J. Central South Univ. **20**(12), 3745–3753 (2013)
19. Sunahara, Y., Yamashita, K.: An approximate method of state estimation for non-linear dynamical systems with state-dependent noise. Int. J. Control **11**(6), 957–972 (1970)
20. Alves, F.S., Dias, R.A., Cabral, J., Gaspar, J., Rocha, L.A.: Thermal compensated pull-in voltage MEMS inclinometers. Procedia Eng. **87**, 831–834 (2014)

An Analytical Solution for the Failure Process of a Shield Tunnel Segmental Joint with a Load-Transferring Gasket

Ting-jin Liu[1](✉), Hong-hao Huang[2], Rao Xu[2], Xin-wei Tang[2],
and Shan-yong Wang[3]

[1] State Key Laboratory of Subtropical Building Science,
South China University of Technology, Guangzhou 510640, China
liu_tingjin@163.com
[2] School of Civil Engineering and Transportation,
South China University of Technology, Guangzhou 510640, China
[3] ARC Centre of Excellence for Geotechnical Science and Engineering,
The University of Newcastle, Callaghan, NSW 2308, Australia

Abstract. The structure of a segmental joint with a load-transferring gasket is complicated and exhibits piecewise and nonlinear deformation characteristics under loads. Joint stiffness largely depends on the properties of the concrete and load-transferring gasket, which are the main components of the joint. A reasonable consideration of their influence is one way to predict the failure process of the segmental joint. Taking the segmental joint with a load-transferring gasket in Guangzhou Metro as an example, an analytical solution for its failure process is proposed based on several basic hypotheses. The uneven stress distribution of the load-transferring gasket, the partial opening of the joint and the contact of concrete at external corner of segment are all considered. On the basis of the mechanical equilibrium conditions and the displacement compatibility, equation sets are established in each stage at first, including a total cross-section of joint under compression, joint opening, the contacting of concrete at external corners of segments and the crushing of concrete. Next, the equations are solved using Mathematica. Finally, a three-dimensional finite element simulation and three experimental results are compared with the analytical solution. The comparison demonstrates that the description and prediction of the deformation characteristics of the segmental joint failure process under heavy loads are relatively successful when using the analytical method proposed in this study.

Keywords: Shield segment · Joint · Load-transferring gasket · Failure process
Analytical solution

1 Introduction

In shield-driven tunnels, segmental lining provides both the structural capacity to resist the ground and water pressures and the necessary reaction frame to thrust the shield machine forwards [1, 2]. The nonlinear mechanical performance of the segmental joints of a shield-driven tunnel plays a key role in the deformation resistance and bearing

© Springer Nature Singapore Pte Ltd. 2018
D. Zhang and X. Huang (Eds.): GSIC 2018, *Proceedings of GeoShanghai 2018 International Conference: Tunnelling and Underground Construction*, pp. 402–421, 2018.
https://doi.org/10.1007/978-981-13-0017-2_41

capacity of a lining ring [3, 4]. Various experimental and theoretical methods have been widely used to study the mechanical behaviour of segmental joints by international scholars.

Several model tests in real-scale and reduced-scale model tests of shield tunnel segmental joints have been conducted in recent years [5–15]. However, loading tests on a segmental joint require massive inputs of both material and financial resources, and great differences exist in the mechanical behaviours of diverse types of segmental joints. Thus, it is not often feasible or achievable to conduct extensive structural tests for various types of segmental joints. Theoretical analysis, by contrast, provides another method to study the mechanical performance of segmental joint at a minimum cost.

As indicated by many previous theoretical studies, the segmental joint presents a complex nonlinear behaviour [16, 17]. This nonlinear behaviour is mainly caused by its inability to transfer tensile stress, and the stiffness decreases significantly after the joint is opened (i.e., a loss of joint contact at one side of the joint). A rotational spring with either the nonlinear [16] or bilinear [17] constitutive model was proposed to describe the relationship between the joint rotational angle and the bending moment. In particular, previous studies involving the analytical solution of a segmental joint can be divided into two types: one type in which the load-transferring gasket exists and the other type that lacks the gasket [18–23]:

(1) Segmental joint without load-transferring gasket

In previous researches on a segmental joint without load-transferring gasket, the compressive stress of concrete in the joint section was considered to have a rectangular or quadratic parabolic distribution [24]. According to the force equilibrium and deformation compatibility, the mechanical behaviour of the joint was analyzed based on the plane section assumption [18, 19]. Li *et al.* [11] and Yan *et al.* [20] considered concrete elastic-plasticity and bolt pre-tightening force and established a mathematical model by solving simultaneous systems of equations to acquire the mechanical and deformation characteristics of a joint without a load-transferring gasket.

(2) Segmental joint with a load-transferring gasket

To investigate structural behaviour of a segmental joint with a load-transferring gasket, the gasket was simplified as a spring merely under compression with either nonlinear [21, 22] or bilinear [23] stiffness. The bolt was considered a perfect elastic-plastic spring merely under tension. The plane section assumption was also made to obtain the force equilibrium between the load-transferring gasket and the bolt. Zhong *et al.* [17] developed a fitting bilinear model of segmental joint flexural stiffness by solving an equation set based on the test results of a load-transferring gasket and a sealing strip.

According to the aforementioned research studies, two issues remain to be considered:

(1) In previous studies, the load-transferring gasket was just simplified as a nonlinear spring merely under compression. As a result, uneven stress distribution of the load-transferring gasket caused by different compressive deformation in a different

location could not be considered. The partial opening of segmental joint under heavy loads also could not be analyzed.

(2) The contribution of concrete in the joint section was not considered. In previous studies, the bearing capacity of the segmental joint depended only on the load-transferring gasket and bolt performance, and the joint failure was confined to the ultimate tensile strain of the bolt. Nevertheless, the structural tests of segmental joint showed that the concrete at the external corner of segmental joint might contact or even be crushed under heavy loads [8–11]. Therefore, joint failure might be caused not only by the tensile fracture of bolts but also by the crushing of concrete at the external corner.

In this paper, an analytical solution is presented to investigate the failure process of the segmental joint with a load-transferring gasket. The influences of the uneven stress distribution of the load-transferring gasket, the partial opening of the joint and the concrete contact of joint section are considered. First, a corresponding simultaneous system of equations for each stage of joint mechanical behavior is established according to the deformation compatibility and static equilibrium. Second, the equation sets are solved through programming in Mathematica. Finally, the proposed method is validated by comparing it with a numerical simulation and three experimental tests based on the segmental joints of Shenyang Metro and Shanghai Metro.

2 Establishment of an Analytical Solution of the Segmental Joint

2.1 Basic Hypothesis

This paper takes a typical segmental joint with a load-transferring gasket of Guangzhou Metro as an example. The details of the segmental joint are shown in Fig. 1.

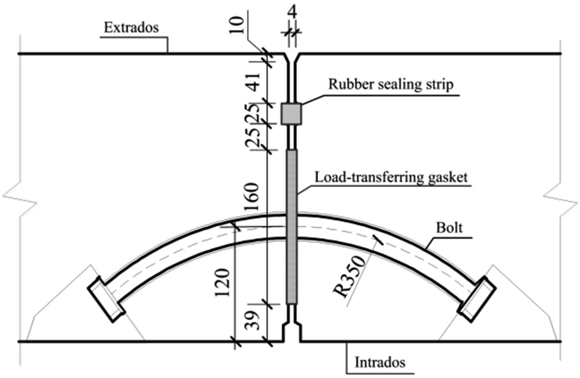

Fig. 1. Schematic diagram of the joint details with load-transferring gasket (unit: mm).

According to the structural features and principles of materials mechanics, the theoretical deduction in this paper is based on the following hypotheses [11, 17, 23]:

(1) The deformation of the segmental joint is determined by the compatible deformation among the concrete, load-transferring gasket, rubber sealing strip and bolt. The original gap between two adjacent segments is also considered.
(2) Small deformation assumption. Compared with the geometric dimension of the segment components, the rotational angle and deformation of the joint under external loads are very small.
(3) Plane section assumption. Cross-section of the segmental joint remains plane during rotation.
(4) The contact relationship between the bolt and the segment is neglected in this study because it is extremely complicated to consider the restraint of the segment on bolt deformation.
(5) Because the longitudinal dimension of tunnel is considerably larger than its transverse dimension, it is reasonable to simplify the deformation of the joint to a plane strain problem to determine the bearing capacity of the joint.

2.2 Physical and Mechanical Parameters

The segmental joint comprises the following components: concrete, load-transferring gasket, rubber sealing strip and bolt. The constitutive relations of these four components are introduced first in this section.

Concrete. To accurately reproduce the mechanical behavior of the segmental joint, the constitutive relation of concrete recommended by Chinese Code for Design of Concrete Structures [25] is adopted:

$$\sigma_c = \begin{cases} f_c\left[1 - \left(1 - \frac{\varepsilon_c}{\varepsilon_{c0}}\right)^2\right] & (\varepsilon_c \leq \varepsilon_{c0}) \\ f_c & (\varepsilon_{c0} < \varepsilon_c) \end{cases} \tag{1}$$

where σ_c is the design value of the concrete compressive strength; ε_c is the actual strain of concrete; f_c is the design value of the concrete compressive strength; and ε_{c0} is the yielding strain of concrete and is equal to 0.002, as recommended by Chinese Code for Design of Concrete Structures [25]. After the concrete reaches yielding strain, σ_c is regarded as being equal to f_c.

Load-Transferring Gasket and Rubber Sealing Strip. The laboratory test results provided by [17] are adopted as the constitutive relations of these two rubber components. For the load gasket, the stress-strain relationship is given by

$$\sigma_t = 2480\varepsilon_t^{1.67} \tag{2}$$

where ε_t is the strain of the load-transferring gasket and σ_t is the corresponding stress of the load-transferring gasket in N/mm^2. For the rubber sealing strip, the optimal fitting formula of the load with respect to deformation is given below:

$$F_D = 0.9388 s_D^2 + 2.6132 s_D \tag{3}$$

where F_D is the load applied on the rubber sealing strip in kN/m and s_D is the amount of compression of the sealing strip in mm.

Bolt. The bolts used to connect the segments are considered to be a perfect elastic-plastic material. The elastic modulus of the bolts is E_b, and the yielding stress is f_y. The total area of the bolts is A_b, and the effective length is l_b. The pre-tightening force of the bolts is T_0.

2.3 Equilibrium Equations at Various Stages

Compression and rotation of the segmental joint occur under the combined action of the axial force N, the bending moment M and the pre-tightening force of bolts T_0. As shown in Fig. 2, we denote the outer corner of the segment cross-section as the referential point (RP). The displacement of the RP is denoted as s_r (positive for relatively closer and negative for relatively further). The rotational angle of the joint is denoted as θ (positive for clockwise and negative for counterclockwise). Note that because θ is small, $\tan\theta \approx \theta$. According to the second basic hypothesis, the deformation of the joint surface at a distance of h from the RP can be represented as $s \approx s_r - h\theta$. Based on the compatibility of deformation, the equilibrium equations of the segmental joint at each working stage are established.

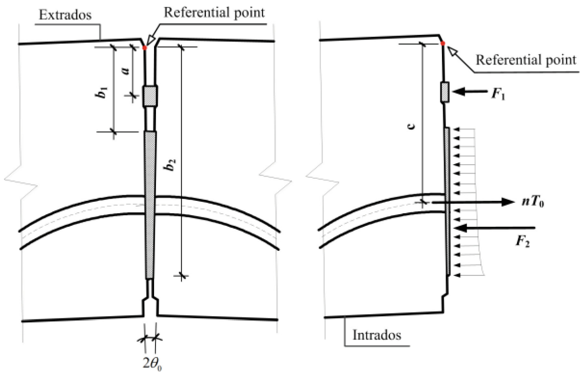

(a) Joint deformation (b) Equilibrium condition

Fig. 2. Applying the bolt pre-tightening force.

Stage I: Apply Pre-tightening Force to Bolts. In the actual assembling process of shield tunnel segments, the pre-tightening force of the bolts is applied first, and then the axial force and bending moment are exerted [11, 17]. After the pre-tightening force of bolts act on the segments and after the locking of the nuts, a certain amount of compression and rotation has already occurred in the segmental joint; moreover, an initial deformation occurs in the bolts. When the axial force and bending moment are exerted, the subsequent deformation will develop on the basis of the initial strain. Therefore, it is necessary to calculate the initial deformation of the bolts and the corresponding initial deformation of the joint surface at the positions of the bolts. After applying the bolt pre-tightening force T_0, the deformation and internal force distribution should be as shown in Fig. 2.

The force equilibrium conditions of the joint cross-section are

$$nT_0 - F_1 - F_2 = 0 \tag{4}$$

$$ncT_0 - aF_1 - bF_2 = 0 \tag{5}$$

where n is the number of bolts of the longitudinal joint, a is the distance between the action point of the rubber sealing strip force F_1 strip and the RP, b is the distance between the action point of the resultant force F_2 on the load-transferring gasket and the RP, and c is the distance between the action point of the bolt pre-tightening force T_0 and the RP.

Because the stiffness and dimensions of the rubber sealing strip are small, the action point of the resultant force is considered the geometrical centre of the sealing strip, as discussed by Xia *et al.* [23]. The integral resultant forces of the rubber sealing strip and the load-transferring gasket can be expressed as

$$F_1 = BF_{\mathrm{D}} \tag{6}$$

$$F_2 = B\int_{b_1}^{b_2} \sigma_t dh \tag{7}$$

$$b = \frac{B\int_{b_1}^{b_2} \sigma_t h dh}{F_2} \tag{8}$$

In the above equations, F_1 and F_2 are the resultant forces of the rubber sealing strip and the load-transferring gasket, respectively. In addition, b is the distance between the action point of the resultant force of the load gasket and the RP, whereas b_1 and b_2 are the distances from the upper and lower boundary of the load-transferring gasket to the RP, respectively. B refers to the width of the segment, and t refers to the thickness of the load-transferring gasket. Thus, the strain of load-transferring gasket is given by

$$\varepsilon_t = \frac{s_r - h\theta}{t}(b_1 < h < b_2) \tag{9}$$

According to Eqs. (4)–(9), the initial displacement s_{r0} and the rotational angle θ_0 of the RP after applying the pre-tightening force of bolts can be obtained. At this moment, the initial deformation Δ_0 of the joint section on the bolt's location and the bolt elongation Δ_{b0} are given by

$$\Delta_0 = s_{r0} - c\theta_0 \tag{10}$$

$$\varDelta_{b0} = \frac{T_0 l_b}{A_b E_b} \tag{11}$$

Stage II: Total Cross-section under Compression. On the basis of pre-tightening of the bolts under T_0, an axial force N is applied subsequently, and the eccentricity e increases gradually until the bending moment reaches $M = eN$. As the bending moment is small, the total segmental joint cross-section is under compression. The deformation and stress distribution of joint are shown in Fig. 3.

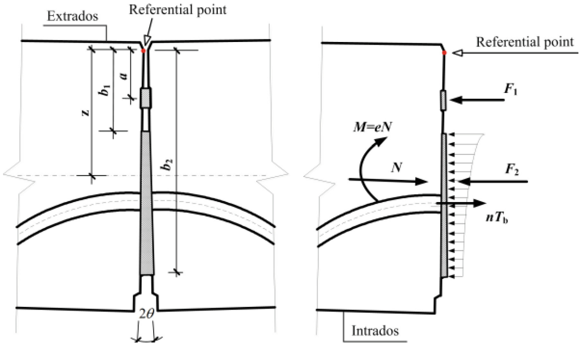

(a) Joint deformation (b) Equilibrium condition

Fig. 3. Total cross-section under compression.

The force equilibrium conditions of the joint cross-section are

$$N + nT_b - F_1 - F_2 = 0 \tag{12}$$

$$(z - e)N + ncT_b - aF_1 - bF_2 = 0 \tag{13}$$

where z is the distance between the geometric centroid of the segment section and the RP; the resultant forces of the rubber sealing strip F_1 and the load-transferring gasket F_2 and corresponding action distance b can be calculated according to Eqs. (6)–(8).

Note that the internal force of bolts T_b is

$$T_b = T_0 - \frac{2E_b A_b (s_r - c\theta - \Delta_0)}{l_b} \tag{14}$$

According to Eq. (14), the amount of compression of the joint section at the bolt's location is larger than its initial deformation when $s_r - c\theta \geq \Delta_0$. Thus, bolt elongation and force decrease or even approach zero. However, the bolt is a component that only bears tension; i.e., T_b must be always positive or zero $(T_b \geq 0)$.

In this stage, the lower boundary stress of the load-transferring gasket must satisfy $\sigma_{b2} \geq 0$ (i.e. $s_r - b_2\theta \geq 0$). Assuming that the applied bending moment is M_c for $s_r - b_2\theta = 0$, then the following must be satisfied:

$$M \leq M_c$$

where M_c is the critical bending moment at which the joint is about to expand. It can be calculated according to $s_r = b_2\theta$.

Stage III: Joint Opening. When the applied bending moment is greater than M_c, a portion of the segmental joint section starts to expand. In other words, the stresses of this portion reduce to zero. In this stage, the deformation and stress distribution of the joint section are shown in Fig. 4.

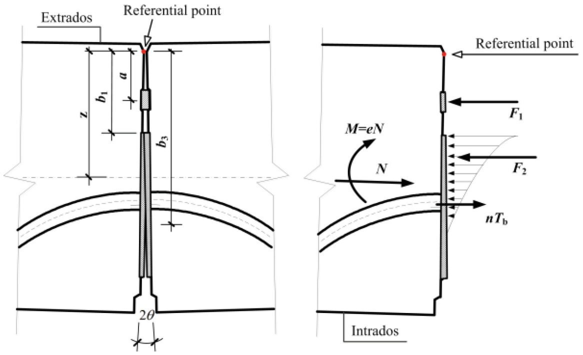

(a) Joint deformation (b) Equilibrium condition

Fig. 4. Joint opening.

According to the second and third hypotheses, the distance between the lower boundary of the load-transferring gasket and the RP, b_3 is given by

$$b_3 = \frac{s_\mathrm{r}}{\theta} \tag{15}$$

In this stage, the force equilibrium conditions of the joint cross-section are the same as Eqs. (12)–(13). Note that b_2 in Eqs. (7)–(8) must be substituted by b_3 to calculate the resultant force F_2 of the load-transferring gasket and the distance b between its action point and the RP.

With the increase of the bending moment, the opening of the joint extends gradually. As $s_r - c\theta < \Delta_0$, the amount of compression of the joint section on the bolt's location is smaller than its initial amount of compression Δ_0 after bolt pre-tightening. In other words, the bolt tension is greater than its pre-tightening force and will increase progressively. Thus, whether the bolt is yielding must be estimated at this moment. The yielding criterion is

$$\frac{T_0}{E_b A_b} - \frac{2(s_r - c\theta - \Delta_0)}{l_b} - \frac{f_y}{E_b} \geq 0 \tag{16}$$

If the above criterion is satisfied, then the internal force of the bolts T_b is equal to f_yA_b in Eqs. (12)–(13). Otherwise, T_b is calculated according to Eq. (14).

In this stage, deformation s_r of the RP must be smaller than half of the initial clearance Δ of its location. Assuming that the applied bending moment is M_t for $s_r = \Delta/2$, the following must be satisfied:

$$M \leq M_t$$

where M_t is the critical bending moment as the concrete at external corners of segmental joint are about to come into contact. It can be calculated according to $s_r = \Delta/2$.

Stage IV: Concrete Contacting at External Corners. When the applied bending moment is greater than Mt, the concrete at the external corner of the two parts of the segmental joint is in mutual contact and begins to bear pressure. The deformation and stress distribution of this stage are shown in Fig. 5.

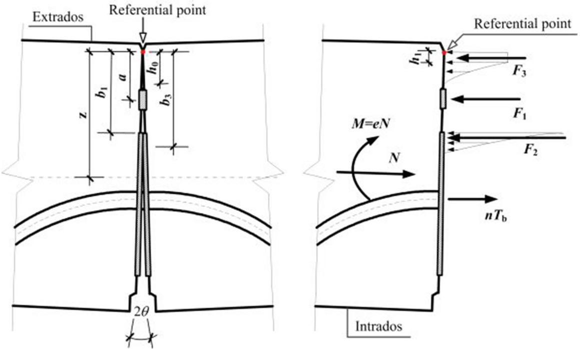

(a) Joint deformation (b) Equilibrium condition

Fig. 5. Contact of the concrete at the external corners of two segments.

The force equilibrium conditions of the joint cross-section are

$$N + nT_b - F_1 - F_2 - F_3 = 0 \tag{17}$$

$$(z - e)N + ncT_b - aF_1 - bF_2 - dF_3 = 0 \tag{18}$$

where F_3 is the resultant compressive force of the contact zone of the external edge concrete and d is the distance between the action point of F_3 and the RP. Note that the bolt tensile force T_b must be estimated, regardless of whether the bolts are yielding, using criterion (16). If the bolt is not yielding, then T_b can be calculated according to Eq. (14); otherwise, it is equal to f_yA_b.

After the concrete at the external corners come into contact, the height of the compressive zone h_0 increases gradually. According to the second and third hypotheses,

$$h_0 = \frac{s_r - \Delta/2}{\theta} \tag{19}$$

The resultant force of concrete F_3 and the distance d between its action point and the RP are

$$F_3 = B\int_0^{h_0} \sigma_c dh \tag{20}$$

$$d = \frac{B\int_0^{h_0} h\sigma_c dh}{F_3} \tag{21}$$

where the concrete stress σ_c is calculated according to Eq. (1) and the concrete strain is obtained by the ratio of the concrete compression amount to the compressive height h_0 according to the following [18, 19]:

$$\varepsilon_c = \frac{s_r - \Delta/2 - h\theta}{h_0}(0 < h < h_0) \tag{22}$$

In this stage, the stress of concrete at the external corner must satisfy $\sigma_c < f_c$. Assuming that the applied bending moment on the segmental joint is M_q for $\sigma_c = f_c$, then the following must be satisfied:

$$M \leq M_q$$

Stage V: Joint Yielding. With the increase of eccentricity, the compressive height of concrete at the joint external corner h_0 increases as well. Moreover, the concrete stress σ_c increases gradually. When the concrete stress σ_c reaches the design compressive strength f_c, the concrete of the joint section begins to yield. With the increase of the bending moment, the yielding height h_1 of the joint concrete expands inwards. In this stage, the deformation and stress distribution of the joint section are shown in Fig. 6.

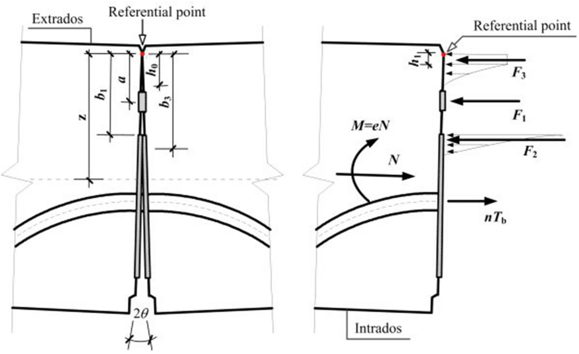

(a) Joint deformation (b) Equilibrium condition

Fig. 6. Joint yielding.

In this stage, the force equilibrium conditions of the joint cross-section remain the same as Eqs. (17)–(18). But note that F_3 is the integral sum of the concrete stress on both the yielding zone and the non-yielding zone:

$$F_3 = B\int_{h_1}^{h_0} \sigma_c dh + Bf_c h_1 \tag{23}$$

The distance d between the action point of F_3 and the RP is:

$$d = \frac{B\int_{h_1}^{h_0} h\sigma_c dh + 0.5Bf_c h_1^2}{F_3} \tag{24}$$

where the yielding height h_1 is calculated by

$$\frac{s_r - \Delta_g - h_1\theta}{h_0} = \varepsilon_{c0} \tag{25}$$

According to the tests performed by Li *et al.* [11] the segmental joint failure may be caused not only by tensile fracture of bolts but also by the contact and crushing of concrete at the external corner. Hence, the failure status of the segmental joint is achieved if one of the situations below occurs:

(1) The concrete strain ε_c at the external corner of the segmental joint exceeds its ultimate compressive strain ε_u:

$$\varepsilon_c \geq \varepsilon_u$$

(2) The resultant force F_3 on the compressive zone of the concrete exceeds the compressive bearing capacity F_c of the section concrete, which can be evaluated using the following equation recommended by Chinese Code for Design of Concrete Structures [25]:

$$F_3 \geq F_c = 1.35\beta_c f_c A_c$$

where β_c is the impact coefficient of the concrete strength (1.0 for concrete strength below C50, 0.8 for concrete strength over C80, and varies linearly between C50 and C80) and A_c is the area of the compressive zone equal to Bh_0.

(3) The bolt strain ε_b exceeds its ultimate tensile strain ε_{bu}:

$$\varepsilon_b = \frac{T_0}{E_b A_b} - \frac{s_r - c\theta - \Delta_0}{l_b} \geq \varepsilon_{bu}$$

2.4 Implementation Procedure of Analytical Solution

To implement the above stages, multiple simultaneous equations must be solved, and explicit solutions that reflect the deformation and mechanical behavior of segmental joint in each stage cannot be obtained directly. Therefore, the solving process in this paper is performed according to the following steps:

(1) Apply a pre-tightening force T_0 of the bolts. Next, calculate the initial deformation $\varDelta_0$ of the joint section on the bolt's location;
(2) Based on a fixed axial force N, assume an eccentricity e. Calculate the compressive amount s_r and the rotational angle θ of the RP, considering the total joint cross-section under compression. Increase the eccentricity e gradually, and then estimate whether the segmental joint is about to open using the corresponding criterion;
(3) Continue to increase eccentricity e. In sequence, the segmental joint enters the fourth stage (concrete at external corner contacting) and the fifth stage (joint yielding). As a result, the relationship between eccentricity e and the deformation/stress of joint can be obtained;
(4) Change axial force N, repeat steps (2) and (3) to analyse the influence of the axial force on the mechanical behavior of the segmental joint;
(5) Change the bolt pre-tightening force T_0, repeat steps (2) and (3) to analyse the influence of the bolt pre-tightening force on the mechanical behavior of the segmental joint.

The solving procedure is implemented in Mathematica to obtain the segmental joint failure process with load-transferring gasket of shield-driven tunnel.

3 Validation of the Analytical Solution

The proposed analytical solution in this paper aims to predict the deformation process until failure for a segmental joint with a load-transferring gasket. But there are few direct experimental investigations focusing on the bearing capacity of the joint involving a gasket, except for the full-scale test conducted by Zhou *et al.* [8, 9], to the authors' knowledge. In addition to the available test, a three-dimensional detailed finite element model is also established in ABAQUS (see Fig. 7), to check the feasibility and validity of the analytical method. The constitutive relations and geometric parameters are identical to those in the analytical solution (see Sects. 2.2. and 3.1.). The detailed configurations including bolt, load-transferring gasket, rubbery sealing strip, and hand-hole, and their contact relations are all considered. The numerical model comprises 482234 C3D10M elements.

Furthermore, two individual segmental joint structural tests without gasket conducted by Liu *et al.* [10] and Li *et al.* [11] respectively are referred as well. However, the measurement programs and specimen details in these three experiments are different, and the acquired data are limited. Hence, the comparisons are carried out separately for each experiment in the following.

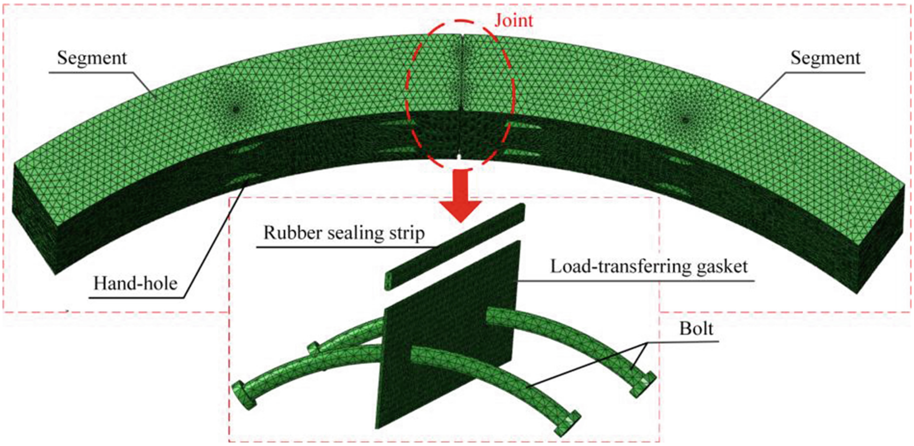

Fig. 7. Three-dimensional finite element model of the segmental joint in Shenyang Metro.

3.1 Overview of the Segmental Joint

Two types of representative segmental joints are selected:

(1) 300-mm-thick segmental joint with a load-transferring gasket of Shenyang Metro [8, 9], which is identical to that of Guangzhou Metro;
(2) 350-mm-thick segmental joint without load-transferring gasket of Shanghai Metro [10, 11].

The detailed configuration parameters of two types of joints are listed below:

Shenyang Metro Segmental Joint with a Load-Transferring Gasket.
(1) Segment and longitudinal joint: $B = 1200$ mm, h = 300 mm, $a = 54$ mm, $b_1 = 79$ mm, $b_2 = 261$ mm, $c = 172$ mm, $t = 4$ mm (thickness of the load-transferring gasket), $\Delta = 4$ mm (original gap between two segments), $z = 142$ mm;
(2) Concrete: Type C50, $f_c = 23.1$ MPa;
(3) Bolt: $E_b = 210$ GPa, $f_y = 640$ MPa, $l_b = 445$ mm, $A_b = 452.4$ mm^2, $T_0 = 20$ kN.

Shanghai Metro Segmental Joint without Load-Transferring Gasket.
(1) Segment and longitudinal joint: $B = 1200$ mm, h = 350 mm, $a = 56.5$ mm, $b_1 = 92$ mm, $b_2 = 286$ mm, $c = 224$ mm, $\Delta = 4$ mm, $z = 169$ mm;
(2) Concrete: Type C55, $f_c = 25.3$ MPa;
(3) Bolt: $E_b = 200$ GPa, $f_y = 400$ MPa, $l_b = 485$ mm, $A_b = 706.9$ mm^2, $T_0 = 108$ kN.

3.2 Results and Discussions

Shenyang Metro Segmental Joint with a Load-Transferring Gasket. Due to the deficiency of test data, only the intrados opening versus axial force for joint with a load-transferring gasket is compared here, as shown in Fig. 8. The initial bolt pre-tightening force is 20 kN. According to the experimental loading scheme, the eccentricity is fixed to 150 mm and the axial force increases gradually. The analytical and experimental curves exhibit similar development process. After the extrados concrete contact, the growth rate of joint opening slows down significantly. And the extrados concrete crushing indicates that the joint reaches its ultimate failure in both analytical and experimental results. Note that under the heavy loads, the analytically attained joint opening and bearing capacity are underestimated, which are 27.9% and 11.0% lower than the experimental results at the most. This difference may be due to the disappreciation of the C50 concrete strength used in the experimental segment specimen, which can be higher than its design value 23.1 MPa recommended by Chinese Code [25]. Therefore, the experimentally obtained ultimate joint opening and bearing capacity when the extrados concrete crushes are relatively larger.

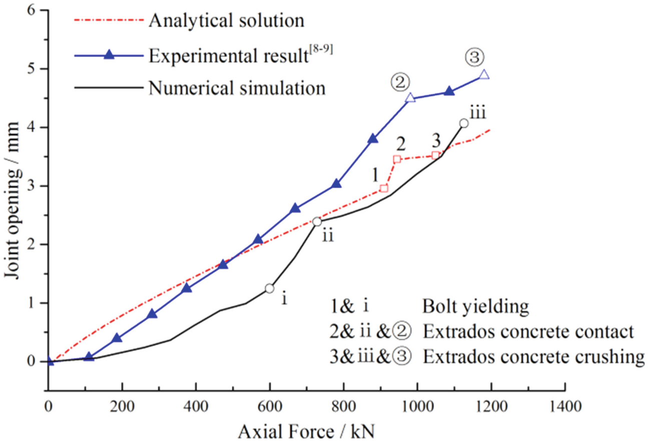

Fig. 8. Comparison of the joint opening between the analytical and numerical solutions and the laboratory test [8, 9] with a load-transferring gasket.

As for the comparison between the analytical solution and numerical simulation, three distinct inflection points (marked by hollow points in Fig. 8) are both observed: (1) bolt yielding; (2) extrados concrete contact; and (3) extrados concrete crushing. If these two curves are observed section by section, then the joint opening calculated by the analytical method is relatively larger than the numerical modeling for the axial force of 0–700 kN. This difference is mainly attributed to the following: round-off error of the analytical method, element contact and penetration of the numerical simulation. In addition, because the interaction between the bolt and the segment concrete cannot be considered temporarily in current theoretical analysis of this study, the constraint on the bolt from the segment concrete is neglected; thus, the analytical joint opening is relatively larger. With the gradual increase of the applied axial force (corresponded to sagging moment), the simulated joint opening increases rapidly, and the influence of the aforementioned factors decreases. The ultimate joint opening and bearing capacity for the analytical solution and the numerical simulation are very close.

Shanghai Metro Segmental Joint without Load-Transferring Gasket. A typical comparison of the proposed analytical solutions and test observations without a load-transferring gasket in reported literature [10] is presented as follows, in terms of the joint rotation angle and bolt strain versus sagging moment (i.e., positive bending moment). Figure 9 gives the joint rotation angle development, which indicates that two curves are generally consistent. Both the analytical and experimental results can be divided into four stages by three distinct places (marked in hollow points in Fig. 9). In the early stage before bolt yielding, the integral rigidity of segmental joint for experimental curve is about 10,388 kN·m/rad. By contrast, the analytical curve shows an initial angular rigidity of 9,895 kN·m/rad, which is slightly smaller. This is due to the existence of soft load-transferring gasket in analytical case, which presents a better deformation capacity under the same bending moment comparing with the direct concrete contact in experimental case. The sagging moment and joint rotation angle obtained analytically when the bolt yielded are 143.5 kN·m and 10.2×10^{-3} rad, which are 8.9% and 8.1% respectively lower than the experimental value of 157.5 kN·m and 11.1×10^{-3} rad. The other data comparisons are listed in Table 1.

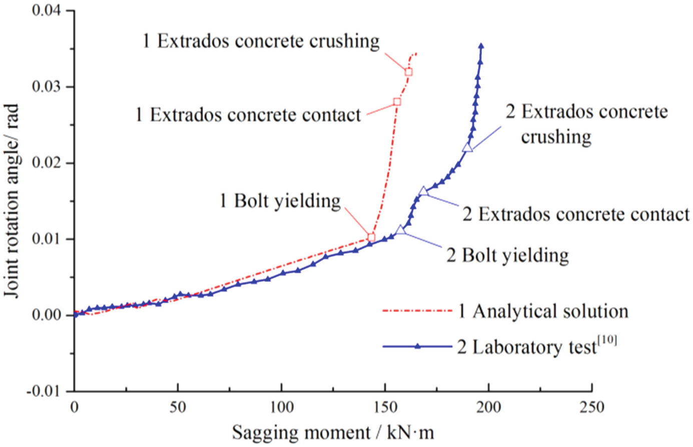

Fig. 9. Comparison of the joint rotation angle between the analytical solution and the experimental test [10] without load-transferring gasket.

It can be seen that the analytical and experimental results differ in the subsequent angle expansion rate after bolt yielding. Since the friction constraint between bolt and hole-wall concrete of segment is neglected, the subsequent joint angular rigidity is 986 kN·m/rad for analytical solution, which is lower than 1,255 kN·m/rad of experimental

Table 1. Comparison of the analytical and test [10] results without load-transferring gasket.

	Bolt yielding		Extrados concrete contact		Extrados concrete crushing	
	Sagging moment/ kN·m	Relative error/ %	Sagging moment/ kN·m	Relative error/ %	Sagging moment/ kN·m	Relative error/ %
Analytical solution	143.5	−8.9	156.0	−7.5	161.7	−15.5
Experimental result	157.5	–	168.6	–	191.4	–

result. As for the ultimate stage, the extrados concrete crushing occurred much earlier for analytical result and a severer joint opening is attained.

Figure 10 gives the comparison between single bolt strain curves of analytical and experimental results. During the stage where sagging moment varies from 0 to 143.5 kN·m, the bolt strain develops almost linearly until its elastic limit 2,000 με for analytical solution, with a larger growth rate than test observations. Thereafter, the bolt tensile strain begins to increase dramatically. The experimentally obtained bolt yielding strain is 1,489 με, little smaller than theoretical value. The analytical obtained bolt strain is basically larger than experimental results under the same load, which indicates that the existence of load-transferring gasket or thicker gasket can lead to more sufficient bolt's contribution to resist bending moment, as stated in previous study by Zhang *et al.* [26, 27].

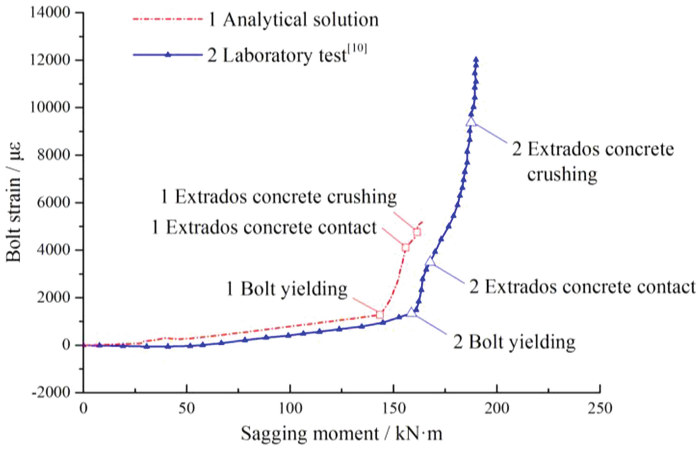

Fig. 10. Comparison of the bolt strain between the analytical solution and the experimental test [10] without load-transferring gasket.

Regarding the comparison between the analytical solution and another structural test carried out by Li *et al.* [11] in term of joint opening, as shown in Fig. 11, good agreement is achieved for the entire process as well. The analytically obtained joint opening curve has an obvious four stages similar to the experimental observations by four critical situations: intrados separating, bolt yielding, extrados concrete contact and crushing.

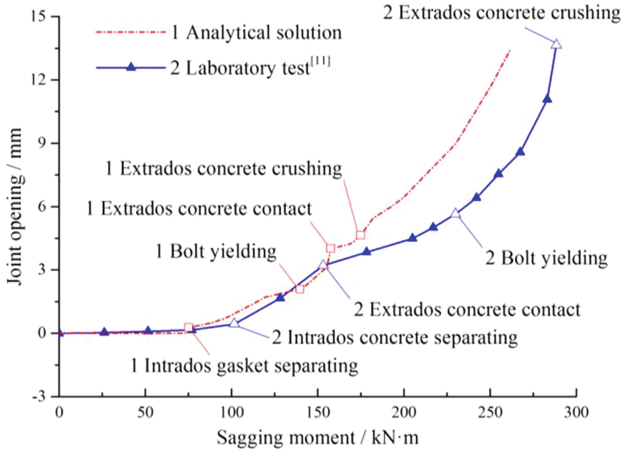

Fig. 11. Comparison of the joint opening between the analytical solution and the experimental test [11] without load-transferring gasket.

It's worth noting that, the integral rigidity of joint for analytical solution with soft load-transferring gasket is relatively smaller, especially at the initial stage under light loads. Besides, the existence of gasket also causes that the predicted joint opening develops more gently than test observed results before extrados concrete contact. In general, the sagging moments corresponding to four critical states for analytical solution are all smaller than test results provided by Li *et al.* [11], which are consistent to the comparison with the experiment carried out by Liu *et al.* [10].

3.3 Limitation and Applicability of the Proposed Analytical Solution

The above-described results demonstrated that the analytical method developed in this paper can well simulate the particular phenomena of a loaded segmental joint, including the separation of two adjacent segments, the tensile fracture of the bolts and the crushing of the concrete at the external corner. Moreover, the deformation and mechanical performance of the joint under heavy loads are well reproduced. But, the following limitations should be paid attention to during the application of this analytical method:

(1) As one of the initial conditions, the pre-tightening force must be determined at first for the proposed analytical solution. However, the pre-tightening force could not be guaranteed because the skill levels and emphasises of different technical workers vary greatly. The bolts were tightened manually during segments

assembling in general. This discrepancy may lead to the inevitable error between the predicted deformation and actual performance of joint.

(2) Note that the segmental joint structural test with gasket taken by Zhou *et al.* [8, 9] used two curved bolts as the connecting components, according to the conventional practice in Shenyang Metro which is identical to that in Guangzhou Metro. In contrast, the other two joint tests without gasket by Liu *et al.* [10] and Li *et al.* [11] used two straight pass-through bolts for connection, based on the design scheme of Shanghai Metro. As pointed by Zhang *et al.* [12] and Zhu *et al.* [13] in their studies, the bearing mechanism and deformation pattern of segmental joint without gasket are similar for curved bolt case and straight bolt case. This is consistent with the exhibited analytical solution which considering the gasket effect, because one of its basic assumptions is that bolt axial force must be perpendicular to the joint section. Whereas, the proposed analytical solution is not suitable for the skew bolt case since the perpendicular assumption is no longer tenable.

(3) The failure process of joint between the wedged segment and adjacent segment could not be well analytically predicted, since the bolt force is not perpendicular to the joint section as well and the stress state is much more complicated.

4 Conclusions

Based on the segmental joint with a load-transferring gasket of Guangzhou Metro Line No. 1, an analytical solution for the joint failure process is proposed in this paper. The influences of the uneven stress distribution of the load-transferring gasket, the partial opening of the joint section and the concrete contact on joint mechanical performance are considered. The particular phenomena of loaded segmental joint including separation of two adjacent segments, tensile fracture of bolts and crushing of concrete at external corners are reasonably described. The opening, rotation angle, bolt strain of the segmental joint are theoretically solved by an analytical method and then compared with the results of a numerical simulation and three laboratory tests. The analytical solution fits well with the experimental observations and the numerical simulation. However, the analytically obtained ultimate bearing capacity of joint may be underestimated. And the bolt pre-tightening force and concrete compressive strength should be carefully determined.

The newly developed analytical solution provides another method to predict the deformation pattern and mechanical behavior of a segmental joint under heavy loads. Note that this study is based on the longitudinal joints that are adopted in Shenyang Metro and Shanghai Metro. For shield tunnels with different dimensions and other types of segmental joints with different detailed configurations, this analytical method may be used after minor modifications, such as skew bolt case. Future studies will focus on the influence and sensitivity of the axial force, the bolt pre-tightening force and the material strength. In addition, the interaction between the bolt and segment must be reproduced more accurately.

Acknowledgements. The authors would like to acknowledge the support from National Natural Science Foundation of China (Grant No. 51678248), and the Independent Research Program of State Key Laboratory of Subtropical Building Science (2016KB16 and 2017KB15), South China University of Technology.

References

1. Koyama, Y.: Present status and technology of shield tunneling method in Japan. Tunn. Undergr. Space Technol. **18**(2), 145–159 (2003)
2. Arnau, O., Molins, C.: Three dimensional structural response of segmental tunnel linings. Eng. Struct. **44**(11), 210–221 (2012)
3. He, C., Zhou, J.M., Feng, K.: An iterative algorithm based on segment joint stiffness nonlinearity and application for shield tunnel structures. China Civ. Eng. J. **45**(3), 166–173 (2012)
4. Tang, Z.C., He, C., Lin, G.: Study on mechanical behavior of segment of shield tunnel of metro with model test. China J. Geotech. Eng. **17**(1), 85–89 (2005)
5. Lu, L., Lu, X., Fan, P.: Full-ring experimental study of the lining structure of Shanghai Changjiang tunnel. In: Proceedings of the 4th International Conference on Earthquake Engineering, Taipei, vol. 56, pp. 1–8 (2006)
6. Teachavorasinskun, S., Chub-Uppakarn, T.: Influence of segmental joints on tunnel lining. Tunn. Undergr. Space Technol. **25**(4), 490–494 (2010)
7. Li, X.X., Yang, Z.H., Cao, W.H.: Experimental investigations on stiffness of segment joints of larger tunnel prefabricated lining. China Civ. Eng. J. **48**(s2), 315–320 (2015)
8. Zhou, H.Y., Chen, T.G., Li, L.X.: Study on joint load test of metro shield tunnelling lining. Ind. Constr. **40**(4), 79–83 (2010)
9. Zhou, H.Y., Chen, T.G., Li, L.X.: Study on joint bending stiffness and influencing factors of metro shield tunnelling lining. Ind. Constr. **40**(7), 59–61 (2010)
10. Liu, X., Zhang, C., Zhang, C., et al.: Ultimate load-carrying capacity of the longitudinal joints in segmental tunnel linings. Struct. Concr. **18**(3), 693–709 (2017)
11. Li, X.J., Yan, Z.G., Zhen, W., et al.: Experimental and analytical study on longitudinal joint opening of concrete segmental lining. Tunn. Undergr. Space Technol. **46**(1), 52–63 (2015)
12. Zhang, H.M., Fu, D.M., Guo, C.: Study on load test of segment joint in shield driven tunnel. Mod. Tunn. Technol. **39**(6), 28–33 (2002)
13. Zhu, Y.H., Liu, X., Zhang, C.G., et al.: Contrast test research on longitudinal joint with different forms of bolts in metro shield tunnel. J. Railw. Sci. Eng. **12**(6), 1427–1435 (2015)
14. Salemi, A., Sereshki, F., Esmaeili, M.: Investigating the mechanical performance of contact point in bolted segments by laboratory tests. Eur. J. Environ. Civ. Eng. **21**(2), 148–171 (2017)
15. Sun, J.: Analysis of internal force and deformation of lining affected by structure stiffness discontinuity of shield tunnel. Chin. J. Undergr. Space Eng. **12**(1), 55–60 (2016)
16. Blom, C.B.M.: Design Philosophy of Concrete Linings for Tunnels in Soft Soils. Dissertation, Technical University of Delft, Netherland (2002)
17. Zhong, X.C., Zhu, W., Huang, Z.R., et al.: Effect of joint structure on joint stiffness for shield tunnel lining. Tunn. Undergr. Space Technol. **21**(3), 406–413 (2006)
18. Chen, B.G., Guo, X.H., Chen, W.Z.: Analytical study of the flexural behaviors of non-gasket segment joints in shield tunnels. Mod. Tunn. Technol. **52**(4), 128–135 (2015)
19. Dong, X.P., Xie, F.: Analytical solution of segment joint model for segmented tunnel lining. China J. Geotech. Eng. **35**(10), 1870–1875 (2013)

20. Yan, Z.G., Ding, W.Q., Shen, B.W., et al.: Structural model for radial joints of water-conveyance shield tunnels. China J. Geotech. Eng. **33**(8), 1185–1191 (2011)
21. Jiang, H.S., Hou, X.Y.: Theoretical study of rotating stiffness of joint in shield tunnel segments. Chin. J. Rock Mech. Eng. **23**(9), 1574–1577 (2004)
22. Zhang, H.M., Guo, C., Fu, D.M.: A study on the stiffness model of circular tunnel prefabricated lining. China J. Geotech. Eng. **22**(3), 309–313 (2000)
23. Xia, C.C., Zeng, G.H., Bian, Y.W.: Method for determining bending stiffness of shield tunnel segment rings longitudinal joint based on fix-point iteration. Chin. J. Rock Mech. Eng. **33**(5), 901–912 (2014)
24. Huang, Z.H.: Study on loading model of joint at longitudinal seam of lining segments in shield tunnel. Chin. J. Undergr. Space Eng. **23**(3), 296–305 (2003)
25. GB50010 Code for Design of Concrete Structures. China Architecture and Building Press, Beijing (2010)
26. Zhang, J.G., He, C.: Analysis on mechanical properties of segment joints with different pressure pads. J. China Railw. Soc. **35**(12), 101–105 (2013)
27. Zhang, J.G., He, C.: Mechanical calculation method of segmental joints: improved strip method. J. China Railw. Soc. **35**(3), 102–107 (2013)

Dynamic Response of Tunnel Lining to Resonance Rubblization Induced Vibration in Pavement Renewal

Mao-Zhu Peng, Dong-Mei Zhang(✉), Yong Zhao, Xiao-Lei Zhang, and Zhong-Kai Huang

Tongji University, Shanghai, China
{1530794,dmzhang}@tongji.edu.cn

Abstract. The resonance rubblization technology can be adopted to reconstruct old concrete pavement and eradicate reflection cracking. This method fractures pavement into fragments quickly and directly casts asphalt on fractures, shortening time cost of reconstruction. Previous studies about this technology mainly concentrated on asphalt-casting methods, and the quality, stiffness, and flatness of reconstructed pavement. Few studies concerned about the resonance rubblization-induced tunnel response. Based on a rock tunnel in China, 3D numerical simulation and field tests were conducted. Acceleration-time history curves of tunnel lining was monitored during field tests, and it was used to validate the numerical model. Then the resonance rubblization caused additional internal stress of tunnel was investigated using the validated numerical model. Results show that the peak additional Mises stress in inverted arch and tunnel lining is about 2 MPa and 1.5 MPa respectively, and it reduces significantly along transverse, longitudinal and vertical directions on tunnel. The effects of isolation trenches were also discussed, and outcomes show that isolation trenches can help reduce the peak additional Mises stress in inverted arch and tunnel lining by 31.7% and 16.0% respectively, demonstrating the effects of isolation trenches.

Keywords: Tunnel · Resonance rubblization · Field test · Reflection cracking

1 Introduction

The amount of tunnels has been increasing in China in past decades, and reflection cracking is a common disease of tunnel pavement [1–4]. However, the traditional treatment needs to reconstruct concrete base of pavement. Considering the base reconstruction-induced expense and traffic delay, resonance rubblization is a more preferred choice in eradicating reflection cracking. This method fractures concrete pavement into fragments while keeping roadbed sound, and directly casts asphalt on fragments [5]. Therefore, reconstruction time is saved.

Resonance rubblization method was firstly brought up in 1986 in America, the transportation research board of America (2006) had thoroughly described the procedures of resonance rubblization method [5]. Timm and Warren studied 9 typical resonance rubblized sections, and evaluated the performance of resonance rubblized pavement [6]. Boyer and Jones discussed the feasibility when use this method in thick

© Springer Nature Singapore Pte Ltd. 2018
D. Zhang and X. Huang (Eds.): GSIC 2018, *Proceedings of GeoShanghai 2018 International Conference: Tunnelling and Underground Construction*, pp. 422–431, 2018.
https://doi.org/10.1007/978-981-13-0017-2_42

concrete pavement, and the subsequent in-service performance of the pavement [7]. Xu et al. had conducted a series of studies on particle size, grading and Young's Modulus of the rubblized pavement [8]. Shi presented an analytical method to calculate the natural vibration frequency of concrete slab [9]. Gui and Zeng discussed influential factors during resonance rubblization construction, and the quality requirements of resonance rubblized pavement [10]. However, previous studies mostly concentrated on single roads, little concerned about using this method in tunnel pavement. To ensure tunnel safety when use this method inside tunnels, it is necessary to study the resonance rubblization-induced tunnel response.

2 Background

A mountain tunnel in China was taken as a typical case for analysis in this paper. Figure 1 shows geological conditions and surrounding rocks' parameters of this tunnel, and Fig. 2 depicts the shape of its cross-section. Parameters of tunnel materials is presented in Table 1. Because there is no underground water existing nearby, underground water was not considered in numerical simulation.

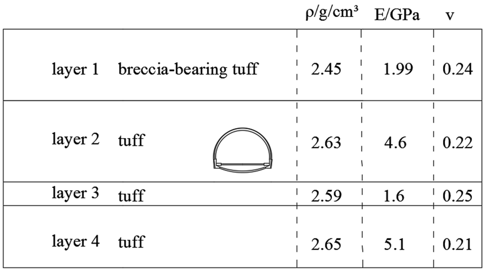

Fig. 1. Rock layers and their parameters

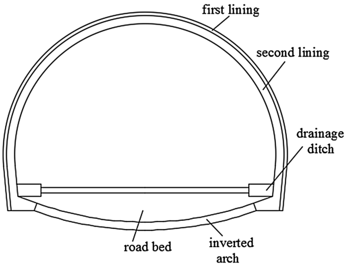

Fig. 2. Cross-section of tunnel

Table 1. Materials of tunnel lining and road

	Concrete type	Unit wight (kN/m^3)	Young's Modulus (Gpa)	Poisson's Ratio
First lining	C20	25	4.1	0.23
Second lining	C25		1.99	0.24
Inverted arch	C25		1.99	0.24
Pavement	C40		4.6	0.22
Road bed	C15		1.51	0.26

3 Field Tests

Field tests were carried out to investigate resonance rubblization-induced tunnel response. During field tests, three sensors (OP1-OP3) were fixed on lining to monitor acceleration-time history curves of lining (see Fig. 3). The breaker of resonance

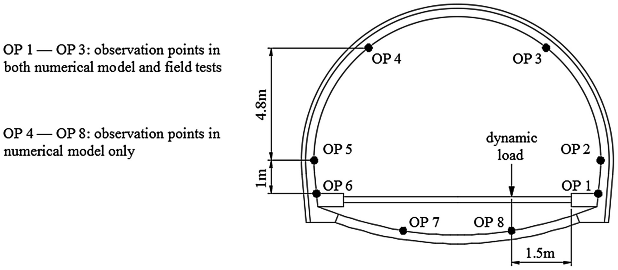
OP 1 — OP 3: observation points in both numerical model and field tests
OP 4 — OP 8: observation points in numerical model only
4.8m
1m
OP 4
OP 3
OP 5
OP 2
OP 6
OP 1
dynamic load
OP 7
OP 8
1.5m

Fig. 3. Distribution of observation points

rubblization machine was located 1.5 m away from the right drainage ditch (see the location of ***dynamic load*** in Fig. 3).

The measured acceleration-time history curves are presented in Fig. 6. It can be noted that the average acceleration of lining reduced significantly from OP1 to OP3, indicating acceleration has a continuous reduction along tunnel lining.

4 Simulation Method

Elastic or Elastic-plastic constitutive models are generally used for rock simulation [11–13]. As can be seen in the following sections, the rubblization-induced additional stress kept low in surrounding rocks, this means rocks are unlikely to yield during the resonance rubblization construction course. Therefore, elastic constitutive model was also adopted for tunnel lining and road to save computing costs.

The effects of resonance rubblization machine on tunnel can be divided into 2 parts: (1) static effect that was caused by self-weight of machine, this effect was simulated by four surface loads at the contact areas of tires and road; and (2) dynamic effect that was caused by breaker. This effect was simplified as a sine-wave dynamic point load, because the breaker hit pavement with a fixed frequency. However, the amplitude of this dynamic load was not necessarily constant during the whole construction process. Considering road surface's amplitude is one of the controlling items in resonance rubblization construction, the dynamic effect of breaker was simulated by a sine-wave surface displacement with constant amplitude in the contact area of road and breaker, instead of a sine-wave surface dynamic load whose amplitude keeps constant.

5 Model Establishments and Parameters

Figure 4 gives an overview of the numerical model (the mesh size has been magnified for clearness). The whole model is made up of 3 parts: rocks (with 4 rock layers), tunnel lining (with first lining, second lining and inverted arch) and road (with pavement, road bed and drainage ditches in both side).

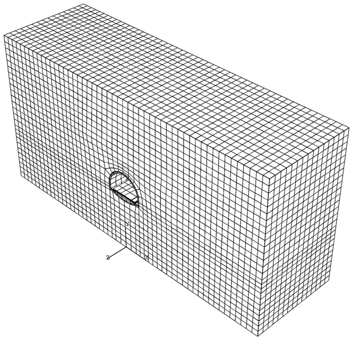

Fig. 4. Overview of numerical model

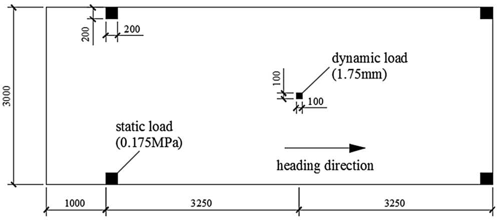

Fig. 5. Layout of resonance rubblization machine

5.1 Parameters of Numerical Model

Size of resonance rubblization machine is approximately 7.5 m × 3 m (see Fig. 5), and its weight is 27.2–31.8t [15]. The machine has one breaker in the middle and 1 tire in each corner. Hitting frequency of breaker usually lies between 45–55 Hz [14–16]. In this paper, weight of resonance rubblization machine was set to be 28t, and 50 Hz was adopted for hitting frequency. The contact area between breaker and road was simplified as a square whose length is 0.1 m, and that of tires and road was also simplified as a square with the length of 0.2 m [16].

Surface load (0.175 MPa) at each contact area between tires and road can be calculated easily according to self-weight of the machine. As to dynamic load of resonance rubblization machine, a series of calculation trials with different surface displacement amplitude were made. By choosing the one whose acceleration of tunnel lining is most close to that of the field tests, the most suitable surface displacement amplitude can be determined, and it turned out to be 1.75 mm.

5.2 Model Size

Former experience suggests that when establish a dynamic FEM model, the distance from model boundary to vibration source should not less than the wave length λ. And mesh size can adopt $1/12\,\lambda - 1/8\,\lambda$ for elements within the range of $1/2\,\lambda$ to vibration source, and $1/2\,\lambda$ for elements outside the range of $1/2\,\lambda$ to vibration source. This experience can be validated by a rule in seismic code of Shanghai that stipulates the model size should be larger than 6d (where d is the diameter of tunnel) in seismic numerical model [17].

Hitting frequency (f) was set to be 50 Hz as described above, and according to field tests, the shear wave velocity (v) of surrounding rocks is about 1400–2310 m/s. Thus the shear wave length can be calculated by Eq. (1). Therefore, the model size was set to be 100 m in x position, 50 m in y position and 30 m in z position respectively. The mesh size is 1 m, 0.5 m and 0.3 m in rocks, tunnel and road respectively. 3D stress elements were used for all components of this model.

$$\lambda = v/f = 20 - 51m \tag{1}$$

5.3 Calculation Steps

Stress distribution is an important indicator of tunnel safety. Whereas the total internal stress of tunnel is influenced by many external factors like geological conditions, which are various and irregular in each case. To get a generalized rule of resonance rubblization-induced tunnel response, additional stress instead of total stress was used in this paper. And the step to calculate initial internal force of tunnel was accordingly omitted in numerical simulation.

6 Transmitting Rules of Rubblization-Induced Acceleration

Figure 6 shows the acceleration-time history curves of numerical modelling and field tests, form it we know that the numerical computed acceleration is more stable than that of field tests (because vehicles, inhomogeneous of tunnel materials, and instability of

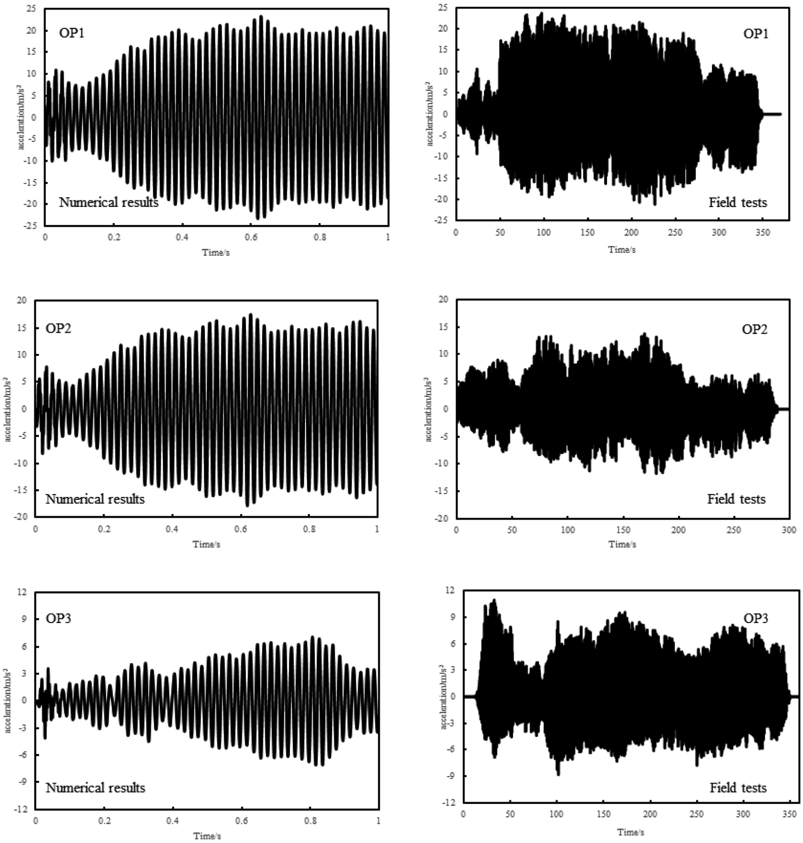

Fig. 6. Acceleration-time history curve of numerical simulation and field tests

resonance rubblization machine all can influence the measurements of sensors). The peak value of numerical computed acceleration was proportional to the total vibration intensity in this point. Hence the peak value of numerical computed acceleration in OP1-OP8 was adopted to represent the vibration intensity of these 8 points.

Figure 7 shows the peak values of numerical computed acceleration in all observation points. Acceleration in OP2 and OP3 decreases by 25.1% and 69.7% respectively compared with OP1, similarly, acceleration in OP5 and OP4 decreases by 23.5% and 48.8% respectively compared with OP6. The acceleration in OP8 is the largest, whereas decreases by 60.3% compared with OP7. From above, we can conclude that: (1) the rubblization induced acceleration decreases fast along tunnel; and (2) OP1 and OP8 are two most severely affected regions that need special attention in the course of resonance rubblization construction.

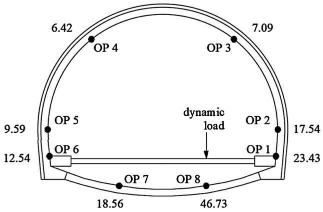

Fig. 7. Peak value of numerical computed acceleration (units: m/s^2)

7 Resonance Rubblization-Induced Additional Stress

7.1 Additional Stress Distribution in Transverse Section

Two typical cases were discussed: (1) breaker reaches its lowest location vertically; and (2) breaker reaches its highest location vertically. Figure 8 shows the additional Mises stress in tunnel and surrounding rocks. It is obvious that additional Mises stress mostly concentrated on a small region directly under the breaker. The average Mises stress is 2–3 times of that in other locations, indicating that rubblization-induced additional stress has a rapid reduce along transverse and vertical direction along tunnel. Additional stress distribution at breaker's lowest and highest locations are almost the same. No tensile stress appears in tunnel and surrounding rocks when breaker reaches its highest location, where the dynamic load applies a tensile force on road surface.

Additional Mises stress of surrounding rocks mainly lies between 20 kPa to 180 kPa, only a small region directly under the breaker has additional Mises stress of 678 kPa–842 kPa. But compared with tunnel, whose Mises stress is averagely 1 MPa out of the stress-concentrated area and 2 MPa within the stress-concentrated area, the additional Mises stress in surrounding rocks are only 10%–35% of that in tunnel.

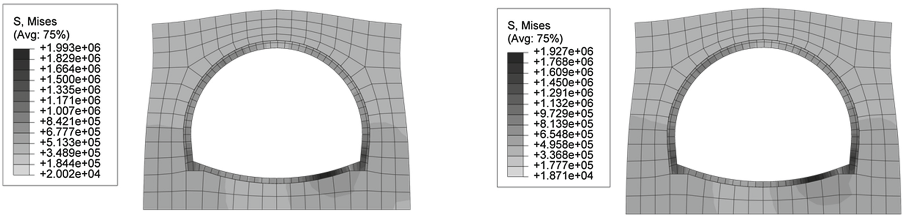
S, Mises
(Avg: 75%)
+1.993e+06
+1.829e+06
+1.664e+06
+1.500e+06
+1.335e+06
+1.171e+06
+1.007e+06
+8.421e+05
+6.777e+05
+5.133e+05
+3.489e+05
+1.844e+05
+2.002e+04
S, Mises
(Avg: 75%)
+1.927e+06
+1.768e+06
+1.609e+06
+1.450e+06
+1.291e+06
+1.132e+06
+9.729e+05
+8.139e+05
+6.548e+05
+4.958e+05
+3.368e+05
+1.777e+05
+1.871e+04

(a) breaker at lowest location (b) breaker at highest location

Fig. 8. Additional Mises stress of tunnel and surrounding rocks (units: Pa)

7.2 Additional Stress Distribution Along Longitudinal Direction

The longitudinal additional stress distribution in inverted arch see Fig. 9, and in tunnel lining (in breaker's side) see Fig. 10. From both figure, no distinct difference of additional stress distribution can be observed at the lowest and highest locations of breaker. The maximum additional Mises stress is about 2 MPa and 1.54 MPa in inverted arch and lining respectively.

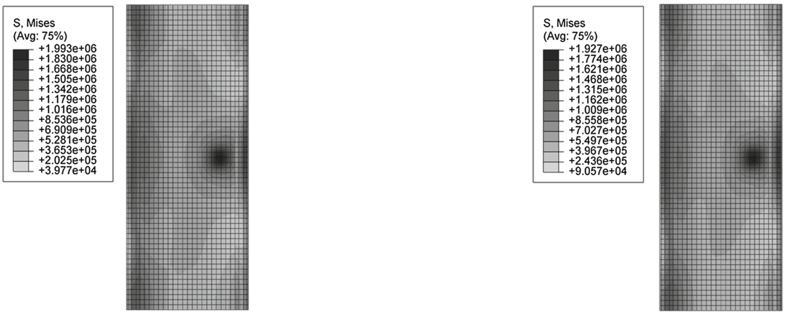
S, Mises
(Avg: 75%)
+1.993e+06
+1.830e+06
+1.668e+06
+1.505e+06
+1.342e+06
+1.179e+06
+1.016e+06
+8.536e+05
+6.909e+05
+5.281e+05
+3.653e+05
+2.025e+05
+3.977e+04
S, Mises
(Avg: 75%)
+1.927e+06
+1.774e+06
+1.621e+06
+1.468e+06
+1.315e+06
+1.162e+06
+1.009e+06
+8.558e+05
+7.027e+05
+5.497e+05
+3.967e+05
+2.436e+05
+9.057e+04

(a) breaker at lowest location (b) breaker at highest location

Fig. 9. Additional Mises stress of inverted arch (units: Pa)

Additional stress in inverted arch concentrates on a small circular whose center is directly under the breaker, and additional stress in this region is about 2 times of Mises stress out of this region. Additional stress in lining concentrates on a small band around breaker. The width of this band is about 1/6 of tunnel height and length is about 1/4 of tunnel length, indicating the propagation of additional stress along longitudinal direction in inverted arch and lining is not obvious.

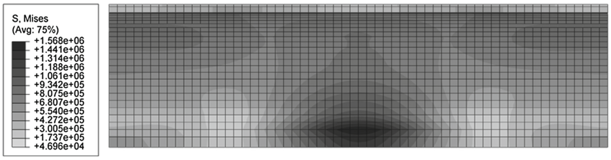

(a) break at lowest location

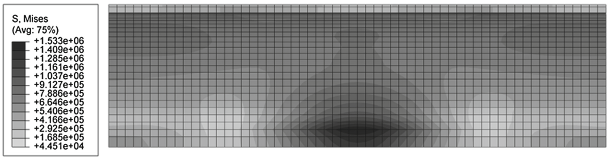

(b) breaker at highest location

Fig. 10. Additional Mises stress of lining in breaker's side (units: Pa)

8 Effects of Isolation Trenches

Isolation trenches (including open or infilled trenches) are a popularly used method to reduce dynamic effects on structures. Beskos et al. suggested when the depth (d) of an open isolation trench meets the criterion of $d/\lambda \geq 0.6$, where λ is the wave length of harmonic wave, this isolation trench is effective in reducing dynamic effects [18].

However, due to the inner space limits of tunnel, Beskos's criterion mentioned above is hard to be met. To study the performance of isolation trenches when this criterion is not met, the two drainage ditches (which are 1 m in width and 0.4 m in height) in both side of tunnel were taken as open isolation trenches. The tunnel response without trenches can be got by filling the two drainage ditches with according materials the same with road bed and pavement (see Figs. 11 and 12).

It can be seen in Fig. 11 that the peak additional Mises stress increased about 31.7% when there are no isolation trenches existing. And from Fig. 12 we know the peak additional Mises stress increased about 16.0% without isolation trenches. From above,

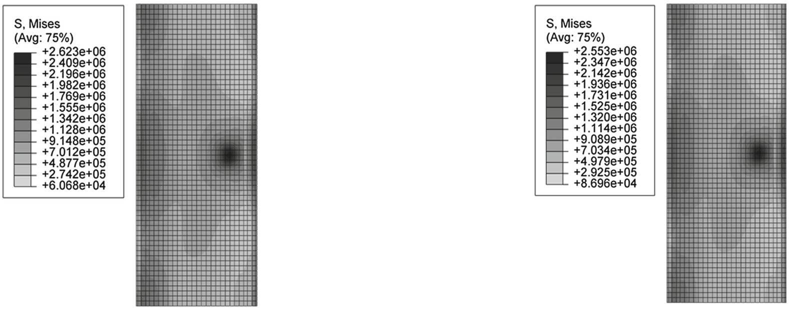

(a) breaker at lowest location (b) breaker at highest location

Fig. 11. Additional Mises stress of inverted arch without trench (units: Pa)

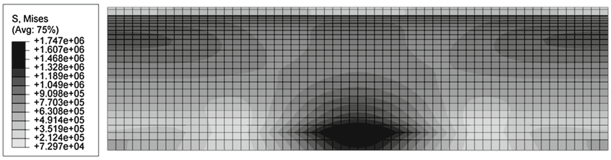

(a) breaker at lowest location

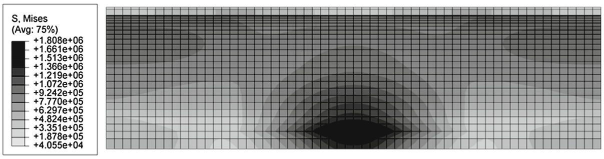

(b) breaker at highest location

Fig. 12. Additional Mises stress of lining without trench (units: Pa)

we can conclude that the isolation trench does have some effects in reducing vibration-induced additional stress. Whereas additional studies may need to be done to optimize the size of isolation trenches whenever isolation trenches are needed, but they were not concerned in this paper.

9 Conclusions

3D numerical simulation and field tests had been conducted to study the tunnel response under resonance rubblization construction inside tunnels. Additional stress was used to get generalized rules of tunnel dynamic response, ignoring different geological conditions. Following conclusions can be got:

(1) the largest vibration-induced acceleration in tunnel lining is about 23 m/s^2, appears at the toe of lining;
(2) the vibration-induced additional stress of tunnel concentrates mainly on a small region directly under the breaker, and its peak value is about 2 MPa and 1.5 MPa in inverted arch and lining respectively. Additional stress also reduces significantly transversely, longitudinally and vertically along tunnel;
(3) compared with when isolation trenches exist in both side, the peak value of additional Mises stress in inverted arch and lining increases by 31.7% and 16.0% respectively when there are no isolation trenches present, so isolation trenches have certain effects on reducing vibration-induced effects on tunnels, but the optimization analysis of isolation trenches is not concerned in this paper.

Acknowledgement. This study was financially supported by National Natura Science Foundation of China (Grants NO. 51478344). The support is gratefully acknowledged.

References

1. Hong-Yu, X.: Research on application of resonance rubblization technology and asphalt overlay technology. Chongqing: Chongqing Jiaotong University (2013) (in Chinese)
2. Khodaii, A., Fallah, S., Nejad, F.M.: Effects of geosynthetics on reduction of reflection cracking in asphalt overlays. Geotext. Geomembr. **27**(1), 1–8 (2009)
3. Cleveland, G.S., Button, J.W., Lytton, R.L.: Geosynthetics in flexible and rigid pavement overlay systems to reduce reflection cracking. Texas Transportation Institute, Texas A&M University System (2002)
4. Adaska, W.S., Luhr, D.R.: Control of reflective cracking in cement stabilized pavements. In: Proceedings of 5th International RILEM Conference on Cracking in Pavements, pp. 309–316 (2004)
5. Fitts, G.L.: Rubblization using resonant frequency equipment. Transportation Research Circular No. E-C087, Transportation Research Board, 20–30 (2006)
6. Timm, D.H., Warren, A.M.: Performance of rubblized pavement sections in Alabama. Final Report. No. IR, 2004, 402
7. Boyer, R., Jones, W.: State-of-the-Practice: Rubblization of Heavy Load Concrete Airfield Pavements. Airfield Pavements: Challenges and New Technologies, 424–435 (2004)
8. Xu, Z., Ling, J., Huang, Q.: Research on resonant rubblized effects of PCC pavement. China J. Highw. Transp. **21**(5), 26–32 (2008)
9. Nai-Chao, S.: Research for the natural frequency of old cement concrete pavement plate and its application in resonance rubblization technology. Changan University (2016) (in Chinese)
10. Qi-Zhi, G., Hui-Zeng.: Research on resonance rubblization technology in Yiyang to changed expressway engineering. Modern Transportation Technology, 24–27 (2016) (in Chinese)
11. Hui-Lun, B.: The numerical simulation of pressure-relief blasting in high geo-stress tunnel. Chengdu University of Technology (2016) (in Chinese)
12. Zhang, S.: Research on the control of deformation during construction of rock tunnel undercrossing buildings. Chongqing University (2013) (in Chinese)
13. Tian, Y.: The numerical simulations of forces acting on TBM disc cutters with the consideration of confining pressure and damage in rocks. Tianjin University (2010) (in Chinese)
14. Qin-Long, H., Zhuang, Y., Lu, Y.: Application and effects evaluation of resonated crushing technology in cement concrete pavement of freeway. Transp. Sci. Technol. **01**, 31–33 (2017). (in Chinese)
15. Wen-Wen, S.: Research on resonance frequency breaker construction technology of Tan Lei highway old concrete pavement. Changsha University of Science and Technology (2013) (in Chinese)
16. Qin-Long, H., Da-Hao, C., Jian-Ming, N., et al.: Performance of rubblization on jointed concrete pavement rehabilitation in Shanghai. J. Changsha Univ. Sci. Technol. **5**(2), 103–106 (2008). (in Chinese)
17. DGJ08-9-2013. Code for seismic design for buildings (2003)
18. Beskos, D.E., Dasgupta, B., Vardoulakis, I.G.: Vibration isolation using open or filled trenches. Comput. Mech. **1**(1), 43–63 (1986)

Analysis and Application Exploration of Smoothed Particle Hydrodynamics (SPH) for Non-circular Shield Tunneling

Peinan Li[1,2(✉)], Jun Liu[3], Yixin Zhai[2], and Wenqi Ding[1]

[1] College of Civil Engineering, Tongji University, Shanghai 200092, China
peinanli411@163.com
[2] Shanghai Tunnel Engineering Co. Ltd., Shanghai 200232, China
[3] College of Urban Railway Transportation, Shanghai University of Engineering Science, Shanghai 201620, China

Abstract. Cutting stirring and synchronous grouting is direct interaction with formation and invisible in shield tunnel construction, which has more uncertainties and risks than other internal visible processes. The selecting of control parameters in constructional step determines the influence of shield tunneling for surrounding environment. At present, grid method has been widely used in various kinds of static, quasi static or dynamic simulation, however, its inherent defect hinders the further refinement study of the numerical analysis. Based on the domestic first non-circular (quasi-rectangular) shield tunnel, this paper introduces a kind of meshless method, smoothed particle hydrodynamics (SPH), to analyze the large deformation characteristics and dynamic effects of cutting soil and grouting material in shield tunneling. Through the comparison to numerical methods, the exposition of motion mechanism and the improvement of SPH algorithms, real-time large deformation simulation and micro-analysis are innovatively performed for the flow plastic medium in shield tunneling, and some guiding conclusions and recommendations are obtained.

Keywords: SPH method · Numerical simulation · Non-circular shield
Cutting stirring · Synchronous grouting

1 Introduction

During the construction of shield tunnel, because of the invisibility, unpredictability and uncertainty of the rock and soil in the underground space, there will be many difficulties, which is usually much more than that in planning and design stage. In shield construction stage, the cutting stirring conditioning and shield tail synchronous grouting are two of the most important processes. Not only the complex geological conditions of surrounding environment, but also the poor control of operation can lead to unpredictable risks in shield tunnel construction period. Therefore, it is necessary to carry out the research on this technology and the materials (cutting soil and synchronous grout), including the dynamic behavior and simulation analysis of the large deformation [1].

© Springer Nature Singapore Pte Ltd. 2018
D. Zhang and X. Huang (Eds.): GSIC 2018, *Proceedings of GeoShanghai 2018 International Conference: Tunnelling and Underground Construction*, pp. 432–441, 2018.
https://doi.org/10.1007/978-981-13-0017-2_43

Similar to the research methods of geotechnical engineering, the research on the key technology of shield tunnel construction is mainly conducted by the following four approaches to understand the behavior of research objectives: theoretical analysis, numerical simulation, laboratorial test, in-site monitoring and etc. [2]. Especially, the numerical simulation has gradually become an important method to solve complex problems. Considering the large errors during the calculation of the large deformation problems by using the Finite Difference Method (FDM) and the Finite Element Method (FEM), the traditional Computational Fluid Dynamics (CFD) and Computational Solid Mechanics (CSM) are limited, when dealing with the problems with free surface, deformation boundary and motion interface. Thus, it is almost impossible to deal with irregular or complex geometric problems [3–5].

In this paper, an exploratory study is carried out in conjunction with adaptive analysis based on the smooth particle hydrodynamics (SPH). The real-time simulation and microscopic analysis of the large deformation fluid in the cutting stirring and synchronous grouting have been explored combining with the elaboration of flow plastic medium movement mechanism and the improvement of SPH algorithm in shield tunnel construction. The guiding conclusions and suggestions can be obtained for the control of the construction parameters, and the sufficient theoretical basis can be provided for the establishment of the fine control system during the construction of the special-shaped shield tunnel.

2 SPH Fundamental Theory

The basic of the SPH method is an interpolation technology [6]. In SPH frame, each macroscopic physical variable (density, pressure, temperature) $f(x)$ can be expressed as integral interpolation by the value of a set of disorder points, including the function smooth and particle approximation, the formula is:

$$f(x_i) = \sum_{j=1}^{N} \frac{m_j}{\rho_j} f(x_j) W(|x_i - x_j|, h) \tag{1}$$

Where, m_j, ρ_j are the mass and density of the particles; W is the interpolated kernel, i is the number of calculated particle and j is the number of adjacent particle.

Based on the hydrodynamic theory and discretization, the Navier-Stokes control equations in SPH format are given below.

The mass conservation equation is:

$$\rho_i = \sum_{j=1}^{N} m_j W_{ij} / \sum_{j=1}^{N} \left(m_j/\rho_j\right) W_{ij} \tag{2}$$

The momentum conservation equation is:

$$\frac{Dv_i^\alpha}{Dt} = \sum_{j=1}^{N} m_j \frac{\sigma_i^{\alpha\beta} + \sigma_j^{\alpha\beta}}{\rho_i \rho_j} \frac{\partial W_{ij}}{\partial x_i^\beta} \tag{3}$$

The energy conservation equation is:

$$\frac{De_i}{Dt} = \frac{1}{2} \sum_{j=1}^{N} m_j \frac{P_i + P_j}{\rho_i \rho_j} v_{ij}^\beta \frac{\partial W_{ij}}{\partial x_i^\beta} + \frac{\mu_i}{2\rho_i} \varepsilon_i^{\alpha\beta} \varepsilon_j^{\alpha\beta} \tag{4}$$

Where v is the speed, e is the heat energy, σ is the stress tensor, P is the pressure, m is the quality, ρ is the density, μ is the dynamic viscosity coefficient, ε is the dynamic shear strain rate and N is the total number of particles. α and β are on behalf of different coordinate axes. i and j represent different particles, which i is the number of calculated particle and j is the number of adjacent particle.

3 Necessity of Elaborate Simulation

Before using SPH method to deal with the large deformation, it is necessary to analyze the microscopic movement mechanism of research object, and consider the partial targeted improvement of SPH simulation algorithm [7].

3.1 Movement Mechanism of Flow Plastic Medium

For the two shield construction steps that interact with the surrounding soil directly the most important feature of the two types of object material is good flow performance by which to make sure that it can be smoothly cut and drained, injected and diffused. For the cutting soil program in shield head chamber, it is a dynamic rotation process which moves around the axis of shield from a plane view and there are both laminar and turbulent flow motion pattern from a longitudinal micro-view. The relative flow velocity of cutting soil is faster near the conditioning hole and the stirring rod, while the soil velocity is slower in other place. The movement of the cutting soil can be seen as a stratified circular motion with local turbulence. The overall flow velocity of soil dross is increasing with the radius, and the relative flow velocity is higher near the conditioning hole and the stirring rod, as shown in Fig. 1a.

On the other hand, it is a dynamic filling process for the synchronous grouting in shield tail gap. Considering the grouting pipeline parallel to the tunnel axis direction, the grout is initially injected along the tunnel longitudinal direction, when it encounters a certain resistance, the grout will turn to ring flow. From a local view, the existed grout in shield tail gap can be driven or extruded by the new injected grout in different degrees depending on its viscosity coefficient. Near the location of grouting hole in shield tail, two flow patterns have present. Therefore, the synchronous grouting process can be seen as a fluid motion with the extrusion diffusion pattern which has both longitudinal and circumferential direction dependently, as shown in Fig. 1b.

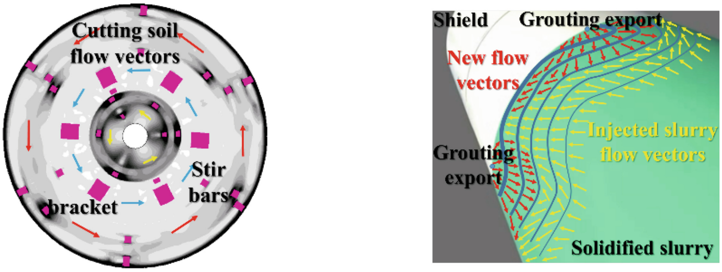
Cutting soil flow vectors
Stir bars
bracket
Shield
Grouting export
New flow vectors
Injected slurry flow vectors
Grouting export
Solidified slurry

(a) Motion pattern of cutting stirring (b) Diffusion pattern of synchronous grouting

Fig. 1. Motion and diffusion patterns concept map of flow plastic medium

3.2 Adaptability Improvement of SPH Method

When the cutting/stirring process and synchronous grouting process in a specific shield tunneling are dynamically simulated by the SPH method, the problem domain shape of the model is a thin layer/strip which is different from the traditional circular shield tunnel. In addition, as the SPH method has a boundary defect problem [8, 9], it is necessary to consider the processing of the rigid boundary condition, especially when the calculated work area of the numerical simulation exhibits a relatively thin distribution. It will be cut off during the integration due to the defects of the particles near the boundary. Hence, the SPH method can not be fully applied to the entire calculation region. In this paper, two types of virtual particles are used to deal with the rigid boundary condition, which contains type I (on fixed boundaries) and type II (outside the boundary) [10]. The arrangement of virtual particles at boundary is shown in Fig. 2.

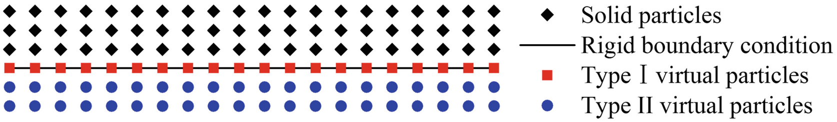
◆ Solid particles
Rigid boundary condition
■ Type Ⅰ virtual particles
● Type II virtual particles

Fig. 2. Solid particles and two types of virtual particles

The SPH simulation is performed in the LS-DYNA software. The treatment of the defects in rigid boundary condition and fluid-solid coupling in irregular space can be realized by a secondary development tool based on FORTRAN, and the rheological parameters and stress patterns are accessed to this program in a custom way.

4 SPH Numerical Model and Calculation Scheme

4.1 Engineering Overview and Mechanical Structure

In this paper, a new type of 11.83 m × 7.27 m earth pressure balance (EPB) quasi-rectangular shield is used for the construction of a running tunnel project in the first phase of Ningbo Rail Transit Line 3. The shield cutting device is based on 2X + I combination cutter form which has two central rotation X-type strip banner large cutter and one eccentric cutter at the center back of X-type cutter plane (see Fig. 3).

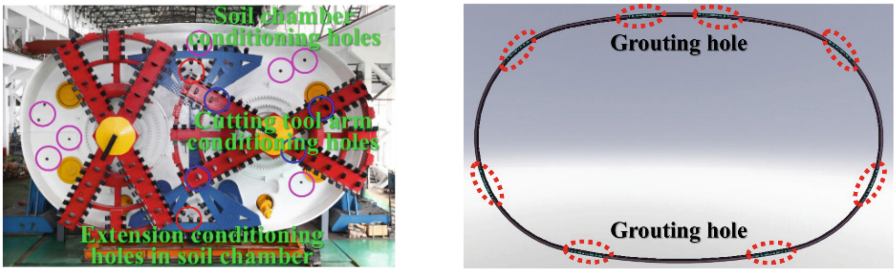
Soil chamber conditioning holes
Cutting tool arm conditioning holes
Extension conditioning holes in soil chamber
Grouting hole
Grouting hole

(a) Cutting stirring system (b) Synchronous grouting system

Fig. 3. Structure form of corresponding equipment in quasi-rectangular shield machine

In order to ensure the easy cutting of soil in incision surface and the grouting soil fluidity in head chamber, 8 + 19 agent injection ports are especially arranged in the main arm and the soil chamber panel, as shown in Fig. 3a. A total of eight grouting holes are symmetrically arranged in the upper and lower side at the back of the shield tail. Considering the poor mobility of quasi-rectangular grouting path, eight standby grouting holes are arranged in the same location, as shown in Fig. 3b.

4.2 Numerical Models and Boundary Conditions

The geometric model is built in 1:1 full-scale. The range of head chamber is composed of shield machine boundary and stratum interface, and the range of annular cavity filled with grouting is defined by shield tail boundary, outer and segment surface and artificial boundary. The cutting soil and grouting material are SPH particles, the surrounding soil layer, the grouting effect layer and the lining are FEM elements. The cutting blade layout is referred to the standard design of the shield head, which consists of two large cutter, one eccentric cutter and two row soil holes as shown in Fig. 4a. The grouting hole is arranged corresponding to the standard piping design, marked with the clockwise number (1 to 8) as shown in Fig. 4b. In simulation, the drop of soil is simulated using SPH particles released with the cutter plate. The speed of shield tail movement is set equal to the average propulsion speed: $3\ \mathrm{cm} \cdot \mathrm{min}^{-1}$.

The stress boundary condition is provided by soil and water pressure corresponding depth range from 8 m to 15 m which is 0.15 MPa – 0.27 MPa from top to bottom.

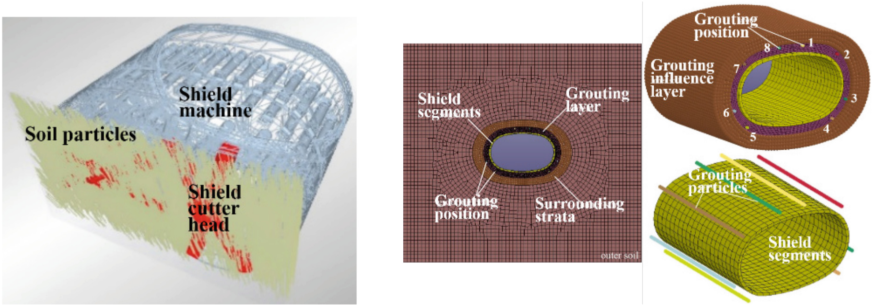
Soil particles
Shield machine
Shield cutter head
Shield segments
Grouting layer
Grouting position
Surrounding strata
outer soil
Grouting position
Grouting influence layer
1
2
3
4
5
6
7
8
Grouting particles
Shield segments

(a) Cutting stirring model (b) Synchronous grouting model

Fig. 4. Numerical calculation models for SPH simulation

4.3 Parameters Setting of Mechanical and Construction

The rheological properties of various Newtonian/non-Newtonian fluids are tested by rotational viscometer in Tongji University laboratory. The result is shown in Fig. 5, the upper curve is for cutting soil and the lower curve is for synchronous grout.

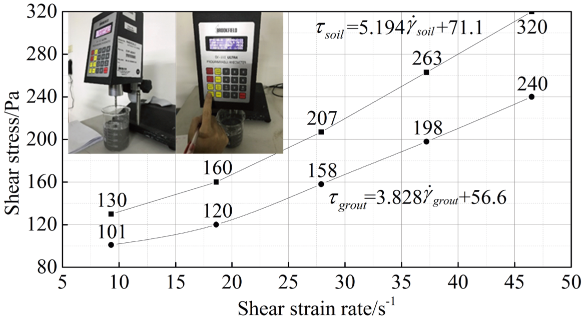

Fig. 5. Rheological tests and results curves of flow plastic medium

The material mechanical parameters for the two types of craft in SPH simulation are listed in Table 1. The corresponding cutting and grouting construction parameters are based on related experience and research, as shown in Table 2.

Table 1. Material mechanical parameters for SPH simulation

Fluid type	Density ρ/g·cm^{-3}	Plastic viscosity coefficient η_0/Pa·s	Shear strength τ_y/Pa
Soil	1.9	5.194	71.1
Grout	2.1	3.828	56.6

Table 2. Construction parameters for SPH simulation

Main cutter rotate speed (r/min)	1
Eccentric cutter rotate speed (r/min)	2
Grout injection rate for whole ring (%)	150
Average grouting speed (m/s)	0.35
Grouting hole pressure (MPa)	0～0.40
Injection rate of up and down hole	4:3:2:1
Velocity distribution of each hole (m/s)	0.56:0.42:0.28:0.14

5 Analysis and Application of SPH Results

5.1 Simulation of Cutting Stirring

During the simulation, six layers particles are arranged to cover the cutting domain, i.e. three planes consisted of large cutter, eccentric cutter and soil chamber are respectively distributed to two layers particles. The number of particles is up to 283922 and the grid spacing is 30 mm. This simulation takes about 60 h in total because the computation domain is relatively large. The interface between particles and cutter is assumed to have no friction. The cutting stirring SPH simulation is shown in Fig. 6a.

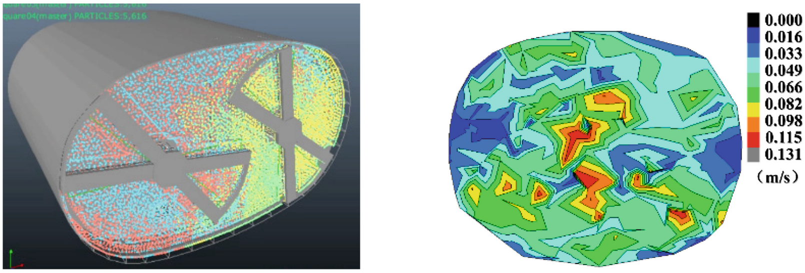

(a) Motion pattern of particles (b) Relative velocity distribution

Fig. 6. Simulation results of cutting stirring based on SPH

Figure 6b shows that with the continuous rotation of shield cutter, on the cutting surface, the relative velocity of cutting soil particles at domain sides is lower than that in middle part because of the combined influence of large central cutter and eccentric cutter. From a vertical view, the relative velocity of cutting soil in lower part of head chamber is larger than that in upper part of head chamber. It is because that the cutting soil in lower part is more compact and its speed and displacement can be transmitted more easily under the function of gravity, while the upper cutting soil is relatively loose resulting in the poor mixing effect from cutter rotation.

5.2 Simulation of Synchronous Grouting

The synchronous grouting is mainly simulated by the particles dynamically generating and launching from the grouting holes location at shield tail. Grouting material and construction parameters are shown in Tables 1 and 2. The constraint force caused by the existed grout in the longitudinal direction is also applied, except the surrounding soil and water pressure. The grout distribution at different times are shown in Fig. 7.

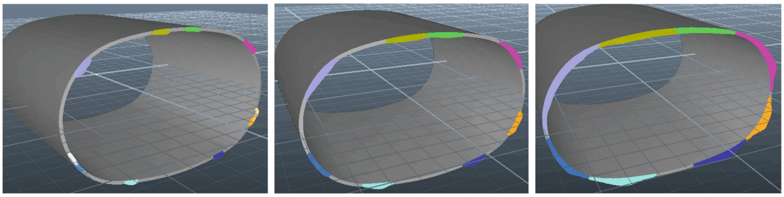

(a) 10s (b) 30s (c) 90s

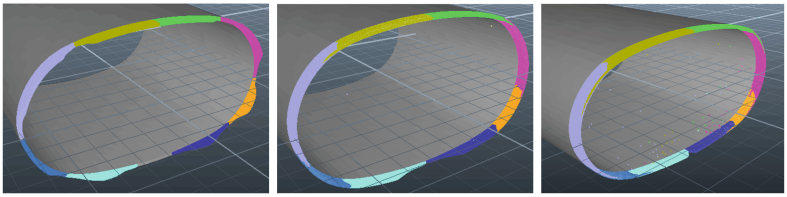

(d) 100s (e) 170s (f) 260s

Fig. 7. Filling and diffusion patterns of synchronous Grouting at different time

At different time, there are different numbers of particles involved in the calculation (the largest number is up to 605340 and costing 72 h), the initial grid spacing is about 10 mm. Considering the narrow computational domain especially for grouting process, the boundary virtual particles are necessary to be set to improve the stability of interpolation calculation. When the calculation time is 10 s, the grout accumulates around grouting holes and spread continually as shown in Fig. 7. The new injected grout distribute thinner with increasing of distance, and the rest space is squeeze filled by the existed grout. The injected grout from upper two grouting holes is closed at the calculation time 30 s. The grout of shield tail from upper to waist is mix together with the grout from waist bottom when the calculation time reach 90 s, and the upper holes are full filled at the same time. The grout in side area and other parts of shield tail is gradually closed over time. Due to a larger pressure at the bottom of shield, the closure and filling process of new injection grout is more slowly. Consequently, the new injected grout in this area is closed at 170 s and full filled at 260 s.

In summary, the flow and filling mechanisms in quasi-rectangular shield are always different from that in circular shield, not only for the cutting program, but also for the grouting process. It is mainly reflected in the irregular distribution of flow velocity during cutting stage and it is difficult to form a perfect circular flow characteristics because of the turbulence effect. The residual soil from shield cutting at the lower part in head chamber is easily accumulated, leading to a low flow efficiency. Furthermore, it is also difficult to explain the laws of closure and filling based on the experiences from conventional circular shield. The grout diffusion pattern at flat upper and lower parts of shield tail is relatively slower, meaning that more grouting amount is needed to achieve closure and diffusion in full section of structure void.

6 Conclusions and Discussion

In this paper, SPH method is used to perform the innovative application exploration of large deformation real-time simulation and the flow micro-analysis for two types of shield construction objects in cutting stirring and synchronous grouting process. Some conclusions and suggestions are summarized as follows:

(1) The simulation results can well capture the dynamic characteristics such as motion configuration, relative velocity distribution pattern, filling and diffusion mechanism of two types of fluid media which are consisted of cutting soil and grouting material. It indicates that SPH method is effective to analyze large deformation movement of flow plastic medium in shield tunnel construction.
(2) Based on the equivalent Newtonian viscosity coefficient, the Bingham fluid model is adopted to solve the motion characteristics and mechanical representation of cutting soil and grouting material. The results show that the flow and filling mechanism of two types of flow plastic medium in quasi-rectangular shield construction is great different with that in conventional circular shield.

Further analysis knows that the SPH simulation results of cutting and stirring can be applied to the structure optimization of cutter form and the arrangement improvement of agent injection ports. Furthermore, it can also guide the selection and determination of grouting material parameters for shield tunneling. In addition, the matching and acquirement scheme of modified additive can be obtained based on the relative velocity of the flow-like residual soil from shield cutting. These calculation results provide a sufficient theoretical reference for the fine management control and micro-disturbance construction of special-shaped shield tunneling. However, the dynamic simulation of shield construction process based on SPH method is still in a stage of exploration and development. More researches will be conducted in the further.

References

1. Fei, Y.E., Jiahua, M.A.O., Ming, J.I., et al.: Research status and development trend of back-filled grouting of shield tunnels. Tunn. Constr. **35**(8), 739–752 (2015)
2. Houmei, Z.: Shield Tunnel Theoretical Research and Construction Practice. China Building Industry Press, Beijing (2010)
3. Huang, Y., Hao, L., Xie, P., Xu, Q.: Numerical simulation of large deformation of soil flow based on SPH method. Chin. J. Geotech. Eng. **31**(10), 1520–1524 (2009)

4. Zienkiewicz, O.C., Taylor, R.L.: The Finite Element Method, 5th ed., Butterworth Herinemann, Oxford (2000)
5. Benson, D.J.: Computational methods in Lagrangian and Eulerian hydrocodes. Comput. Methods Appl. Mech. Eng. **99**, 235–394 (1992)
6. Liu, G.R., Liu, M.B.: Smoothed particle hydrodynamics—a meshfree particle method. World Scientific Publishing Company, New Jersey (2003)
7. Xiao, G., Li, P., Zhu, Y., et al.: Explorative research on SPH fluid dynamics applied in quasi-rectangular shield construction. Mod. Tunn. Technol. **53**(S1), 181–188 (2016)
8. Monaghan, J.J.: Smoothed particle hydrodynamics. Annu. Rev. Astron. Astrophys. **30**, 543–574 (1992)
9. Morris, J.P., Fox, P.J., Zhu, Y.: Modeling low Reynolds number incompressible flows using SPH. J. Comput. Phys. **136**, 214–226 (1997)
10. Liu, M.B., Liu, G.R., Zong, Z., Lam, K.Y.: Numerical simulation of incompressible flows by SPH. In: International Conference on Scientific & Engineering Computing, Beijing (2001)

Mechanical Analysis of a Super-large-diameter Shield Tailskin Under Deep Ground Load

Chen Zhou(✉), Xuehui Zhang, and Yun Bai

Department of Geotechnical Engineering, Tongji University,
Shanghai 200092, People's Republic of China
chen.zhou@tongji.edu.cn

Abstract. The deformation and stress of a super-large-diameter shield tailskin are analyzed in this paper. Four kinds of structure analysis models, i.e. the perfect solid shell model, the defected solid shell model, the perfect hollow-layered shell model, and the defected hollow-layered shell model are formed to study the effects of initial geometrical defects and the hollow-layered shell formation on the deformation properties of the tailskin. Using the FEM modelling, the defected hollow-layered shell model gets a maximum deformation of 18.8 mm and a maximum Mises-stress of 304 MPa under the ultimate load condition, which indicates plastic deformation; while the perfect solid shell model shows a corresponding result of 3.6 mm and 71.6 MPa. The study shows initial geometrical defects and hollow-layered shell formation lead to much larger deformation and higher stress value, compared with the perfect solid shell model. It is necessary to consider these two factors when designing super-large-diameter shields for deep-buried tunnels.

Keywords: Super-large-diameter shield · Tailskin · Mechanical property
Initial geometrical defects · Hollow-layered shell

1 Introduction

With the increasing traffic flow of urban roads and the gradual saturation of shallow underground space, the construction of highway tunnels with large diameter (D > 14 m) and large depth at home and abroad began to develop. The Shanghai North Cross Channel uses a large diameter shield for construction, and over 2.6 km of its tunnel section has the depth of more than 40 m.

As usual, the shield is composed of a cut ring (front shield), a support ring (shield) and a shield tail as shown in Fig. 1. The shield tail consists of the hollow-layered shell and the solid shell. The hollow-layered shell are designed to lay the grouting lines.

Large deformation in shield tail will make the shield tail gap too small, and the assembly difficult. It may even cause the contact of the shield and the assembled segment, making the shield difficult to push on. In actual construction, accidents caused by large deformation of shield tails have occurred. Large deformation of the shield tail resulted in the failure of construction in Yaohua slip road tunnel in Shanghai. In the Westerschelde tunnel project, the large deformation of shield tail made the shield stuck for several

© Springer Nature Singapore Pte Ltd. 2018
D. Zhang and X. Huang (Eds.): GSIC 2018, *Proceedings of GeoShanghai 2018 International Conference: Tunnelling and Underground Construction*, pp. 442–450, 2018.
https://doi.org/10.1007/978-981-13-0017-2_44

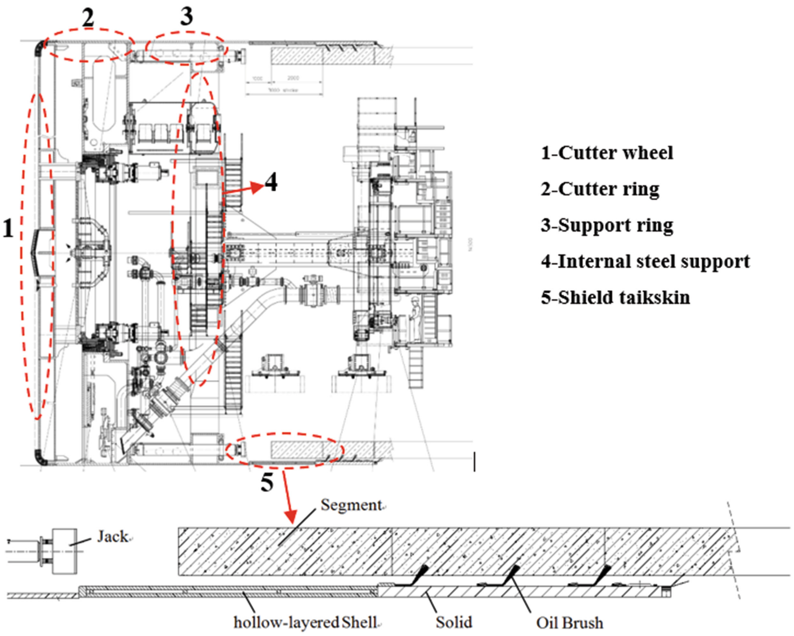

Fig. 1. Schematic diagram of shield tailskin

months and led to high cost and increase of risks. Therefore, possible causes of large deformation of the shield tail are necessary to be researched to prevent further accidents.

Researchers have studied the stress of shield shell under water and soil pressure. Deng *et al*. [1] analyzed the Φ6.34 m shield tail structure of an earth pressure balance shield, and found that the unequal loading is the most harsh condition for a solid shield machine. Guan [2] considered the shield as a homogeneous cylinder structure and derived the formula for calculating the internal force of the shell using the structural mechanics method. Coen *et al*. [3] analyzed the engineering case of the shield shell deformation in the Westerschelde tunnel project, and concluded that the lead factors contributing to the excessive deformation of the shield tail are the shield design defect and the larger grouting pressure.

In this paper, based on the Shanghai North Cross Tunnel Project and taking the initial geometric defect and the hollow laminated structure into consideration, a three-dimensional finite element model is established to study the deformation and stability of the shield tail (D = 15.8 m) under high water and soil pressure. It will provide a reference for the design and manufacturing of large diameter shields.

2 Basic Parameters of the Shield Tail Analysis

2.1 Shield Geometry Size

The parameters of the shield machine used for the North Cross Tunnel are shown in Table 1 below (provided by Herrenknecht).

Table 1. Geometry parameters of the studied shield

Shield machine parts	Parameter value
Outer diameter of shield	15.4 m
Length of shield machine	12 m
Length of cut ring and support ring	7 m
Length of shield tail	5.0 m
Shield tail gap	0.11 m
Length of hollow board	2.52 m
Length of solid plate	2.48 m
Outer diameter of shield tail	15.4 m

2.2 Ground Geological Condition

The depth of the tunnel is from 28 m to 60 m. Considering that most of the shield segments are located at a depth of about 40 m, 40 m is selected as the depth of the section model. According to the geological investigation report, the groundwater level is +0.00 m. The soil thickness above the shield section is 40 m. The tunnel section is located in silty clay and silty sand layer horizontally, and the average gravity of both soils is 19 kN/m^3.

2.3 Shield Tail Load Determination

We use the load-structure model (Fig. 2) to consider formation resistance. The ground resistance is calculated using the spring model. Only the compression state of spring is taken into account in the calculation, and the tension spring is removed by iteration. At present, China's shield design mainly refers to the Japanese standard [4]. In this paper, we mainly study the force and deformation of the shield tail under normal construction conditions (in straight direction). This calculation considers the soil and water pressure, self-weight and ground resistance. For shields, soil and water pressure is the main load. The full earth-covering theory is used to calculate the vertical earth pressure σ_v of the shield in soft soil strata in Shanghai. The horizontal earth pressure σ_h can be calculated from the vertical earth pressure and the lateral earth pressure coefficient:

$$\sigma_v = \sum rihi \tag{1}$$

$$\sigma_h = k \cdot \sigma_v \tag{2}$$

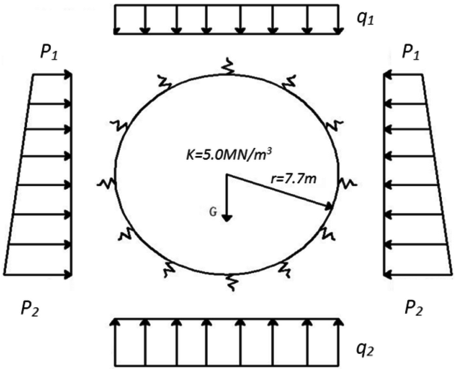

Fig. 2. Load model of the shield tailskin

Where: k is the lateral earth pressure coefficient; σ_h is the lateral earth pressure; σ_v is the vertical earth pressure [5].

The external load of the shield tail is determined as follow (Table 2):

Table 2. Load on the tailskin

Load	q_1	q_2	p_1	p_2
Value *(KN/m²)*	703.6	727.2	492.5	697.3

3 Finite Element Analysis of Shield Tail Structure

3.1 FEM Model Assumption

We use the load-structure model to consider the formation resistance. The ground resistance is calculated using the spring model. Since the study mainly focuses on the initial defects and the effect of hollow-layered shell on the mechanical properties of shields, the following assumptions are made in the calculation for simplicity: (1) the internal weakening impact of the tail pipe grouting on the cross-section is not considered; (2) the impact of sealing grease on the shield tail is not considered; (3) the connection boundary between the shield tail and shield support ring has fixed constraints.

Here, four kinds of structure analysis models are formed: (1) the perfect solid shell model which considers the shield tailskin as an ideal single-layered round shell; (2) the defected solid shell model which considers the initial geometrical defects separately; (3) the perfect hollow-layered shell model which considers the hollow-layered shell formation separately and (4) the defected hollow-layered shell model which takes both initial geometrical defects and hollow-layered shell formation into consideration.

We adopt the load combination under ultimate bearing capacity. In the four models, the effect of ground resistance is considered. The ground resistance is simulated by the spring element. The shield tail calculation model is shown in Fig. 3.

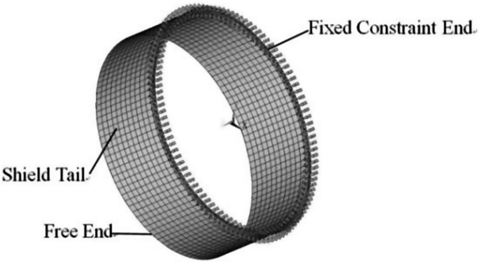

Fig. 3. Mechanical model and meshing of the tailskin

3.2 Analysis of the Perfect Solid Shell Model

The finite element analysis of the shield of the perfect solid shell model is simulated by the SHELL43 shell element. The SHELL43 unit can consider the motion and deformation inside and outside of the plane, and has good simulation effect on geometric nonlinearity.

As shown in Fig. 4, the maximum displacement of the shield tail is 3.6 mm, much smaller than the shield tail gap (110 mm). The maximum Mises-stress on the tail is 71.6 MPa, which is much smaller than the yield stress (235 MPa). The largest equivalent stress region appears near the boundary of the constraint, and no plastic deformation occurs.

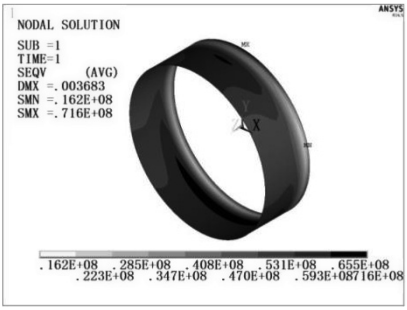

Fig. 4. Deformation and stress of perfect circular tailskin under load

3.3 Analysis of the Defected Solid Shell Model

The structural instability has three types: branch buckling, maximum point instability, and snap-through instability. The maximum point instability may occur in the shield tail, and the initial defect can be simulated using uniform modal analysis [6]. The geometric nonlinear analysis of the initial defect model is further studied.

The following steps are taken to analyze the geometrical defect of the shield tail: (1) use the eigenvalue method for buckling analysis, and extract the first-order buckling mode; (2) limit the maximum initial defect within the maximum manufacturing error; (3) re-apply the external load and the reaction spring, do the geometric nonlinear calculation, and obtain the final calculation results.

The maximum value of the initial defect is measured using the data 3.75 cm provided by Herrenknecht (based on the German specification for manufacturing errors in steel construction).

The first-order buckling mode is extracted and the maximum deformation is set to 3.75 mm. The model is set to the original perfect solid shell model to obtain the defective circular shell model, and then reload for geometric nonlinearity solution.

Figure 5 shows the results of the defective circular shell model with a maximum displacement of 15.1 mm, which appears at the distal end of the shield bottom. The maximum equivalent stress is 171 MPa and it also appears at the distal end of the shield bottom. The maximum equivalent stress is less than the yield load (235 MPa), indicating that the structure does not yield.

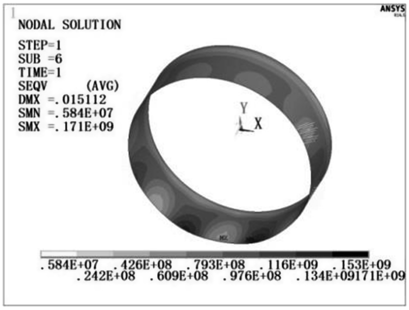

Fig. 5. Deformation and stress of the circular tailskin with initial defects

3.4 Analysis of the Perfect Hollow-Layered Shell Model

In the above analysis, the shield tail is regarded as a single layer of uniform real shell, and we do not consider the impact the shield tail hollow-layered structure has on its mechanical properties. As shown in Fig. 1, the shield tail structure can be divided into two parts, with the hollow-layered shell connecting to the support ring and the cantilever solid plate. The hollow-layered shell has three layers: the shell, the inner shell and the ribs. The connection between the ribs and the shell is considered to be rigid. Furthermore, the ribs and the inner shell are plug welding connected. The result of the perfect hollow-layered shell model shows that the maximum equivalent stress is 219 MPa, which appears near the boundary and has a maximum deformation of 4.9 mm (Fig. 6).

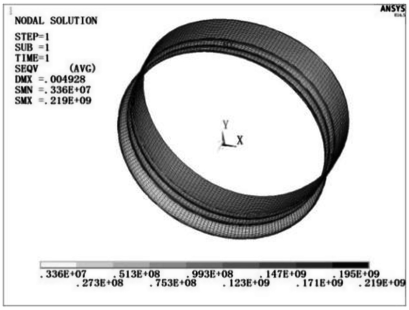

Fig. 6. Stress and deformation of perfect layered tailskin

3.5 Analysis of the Defected Hollow-Layered Shell Model

We use the same modal analysis method to simulate the initial geometric imperfections. The largest manufacturing error of the shield tail was set to 3.75 mm, and the initial defects are applied to the shield tail.

The results show the buckling load factor FREQ = 2.19 > 1, which means that the buckling instability does not occur under the load. Figure 7 shows that the shield with the hollow-layered structure and the initial geometric imperfections has the maximum deformation of 18.8 mm and the maximum equivalent stress of 304 MPa, which has exceeded the yield strength (235 MPa) of the shielded steel. This indicates that this part of the shield tail enters into the plastic phase. It is also observed that the plastic deformation zone is mainly present at the end of the shield and the rib ring.

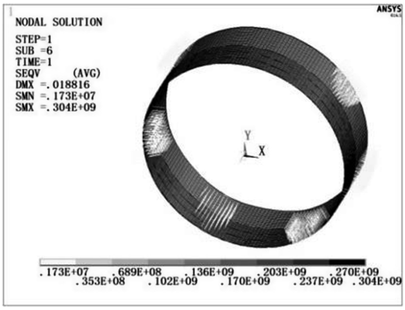

Fig. 7. Stress and deformation of layered tailskin with initial defects

4 Results Analysis

In order to facilitate the comparative analysis, the four calculation models under the shield tail stress and deformation calculation results are summarized in Table 3.

The results show that under the same load, the shield tail model considering the initial geometric imperfections and the hollow-layered shell structure has the maximum

Table 3. Result comparison of the 4 analysis models

Model	Largest deformation of shield tail (mm)	Maximum equivalent stress of shield tail (MPa)
The perfect solid shell model	3.65	71.6
The perfect hollow-layered shell model	4.90	219
The defected solid shell model	15.1	171
The defected hollow-layered shell model	18.8	304

deformation and the equivalent stress is 5 times that of the perfect solid shell model. The effect of the initial geometric imperfections on the deformation and the equivalent stress is greater than that of the hollow-layered shell structure.

Compared with the case of considering the hollow-layered shell structure separately, the initial geometrical defects have a greater influence on the maximum deformation of the shield (increasing from 4.90 mm to 18.8 mm). It is suggested that the effect of the initial geometrical defects should be paid more attention to in actual shield structure inspections. In addition, in the assumed model and load conditions, the deformation of shield tail under ultimate bearing capacity does not exceed the shield clearance value, and has a large margin.

However, considering the hollow-layered shell structure, the maximum equivalent stress (304 MPa) of the shield tail exceeds the yield strength of the material (Q235 steel), which means that the shield tail may undergo plastic deformation under the influence of large depth soil and water pressure. It can be seen that the plastic deformation zone mainly exists at the end of the shield and the rib ring. Therefore, the rib ring is the weak part of a shield, which needs to be strengthened in design and manufacturing.

5 Conclusions

In this paper, based on the Shanghai North Cross Tunnel, the mechanical properties of the shield at 40 m depth are analyzed. The results show that the initial geometrical defects and the hollow-layered shell structure have great influence on the deformation of the shield, which must be considered in structural design.

Therefore, it is suggested that the size of the shield cross section should be increased based on the analysis result in design, or steel with higher strength should be partially used. At the same time, manufacturing defects should be reduced in the process.

It should be noted that, in this paper, the shield tail support is considered as a fixed end to some extent, ignoring the weakening effect of the rigid constraint on the support side. In addition, this paper does not consider the impact of shield tail grouting and bias effects either. Therefore, further in-depth study is recommended to follow up the issues.

References

1. Deng, H.: ANSYS-based FEM analysis of shield tail. Machinery **05**, 7–9 (2005)
2. Guan, H.: Calculation and analysis of a shield tail strength. Constr. Mach. Equip. **08**, 34–37 (2008)
3. Van der Vliet, C., Bijlaard, F., Kooijman, G., et al.: Shield Tail Deformations: Experience, Mechanics and Lessons, pp. 156–158. World Tunnel Congress, Vancouver (2016)
4. Japanese Institute of Civil Engineering, Code for Shield Tunneling and Interpretation, Translated by Zhu Wei, China Architecture & Building Press (2011)
5. Qian, S.: Soil Mechanics, 2nd edn. Wuhan University Press, Wuhan (2010)
6. Gum, M., Zhang, Q.: Study of primary defects by adopting first buckling mode. In: The Third Symposium on Modern Structure Engineering, pp. 1188–1192. Industrial Construcion, Guangzhou (2005)

Numerical Analysis of Influence of Ground Variation on Deformation and Internal Forces of Large Diameter Shield Tunnel

Jingkang Shi, Dongming Zhang(✉), and Hongwei Huang

Tongji University, 1239 Siping Rd, Shanghai, China
{1710704,09zhang,huanghw}@tongji.edu.cn

Abstract. Large diameter shield tunnel becomes increasingly popular for under water and undersea channels built in cities. The probability of going through multi-layered ground formation within the tunnel depth is increasing as the diameter of shield tunnel increases. So it is necessary to consider the influence of ground variation on deformation and internal forces of shield tunnel within the range of tunnel depth. In this paper, two dimensional elastic modulus random field model which is lognormal distributed is employed to characterize the ground variation. Five parameters including tunnel diameter, tunnel buried depth, mean value and COV of ground elastic modulus, and vertical SOF of elastic modulus random field are changed in orthogonal test to study how these parameters influence tunnel internal forces and deformation. Monte Carlo simulation is performed and distributions of tunnel deformation and internal forces are all normally distributed. Mean value of tunnel deformation and internal forces are almost negative linear with mean value of ground elastic modulus, but not sensitive to COV of ground elastic modulus. Tunnel crown bending moment has the largest variability while invert axial force has the smallest variability among all structural response indicators.

Keywords: Random field · Spatial variability · Orthogonal test
Large diameter shield tunnel · Tunnel deformation · Tunnel internal forces

1 Introduction

With the advances in tunneling technology, large shield tunnel becomes increasingly popular in cross-sea and urban subway projects. In China, many super large shield tunnel project was completed in the past few years. Shanghai Yangtze River Tunnel was finished in 2009, the diameter of which is 15 m. Large diameter tunnel allows more versatile configurations to allow stacking of traffic lanes and the combination of different uses, such as highway and transit. Although many large shield tunnel real projects have been completed, the design method is still deterministic [1]. Calculated loads imposed by ground directly act on shield tunneling then internal forces and deformation of tunneling lining can be obtained determinately. The effect of soil spatial variability on structural behavior of tunnel lining has received little attention so far [2]. Reliability design of tunnel lining cannot be applied without considering ground variation. Since Vanmarcke first introduced random field theory to analyze the spatial variability in

© Springer Nature Singapore Pte Ltd. 2018
D. Zhang and X. Huang (Eds.): GSIC 2018, *Proceedings of GeoShanghai 2018 International Conference: Tunnelling and Underground Construction*, pp. 451–459, 2018.
https://doi.org/10.1007/978-981-13-0017-2_45

1977, many works about the influence of soil spatial variability on geosystems have been done [3–6]. The results show that deformation and internal forces of those geosystems can be underestimated without considering the ground variation.

In this paper random field theory is employed to characterize ground spatial variability and Monte Carlo simulation is applied to calculated the distribution of internal forces and convergences of tunnel lining. This paper adopts commercial finite difference analysis code FLAC3D to model the structural performance of shield tunnel considering ground variation. There is no doubt that tunnel buried depth and tunnel diameter exert great influence on lining structural performance. In terms of soil parameters, it is widely accepted that elastic modulus and Poisson's ratio are the dominant parameters which influence the deformations of soils and embedded structures [3]. Furthermore, Poisson's ratio is believed to be less varied compared to elastic modulus. Consequently, elastic modulus random field is always simulated by random field for structural analysis of geotechnical system [2]. Apart from mean and coefficient of variance (COV), one of the key parameters for spatial variability is scale of fluctuation (SOF). Due to the depositional process, soils generally exhibit a stronger horizontal correlation than in vertical direction [7]. So vertical SOF is paid more attention to than horizontal SOF in this paper. From what has been discussed above, five parameters which are tunnel buried depth, tunnel diameter, mean, COV and vertical SOF of elastic modulus random field are chosen to see how they affect the structural performance of shield tunnel lining. The orthogonal test is employed to improve efficiency when do parameter studies.

This paper is structured as follows: first, set five levels of each parameter according to the real shield tunnel projects and literature review; second, design the orthogonal test and build finite difference numerical model in FLAC3D for different parameter groups; third, two dimensional random field for the elastic modulus are generated and Monte Carlo simulations are performed for each parameter group; Fourth, computation results are analyzed and reasonable conclusions are reached.

2 Orthogonal Test Design

This paper aims to study the influence of five chosen parameters on the internal forces and deformation of shield tunnel. In order to do parameter studies more efficiently, orthogonal test is employed to decrease the number of parameter combinations. According to the literature review and the experience from Shanghai shield tunnel projects, five levels of each parameter are set. The tunnel diameter (D) is set 6.2 m, 8 m, 11 m, 13 m and 15 m. The rest four parameters are tunnel buried depth (H), mean value of elastic modulus (E), COV of elastic modulus and vertical SOF of elastic modulus random field. D. Z. Gao in 1996 calculated the vertical SOF for Shanghai soil based on experiment data and he figured out that vertical SOF for Shanghai soil is around 1 meters [8]. So in this paper the vertical SOF value is set around 1 m to fit in with the real condition for Shanghai soil. There are some assumptions for orthogonal test design: (1) the correlation between any two of the five parameters is not considered. That is, the five parameters are independent from each other. Table 1 illustrates

Table 1. Levels for each parameter

D/m	6.2	8	11	13	15
H/m	10	15	20	25	30
E/MPa	4	8	12	16	20
COV	0.10	0.15	0.20	0.25	0.30
SOF/m	0.6	0.8	1.0	1.2	1.4

different levels for each parameter. Then according to the principles of orthogonal test, the experiment table is designed as follows.

3 Finite Difference Analysis

A shield tunnel embedded into spatially varied soil is considered in this paper. According to the orthogonal test design, finite difference numerical model is built in commercial software FLAC3D for each parameter group. Take group 10 in Table 2 as example to simply explain the model building process. For group 10, the diameter is 6.20 m and tunnel buried depth is 20.00 m. The lining thickness is 350 mm, which is commonly employed in Shanghai Metro Tunnel. The inter diameter of the segment is 5.5 m and the longitudinal ring width is 2 m for consistency with large diameter cases. Beam-spring model is used to consider the structural behavior of segmental ling and the joint bending stiffness is 1000 MN.m/rad. In commercial FLAC3D code, tunnel lining is modeled by means of shell element and the friction between lining and soil mass is not considered in this paper. As for material parameters of concrete lining, unit weight is 24.5 kN/m^2, the elastic modulus is 35.5 GPa and Poisson's ratio is 0.3.

The soil domain is set as 19.3 D in width and 10.2 D in depth to avoid boundary effect as shown in Fig. 1. The whole domain is made up of 1170 grid points and 585 zones. The plane strain is assumed for the longitudinal length is significant larger than the tunnel diameter. Since this paper focuses on the long term structural performance of tunnel lining, the drained condition is assumed for soils. Due to easy access to parameters, the elastic perfectly plastic soil model with Mohr-Coulomb yield criteria is widely used in numerical simulation, especially in random field analysis [9]. Thus, this paper also adopts Mohr-Coulomb model for soils. And parameters in this model are set as follow: Poisson's ratio, soil's unit weight, the effective cohesion and the internal friction angle are all held constant at 0.33, 20 kN/m^3, 30 kPa, 15° respectively in different cases, as those values are frequently used for Shanghai soil. As mentioned above, the elastic modulus of soil mass is spatially variable. In order to avoid the occurrence of negative value, lognormal distribution instead of norm distribution is employed here to characterize the variability of elastic modulus with mean value and coefficient of variance given by Table 1. Random fields of elastic modulus are generated using the Karhunen-Loève expansion [10] and this is done by commercial software MATLAB specifically. For each parameter group, Monte Carlo simulation is performed and the simulation time is N = 500. In the finite difference numerical model, the calculation will be stopped if the maximum unbalanced force is smaller than 500 N. Generally, the calculation step is about 15 thousand for each simulation.

Table 2. Orthogonal test table

Group	D/m	H/m	E/MPa	COV	SOF/m
1	15.00	20.00	16.00	0.15	1.20
2	13.00	15.00	20.00	0.25	1.40
3	6.20	10.00	4.00	0.10	0.60
4	13.00	10.00	16.00	0.20	1.00
5	8.00	15.00	16.00	0.30	0.60
6	15.00	15.00	12.00	0.10	0.80
7	13.00	20.00	4.00	0.30	0.80
8	15.00	25.00	20.00	0.20	0.60
9	15.00	10.00	8.00	0.30	1.40
10	6.20	20.00	12.00	0.20	1.40
11	8.00	20.00	20.00	0.10	1.00
12	6.20	15.00	8.00	0.15	1.00
13	11.00	15.00	4.00	0.20	1.20
14	13.00	30.00	12.00	0.15	0.60
15	8.00	10.00	12.00	0.25	1.20
16	13.00	25.00	8.00	0.10	1.20
17	11.00	30.00	16.00	0.10	1.40
18	6.20	25.00	16.00	0.25	0.80
19	15.00	30.00	4.00	0.25	1.00
20	6.20	30.00	20.00	0.30	1.20
21	8.00	25.00	4.00	0.15	1.40
22	8.00	30.00	8.00	0.20	0.80
23	11.00	20.00	8.00	0.25	0.60
24	11.00	25.00	12.00	0.30	1.00
25	11.00	10.00	20.00	0.15	0.80

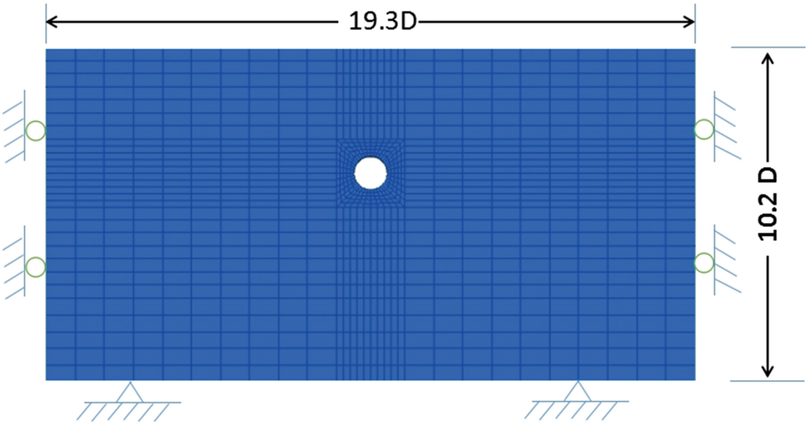

Fig. 1. Finite difference model and boundary conditions.

4 Computation Result Analysis

4.1 Influence of Mean Value of Elastic Modulus on Tunnel Deformation and Internal Forces

Ii is widely accepted that mean value of ground elastic modulus exerts large effects on tunnel deformation and internal forces. From the results of 25 groups calculation, we find that bending moment of tunnel crown and axial force of tunnel invert are usually the largest among all tunnel sections. What's more, tunnel horizontal convergences are always a little bit larger than vertical convergences. Thus in the following discussion, tunnel crown bending moment and invert axial force are mainly concerned. Figure 2 shows that horizontal convergence, vertical convergence and tunnel invert axial force are all linear with mean value of ground elastic modulus and the three values are decreasing as elastic modulus increases. Meanwhile, although crown bending moment decreases as elastic modulus increases, the linearity is not so obvious compared to other three indexes. Figure 3 gives the specific distribution of tunnel internal forces and convergences and they are all norm distribution according to K-S test. As the mean of elastic modulus decreases, crown bending moment and convergences are more variable

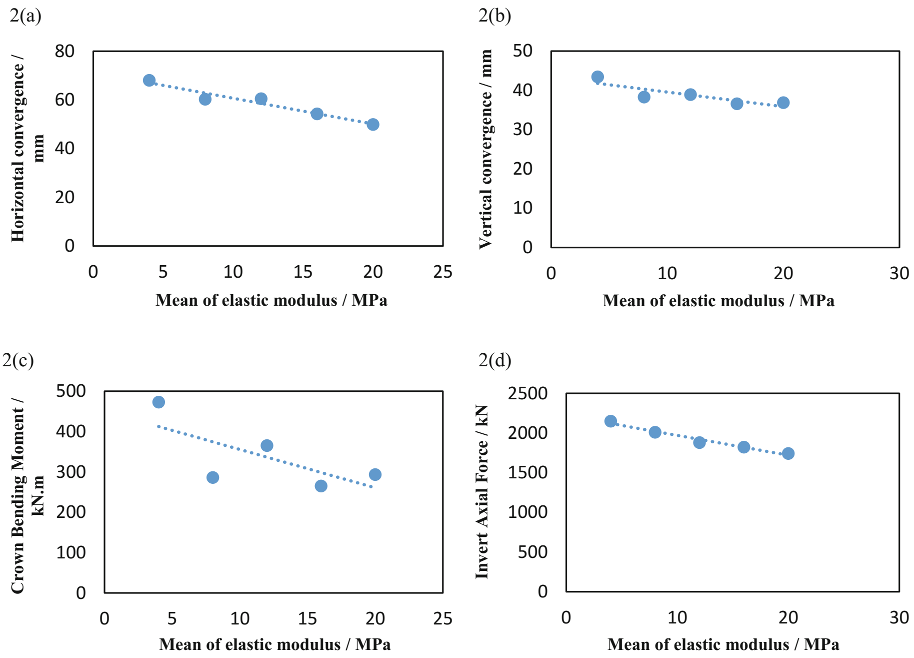

Fig. 2. Relationships between tunnel deformation, internal forces and mean value of ground elastic modulus: (a) horizontal convergence; (b) vertical convergence; (c) crown bending moment; (d) invert axial force.

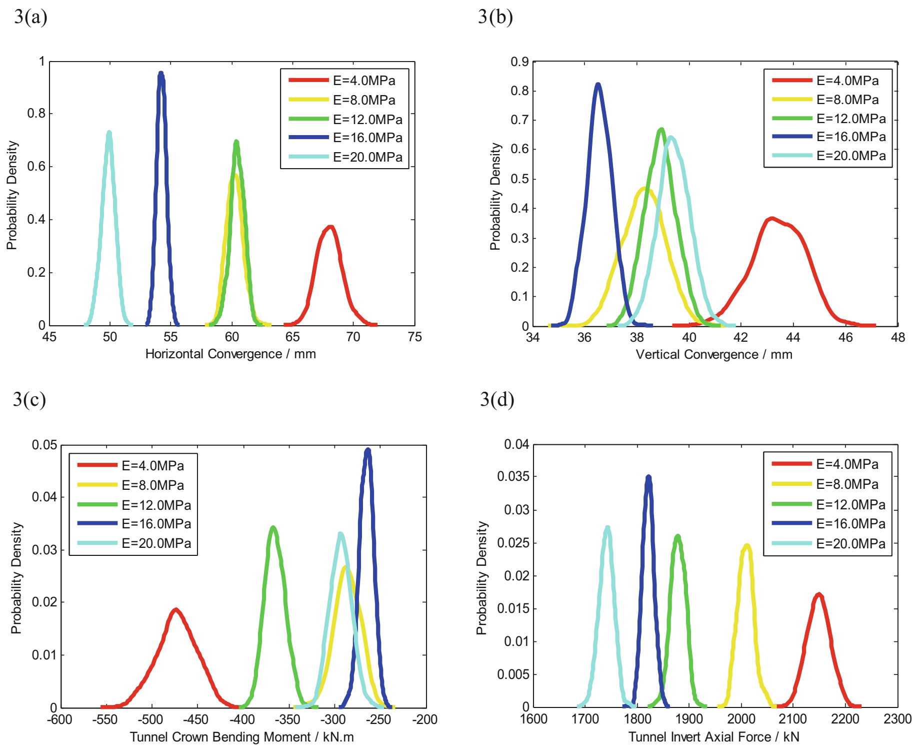
3(a)

3(b)

3(c)

3(d)

Fig. 3. Probability distribution of tunnel internal forces and deformation: (a) horizontal convergence; (b) vertical convergence; (c) crown bending moment; (d) invert axial force.

especially when elastic modulus is 4 MPa. Only tunnel invert axial force behaves relatively stable as elastic modulus decreases. Adversely, the variability of crown bending moment is the largest compared to other structural responses. When the elastic modulus is very small, mean value and COV are all large, meaning that tunnel internal forces and deformation could be unexpected huge, which is very disadvantage for lining structural performance.

4.2 Influence of COV of Elastic Modulus on Tunnel Deformation and Internal Forces

The ground in real projects are spatially variable and in this paper two dimensional elastic modulus random field are employed to simulate the ground spatial variety. It is generally accepted that coefficient of variance (COV) is one of the most important indexes in characterizing ground variety. Consequently, it is of great necessity to study how the COV of elastic modulus influence tunnel deformation and internal forces. Figure 4 shows the computation results of Monte Carlo simulation. In general, if the

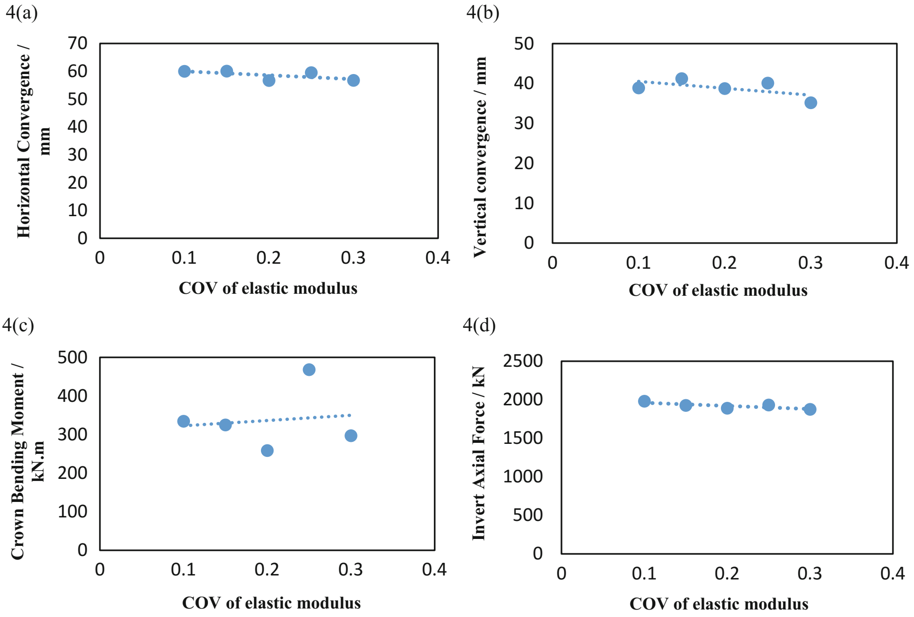

Fig. 4. Relationship between tunnel deformation, internal forces and COV of ground elastic modulus: (a) horizontal convergence; (b) vertical convergence; (c) crown bending moment; (d) invert axial force.

mean value of elastic modulus is given, tunnel deformation and axial forces are not sensitive to COV of elastic modulus, which can be known from Fig. 4(a), (b) and (d). But Fig. 4(c) reveals that bending moment is sensitive to COV of elastic modulus and the relationship between crown bending moment and COV of elastic modulus seems random. This randomness proves that the soil spatial variability could have a large impact on tunnel internal forces and this phenomenon cannot be figured out by deterministic method. In other words, random field theory is indeed a practical method to help us get better knowledge of soil spatial variability. Figure 5 shows the distributions of tunnel internal forces and deformation in different COV of soil elastic modulus. Tunnel horizontal and vertical convergence are notably more variable than in other cases as the COV of soil's elastic modulus increases. This illustrates that the variability of tunnel deformation is directly concerned with the spatial variability of soil elastic modulus. And Fig. 5 also proves that tunnel crown bending moment is most variable among all structural response indicators.

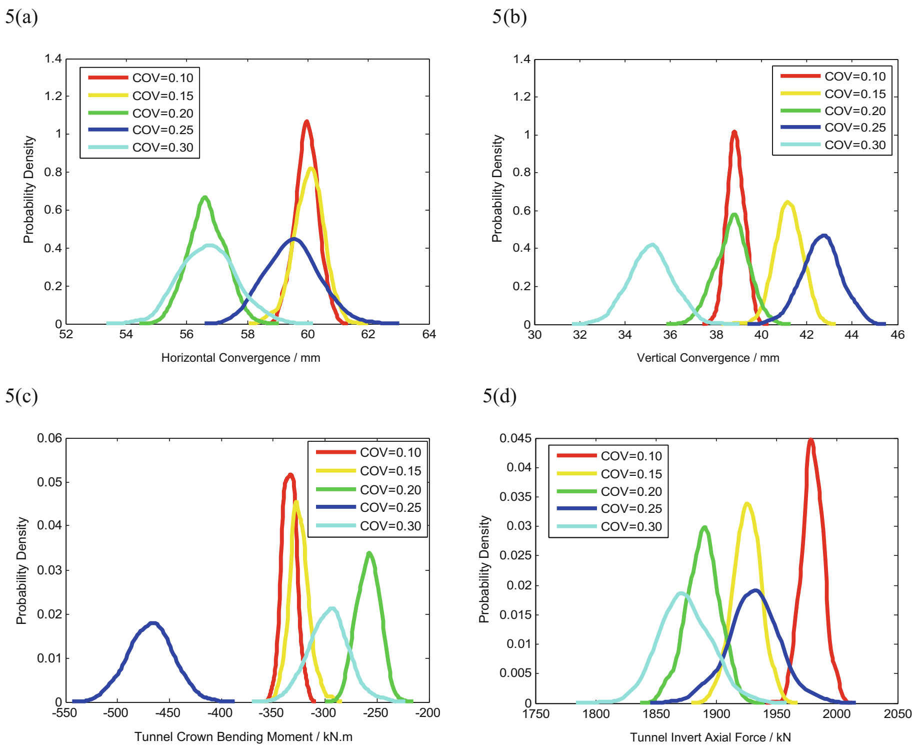

Fig. 5. Probability distribution of tunnel internal forces and deformation: (a) horizontal convergence; (b) vertical convergence; (c) crown bending moment; (d) invert axial force.

5 Conclusion

From what has been discussed above, reasonable conclusions can be arrived at as follows:

(1) Given a two dimensional elastic modulus random field, which the elastic modulus is lognormal distribution, the distribution of tunnel deformation and internal forces are all norm distributions according to K-S test. The variability of tunnel crown bending moment is the largest and invert axial force is the smallest among all internal forces and deformation indicators. The increasing of COV and decreasing of mean value of soil elastic modulus will increase the variability of tunnel internal forces and convergences.

(2) For a given parameter group in orthogonal test, tunnel horizontal convergence always larger than vertical convergence and tunnel invert axial force is the largest among all sections. Meanwhile, tunnel crown bending moment is the largest moment among all sections in most cases and for small tunnel diameter cases, tunnel invert bending moment can be larger than crown bending moment. Tunnel deformation and internal forces are almost negative linear with mean value of ground elastic modulus while they are not sensitive to COV of elastic modulus.

Acknowledgements. This study is substantially supported by the Natural Science Foundation Committee Program (No. 51608380, 51538009), by Shanghai Rising-Star Program (17QC1400300) and by Shanghai Science and Technology Comminttee Project (17DZ1204205). Hereby, the authors are grateful to these programs.

References

1. International Society of Tunnelling Association: Guidelines for the design of shield tunnel lining - Working Group No. 2. Tunn. Undergr. Space Technol. **2000**(3), 303–331 (2000)
2. Huang, H.W., Xiao, L., Zhang, D.M., Zhang, J.: Influence of spatial variability of soil Young's modulus on tunnel convergence in soft soils. Eng. Geol. **228**, 357–370 (2017)
3. Fenton, G.A., Griffiths, D.V.: Risk Assessment in Geotechnical Engineering. Wiley, Hoboken (2008)
4. Srivastava, A., Babu, G.L.S., Haldar, S.: Influence of spatial variability of permeability property on steady state seepage flow and slope stability analysis. Eng. Geol. **110**, 93–101 (2010)
5. Liu, Y., Lee, F.H., Quek, S.T., Chen, E.J., Yi, J.T.: Effect of spatial variation of strength and modulus on the lateral compression response of cement-admixed clay slab. Géotechnique **65** (10), 851–865 (2015)
6. Huang, H.W., Gong, W.P., Khoshnevisan, S., Juang, C.H., Zhang, D.M., Wang, L.: Simplified procedure for finite element analysis of the longitudinal performance of shield tunnels considering spatial soil variability in longitudinal direction. Comput. Geotech. **64**, 132–145 (2015)
7. Xiao, L., Huang, H., Zhang, J.: Effect of soil spatial variability on ground settlement induced by shield tunnelling. In: Geo-Risk 2017: Impact of Spatial Variability, Probabilistic Site Characterization, and Geohazards, GSP 284, Colorado (2017)
8. Gao, D.Z.: The design of safety index and its application in geotechnical engineering. Geotech. Investig. Surv. **01**, 1–6 (1996)
9. Mollon, G., Phoon, K.K., Dias, D., Soubra, A.H.: Validation of a new 2D failure mechanism for the stability analysis of a pressurized tunnel face in a spatially varying sand. J. Eng. Mech. **137**(1), 8–21 (2011)
10. Huang, S.P., Quek, S.T., Phoon, K.K.: Convergence study of the truncated Karhunen-Loeve expansion for simulation of stochastic processes. Int. J. Numer. Anal. Methods Geomech. **52** (9), 1029–1043 (2001)

A Shield Tunnel Model Based on Generalized-Node Solid-Shell and Spacial Joint Element

Lin Yifeng(✉)

Shanghai Investigation, Design & Research Institute, Shangai 200434, China
lyf@sidri.com

Abstract. In order to overcome the demerits of traditional beam(shell)-spring model and solid finite element model for shield tunnel lining, A new model based on generalized-node solid-shell and three dimensional joint element was introduced. The partition of unity-based finite element method was employed to establish a generalized-16 nodes hexahedron element to model tunnel lining, in which the element possess of three dimensional geometric and mechanic behavior and it's performance is greatly improved by high order local cover function in coarse mesh so the mesh generation process is evidently simplified. Based on the partition of unity-based finite element method and the theory of combinational elements a three dimensional combination joint element was also established which compose of surface contact elements for segment & longitudinal joint and embedded bolts. The new combination joint element can be used to simulate the details of bolts, interleaver and local contact behaviors and the mesh generation process is comparatively convenient. The two present elements were combined to establish a new shield tunnel structure model. In the end the new model was employed to analysis a typical shield tunnel lining with segment seams in stagger.

Keywords: Shield tunnel lining · Generalized finite element · Solid-shell Joint element · Contact element

1 Introduction

The conventional model of shield tunnel lining can be divided into beam-spring, shell-spring and three-dimensional solid finite element model. In beam-spring model, beam element is used to model the segment, and the joint is modeled by springs [1]. The beam-spring model can reflect the main mechanical characteristics of the shield tunnel lining and is simple. The main deficiency of this model is due to the use of the plane model, which can not reflect the three-dimensional mechanical characteristics of segment structure. Additionally spring element cannot accurately account for the important considerations such as bolts, interleaver and contact states. Shell-spring model simulates the segment with shell element [2], which can be used for three-dimensional analysis. However shell element can not accurately simulate the geometric and mechanical characteristics of the segment structure in thickness direction. The deficiency of joints for shell-spring model also remains the same as

© Springer Nature Singapore Pte Ltd. 2018
D. Zhang and X. Huang (Eds.): GSIC 2018, *Proceedings of GeoShanghai 2018 International Conference: Tunnelling and Underground Construction*, pp. 460–467, 2018.
https://doi.org/10.1007/978-981-13-0017-2_46

beam-spring model. Theoretically, the conventional 3-D solid finite element method can be used to precisely model the segment, bolt and contact states and carry out mechanical analysis of the 3-D nonlinear discontinuous deformation [3]. However, as the conventional FEM is a mesh-dependent numerical method, the computational accuracy is heavily depended on mesh density. As the lining structures of shield tunnel is a complex and composite structure composed of segments, bolts, interleaver materials, a complex finite element mesh with high density is needed, which is a time consuming task. So it is needed to develop a new three dimensional solid shield tunnel model with simple mesh.

Generalized FEM based on the unity-partition method is a new FEM proposed by Babuska et al. [4]. The solution field is coved with finite covers in the Partition of Unity-Based Finite Element method (PU-Based FEM). Local approximate spaces defined in separate local covers are stick together with partition of unity functions, which constitutes global approximate spaces of PU-Based FEM. The independence of local space from element mesh makes the global spaces independent from mesh, which indicates that global estimative precision can be enhanced by improvement of local space instead of mesh modification. This new scheme of PU-Based FEM affords a powerful resort to build high-performance element. PU-Based FEM is used to develop new shell/plate element with no special treatments for fulfilling the Kirchhoff condition, C-1 displacement continuity and shearing/membrane locking [5–8]. In this paper, based on the advantages of the generalized finite element method and the characteristics of the shield tunnel structure, a 3-D generalized solid model of shield tunnel including segment and joint is established. Based on high order polynomial function as local cover function of generalized finite element, a 16-nodes hexahedral generalized solid shell element Ghex16 is established to simulate the lining segment and a generalized 12-nodes contact element is used to simulate the segment longitudinal seam and annular contact. Based on element combination ideas a generalized implicit connection bolt finite element is also established.

2 Generalized Solid-Shell and 3-D Joint Model

2.1 Basic Principle of Generalized FEM

In Generalized FEM based on the unity-partition method, finite covering technique is used to discretize the solution domain. Firstly the local coverage function is constructed according to the characteristics of the problem, and the definition of the local coverage function does not depend on the finite element mesh. Then the finite element shape function is used as the unity-partition function, and the local coverage functions are weighted to sum up to obtain the whole approximation function. In generalized FEM, the finite element mesh is only used to construct the unity-partition function, while the local coverage function is independent of the mesh. Therefore, the solution accuracy can be improved by increasing the accuracy of the local coverage function instead of increasing the mesh density of the finite element, or by using a high order local cover function which can achieve a higher accuracy in poor grid conditions. By using the generalized finite element theory, a new element with high performance can be built up in the framework of conventional FEM.

2.2 Generalized Solid-Shell Element Ghex16

To adapt to the characteristics that the plane of the plate is larger than the thickness and the surface of the shell is curved, a 16-nodes hexahedron element is used to establish generalized solid shell element Ghex16. Only one layer is arranged in the thickness direction, the shape, node, and face number of the element are defined as shown in Fig. 1.

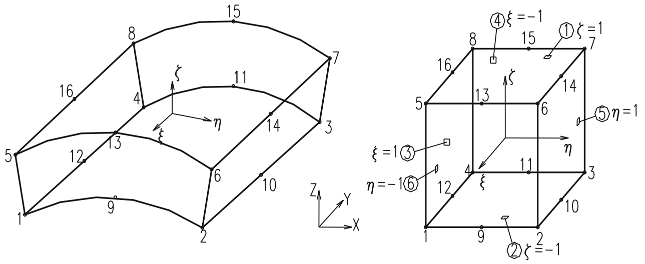

Fig. 1. Geometry of generalized solid-shell Ghex16

Unity Partition Function of Element Ghex16

The shape function φ_i of conventional 16 nodes hexahedron element Thex16 is used as the unity partition function.

Local Coverage Function of Element Ghex16

A 1st-order complete polynomial function is applied as the local coverage function as following:

$$\mathbf{u}_i^{LC} = \mathbf{F}_i \mathbf{U}_i \tag{1}$$

$$\mathbf{F}_i = \begin{bmatrix} 1 & 0 & 0 & x_i & 0 & 0 & y_i & 0 & 0 & z_i & 0 & 0 \\ 0 & 1 & 0 & 0 & x_i & 0 & 0 & x_i & 0 & 0 & z_i & 0 \\ 0 & 0 & 1 & 0 & 0 & x_i & 0 & 0 & x_i & 0 & 0 & z_i \end{bmatrix} \tag{2}$$

$$\mathbf{U}_i = \begin{pmatrix} a_{i,1} & a_{i,2} & \cdots & a_{i,11} & a_{i,12} \end{pmatrix}^T \tag{3}$$

Unity Generalized Shape Function

According to the generalized finite element theory, the global displacement function of generalized element is the sum of products of unity partition function and local coverage function on each local covering.

$$\mathbf{u}^{\mathrm{e}} = \begin{Bmatrix} u \\ v \\ w \end{Bmatrix} = \begin{bmatrix} \mathbf{N}_1 & \mathbf{N}_2 & \cdots & \mathbf{N}_{15} & \mathbf{N}_{16} \end{bmatrix} \begin{Bmatrix} \mathbf{U}_1 \\ \mathbf{U}_2 \\ \vdots \\ \mathbf{U}_{15} \\ \mathbf{U}_{16} \end{Bmatrix} = \mathbf{NU} \tag{4}$$

$$\mathbf{N}_i = \varphi_i \mathbf{F}_i \tag{5}$$

After the generalized shape function is established, the generalized element stiffness matrix and load array can be obtained by using the same analysis procedure as the traditional FEM.

Validation for the Performance of Ghex16

A cylindrical shell fixed at both ends, shell outer radius is 2.75 m, thickness is 0.35 m and width is 1.50 m, corresponding center angle is 90°. The elastic modulus and posisson's ratio is 21000 MPa and 0.1678. a uniform pressure of 200 kPa distributed on the top of shell. The midpoint deflections under different mesh density for the Ghex16 and Thex16 is shown is Table 1 which indicates that Ghex16 has significantly higher performance than Thex16, for instance under very loose mesh density of 2 × 1 × 1, Ghex16 nearly gets the accuracy value while the Thex16 reaches the same at 6 × 1 × 1.

Table 1. Calculation results of cylinder shell

Mesh density	2 × 1 × 1	4 × 1 × 1	6 × 1 × 1	Accuracy solution
Thex16	−2.971	−3.947	−3.982	−4.010
Ghex16	−3.992	−4.008	−4.010	

2.3 Generalized Special Joint Element

Generalized Contact Surface Element

Generalized Contact Surface Element Stiffness Matrix

Based on Ghex16 as segment element, 12-nodes surface-to-surface generalized contact element Gsszc12 is used to simulate the longitudinal joint contact surface as shown in Fig. 2.

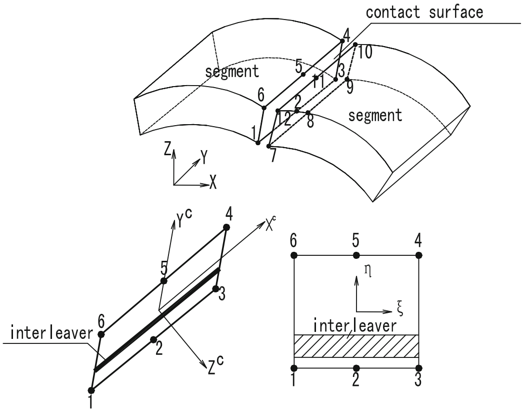

Fig. 2. Geometry of generalized segments contact element Gsszc12

The conventional 6-nodes plane element shape function is used as unity partition function and 1-st order complete polynomial is employed for the local coverage function. The strain of Gsszc12 can be obtained as follows.

$$\boldsymbol{\varepsilon}=\begin{Bmatrix} \varepsilon_x \\ \varepsilon_y \\ \varepsilon_z \end{Bmatrix} = [\mathbf{N}_1 \quad \cdots \quad \mathbf{N}_6 \quad -\mathbf{N}_1 \quad \cdots \quad -\mathbf{N}_6][\mathbf{U}_1 \quad \cdots \quad \mathbf{U}_6 \quad \mathbf{U}_7 \quad \cdots \quad \mathbf{U}_{12}]^T \\ = \mathbf{B}_\mathrm{c}\mathbf{U} \tag{6}$$

The stiffness matrix of Gsszc12:

$$\mathbf{K}_\mathrm{c} = \int\limits_\mathrm{A} \mathbf{B}_\mathrm{c}^T \mathbf{T}^T \mathbf{D}_\mathrm{c} \mathbf{T} \mathbf{B}_\mathrm{c} dA \tag{7}$$

The stiffness of the contact element consists of two parts: interleaver contact and concrete surface contace as follows.

$$\mathbf{K}_\mathrm{c} = \mathbf{K}_\mathrm{L} + \mathbf{K}_\mathrm{s} \tag{8}$$

The idea of combinational elements and subregional integral of element stiffness matrix is employed to incorporated the two parts of stiffness into Ghex16 [9].

The Contribution of Interleaver Stiffness

The contribution of the interleaver stiffness to the contact element can be obtained as follows:

$$\mathbf{K}_\mathrm{L} = \sum_i^m \sum_j^n \mathbf{B}_\mathrm{c}^T \left(\xi_i^L \to \xi_i^n, \eta_j^L \to \eta_j^n\right) \mathbf{T}^T \mathbf{D}_\mathrm{L} \mathbf{T} \mathbf{B}_\mathrm{c} \left(\xi_i^L \to \xi_i^n, \eta_j^L \to \eta_j^n\right) |\mathbf{J}_\mathrm{L}| w_i w_j \tag{9}$$

ξ_i^L, η_j^L represent the integral point of the interleaver area, and $\xi_i^L \to \xi_i^n$, $\eta_i^L \to \eta_i^n$ represent the coordinates of the ξ_i^L, η_j^L in natural coordinates system.

Generalized Implicit bolt Joint Element

To connect bolt and segment, the implicit modeling technique is employed. The basic idea of this procedure is coupling the contribution of bolt stiffness into segment by displacement interpolation instead of generation a common node between bolt and segment.

Element Stiffness Matrix of Generalized Implicit Bolt Joint

As shown in Fig. 3, the virtual displacement $\mathbf{u}^{\mathrm{e}*}$ of two end points of bolt can be interpolate by the segments as follows

$$\mathbf{u}^{\mathrm{b}*} = \mathbf{N}_\mathrm{b} \mathbf{u}^{\mathrm{e}*} \tag{10}$$

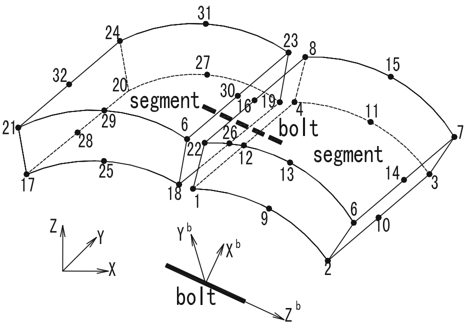

Fig. 3. Geometry of generalized hidden-bolt joint element

where $\mathbf{N}_b$ is the value of segment generalized shape function at two point of the bolt. The virtual strain of bolt $\boldsymbol{\varepsilon}^{b*}$ in its local coordinate system is as follows:

$$\boldsymbol{\varepsilon}^{b*} = \left(\varepsilon_{bx} \quad \varepsilon_{by} \quad \varepsilon_{bz} \right)^T = \frac{1}{L}\mathbf{B}_b\mathbf{T}\mathbf{u}^{\mathbf{b}*} \tag{11}$$

where, L is bolt length, **T** is transformation matrix from the global coordinate system to the bolt local coordinate system, and $\mathbf{B}_b$ is bolt strain matrix.

According to the principle of virtual work, the contribution of bolts to the stiffness of segment elements can be obtained as follows:

$$\mathbf{K}_{be} = \frac{A}{L}(\mathbf{N}_b)^T\mathbf{T}^T(\mathbf{B}_b)^T\mathbf{D}_b\mathbf{B}_b\mathbf{T}\mathbf{N}_b \tag{12}$$

3 Tunnel Examples Analysis

3.1 Primary Parameters

A 45° stagger-jointed segment shield tunnel with buried depth of 20.10 m is shown in Fig. 4. Five lining rings are modeled by the present generalized solid-shell and 3-D joint model to get segment deflections and bolt force.

3.2 Calculation Results Analysis

Segment Deformation

The calculation results show that there exist great deflection differences between adjacent lining rings due to the shearing-effect. The maximum vertical displacements of the lining rings occurs near the top of the tunnel, but the values of the adjacent rings are different. The first, third and fifth ring are 8.1 mm and appears at 80° position. The second and fourth ring are 7.3 mm and appear at 90° position. The maximum

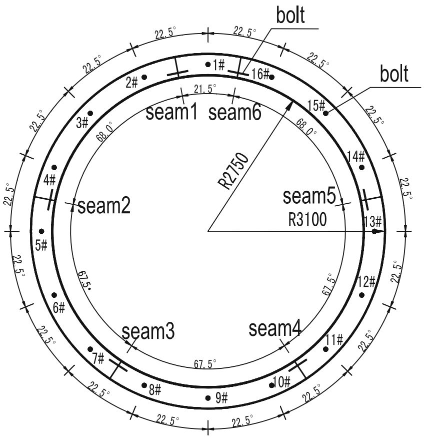

Fig. 4. Geometry of shield tunnel lining ring

horizontal displacements appears at the horizontal diameter of the tunnel. The first, third, fifth ring are 2.05 mm, and the second and fourth ring are 1.92 mm.

Joint Opening

The longitudinal joint opening is shown in Table 2. The positive and negative opening indicates the inside and outside opens respectively.

Table 2. Opening of longitudinal gaps for segment joints (mm)

	Seam 1	Seam 2	Seam 3	Seam 4	Seam 5	Seam 6
1st, 3rd, 5th ring	0.49	0.43	−1.73	0.14	0.33	−1.97
2nd, 4th ring	0.41	−1.63	−0.82	0.75	−2.08	0.28

Circumferential Bolt Force

The Circumferential bolt tension are shown in Table 3.

Table 3. Tensive force of bolts for segment joints (kN)

	Seam 1	Seam 2	Seam 3	Seam 4	Seam 5	Seam 6
1st, 3rd, 5th ring	81.8	68.2	/	5.9	67.4	/
2nd, 4th ring	58.0	/	/	163.2	/	48.6

4 Conclusion

Based on the generalized FEM and the characteristics of shield tunnel lining, a generalized solid-shell 3D joint model is proposed. The primary research results is following:

A 16-nodes hexahedral generalized element Ghex16 for solid shell analysis is derived based on unity-partition generalized FEM. The Ghex16 element has significantly higher performance than the traditional Thex16 element. The present element behave 3-D geometry and mechanical properties and can be used to model shield tunnel segment.

A generalized contact element is developed to simulate the contact behavior of segments. The effect of interleaver contact stiffness is considered with the idea of partition integration instead of interleaver mesh generation, which greatly reduces the modeling difficulty.

Based on the idea of implicit bolt, the tensile and shear stiffness of the bolt are directly coupled into segment stiffness instead of separated bolt mesh generation, which remarkably simplify the mesh procedure.

Based on load-structure method, The present Ghex16 element and 3D generalized joint element was composed to established a shield tunnel structure calculation model and the corresponding simulation code is developed. A typical staggered joint shield tunnel was calculated with the present model and the lining deflection, joint opening and bolts force was studied.

References

1. Murakami, H., Koizami, A.: Study on load bearing capacity and mechanics of shield segment ring. Proc. Jpn. Soc. Civ. Eng. **2**(4), 103–115 (1978)
2. Zhu, W., Huang, Z., Liang, J.: Studies on shell-spring design model for segment of shield tunnels. Chin. J. Geotech. Eng. **28**(8), 940–948 (2016)
3. Zhang, H., Yin, Z., Zhu, J., et al.: Three dimensional FEM simulation of shield driven tunnel lining during construction stage. Rock Soil Mech. **26**(6), 990–994 (2005)
4. Melenk, J., Bubska, I.: The partition of the unity finite element method: basic theory and application. Comput. Methods Appl. Mech. Eng. **139**, 289–314 (1996)
5. Nguyen-Thanh, N., Valizadeh, N., Nguyen, M.N., et al.: An extended isogeometric thin shell analysis based on Kirchhoff-Love theory. Comput. Methods Appl. Mech. Eng. **284**, 265–291 (2015)
6. Nguyen-Thanh, N., Zhou, K., Zhuang, X., et al.: Isogeometric analysis of large-deformation thin shells using RHT-splines for multiple-patch coupling. Comput. Methods Appl. Mech. Eng. **316**, 1157–1178 (2017)
7. Areias, P., Rabczuk, T., Msekh, M.A.: Phase-field analysis of finite-strain plates and shells including element subdivision. Comput. Methods Appl. Mech. Eng. **312**(C), 322–350 (2016)
8. Rabczuk, T., Areias, P., Rabczuk, T.: A meshfree thin shell method for non-linear dynamic fracture. Int. J. Numer. Methods Eng. **72**(5), 524–548 (2007)
9. Xu, X., Ling, D.: Series of degenerated solid FA elements. Solid Mech. (Comput. Mech. Spec.) **22**, 1–12 (2001)

Numerical Validation of a New Testing Setup for Mechanical Test of Tunnel Lining Joints

Z. X. Zhang[1,2], W. Liu[1,2], X. Huang[1,2(✉)], and Q. W. Zhuang[3]

[1] Department of Geotechnical Engineering, College of Civil Engineering,
Tongji University, Shanghai 200092, People's Republic of China
xhuang@tongji.edu.cn
[2] Key Laboratory of Geotechnical Engineering, Ministry of Education,
Tongji University, Shanghai 200092, People's Republic of China
[3] Shanghai Shield Research Center Co. Ltd., Shanghai, China

Abstract. When designing a shield tunnel, there is often a need to carry out mechanical tests on tunnel lining joints to obtain joint stiffness. As tunnel excavation goes deeper, the moment and axial force acting on the lining segments increase, which requires a more rigid backup frame and a stronger foundation for the traditional testing setup. A new testing setup, named as Compression Steel Butterfly (CSB), was developed. CSB is biaxially symmetric in geometry, consisting of two steel frames connected by horizontal tensile pulling rods passing through the mounting holes of hollow hydraulic ram jacks. Using CSB, different combinations of axial force and bending moment can be effectively and conveniently imposed on the testing segments by varying the magnitudes of pulling force of each pair of pulling rods. Since the jacking forces are self-balanced, there is no need for a strong backup frame. A series of finite element simulations were carried out to validate the loading capacity and correctness of load transmission for the new testing setup. It is shown that the axial force and moment obtained in numerical simulations agree well with the theoretical values.

Keywords: Segment joint · Mechanical test · Finite element simulation

1 Introduction

Nowadays in urban areas, the underground space is crowded with a variety of facilities, such as foundations of over-ground structures, metro and sewage tunnels, and pipelines, which has made the mechanized shield tunnelling method one of the most popular tunnelling approaches [1, 2]. The stability of a shield tunnel lining highly depends on the water and soil conditions, fabrication pattern, mechanical state, properties and distribution of joints [3]. When designing shield tunnel lining, the joint is often treated as elastic pins characterized by different types of springs, e.g., axial, shear and rotation [4]. The stiffnesses of joint springs control the overall deformation and force transmission of segmental lining structures. Joint stiffnesses are highly variable and can be influenced by a number of factors including section size, contact condition between bearing surfaces of adjacent segments, bolt type, position of bolt holes, pre-tightening stress and loading conditions [3, 5]. Due to the high variability, a reliable way to

© Springer Nature Singapore Pte Ltd. 2018
D. Zhang and X. Huang (Eds.): GSIC 2018, *Proceedings of GeoShanghai 2018 International Conference: Tunnelling and Underground Construction*, pp. 468–476, 2018.
https://doi.org/10.1007/978-981-13-0017-2_47

determine joint stiffnesses is to carry out full-scale or model tests [3, 6]. In some cases, the testing segments are simplified as flat beams [7]. Usually, the segmental joint tests were conducted through two-point bending tests as shown in Fig. 1 [3, 8].

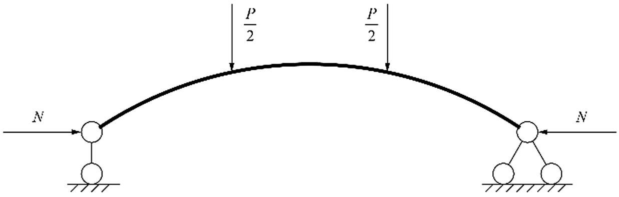

Fig. 1. Schematic illustration of two-point bending test setup

Recently, as the expansion of cities and development of advanced tunneling technology, shield tunnel excavation has gone increasingly deeper. This increase of buried depth indicates extremely high water-soil pressures, which makes two-point bending test setup that requires high rigidity of the backup frame and a strong foundation inadequate and uneconomic.

The design and numerical validation of a novel testing setup are presented. The theoretical consideration of the new testing setup will be introduced first. The loading capacity of the testing setup is then verified through finite element modelling. Finally, a series of numerical validation simulations on flat beam are performed to confirm its correctness in force and moment transmission.

2 Design of the New Testing Setup

2.1 Theoretical Consideration

In a real lining ring, segments bear axial force, bending moment and shear force at the same time. The shear force is usually neglected in the joint model test [3, 5]. To directly generate axial force and bending moment at the boundary ends of the testing segments similar to the real mechanical state, a new testing setup is designed. The mechanical model of the new testing setup is shown in Fig. 2. In the testing setup, the testing segments are clamped by steel frames at both ends. Axial force and bending moment are applied to the segments through steel frames. To maintain the overall stability, the testing setup has to lie on the ground rather than stand up. Axial force (N_0) and bending moment (M_0) at the ends of the testing segment can be calculated with Eq. 1.

$$\begin{cases} N_0 = \sum F_i^U + \sum F_i^L \\ M_0 = \sum F_i^U l_i^U + \sum F_i^L l_i^L \end{cases} \tag{1}$$

After N_0 and M_0 have been determined, the distributions of axial force (N) and bending moment (M) along the testing segments can be derived.

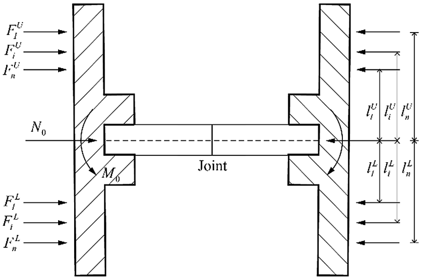

Fig. 2. Schematic illustration of the new testing setup

2.2 Design of the Testing Setup

The configuration of the testing setup is illustrated in Fig. 3. Two identical steel frames, connected by horizontal tensile pulling rods passing through the mounting holes of six sets of hollow hydraulic ram jacks, form the new testing setup. The new setup is in a shape of butterfly with the two steel frames acting as wings, and thus is named as Compression Steel Butterfly (CSB). The steel frame, with seven layers of paralleled steel rib plates, is 4.5 m in length and 1.5 m in height. The width of the rib plates increases linearly from 100 mm at the two ends to 750 mm close to the middle of the steel frame. Four replaceable steel pads are used to adapt to segments with different size. The horizontal loads are driven by six layers of hollow hydraulic ram jacks. The hollow hydraulic ram jacks pull the two steel frames against each other, generating a self-balanced system. Details of the new setup can be found in Fig. 3. Equation 1 can be expressed as follows:

$$\begin{cases} N_0 = F_1 + F_2 + F_3 + F_4 + F_5 + F_6 \\ M_0 = F_1 l_1 + F_2 l_2 + F_3 l_3 - F_4 l_4 - F_5 l_5 - F_6 l_6 \end{cases} \tag{2}$$

3 Numerical Validation of CSB

To confirm CSB's loading capacity and correctness in transferring the required internal forces/moment throughout the testing segment, a series of FE numerical simulations were carried out. 3D FE models were created in ABAQUS (version 6.14) [9].

3.1 Loading Capacity of CSB

Figure 4(a) illustrates the configuration of the capacity validation model. Due to symmetry, only one of the two steel frames was picked out for data analysis. 3D FE model of the same size illustrated in Sect. 2 was built. To simplify simulation, some of unimportant holes (holes for tensile pulling rods, etc.) that will not largely change the capacity of the whole model were neglected. Due to the high irregularity of the model,

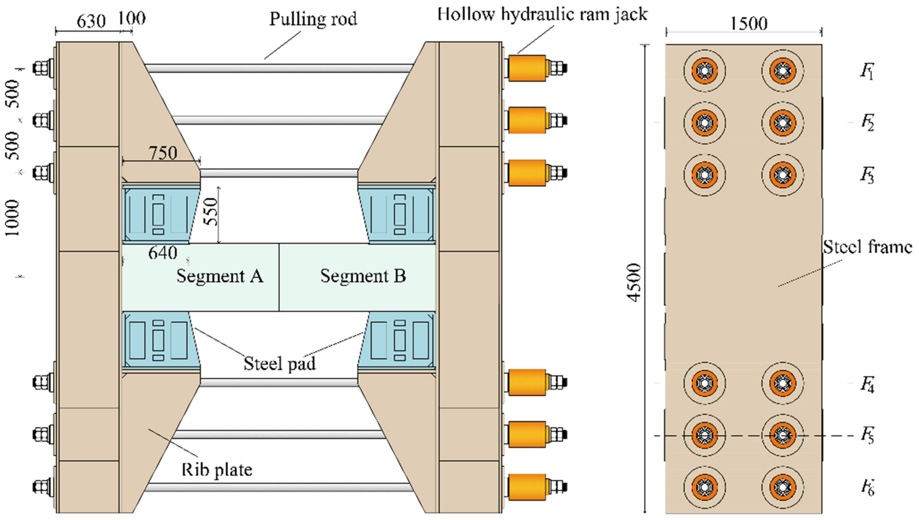
630
100
Pulling rod
Hollow hydraulic ram jack
1500
500
500
1000
750
550
640
Segment A
Segment B
Steel pad
Rib plate
4500
Steel frame
F_1
F_2
F_3
F_4
F_5
F_6

(a) Top view (b) side view

Fig. 3. Configuration of the new testing setup (Unit: mm)

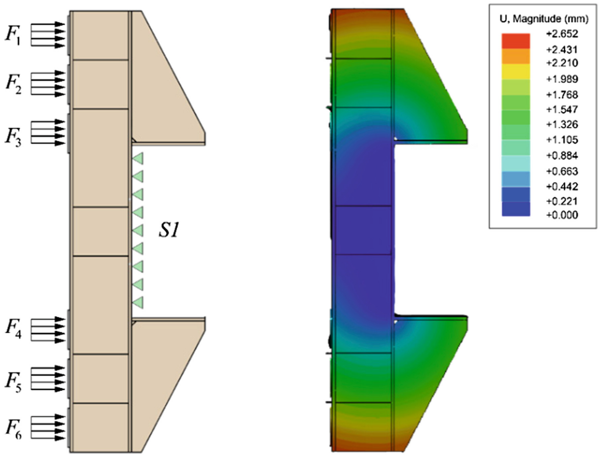

(a) numerical model of the steel frame (b) contour of deflection

Fig. 4. Loading capacity of the testing setup

10-node quadratic tetrahedron(C3D10) elements were used to generate model meshes. The element type and material properties of the steel frame are presented in Table 1.

The self-weight of the frame was ignored as the testing setup lies horizontally. Twelve uniform pressures whose resultant force are F_i ($i = 1 - 6$) were applied to simulate the pressures imposed by the 6 pairs of hollow hydraulic ram jacks. F_i equals

Table 1. Element type and material properties

Model part	Element type	Density (kg/m^3)	Young's modulus (GPa)	Poisson's ratio	Yield stress (MPa)
Steel frame	C3D10	7850	206	0.28	295

to 1500 kN, which corresponds to a capacity of 150 ton of each jack. Horizontal displacements of the interface between the steel frame and steel pads and the interface between the steel frame and the testing segments, are fixed to keep the frame balanced.

3.2 Load Transmission Correctness of CSB

Figure 5 illustrates the configuration of the load transmission correctness validation model. The validations were performed on a flat concrete beam which has a rectangular cross-section of 0.65 m × 1.5 m and is 3.0 m in length, containing no joint. Steel panels (0.65 m in length, 1.5 m in width, 20 mm in thickness) were cast onto the inner and outer surface of the flat beam in the clamped area to avoid crushing of concrete due to stress concentration.

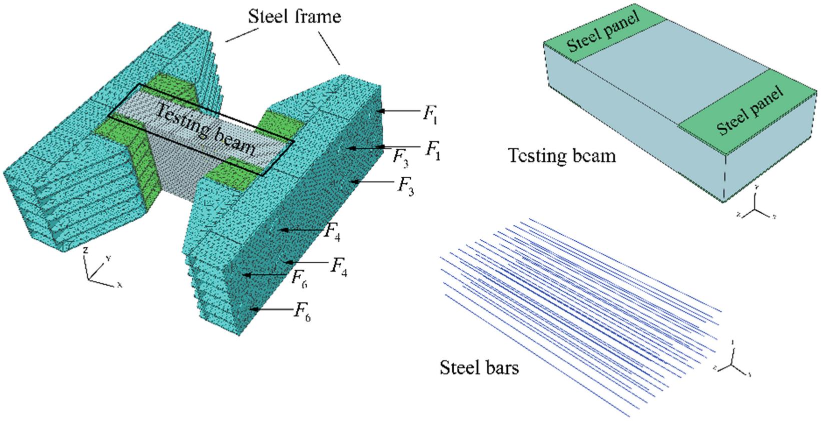

Fig. 5. Configuration of the numerical model

The element types, material properties of different model parts and contact conditions are presented in Tables 2 and 3. Steel and concrete were treated as elastic-perfectly-plastic materials following [3]. The pulling rods were not simulated, and the horizontal forces were imposed directly onto the frame.

Table 2. Element type and material properties

Model part	Element type	Density (kg/m^3)	Young's modulus (GPa)	Poisson's ratio	Yield stress (MPa)
Concrete	C3D8	2850	360	0.2	38.5
Steel panel	C3D8	7850	206	0.28	295
Reinforcing Bar	T3D2	7850	210	0.28	360
Steel frame	C3D10	7850	206	0.28	295

Table 3. Contact conditions between different material parts

Contact parties	Contact type
Concrete-reinforcing bar	Embedded
Concrete-steel box & steel box-steel frame	Hard contact, friction ($\mu = 0.15$)
Concrete-steel panel	Tie

The self-weight of the frame and beam was ignored as they lie horizontally. To simplify calculation, the second (F_2) and fifth (F_5) pairs were removed. Then, Eq. 2 can be expressed as follows:

$$\begin{cases} N_0 = F_1 + F_3 + F_4 + F_6 \\ M_0 = F_1 l_1 - F_6 l_6 \end{cases} \tag{3}$$

Two loading scenarios were considered including: (a) axial compression test, where no moment is generated at the boundary ends of the testing segment; (b) bias compression test, where the axial force N is fixed at 4000 kN, while the bending moment at the boundary ends of the testing segment was increased stepwisely from 0 to 1600 kN·m by changing the combinations of the horizontal forces (F_1, F_3, F_4 and F_6). The loading grades for the axial compression test and the bias compression test are listed in Tables 4 and 5, respectively.

Table 4. Applied load grades for axial compression test

Grade	1	2	3	4	5	6	7	8
N (kN)	500	1000	1500	2000	2500	3000	3500	4000

Table 5. Applied load grades for bias compression test (N = 4000 kN)

Grade	1	2	3	4	5	6	7	8	9
M (kN·m)	0	200	400	600	800	1000	1200	1400	1600

3.3 Numerical Results

Loading Capacity of CSB

Contour of deflection illustrating the deformation of the frame is shown in Fig. 4(b). It can be found that when all the hollow hydraulic ram jacks reach their full capacities, the maximum deflection at the two ends of the steel frame is smaller than 2.65 mm, which corresponds to a deflection angle of 0.07° for the cantilevered arms. This level of deflection can be negligible.

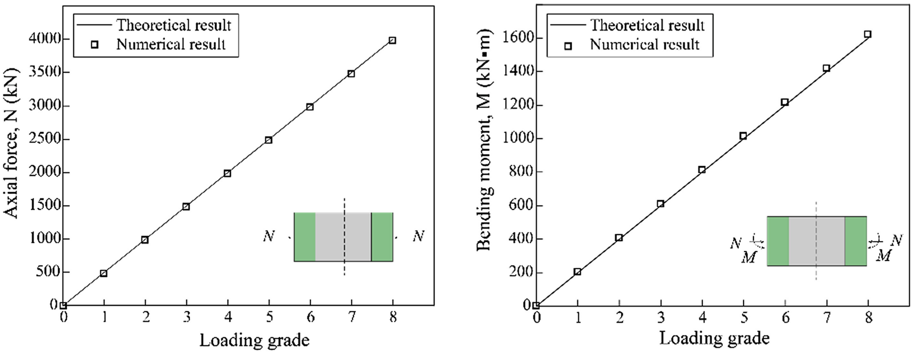

(a) axial force (axial compression) (b) bending moment (bias compression)

Fig. 6. Comparing numerical internal forces in the middle section at different loading grades with theoretical values.

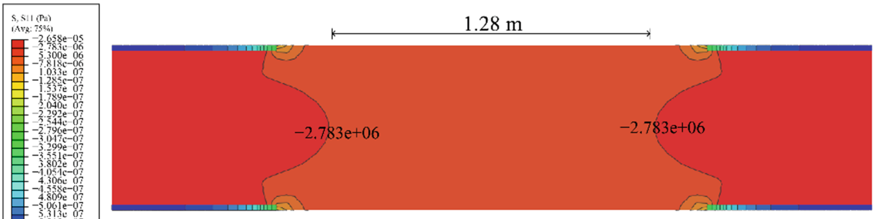
S, S11 (Pa)
(Avg: 75%)
−2.658e+05
−2.783e+06
−5.300e+06
−7.818e+06
−1.033e+07
−1.285e+07
−1.537e+07
−1.789e+07
−2.040e+07
−2.292e+07
−2.544e+07
−2.796e+07
−3.047e+07
−3.299e+07
−3.551e+07
−3.802e+07
−4.054e+07
−4.306e+07
−4.558e+07
−4.809e+07
−5.061e+07
−5.313e+07
−5.565e+07
−5.816e+07
−6.068e+07
1.28 m
−2.783e+06
−2.783e+06

(a) Axial compression

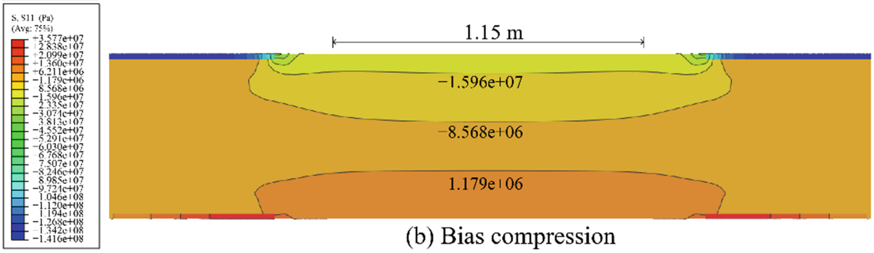
S, S11 (Pa)
(Avg: 75%)
+3.577e+07
+2.838e+07
+2.099e+07
+1.360e+07
+6.211e+06
−1.179e+06
−8.568e+06
−1.596e+07
−2.335e+07
−3.074e+07
−3.813e+07
−4.552e+07
−5.291e+07
−6.030e+07
−6.768e+07
−7.507e+07
−8.246e+07
−8.985e+07
−9.724e+07
−1.046e+08
−1.120e+08
−1.194e+08
−1.268e+08
−1.342e+08
−1.416e+08
1.15 m
−1.596e+07
−8.568e+06
1.179e+06

(b) Bias compression

Fig. 7. Stress contours along the longitudinal direction of the flat beam

Load Transmission Correctness of CSB

Axial force and bending moment were calculated in middle section of the beam. As Fig. 6 shows, the numerical simulation results are almost identical to the theoretically predicted values.

Figure 7 illustrates the contours of stress in the longitudinal direction of the flat beam in axial and bias compression tests. The unaffected length, where stress changing rate is below 1% in the longitudinal direction, is marked in Fig. 7. It can be inferred that the stress distribution in the section away from the boundaries agrees with plane cross-section assumption. This makes joint mechanical test, in which behaviors of joint are the main concern, calculable and feasible

4 Conclusion

This paper presented the design and numerical validation of a new testing setup for the mechanical test of tunnel lining joints.

A new testing setup named as 'Compression Steel Butterfly' (CSB) is designed considering the real segmental mechanical state and the need of deep-buried tunnel. The CSB is a self-balanced system consisting of two identical steel frames connected by horizontal tensile pulling rods passing through the mounting holes of six sets of hollow hydraulic ram jacks. By varying the magnitudes of the horizontal loads, different combinations of axial force and moment at the joint can be achieved. By changing the steel pads, segments of different sizes can be tested.

The required loading capacity of the testing setup was confirmed through finite element modelling. The maximum deflection at the two ends of the steel frame when the required loads were reached was smaller than 2.65 mm, which can be neglected.

A series of numerical validations were performed on a flat concrete beam with no joint to confirm the correctness of CSB in force and moment transmission. The simulation results showed good agreement with the values predicted by the theoretical model.

In conclusion, the new testing setup is theoretically feasible.

Acknowledgement. The research was financed by the Natural Science Foundation of China (No. 41372276). The technical supports from the staff of Shanghai Tunnel Engineering Co. Ltd. are highly appreciated.

References

1. Zhang, Z.X., Zhang, H., Yan, J.Y.: A case study on the behavior of shield tunneling in sandy cobble ground. Environ. Earth Sci. **69**(6), 1891–1900 (2013)
2. Lin, C., Zhang, Z., Wu, S., Yu, F.: Key techniques and important issues for slurry shield under-passing embankments: a case study of Hangzhou Qiantang River Tunnel. Tunn. Undergr. Space Technol. **38**, 306–325 (2013)
3. Jin, Y.L., Ding, W.Q., Yan, Z.G., Soga, K., Li, Z.L.: Experimental investigation of the non-linear behavior of segmental joints in a water-conveyance tunnel: tunnelling and under-ground. Space Technol. **68**, 153–166 (2017)

4. Lee, K.M., Ge, X.W.: The equivalence of a jointed shield driven tunnel lining to a continuous ring structure. Can. Geotech. J. **38**, 461–483 (2001)
5. Yan, Z.G., Peng, Y.C., Ding, W.Q., Zhu, H.H., Huang, F.: Load tests on segment joints of single lining structure of shield tunnel in Qingcaosha water conveyance project. Chin. J. Geotech. Eng. **33**(9), 1385–1390 (2011). (In Chinese)
6. Cheng, S.J.: The analysis of the joint mechanism of shield-driven tunnel lining. M.Phil. Thesis, Department of Geotechnical Engineering, Tongji University, P.R. China (1985). (in Chinese)
7. Thomas, H.: Measuring the structural performance of cast Iron tunnel linings in the laboratory. Geotechnics Division, Building Research Station, Building Research Establishment, Department of the Environment, pp. 29–36 (1977)
8. Shalabi, F.I., Cording, E.J., Paul, S.L.: Concrete segment tunnel lining sealant performance under earthquake loading. Tunn. Undergr. Space Technol. **31**, 51–60 (2012)
9. ABAQUS Inc.: ABAQUS User's Manual, Version 6.14 (2014). SIMULIA www.simulia.com

Dynamic Response Analysis of Underground Station Under the Action of Falling Ground Vibration

Shan Ji(✉), Jun Hu, and Wei-Ping Xie

School of Civil Engineering and Architecture,
Wuhan University of Technology, Wuhan, China
ghj0113@163.com

Abstract. In recent years, because of the controlled blasting engineering in China concentrated in the downtown area, the surrounding environment of the downtown area is complex and the underground pipeline is dense, which poses a great challenge to the controlled blasting. It is of great significance to study the impact of falling ground vibration caused by controlled blasting on the underground station. Based on the numerical simulation analysis of ground contact vibration, the dynamic response of underground stations under the action of falling ground vibration is studied by using finite element software. Discuss the propagation rules of acceleration and velocity of ground surface of dynamic response caused by the collapsing touchdown vibration and the propagation law of the velocity, acceleration and displacement of the top and bottom plate of the underground station, and the research shows that: (1) In the area of 5–20 m from the collapse point, the vibration caused by the collapse is dominated by vertical vibration, and the vertical vibration decays faster; (2) The vibration of the roof and floor of the underground station is also dominated by vertical vibration, and the phase difference of vibration exists.

Keywords: Falling ground vibration · Underground station
Dynamic response · Vibration

1 The Introduction

With the rapid development of urban underground structure, the scale of controlled demolition is also increasing. Demolition work often occurred near underground structures. The impact of the falling ground vibration caused by the controlled blasting technique on the surrounding underground structure is very prominent. A lot of testing and practice proved that compared with the vibration caused by blasting, the vibration amplitude of the collapse vibration is larger and the frequency is smaller. The damage to underground structure such as subway and underground pipeline is more significant. Such as the destruction of the mountain tunnel in Taiwan (1999), the damage of Turkey's Bolu expressway (1999). Especially in 1995, the massive destruction of the subway station and underground composite pipe racks in Kobe city, Japan during the Han Shin earthquake which makes the attention to the seismic design method of urban underground structure [1]. The intensive study of the dynamic response of underground

© Springer Nature Singapore Pte Ltd. 2018
D. Zhang and X. Huang (Eds.): GSIC 2018, *Proceedings of GeoShanghai 2018 International Conference: Tunnelling and Underground Construction*, pp. 477–485, 2018.
https://doi.org/10.1007/978-981-13-0017-2_48

structure under the influence of falling ground vibration has important engineering guiding value and disaster prevention significance.

The study on the vibration of demolition and collapse of buildings in foreign countries has been rapid development. In 1927, the American scholar Rokewell proposed the safety standards of buildings under the effect of blasting seismic effect. In 1979, Henrych first proposed the estimation formula for the vibration of the ground based on engineering experience [2]. Some foreign scholars, such as Sharma [3], Hashash [4], Kontogianni et al. [5] made a great deal of research and investigation on the damage mechanism of underground structural dynamic response. The result showed that the vibration of underground structure is affected by the surrounding soil, and the vibration characteristic is not generally expressed. The deformation of foundation soil is the main cause of underground structure damage. The damage caused by dynamic response is more serious when the underground structure passes through the bad geological belt, such as soft soil layer and sandy soil layer. The damage mechanism of underground structure is related to geometrical shape, depth, stiffness and construction technology, and the shallow buried tunnel is more severely damaged than deep buried tunnel.

A few scholars have done some research about the influence of the vibration impact on the underground structure. Baziar et al. conducted a series of dynamic centrifuge tests and seismic performance studies of buried box tunnels and did the numerical simulation work using finite difference method software. The results show that the ground acceleration has great influence on the underground structure, and should be paid attention to when conducting seismic zoning [6]. The stability of the underground roadway and the security of the strut based on the surface blasting vibration were studied by Fourier and noticed that if the particle velocity is less than 10 m/s, the size of the gravel will be smaller, and the amount of gravel is related to the energy of the surface blasting [7]. Karinshki et al. studied the structural response of the two-dimensional model of the square underground structure under the action of gravity and surface static load [8]. Jiang et al. used the LS-DYNA finite element software to perform numerical calculation of the adjacent railway tunnel structure under the influence of surrounding rock blasting vibration. Through the analysis of the vibration velocity and the effective stress of the tunnel floor, the vibration velocity peak is determined as the safety criterion of railway tunnel structure [9]. Chen et al. studied the dynamic response of the underground arch structure under the action of explosion load, obtained numerical solutions using the mode superposition method, and discussed the interaction between different soil layers [10]. Miller and Pursey studied the energy distribution of semi-infinite elastic surfaces under circular vertical resonance, obtained that the resulting wave energy distribution is feasible in the distance. The reasons are as below: ① in the far distance from the source, the body wave is much weaker than the Rayleigh wave; ② different forms of wave in the different distance, their energy density is different; ③ the stress displacement solution is not a linear function of the distance [11]. According to the study on the influence of the impact of collapse contact on the underground structure in recent years, we can see that the study on influence of collapsing touchdown vibration to underground structures is limited. So related test and numerical simulation study on underground structures are necessary. This paper based on the numerical simulation analysis of ground contact vibration, the dynamic response of underground station under the action of collapse vibration is studied by using the finite element software ABAQUS.

2 Calculation Method

2.1 Calculation Principle

The finite element method is used to analyze the numerical simulation to study the effect of the impact vibration on the dynamic response of the underground station. Using ABAQUS to show the dynamic analysis process to simulate the propagation rule and vibration response of collapsed vibration is a more complex and comprehensive dynamic process. On the basis of numerical simulation, especially for the study of the vibration propagation law of the geotechnical, ABAQUS can effectively solve the problem of initial condition of discontinuity, can model the relevant information accurately, and can provide guidance for practical engineering experience, improve the level of parameter design.

2.2 Calculation Model

In order to study the influence of the ground vibration on the underground station, the software ABAQUS is employed for analysis and calculation. The response of the soil surface along wide direction from near to far points (C–I, see Fig. 1) were monitored to analysis vibration attenuation rules, which are 5 m, 7.5 m, 10 m, 12.5 m, 15 m, 17.5 m, 20 m far away from the falling blocks. And the response of top and bottom point A, B of station column (see Fig. 1) are also monitored to study deformation of subway structure.

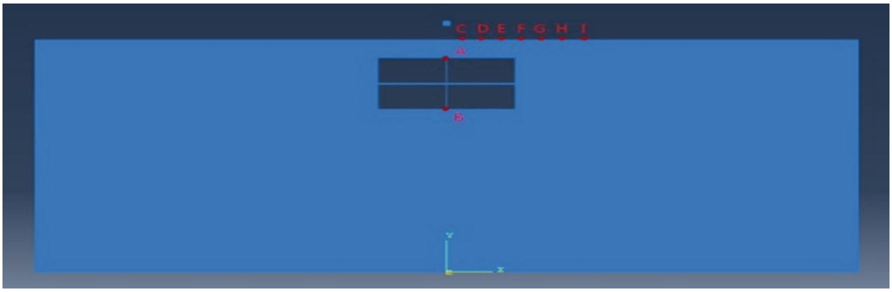

Fig. 1. Calculation model

The X axis is the soil's transverse direction and the Y axis is the vertical direction. The soil model sizes are 120 m in width and 50 m in depth. The soil model was meshed by quadrilateral with 1 m in length. The top plate of the underground station is 3 m from soil surface. The station sizes are 13 m in width and 22 m in height, the top and side concrete thickness are both 1000 mm. The thickness of concrete is 400 mm for middle plate. The square column size is 600 mm. The soil layers, parameters and concrete block parameters are shown in Table 1.

Table 1. Parameters of soil and concrete

Parameter category	Elastic modulus (MPa)	Density (kg/m^3)	Poisson's ratio	Cohesion (MPa)	Internal friction angle (°C)
Silty clay 1	200.87	1917	0.35	25.00	10.80
Silty clay 2	400.98	2000	0.35	61.00	15.80
Residual silty clay	428.71	2030	0.30	56.00	15.20
Red clay	254.40	1837	0.38	37.00	8.30
Concrete	30000	2500	0.20		

2.3 Calculation Model

(1) Unit setting

The CPS4R unit was adopted in the surrounding area of the earth, concrete collapse and the station.B21 was adopted in the station.

(2) Grid division

Grid division is an important factor affecting the calculation speed and accuracy. Smaller unit size will cause higher calculation precision, longer calculation time. Larger unit size will cause lower calculation accuracy and the shorter calculation time. Therefore, in order to ensure sufficient calculation accuracy and improve the computational efficiency, the grid unit edge length of this numerical analysis is 0.5 m. Using this method to divide the grid, there are about 24,000 units and nodes.

(3) Boundary condition setting

The freedom in the vertical direction on soil two sides are constrained to allow soil shear deformation, soil bottom was constraint both in horizontal and vertical direction, the top surface is free. The contact between the concrete block and the earth body is in contact. The surface of the earth is from the surface. The concrete base surface is the main surface. Since the collision should be separable, non-penetrating and retractable, hard contact is required, and the friction coefficient is 0.15 according to the experience.

(4) Apply load

In this numerical simulation, the concrete block is free falling body, so it is only possible to apply gravity field to the collapsed concrete block in numerical simulation.

(5) Calculation time, damping, etc.

The total length of the simulation is 5 s, the time step is 0.005 s, and the Rayleigh damping is set, according to the equivalent shear wave speed and the frequency prediction formula:

$$V_{se} = \frac{d}{\sum_{i=1}^{n} \frac{d_i}{v_i}}, f = \frac{V_{se}}{4H} \tag{1}$$

where V_{se} is the equivalent velocity of shear wave, d is the Stratified thickness of soil layer, V_i is the measured value of soil shear wave velocity per layer, H is the total soil thickness. By the calculation, we can get system first natural frequency ω_1 was equal to *8.0* rad/s. Take the damping ratio of the soil layer, $\xi = 0.08$, $\omega_1 = \omega_2$ according to the formula of mass coefficient and stiffness coefficient

$$\alpha = 2\xi\frac{\omega_1\omega_2}{\omega_1 + \omega_2}, \beta = 2\xi\frac{1}{\omega_1 + \omega_2} \tag{2}$$

It can be obtain that the mass and stiffness coefficient are equal to 0.0808 and *0.0785* respectively.

3 Dynamic Response Analysis Caused by Falling Ground Vibration

In order to study the dynamic response of the surface and underground stations under the action of falling ground vibration, we need to study the propagation law of the dynamic response along the surface acceleration and velocity, which caused by touchdown vibration, as well as the propagation laws of velocity, acceleration and displacement of the roof and floor center of underground station.

3.1 Study on the Propagation Law of Surface Vibration

In order to study the ground response caused by touchdown vibration, we compare the data of near point C and far point I, and analyze the similarities and differences of the velocity and acceleration at near and far point.

3.1.1 Acceleration Amplitude Attenuation Trend on Soil Surface at Point C–I

It can be seen from Fig. 2a, b that both the horizontal acceleration and the vertical acceleration along the surface direction decrease with the increase of the collapse point. This indicates that the acceleration response is gradually attenuated along the surface direction. As can be seen from Fig. 2c, the amplitude of the vertical vibration acceleration is much larger than that of the horizontal, indicating that the vibration is dominated by vertical vibration and the declining rate of the vertical vibration is larger than the horizontal vibration.

3.1.2 The Acceleration Time History Curves of Point C and Point I

Comparing Fig. 3a and b and combining the argument in Sect. 3.1.1, it can be seen that the acceleration response at point C is significantly larger than that at point I. The maximum horizontal acceleration is about 0.16 m/s^2 and the maximum vertical acceleration is about 4.20 m/s^2. It is shown that the vibration acceleration in the vertical direction is greater than the vibration acceleration in the horizontal direction in the distance of 5–20 m; the vibration velocity attenuation in the vertical direction is faster than the horizontal direction.

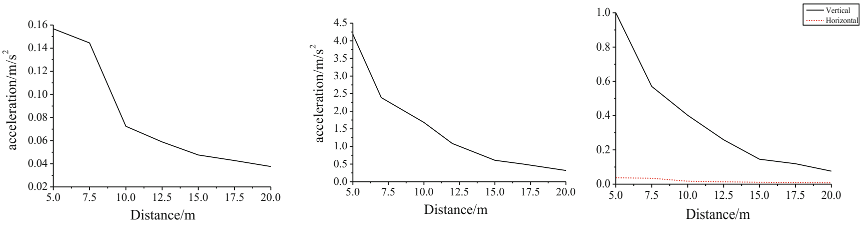

(a) Horizontal (b) Vertical (c) Comparison

Fig. 2. Soil surface acceleration amplitude attenuation curves in horizontal and vertical direction and their comparison

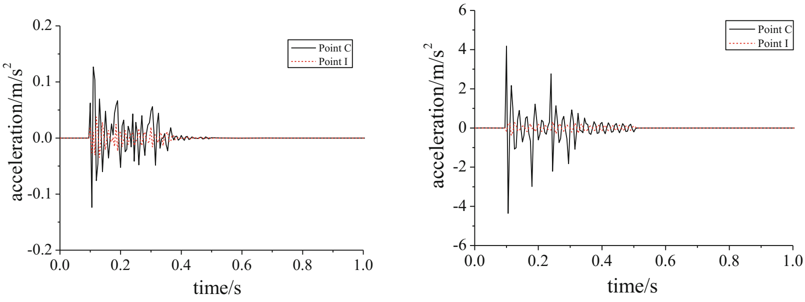

(a) (b)

Fig. 3. Acceleration time history curves comparison between soil surface at point C and I

3.2 Vibration Response Analysis of Underground Station

In order to study the response of the underground station caused by touchdown vibration, we compare the data of the station, which include the center point A of the roof and the center point B of the bottom, and analyze the similarities and differences of the velocity, acceleration and displacement at point A and B.

3.2.1 Acceleration Time Histories and Fourier Spectrum Curves at Points A and B

From Fig. 4a and b, we can see that the horizontal and vertical acceleration responses of point A are obviously greater than those of point B, and the maximum horizontal acceleration is about 0.40 m/s^2 and the maximum vertical acceleration is about 3.00 m/s^2. As in the previous analysis, the vibration of A and B is dominated by vertical vibration.

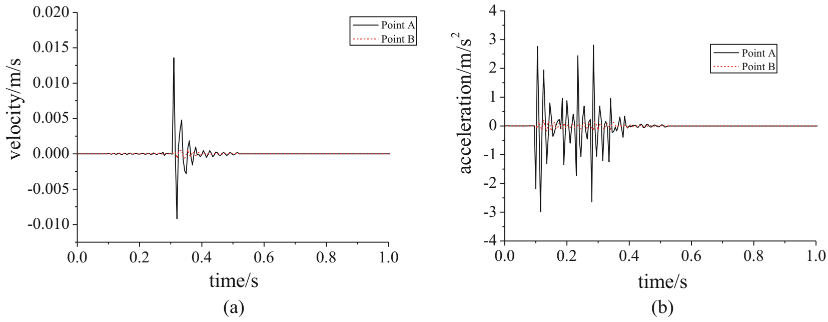

Fig. 4. Acceleration time history curves comparison between structure column at point A and B

3.2.2 Comparison of Horizontal Displacement Change Trend at Point A and Point B

It can be seen from Fig. 5a that the maximum horizontal displacement at the center point of the top plate is greater than that of the point A, and the value is about 3×10^{-13} m. The reason for the maximum displacement value so small is probably because the measurement point is below the collapse point and the horizontal vibration is not obvious. As is shown in Fig. 5b, the maximum vertical displacement is also present in point A, the value is about 3×10^{-3} m; compared with Fig. 5a and b, the vertical displacement of the monitoring point under the collapse point is larger than horizontal displacement, and the vertical vibration is obvious, which is consistent with the previous analysis.

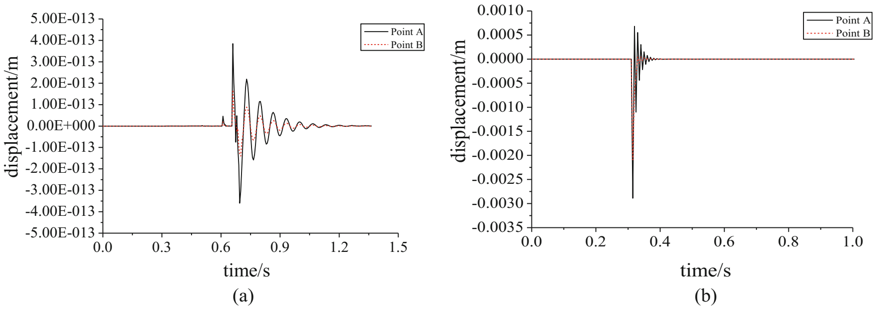

Fig. 5. Displacement time history curves comparison between structure column at point A and B

4 Conclusions

Based on the above analysis, the following conclusions can be drawn:

(1) When the touchdown vibration wave propagates along the surface, the acceleration of particle vibration in the near field is higher than the far point in the range of 5–20 m, which is due to the gradual attenuation of Rayleigh wave under the

action of geometric diffusion and the suction of rock and soil medium. The maximum vibration acceleration in vertical direction is greater than that in horizontal direction, and the acceleration attenuation in vertical direction is faster than that in horizontal direction. The particle vibration velocity in the near field is higher than that in the far field, and the maximum vibration velocity in vertical direction is larger than that in the horizontal direction, and the vertical vibration velocity attenuates rapidly.

(2) For the underground station, we study the response of point A and B caused by touchdown vibration. For the acceleration, the acceleration response of point A is obviously larger than that of point B and the maximum amplitude of point A is significantly higher than that of point B. It indicates that the vibration of point A is greater. For the velocity, the velocity response of point A is obviously greater than that of point B, and the particle vibration velocity in vertical is greater than that in horizontal. For the displacement, the vertical displacement of point A and B is obviously larger than the horizontal displacement, probably because the point is below the collapse point, the horizontal displacement is not obvious, and referring to the relative displacement curve, the phase difference between point A and B is indicated.

In this numerical simulation, the soil properties (such as material parameters, geological characteristics, etc.), the relevant stress and strain data are not considered in detail, because this article only do the relevant regular discussion, the analysis is intuitive two-dimensional finite element analysis. Later, we will analyze the parameters of the size of the slump, soil properties, underground station materials and other related indicators.

References

1. Moss, R.E.S., Crosariol, V.A.: Scale model shake table testing of an underground tunnel cross section in soft clay. Earthq. Spectra **29**(4), 1413–1440 (2013)
2. Henrych, J.: The Dynamics of Explosion and Its Use. Elsevier Scientific Publishing Company, Amsterdam (1979)
3. Sharma, S., Judd, W.R.: Underground opening damage from earthquake. Eng. Geol. **30**(3), 263–276 (1991)
4. Hashash, Y.M., Hook, J.J., Schmidt, B., et al.: Seismic design and analysis of underground structure. Tunn. Undergr. Space Technol. **16**(4), 247–293 (2001)
5. Kontogianni, V.A., Stiros, S.C.: Earthquakes and seismic faulting: effect on tummels. Turk. J. Earth Sci. **12**(1), 153–156 (2003)
6. Baziar, M.H., Moghadam, M.R., Kim, D.S.: Effect of underground surface acceleration. Tunn. Undergr. Space Technol. **44**, 10–22 (2014)
7. Fourie, G.A.: The influence of surface blasting on the stability of underground workings. In: Advances in Mining Science and Technology, vol. 1, pp. 281–296 (1987)
8. Karinski, Y.S., Dancygier, A.N.: Analytical model to evaluate the static soil pressure on a buried structure. Eng. Struct. **25**(1), 91–101 (2003)
9. Jiang, N., Zhou, C.: Blasting vibration safety criterion for a tunnel liner structure. Tunn. Undergr. Space Technol. **32**, 52–57 (2012)

10. Chen, H.L., Xia, Z.C.: Dynamic responses of underground arch structures subjected to conventional blast loads: curvature effects. Arch. Civ. Mech. Eng. **13**(3), 322–333 (2013)
11. Miller, G.F., Pursey, H.: The field and radiation impedance of mechanical radiations on the free surface of a semi-infinite isotropic solid. Proc. R. Soc. Lond. A Math. Phys. Eng. Sci. **223**(1155), 521–541 (1954)

Reliability-Based Analysis of Segmental Linings for Underwater Shield Tunnels

Youwen Wang(✉), Zhe Luo, and Biao Hu

The Key Laboratory of Road and Traffic Engineering, Ministry of Education,
Tongji University, Shanghai 201804, China
`{wangyouwen, zluo}@tongji.edu.cn`

Abstract. In this paper, an efficient reliability-based approach for the analysis of segmental linings of underwater shield tunnels under high water pressure is developed. It is known that the lining analysis is subjected to the influence of uncertain factors such as soil property, structural material strength, which are modeled as random variables in reliability-based design. The modified elastic method is adopted to analyze the internal forces of segmental lining. The performance of the segmental lining against cracking is assessed. To facilitate the reliability analysis, a tool for reliability-based lining design is developed by implementing the first-order reliability method (FORM) into spreadsheet. It is shown that the performance of the tunnel lining is significantly affected by the uncertainty in soil property and height of water over tunnel crown. The developed reliability-based design tool can assess the failure probability and effectively guide the design of lining for underwater shield tunnel. The FORM is more computationally efficient, and can be a practical tool for tunnel lining design.

Keywords: Underwater shield tunnel · Reliability-based analysis
Elastic equation method · Uncertainty · Cracking

1 Introduction

The shield tunnels are widely used for metro, underwater highway, water supply and drains in urban areas. Due to the demand of cross river traffic, there are more and more underwater shield tunnels built around the world, such as Tokyo Bay Aqualine Tunnel, Channel Tunnel and Storebaelt Tunnel. The stability and serviceability design of shied tunnels are challenged by the complicated and volatile soil layer, geological condition and seasonal fluctuation of the groundwater table. In the underwater environment, the deteriorated structural serviceability performance of shield tunnels, in terms of excessive deformation and stress and tensile crack, is typically observed. For the underwater shield tunnels, the development of lining crack drastically accelerates the aging and degradation of concrete segment [1]. In traditional geotechnical practice, the factor of safety (*FS*) is used in design based on experience, which is also known as allowable stress design (ASD). Under ASD framework, the uncertain soil property and random factors are simply considered by enlarging the target *FS*, which may lead to high maintenance, repair and rehabilitation (MR&R) cost. To account for the effect of

© Springer Nature Singapore Pte Ltd. 2018
D. Zhang and X. Huang (Eds.): GSIC 2018, *Proceedings of GeoShanghai 2018 International Conference: Tunnelling and Underground Construction*, pp. 486–495, 2018.
https://doi.org/10.1007/978-981-13-0017-2_49

uncertainty, the reliability-based design (RBD) is widely used in various engineering fields instead of the ASD method [2].

A number of research on the reliability analysis of structural performance of shield tunnels has been reported. For example, the reliability-based approaches are proposed to access the face stability and maximum settlement for both Ultimate Limit State (ULS) and Serviceability Limit State (SLS) [3, 4], and bearing capacity in accordance with large eccentricity scenarios and small eccentricity scenarios [5]. Yet, the research in this field on reliability analysis for lining cracking resistance is still very limited. The first-order second-moment [6], second-order second-moment method [7] and random finite element combined with second-order second-moment method [8] are adopted to conduct reliability analysis of tunnel linings considering multiple performance functions. Further research to quantify various types of uncertainty in tunnel lining design is still needed. It is necessary to develop an efficient and convenient reliability analysis approach for the design of segmental linings for underwater shield tunnels.

In this paper, a reliability-based design tool for the underwater shield tunnel with large section under high water pressure is developed. The tunnel design and construction are more challenging than those in urban areas due to the high water pressure. In addition, the effect of uncertainty in soils has considerable negative effect on the segmental lining design. All those detrimental factors will cause the excessive lining cracking, which is one key concern in the tunnel serviceability limit state assessment. In this regard, the first-order reliability method is implemented into spreadsheet to facilitate the reliability analysis of tunnel lining cracking in this study. Using this approach, the effect of uncertain soil property, and height of water and soil thickness over the tunnel crown on the probability of cracking failure (P_f) is investigated.

2 Elastic Method for Lining Analysis – an Analytical Solution

The traditional design method for lining of shield tunnels is mainly based on the load-structure method, an elastic equation method. The loading model is shown in Fig. 1 [9]. In this model, it is assumed that the segmental ring has uniform bending stiffness, without considering the reduction in local stiffness at the joints between adjacent linings. To address the non-uniform stiffness caused by joints, the effective ratio of flexural stiffness η and moment increment ratio ξ are employed in the modified elastic method. Due to the influence of joint stiffness, flexural stiffness of the equivalent uniform ring is reduced to ηEI. The redistribution of moment will occur at adjacent segments owing to the existence of joint. Correspondingly, $(1 + \xi)M$ is transmitted through segment and $(1 - \xi)M$ is transmitted through joint. It is reported that η ranges from 0.4 to 0.9, and ξ ranges from 0.3 to 0.6, respectively [10].

In view of the Winkler theory, the horizontal subgrade reactions (q_r) are in triangle distributions located within the two side-quarters of tunnel, as shown in Fig. 1. The subgrade reactions applied on the ring can be determined under the premise that the surrounding stratum is in ultimate limit state. By adopting Winkle' type of soil, q_r can be calculated as follows:

$$q_r = K_h \cdot \delta \tag{1}$$

$$\delta = \frac{(2p_1 - q_1 + p_g)R_c^4}{24(EI\eta + 0.0454K_hR_c^4)} = \frac{[2(p_{e1} + p_{w1}) - (q_{e1} + q_{w1}) - (q_{e2} + q_{w2}) + \pi\gamma_c t]R_c^4}{24(EI\eta + 0.0454K_hR_c^4)} \tag{2}$$

where K_h = coefficient of horizontal subgrade reaction; δ = horizontal radial displacement of lining; q_{e1}, q_{w1} = horizontal earth and water pressure at crown of lining; q_{e2}, q_{w2} = horizontal earth and water pressure at bottom of lining; p_g = dead load; E = elastic modulus of concrete; I = inertia moment for unit width of lining; R_c = calculating radius of lining.

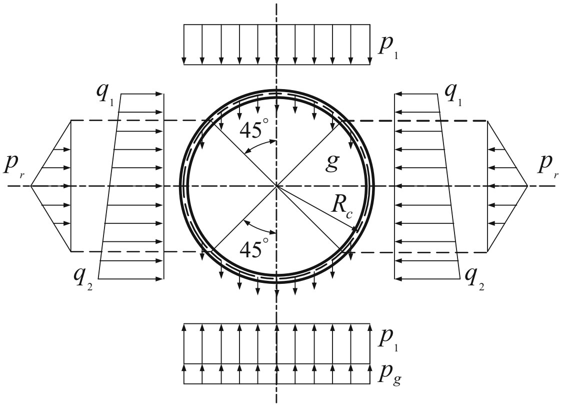

Fig. 1. Sketch of load calculation of shield tunnel.

The vertical earth pressure applied on the lining crown is a uniform load. The vertical earth pressure (p_{e1}) can be calculated by Terzaghi's formula with the consideration of groundwater and multiple soil layers, as shown in the following equations:

$$\sigma_{v1} = \frac{B_1(\gamma_1 - c_1/B_1)}{K_0 \tan\varphi_1} \cdot \left(1 - e^{-K_0 \tan\varphi_1 \frac{H_1}{B_1}}\right) \tag{3}$$

$$\sigma_{vi} = \frac{B_1(\gamma_i - c_i/B_1)}{K_0 \tan\varphi_i} \cdot \left(1 - e^{-K_0 \tan\varphi_i \cdot \frac{H_i}{B_1}}\right) + \sigma_{vi-1} e^{-K_0 \tan\varphi_i \cdot \frac{H_i}{B_1}} \tag{4}$$

where σ_{vi} = vertical earth pressure at top of each soil layer; K_0 = ratio of vertical stress and horizontal stress in each soil layer; γ_i, c_i, φ_i = unit weight, cohesion and internal friction angle in each soil layer, respectively; H_i = thickness of each soil layer over crown; φ_v = internal friction angle of crossing soil; B_1 = influencing width of tunnel excavation, given as $R_0 \cot(\pi/8 + \varphi_v/4)$.

The horizontal earth pressure acting on the lining can be obtained by the following equation:

$$\sigma_h = \lambda \sigma_v \tag{5}$$

where λ = lateral earth pressure coefficient. Thus, the horizontal earth pressure linearly increases from the top to bottom of lining, as shown in Fig. 1.

The internal forces in tunnel linings induced by the aforementioned earth and water pressure can be estimated using the elastic equation method. In this study, the solutions of the internal forces in linings follow the related literature [10]. After the internal forces of lining are obtained, the stress state at the extreme fiber of linings can be determined.

The factor of safety (FS) against cracking in the modified elastic method is defined as the ratio of limiting crack width (ω_{lim}) and maximum crack width ($\omega_{\max}$):

$$FS = \frac{\omega_{\text{lim}}}{\omega_{\max}} \tag{6}$$

where ω_{lim} = 0.2 mm [11].

As reflected in Eq. (6) and the solution for $\omega_{\max}$, FS is a function related with material property of soils and linings. The magnitude of $\omega_{\max}$ can be determined with the following equation [12]:

$$\omega_{\max} = \alpha_{cr} \psi \frac{\sigma_s}{E_s} \left(1.9 c_s + 0.08 \frac{d_{eq}}{\rho_{te}} \right) \tag{7}$$

where α_{cr} = mechanical characteristic coefficient of member; c_s = distance between the outer boundary of the outermost layer of longitudinal tension rebars and the base of tension zone; ψ = nonuniform coefficient of strain for longitudinal tension rebars between cracks, given as $[\min(\max(1.1 - 0.65 \frac{f_{tk}}{\rho_{te}\sigma_s}, 0.2), 1.0)]$; f_{tk} = standard value of axial tension strength for concrete; ρ_{te} = reinforcement ratio of longitudinal tension rebars obtained by the effective area of tension concrete; σ_s = normal stress of longitudinal tension rebars; d_{eq} = equivalent diameter of longitudinal rebars at the tension zones.

3 Efficient Reliability-Based Analysis for Lining of Underwater Shield Tunnel

There are several probability/reliability methods for lining structure design, including the first-order reliability method (FORM), second-order reliability method (SORM), and Monte Carlo Simulation (MCS). The FORM approaches are widely used in engineering because of its computational efficiency and acceptable accuracy. In this study, the performance function for cracking resistance is established as

$$Z = g(X_1, X_2, \ldots, X_n) \tag{8}$$

in which X_1, X_2,…, X_n = fundamental random variables, expressed as $X_i \sim N(\mu_i, \sigma_i^2)$.

The widely used reliability index β, Hasofer and Lind index [13], is considered as the shortest distance between the origin and limit state surface in the normalized space. By incorporating the correlations between random variables, the reliability index β is given as

$$\beta = \min_{x \in F} \left\{ \left[\frac{x_i - \mu_{X_i}}{\sigma_{X_i}} \right]^T [\boldsymbol{\rho}] \left[\frac{x_i - \mu_{X_i}}{\sigma_{X_i}} \right] \right\}^{\frac{1}{2}} \tag{9}$$

where x_i = coordinate value of variable X_i in normalized space; μ_{X_i}, σ_{X_i} = mean value and standard deviation of variable X_i; $\boldsymbol{\rho}$ = correction matrix for random variables. Correspondingly, the failure probability is calculated with

$$P_f = 1 - \Phi(\beta) \tag{10}$$

where Φ = standard normal cumulative distribution function.

The evaluation of lining crack width can be established by applying reliability-based methods on the limit state function. Among the various parameters involved in the relationship between loads and internal forces in elastic solutions, seven leading parameters are chosen as random variables, including the height of water over tunnel crown (h_w), unit weight of crossing soil (γ), cohesion of crossing soil (c), friction angle of crossing soil (φ), cover depth of crossing soil (h_n), coefficient of horizontal subgrade reaction (K_h), as well as standard value of axial tension strength for concrete (f_{tk}). The uncertainty propagation in probabilistic analysis of shield tunnel for crack resistance is shown in Fig. 2. In reference to the resulting probability density distribution for *FS* against a certain failure mode, the shaded area indicates the failure probability with $Z < 0$ or $FS < 1.0$.

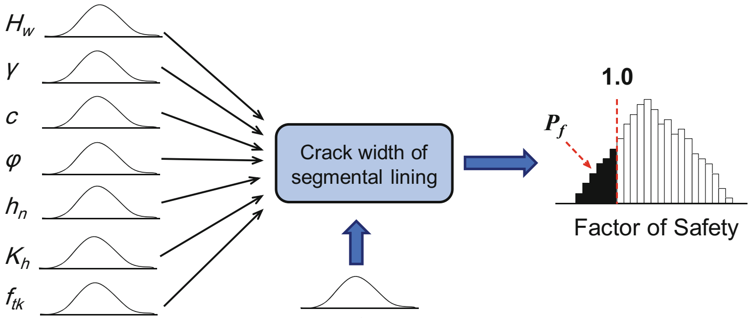

Note:
H_w = height of water over crown; γ = unit weight of crossing soil;
c = cohesion of crossing soil; φ = friction angle of crossing soil;
h_n = cover depth of crossing soil; K_h = coefficient of horizontal subgrade reaction;
f_{tk} = standard value of axial tension strength for concrete.

Fig. 2. Uncertainty propagation in probabilistic analysis of shield tunnel against cracking.

4 Case Study - Underwater Shield Tunnel Crossing the Yangtze River

A shield tunnel project under high water pressure [14] is used herein as an example to illustrate the first-order reliability method (FORM) for the analysis of cracking resistance with considering the variability in soil and lining property. The physical and mechanical parameters of each soil layer are listed in Table 1. The sandy soils are the major soil layer within which the tunnel was constructed. In the transition zone, the groundwater table is located below the ground surface. In this project, the depths of overburden soils and height of groundwater are deeper than the situation for urban tunnel. For simplicity, the adjacent soil layers with similar property are combined into a layer in analysis. The soil thickness (H) and height of water (h_w) over crown are 34 m and 30.7 m, respectively. Other parameters for the analysis against cracking resistance are shown in Tables 2 and 3.

Table 1. Physical and mechanical parameters of each soil layer over tunnel crown.

Layer no.	h (m)	γ (kN/m^3)	c (kPa)	φ (°)	λ	K_h (MPa/m)
1	0–1.85	19.2	22	22.3	0.64 [15]	3 [15]
2	1.85–6.8	19.1	20	11.7	0.6 [15]	14 [15]
3	6.8–34	19.5	11	31.4	0.42	28

Table 2. Parameters as random variables in the analysis of lining against crack resistance.

Input parameters	Notation	Unit	Mean	COV
Height of water over crown	H_w	m	30.7	0.1
Unit weight of crossing soil	γ	kN/m^3	19.5	0.05
Cohesion of crossing soil	c	kPa	11	0.11 [16]
Friction angle of crossing soil	φ	degree	31.4	0.18 [16]
Cover depth of crossing soil	h_n	m	27.2	0.05
Coefficient of horizontal subgrade reaction	K_h	MPa/m	28	0.25 [8]
Standard value of tension strength for concrete	f_{tk}	MPa	2.85	0.12 [8]

The vertical and horizontal earth pressures depend on the geological condition where the tunnel is located. The horizontal subgrade reaction occurs under the earth and water pressures. These combined actions comprehensively dominate the stress state of tunnel linings. However, the uncertainty in the geological condition leads to the design challenges. Hence, the effect of uncertain soil parameters, including γ, c and φ are explored. The probability of cracking failure (P_f) due to uncertain soil property is carried out with the FORM procedure shown in Fig. 3.

Figure 4(a) and (b) show the effect of uncertain γ and φ, respectively. Remarkably, the probability of failure (P_f) decreases with the thickness of lining. These results show that the soil property has a significantly influence on the earth pressure, which further affects the probability of failure (P_f) against cracking. However, the probability of failure (P_f) increases slightly with the COV for cohesion (c) of crossing soil. The uncertain soil property is a key factor for crack resistance evaluation.

Table 3. Material property of segmental lining.

Basic calculation parameters	Notation	Unit	Value
Cover depth of tunnel	H	m	34
Calculated diameter	R_c	m	5.35
Thickness of segment	t	m	0.5
Width of segment	b	m	2
Unit weight of concrete	γ_c	kN/m^3	26
Elastic modulus of concrete	E_c	GPa	36
Distance between resultant acting point and outer boundary of concrete	$a(a')$	mm	50
Diameter of rebar at each side	d	mm	25
Number of rebar at each side	n	–	20
Elastic modulus of rebar	E_s	MPa	210

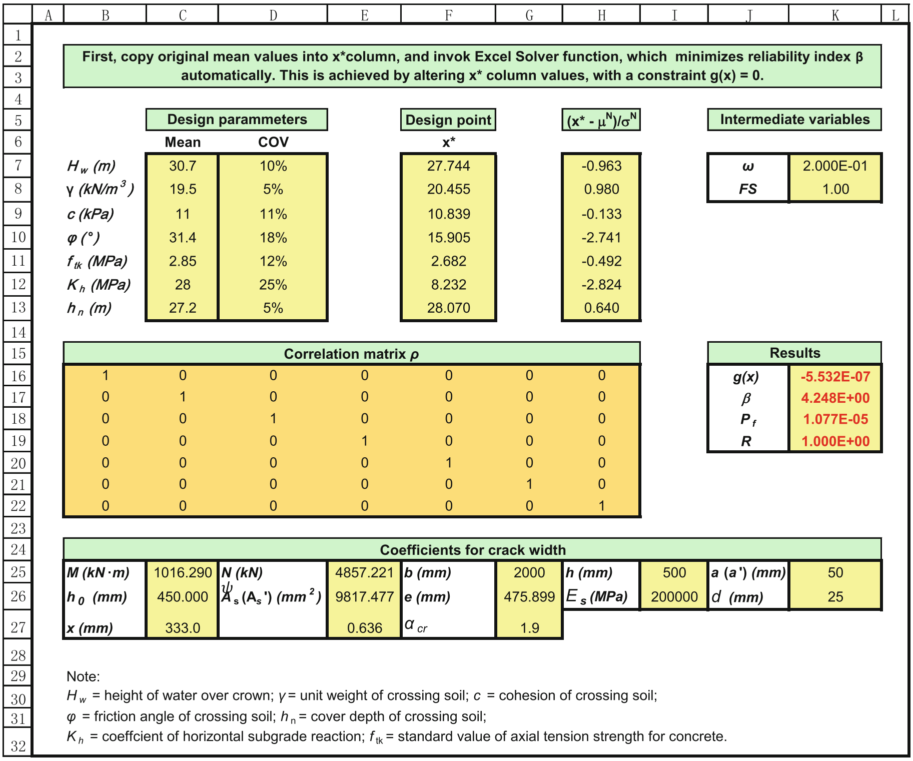

First, copy original mean values into x*column, and invok Excel Solver function, which minimizes reliability index β automatically. This is achieved by altering x* column values, with a constraint g(x) = 0.

	Design parammeters Mean	Design parammeters COV	Design point x*	$(x^* - \mu^N)/\sigma^N$
H_w (m)	30.7	10%	27.744	-0.963
γ (kN/m^3)	19.5	5%	20.455	0.980
c (kPa)	11	11%	10.839	-0.133
φ (°)	31.4	18%	15.905	-2.741
f_{tk} (MPa)	2.85	12%	2.682	-0.492
K_h (MPa)	28	25%	8.232	-2.824
h_n (m)	27.2	5%	28.070	0.640

Intermediate variables	
ω	2.000E-01
FS	1.00

Correlation matrix ρ

1	0	0	0	0	0	0
0	1	0	0	0	0	0
0	0	1	0	0	0	0
0	0	0	1	0	0	0
0	0	0	0	1	0	0
0	0	0	0	0	1	0
0	0	0	0	0	0	1

Results	
$g(x)$	-5.532E-07
β	4.248E+00
P_f	1.077E-05
R	1.000E+00

Coefficients for crack width

M (kN·m)	1016.290	N (kN)	4857.221	b (mm)	2000	h (mm)	500	a (a') (mm)	50
h_0 (mm)	450.000	A_s (A_s') (mm^2)	9817.477	e (mm)	475.899	E_s (MPa)	200000	d (mm)	25
x (mm)	333.0	ψ	0.636	α_{cr}	1.9				

Note:
H_w = height of water over crown; γ = unit weight of crossing soil; c = cohesion of crossing soil;
φ = friction angle of crossing soil; h_n = cover depth of crossing soil;
K_h = coeffcient of horizontal subgrade reaction; f_{tk} = standard value of axial tension strength for concrete.

Fig. 3. Layout for spreadsheet-based first-order reliability analysis.

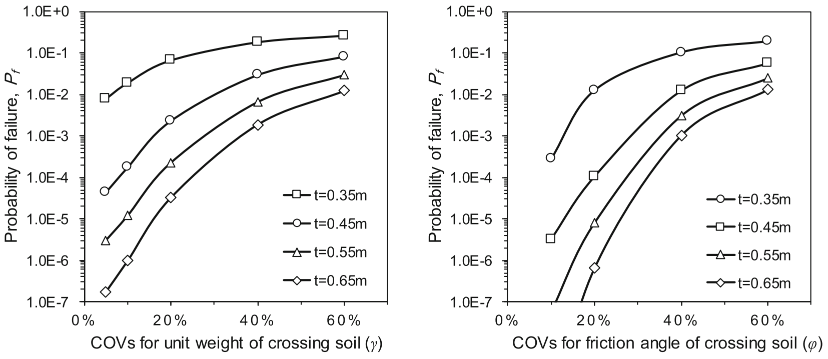

(a) Unit weight of crossing soil, γ (b) Friction angle of crossing soil, φ

Fig. 4. Effect of uncertainty in material property of crossing soil for different thickness of lining on probability of failure (P_f) against cracking.

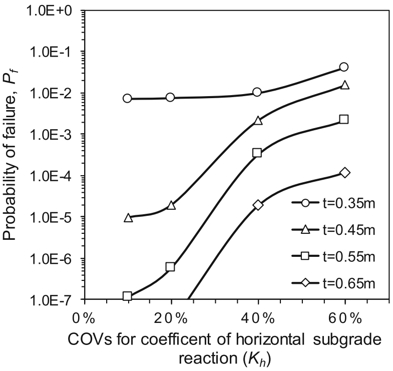

Fig. 5. Effect of uncertainty in coefficient of horizontal subgrade reaction (K_h) for different thicknesses of lining on probability of failure (P_f) against cracking.

The effect of uncertain K_h on the probability of failure (P_f) against cracking is investigated and the results are shown in Fig. 5. For the thickness of lining = 0.35 m, the probability of failure (P_f) increases slightly with the COV for K_h. Yet, when the thickness of lining > 0.45 m, the probability of failure (P_f) increases sharply with the COV between 20% and 60%. The probability of failure (P_f) increases with the decrease in lining thickness. In this study, the COV for K_h is assumed to be 25% as in Table 2.

For the underwater shield tunnel with large section under high water pressure, the condition of cover depth should mainly consider two factors, including the height of water over crown (h_w) and soil thickness over crown. For the geological condition shown on Table 1, the depth of overlaying soil is merely 6.8 m, which is relatively smaller compared with the cover depth of crossing soil (h_n). For convenience, the cover depth of crossing soil (h_n) is considered as a random variable instead of soil thickness over crown.

Figure 6(a) and (b) illustrate the effect of uncertainty in height of water over crown (h_w) and cover depth of crossing soil (h_n) on probability of cracking failure (P_f), respectively. The possibility of failure (P_f) decreases with the height of water (h_w). The decreasing tendency gradually becomes gentle with COV for the height of water over crown (h_w). There is almost no variation with high probability of failure (P_f) for COV of h_w = 40%. Larger height of water over crown (h_w) will lead to more uniform surrounding pressure to tunnel. When the groundwater table is located below the ground surface under high water pressure, the water pressure or the height of water (h_w) becomes the control factor. As shown in Fig. 6(b), the probability of failure (P_f) increases with the cover depth of crossing soil (h_n). Consequently, the crack is unlikely to develop for high ratio of height of water (h_w) to soil thickness over crown.

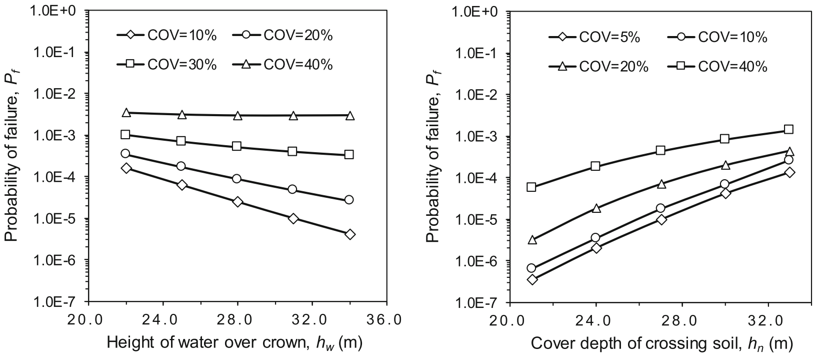

(a) Height of water over crown, h_w (b) Cover depth of crossing soil, h_n

Fig. 6. Effect of uncertainty in height of water over crown (h_w) and cover depth of crossing soil (h_n) on probability of failure (P_f) against cracking.

5 Conclusion

In this paper, the reliability analysis of shield tunnel lining is presented using the spreadsheet implemented with FORM. The probability of lining cracking failure (P_f) considering the uncertain soil property is evaluated using this spreadsheet tool. The conclusions are summarized as follows:

(1) The uncertain soil property has a significant effect on lining cracking analysis. It is also worth noting that the larger variation in coefficient of horizontal subgrade reaction (K_h) leads to higher probability of cracking failure (P_f).
(2) The high water level above the tunnel is beneficial to control the development of lining cracks in tunnel transition zone. The larger height of water over crown (h_w) will lead to more uniform confining pressure to shield tunnel. On the contrary, the larger soil thickness over crown has negative effect on cracking resistance.

Acknowledgment. The study on which this paper is based was supported by the National Natural Science Foundation of China through Grant No. 41702296.

References

1. Lees, J.M., Burgoyne, C.J.: Experimental study of influence of bond on flexural behavior of concrete beams pretensioned with aramid fiber reinforced plastics. ACI Struct. J. **96**(3), 377–385 (1999)
2. Duncan, J.M.: Factors of safety and reliability in geotechnical engineering. J. Geotech. Geoenvironmental Eng. **126**(4), 307–316 (2000)
3. Mollon, G., Dias, D., Soubra, A.H., Asce, M.: Probabilistic analysis and design of circular tunnels against face stability. Int. J. Geomech. **9**(6), 237–249 (2009)
4. Rom, M., Avriel, M.: Probabilistic analysis of circular tunnels in homogeneous soil using response surface methodology. J. Geotech. Geoenvironmental Eng. **135**(9), 1314–1325 (2009)
5. Zhao, Q., Yuan, Y., Gao, S., Yu, G.: Reliability of a tunnel segment account for section bearing capacity. Am. Soc. Civ. Eng. **345**, 1717–1723 (2009)
6. Yan, J., Yang, L.: Reliable design method of tunnel lings in soft soil. Urban Mass Transit **12** (10), 45–47 (2009)
7. Huang, Q., Yuan, D., Wang, M.: Study on utility method of reliability analysis for segment lining. J. Beijing Jiaotong Univ. **33**(1), 104–108 (2009)
8. Tan, Z., Wang, M.: Second-order second-moment method for structural reliability analysis of tunnel lining. Chin. J. Rock Mech. Eng. **23**(13), 2243–2247 (2004)
9. Working Group No. 2 International Tunneling Association: Guidelines for the design of Shield Tunnel lining. Tunn. Undergr. Space Technol. **15**(3), 303–331 (2000)
10. Koyama, Y.: Present status and technology of shield tunneling method in Japan. Tunn. Undergr. Space Technol. **18**(2–3), 145–159 (2003)
11. Ministry of Housing and Urban-Rural Development of the People's Republic of China. Code for design of concrete structure (GB50010-2010). China Architecture and Building Press, Beijing (2010)
12. Beijing Municipal Commission of Urban Planning. Code for Design of Metro (GB 50157-2013). China Architecture and Building Press, Beijing (2013)
13. Hasofer, A.M., Lind, N.C.: Exact and invariant second-moment code format. J. Eng. Mech. **100**(1), 111–121 (1974)
14. Zhou, S., Liu, C., Li, X., Jin, H.: Reverse calculation and analysis of measured internal force of deeply shield tunnels with large cross-section under high water pressure conditions. J. Tongji Univ. (Nat. Sci.) **45**(07), 970–977 (2017)
15. Ji, D.: Comparison and analysis of calculating model for the internal force of shield tunnel lining. Railw. Surv. Des. **4**, 21–25 (2006)
16. Zhang, J., Miao, L.: Types and selection criteria of probability distribution of rock and soil parameters. Chin. J. Rock Mech. Eng. **28**(s2), 3526–3532 (2009)

Three-Dimensional Transient Response of Deep Embedded Tunnels to Internal Explosions

F. Y. Liu[1(✉)], X. Wang[1], Y. Q. Cai[2], and C. J. Xu[3]

[1] Shanghai University, Shanghai 200444, China
`lfyzju@shu.edu.cn`
[2] Zhejiang University, Hangzhou 310014, China
[3] East China Jiaotong University, Nanchang 330013, China

Abstract. Internal explosions in underground spaces can lead to enormous economic losses and cause security hazards to society. Therefore, understanding the dynamic response of embedded tunnels to explosions is extremely important. Using the theory of elastic media, we studied the three-dimensional transient dynamic responses of coupled soil-lined systems under blast loads. First, general solutions for the dynamic responses of infinite elastic soils and linings in the Laplace and Fourier domains are derived. Second, analytical solutions for the displacement and stress of elastic soils and linings under axially-symmetric explosion loads in the Laplace and the Fourier domains are deduced by exploiting the continuity of the contact area between the lining and elastic soil. An interior boundary condition for linings is also derived. Finally, three-dimensional dynamic responses in the time-space domain are calculated using Fourier transforms and the Durbin approach to Laplace inverse transforms. The soil displacement and stress distributions caused by the blast load, as well as the influence of different parameters are analyzed. Additionally, optimal ranges are provided for the lining thickness and the ratio between the shear modulus of linings and the modulus of soil.

Keywords: Internal explosions · Tunnel linings · Dynamic response
Laplace transform · Fourier transform

1 Introduction

The explosion of an underground structure induces a large, short-duration instantaneous response, with high vibration speeds and frequencies, causing significant structural damage. As a result, the dynamic responses of tunnels to internal explosions is of great concern to engineers and academics alike.

The study of steady-state responses of tunnels to internal explosions is mature. Mohsenimonfared [1] used a potential function and Fourier series to study the steady-state responses of infinitely-long elastic tunnels to dynamic loads. Coskun [2] considered the dynamic responses of circular tunnels with elastic half-spaces. Datta [3] combined numerical calculations with finite element methods to study the steady-state responses to dynamic stresses and displacements of different tunnel shapes. Yi [4] used

© Springer Nature Singapore Pte Ltd. 2018
D. Zhang and X. Huang (Eds.): GSIC 2018, *Proceedings of GeoShanghai 2018 International Conference: Tunnelling and Underground Construction*, pp. 496–505, 2018.
https://doi.org/10.1007/978-981-13-0017-2_50

a wave function expansion approach to obtain a steady-state analytical solution for circular tunnel linings.

To investigate the transient responses of tunnels to internal explosions, Li [5] used Flügge shell theory to derive an equation of motion for the transient response of circular-shell linings under external hydrostatic pressure. Gao [6] applied the Fourier and Laplace transforms to deduce a dimensionless solution for the transient dynamic response of cylindrical lining holes. Wang [7] studied the dynamic responses to permanent, stage-jumping, and triangular loads on tunnel linings. Ceng [8] investigated the three-dimensional dynamic response of a circular tunnel lining.

Such studies have been performed primarily in two dimensions. However, explosive loads cause spherically-propagating shockwaves, and thus considering the impact of such effects is necessary. Koneshwaran [9] used arbitrary Lagrangian-Eulerian (ALE) approach and smoothed particle hydrodynamics (SPH) to study the responses of deeply buried tunnels to explosions, comparing the results of the two methods. Uystepruyst [10] used numerical calculations to study shockwaves caused by internal explosions in rectangular tunnels, and Yan [11] used the finite element software Abaqus to define a 3D model of double-lined tunnels to study their dynamic responses.

We consider the three-dimensional transient responses of internal explosions on shell-lined circular tunnels buried in soil. The responses of these deeply-buried linings can be derived with the Laplace and Fourier transforms and their inverses. We attempt to characterize the axial dynamic response of such an infinite system over time with different parameters.

2 Control Equation and Solution

As shown in Fig. 1, we assume that an infinitely-long elastic circular tunnel has a lining thickness h. If the inner radius of the lining is ρ_s, its outer radius is R_2, and its average radius is a, then $a = (R_1 + R_2)/2$, $h = R_2 - R_1$. We assume that the dynamic response of the elastic soil-lined system creates a small deformation. The soil is in complete contact with the lining with no relative slip.

Let λ_s and μ_s be the Lamé constants of the soil, and ρ_s its true density.

The propagation of explosive waves in closed containers can understood via a simplified model, by simulating the internal explosions acting on the inner wall of the tunnel lining. Consider the rapid expansion of internal explosions over a short period of time. The internal energy rapidly increases from zero to a peak at the moment of the explosion, then decays back to zero. An explosive blast wave will impact the inner wall of the lining and reflect, resulting in the appearance of two peaks and a triangular load. Figure 2 depicts the radial profile of the internal explosion function, also described in Eq. (1):

$$P(t) = \begin{cases} P_0 \times 10^3 t & 0 < \mathrm{t} \leq 10^{-3} \\ (-P_0 t/2 + 3P_0/2) \times 10^3 & 10^{-3} < \mathrm{t} \leq 3 \times 10^{-3} \\ 0 & 3 \times 10^{-3} < \mathrm{t} \leq 5 \times 10^{-3} \\ (-P_0 t/6 + 3P_0/2) \times 10^3 & 5 \times 10^{-3} < \mathrm{t} \leq 8 \times 10^{-3} \\ 0 & 8 \times 10^{-3} < \mathrm{t} \leq 10 \times 10^{-3} \\ (-P_0 t/6 + 3P_0/2) \times 10^3 & 10 \times 10^{-3} < \mathrm{t} \leq 13 \times 10^{-3} \\ 0 & 13 \times 10^{-3} < \mathrm{t} \leq 15 \times 10^{-3} \end{cases} \tag{1}$$

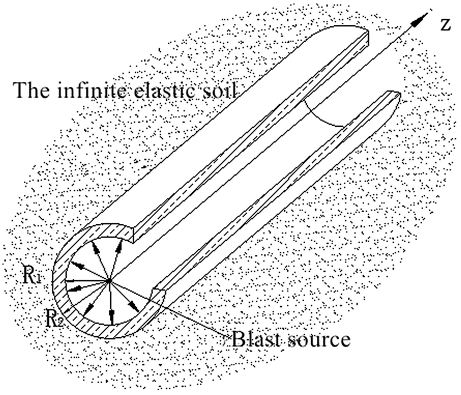

Fig. 1. Analysis model.

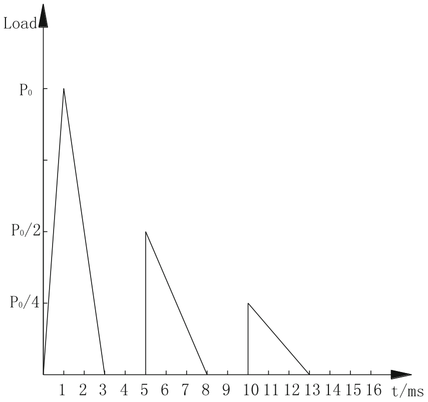

Fig. 2. Blast model.

The time-pressure curves of the shockwaves impinging on a structure after an explosion can be viewed as primary pulse-type dynamic loads. Such loads are generally simplified to sudden triangular loads, as shown in Eq. (2):

$$\Delta P(t) = \Delta P_+ \left(1 - \frac{t}{t_0}\right) \tag{2}$$

where $\varDelta P_+$ is the overpressure peak of a surface near the explosive shock wave, $P_0 = 1.06/\overline{R} + 4.3/\overline{R}^2 + 14/\overline{R}^3$, $\overline{R}$ is equivalent distance, $\overline{R} = R/\sqrt[3]{\mathrm{m}_0}$, R is the distance between the measurement point and explosion core, defined as $R = \sqrt{r^2 + z^2}$, and m_0 is the weight of the explosive.

In this study, we consider the following situation to calculate the specific parameters of a shockwave [12]: terrorists use a 200 mm × 600 mm × 350 mm bag to carry approximately 70 kg of TNT for an explosive attack, with an explosive density of 1.654×10^3 kg/m^3.

2.1 Elastic Soil Control Equation

Soil can be modeled as an infinite elastomer. To obtain the column coordinates by the principle of flexible media, the control equation for the elastic soil can be represented by its displacement under an axially-symmetric dynamic load, as shown in Eq. (3) [13]:

$$\left.\begin{array}{l} \mu_s \nabla^2 u_r + (\lambda_s + \mu_s)\frac{\partial e}{\partial r} - \mu_s \frac{u_r}{r^2} - \rho_s \frac{\partial u_r}{\partial t^2} = 0 \\ \mu_s \nabla^2 u_z + (\lambda_s + \mu_s)\frac{\partial e}{\partial z} - \rho_s \frac{\partial^2 u_z}{\partial t^2} = 0 \end{array}\right\} \tag{3}$$

where λ_{s} and μ_{s} are the Lamé constants of the soil, μ_{r} and μ_z are its radial and axial displacement, respectively, ρ_{s} is its density, e is its volumetric strain, defined as $e = \frac{\partial u_r}{\partial r} + \frac{u_r}{r} + \frac{\partial u_z}{\partial z}$, and ∇^2 is the Laplace operator $\nabla^2 = \frac{\partial^2}{\partial r^2} + \frac{1}{r}\frac{\partial}{\partial r} + \frac{\partial}{\partial z^2}$.

Using an axially-symmetric potential function, we now introduce two potential functions ϕ and ψ. We consider the initial conditions in Eq. (4):

$$\left.\begin{array}{l} u_r(r,t)|_{t=0} = \left.\frac{\partial u_r(r,t)}{\partial t}\right|_{t=0} = 0 \\ u_z(r,t)|_{t=0} = \left.\frac{\partial u_z(r,t)}{\partial t}\right|_{t=0} = 0 \end{array}\right\} \tag{4}$$

The Laplace and Fourier transforms are applied on the time variable t of the control equation Eq. (3) to derive the governing equations in Eq. (5):

$$\left.\begin{array}{l} \left(\frac{\partial^2}{\partial r^2} + \frac{1}{r}\frac{\partial}{\partial r} + \omega^2 - \frac{s^2}{a^2}\right)\tilde{\phi} = 0 \\ \left(\frac{\partial^2}{\partial r^2} + \frac{1}{r}\frac{\partial}{\partial r} - \frac{1}{r^2} + \omega^2 - \frac{s^2}{b^2}\right)\tilde{\psi} = 0 \end{array}\right\} \tag{5}$$

where $\alpha^2 = \frac{s^2}{a^2} - \omega^2$ and $\beta^2 = \frac{s^2}{b^2} - \omega^2$.

The strain components of the column coordinates are expressed in Eq. (6):

$$\left.\begin{array}{l} \varepsilon_{rr} = \frac{\partial u_r}{\partial r} \\ \varepsilon_{zz} = \frac{\partial u_z}{\partial z} \\ \varepsilon_{zz} = \frac{1}{2}\left(\frac{\partial u_r}{\partial z} + \frac{\partial u_z}{\partial r}\right) \end{array}\right\} \tag{6}$$

According to Hooke's law, the boundary conditions $\lim\limits_{r\to\infty} \tilde{u}_s = \lim\limits_{r\to\infty} \tilde{u}_z = 0$ and the coupling relationship between the potential functions can be combined with Eqs. (5) and (6) to derive the general solution [14, 15] shown in Eq. (7).

$$\left.\begin{array}{l} \tilde{\sigma}_{rr} = \left[[(\lambda_s + 2\mu_s)\alpha^2 + \lambda_s\omega^2]K_0(\alpha r) + \frac{2\mu_s \alpha K_1(\alpha r)}{r}\right]B_1 + \left[-2(\lambda_s + \mu_s)\omega\beta K_0(\beta r) + \frac{2\mu_s \omega K_1(\beta r)}{r}\right]B_2 \\ \tilde{\sigma}_{\theta\theta} = \left[\lambda_s(\alpha^2 + \omega^2)K_0(\alpha r) - \frac{2\mu_s \alpha K_1(\alpha r)}{r}\right]B_1 + \left[-2\lambda_s\omega\beta K_0(\beta r) + \frac{2\mu_s \omega K_1(\beta r)}{r}\right]B_2 \\ \tilde{\sigma}_{zz} = [\lambda_s\alpha^2 + (\lambda_s + 2\mu_s)\omega^2]K_0(\alpha r)B_1 - 2(\lambda_s + \mu_s)\omega\beta K_0(\beta r)B_2 \\ \tilde{\sigma}_{rz} = -\mu_s(1+\omega)\alpha K_1(\alpha r)B_1 + \mu_s\left[\beta^2 - \left(\frac{1}{r^2} + \omega\right)\right]K_1(\beta r)B_2 \end{array}\right\} \tag{7}$$

2.2 Control Equation and Boundary Condition of Shell Lining

A lining is a shell-like structure around a cylinder. We define a coordinate system with the source of the explosion at its center. As shown in Fig. 3a, the vibration equation for the lining in the axial x-axis, ring y-axis, and radial z-axis is similar to that in the literature [16].

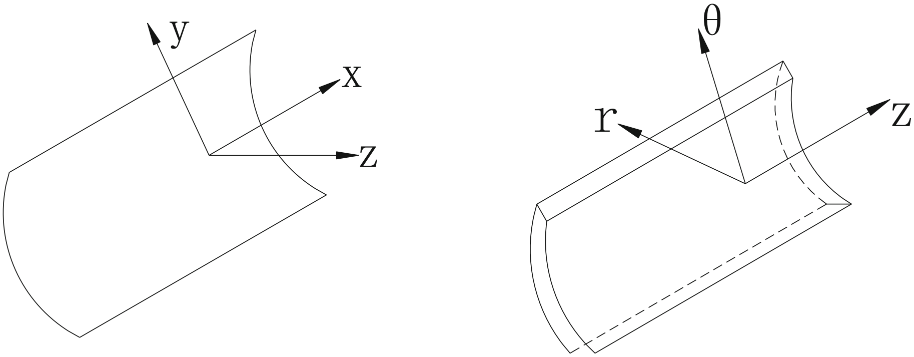

(a) (b)

Fig. 3. Three-dimensional coordinate systems for (a) lining and (b) elastic soil.

Because of the cylindrical lining and axial symmetry of the explosive load, v = 0, $q_y = 0$, and $q_x = 0$. The governing equations are simplified to those in Eq. (8),

$$\left.\begin{array}{l} a\frac{\partial^2 u_x}{\partial x^2} - v\frac{\partial w}{\partial x} + \frac{h^2}{12}\frac{\partial^3 w}{\partial x^3} + a\frac{1-v^2}{Eh}q_x = \rho a\frac{1-v^2}{E}\frac{\partial^2 u_x}{\partial t^2} \\ v\frac{\partial u_x}{\partial x} - \frac{w}{a} - \frac{h^2}{12}a\frac{\partial^4 w}{\partial x^4} - \frac{h^2}{12}\left(\frac{\partial^3 u_x}{\partial x^3} + \frac{1}{a^3}w\right) + a\frac{1-v^2}{Eh}q_z = \rho a\frac{1-v^2}{E}\frac{\partial^2 w}{\partial t^2} \end{array}\right\} \tag{8}$$

Both sides of Eq. (8) represent a Laplace transformation of the variable t (noting that $L[u(x,t)] = \bar{u}(x,s)$) and a Fourier transformation of the variable x (noting that $F[\bar{u}(x,s)] = \tilde{u}(\omega,s)$).

The stress components of the soil acting on the outer surface of the lining are denoted T_{zx} and T_{zz}. It is assumed that the elastic soil is in complete contact with the shell lining and with no relative slip. The contact surface is comprised of water that cannot pass through the lining. In the Laplace and Fourier transform domains, the continuity condition between the elastic soil and the lining contact surface $r = R_2$ is that the stress on the shell lining is equal to the difference between the stress generated by the inner and outer surfaces of the lining:

$$\frac{-Eh}{a(1-v^2)}[A]\begin{bmatrix}\tilde{u}_x \\ \tilde{w}\end{bmatrix} = \begin{bmatrix}\tilde{q}_x \\ \tilde{q}_z\end{bmatrix} = \begin{bmatrix}\tilde{P}_x \\ \tilde{P}_z\end{bmatrix} - \begin{bmatrix}\tilde{T}_{zx} \\ \tilde{T}_{zz}\end{bmatrix} \tag{9}$$

In the Laplace and Fourier transform domains, the stress components produced by the explosion in the x- and y-directions are $\tilde{P}_x = \tilde{P}_y = 0$, and $\tilde{P}_z$ is the component from Eq. (1).

The displacement and stress are continuous on the contact surface $(r = R_2)$ of the lining. The main directions in the cylindrical coordinate system are not exactly consistent between the lining and the soil. As shown in Fig. 3, the continuous condition is represented by Eq. (10).

$$\left.\begin{aligned} w &= -u_r, \\ \tau_{zx} &= -\sigma_{rz}, \\ \tau_{zz} &= \sigma_{rr}. \end{aligned}\right\} \tag{10}$$

where τ_{zx} and τ_{zz} are the stresses in Fig. 3a, where T_{zx} and T_{zz} come from Eq. (9).

A joint solution for Eqs. (7), (9) and (10) is shown in Eq. (11).

$$\begin{bmatrix} B_1 \\ B_2 \end{bmatrix} = \begin{bmatrix} \frac{c_{12}\tilde{P}_z}{c_{12}c_{21} - c_{11}c_{22}} \\ \frac{c_{11}\tilde{P}_z}{-(c_{12}c_{21} - c_{11}c_{22})} \end{bmatrix} \tag{11}$$

This equation can be solved to find the undetermined constants B_1 and B_2 by using the inverse transforms described by Durbin [17] and Fourier to obtain the dynamic response of an elastic circular tunnel lining buried in deep soil in the Laplace and Fourier domains under an explosive load. Through the use of an inverse Fourier transform, the dynamic response of an infinitely elastic lining system under an explosive load along the axial direction can also be calculated.

3 Parameter Analysis

As shown in Fig. 4, with different values of the lining thickness h and other parameters prescribed as listed in Table 1, the dynamic responses of the displacement and stress over time at the contact surface ($r = R_2$) between the shell lining and soil changed. To be specific, $z = 0$ represents the dynamic response of μ_r, σ_rr, and $\sigma_{\theta\theta}$, and $z = -3$ represents the dynamic response of μ_z and σ_rz.

As h varied, each response oscillated with a decaying trend. The largest response occurred when the first wave of maximum stress arrived. When $t \approx 10$ ms, the response peaked and then the shock attenuated as time progressed until the displacement and stress stabilized. As h increased from 0.1 m to 0.25 m, the response amplitude decreased by approximately 50%. As h increased from 0.25 m to 0.4 m, the response amplitude gap was relatively small.

Figure 5 shows the dynamic responses of displacement and stress over time at the contact surface $(r = R_2)$ between the shell and soil by varying the relative stiffness $I = \mu_L/\mu_S$ and assigning other parameters to those in Table 1. To be specific, $z = 0$ is the dynamic response of u_r, σ_{rr}, and $\sigma_{\theta\theta}$, and $z = 3$ is the dynamic response of u_z and σ_{rz}.

As the relative stiffness I changed to 10, 100, 1000, and 10,000, the response again oscillated with a decaying trend. As before, as the first wave of maximum stress

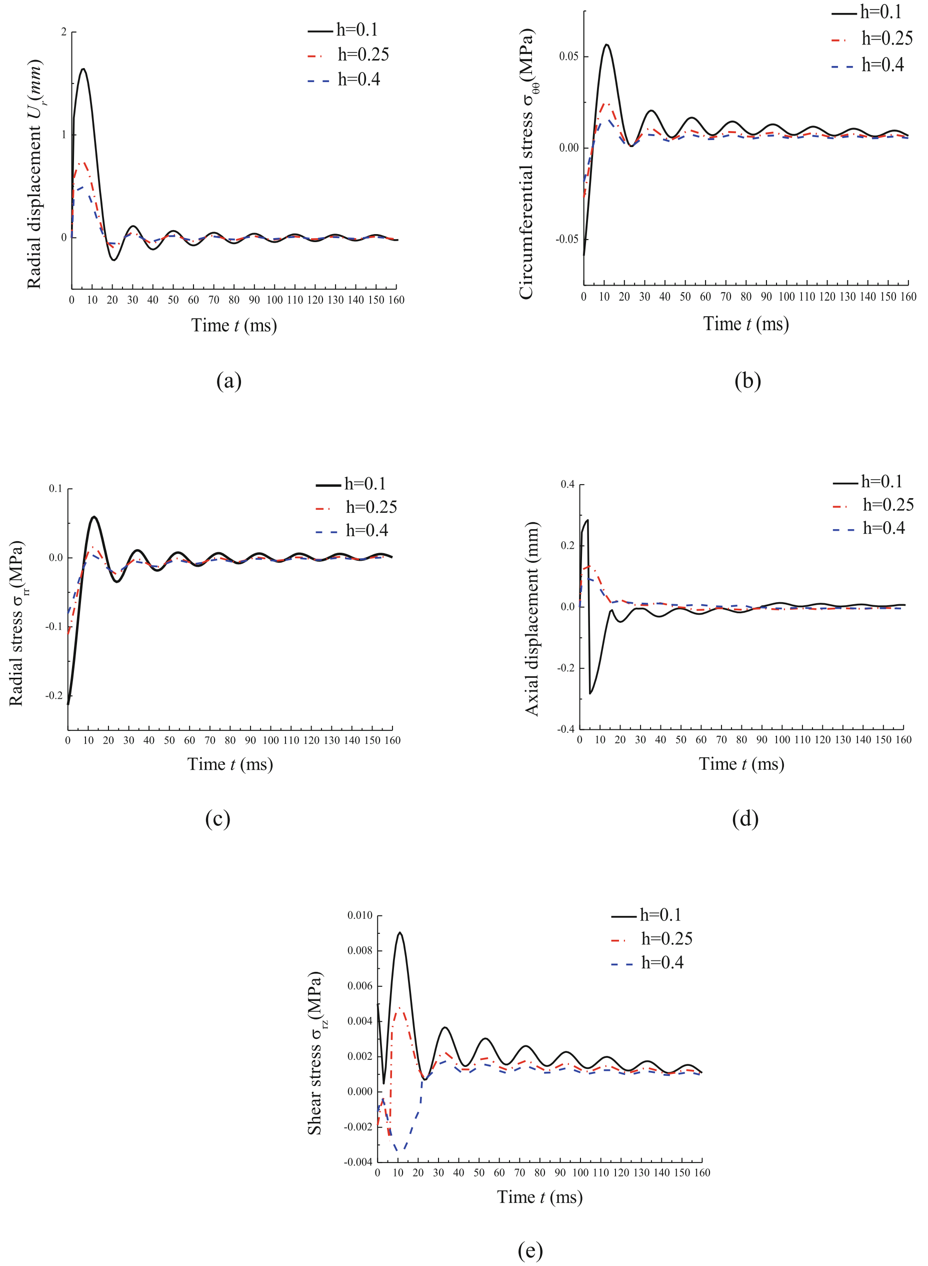

(a)

(b)

(c)

(d)

(e)

Fig. 4. Responses of soil (a) radial displacement, (b) circumferential stress, (c) radial stress, (d) axial displacement, and (e) shear stress over time.

Table 1. Calculation parameters.

Lining					Elastic soil		
E/MPa	ρ/(g/cm^3)	ν	*a*/cm	*h*/cm	λ/MPa	μ/MPa	ρ_s/(g/cm^3)
5×10^4	2.5	0.3	300	25	30	20	2.50

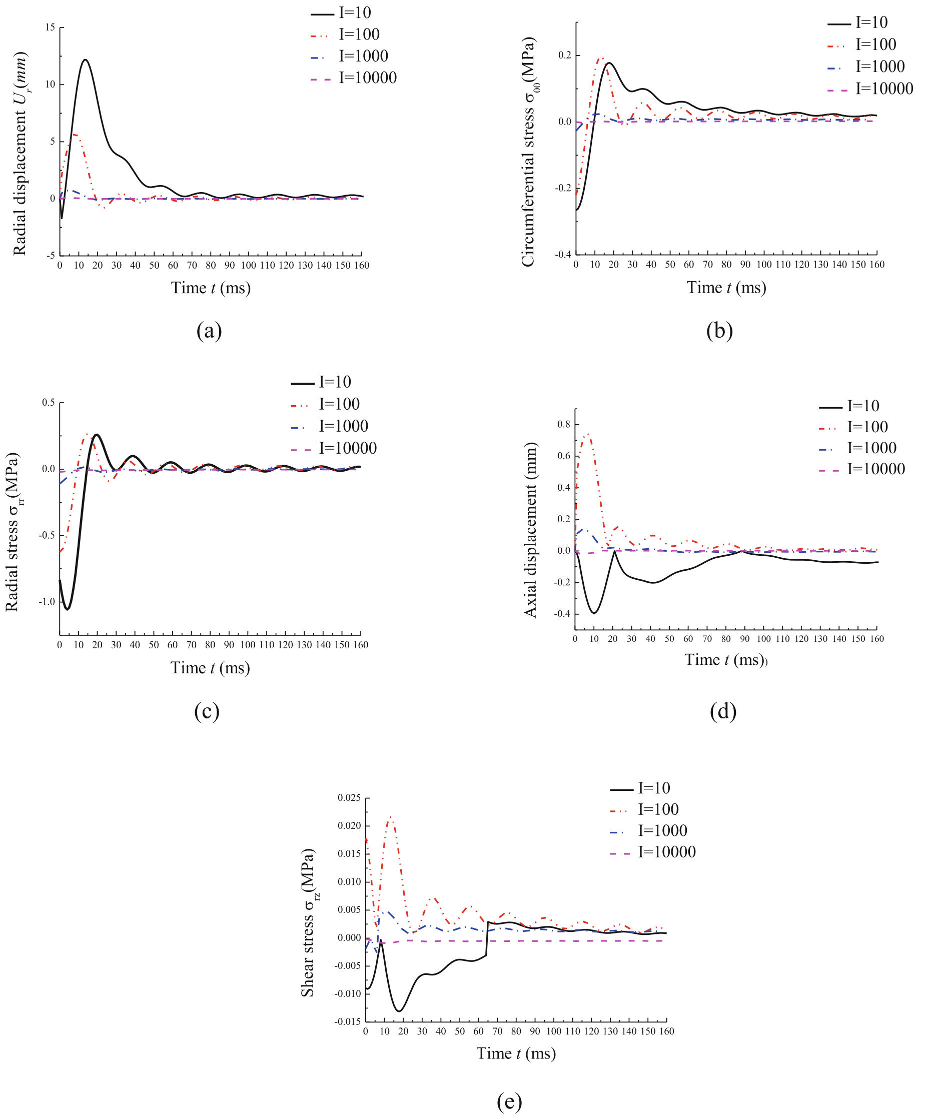

(a)

(b)

(c)

(d)

(e)

Fig. 5. Responses of soil to (a) radial displacement, (b) circumferential stress, (c) radial stress, (d) axial displacement, and (e) shear stress over time for different values of the parameter *I*.

arrived, the response peaked and the shock attenuated, and the displacement and stress stabilized. As the rigidity of the shell lining increased, the vibration cycle of each response increased and the maximum absolute values of the soil displacement and stress decreased.

A comparison of Fig. 5a and b shows that the displacement had a certain delay relative to stress, and a comparison of Fig. 5d and e shows that axial displacement was delayed relative to axial stress.

4 Conclusion

(1) The primary dynamic responses of the soils were independent of lining size and relative stiffness. The response oscillations decayed over time, and rapidly decayed along the axial direction of the tunnel. The dynamic response of the soil farther away from the explosion was much smaller than that near the explosion.
(2) The rigidity and thickness of the lining had significant effects on the three-dimensional dynamic responses of the soil displacement and stress. As the shell lining stiffness and thickness increased, the response amplitude and period decreased and the vibration weakened.
(3) An appropriate increase in the thickness of the lining can effectively reduce the responses to explosions. However, when the lining thickness exceeds a certain threshold, increasing its value further likely provides little benefit. The optimum value should be between 0.1 m and 0.25 m.
(4) An appropriate increase in the rigidity of the shell lining can effectively reduce dynamic responses. However, if the relative stiffness is too large, the stability of the lining structure can become unfavorable. The relative stiffness optimal value should be between 1,000 and 10,000.

Acknowledgments. The writers wish to acknowledge the National Natural Science Foundation of China (No. 51478255 and 51678352).

References

1. Mohsenimonfared, H., Nikkhahbahrami, M.: Dynamic stresses and displacements around cylindrical cavities in an infinite elastic medium under moving step loads on the cavity's surface. Life Sci. J. **9**(2), 812–822 (2012)
2. Coşkun, İ., Dolmaseven, D.: Dynamic response of a circular tunnel in an elastic half space. J. Eng. **2017**(3), 1–12 (2017)
3. Datta, S.K., Wong, K.C., Shah, A.H.: Dynamic stresses and displacements around cylindrical cavities of arbitrary shape. Trans. ASME J. Appl. Mech. (USA) **51**(4), 798–803 (1984)
4. Yi, C.P., Zhang, P., Johansson, D., et al.: Dynamic response of a circular lined tunnel with an imperfect interface subjected to cylindrical P-waves. Comput. Geotech. **55**, 165–171 (2014)

5. Li, X., Chen, Y.: Transient dynamic response analysis of orthotropic circular cylindrical shell under external hydrostatic pressure. J. Sound Vibr. **257**(5), 967–976 (2002)
6. Gao, M., Zhang, J.: Transient response of cylindrical lined tunnel in infinitely elastic soil under internal source explosive loading. Geotech. Eng. **39**(08), 1366–1373 (2017)
7. Wang, Y., Gao, G.: Study on dynamic response of transient loaded tunnels in saturated half – space. Geomechanics **37**(03), 850–858 (2016)
8. Zeng, C., Sun, H.L., Cai, Y.Q. et al.: Analysis of three-dimensional dynamic response of a circular lining tunnel in saturated soil to harmonic loading. Rock Soil Mech. **35**(4), 1147–1156 (2014)
9. Koneshwaran, S., Thambiratnam, D.P., Gallage, C.: Response of segmented bored transit tunnels to surface blast. Adv. Eng. Softw. **89**, 77–89 (2015)
10. Uystepruyst, D., Monnoyer, F.: A numerical study of the evolution of the blast wave shape in rectangular tunnels. J. Loss Prev. Process Ind. **34**, 225–231 (2015)
11. Yan, Q.X., Bin, L., Ping, G., et al.: Dynamic response of a double-lined shield tunnel to train impact loads. Tunn. Undergr. Space Technol. **53**, 33–45 (2016)
12. Pan, J.L., Luo, M., Zhou, J.J.: Dynamic responses and failure mechanism of reinforced concrete cylindrical column wrapped with CFRP under blast loading. J. Tianjin Univ., 43(9), 755–761 (2010)
13. Achenbach, J.D.: Wave Propagation in Elastic Soilds. North-Holland Publishing Co., Amsterdam (1973)
14. Wang, Y., Gao, M., Gao, G.Y., et al.: An analytical solution for the transient response of a cylindrical lined cavity in a poroelastic medium. Soil Dyn. Earthq. Eng. **46**(3), 30–40 (2013)
15. Xiao, Y., Wen, M.J.: Dynamic characteristics of saturated fraction derivative derived viscoelastic soil-shallow circular tunnel lining system. Eng. Mech. 29(12), 248–255 (2012)
16. Forrest, J.A., Hunt, H.E.M.: A three-dimensional tunnel model for calculation of train-induced ground vibration. J. Sound Vibr. **294**(4–5), 678–705 (2006)
17. Durbin, F.: Numerical inversion of Laplace transform efficient improvement to Durbin and Abate's method. Comput. J. **17**(4), 371–376 (1974)

A Coupled Hydro-Mechanical Modeling of Tunnel Leakage in Sand Layer

Jie Yang[1,2], Zhen-Yu Yin[2,3,4](✉), Dong-Mei Zhang[3,4],
Pierre-Yves Hicher[2], and Farid Laouafa[1]

[1] INERIS, 60550 Verneuil en Halatte, France
[2] Research Institute of Civil Engineering and Mechanics (GeM),
UMR CNRS 6183, Ecole Centrale de Nantes, 44300 Nantes, France
zhenyu.yin@gmail.com
[3] Department of Geotechnical Engineering, College of Civil Engineering,
Tongji University, Shanghai, China
[4] Key Laboratory of Geotechnical and Underground Engineering of Ministry
of Education, Tongji University, Shanghai 200092, People's Republic of China

Abstract. The tunnel leakage in sand layer plays an important role in the evolution of the lining stresses and the ground movement. The phenomenon of internal erosion occurs when underground water leaks into the tunnel from the damaged joints or the cracks of the linings. Fines in sand are pulled off by seepage forces and transported throughout the soil matrix into the tunnel. The loss of fines due to seepage flow affects the mechanical behavior of the soil around the tunnel. Conversely, the change of porosity influences the permeability of the soil and, therefore, its hydraulic conductivity. In this study, the effect of tunnel leakage in sand layer is investigated numerically with a coupled hydro-mechanical approach, considering the internal erosion phenomenon induced by the local flows of underground water, using the continuous porous medium theory and a critical-state based constitutive model. Simulation results show that the loss of fines as well as the leakage locations have significant impacts on the tunnel lining and the ground movement.

Keywords: Tunnel leakage · Sand · Fine particles
Hydro-mechanical modeling · Internal erosion

1 Introduction

Tunnels are considered to be one of the widely used underground structure. It has been observed that during the service life of a tunnel, the ground movement induced by tunneling is significant and can continue for many years [1–3]. The cause of tunnel settlement and deformation have been discussed, including land subsidence, variation of ground water table, leakage of tunnel, dynamic response of train, etc. [4–6] Tunnel leakage is an important factor that has been widely studied [7, 8]. However, the effect of the loss of fines has not been deeply discussed in the previous study. The leakage of underground water through the cracks and joints of lining commonly carries fines in the form of silt and clay from the surrounding ground, i.e. internal erosion [9]. The change

© Springer Nature Singapore Pte Ltd. 2018
D. Zhang and X. Huang (Eds.): GSIC 2018, *Proceedings of GeoShanghai 2018 International Conference: Tunnelling and Underground Construction*, pp. 506–514, 2018.
https://doi.org/10.1007/978-981-13-0017-2_51

of porosity due to loss of fines affects the mechanical behavior of the surrounding soil [10, 11]. Conversely, the change of porosity influences the permeability of the sand and, therefore, its hydraulic conductivity.

In this study, the effect of leakage on the tunnel in sand layer was investigated numerically with a coupled hydro-mechanical approach, considering the internal erosion phenomenon induced by the local flows of underground water.

2 Formulation of the Time Dependent Physical Problem

2.1 Mass Balance and Particle Transport

The mass balance equations are based on the porous media theory [12, 13]. The saturated porous medium is modeled as a system of 4 constituents: the solid skeleton (*ss*), the erodible fines (*se*), the fluidized particles (*fp*) and the fluid (*ff*). The fines can either behave as a fluid-like (described as fluidized particles) or a solid-like (described as erodible fines) material. Thus, a liquid-solid phase transition process is taken into account in the present model by a mass production term in the corresponding mass balances for erodible fines and fluidized particles.

In a given Representative Elementary Volume (dV) consisting of the four constituents, the volume fraction n^x of a single constituent x is expressed as:

$$n^x = dV^x/dV \tag{1}$$

with dV^x denoting the volume of the corresponding constituent.

At a material point level, the volume balance for the x phase is reduced from the mass balance, neglecting the hydro-mechanical dispersion tensor [12]:

$$\partial_t(n^x) + div(n^x\mathbf{v}^x) = n^{ex,x} \tag{2}$$

where $n^{ex,x}$ is the volume exchange term, $\mathbf{v}^x$ is the velocity.

Moreover, it is assumed that fluid and fluidized particles have at any time the same velocity. The solid skeleton is assumed to be deformable but non-erodible. The porosity field ϕ, the amount of erodible fines f_c, the concentration of the fluidized particles c are defined as follows:

$$\phi = n^{ff} + n^{fp}, f_c = n^{se}/(1-\phi) \text{ and } c = n^{fp}/\phi \tag{3}$$

The transformation of the state of fines from part of the solid skeleton to fluidized particles leads to:

$$n^{ex,a} = -n^{ex,se} = \hat{n},\ n^{ex,ss} = 0 \text{ and } n^{ex,ff} = 0 \tag{4}$$

The mass balance equations are then given by the following expressions:

$$-\partial_t \phi + div(\mathbf{v}_s) - div(\phi \mathbf{v}_s) = -\hat{n} \tag{5}$$

$$\partial_t(f_c) - \partial_t(f_c \phi) + div(f_c \mathbf{v}_s) - div(f_c \phi \mathbf{v}_s) = -\hat{n} \tag{6}$$

$$\partial_t(c\phi) + div(c\mathbf{q}_\mathbf{w}) + \partial_t(c\phi \mathbf{v}_s) = \hat{n} \tag{7}$$

$$div(\mathbf{q}_w) + div(\mathbf{v}_s) = 0 \tag{8}$$

where $\mathbf{q}_\mathbf{w}$ denotes the total discharge of liquid, $\mathbf{q}_\mathbf{w} = \phi\left(\mathbf{v}_f - \mathbf{v}_s\right)$, $\mathbf{v}_s = \partial_t \mathbf{u}$ denotes the soil skeleton velocity, reduced from the displacement of soil skeleton $\mathbf{u}$.

2.2 Darcy's Law

In this study, the flow in the porous medium is governed by Darcy's law:

$$\mathbf{q}_\mathbf{w} = -\frac{k(\phi)}{\eta_k \bar{\rho}(c)}(\mathbf{grad}(p_w) - \bar{\rho}(c)\mathbf{g}) \tag{9}$$

where k is the intrinsic permeability of the medium depended on porosity [13], η_k is the kinematic viscosity of the fluid, p_w is the pore fluid pressure, $\mathbf{g}$ is the gravity vector, $\bar{\rho}$, ρ_s and ρ_f are the density of the mixture, the solid and the fluid:

$$\bar{\rho} = c\rho_s + (1-c)\rho_f \tag{10}$$

$$k = k_0 \frac{\phi^{k_1}}{(1-\phi)^{k_2}} \left(\frac{\phi_0^{k_1}}{(1-\phi_0)^{k_2}}\right)^{-1} \tag{11}$$

2.3 Constitutive Equation for Mass Exchange

A model for the mass exchange is given by the following relation [14]:

$$\hat{n} = \lambda_e(1-\phi)\left(1 - \frac{c}{c_r}\right)|\mathbf{q}_\mathbf{w}|\{f_c - f_{c0}[(1-\beta)\exp(-\alpha|\mathbf{q}_\mathbf{w}|) + \beta]\} \tag{12}$$

where c_{cr} is the critical value of c for which the two competing phenomena, erosion and plugging, balance each other; λ_e, α and β are the material parameters.

2.4 A Critical State Based Constitutive Model for the Solid Phase

The mechanical behavior of the solid skeleton is controlled by:

$$\sigma'_{ij,j} + (p_w)_{,j} - w_j = 0 \tag{13}$$

where σ'_{ij} denotes the component of the effective stress tensor, p_w is the pore pressure, w_i is the body forces per unit volume. A critical state based constitutive model [15–19] is adopted. It is able to take into account the influence of the change of porosity on the mechanical behavior of the soil during the process of internal erosion. The main constitutive equations are summarized in Table 1.

Table 1. Basic constitutive equations of SIMSAND

Components	Constitutive equations
Elasticity	$\dot{\varepsilon}^e_{ij} = \frac{1+v}{3K(1-2v)}\sigma'_{ij} - \frac{v}{3K(1-2v)}\sigma'_{kk}\delta_{ij}$ $K = K_0 \cdot p_{at}\frac{(2.97-e)^2}{1+e}\left(\frac{p'}{p_{at}}\right)^{\zeta}$
Yield surface in shear	$f_s = q/p' - H$
Potential surface in shear	$\frac{\partial g_s}{\partial p'} = A_d\left(M_{pt} - \frac{q}{p'}\right); \frac{\partial g_s}{\partial s_{ij}} = \{1 \quad 1 \quad 1 \quad 1 \quad 1 \quad 1\}$
Hardening rule for shear	$H = M_p\varepsilon^p_d / \left(k_p + \varepsilon^p_d\right)$
Critical state line and inter-locking effect	$e_c = e_{ref} - \lambda(p'/p_{at})^{\xi}$ $\tan\phi_p = (e_c/e)\tan\phi_\mu; \tan\phi_{pt} = (e/e_c)\tan\phi_\mu$
Three-dimensional strength criterion	$M = M_c\left[\frac{2c^4}{1+c^4+(1-c^4)\sin 3\theta}\right]^{\frac{1}{4}}$ with $c = \frac{3-\sin\varphi}{3+\sin\varphi}$

*K is the bulk modulus; v is the Poisson's ratio; p_{at} is the atmospheric pressure (p_{at} = 101.325 kPa); p' is the mean effective stress; q is the deviatoric stress; k_p is the plastic shear modulus; A_d is the stress-dilatancy parameter; ϕ_p is peak fiction angle; ϕ_{pt} is phase transformation friction angle; ϕ_μ is critical fiction angle; M_p and M_{pt} is the stress ratio corresponding to peak strength and phase transformation strength respectively; e_c is the critical void ratio; e_{ref} is the reference critical void ratio corresponding to $p_{ref} = p_{at}$; λ is the slope of the CSL in the e–log p' plane.

2.5 Hydro-Mechanical Coupling

The hydro-mechanical coupling effect can be conceptually divided into two parts. In the first part, the internal erosion results in an evolution of the porosity, which in turn leads to the change of permeability. As a consequence, the pore pressure and the effective stresses will change. In the second part, the loss of fines affects the void ratio, which in turn leads to the change of the mechanical behavior of the soil.

3 Numerical Analysis of Tunnel Leakage in Sand Layer

Weak forms of Eqs. (5)–(8) and (13) are implemented into a finite element formulation by using isoparametric 8-node elements. Euler backward implicit scheme is used for time. The weak forms are linearized and solved by Newton-Raphson method iteratively at each time step.

3.1 Description of the Problem

The numerical model was conducted to investigate the hydro-mechanical response of an existing tunnel installed in sand layer and experiencing a local internal erosion due to the leakage of underground water from the damaged joints or cracks. The tunnel was assumed to have a circular shape with an inner diameter of 5.5 m and to be constructed at a depth of 10 m below the ground surface as shown in Fig. 1.

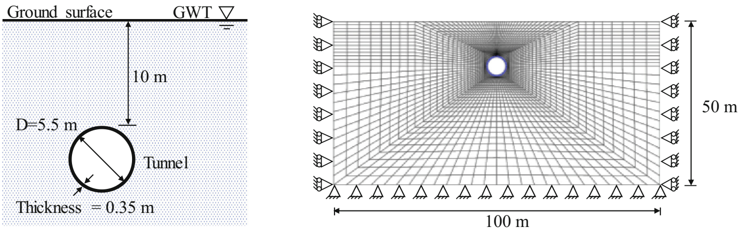

Fig. 1. Problem geometry used in the numerical analysis.

A plain strain finite element model was used to represent the soil and tunnel lining, using 8-noded quadratic elements. The finite element mesh and boundary conditions are shown in Fig. 1. The interaction between the lining and soil was assumed to be rigid in the normal direction and rough friction in the tangent direction.

A series of simplified leakage cases were analyzed. The leakage points were supposed to be at ±45° or ±135°, as shown in Fig. 2.

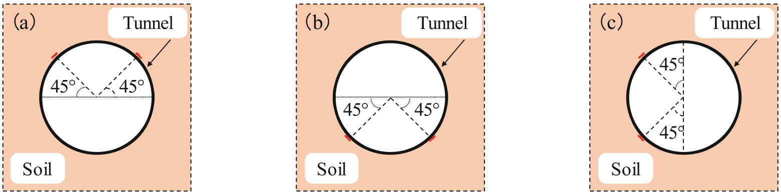

Fig. 2. Leakage location at tunnel lining. (a) Top; (b) Bottom; (c) Left.

The material constants are summarized in Tables 2 and 3. The model parameters of Toyoura sand with initial void ratio $e_0 = 0.73$ [20] were adopted.

Table 2. Material constants of erosion

Density of fluid	ρ_f	1.0	Kinematic viscosity of fluid	η_k	5.0E-6 m^2s
Density of solids	ρ_s	2.65	Intrinsic permeability	k_0	5.0E-10 m^2
Permeability constants	k_1, k_2	3.0, 2.0	Erosion constants	λ_e, α, β	9E-6,0.01,0.1

Table 3. Material properties of Toyoura sand and concrete lining

Parameters	K_0	ν	ζ	ϕ_μ	e_{ref}	λ	ξ	k_p	A_d
Toyoura sand	130 pat	0.3	0.52	31.5	0.977	0.0596	0.365	0.0041	0.7
Concrete lining	30 GPa	0.2	-	-	-	-	-	-	-

3.2 Hydro-Mechanical Responses

Figure 3 shows the evolution of the fines during the leakage process. Internal erosion took place, leading to the decrease of the fines which was initially uniform in the whole soil volume. The decrease was critical in the vicinity of the cavity, which created to a highly eroded zone. By comparing the three cases, when the leakage occurred at the lower part of the tunnel, a more significant eroded area is obtained.

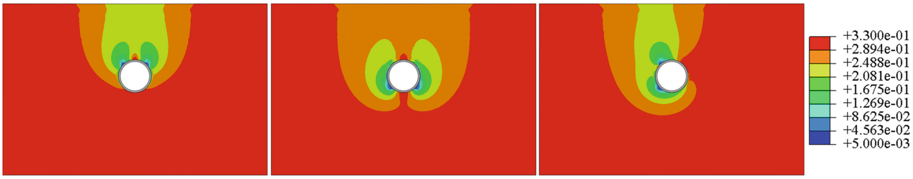

(a) Top (b) Bottom (c) Left

Fig. 3. Spatial distribution of fines f_c for the three cases at the 300th day of leakage.

Figure 4(a) and (b) show the profiles of ground surface settlement at 300d for the three and the time history of maximum ground surface settlements for different leakage location during leakage process. It is observed that for two-dimensional simulation, the lower leakage location results in a larger ground surface settlement. Moreover, about 50% of the total settlement during 300 days is produced at very early stage of leakage. This is due to the change of effective stress induced by the change of boundary condition of pore pressure at the leakage point before the development of eroded area. After that the settlement keeps increasing and tend towards stabilizing.

The profiles of calculated bending moments of the tunnel lining at 300d for the three cases are presented in Fig. 5(a)–(c). Significant increase in bending moment was obtained. It was also observed that the moment change for lower leakage location is larger compared to the other two cases. To visualize the relative changes in bending moment along the tunnel circumference, the results are summarized in Fig. 5(d). For each leakage location, the bending moment at the top heading of the tunnel increased

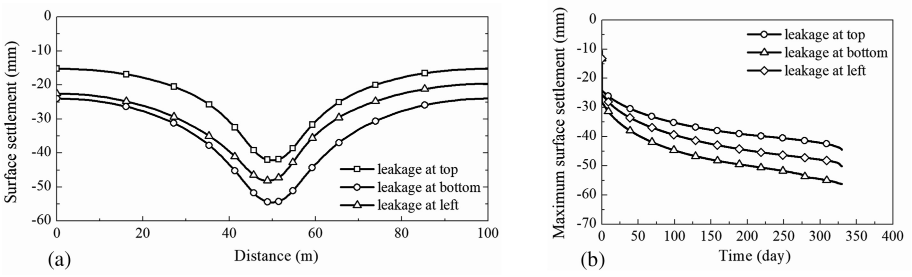

Fig. 4. (a) Profiles of ground surface settlement at 300d for different leakage location; (b) Time history of maximum ground surface settlement for different leakage location

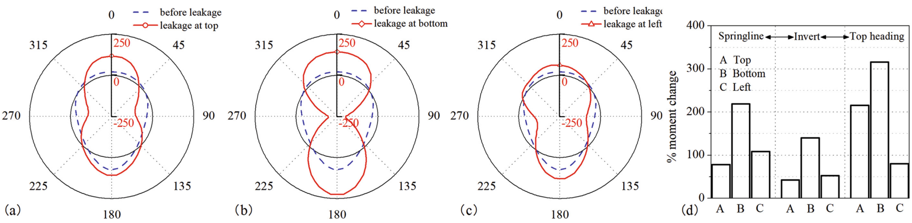

Fig. 5. Bending moment (kN·m/m) of tunnel lining at 300d: (a) leakage at upper tunnel, (b) leakage at lower tunnel, (c) leakage at left side of tunnel; (d) Percentage change in bending moment of tunnel lining due to the leakage at different location.

by 215%, 315% and 80% in excess of the values without considering the erosion process. The maximum bending moment was obtained at the invert of tunnel, which increased by 42%, 140% and 52% for the three leakage locations respectively. This is considered to be significant changes that could lead to undesirable stress levels in tunnel lining.

4 Summary and Conclusions

In this study, the effect of leakage on the tunnel in sand layer was investigated numerically with a coupled hydro-mechanical approach, considering the internal erosion phenomenon induced by the local flows of underground water. The internal erosion of the soil skeleton and the transport of fine particles by the fluid were modeled by the mass exchange between the solid skeleton and the pore water. Furthermore, a simple critical-state based constitutive model was applied to describe the behaviors of eroded soil. The investigations indicated that the loss of fines has significant impact on the concrete lining of tunnel and the ground settlement. With the development of underground water leakage and internal erosion, there is an obvious increase in the maximum bending moment in the tunnel lining and the ground surface settlement.

This work focuses on the evolution of fines by hydro-mechanical coupling method. Future work will consider the effects of fines content on mechanical behavior of sand for full coupling.

Acknowledgement. The financial supports provided by the National Institute for Industrial Environment and Risks of France (INERIS) and National Natural Science Foundation of China (41372285 and 51579179) are gratefully acknowledged.

References

1. Shen, S.-L., Wu, H.-N., Cui, Y.-J., Yin, Z.-Y.: Long-term settlement behaviour of metro tunnels in the soft deposits of Shanghai. Tunn. Undergr. Space Technol. **40**, 309–323 (2014)
2. Jiang, M., Yin, Z.-Y.: Influence of soil conditioning on ground deformation during longitudinal tunneling. C.R. Mec. **342**, 189–197 (2014)
3. Jiang, M., Yin, Z.-Y.: Analysis of stress redistribution in soil and earth pressure on tunnel lining using the discrete element method. Tunn. Undergr. Space Technol. **32**, 251–259 (2012)
4. Wu, H.-N., Shen, S.-L., Chai, J.-C., Zhang, D.-M., Xu, Y.-S.: Evaluation of train-load-induced settlement in metro tunnels. Proc. Inst. Civ. Eng. Geotech. Eng. **168**, 396–406 (2014)
5. Wu, H.-N., Shen, S.-L., Liao, S.-M., Yin, Z.-Y.: Longitudinal structural modelling of shield tunnels considering shearing dislocation between segmental rings. Tunn. Undergr. Space Technol. **50**, 317–323 (2015)
6. Li, P., Du, S.-J., Ma, X.-F., Yin, Z.-Y., Shen, S.-L.: Centrifuge investigation into the effect of new shield tunnelling on an existing underlying large-diameter tunnel. Tunn. Undergr. Space Technol. **42**, 59–66 (2014)
7. Wongsaroj, J., Soga, K., Mair, R.: Tunnelling-induced consolidation settlements in London clay. Géotechnique **63**, 1103 (2013)
8. Zhang, D., Huang, Z., Yin, Z., Ran, L., Huang, H.: Predicting the grouting effect on leakage-induced tunnels and ground response in saturated soils. Tunn. Undergr. Space Technol. **65**, 76–90 (2017)
9. Bonelli, S., Marot, D.: Micromechanical modeling of internal erosion. Eur. J. Environ. Civ. Eng. **15**, 1207–1224 (2011)
10. Yin, Z.-Y., Zhao, J., Hicher, P.-Y.: A micromechanics-based model for sand-silt mixtures. Int. J. Solids Struct. **51**, 1350–1363 (2014)
11. Yin, Z.-Y., Huang, H.-W., Hicher, P.-Y.: Elastoplastic modeling of sand–silt mixtures. Soils Found. **56**, 520–532 (2016)
12. Schaufler, A., Becker, C., Steeb, H.: Infiltration processes in cohesionless soils. ZAMM - J. Appl. Math. Mech./Z. Angew. Math. Mechanik **93**, 138–146 (2013)
13. Yang, J., Yin, Z.-Y., Hicher, P.-Y., Laouafa, F.: A finite element modeling of the impact of internal erosion on the stability of a dike. In: Poromechanics VI, pp. 354–361 (2017)
14. Vardoulakis, I., Stavropoulou, M., Papanastasiou, P.: Hydro-mechanical aspects of the sand production problem. Transp. Porous Media **22**, 225–244 (1996)
15. Yin, Z.-Y., Xu, Q., Hicher, P.-Y.: A simple critical-state-based double-yield-surface model for clay behavior under complex loading. Acta Geotech. **8**, 509–523 (2013)
16. Jin, Y.-F., Wu, Z.-X., Yin, Z.-Y., Shen, J.S.: Estimation of critical state-related formula in advanced constitutive modeling of granular material. Acta Geotech., **12**(6), 1–23 (2017)

17. Yin, Z.-Y., Jin, Y.-F., Shen, S.-L., Huang, H.-W.: An efficient optimization method for identifying parameters of soft structured clay by an enhanced genetic algorithm and elastic–viscoplastic model. Acta Geotech., **12**(4), 849–867 (2016)
18. Jin, Y.F., Yin, Z.Y., Shen, S.L., Hicher, P.Y.: Selection of sand models and identification of parameters using an enhanced genetic algorithm. Int. J. Numer. Anal. Methods Geomech. **40**, 1219–1240 (2016)
19. Jin, Y.-F., Yin, Z.-Y., Shen, S.-L., Hicher, P.-Y.: Investigation into MOGA for identifying parameters of a critical-state-based sand model and parameters correlation by factor analysis. Acta Geotech. **11**, 1131–1145 (2016)
20. Wu, Z.-X., Yin, Z.-Y., Jin, Y.-F., Geng, X.-Y.: A straightforward procedure of parameters determination for sand: a bridge from critical state based constitutive modelling to finite element analysis. Eur. J. Environ. Civ. Eng., 1–23 (2017)

Tunnelling in Challenging Situations

Evolution of Frost Penetration and Ablation in the Surrounding Rock of Cold Region Tunnels

Zhitao Lv[1,2], Caichu Xia[1,2(✉)], Yu Zhou[1,2], Changling Han[3], and Yuesong Wang[1,2]

[1] Department of Geotechnical Engineering,
Tongji University, Shanghai 200092, China
`tjxiaccb@126.com`
[2] Key Laboratory of Geotechnical and Underground Engineering of Ministry of Education, Tongji University, Shanghai 200092, China
[3] First Highway Consultants Company Limited, China Communications Construction Company Limited, Xi'an 710075, Shanxi, China

Abstract. Taking Jiangluling tunnel as an example, a numerical model for investigating the evolution of the frost penetration and ablation in the surrounding rock of cold region tunnels is presented based on the governing equations of the coupling problem of temperature and air flow fields in cold region tunnels. As the tunnel starts to operate and cold air flows in, frost penetration starts. The thawed permafrost section near the entrance and exit freezes again after 5 years of operation, and the unfrozen surrounding rock section in the middle part starts to transform to permafrost gradually in the 6th to 10th year of operation. Thereafter, the frozen circle becomes thicker slowly. From the 20th year to the 40th year, the temperature of surrounding rock maintains stable approximately. Thereafter, the temperature of surrounding rock starts to increase, and the entrance and exit part starts to re-melt due to the climate warming. Frost ablation starts. After the 80th year, the frozen surrounding rock in the range of 500 m from the entrance and 150 m from the exit approximately re-melts. To the 100th year, the surrounding rock in the whole tunnel re-melts as the result of frost ablation. Moreover, frost penetration and frost ablation develop much faster from the entrance along the wind direction than those from exit.

Keywords: Cold region tunnels · Frost penetration · Frost ablation
Temperature field

1 Introduction

Many cold region tunnels have been constructed in China, Canada, Japan, Russia, and Norway. The frost and thaw situation of the surrounding rock in cold region tunnels after construction has been paid much attention, because it's a basis to protect cold region tunnels from frost and thaw damage. Thus, plenty of work has been done on predicting temperature field, frost and thaw situation of cold region tunnels.

Lai et al. [1] derived an approximate analytical solution of temperature field in cold region circular tunnels, using dimensionless and perturbative method. He et al. [2]

© Springer Nature Singapore Pte Ltd. 2018
D. Zhang and X. Huang (Eds.): GSIC 2018, *Proceedings of GeoShanghai 2018 International Conference: Tunnelling and Underground Construction*, pp. 517–527, 2018.
https://doi.org/10.1007/978-981-13-0017-2_52

proposed a numerical model of coupled problem of heat conduction and convective exchange between air inside the tunnel and the surrounding rock, to predict the temperature field variation, but in the model the tunnel was assumed as axial symmetry; and then, a three-dimensional calculating model of the coupled problem are presented by Lai et al. [3]. Moreover, Tan et al. [4] developed a temperature field model assuming the wind flow as turbulence flow, to show the influence of airflow on the temperature of the surrounding rock in a cold region tunnel. Zeng et al. [5] performed a model test based on practical horseshoe railway tunnel section to investigate the couple effect of convection-conduction with low inlet temperature airflow. In addition, Zhang et al. [6] investigated the re-frozen process of Feng Huoshan permafrost tunnel, and the results showed that the melt circle induced during construction may re-frozen after four years of operation.

While, the present researches are mainly focus on the cold region tunnels passing through permafrost layer or the frost and thaw situation of permafrost in cold region tunnels. For a cold region tunnel passing through seasonal permafrost layer, permafrost layer, and unfrozen surrounding rock in longitudinal direction, as shown in Fig. 1, less attention has been paid. During the operation process, due to the negative annual average temperature, the frost may penetrate from the entrance and the exit into the middle part gradually; after the permafrost in the entrance and exit parts is re-frozen, the unfrozen surrounding rock in the middle part freezes progressively. Thus, the frost penetration tunnel forms. Frost penetration in the surrounding rock may freeze the drainage system and lead to the increase of frost heaving force, which may damage the lining. On the other hand, studies have shown that climate warming is a considerable issue which affects the stability of the permafrost [7, 8]. Most researchers suggest that the rate of the climate warming is 0.05 °C/a, and thus the annual average temperature may increase 5.0 °C during the design life (100 years) of a tunnel. Hence, for tunnels in areas where the annual average temperature is between 0 °C and −5 °C, the temperature of the surrounding rock would increase and the frost ablation may occur during the operation process. Frost ablation in surrounding rock may induce thawing settlement. Hence, the frost penetration and ablation should be considered in cold region tunnel design. Therefore, in the paper, a numerical model is presented based on the governing equations of the coupling problem of temperature and air flow fields in cold region tunnels with the assistance of COMSOL multiphysics. Taking Jiangluling tunnel as an example, numerical simulations are carried out to investigate the evolution of the frost penetration and ablation in the surrounding rock of the cold region tunnel.

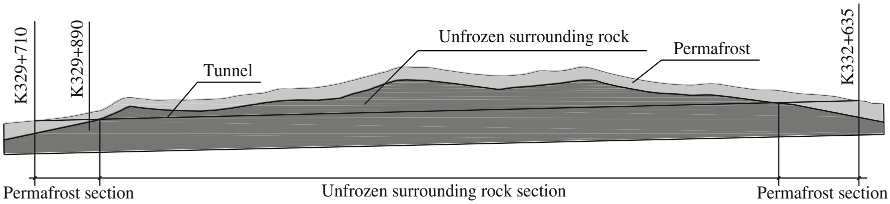

Fig. 1. Longitudinal profile of Jiangluling tunnel

2 Governing Equations of Coupling Problem of Temperature and Air Flow Fields in Cold Region Tunnels

2.1 Air Flow and Temperature Fields in the Tunnel

To simplify the govern equations of the air flow field in the tunnel, the following assumptions are introduced:

(1) Air is incompressible and the air pressure is not varied with temperature.
(2) Air flow in the tunnel is considered as laminar flow [2, 3].

Thus, the mass conservation equation takes the form as:

$$\nabla \cdot \boldsymbol{u} = 0, \tag{1}$$

where $\boldsymbol{u}$ is the velocity vector.

The momentum conservation equations can be simplified as:

$$\frac{\partial \boldsymbol{u}}{\partial t} + (\boldsymbol{u} \cdot \nabla)\boldsymbol{u} = \nabla \cdot \left[-p\mathbf{I} + v\left(\nabla \boldsymbol{u} + (\nabla \boldsymbol{u})^{\mathrm{T}}\right)\right], \tag{2}$$

where p is the ratio of air pressure to air density, v is kinematic viscosity coefficient of air, $\mathbf{I}$ is a unit matrix.

The air temperature field is governed by energy conservation equation:

$$c_a \frac{\partial T}{\partial t} + c_a \boldsymbol{u} \cdot \nabla T = \nabla \cdot (\lambda_a \nabla T), \tag{3}$$

where T is air temperature, c_a and λ_a are volumetric heat capacity and thermal conductivity of air, respectively.

2.2 Temperature Field of the Surrounding Rock

The temperature governing equation of surrounding rock considering the latent heat of pore water can be given as [9]:

$$C_{eq} \frac{\partial T}{\partial t} - \nabla\left(\lambda_{ef} \nabla T\right) = 0, \tag{4}$$

where $C_{eq} = \begin{cases} C + L\rho_w \frac{\partial \theta_w}{\partial T} & T \le T_0 \\ C & T > T_0 \end{cases}$, λ_{ef} and C are the effective thermal conductivity and volumetric thermal capacity of rock composite, L is the latent heat of water per unit mass, ρ_w is the density of water, θ_w is the volumetric unfrozen water content, T_0 is the freezing point of pore water and is considered to be 0 °C in this paper.

θ_w can be given as:

$$\theta_w = \frac{(1-n)\rho_s}{\rho_w}\omega, \tag{5}$$

where ρ_s is the density of rock grains, n is the porosity of rock, ω is the unfrozen water content.

Equation (6) is chosen to describe the unfrozen water content ω in freezing rock [10, 11]:

$$\omega = \omega^* + (\omega_0 - \omega^*)e^{a(T-T_0)}, \tag{6}$$

where ω^* is the residual unfrozen water content at some low reference temperature, ω_0 is the minimum unfrozen water content at freezing point T_0, a is a material parameter describing the decay rate of unfrozen water.

C can be expressed as [9]:

$$C = (1-n)C_s + \theta_w C_w + \theta_i C_i, \tag{7}$$

where C_s, C_w, C_i are the volumetric thermal capacity of rock grains, water, ice, respectively, θ_i is the volumetric ice content, and $\theta_i = n - \theta_w$.

A logarithmic law is employed in this paper for calculation of λ_{ef} [9]:

$$\lambda_{ef} = \lambda_s^{1-n}\lambda_w^{\theta_w}\lambda_i^{\theta_i}, \tag{8}$$

where λ_s, λ_w, λ_i are the thermal conductivity of rock grains, water and ice, respectively.

3 Numerical Simulation of Jiangluling Tunnel in Cold Region

The governing Eqs. (1), (2), (3) and (4) of the coupling problem are solved with the assistance of COMSOL multiphysics. Numerical simulations are carried out taking Jiangluling tunnel as an example to investigate the evolution of the frost penetration and ablation in the surrounding rock of the cold region tunnel.

3.1 Introduction to Jiangluling Tunnel

Jiangluling tunnel is a key project of Gonghe-Yushu highway in Qinghai-Tibet Plateau with the altitude over 4280 m. In the tunnel site, the winter is cold with plenty of snow and the freezing period exceeds 7 months in a year. The average annual air temperature is –4.2 °C, and the extreme minimum temperature is –48.1 °C. The top surface of the permafrost is 1.2–2.2 m in depth, and bottom surface is 31–39 m in depth, as shown in Fig. 1. The tunnel is 2925 m in length, and the permafrost sections are about 240 m and 200 m at the entrance and exit, respectively. The unfrozen surrounding rock section is about 2485 m long.

3.2 Numerical Model and Boundary Conditions

Since the tunnel is too long, only an approximation 2D model is built, as shown in Fig. 2. A 5 cm thick thermal insulation layer is paved on the outside of the lining and the lining is 50 cm thick. The thermal conductivity of the insulation layer and lining are 0.05 W m^{-1} $°\text{C}^{-1}$ and 0.5 W m^{-1} $°\text{C}^{-1}$, respectively. In the model, the thermal insulation layer and the lining are equivalent to one layer with 1 m thick, and the thermal conductivity of this layer set to 0.516 W m^{-1} $°\text{C}^{-1}$. Thus, the thermal resistance of the layer equals to the sum of the thermal resistance of thermal insulation layer and lining. According to the monitoring data of meteorological station near the tunnel, and assuming the climate warming rate is 0.05 °C/a, the air temperature outside the tunnel can be simplified as:

$$T = -4.2 + 6.9\sin(\frac{2\pi t}{365} + \frac{3\pi}{2}) + \frac{0.05t}{365}. \tag{9}$$

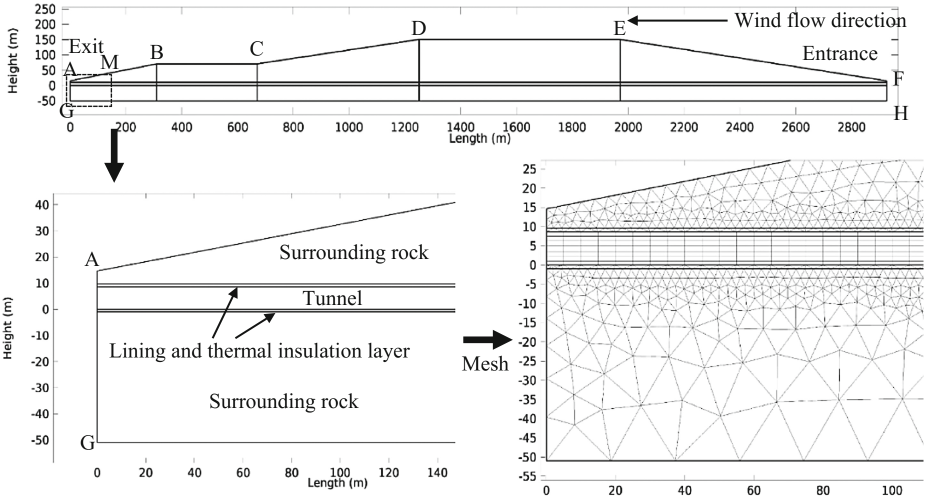
Height (m)
250
200
150
100
50
0
-50
Exit
A
M
B
C
D
E
Wind flow direction
Entrance
F
G
H
0
200
400
600
800
1000
1200
1400
1600
1800
2000
2200
2400
2600
2800
Length (m)
Height (m)
40
30
20
10
0
-10
-20
-30
-40
-50
A
Surrounding rock
Tunnel
Lining and thermal insulation layer
Surrounding rock
G
0
20
40
60
80
100
120
140
Length (m)
Mesh
25
20
15
10
5
0
-5
-10
-15
-20
-25
-30
-35
-40
-45
-50
-55
0
20
40
60
80
100

Fig. 2. Numerical model of Jiangluling tunnel

The solar radiation is strong in Qinghai-Tibet Plateau, and thus, it should be considered when computing the temperature of the ground surface. The influence of the solar radiation can be equivalent to the increments of the annual average air temperature (ΔT) and the amplitude of the air temperature (ΔA). At the sunny slope of the Jiangluling tunnel, $\Delta T_1 = 4.8\,°\text{C}$ and $\Delta A = 0.5\,°\text{C}$; at the shady slope, $\Delta T_1 = 3.9\,°\text{C}$ and $\Delta A = 1.6\,°\text{C}$ [12]. Thus, the temperature of the ground surface at the sunny slope and the shady slope of the Jiangluling tunnel can be derived as:

$$T_{su} = 0.6 + 7.4\sin(\frac{2\pi t}{365} + \frac{3\pi}{2}) + \frac{0.05t}{365}, \tag{10}$$

$$T_{sh} = -0.3 + 8.5\sin(\frac{2\pi t}{365} + \frac{3\pi}{2}) + \frac{0.05t}{365}. \tag{11}$$

Boundaries A-B-C-D-E are sunny slope, and boundary EF is shady slope. The convective heat transfer coefficient of the boundaries which contact with air is 15.0 W/(m^2 °C) [13]. The heat flux of boundary GH is 0.06 W/m [3]. At the entrance and the exit, the temperature boundary set as Eq. (12).

According to the meteorological station near the tunnel, the maximum and minimum of monthly average wind speed is about 3.5 m/s and 2.5 m/s, respectively. Hence, at the entrance, the wind speed in one year can be given as [2]:

$$u = 0.028\left[\frac{12(t-183)}{365}\right]^2 + 2.5, \tag{12}$$

where 0 < t < 365 d and assumed that the wind speed is given as Eq. (12) every year. At the exit, P = 101.3 kPa. Parameters related are listed in Table 1.

Table 1. Parameters for the numerical simulation

Parameter	Value	Parameter	Value	Parameter	Value	Parameter	Value
λ_a (W m^{-1} °C^{-1})	0.02	ρ_s (kg/m^3)	2600	ω^*	0.00475	λ_i (W m^{-1} °C^{-1})	2.22
C_a (kJ m^{-3} °C^{-1})	0.713	λ_s (W m^{-1} °C^{-1})	3.87	ω_0	0.06787	C_w (kJ m^{-3} °C^{-1})	4180
v (10^{-6} m^2/s)	1.298	C_s (kJ m^{-3} °C^{-1})	1742	n	0.15	C_i (kJ m^{-3} °C^{-1})	1916
ρ_w (kg/m^3)	1000	ρ_i (kg/m^3)	917	L (kJ/kg)	334	λ_w (W m^{-1} °C^{-1})	0.58

3.3 Initial Temperature Field

The initial temperature field of the mountain without tunnel is obtained first. According to the survey data, the average depth of permafrost is 35 m, and the average temperature of permafrost is –2.5 °C. In the model, set the initial temperature of upper 35 m to −2.5 °C, and the initial temperature of the lower part increases by 0.03 °C/m [2, 13]. Then the temperature field of the mountain is simulated, and it is found that when the calculation time reaches 13 years, the temperature field changes slightly. This temperature field can be seen as the initial temperature field before the excavation of the tunnel.

During the excavation process, the temperature of the surrounding rock increases due to the hydration heat of the concrete and the heat of blasting. Temperature of surrounding rock at different depth was measured with a 4 m deep drilling hole during the excavation. Figure 3 shows the measured temperature increase of the surrounding rock at section ZK332 + 505 and section ZK329 + 890. The temperature increase ($\Delta T'$) is nearly linear to the depth of the measure position (D). The fitting curve is $\Delta T' = -1.364D + 6.462$, and the correlation coefficient R^2 = 0.938. Increase the temperature of the surrounding rock within 4.7 m according to the fitting curve, and thus, the temperature field after excavation can be obtained.

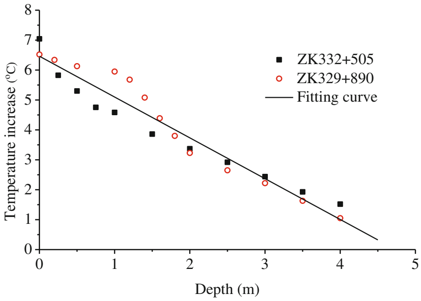

Fig. 3. Temperature increase of surrounding rock due to excavation

3.4 Comparison Between Numerical Results and Monitoring Data

The temperature of the ground surface at point M (shown in Fig. 2) and surrounding rock at section ZK329 + 890 were measured during and after the construction. Comparisons between the numerical results and the measured temperature are given in Fig. 4. The numerical results are consistent with the measured data.

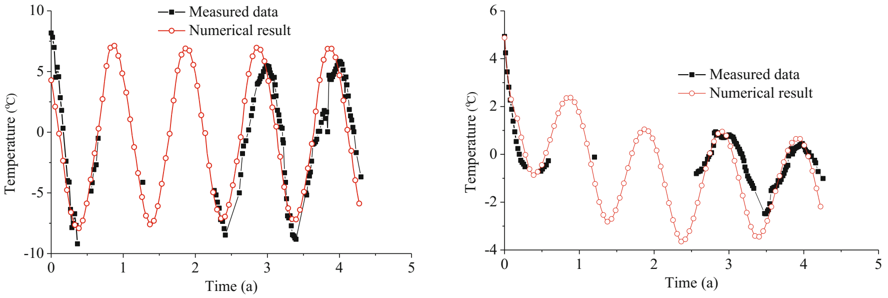

(a) Ground surface at point M (b) Surrounding rock at section ZK329+890

Fig. 4. Comparison between the numerical results and measured data

4 Evolution of the Frost Penetration and Ablation of Jiangluling Tunnel

Figure 5 shows the temperature field of the entrance part (1250 m to 2925 m) before construction and 5 years after construction. Figure 6 shows temperature variation of surrounding rock with 1.0 m depth along longitudinal direction before construction and 5, 10, 20, 40, 60, 80, 100 years after construction, respectively. As shown in Figs. 5(a), and 6(a), before excavation, only the temperature of the part 2700 m to 2925 m is below 0 °C, and this is consistent with the in situ permafrost survey data. After excavation, due to the heat induced during the construction process, the temperature of the surrounding rock increases and nearly the temperature of the surrounding rock within 1 m depth in the whole tunnel is greater than 4 °C, as shown in Fig. 6(a). Then, as the tunnel begins to operate, cold air flows in the tunnel, and the frost penetration starts. 5 years after construction, the thawed permafrost section near the entrance and exit freezes again; moreover, in the range of 900 m from the entrance and 250 m from the exit approximately, the unfrozen surrounding rock forms the permafrost, as shown in Figs. 5(b) and 6(a). 10 years after construction, the surrounding rock in the whole tunnel begins to form the permafrost, and 12 years after construction, the frozen surrounding rock reaches about 3 m, as shown in Fig. 7. As the result of frost penetration, the unfrozen surrounding rock section gradually transforms to permafrost in the 12 years of operation.

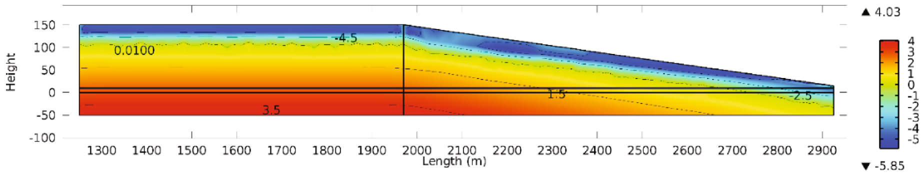

(a) Initial temperature before construction (December)

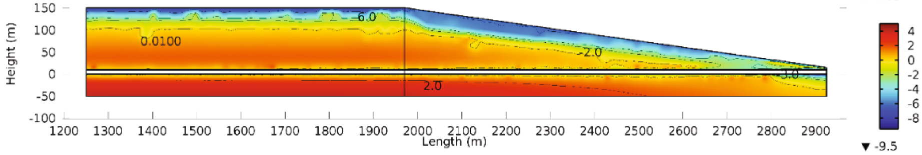

(b) 5 years after construction (December)

Fig. 5. Temperature field of the surrounding rock at the entrance

From the 10th year to the 20th year, the temperature of surrounding rock continue to decrease, and the temperature in the middle part is greater than the entrance or the exit part. From the 20th year to the 40th year, the temperature of surrounding rock maintains stable approximately, but the temperature in the middle part gradually becomes smaller than the entrance or the exit part, due to the climate warming, as shown in Fig. 6(a). After the 40th year, as the climate warming continues, the temperature of surrounding rock starts to increase, and the entrance and exit part starts to re-melt to the 60th year, as shown in Fig. 6(b). Frost ablation starts. After the 80th year, in the range of 500 m from the entrance and 150 m from the exit approximately, the frozen surrounding rock re-melts. To the 100th year, as the result of frost ablation, the surrounding rock in the whole tunnel re-melts.

Figure 8(a) shows the frost penetration length from the entrance and exit during the 1st to 11th year. Cold air flows in the tunnel from the entrance, and thus, frost penetration develops much faster from the entrance than that from exit. To the 11th year when the frost action penetrates through the whole tunnel, the frost penetration length is about 2375 m from entrance, while it is only 550 m from exit. Figure 8(b) shows the frost ablation length from the entrance and exit during the 55st to 90th year. The frost ablation process is similar to the frost penetration process; frost ablation develops much

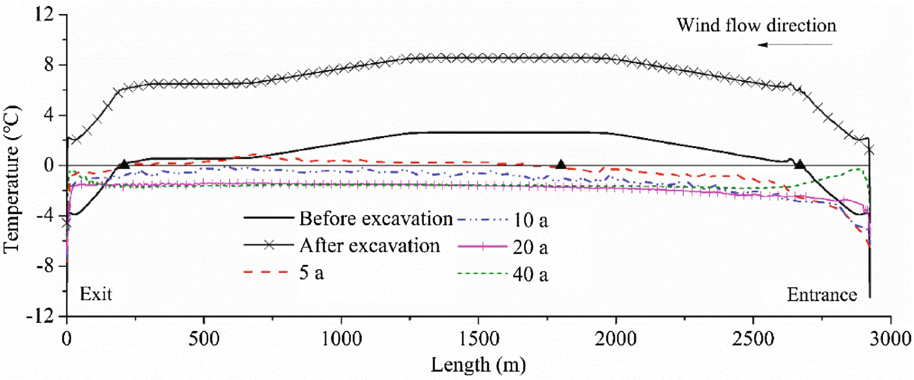

(a) Before excavation to 40 years after excavation (December)

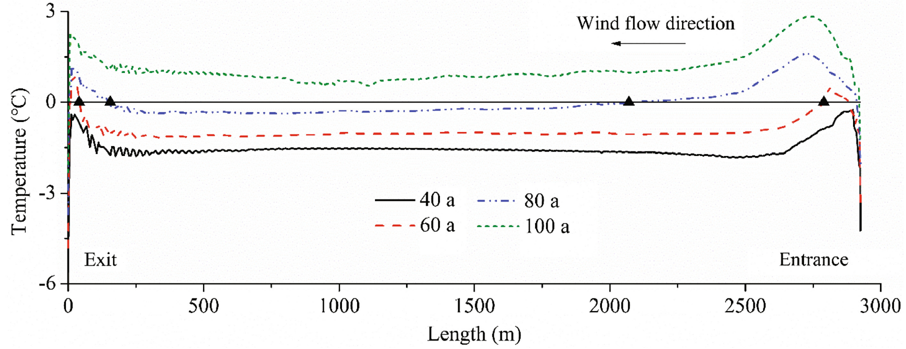

(b) 40 to 100 years after excavation (December)

Fig. 6. Temperature variation of surrounding rock along longitudinal direction at different time

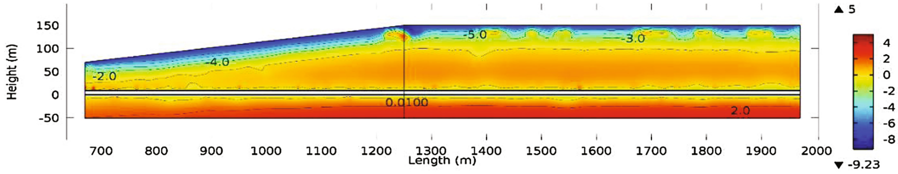

Fig. 7. Temperature field of the surrounding rock (12 years after construction, December)

faster from the entrance than that from exit. To the 90th year when the frost ablation penetrates through the whole tunnel, the frost ablation length is about 2325 m from entrance, while it is only 600 m from exit.

Figure 9 shows the temperature variation of two points of surrounding rock at cross sections 1600 m and 2825 m with 2 m depth versus time. The cross section 1600 m is 1325 m from the entrance, which is in the middle part, and the cross section 2825 m is 100 m from the entrance, which is in the entrance part. As shown in Fig. 9, the temperature variation in the middle part is lagging behind that in the entrance part. The permafrost at section 2825 m melts during the excavation, and freezes again at the 2nd

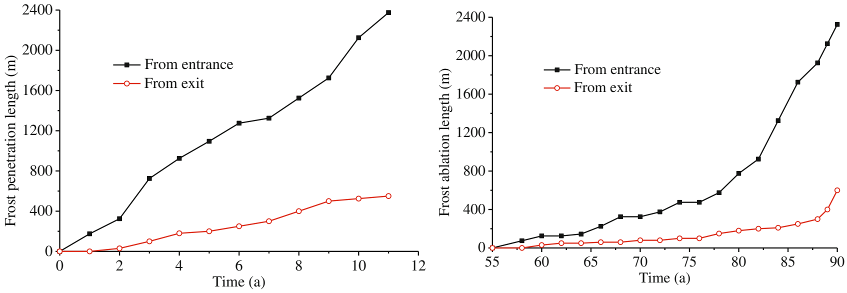

Fig. 8. Frost penetration and ablation length from entrance and exit

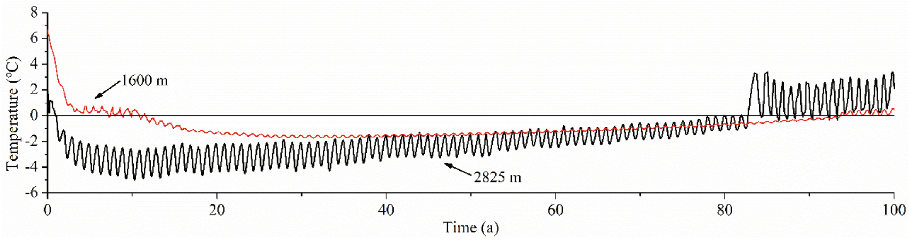

Fig. 9. Temperature variation of surrounding rock versus time

year after excavation. With the continued development of frost penetration, the temperature in the middle part decreases continuously, and the unfrozen surrounding rock at section 1600 m transforms to permafrost at the 12th year after construction. As the climate warming develops, the temperature of the surrounding rock at section 2825 starts to increase 40 years after construction. While, the temperature at section 1600 m starts to increase 60 years after construction. As the climate warming further develops, the permafrost at section 2825 m starts to melt 80 years after construction; while, the permafrost starts to melt until 95 years after construction. Moreover, the amplitude of the temperature in the middle part is much smaller than that in the entrance part.

5 Conclusion

A numerical model is presented based on the governing equations of the coupling problem of temperature and air flow fields in cold region tunnels. Taking Jiangluling tunnel as an example, numerical simulations are carried out to investigate the evolution of the frost penetration and ablation in the surrounding rock of the cold region tunnel. The results show that as the tunnel begins to operate, cold air flows in the tunnel, and the frost penetration starts. 5 years after construction, the thawed permafrost section near the entrance and exit freezes again; 10 years after construction, the surrounding rock in the whole tunnel begins to form the permafrost, and 12 years after construction, the frozen surrounding rock reaches about 3 m. From the 20th year to the 40th year, the temperature of surrounding rock maintains stable approximately. After the 40th year, the temperature of surrounding rock starts to increase, and the entrance and exit part starts to re-melt. Frost ablation starts. After the 80th year, in the range of 500 m from the entrance and 150 m from the exit approximately, the frozen surrounding rock re-melts. To the 100th year, as the result of frost ablation, the surrounding rock in the whole tunnel re-melts. Moreover, frost penetration and frost ablation develops much faster from the entrance along the wind direction than those from exit.

Acknowledgements. This research was supported by National Natural Science Foundation of China (41472248, 51778475).

References

1. Lai, Y., Liu, S., Wu, Z., Yu, W.: Approximate analytical solution for temperature fields in cold regions circular tunnels. Cold Reg. Sci. Technol. **34**, 43–49 (2002)
2. He, C., Wu, Z., Zhu, L.: A convection-conduction model for analysis of the freeze-thaw conditions in the surrounding rock wall of a tunnel in permafrost regions. Sci. China, Ser. D Earth Sci. **42**, 1–8 (1999)
3. Lai, Y., Zhang, X., Yu, W., et al.: Three-dimensional nonlinear analysis for the coupled problem of the heat transfer of the surrounding rock and the heat convection between the air and the surrounding rock in cold-region tunnel. Tunn. Undergr. Space Technol. **20**, 323–332 (2005)
4. Tan, X., Chen, W., Yang, D., et al.: Study on the influence of airflow on the temperature of the surrounding rock in a cold region tunnel and its application to insulation layer design. Appl. Therm. Eng. **67**, 320–334 (2014)
5. Zeng, Y., Liu, K., Zhou, X., Fan, L.: Tunnel temperature fields analysis under the couple effect of convection-conduction in cold regions. Appl. Therm. Eng. **120**, 378–392 (2017)
6. Zhang, X., Lai, Y., Yu, W., Wu, Y.: Forecast analysis for the re-frozen of Feng Huoshan permafrost tunnel on Qing-Zang railway. Tunn. Undergr. Space Technol. **19**, 45–56 (2004)
7. Frauenfeld, O.W., Zhang, T., Barry, R.G., Gilichinsky, D.: Interdecadal changes in seasonal freeze and thaw depths in Russia. J. Geophys. Res. Atmos. **109**, D05101 (2004)
8. Wu, T., Zhao, L., Li, R., et al.: Recent ground surface warming and its effects on permafrost on the central Qinghai-Tibet Plateau. Int. J. Climatol. **33**, 920–930 (2013)
9. Tan, X., Chen, W., Tian, H., Cao, J.: Water flow and heat transport including ice/water phase change in porous media: Numerical simulation and application. Cold Reg. Sci. Technol. **68**, 74–84 (2011)
10. Michalowski, R.: A constitutive model of saturated soils for frost heave simulations. Cold Reg. Sci. Technol. **22**, 47–63 (1993)
11. Michalowski, R.L., Zhu, M.: Frost heave modelling using porosity rate function. Int. J. Numer. Anal. Meth. Geomech. **30**, 703–722 (2006)
12. Lu, M.: Study on the technique of design and construction controlling of tunnel portal in permafrost region, dissertation for Master's degree, Tongji University, Shanghai (2014)
13. Zhang, X., Lai, Y., Yu, W., Zhang, S.: Nonlinear analysis for the three-dimensional temperature fields in cold region tunnels. Cold Reg. Sci. Technol. **35**, 207–219 (2002)

TBMs: Capabilities, Limitations and Challenges

Yun Bai[1](✉), Xi Jiang[1], Diana Diaz[1], Xuehui Zhang[1],
and ZhuanZhuan Zhang[2]

[1] Department of Geotechnical Engineering, Tongji University, Shanghai, China
baiyun1958@tongji.edu.cn
[2] China Tiesiju Civil Engineering Group Co., Ltd., Hefei, China

Abstract. The Tunnel Boring Machine (TBM) technology has significant advantages over conventional Drill & Blast method, and it has become one of the most common tunnel excavation methods in the world. However, weaknesses of TBM such as the poor adaptability to complex geological conditions create a bottleneck in its functionality, and restrict its further development. Therefore, factors such as engineering geological conditions, construction schedule, cost, environmental impact and other multi-disciplinary influences should be well considered in the TBM selection. This paper presents the capabilities, limitations and challenges of TBM method by a study of various case projects, and proposes effective countermeasures towards bad geological conditions. The results of this research are helpful for improving the TBM working efficiency and ensuring a smooth and safe construction.

Keywords: Tunnel excavation · TBM method · Capacity · Limitations
Complex geology

1 Introduction

In the 21st century, a new trend in development has emerged, which is called "sustainable development" and most policies and processes must follow up its goals and considerations. As a result, the underground space is again valuable as a space for human beings to survive on earth [1]. After more than two centuries of wide application of TBMs (Tunnel Boring Machines), and thanks to continuous scientific and technological advances, such mechanized excavation technology is being extensively used around the world for tunnel construction in all kinds of infrastructure projects (like railway, highway, hydropower, etc.).

Among its multiple functions, a TBM can excavate, support, install lining and remove muck synchronously. Moreover, with the extensive use of electronic information technology, such as real-time monitoring and distant control, full access to the construction process becomes possible, allowing it to reach a relatively optimized state. Until today, these were the key advantages of TBM technology.

TBM's construction speed is probably the biggest advantage, which is 4 to 10 times as high as the conventional Drill & Blast (D&B) method. In addition, TBM tunneling offers a lower life-time cost, saves much labor force, and is environmentally friendly.

© Springer Nature Singapore Pte Ltd. 2018
D. Zhang and X. Huang (Eds.): GSIC 2018, *Proceedings of GeoShanghai 2018 International Conference: Tunnelling and Underground Construction*, pp. 528–535, 2018.
https://doi.org/10.1007/978-981-13-0017-2_53

The D&B method usually produces a larger severe rock mass damage zone (see Fig. 1), while the TBM method will only induce a small damage zone in the surrounding rock, thus decreasing the risk during construction. According to estimations, by the end of 2000, more than 100 tunnels over 10 km in length were excavated by the TBM method, totaling more than 10,000 km.

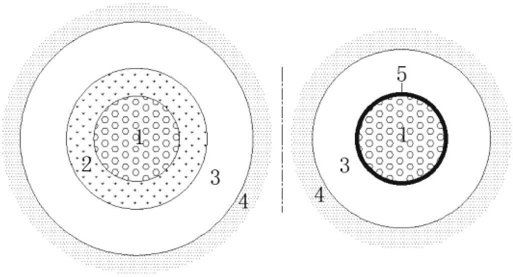

(a) D&B (b) TBM

Fig. 1. Influence of two excavation methods on the surrounding rock. (*1-Tunnel area; 2-Crack zone of surrounding rock; 3-Perturbance of surrounding rock; 4-Non-affected zone; 5-Void or grouting area*).

However, the TBM method does have limitations. The following are bottlenecks summarized from previous construction processes: (i) A TBM is difficult to transport due to its large weight and size, additionally it cannot be retreated after the lining support is installed; (ii) The initial capital investment is higher than D&B method; (iii) No obvious advantages over traditional D&B methods for short tunnels; (iv) Its support capacity is far less than the tunneling driving ability, and the initial support is not as timely as the conventional method; (v) The rock exposure time is longer, (the time before the primary support can be finished), resulting potential hazard risk for the equipment; (vi) Once the initial support is fixed, it is no longer as flexible as the conventional method. Due to these weaknesses, the adaptability of the TBM method needs to be considered for complex geology, especially when confronting adverse conditionals such as weak strata, rock burst, water ingress, etc. if the TBM is wrongly chosen for bad situation, it not only suffers more impact than the conventional D&B method, but also diminishes the efficiency and even to cause major accidents (such as equipment damage and casualties).

The lessons learned from tunnel projects show that, besides serious problems encountered in TBM construction such as the stuck of TBMs for long periods or even the probability of it to remain buried, the TBM method also encounters accidents like water inflow and surrounding ground collapse. These factors can lead to a rearrangement of original project plans, where the traditional drilling and blasting method has to be employed for the rest of the tunnel construction, the Yunnan Zhangjiu River Diversion Water Supply project in China and Dul Hasti Hydropower project in India are both such cases, TBM encountered unexpected bad geological conditions which posed a threat to the safety of the personnel and equipment [2].

Thus, it is important to select the appropriate type of TBMs according to each engineering situation and take reasonable measures to ensure the safety and efficiency. The capabilities, limitations and challenges of the TBM method are presented here. Finally, current deficiencies of the TBM tunneling technology are analyzed through typical engineering case studies in order to propose helpful countermeasures.

2 Overview of the Tunnel Boring Construction Method

A TBM consists basically of two main parts: the main body or front section (also called shield) and the backup system components, with an overall length of generally up to 150–200 m. The main body consists of a cutterhead, a thrust system, a trailing support mechanism, a conveyor and a control room for an operator to run the rock breaking, mucking and transport system. The cutterhead is a rock breaking component; the vertical, side and roof support together with the gripper or trailing mechanism allow the TBM to move forward and push the cutterhead. The backup system components include a slag system, the support equipment, a laser guidance system, power and water supply system, and a drainage and ventilation system. Since a TBM has large weight and volume, it is usually assembled and disassembled at the launching and retrieval shafts, respectively.

The construction process of the TBM method can be divided into pre-construction preparation, transport and assembly of a TBM, excavation operation, lining installation, muck removal. TBM's working cycle includes digging and a step-by-step process that involves the hydraulic cylinder system, and its support system, pressing the TBM forward continuously. The excavation of a TBM tunnel must follow the project design documents in order to ensure a successful construction [3].

3 Capabilities of the TBM Method

3.1 Development and Application of the TBM Construction Method

Since the 1950s, the TBM method has been widely used, achieving tremendous breakthroughs. Over the last half-century, big projects like the Channel Tunnel, the Tokyo Bay Aqualine Tunnel and the Green Heart Tunnel in the Netherlands, represent a landmark in the history of the TBM (refer to Table 1). Undoubtedly, in recent years, a large number of super-engineering projects have successfully used TBMs as the construction method, popularly called the "Tunnel Century" [4].

Table 1. Tunnels constructed using TBMs.

Project name	Location	Length (km)	Diameter (m)	Construction time
Tokyo Bay Aqualine Tunnel	Japan	20	14.14	1994.8–1997.12
Celtic Creek Tunnel	Netherlands	13.2	11.34	1998.3–2003.11
Great Denmark Tunnel	Denmark	14.8	7.7	1988.11–1997.2
Mohale Tunnel	South Africa	30.5	4.9–5.4	1999.3–2002.6

The Gotthard Base Tunnel beneath the Alps is one of the most representative projects, with a maximum overburden of approx. 2400 m, consisting of two parallel single-track tubes with an excavation diameter varying from 8.8 to 9.5 m and linked by cross-passages approximately every 312 m. Around 65% of the entire tunnel system was excavated by TBMs. Before the project could start, many preliminary studies were conducted in order to decide which construction method was most suitable. The TBM method was selected considering factors such as safety and efficiency.

China also researched and developed various types of TBMs to meet the increasing demand of tunnel construction. According to current predictions, the length of tunnels built in China will exceed 3000 km in the next 20 years [5], far more than the overall length of the Western countries. Hence, there is no doubt that the use of high-tech TBMs will continue to increase.

4 TBM Method's Limitations, Challenges and Countermeasures

Despite numerous achievements gained throughout years of experience with the TBM method, there are still many challenges. For example, multiple soil layers can be encountered, which means a drawback for the cutterheads; the TBM can be damaged or even stuck by rock bursting or under high-stresses relief of the surrounding ground; water inflows into the tunnel can delay the project, etc. Cases like the diversion tunnel of Tianshengqiao hydropower station of Yunnan Province in China, the Mont Blanc Tunnel in Italy and the under construction Brenner Base Tunnel in Austria have faced such challenges. However, if the TBM type and configuration are not appropriately assessed, once it encounters complex geology conditions as mentioned before, it could lead to major problems as shown in Table 2 [6].

Table 2. Engineering problems encountered in tunnels [6]

Project name	Problem encountered
Channel Tunnel	Water gushing
Celtic Creek Tunnel	Compressional formation & High water pressure
Great Denmark Tunnel	Cutter wear & Water gushing
Mohale Tunnel	Water inrush
Grand entry into Qin Project	Rapid deformation of surrounding rock
Wanjiazhai Yellow River Diversion Project	Fault fracture zone and Water inrush
Qinling Tunnel	Rock burst and Fault fracture zone
Mogouling Tunnel	Collapse of surrounding rock
Shanggongshan Tunnel	Collapse of fault fracture zone & Water inrush

Evidence of plate tectonics shows that fractured rock mass and abundance of groundwater as well as complex geological conditions increase during tunnel excavation. These uncertainties are major problems for engineers. If one overestimates the capability of the TBM method, without studying its deficiencies and limitations in each specific project, it could lead to project failure. The common problems faced during excavation by TBMs are compiled below.

4.1 Engineering Geological Problems

Adverse geological conditions mainly refer to conditions that impede the project's progress. For TBM construction, it relates to the geological structure, lithology, ground stress and groundwater. The analysis of a large number of TBM engineering cases, indicates that large deformation of the surrounding ground and water inflow are the two main problems that lead to major engineering accidents. In 2005, 98 TBM accidents were recorded [7], of which 72% of the accidents were caused by these two factors (see Fig. 2). Other factors included rock burst, karst zones, fault formations, composite strata, etc.

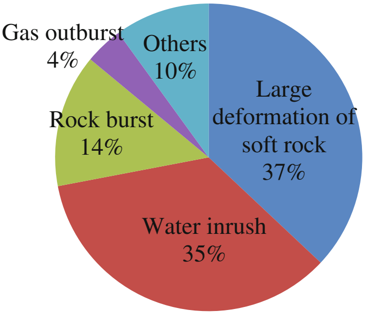

Fig. 2. Main engineering geological problems encountered by TBM method in 2005.

The Snow Mountain Tunnel in Taiwan is the second longest road tunnel in Asia, a double-tube, and double-track tunnel 12.9 km long. Due to difficulties presented during construction, it took 13 years to complete. The Snow Mountain range consists of mildly metamorphic and sedimentary rocks. Its location where the collision of the Philippine plate with the Eurasian plate takes place further induced squeezing and upheaves of the tunnel. The two main tunnels have a diameter of 11.74 m and the three ventilation shafts are 4.8 m in diameter. The project planned to adopt the TBM method due to its efficiency: the construction times were to be 4.5 years and 15 years, respectively [8]. However, all parties involved in the design agreed in that the TBM could only show superiority at the west part of the alignment, where there was a stable compact rock zone.

Weathering and dense vegetation could make the drilling even more difficult. Due to the over-complexity faced in the construction stage, the construction methods used were different from the ones suggested in the original plan (see Fig. 3). This experience

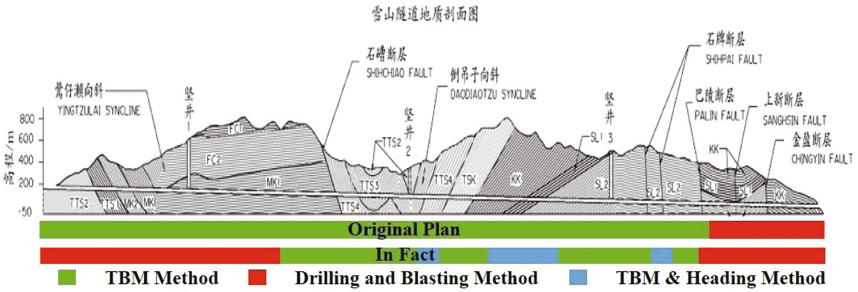
雪山隧道地质剖面图
鶯仔瀨向斜
YINGTZULAI SYNCLINE
石磜斷层
SHIHCHIAO FAULT
倒吊子向斜
DAODIAOTZU SYNCLINE
石牌断层
SHIHPAI FAULT
巴陵断层
PALIN FAULT
上新断层
SANGHSIN FAULT
金盈断层
CHINGYIN FAULT
坚井 1
坚井 2
坚井 3
高程/m
800
600
400
200
-50
FC1
FC2
MK1
MK2
TTS1
TTS2
TTS3
TTS4
TSK
KK
SL1
SL2
Original Plan
In Fact
TBM Method
Drilling and Blasting Method
TBM & Heading Method

Fig. 3. Geological profile of Snow Mountain Tunnel in Taiwan.

indicates that severe fractures, shearing zones and large underground water inflow can bring great difficulties to the construction.

Dul Hasti Hydroelectric Project in Kashmir, India includes a 65 m dam, a 10.6 km long tunnel and an underground powerhouse, and is built within the Himalayan Range. The crossing rock formation is mainly quartzite and phyllite. Due to the differences between the ancient Kishtwar plateau deposition and drilling tests, many accidents occurred, which includes mud and water ingress. In 2000, the TBM was stuck at a severe-fractured zone for 8 months, damaging the machine. The project was delayed by more than 20 months, finally completed after 12 years (1991–2003).

The above TBM accidents show that although the TBM method has been developed over two hundred years, complex geology is continuously demanding higher technology in order to avoid major engineering accidents, which result in significant economic losses.

4.2 Challenges and Countermeasures of the TBM Method

The challenges encountered by TBMs during construction are various, and some possible solutions from former projects are summarized as follows:

(1) **Large deformation of weak surrounding rock**
Large deformation of the weak surrounding rock will lead to rapid convergence of tunnels, resulting in deformation and damage of the segment or even of the TBM. The following measures can be taken: ① Over-excavation, which leaves enough space for the deformation of surrounding rock; ② Use of an auxiliary hydraulic cylinder to allow the TBM to pass rapidly through soft rock formation.

(2) **Gushing water**
Gushing water usually has the following characteristics: large volume, high water pressure and sudden outburst. It will cause severe harm to staff and equipment. Therefore, is important to: ① Strengthen monitoring by drilling ahead; ② Detect water gushing point and discharge the possible water.

(3) **Rock burst**
Rock burst is a kind of dynamic instability caused by sudden release of strain energy. It's important to consider the rock burst criteria, according to the Chinese standard for engineering classification of rock masses (GB/T 50218-2014) [9].

Table 3. Rock burst criteria according to Chinese code (GB/T 50218-2014) [7]

σ_c/σ_{max}	>7	4–7	<4
Level of rock burst	No	Slight or medium	Strong
Influence depth	0	0.5–1 m	1/3 m or more

It is the ratio of the rock strength to the maximum ground stress that matters (see Table 3.). In order to safely pass through the rock burst section, the following measures can be taken: ① Use of boreholes to release the crustal stress and inject water into the boreholes to dampen the rock mass; ② Timely support by appropriate support methods, and strengthen real-time monitoring work.

(4) **Mixed formations**

Mixed formation is usually encountered during TBM tunneling in mountain tunnels. According to case studies, mixed formation can be generally classified into three types [10, 11]. Stability of excavation surface and deformation of surrounding strata have to be considered during the excavation in a mixed formation.

(5) **Karst Zone**

In order to pass through the karst zone smoothly, the following treatment methods can be adopted when the large karst section is encountered during the construction process: ① If the cave is located in the upper face, steel bolt and half ring steel support should be adopted; ② If the cave is located in the lower part of the tunnel, rock bolt reinforcement can be used on both sides of karst cave; ③ If the above methods are not applicable, circuitous heading can be helpful and the karst cave can be treated from the side or top of the tunnel.

(6) **Coal seam and harmful gas**

Coal seam and harmful gas are twin brothers, which are often associated with each other, resulting in the damage of tunnel construction and operation. During the construction of Wuhan, China Metro Line 2, the tunnel from Hankou Railway Station to Fan Lake Station crossed the gas reservoir, which has great potential safety hazard to operators and mechanical safety in the process of TBM construction.

Therefore, corresponding measures must be taken for safety: ① Advance forecast is needed according to geological conditions of gas development; ② Strengthen ventilation in tunnel to reduce harmful gas concentration; ③ Explosion proof equipment is adopted to control and ensure safe use of electricity during construction; ④ Make strict management and fire prevention measures to ensure construction safety.

Although the TBM construction method has many advantages, if the above problems are not paid enough attention to, it will cause disastrous losses.

5 Conclusions

The demand for tunnel construction and underground space development is still expanding all over the world. However, the TBM method may not be adapted to complex geological conditions, and other associated problems also restrict its further development. Through the analysis and summary of the above engineering cases, the following issues should be paid attention to during the construction of tunnel projects:

(1) In the process of geological investigation, the information of drilling, geophysical prospecting and geological logging should be comprehensively analyzed. Detailed forecast and pretreatment work should be done from the beginning of the project.
(2) If most of the geological conditions are not figured out or if known to be poor, construction workers need to carefully consider whether to use the TBM method. An optimal scheme should be suggested after analyzing geological conditions, construction progress, economic benefits and environmental impact.
(3) One or more risk-sharing methods should be taken during the construction. Working with experienced construction teams will help to ensure the smooth progress of the project.

References

1. Wang, M.: Tunneling by TBM/shield in China: state-of-art, problems and proposals. Tunn. Constr. **03**, 179–187 (2014)
2. Vibert, C., et al.: Dul Hasti HPP (India): experience gained from back-analysis of the excavation of the headrace tunnel. In: Proceedings of Geoline 2005 International Symposium, Lyon, p. 154 (2005)
3. Liu, Q., et al.: Application and development of hard rock TBM and its prospect in China. Tunn. Undergr. Space Technol. **46**, 33–46 (2016)
4. Zhang, J.: The application and some problems of TBM and its prospects. Chin. J. Rock Mech. Eng. **18**(3), 363–366 (1999)
5. Wang, Z.: Safe driving technology for TBM across poor geologic zones. Chin. Saf. Sci. J. **12** (4), 55–59 (2002)
6. Hong, K.: State-of-art and prospect of tunnels and underground works in China. Tunn. Constr. **35**(02), 95–107 (2015)
7. Shang, Y., et al.: Retrospective analysis of TBM accidents from its poor flexibility to complicated geological conditions. Chin. J. Rock Mech. Eng. **12**, 2404–2411 (2007)
8. Walls, S., et al.: Recent situation of pinglin tunnel in Taiwan. Tunn. Undergr. Eng. **2**, 5–15 (1999)
9. GB/T 50218: Standard for engineering classification of rock mass (2014). (in Chinese)
10. Zhao, J., et al.: Tunnelling through a frequently changing and mixed ground: a case history in Singapore. Tunn. Undergr. Space Technol. **22**(4), 388–400 (2007)
11. Gong, Q., et al.: TBM tunnelling under adverse geological conditions: an overview. Tunn. Undergr. Space Technol. **57**, 4–17 (2016)

Progress of Research Advance on the Model Tests on the Interaction Between New Constructions and Adjacent Existing Buildings

Mingyu Li(✉) and Jibin Zhao

Zhengzhou University, Zhengzhou 450001, China
150302137@qq.com, 827383002@qq.com

Abstract. The model tests on the interaction between new constructions and adjacent existing buildings were summarized and analyzed from four aspects: the preparation methods of the model soil, the selection of pile model and tunnel model, the simulation methods of excavation process, and the loading methods of model tests. Several conclusions can be drawn as follows: (I) the influence of the superstructure stiffness and the pile cap is almost not considered in the past; (II) the influence of the sequence between installing the supporting structure and filling the soil still not be completely avoided, and more advanced supporting structure system should be designed; (III) most model tests on tunneling are based on two-dimensional hypothesis, and three-dimensional tests need to be conducted in the future; (IV) adverse influences of segment joints are seldom considered in the present tests on shield tunnels, and better tunnels model reflects the effect of segment joints should be adopted.

Keywords: Tunnel engineering · Foundation pit engineering
Existing building · Crossing engineering · Model test · Interaction

1 Introduction

Due to the limitation of public space, the influence of adjacent buildings must be considered when building new constructions. At the same time, the construction of new buildings can also have some influence on adjacent buildings. Unfortunately, the theories and the technologies for solving these problems are still not perfect, leading to more and more challenges. Furthermore, incalculable consequences (casualties, economic losses, etc.) will happen if the related influence factors are not fully considered. Therefore, it's self-evident that researching on the interaction between new constructions and adjacent existing buildings is significant.

Generally, numerical analyses and model tests were chosen by most researchers to investigate the geotechnical problems since the size of actual projects is very large, field conditions are complex and in-situ tests are very time-consuming. Geotechnical model tests can be divided into two parts, one is static geotechnical model test, or the indoor model test, the other is dynamic geotechnical model test, namely the centrifuge

© Springer Nature Singapore Pte Ltd. 2018
D. Zhang and X. Huang (Eds.): GSIC 2018, *Proceedings of GeoShanghai 2018 International Conference: Tunnelling and Underground Construction*, pp. 536–547, 2018.
https://doi.org/10.1007/978-981-13-0017-2_54

test. In the recent ten years, many researchers have focused on the interaction between new constructions and adjacent existing buildings, and it has become a popular research direction.

2 The Research Status of the Model Tests on the Interaction Between Constructions and Environment

2.1 Responses of Piles Subject to Lateral Load and Lateral Displacement

In 1993, Anagnostopoulos and Michael [1] conducted 6 model tests for investigating the interaction among axial and lateral responses of piles in clay. Poulos et al. [2, 3] performed a series of laboratory tests on single instrumented model piles and instrumented pile groups embedded in calcareous sand undergoing lateral movement during the period 1995–1997. Guo and Ghee [4–7] conducted a series of laboratory tests on single piles and pile groups subjected to lateral soil movement. Guo and Qin [8], studied the response of the pile subjected to triangular and rectangular soil movement profiles using 4 laboratory model tests. Wu [9] investigated the behavior of axially loaded pile and pile groups subjected to tunneling by laboratory model tests. Yao [10] chose the axially loaded pile subjected to lateral soil movement as the research object, and used laboratory model tests to research on the characteristics of passive pile under coupling of lateral soil movements and axial loads. Liang, Yao, Chen and Li [11, 12] investigated the behavior of single pile and group piles subjected to the lateral soil movement in rectangle mode, and the behavior of axially loaded piles subjected to lateral soil movement.

2.2 The Interaction Between Foundation Pit and Adjacent Existing Buildings

In Singapore, Leung et al. [13] used the centrifuge model test to investigate the influence of an unstrutted deep excavation in dense sand on an adjacent single pile foundation behind the retaining wall. Leung et al. [14]. have conducted centrifuge model tests on free-head and capped-head pile groups located adjacent to a deep excavation in sand. Ong, Leung and Chow [15–17] have conducted a series of centrifuge model tests, investigating the behavior of single piles behind a retaining wall (stable wall or collapsed wall) and pile groups in soft clay subject to excavation-induced soil movement. Ma et al. [18]. conducted centrifuge model tests to study the effect of excavation super-deep foundation pits on adjacent high-rise buildings in 2008. Choudhury et al. [19]. did centrifuge model tests to investigate the pile responses due to excavation-induced soil movements in sand with various relative densities. Choudhury et al. [20]. conducted centrifuge model tests on a 4-pile group connected by pile caps with different rigidities, and studied the responses of piles due to the staged excavation. Tian [21] studied on a high-rise building which has a CFG composite foundation next to the foundation pit through laboratory model tests. Jin [22] conducted some laboratory model tests to research on the interaction and influence law between the deformation of and the foundation settlement of the surrounding building s during excavation. Hu [23] carried out centrifuge model tests to study the influence of excavation on adjacent pile foundation in six different conditions based on the background of Shuangliu Airport Station foundation pit. Fu [24] conducted some centrifuge model tests to investigate the load transfer law and lateral behavior of composite foundation and their responses due to adjacent excavation.

2.3 The Mutual Effects Between Tunneling and Environment

Yashima et al. [25]. carried out a series of laboratory model tests to investigate the effect of tunneling in sand deposits upon the adjacent, existing structures with pile foundations. Ghahremannejad et al. [26]. performed laboratory model tests to simulate the tunnelling-induced effects on adjacent pile foundations in dense sand and ground movement. Shahin et al. [27]. conducted two-dimensional model tests of shallow tunnels to investigate the interaction between the tunnel excavation and the adjacent foundation, varying the lateral distance between the tunnel and the foundation. Loganathan et al. [28]. performed three centrifuge model tests to assess tunneling-induced ground deformations in clays and their effects on adjacent pile foundations. Ran [29] conducted three centrifuge model tests to evaluate the effects of distance between pile and tunnel, pile length and ground loss on pile due to tunneling. Jacobsz et al. [30]. carried out a centrifuge model study to investigate the effects of tunneling on nearby single piles in dense dry sand. Lee and Chiang [31, 32] performed a series of centrifuge model tests to research the responses of single piles to tunneling-induced soil movements and the load transfer mechanism of a single pile near new tunneling in sandy ground. Marshall [33] conducted some centrifuge model tests to study tunneling in sand and its effect on pipelines and piles. Marshall and Mair [34] used centrifuge model tests to investigate the problem of tunneling beneath driven or jacked end-bearing piles in sand.

Xia [35] conducted a series of laboratory model tests for studying on influence of tunneling to surrounding environments. An [36] studied the interaction between shallow tunnel excavation and the foundation load of existed buildings by laboratory model tests. Ng et al. [37, 38] carried out a series of three-dimensional centrifuge model tests to research on the effects of piggyback twin tunnel on pile groups, side-by-side twin tunneling on pile groups. Ng et al. [39]. used three-dimensional centrifuge model tests to investigate twin construction on an existing single pile in dry sand, considering the influence of the depth of each tunnel relative to the pile. Ng and Lu [40] investigated the effects of construction sequence of twin tunnels on an existing pile in dry sand by centrifuge model tests. Sun et al. [41]. conducted three centrifuge tests to evaluate the effects of distance between pile and tunnel on pile responses in both short and long terms in clay due to tunnel excavation. Boonsiri and Takemura [42] researched on the movement of both soil surface and subsurface layers of dry sand with two pile groups of different length at both sides of the tunnel through centrifuge model tests. In 1996, Kim [43] carried out two groups of tests, researching on closely spaced parallel tunnels and perpendicular tunnels. Huang et al. [44]. used the method of centrifuge modeling together with the field measurement to study the effects shied tunneling on nearby strata and existing tunnels. Ma et al. [45]. investigated the effects of shielding tunneling on the nearby strata and the existing tunnels by a centrifuge model test. Wei [46] studied on the influence of basement excavation on the underlying tunnel by a centrifuge test. Liang et al. [47]. investigated a deep foundation pit adjacent to metro tunnels in Shanghai, and researched on deformation behaviors of deep foundation pit adjacent to metro stations through conducting a centrifuge model test.

3 Key Technologies Affecting the Effectiveness of Model Tests

3.1 The Preparation of the Model Soil

In general, the foundation soil in the model test is natural soil treated by some methods (Table 1). However, there are some academics [36] who choose a kind of quasi dispersed grain material as the foundation, this material has characteristics of high density, close to the soil Poisson's ratio, low elastic modulus, stable mechanical properties, reutilization and etc. And there still are other researchers [25, 27] who use aluminum rods as foundation materials.

Table 1. The preparation methods of the model soil.

Method	Model Soil	Type	Evaluation		Introduction
Sand-rain method [2–8, 13–16, 19, 20, 26, 30–40, 42, 46]	Sandy soils	Laboratory model test, centrifuge test	Advantage	Due to the uniform laying, the uniformity is well ensured, and the property is also close to the natural sand layer	Using a container filled with sand to continuously scatter sand from a certain height back and forth, similar to raining
			Disadvantage	Requiring very careful operation and taking a long time.	
Compaction method [10–12, 21, 22, 24]	Sandy soil, clayey soil	Laboratory model test, centrifuge test	Advantage	Simple equipment and method; easy to operate; economical	Applying impact load on soil surface to drain pore water and make soil consolidated
			Disadvantage	Poor controllability; poor repeatability; the homogeneity of the clay foundation need to be further studied	

(*continued*)

Table 1. (*continued*)

Method	Model Soil	Type	Evaluation		Introduction
Centrifugal consolidation method [15, 18, 23–29, 41, 47]	Clayey soil	Centrifuge test	Advantage	The forming process of natural clay can be better reflected; more similar to the prototype	Using centrifugal force to force the water to the surface and consolidate the soil
			Disadvantage	Difficult to reach the strength of the prototype soil; difficult to accurately control the physical and mechanical parameters of soil samples	
Pressure consolidation method [43]	Clayey soil	Laboratory model test	Advantage	Convenient to control the consolidation state	Using static pressure that cover the soil to drain pore water and make soil consolidated

3.2 The Selection of Model Piles and Model Tunnels

The principle of equivalent stiffness should be considered in the fabrication of pile model and tunnel model. In most of model tests, pile models were made of aluminum alloy. However, other materials have also been chosen according to actual conditions. Ma et al. [18]. used screw thread steel to make model pile foundations in their test; Tian [21] made CFG pile model by cement, fly ash and round gravel in a certain proportion, for better reflecting the influence of adjacent composite foundation on foundation pit. Jin [22] selected the reinforced concrete as the raw material of model pile. Loganathan et al. [28]. used brass model piles. An [36] adopted the plain concrete to produce model piles. In addition, there are other people using acrylic tubes as pile model [42]. As for the material of the tunnel model, the aluminium alloy is the most widely used. Copper foils and copper tubes, and other materials are also used. Some researchers [31, 32, 37–40] mentioned that choosing rubber bags to make model tunnels, and using such a model tunnel is convenient for storing gas or heavy liquid.

3.3 The Simulation of Excavation Process

On the basis of analysis, the simulation of the excavation process of foundation pits and tunnels has to be relatively simple and fully reflect the engineering practice, and it also should be time-saving, labor-saving, and economic. Of course, accurate results must be ensured at the same time (Table 2).

Table 2. Methods of the simulation for excavation process

Method	Description	Type	Research object	Evaluation	
				Advantage	Disadvantage
Stop and restart method [18, 23]	Stopping the centrifuge and then artificial excavating or mechanical excavating	Centrifuge test	The excavation of foundation pits	The most direct and simplest method; high operating accuracy during machine halt	The tangential acceleration caused by the start and stop of the centrifuge is bound to have influence on the test results; the process of unloading and reloading, with the addition of time effect, makes the measured stress and strain inevitably have an error
Removing heavy liquid (or gas) method [28, 31–34, 44, 45]	Orderly removing liquid(gas) prefilled in the model tunnel, which simulating the excavation	Centrifuge test	The excavation of foundation pits and tunnels	Able to excavate without stopping the centrifuge; simplified the complex excavation process; can simulate the ground loss	Difficult to control the removing process in the supergravity field; unable to reflect the distribution of lateral earth pressure since the liquid(gas) has the same pressure in every direction in a certain depth

(*continued*)

Table 2. (*continued*)

Method	Description	Type	Research object	Evaluation	
				Advantage	Disadvantage
Auto-excavation device method [24]	Packing soil into several bags, and then lifting bags in sequence for simulating the stage excavation	Centrifuge test	The excavation of foundation pits	The stress path of the soil will not change during excavation; earth pressure is more similar to reality; easy to control the excavation volume of soils	Soil bags are lifted rapidly in sequence, and it can affect the stress transfer and deformation of foundation soil
Lowering-panel test [25]	Lowering lowering-panel set at the bottom to simulating the soil movement in tunneling	Laboratory model test	Tunneling	Not necessary to design complicated equipment and devices; simple and convenient to operate	The factors considered are too simple to simulate actual excavation; can't simulate the ground loss
Model shield tunneling machine method [42, 43]	Simulating the tunneling process by a self-designed model shield tunneling machine	Laboratory model test	Tunneling	The actual excavation process of tunneling is greatly reflected	Simplified model tests ignore some factors in shield tunneling method and can affect the accuracy of results; complicated devices and inconvenient operation

(*continued*)

Table 2. (*continued*)

Method	Description	Type	Research object	Evaluation	
				Advantage	Disadvantage
Drawing tube method [26, 35, 36]	Setting a series of tubes with various diameters in soil, and simulating ground volume loss by pulling out tubes	Laboratory model test	Tunneling	Simple devices and operation; simple principle; better for simulating the ground loss through flexible variation of the diameter of model tunnels	There is shear force on the contact surface between the tube wall and soils during drawing the tube, and the effect is needed to eliminated, and improper handling may affect the correctness of the result
Dissolution method [29, 41]	Burying the tube soil filled with organic matter into soil, and then deliver the organic solvent to dissolve it	Centrifuge test	Tunneling	Simple devices and operation	Cannot reflect the real excavation process; the physical and mechanical properties of dissolved materials do not conform to soils; not easy to control the dissolution process

3.4 Loading Methods of Model Tests

Many construction conditions should be simulated. Such as applying concentrated load and uniformly distributed load, driving piles, forming displacement patterns of different soils, and etc. The proper choosing of loading methods can reflect actual situations better, improve the precision, and get more accurate results (Table 3).

Table 3. The loading methods of model tests

Methods	Description	Evaluation	
		Advantages	Disadvantages
Jack loading method	Using traditional jacks to apply load or to form soil displacement mode	Simple operation; broad scope of application; able to form different patterns of the soil displacement	Not suitable for applying the uniform distributed load; difficult to ensure the precision of loading
Dead load method [1, 18, 21, 22, 25, 28, 30]	Using the weight to generate static load on objects directly	Simple devices and operation	Unable to simulate the process of load distribution and transfer; easy to produce stress concentration; can produce dead load only
Air (Water) bag loading method [24]	Making the bag and the object contact widely and completely, and producing uniform distributed load after load transfer completed in fluid	Suitable for applying the uniform distributed load; able to simulate the process of load distribution and transfer; convenient for controlling the load value	Unable to apply the concentrated load
Motor loading method [23, 38]	Using the energy provided by motor to generate load	Remote and easy operation; able to ensure the precision of loading	Not suitable for applying the uniform distributed load
Air cylinder loading method [30, 33, 34]	Using the energy provided by air cylinder to generate load	Able to recreate the process of setting up driving piles	Not suitable for applying the uniform distributed load

4 Conclusions

Only the effect of elevated pile caps to pile foundation were analyzed in most of the present study, but the effect of low pile caps was paid less attention. In this case, the influences caused by the interaction between the pile cap and the soil and the embedded depth were ignored.

Nearly all model tests merely considered the load generated by the superstructure without considering the influence of the superstructure stiffness, simplifying the test difficulty. However, this factor should not be ignored in order to getting high accuracy.

The supporting structure was installed before the filling of soil in most tests in simulating the excavation process of foundation pits, being not consistent with the reality. Once the setting sequence and the type of supporting structure changes, the stiffness of the supporting structure will not be a constant value during construction. While constructing the supporting structure, the surrounding soil will move towards the interior of foundation pit, causing the ground settlement. The supporting structure will also produce additional stress and deformation. Ignoring these factors will inevitably affect the test result.

Most model tests on tunneling were based on two-dimensional hypothesis, and the three-dimensional model was gradually adopted in recent years. It is well-known that tunneling is not strictly conform to the plane strain model, for improving the accuracy of the study, it should be improved from the model principle firstly.

The tunnel lining is not ideal smooth due to the existing of the joints between two segments, and thus the tunnel model should not be treated as a uniform stiffness tube. But most tunnel models are simplified, and the negative influence of segment joints is seldom considered, leading to less study on the relative displacement of the different parts of the lining, and the interaction between different parts.

References

1. Anagnostopoulos, C., Georgiadis, M.: Interaction of axial and lateral pile responses. J. Geotech. Eng. **119**(4), 793–798 (1993)
2. Poulos, H.G., Chen, L.T., Hull, T.S.: Model tests on single piles subjected to lateral soil movement. Soils Found. **35**(4), 85–92 (1995)
3. Chen, L.T., Poulos, H.G., Hull, T.S.: Model tests on pile groups subjected to lateral soil movement. Soils Found. **37**(1), 1–12 (1997)
4. Guo, W.D., Ghee, E.H.: Model tests on single piles in sand subjected to lateral soil movement. In: 18th Australasian Conference on the Mechanics of Structures and Materials, Perth, Australia, pp. 997–1003 (2004)
5. Guo, W.D., Ghee, E.H.: Response of axially loaded pile groups subjected to lateral soil movement-an experimental investigation. In: 6th International Conference on Tall Buildings (ICTB-VI), pp. 333–338. World Scientific Publishing Co. Pte. Ltd, Hong Kong (2005)
6. Guo, W.D., Ghee, E.H.: A preliminary investigation into the effect of axial load on piles subjected to soil movement. In: 1st International Symposium on Frontiers in Offshore Geotechnics, pp. 865–871. Taylor & Francis, London (2010)

7. Guo, W.D., Ghee, E.H.: Behavior of axially loaded pile groups subjected to lateral soil movement. In: Proceedings of Sessions of GeoShanghai, GSP2006, Shanghai, pp. 174–181 (2010)
8. Guo, W.D., Qin, H.Y.: Vertically loaded single piles in sand subjected to lateral soil movement. In: 6th International Conference on Tall Buildings (ICTB-VI), pp. 333–338. World Scientific Publishing Co. Pte. Ltd, Hong Kong (2005)
9. Wu, T.X.: Research on the effect of tunnelling on the bearing behavior of piles. Doctoral dissertation, Xi'an University of Science and Technology, Xi'an (2013)
10. Yao, G.S.: Numerical analysis and Model tests of behavior of axially loaded piles subjected to lateral soil movement. Doctoral dissertation, Tongji University, Shanghai (2009)
11. Yao, G.S., Liang, F.Y., Chen, H.B., et al.: Model test investigation on behavior of adjacent piles subjected to lateral soil movements with rectangle mode. Chin. J. Undergr. Space Eng. **5**(s2), 1542–1544 (2009)
12. Liang, F.Y., Yao, G.S., Chen, H.B., et al.: Model tests on behavior of axially loaded piles subjected to lateral soil movement. Chin. J. Geotech. Eng. **32**(10), 1603–1609 (2010). (in Chinese)
13. Leung, C.F., Chow, Y.K., Shen, R.F.: Behavior of pile subjected to excavation-induced soil movement. J. Geotech. Geoenviron. Eng. **126**(11), 947–954 (2000)
14. Leung, C.F., Lim, J.K., Shen, R.F., et al.: Behavior of pile groups subject to excavation-induced soil movement. J. Geotech. Geoenviron. Eng. **129**(1), 58–65 (2003)
15. Ong, D.E.L., Leung, C.F., Chow, Y.K.: Pile behavior due to excavation- induced soil movement in clay I: stable wall. J. Geotech. Geoenviron. Eng. **132**(1), 36–44 (2006)
16. Leung, C.F., Ong, D.E.L., Chow, Y.K.: Pile behavior due to excavation- induced soil movement in clay II: collapsed wall. J. Geotech. Geoenviron. Eng. **132**(1), 45–53 (2006)
17. Ong, D.E.L., Leung, C.F., Chow, Y.K.: Behavior of pile groups subject to excavation-induced soil movement in very soft clay. J. Geotech. Geoenviron. Eng. **135**, 1462–1474 (2009)
18. Ma, X.F., Zhang, H.H., Zhu, W.J., et al.: Centrifuge model tests on effect of excavation super-deep foundation pits on adjacent high-rise buildings. Chin. J. Geotech. Eng. **30**(1), 499–504 (2008)
19. Choudhury, D., Shen, R.F., Leung, C.F., et al.: Centrifuge model study on pile responses due to adjacent excavation. In: Geoshanghai International Conference, pp. 145–151 (2006)
20. Choudhury, D., Shen, R.F., Leung, C.F.: Centrifuge model study of pile group due to adjacent excavation. In: Proceedings of GEOCONGRESS 2008, pp. 141–148 (2008)
21. Tian, J.C.: Model tests on foundation pit engineering that excavate nearby a high-rise building who has composite foundation. Master's dissertation, China University of Geosciences, Beijing, China (2009)
22. Jin, X.: Model experimental study of interaction between deep excavations and adjacent building foundation. Master's dissertation, Lanzhou Jiaotong University, Lanzhou, China (2013)
23. Hu, Q.: Centrifuge modeling of deep foundation pit and adjacent inclined arch interaction mechanism of pile foundation. Master's dissertation, Southwest Jiaotong University, Chengdu, China (2014)
24. Fu, Q.H.: Behavior of composite foundation due to adjacent excavation: centrifuge model tests. Master's dissertation, Shandong University, Jinan, China (2016)
25. Yashima, A., Shibata, T., Sekiguchi, H., et al.: Soil movements associated with tunneling and their effects on an adjacent pile foundation. Bull. Disaster Prev. Res. Inst. **35**, 115–135 (1985)

26. Ghahremannejad, B., Surjadinata, J., Poon, B., et al.: Effects of tunnelling on settlements and structural forces within model pile foundations. In: International Conference on Physical Modelling in Geotechnics, Hong Kong (2006)
27. Shahin, H.M., Nakai, T., Kuroi, S.: Interaction of tunneling and existing structure considering the location of foundation. Jpn. Geotech. Soc. Spec. Publ. **2**(40), 1428–1432 (2016)
28. Loganathan, N., Poulos, H.G., Stewart, D.P.: Centrifuge model testing of tunnelling-induced ground and pile deformations. Geotechnique **50**(3), 283–294 (2000)
29. Ran, X.: Tunnel pile interaction in clay. Master's dissertation, National University of Singapore, Singapore (2005)
30. Jacobsz, S.W., Standing, J.R., Mair, R.J., et al.: Centrifuge modelling of tunnelling near driven piles. J. Jpn. Geotech. Soc. Soils Found. **44**(1), 49–56 (2004)
31. Lee, C.J., Chiang, K.H.: Load transfer on single pile near new tunneling in sandy ground. In: Proceedings of the International Symposium on Engineering Practice and Performance of Soft Deposit, pp. 501–506. JGS, Osaka (2004)
32. Lee, C.J., Chiang, K.H.: Responses of single piles to tunneling-induced soil movements in sandy. Can. Geotech. J. **44**(10), 1224–1241 (2007)
33. Marshall, A.M.: Tunnelling in sand and its effect on pipelines and piles. Doctoral dissertation, University of Cambridge, Cambridge, UK (2009)
34. Marshall, A.M., Mair, R.J.: Tunneling beneath driven or jacked end-bearing piles in sand. Can. Geotech. J. **48**(12), 1757–1771 (2010)
35. Xia, F.: Displacement controlled model test study on influence of tunneling to surrounding environments. Master's dissertation, Shanghai Jiaotong University, Shanghai (2014)
36. An, J.Y.: Model experiments and theoretical calculations for the interactions between shallow tunnel excavations and pre-existing building foundation loads. Doctoral dissertation, Beijing Jiaotong University, Beijing (2015)
37. Ng, C.W.W., Soomro, M.A., Hong, Y.: Three-dimensional centrifuge modelling of pile group responses to side-by-side twin tunnelling. Tunn. Undergr. Space Technol. **43**(7), 350–361 (2014)
38. Ng, C.W.W., Hong, Y., Soomro, M.A.: Effects of piggyback twin tunnelling on a pile group: 3D centrifuge tests and numerical modelling. Geotechnique **65**(1), 38–51 (2015)
39. Ng, C.W.W., Lu, H., Peng, S.Y.: Three-dimensional centrifuge modelling of the effects of twin tunnelling on an existing pile. Tunn. Undergr. Space Technol. **35**(4), 189–199 (2013)
40. Ng, C.W.W., Lu, H.: Effects of the construction sequence of twin tunnels at different depths on an existing pile. Can. Geotech. J. **51**(2), 173–183 (2012)
41. Sun, Q., Yang, M., Ran, X., et al.: Test study on tunnelling-induced soil movements and pile responses. J. Tongji Univ. (Nat. Sci.) **39**(7), 989–993 (2011)
42. Boonsiri, I., Takemura, J.: Observation of ground movement with existing pile groups due to tunneling in sand using centrifuge modelling. Geotech. Geol. Eng. **33**(3), 621–640 (2015)
43. Kim, S.H.: Model testing and analysis of interactions between tunnels in clay. Doctoral dissertation, University of Oxford, Oxford, UK (1996)
44. Huang, D.Z., Ma, X.F., Wang, J.S., et al.: Centrifuge modelling of effects of shield tunnels on existing tunnels in soft clay. Chin. J. Geotech. Eng. **34**(3), 520–527 (2012)
45. Ma, X.F., He, L.Q., Wang, J.S.: Centrifuge modeling on the effects of shield tunnel crossing below the existing tunnels in soft clay. J. Yangtze River Sci. Res. Inst. **29**(1), 79–84 (2012)
46. Wei, S.W.: Centrifuge and Numerical studies of the influence of basement excavation on the underlying tunnel. Master's dissertation, Tianjin University, Tianjin, China (2010)
47. Liang, F.Y., Chu, F., Song, Z., et al.: Centrifugal model test research on deformation behaviors of deep foundation pit adjacent to metro stations. Rock Soil Mech. **33**(3), 657–664 (2012)

Studies on the Key Technologies for Underground Construction of High-Speed Rail Station Design

Chuanping Liu(✉) and Jian Jia

Architectural Design and Research Institute of Tongji
University (Group) Co., Ltd., Shanghai, China
liuchuanping@126.com

Abstract. Using the practice of Ningbo high-speed railway station transportation hub as an example, we studied and reported on the key technologies for the construction of an urban railway transportation hub that integrated the functionalities and structures of a railway, subway, city bus, and taxi stations for traffic and passenger transportation. Specifically, we first studied the impact of deep foundation pit excavation on the normal operation of existing train line and corresponding protection plans. We also carried out force analyses and foundation subsidence coupling studies for the co-construction structure of the railway station building and the subway system at Ningbo station. Finally, we explored the informatics control of an underground engineering project. Based on our technical studies and analyses, we proposed targeted project designs, which contributed substantially to the success of the construction of Ningbo high-speed railway station.

Keywords: High-speed railway · Deep foundation pit excavation
Co-construction structure · Temporary railway trestle bridge
Subsidence coupling

1 Introduction

Over the past decade, China's high-speed railway constructions and urban rail transit constructions have earned the world's attention, a large number of "hub-type, complex" traffic-engineering projects in large and medium-sized cities have emerged. These projects share common characteristics: (1) they utilize the high-speed railway stations as the main building, to integrate the infrastructures and functionalities of high-speed railroad, subway system, long-distance shuttle service, public transit, as well as taxi service to form complex transportation hubs; (2) they are urban complex projects that follow the principle of "people-oriented and zero transfer". Therefore, such projects are often designed to have the high-speed railroad station building and the yard stay above ground; and underneath them are subway stations allowing easy transfers for passengers. Bus stops, taxi stops, public parking lot and other supporting services are located in the plaza in from of the station building, forming an urban complex building; thus, achieved the full development and utilization of underground space for the "economical" city planning. (3) They usually locate at the key nodes and the core areas for

© Springer Nature Singapore Pte Ltd. 2018
D. Zhang and X. Huang (Eds.): GSIC 2018, *Proceedings of GeoShanghai 2018 International Conference: Tunnelling and Underground Construction*, pp. 548–558, 2018.
https://doi.org/10.1007/978-981-13-0017-2_55

urban traffic. Therefore, requirements are stringent for the project duration and surrounding environment protection, which can be difficult to achieve due to the complexity of construction sites.

Many issues that require immediate attention have arisen during the construction of railway transportation hub and complex urban infrastructures. These problems include the protection of safe operation of existing railway during deep pit excavation; the evaluation and analyses of the influence of deformation of the supporting and protecting structures on surrounding environment during and after deep pit excavation; key technical problems regarding force analysis of the composite structure of railway station building and subway infrastructure, and the coupling base structure subsidence. These technical issues are pertinent to the safety of the excavation project, the operating railway lines and the to-be finished station building, therefore, need to be investigated and resolved by engineers and constructors.

Based on the practice of Ningbo railway station hub construction, this paper introduced the analyses and protection measures of the impact of deep pit excavation construction on existing railroad line operations within the soft soil areas of China's coastal railway. We also carried out the force analyses for the co-construction of railroad station building and subway station. At the same time, we investigated the coordination of the coupling base structural subsidence and proposed technical solutions. Last, we studied the monitoring data collected during construction and discussed the possibilities of using these data for project control purposes during the construction.

2 Analyses on the Influence of Deep Pit Excavation on Safety of Existing Railway Operation and Corresponding Protection Measures

2.1 Background for the Co-construction of Ningbo High-Speed Railway Station and Subway Systems

Ningbo station is an important hub of the high-speed rail network in the Yangtze River Delta region. It is also a reconstruction on the site of the old Ningbo station after its demolition. Figure 1 is the overall aerial view of Ningbo station redevelopment project. Ningbo station construction site and its relationships with existing railway lines are shown in Fig. 2. During the alteration of Ningbo station, it was mandatory to ensure the normal operation of two existing railroad lines, Hangzhou-Ningbo and Ningbo-Taizhou-Wenzhou that go across the construction site. It was also required to rebuild Ningbo station and the subway line 2 train station simultaneously, and to finish them within two years. To put Ningbo station to use and make social and economic impacts as soon as possible, the time allowance for this project is therefore stringent.

In this project, the deep pit excavation of high-speed train station building and the subway system crossed the existing railway lines, and the normal operation of the existing high-speed rail lines cannot be disrupted during Ningbo station construction. The excavation underneath the station building went as deep as 13 m, and it includes two stages of excavation, the width of which are 123.5 m and 75 m, respectively. The subway foundation pit is located in the center of the station building foundation pit,

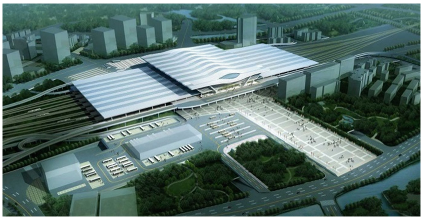

Fig. 1. Aerial view of Ningbo station reconstruction project

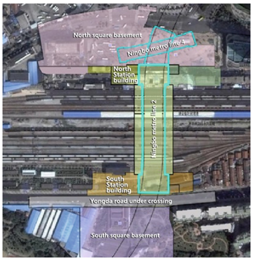

North square basement
Ningbo metro line 4
North Station building
Ningbo metro line 2
South Station building
Yongda road under crossing
South square basement

Fig. 2. General layout plan for the reconstruction and co-construction of Ningbo railway station and subway

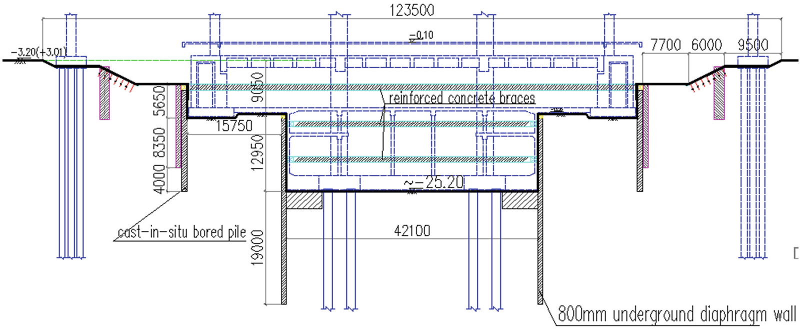

123500
-3.20(+3.01)
±0.10
7700
6000
9500
5650
8350
4000
9050
15750
12950
reinforced concrete braces
~-25.20
cast-in-situ bored pile
42100
19000
800mm underground diaphragm wall

Fig. 3. Sectional view of the pit excavation for the station building and the subway system

forming a pit within pit structure, the maximum excavation depth is 24 m, and the width is 42.1 m. Station and subway pit section view is shown in Fig. 3.

According to the traditional practice for handling the existing railroad lines during construction transition, a “zoning” scheme can be used, that is, to divide the main foundation pit excavation into two sections. Regions containing the existing railroad lines was designated Section 2, while the other part was designated Section 1 (1) (2), which shall be finished first. After the completion of both aboveground and underground constructions in Section 1, move the existing operating line from Section 2 to Section 1 and then complete the construction in Section 2, as illustrated in Fig. 4. An alternative strategy is to create a detour of the existing railroad lines so that it goes around the pit excavation during the construction. However, both strategies were not applicable to the case of Ningbo station due to time constraints and technical difficulties.

In view of the above-mentioned problems, after repeated investigations, comparisons and discussions of different plans, the final design was determined and it requires simultaneous excavation of the pits for both station building and the subway with the laying of a temporary bridge over the pit to ensure the continuous operation of the existing railway, as shown in Fig. 5. This design ensured the normal operation of the existing lines. And as compared with the “zoning” method, it greatly shortened the

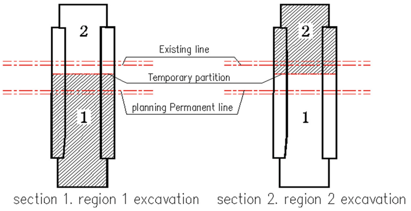
2
Existing line
Temporary partition
planning Permanent line
1
2
1
section 1. region 1 excavation
section 2. region 2 excavation

Fig. 4. Traditional partition transition plan in foundation pit operating

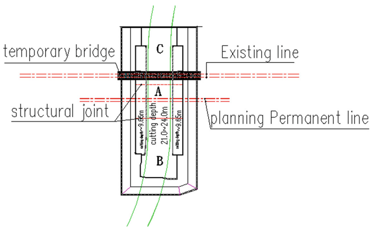
temporary bridge
C
Existing line
A
structural joint
cutting depth:
21.0~24.0m
planning Permanent line
B

Fig. 5. A plan view of the foundation pit and the temporary bridge

construction time by a year and a half, hence, meets the overall timing requirements for Ningbo station project.

The main design parameters for the temporary railway bridge structure are as follows: The temporary railway bridge adopts a composite of steel lattice column with cast-in-place reinforced concrete beam and slab structure. The composite steel grid column has a sectional area of 550 × 550 mm, and it consists of four L200 × 20 steel angles and gusset plate. The Bridge deck was made with C40 cast-in-place concrete with a thickness of 350 mm. The sectional area of the main beam slab of the bridge was 1000 × 1000 mm, and the secondary beam slab has a sectional area of 600 × 800 mm. The designed passing speed on the bridge is less than 80 km/h for cars, and less than 45 km/h for small cargo vans. Figure 6 for the sectional view of the temporary bridge.

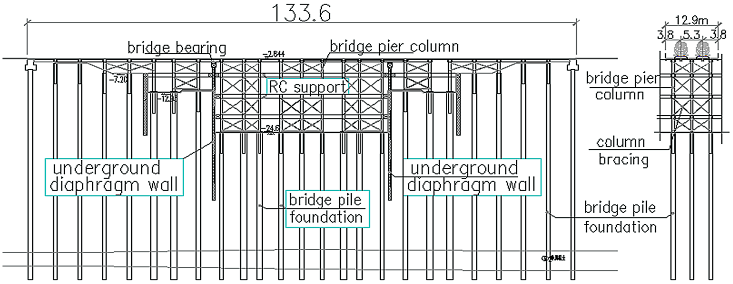
133.6
bridge bearing
bridge pier column
RC support
underground diaphragm wall
underground diaphragm wall
bridge pile foundation
12.9m
3.8 5.3 3.8
bridge pier column
column bracing
bridge pile foundation

Fig. 6. Sectional view of the temporary railway bridge structure

2.2 Analyses on the Impact of Deep Foundation Pit Excavation on Safety and Stability of the Railway Bridge Structure and the Operating Trains

The use of the innovative rail trestle bridge, which is constructed with the composite of steel lattice column + cast-in-place reinforced concrete beam and slab, created favorable conditions for the overall deep pit excavation and therefore contributed significantly to the timely completion of Ningbo railway station reconstruction project.

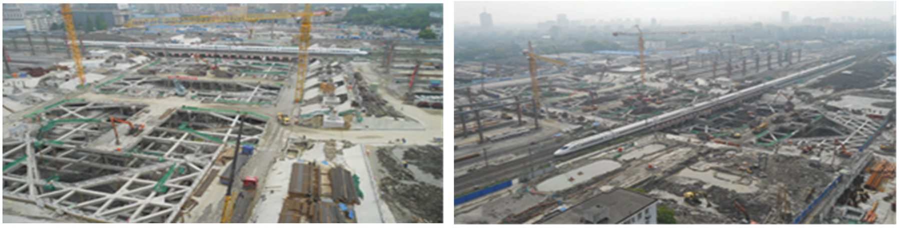

Fig. 7. A train passing over the excavation of the construction site of Ningbo railroad station

Figure 7 showed a train that is passing over the excavation of the construction site of Ningbo railroad station.

The application of the steel – concrete combination in temporary railway trestle bridge was innovative and has no precedent, therefore, many technical difficulties and safety issues have arisen, especially for the ultra - deep large pit excavation projects within coastal soft soil area. To ensure the overall safety of pit excavation projects and the operation of railway trains, it is urgent to carry out studies regarding soft the construction of soil deep pit excavation, the development of foundation pit deformation, the uplift of the soil within the pit; and evaluate the effects of abovementioned issues on structural stability of the temporary trestle bridge and safety of the operation of the railroad.

Analyses on the temporary trestle bridge were done with the finite element model, which was established by using MIDAS /GEN. The bridge deck was simulated by the plate element, and the bridge deck beam and bridge pier column were simulated by the space beam element. Bridge pier column and bridge deck beam consolidation. Considering the geological conditions of the project and the embedding condition of the bridge pier column foundation, the equivalent elastic stiffness matrix was applied in the model for the evaluation of the elastic restraint of the pier column foundation and the reinforced soil on the bridge (Fig. 8).

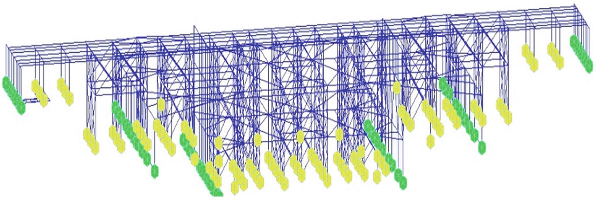

Fig. 8. A diagram of the calculated model for construction condition IV

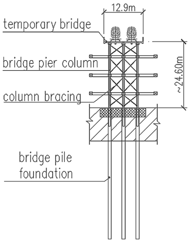

Fig. 9. An illustration of the temporary trestle bridge in construction condition IV

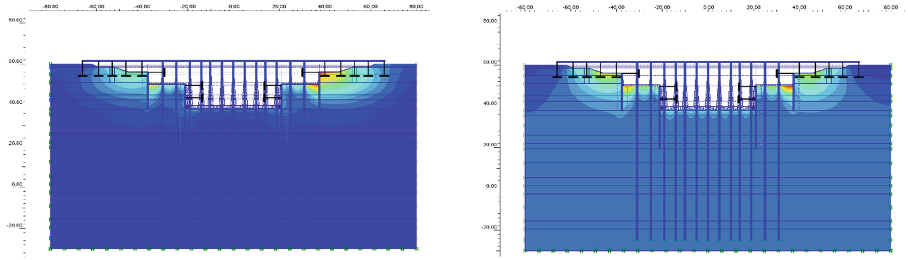
A. Horizontal displacement contour map

B. vertical displacement contour map

Fig. 10. Displacement contour map for working condition IV of the pit and trestle bridge structure

According to the order of excavation and supporting construction, four main construction conditions were selected for the analyses of the dynamic characteristics of the bridge. Figures 9 and 10 illustrated the diagram of the calculated model of the most unfavorable conditions IV that is when the foundation pit excavation reached the bottom. The calculation results of the vertical and horizontal fundamental frequencies in the four construction stages (working conditions I to IV) of the excavation are shown in Table 1 [1].

Table 1. The calculation results of the natural frequencies of the bridge structures at different stages of excavation

Construction conditions	Horizontal				Vertical			
	I	II	III	IV	I	II	III	IV
Excavation depth (m)	5.53	11.50	17.50	21.75	5.53	11.50	17.50	21.75
Trestle bridge fundamental frequency (Hz)	5.87	5.16	4.84	4.73	8.24	7.93	7.11	6.57
Normalized value (Hz)	4.40	2.84	2.07	1.85				

Normalized Value-The transverse self - vibration frequency limits of the pier column Calculated by Code for Rating Railway Bridges.

Calculation of the effects of excavation on the additional deformation of the temporary railway trestle bridge is shown in the following figure.

Analyses on the Influence of Foundation Pit Excavation on the Safety of Railway Trestle Bridge. Based on the analyses of the finite element calculation results of the bridge structure at different construction conditions, the following conclusions can be drawn:

(1) The vertical stiffness of the bridge structure is greater than the horizontal stiffness, while the dynamic characteristics of the bridge are determined by its horizontal stiffness.

(2) As the excavation of the foundation pit goes deeper, and the bridge pier column goes higher, the lateral stiffness of the bridge gradually decreases. The overall vertical and horizontal fundamental frequencies of the bridge pier column also gradually decrease. Therefore, it is necessary to follow the different stages of foundation pit excavation separately to monitor the amplitude and frequency of the railway bridge to ensure the safety of the bridge and train operation.

(3) The calculation results show that the performance of the bridge structure (shows in the fourth row of Table 1) can meet the standards and the safety requirements (the minimum transverse self-vibration frequency of the pier column calculated by Code for Rating Railway Bridges shows in the fifth row of Table 1) for train operation during foundation pit excavation. The results of finite element calculation shows in Fig. 10.

Analyses on the Influence of Foundation Pit Excavation on the Safety Operation of Railway. The calculation and analysis of the train-bridge coupling vibration response of the bridge structure show that when excavation reached the bottom of the pit (at the maximum calculated height of the bridge pier column), cars can pass through the bridge at ≤ 80 km/h, while cargo van can pass through at ≤ 45 km/h. The operational safety parameters of the trains (derailment coefficient, wheel load shedding rate, and wheel/rail lateral force, vertical and lateral acceleration of the vehicle body) meet the standards specifications and thus ensure the safety of the trains. The smoothness parameters for train operations achieved an excellent level. However, the smoothness of operation decreased as the speed increased. The calculation results showed that the speed limitation (≤ 80 km/h) for passing over the trestle bridge is appropriate as it ensured the stability of the bridge, while at the same time guaranteed the passengers a comfortable train ride.

The calculation results show that the horizontal stiffness of the bridge is the controlling factor of the stiffness of the bridge. Therefore, the two underground girders with large lateral stiffness in the deep foundation pit of the middle subway area were utilized as the vertical support structures of the bridge. (See Fig. 5), and the bridge bearing is designed to allow the bridge deck to slide along the longitudinal direction (to avoid the temperature inducing additional horizontal shear force on bridge pier column, which is a result of longitudinal expansion of the bridge deck), horizontally fixed, greatly constrained the bridge structure horizontally and thus, relatively reduced the impact of deep pit excavation on the horizontal stiffness of the bridge pier column.

3 Control of the Force on High-Speed Railway Station and Subway System Co-construction and Settlement Coupling

Ningbo station uses the station layout of “upper-lever-enter and lower-level-exit”, and the passenger waiting room lays across the railroad track above. The elevated station building as well as the elevated railroad track were co-constructed with the subway train station at the underground level 2 to 3. According to the requirements for the design and application of high-speed railway bridge, the subsidence of the pier column for the elevated high-speed railway bridge shall not exceed 40 mm, and the difference between the pier column should be less than 20 mm.

The spacing between pier column of the elevated railway bridge for Ningbo station was big, with a dimension of 21 × (21–24) m, and the differences in the designated pillar load are relatively large (the column force ranging from 6000 KN to 44000 KN). The larger difference between the loads of the pier column not only lay a great influence on the structure of the co-construction of elevated railway bridge and system but also on the subway. Because the subway station structure in the soft soil strata is slender and has a small overall stiffness along the longitudinal direction, with the impact of uneven load, it easily causes the uneven settlement and crack of the subway base platform, and thus leading to breakage and water leakage at the subway entrance. These will affect not only the safety of the subway system, but the secondary stress induced on the main station building will also impact the safety of the overall station building structure.

In order to study and analyze the law and characteristics of the force and coupling of settlement deformation of this co-construction structure, the elevated bridges for main station building, the north-south transfer aisles, the subway, and the foundation structure were modeled as a whole, using Boussinesq solution, Mindlin Elastic half-space theory and the elastic analysis, and methods based on Mindlin plate theory to analyze the force and the coupling subsidence of foundation plate [2]. Figure 13 illustrated a model for the force and coupling subsidence analysis of national railway and subway structure. Analyses were done using a general large-scale finite element software ABAQUS, according to the actual size of the project. Linear elastic model is used for the pile, and soil analyses, while between pile and soil lies the tie contact.

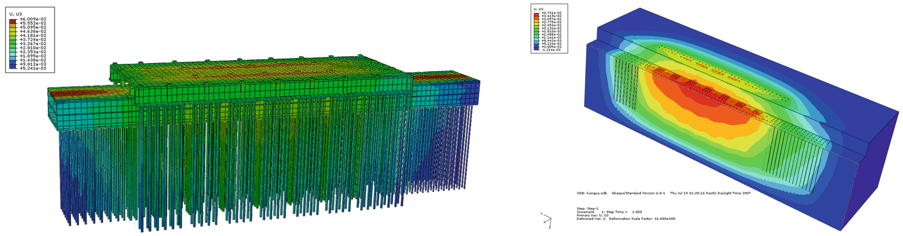

Fig. 11. The calculation model and the results of the coupling subsidence of the co-construction structure

The analysis results show that the subsidence deformation of foundation piles of the station building and the subway was significant on both ends and small at the center, which is a result of pile group effect. The largest subsidence was located at the center of the station, as shown in Fig. 11.

After repeated experiments and careful calculations, we eventually determined that the design shall follow the principle that requires the pile set-up to be concentrated underneath the high-speed railway station building and the elevated bridge pier column. Meanwhile, a certain number of the regulation piles for subsidence control should be set-up underneath the subway base plate. These measures were meant to control the uneven subsidence and base plate deformation of the foundation. At the same time, the subway structure is designed to make full use of the underground wall of the subway pit to form the overlapping wall structure to enhance the longitudinal stiffness of the subway station structure. Under the combined action with the national railway and the subway pile foundation, the goal of preventing uneven vertical subsidence of the baseplate of the station was achieved.

The calculation results show that we can control the subsidence differences within the station building by appropriate pile set-up for altered stiffness. The calculation results can also meet the standard criteria for railway and subway construction simultaneously.

4 Monitoring Data Analysis and Informatics Control of Underground Engineering

4.1 Informatics Monitoring of Foundation Pit and Trestle Bridge

In addition to the conventional monitoring for deformation and internal force of the foundation pit during the implementation of the project, the 24-h dynamic monitoring of the railway trestle bridge was carried out, including indicators for Train operation safety, such as the three-dimensional dynamic displacement of the bridge, the dynamic acceleration, the dynamic stress responses, and the uplift or subsidence of the trestle bridge pier column. Through the comparison between the real-time statistical analyses of the monitoring data with the theoretical calculations, we were able to grasp the true force and deformation of foundation pit and the trestle bridge, to achieve dynamic design and informatics management of the construction.

4.2 Analysis of Acquired Data

Figure 12 illustrated the deformation changes of the soil body inside and outside the foundation pit over time. The curve below the horizontal axis is the subsidence curve of the soil body outside the pit, and the curve above the horizontal axis is the soil body uplift inside the pit. It can be seen that as the excavation proceeded, there was a tendency that the soil inside the pit is gradually uplifted, while the soil body outside gradually subsidized. When the subway excavation finished, the maximum uplift of the soil in the pit has reached 18.7 mm, and the maximum settlement of the soil outside the pit was about 10.0 mm, which is close to the finite element numerical simulation results.

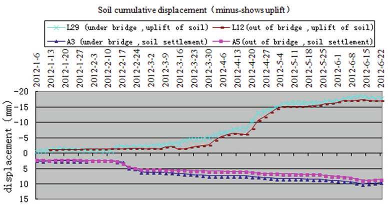

Fig. 12. Soil body deformation dynamics

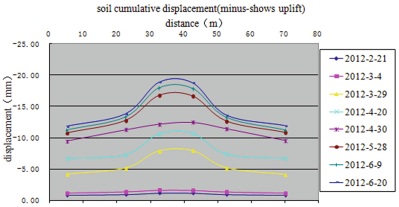

Fig. 13. Soil body uplift deformations in the foundation pit

Figure 13 showed the curves of the uplift deformation measured of the soil body from the cross section of the pit. As the excavation proceeds, the soil in the pits is uplifted, and the deformation gradually expanded. The deformation from a sectional view resembles a saddle shape with a downward opening.

Table 2. Expected and measured data for bridge deformation.

Construction conditions	Horizontal displacement/mm		Uplift deformation/mm		
	Limit	Measurements	Limit	Measurements	Expected values
The 2nd layer excavation	5	1.8	25	8.4	12.77
The 3rd layer excavation		2.2		18.5	21.86
The 4th layer excavation		2.7		24.5	30.08

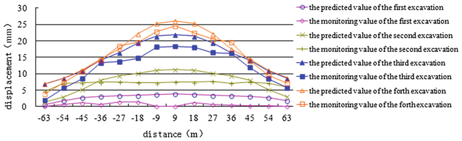

Fig. 14. The measured horizontal amplitude of the bridge

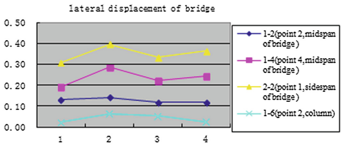

Fig. 15. The measured horizontal amplitude of the bridge

As the depth of excavation underneath the trestle bridge increased, the static displacement of the trestle bridge was observed through the uplift of the bridge deck in company with the soil body uplift. When the excavation reached its bottom, the maximum vertical deformation reached 24.5 mm, which is very close to the calculated data, 30.08 mm. As shown in Table 2. Figure 14 shows the curves of theoretical calculation and actual measured data from different construction conditions. Both the calculations and measurements directly reflected a tendency of the trestle bridge uplift deformation as the excavation proceeded. And the theoretical calculation data were very close to the acquired measurements. Figure 15 shows the curves for the changes of horizontal amplitude of trestle bridge at different construction stages.

During the foundation pit excavation, protection measures for trestle bridge were as follows: (1) increase the diameter of the base piles foundation and enhance the rigidity of the foundation of the bridge; (2) add support structure between pier columns and strengthen the horizontal rigidity; (3) use high pressure spraying pile reinforcement to strengthen the soft soil layer underneath the bridge and thus increase the constrains of the base piles; (4) Limit the timing for under-bridge excavation and support set-up under 12 h to ensure the timely formation of proper rigidity for the base piles.

The monitoring data collected during the construction indicated that our project design is effective and we can limit the impact of excavation on trestle bridge deformation and train operation within the accepted safety range.

5 Conclusion

Underground constructions are a precedent for large-scale integrated transportation hub projects that are built on or around railway stations. The implementation of such underground constructions usually has high technical difficulties, high construction risk, and affects the overall duration of the projects. Many critical issues to considers are, transition plans for existing operating railway lines, protection measures of the existing railway line during foundation pit excavation, plan for station building construction, and environmental preservation. In this article, based on our practice of the underground engineering for Ningbo High-speed railway station, we proposed a plan of temporary trestle bridge for the continuous operation of existing railway line. By establishing finite element computing model on deep foundation pit and railway trestle bridge, we studied the influence of deep pit excavation on innovative railway trestle bridge and safety operation of trains. Our results showed that the railway trestle bridge structure and train operation in the deep foundation pit are safe and controllable. We also studied, in theory, the coupling subsidence of national railway station and subway station co-construction structure. Based on the analysis results, the variable stiffness leveling method is used to arrange the foundation piles, by which we can control the uneven subsidence of the foundation of the co-construction structure within a safety limit. Both the analysis of the monitoring data and the implementation of informatics control of the construction indicate that our plan and strategy for Ningbo station project has led good results and thus ensures the smooth complementation of the construction of an integrated transportation hub. The research presented in this paper can serve as a reference and set an example for similar transportation hub projects.

References

1. Jia, J., Liu, C., Zhang, Y.: Safety and stability technology for railway trains running on trestle bridges above soft soil excavations. Chin. J. Geotech. Eng., **34**(Suppl) 324–329 (2012)
2. Jia, J., Xie, X., Zhang, Y., Yang, K.: Techniques of the integration construction of underground space in comprehensive urban transportation hub. J. Shanghai Jiaotong Univ., **46**(1), 7–12 (2012)

Centrifuge Investigation into the Effect of New Shield Tunneling on an Existing Overlying Large-Diameter Tunnel

Xiao-Guang Liu[1], Shou-Ji Du[1(✉)], and Peng Li[2]

[1] Department of Civil Engineering, Shanghai Jiao Tong University,
Shanghai, China
dusj@sjtu.edu.cn
[2] Electric Power Planning & Engineering Institute, Beijing, China

Abstract. Two centrifuge model tests with different vertical clearances were carried out to investigate the new shield tunneling on an existing overlying large-diameter tunnel. The difference of the two centrifuge model tests lies in different vertical clearance between the two tunnels. Two construction steps of a new shield tunnel were simulated in the test. The vertical displacement and the longitudinal strain of the existing tunnel, as well as the pore water pressure at its invert and spring line, were measured. Results show that the vertical displacement and the longitudinal stress and the longitudinal differential settlement of the existing tunnel increase along with the vertical clearance of the two tunnel. The vertical displacement and the longitudinal stress of the existing tunnel and the pore water pressure increase because of the excavation while decrease as a result of grouting. The longitudinal differential settlement of the existing tunnel increases with the proceeding of the construction steps of a new shield tunnel.

Keywords: Shield tunneling · Centrifuge model test · Vertical clearance
Pore water pressure · Differential settlement

1 Introduction

With the development of urban rail transit, many new tunnels are constructed adjacent to existing tunnels [1, 2]. The influence of new tunneling on adjacent existing tunnels is essential to be investigated to ensure the safety of existing tunnels in soft clay [3]. In order to investigate this problem, field observations and theoretical analyses and numerical analyses have been used [4–6]. In recent decades, centrifuge model testing in shield tunnel modeling has developed as the centrifuge model test is highly reliable, controllable and stable [7]. A centrifuge model test was used to investigate the effect of new shield tunneling on an existing underlying large-diameter tunnel by Li [8]. However, the effect of overlying tunneling on large-diameter has not been investigated.

In this paper, two centrifuge model tests with different vertical clearances were carried out to investigate the new shield tunneling on an existing overlying large-diameter tunnel. The difference of the two centrifuge model tests lies in different vertical clearance between the two tunnels. Two construction steps (ground loss and grouting) of a new shield tunnel were simulated in the test. The vertical displacement

© Springer Nature Singapore Pte Ltd. 2018
D. Zhang and X. Huang (Eds.): GSIC 2018, *Proceedings of GeoShanghai 2018 International Conference: Tunnelling and Underground Construction*, pp. 559–566, 2018.
https://doi.org/10.1007/978-981-13-0017-2_56

and the longitudinal strain of the existing tunnel, as well as the pore water pressure at its invert and spring line, were measured.

2 Centrifuge Model Test

2.1 Model Configuration and Materials

The test was carried out using the geotechnical centrifuge in Tongji University, which has an effective radius of 3 m, a maximum payload of 2 tons (at 75 g), and a maximum centrifugal acceleration of 200 g. The centrifuge strong box, which held soil and model tunnels, has an internal plan area of 700 mm by 900 mm and an internal height of 700 mm.

Considering the space limitation of the strong box and the prototype scale, the geometric similarity ratio (prototype to model), N, is set to be 100. The basic characteristic of geotechnical centrifuge testing is that the model soil can be made using prototype soil. Based on the dimensional analysis method, the test should be conducted at an acceleration level of 100 g if the model soil is simulated by the prototype soil. At the same time, the bending stiffness similarity ratio for the existing tunnel, E_pI_p/E_mI_m, should be equal to N^4, where E_pI_p and E_mI_m are the longitudinal bending stiffness of the existing tunnel in prototype and in model, respectively. The existing tunnel in prototype is a shield tunnel which is constructed ring by ring in the longitudinal direction. This structural type weakens the longitudinal bending stiffness of the existing tunnel should be reduced. According to the equivalent bending stiffness [9, 10] theory, E_pI_p is equal to ξEI, where ξ is the reduction coefficient and EI is the longitudinal bending stiffness of the existing tunnel in prototype without consideration on the effect of structural type. The layout and dimensions of the model are presented in Fig. 1, in which the model unit is used. The parameters of the existing tunnel and the new shield tunnel, as well as the soil properties are the same as these presented in another paper by Li [8]. The difference of the two centrifuge model tests lies in different vertical clearance (2 and 5 m) between the two tunnels. And the purpose of this paper is to investigate the new shield tunneling on an existing overlying large-diameter tunnel. The properties of the soil are given in Table 1.

2.2 Date Acquisition

Three displacement transducers, arranged in a line at the crown of the existing tunnel model, were used to measure the vertical displacement of the existing tunnel, and their intervals are shown in Fig. 2. Two pore water pressure gauge were located at the spring line and the invert of the existing tunnel. Strain gauges were pasted at the crown and the invert of the existing tunnel model in a longitudinal direction with the interval of 100 mm, especially, three more strain gauges were pasted at the middle of the existing tunnel model as shown in Fig. 2.

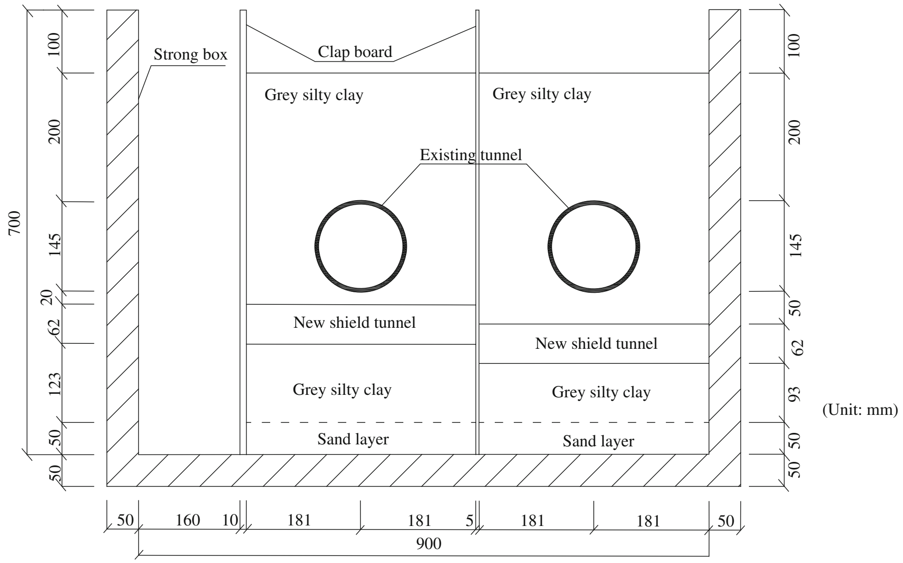
Strong box
Clap board
Grey silty clay
Grey silty clay
Existing tunnel
New shield tunnel
New shield tunnel
Grey silty clay
Grey silty clay
Sand layer
Sand layer
(Unit: mm)
700
100
200
145
20
62
123
50
50
100
200
145
50
62
93
50
50
50
160
10
181
181
5
181
181
50
900

(a) Front view

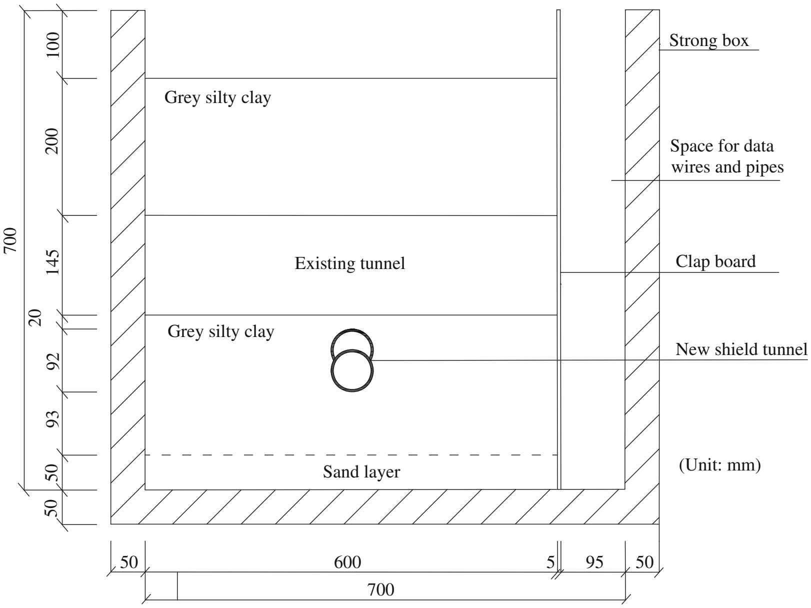
Strong box
Grey silty clay
Space for data wires and pipes
Existing tunnel
Clap board
Grey silty clay
New shield tunnel
Sand layer
(Unit: mm)
700
100
200
145
20
92
93
50
50
50
600
5
95
50
700

(b) Side view

Fig. 1. Configuration of centrifuge model

Table 1. Soil properties.

Parameters	Value
Modulus of compressibility (MPa)	3.34
Void ratio	1.2
Water content (%)	44
Unit weight (kN/m^3)	17.8
Cohesion (kPa)	14
Angle of friction (degrees)	19.2
Permeability coefficient (cm/s)	$9 * 10^{-8}$

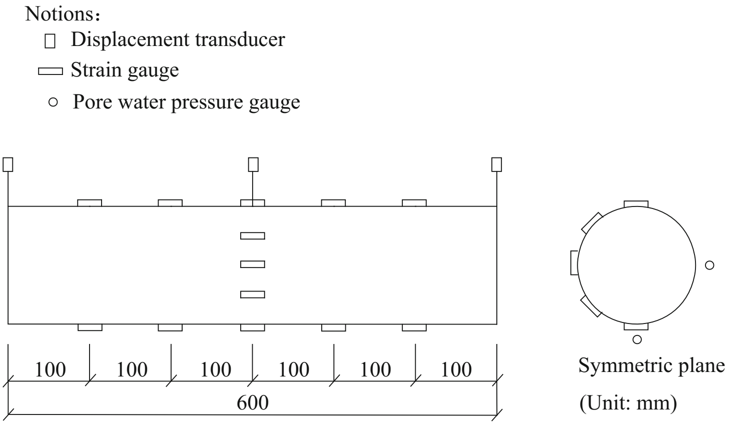

Fig. 2. Layout of measuring instruments

2.3 Experimental Procedure

The key issue in the centrifuge test was to simulate the construction of the shield tunnel. A hollow aluminum alloy tube was used to simulate the new shield tunnel, which was divided into 2 segments to simulate 2 construction steps. Excavation lengths were 175 mm in each step in the centrifugal simulation. Each segment was sealed within a latex membrane. The gaps between the latex membrane and the aluminum alloy tube were filled with saturated $CaCl_2$ solution. The solution was used to simulate ground loss and grouting by discharging and injecting it. Four solenoid values were used to control the discharge and injection of the solution. The magnitude of ground volume loss and grouting volume was controlled by a hydraulic jack connected to a piston of a fluid-filled sealed cylinder. This cylinder was connected to the new shield tunnel model and had an inter diameter of 30 mm. A given displacement of the hydraulic jack corresponds to a specific volume of solution between the latex membrane and the aluminum alloy tube. Figure 3 illustrates the above method.

By statistically analyzing the data of ground loss induced by shield tunnel construction, it is found that the ground loss ratio ranges from 0.35% to 2.02% for cohesive soil area in Shanghai. The magnitudes of ground loss ratio and grouting ratio were

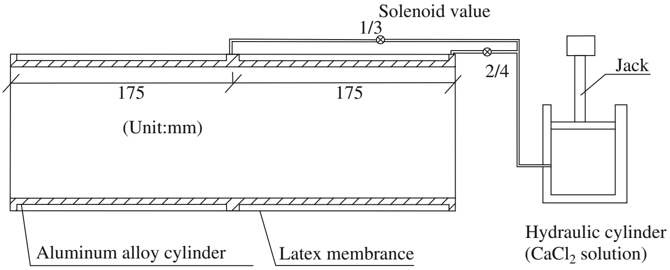

Fig. 3. Simulation of new shield tunnel construction

specified to be 1% and 150% in the centrifuge test, respectively. The simulation procedure of the new shield tunnel construction is given in detail as follows:

(a) Progress in step 1. As for the situation which the vertical clearance between the existing tunnel and new shield tunnel is 2 m, turn on solenoid 1. Give the hydraulic jack an upward displacement of 9.4 mm to simulate ground loss ratio of 1%. After this operation, give the hydraulic jack a downward displacement of 14.2 mm to simulate grouting ratio of 150%. After all, turn off solenoid values 1.
(b) Progress in step 2. Turn on solenoid 2. Give the hydraulic jack an upward displacement of 9.4 mm to simulate ground loss ratio of 1%. After this operation, give the hydraulic jack a downward displacement of 14.2 mm to simulate grouting ratio of 150%. After all, turn off solenoid values 2.
(c) Progress in step 3. Redo the step above with solenoid 3 and 4 to simulate the situation which the vertical clearance between the existing tunnel and new shield tunnel is 5 m.

3 Result and Analysis

3.1 Vertical Displacement of Existing Tunnel

Figures 4 and 5 show the vertical displacement pattern of the existing tunnel. It can be seen that the changes of displacement of the existing tunnel occurred in a period of after drainage or grouting, implying that the deformation of soil lags behind the load of soil. It proves that the additional stress is undertaken by water under moment load.

The displacements at the middle and terminals of the existing tunnels are different and the displacements at the middle are large than at the terminals, implying that longitudinal bending occurred in the existing tunnels. For the situation with vertical clearance as 2 m, the displacement at the middle of the existing tunnel is 9 mm in drainage of step 1, 21 mm in drainage of step 2, and 23 mm at the end of the construction of the new shield tunnel. The longitudinal differential settlement is 4 mm. As for the situation with vertical clearance as 5 m, the displacement at the middle of the existing tunnel is 4 mm in drainage of step 1, 8 mm in drainage of step 2, and 8 mm at the end of the construction of the new shield tunnel. The longitudinal differential

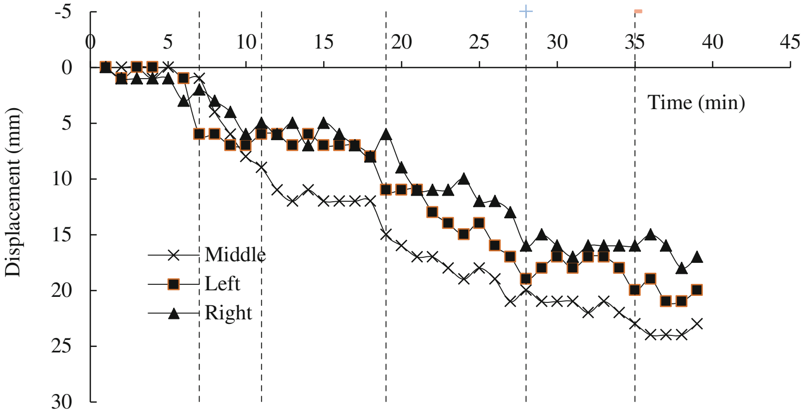

Fig. 4. Displacement of the existing tunnel with vertical clearance as 2 m

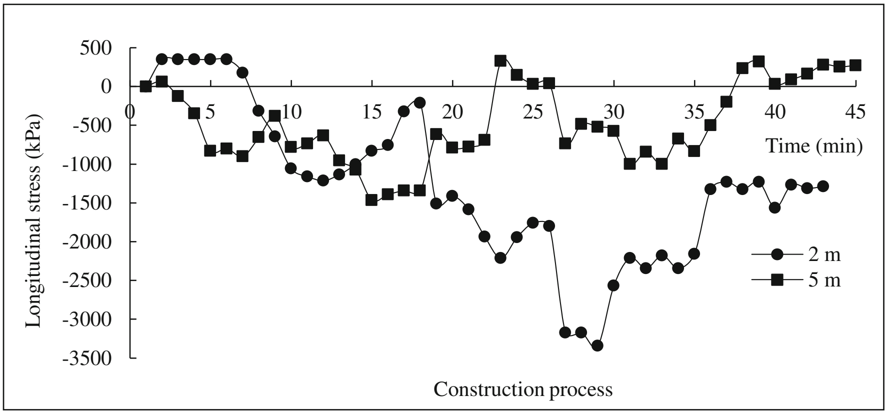

Fig. 5. Displacement of the existing tunnel with vertical clearance as 5 m

settlement is 2 mm. It can be drawn that the vertical displacement and the longitudinal differential settlement of the existing tunnel increase along with the vertical clearance of the two tunnel.

3.2 Longitudinal Stress of Existing Tunnel

Due to the new shield tunnel cross at the middle of the existing tunnel, the stresses of the most dangerous section (the middle of the existing tunnel) are presented in Figs. 6 and 7.

New shield tunnel stratum loss leads to a compressive stress on the surface of the existing tunnel, while new shield tunnel grouting leads to a tension stress on the surface of the existing tunnel. For the situation with vertical clearance as 2 m, the change of the longitudinal internal force of existing tunnel is 3690 kPa. As for the situation with

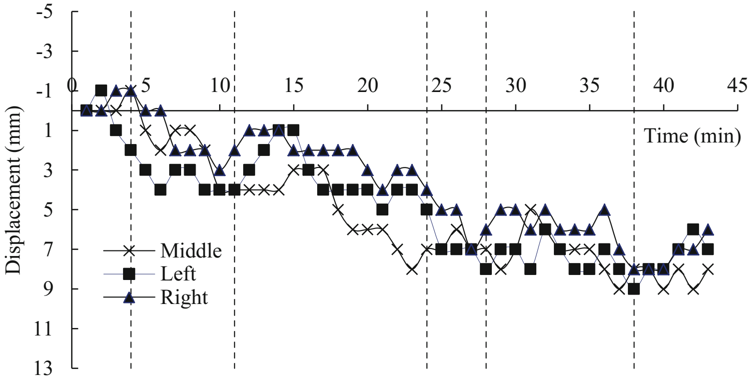

Fig. 6. Longitudinal stress of the existing tunnel with vertical clearance as 2 m and 5 m

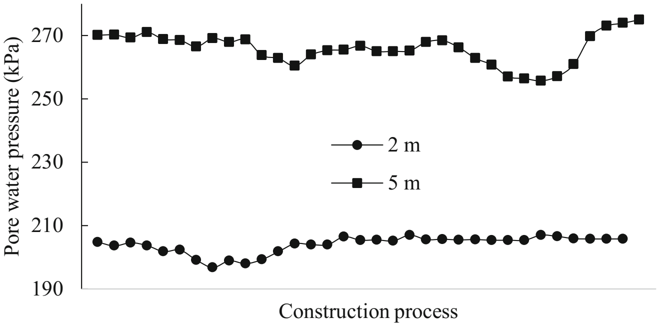

Fig. 7. Pore water pressure of the existing tunnel with vertical clearance as 2 m and 5 m

vertical clearance as 5 m, the change of the longitudinal internal force of existing tunnel is 1795 kPa. It can be drawn that the longitudinal stress of the existing tunnel increase along with the vertical clearance of the two tunnel.

3.3 Pore Water Pressure of Existing Tunnel

During the test process, pore water pressure data at the invert of existing tunnel with vertical clearance as 2 m and at the spring line of existing tunnel with vertical clearance as 5 m are not obtained. For the situation with vertical clearance as 2 m, the pore water pressure decreased 10 kPa in the drainage of step 1 and increased 10 kPa in the grouting of step 1. The change of the pore water pressure is not obvious in step 2 because the pore water pressure gauge is pasted closely to the first section of new shield tunnel. As for the situation with vertical clearance as 5 m, the pore water pressure decreased 8 kPa in the drainage of step 1 and increased 10 kPa in the grouting of step 1, and the pore water pressure decreased 15 kPa in the drainage of step 1 and increased 18 kPa in the grouting of step 2. It can be drawn that the pore water pressure increase because of the excavation while decrease as a result of grouting.

4 Conclusions

The process of the centrifuge test and the result of the test are presented and analyzed above, the conclusion can be drawn as follows: the vertical displacement and the longitudinal stress and the longitudinal differential settlement of the existing tunnel increase along with the vertical clearance of the two tunnel. The vertical displacement and the longitudinal stress of the existing tunnel and the pore water pressure increase because of the excavation while decrease as a result of grouting. The longitudinal differential settlement of the existing tunnel increases with the proceeding of the construction steps of a new shield tunnel.

References

1. Li, X.G., Yuan, D.J.: Response of a double-decked metro tunnel to shield driving of twin closely undercrossing tunnels. Tunn. Undergr. Space Technol. **28**, 18–30 (2012)
2. Marshall, A.M., Klar, A., Mair, R.J.: Tunneling beneath buried pipes: view of soil strain and its effect on pipeline behavior. J. Geotech. Geoenviron. Eng. **136**(12), 1664–1672 (2010)
3. Shen, S.L., Wu, H.N., Cui, Y.J., Yin, Z.Y.: Long-term settlement behavior of the metro tunnel in Shanghai. Tunn. Undergr. Space Technol. **40**, 309–323 (2014)
4. Zhang, J.F., Chen, J.J., Wang, J.H., Zhu, Y.F.: Prediction of tunnel displacement induced by adjacent excavation in soft soil. Tunn. Undergr. Space Technol. **36**, 24–33 (2013)
5. Li, P., Du, S.J.: Responses of cross-river tunnel due to overlying shield tunnel construction (I): Influence of construction procedure. In: Proceedings of the International Conference on Pipelines and Trenchless Technology, pp. 1585–1594. ASCE, United States (2012)
6. Li, P., Du, S.J.: Responses of cross-river tunnel due to overlying shield tunnel construction (I): Influence of distance. In: Proceedings of the International Conference on Pipelines and Trenchless Technology, pp. 1595–1605. ASCE, United States (2012)
7. Ng, C.W.W., Lu, H., Peng, S.Y.: Three-dimensional centrifuge modelling of the effects of twin tunneling on an existing pile. Tunn. Undergr. Space Technol. **35**, 189–199 (2013)
8. Li, P., Du, S.J.: Centrifuge investigation into the effect of new shield tunneling on an existing underlying large-diameter tunnel. Tunn. Undergr. Space Technol. **42**, 59–66 (2014)
9. Liao, S.M., Liu, J.H., Wang, R.L., Li, Z.M.: Shield tunneling and environment protection in Shanghai soft ground. Tunn. Undergr. Space Technol. **24**(4), 454–465 (2009)
10. Liao, S.M., Peng, F.L., Shen, S.L.: Analysis of shearing effect on tunnel induced by load transfer along longitudinal direction. Tunn. Undergr. Space Technol. **23**(4), 421–430 (2008)

Study on Construction Control Measures of Shield Tunnel Overpassing Existing Tunnel in Sandy Silt

Yahui Wang[1], Yan Liu[1,2](✉), Junyan Liu[1,2], and Liangliang Zhang[3]

[1] School of Civil Engineering and Architecture,
University of Jinan, Jinan, China
wyhegz@163.com, liuyan322@163.com
[2] The Engineering Technology Research Center for Urban Underground
Engineering Supporting and Risk Monitoring of Shandong Province,
Jinan, China
[3] China Railway Siyuan Survey and Design Group Co., Ltd., Hubei, China

Abstract. Nowadays the problem of soil loss during construction of shield driving has attracted much attention, especially in sandy silt. Moreover, it is easy to cause ground subsidence and destruction of surrounding environment because of the soil's sensitivity and disturbing characteristic. Factually, existing tunnel has high control standards for deformation as well as its deformation occurs easily when shield tunnel overpasses it at short distance, so it has always been valued the highest risk. This article will take Xuzhou Metro Line 3 first-stage project as the background and it adopt numerical method to consider the whole process of tunneling construction, including the effect of external pressures of segment. On the one hand, the evolution mechanism of soil displacement field and the responses on displacement and stress of the existing tunnel under various loads will be studied during the construction of shield tunnel overpassing existing tunnel. On the other hand, the optimal reinforcement scheme will be explored according to the different responses of the vault, the haunch and the arch bottom of the tunnel. And the validity of reinforcement design parameters combined with sandy silt's characteristics will be researched furtherly. As a result, the paper can provide the theoretical basis for the similar project design and construction of subway tunnel overlapping tunnel.

Keywords: Shield tunnel · Finite element analysis · Existing tunnel
Grouting reinforcement · Overpassing

1 Introduction

In the projects of new tunnel crossing existing tunnel, the excavation of shield tunnel and soil under unloading will cause large deformation of the existing tunnel structure [1, 2]. Therefore, such projects are listed as important sources of risk. Further, the issue about crossing existing tunnel in the complex geological situation is the major problem.

For the problems, domestic and foreign scholars have carried out extensive research and they have achieved a series of results. Zhang et al. analyzed the influence of new

© Springer Nature Singapore Pte Ltd. 2018
D. Zhang and X. Huang (Eds.): GSIC 2018, *Proceedings of GeoShanghai 2018 International Conference: Tunnelling and Underground Construction*, pp. 567–575, 2018.
https://doi.org/10.1007/978-981-13-0017-2_57

tunnel on old tunnel during shield tunneling in the clay layer and they concluded that the relative position and net distance between the runnels have great influence on the interaction [3]. Zhang revealed the deformation prediction of subway tunnel in service induced by EPB shield in soft clay during above and down overlapped traversing process and its construction control [4]. Zan analyzed the influence of the vertical and horizontal deformation of existing tunnel and he concluded that the shield construction uplifts the existing tunnel and the horizontal deformation is far less than the vertical [5]. The interactions between perpendicularly crossing tunnels in the Sydney region are investigated by Liu etc. The results of the analysis showed that installation of the new tunnel causes the shotcrete lining of the existing tunnel to be in tension in the side facing towards the tunnel opening and in compression at the crown and invert [6].

Many scholars have concentrated on the cross engineering of soft soil geological conditions. But the research on sandy silty is rare. This paper takes Xuzhou Metro Line 3 shield tunnels overpassing Line 1 tunnels as its background, and it analyzes the soil loss in sandy silt and the influence on the existing tunnel by using the method of 3D finite element analysis.

2 Engineering Background

It overpasses Metro Line 1 tunnels and the net distance between them is about 1.6 m after the subway route of Xuzhou Metro Line 3 first-stage project leaves XuZhou Railway Station station.

According to “Code for risk management of underground works in urban rail transit” (GB 50652), the project belongs to I risk source. Secondly, the train vibration has adverse effects on sandy soil layer during the subway operation. Therefore, considering construction and operation comprehensively, simulation analysis shall be carried out before construction [7, 8]. The soil layers of the tunnels crossing node and the main physical and mechanical parameters are shown in Table 1. The relation between the tunnels is shown in Fig. 1.

Table 1. Physical and mechanical parameters of soils.

Number	Layer	γ(kN/m^3)	E_0 (MPa)	Y	c(kPa)	φ_k(°)
1-1	Miscellaneous fill(1-1)	18#	4#	0.35#	15#	12#
2-4-2	Sandy silty soil (liquefaction)(2-4-2)	19.3	6#	0.30	12.4	29.8
2-3B-3	Silty clay(2-3B-3)	18.92	5.95	0.35	19.2	13.2
2-4-3	Sandy silty soil(2-4-3)	19.31	8.0#	0.30	12.1	29.8
2-3A-4	Clay(2-3A-4)	19.54	10.0#	0.30	72.0	12.0
5-3A-4	Clay(5-3A-4)	19.07	13.02	0.30	75.1	12.6
12-1-3	Intermediate weathered limestone(12-1-3)	27.2	9000#	0.25#	1000#	40#
11-2B	Limestone cave(11-2B)	19.5#	13#	0.35#	75#	15#

Note. Mechanical index with the “#” is experience value.

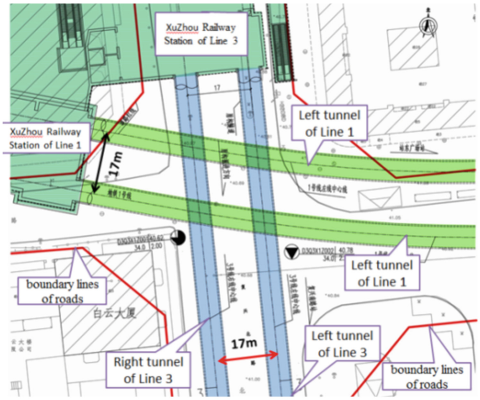
XuZhou Railway Station of Line 3
XuZhou Railway Station of Line 1
17m
Left tunnel of Line 1
Left tunnel of Line 1
boundary lines of roads
白云大厦
Right tunnel of Line 3
17m
Left tunnel of Line 3
boundary lines of roads

(a) Plan

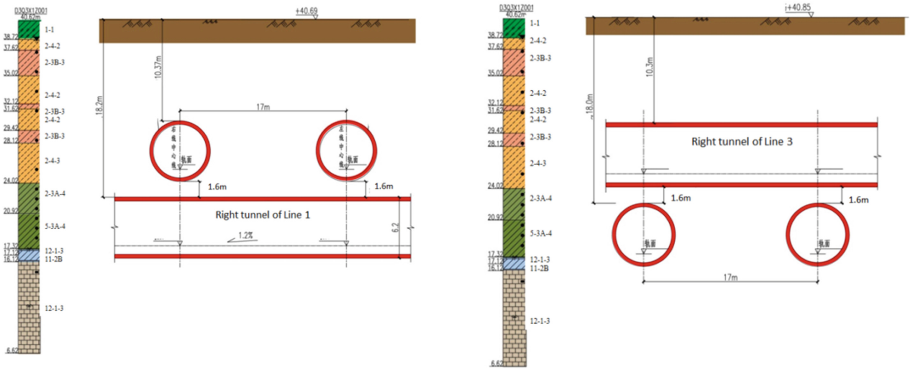
+40.69
10.37m
18.2m
17m
1.6m
1.6m
Right tunnel of Line 1
1.2%
6.2
1-1
2-4-2
2-3B-3
2-4-3
2-3A-4
5-3A-4
12-1-3
11-2B
+40.85
10.3m
18.0m
Right tunnel of Line 3
1.6m
1.6m
17m

(b)Transverse section drawing (c)Vertical section drawing

Fig. 1. Sketch of the location of the tunnels

3 Model Establishment

3.1 Numerical Model and Selection of Calculation Parameters

According to the actual situation and characteristics of this project, there are the following considerations in the 3D finite element static analysis.

(a) The Mohr-Coulomb elastoplastic model is used in the soil and the linear elastic constitutive relation is used in structural material of segment.

(b) It supposed that there is an external pressure (1000 kN/m^2) around the segment when shield driving and this force be made of the slurry pressure after the wall grouting.

(c) In the model, the distance between the model boundary line and the edge of the tunnel is about 4D(hole diameter), the size is 75 m × 60 m × 34 m (x, y, z direction). The model is shown in Fig. 2.

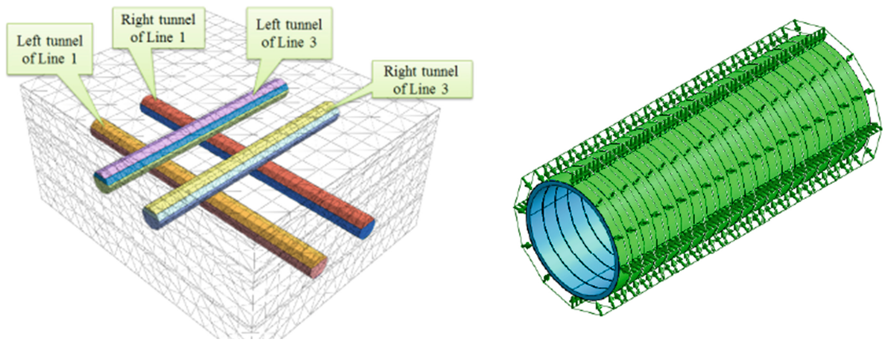

(a) Axial side view (b) Tunnel force diagram

Fig. 2. Three-dimensional numerical model.

The simulation process of shield tunnel construction is as the following.

(a) Calculating the initial stage of stress distribution.
(b) The value of soil stress release is 10% and the segments and external pressure are applied when the existing tunnel is tunneling. Finally, it calculate to equilibrium state.
(c) Clear displacement.
(d) With the stress release of 10% and the application of shield segments and external pressure, the left and right tunnels of Line 3 were excavated successively. Finally, it calculate to equilibrium state.

4 Simulation Analysis and Results

Line 1 tunnels has been completed when Metro Line 3 tunnels is in construction. The mechanism of soil displacement field is as the following (Fig. 3).

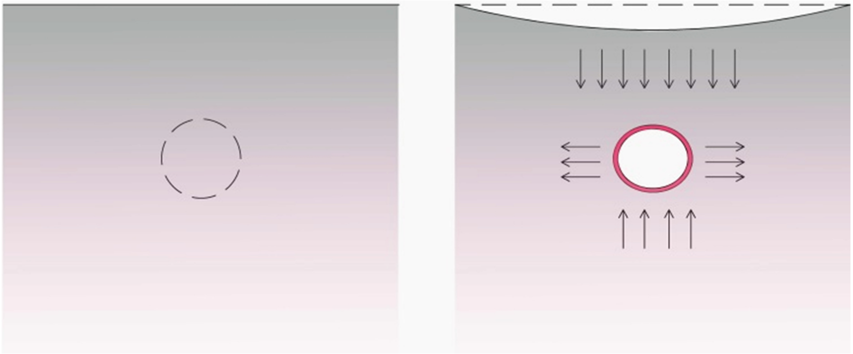

Fig. 3. Mechanism of soil displacement field.

Table 2. The displacement results of shield tunnel overpassing existing tunnel.

Step	Maximum vertical displacement		Maximum horizontal displacement		Subsidence
Left line tunnel through node	Vault	4.4	Left side	1.1	–8.6
	Arch bottom	1.9	Right side	–1.1	
Double track tunnels through node	Vault	6.9	Left side	1.4	–10.3
	Arch bottom	3.0	Right side	–1.5	

Note: "+" means displacement is positive; "–" means displacement is negative.

(1) The displacement results of Line 1 tunnels after left and right shield tunnels of Line 3 through the cross-node are shown in Table 2.

(2) Interpretation of result.

(a) Soil unloading caused uplift deformation of vault of Line 1 shield tunnel when left line tunnel of Line 3 passed through the cross-node. The maximum value is 4.4 mm; The soil at the tunnel arch waist has a tendency to move into the carve and the shield segments will be squeezed. The maximum lateral displacement of the tunnel arch waist is 1.1 mm and the maximum value of surface settlement is 8.6 mm.

(b) The uplift deformation of Line 1 tunnel segments has an increasing trend when double tunnels of Line 3 passed through the node. The maximum value is 6.9 mm. The maximum lateral displacement of the tunnel arch waist is 1.5 mm and the maximum value of the surface settlement is 10.3 mm.

(c) The top stress values of Line 1 tunnels are positive after Line3 tunnels overpassed Line 1 tunnels and the trend of it has increased. The maximum value is 1266kN/m^2.

(d) The uplift value of existing tunnel structure shall be controlled within 5 mm. After the Line 3 overpassed the node, the maximum uplift value of Line 1 tunnel structure is 6.9 mm, greater than 5 mm. So it does not meet the deformation requirement. Therefore, the design of reinforcement must be carried out.

5 Study on Reinforcement Scheme

From the simulation results, it can be seen that the crossing area is weak. In particular, the deformation is more obvious in the 30 m range along Line 3 tunnel and in the 40 m range along Line 1 tunnel.

Considering that the crossing area is limited by the surrounding environment, traffic ease and pipeline relocation, the design of in-tunnel grouting reinforcement of PVC sleeve valve pipe in the tunnel is preferred [9, 10]. The reinforcement strength index is that the unconfined compressive strength of soil(qu) should not be less than 1.0 MPa. And the osmotic coefficient should not be greater than 1×10^{-7}cm/s. The grout material is double slurry, made of cement-water glass. Grouting pressure are 0.5–1.0 MPa (for line 1) and 0.2–0.5 MPa (for line 3). In addition, the diffusion radius is 0.8 m.

The reinforcement design is shown in Fig. 4.

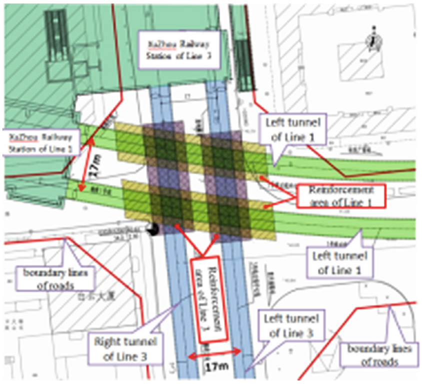
KaiZhou Railway Station of Line 3
KaiZhou Railway Station of Line 1
Left tunnel of Line 1
17m
Reinforcement area of Line 1
Left tunnel of Line 1
boundary lines of roads
Reinforcement area of Line 3
Left tunnel of Line 3
Right tunnel of Line 3
17m
boundary lines of roads

(a)Plan

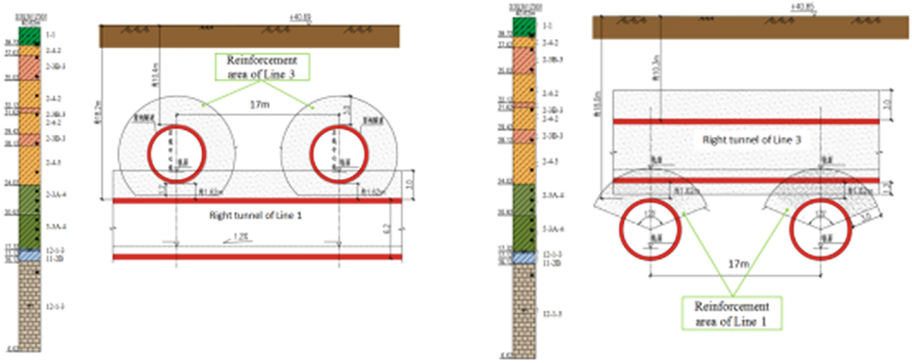
Reinforcement area of Line 3
17m
Right tunnel of Line 1
Right tunnel of Line 3
17m
Reinforcement area of Line 1

(b) transverse section drawing (c) vertical section drawing

Fig. 4. Drawings of grouting reinforcement in tunnel at crossing node

5.1 Establishment of Reinforcement Model and Selection of Parameters

The selection of reinforcement soil parameters is shown in Table 3.

Table 3. Reinforcement soil parameter value

Serial number	Project	γ(kN/m^3)	E_s(MPa)	Y
1	Grout	22.5	10000	0.3

The grouting reinforcement model in the tunnel is shown in Fig. 5

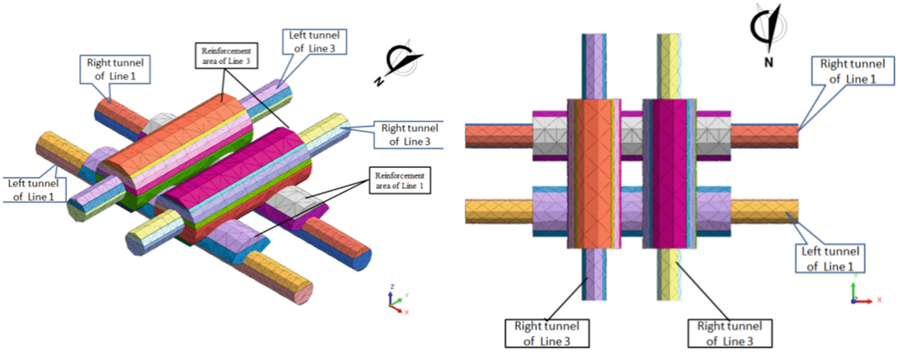
Right tunnel of Line 1
Reinforcement area of Line 3
Left tunnel of Line 3
Right tunnel of Line 3
Reinforcement area of Line 1
Left tunnel of Line 1
N
Right tunnel of Line 1
Left tunnel of Line 1
Right tunnel of Line 3
Right tunnel of Line 3

(a) (b)

Fig. 5. Model drawings of reinforcement.

5.2 Interpretation of Result

In this process of construction, in-tunnel grouting reinforcement on the soil was considered. And the simulation of grouting reinforcement was conducted.

(1) The displacement results of Line 1 after left and right shield tunnels of Line 3 through the cross-node are shown in Table 4.

Table 4. The displacement results of shield tunnel overpassing existing tunnel.

Step	Maximum vertical displacement		Maximum horizontal displacement		Subsidence
Left line tunnel through cross node	Vault	1.7	Left side	0.4	–3.6
	Arch bottom	1.3	Right side	–0.4	
Double track tunnel through cross node	Vault	2.2	Left side	0.4	–3.9
	Arch bottom	1.9	Right side	–0.4	

Note: "+" means displacement is positive; "–" means displacement is negative.

(2) Interpretation of result.

In the conditions with reinforcement, the displacement and the stress of Line 1 tunnel and the surface subsidence value are significantly less than the results of no-reinforcement conditions. And Line 1 tunnel structural uplift value is 2.2 mm < 5 mm, the surface settlement value is 3.9 mm < 10 mm. They all meet the deformation requirements.

5.3 The Design of Reinforcement Measures

From the simulation results, it is feasible to conduct grouting reinforcement in tunnel for the cross section in theoretical analysis. On this basis, the design with reinforcement will be further materialized.

(a) Before the construction of Line 3 tunnel, grouting reinforcement in the Line 1 tunnel is carried out on the sandwiched soil of two lines (namely 135° of the Line 1 tunnel vault top, 3 m soil boundary outside the tunnel structural line). And the longitudinal length along the Line 1 tunnels is 45 m.

(b) In the construction of Line 3, the grouting reinforcement of full ring tunnel is conducted on sandwiched soil between two tunnels and 2-4-2 liquefiable soil layer. The longitudinal length along the Line 3 tunnels is 33 m and the distance between the reinforcement boundary and the tunnel structural line is 3 m. However, the vertical reinforcement length of two tunnels clamp soil is 1.2 m.

6 Epilogue

The project of shield tunnel overpassing existing tunnel in sandy silt is simulated by using the finite element software Midas GTS NX. And the Line 3 shield tunnel construction's influence about Line 1 shield tunnel structure and the upper surface settlement is analyzed under two conditions. From the result, it can be concluded as the following.

(a) In the case without reinforcement, the soil disturbance around the tunnels is caused by unloading soil when Line 3 shield tunnels overpasses existing tunnels. Meanwhile, stress redistribution of the surrounding rock occurs. All these lead to the result that Line 1 shield tunnels rises, and the maximum uplift value is 6.9 mm. The complex soil disturbance leads to the extrusion deformation of Line 1 tunnel segments, resulting in the maximum horizontal displacement at 1.5 mm, which occurs at the hance of Line 1 tunnel. In addition, there is an increasing trend of the normal stress at the top of Line 1 tunnels. The maximum surface settlement is 10.3 mm.

(b) In the case without reinforcement, the maximum uplift value of Line 1 tunnel structure is 6.9 mm after Line3 tunnel overpassed Line 1 tunnel, greater than 5 mm. So it does not meet the deformation requirement. In addition, the sandy silt 2-4-2 belongs to liquefaction soil. Therefore, the reinforcement design must be carried out for the normal operation and the shield construction safety consideration.

(c) In the condition with reinforcement, the maximum uplift value of Line 1 tunnels structure is 2.2 mm after shield tunnel overpass existing tunnels, less 4.7 mm than that of no reinforcement. The maximum horizontal displacement of Line 1 tunnel structure is 0.4 mm, less 1.1 mm than that without reinforcement. The stress value of reinforcing zone at the top of Line 1 tunnels is obviously reduced. The maximum surface settlement at the top of Line 3 tunnels is 3.9 mm, less 6.4 mm than that without reinforcement. According to the results of simulation, the design of reinforcement can effectively reduce the deformation and the stress of existing tunnel caused by the construction of new tunnel.

(d) In the design and construction of the old and new tunnels close crossing, in addition to the grouting reinforcement in the tunnel, there are the ground high-pressure jet grouting reinforcement. Meanwhile, the corresponding engineering control measures are also recommended (such as, strict control of synchronous grouting and slurry quality, increasing segment grouting hole to reinforce grouting two times around the existing tunnel, strengthening segment reinforcement, monitoring and measurement, information construction, etc.). It can effectively control the deformation of the shield tunnel structure.

Acknowledgments. The author would like to thank for the support from the Science and Technology Plan Projects of the Ministry of Housing and Urban-Rural Development of the People's Republic of China (No. 2015-K3-022), Department of Housing and Urban-Rural of Shandong Province (No. KY010 and No. KY011) of China, the Doctoral Fund Project of University of Ji'nan (XBS1355).

References

1. Fang, X-H.: Research on the shield tunnel exerts negative influences on nearby existing tunnels. Central South University (2014)
2. Liao, S.-M., Yu, Y., Bai, T., et al.: Distribution of ground displacemeng field owing to two overlapped shield tunneling interaction. Chin. J. Geotech. Eng. **28**(04), 485–490 (2006)
3. Zhang, H.-B., Yin, Z.-Z., Zhu, J.-G.: Numerical simulation of influence of new tunnel on short distance overlapped old tunnel during shield tunneling. Rock Soil Mech. **26**(2), 282–286 (2005)
4. Zhang, Z.-G., Zhang, M.-X.: Deformation prediction of subway tunnel induced by EPB shield in soft caly during above and down overlapped process and its constrction control. Rock Soil Mech. **32**(S2), 3428–3439 (2013)
5. Zan, Z.-H.: Influence of up-crossing shield tunnel construction on deformation of adjacent existing tunnels. J. Wuhan Inst. Technol. **S2**, 3428–3439 (2016)
6. Liu, H.Y.: Effects of tunnelling on existing support systems of perpendicularly crossing tunnels. Comput. Geotech. **36**(5), 880–894 (2009)
7. Ma, X.-F., Wang, J.-S., Li, X.-Y., et al.: Centrifuge modeling of grouting loss and settlement cansed by shield tunnelling in soft ground. Chin. J. Geotech. Eng. **05**, 942–947 (2012)
8. Liao, S.-M., Yang, Y.-H.: Deformation analysis and control of a running subway crossed by upper- and lower-shield in succession. Chin. J. Geotech. Eng. **05**, 812–818 (2012)
9. Ruan, W.-J.: Research on diffusion of grouting and basic properties of grouts. Chin. J. Geotech. Eng. **01**, 69–73 (2005)
10. Song, T.-T., Zhou, S.-H., Xu, R.-Z.: Mechanism and determination of parameters of synchronous grouting in shield tunneling. Chin. J. Undergr. Space Eng. **01**, 130–133 (2008)

Research on the Shield Tunneling Construction Passing Through the Maglev Pile Foundations in Saturated Soft Soil Strata

Di Wu(✉)

Shanghai Shentong Metro Group Co., Ltd., Shanghai 201103, China
`wd_mtr@163.com`

Abstract. Shield tunneling projects in the central city of the soft soil area usually have limited conditions of auxiliary reinforcement protection measures. In this paper, the influence of the shield tunneling construction on the nearby maglev pile foundations, which is carried out by means of the non-reinforcement protection measures, is studied by numerical analysis and field measurement method. By setting the field test section and the simulation section, this paper puts forward the construction plan and the key parameters of the shield tunneling construction to meet the requirements of the maglev operation and deformation control. The influence of the shield tunneling on the deformation of the maglev bridge pier and the track is analyzed. The results of the research and engineering implementation show that the pressure setting of the shield tunnel is the key parameter to control the settlement of the bearing cap. For the pressure-type pile foundation, the undervoltage range of the shield tunneling pressure is 0.01–0.02 MPa to maintain the pile foundation cracking and the external balance, which can be determined according to the test section with a multi-stage method proposed in this paper; the filling rate of the synchronous grouting is 150%–180%, for filling the formation loss to ensure that the surface subsidence within the allowable range.

Keywords: Saturated soil · Shield tunneling · Under passing construction
Operating maglev · Construction control

1 Introduction

Shield tunneling projects will inevitably have significant influence on the deformation of the surroundings due to the excavation surface support pressure, synchronous grouting effect, grouting pressure and other construction effects [1, 2]. Sun et al. [3] used numerical method to analyze the distribution law of earth pressure beneath the existing tunnel with different burial depth, and put forward reinforcement protection measures to ensure the safety of the existing tunnels. Xu et al. [4]. used soap water, foam and other materials to study the increase of dumping speed through a field test. The driving speed is improved and the cutter wheel torque is reduced, a good construction effect is reached according to their research results. Ji et al. [5]. studied the impact of various factors on the segment floating problem by relying on the field test section during the shield tunneling construction. Anti-floating measures were suggested

© Springer Nature Singapore Pte Ltd. 2018
D. Zhang and X. Huang (Eds.): GSIC 2018, *Proceedings of GeoShanghai 2018 International Conference: Tunnelling and Underground Construction*, pp. 576–584, 2018.
https://doi.org/10.1007/978-981-13-0017-2_58

to reduce the floating amount of the tunnel. Wu et al. [6]. carried out filter cake performance test of the slurry shield tunneling in the sandy soil. Proposed slurry density and preparation method was obtained in coarse sand and gravel stratum, which ensured the balance between the earth pressure and the unloading pressure of the excavation surface, and reduced the settlement of the surface and the deformation of the building.

According to the theoretical analysis, Dai [7] adjusted the shield machine attitude in the curve segments and analyzed the over-excavation law of different modes. The calculation method of surface settlement under different tunneling modes was proposed. Wang [8] deduced the relationship between the construction parameters when the shield is in the equilibrium state, and put forward the method of using the model test to determine the equilibrium state parameter. Huang et al. [9]. analyzed the settlement and safety control method of shield tunneling under a new railway subgrade by theoretical and numerical methods, before they put forward a reasonable construction scheme of pile and plate reinforcement. Song et al. [10]. established a excess pore water pressure analysis model based on a highway tunnel project in Shanghai to ensure the surface settlement. Yan et al. [11]. proposed the reference value of the shield parameters under various operating conditions through statistical method and theoretical analysis, which had a certain significance on the Guangzhou subway passing under the important roads engineering. Anagnostou [12] studied the failure mechanism of the slurry tunneling surface, and quantitatively analyzed the relationship between soil strength, formation permeability, mud parameters, tunnel section size and safety factors. Li et al. [13]. studied the Shanghai Yangtze River Tunnel using the upper bound limit analysis method and finite element method, the local damage and overall damage in the collapse and extrusion of excavation face were disscussed.

According to the existing theoretical research results and the engineering practice, the implementation of the shield tunnel project in the soft soil is usually accompanied by the corresponding reinforcement protection measures to cut off the influence of the tunneling construction deformation on the penetrating body and ensure the normal use function. However, when tunneling under the central city, due to the complex surrounding environment, the reinforcement conditions are usually limited. In this paper, the influence of the construction of the shield tunnel is studied by numerical analysis and field measurement method. The influence of the shield tunneling construction on the maglev pile foundations is carried out by means of the non-reinforcement protection measures. By setting the field test section and the simulation section, this paper puts forward the construction plan and the key parameters of the shield construction to meet the requirements of the maglev operation and deformation control. The influence of the shield tunneling on the deformation of the maglev bridge pier and the track is analyzed.

2 Project Overview

A section of Shanghai rail transit has passed the magnetic levitation pile foundation. The project plane shows in Fig. 1. The length of the up/down lines are 1768.1 m, and the thickness of the covering soil is 10.0–23.1 m, the outer diameter of the shield

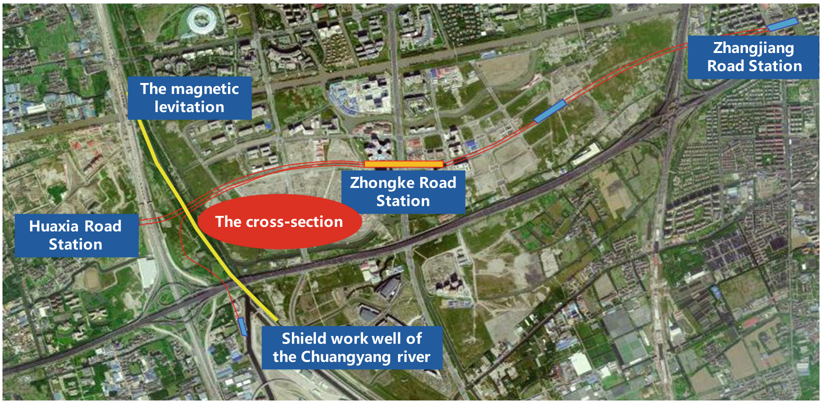
Zhangjiang Road Station
The magnetic levitation
Zhongke Road Station
Huaxia Road Station
The cross-section
Shield work well of the Chuangyang river

Fig. 1. The project plane of Shanghai rail transit passing the magnetic levitation pile foundation.

tunnel is 6.6 m; The distance of the entrance/exit line are 2340.4 m, and the thickness of the covering soil is 9.4–16.4 m, the tunnel diameter is 6.2 m. The curve radius is 250 m in the through section of the entrance/exit lines.

The illustration and the cross-section view is shown in Fig. 2. It can be seen from Fig. 2 that the up/down lines passed through the magnetic levitation pile foundations between piles named PO182, PO183, PO184 respectively; The entrance/exit line passed through the magnetic levitation pile foundations between the piles named PO184 and PO185. The elevation of the magnetic levitation piers are 2.9 m, and the length of the Φ1000 drilling piles are 72.5 m and 74.5 m. The elevations of the piles bottom are −71.4 m and −73.5 m.

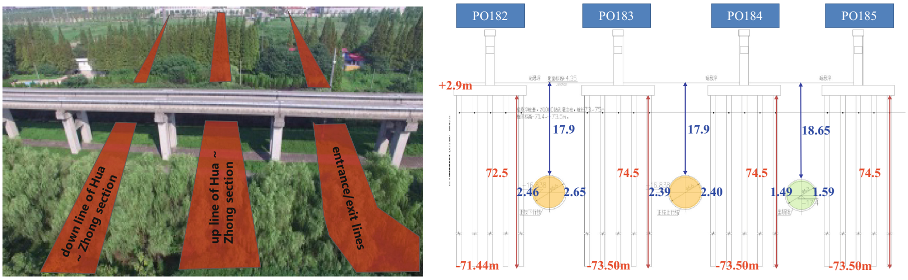
down line of Hua ~ Zhong section
up line of Hua ~ Zhong section
entrance/exit lines
PO182
PO183
PO184
PO185
+2,9m
17.9
17.9
18.65
72.5
74.5
74.5
74.5
2.46
2.65
2.39
2.40
1.49
1.59
-71.44m
-73.50m
-73.50m
-73.50m

(a) Schematic diagram of the through section **(b)** Interval of the metro tunnel and the maglev pile foundation

Fig. 2. The relationship between the metro section and the maglev pile foundation.

The minimum distance between the tunnel of the up/down lines and the magnetic pile foundations is 2.39 m, the depth of the tunnel is 17.9 m in the cross-section; The minimum distance between the tunnel of the entrance/exit line and the maglev pile foundations is 1.49 m, and the tunnel depth is 18.6 m. The main layer within the cross section is ④, ⑤$_1$, ⑤$_2$ and ⑤$_{3-1}$, the main physical parameters of the stratum shown in Table 1.

Table 1. Main physical parameters of the stratum in the through section.

Layer number	Soil name	Cohesion (kPa)	Friction angle (°)	Thickness (m)
①$_1$	Miscellaneous fill	/	/	1.1
①$_2$	Hamamatsu silt	/	/	0.7
②	Silty clay	17	19	1.7
③	Silty clay	12	18	3.5
④	Muddy clay	10	11	7.4
⑤$_1$	Clay	13	12	4.8
⑤$_2$	Sandy silt	6	30	3.6
⑤$_{3-1}$	Silty clay	16	20	2.0

3 Numerical Analysis of the Through Section

The finite element method is used to calculate the influence of shield tunneling on the magnetic pile foundation, which provides the basis for the follow-up parameters and control measures. The finite element model is shown in Fig. 3.

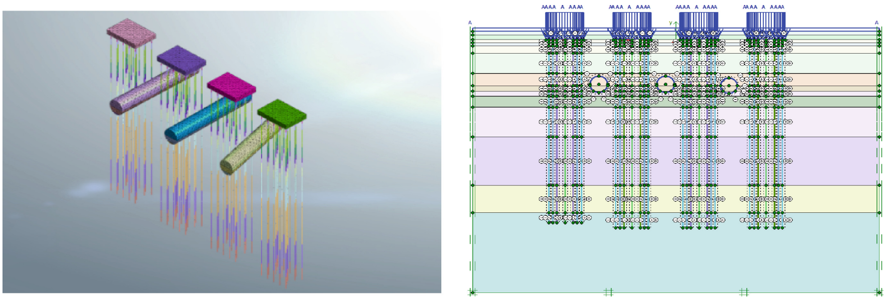

(a) Diagram of the three-dimensional model in numerical method

(b) Cross section of the numerical model

Fig. 3. The finite element analysis model of the though section of the magnetic pile foundation.

As shown in Fig. 3, the pile foundations of the magnetic levitation are simulated with the beam element, and the plate element is used when modeling the concrete segments and the bridge piers. The surface overload is 10 kPa, the dead load and the live load of the magnetic platform are 3600 kN and 1250 kN respectively. The soil model is based on the 15-node Mohr-Coulomb model. According to the experience of

Shanghai area, the elastic modulus is taken from 5 to 10 times the consolidation modulus, other main physical and mechanical parameters are shown Table 1.

To reduce the impact of adjacent tunnel construction, shield construction planning for the first line is the up line (midline) construction, and then the construction of the down line (left line), the entrance/exit line (right line) comes last. According to the requirements of construction planning, the settlement value of the magnetic pile foundation at the formation loss rate of 0.1%, 0.2%, 0.3% and 0.5% is calculated respectively.

The additional deformation limits of the maglev structure are shown in Table 2. According to the numerical analysis results, the formation loss rate which is less than 0.1% can meet the requirements of magnetic deformation.

Table 2. Additional deformation limits for the maglev structures.

Control index	Cumulative deformation (mm)	Deformation rate (mm/d)
Settlement of the pier column	2.0	0.4
Unfair settlement of adjacent pier	1.0	0.4
Horizontal displacement difference of adjacent pier	1.0	0.4
Unfair settlement of platform	0.5	0.2

4 Design and Results of Full - Scale Test

According to the numerical results, it is necessary to set the field full-scale test to set the parameters of the tunneling and to test the control measures before the formal crossing construction. The test section settings are shown in Fig. 4.

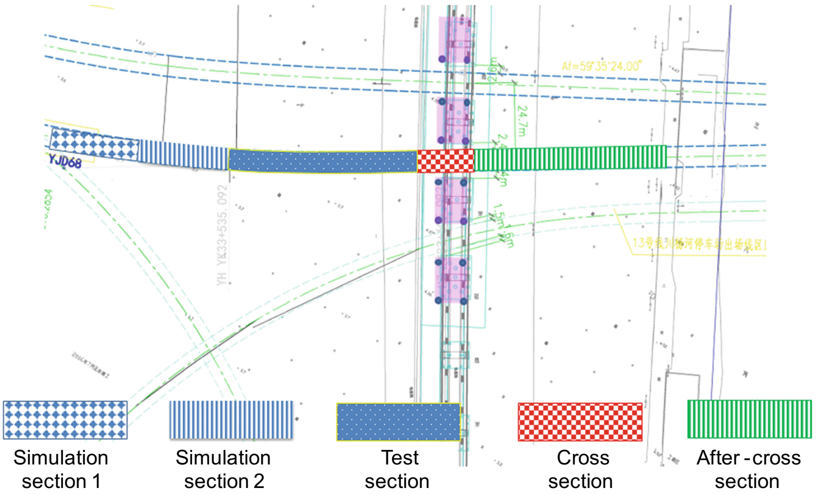

Fig. 4. The test section settings of the field full-scale test.

It can be seen from Fig. 4 that the full field test section consists of the simulation Sect. 1, the simulation Sect. 2 and the test section. The continuous advance conditions and the window period conditions are simulated in the simulation section. In this case, the length of the continuous advance condition in simulation Sect. 1 is 24 m (20 rings), 3–5 rings per day, about 4–5 days; the window period for the simulation Sect. 2 is also for 24 meters (20 rings), the window period is set at 11:00 pm–5:00 am next day (according to the first time of the first time), the daily promotion is 2 rings, about 12 days. Simulation Sects. 1 and 2 are set before the test section.

The field full-scale test mainly analyzes the relationship between the earth pressure, drive speed, amount of unearthed volume, grouting volume, grouting pressure and the ground subsidence, and grasps the variation law of the soil in this section when tunneling underground to control the settlement of soil. Finally, the suitable construction parameters can be obtained and appropriate measures can be taken to ensure the safety of magnetic levitation.

The control target for the shield tunneling in the field full-scale test is the formation loss rate less than 1‰ according to the numerical simulation. The earth pressure setting is determined in three stages, as shown in Table 3.

Table 3. The three-stage earth pressure determination process.

Stage	Ring number	Depth (m)	Lateral coefficient	Earth pressure (MPa)
Test stage	0	20.9	0.75	0.283
	10	21.0	K1	/
	15	21.0	K2	/
Verify stage	20	21.1	K3	/
	30	21.1	K4	/
Confirm stage	40	21.2	K5	/
	50	21.2	K6	/

It can be seen from Table 3 that, in the test stage (ring 0 to ring 15), the earth pressure is adjusted according to the soil settlement and the initial determination of K0 value is reversed; in the verify stage (ring 16–ring 30), to ensure that the soil settlement control in the range from 0 to +0.5 mm, the value of K0 is fine adjusted; in the confirm stage (ring 31 to ring 49), the value of K0 is determined, which can be used as earth pressure setting value during the formal through section.

Similarly, the drive speed, synchronous grouting parameters and the amount of unearthed volume control can be determined through the multi-stage confirmation.

According to the test section, there are:

(1) The lateral coefficient in this section is K0 = 0.7;
(2) The drive speed ranges from 10 to 20 mm/min;
(3) The filling rate of the synchronous grouting is 150% which can ensure the soil settlement in the range of 0 to +0.5 mm;
(4) The reasonable amount of the shield unearthed volume is 98% to 100% of the excavation section.

5 Construction Control and Result Analysis of the Through Section

According to the test results, the actual construction parameters of the crossing process are set to:

1. (1) The earth pressure setting P = K0 × h = 0.70 × 18 × 23.5/1000 = 0.296 MPa;
2. (2) The amount of the unearthed is 98% to 100% of the excavation section;
3. (3) The drive speed is 10 mm/min;
4. (4) The filling rate of the synchronous grouting is 150%.

The up line passed through the maglev foundation between pile PO183 and pile PO184. The pier column displacement and the surface settlement caused by the tunneling is analyzed as shown in Figs. 5 and 6.

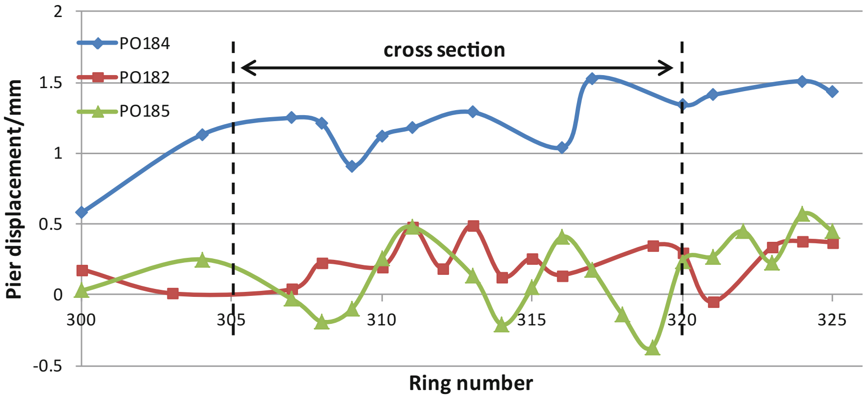

Fig. 5. Displacement monitoring results of adjacent pier columns during shield crossing.

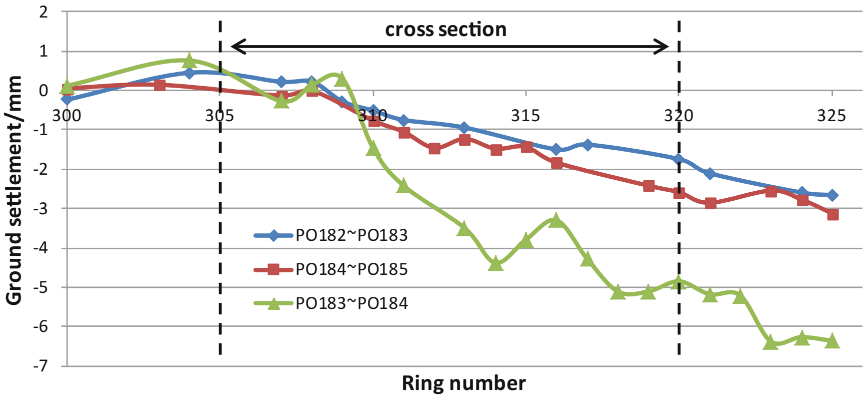

Fig. 6. Settlement monitoring results in the shield cross section

Figure 5 shows the results of the adjacent pier displacement when tunneling through the maglev projection line. As one can see from Fig. 5, the overall displacement of PO184 is larger than that of PO182 and PO185, and the lift is higher. In addition, during the construction we found that the shield machine from the magnetic levitation projection line 10 m (the ring number is 300) has a great impact on the maglev pier column PO184: maglev pier began to lift gradually under the influence of construction. The main reason is due to the maglev pile foundations are pressure design, which are weak in pull capacity. As a result, when higher thrust or earth pressure is set, the upward force will pillar pillars, and ultimately lead to the move up of the platform.

In order to ensure the safety of magnetic levitation operation, according to the monitoring results, the earth pressure setting is readjusted. A slight undervoltage pressure is used, the undervoltage range from 0.01 MPa to 0.02 MPa. It can be seen from Fig. 5 that the adjusted displacement of the maglev pile tends to be smooth and the final deformation satisfies the maglev deformation requirements.

Figure 6 shows the results of the monitoring of the surface subsidence. In Fig. 6, on can see that before the shield to reach the projection line, the measuring point directly above the excavation face appears a slightly rise because of the higher thrust and the earth pressure. When the undervoltage strategy is used, the value of surface uplift decreases.

According to the numerical analysis and field test results, the loss rate of excavation strata should not be too large. Therefore, it is necessary to provide a precise synchronous grouting filling rate to supplement the formation loss caused by the excavation and to reduce the surface deformation. Considering the undervoltage strategy, the synchronous filling rate is raised to 150%–180%. It can be seen from Fig. 6 that the adjusted filling rate can timely control the development of the surface subsidence and the final surface deformation can meet the requirements.

6 Summary

This paper studies the influence of the shield tunneling construction on the nearby maglev pile foundations, which is carried out by means of the non-reinforcement protection measures. The main conclusions are as follows:

(1) According to the numerical simulation, the formation loss rate which is less than 0.1% can meet the requirements of magnetic deformation.
(2) The pressure setting of the shield tunnel is the key parameter to control the formation loss rate and the reduce the settlement of the ground. This paper proposed a multi-stage method during the test section to determine the pressure setting parameters.
(3) When passing through the pile foundation, the soil pressure and thrust is too large likely to cause the pile body cracking and pier column lift, it is recommended to use micro undervoltage method for excavation construction, undervoltage range of 0.01–0.02 MPa.

(4) The synchronous grouting rate is another key parameter to ensure the formation loss rate caused by the tunneling construction. In the case of under-passing construction, the control range of the synchronous grouting rate should be 150%–180%. The main purpose is to fill the formation loss caused by the undervoltage excavation and ensure that the surface subsidence is within the allowable range.

References

1. Niu, Q., et al.: Shield Tunneling Method of Investigation. Design. Construction. China Construction Industry Press, Beijing (2011). (in Chinese)
2. Liu, J., Hou, X.: The Shield Tunneling Method. China Railway Press, Beijing (1991). (in Chinese)
3. Sun, Y., Zhou, S., Xiang, K., et al.: Study on the construction parameters of shield tunneling in short-distance undercrossing the existing tunnel. China Railway Sci. **31**(1), 54–58 (2010). (in Chinese)
4. Xu, K., Ji, C., Zhou, S.: Soil conditioning field test before heading face of EPB shield in sandy soil. China Civ. Eng. J. **9**, 147–155 (2012). (in Chinese)
5. Ji, C., Zhou, S., Xu, K., et al.: Field test research on influence factor of upward moving of shield tunnel shield tunnel segments during construction. Chin. J. Rock Mech. Eng. **32**(z2), 3619–3626 (2013). (in Chinese)
6. Wu, D., Zhou, S., Wen, X.: Laboratory test and application of filter cake formation in sand during slurry shield construction. Chin. J. Rock Mech. Eng. **S1**, 3460–3467 (2015). (in Chinese)
7. Dai, R.: Calculation Method of Ground Settlement During Construction Based on Overbreak Mode of Shield Tunnelling. Tongji University (2011). (in Chinese)
8. Wang, H.: Calculation of Device Parameters and Balance Control of EPB Shield in Soft Soil Strata. Tongji University (2009). (in Chinese)
9. Huang, L., Zhou, S., Gong, Q.: Analysis on foundation treatment in soft soil crossed underground by shield tunneling. Uban Mass Transit **16**(02), 56–61 (2013). (in Chinese)
10. Song, J., Miao, L., Dai, S., Ma, Y.: 3D coupled mechanical and hydraulic analysis of pore water pressure disturbed by shield tunneling. Chin. J. Geotech. Eng. **35**(02), 302–312 (2013). (in Chinese)
11. Yan, B., Yang, G., Lin, H., Lin, P., Wu, W.: Reasearch on shield tunneling parameters optimization and surface subsidence control. Chin. J. Undergr. Space Eng. **7**(S2), 1683–1687 (2011). (in Chinese)
12. Anagnostou, G., Kovári, K.: The face stability of slurry-shield-driven tunnels. Tunn. Undergr. Space Technol. **9**(2), 165–174 (1994)
13. Li, Y., Emeriault, F., Kastner, R., et al.: Stability analysis of large slurry shield-driven tunnel in soft clay. Tunn. Undergr. Space Technol. **24**(4), 472–481 (2009)

Planning, Sustainability, Maintenance and Emergency Counter-Measures

Layout Patterns of Underground Space Comprehensive Utilization Around Metro Station for Urban Commercial Area

Jian Peng[1,2,3](✉) and Fang-Le Peng[1,2]

[1] Department of Geotechnical Engineering, Tongji University,
Shanghai, People's Republic of China
`pj53129544@163.com`
[2] Research Center for Underground Space, Tongji University,
Shanghai, People's Republic of China
[3] Sustainable Energy and Environmental Engineering,
Graduate School of Engineering, Osaka University, Osaka, Japan

Abstract. In order to satisfy contemporary urban development requirements, it is essential to utilize urban underground space (UUS) effectively when planning new metropolitan subway (metro) stations, especially in commercial areas. Herein, two cases involving metro stations in commercial areas, the Xujiahui zone in Shanghai, China and the Namba zone in Osaka, Japan, are investigated with respect to land use and UUS utilization, after which their underground space distribution situations are summarized in terms of function and layout, and the differences between the two cases are discussed. Two kinds of comprehensive UUS utilization layout patterns are elucidated, i.e., station center layout and commercial street center layout. The station center layout emphasizes the smooth transfer of people between transportation modes, while the commercial street center layout emphasizes not only transportation transfer, but also more intensive commercial exploitation of space under municipal roads and higher floor area ratios. Here, it should be noted that the former can transform to the latter as the city develops. Our study also shows that the development of UUS around metro stations in urban commercial areas is based on urban "function and layout" interaction characteristics, but the layout pattern may also be different depending on different national context.

Keywords: Layout pattern · Urban underground space · Commercial area
Function · Interaction characteristics

1 Introduction

In recent years, serious traffic jams have become a significant issue in a number of large Chinese cities due to their rapidly increasing population levels. Rail transit offers many advantages in terms of urban traffic jam mitigation, and has been widely used. Correspondingly, urban underground space (UUS) developed in tandem with urban metro stations can be utilized to create commercial opportunities and transport space in ways that promote economic and social developments around the station. Thus, in order to

© Springer Nature Singapore Pte Ltd. 2018
D. Zhang and X. Huang (Eds.): GSIC 2018, *Proceedings of GeoShanghai 2018 International Conference: Tunnelling and Underground Construction*, pp. 587–596, 2018.
https://doi.org/10.1007/978-981-13-0017-2_59

maximize benefits from rail transit network improvements, it is essential to approach metro station area planning from the standpoint of effective UUS utilization – and function and layout are key factors when planning UUS.

Such planning has been explored in a number of studies. For example, Boivin (1991) described the Montreal underground pedestrian network, which at that time linked 44 buildings and nine subway stations. Polzin (1999) analyzed the relationship between metro and land use in ways that challenged some conventional perceptions. Additionally, Hui (2002) studied the planning and construction of urban rail transit stations and classified them into four types. In addition, Be'langer (2007) discussed the underground network development patterns and their futures as important urban infrastructures while focusing on the origins and transformations of Toronto's underground pedestrian network in order to illustrate its multi-dimensionality. Furthermore, Li et al. (2016) studied the demand and driving factors of three metro station areas with respect to underground space. However, since none of the previous studies established a concrete relationship between the function and layout of UUS around metro stations, this paper will examine those issues and discuss classic UUS layout patterns around metro stations, with a particular focus on urban commercial areas.

2 Methodology

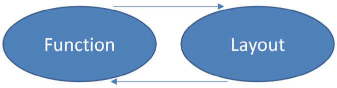

Fig. 1. Function and layout interaction

City developments along metro lines tend to be directed by metro construction. In this process, the establishment of metro stations tips the balance of the original spatial structure and promotes regional accessibility. More specifically, the closer an establishment is to a metro station, the higher its accessibility and land value are, and vice versa (Bajic 1983; Du and Mulley 2007). Here, the environs of metro stations in commercial areas are defined. Choi and Asami (2002) defined close proximity to a station as within a distance of 200 m in a commercially dense area, and the first 500 m distance as a buffer zone, while Roukouni et al. (2012) presented a buffer zone with a radius of 500 m around metro stations. Thus, the scope of this study is defined as the area within 500 m of a commercial metro station area, within which commercial activities account for the biggest percentage of land use. Proper land use designations help fuse a supra-space city within a UUS city into one cohesive urban organism (Golany and Ojima 1996). However, UUS functions will vary depending on the land use. The concept of a proper UUS layout addresses how different functions should be considered, and what their plain and vertical form should be. To accomplish this, UUS function and layout must maintain relationships based on mutual coordination and mutual promotion. On one hand, function changes almost always cause layout changes; but on the other hand, layout changes need new functions to fit those changes. A conceptual image of this interaction is shown as Fig. 1. Based on site investigations and data provided by local institutes, this paper will compare two cases of comprehensive UUS utilization in commercial metro station areas in terms of function and layout, and will then illustrate their relationships in order to clarify their interaction characteristics.

3 Data Collection

3.1 Xujiahui Zone, Shanghai Study Area

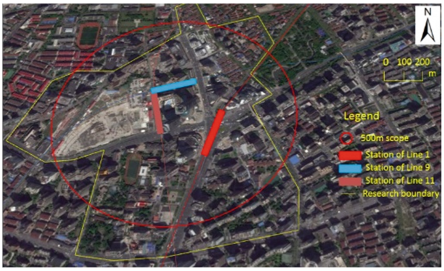

Fig. 2. Study area – Xujiahui

The Xujiahui zone, which is one of the city's commercial centers, is located in southwest part of Shanghai, China. It is also an area where substantial crowds aggregate and disperse, especially on weekends and holidays. Three metro lines cross the zone and three separate metro stations are situated there. The study area is defined as a radius of 500 m around each of the barycenter locations centered on the three stations. For the purposes of this research, due to the fact that the study area is surrounded by roads, only those blocks that are more than one half included in the buffer zone are considered (Fig. 2). Combining with site investigation and the datum from Shanghai Urban Planning and Design Research Institute, it is found that there are several land use function categories present in the zone, the specifics of which are presented in Fig. 4 and Table 1. Commerce and residential uses are dominant functions. The total area is approximately 80 ha. As shown in Fig. 4 and Table 2, the primary UUS function in the study area is parking, which accounts for more than 60% of the underground land use. Other underground commercial uses include shopping centers, retail outlets, clothing stores, entertainment centers, and catering establishments, while pedestrian passages provide access among the different facilities. Most commercial uses aggregate in the B1F of the buildings surrounding the Line 1 station, which was completed in the 1990s. Pedestrian passageways connecting different land parcels are almost always located under municipal roads. The total area utilized is approximately 445,000 m^2 from the B1F to B3F levels. As for layout, the underground space relatively close to the stations consists of an irregular assortment of basements and pedestrian passages, including an underground street on the B2F level. The transfer access passageways between the different stations on the B1F level are isolated from most of those basements, and underground space in areas relatively far from the stations do not appear to be connected to those stations.

3.2 Namba Zone, Osaka Study Area

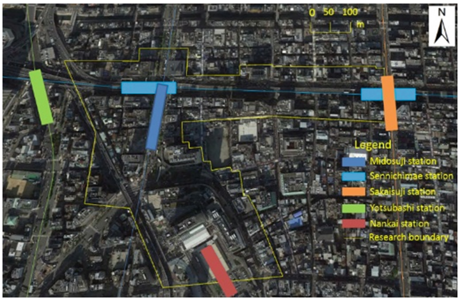

Fig. 3. Study area – Namba

As one of the city's major commercial centers, the Namba zone is located in the downtown area of Osaka, Japan, in an area serviced by multiple metro lines. From the Xujiahui zone case study, it was found that UUS is mainly located in the blocks adjacent to roads, so the scope of the Osaka study area was narrowed and the Midosuji Line was chosen as the

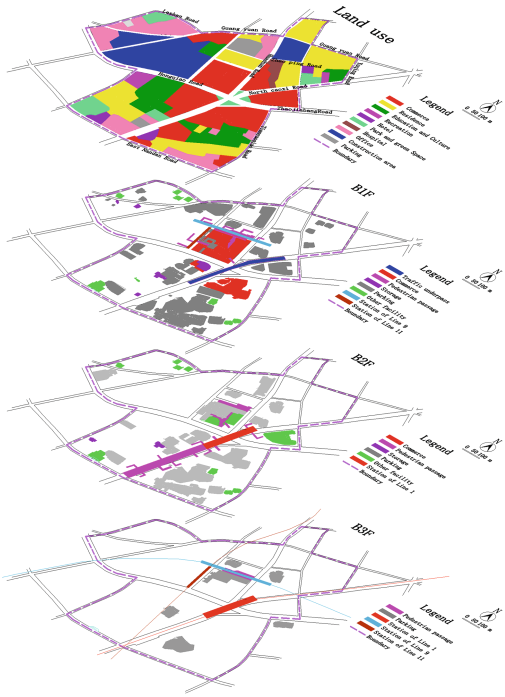
Land use
Leshan Road
Guang yuan Road
Guang yuan Road
Huashan Road
Zhao ping Road
Yuqing Road
Hongqiao Road
North caoxi Road
ZhaojiabangRoad
Tianyaoqiao Road
East Nandan Road
Legend
Commerce
Residence
Education and Culture
Recreation
Hotel
Park and green Space
Hospital
Office
Construction area
Parking
Boundary
N
0 50 100 m
B1F
Legend
Traffic underpass
Commerce
Pedestrian passage
Storage
Parking
Other facility
Station of Line 9
Station of Line 11
Boundary
B2F
Legend
Commerce
Pedestrian passage
Storage
Parking
Other facility
Station of Line 1
Boundary
B3F
Legend
Pedestrian passage
Parking
Station of Line 1
Station of Line 9
Station of Line 11
Boundary

Fig. 4. Land use and UUS distribution of Xujiahui zone

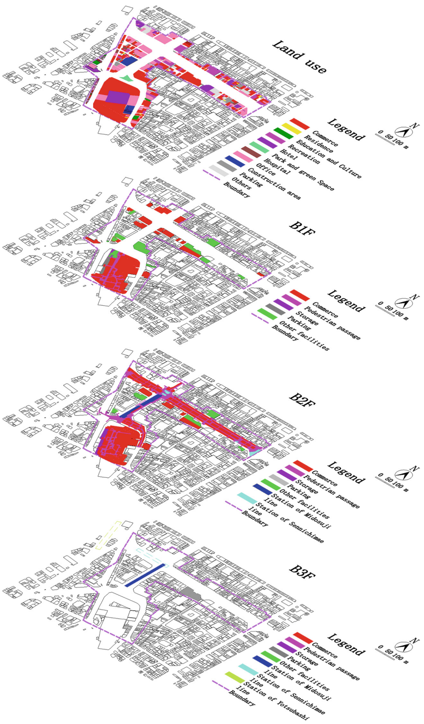
Land use
Legend
Commerce
Residence
Education and Culture
Recreation
Hotel
Park and green Space
Hospital
Office
Construction area
Parking
Others
Boundary
N
0 50 100 m
B1F
Legend
Commerce
Pedestrian passage
Storage
Parking
Other facilities
Boundary
B2F
Legend
Commerce
Pedestrian passage
Storage
Parking
Other facilities
Station of Midosuji line
Station of Sennichimae line
Boundary
B3F
Legend
Commerce
Pedestrian passage
Storage
Parking
Other facilities
Station of Midosuji line
Station of Sennichimae line
Station of Yotsubashi line
Boundary

Fig. 5. Land use and UUS distribution of Namba zone

center, as shown in Fig. 3. In this study area, the specific land use categories are presented in Fig. 5 and Table 1 (Osaka City Planning Bureau 2017). It is obvious that the dominant land use is commerce. The total area is approximately 20.5 ha. Based on our site investigation, it is found that the primary UUS function of the study area is commerce, which accounts for 56.6% of the land use. Underground commercial uses also include shopping centers, retail outlets, clothing stores, restaurants, entertainment centers, and catering, and an extensive pedestrian passage system connects almost all of the underground areas. Most commercial area use is found below the municipal roads and in the B1F and B2F levels of the buildings surrounding the stations. Pedestrian passageways connecting the different land parcels almost always follow below the municipal roads. The total area utilized from the B1F to B3F levels is approximately 146,000 m^2 (Table 2). As for layout, the underground space consists of major four parts: Namba Walk, Namba Ekimo, Namba NanNan, and Namba City (Fig. 6), which together connect practically all the building basements and metro stations.

Table 1. Land use function categories in Xujiahui zone and Namba zone

Zone		C	R	E	Rn	H	G	Hl	O	Cn	P	Os	Rd	Sum
Xujiahui	Area (ha)	17.2	14.2	8.0	0.2	2.1	3.6	0.9	8.6	11.2	1.3	0.0	15.0	80.3
	Ratio (%)	21.4	17.7	10.0	0.2	2.6	4.5	1.1	10.7	13.9	1.6	0.0	18.7	100.0
Namba	Area (ha)	4.8	0.1	0.1	0.9	1.1	0.1	0.1	2.2	0.4	0.3	0.4	10.0	20.5
	Ratio (%)	23.4	0.5	0.5	4.4	5.4	0.5	0.5	10.7	2.0	1.5	2.0	48.8	100.0

Note: C-Commerce, R-Residence, E-Education and culture, Rn-Recreation, H-Hotel, G-Green space, Hl-Hospital, O-Office, Cn-Construction area, P-Parking, Os-Others, Rd-Road.

Table 2. UUS function categories in Xujiahui zone and Namba zone

Zone		F	S	Tu	Pp	C	P	Se	Os	Sum
Xujiahui	Area (m^2)	B1F	8195	10025	8814	46672	130188	2892	10567	217353
		B2F	9753	0	25600	0	112996	0	26724	175073
		B3F	17400	0	1946	0	33374	0	0	52720
		Sum	35348	10025	36360	46672	276558	2892	37291	445146
	Ratio (%)		7.9	2.3	8.2	10.5	62.1	0.6	8.4	100.0
Namba	Area (m^2)	B1F	0	0	5292	34771	1440	424	10515	52442
		B2F	4765	0	25000	47940	0	1934	5318	84957
		B3F	5270	0	0	0	3570	0	0	8840
		Sum	10035	0	30292	82711	5010	2358	15833	146239
	Ratio (%)		6.9	0.0	20.7	56.6	3.4	1.6	10.8	100.0

Note: F-Floor, S-Station, Tu-Traffic underpass, Pp-Pedestrian passage, C-Commerce, P-Parking, Se-Storage, Os-Others.

4 Discussion

From the land use situation, it was found that commercial use occupies the main function in both study areas because the two zones are commercial centers servicing their entire cities. Commercial use is almost always found adjacent to the stations or roads, while other land uses do not seem to have any distinctive distribution characteristic with regard to distance to the station. For the Xujiahui zone, residential use and construction areas come in second and third, respectively. While for the Namba zone, office areas come in second, and there is little in the way of residential areas. The authors infer that this difference may be correlated to early stage urban renewal and residential district planning.

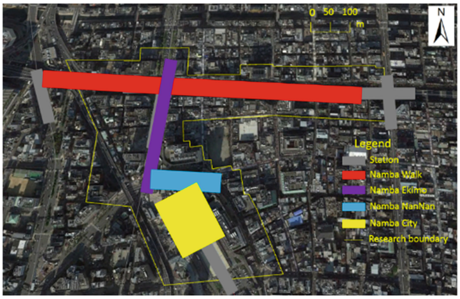

Fig. 6. Layout of Namba zone

As for UUS utilization in the Xujiahui zone, it is found that underground parking occupies an overwhelming ratio of more than 60% of the land use, with the remainder widely distributed over almost all other usage types. Furthermore, it is found that, on the whole, this parking use was concentrated primarily in the B1F and B2F levels of the high-rise buildings completed after the year 2000. This can be explained by the fact that there were not so many cars in the years prior to that period, and that the impending scarcity of land resources had not yet attracted government attention. However, the situation in the Namba zone is quite different. There, underground parking is rare, accounting for just 3.4% of the study area. The authors infer that it is possible that the Japanese government's efforts to encourage public transportation use is more effective, and that the use of above-ground mechanical parking lots is more popular based on our investigation.

For both study zones, in addition to the underground commercial streets (called underground shopping malls in Japan, "*underground facility integrated with underground footpaths provided for public purposes and shops, offices and other similar facilities built on such footpaths that are linked to roads or station square areas provided for public purpose*", Kishii 2016), a large percentage of the underground commerce is located in the basements of buildings located within a 200-m distance from the metro stations. In the case of the Xujihui zone, almost all such commerce is located on the B1F level; while for Namba, it can be found on both the B1F and B2F levels. Here, the authors infer that it is influenced by the passenger flow rate as well as commercial land prices. In other words, it is plain that the UUS function distribution is strongly connected with metro stations located within a 200-m radius. Meanwhile, the vertical function of UUS distribution depends on different environmental and economic situations. As for layout, it was found that commercial underground space under the municipal roads in the Xujiahui zone is not exploited substantially, even though one pedestrian passage (or underground street), the Shanghai Metro Culture and Art Walkway, is located under the North Caoxi Road in the south of the Line 1 station (Fig. 4, B2F). However, there are almost no commercial uses along this passage. The access ways among the stations are located beneath the land parcel making up the study area, but are isolated from the building basements (Fig. 4, B1F), which means that passengers never go through those basements when they transfer from one station to another. As a result, the people flow tends to aggregate around the stations and transfer access areas, but not in the commercial areas. This utilization pattern can be called the station center layout pattern. In this layout pattern, commercial activities are almost always located in basements, and pedestrian passage between stations takes place below roads, separately from basements in the land parcel.

This pattern is significantly different from that seen in Japan. Although the Namba stations are transfer points for multiple subway lines, as shown in Fig. 3, it is found that commercial underground space is exploited substantially under the roads, with a variety of underground commercial streets present under main roads, and numerous commercial ventures alongside the underground streets. Transfer access ways among these multiple stations, i.e., underground streets, are also located beneath the roads. Passengers almost get off from one station, arrive at underground streets, and then either transfer to another line or go shopping in the commercial basement of the buildings. As a result, the people flow tends to aggregate in the commercial streets. This utilization form can be called the commercial street center layout pattern. For this layout pattern, large amounts of commercial activities are located in the commercial streets where pedestrian passage is amalgamated. Passengers can also transfer from one station to another through the commercial streets that are connected to the building basements in the area. For this pattern, UUS zoning (Fig. 6) is necessary for efficient wayfinding. Meanwhile, the flowrate of people along another access way, named the Chicago Gallery and located in the west side of Namba Walk, is much higher than that of Xujiahui. From this observation, the authors infer that the location of underground streets should be planned between two stations, not at one side of any station, so as to avoid decreased flowrates. Furthermore, the underground street exits should be amalgamated with the building basements in order to prevent flowrates from decreasing, especially when they are farther than 200 m from the metro stations. The importance of mobility and access in a contemporary metropolis brings to infrastructure the character of collective space. Based on these rough classifications, with respect to layout, UUS patterns around metro stations in urban commercial area can be divided into station center and commercial street center layouts. Their conceptual images are shown in Fig. 7.

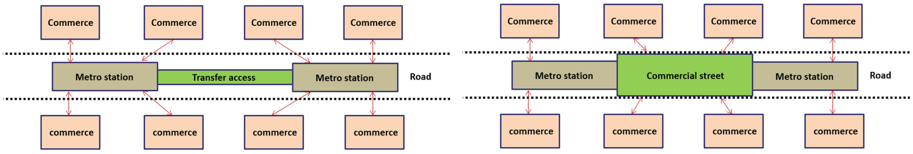

(1) Station center layout (2) Commercial street center layout

Fig. 7. Layout patterns of UUS around metro station in urban commercial area

Based on our site investigations, it is found that most of the UUS utilization around metro stations in the Shanghai commercial area, such as Zhongshan Park and People's Square Stations, follow the station center layout. In contrast, UUS around most of the metro stations in the commercial areas of Osaka, such as Shinsaibashi and Umeda Stations, follow the commercial street center layout. The authors infer that this is the result of differences in national context. The Shanghai underground pedestrian system development is largely based on metro stations and the connection layouts are determined by the principle of ensuring the quick movement of pedestrians to street level (Cui et al. 2012). However, while the Japanese government paid more attention to high intensive utilization of UUS several decades ago due to land scarcity, it is definitely the case that distances between adjacent metro stations in Osaka are shorter than those in Shanghai. Thus, there is more potential to exploit underground streets along municipal roads in order to connect adjacent stations in Japan. The authors contend that this consideration is extremely important when planning the location of an underground street in order to maximize benefits from rail transit networks, and is also why underground streets are developed only in relatively high-density commercial areas. For the Namba zone, the floor area ratio is 10.0 (Osaka City Planning Bureau 2017), although it is just 3–4 for Xujiahui zone (Mo et al. 2009). However, a station center layout can transform into a commercial street center layout over time. For example, Namba Station would have been considered to have a station center layout before 1970, when the Namba Walk and Sennichimae Line were still under construction. At that time, passengers transferred from the Midosuji to Yotsubashi Lines just through normal access ways, but underground streets connected all the underground facilities after they were completed. Thus, the layout pattern changed as the zone developed, which included the effects of traffic congestion due to population expansion. UUS function, e.g., commerce, cannot meet the needs of urban development on its own, so functions need to be improved, and such function changes almost always causes layout changes, thereby strengthening the presence of underground networks as dynamic public systems. Meanwhile, layout changes need new functions that take advantage of their features. This reflects the point that UUS function and layout should maintain a relationship of mutual coordination and promotion. Ultimately, upon adopting a commercial street center layout, the Namba Station area became a complex underground system with highly intensive space utilization.

5 Conclusion

The conclusions based on the research of UUS development around metro stations in urban commercial metro areas can be summarized as follows:

(1) Most of the observed UUS is located within 200 m of the metro station, especially in the blocks adjacent to roads, and in the underground street below those roads. In the case of Shanghai's Xujiahui zone, almost all commercial activity is located on the B1F level, and a substantial amount of underground parking scattered around the area. In the case of the Osaka's Namba zone, commercial use is located both on the B1F and B2F levels, and there is little underground parking. Thus, function and layout in the vicinity of the stations may vary according to national context, including city development history, construction regulation, property law, political issues, etc.

(2) Underground streets should be planned between two stations and the exits should be connected to the basements of surrounding buildings, in order to maximize commercial benefits. Meanwhile, commercial space should be mainly planned in B1F, and whether it can be planned in B2F, even B3F, should depend on the depth of underground street and other factors, such as passenger flow rate, etc.

(3) Two kinds of UUS comprehensive utilization layout patterns around metro station in commercial areas were elucidated: station center layout and commercial street center layout. Station center layout emphasizes smooth passenger transfers between transportation modes, while commercial street center layout emphasizes not only passenger transfer, but also higher intensive exploitation of commercial activities that are made possible by utilizing the available space under the municipal roads with higher floor area ratios. While the former can transform into the latter as the city develops, the layout pattern transformation process requires a greater level of integration between the metro station and surrounding streets. So we argue that exploitative space surrounding metro station should be reserved

from a long view when it is in station center layout stage. This may also sound an alarm to the planners that utilizing underground space randomly runs counter to sustainable development.

(4) The development of UUS in a commercial metro station area is based on urban "function and layout" interaction characteristics. UUS function and layout are predicated on maintaining a relationship of mutual coordination and mutual promotion.

However, the patterns elucidated in this paper were developed based on ideal situations. In reality, commercial metro station areas may be a combination of both patterns, or something in between. Herein, a representative concept was introduced, which is critical to promoting further development, even though the classic UUS patterns discussed may not be applied directly. Meanwhile, our future work will focus on additional site investigations.

Acknowledgements. The authors gratefully acknowledge support provided by funds from the National Key Technology R&D Program grant 2012BAJ01B04, the National Basic Research Program (973 Program) grant 2015CB057806 and the China Scholarship Council grant 201606260162.

References

Bajic, V.: The effects of a new subway line on house prices in Metropolitan Toronto. Urban Stud. **20**, 147–158 (1983)

Be'langer, P.: Underground landscape: the urbanism and infrastructure of Toronto's downtown pedestrian network. Tunn. Undergr. Space Technol. **22**, 272–292 (2007)

Boivin, D.: Montreal's underground network: a study of the downtown pedestrian system. Tunn. Undergr. Space Technol. **6**(1), 83–91 (1991)

Choi, J., Asami, Y.: Analysis of distribution and attributes of redevelopment projects by the distance from railway stations. Jpn. J. Real Estate Sci. **16**, 91–101 (2002). (In Japanese)

Cui, J., Allan, A., Taylor, M.A., Lin, D.: Developing Shanghai underground pedestrian system under urbanization: mobility, functionality and equity. J. Archit. Urban. **36**(4), 283–297 (2012)

Du, H., Mulley, C.: The short-term land value impacts of urban rail transit: quantitative evidence from Sunderland, UK. Land Use Policy **24**, 223–233 (2007)

Golany, G., Ojima, T.: Geo-space Urban Design. Wiley, New York (1996)

Hui, Y.: Research for urban rail transit station area planning and construction. Urban Plan. Forum **138**(2), 30–33 (2002). (In Chinese)

Kishii, T.: Utilization of underground space in Japan. Tunn. Undergr. Space Technol. **55**, 320–323 (2016)

Li, X., Xu, H., Li, C., Sun, L., Wang, R.: Study on the demand and driving factors of urban underground space. Tunn. Undergr. Space Technol. **55**, 52–58 (2016)

Mo, Y., Deng, J., Wang, J.: A land use model for urban rail station area planning based on TOD strategy. Archit. Environ. Eng. **31**(2), 116–120 (2009). (In Chinese)

Osaka City Planning Bureau (2017). https://www.mapnavi.city.osaka.lg.jp/webgis/

Polzin, S.: Transportation/land-use relationship: public transit's impact on land use. J. Urban Plan. Dev. **125**(4), 135–151 (1999)

Roukouni, A., Basbas, S., Kokkalis, A.: Impacts of a metro station to the land use and transport system: the Thessaloniki Metro case. Soc. Behav. Sci. **48**, 1155–1163 (2012)

Influence of Aspect Ratio of the Exhaust Opening on Smoke Propagation in a Large Cross-section Tunnel

Zhiguo Yan[1,2,3], Yuxin Zhang[1,2,3](✉), and Hehua Zhu[1,2,3]

[1] State Key Laboratory for Disaster Reduction in Civil Engineering,
Tongji University, 1239 Siping Road, Shanghai 200092, China
13162559391@163.com
[2] Department of Geotechnical Engineering, Tongji University,
1239 Siping Road, Shanghai 200092, China
[3] Key Laboratory of Geotechnical and Underground Engineering of the Ministry
of Education, Tongji University, 1239 Siping Road, Shanghai 200092, China

Abstract. The point extraction system (PES) is effective and popular especially for long and large cross-section tunnels. To clearly comprehend the fire characteristics on the cross-section and correctly apply the smoke strategy, we conduct a series of numerical Computation Fluid Dynamics (CFD) simulations according to the dimensions of the South Hongmei Rd. tunnel, located in Shanghai, China. We set the tunnel in three fire scenarios i.e. 5 MW, 20 MW, and 50 MW and use three index, namely temperature, minimum visibility and carbon monoxide (CO) concentration to evaluate the effect of the PES according to the standard safety criteria on three sections with different distance from the fire source. By testing the PES, we change dimensions of smoke exhaust openings. The results show that with the same area, the slender exhaust perpendicular to the length of the tunnel can control the smoke better than the short one, especially far away from the fire source.

Keywords: Smoke control · Large cross-section tunnel
Point smoke extraction · Exhaust opening

1 Introduction

With the increase in traffic volume, the chance of tunnel traffic accidents and associated fires has increased. Fires in tunnels have caused great risk to human life and damage to property and the economy. Fires usually result in the significant accumulation of hot smoke in the tunnel because of the confined space and insufficient exits. Tunnel disasters, such as the accidents in the Mont Blanc Tunnel in 1999 and in the San Gottardo Tunnel in 2001, have demonstrated the shortage of emergency evacuation and rescue in tunnels (Vega et al. 2008) using normal ventilation system. In PES, fresh air is induced by jet fans located under the exhaust duct. If a fire occurs, a number of exhaust openings near the fire source will open to keep the smoke at the top of the tunnel cross-section; smoke would then be extracted through the duct to the outside of the tunnel.

© Springer Nature Singapore Pte Ltd. 2018
D. Zhang and X. Huang (Eds.): GSIC 2018, *Proceedings of GeoShanghai 2018 International Conference: Tunnelling and Underground Construction*, pp. 597–604, 2018.
https://doi.org/10.1007/978-981-13-0017-2_60

Many previous studies on tunnel fire ventilation have been conducted with the help of CFD technology (Woodburn and Britter 1996a, 1996b; Lin and Chuah 2008; Hu et al. 2006). Lin and Chuah (2008) investigated the performance of different smoke extraction strategies for a long vehicle tunnel under a 100 MW fire load and found that the single-point extraction opening system was more effective than the multi-point extraction opening system for partial transverse ventilation systems. Hu et al. (2006) studied the smoke temperature above the fire source under the ceiling for tunnel fires using both full-scale burning tests and CFD simulations and achieved fairly good agreement. Vu-Bac et al. (2016) analyzed probabilistic sensitivity analysis for computationally expensive models, which provided offer utilities for quantifying the influence of uncertain input parameters on uncertain model outputs. Zhu et al. (2016) conducted the numerical study on the feasibility and efficiency of point smoke However, little investigation has been documented on transverse fire characteristics on the cross-section and the evaluation of evacuation environments in a shield TBM (Tunnel Boring Machine) tunnel using point smoke extraction, especially for a large cross-section tunnel.

In this paper, we present comprehensive numerical simulation results of fire characteristics on the cross section and the evaluation of the evacuation environment of a large cross-section shield TBM tunnel in case of fire accidents.

2 CFD Numerical Modeling

2.1 CFD Model

CFD as a predictive tool for fire safety engineering has become widespread. It is designed for engineers from different disciplines in pursuing optimum designs due to the high cost, complexity, and limited information obtained from experimental methods (Li and Chow 2003). SMARTFIRE aims to assist the CFD novice using its automated meshing system component. The key benefit of Smartfire is the automated mesh generation system that adjusts to the requirements of fire analysis with embedded expertise specific to the type of geometry being modeled.

2.2 Configuration of Large Cross-section Shield TBM Tunnel

This study has reached out some conclusions and those have been applied in South Hongmei Road Tunnel (SHM Tunnel, for short) operating early in 2016, in Shanghai, China (refer to Fig. 1). This tunnel is a 3390-m-long large cross-section shield TBM tunnel consisting of two one-way traffic tubes with external and internal diameters of 14.5 m and 13.3 m, respectively. The PES uses an exhaust duct with discrete openings in the ceiling every 50 m along its length (Fig. 2).

Fig. 1. Photos of the construction site of the SHM Tunnel in Shanghai.

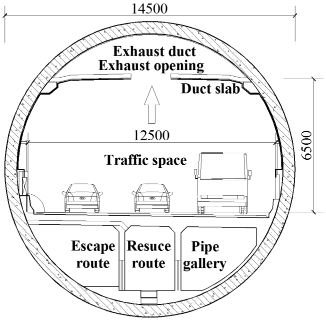
14500
Exhaust duct
Exhaust opening
Duct slab
12500
Traffic space
6500
Escape route
Resuce route
Pipe gallery

Fig. 2. Cross section of the SHM Tunnel (unit: mm).

2.3 Fire Scenarios

Three different fire sizes are carried out to simulate small (i.e., 5 MW), medium (i.e., 20 MW) and large scale fires (i.e., 50 MW) according to the Permanent International Association of Road Congress (PIARC) (PIARC, 1999) (Figs. 3 and 4).

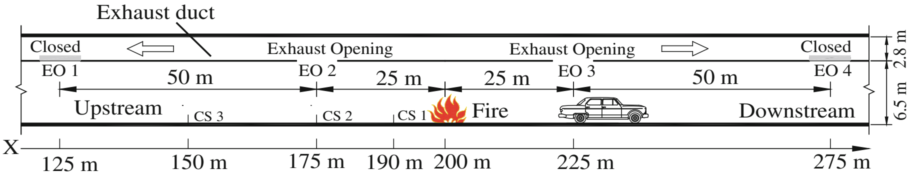
Exhaust duct
Closed
Exhaust Opening
Exhaust Opening
Closed
EO 1
EO 2
EO 3
EO 4
50 m
25 m
25 m
50 m
2.8 m
6.5 m
Upstream
CS 3
CS 2
CS 1
Fire
Downstream
X
125 m
150 m
175 m
190 m
200 m
225 m
275 m

Fig. 3. Side view of fire location in longitudinal direction.

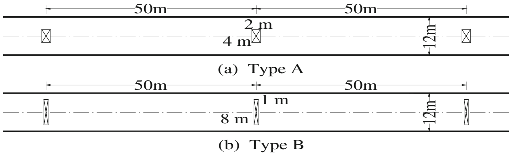
50m
50m
2 m
4 m
12m
(a) Type A
50m
50m
1 m
8 m
12m
(b) Type B

Fig. 4. Configuration of smoke exhaust openings.

2.4 Grid Meshing and Boundary Conditions

In this study, the size of CFD model is set as 400 m long, 12 m wide and 9 m high to shorten computation time, which is based on the actual dimensions of the SHM tunnel. As to the SHM Tunnel, the slope in the middle of it is less than 0.3% and not considered in this study. The distance between the duct slab and the road surface is 6.5 m and the thickness of the duct slab is 0.2 m. The cross-sectional area of the exhaust duct is 9.2 m^2 (Table 1).

Table 1. Configuration of simulation cases

Group	Case	HRR (MW)	Exhaust opening type	Fire location	Smoke exhaust rate (m^3/s)	Mesh ($L \times H \times W$)
Group-I	I-5	5	A	FL-M	120	$93 \times 37 \times 46$
	I-20	20	A	FL-M	120	$108 \times 55 \times 70$
	I-50	50	A	FL-M	120	$108 \times 55 \times 70$
Group-II	II-5	5	B	FL-M	120	$100 \times 55 \times 69$
	II-20	20	B	FL-M	120	$100 \times 55 \times 69$
	II-50	50	B	FL-M	120	$100 \times 55 \times 69$

2.5 Safety Criteria for Emergency Evacuation

According to the criteria for safe evacuation established by PIARC in 1999, the evacuation environment within the tunnel is carefully evaluated Air temperature is set to be acceptable when <353 K, and S_{smoke} (Visibility, m)/(Light Extinction Coefficient, k_{smoke}, m^{-1}) > 10/(0.8), Carbon Monoxide Concentration <225 ppm.

3 Simulation Results and Discussions

3.1 Influence of Aspect Ratio on Temperature

This paper compares the influence of two aspect ratios of the exhaust openings on ventilation and smoke extraction efficiency. Type A is 2×4 m^2, with an aspect ratio of 2, while Type B is 1×8 m^2, with an aspect ratio of 8.

From Fig. 5, all the key parameters keep in a relatively safe condition in 5 MW and 20 MW. As to 50 MW, the temperature is much higher and the visibility cannot meet the demands on CS1 and CS2. Since large scale fires bring worse evacuation environment and expose more security issues, we emphatically analyze the large-scale fire (50 MW). The temperature variations during the simulation time of 900 s, along the vertical direction at CS1 (CS2, CS3) for Case I-50 to Case V-50 can be seen in Figs. 5, 6 and 7, respectively. We discuss the influence of the size of the exhaust openings in this chapter, and choose the two curves: Case I-50 and Case II-50. In both cases, the temperature rises slowly at CS1 below 3.5 m, and it rises sharply from 3.5 m to 4.0 m as seen from Fig. 5. The trend of increase slows down from 4.0 m to 6.0 m and it speeds up from 6.0 m. It brings great challenge to the concrete in the upper zone of the tunnel. Considering the two temperature curves at CS1, the distinction is quite tiny. Similarly, the temperature variation of two cases at CS2 is small as seen in Fig. 6, which means that the change in the aspect ratio of the exhaust opening has little effect on CS2, either.

Different from the changeable trend at CS1, the temperature variation is simple at CS2, which goes slowly below 4.5 m and rises fast above 4.5 m. Due to the fact that the smoke exhaust openings is set right above at CS2 and away from the fire source, the rise is weaker than that at CS1 and the maximum temperature at CS2 is 369 K for Case

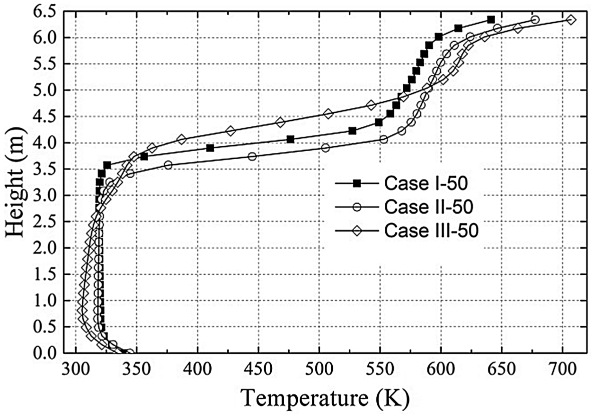

Fig. 5. Temperature variation along the vertical direction at CS1 at 900 s.

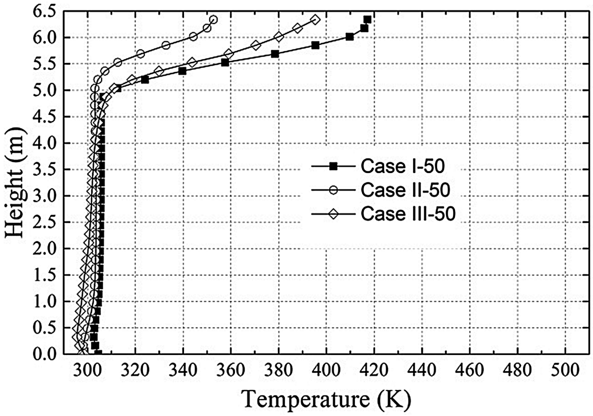

Fig. 6. Temperature variation along the vertical direction at CS2 at 900 s.

II-50, which is 54% less than at CS1. As seen from Fig. 7, the temperature increases rapidly in Case I-50 and Case II-50 at CS3 in the region higher than 5.0 m in height, and the temperature of Case I-50 is higher than that of Case II-50 at the same height. As shown in Fig. 5, the maximum temperature is approximately 417 K for Case I-50 at CS-3, while Case II-50 is 353 K, 15% less. This indicates that Case II-50 provides better evacuation environment than Case I-50 away from the fire source. According to the standard we set before that 353 K is the boundary of a tolerable temperature, the temperature is still very high under the exhaust duct 10 m away from the center of the fire source, but decreases rapidly at 25 m away. So the rescue reinforcement should be involved in the center of the fire.

The temperatures of Case I-50 and Case II-50 are approximately 300 K at 2.0 m in height at CS3, which are much lower than the tolerable values for the lower space of the traffic layer. The results showed that the transverse rectangular shape improves efficiency slightly than the other two.

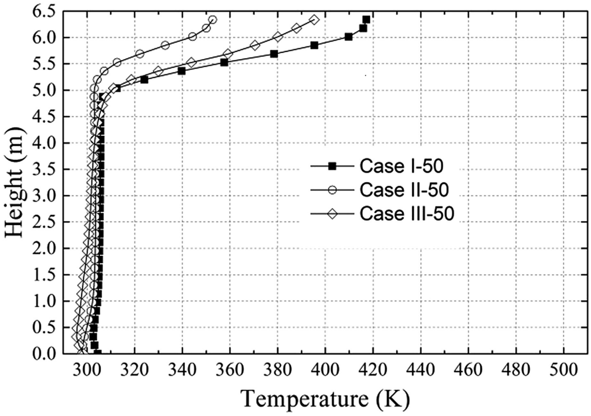

Fig. 7. Temperature variation along the vertical direction at CS3 at 900 s.

3.2 Influence of Aspect Ratio on Visibility

The effect on visibility is quite obvious. The k_{smoke} of Case I-50 is significantly greater than Case II-50 at the same position in the region above 5 m in height at CS3, as seen in Fig. 8. The visibility at 2.0 m high in Case II-50 is much farther than that in Case I-50 at CS1 CS2 and CS3, which means that the visibility of the evacuation environment is notably improved when applying the exhaust opening of $1 \times 8\ \mathrm{m}^2$.

3.3 Influence of Aspect Ratio on CO Concentration

A similar result is found for C_{co} of Case I-50 and Case II-50, as shown in Fig. 9. The CO concentration in Case I-50 is much higher than that in Case II-50, which implies the excellent effect on extraction of CO when lengthen the aspect ratio. The concentrations for all cases are far less than 225 ppm in the entire space, which is allowable according to the safety criteria.

Based on the simulation results, the dimensions of the exhaust opening of the SHM Tunnel are optimized from Type A ($2 \times 4\ \mathrm{m}^2$) to Type B ($1 \times 8\ \mathrm{m}^2$). The latter shows great improvement in lowering the temperature, enhancing the visibility and diluting the CO concentration and assures relative safer environment in the upper zone away from the fire source.

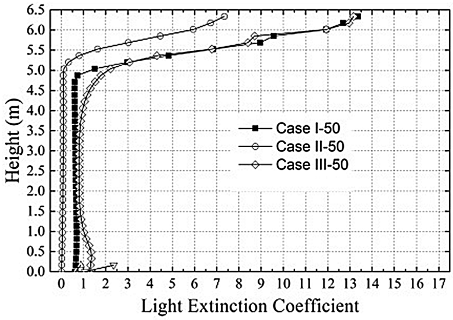

Fig. 8. k_{smoke} variation along the vertical direction at CS3 at 900 s.

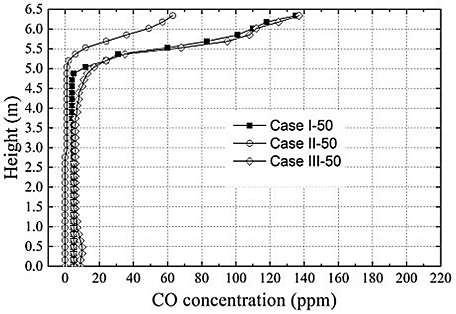

Fig. 9. C_{co} variation along the vertical direction at CS3 at 900 s.

4 Conclusions

This study employs CFD to simulate smoke extraction in a large cross-section tunnel, the South Hongmei Road Tunnel using point smoke extraction for fire emergency. The point extraction method has been shown to successfully control the smoke in the upper region, and a steady smoke layer can be maintained for the safety of people farther away from the fire location. Some direct and deductive conclusions and some smoke control strategies can be derived from the analysis.

(1) For the same location and same area of the exhaust openings, 1 × 8 m^2 smoke extraction openings brings a better evacuation environment and have been chosen in SHM tunnel.
(2) In an emergency fire situation, the PES can effectively control smoke movement for small-scale and medium-scale fires.
(3) For fire size of 50 WM, the PES needs to be improved. Instant rescue operation and corresponding strategy to control the fire are necessary.

References

Vega, M.G., Diaz, K.M.A., Oro, J.M.F., Tajadura, R.B., Morros, C.S.: Numerical 3D simulation of a longitudinal ventilation system: memorial tunnel case. Tunn. Undergr. Space Technol. **23** (5), 539–551 (2008)

Li, J.S.M., Chow, W.K.: Numerical studies on performance evaluation of tunnel ventilation safety systems. Tunn. Undergr. Space Technol. **18**, 435–452 (2003)

Woodburn, P.J., Britter, R.E.: CFD simulations of a tunnel fire-Part I. Fire Saf. J. **26**(1), 35–62 (1996a)

Woodburn, P.J., Britter, R.E.: CFD simulations of a tunnel fire-Part II. Fire Saf. J. **26**(1), 63–90 (1996b)

Lin, C., Chuah, Y.K.: A study on long tunnel smoke extraction strategies by numerical simulation. Tunn. Undergr. Space Technol. **23**, 522–530 (2008)

Hu, L.H., Huo, R., Peng, W., Chow, W.K., Yang, R.X.: On the maximum smoke temperature under the ceiling in tunnel fires. Tunn. Undergr. Space Technol. **21**, 650–655 (2006)

Vu-Bac, N., Lahmer, T., Zhuang, X., Nguyen-Thoi, T., Rabczuk, T.: A software framework for probabilistic sensitivity analysis for computationally expensive models. Adv. Eng. Softw. **100**, 19–31 (2016)

Zhu, H.H., Shen, Y., Yan, Z.G., Guo, Q.C., Guo, Q.H.: A numerical study on the feasibility and efficiency of point smoke extraction strategies in large cross-section shield tunnel fires using CFD modeling. Loss Prev. Process Ind. **44**, 158–170 (2016)

Study on the Grade Evaluation of Highway Tunnel Cracks Based on PFC Simulation and BP Neural Network

Hao Ding[1,2], Ke Li[1,2(✉)], Yuyu Xiayang[1,2], and Jing Bi[3]

[1] China Merchants Chongqing Communications Research and Design Institute Co., Ltd., Chongqing 400067, China
`364842342@qq.com`
[2] National Engineering Laboratory for Highway Tunnel Construction Technology, Chongqing 400067, China
[3] Chongqing University, Chongqing 400044, China

Abstract. In China, there are 15,181 highway tunnels with a total length of 14,039.7 km have been put into service by 2016. Tunnel lining cracks is the most critical risk, therefore, how to control the structural safety of highway tunnels has become one of the prominent issues. In this paper, effects of length, width, depth and position of highway tunnel lining cracks on the safety of lining structure has been studied based on PFC discrete element model. BP neutral network algorithm is also introduced to select critical factors for grading and assessment to establish an assessment system for highway lining crack.

Keywords: Highway tunnel · Lining crack · Grade evaluation
PFC

1 Introduction

In China, there are 15,181 highway tunnels with a total length of 14,039.7 km have been put into service by 2016 [1]. In addition, the numerical scale of highway tunnels in China will increase continuously in the future. According to the previous studies, highway tunnels in China have some common defects, *e.g.,* cracking, leakage, peeling, extremely thin lining and hollowing, among which lining cracking is the most common issue [2, 3]. In fact, almost all defects are associated with tunnel cracking. Failing to control tunnel cracking in time may result in peeling or collapse of tunnel, which may affect the safety assurance of vehicle and drivers.

Domestic and foreign scholars had studied a lot on the grading evaluation of tunnel cracks. Highway and Rail Transit Tunnel Inspection Manual (the U.S.) divided non-pre-stressed concrete lining cracks into three grades according to the crack width [4]. Brief Guide to Maintenance and Management of Highway Tunnel (Japan) [5] classified the tunnel cracks into two categories according to their expansibility, and provided gradation of those two types of tunnel cracks according to their width and length. Both quantitative and qualitative approaches were used to divide tunnel cracks into five grades based on comprehensive consideration of crack length, width and so on [6]. In general, as

© Springer Nature Singapore Pte Ltd. 2018
D. Zhang and X. Huang (Eds.): GSIC 2018, *Proceedings of GeoShanghai 2018 International Conference: Tunnelling and Underground Construction*, pp. 605–611, 2018.
https://doi.org/10.1007/978-981-13-0017-2_61

compared with railway tunnels, the highway tunnels of China lack of engineering experience and techniques in classification and evaluation. Therefore, it is very necessary to conduct related studies to resolve above defects of highway tunnels in China.

This paper aims at simulating safety assessment on the lining cracks of highway tunnels by discrete element analysis software PFC under different conditions, including grade of surrounding rock, position, length, width and depth of cracks in tunnel lining. In addition, based on the modeling sample and BP (back propagation) neural network, this paper established an assessment system of highway tunnel lining cracks.

2 Discrete Element Numerical Model

2.1 Micro Parameters of Particles

Physical properties of materials can be reflected by the overall motion track of particles when using PFC particle flow as numerical simulation. Microscopic - parameters of particles will affect their motion track. Therefore, macro changes of materials are determined by the micro parameters of particles. However, due to the uncertainty and complexity of micro-parameters of particles, there is not a uniform formula to connect micro and macro parameters of materials [7–9]. This paper calibrated the micro parameters of C30 concrete materials by the uniaxial compression numerical simulation test, as shown in Fig. 1. In order to make sure that the macroscopic mechanical behaviors of materials are consistent with actual circumstance through analyzing the micro parameters of particles, and thereby obtain reasonable and accurate micro parameters, as shown in Table 1.

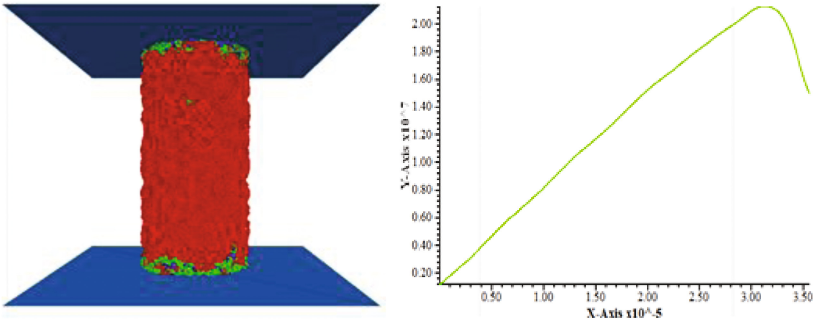

Fig. 1. Uniaxial compression numerical simulation test

2.2 Model Establishment

A two-lane tunnel was taken as the study sample. Specific parameters were as follows: arch radius (R1) is 14.75 m; arch radius of tunnel foot (R2) is 1.95 m; arch radius of tunnel body (R3) is 5 m. PFC2D and PFC3D models were used in this paper as shown in Figs. 2 and 3, respectively.

Table 1. Micro parameters of particles

Parameters	Density (kg/m^3)	Equivalent elastic modulus of particles (GPa)	Friction coefficient	Rigidity ratio	Tensile strength of parallel bond (Pa/m)	Cohesive force of parallel bond (Pa/m)
Values	2040	30	0.577	2	2.01e+07	15.00e+06

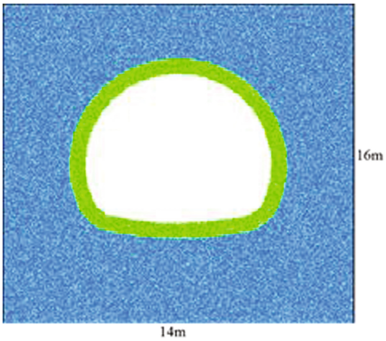

Fig. 2. PFC 2D computational model

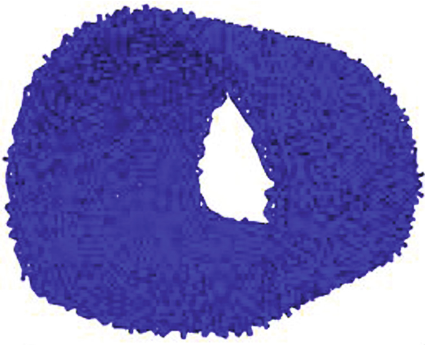

Fig. 3. PFC 3D computational model

PFC2D model, with a length of 14 m, a height of 16 m, and particle radius of 0.03 and 0.05 rad/m (Fig. 2), was used to study the influence of crack depth and position on the safety performance of tunnel.

PFC3D model, with a length of 14 m, a height of 16 m, a width of 10 m, and particle radius of 0.15–0.215 rad/m (Fig. 3) was used to study the influence of crack length on safety performance of tunnel.

The model was be endowed bond strength of particles after becoming stable. It should be noted that parallel bonding is applicable to particles while point bonding is used to surrounding rock of tunnel.

In the process of calculation, a strength reduction method was used to control the decrease of safety through continuously changing the length, width and depth of cracks under different surrounding rocks, tunnel depth, and crack positions to reach a dynamic transition from stability to instability.

3 Algorithm of BP Neural Network

BP neural network is a kind of neutral network based learning algorithm, which has been widely used in engineering. In the view of structure, BP neural network has input layer, concealed layer, and output layer. Moreover, it is characterized by the ability of complicated mode classification and multi-dimensional function mapping. Therefore, BP neural network can be used for assessment and analysis from multi-factors.

3.1 Evaluation Index of Model

In this paper, eight factors (surrounding rock grade, tunnel depth, vertical load, lateral load, lining thickness and crack position, length, width and depth) were selected as input vectors in the analysis model of BP neural network.

Input vector is:

$$P_x = \{i, h, o, l, w, d, p1, p2, t\} \quad (1)$$

where, i is surrounding rock grade; h is tunnel lining depth; o is crack position; l is crack length; w is crack width; d is crack depth; $p1$ is vertical load; $p2$ is lateral load; t is lining thickness.

3.2 Construction of Learning Sample

471 sets of data under the surrounding rock condition of grade V were selected as learning samples from the results of PFC simulation. Where, the depths of 27 m and 21.6 m, cracks positions (arch roof, spandrel, and haunch), lining thickness of 0.45 m, 0.5 m, and 0.55 m, crack length and depth of 3–8 m and 0.1–0.5 m were considered respectively.

Numerical simulation result of S is the safety status of tunnel lining, which including 000 status and 001 status. 000 status refers to stability; while 001 status refers to the damage incurred by anyone of pre-set cracks length, width or depth. More seriously, when the damage is incurred by any two factors of pre-set cracks length, width or depth, the 001 status refers to serious damage.

3.3 Network Training

471 sets of learning samples were put into the analysis model with the analysis error below 0.005 for convergence. The maximum iteration step was set to 20000 times.

To compare with BP calculation, the depths of 13.5 m and 5.4 m were selected in simulation model under the Grade V surrounding rock condition. The results show that the BP calculations are in good agreement with numerical simulation results, indicating that this method can be applied to the system for assessment safety of tunnel lining cracks. The following conclusions can be obtained when the 8 factors are input into the model during practical engineering monitoring of tunnel lining cracks: (1) 000 refers to a safe condition of lining; (2) 011 refer to the forthcoming damage of lining, which needs to support.

4 Establishment of Assessment System

Based on the above calculations of neural network, various parameters are scored. In order to simplify the assessment system, it is not necessary to consider vertical and lateral loading related to surrounding rock and burial depth when calculating neural network samples. There are seven main factors considered in this safety assessment system, as follows:

(1) Surrounding rock grade: effect on the safety of lining cracks under Grade III and VI surrounding rock conditions is the main factor in this assessment system.
(2) Tunnel burial depth: According to the critical burial depth from Specifications for Design of Highway Tunnels (SDHT), 4 shallow burial depths and 1 deep burial depth are considered respectively.
(3) Thickness of 2nd lining: According to the SDHT, effects of different 2nd lining thickness on the safety of cracks under different surrounding rock conditions are considered.
(4) Crack position: According to numerical simulation results, cracks on the spandrel may most likely incur damages, compared to haunch and vault.
(5) Crack width: According to numerical simulation results, pre-set cracks width of 1 mm–10 mm do not incurred damages in lining. Therefore, this item has a relatively low score.
(6) Crack depth: According to numerical simulation results, crack depth has the strongest influence on cracking and expansion. Therefore, crack depth is a major factor that affects the safety of lining, showing the maximum score.
(7) Crack length: According to numerical simulation results, crack length has the same effect of crack width on lining cracking and expansion.

The score of each parameter is determined during assessing tunnel lining cracks, and obtain a total score from each scores of 7 parameters to. Therefore, we can describe the safety of tunnel lining through the total score (Tables 2, 3, 4 and 5).

Table 2. Assessment of highway tunnel lining crack under grade III surrounding rock condition

	Values				
Surrounding rock grade	III				
Score	10				
Tunnel depth	<1.08 m	2.7 m	4.32 m	5.4 m	>5.4 m
Score	15	15	13	12	13
2nd lining thickness	35 cm			40 cm	
Score	3			4	
Crack width	<2 mm	2–6 mm	6–10 mm	>10 mm	
Score	5	4	3	1	
Crack depth	<10 cm	20–40 cm	40–60 cm	>60 cm	
Score	30	28	20	10	
Crack length	<1 m	1–4 m	4–8 m	>8 m	
Score	20	16	10	5	
Crack position	Vault	Spandrel		Haunch	
Score	12	5		8	

Table 3. Assessment of highway tunnel lining crack under grade IV surrounding rock

	Values				
Surrounding rock grade	IV				
Score	5				
Tunnel depth	<2.7 m	6.75 m	10.8 m	13.5 m	>13.5 m
Score	15	10	6	5	8
2nd lining thickness	35 cm	40 cm		45 cm	
Score	3	4		5	
Crack width	<2 mm	2–6 mm	6–10 mm	>10 mm	
Score	5	4	3	1	
Crack depth	<10 cm	20–40 cm	40–60 cm	>60 cm	
Score	30	22	15	5	
Crack length	<1 m	1–4 m	4–8 m	>8 m	
Score	20	12	5	1	
Crack position	Vault	Spandrel		Haunch	
Score	12	5		8	

Table 4. Assessment of highway tunnel lining crack under grade V surrounding rock

	Values				
Surrounding rock grade	V				
Score	2				
Tunnel depth	<5.4 m	13.5 m	21.6 m	27 m	>27 m
Score	10	4	2	1	8
2nd lining thickness	45 cm	50 cm		55 cm	
Score	3	4		5	
Crack width	<2 mm	2–6 mm	6–10 mm	>10 mm	
Score	5	4	3	1	
Crack depth	<10 cm	20–40 cm	40–60 cm	>60 cm	
Score	30	20	12	3	
Crack length	<1 m	1–4 m	4–8 m	>8 m	
Score	20	8	2	1	
Crack position	Vault	Spandrel		Haunch	
Score	12	5		8	

Table 5. Assessment of values of highway tunnel lining crack

Assessment indicators	Assessment			
Assessment value	80–61	60–41	40–21	<20
Classification	I	II	III	IV
Safety status description	Safe	Common	Poor	Very poor
Shoring or not	No	No	Yes	Yes

5 Conclusions

This paper established a safety assessment system of lining cracks in highway tunnel based on PFC numerical simulation and BP neural network. The following findings and conclusions are concluded:

(1) Micro parameters of concrete materials are calibrated through the uniaxial numerical simulation test. PFC-2D and PFC-3D models are established based on research contents.
(2) Based on the learning sample from PFC numerical simulation, the BP neural network algorithm for safety assessment of highway tunnel lining is established through selection of assessment index and network training.
(3) Based on neural network calculations, the critical factors of surrounding rock grade, tunnel depth, thickness of 2nd lining, crack position, crack width, crack depth and length are selected as the evaluation indexes to establish the assessment system of highway tunnel lining crack.

Acknowledgements. This work was financially supported by the National Key R&D Program of China (2017YFC0806000) and the Chongqing Research Program of Basic Research and Frontier Technology (cstc2015jcyjBX0118).

References

1. Ministry of transport of the people's Republic of China. In 2016, the [1] transportation industry development statistics bulletin [EB]. Beijing: the people's Republic of China Ministry of transport (2017). (in Chinese)
2. Lee, J.S., Choi, I.Y., Lee, H.U., et al.: Damage identification of a tunnel liner based on deformation data. Tunn. Undergr. Space Technol. Inc. Trenchless Technol. Res. **20**(1), 73–80 (2005)
3. Liu, H.Y.: Measures and control mechanism of cause of disease of highway. Southwest Jiao Tong University (2007). (in Chinese)
4. Federal Highway Administration & Federal Transit Administration. Highway and rail transit tunnel inspection manual (2003)
5. Road Tunnel Maintenance Management Handbook. Japan Road Association, Tokyo (1993)
6. Transportation Bureau of Ministry of railways. Maintenance rules for overhaul of railway bridges and tunnels. China Railway Press, Beijing (1997). (in Chinese)
7. Itasca Consulting Group, Inc. Particle flow code in 2 dimension. Itasca Consulting Group, Inc., Minneapolis (2008)
8. Yoon, J.: Application of experimental design and optimization to PFC model calibration in uniaxial compression simulation. Int. J. Rock Mech. Min. Sci. **44**, 871–889 (2007)
9. Potyondy, D.O., Cundall, P.A.: A bonded-particle model for rock. Int. J. Rock Mech. Min. Sci. **41**, 1329–1364 (2004)

Study on the Temperature Distribution and Thermal Damage of Concrete Lining in the Maximum Temperature Section of Tunnel Under Fire Condition

Baoping Xi[1(✉)], Yangchun Wu[1], Luhai Chen[1], Qinghua Guo[2],
and Hehua Zhu[2]

[1] Department of Underground Engineering, Taiyuan University of Technology,
Taiyuan 030024, China
xibaoping@163.com
[2] Department of Geotechnical Engineering, Tongji University,
Shanghai 200092, China

Abstract. 50 MW heat release rate fire is the most representative in tunnel fire. The paper has a systematic study on the temperature distribution and thermal damage of the maximum temperature section with a heat release of 50 MW by means of theoretical analysis, numerical simulation and experimental investigations. Research results show that with the increase of ventilation velocity, the maximum temperature point of tunnel lining distributes within the range of 5 m of the upper and lower reaches of the fire source. The surface temperature of cross section lining lies in the maximum temperature section showing a continuous decrease trend from the vault to the side wall. The threshold temperature value of strength damage is 400 °C when the fire temperature lowers than 700 °C. The heat causes serious damage in the tunnel vault for concrete lining with a thickness of 35 cm whose heat damage could be 9.80 cm. Also, the damage region distributes within the range of 5 m of the upper and lower reaches of the fire source and shows a continuous decrease trend from the vault to the side wall. The results can provide reference for the stability and safety assessment of tunnel lining and the repair of tunnel lining damage after fire.

Keywords: Tunnel fire · Concrete lining · Maximum temperature section
Temperature distribution · Thermal damage

Tunnel fire has some characteristics, such as high temperature, long duration, large smoke flow, low visibility. It has a great damage to person and equipment in the tunnel, and the fire can also cause different degrees of damage to lining structure of tunnel, which seriously reduced the safety of the concrete lining structure. There are many typical cases, for example, French-Italian Mont Blanc Highway Tunnel Fire in 1999 [1], Austrian kaitelan Highway Tunnel Fire in 1999 [2], and Chinese maoliling tunnel fire in 2002. In addition, in the fire of Britain-French Channel Tunnel in 1996, it has a great damage to the tunnel lining, the length of completely destroyed in this fire is about 46 m, the thickness is only left 4 cm from the previous 45 cm in the most serious damage [3, 4]. We can draw a conclusion from these fire cases, there is lots of high

© Springer Nature Singapore Pte Ltd. 2018
D. Zhang and X. Huang (Eds.): GSIC 2018, *Proceedings of GeoShanghai 2018 International Conference: Tunnelling and Underground Construction*, pp. 612–624, 2018.
https://doi.org/10.1007/978-981-13-0017-2_62

temperature flu gas filled the entire tunnel space in a quick time, a large amount of heat is transferred to the concrete lining structure by radiation and convection, the temperature of the concrete lining rised rapidly and it can reach above 1000 °C. And then, the mechanical properties of concrete caused by the deterioration process is known as temperature rising, so the bearing capacity and reliability of the concrete lining system is reduced, it can cause a serious damage to the lining structure [5–8].

The degree and range of damage to tunnel lining structure are closely related to the scale and size of fire. The heat release rate of fire source is an important index to evaluate the scale of fire, and the heat release rate (HRR) of fire source is the value of the heat released unit interval. According to the World Road Association PIARC document (1999), the British Highway and Bridge Design Handbook BD78/99 standard, the American Fire Protection Association NFPA 502 Standard (2004), in the tunnel fire protection design [9–11], the fire heat release rate of the small passenger car is 5 MW, the box-type trucks is 15 MW, the bus is 20 MW, the heavy-duty trucks is 20–100 MW, the gasoline tanker is 100 MW. In recent years, whether passenger cars or trucks, the maximum heat release rate has a growing trend during the fire. So some researchers believe that the heat release rate of bus is 30 MW and heavy duty truck is 50 WM.

The tunnel fire caused by one or several heavy trucks is a common scene in our daily life, this is a typical case. In this paper, we selected the concrete lining with maximum temperature range in the fire of 50 MW heat release rate as research object, and analyzed the laws of the distribution of flue gas flow and temperature by numerical simulation. We found the location of the maximum temperature, and analyzed the temperature distribution of the outer surface of the lining. And then we provided the range of thermal damage of concrete lining, by analyzing the characteristics of heat transfer at internal lining and the mechanical test conclusion of the concrete strength after high temperature.

1 The Scene Tunnel Fire Under 50 MW Heat Release Rate

The scene of fire determines the energy input to the destruction on tunnel lining structure when the fire occurs. Different fire scenes determine the different temperature distribution and degree of thermal damage in tunnel. And it is very important to select a appropriate fire scene to study the damage of concrete lining in tunnel.

1.1 Tunnel Model and Its Lining Structure

At present, the often-used forms of road tunnel sections are mostly arched or horseshoe-shaped, and the forms of shield tunnel are mostly round [12], we select 160 m of the tunnel longitudinal length range as the fire research object, the tunnel section as shown in Fig. 1. The thickness of concrete lining structure is 35 cm. The concrete strength ranges from C10 to C40 at different parts of tunnel. The net width (x axis) of the tunnel is 9.0 m and the net height (Y axis) is 8.0 m.

Note: In the cross-section of the tunnel, from the vault to the lowest side of the sidewall mark the temperature monitoring point successively at an equal distance which are T0, T1, T2, T3 and T4 respectively.

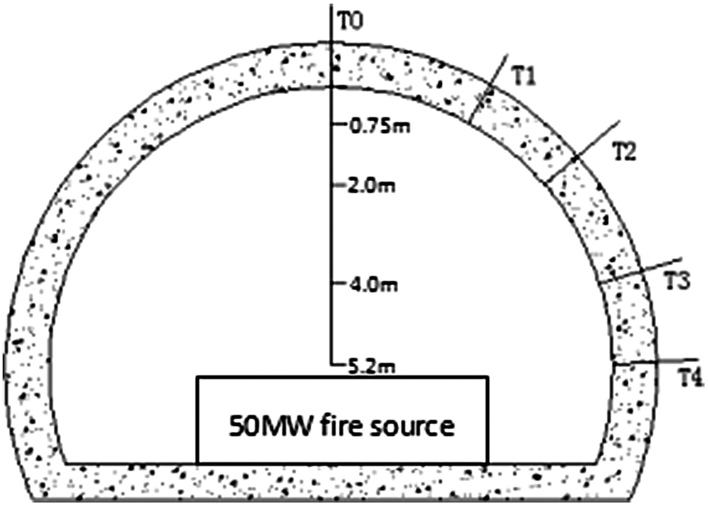

Fig. 1. The tunnel model and monitoring points of temperature on lining

Fire source location: The fire source is arranged in the tunnel inlet 40 m. The air inlet is close to the fire source, and the other side is an open boundary. The length of the fire upstream is 40 m from fire source to the air inlet; The length of the fire source downstream is 160 m from fire source to the other side.

Monitoring of temperature and smoke layer thickness: Several temperature monitoring points and flue gas detection points are arranged at different locations within the tunnel model on the basis of monitoring purposes.

1.2 Critical Wind Speed Selection

During the tunnel fire, the thermal power caused by the flame and the high temperature flue gas will have an important influence on the airflow structure in the tunnel. The countercurrent of the flue gas is a relatively important thermodynamic effect. After the fire in the tunnel, when the tunnel in the condition of natural ventilation or longitudinal ventilation velocity is small, most of the flue gas and the air flow to the fire area downstream side together, part of smoke along the roof of the tunnel do the upwind flowing, which formed the countercurrent smoke layer [13], as shown in Fig. 2.

The flue gas countercurrent layer has a serious threat to the fire rescue persons at the source of upstream, and it will also block the escape and evacuation path of the victims. The flue gas countercurrent layer can be usually eliminated by the way of increasing the wind speed. The wind speed that can exactly eliminate the flue gas countercurrent layer is called critical wind speed [14]. Critical wind speed is an important parameter that affects the position of the highest temperature in the longitudinal direction of the tunnel. In 1987, PIARC [9] recommend to control the flue gas on the side of the fire by using the following wind speed: passenger car fire (2.5 MW–5 MW) is 1–2 m/s, bus or truck fire (20 MW–30 MW) is 3 m/s, and gasoline tanker fire (50 MW–100 MW) is 5 m/s. In this paper, the critical wind speed under the scale of 50 MW fire heat release rate is 5 m/s.

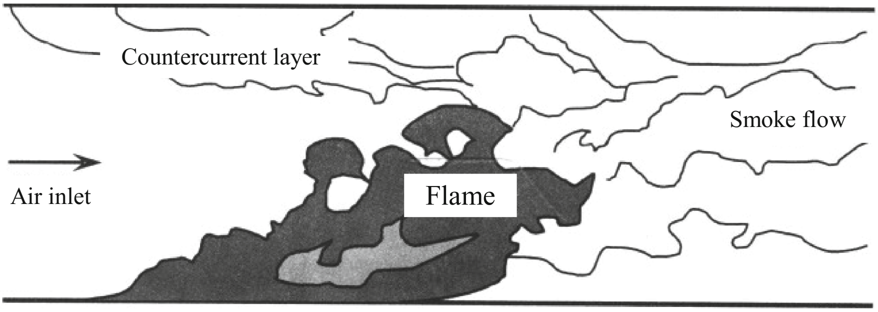

Fig. 2. The diagrammatic drawing of countercurrent smoke layer of tunnel fire [13]

2 Movement of Smoke Flow and Its Temperature Distribution in Tunnel During Fire

2.1 Smoke Movement and Its Temperature Field in the Longitudinal Direction of Tunnel Under 50 MW Fire Heat Release Rate

As it shown in Fig. 3, when the tunnel is natural ventilation, that is v = 0 m/s, the smoke layer thickness has some change between the upstream and downstream of the fire, but the change is weaker than that of v $\geq$ 4 m/s. The thickness of the smoke layer at the entrance of the tunnel is about 1.6 m, and at range from 10 m to 30 m of fire upstream, the smoke layer thickness is same basically. But the thickness of smoke layer downstream is gradually increasing from 2.5 m to about 3.2 m. When the ventilation

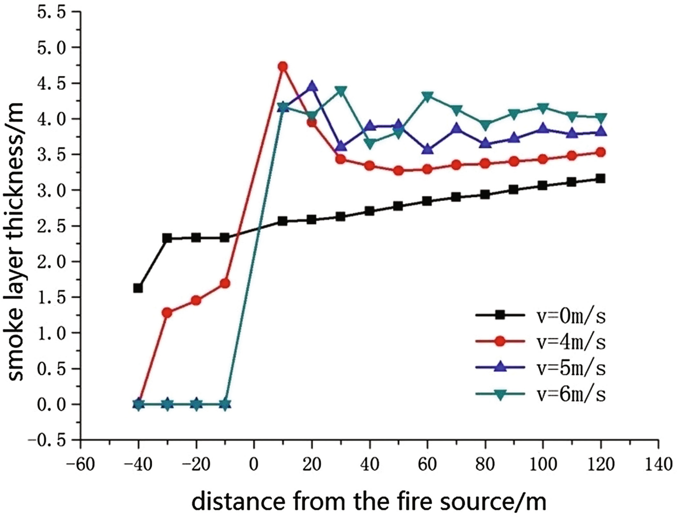

Fig. 3. Variation of smoke layer thickness in tunnel under 50 MW fire heat release at different wind speed

velocity is 4 m/s, 5 m/s and 6 m/s, the thickness of the smoke layer downstream in the range from 10 m to 30 m reaches the peak, and the greater the wind speed, the greater the thickness of the smoke layer is moving downwards. At the range of above 20 m, that is v = 4 m/s, the thickness of smoke layer keeps about 3.5 m. When v = 5 m/s, 6 m/s, the thickness of smoke layer varies from 20 m to 80 m in the downstream, which is in a state of fluctuation, and it tends to be stable after 80 m.

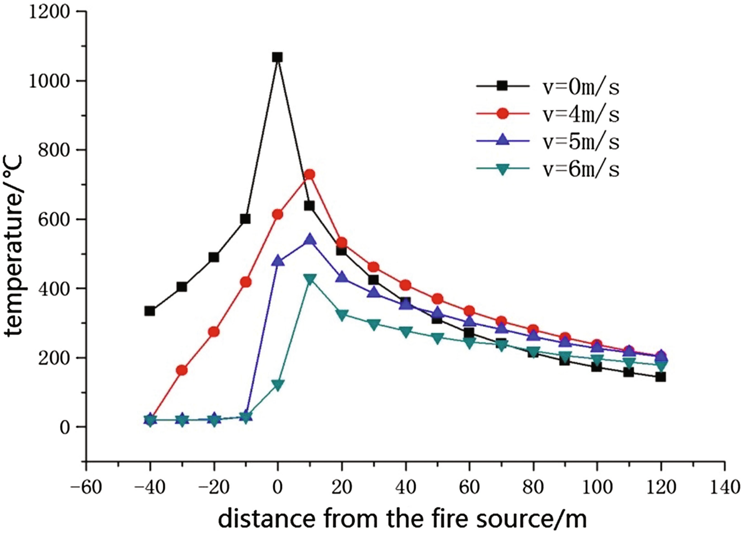

Fig. 4. The temperature distribution of tunnel vault under 50 MW fire heat release at different wind speed

It shows that the temperature distribution of tunnel vault under 50 MW fire heat release at different wind speed in Fig. 4. We study the stabilization stage under 50 MW fire heat release, when v = 0 m/s, the maximum temperature of the tunnel vault reaches to 1085 °C. When v = 4 m/s, the maximum temperature of the tunnel vault reaches to 770 °C. When v = 5 m/s, the maximum temperature of the tunnel vault reaches to 546 °C. When v = 6 m/s, the maximum temperature of the tunnel vault reaches to 429 °C. So the wind speed is an important factor to affect the maximum temperature in tunnel. Ventilation, it can not only suppress effectively the temperature of the fire upstream and reduce the maximum temperature in tunnel, but also it can move the temperature to the fire downstream conducive. When v = 4 m/s, the temperature beyond 20 m of fire downstream is higher than the temperature without ventilated. When v = 5 m/s, the temperature beyond 40 m of fire downstream is higher than the temperature without ventilated. When v = 6 m/s, the temperature beyond 80 m of fire downstream is higher than the temperature without ventilated. That is to say, with the increase of wind speed, the temperature in the longitudinal direction is increasing. And along the tunnel longitudinal extension, under different ventilation conditions, the temperature is getting closer and reaching a stable value.

2.2 The Temperature Distribution on the Surface of Tunnel Lining at the Highest Temperature Section

We can find the location of highest temperature under 50 MW fire release rate according to the laws of the distribution of flue gas flow and temperature. So, at the highest temperature section, how about the temperature distribution on the surface of tunnel lining?

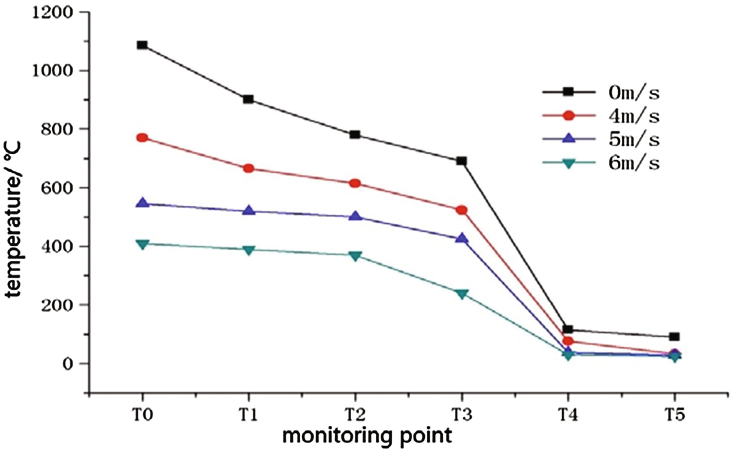

Fig. 5. The temperature distribution of different location at the transverse of highest temperature section under 50 WM fire heat release at different wind speed

As shown in Fig. 5, the temperature distribution on the surface at the transverse of highest temperature section of tunnel lining is decreasing from the vault to the side wall. Under the conditions of the 50 MW fire heat release rate, when the wind speed is 0 m/s, 4 m/s, 5 m/s and 6 m/s, the highest temperature of T0 at the vault is 1085 °C, 770 °C, 546 °C and 410 °C, the highest temperature of T3 at the side wall is 690 °C, 524 °C, 425 °C and 240 °C. With the increase of wind speed, the temperature distribution on the surface at the transverse of highest temperature section of tunnel lining shows a decreasing trend from vault to side wall.

So, to the same transverse of highest temperature section, due to the high temperature smoke flow to the tunnel vault to gather, and the air temperature at the bottom of side wall is relatively low, and the temperature decreases gradually from the vault to the side wall.

3 The Property of Heat Conduction Inside the Concrete Lining at the Highest Temperature Section

We considered the most unsafe situation under 50 MW fire heat release, that is, the ventilation speed is 0 m/s. At this time, the temperature of surface from T0 toT4 is 1085 °C, 888 °C, 831 °C, 764 °C, 220 °C. So, when the fire go into stabilization, how about the heat conduction inside the concrete lining? How about the distribution of temperature?

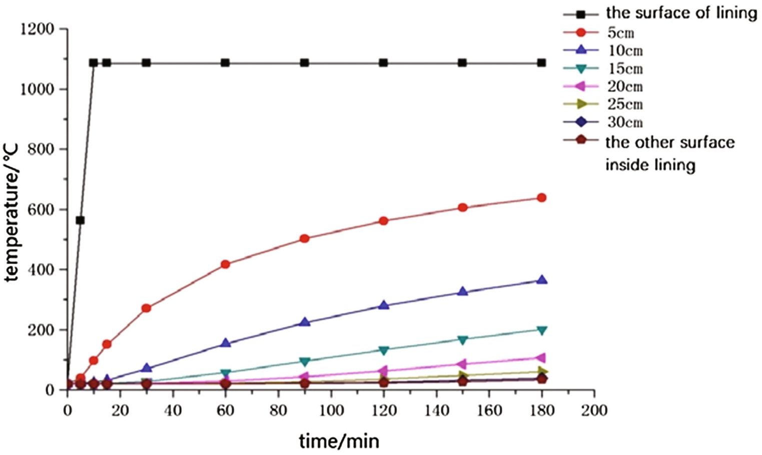

Fig. 6. The relationship between temperature and time of measuring point T0 at different depth of concrete lining under 50 WM fire heat release

It can be seen from Fig. 6 that the temperature on the surface of tunnel lining is the fire temperature. The temperature inside the tunnel lining increases with the increasing time. When the time exceeds a certain value, the increase of temperature inside the tunnel lining tends to be gentle. And with the increase of depth, the time of temperature rising stage and leveled off stage goes backward. The duration of the fire has a greater impact on the lining of tunnel, and with the increase of time, the internal temperature of tunnel lining rises faster.

As shown in Fig. 7, although the initial temperature on the surface of tunnel lining is different greatly, the temperature decay is larger with the increase of the depth of the

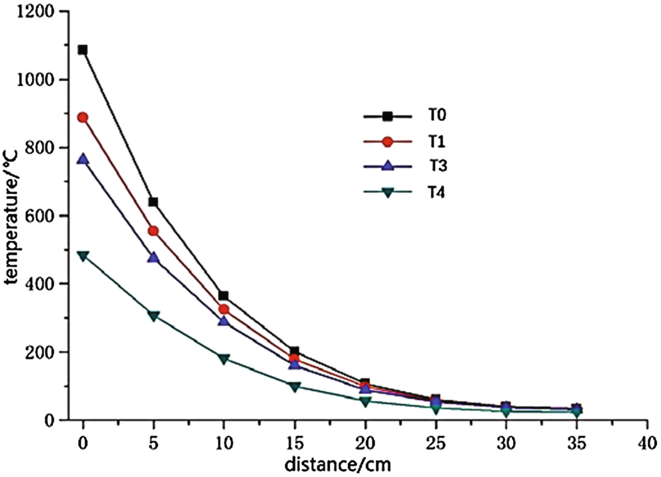

Fig. 7. Curve of the temperature about T0, T1, T2 and T3 with depth under constant fire

lining, and the temperature changed is not obvious inside the lining, it keeps at about 30 °C finally. The temperature changes obviously within 20 cm depth from Fig. 7, but the depth reaches to 20 cm, the temperature changes slightly.

4 Analysis of Strength Damage on Tunnel Lining Concrete by High Temperature

We can see from the previous analysis, the temperature on surface of tunnel lining can reach to 1100 °C under the fire of 50 MW heat release, and the temperature among the depth of 5 cm is mostly concentrated at 700 °C inside the lining. So we should play an emphasis on the evaluation of strength of lining concrete under 700 °C.

4.1 Experimental Study on Mechanical Properties of High Temperature Concrete Strength Within 700 °C

We carried out some experimental study on compressive strength of concrete cubes after high temperature cooling from 700 °C by using the WAW-600 servo-controled experimental machine. The test results are shown in Table 1. the fcuT refers to compressive strength of concrete cube after high temperature, and the fcu refers to compressive strength of concrete cube at room temperature.

It can be seen from Table 1 that the changed law of fcuT on C10–C40 concrete cube after high temperature is basically same: the variation range of the compressive strength on the concrete is lower before 400 °C, and then decreases obviously after 400 °C. Among them, the strength of C10 concrete dropped sharply after 400 °C, and the strength of C20, C30 and C40 concrete strength decreased gradully.

Table 1. The fcuT of concrete within the high temperature of 700 °C

Concrete strength grade	fcu/(MPa)	fcuT/(MPa)						
	20 °C	100 °C	200 °C	300 °C	400 °C	500 °C	600 °C	700 °C
C10	16.6	14.5	17.6	16.9	16.7	5.25	5.46	7.23
C20	24.1	19.7	25.6	25.3	18.7	16.0	13.0	8.1
C30	30.1	28.6	31.1	31.4	28.4	21.0	13.2	10.4
C40	41.1	31.1	39.5	35.8	30.7	17.9	20.3	13.1

In order to reveal the law on decrease of compressive strength of concrete after high temperature, it is shown that the curve on relative compressive strength fcuT/fcu of concrete with temperature in Fig. 8. It can be obtained that the compressive strength of C10, C20, C30, C40 concrete cube after high temperature presented the same trend obviously. When T = 100 °C, fcuT/fcu = 0.82–0.95, it is decreased for the compressive strength of concrete cube. T = 200 °C–300 °C, fcuT/fcu = 0.89–1.06. In this temperature range, the compressive strength of concrete cube will be a certain increase, even higher than the compressive strength at room temperature. When T > 400 °C, the compressive strength of concrete cube decreases uniformly and decreases greatly.

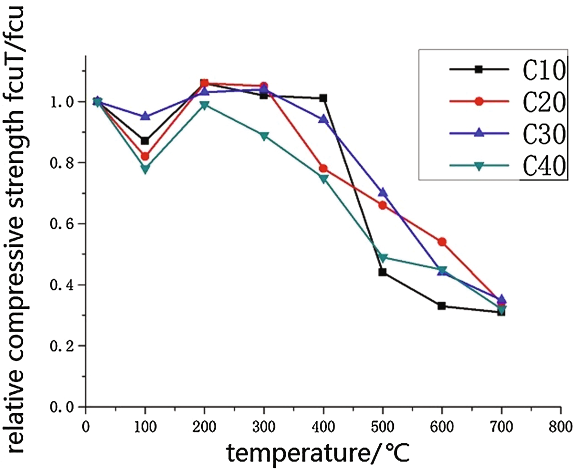

Fig. 8. The curves on relative compressive strength fcuT/fcu of concrete

When T = 500 °C, the residual compressive strength of C10 concrete was 7.23 MPa, which is 56% lower than that of 16.6 MPa at normal temperature; the strength of C20 concrete decreased by 34%, C30 decreased by 30%, C40 decreased by 41%. When T = 600 °C, fcuT/fcu = 0.33–0.54. When T = 700 °C, the compressive strength of C10 concrete cube decreased from 16.6 MPa to 7.23 MPa, it is decreased by 69%, and the compressive strength of C20 concrete cube decreased from 24.1 MPa to 8.1 MPa, it is decreased by 66%, and the compressive strength of C30 concrete cube decreased from 30.1 MPa to 10.4 MPa, it is decreased by 65%, and the compressive strength of C40 concrete cube decreased from 41.1 MPa to 13.1 MPa, it is decreased by 68%. We can conclude that the compressive strength of concrete material has been seriously damaged after high temperature within 700 °C, it has a great impact on the safety of the structure. That is, fcuT/fcu = 0.30–0.35. And the higher temperature experienced, the more obvious decreased.

4.2 Temperature Threshold of Concrete Strength Damage at High Temperature

Concrete is an artificial material made up of cement, water, sand, stone. It can be mixed with chemical admixtures and mineral admixtures under necessary condition. And then it is formed by appropriate proportion mixture, uniform stirring, compacted molding and curing hardening.

The interior of concrete will change obviously under the action of temperature, specific performance as follow: When the concrete material is heated to about 100 °C, the free water, including original crack and the junction of the aggregate and the cement, gradually evaporates, resulting in the decrease of the pore pressure and producing stress concentration in crack during loading, which promote crack expansion and lead to the decline of strength. When the temperature is heated to 200 °C–300 °C, the complexity of concrete material lead to a series of complex physical and chemical reactions, stress concentration at the crack. As the thermal expansion coefficients of coarse aggregate and cement stone with great difference, it leads to a uncoordinated deformation between aggregate and cement stone bonding interface. The compressive strength of concrete is weaken because of the decrease of cohesive force and the increase of crack. However, at about 200 °C–300 °C, the amount of water vapor in concrete increases, which further promotes the hydration of cement, enhances the strength of cement stone, alleviates the stress concentration at crack and enhances the strength of concrete. So, at this temperature, the concrete compressive strength will rise, not decline. When T > 400 °C, as cement mortar particles dehydration carbonization under the action of high temperature, it becomes from original dense to careless, the cohesive force greatly decreased. With the temperature increasing, there is no adhesion between the cement mortar particles, and thermal cracking aggravates the loss of concrete bearing capacity. So, the compressive strength of concrete cube decreased significantly.

It can be seen from the analysis that the compressive strength of the concrete experienced different fire temperatures has a same change rule. So, the temperature threshold value of concrete strength damage is 400 °C. In consideration of safety, we can conclude that its strength has been seriously damaged when the lining concrete experienced 400 °C.

5 Analysis of Thermal Damage Range of Concrete Lining Structure in Tunnel Under Highest Temperature

For the stability, the safety assessment and the repairing of the tunnel lining damage after fire, it is the key that we have mastered clearly the thermal damage range and mechanical properties deterioration of lining concrete after high temperature.

The heat is transferred to the concrete inside the tunnel lining in fire, with the increase of concrete temperature, when the temperature reaches the temperature threshold of concrete strength damage value 400 °C, the strength of concrete decreased significantly. So, the range of thermal damage can be determined by examining the distribution of temperature 400 °C in the tunnel lining.

5.1 Thermal Damage Thickness of Tunnel Concrete Lining Structure Under 50 MW Fire Heat Release Rate

Under 50 MW fire heat release rate, we regard ventilation speed v = 0 m/s as the most unsafe situation. We can know the range of concrete strength damage from the depth of temperature 400 °C reaching by T0–T4 temperature monitoring point. As shown in Table 2.

Table 2. The reaching depth on the temperature of concrete strength damage

Temperature monitoring point	T0	T1	T2	T3	T4
Reaching depth of 400 °C(cm)	9.80	8.75	7.51	2.53	1.25

From the results of Table 2 and Fig. 9, it shows that the tunnel lining has suffered from a serious thermal damage under 50 MW fire heat release rate. The thickness of thermal damage on the top of vault T0 reaches to 9.8 cm for the 35 cm thick lining, the damage of T0 is the most serious, the thickness of thermal damage on the sidewall T4 is 1.25 cm, it has a reduced trend from the vault to side wall. So, a large number of vault concrete will fall off, the stability and safety of the lining will be seriously affected.

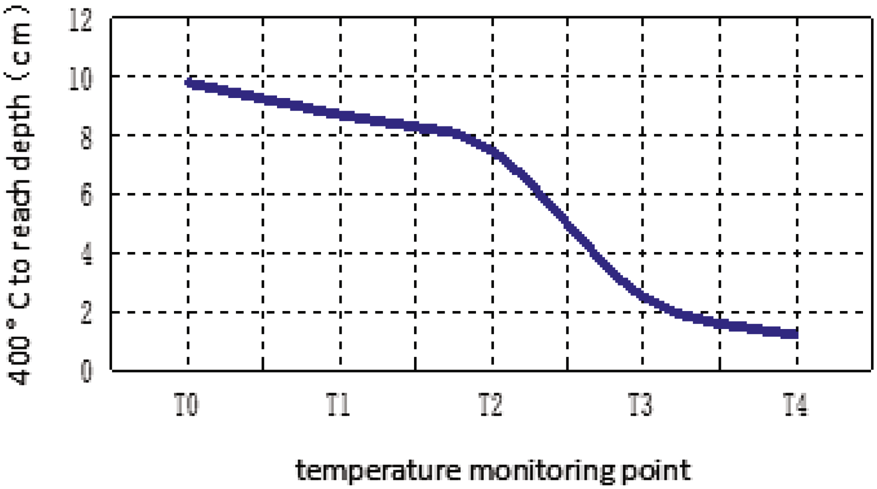

Fig. 9. The reaching depth on the temperature of concrete strength damage reaching under 50 MW fire heat release rate

5.2 Longitudinal Length of Thermal Damage of Tunnel Concrete Lining Structure Under 50 MW Fire Heat Release Rate

We can know from the distribution of vault temperature in longitudinal direction at different wind speed under 50 MW fire heat release rate in Fig. 4. Because of the different ventilation pattern, the maximum temperature point of the fire section in the tunnel will move with the ventilation speed, generally kept at a distance of 10 m from the fire point. So, along the longitudinal length of the tunnel, the range from upstream 5 m to downstream 5 m is the most serious thermal damage in the tunnel.

6 Conclusion

50 MW heat release rate fire is the most representative in tunnel fire. Generally, the fire caused by one or several heavy trucks is defined as a 50 MW fire heat release rate. This paper has a systematic study on the temperature distribution and thermal damage of the maximum temperature section with a heat release of 50 MW by means of theoretical

analysis, numerical simulation and experimental investigations. The results are as follows:

(1) The ventilation speed has an important influence on the movement of the smoke flow in the longitudinal direction and the temperature distribution. With the change of ventilation speed, the maximum temperature of the tunnel lining is centered on the fire source, and it moves in the 5 m range from the upstream to downstream. along the longitudinal length of the tunnel, the temperature tends to be more stable.

(2) The surface temperature of the cross-section lining of the tunnel's highest temperature section is decreasing from the vault to the side wall. Under 50 MW fire heat release rate, natural ventilation and wind speed of 4 m/s, 5 m/s and 6 m/s, the maximum temperature of the vaults were 1085 °C, 770 °C, 546 °C and 410 °C.

(3) With the increase of time, the temperature of each point in the tunnel lining is increasing, but the temperature decreases with the increase of the depth inside lining, and the change in temperature between the outer boundary of the lining is not big, it is maintained at about 30 °C.

(4) The compressive strength test of the concrete cube after high temperature cooling within 700 °C shows that the concrete has a small change range before 400 °C, and the compressive strength is obviously decreased after 400 °C. And the temperature threshold of concrete strength damage is 400 °C.

(5) Under 50 MW fire heat release rate, considering the most unsafe situation (ventilation speed v = 0 m/s), the thickness of thermal damage on the top of vault reaches to 9.8 cm, it has a reduced trend from the vault to side wall. the range from upstream 5 m to downstream 5 m is the most serious thermal damage in the tunnel.

Acknowledgements. The authors would like to thank for the Project supported by the Natural Science Foundation of Shanxi Province, China (Grant No. 201701D22111320).

References

1. Yan, Z.: A Study on Mechanical Behaviors and F1re Proof Methods of Tunnel Lining Structure during and after Fire Scenarios. Tongji University. College of Civil Engineering, Shanghai (2007)
2. Zhou, H., Zhou, Y.: Numerical analysis of the rock mass conditions for rock burst occurrences in deep underground caverns. Mordern Tunn. Technonl. **05**, 32–39 (2015)
3. Xu, P., Jiang, S., Zhou, J., Chen, D., Xie, Y.: Experimental study on smoke temperature distribution in immersed tunnel fire scenarios. Mordern Tunn. Technonl. **05**, 79–83 (2015)
4. Yan, Z., Zhu, H., Liang, L.: Experimental study on mechanical performance of lining segments in fire accidents. J. Tongji Univ. (Natural Science) **06**, 823–828 (2012)
5. Yan, Z., Zhu, H., Zhang, J.: A study on fire damage to tunnel lining and fire-control measures. Chin. J. Undergr. Space Eng. **2006**(04), 683–687 (2006)
6. Wang, F., Dong, G., Wang, M.: On the critical air velocity for fire smoke control in a curved tunnel. Mordern Tunn. Technonl. **05**, 84–89 (2015)

7. Chang, Q., Yan, Z., Zhu, H., Guo, Y.: Numerical analysis of thermal coupling in the mechanical behaviors of tunnel lining structure under fire. Chin. J. Undergr. Space Eng. S1, 1425–1428 + 1447 (2010)
8. Rabczuk, T., Zi, G., Bordas, S., Nguyen-Xuan, H.: A geometrically non-linear three-dimensional cohesive crack method for reinforced concrete structures. Eng. Fract. Mech. **75**(16), 4740–4758 (2008)
9. Technical Committee 5 Road Tunnels. Fire and Smoke Control in Road Tunnels. PIARC (1999)
10. Design Manual for Road and Bridge V 2 S 2: Part9 BD 97/99 Design of Road tunnels. H M S0 (2011)
11. NFPA 502. Standard for Road Bridges and other Limited Access Highways. National Fire Protection, Quincy, Massachusetts, USA; 2004 edition
12. Zhu, H., Yan, Z., Liang, L., et al.: Numerical study on temperature distribution in tunnel linings under fire cases. Chin. J. Undergr. Space Eng. **S1**, 1595–1600 (2012)
13. Zhou, Y.: Study on Thermal Dynamic Phenomena in Tunnel and Network Fire, pp. 3–8. China University of Mining and Technology Press, Xuzhou (2006)
14. Caliendo, C., Ciambelli, P., Guglielmo, M.L.D., Meo, M.G., Russo, P.: Simulation of fire scenarios due to different vehicle types with and without traffic in a bi-directional road tunnel. Tunn. Under. Space Technol. **37**, 22–36 (2013)

Fire Response Performance and Social Behavior in Tunnels Distinguishing from Buildings in Evacuation

Yuxin Zhang[1,2,3](✉), Zhiguo Yan[1,2,3], Hehua Zhu[1,2,3], and Yi Shen[4]

[1] State Key Laboratory for Disaster Reduction in Civil Engineering,
Tongji University, Shanghai, China
13162559391@163.com
[2] Department of Geotechnical Engineering, Tongji University, Shanghai, China
[3] Key Laboratory of Geotechnical and Underground Engineering of the Ministry
of Education, Tongji University, Shanghai, China
[4] Shanghai Municipal Engineering Design Institute (Group) Co. Ltd.,
Shanghai, China

Abstract. The most decisive factor of tunnels' safety in the face of fire is the chance of evacuation safely. Immediate response and proper movement in evacuation from tunnels in fire is essential, which can largely improve the rescue efficiency and reduce the casualties. Tunnels, different from buildings, provide significantly different influence on evacuees due to its unique environment, layout, fire facilities etc. These external distinction not only affect the objective escape conditions directly, but also social behavior indirectly. Consequently, understanding how people behave in the case of fire is of great benefit to bring fire safety measures in line with their need and render valid escape guide in emergency. This paper makes a comparison of people's behavior affected by smoke accumulation, visibility, complexity of structure and fire safety facilities in tunnels and buildings according to available literature. Moreover, psychological comparison namely property attachment, affinity to the surroundings and influence by other evacuees are presented. The discrepancy between tunnels and buildings indicates that corresponding strategies should be applied on different scenarios in tunnel and there is a need to distinguish fire safety education separately.

Keywords: Fire response performance · Social behavior · Tunnel fire
Fire safety strategies

1 Introduction

With the increase in traffic volume, the chance of tunnel traffic accidents and associated fires have increased, which lead to great risk to human life and damage to property and the economy. Moreover, the trucks occupy a large portion of vehicles in tunnels which are much likely to trigger explosion and release much toxic gas. The burning gas and smoke, on one hand, is a vital threat to occupant's safety with the possibility of asphyxia and intoxication. On the other hand, it affects the visibility in tunnels which lowers the moving speed and lengthens the evacuation time finally.

© Springer Nature Singapore Pte Ltd. 2018
D. Zhang and X. Huang (Eds.): GSIC 2018, *Proceedings of GeoShanghai 2018 International Conference: Tunnelling and Underground Construction*, pp. 625–632, 2018.
https://doi.org/10.1007/978-981-13-0017-2_63

Many casualties are induced due to the fact that occupant stay still in their vehicles and don't take any steps escaping, for instance, where most of the victims were found inside their cars in the fire in the Mont Blanc tunnel (Kouabenan et al. 2005; Gandit et al. 2009). Different from buildings on the ground, the assistance of the professional emergency services like rescue it is much more difficult for fire brigades to extinguish tunnel fires since fire engine has trouble driving into the tunnel through traffic jam caused by fire and also the precise location of fire cannot guarantee underground. In such unclear situations, adequate self-evacuation can help occupants out of the danger or at least prolong survival time until the rescue. However, a large portion of people don't behave correctly: stop the vehicle distant from the fire source of 50 m or more on the side of carriageway, switch off the engine, switch on the hazard flasher, and leave the vehicle immediately while leaving the keys in the ignition lock. They should move to the nearest emergency exit as soon as possible (Egger 2012). Unfortunately, observations from various tunnel fires show that occupants do not evacuate immediately.

2 Evacuees' Reaction and Pre-movement Time

Evacuees' reaction and time to react determine the number of casualties since any delay and hesitation during a fire will shorten available time to escape. On the one hand, with strong social bonds between occupants involved in a fire, such as between family members, they tend to go and find their group at the very first time instead of escaping. On the other hand, task commitment which people cling to role patterns or expectations is in their first instance when unexpected events occur (Averill et al. 2005). This inhibits the recognition of danger and increases the processing time of information about the risks that a fire poses. People are often inclined to finish the job they are doing firstly before making their escape. And those who have organizational responsibilities for a building, by virtue of their roles or positions, such as waitresses and department managers, are also inclined to assume these duties during an emergency situation. Incident analyses have discovered that there is a connection between a delayed evacuation and a high number of fire deaths or injuries, particularly in residential buildings and hotels. Earlier evaluations, in particular those of the Beverly Hills Supper Club fire and the Cocoanut Grove Dance Hall fire, had already revealed that a delayed evacuation had resulted in a large number of fatalities. Since the tunnel is filled with a group of strangers, the delay resulting from role and social connection weakens. Occupants lack reliance on other people or their work, hence, they regard cars as the safest place and choose to hide in them. In the first few seconds, they stay still inside vehicles until further instructions or drive faster to rush out the fire zone as long as they believe they could survive through the rush, which would trigger server car accidents or crash with the possibility of fuel leakage. According to the handbook of tunnel fire safety, correct behavior is as followed in Table 1:

Table 1. Correct behavior for drivers in case of tunnel fire

1	Switch on warning lights	necessary
2	Switch off the engine	necessary
3	Leave your vehicle	necessary
4	Administer first-aid to injured people	unnecessary
5	Call for help from an emergency point	necessary

Among all the reaction, Sime, Proulx and Fahy have done the research which have revealed that pre-movement time is a more important element since required escape time is provided and movement to a safe place does not differ a lot. Though pre-movement time and pre-movement behavior are currently regarded as key aspects of the evacuation process, little document and research has put it into quantitated calculation, and less research in tunnels.

3 Movement Speed and Path

At the beginning of the 20th century, people firstly turned their attention to investigations of movement velocity and movement time, and now thousands of scientists from across the globe have conducted major research into this issue, including Fruin (USA), Pauls (USA), Predtetschenski and Milinski (Germany), Habicht and Braaksma (Canada) and Jin in particular. Several mainstream types of velocity in corresponding buildings and the time needed for movement purposes are relatively well documented. Among those, Paul and Fruin's investigations have been converted into calculation tools and are taken down in fire safety legislation and codes of practice. Jin discovered that walking in smoke behaves differently from that in previous study which focused on places without smoke. Also, some attention has been paid to the functionally impaired including young children and the elderly from the 1970s by Bpyce, Shields and Silcock, which proved to deviate from expectation and previous calculation. Two main experiments conducted by Jin and Frantzich and Nilsson. Jin investigated both irritant and non-irritant smoke and the results for irritant and non-irritant were 0.3 and 1 m/s and 0.5–1 m/s respectively. Experiments by Frantzich and Nilsson were devoted to a wider range of extinction coefficients and the obtained speed covered 0.2–0.8 m/s. Another factor is mobility which determines an individual's ability to move, distinguishing four levels, namely high, temporarily reduced, permanently reduced, and dependent mobility [lr38]. The average movement speed was relatively higher than that in buildings with less complicated engineered features like corners, stairs and obstacles, found to be approximately 0.9 m/s, independent of tunnel floor material examined. Moreover, during an experiment by Karl Fridolf and Enrico Ronchi etc., many participants walked with a crouched posture as shown in Figs. 1 and 2 due to an uncertainty about the tunnel height, improvement of the walking balance and an increase of perceived level of safety inside the tunnel.

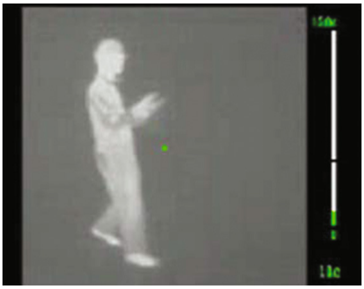

Fig. 1. Walking with a crouched posture.

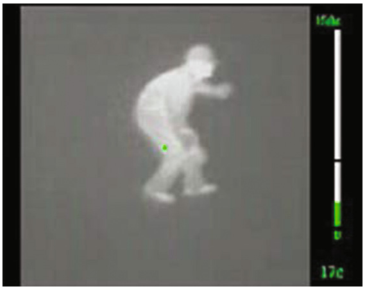

Fig. 2. Walking with the hands in front of the body.

4 Movement Speed and Path

Occupation density, the number of people in a building affects evacuation largely. High occupation density relates to a high probability of fatalities in the event of fire according to the literature. While congestion around the exit door or staircase is a huge problem in building evacuation, it troubles rather little in tunnels.

Shinji Emoto in Japan did an experiment and found congestion did not occur because the diagonal tunnel, constructed with a width of 8 m, had a large capacity for evacuees from one site to another (Emoto et al. 2016). According to many simulations via pathfinder and Building Exodus, people won't gather in front of either emergency doors or staircases normally, for its low occupation density and large size of tunnel installation. However, congestion at an emergency door was observed once because many participants arrived from both sides simultaneously. And there is possibility that people gather together in front of doors waiting others on their way to doors, which lead to serious congestion probably. Those situations are extremely hazardous with unimaginable damage to escapers once occur. It is expected to eliminate the congestion by guiding clearly and precisely with signage and some researchers are trying to guide and command occupants in emergency with artificial intelligence.

5 Safe Destination

Destination, referring to locations or areas that pedestrians move towards plays an important role in escaping for they move to their destination based on a shortest path algorithm according to distance potential maps in their mind. Thus, a clear destination brings about a quick reaction and a specific route (Sime 1999). In modelling, the behavior control moves the individual from one cell to another based on the shortest distance to a destination, supervising the waiting periods, and other behaviors such as overtaking or sidestepping. The method is usually based on "potential maps" which identifies a discrete approximation of the shortest path towards the destination and stores this information in the cells in order to achieve an efficient simulation and the path varies along with the destination.

Though exit doors are regarded as destination generally, people would feel safe when they reach a place where they are familiar with. People in building fires aim to run out of the building and the surrounding outside is explicit and secure. In contrast, people escape with hesitation more or less due to the uncertainty outside the emergency door. The current three destinations in tunnels are namely refugee room, another adjacent tunnel or road surface all connecting with a cross aisle, which would bring less sense of security in escaping.

6 Property Attachment

According to research data in accidents before, the most two common actions drivers would take are to stop their cars and remain seated in the cars or to make a U-turn to the entrance of tunnels. The first would waste precious evacuation time on first stages of fire and lose the chance of running away. The second is more dangerous and detrimental since it may lead to traffic jam and accidents in tunnels and may hit evacuees badly. Admittedly, compared to the tunnel environment, drivers perceives relative safe inside their own vehicle is a main reason and reluctance to leave property behind is another undeniable cause of passivity. (Gandit et al. 2009; Ronchi et al. 2013). Similarly, property attachment has been shown to be a main account of non-evacuation in buildings in fire. This can be proved on the discrepancy of evacuation in home and office. Mostly, people at home cost longer time before taking action since they spend time gathering cash, jewelry and significant document. In contrast, the evacuation time is relatively short if task commitment, which means that people cling to role patterns or expectations, is neglected. This psychological tendency has no possibility to eliminate entirely but can only be overcome to some extent by announcement and instructions in tunnels. It is essential to distinguish various instruction ways including vocal message, signage and other ways and release effective information.

7 Affinity to the Surroundings

People's behavior towards surroundings is based on the acknowledgement and interpretation on it. The more familiar people are to the environment, the more effective and adequate measures they are tend to take. Affinity to the surroundings are the key to correctly and actively interpret what is happening around. It influences people's moving speed directly and disturb people mentally which would affect their react time and way finding choice indirectly. It can be divided into two aspects. On one hand, it is the basic surrounding that the structure provides including layout, dimensions, exit etc. On the other hand, it relies on the changeable parameters when an accident occurs such as the visibility and noise. Tunnels are unfamiliar from daily life and they are designed quite differently from normal buildings. Sometimes, even experienced drivers have had rare chance to move through tunnels without vehicles. Except from the lanes, other parts such as cross passages are black box especially when drivers are exposed to the dark surroundings. In contrast with tunnels, office and home are mostly alike with common structure, providing more sense of familiarity and security. Apart from the natural characteristic, lights along the ceiling are obscured by dense and stratified smoke and fans for smoke ventilation will create much noise which would aggravate the horror in the dark. The change in illumination and huge noise would cause panic in a strange environment, which would worsen mobility and awareness. The perception of surroundings also plays a decisive role in fire response performance. It has been found that it is not the actual length of an escape route, but how it is perceived, which determines which way is chosen. Little affinity to surroundings increases the chance of misjudging distance when choosing exits.

8 Conclusion

It is widely agreed that clear and profound cognition towards human behavior is essential when meeting a fire in a compartment fire and research concerning to human response performance and social behavior has been conducted from the beginning of the 20th century. In contrast with masses of experiment and modelling focusing on fire in buildings, little attention has been paid to tunnel fires due to relatively less number of fire accidents in tunnel. Nevertheless, tunnel fires can never be taken too serious since its immeasurable destroy and large causalities usually companying with large explosion ignited by fuel tanks of vehicles. Though tunnel fires and building fires share quite a few in common in occupants' behavior facing emergency, tunnel fires differs a lot due to its weak illumination, relative confined space and unfamiliarity to occupants, containing some HGVs, which brings about various pressure and problem for evacuees. Currently, most investigations are based on building fires and the discrepancy between them lack thorough research with masses of modelling and experiments. New advanced technology like virtue reality provides convenience and facility and cuts down expense in both human and material resource, and thus should be put into use in quantity. Fire response performance is dependent upon the environment where an individual stands, the point should be stressed on the interaction between human and the features of tunnels. According, further research is demanded based on tunnel psychonomics in tunnel fires.

References

Amundsen, F.H.: Studies of driver behavior in Norwegian road tunnels. Tunn. Undergr. Space Technol. **9**, 9–17 (1994)

Amundsen, F.H., Ranes, G.: Studies on traffic accidents in Norwegian road tunnels. Tunn. Undergr. Space Technol. **15**, 3–11 (2000)

Burns, P., Stevens, G., Sandy, K., Dix, A., Raphael, B., Allen, B.: Human behaviour during an evacuation scenario in the Sydney Harbour Tunnel. Aust. J. Emerg. Manag. **28**, 20 (2013)

Kouabenan, D.R., Caroly, S. Gandit, M.: Comprendre la perception des risques et les modalités de gestion des incendies dans les tunnels routiers par les usagers: une voie pour une stratégie de prévention durable. In: Ergonomie et développement durable, Actes du 40 (2005)

Purser, D.A.: Assessment of hazards to occupants from smoke, toxic gases and heat. In: National Fire Protection Association (ed.) SFPE Handbook of Fire Protection Engineering. National Fire Protection Association, Quincy MA, USA, 2-96-92-193 (2008)

Gandit, M., Kouabenan, D.R., Caroly, S.: Road-tunnel fires: risk perception and management strategies among users. Saf. Sci. **47**(1), 105–114 (2009)

Egger, M.: Recommended behaviour for road tunnel users. In: Beard, A., Carvel, R. (eds.) The Handbook of Tunnel Fire Safety, pp. 399–420. Thomas Telford Publishing, London (2012)

Shields, J.: Human behaviour in tunnel fires. In: Beard, A., Carvel, R. (eds.) The Handbook of Tunnel Fire Safety, pp. 323–342. Thomas Telford Ltd., London (2005)

Beard, A.N.: Fire safety in tunnels. Fire Saf. **44**, 276–278 (2009)

Kinateder, M., Pauli, P., Müller, M., et al.: Human behaviour in severe tunnel accidents: effects of information and behavioural training. Transp. Res. Part F: Traffic Psychol. Behav. **17**, 20–32 (2013)

Kinateder, M., Müller, M., Jost, M., Mühlberger, A., Pauli, P.: Social influence in a virtual tunnel fire-Influence of conflicting information on evacuation behavior. Appl. Ergon. **45**(6), 1649–1659 (2014)

Latane, B., Darley, J.M.: Group inhibition of bystander intervention in emergencies. J. Pers. Soc. Psychol. **10**, 215–221 (1968)

Fischer, P., Krueger, J.I., Greitemeyer, T., Vogrincic, C., Kastenmuller, A., Frey, D., et al.: The bystander-effect: a meta-analytic review on bystander (2011)

Kobes, M., Helsloot, I., de Vries, B., Post, J.: Exit choice, (pre-) movement time and (pre-) evacuation behavior in hotel fire evacuation Behavioural analysis and validation of the use of serious gaming in experimental research. Procedia Eng. **3**, 37–51 (2010a)

Kobes, M., Helsloot, I., de Vries, B., Post, J.G., Oberije, N., Groenewegen, K.: Way finding during fire evacuation; an analysis of unannounced fire drills in a hotel at night. Build. Environ. **45**, 537–548 (2010b)

Sime, J.D.: Crowd facilities, management and communications in disasters. Facilities **17**, 313–324 (1999)

Sime, J.D.: An occupant response shelter escape time (ORSET) model. Saf. Sci. **38**, 109–125 (2001)

Boer, L.C.: Behaviour by Motorists on Evacuation of a Tunnel. Rapport TNO Human Factors (2002)

Boer, L.C., van Zanten, D.V.: Behavior on tunnel fire. Pedestr. Evacuation Dyn. **2005**, 91–98 (2007)

Fridolf, K., Nilsson, D., Frantzich, H.: Fire evacuation in underground transportation systems: a review of accidents and empirical research. Fire Technol., (2), 451–475 (2011)

Kaptein, N., Theeuwes, J., Van Der Horst, R.: Driving simulator validity: some considerations. Transp. Res. Rec. J. Transp. Res. Board **1550**, 30–36 (1996)

Yan, Z.G., Guo, Q.H., Zhu, H.H.: Full-scale experiments on fire characteristics of road tunnel at high altitude. Tunn. Undergr. Space Technol. **66**, 134–146 (2016)

Godley, S.T., Triggs, T.J., Fildes, B.N.: Driving simulator validation for speed research. Accid. Anal. Prev. **34**, 589–600 (2002)

Nilsson, D., Johansson, A.: Social influence during the initial phase of a fire evacuation – analysis of evacuation experiments in a cinema theatre. Fire Saf. J. **44**, 71–79 (2009a)

Nilsson, D., Johansson, M., Frantzich, H.: Evacuation experiment in a road tunnel: a study of human behavior and technical installations. Fire Saf. J. **44**, 458–468 (2009b)

Ribeiro, J., Almeida, J.E., Rossetti, R.J., Coelho, A., Coelho, A.L.: Using serious games to train evacuation behavior. In: 2012 7th Iberian Conference on Information Systems and Technologies (CISTI), pp. 1–6. IEEE (2012)

Shields, T.J., Boyce, K.E.: A study of evacuation from large retail stores. Fire Saf. J. **35**(1), 25–49 (2000)

Ribeiro, J., Almeida, J.E., Rossetti, R.J., Coelho, A., Coelho, A.L.: Using serious games to train evacuation behavior. In: 2012 7th Iberian Conference on Information Systems and Technologies (CISTI), pp. 1–6. IEEE (2012)

Pelechano, N., Malkawi, A.: Evacuation simulation models: challenges in modeling high rise building evacuation with cellular automata approaches. Autom. Constr. **17**, 377–385 (2008)

Averill, J.D., Mileti, D.S., Peacock, R.D., Kuligowski, E.D., Groner, N., Proulx, G., Reneke, P. A., Nelson, H.E.: Occupant Behavior, Egress, and Emergency Communications, NIST NCSTAR 1-7, Federal Building and Fire Safety Investigation of the World Trade Center Disaster, NIST, USA (2005)

Valasek, L., Glasa, J.: Simulation of the course of evacuation in tunnel fire conditions by FDS + Evac. In: Proceedings of the 2013 International Conference of Applied Mathematics and Computational Methods in Engineering, pp. 288–295 (2013)

Ronchi, E., Nilsson, D.: Fire evacuation in high-rise buildings: a review of human behavior and modelling research. Fire Sci. Rev. **2**(1), 7 (2013)

Kohl, B., Botschek, K., Hörhan, R.: Austrian risk analysis for road tunnels: development of a new method for the risk assessment of road tunnels. In: 3rd International Conference. Tunnel Safety and Ventilation, pp. 204–211 (2006)

Kohl, B., Forster, C.: Risk analysis as decision making tool for tunnel design and operation. In: 6th International Conference. Tunnel Safety and Ventilation, pp. 17–25 (2012)

Alonso, V., Abreu, A., Cuesta, A., Alvear, D.: An evacuation model for risk analysis in Spanish road tunnels. Procedia Soc. Behav. Sci. **162**, 208–217 (2014)

Emoto, S., Kawabata, N., Hasegawa, M., Seike, M.: Proposed evacuation tunnels for wide-area disaster. Tunn. Undergr. Space Technol. **65**, 12–21 (2016)

Kudikyala, U.K., Vaughn, R.B.: Software requirement understanding using Pathfinder network: discovering and evaluating mental models. J. Syst. Softw. **74**, 101–108 (2005)

Thompson, P.A., Marchant, E.W.: Testing and application of the computer model 'SIMULEX'. Fire Saf. **24**, 149–166 (1995)

Natural Ventilating Behavior of Z-Shaped Pedestrian Underpass in Wuhan

Xiongwei Li[1(✉)], Yu Qin[1,2], and Yong Wang[3]

[1] School of Civil Engineering and Architecture, Changzhou Institute of Technology, Changzhou 213002, Jiangsu, People's Republic of China
lixww@126.com

[2] Department of Civil Engineering, Changzhou University, Changzhou 213164, Jiangsu, People's Republic of China
1730459487@qq.com

[3] State Key Laboratory of Geomechanics and Geotechnical Engineering, Institute of Rock and Soil Mechanics, Chinese Academy of Sciences, Wuhan 430071, Hubei, People's Republic of China
wang831yong@126.com

Abstract. In southern China, The moisture condensation is common in the urban underground facilities due to the humid and rainy climate. In order to reduce the maintenance costs the natural ventilation should be used in urban pedestrian underpass as far as possible. The planar layout of the underpass is very important for its ventilation effect so as to avoid condensation problem. Taking the Cuiliu street pedestrian underpass in city of Wuhan as a typical case, the field test was carried out in this paper on the Z-Shaped pedestrian underpass, and analyzed its ventilation effect by the computational fluid dynamic (CFD) numerical simulation. Results show that outcomes of the numerical simulation are close to the measured data, which verifies the reliability of simulation method. Thus Z-Shape is a good layout plan because of the better ventilation effect so that it can effectively prevent the moisture condensation for the urban pedestrian underpass even in moist environment.

Keywords: Pedestrian underpass · CFD · Natural ventilation
Moisture condensation

1 Introduction

The underground facilities of urban pedestrian underpass are constructed to relieve the traffic pressure and ensure the safety of pedestrians. However the cost is large. In order to make its best use, the design needs to consider many factors and give full play to its advantages to attract pedestrians. In southern China, since the humid and rainy climate is predominated, Condensation problems often happen in underground facilities. If the moisture in the air condensed into dews on the wall, accumulated water will result in mildew and accelerate the corrosion on the wall, influencing the structural serviceability and working life span. At the same time, dewing make the air muddy and dull. So the environment is seriously affected in pedestrian underpass. It is harmful for the health of pedestrians [1, 2].

© Springer Nature Singapore Pte Ltd. 2018
D. Zhang and X. Huang (Eds.): GSIC 2018, *Proceedings of GeoShanghai 2018 International Conference: Tunnelling and Underground Construction*, pp. 633–641, 2018.
https://doi.org/10.1007/978-981-13-0017-2_64

To prevent dewing on the wall, a good ventilation environment should be ensured, and in order to reduce the cost of management and maintenance of the channel and consider the energy conservation requirements, the channel design must make use of natural ventilation as much as possible to overcome the condensation. Its effect is closely related to the selection and layout of the tunnel. The current industry standard urban pedestrian bridge and pedestrian underpass technical specification' (CJJ69-95) (hereinafter referred to as 'standard') only makes a simple provision for channel natural ventilation: using natural ventilation when the main channel length is less than or equal to 50 m. In the engineering practice, according to the fact that the moisture condensation occurs frequently in the southern China, it's irresponsible to ignore some factors likes local weather and simply follow the standard. The problem whether the natural ventilation is partly adopted for underground channel layout is demanding solution. For the design of urban pedestrian underpass, it is very important to evaluate the ventilation effect of different layout channels in advance.

Ventilation effects can be tested by field testing and numerical simulation methods. Field tests can accurately measure temperature, humidity, wind speed and other information in local areas of the channel, but it must be a completed channel. And because of the limited amount of measuring points, it can not fully reflect the condition inside the channel. The numerical simulation test with no limitation of measured points can simulate any tunnel layout forms, dates of each location in different time, but need to be based on the measurements by field tests. If the two methods are combined, the complementary advantages can be realized to meet the requirements of the design for the evaluation of the tunnel ventilation effect [3].

This paper takes Hubei city of Wuhan province East Lake road Cuiliu street Z underground tunnel as the research object, field test is conducted to survey the ventilation effect and the whole condition of tunnel is analyzed by means of CFD numerical simulation,\. Both of them verified the reliability method, and provide a reference for natural ventilation city in South China underground pedestrian underpass design.

2 Project Overview

The plane layout of the Cuiliu street pedestrian underpass in city of Wuhan is Z-shaped. The length of the main channel is about 65 m, across the East Lake Road, and the net width is 5.0 m, while net height is 3.0 m and buried depth is about 8 m. The channel has two entrances at both ends of the Z-shaped, with a slope of 1:4.

The moisture content of air is one of the important factors that affect the inner wall of the subway underpass. According to the survey, the monthly average air humidity in Wuhan reached its peak in July and August every year (see Table 1). Therefore, in this paper, the field test and data collection of the ventilation environment in the pedestrian underpass of Cuiliu street in July and August are conducted. Three weather conditions, including hot, rainy and hot flashes, were selected to conduct repeated tests three times before and after the passage. In addition, according to the research results, the highest Summer Dew point temperature appeared in the morning. Based on the collected data of each field the interval is from 10 PM to 6 AM in the next day, and the maximum value can be obtained in the case of condensation in the tunnel ventilation environment.

Table 1. Monthly average moisture of Wuhan

Month	Jan.	Feb.	Mar.	Apr.	May.	June.	July.	Aug.	Sept.	Oct.	Nov.	Dec.
Monthly average moisture content (g/kg dry air)	4.1	4.2	6.4	8.9	13.0	16.8	19.6	19.4	14.3	10.3	6.6	3.7

3 Field Test

A series of advanced professional measurement equipment are used in the test to ensure the reliability of the measurement data, The main test instruments are shown in Table 2. In order to know as much as possible about the ventilation of underground pedestrian underpass, 5 scattered cross-sections are selected in the tunnel, and the sections are shown in Fig. 1. The measuring instruments were installed at the entrance to collect relevant data, and the time points of measurement are consistent with other conditions. The data are collected every 3 h for 1 time. The collected data include section, air temperature and humidity, wind speed, dew point temperature, wall temperature and wall thermal conductivity, etc.

Table 2. Measuring instruments

Equipment name	Testing object
Mechanical, hand-held hygrometer	Measured air temperature, humidity
Handheld anemometer	Measured air speed
Wall thermometer	Measuring wall temperature
Multi-channel acquisition instrument	Collect measurement data

The measurement work is conducted at three time points, so there are three sets of data at each point. The data are analyzed by error and then processed by the mean value to obtain representative values for analysis, as seen in Table 3 and 4. From the table surface relative humidity is close to 80%, the relative humidity of the air hole tunnel ratio is slightly higher than the entrance of cave. But the air temperature and surface temperature near the channel wall presented in dew point temperature inside the channel does not meet the conditions of condensation. The actual test results are consistent with the field observation.

4 Finite Element Model

FLUENT software has high precision in solving fluid flow and heat conduction problems [4–9]. Therefore, In this paper, a three-dimensional model is established by means of general fluid analysis finite element program to simulate the natural ventilation of underground passage. For simplicity, the midpoint of the section of the underpass is analyzed in numerical analysis.

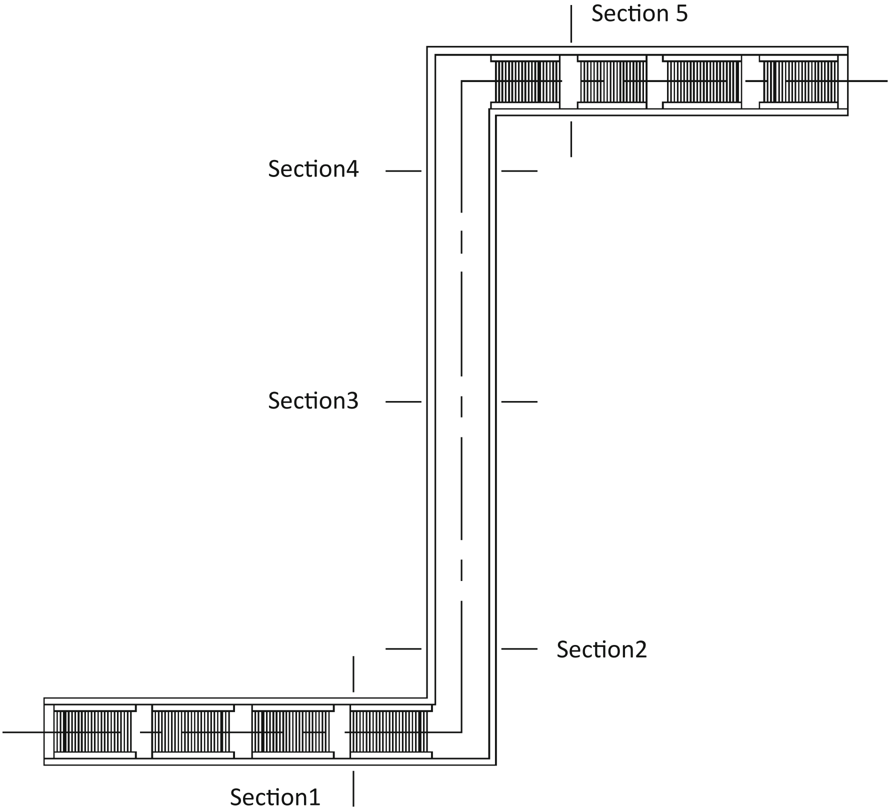

Fig. 1. Plan of Cuiliu street pedestrian underpass

Table 3. Data at the entrance of passage

Measuring position	Air temperature T (°C)	Air humidity φ (%)	Wind speed V (m/s)
Entrance	26.79	75.25	0.84

Table 4. Data of each section

Measuring position	Wind speed V (m/s)	Air temperature T (°C)	Wall temperature T (°C)	Air humidity φ (%)	Dew point temperature T (°C)	Whether dew
Section 1	0.94	27.39	26.55	75.67	24.71	No
Section 2	1.25	27.2	26.49	75.81	24.54	No
Section 3	1.13	27.17	26.57	75.27	24.23	No
Section 4	0.74	26.59	25.53	75.94	24.62	No
Section 5	1.34	26.62	26.2	76.23	24.97	No

4.1 Model Assumptions

The following basic assumptions are made to simplify the simulation process [9]:

(1) The airflow in an underground pedestrian passage is three-dimensional stationary incompressible viscous turbulence.
(2) Ignore the impact of the flow of people.
(3) Ignore the influence of channels, handrails, wall hangings, advertising and fire extinguishers, etc.
(4) Treating the stairway as a ramp without considering the influence of the rest platform.
(5) The influence of heat conduction and seepage on the inner wall of the channel is not taken into consideration.

4.2 Boundary Conditions

The simulated boundary conditions are determined by processing the measured data of the pedestrian underpass in Cui Liu street.

(1) Temperature boundary conditions

The air temperature at the entrance of the channel is 26.79 °C. The temperature of the left and the right walls are 26.6 °C, the top temperature is 26.2 °C, and the bottom temperature is 26.39 °C. The inner wall of the channel is considered as an insulating material without thermal conduction.

(2) Humidity boundary conditions

The humidity at the entrance of the channel is 76.25%, regardless of the influence of the water seepage on the wall and the influence of pedestrian wetting.

(3) Wind speed boundary conditions

The wind speed at the entrance of the channel is 0.84 m/s, and the direction of wind is parallel to the direction of the entrance of the channel.

5 Simulation Results Analysis

5.1 Wind Speed

The wind speed simulation in the pedestrian underpass of Chui Liu street is shown in Fig. 2. From the figure, the natural wind flows into the channel with the initial speed 0.84 m/s. With the same wind speed setting, wind speed increases in some parts of the channel, close to 1.6 m/s, and then directly outflow from the opposite outlet. There is a vortex at the corner of the entrance and exit, but it does not affect the overall ventilation effect. The wind speed in the main channel is between 0.5 m/s – 1.4 m/s, the variation is large, which is basically consistent with the measured data.

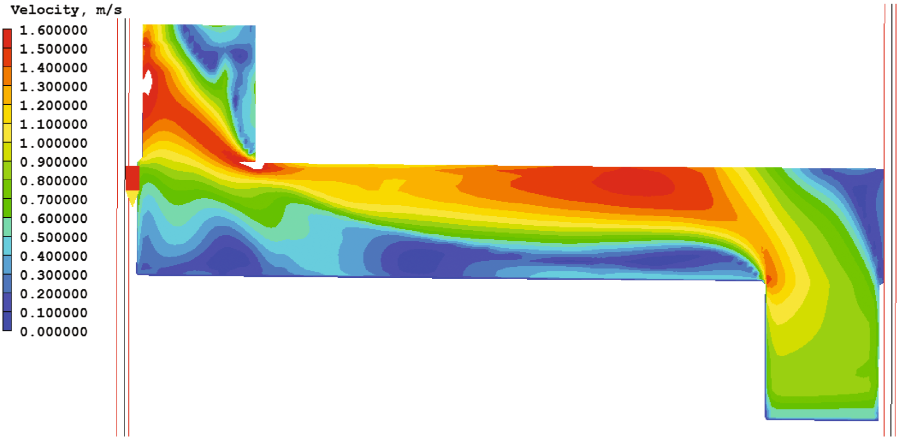

Fig. 2. Elevation wind speed picture of Cuiliu street urban pedestrian underpass

5.2 Air Age

Air age is the residence time of air in a channel. The smaller the air age is, the faster the wind speed is. The faster the air replacement rate is, and the better the air quality is. The air age distribution in the underpass of Chui Liu street is shown in Fig. 3. From the figure, the air age inside the channel is basically less than 250S, and the number of air changes is more than 14 times/h. At the junction of the entrance and the channel there is a vortex, and the air age is slightly larger, however the overall ventilation of the underground passage is better. Therefore, the air inside the channel is relatively fresh, which can meet the comfort requirements of pedestrians.

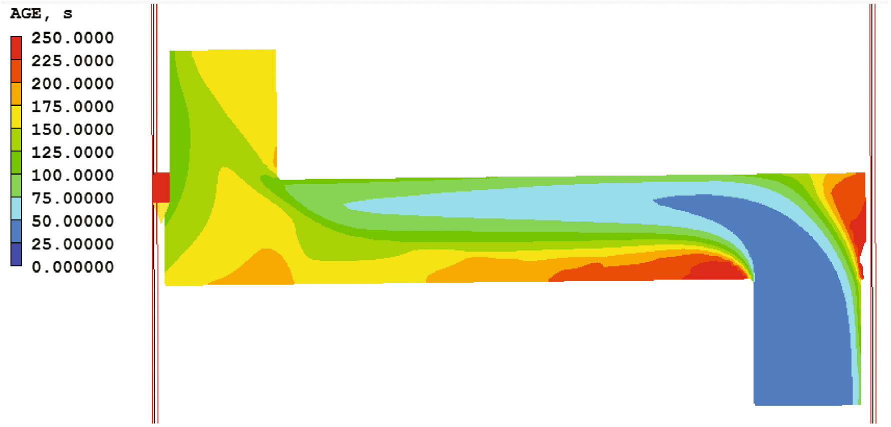

Fig. 3. Elevation air age picture of Cuiliu street urban pedestrian underpass

5.3 Temperature

The temperature distribution of Cuiliu Street pedestrian underpass shown in Fig. 4, we can observe from the figure that the air temperature inside the channel is basically between 26.71 °C to 26.79 °C, while the inlet temperature of the channel is the same as the set temperature and the outlet temperature is 0.8 °C lower than the setting temperature. The measured data is the inner cross section temperature of the channel, which is slightly higher than the inlet temperature. And the simulation and measurement are slightly deviation, mainly due to the influence of the personnel and lighting on the internal temperature of the channel.

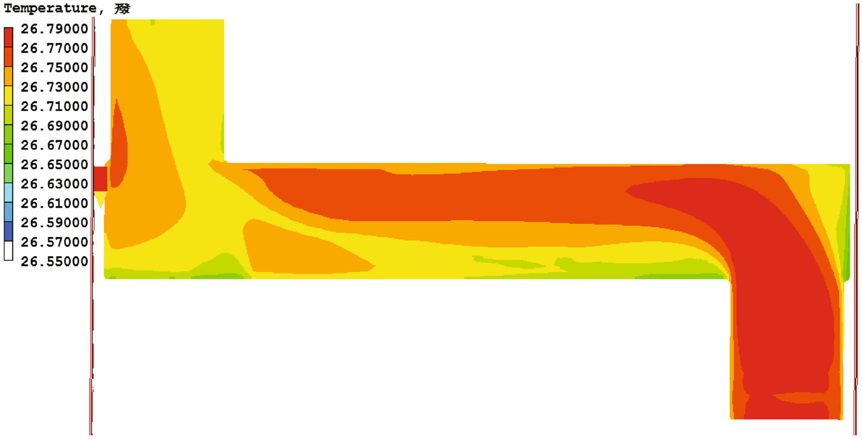

Fig. 4. Elevation temperature picture of Cuiliu street urban pedestrian underpass

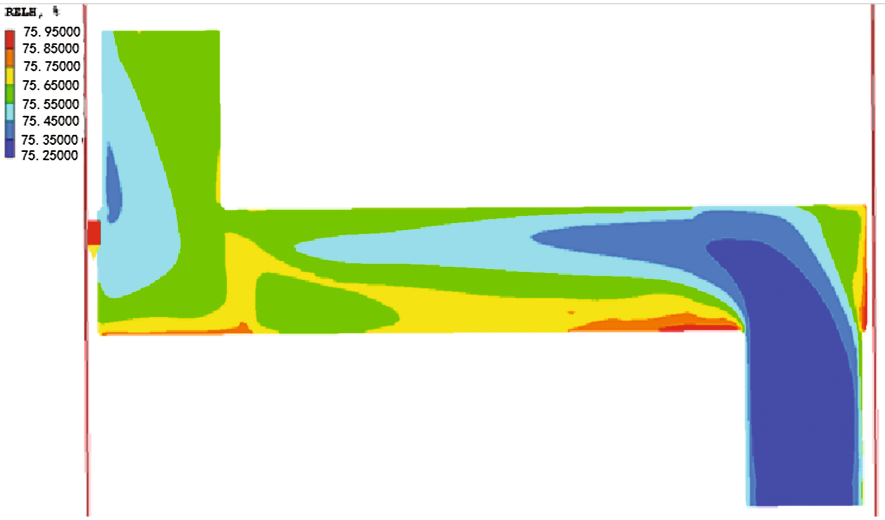

Fig. 5. Elevation humidity picture of Cuiliu street urban pedestrian underpass

5.4 Humidity

The humidity distribution in the pedestrian underpass of Cui Street is shown in Fig. 5, The relative humidity at the entrance of the channel is set at 75.25%, and the relative humidity inside the channel is basically between 75.25% – 75.95%. As difference between the wall temperature and air temperature is not large, it will not appear condensation phenomenon.

6 Conclusions

The method to avoid wet dew of underground facilities under natural ventilation is an evitable urge of the preliminary plan optimization evaluation for urban underground engineering design in southern china. In this paper, the field test to Z-shaped pedestrian underpass of Cuiliu Street in Wuhan city is carried out, along with the finite element numerical simulation set as compared test, we can draw the following conclusions:

(1) The numerical simulation results are close to the measured data, and the reliability of the CFD simulation method is verified. The method can be used to select the design scheme in advance.
(2) In the Z-shaped underground pedestrian underpass, the air flow rate is fast and the air age is shorter. Since the air is updated frequently, the ventilation effect is evident, and it is difficult to dew. The layout form is a better channel type for natural ventilation.
(3) For the poor ventilation channels in the corner area, considering the use of special materials, a circular arc shape and other measures are suggested to avoid condensation.

Acknowledgments. The research is supported by the Project for Building Science and Technology of Hu-bei Province, China (Grant Number 2013014), and the fifth phase of '333 project' in Jiangsu Province of China (Grant No. BRA2016113).

References

1. Ning-han, X.: Ventilation problem of shallow buried underground walkway. Build. Therm. Energy Vent. **20**(4), 46–48 (2001)
2. Guodong, W., Angui, L., Shaohui, Q.: Study on hot and humid environment test of underground pedestrian crossing in Xi'an. Build. Therm. Vent. Air Cond. **28**(2), 25–28 (2009)
3. Jingxuan, W., Haibo, S.: Experimental study and numerical simulation of flow field in subway station model. Energy Res. Inform. **24**(1), 39–43 (2008)
4. Blocken, B., Carmeliet, J., Stathopoulos, T.: CFD evaluation of wind speed conditions between passages between parallel buildings-effect of wall-material roughness modifications for the atmospheric boundary layer flow. J. Exp. Med. **95**(9–11), 941–962 (2007)

5. Limtrakarn, W., Nuansirikomon, S., Bunmongkolruksa, P., Kruenate, J.: Air ventilation and temperature distributions in strawberry greenhouse by computational fluid dynamics. Acta Hort. **719**(719), 173–180 (2006)
6. Bo, Z., Zhimin, G.: Numerical simulation of ventilation effect induced by underground garage. Sci. Technol. Eng. **9**(7), 1766–1771 (2009)
7. Fengdong, Y., Jun, Y.S., Xiangjin, Y.: Subway side platform air conditioning airflow CFD simulation. J. Southwest Jiaotong Univ. **40**(3), 303–307 (2005)
8. Xiyan, G., Chunsheng, Y., Xiangling, C., et al.: Study on CFD simulation of ventilation scheme in Harbin subway station. J. Archit. Sci. **23**(10), 23–27 (2007)
9. Gao, C.M., Weiliang, W.: Optimization of Underground Space Ventilation. Sci. Technol. Eng. **15**(12), 265–269 (2015)

Risk Assessment and Alignment Comparison Research on a Proposed Subsea Tunnel in Operation Periods

Lin Zhi and Chen Si(✉)

Chongqing Jiaotong University, Chongqing 400072, China
1154228184@qq.com

Abstract. The risk assessment process and method of subsea tunnel which from the point of risk identification, risk probability, consequences of loss grade, single risk and overall risk in the operation period was researched in this paper. We performed comparative study to the alignment selection and construction method of the subsea tunnel in the view of technical risk. We perform risk assessment and comparison analysis to the operational risk assessment and risk of each alignment plan with the method of investigation and expert scoring method and analytic hierarchy process, and combined with the risk assessment standards and methods at home and abroad from the eight points of fire, explosion, long distance ventilation system reliability, reliability of fire protection facilities, reliability and durability of tunnel under high water pressure, structural stability and durability, earthquake and flooding. Finally we concluded the minimum value of the alignment plan and construction methods and put forward the corresponding suggestions for the risk of the operation period of the project.

Keywords: Subsea tunnel · Technical risk · Risk assessment
Scheme comparison

1 Introduction

The cross sea tunnel generally has the characteristics of long axis, closed space, dense traffic flow, great difficulty in escaping and rescuing, and the probability of fire accident and the loss of the accident are greater. The risk accidents are often raised by a lot of complex and uncertain factors [1, 2]. These uncertain factors can be analyzed reasonably by risk assessment, and the unforeseen risk factors can be turned to quantitative indicators which provide the basis for the selection and decision of the project. However, there are few researches on the risk assessment of cross river tunnel operation at home and abroad, and the date is limited [3, 4]. Therefore, in order to accurately assess the cross river tunnel in construction period and operation period of the risk situation, it is necessary to introduce the advanced risk analysis theory for the specific characteristics of the project, and carry out further research work through the method of probability model to provide support for the scheme comparison in the feasibility study phase of the project [5].

© Springer Nature Singapore Pte Ltd. 2018

D. Zhang and X. Huang (Eds.): GSIC 2018, *Proceedings of GeoShanghai 2018 International Conference: Tunnelling and Underground Construction*, pp. 642–651, 2018.
https://doi.org/10.1007/978-981-13-0017-2_65

2 The General Situation of the Project

A cross-sea project spans the river. The recommended route is 24.005 km long. The length of the sea crossing is 22.365 km and the distance of the land is 1.64 km. In order to meet the driving demand and the future economic development plan, a two-way eight Lane Expressway with a maximum longitudinal gradient of 4% is proposed. (The risk assessment in this paper is to consider the traffic situation of vehicles without restriction of dangerous goods.) Through preliminary project feasibility study, three technical routes were preliminary selected. As shown in Table 1 below.

Table 1. Technical route chart for a cross sea project

Alignment project		Alignment A3	Alignment A4	Alignment A4-1
1	Structural type	East Tunnel + West Bridge	Long Tunnel	Long Tunnel
2	Tunnel length	6720 m	15190 m	13120 m
3	Route length	24005 m	22940 m	22755 m
4	Excavation method	Immersed tube method, Shield method	Immersed tube method, Shield method, Mining method	Immersed tube method, Shield method, Mining method

3 The Process and Method of Risk Assessment

3.1 Risk Source Identification and Risk Event Analysis

When undertaking system engineering, there are many factors that can cause risk, and the severity of the consequences is different. It is wrong to ignore these or omit the main factors completely [6]. However, consideration of every factor can lead to complicated problems and it is not appropriate. Risk identification is to reduce the uncertainty reasonably [7]. As shown in Fig. 1, we deeply analyze the risk events and risk source characteristics of each alignment based on extensive investigation of the domestic and foreign large scale river crossing tunnel engineering research results. At last, we get the main risk source of the cross-river tunnel on operation period are fire, explosion, reliability of long distance ventilation system, reliability of fire-fighting facilities, reliability and durability of tunnel waterproof on high hydraulic pressure, Structural stability and durability, earthquake and flooding etc.

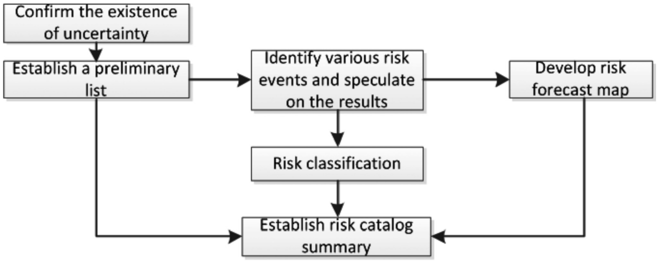
Confirm the existence of uncertainty
Establish a preliminary list
Identify various risk events and speculate on the results
Develop risk forecast map
Risk classification
Establish risk catalog summary

Fig. 1. Risk identification flow

3.2 Probability of Occurrence of Risk Event and Assessment Method of Consequence Loss

Engineering risk loss refers to any potential or external negative effects or adverse consequences in the process of construction or operation of the project which include casualties, economic losses, environmental impacts and other losses [8]. As shown in Fig. 2 is the overall risk assessment process.

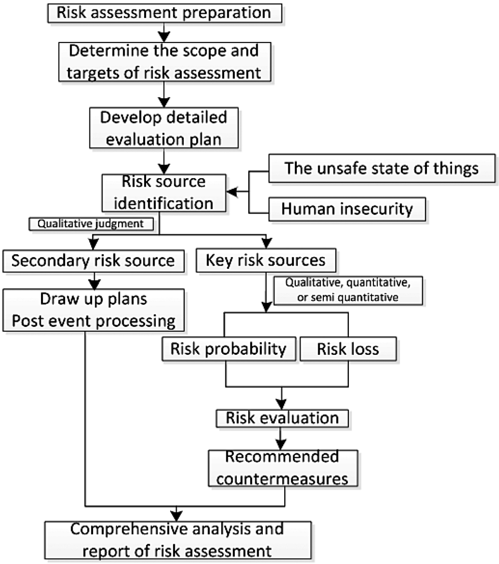
Risk assessment preparation
Determine the scope and targets of risk assessment
Develop detailed evaluation plan
The unsafe state of things
Human insecurity
Risk source identification
Qualitative judgment
Secondary risk source
Key risk sources
Qualitative, quantitative, or semi quantitative
Draw up plans Post event processing
Risk probability
Risk loss
Risk evaluation
Recommended countermeasures
Comprehensive analysis and report of risk assessment

Fig. 2. Risk assessment flow chart

The risk occurrence level of the cross-sea tunnel is referred to “the guidelines of design safety risk assessment for highway, bridge and tunnel”, and determined by expert investigation results and similar domestic engineering cases [9, 10]. The consequences of risk sources are mainly from the number of casualties, economic losses and environmental impact. Consider the differences of risk loss acceptance, we set different weight loss grade which is integrated with relevant risk assessment standards and expert findings at home and abroad. The risk occurrence probability and the consequence loss grade are shown in Tables 2 and 3 respectively.

Table 2. Risk occurrence level and criteria

Consequences	1	2	3	4	5
Probability	<0.03%	0.03%–0.3%	0.3%–3%	3%–30%	>30%
Risk describe	Rarely occur	Seldom occur	Occur by chance	May occur	Frequent occur

Table 3. Levels and criteria of risk consequences

Loss level	1	2	3	4	5
Casualties L_1	si < 5	dt < 3 or 5 < si < 10	3 < dt < 10 or 10 < si < 50	10 < dt < 30 or 50 < si < 100	dt > 30 or si > 100
Economic loss L_2	<5 mln	5–10 mln	10–50 mln	50–100 mln	>100 mln
Environment impact L_3	Covers a very small field, no groupment influence, resettlement < 50 persons	Covers a relatively small field, general groupment influence, resettlement 50–100 persons	Covers large field, regional economic and social activities influenced, resettlement 100–500 persons	Covers very large field, regional ecologic function missing, resettlement 500–1000 persons	Covers quite large field, ecological function severely disabled, resettlement > 1000 persons, normal economic and social activities strongly influenced
Weight value	0.8	0.9	1.0	1.1	1.2

3.3 Risk Level Determination

Different risk levels need to adopt different risk control measures, and in conjunction with risk evaluation matrix. As shown in Table 4 is the risk acceptance criteria of different levels.

Table 4. Risk level acceptance criteria

Risk level	Definition
I	Low risk, acceptable risk, effective current control measures
II	Moderate risk, accept the risk level conditionally, further preventive measures should be taken, improve the safety of bridge and tunnel
III	High risk, accept the risk level conditionally, we must implement control measures to reduce risk and contingency plans should be worked out
IV	Sky-high risk, effective control measures must be taken to reduce the risk level to level III and below, the project should be abandoned when the cost of the control measures is beyond the capacity of the risk taker

The risk should be graded quantitatively when we ensure the risk. In the alternatives, the highest level of risk will dominate the decisions made in the alternatives. The security risk level is sorted according to the score of each risk. As shown in the formula (1) is the calculation formula of risk score.

$$R = P \times \left(\sum\nolimits_{i=1}^{n} L_i \times W_i \right) \tag{1}$$

Where:

R—Risk score, Value range from 2.4 to 90;
P—Consequences, Value range from 1 to 5;
L_i—Risk level, Value range from 1 to 5;
W_i—Weight value of each risk, as shown in the Table 3;
n—Number of risk event, select in 1, 2, 3, represent Casualties, Economic loss and Environment impact.

3.4 Risk Grade Assessment Method for Single Risk Event

In this cross-sea tunnel project, the single risk events on operation periods include fire, explosion, long distance ventilation system reliability, reliability of fire protection facilities, reliability and durability of tunnel under high water pressure, structural stability and durability, earthquake and flooding. The expert investigation method is used for this project to research the domestic and foreign single risk event and assess the risk probability of a single risk event [11]. Through the single event scenario simulation, and through expert consultation, accident investigation and analytic hierarchy process (AHP), a comprehensive analysis of single event risk loss is made. From the three aspects of personnel loss, economic losses and social impact, the single event risk loss grade and the corresponding weight is obtained which are shown in Table 2.

$$R_i = P_i \times C_i \tag{2}$$

$$C = \sum (L_1 \cdot W_1, L_2 \cdot W_2, L_3 \cdot W_3) \tag{3}$$

3.5 Overall Risk Assessment Method of the Alignment

Based on the similar engineering case study at home and abroad, the combination of different single risk event probability and risk consequences of loss level and other factors, the expert investigation method was used to get the weight of different single event values, and then calculate the total risk score [12]. At the same time, according to the importance of the tunnel in different alignments, the weight of each risk event in different alignments plans is determined, and the overall risk line of different route schemes is obtained. As shown in the formula (4), the overall risk value of each line is calculated.

$$R = \sum R_i \times W_i \tag{4}$$

Where:

R_i—Risk value of single event;
W_i—Weight of single risk event, as shown in Table 5;
i—Single event count (Relating to structure).

Table 5. Weight of single risk event

Risk event	Fire	Explosion	Long distance ventilation system a reliability	Reliability of fire protection facilities	Reliability and durability of tunnel under high water pressure	Structural stability and durability	Earthquake	Flooding
Weigh	0.2	0.13	0.13	0.11	0.14	0.11	0.09	0.09

4 Risk Analysis of Each Line Scheme

4.1 The Same Risk Comparison of Each Alignment

There are fire and seismic risks in the alignment A3, A4 and A4-1 in the engineering feasibility study report. Tunnel fire and earthquake risk in each alignment were illustrated in Table 6.

Table 6. The same risk comparison of each alignment

Risk event	Method	Fire	Earthquake
A3	Immersed tube/Shield	28.2	18.0
A4	Immersed tube/Shield	37.6	52.8
	Drill-and-blast + Shield	41.6	
A4-1	Immersed tube/Shield	37.6	52.8
	Drill-and-blast + Shield	41.6	

The risk score of fire and earthquake to Alignment A4 and A4-1 are fairly similar, but they are all higher than the alignment A3.

(1) The fire risk of alignment A4 = the fire risk of alignment A4-1 > the fire risk of alignment A3;
(2) The earthquake risk of alignment A4 = the earthquake risk of alignment A4-1 > the earthquake risk of alignment A3.

4.2 The Comparison of Alignment A3

Due to the limitation of the aviation limit, a shallow tunnel plan of alignment A3 is put forward. Therefore, the immersed line method and shield method are preferred for the alignment A3 tunnel. According to the risk grade evaluation method of single risk event proposed in the Sect. 3.4, the single risk event assessment table of alignment A3 in Table 7 is obtained. According to the single risk event analysis, it can be seen that whether immersed tunnel or shield tunnel, there are 3 level III risks which are fire, structural stability and durability, earthquake and 1 level IV risk which are explosion. As shown in the Table 7, the risk ranks are same. But the alignment A3 should be recommend due to the considering of better connection between the tunnel and the network of road, the advantages of the traffic function and the driving safety, comfort and traffic function of operation period.

Table 7. Overall risk assessment of Alignment A3

Excavation Method	Risk rank	Tunnel length	Section size	Risk score $(\sum_{i=1}^{n} R_i \times W_i)$
Immersed tube	IV × 1, III × 3, II × 4	Full length 6720 m, dark hole 6085 m, immersed tube section 5700 m	47.2 m × 11.5 m	21.732
Shield	IV × 1, III × 3, II × 4	Full length 7760 m, dark hole 7100 m, shield section 6100 m	14.3 m (diameter)	21.732

4.3 The Comparison of Alignment A4

As can be seen from the engineering feasibility study document, the alignment A4 has no interference to navigation, flood control, aviation limitation and riverbed evolution. It is the least contradictory scheme. There are three kinds of evacuation method for alignment A4. They are immersed tube method, shield method and two ends shield and middle drilling method. From the single risk event analysis, regardless of the immersed tube method, shield method or shield + combination of drilling and blasting method, there are 3 level IV risks which are tunnel fires, explosions and earthquakes. There are 3 level III risks in the immersed tube method and shield construction method which are the stability and durability of the tunnel structure, the reliability of long distance ventilation and water flooding. The shield and drilling and blasting combination method has 4 level III risks which are structural stability and durability, waterproof reliability and durability, reliability of long distance ventilation and flooding. As shown in Table 8, the risk score of combination method of shield and drilling and blasting is larger than immersed tube method and shield method. And it is recommended to abandon the construction method of shield and drilling and blasting. Considering of better connection between the tunnel and the network of road, the advantages of the traffic function and the driving safety, comfort and traffic function of operation period, the whole immersed tunnel project were recommended to alignment A4.

Table 8. Overall risk assessment of Alignment A4

Excavation Method	Risk rank	Tunnel length	Section size	Risk score ($\sum_{i=1}^{n} R_i \times W_i$)
Shield + drilling blasting	IV × 3, III × 4, II × 1	Full-length 16410 m	Shield (diameter) 14.3 m Drilling and blasting (diameter) 13.0 m	33.682
Immersed tube	IV × 3, III × 3, II × 2	Full length 15190 m, dark hole section 14620 m, immersed tube section 14245 m	47.2 m × 11.5 m	31.7
Shield	IV × 3, III × 3, II × 2	Full length 16410 m, dark hole section 15870 m, shield section 14770 m	Shield (diameter) 14.3 m	31.7

4.4 The Comparison of Alignment A4-1

The alignment A4-1 scheme is a long tunnel plan. In this scheme, the tunnel has 3 recommended schemes which are drilling blasting and shield scheme, fully immersed tube scheme and full shield scheme. As shown in Table 9, the operational period risk is the least and the risk score is 31.37 when alignment A4-1 uses the immersed tube or shield tunnel scheme. When drilling and blasting + shield are adopted, the risk is the highest, and the risk score is 33.862. From the analysis of single risk event, alignment A4-1 regardless of the immersed tube method, shield method or shield + drilling and blasting method, there are three level III risks which are the tunnel fire, explosion and earthquake. There are three level III risks in the immersed tube method and shield construction method which are the stability and durability of the tunnel structure, the reliability of long distance ventilation and water flooding. Three are four level III risks in the shield + drilling and blasting method which are structural stability and durability, waterproof reliability, durability, reliability of long distance ventilation and flooding. Considering of better connection between the immersed tunnel and the network of road, the advantages of the traffic function and the driving safety, comfort and traffic function of operation period, the whole immersed tunnel project were recommended to alignment A4-1. From the view of operation risk, the risk score of alignment A4-1 is higher than alignment A4. So the alignment A4-1 isn't as thorough scheme selection.

Table 9. Overall risk assessment of alignment A4-1

Excavation method	Risk rank	Tunnel length	Section size	Risk score ($\sum_{i=1}^{n} R_i \times W_i$)
Shield + drilling blasting	II × 1, III × 4, IV × 3	Full-length 16410 m	Shield (diameter) 14.3 m drilling blasting 13.0 m	33.682
Immersed tube	II × 4, III × 3, IV × 1	Full length 15190 m, dark hole section 14620 m, immersed tube section 14245 m	47.2 m × 11.5 m	31.37
Shield	II × 4, III × 3, IV × 1	Full length 16410 m, dark hole section 15870 m, shield section 14770 m	Shield (diameter) 14.3 m	31.37

4.5 Overall Risk Comparison of Each Alignment

In summary, it can be seen from the quantity of risk that the number of operational A3 alignment III Risk and the risk of IV (very high risk) are less than the A4 and A4-1 (Table 10). That is A3 < A4 < A4-1. From the point of view of the risk score, the overall risk size of each route plan during the operation period is: A3 < A4 = A4-1. That is the A3 line scheme has the lowest overall risk during operation.

Table 10. Overall risk comparison of each alignment

Alignment	Excavation method	Risk rank	IV risk events	Risk score
A3	Shield	II × 5, III × 3	None	15.88
	Immersed tube	II × 5, III × 3		15.88
A4	Shield	II × 3, III × 4, IV × 1	Earthquake	21.02
	Immersed tube	II × 3, III × 4, IV × 1		21.02
	Shield + drilling blasting	II × 2, III × 5, IV × 1		21.97
A4-1	Shield	II × 3, III × 4, IV × 1	Earthquake	22.24
	Immersed tube	II × 3, III × 4, IV × 1		22.24
	Shield + drilling blasting	II × 2, III × 5, IV × 1		22.94

5 Conclusion

(1) This paper carried out risk identification and evaluation calculation which aiming at proposed submarine tunnel. And the occurrence probability of risk model, consequential loss model and security risk rating were put forward. The risk score of each alignment and the excavation method were got through the assessment of eight single risk events.

(2) The full shield scheme of alignment A3 was chosen as the minimum overall risk plan through the risk score comparison of the number of casualties, economic

losses and environmental impact. And the comparisons provide scientific and reasonable support for the project feasibility study phase comparison.

(3) The risk assessment methods and processes used in this paper are of universal applicability, and have certain reference value for similar projects across the sea. If further analysis of each risk source is carried out, a risk tracking analysis system can be established to implement dynamic risk assessment, thereby improving the accuracy of risk assessment.

(4) According to the risk assessment results of each line plan, combining with the most basic calculation formula R = P C. If we want to reduce or avoid the risk of transporting dangerous articles in the tunnel, one is to reduce the probability of the risk. Two, once the risk event occurs, try to reduce the loss. Through the investigation and analysis of domestic and foreign dangerous goods vehicle control of the basic measures are as follows: to limit the dangerous goods vehicle transit time, speed limit or to maintain the minimum driving distance, guided vehicle escort passage.

In view of the difficulty of dangerous goods vehicle traffic control, the study on how to control the dangerous goods vehicles was proposed in the next phase. And the study was based on the conclusion of operation period and the characteristics of this project.

References

1. Yonghong, W., Bing, L., Yonggang, Z.: Risk assessment on Bohai bay subsea tunnel in its operational period. China Eng. Sci. **12**, 107–112 (2013)
2. Haoran, S., Dingli, Z., Guangzong, T.: Study on risk assessment and control of Dalian bay subsea tunnel. J. Beijing Jiaotong Univ. **37**(4), 1–6 (2013)
3. Shiyang, L.: Case Study on design of Dangjinshan super-long tunnel on Dunhuang-Golmud railway. Tunn. Constr. **5**, 452–459 (2014)
4. Leiyu, G., Hongwei, H., Qunfang, H.: Risk assessment on one sub-sea tunnel in its operational period. J. Underg. Space Eng. **3**(s1), 1236–1240 (2007)
5. Feng, Z., Yongdi, Z., Yongxu, X.: Research on quantitative analysis model of operating risk in road tunnel. West. Traffic Sci. Technol. **5**, 67–71 (2010)
6. Zhou, J., Baojun, D., Limao, Z., et al.: Risk assessment of the operational tunnel leakage based on bayesian networks. Environ. Eng. (s1), 922–927 (2014)
7. Shufei, C.: Highway tunnel operation risk evaluation based on fuzzy hierarchical analysis. Railw. Constr. Technol. (s1), 922–927 (2014)
8. Zhongsheng, T., Mengshu, W., Shixiang, L.: Simulation experiment of pumped sand on immersed tunnel. Chin. Eng. Sci. **11**(7), 39–44 (2009)
9. Zhi, L., Senyang, W.: Tunnel operation safety risk assessment methods. China Highw. **5**, 110–114 (2016)
10. Jun, S.: Risk analysis on construction of taiwan strait tunnel. Tunn. Constr. **29**(3), 257–262 (2009)
11. Jianxun, C., Yanbing, L., Jiuchun, J.: Operating highway tunnel safety evaluation. Mod. Tunn. Technol. **43**(4), 68–71 (2006)
12. Gengyao, S.: River-crossing or sea-crossing project: bridge, tunnel or bridge-tunnel combination. Tunn. Constr. **35**(7), 611–615 (2015)

Ventilation Effect and Optimum Design of an Urban I-Shaped Pedestrian Underpass

Yong Wang[1,2(✉)], Xiongwei Li[3], Min Wang[4], Yanli Wang[5],
and Jianbin Chen[6]

[1] State Key Laboratory of Geomechanics and Geotechnical Engineering,
Institute of Rock and Soil Mechanics, Chinese Academy of Sciences,
Wuhan 430071, China
[2] College of Engineering, Swansea University, Swansea SA2 8PP, UK
wang831yong@126.com
[3] School of Civil Engineering and Architecture, Changzhou Institute
of Technology, Changzhou 213002, China
lixww@126.com
[4] Rockfield Software Ltd., Swansea SA1 8AS, UK
sacewangmin@gmail.com
[5] Key Laboratory of Geotechnical Mechanics and Engineering of the Ministry
of Water Resources, Yangtze River Scientific Research Institute,
Wuhan 430010, China
wyldhh@126.com
[6] Wuhan Municipal Engineering Design & Research Institute Co., Ltd.,
Wuhan 430023, China
409976046@qq.com

Abstract. To reveal the reason for moisture condensation of an I-shaped pedestrian underpass in the summer, which is widely constructed in many large southern cities of China, its ventilation effect was investigated under a hot, rainy, and humid climate condition. Through in situ monitoring of the Yuejiazui I-shaped pedestrian underpass in Wuhan City, China, some internal environment parameters, such as the wind speed, relative humidity, air temperature, and wall temperature, were recorded and analyzed systematically. Then, with computational fluid dynamics (CFD), numerical simulation studies were conducted by comparing the field measured data. The results show that the main tunnel of the I-shaped underpass cannot achieve effective natural ventilation, and the underpass is often in a higher humidity state in the summer; therefore, it is prone to serious moisture condensation. Meanwhile, the Magnus formula was used to investigate the cause of moisture condensation. To improve the ventilation effect of the underpass, different optimization models were compared by CFD numerical simulations to further validate the rationality of the optimization scheme. The results can provide references for the design of urban pedestrian underpasses in hot-moist climate regions.

Keywords: Urban transportation · Pedestrian underpass · Ventilation
Moisture condensation

© Springer Nature Singapore Pte Ltd. 2018
D. Zhang and X. Huang (Eds.): GSIC 2018, *Proceedings of GeoShanghai 2018 International Conference: Tunnelling and Underground Construction*, pp. 652–665, 2018.
https://doi.org/10.1007/978-981-13-0017-2_66

1 Introductions

Urban pedestrian underpasses are an important way to resolve the problems of urban pedestrian road crossings, traffic jams and three-dimensional transportation. Underpasses can solve heavy traffic flow from various directions, which is preferable in view of road safety and saving time [1]. In recent years, with rapid socio-economic development in China, many cities are beginning to construct pedestrian underpasses below city expressways, especially in big cities located in southern economic developed areas. I-shaped underpasses are widely adopted and constructed. The main tunnel of an I-shaped underpass is vertical to the municipal road, while the stairs and ramps of the entrance and exit are parallel to the sidewalks. This layout plan has many advantages, such as good entrance visibility, easy pedestrian guidance and saving space. However, because there is a hot-moist and rainy climate in the southern regions of China, I-shaped underpasses are prone to moisture condensation in the summer. The interior of the main tunnel is often in a "wet" state for a long time, and the interior even produces water droplets like rain falling on the ground. This problem is inconvenient to passersby.

In China, because the current specification "Technical specifications of urban pedestrian overcrossing and underpass (CJJ69-95)" [2] does not provide specific criteria for the internal environment of pedestrian underpass, the designer only refers to other relevant specifications, such as "Code for design of civil air defense basement" [3], "Thermal environmental conditions for human occupancy" [4], and "Code for design of metro" [5]. In fact, as a transitional space structure, the underpass is different from the subway or subterranean commercial streets, so the structure cannot be copied blindly. It is necessary to put forward specific indexes to control the internal environment, especially for ventilation.

Ventilation has a significant effect on the internal environment of a pedestrian underpass. Improving ventilation is also the basic means to solve the problem of moisture condensation in underpasses. As a transitional space structure, an underpass should be designed for energy conservation and emission reduction. Under the requirement to meet the basic functions, it should adopt as much natural ventilation as possible to reduce late operation and management costs. Only when natural ventilation is insufficient to meet requirements should auxiliary mechanical ventilation be used. Van Der Voordt [1] earlier studied the requirements for design of pedestrian underpasses, but he thought natural ventilation was enough. Yang et al. [6], and Wang et al. [7] conducted an internal environmental survey of six pedestrian underpasses in Xi'an, explored the variation laws and influencing factors of each parameter, and gave a preliminary evaluation for the environmental conditions of urban pedestrian underpasses. Ning et al. [8] and Xie et al. [9] surveyed and simulated the ventilation environment of urban pedestrian underpasses. However, until now, much research focuses on the ventilation of traffic, railway and subway tunnels as well as building basements [10–15], but few studies exist on pedestrian underpasses.

In this work, the Yuejiazui I-shaped pedestrian underpass in Wuhan, China, was selected to monitor its internal environmental parameters in the hot-moist and rainy summer climate. To explore the cause of moisture condensation for the I-shaped pedestrian underpass in the summer, its natural ventilation effect and variation of internal environment parameters, such as the wind speed, air temperature, air age, relative humidity, and wall temperature, were analyzed using computational fluid dynamics (CFD), and the measurement results were compared. Then, the optimization design and improvement suggestions were proposed, and the rationality was validated at the same time.

2 Field Test

The Yuejiazui pedestrian underpass is located at the inner ring municipal road of Wuhan. Near the underpass, there is a large commercial shopping center metro, and it is very crowded. The main tunnel length of the Yuejiazui underpass is 77 m, and the depth is approximately 10 m. Its plane layout is I-shaped, as shown in Fig. 1. Although a ventilation system of jet fans has been installed in the underpass, the moisture condensation problem is still very serious in the summer. Therefore, typical sections of the underpass were selected for field tests to analyze the reasons for moisture condensation.

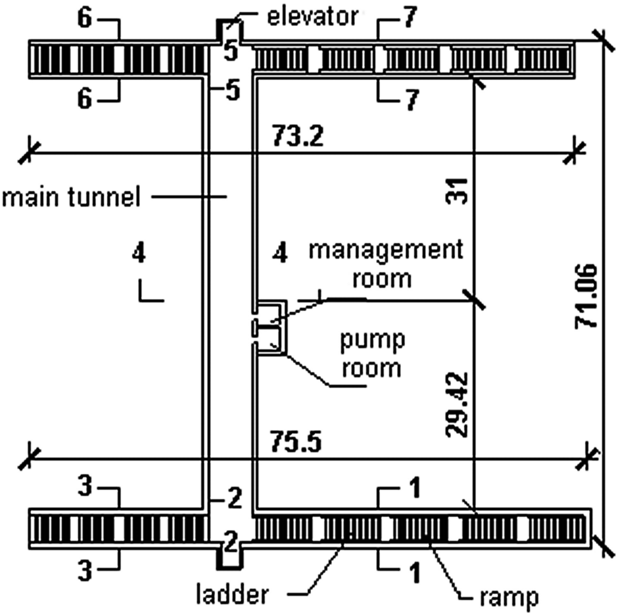

Fig. 1. Floor plan of Yuejiazui pedestrian underpass (unit: m).

2.1 Test Contents

The field monitoring test was carried out during the Wuhan summer (from July to August), which is a hot, rainy, and humid climate. It is the season most prone to causing moisture condensation in the underpass. There were six typical internal sections to be measured, including the parts of the entrance and exit on both sides of main tunnel. Each section tested the concerned parameters, such as the wind speed, air temperature, relative humidity, wall temperature, wall thermal conductivity, dew point temperature, ventilation rate and so on. The field monitoring and data collection are shown in Fig. 2.

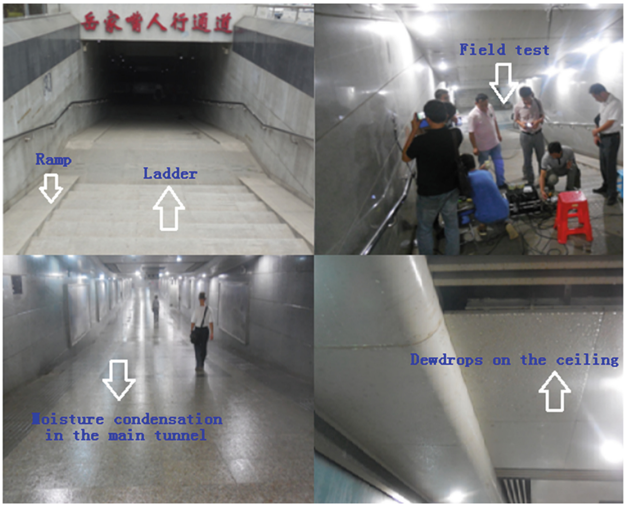

Fig. 2. Field monitoring and data collection in the Yuejiazui pedestrian underpass.

2.2 Test Equipment

The test equipment includes a mechanical thermo-hygrometer, a handheld thermo-hygrometer, a hand-held anemometer, an electronic hygrometer, an infrared thermometer, a wall heat flow meter, a dew point hygrometer, and a multi-channel data acquirement and process system.

2.3 Test Plan

The relative humidity of the atmosphere in Wuhan is high throughout a year, and the mean monthly humidity is more than 70%. Especially in July and August, the average air moisture content is the highest, approximately 19.5 g in per kilogram of dry air. We selected a typical sunny day in July and August, 2014 as the research object and investigated the hourly report of meteorological parameters of the day. It was found that the maximum dew point temperature occurred at 23:00 on July 22 and at 0:00 on August 22. Then, it is concluded that the early hours of a day in the summer are prone to condensation. Therefore, the monitoring test was conducted from 22:00 to 8:00 the next day to record the environmental parameters of each section under the most likely condensation conditions. To ensure the representation and accuracy of the sampling data, the field works for data collection were completed in three days, respectively, a rainy day (July 21), a sunny (July 31) and a cloudy day (August 11). During each day, the monitoring sections of the underpass were tested back and forth four times to observe the change law of the cross-section measuring point parameters.

2.4 Test Results and Analysis

Figure 3 shows the temperature difference curves between the air and the wall as well as the relative humidity of a central point section, which is located at the average height of a pedestrian. During the test, the air relative humidity at the entrance and exit on both sides is 67.62%. It can be seen from Fig. 3 that the air relative humidity inside the main tunnel is higher than 80% and is even higher than 85% on July 21. Generally, the air temperature inside the underpass is higher than the wall temperature of 1–4 °C. The temperature difference and relative humidity in Section 4-4 are higher. In addition, during the triple tests under typical weather, different degrees of condensation phenomenon occurred on the wall and ceiling of the main tunnel. Especially on July 21, the condensation was the most serious, and it caused the emergence of continuous water drops. Figure 4 shows that because of the four jet fans installed on the ceiling in the middle of the main tunnel, the data of the internal wind speed are unstable; however, the data on July 31 (the jet fans worked on the day) including the internal wind speeds of the section points are smaller than those near the entrance and exit. Thus, it can be found that the ventilation effect is not obvious; although, jet fans were used to improve the internal ventilation. Furthermore, the relative humidity inside the underpass is still high, which causes the problem of moisture condensation.

According to the Magnus formula, $T > 0$ °C

$$E = E_0 \times 10^{\left(\frac{17.27T}{235+T}\right)} \tag{1}$$

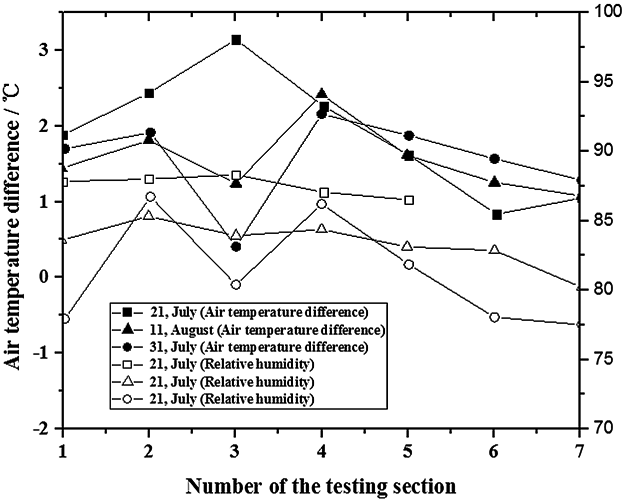

Fig. 3. Curves of air temperature difference and relative humidity in different testing sections.

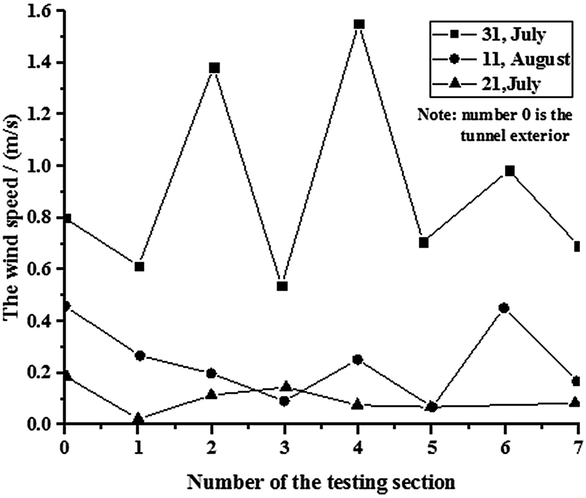

Fig. 4. Wind speed curves in different testing sections of the underpass.

T $\leq$ 0 °C,

$$E = E_0 \times 10^{\left(\frac{9.5T}{265+T}\right)} \tag{2}$$

where E is the saturation vapor pressure at a temperature, E_0 is the saturation vapor pressure at 0 °C, and E_0 = 611 hPa; T is the current temperature, °C.

The relative humidity is found by the following:

$$rh = \frac{e}{E} \times 100\% \tag{3}$$

Where rh is the relative humidity, and e is the actual vapor pressure in per unit volume of air.

According to formulas (1), (2) and (3), the saturation vapor pressure increases with the increase of temperature, and the dew point temperature can be calculated in the case that the absolute moisture content when the temperature in per unit volume of air is known. As seen from Fig. 3, the wall temperature is generally lower than the air temperature inside the underpass, and the air relative humidity is greater than 80%. Therefore, the moisture condensation phenomenon is because the air humidity inside the underpass reaches or exceeds the vapor saturation value under the vapor pressure corresponding to the wall temperature. In other words, at any time, if the air absolute humidity around the wall is larger than the saturation absolute humidity corresponding to the wall temperature, the condensation will appear on the wall. From the above formula, we can also draw the conclusion that to solve the problem of moisture condensation in the underpass, ultimately, the air humidity inside the underpass needs to be reduced or the temperature difference between the air and wall inside the tunnel needs to be decreased.

For the Yuejiazui I-shaped pedestrian underpass, even though jet fans are installed to improve ventilation, the fans did not reduce the air humidity inside the tunnel, so the effect was not obvious. The main reason is that the air temperature inside the tunnel is usually lower than that of the outdoor air in the summer. Cold air drops and warm air rises, so air with higher humidity and lower temperature gathers in the main tunnel of the underpass, which is in a relatively deep location. The jet fans can only promote the air to flow within the main tunnel but cannot achieve air circulation between the inside and outside of the underpass. Therefore, there is no obvious effect on reducing the relative humidity and increasing the air temperature inside the main tunnel with this type of mechanical ventilation.

3 Analysis of Numerical Simulation

3.1 Numerical Model

In recent years, the CFD method has been widely used in many research areas [16–20]. In this work, the three-dimensional numerical models of underpasses were built with the Fluent software, and the CFD method was adopted to analyze their internal environment parameters, such as the air flow, temperature, air humidity, air age, and wind speed, based on the meteorological data in Wuhan.

3.2 Boundary Condition

The measured data of the Yuejiazui I-shaped pedestrian underpass were screened to yield their average values as the boundary condition of the numerical models. In three-dimensional numerical models, the air temperature near both sides of the entrances is 29.5 °C, the air relative humidity is 67.6%, the wind speed is 0.80 m/s, the wall temperature inside underpass is 25.5 °C, the top ceiling temperature is 26.1 °C, and the ground floor temperature is 25.3 °C.

3.3 Numerical Simulation Results

According to the construction structure of Yuejiazui pedestrian underpass, a three-dimensional simulation model was established to conduct the computational analysis. The ventilation volume of the I-shaped underpass is selected as 32.20 kg/s.

Figures 5(a) and (b) are the vector graphs of wind speed inside the underpass yielded by the simulation. It can be seen from the figures that natural wind flows into the underpass from both sides of the entrance, but the wind outflows directly from the opposite exit. At the junction of the main tunnel and the stairs and ramps, the vortex phenomenon emerges; there is no natural airflow in the main tunnel, so the I-shaped underpass does not achieve good natural ventilation. Figures 5(c) and (d) are the calculated wind speed distributions. After investigating the data of the same sections of the field measurements, it can be found that the wind speed at the stairs and ramps section changes from 0.6 m/s to 1 m/s. The wind speeds at different areas of the main

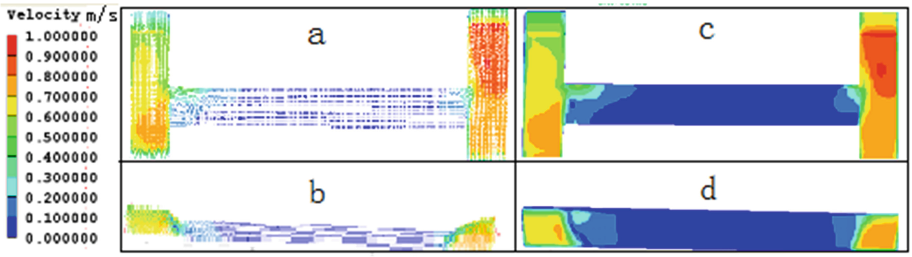

Fig. 5. Wind speed yielded by CFD simulations inside the underpass: (a) vector graph of wind speed in the floor plan, (b) wind speed vector graph of main tunnel in the elevation, (c) wind speed distribution in the floor plan, and (d) wind speed distribution of main tunnel in the elevation.

tunnel are 0–0.1 m/s. The jet fan in the actual underpass causes the wind speed simulation results to be different from the measured data.

Figures 6(a) and (b) are the air age distributions inside the underpass yielded by simulations. It can be seen from the figures that the air age inside the main tunnel is within 200 s–600 s, and the ventilation frequency is from 6 to 18 times per hour. The natural ventilation effect inside the main tunnel of the I-shaped underpass is very poor. However, the air ages in the stairs and ramps section near the entrance are smaller, and most of ages are less than 150 s. The ventilation frequency is approximately 24 times per hour, where the better ventilation can be achieved.

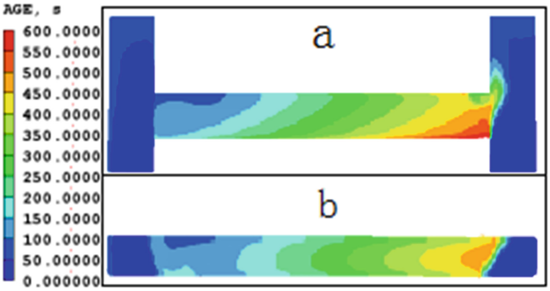

Fig. 6. Air age yielded by CFD simulations inside underpass: (a) air age distribution in the floor plan, and (b) air age distribution of main tunnel in the elevation.

Figures 7(a) and (b) are the air temperature distributions inside the underpass, The air temperature distribution in the main tunnel of the Yuejiazui underpass is relatively lower than that outside, which is between 26.4 °C and 28.1 °C. However, the air temperature in the stairs and ramps section near the entrance is very close to the outdoor temperature, approximately 28.8 °C to 29.5 °C. The simulated air temperature inside the underpass is slightly higher than the field measures, but the laws of their overall distribution are similar.

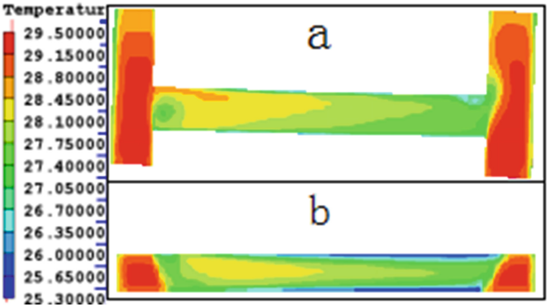

Fig. 7. Air temperature yielded by CFD simulations inside underpass: (a) air temperature distribution in the floor plan, and (b) air temperature distribution of main tunnel in the elevation.

Figures 8(a) and (b) are the air relative humidity distribution yielded by CFD simulations inside the underpass. It can be seen from the figures that the relative air humidity inside main tunnel of the Yuejiazui underpass is large, from 67.6% to 86.5%; while the air humidity in the stairs and ramps section is close to the set value, approximately 67.6% to 73.27%. The calculated internal air humidity distribution agrees well with the field measurements.

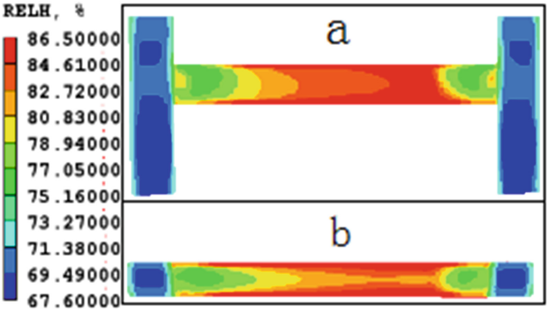

Fig. 8. Relative humidity yielded by CFD simulations inside underpass: (a) relative humidity distribution in the floor plan and (b) relative humidity distribution of main tunnel in the elevation

On the whole, the simulation results have a good correspondence with the measured data, illustrating that the CFD simulation is an effective method to analyze the internal environment conditions of pedestrian underpasses. Meanwhile, it can intuitively reflect that poor natural ventilation exists inside the main tunnel of the Yuejiazui I-shaped pedestrian underpass.

4 Optimization Design

4.1 Optimization Model

As the pedestrian underpass is built below the ground, the air temperature inside the underpass is lower than that of the outdoor air in the summer, so it is difficult to form an air pressure difference on both sides of the main tunnel to promote airflow. Furthermore, the stairs and ramps are vertical to the main tunnel, causing difficult air circulation inside the main tunnel. As can be seen from Fig. 9, if the plane layout of the I-shaped underpass changes from Fig. 9(a) to (b) or (c), natural wind will be introduced into the main tunnel to improve the ventilation effect. In other words, a certain angle should exist between the inlet and outlet, avoiding parallel operation. In the following section, the method is the same as the above CFD simulation. The internal environment of underpasses in Fig. 9(b) and (c) were analyzed for comparison with the conventional I-shaped underpass in Fig. 9(a).

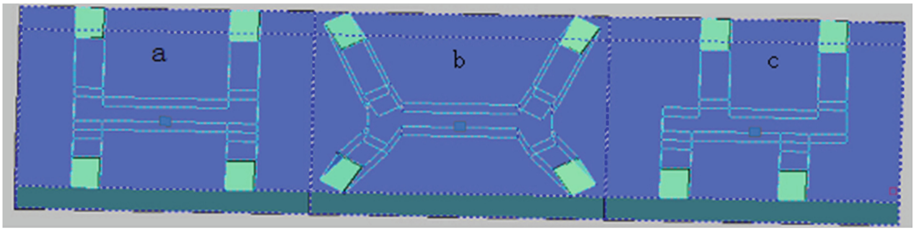

Fig. 9. I-shaped underpass and its optimization models.

The underpass main tunnel of the numerical model is 50 m long, the width is 8 m, and the height is 5 m. The length of the stairs and ramps on both sides of the main tunnel is 25 m, and the width is 6 m. The boundary conditions of the models were set referring to the field measured data of the Yuejiazui pedestrian underpass. The air temperature at the entrance was set as 30 °C, the air relative humidity is 70%, the wind speed is 1 m/s, and the wall temperature of the interior was set as 26 °C.

4.2 Numerical Simulation Analysis

Figures 10(a), (b), (c) and (d) are the wind speed comparisons between the conventional I-shaped underpass and the optimization models yielded by the CFD simulations. For the conventional underpass shown in Fig. 9(a), the natural wind flows into the entrance of the underpass and directly out of the opposite exit, so there is relatively no wind to flow into the main tunnel. Comparatively, the condition of the mode in Fig. 9 (c) is the best, in which most of the natural wind flows through the underpass. The model in Fig. 9(b) is slightly better than that of Fig. 9(a). Although there is natural wind flowing through the stairs and ramps on both sides, the wind speed inside the main tunnel is nearly equal to zero. However, for the model in Fig. 9(c), the wind speed inside the main tunnel is above 0.3 m/s.

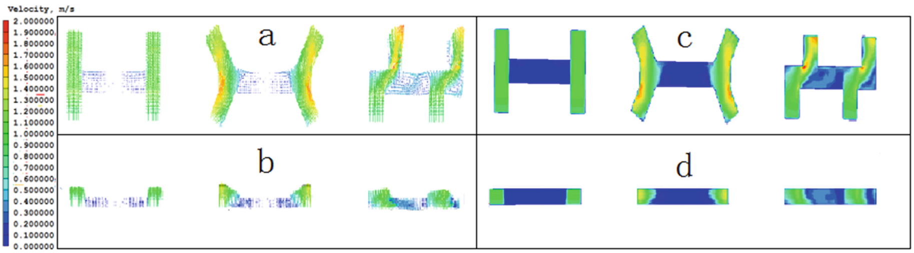

Fig. 10. Wind speed of optimization models yielded by CFD simulations: (a) wind speed vector graph in the floor plan, (b) wind speed vector graph of main tunnel in the elevation, (c) wind speed distribution in the floor plan, and (d) wind speed distribution of main tunnel in the elevation.

Figures 11(a) and (b) show the air age comparisons between the conventional I-shaped underpass and the optimization models yielded by CFD simulations. For the model in Fig. 9(a), air ages inside the main tunnel of the underpass are larger than 1200 s, and the ages are above 2000 s in the middle area. For the model in Fig. 9(b), the air ages in a small area of the main tunnel are approximately 1000 s, and most of areas have ages less than 500 s. Comparatively, the ventilation condition of the model in Fig. 9(c) is the best, in which air ages of the main tunnel are mainly less than 200 s.

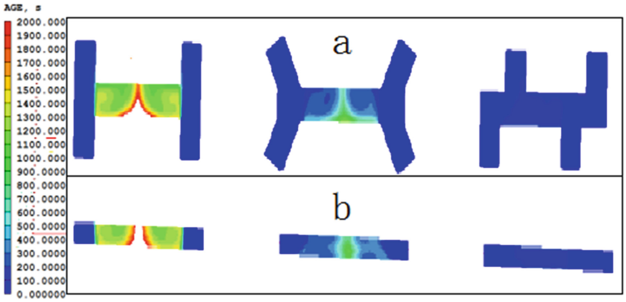

Fig. 11. Air age of underpass optimization models yielded by CFD simulations: (a) air age distribution in the floor plan, and (b) air age distribution of main tunnel in the elevation.

Figures 12(a) and (b) are the comparisons of air temperature distribution between the conventional and optimized models of the underpass yielded by CFD simulations. It can be seen that air temperatures near the inlet and outlet are close to the outdoor atmospheric temperature of 30 °C, while that inside the main tunnel is close to the wall temperature of 26 °C, without considering disturbances from the lights and pedestrians. There is an approximate 4 °C temperature difference of air between the main tunnel and the outdoor environment. For the model in Fig. 9(b), the air temperature in the middle area of the main tunnel is the lowest; the temperature is higher on both sides, but most areas have temperatures between 27.5 °C and 29 °C. Similarly, the air

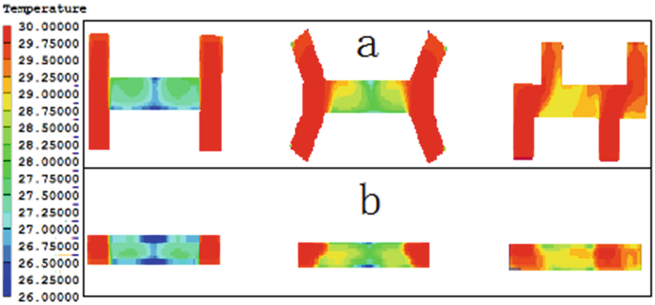

Fig. 12. Temperature of optimization models yielded by CFD simulations: (a) temperature distribution in the floor plan, and (b) temperature distribution of main tunnel in the elevation.

temperatures of the main tunnel of the model in Fig. 9(c) are mostly above 28.75 °C, which are close to the outdoor atmospheric temperature.

Figures 13(a) and (b) show the relative humidity comparisons yielded by CFD simulations. For the conventional I-shaped underpass in Fig. 9(a), not considering disturbances from lights and pedestrians, the air relative humidity near the inlet and outlet are close to the outdoor atmospheric humidity of 70%, while that in the middle area of the main tunnel is the largest but lower on both sides. Most areas inside the main tunnel are 80% to 88%. Comparatively, the law of air humidity in the main tunnel is the same as the model in Fig. 9(a), but the values of air humidity are within 74% to 80%. For the optimization model as Fig. 9(c), the air humidity in most areas of the main tunnel is lower than 75%, which is very close to the outdoor atmospheric relative humidity.

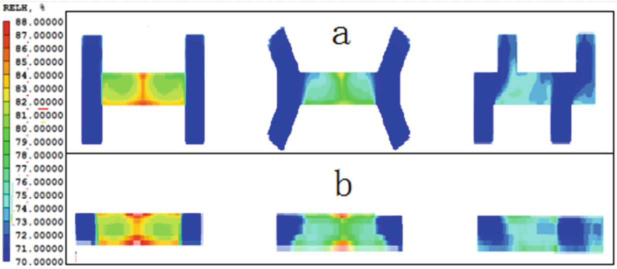

Fig. 13. Relative humidity of underpass optimization models yielded by CFD simulations: (a) relative humidity distribution in the floor plan, and (b) relative humidity distribution of main tunnel in the elevation.

Through the above simulation analysis, we can be clearly distinguished the pros and cons of design plans. For the effect of ventilation, the model in Fig. 9(c) is the best, followed by the model in Fig. 9(b), and the conventional I-shaped pedestrian underpass is the worst. Therefore, if conditions permit, the I-shaped underpass should layout be optimized as often as possible.

5 Conclusions

Based on the field monitoring and numerical simulation of the Yuejiazui I-shaped pedestrian underpass in Wuhan, China, under hot, moist and rainy climate conditions, this paper investigated the natural ventilation effect and internal environmental parameters of the underpass. The layout plan of I-shaped underpass was optimized, and the following conclusions can be drawn:

Natural ventilation is insufficient for conventional I-shaped pedestrian underpass usage. It relies on the weather (wind, temperature, and pressure difference) to maintain air flow. There is a smaller pressure-difference caused by heat between the inside and outside of tunnel in the summer, so the inside environment of an I-shaped pedestrian tunnel is often in a high humidity state, and the air does not circulate effectively with the outside atmosphere. Therefore, this layout it is prone to moisture condensation.

For cities in hot, moist and rainy regions, I-shaped pedestrian underpasses are not recommended. If conditions permit, the underpass optimization model in Fig. 9(b) or (c) should be adopted. For pedestrian underpasses with shorter main tunnels, natural ventilation should be adopted under the premise of meeting the internal environment quality. It is a poor choice to improve the internal ventilation effect through the installation of jet fans; alternatively, ventilation ducts should be installed to strengthen the air circulation inside tunnels with exposure to the outside atmosphere.

The CFD computing method can well simulate the internal airflow, temperature, air relative humidity, air ages and ventilation conditions of an underpass. Designers can use this method to optimize their design schemes in advance, according to internal environmental standard requirements.

Acknowledgments. This work was supported by the Project for Building Science and Technology of Hubei Province, China (Grant Number 2013014) and the 333 Project Training Fund of Jiangsu Province (BRA2016113).

References

1. Van Der Voordt, D.J.M., Van Wegen, H.B.R.: Underpasses for pedestrian and cyclists – user requirements and implications for design. Transp. Plan. Technol. **8**, 1–14 (1983)
2. Technical specifications of urban pedestrian overcrossing and underpass (CJJ69). China Architecture & Building Press, Peking (1995)
3. Design of civil air defense basement (GB 50038). China Planning Press, Peking (2005)
4. Indoor thermal environmental conditions (GB/T 5701). China Standards Press, Peking (2008)
5. Subway design specifications (GB 50157). China Architecture & Building Press, Peking (2013)
6. Yang, Y.S.: Study on the environment of underground pedestrian passage in Xi'an. Thesis of Xi'an University of Architecture and Technology, Xi'an (2007)
7. Wang, G.D., Li, A.G., Qiu, S.H.: Study on hot and humid environment test of underground pedestrian crossing in Xi'an. Build. Therm. Ventilating Air Conditioning **28**(2), 25–28 (2009)

8. Ning, Z.Z., Shen, H.F., Wang, D.G., Ni, Y.F., Ling, Q.: Discussion on air quality evaluation of underground building ventilation measures and comfort zone of underground environment. Editorial Off. Undergr. Space **1**, 35–38 (1986)
9. Li, P., Liu, Z., Wang, X.H.: Numerical simulation and experimental study on the thermal environment in staff room. Contam. Control Air-Conditioning Technol. **4**, 33–39 (2012)
10. Ohashi, H., Mizuno, A., Nakahori, I.: A new ventilation method for the Kan-Etsu Road Tunnel. In: 4th International Symposium on the Aerodynamics and Ventilation of Vehicle Tunnels, pp. 31–48. BHRA Fluid Engineering, York (1982)
11. Diaz, J., Kramesberger, F.: Safe and economic ventilation of a motorway tunnel. In: Proceedings of the 5th International Symposium on the Aerodynamics and Ventilation of Vehicle Tunnels, Lille, France (1985)
12. Armstrong, J.: The ventilation of vehicle tunnels by jet fans – the axisymmetric case. In: Proceedings of the Seminar on Installation Effects in Fan Systems. Mechanical Engineering Press, London (1993)
13. Li, J.S.M., Chow, W.K.: Numerical studies on performance evaluation of tunnel ventilation safety systems. Tunn. Undergr. Space Technol. **18**(5), 435–452 (2003)
14. Jiang, Y., Alexander, D., Jenkins, H., Arthur, R., Chen, Q.Y.: Natural ventilation in buildings: measurement in a wind tunnel and numerical simulation with large eddy simulation. J. Wind Eng. Ind. Aerodyn. **91**(3), 331–353 (2003)
15. Tabarra, M., Sadokierski, S.: Design of a modern subway ventilation system. Technical review: ventilation, Tunnels & Tunnelling International. http://worldcat.org/issn/0041414X. Accessed 21 Nov 2017
16. Yuan, F.D., You, J.: CFD simulation and optimization of the ventilation for subway side-platform. Tunn. Undergr. Space Technol. **22**(4), 474–482 (2007)
17. Xu, L., Zhang, X.: CFD analysis of critical wind speed for horizontal ventilation of super-large horizontal tunnel. Chin. J. Undergr. Space Eng. **3**(1), 124–127 (2007)
18. Guo, X., Zhang, Q.: Analytical solution, experimental data and CFD simulation for longitudinal tunnel fire. Tunn. Undergr. Space Technol. **42**(5), 307–313 (2014)
19. Jiang, M.J., Zhang, W.C.: CFD-DEM coupling numerical method considering fluid equation of state. J. Geotech. Eng. **5**, 793–801 (2014)
20. Diego, I., Torno, S., Toraño, J., Menéndez, M., Gent, M.: A practical use of CFD for ventilation of underground works. Tunn. Undergr. Space Technol. **26**(1), 189–200 (2011)

Research Methods in Tunnel Fire Distinguishing from Buildings in Evacuation

Jingtao Dong[1,2], Zhiguo Yan[1,2,3(✉)], Yuxin Zhang[1,2,3(✉)],
and Hehua Zhu[1,2,3]

[1] State Key Laboratory for Disaster Reduction in Civil Engineering,
Tongji University, Shanghai, China
1454605223@qq.com, yanzguo@tongji.edu.cn
[2] Department of Geotechnical Engineering, Tongji University, Shanghai, China
[3] Key Laboratory of Geotechnical and Underground Engineering of the Ministry
of Education, Tongji University, Shanghai, China

Abstract. Road tunnels, with large cross-section and long distance, brings about vital danger to occupants once in fire. The first few minutes in fire is extremely precious for escapers. Meanwhile, professional aid cannot be obtained. Therefore, it is quite necessary to improve the performance in fire to reduce injury and lost to a large extent. However, current research in evacuation behavior mostly focuses on building fires and has already gained some advanced and practical achievement while less on tunnel fires. Therefore, it is beneficial and efficient to study tunnel evacuation in fire based on buildings. The passage lists mainstream research methods in evacuation in tunnel fires distinguishing from building fires. It summaries the methods on the one hand. On the other hand, it provides reference for tunnel fires research.

Keywords: Tunnel fire · Research methods · Fire · VR experiment

1 Introduction

Road tunnels, as essential public works, provide both practical and economic function to transportation and physical distribution. Explosive increase in industry and related trades exerts unimaginative pressure on the efficiency and safety to tunnels and brings several tragic fire disasters. Fires in tunnels have caused great risk to human life and damage to property and the economy (Amundsen 1994; Amundsen and Ranes 2000). Prompt self-evacuation is extremely essential in tunnel fires since fires spread rapidly and violently (Burns et al. 2013). In early stages of a fire, people in tunnels typically have to rely on themselves or rescued by other people in their immediate vicinity instead of professional teams with such a confined space too narrow to reach out at once. Besides, unlike other fires in buildings or open sites, the fires in tunnels burn more fiercely in the confined space due to heat feedback (Purser 2008).

The field of scientific research in human behavior in fire is relatively new, although numerous studies have been conducted into this issue from the start of the 20th century, and are continuing (Latane and Darley 1968; Fischer et al. 2011). First studies of evacuation in building concerning human focused on people’s movement in corridors,

© Springer Nature Singapore Pte Ltd. 2018
D. Zhang and X. Huang (Eds.): GSIC 2018, *Proceedings of GeoShanghai 2018 International Conference: Tunnelling and Underground Construction*, pp. 666–673, 2018.
https://doi.org/10.1007/978-981-13-0017-2_67

on stairs and through doors (Kobes et al. 2010a, b). Occupant density and moving speed were the main heed instead of human behavior which aimed at optimizing the dimensions of inner building structure. Scientists paid more attention to behavioral aspect from technological in the last years in the 20th century (Sime 1999, 2001). Recent years, researches emphasize people's inner motivation other than observing and recording how they behave.

In contrast with quantitative research on building, human research in tunnel fire perform relatively poorly. That Sime discovered that drivers were likely to move back forward to the tunnel entrance and did not use the closet emergency exits and other efficient way for evacuation in 1985 can be regarded as the start of research about human behavior in tunnel fire and most studies began from the beginning of the 21st century (Boer 2002; Boer and van Zanten 2007). An evacuation study found that a few drivers realized the danger during accidents but did not behave properly due to lack of concerning knowledge. A questionnaire also proved this which many of them owned the intention of using safety devices in tunnels but could not operate properly and internalizedly. Egger and Shields analyzed the designed environment of building and tunnels (Egger 2012). They pointed out that structure in tunnels were clearly visible as well as signage and finding an emergency exit should be easy. However, there were no obvious evidence showing that people in tunnel are easier to find ways than in buildings which would attribute to the dim and depressing environment underground. Decision-making about destination and route choice is required in a short period while people are apt to behave passively with less responsibility while may thwart immediate evacuation (Nilsson and Johansson 2009; Fridolf et al. 2013).

At present, our knowledge of occupants' performance confronting with tunnel fire is still very limited, much scantier than knowledge facing building fires. It is beneficial and inspiring to learn fire response performance and social behavior from building fires on condition that fully distinguishing tunnels from buildings.

2 Accidents Data

Tunnel fire accidents are relatively rare compared to building fires. On one hand, it attributes to the small amount of tunnels worldwide. On the other hand, accidents do occur less frequently in road tunnels and only a small portion required the intervention of fire brigade or resulted in fatalities due to strict safety norms and strong over-sight. However, the consequence of a tunnel fire can be far more serious than a fire in the open air and several tragedies have taught us lessons. For instance, the incident in the Mont Blanc Tunnel was the 18th fire recorded in this tunnel since 1965 but it caused 39 death. The potential of worse consequence cannot be neglected with longer and more complex tunnels and higher traffic densities. As the only accurate evidence to study tunnel fires, accidents data are precious since it can reflect real reaction and human behavior. Some data were obtained and recorded by interviews with staff, passengers and other witness and some were discovered indirectly by the badly damaged scene. But little can be recorded by monitoring record system since many old tunnels don't equipped with that and smoke would cover the camera when the fire burns out.

Tunnels are tougher and stronger with tests showing that most tunnels won't collapse in big fires but human's capacity is far less. Some researches pointed out that human behavior is a major factor in bringing about fatalities in road tunnel fires. Both fires in Nihonzaka and Caldecott were started from collision from vehicles but the consequence differed a lot. The tragedy in the Mont Blanc incident could have been avoided if the occupants gave up their cars and escaped promptly. The evacuation in Nihonzaka tunnel fire, which destroyed 173 vehicles, as a successful example, brought about only seven deaths which were as a result of crash but not fire. To point out, 200 people ran out of the tunnel on foot in about half an hour instead of waiting inside the tunnel for rescuing in this positive human evacuation. Though ventilation system and other assorted facilities affected the fire to some extent, it came to an apparent conclusion that human behavior is a decisive factor in tunnel fire especially concerning to casualties. Accidents data, on one hand, records human reaction and provides direct proof to analyze human behavior. On the other hand, it is a useful and precious database for calibration in simulation models.

3 Experiment

Experiments and tests in tunnels are a common way to learn fire from 1960s. Among several reasons, the following two are mainstream: understand fire dynamics and related phenomena in tunnels, and test the security and efficiency of facilities and equipment in tunnels namely ventilation system, sprinkler system and tunnel escape. Recent large experiments include Carleton University Laboratory Train Tests in 2011 aiming to determining fire development and HRR of intercity railcar and a subway car, SP Fire Research in Sweden in cooperation with TNO in the Netherlands and SINTEF-NBL in Norway in 2003 for fire development and other characteristics, and Baimang Snow Mountain No. 1 Tunnel experiment in China in testing fire characteristics at high altitude (Yan et al. 2017).

It is applicable and feasible to test the performance of system and other physical equipment. However, it is a tough task to test human behavior when considering the authenticity of experiments and harm to participants. Experiments in all other fields except concerning human factor pursue as much as similarity to reemerge the external condition and environment. Meanwhile, it is not suitable and lacks of humanism to set human in such a disastrous environment which may bring post-traumatic stress disorder. It concerns ethical consideration requiring sufficient preparation and precaution to protect participant which affect the authenticity reversely unavoidably.

Moreover, experiments in tunnels are comparably hard to test than in buildings due to the uncertainty of people's reaction. No natural light, reduced visibility and poor visual accessibility, tunnels are alien environment where people would feel claustrophobic and fear entrapment not like buildings where people live daily without undue and unnecessary psychological stress. People in buildings which they are familiar to are tend to escape rapidly and focus is mainly on the congestion and potential stampede on stairs. Therefore, large numbers of experiments concentrate on the flow of people and choice of path which can be tested even without accidents and fires. In contrast, due to a low density of crowd, people in tunnels do not come across blocking up in escaping, but the key problem is their passive behavior towards evacuation which is impossible to simulate without vivid emergency and stress.

Besides, all experiments about human behavior in tunnels are full-scale experiments since people are set in tunnel environment while both large-scale and intermediate size experiments are common in other fields (Shields and Boyce 2000). Full-scale experiments with large group of experimenters are time consuming and logistically complicated to perform. Though the tough balance between ethical problem and authenticity and large cost in time and finance, many researches have been conducted. Nilsson et al. (2009) investigated motorists' behavior and emotional response when exposed in tunnel fire and discovered people's reaction to acoustic signals and information signs. These days, more advanced and technological methods are applied in exploring human behavior in tunnel fires.

4 Simulations

A variety of evacuation models for simulating accidents in tunnels are widely used with the fast development of computer science. It appears the trend from an assistant and supportive role combining with other source of knowledge/experience/intuition (The handbook of tunnel fire safety) to an independent or decisive role to test and explore in many fields. Though favored by the advanced technology, evacuation modelling is a new and immature field (Kuligowski et al. 2010) since it is almost impossible to mimic people's behavior accurately. Evacuation modelling methodology aims at providing a set of precise measures and data of the tunnel and reproduce behavioral factors as far as possible. Mainstream models (Valasek and Glasa 2013; Ronchi et al. 2012; Ronchi and Nilsson 2013; Kohl et al. 2006; Kohl and Forster 2012; Alonso et al. 2014) namely FDS+Evca, BuildingEXODOS, STEPS, Pathfinder (Kudikyala and Vaughn 2005), Gridflow and Simulex (Thompson and Marchant 1995) etc. presenting three scales of modelling: analytical calculation, individual use of models and multi-model approach (Ronchi and Nilsson 2013).

Kuligowski and Peacock categorized models into three types by their function and purpose, namely behavioral models, movement models and partial behavior models (Kuligowski et al. 2010). Behavioral models are aiming at occupants' performance, the process of decision-making and reactions to the change of environment; movement models set that occupants move from one point to another and simulate their speed and path; partial behavior models include calculating people's movement but repeat some behavior like pre-movement time and path choice indirectly. Though restricted by several conditions and inadequate simulation of human behavior, evacuation model has its own advantage like high control of parameters, low cost and saving time, and no harm to experimenters in daily life. It shows great potential in reappearance of fire accidents and analyzes human behavior. Most of them like EXODUS, STEPS, and Simulex etc. originate from building evacuation models which classified into two subsets: macroscopic and microscopic models which focus on a whole system and individual pedestrians' behavior, decision and influence by other pedestrians respectively (Gwynne et al. 2001; Galea et al. 2004; Blake et al. 2004).

Though sharing similar software, tunnels and buildings emphasis diversely and those limitations vary a lot due to their structure and environment. Unlike limitations in buildings like grid-size and fatigue factor of high rise, collision induced by uneven use of stairs, and conflicting route choice because of familiar parts of the buildings (Pelechano and Malkawi 2008), those in tunnels are concentrated on the little cognition of tunnels and mental condition underground. Also, it is intractable to calibrate models with lack of examples of accidents. Ronchi compared three common evacuation models (FDS+Evac, STEPS, Pathfinder) in the case of Lantueno tunnel in Spain and listed difference influenced by pre-movement time, modelling method, depth of analysis, inputs calibration (Ronchi et al. 2012). Hopefully, it owns large potential to improve and overcome the deficiency little by little along with growing understanding of tunnels and progressive computer technology.

5 VR Experiment

VR (virtual reality), as a novel approach studying evacuation, has brought large progress deriving from its unique advantage. It has been applied in the following fields: the effect of occupant training on tunnel evacuation (Kinateder et al. 2013; Ribeiro et al. 2012), pre-evacuation behaviors (Kobes et al. 2010a; Kobes et al. 2010b), mass evacuation from underground transportation, and the impact of way-finding installations (Kobes et al. 2010b). Its effectiveness has been confirmed in medical field by transferring response in virtual reality into real world adequately.

The application of VR would trace back to 2003 when Gamberini, Cottone, Spagnolli, Varotto, and Mantovani studied evacuation from a virtual library fire. From then on, several VR experiments have been conducted to test emotional response in VR environment as well as obtaining a proper relationship between real world and VR. These experiments proved that training in VR can improve people's performance in real world. The improvement include better sense of orientation after training in a virtual maze compared to studying a map, or even training in real world, strong spatial acknowledgement through an active virtual scenario compared to a passive navigation in the scenario, and a swift response to accidents after VR behavioral training on self-evacuation during a simulated emergency situation (Kinateder et al. 2013). Apart from those, Max Kinateder investigated the function of SI (social influence) in decision making and route choice, and occupants' response to conflicting social information successively. To sum up, VR has brought qualitative change in exploring human behavior in evacuation.

Economical, safe, and replicable, VR owns its unrivalled advantage comparing to data studying or traditional laboratory study with lack of experimental control and causal interpretation, or complex control with large cost in time and finance respectively. It is worth mentioning that VR experiments bring about less harm and PTSD to experimenters than classical ones. However, there are still much methodological challenge and ethical limitations. Participants in VR studies always remember that their perception is based on simulation using current technology, which cannot present real reaction to 100%. VR performs better and persuadably on condition that accurate interpretation from manners into human behavior are established. Another problem is about the uncanny valley effect, whose existence is still under debate.

6 Summary

In contrast with masses of experiment and modelling focusing on fire in buildings, little attention has been paid to tunnel fires due to relatively less number of fire accidents in tunnel. Nevertheless, tunnel fires can never be taken too serious since its immeasurable destroy and large causalities usually companying with large explosion ignited by fuel tanks of vehicles. By contrasting and comparing the differences and similarities between buildings and tunnels, we could build a better evacuation environment in tunnel fire for evacuees in the future.

(1) Though tunnel fires and building fires share quite a few in common in occupants' behavior facing emergency, tunnel fires differs a lot due to its weak illumination, relative confined space and unfamiliarity to occupants, containing some HGVs. This brings about various pressure and problem for evacuees.
(2) As to research task, the main problem in building fires focuses on the congestion in corridors and necessary escaping time during the whole process. In contrast, the prior issue in tunnel fires is to solve the spontaneity to escape in tunnels.
(3) The research methods including accident data, experiment, simulation and VR test has not formed rigorous and complete system. There is still improvement in the digitalization of tunnel facilities. Moreover, there is still a long way in terms of simulation and experiment in human nature, morality and experimental authenticity.

References

Amundsen, F.H.: Studies of Driver behavior in Norwegian road tunnels. Tunn. Undergr. Sp. Tech. **9**, 9–17 (1994)

Amundsen, F.H., Ranes, G.: Studies on traffic accidents in Norwegian road tunnels. Tunn. Undergr. Sp. Tech. **15**, 3–11 (2000)

Burns, P., Stevens, G., Sandy, K., Dix, A., Raphael, B., Allen, B.: Human behaviour during an evacuation scenario in the Sydney Harbour Tunnel. Aust. J. Emerg. Manag. **28**, 20 (2013)

Purser, D.A.: Assessment of hazards to occupants from smoke, toxic gases and heat. In: National Fire Protection Association (ed.) SFPE Handbook of Fire Protection Engineering. National Fire Protection Association, Quincy MA, USA, pp. 2-96–92-193 (2008)

Latane, B., Darley, J.M.: Group inhibition of bystander intervention in emergencies. J. Pers. Soc. Psychol. **10**, 215–221 (1968)

Fischer, P., Krueger, J.I., Greitemeyer, T., Vogrincic, C., Kastenmuller, A., Frey, D., et al.: The bystander-effect: a meta-analytic review on bystander intervention in dangerous and non-dangerous emergencies. Psychol Bull. **137**(4), 517–537 (2011)

Kobes, M., Helsloot, I., de Vries, B., Post, J.: Exit choice, (pre-) movement time and (pre-) evacuation behavior in hotel fire evacuation - behavioural analysis and validation of the use of serious gaming in experimental research. Procedia Eng. **3**, 37–51 (2010a). https://doi.org/10.1016/j.proeng.2010.07.006

Kobes, M., Helsloot, I., de Vries, B., Post, J.G., Oberije, N., Groenewegen, K.: Way finding during fire evacuation; an analysis of unannounced fire drills in a hotel at night. Build. Environ. **45**, 537–548 (2010b). https://doi.org/10.1016/j.buildenv.2009.07.004

Sime, J.D.: Crowd facilities, management and communications in disasters. Facilities **17**, 313–324 (1999)

Sime, J.D.: An occupant response shelter escape time (ORSET) model. Saf. Sci. **38**, 109–125 (2001). https://doi.org/10.1016/s0925-7535(00)00062-x

Boer, L.C.: Behaviour by Motorists on Evacuation of a Tunnel. Rapport TNO Human Factors (2002)

Boer, L.C., van Zanten, D.V.: Behavior on tunnel fire. In: Pedestrian and Evacuation Dynamics 2005, pp. 91–98. Springer, Heidelberg (2007)

Egger, M.: Recommended behaviour for road tunnel users. In: Beard, A., Carvel, R. (eds.) The Handbook of Tunnel fire Safety, pp. 399–420. Thomas Telford Publishing, London (2012)

Nilsson, D., Johansson, A.: Social influence during the initial phase of a fire evacuation – analysis of evacuation experiments in a cinema theatre. Fire Saf. J. **44**, 71–79 (2009)

Nilsson, D., Johansson, M., Frantzich, H.: Evacuation experiment in a road tunnel: a study of human behavior and technical installations. Fire Saf. J. **44**, 458–468 (2009)

Fridolf, K., Nilsson, D., Frantzich, H.: Fire evacuation in underground transportation systems: a review of accidents and empirical research. Fire Technol. **49**(2), 451–475 (2013)

Kinateder, M., Pauli, P., Müller, M., et al.: Human behaviour in severe tunnel accidents: Effects of information and behavioural training. Transp. Res. Part F Traffic Psychol. Behav. **17**, 20–32 (2013)

Ribeiro, J., Almeida, J.E., Rossetti, R.J., Coelho, A., Coelho, A.L.: Using serious games to train evacuation behavior. In: 2012 7th Iberian Conference on Information Systems and Technologies (CISTI), pp. 1–6. IEEE (2012)

Yan, Z., Guo, Q., Zhu, H.: Full-scale experiments on fire characteristics of road tunnel at high altitude. Tunn. Undergr. Sp. Technol. **66**, 134–146 (2017)

Shields, T.J., Boyce, K.E.: A study of evacuation from large retail stores. Fire Saf. J. **35**(1), 25–49 (2000)

Kuligowski, E.D., Peacock, R.D., Hoskins, B.L.: A review of building evacuation models. NIST Technical Note 1680 (2nd edn.). National Institute of Standards and Technology (2010)

Valasek, L., Glasa, J.: Simulation of the course of evacuation in tunnel fire conditions by FDS +Evac. In: Proceedings of the 2013 International Conference of Applied Mathematics and Computational Methods in Engineering, pp. 288–295 (2013)

Ronchi, E., Colonna, P., Capote, J., Alvear, D., Berloco, N., Cuesta, A.: The evaluation of different evacuation models for assessing road tunnel safety analysis. Tunn. Undergr. Space Technol. **30**, 74–84 (2012)

Ronchi, E., Nilsson, D.: Fire evacuation in high-rise buildings: a review of human behavior and modelling research. Fire Sci. Rev. **2**, 7 (2013)

Kohl, B., Botschek, K., Hörhan, R.: Austrian risk analysis for road tunnels: development of a new method for the risk assessment of road tunnels. In: 3rd International Conference "Tunnel Safety and Ventilation" 2006, Graz, pp. 204–211 (2006)

Kohl, B., Forster, C.: Risk analysis as decision making tool for tunnel design and operation. In: 6th International Conference 'Tunnel Safety and Ventilation' 2012, Graz, pp. 17–25 (2012)

Alonso, V., Abreu, A., Cuesta, A., Alvear, D.: An evacuation model for risk analysis in Spanish road tunnels. Procedia Soc. Behav. Sci. **162**, 208–217 (2014)

Kudikyala, U.K., Vaughn, R.B.: Software requirement understanding using Pathfinder network: discovering and evaluating mental models. J. Syst. Softw. **74**, 101–108 (2005)

Thompson, P.A., Marchant, E.W.: Testing and application of the computer model ‘SIMULEX’. Fire Saf. J. **24**, 149–166 (1995)

Gwynne, S., Galea, E.R., Lawrence, P.J., Filippidis, L.: Modelling occupant interaction with fire conditions using the building EXODUS evacuation model. Fire Saf. J. **36**, 327–357 (2001)

Galea, E., Lawrence, P., Blake, S., Gwynne, S., Westeng, H.: A preliminary investigation of the evacuation of the WTC North Tower using computer simulation. In: Proceedings of the 3rd International Symposium on Human Behavior in Fire, pp. 167–180. Interscience Communications Ltd. (2004)

Blake, S., Galea, E., Westeng, H., Dixon, A.: An analysis of human behavior during the WTC disaster of 11 September 2001 based on published survivor accounts. In: Proceedings of the 3rd International Symposium on Human Behavior in Fire, pp. 181–192 (2004)

Pelechano, N., Malkawi, A.: Evacuation simulation models: challenges in modeling high rise building evacuation with cellular automata approaches. Autom. Constr. **17**, 377–385 (2008)

Cutter Ring Breakage Induced by Unbalanced Side Force in Circular Cutting Process

Dong-Jie Ren[1,2], Shui-Long Shen[1,2(✉)], Jin-Chun Chai[1],
and Da-Jun Yuan[3]

[1] State Key Laboratory of Ocean Engineering, Department of Civil Engineering,
School of Naval Architecture, Ocean, and Civil Engineering,
Shanghai Jiao Tong University, Shanghai 200240, China
slshen@sjtu.edu.cn
[2] Collaborative Innovation Center for Advanced Ship and Deep-Sea Exploration
(CISSE), Shanghai Jiao Tong University, Shanghai 200240, China
[3] School of Civil Engineering, Beijing Jiaotong University,
Beijing 100044, China

Abstract. The cutter ring breakage as a cutter failure mode in shield tunnel construction is more likely to occur in the centre zone of cutterhead. Given the inconsistence of this phenomenon with the linear cutting theory, the present paper suggests the use of the circular cutting theory to explain the cutter ring breakage and find the correlation between the unbalanced side force and cutter ring breakage. The numerical simulation performed by LS-DYNA demonstrates the difference existing between the inner side and outer side forces. The rock breakage in circular cutting process shows that the difference of side force is more remarkable in the centre zone than in the outer region of cutterhead.

Keywords: Cutter ring breakage · Side force · LS-DYNA

1 Introduction

Tunnel boring machines (TBMs) have been extensively used in tunnel constructions. Disc cutters as the most important components of these machines have a great influence on the working efficiency. For this reason, several researchers, e.g. Frenzel [1], Macias [2], and Liu et al. [3], focused their interests on the different types of disc cutter failures such as uniform cutter wear, non-uniform cutter wear, and cutter ring breakage. However, the existing methods usually adopt simplified research processes that do not reliably integrate the cutter ring breakage. Moreover, in addition of being mainly focused on the uniform and non-uniform cutter wears, the previous studies have been mostly based on the linear cutting process, which only addresses the effect of thrust force and rolling force in the tangential direction [4, 5]. Actually, the cutter ring breakage has a great influence on the performance of TBM, given that a partial breakage of cutter ring may cause the failure of the entire disc cutter. Furthermore, field observations revealed that the cutting process of the disc cutter is achieved following a circular fashion [6], which means, the lateral rock shearing may cause unbalanced side forces on the cutter ring. It therefore seems more reasonable to use the circular cutting

© Springer Nature Singapore Pte Ltd. 2018
D. Zhang and X. Huang (Eds.): GSIC 2018, *Proceedings of GeoShanghai 2018 International Conference: Tunnelling and Underground Construction*, pp. 674–681, 2018.
https://doi.org/10.1007/978-981-13-0017-2_68

theory, which has the advantage of considering the side force effect. Also, by comparing the characteristics of cutter ring breakage and side forces, the mechanism of cutter ring breakage may be clarified.

In this paper, the characteristics of cutter ring breakage are summarised based on a field observation. The theoretical analysis is conducted to explain the differential of side forces in a circular cutting process. A three-dimensional numerical model is first established to simulate the circular cutting process. Then, the change of unbalanced side forces is addressed. Finally, the correlation between unbalanced side force and cutter ring breakage is discussed.

2 Characteristics of Cutter Ring Breakage and Side Force

According to existing researches, the cutter ring breakage occurs due to normal impact loads from the cutting face [4, 5]. These Normal impact loads tend to increase with the rise of the tangential velocity, so that the disc cutter with larger spacing ratio will more easily suffer from the cutter ring breakage. However, the recent observation from a case study in Guangzhou, shows the total different phenomenon. Figure 1 shows the distribution of cutter ring breakage encountered in Xie-Zhong section of Guangzhou Metro Line 7. The cutter ring breakage mostly occurred in the centre region of cutterhead, rather than the outer region, with severer impact loading. Based on characteristics of cutter ring breakage and the properties of materials, it is legitimate to elaborate the hypothesis that the cutter ring breakage is directly correlated to the side force on the cutter ring.

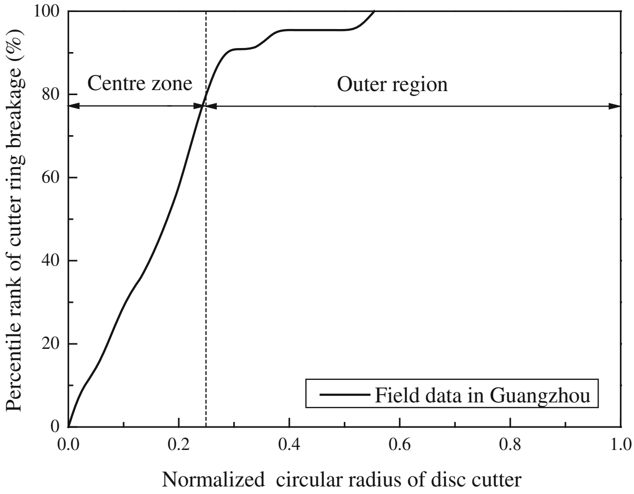

Fig. 1. Distribution of cutter ring breakage in the TBM cutterhead

Figure 2 shows a circular cutting process of a disc cutter on the cutterhead. In Fig. 2(a), there is a centripetal acceleration pointing to the centre of cutterhead in the actual cutting process. Especially in the centre zoom of cutterhead, the side force acting on the cutter ring is significant during the circular cutting process, as shown in Fig. 2(b).

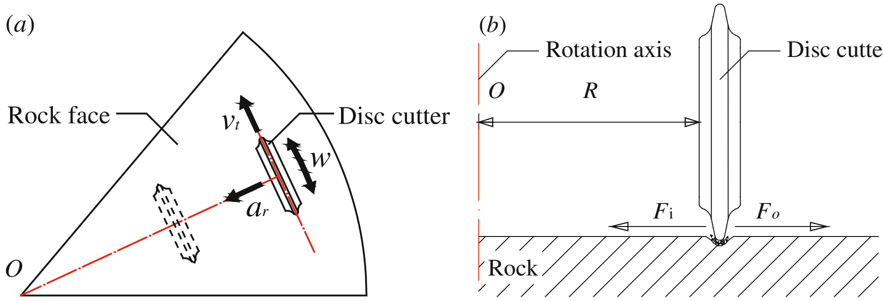

Fig. 2. Lateral mechanical analysis during circular cutting process

3 Numerical Simulation of Circular Cutting Process

3.1 Configuration of Numerical Model

A numerical method is generally adopted for modelling and monitoring the stress condition of cutter ring and rock breakage. In this case, LS-DYNA was used to simulate the circular cutting process of disc cutter. The numerical model including rock sample, cutter ring for cutting the rock and cutter body for controlling the moving of cutter ring is shown in Fig. 3. Except for the top boundary which was free for deformation, all the other boundaries (for the rock model) were fixed in displacement and rotation. Additionally, a non-reflect boundary condition was employed to mitigate the unexpected failure induced by the reflecting waves. For analysing the effect of factors on stress status of cutter ring, several cases with different radius were considered. Six monitoring points on cutter ring were used to record the value of side force.

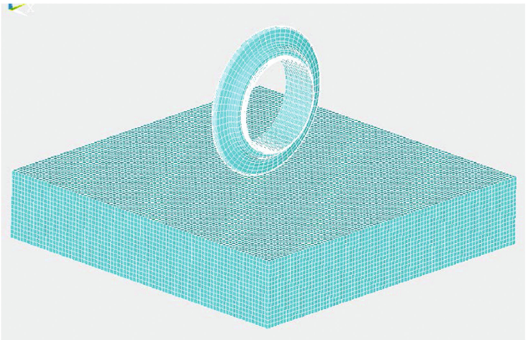

Fig. 3. Numerical model for circular cutting process

3.2 Simulation of Circular Cutting Process

A single disc cutter was established in LS-DYNA to predict the breaking behaviour of rock sample and the stress status of cutter ring. The developments of rock failures and the contour plots of stress on the cutter ring surface were carried out to validate the mechanical analysis of side force acting on the cutter ring. In numerical simulation, the penetrating depth was employed at 0.01 s, and the circular cutting process started at 0.03 s, ending at 0.05 s. The development of rock failure during cutting process was performed with a circular radius of 0.5 m (Fig. 4). At the normal penetrating period, the contour of rock's von-Mises strain was nearly symmetric, indicating that the side force acting on both sides of the cutter ring were balanced. When the circular cutting started, along the tangential direction the von-Mises strain for the inner side of rock became larger than that of the outer side. Moreover, the von-Mises strain contour on both sides of cutter ring shown less differences between a cutter disc of 2.0 m radius (Fig. 4f) and that of 0.5 m radius (Fig. 4d), computed at the same step. These results indicate that with the increase of spacing radius (R), the phenomenon observed by applying the circular cutting theory gradually tends to be similar to the one observed while using the linear cutting theory.

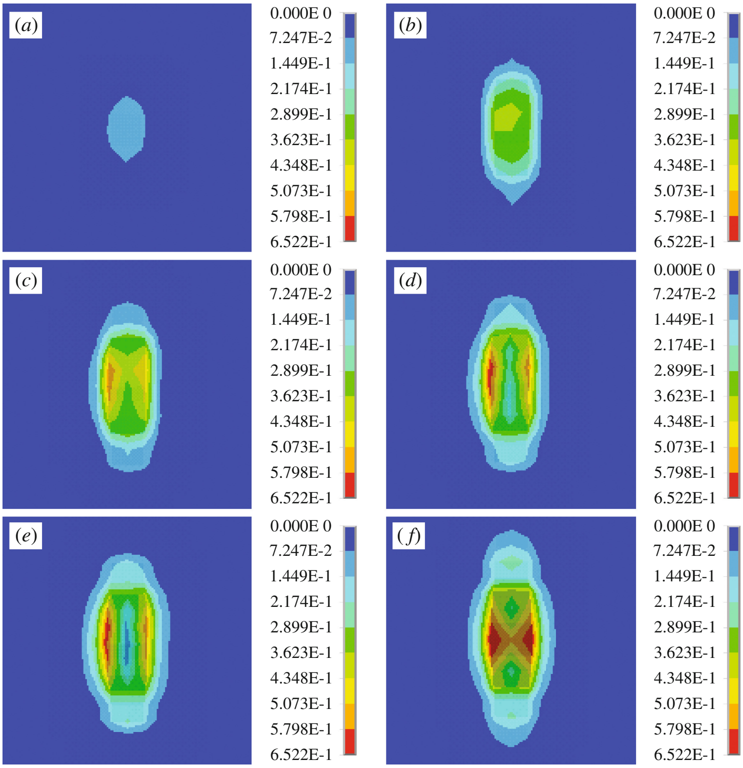

Fig. 4. Von-Mises strain of rock sample during circular cutting process: (a) T = 0.01 s, R = 0.5 m; (b) T = 0.02 s, R = 0.5 m; (c) T = 0.03 s, R = 0.5 m; (d) T = 0.04 s, R = 0.5 m; (e) T = 0.05 s, R = 0.5 m; (f) T = 0.04 s, R = 2.0 m

3.3 Simulation Results

During the circular cutting process, the side force acting on the cutter ring were recorded. Three monitoring points were located at the inner side of cutter ring, as shown in Fig. 5. With the rolling of disc cutter, the points M_i were successively under pressure. Another set of three points (m_i) was located at the opposite position on the outer side. The average value of monitored surface stress was employed to represent the general status of surface stress. After calculating the influence area, the side force was readily determined. Figure 5 also shows the value of inner side force on cutter ring with the penetration depth of 10 mm. The fluctuation of monitored results can be attributed to the brittleness of rock, which imposes irregular side force on the cutter ring. In order to verify the numerical results, the Roxborough method was introduced [7]. Generally, the results calculated by Roxborough method were in good agreement with the numerical results. This particularly attests of the reliability of the side force values obtained from the numerical simulation.

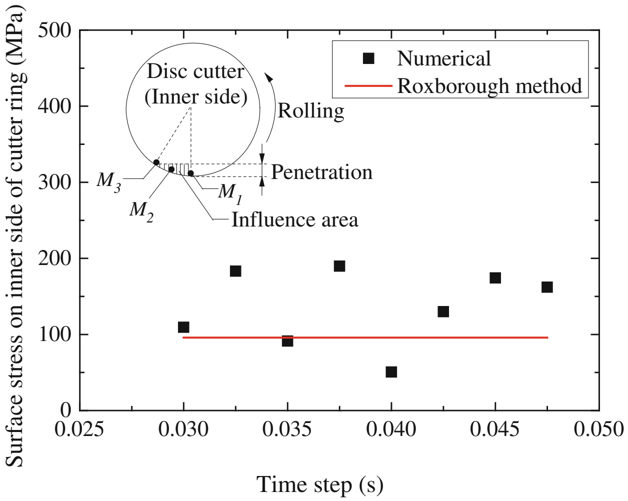

Fig. 5. Surface stress on cutter ring calculated by numerical modelling and Roxborough method

4 Discussion

4.1 Comparison of Circular and Linear Cutting Process

Choi and Lee [8] monitored the side force in the linear cutting process by numerical modelling. Figure 6 shows the comparison of side force in linear cutting process. Generally, the right side force and the left side force of disc cutter are balanced. However, the effect of the balanced side forces is inconsistent with the rock breakage behaviour shown in Fig. 4(d) and (e). It is believed that the balanced side forces cause the similar rock failure on the two side of cutting groove. The symmetrical distribution

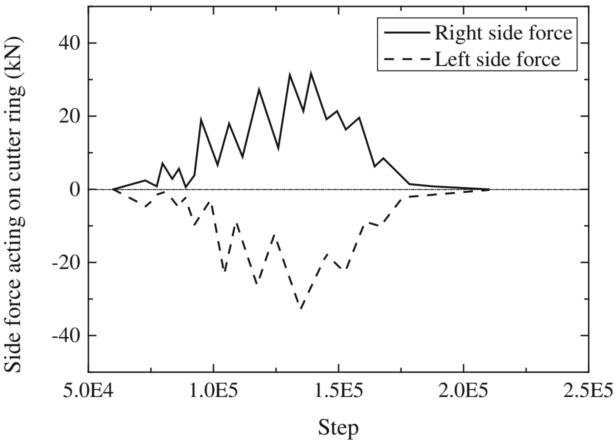

Fig. 6. Side force of disc cutter in linear cutting process (data from Choi and Lee, 2015 [6])

of side forces in Fig. 5 matches well with the breakage behaviour of rock in Fig. 4(f), whose spacing radius of disc cutter is large and cutting process has been considered as linear.

In the circular cutting process, the side forces acting on the cutter ring induced some discrepancies in von-Mises stress of cutter ring as shown in Fig. 7. Generally, the proportion of inner and outer von-Mises stress gathered from the monitoring points were larger than “1”, indicating that the inner side force acting on the cutter ring was larger than the outer side force. Therefore, the average value of the three points was reasonable to estimate the side force acting on the surface of cutter ring, as the average value could largely eliminate the fluctuation of stress caused by rock brittle failure.

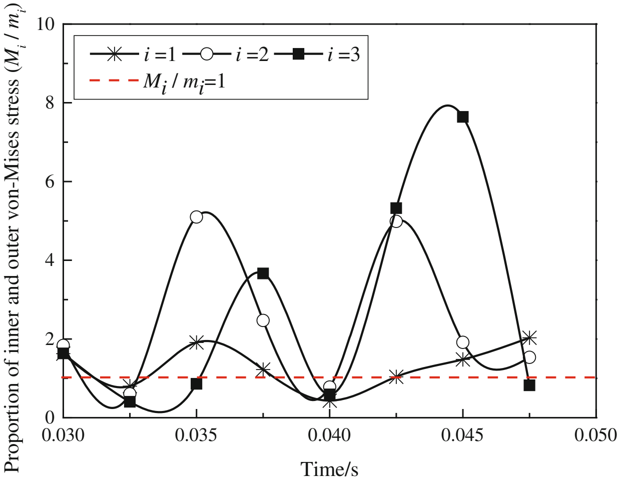

Fig. 7. Von-Mises stress of monitoring points in two sides of cutter ring

4.2 Significance of Numerical Simulation

With the numerical modelling, the unbalance repartition of side forces on two sides of cutter ring has been confirmed. Based on rock breakage behaviour, this unbalanced phenomenon was found more pronounced for circular cutting with small radius than that with large radius. This was also true for the distribution of cutter ring breakage, indicating to this effect that the side force may have a great influence on the cutter ring breakage. In order to prevent the cutter ring breakage, the side force in field can be evaluated by the numerical modelling. By estimating the numerical side force, the parameters for the design of cutterhead and the TBM operation can be optimized.

5 Conclusion

After summarising the characteristics of cutter ring breakage, we can conclude that the cutter ring breakage have a significant correlation with the inner side force acting on the cutter ring surface. Utilizing numerical simulation, the side force acting on the cutter ring was evaluated. More specific conclusions are as follows:

1. Based on the data gathered from Guangzhou Metro Line 7, the cutter ring breakage was found more likely to occur in the centre zone of cutterhead. The side force caused by circular cutting was introduced to shed a light on the limitations of the linear cutting theory.
2. The numerical simulation was used to estimate the influence factors for the side force. The numerical results shown that the inner side force and outer side force are different in circular cutting process.
3. Numerical cases with different spacing radius were conducted. The rock breakage demonstrated that the difference of side force was more remarkable with small spacing radius. Moreover, the unbalanced side force was correlated to the cutter ring breakage.

Acknowledgements. The research work described herein was funded by the National Basic Research Program of China (973 Program: 2015CB057802). These financial supports are gratefully acknowledged.

References

1. Frenzel, C.: Disc cutter wear phenomenology and their implications on disc cutter consumption for TBM. In: 45th US Rock Mechanics/Geomechanics Symposium, pp. 1–7. American Rock Mechanics Association, San Francisco (2011)
2. Macias, F.J.: Hard Rock Tunnel Boring: Performance Predictions and Cutter Life Assessments. Dissertation, Norwegian University of Science and Technology (2016)
3. Liu, Q.S., Liu, J.L., Pan, Y.C., Zhang, X.P., Peng, X.X., Gong, Q.M., Du, L.J.: A wear rule and cutter life prediction model of a 20-in TBM cutter for granite: a case study of a water conveyance tunnel in China. Rock Mech. Rock Eng. **50**(5), 1303–1320 (2017)

4. Rostami, J.: Study of pressure distribution within the crushed zone in the contact area between rock and disc cutters. Int. J. Rock Mech. Min. Sci. **57**, 172–186 (2013)
5. Wang, L.H., Kang, Y.L., Zhao, X.J., Zhang, Q.: Disc cutter wear prediction for a hard rock TBM cutterhead based on energy analysis. Tunn. Undergr. Space Technol. **50**, 324–333 (2015)
6. Liu, Q.S., Liu, J.L., Pan, Y.C., Zhang, X.P., Peng, X.X., Gong, Q.M., Du, L.J.: A wear rule and cutter life prediction model of a 20-in. TBM cutter for granite: a case study of a water conveyance tunnel in China. Rock Mech. Rock Eng. **50**, 1303–1320 (2017)
7. Roxborough, F.F., Phillips, H.R.: Rock excavation by disc cutter. Int. J. Rock Mech. Min. Sci. Geomech. Abstr. **12**(12), 361–366 (1975)
8. Choi, S.O., Lee, S.J.: Three-dimensional numerical analysis of the rock-cutting behavior of a disc cutter using particle flow code. KSCE J. Civ. Eng. **19**(4), 1129–1138 (2015)

New Frontiers and Innovative Technologies

Large-Scale Mine Water Geothermal Applications with Abandoned Mines

Ting Bao[1], Zhen Liu[1](✉), Jay Meldrum[2], and Christopher Green[2]

[1] Michigan Technological University, Houghton, MI 49931, USA
{tbao, zhenl}@mtu.edu
[2] Michigan Technological University, Calumet, MI 49913, USA

Abstract. This paper reports on the first large-scale project in the U.S. for utilizing water from abandoned mines for geothermal applications. This project proved the high potential of turning water in deep abandoned mines into a renewable energy resource, which is safer, greener, and more abundant than other conventional low-enthalpy geothermal applications. In this paper, a real demonstration project is introduced for recovering geothermal energy from the mine water for heating and cooling to a 1022 m^2 building in the Upper Peninsula of Michigan. A field test in a mine shaft with a depth of 1219.2 m is then presented to show the key issue in the use of the mine water as a geothermal resource: the temperature distribution. Complex multiphysics simulation with unique non-isothermal hydrodynamics is conducted to provide a physical explanation for the data obtained in the field test. Simulation results shed light on the scientific myth regarding water stratification and energy flow observed in the field study.

Keywords: Mine water · Water stratification · Geothermal application
Temperature distribution

1 Introduction

Geothermal energy is a renewable, abundant, and clean resource and thus has been considered as a good renewable energy resource to supply humanity's energy needs [1]. In recent years, the exploration of the mine water from abandoned mines as a geothermal resource has been gaining increasing research attention [2–4]. Mine water in the lower portions of mines can be heated by the surrounding geologic formations due to geothermal gradients, leading to sizeable man-made reservoirs of warm water. Therefore, the mine water has huge energy potential to provide heating to buildings in the U.S. and around the world. The conceptual model of using the mine water for heating buildings in winter is shown in Fig. 1.

The use of the mine water as a geothermal resource inherits most of the environmental benefits of conventional geothermal heat pump applications: safe, green, relatively renewable, and adaptable [5, 6]. In addition, from a technical perspective, the nature of using the mine water for geothermal applications provides more attractive advantages, making it a much higher grade geothermal resource: eco-friendly and environmental utilization of waste materials (abandoned mine water), higher-quality

© Springer Nature Singapore Pte Ltd. 2018
D. Zhang and X. Huang (Eds.): GSIC 2018, *Proceedings of GeoShanghai 2018 International Conference: Tunnelling and Underground Construction*, pp. 685–695, 2018.
https://doi.org/10.1007/978-981-13-0017-2_69

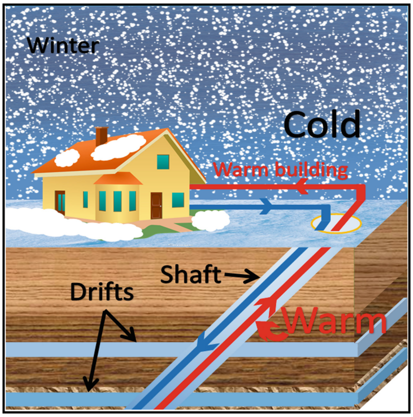

Fig. 1. Graphics for the mine water geothermal applications.

geothermal energy (higher geothermal gradient), highly efficient exploration (heat transport of bulk water), and economical (utilization of existing facilities).

The exploitation of the mine water as a geothermal resource has been pioneered in projects around the world. The utilization of the mine water for heating and cooling of buildings and industrial processes started officially in 1989 when the Town of Springhill developed an industrial park where companies could utilize geothermal energy supply from the local abandoned coal mines. Since this pioneering work in Canada [7, 8], the idea of using the mine water as a geothermal resource has been gaining momentum worldwide. As a result, a number of demonstration projects are in progress around the world, e.g., Germany [9] and the UK [10, 11]. In the U.S., this application lags behind compared to the above countries. However, the potential mine sites for the potential geothermal use is huge in the U.S., as shown in Fig. 2. In addition, active mines will be closed at future time point. Therefore, the number of potential sites will increase over the following decades, leading to a huge number of potential sites in the U.S.

The scientific understanding of using the mine water as a geothermal resource, however, is far behind its application. The mine water has a unique feature which is extremely complex and hard to predict. To be more specific, the mine water is mobile and driven by temperature and salinity differences [13], i.e., double-diffusive natural convection. This water movement can be influenced by the configuration of the mining space [11, 14], interaction between the mine water and pore/surface water [8, 15], and exploration strategies (e.g., locations of water in/out, pumping rate), etc. The mine water in a shaft, for example, can form one to several layers, within which water is well mixed with the same salinity and temperature [11]. Since the key to the efficiency and sustainability of the geothermal energy exploration is the distribution and variation of temperature in the mine water [16], it is very critical to understand this water movement as it determines the temperature distribution. However, because of the high level of complexity of the physical mechanisms in the natural process, the formation and variation of the layers within the mine water have not been well understood and no

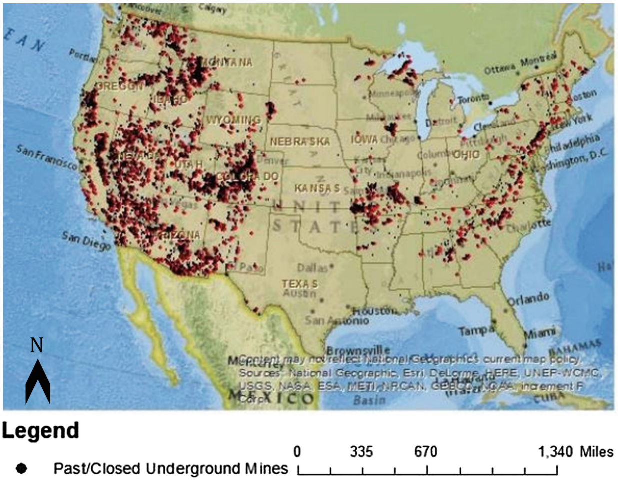

Fig. 2. Potential sites for the mine water geothermal applications in the U.S. (Modified after [12]. Data from USGS).

research has successfully explained the layer development and heat transfer mechanisms in the mine water.

This paper reports on the first large-scale project of recovering geothermal energy for heating and cooling and the first study around the world of this kind for deep mines. A real demonstration project, which has been recovering geothermal energy from the mine water to provide heating and cooling to a 1022 m^2 building in the Upper Peninsula of Michigan (U.P.) since 2009, is introduced. The field study for a deep mine shaft (over 1000 m) is then presented to show the temperature distribution, which is the key issue in the use of the mine water as a geothermal resource. Complex multiphysics simulation involving large-scale non-isothermal hydrodynamics is finally conducted for the mine where the field test was implemented to provide critical insights and explanations to the natural phenomenon observed from the field test from a scientific perspective.

2 Min Water Geothermal Application Demonstration

The Keweenaw Research Center (KRC) in the U.P. launched a demonstration project in 2009 to explore the possibility of using the mine water for geothermal applications in the region. In this project, geothermal energy was tapped from the mine water to provide heating and cooling to a 1022 m^2 building (see Fig. 3) near the Houghton County Airport from the New Baltic No. 2 mine shaft. The initial KRC geothermal system installation consisted of 14 heat pumps with a nominal heating capacity of 435,000 BTU/hr. The geothermal pipes were distributed in the engineering center of the KRC including reception areas, offices, conference rooms, computer centers, lunch rooms, and bathrooms.

A 90 gpm (gallon per minute) pump pulls the mine water from a 92 m depth and sends it through a double wall plate heat exchanger. On the building side of the heat

building area: 1022 m^2

heating room number: over 6

approximate cost: $100,000

cost saving: 30% over gas

Fig. 3. The use of the mine water for heating and cooling the KRC building.

exchanger a 160 gpm pump circulates water to all the heat pumps. The initial heating design point was based on an entering water temperature of 4.4 °C and a leaving water temperature of 1.4 °C. In 2014, a 372 m^2 addition required the installation of four more heat pumps with a heating capacity of 149,000 BTU/hr. The KRC geothermal system cost approximate $100,000 to install during the building's construction phase. Based on the condition of its service, the director of the KRC estimated that a payback period is three to five years and the rough cost savings are about 30% over a conventional natural gas system. Because of its benefits, the KRC is intended to expand this mine water-based geothermal on the site to install a new and smaller system in a separate building.

3 Field Test

This section introduces a field study for measuring the temperature and chemical distributions in an abandoned mine shaft located in the U.P. A nearly vertical shaft, Shaft 2 of the Hancock mine, was chosen for the measurements. Hancock Shaft 2 was close to the downtown of Hancock City. The final depth of this shaft was estimated to be 1219.2 m. Sensors for temperature and electrical conductivity were sent down into the shaft using a pulley system.

Shown in Fig. 4 is the measured temperature and electrical conductivity variations with depth. It is seen that the water level is at 60 m below the ground surface. Therefore, data at positions above that point are of limited value. The water temperature is not linearly distributed along the depth. Instead, the data clearly demonstrate the existence of two constant temperature layers (layer 1 and layer 2) with an average temperature of 12.6 °C and 15.2 °C, respectively. The existence of the two constant temperature layers indicates that the water is stratified into two layers with a sudden temperature change between them (see Fig. 4). This stratification is also supported by the distribution of the electrical conductivity, which indirectly reflects the distribution of the total salt concentration. As can be seen, the changes in the temperature and electrical conductivity happen at about the same depths. The distributions of both the temperature and electrical conductivity led us to the same deduction: water moves relatively fast within individual layers and consequently, results in a constant temperature and electrical conductivity in each layer (see Fig. 4).

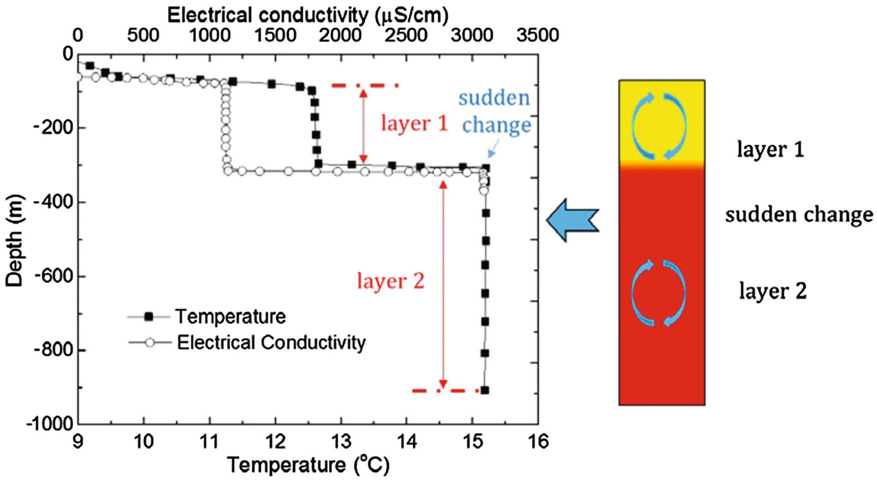

Fig. 4. Temperature and electrical conductivity distributions along Shaft 2.

4 Numerical Investigation

4.1 Theoretical Formulation

This section outlines a theoretical framework for modeling the mine water movement involving the double-diffusive convection. For the large-scale hydrodynamics, water can be reasonably assumed to be incompressible. The mass of a moving fluid element is conserved and formulated as

$$\nabla \cdot \mathbf{U} = 0 \tag{1}$$

where **U** is the velocity of the mine water (m/s). The momentum balance of water is formulated as

$$\frac{\partial \mathbf{U}}{\partial t} + \nabla \cdot (\mathbf{U}\mathbf{U}) - \nabla \cdot [\frac{\mu_{\text{eff}}}{\rho}(\nabla \mathbf{U} + \nabla \mathbf{U}^T) - \frac{2}{3\rho}\mu_{\text{eff}}(\nabla \cdot \mathbf{U})\mathbf{I}] = -\frac{1}{\rho}(\nabla p_{\text{d}} + \rho_{\text{eff}}\mathbf{g}h_e) \tag{2}$$

where ρ is the density of the mine water (kg/m^3); **I** is the identity matrix; h_e is the elevation (m); μ_{eff} (Pa s) is the effective viscosity given by $\mu_{\text{eff}} = \mu_{\text{laminar}} + \mu_{\text{turbulent}}$, in which μ_{laminar} and $\mu_{\text{turbulent}}$ are the laminar dynamic viscosity and the turbulent dynamic viscosity (kg/(m s)), respectively; **g** is the acceleration (m/s^2); and p_{d} is the dynamic pressure (Pa) and is formulated as

$$p_d = p - \rho g h_e \tag{3}$$

where p is the total pressure (Pa). ρ_{eff} in Eq. (2) is the effective density (kg/m^3), which can be assumed to linearly vary with T(K) and S(%) using the following equation:

$$\rho_{\text{eff}} = \rho[1 - \beta_T(T - T_0) + \beta_S(S - S_0)] \tag{4}$$

where T_0 and S_0 are the reference temperature and salinity, respectively; β_T is the coefficient of thermal expansion (K^{-1}); and β_S is the coefficient of salt expansion ($\%^{-1}$).

The governing equation for salt transport is formulated as

$$\frac{\partial S}{\partial t} + \mathbf{U} \cdot \nabla S = \nabla \cdot \left(\alpha^S_{\text{eff}} \nabla S\right) \tag{5}$$

where $\alpha^S_{\text{eff}} = \alpha^S_{\text{laminar}} + \alpha^S_{\text{turbulent}}$, which is the effective salt diffusivity coefficient of the mine water (m^2/s).

The energy conservation within the moving fluid element can be formulated as

$$\frac{\partial T}{\partial t} + \mathbf{U} \cdot \nabla T = \nabla \cdot (\alpha^T_{\text{eff}} \nabla T) \tag{6}$$

where α^T_{eff} is the effective thermal diffusivity of the mine water (m^2/s) and is given by $\alpha^T_{\text{eff}} = \alpha^T_{\text{laminar}} + \alpha^T_{\text{turbulent}}$. The governing equations presented above were discretized and solved using OpenFOAM. The PISO algorithm was used in this paper to solve the iteration of this coupled system [17, 18].

4.2 Simulation Results and Discussion

According to field observations in Fig. 4, there are two constant temperature and salinity (indirectly measured by electrical conductivity) layers in the mine water. The temperature and salinity are well mixed in each layer. Therefore, Hancock Shaft 2 was chosen for the simulation in this section. The model consists of a vertical mine shaft with 8 horizontal drifts. The total depth of the shaft in the model is 1159.2 m, which is 60 m shorter than the actual depth (1219.2 m) because the water level is at 60 m below the ground surface. To consider the buoyancy effect, the buoyancy ratio N was used and formulated as

$$N = \frac{\beta_S \Delta S}{\beta_T \Delta T} \tag{7}$$

where ΔS and ΔT are the salinity difference and temperature difference, respectively. In this paper, N was defined to be 1.2 for the simulation.

Shown in Fig. 5 are the vertical temperature distributions along Shaft 2 at different times. The initial temperature is linearly distributed from 282.15 K to 288.35 K along the depth of the shaft (see Fig. 5a). As time elapses, a very interesting phenomenon was observed. The temperature distribution exhibits a "staircase" shape, as shown in Fig. 5b. When t = 12 h, the number of the staircase decreases (see Fig. 5c), because some of the small staircases merged to form staircases with a larger thickness. This interesting phenomenon was also observed from the vertical salinity distribution in Fig. 6. The "staircase" shape for salinity is formed at t = 1.5 h, and then some of the small staircases merged into larger ones, which is similar to what we observed in

Fig. 5. For both the temperature and salinity, the number of the staircases and the location to form the staircases are identical. The temperature and salinity distributions in Figs. 5 and 6 exhibit the same structure as the field measurements in Fig. 4. This may imply a significantly scientific breakthrough.

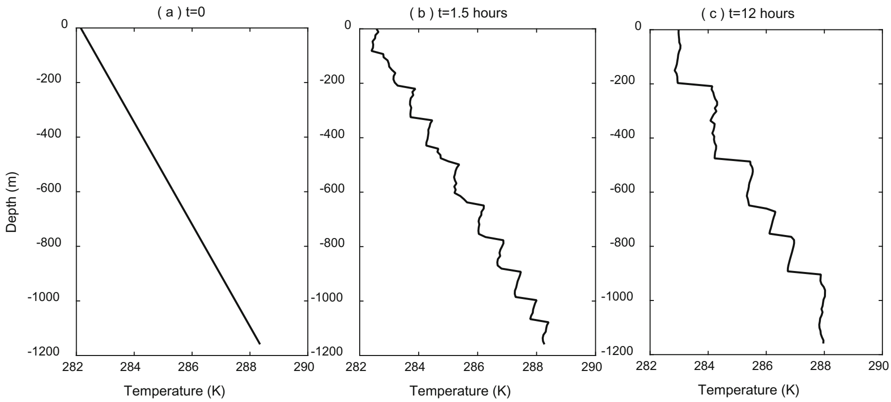

Fig. 5. Vertical temperature distributions along Shaft 2 at different times: (a) the initial condition, (b) t = 1.5 h, and (c) t = 12 h.

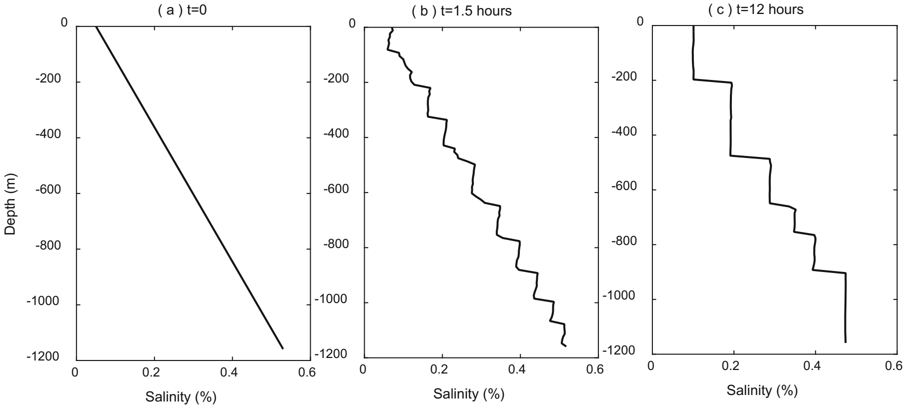

Fig. 6. Vertical salinity distributions along Shaft 2 at different times: (a) the initial condition, (b) t = 1.5 h, and (c) t = 12 h.

Typical flow patterns can help understand how the heat and mass in the mine water are distributed and vary, which trigger the formation of the staircases. Figure 7 presents typical flow patterns at the location between $z = -975$ m and $z = -1159.2$ m at different times. Due to the density difference caused by the temperature and salinity, as can be seen in Fig. 7a, the mine water is not stagnant. The mine water circulates in the shaft to form separate layers. At the interface between the two adjacent layers, the velocity is

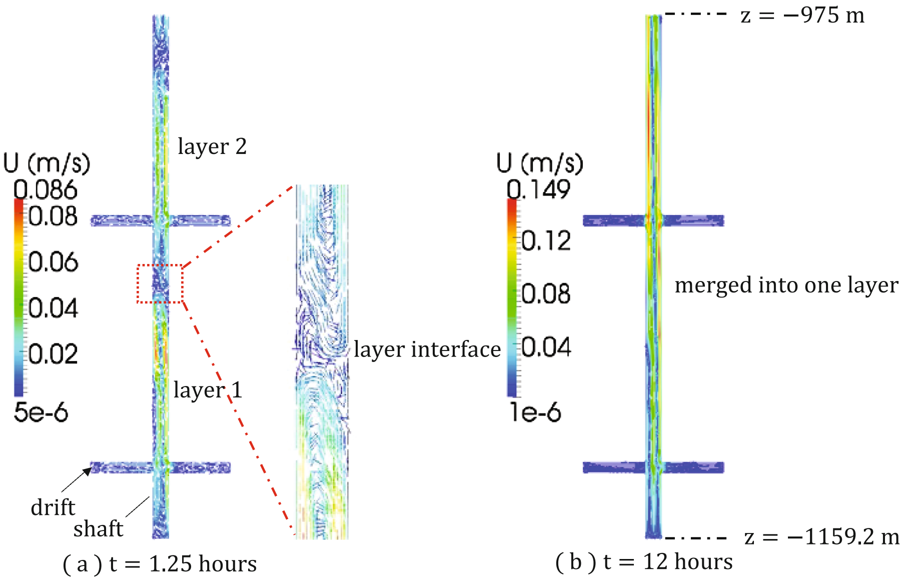

Fig. 7. Typical flow patterns at the location between $z = -975$ m and $z = -1159.2$ m: (a) $t = 1.25$ h and (b) $t = 12$ h.

very slow. Due to this slow velocity, the connection between the two adjacent layers is intercepted and the water moves relatively fast within individual layers. When $t = 12$ h, these two layers merged to form one large layer (see Fig. 7b). These observations clearly explain what we observed on the temperature and salinity distributions in Figs. 5 and 6.

Another angle for directly showing the heat and mass distribution within the mine water is the temperature and salinity contour. As shown in Fig. 8a, the temperature of each layer is almost the same. There is a sudden temperature change at the interface between the two layers, which is consistent with the flow interface in Fig. 7a. When $t = 12$ h, the two layers are merged to form one layer that has the uniform temperature but a larger thickness (see Fig. 8b). Similar observations also can be seen in Fig. 9 for salinity contours. A clearly sudden salinity change is observed when the two layers are formed at $t = 1.25$ h (see Fig. 9a). Then, one large layer is formed via merging the two small layers as time elapses, as shown in Fig. 9b.

The mine water movement due to the double-diffusive convection (Fig. 7) essentially mixes the water to form separate layers. In each layer, the temperature and salinity will approach an equilibrium value, making all the water in this shaft appear as several layers. The mechanism inferred from the above simulation well explains the thermal and salt stratification in the mine water from the field study in Fig. 4, in which the temperatures and chemical concentrations in each layer are approximately constants.

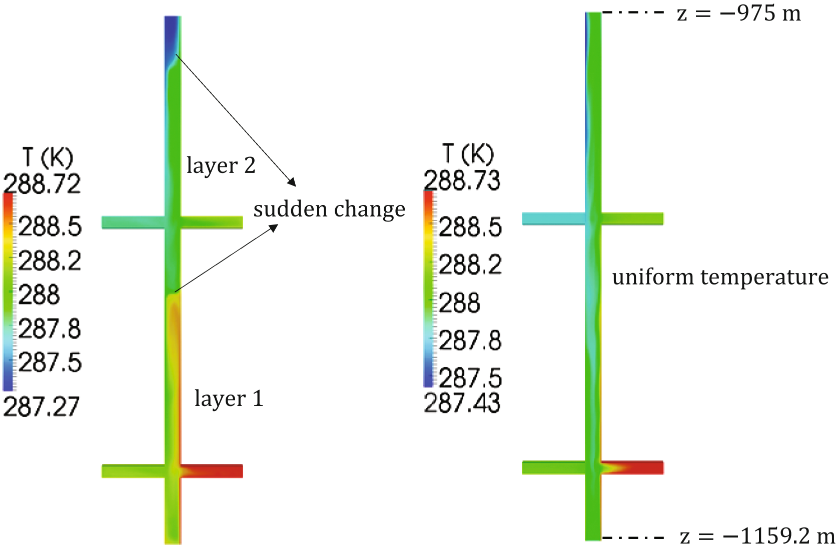

(a) t = 1.25 hours (b) t = 12 hours

Fig. 8. Temperature contours at the location between $z = -975$ m and $z = -1159.2$ m: (a) $t = 1.25$ h and (b) $t = 12$ h.

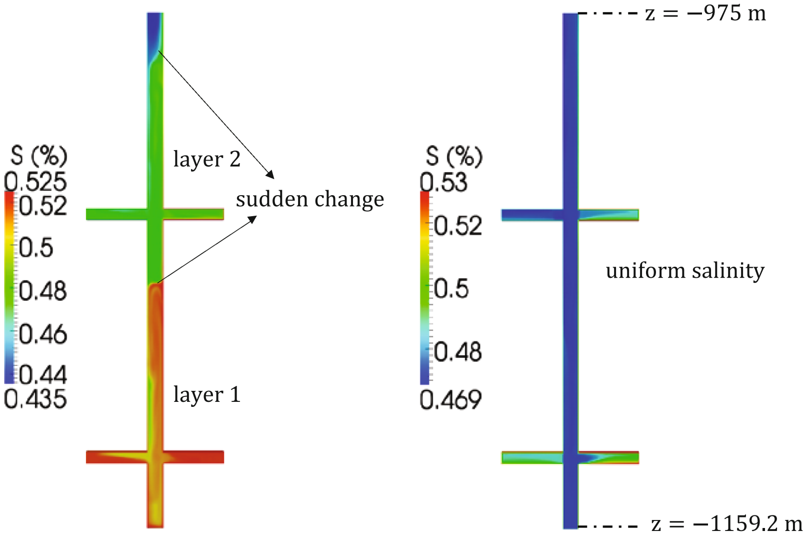

(a) t = 1.25 hours (b) t = 12 hours

Fig. 9. Salinity contours at the location between $z = -975$ m and $z = -1159.2$ m: (a) $t = 1.25$ h and (b) $t = 12$ h.

5 Conclusions

This paper reports on the first large-scale project in the U.S for recovering geothermal energy from the mine water for heating and cooling buildings. A real demonstration project, which has been recovering geothermal energy from the mine water to provide heating and cooling to a 1022 m^2 building in the U.P. of Michigan since 2009, was introduced. The field study for a deep mine shaft yielded measurements of temperature and electrical conductivity distributions, which provided valuable first-hand field data for understanding the physical mechanisms underlying the use of mine water as a geothermal resource. Multiphysics simulation with unique non-isothermal hydrodynamics was conducted to provide explanations to the data measured in the field test. No research has been reported prior to the current study for presenting these significant insights and explanations. The simulation has succeeded in reproducing the key mechanisms explaining heat and mass transfer in the complicated multiphysical processes and shedding light on water stratification observed in the field study.

References

1. Kagel, A., Bates, D., Gawell, K.: A Guide to Geothermal Energy and the Environment. Geothermal Energy Association, Washington, D.C. (2005)
2. Raymond, J., Therrien, R., Hassani, F.: Overview of geothermal energy resources in Québec (Canada) mining environments. In: 10th International Mine Water Association Congress: mine water and the environment, IMWAC. Technical University of Ostrava, Ostrava, Czech Republic, Santiago, Chile (2008)
3. Behrooz, B.S, Elianne, D., Jan-Jaap, V.B.: Geothermal use of deep flooded mines. In: International Symposium on Post-Mining, ISPM, Nancy, France, pp. 1–10 (2008)
4. Bao, T., Liu, Z.: Large-scale thermo-hydrodynamic modeling of a flooded underground mine for geothermal applications. In: Geo-Chicago 2016, pp. 72–83 (2016)
5. Limanskiy, A., Vasilyeva, M.: Using of low-grade heat mine water as a renewable source of energy in coal-mining regions. Ecol. Eng. **91**, 41–43 (2016)
6. Ramos, E.P., Falcone, G.: Recovery of the geothermal energy stored in abandoned mines. In: Clean Energy Systems in the Subsurface: Production, Storage and Conversion, pp. 143–155. Springer (2013)
7. Jessop, A.: Geothermal energy from old mines at Springhill, pp. 463–468, Nova Scotia, Canada (1995)
8. Jessop, A.M., MacDonald, J.K., Spence, H.: Clean energy from abandoned mines at Springhill. Energy Sources **17**, 93–106 (1995)
9. Rottluff, F.: Neue Warmepumpenanlage im Besucherbergwerk Zinngrube Ehrenfriedersdorf. Geotermische Energie. **21**, 811 (1998)
10. Hall, A., Scott, J.A., Shang, H.: Geothermal energy recovery from underground mines. Renew. Sustain. Energy Rev. **15**, 916–924 (2011)
11. Wolkersdorfer, C.: Water Management at Abandoned Flooded Underground Mines: Fundamentals, Tracer Tests, Modelling, Water Treatment. Springer, München, Germany (2008)
12. Louie, E.P.: Writing a community guidebook for evaluation low-grade geothermal energy from flooded underground mines for heating and cooling buildings (2015)

13. Reichart, G., Vaute, L., Collon-Drouaillet, P., Buès, M.A.: Modelling heat and salinity related convective processes in deep mining flooded wells. In: 11th International Mine Water Association Congress, IMWA, Aachen, Germany, pp. 183–187 (2011)
14. Kories, H., Rüterkamp, P., Sippel, M.: Field and numerical studies of water stratification in flooded shafts. In: Proceedings International Mine Water Association Symposium, IMWA, Newcastle upon Tyne, UK, pp. 149–159 (2004)
15. Renz, A., Rühaak, W., Schätzl, P., Diersch, H.: Numerical modeling of geothermal use of mine water: challenges and examples. Mine Water Environ. **28**, 2–14 (2009)
16. Malolepszy, Z.: Low temperature, man-made geothermal reservoirs in abandoned workings of underground mines. In: Proceedings of the 28th Workshop on Geothermal Reservoir Engineering, Stanford, California, USA, pp. 259–265. Stanford University (2003)
17. Oliveira, P.J., Issa, R.I.: An improved PISO algorithm for the computation of buoyancy-driven flows. Numer. Heat Transfer, Part B: Fundam. **40**, 473–493 (2001)
18. Ferziger, J.H., Peric, M.: Computational Methods for Fluid Dynamics. Springer, Heidelberg (2012)

Investigation on the Thermo-Mechanical Behavior of an Energy Pile and the Surrounding Soil by Model Test and 2D Finite Element-Finite Difference Method

X. H. Bao[1(✉)], Y. L. Xiong[2], H. Y. Mingi[1], H. Z. Cui[1], G. B. Liu[2], and R. Y. Zheng[2]

[1] Shenzhen University, Shenzhen 518060, China
bxh@szu.edu.cn
[2] Ningbo University, Ningbo 315211, China

Abstract. The exploitation of geothermal energy could cause additional thermal load imposed to the foundation and surrounding soils. The effects of temperature changes on the response of energy piles which can induce thermal expansion and contraction of both piles and soils need to be examined. This study investigated the behaviors of an energy pile and the surrounding soil using the model test and 2D thermo-hydro-mechanical finite element-finite difference (FE-FD) method that can solve soil-water-temperature coupling problems based on three phase field theory. In the numerical analysis, the thermo-mechanical property of soil could be described by a new thermo-elastoplastic constitutive model, in which, the concept of equivalent thermal stress was adopted. Time change of temperature and displacement of the pile and soil, axial stress of pile are investigated. The simulated results are in good agreement with those obtained from the laboratory test on a model energy pile. Attention is dedicated to the development of pore water pressure that could cause thermo-consolidation of soil and bring the settlement of pile-soil system. In some circumstances, long-term instability of the pile-soil might happen through years of heating and cooling cycles.

Keywords: Energy piles · THM · Model test · FE-FD method

1 Introduction

The use of sustainable geothermal energy has significant meaning in saving of conventional energy sources and protecting the environment. The energy pile, also referred to as heat exchange pile, is an innovative and sustainable foundation solution because of its dual function of supporting superstructure load and harvesting geothermal energy. The performance of the energy pile is based on absorbing and injecting heat in ground and this kind of heat transfer in the energy pile can result in temperature variation in the pile and surrounding soil, which cause pile and soil to expand and contract, further affect the bearing capacity of pile or cause thermo-consolidation of soil, then influence the foundation and structure resistance.

© Springer Nature Singapore Pte Ltd. 2018
D. Zhang and X. Huang (Eds.): GSIC 2018, *Proceedings of GeoShanghai 2018 International Conference: Tunnelling and Underground Construction*, pp. 696–709, 2018.
https://doi.org/10.1007/978-981-13-0017-2_70

Within the past decade, energy piles have been used in many large construction projects, however, most of the energy pile design is still based on experience and empirical methods derived from field tests (Gao et al. 2008; Katsura et al. 2009; Jalaluddin et al. 2011; Loveridge et al. 2013). Most of these studies focused on the heat transfer behavior of the energy pile system, some also focus on the thermo-mechanical behavior of piles influenced by temperature changes (Laloui et al. 2006; Bourne-Webb et al. 2009; Olgun et al. 2012; Murphy et al. 2014). Except for the field tests, laboratory model tests including material tests for energy piles (Wang et al. 2011; Stewart and McCartney 2014; Yavari et al. 2014; Kramer et al. 2015; Marto and Amaludin 2015; Bao et al. 2017; Yang et al. 2017) and numerical analysis (Ghasemi-Fare and Basu 2015; Saggu and Chakraborty 2015; Di Donna et al. 2016; Caulk et al. 2016) are also performed to investigate thermo-mechanical behavior of the energy pile, particularly the composite energy pile or under different thermo-load conditions. However, in most of the numerical models, a fairly simple method was used for calculating the thermo-mechanical behavior of pile and soil system. The models were unable to analysis the effect of thermo-consolidation and thermo-plastic property of soil which is of importance for considering soil-pile interaction behavior, especially the saturated clay that temperature change may cause large pore water pressure, and then lead to large amount of settlement of the ground and pile under long-term cyclic heating-cooling cycles.

Full-scale pile heating tests in field can help in understanding the thermal and mechanical performance of piles. However, large-scale laboratory tests on model piles can be advantageous over full-scale pile heating tests because of the high cost and uncertain field conditions associated with field tests. Moreover, soil properties can be controlled and measured more easily in laboratory than in the field. Thus, as pointed out by Kramer et al. (2015), results from controlled laboratory tests can be helpful in providing meaningful insight into the physics of a complex process and the tests results can be used to verify predictions from numerical analysis of energy piles, as presented in this paper.

Therefore, in the present study, using the finite element-finite difference (FE-FD) method, the thermo-mechanical behavior of a large model-scale energy pile with an embedded U tube was investigated. The model pile was installed in saturated clay prepared through compaction layer by layer. In the simulation, the thermo-mechanical property of the saturated clay was described using a new thermo-elastoplastic constitutive model, in which, the concept of equivalent thermal stress was adopted and the mechanical behavior of soil including structure, overconsolidation and anisotropy at different temperature states could be described in a unified way. Time change of temperatures and displacements of the pile and soil are investigated. Attention is dedicated to the development of pore water pressure which could cause thermo-consolidation of soil. The calculated results are in good agreement with those obtained from the laboratory test.

2 FE-FD Method

2.1 Basic Theory

The problem is presented by a reinforced concrete model pile which is subjected to vertical mechanical loads and exchanges heat with the surrounding soil at the same time. The soil is considered as porous material, composed of solid phase and fluid phase and the entire medium is considered to be fully saturated by water. Thus, the study is a typical thermal-hydraulic-mechanical (THM) problem, that mechanical, thermal and hydraulic are fully coupled because the volume change of the materials is effected by temperature. Moreover, the heat exchange between pile and soil depends on the pore water flow and the mechanical response of soil also depends on the pore water pressure. Therefore, a fully coupled thermo-hydro-mechanical formulation is needed for the numerical simulation.

In this study, a finite element-finite difference (FE-FD) theory proposed by Oka et al. (1994) was adopted to formulate the THM coupling equations which were incorporated in the software SOFT and then numerical simulation could be performed using the program SOFT. In this program, the equilibrium equation and energy conservation equation were discretized by FEM, while the continuity equation was discretized by backward FDM. The displacement, pore water pressure and temperature were taken as the variables in the field equations as shown in the following:

(1) Equilibrium equation:

$$\rho \ddot{u}_i^s = \frac{\partial \sigma_{ij}}{\partial x_j} + \rho b_i \tag{1}$$

(2) Continuity equation for soil-water:

$$\frac{\dot{\varepsilon}_{ii}^s}{n} - \frac{k}{\gamma_w}\frac{\partial^2 P_d}{\partial x_i \partial x_i} - \frac{\dot{P}_d}{K^w} - 3\alpha_t^w \dot{T} = 0 \tag{2}$$

(3) Energy equation:

$$\rho c \frac{\partial T}{\partial t} + n(\rho c)^w v_i \frac{\partial T}{\partial x_i} = k_t \frac{\partial^2 T}{\partial x_i \partial x_i} + Q \tag{3}$$

Where, ρ is the bulk density of the porous material including soil particles and water, $\bar{\rho}^s = (1-n)\rho^s$ is the apparent density of solid, $\bar{\rho}^w = n\rho^w$ is the apparent density of water $(\rho = \bar{\rho}^s + \bar{\rho}^w = (1-n)\rho^s + n\rho^w)$, n is the porosity, u^s is the displacement vectors of solid and water respectively, σ_{ij} is the stress tensor, b_i is the body force, w_i is the relative displacement vector between liquid and solid phases, ε_{ij}^s is the strain tensor of solid, k is the soil permeability, P_d is the excess pore water pressure, K^w is the bulk modulus of water, α_t^w is the linear thermal expansion coefficient of water, c is the specific heat of soil including solid and water $(\rho c = (1-n)(\rho c)^s + n(\rho c)^w)$, k_t is the average heat conductivity including solid and water $\left(k_t = (1-n)k_t^s + nk_t^w\right)$, v_i is the velocity of fluid, T is the temperature and Q is energy produced by the heat source per unit volume.

After discretization, the final THM FE-FD field equation can be obtained as:

$$\begin{aligned}
&\begin{bmatrix} [K] & \vec{K}_v \\ \vec{K}_v^{T} & -(\bar{A}+\bar{\alpha}) \end{bmatrix} \begin{Bmatrix} \Delta\vec{u}_N|_{t+\Delta t} \\ h_{|t+\Delta t} \end{Bmatrix} + \begin{Bmatrix} 0 \\ \sum_{i=1}^{m} \bar{\alpha}_i h_{i|t+\Delta t} \end{Bmatrix} \\
&= \begin{Bmatrix} \Delta\vec{F}_{|t+\Delta t} + \Delta\vec{F}_{|Rt+\Delta t} + \vec{K}_v h_{|t} + \vec{F}_T \Delta\vec{T}_{N|t+\Delta t} \\ \left[\vec{K}_{vT}\right] \Delta\vec{T}_{N|t+\Delta t} - \bar{A} h_{|t} \end{Bmatrix} \left([C^t] + \bar{\beta}\Delta t[K^t]\right)\dot{\vec{T}}_{N|t+\Delta t} \\
&= [F^t] - [K^t]\left(\vec{T}_{N|t} + (1-\bar{\beta})\Delta t \dot{\vec{T}}_{N|t}\right)
\end{aligned} \tag{4}$$

The detailed information about the field equation can be seen in the reference (Xiong et al. 2014).

2.2 Thermo-Elastoplastic Constitutive Model

In the numerical simulation, the behavior of the reinforced concrete is considered thermo elastic, whereas the soil behavior should be described by thermo-elastoplastic constitutive model. The temperature change can cause elastic and plastic volumetric strain, which is similar to the behavior that the stress performances, so the concept of "equivalent stress" is introduced. The similarity of volumetric strain caused by real stress and equivalent stress due to temperature change was clearly described in the work by Xiong et al. (2016). According to the Hooke's law, the equivalent stress $\Delta\tilde{\sigma}_{ij}$ can be expressed as:

$$\Delta\tilde{\sigma}_{ij} = 3K\alpha_T(T - T_0)\delta_{ij} \tag{5}$$

Where, K is the bulk modulus of the soil, α_T is the linear thermal expansion coefficient, T is the actual temperature and T_0 is the reference temperature (usually assumed to be 15 °C).

The result that the change of temperature can cause elastic and plastic volumetric strain was confirmed by experimental date (Eriksson 1989). Therefore, based on the elastoplastic constitutive model at normal temperature condition (Zhang et al. 2011, 2012), the thermo-elastoplastic constitutive model can be obtained by changing overconsolidation state variable R to temperature state variable $\tilde{R}$. The yield function adopted in the model is the function of the modified Cam-clay model considering the overconsolidation, structure and saturation of clay soil, which can be written as:

$$f = \ln\frac{p}{p_0^*} + \ln\frac{\mathrm{M}^2 - \varsigma^2 + \eta^{*2}}{\mathrm{M}^2 - \varsigma^2} + \ln R^* - \ln R - \frac{\rho_s}{1+e_0}\frac{1}{C_p} - \frac{\varepsilon_v^p}{\mathrm{C_p}} = 0 \tag{6}$$

Where,

$$C_p = \tfrac{\lambda - \kappa}{1 + e_0}, \qquad \eta^* = \sqrt{\tfrac{3}{2}\hat{\eta}_{ij}\hat{\eta}_{ij}}, \qquad \eta = \sqrt{\tfrac{3}{2}\eta_{ij}\eta_{ij}}, \quad \varsigma = \sqrt{\tfrac{3}{2}\beta_{ij}\beta_{ij}},$$
$$\hat{\eta}_{ij} = \eta_{ij} - \beta_{ij}, \quad \eta_{ij} = \tfrac{S_{ij}}{\sigma_m} \qquad \eta^{*2} = \tfrac{3}{2}\hat{\eta}_{ij}\hat{\eta}_{ij} = \tfrac{3}{2}\left(\tfrac{S_{ij}}{\sigma_m} - \beta_{ij}\right)\left(\tfrac{S_{ij}}{\sigma_m} - \beta_{ij}\right)$$

η is the stress ratio *q/p* in $p-q$ space *q/p*, ζ is the anisotropy parameter, β is the anisotropy stress tensor, M is the critical state line ratio of the normally consolidated soil.

Based on the consistency law, Eq. (5) can be written as:

$$\begin{aligned} & df = 0 \\ & \Rightarrow \frac{\partial f}{\partial \sigma_{ij}} d\sigma_{ij} + \frac{\partial f}{\partial \beta_{ij}} d\beta_{ij} + \frac{1}{R^*} dR^* - \frac{1}{R} dR - \frac{d\rho_s}{1 + e_0}\frac{1}{C_p} - \frac{1}{\mathrm{C_p}} d\varepsilon_v^p = 0 \end{aligned} \tag{7}$$

Associated flow rule is adopted, the increment of plastic strain tensor can be obtained as:

$$d\varepsilon_{ij}^p = \Lambda \frac{\partial f}{\partial \sigma_{ij}} \tag{8}$$

$$\Lambda = \frac{\frac{\partial f}{\partial \sigma_{ij}} E_{ijkl}\, d\varepsilon_{kl} + \frac{Q}{C_p}\frac{1}{1 + e_0} dS_r}{h_p + \frac{\partial f}{\partial \sigma_{ij}}\, E_{ijkl} \frac{\partial f}{\partial \sigma_{kl}}} \tag{9}$$

Where,

$$h_p = \frac{1}{\mathrm{C_p}(\mathrm{M}^2 - \zeta^2 + \eta^{*2})\sigma_m}\left[M_s^2 - \eta^2\right] \tag{10}$$

The loading criteria is given as:

$$\begin{cases} \Lambda > 0 & \textit{loading} \\ \Lambda = 0 & \textit{neutral} \\ \Lambda < 0 & \textit{unloading} \end{cases} \tag{11}$$

The detailed explanation about the deviation of the constitutive model can be found in the reference (Xiong et al. 2016).

2.3 Material Parameters

The parameters of clay and pile used in the constitutive model are listed in Table 1. For the initial constitutive model parameters of clay and concrete, most of the parameters were obtained by laboratory tests, except for the overconsolidation, structure and anisotropy parameters which are decided according to the references (Bao et al. 2016; Ye and Ye 2016). The initial thermal property parameters of clay and concrete related to thermal properties as shown in Table 2 are also obtained from laboratory thermal tests.

Table 1. Constitutive model parameters of soil and concrete pile used in calculation.

Parameters	Clay	Concrete
Compression index λ	0.25	Null
Swelling index κ	0.06	Null
Critical state parameter M	0.82	Null
Void ratio N (p' = 98 kPa on *N.C.L.*)	2.4	Null
Poisson's ratio v	0.35	0.2
Over consolidation parameter m	2.2	Null
Structure parameter a	0.06	Null
Anisotropy parameter b_r	0.1	Null
Gravity γ (kN/m^3)	18	24
Permeability (m/s)	$2.3 * 10^{-7}$	$1.0 * 10^{-9}$
Elastic module E (GPa)	Null	30

Table 2. Thermal properties of soil and concrete pile used in calculation.

Parameters	Clay	Concrete
Thermal expansion coefficient α (1/K)	$5.0 * 10^{-6}$	$1.1 * 10^{-5}$
Thermal conductivity k (W/m/K)	1.51	2.94
Specific heat c (kJ/kg/K)	1.52	0.96
Specific heat of water c^w (kJ/kg/K)	4.184	

3 Test Description and Numerical Model

3.1 Test Description

The laboratory test was conducted in Ningbo University (Ningbo, China) and the schematic profile is shown in Fig. 1. The model concrete pile which was precast has a total length of 1.25 m and diameter of 0.2 m, in which a heat exchange U tube was set. The lengths of the pile and tube that buried in clay were 1 m and 0.95 m respectively. The pile was made by concrete with the strength of C30, and reinforced by 4 HRB335 type steel with diameter of 10 mm. In the present numerical simulation, the pile was assumed to be concrete material and the steel was not considered.

In this experiment, the initial temperature of the soil and pile was set to 28 °C (room temperature in summer), and then the pile was heated by keeping inlet water temperature in The U tube in a constant value of 50 °C. The heat gradually diffuses from the tube to pile and soil, when the adjacent pile soil temperature differences is less than 10%, the heat exchange can be considered stable. Keep the stable state until the excess pore water pressure fully dissipated in the soil, and then stop heating so that the temperature of pile and soil naturally returned to the room temperature of 28 °C. The effect of temperature change on the working performance of heat exchange pile can be studied in this heating-cooling cycle.

Temperature measurements were placed at several locations within soil (T1, T2, T3, T4, T5) and on pile surface (T6) to characterize the temperature evolution in soil

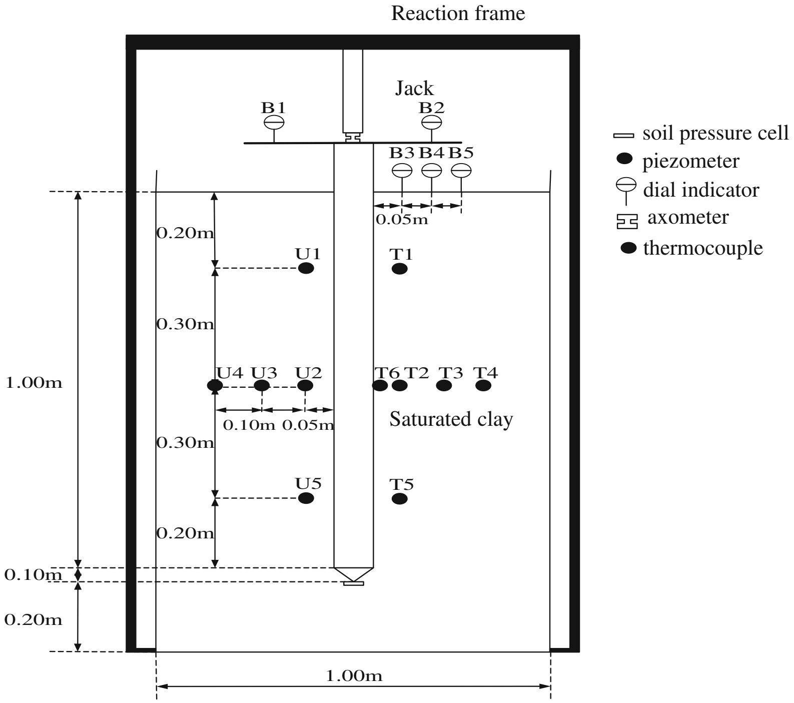
Reaction frame
Jack
B1
B2
B3 B4 B5
0.05m
U1
T1
U4 U3 U2
T6 T2 T3 T4
0.10m 0.05m
Saturated clay
U5
T5
0.20m
0.30m
0.30m
0.20m
1.00m
0.10m
0.20m
1.00m
soil pressure cell
piezometer
dial indicator
axometer
thermocouple

Fig. 1. Schematic diagram of pile and soil.

surrounding the pile with time change. Pore pressure measurements were also placed at several locations within soil (U1, U2, U3, U4, U5) to investigate the influence of temperature on soil behavior. Moreover, several dial indicators were placed on top of pile (B1, B2) and soil surface near pile (B3, B4, B5) to measure the displacement of pile and soil caused by temperature change. The exact locations of these instruments are clearly shown in Fig. 1.

3.2 Numerical Model

The FE-FD analysis was performed to simulate the laboratory test of the energy pile under the same conditions as those in the test. A constant inlet flow temperature T_{inlet} = 50 °C of the circulation fluid at the inlet point was set. According to the laboratory test model and symmetry properties of pile and soil, the 2-D half domain of the numerical model is shown in Fig. 2, in which the red part represents the heater tube with inlet fluid and the blue part represents half of the model pile. All the size is the same as that in the laboratory test. Only the inlet flow was considered and modeled as a heat pipe with the size of 0.95 m × 0.02 m according to the tube size in the laboratory test. The thermal loading of the pile is numerically reproduced by imposing temperature paths on all of the nodes of the elements that characterize the heat pipe mesh in pile body.

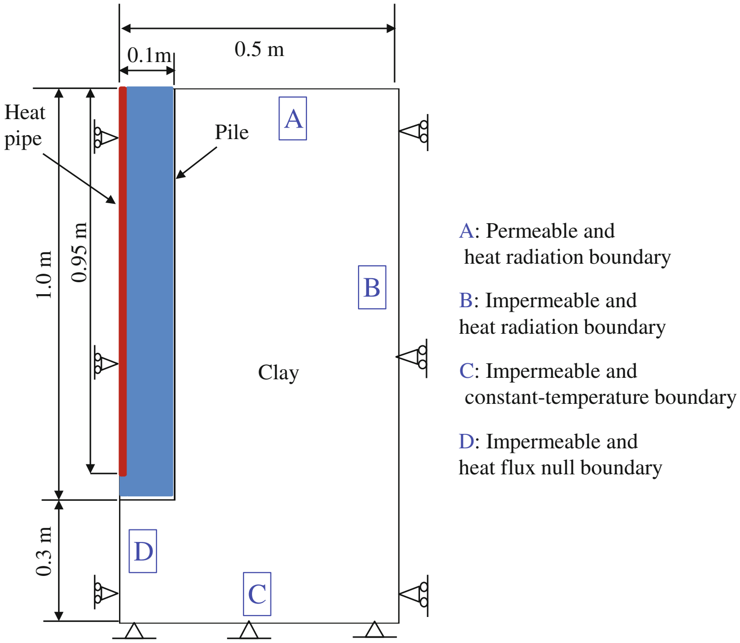
0.5 m
0.1m
Heat pipe
Pile
A
B
C
D
Clay
1.0 m
0.95 m
0.3 m
A: Permeable and heat radiation boundary
B: Impermeable and heat radiation boundary
C: Impermeable and constant-temperature boundary
D: Impermeable and heat flux null boundary

Fig. 2. Numerical model for the FE-FD analysis.

For the boundary conditions, the initial boundary condition was set according to the test condition that the vertical boundaries at the two sides have been restrained in horizontal direction and the bottom soil boundary has been restrained in both vertical and horizontal direction. As the clay was saturated, so the top soil boundary is assumed to be permeable, while the bottom boundary, left vertical soil boundary and right side boundary are impermeable. The pile is also assumed to be impermeable. The thermal boundary conditions applied in the model were heat radiation through top and right side boundaries, constant-temperature at the bottom boundary. Heat flux is assumed to be zero along the axis of symmetry of pile and soil. This method of setting of thermal boundary conditions used in FE method can be founded in references (Ghasemi-Fare and Basu 2015; Saggu and Chakraborty 2015; Di Donna et al. 2016; Caulk et al. 2016). For the initial thermal condition, the initial temperature of pile and soil was set the same as in the model tests measured before heating with a value of 28 °C, and the initial inlet flow temperature was also set he same as in test condition T_{inlet} = 50 °C.

The interface between the pile and soil surface has been modeled as frictional contact in tangential direction with a coefficient friction tan φ (φ is the internal friction angle of clay). In another word, pile-soil interface is modeled by a thin layer of element that soil and pile can slide relatively, and the pile-soil interface parameters are the same as those assumed for the soil. At the bottom of the pile soil surface, hard contact with zero penetration has been considered.

4 Comparison of Results from Numerical Simulation and Laboratory Test

This section compares the numerical results with the laboratory test results conducted in Ningbo University (Ningbo, China). As the entire test data were available to the numerical model, the numerical simulation is considered suitable for reproducing the response of the thermo-mechanical behavior of pile and soil in the heating and naturally cooling circle.

4.1 Temperature Distribution

The time-temperature curves of the points T1 (0.2 m below soil surface), T2 (0.5 m below soil surface) and T5 (0.8 m below soil surface) along the depth direction near pile (0.05 m away from pile side) are shown in Fig. 3(a). It can be seen from the figure that it took about 50 h for the thermal transfer from pile to soil and the heat exchange reached the stable state. The maximum temperature of the soil near pile side is 45.2 °C, 40.3 °C and 36.7 °C at depth of 0.2 m (T1) 0.5 m (T2) and 0.8 m (T5) below the soil surface. At the same time and the same distance of 0.05 m from the pile side, along the pile depth direction, the greater the depth of the soil, the smaller the temperature rose. The test and simulated results showed almost the same values. In Fig. 3(b), it can be seen that when the heat exchange reached the stable state, at the points 0.05 m below the soil surface, the temperatures of the soil at the distance of 0.05 m (T2), 0.15 m (T3), 0. 25 m (T4) from the pile side and on the pile surface (T6) are 40.2 °C, 35.3 °C, 32.1 °C and 45.0 °C, respectively. It is clear that at the same time, soil temperature decreased with the increase of horizontal distance from the pile side. The simulated results are in good agreement with the laboratory test results. When the heat exchange reached the stable state, the simulated temperature distribution of pile-soil is shown in Fig. 4. When the thermal cycle reached stable state, the maximum temperature appeared in the upper part of the pile, reaching 49.7 °C, the temperature gradually reduced along the pile from top to bottom.

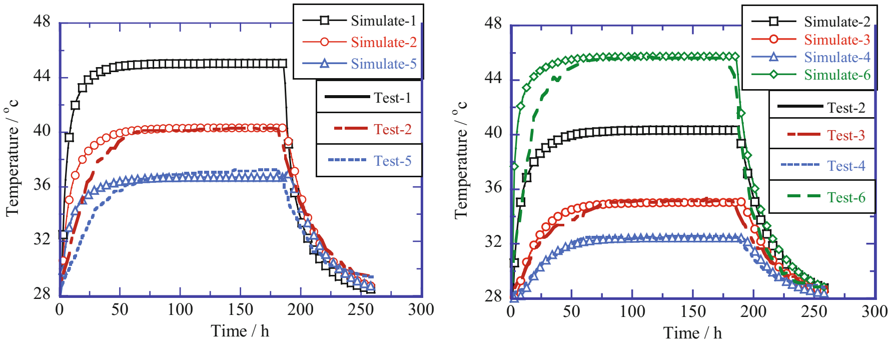

(a) Different depths (b) Different horizontal distances

Fig. 3. Time-temperature curves of soil at different depths and horizontal distances.

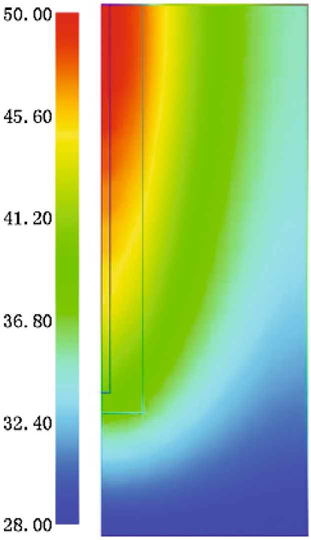

Fig. 4. Simulated distribution of temperature in pile and soil (unit: °C).

4.2 Pore Pressure in Soil

The time-excess pore water pressure (EPWP) curves at points U1 (0.2 m below soil surface), U2 (0.5 m below soil surface) and U3 (0.8 m below soil surface) 0.05 m away from the pile side are presented in Fig. 5(a). The test and simulated results showed almost the same values. It can be seen from Fig. 5(a) that the pore pressure increased sharply with the increase of temperature, and the maximum pore pressure at the points U1, U2 and U5 reached 0.70 kPa, 2.69 kPa and 4.54 kPa respectively and then slowly dissipated to the stable state. At the same time and the same distance from the pile side, the greater the depth, the higher the soil pressure caused by the

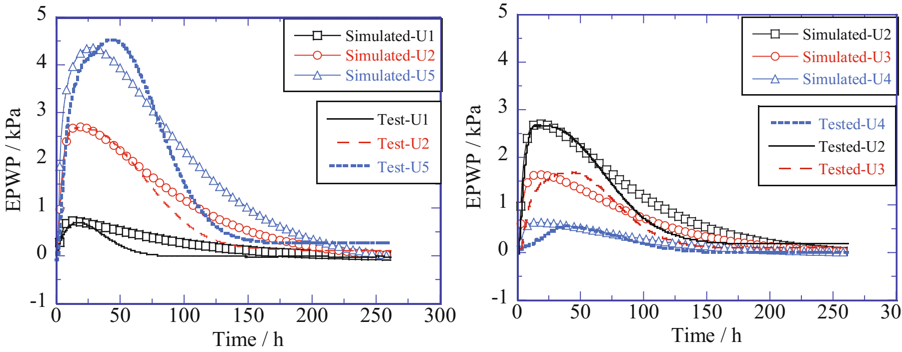

(a) Different depths (b) Different horizontal distances

Fig. 5. Time-pore pressure curves of soil at different depths and horizontal distances.

temperature, and the longer time before the pore pressure to reach the peak value. Figure 5(b) presents the time-EPWP curves at different horizontal distance away from pile side 0.5 m below the soil surface. It can be seen from the figure that the maximum value of EPWP at points U2 (0.05 m away from pile side), U3 (0.15 m away from pile side) and U4 (0.25 m away from pile side) reached 2.69 kPa, 1.69 kPa and 0.56 kPa, respectively, and then slowly dissipated to the stable state. At the same time and the same depth, the closer to the pile side, the higher the EPWP caused by the temperature change, and the shorter the time required for the EPWP to reach the peak values. The numerical simulation results are in good agreement with the laboratory test results.

4.3 Displacement

For the sign conventions, upward displacements are considered to be positive while downward displacements are considered to be negative. Figure 6(a) shows the variation of the vertical displacement at the pile top under the heating-cooling cycle. In the heating stage, the pile uplift due to thermal expansion and arrived at the peak value at the end of heating, which means that the effect of temperature could reduce the settlement of the pile under the condition of pure heating cycle. After heating, the vertical displacement at the pile top dropped quickly. During the naturally cooling stage, the pile-soil expansion disappeared and the downward displacements increased. When arrived at the stable state, the total settlement of the pile reduced 0.16 mm, indicating that the unrecoverable plastic deformation occurred. The simulated value is slightly larger than the test value at the thermal expansion stage and slightly smaller than the total settlement value from the test. However the overall tendency is consistent with test results.

Figure 6(b) shows the variation of the vertical displacement at soil surface 0.05 m away from the pile side under the heating-cooling cycle. The simulated results and test results showed the same tendency. In the early stage of heating, the test value and simulated value of the surface uplift showed a rapid increase, and the rate of simulated uplift was faster than that of the test. When the temperature of pile and soil reached the stable state, consolidation settlement began to accumulate and soil settlement become large quickly in the naturally cooling cycle. It is clear that unrecoverable plastic deformation of soil occurs and the total settlement is about 0.25 mm when the soil-pile recovered to the initial room temperature of 28 °C. In another word, the thermo-consolidation occurred when the pore water dissipated. On the whole, the simulation results fit the test value quite well. For the displacements of pile and soil, the trends and the maximum values are comparable between the simulation and the test, while there is a significant difference in the computing time. In another word, the rate of simulated deformation is faster than that of the test. This phenomenon might be the following reasons:

(1) The permeability of soil. In test, soil permeability changed with the temperature change and the development of pore water pressure. However, in the simulation, the permeability value of soil kept constant as the initial value obtained from laboratory test.

(2) Constitutive model of soil. The thermo-elastoplastic constitutive model did not consider the creep behavior of clay that the deformation kept developing slowly for a long time after the change of loading and temperature condition. However, the used constitutive model just considered the elastic and plastic deformation in the loading and temperature change processes.

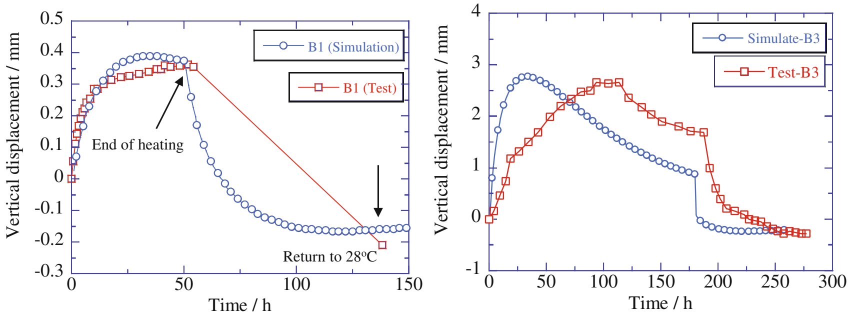

(a) Top of the test pile (b) Ground surface 0.05 m away from pile side

Fig. 6. Time-vertical displacement curves at different places.

5 Conclusions

This study comprised both the model test and 2-D numerical simulation of the thermo-hydro-mechanical (THM) behavior of an energy pile embedded in saturated clay subjected to the heating-cooling cycle. In the used THM coupled FE-FD method, a thermo-elastoplastic constitutive model based on the concept of thermal equivalent stress was used to describe the thermo-plastic behavior of soil. The simulation results are in good agreement with the laboratory model test results, and the following conclusions can be drawn.

(1) It took about 50 h for the thermal transfer from pile to soil and the heat exchange reached the stable state when the maximum temperature appeared in the upper part of the pile. The greater the depth of the soil, the smaller the temperature rose. In another hand, soil temperature decreased with the increase of horizontal distance from the pile side.

(2) For the excess pore pressure, the greater the depth, the higher the soil pressure caused by the temperature, and the longer time required for the pore pressure to reach the peak value after the heat exchange reached the stable state. In another hand, the closer to the pile side, the higher the EPWP caused by the temperature change, and the shorter the time required for the EPWP to reach the peak value.

(3) The effect of temperature could reduce the settlement of the pile under the condition of pure heating cycle, while during the naturally cooling stage, the pile-soil expansion disappeared and the downward displacements increased indicating that the unrecoverable plastic deformation occurred.

(4) In the early stage of heating, the surface uplift showed a rapid increase, however, after the heat exchange reached the stable state, consolidation settlement began to accumulate and soil settlement become large quickly in the naturally cooling cycle indicating that the thermo-consolidation occurred due to the dissipation of pore water.

Acknowledgement. This work was supported by the National Natural Science Foundation of China (Grant No. 51678369) and Technical Innovation Foundation of Shenzhen (Grant No. JCYJ20170302143610976).

References

Bao, X., Memon, S., Yang, H., et al.: Thermal properties of cement-based composites for geothermal energy applications. Materials **10**(5), 462 (2017)

Bao, X., Ye, B., Ye, G., Zhang, F.: Co-seismic and post-seismic behavior of a wall type breakwater on a natural ground composed of liquefiable layer. Nat. Hazards **83**(3), 1799–1819 (2016)

Bourne-Webb, P., Amatya, B., Soga, K., et al.: Energy pile test at Lambeth College, London; geotechnical and thermodynamic aspects of pile response to heat cycles. Géotechnique **59**(3), 237–248 (2009)

Caulk, R., Ghazanfari, E., McCartney, J.: Parameterization of a calibrated geothermal energy pile mode. Geomech. Energy Environ. **5**, 1–15 (2016)

Di Donna, A., Rotta Loria, A., Laloui, L.: Numerical study of the response of a group of energy piles under different combinations of thermo-mechanical loads. Comput. Geotech. **72**, 126–142 (2016)

Eriksson, L.: Temperature effects on consolidation properties of sulphide clays. In: 12th International conference on soil mechanics and foundation engineering, Rio de Janeiro, pp. 2087–2090. Taylor and Francis, London, UK (1989)

Ghasemi-Fare, O., Basu, P.: Thermal operation of geothermal piles installed in sand - a comparative assessment using numerical and physical models. In: IFCEE 2015 ASCE, pp. 1721–1730 (2015)

Gao, J., Zhang, X., Liu, J., Li, K., Yang, J.: Thermal performance and ground temperature of vertical pile-foundation heat exchangers: a case study. Appl. Therm. Eng. **28**(17–18), 2295–2304 (2008)

Jalaluddin, A., Tsubaki, K., Inoue, S., Yoshida, K.: Experimental study of several types of ground heat exchanger using a steel pile foundation. Renew. Energy **36**, 764–771 (2011)

Katsura, T., Nakamura, Y., Okawada, T., Hori, S., Nagano, K.: Field test on heat extraction or injection performance of energy piles and its application. In: The 11th International Conference on Energy Storage (Effstcok2009), p. 146 (2009)

Kramer, C., Ghasemi-Fare, O., Basu, P.: Laboratory Thermal performance tests on a model heat exchanger pile in sand. Geotech. Geol. Eng. **33**, 253–271 (2015)

Loveridge, F., Holmes, G., Powrie, W., Roberts, T.: Thermal response testing through the chalk aquifer. ICE Proc. Geotech. Eng. **166**(2), 197–210 (2013)

Laloui, L., Nuth, M., Vulliet, L.: Experimental and numerical investigations of the behavior of a heat exchanger pile. Int. J. Numer. Anal. Meth. Geomech. **30**, 763–781 (2006)

Murphy, K., McCartney, J., Henry, K.: Thermo-mechanical characterization of full-scale energy foundations. In: Proceedings of the GeoCongress, ASCE, pp. 617–628 (2014)

Marto, A., Amaludin, A.: Response of shallow geothermal energy pile from laboratory model tests. In: International Symposium on Geohazards and Geomechanics (ISGG2015) IOP Conference Series on Earth and Environmental Science, vol. 26, p. 012038 (2015)

Oka, F., Yashima, A., Shimata, T., Shibata, T., Kato, M., Uzuoka, R.: FEM-FDM coupled liquefaction analysis of a porous soils using an elasto-plastic model. Appl. Sci. Res. **52**, 209–245 (1994)

Olgun, G., Martin, J., Abdelaziz, S., et al.: Field testing of energy piles at Virginia Tech. In: Proceedings of the 37th Annual Conference on Deep Foundations, Houston, TX, USA (2012)

Saggu, R., Chakraborty, T.: Cyclic thermo-mechanical analysis of energy piles in sand. Geotech. Geol. Eng. **33**, 312–342 (2015)

Stewart, M., McCartney, J.: Centrifuge modeling of soil structure interaction in energy foundations. J. Geotech. Geoenviron. Eng. **140**(4), 04013044 (2014)

Wang, B., Bouazza, A., Haberfield, C.: Preliminary observations from laboratory scale model geothermal pile subjected to thermo-mechanical loading. In: Geo-Frontiers, pp, 430–439 (2011)

Xiong, Y., Ye, G., Zhu, H., Zhang, S., Zhang, F.: Thermo-elastoplastic constitutive model for unsaturated soils. Acta Geotech. **11**, 1287–1302 (2016)

Xiong, Y., Zhang, S., Ye, G., Zhang, F.: Modification of thermo-elasto-viscoplastic model for soft rock and its application to THM analysis of heating tests. Soils Found. **54**(2), 176–196 (2014)

Yang, H., Memon, S., Bao, X., et al.: Design and preparation of carbon based composite phase change material for energy piles. Materials **10**(4), 391 (2017)

Yavari, N., Tang, A., Pereira, J., Hassen, G.: Experimental study on the mechanical behavior of heat exchange pile using physical modeling. Acta Geotech. **9**(3), 385–398 (2014)

Ye, G., Ye, B.: Investigation of the overconsolidation and structural behavior of Shanghai clays by element testing and constitutive modeling. Undergr. Space **1**(1), 62–77 (2016)

Zhang, F., Ikariya, T.: A new model for unsaturated soil using skeleton and degree of saturation as state variables. Soil Found. **51**(1), 67–81 (2011)

Zhang, S., Leng, W., Zhang, F., Xiong, Y.L.: A simple thermo-elastoplastic model for geomaterials. Int. J. Plast **34**, 93–113 (2012)

Bearing Performance of Geothermal Energy Pile Subjected to Thermal Loading

Pengfei Fang[1(✉)], Abdelmalek Bouazza[2], Zhongjin Wang[1],
and Xinyu Xie[1]

[1] Ningbo Institute of Technology, Zhejiang University, Ningbo 315100, China
`fpf@nit.zju.edu.cn`
[2] Monash University, Melbourne, VIC 3800, Australia

Abstract. As a kind of Ground Source Heat Pump (GSHP), geothermal energy piles is the economic, stable, efficient, and environmentally friendly way of cooling and heating building. Though the usage of geothermal energy piles has rapidly increased in the past three decades, there is so far limited understanding of their thermo-mechanical performance, and its application is earlier than theoretical investigation. Based on four published research findings, the bearing capacity and the mobilized shaft resistance of pile under thermal loading are analyzed. When geothermal energy pile (GEP) is heated, its bearing capacity will be increased, and the friction resistance of the upper section will be decreased. At the same time, friction resistance of the lower section is increased, and the axial force along pile will be enlarged. Whilst geothermal energy pile is cooled, friction resistance of the upper section will be increased, and that of the low pile is decreased. The mobilized strain, stress and shaft resistance profile are related to the constraint condition of pile ends. There is even tensile stress in pile under the special case with cooling load, which is adverse to its bearing capacity. The results is reference to design geothermal energy pile under similar circumstance.

Keywords: Thermal loading · Geothermal energy pile · Bearing performance

1 Introduction

As a building energy consumption technology, ground source heat pump (GSHP) can be used to harness the geothermal energy via the closed-loop pipe in soil, which is employed widely in the field of building HVAC and air conditioning all over the world [1–3]. Whilst the pipes carrying a heat transfer fluid in GSHP are mounted along the reinforcement cages in pile (a vertical slender structure), it is known as Geothermal Energy Pile (GEP). So GEP plays two roles, one is pile foundation of building (or underground structure) and the other is ground heat exchanger, which extracts shallow ground energy via heat pump. For the pile foundation used as vertical borehole ground-coupled heat pump, its cost of drill hole and backfill can be saved. The acquired energy from GEP is renewable, stable, clean and durable, which have the advantage of reliable and environmentally friendly resource.

The geothermal energy pile technology had been rapidly developed during the past three decades, since the beginning of the 1984 [4]. There are so far many cases of

© Springer Nature Singapore Pte Ltd. 2018
D. Zhang and X. Huang (Eds.): GSIC 2018, *Proceedings of GeoShanghai 2018 International Conference: Tunnelling and Underground Construction*, pp. 710–717, 2018.
https://doi.org/10.1007/978-981-13-0017-2_71

geothermal energy pile in UK, Austria, Germany and Ireland, etc. [4–7]. Particularly, there are very costly penalties for buildings that do not achieve the 40% energy savings above Building Regulations in UK [5], and GEP is becoming increasingly popular as some energy prices are rising. In addition, more than 5012 geothermal energy piles were used for building in UK till 2012, and there was the reduction of carbon dioxide emission with 6640 tons every year. So the GEP system represents an effective contribution to environmental protection by providing clean and self-renewable energy.

So far, there is little published, quantitative evidence regarding the bearing performance of GEP subjected to thermal loading. Notwithstanding there is no report on damage case of GEP, its safety and reliability is uncertainty, which will affect its popularization and application.

When a geothermal energy pile is heated or cooled, there is the expansion or contraction deformation in pile-soil interface. And the mobilized pile-soil interface sliding and normal stress come into being. So the impact on load transfer behavior and shaft resistance of pile under thermal loading cannot be negligible, which affects the bearing capacity and settlement of pile.

In this paper, results from the centrifugal model test and the field trials are synthesized in order to understand the mechanism of the load-settlement, lateral friction and axial stress along pile under thermal loading. And the development of the pile-soil interaction mechanism may be helpful for GEP design in similarly circumstances.

2 Load-Settlement Curves Under Thermo-Mechanical Loading

Whilst a pile is free body without a head load, it will expand or contract in proportion to the coefficient of thermal characteristics under temperature loading. The relation of thermal strain and temperature change is according to the equation

$$\varepsilon_{\mathrm{T}} = \alpha_{\mathrm{T}} \times \Delta T \tag{1}$$

where ε_{T} is the free axial thermal strain without restraint in head and toe of pile, α_{T} is the coefficient of thermal expansion or contraction of concrete and ΔT is the change of temperature in pile.

In fact, the pile is restrained by the surrounding ground and superstructure. As the results of the restraint (full or partial) and thermal loading, axial and radial strain will be mobilized, which will affect the shift of pile body (head and toe), pile-soil interface stress, lateral friction and axial force along pile. So the mobilized axial stress and settlement must be considered under thermal loading in the design of GEPs.

2.1 Centrifuge Model Test

Owing to the load-settlement curves of pile obtained from the in-situ static load test, the significant cost and time are required. It is very difficult to perform the field test to investigate the effect of thermal loading on the load-settlement curves. So a centrifuge-scale testing setup was developed to evaluate the bearing capacity of GEP by

Dr. McCartney of University of Colorado at Boulder [8]. A large-scale soil container was designed, which was a cylindrical aluminum tank with an inside diameter of 600 mm, wall thickness of 13 mm, and a height of 540 mm. There was an insulation sheet around the tank to prevent heat loss. Four piles with the length of 381 mm and the diameter of 76.2 mm were buried around the compacted silt in container. The pile spacing was 3 times diameter. Each test was performed at 14 g acceleration level after the soil and pile had recovered to ambient conditions from the previous test. The maximum mechanical load on pile head was 1000 kN, and the loading rate adopted was a constant displacement rate of 0.2 mm/min. Among the four tests, two baseline tests were performed under the ambient temperature of 15 °C, other tests were under 50 °C and 60 °C respectively.

The test results are shown in Fig. 1. The two baseline tests indicate a good compatibility in load-settlement curves. Whilst the temperature is increased by 29 °C (the ambient temperature of 21 °C) and 41 °C (the ambient temperature of 19 °C), theirs load-settlement curves behave steep characteristic type. In case of the pile heated, the temperature-induced radial strain will enlarge the normal stress in pile-soil interface, and raise the lateral friction and bearing capacity. According to the criterion of ultimate bearing capacity from the load-settlement curve [9], the ultimate bearing capacity of four testing piles are 1400 kN, 1400 kN, 1630 kN and 1820 kN respectively. When the pile was heated from 15 °C to 60 °C, the ultimate bearing capacity was increased by 30%.

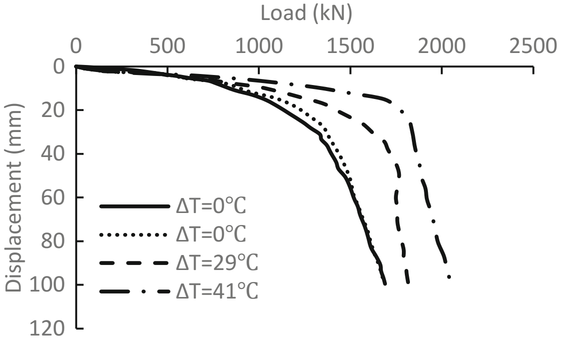

Fig. 1. Load-displacement curves under thermal loading from centrifugal model test [8]

2.2 Field Test in Monash

A field test of geothermal energy pile was conducted in Monash University, Melbourne, Australia [10]. The cast-in-place bored pile had the diameter of 600 mm and the length of 16.1 m. The stratigraphy along pile consist of fill material of 1.5 m, sandy clay of 1 m, sand (with traces of clay) of 13.6 m. Two O-cell testing system were installed at 10 m and 14.5 m depth. During the initial loading, the cell of 14.5 m depth could not work. Three static load tests were carried out, including: (1) the initial test under the ambient circumstance without thermal load; (2) the heating test, pile heated for 9 days; (3) the cooling test, pile cooled naturally for 6 months. The test results are shown in Fig. 2.

According to the three static load tests, the ultimate frictional resistances of upper section above the 10 m O-cell are 1650 kN (initial test), 1885 kN (heating test) and 1700 kN (cooling test) respectively. In comparison with the initial test, the ultimate lateral friction of the heating test was enlarged by 235 kN. So the shaft resistance will be increased under heating load, for the heated pile is expanded to raise the pile-soil interface stress. Whilst the pile was cooled, the ultimate side friction fell to 1700 kN, which was close to that of the initial test.

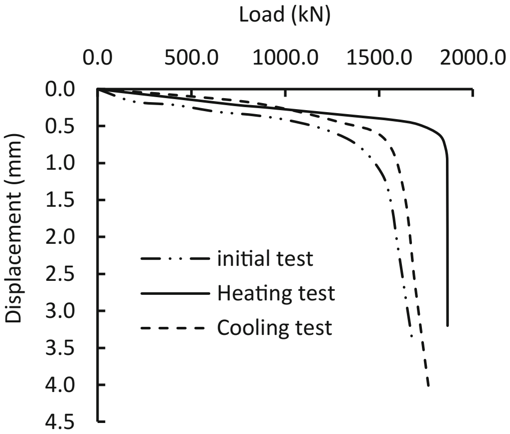

Fig. 2. Load-displacement curves under thermal loading from field test [10]

3 Lateral Friction and Axial Force Under Thermo-Mechanical Loading

3.1 Field Test in Lambeth College

The site for the test pile was located on the south-east of South London [11]. Ground condition around the test pile was the typical London Clay Formation. The test pile was 23 m long with an upper diameter of 610 mm (5 m long) and a lower diameter of 550 mm. According to project design, the anchor pile method and the working load of 1200 kN were adopted. There were 18 vibration-wire strain gauges with 6 levels, 6 thermocouples and 5 external load control elements (LVDTs) along pile shaft. At the same time, the continuous strain and temperature profiles were measured by the optical fiber sensors. There were three tests including the initial test, heating test and cooling test. The lateral friction and the axial force profiles are shown in Fig. 3. The lateral friction distribution along pile under the mechanical load only in initial test is uniform beside the pile head. In case of the pile cooled, the volume contraction will mobilize the downward shift for the upper section and the upward for the lower section. Therefore, the lateral friction for the upper section will be increased and that of the lower section decreased. Particularly, for the lower section of pile the negative friction and the tensile stress in concrete will be mobilized, which is very unfavorable to its bearing capacity. So it is necessary to consider the extreme cooling condition during the GEP design.

Whilst the pile is heated, the upward shift for the upper section and the downward for the lower section are mobilized. The pile-soil interface sliding for the upper section is decreased, which may reduce the lateral friction. And the pile-soil sliding for the lower section is increased, which may enlarge the shaft resistance. The maximum axial stress was 8000 kPa under thermo-mechanical load, and the tensile stress near pile toe was 560 kPa. But the values were less than the ultimate compressive or tensile strength of concrete.

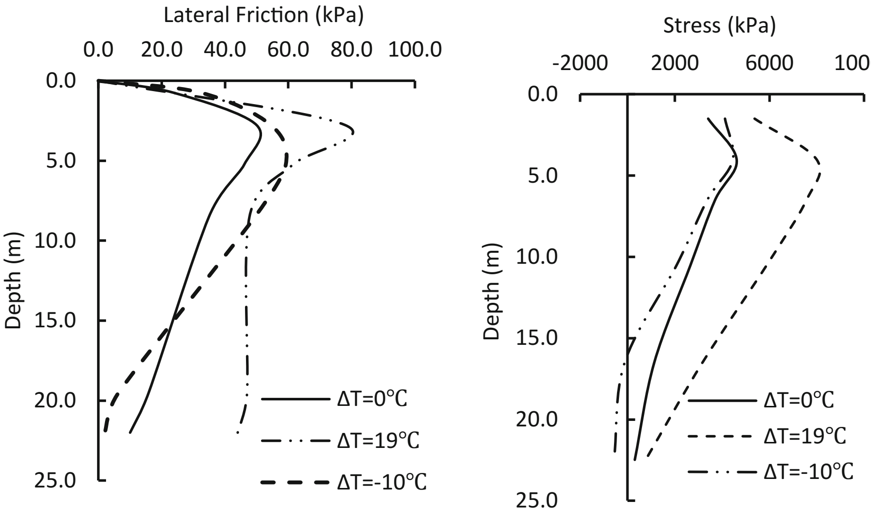

(a) Lateral Friction (b) Axial Stress

Fig. 3. Lateral friction and axial stress profile under thermal loading in Lambeth College test [11]

3.2 Field Test in EPFL

A geothermal energy pile was installed below the four-storey building in Ecole Polytechnique Fédérale de Lausanne [12]. Its length was 25.8 m and diameter was 880 mm. There were alluvial soil of 12 m depth, sandy gravelly moraine of 9.6 m, and bottom moraine of 3.6 m in soil profile. The instrumentation for measuring strain, temperature and load were made up of 62 gauges, including 28 vibration-wire extensometers and 29 fiber-optic extensometers along pile shaft, 1 load cell on pile toe, and 4 extensometers on pile head. The strain, load and temperature were monitored during the construction of building. There were 7 heating and cooling cycle testing process. During each temperature cycle test, the pile was heated by 15 °C and cooled naturally. In this paper, the 7th test for the building construction finished is discussed.

When the pile is heated, the expansion brings the upward shift for the upper section of pile. Because there existed the strong constraint in pile head, the upward shift mobilized was not uniform, which caused the reduced shaft resistance on the upper section (See in Fig. 4(a)). For the lower section under the heating load, its lateral friction was increased. According to the measurement, the mobilized shaft resistance near the pile toe was 90 kPa, which did not exceed the ultimate value of 120 kPa. The mobilized lateral friction for mid-depth in test pile was the minimum for the least pile-soil sliding under heating load.

The vertical stress under the mechanical load only was the maximum at pile head and diminished with depth. The thermal stress was larger and behaved uniform along pile. For there existed constraints on pile top and toe, it is very difficult to deliver the expansion strain for middle part of pile, and its thermal-induced vertical stress reach the maximum. So the vertical stress profile under the thermos-mechanical load is different to that of traditional pile (See in Fig. 4(b)). The vertical stress of pile top and pile tip are 2.6 MPa and 2.1 MPa separately, which exceed the design stress of 2 MPa and 1.2 MPa. In short, the safety in GEPs design deserves our attention from the experimental results.

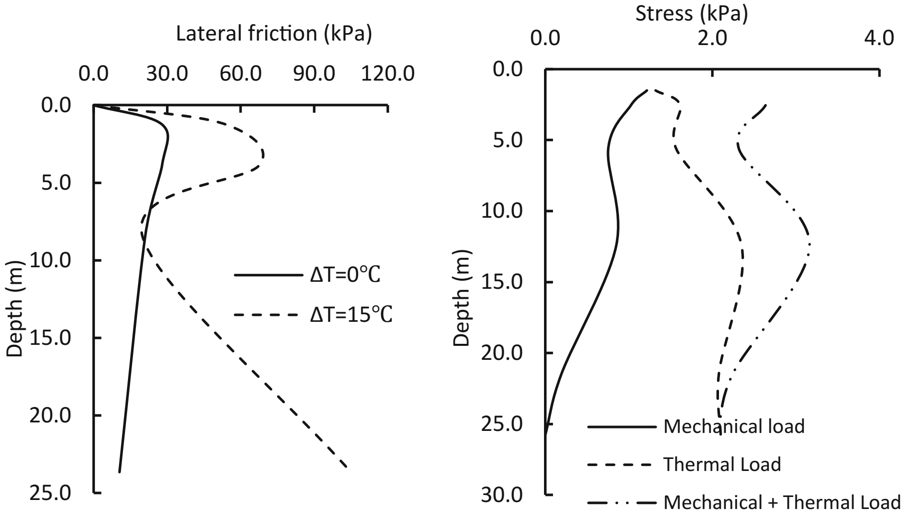

(a) Lateral Friction (b) Axial Stress

Fig. 4. Lateral friction and axial stress profile under heating and cooling in EPFL test [12]

4 Pile-Soil Interaction Mechanism Under Thermo-Mechanical Loading

4.1 Thermal Loading Only

When a pile is heated and expanded, the upper part has the upward shift and the lower part has the downward one, which mobilized the positive shaft resistance and the negative one separately. As the pile cannot be expanded freely for the surrounding soil, the pile-soil interface shift is less than the value calculated by Eq. (1). If the pile head and pile toe are free to move, there is no mobilized vertical stress on pile ends. For the soil restraint, the mobilized vertical stress at mid-depth of pile is larger than other points, but its strain and shaft friction are the minimum.

If the pile head and toe are restrained fully, the expansive strains will be restricted. The strain and lateral friction of pile ends are zero. However, theirs mobilized vertical stress will be maximum. The maximum mobilized strain and shaft resistance are at the mid-depth of pile.

If the pile is cooled, its contraction will induce the downward shift over the upper part and the upward shift over the lower part, which generate positive shaft friction and negative shaft friction separately. If the pile head and pile toe are free to move, the mobilized strain and pile-soil interface shift are maximum for the pile ends. At the mid-depth of pile, the mobilized strain is minimum, however its axial force is maximum. There exits the tensile stress along pile shaft. If the pile top and pile toe are restrained fully, the temperature-induced shift of pile-soil interface, lateral friction and axial force at mid-depth are maximum. Because the axial deformation is restrained, mobilized axial load is larger than for the case of the pile without end-restraint.

4.2 Thermo-Mechanical Loading

When there is no constraint on the pile top and pile toe, the lateral friction of upper part will be decreased and that of lower part is increased under the mechanical and heating load. The gradient of the axial load with depth is greater than that under mechanical load only. The maximum strain is mobilized on pile top and pile toe. When the pile top and pile toe are restrained fully, the mobilized vertical stress along pile shaft becomes more uniform and the mobilized lateral friction at mid-depth is maximum.

During cooling, whilst the pile top and pile toe is free to move, the lateral friction of upper part will be increased and that of lower part is decreased. The diminishing rate of axial load along pile shaft becomes larger. When there are constraint on pile ends, the lateral friction at mid-depth is increased greatly. The tensile stress on the lower part may be occurred.

5 Conclusions

Under the thermo-mechanical loading, the pile-soil interaction characteristic will be changed for its expansion or contraction, such as the tensile stress, addition settlement, and large axial force, etc. Some adverse factors must be considered in designing GEP. According to the several published tests, the bearing performance of GEP under thermo-mechanical loading is investigated. The results show that load-settlement, lateral friction and axial force along pile will be impacted distinctly by the heating and cooling load.

According to the centrifugal model test, the bearing capacities of model pile were increased by 16.4% ($\Delta T = +29$ °C) and 30% ($\Delta T = +41$ °C) individually. Three static load tests were conducted in Monash. The ultimate lateral friction of upper section of GEP were 1650 kN, 1885 kN and 1700 kN corresponding to initial test, heating test and cooling test. During heated, the bearing capacity can be increased by 14.2%. And after the pile was cooled to natural temperature, the bearing capacity can be recovered.

From the field tests of Lambeth College and EPFL, the results show that lateral friction of upper part of pile is decreased and that of lower part is increased when pile heated. Cooling will result in the opposite response. The mobilized shaft resistance near pile toe reached 90 kPa, which was less than the ultimate value of 120 kPa. It is also shown that the axial load along pile will be increased during heated, and decreased when cooling. According to the EPFL test, the maximum axial stress was about 3.1 MPa under thermo-mechanical load (less than ultimate compressive strength of concrete). The total axial stress is twice as large as that one with mechanical load only.

When pile heated and cooled, the mobilized strain, stress and shaft resistance profile are related to the constraint condition of pile ends. If the pile top and pile toe are free to move, heating and cooling load can cause the large mobilized stress and shaft resistance, and the less mobilized axial stress. In case of restraint on pile ends, thermal load will generate the less mobilized strain and lateral friction, and the larger mobilized axial stress.

References

1. Buker, M.S., Riffat, S.B.: Solar assisted heat pump systems for low temperature water heating applications: a systematic review. Renew. Sustain. Energy Rev. **55**, 399–413 (2016)
2. Rosen, M.A., Koohi-Fayegh, S.: Geothermal Energy: Sustainable Heating and Cooling Using the Ground. Wiley, New Jersey (2017)
3. Hein, P., Kolditz, O., Görke, U.J., et al.: A numerical study on the sustainability and efficiency of borehole heat exchanger coupled ground source heat pump systems. Appl. Therm. Eng. **100**, 421–433 (2016)
4. Brandl, H.: Energy foundations and other thermo-active ground structures. Geotechnique **56** (2), 81–122 (2006)
5. Amis, A., Loveridge, F.A.: Energy piles and other thermal foundations for GSHP developments in UK practice and research. REHVA J. **2014**(1), 32–35 (2014)
6. Pahud, D., Hubbuch, M.: Measured thermal performances of the energy pile system of the dock midfield at Zürich Airport. In: Proceedings of European Geothermal Congress, Unterhaching, Germany, pp. 1–7 (2007)
7. Loveridge, F., Powrie, W., Nicholson, D.: Comparison of two different models for pile thermal response test interpretation. Acta Geotech. **9**(3), 367–384 (2014)
8. McCartney, J.S.: Engineering performance of energy foundations. In: Pan-American CGS Geotechnical Conference, Toronto, pp. 2–6 (2011)
9. China Academy of Building Research: Technical Code for Building Pile Foundation. China Architecture & Building Press, Beijing, (2008). (in Chinese)
10. Wang, B., Bouazza, A., Barry-Macaulay, D., et al.: Geothermal energy piles subjected to thermo-mechanical loading. In: 11th ANZ Conference Proceeding, pp. 626–630. Engineers Australia, Australia (2012)
11. Amatya, B.L., Soga, K., Bourne-Webb, P.J., et al.: Thermo-mechanical behaviour of energy piles. Géotechnique **62**(6), 503–519 (2012)
12. Laloui, L., Nuth, M., Vulliet, L.: Experimental and numerical investigations of the behaviour of a heat exchanger pile. Int. J. Numer. Anal. Meth. Geomech. **30**(8), 763–781 (2006)

Optimal Shock Absorption Layout of Lead Rubber Bearing in a Multi-story Underground Structure

Zhiyi Chen[1,2(✉)] and Zhiqian Liu[1]

[1] Department of Geotechnical Engineering, Tongji University,
Shanghai 20092, China
`zhiyichen@tongji.edu.cn`

[2] Key Laboratory of Geotechnical and Underground Engineering of Ministry
of Education, Shanghai 200092, China

Abstract. The damping effect of lead rubber bearing (LRB) on the seismic response of simple subway station structures has been verified. Because the structure style of the multi-story subway station structure is more complex, the damping effect of LRB on the seismic response of the multi-story subway station structure and the optimal layout strategy need to be further studied. In this paper, a four-story three-span subway station structure is taken as the research object. Based on the finite element code ABAQUS, a series of time history analyses of the structure with various layout conditions of LRB are carried out, and the influence of different layout story on the damping effect of the multi-story subway station structure is studied. It is found that the damping effect of the central column equipped with LRB is obvious. The column shear force is reduced by 50%–80%, and the sidewall with high design security is only increased by 10–15% by contrast. With the increase of the number of LRB layout stories, story drifts increase obviously but still within the allowable range.

Keywords: Lead rubber bearing · Multi-story underground structure
Seismic performance · Optimal layout

1 Introduction

Researches on the seismic damage of Daikai station show that the central column is the weakest component of the subway station structure [1, 2]. Therefore, improving the seismic performance of the central column is an effective way to upgrade the seismic performance of the whole structure. Drawing lessons from using the lead rubber bearing (LRB) for seismic isolation of ground structures, Chen et al. [3] proposed the method of installing LRB at the central column end of subway station structure to reduce the dynamic response and seismic damage of the central column. Daikai station was taken as an example, and the seismic effect of LRB on the simple subway station structure was verified. However, for the multi-story subway station structure, the damping effect of LRB is closely related to its layout scheme. On the one hand, low stiffness of the multi-story subway station structure lead to the large deformation during the earthquake, and the layout of the LRB will further reduce the structural stiffness,

© Springer Nature Singapore Pte Ltd. 2018
D. Zhang and X. Huang (Eds.): GSIC 2018, *Proceedings of GeoShanghai 2018 International Conference: Tunnelling and Underground Construction*, pp. 718–727, 2018.
https://doi.org/10.1007/978-981-13-0017-2_72

thus too many LRB may lead to excessive structural deformation. On the other hand, the layout position of LRB will affect the deformation and stress of different stories. Therefore, in order to get the best damping effect, it is necessary to optimize the layout of LRB in a multi-story subway station structure.

In this paper, a four-story three-span subway station structure is taken as the research object. Based on the finite element code ABAQUS [4], a series of time history analyses of the structure with various layout conditions of LRB are carried out, and the influence of different layout story of LRB on the damping effect of the multi-story subway station structure is studied.

2 Numerical Model

2.1 Soil-Structure Interaction Numerical Model

The four-story three-span subway station structure is located in Shanghai, China. Figure 1 shows the cross section of the subway structure. Total length of the station is 155 m, and the width varies from 23.6 m to 28.35 m. The structure height is 29.1 m. Diaphragm wall is adopted as the building envelope and composite lining is used. All central column spacing is 8 m. Central columns in the B1 and B2 floors are 1.1 m long and 0.7 m wide, while the sizes of columns in B3 and B4 floors are 1.4 m long and 0.7 m wide. Table 1 shows the soil parameters around the station. The stratum around the station is mainly composed of clay, silty soil, mucky soil and deep sandy soil, and the soil layer is relatively stable. The groundwater depth is 0.50 m.

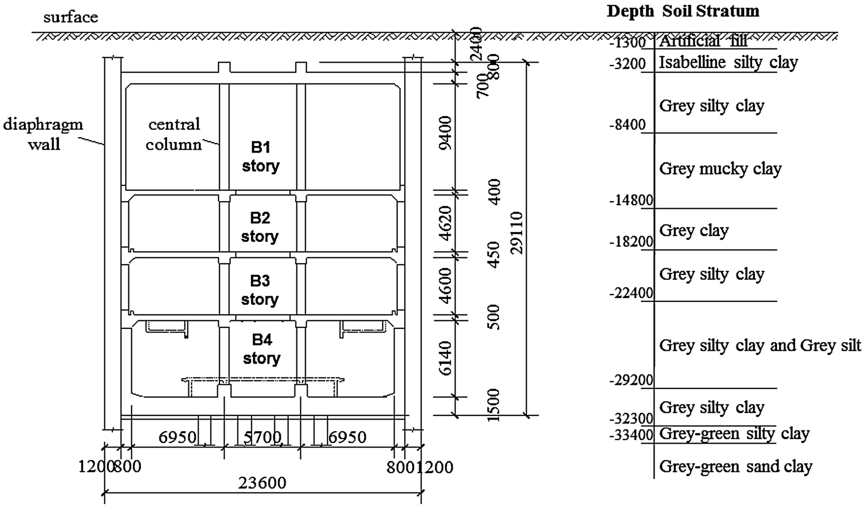
surface
diaphragm wall
central column
B1 story
B2 story
B3 story
B4 story
2400
700
800
9400
400
4620
450
29110
4600
500
6140
1500
6950
5700
6950
1200
800
800
1200
23600
Depth
Soil Stratum
-1300 Artificial fill
-3200 Isabelline silty clay
Grey silty clay
-8400
Grey mucky clay
-14800
Grey clay
-18200
Grey silty clay
-22400
Grey silty clay and Grey silt
-29200
Grey silty clay
-32300
-33400 Grey-green silty clay
Grey-green sand clay

Fig. 1. Cross section of the subway station and soil stratums, dimensions in mm.

Table 1. Soil parameters of the Shanghai station model

Sequence	Name	Depth (m)	Unit weight (kN/m^3)	Cohesion yield stress (kPa)	Friction angle (°)	Poisson's ratio	Elastic modulus (MPa)
1	Artificial fill	0–1.3	18.2	21	14.5	0.32	14
2	Isabelline silty clay	1.3–3.2	18.2	21	14.5	0.32	14
3	Grey silty clay	3.2–8.4	17.6	14	12.5	0.33	10
4	Grey mucky clay	8.4–14.8	16.8	14	9.5	0.37	7
5	Grey clay	14.8–18.2	17.6	15	13.5	0.34	11
6	Grey silty clay	18.2–22.4	17.9	17	16.5	0.31	13
7	Grey silty clay and Grey silt	22.4–29.2	18.0	16	18	0.29	17
8	Grey silty clay	29.2–32.3	18.4	24	16	0.31	16
9	Grey-green silty clay	32.3–33.4	19.8	34	19	0.26	26
10	Grey-green sand clay	33.4–39.1	19.0	5	29	0.26	33
11	Grey-green silty sand	39.1–66.6	18.7	3	31.5	0.24	43
12	Grey silty clay	66.6–71.6	18.2	26	14.5	0.23	17
13	Grey silty sand	71.6–85	18.9	0	34.5	0.25	45

The concrete damaged plasticity model is adopted to better simulate the dynamic response of the structure. The calculation of damage parameters has been done in previous studies [5, 6]. Beam element (B21) was chosen to simulate the structure. Central columns of the structure were made of C45 concrete [7]. Other parts of the structure were made of C35 concrete. Idealized elastic-plastic model was selected for rebar. Rebar used in central columns and other parts were HRB400 and HRB335, respectively. And the yield strength of HRB400 and HRB335 is 400 MPa and 335 MPa, respectively.

Mohr-Coulomb model is applied for soils. The soil-structure interaction is defined by the Coulomb friction law. The coefficient of friction is assumed to be 0.4, which is equivalent to the friction angle of 22°.

According to Code for Seismic Design of Buildings [8], unilateral soil width around the structure should be at least 3 times larger than the width of the structure.

In this paper, the width of soil unilateral is 250 m. And infinite element boundary is used in soil lateral boundary. The soil depth of the numerical model is 85 m below the ground surface. Besides, the X and Y direction degrees of freedom of the soil element nodes in the bottom boundary are imposed before the time history analysis. The established SSI numerical model is shown in Fig. 2.

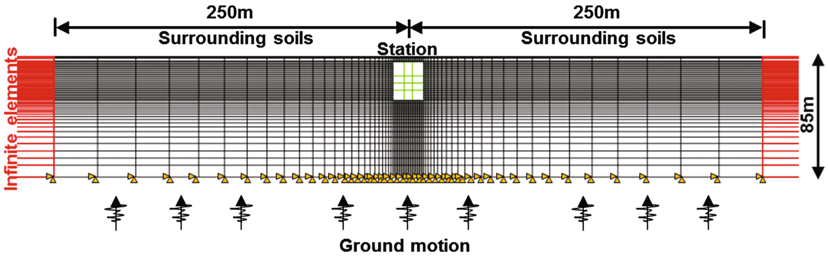
250m
Surrounding soils
Station
250m
Surrounding soils
Infinite elements
85m
Ground motion

Fig. 2. Numerical model of the underground subway station with surrounding soils

2.2 Lead Rubber Bearing

Lead rubber bearing (LRB) is mainly composed of internal rubber layer, steel shim, lead core, outer rubber cover, mounting plate and anchorage component, as can be seen in Fig. 3. Lead core can provide initial horizontal stiffness during small earthquakes and consume seismic energy through plastic deformation during large earthquakes; the internal laminated rubber reduces the horizontal stiffness of LRB and provides restoring force; the steel shim is used to increase the vertical stiffness of LRB and limit the horizontal expansion deformation of LRB, thus it can support the upper structure effectively.

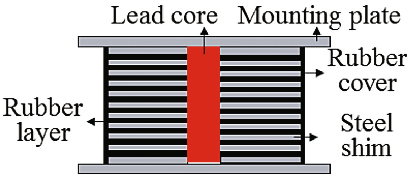
Lead core
Mounting plate
Rubber cover
Rubber layer
Steel shim

Fig. 3. Composition of LRB

Hysteretic behavior of LRB is simulated by bilinear model [9–11]. The main parameters, characteristic strength Q_d, yield stiffness K_d and initial stiffness K_u are defined as follows [12, 13]:

$$Q_d = \sigma_y A_{pl} \tag{1}$$

$$K_d = \frac{GA_r}{T_r} \tag{2}$$

$$K_u = 6.5K_d(1 + \frac{12A_{pl}}{A_r}) \quad (3)$$

Where, σ_y, A_{pl}, G, A_r, T_r are represented the shear yield strength, lead core area, rubber shear modulus, reduced rubber area and rubber layer thickness, respectively. Referring to the design process of the LRB in the ground structure proposed by [13] and considering the section size of the central column of the four-story three-span station structure, each column in B1 and B2 stories is equipped with a single 700 mm × 700 mm LRB (whose lead core diameter D_{pl} is 100 mm) while each column in B3 and B4 stories is equipped with two 600 mm × 600 mm LRB (whose D_{pl} is 80 mm). Shear modulus of rubber G, thickness of single layer rubber t_r, the number of rubber layers and the thickness of laminated steel are 0.4 MPa, 6 mm, 10 mm and 3 mm, respectively. Q_d, K_d and K_u of each single LRB equipped in different stories are calculated according to formula (1)–(3), as shown in Table 2.

Table 2. Design parameter of single LRB

LRB parameter	B1 story	B2 story	B3 story	B4 story
Q_d (kN)	67	67	43	43
K_d (kN/m)	1988	1988	1333	1333
K_u (kN/m)	17004	17004	11279	11279

2.3 Input Ground Motion

The input ground motion is Shanghai artificial wave. Shanghai artificial wave is a kind of stochastic seismic wave, which is based on the specific site conditions of Shanghai and meets certain conditions like spectrum characteristics, vibration duration and earthquake energy, etc. Time history of Shanghai artificial wave and Fourier amplitude spectrum are shown in Fig. 4. The intensity of the input ground motion is determined by “7° rare earthquake” as specified in “Code for Seismic Design of Buildings” [8], which means PGA equals to 0.22 g.

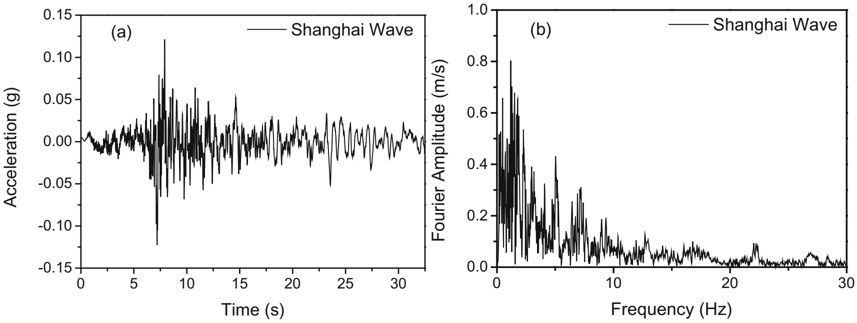

Fig. 4. (a) Acceleration time history; (b) Fourier amplitude spectrum of Shanghai wave

3 Calculation Cases

Figure 5 shows the layout of LRB in each calculation cases. The structure is not arranged LRB in Case 1. According to the previous research [14], the B4 and the B1 story of the four-story station structure are easy to be damaged in the earthquake. Therefore, to study the influence of the number of stories equipped with LRB on the damping effect of structures, in Case 2, Case 3 and Case 4, LRB is arranged in 1 story (B4), 2 stories (B1 and B4) and all 4 stories (B1, B2, B3, and B4) of the structure, and LRB are arranged at the column top.

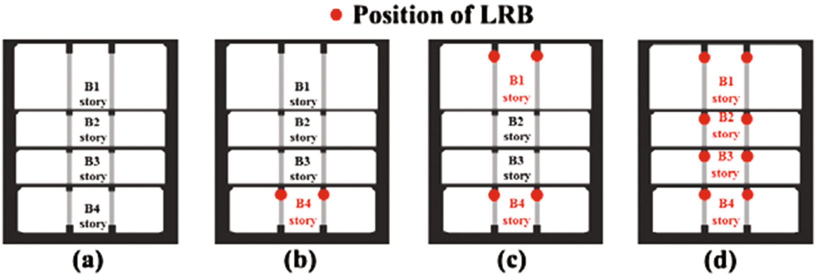

Fig. 5. Layout of LRB in (a) Case 1; (b) Case 2; (c) Case 3; (d) Case 4

4 Results and Analyses

Figure 6 shows the maximum deformation of the structure during the earthquake process in each case. It can be seen from Fig. 6 that the horizontal relative deformation of the structure is increasing from Case 1 to Case 4, and the deformation of the central columns equipped with LRB is obviously reduced. The deformation and shear forces of the structure in each case will be discussed below.

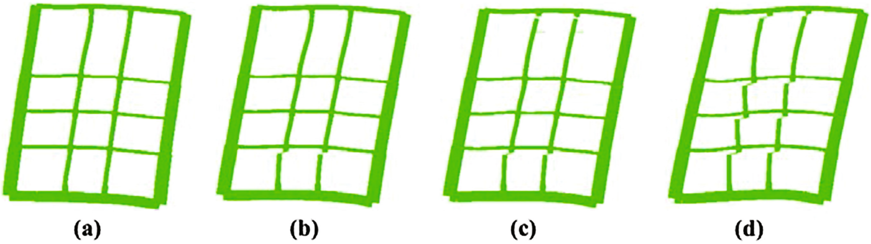

Fig. 6. Maximum structural deformation in (a) Case 1; (b) Case 2; (c) Case 3; (d) Case 4 (Deformation scale factor: 100)

The observation positions of the story drifts as well as the shear forces of the columns and sidewalls are marked in Fig. 7. As shown in Fig. 7, story drift, θ_i, is defined as follows:

$$\theta_i = \frac{\Delta u_i}{h_i} \tag{4}$$

where, i refers to the story number of the structure, and $i = 1, 2, 3, 4$; Δu is horizontal relative displacement of the two ends of the sidewall; Δh is the height of the sidewall of each story. The shear forces of the central column and the sidewall are taken from the bottom cross-section in each story, as shown in Fig. 7.

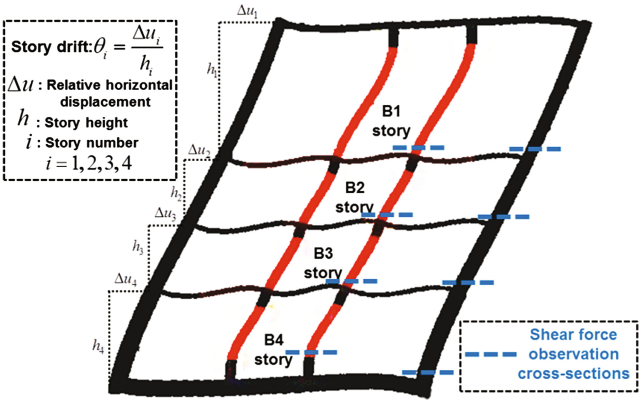
Story drift: $\theta_i = \frac{\Delta u_i}{h_i}$
Δu : Relative horizontal displacement
h : Story height
i : Story number
$i = 1,2,3,4$
Δu_1
h_1
Δu_2
h_2
Δu_3
h_3
Δu_4
h_4
B1 story
B2 story
B3 story
B4 story
Shear force observation cross-sections

Fig. 7. Observation positions of story drifts and shear forces

4.1 Story Drifts

Figure 8 gives the maximum values of story drifts in each case. As can be seen from Fig. 8, the story drifts of four stories in Case 2, Case 3 and Case 4 increase by 14.8%, 24.8%, 75.2%, respectively compared with it in Case 1. This shows that structure deformation increases with the increase of the number of stories equipped with LRB. This is because the stiffness of the structure is reduced when stories equipped with LRB, and soil-structure stiffness ratio is increased, which leads to the increase of the structure deformation. In addition, the story drifts in all cases are less than 0.004 (1/250) under rare earthquake, which is the limit value according to “Code for Seismic Design of Buildings” [8], which indicates that the structural deformation is still within the allowable range.

4.2 Shear Forces

The structure stiffness is decreased after the layout of LRB while the story drifts is obviously increased, and the total lateral force of the structure is related to both.

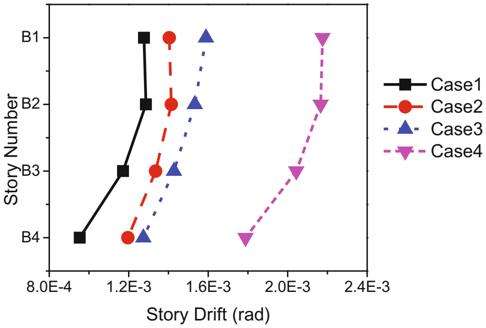

Fig. 8. Maximum story drifts

Therefore, the change of the total lateral force of the total structure cannot be inferred directly. The total shear force at the bottom of the sidewall and column can be considered as the total lateral force input into structure. According to the calculation results, the total shear forces at the bottom of the structure in Case 1–Case 4 are 14120 kN, 14128 kN, 14152 kN and 14358 kN, respectively. Compared with it in Case1, the total shear force in Case 2–Case 4 increases by 0.0006%, 0.002%, 1.7%, respectively, which are almost negligible. This shows that the total lateral force of the structure is almost unchanged, and the number of stories equipped with LRB has no obvious relation with the total lateral force input into the structure.

Figure 9(a), (b) gives the maximum shear forces at the bottom of the column and the sidewall in each case. The influence of the equipment of LRB on the central column shear force is evident. In Fig. 9(a), it can be seen that the column shear force of B4 story which is equipped with LRB in Case 2 is reduced from 810 kN to 114 kN compare to it in Case 1. In the adjacent B3 story, the column shear force rises from 682 kN to 864 kN, while the column shear force of the B1 and B2 stories do not change significantly. In Case 3, the column shear force of the B1 and B4 stories which is equipped with LRB are reduced from 253 kN and 810 kN to 68 kN and 116 kN, respectively; while the column shear force of the B2 and B3 stories which is not

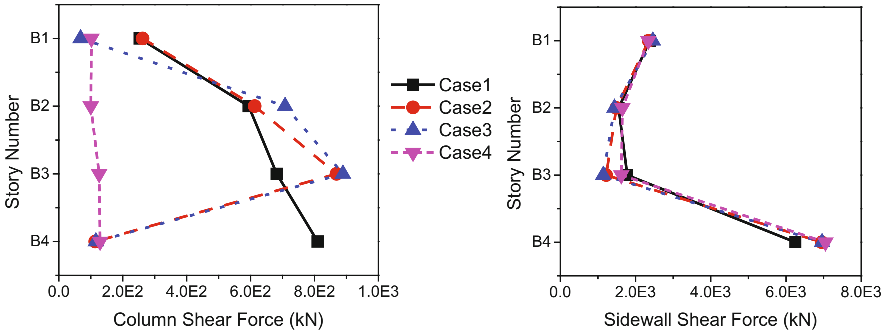

Fig. 9. Maximum shear forces of (a) central columns; (b) sidewalls

equipped with LRB are increased from 594 kN and 682 kN to 708 kN and 889 kN, respectively. This indicates that the shear force of the column equipped with LRB is greatly reduced due to the stiffness decrease of the central column equipped with the LRB (about 85% reduction), and the column shear force in the adjacent stories is obviously increased.

From the Fig. 9 (b), it can be seen that the sidewall bottom shear force of B4 story in Case 2–Case 4 has obvious trend of increase compared with the Case 1 in which all columns are not equipped with LRB (Case 2–Case 4 increase by 11.2%, 11.4%, 12.8%, respectively). This is because the B4 story is equipped with LRB in these cases, so that the column stiffness of B4 story decreases, then the relative linear stiffness of sidewall to the central column increases (from 8 to 55 approximately). Because the total lateral force remains almost constant and the distribution of story shear force according to the relative linear stiffness of sidewall to the central column, the sidewall shear force increases accordingly. The sidewall shear force of B2 and B3 stories decreases because the column shear force of the same stories increases obviously. And there is no obvious change in the sidewall shear force of B1 story in all cases, all of which are in the range (−3%–3%). Overall, when the structure is equipped with LRB, although part of the shear force of central column is transferred to sidewall, the wall shear increases is not large (no more than 15%). Because of the large reduction of 50%–80% of column shear force, it can be seen that the LRB damping effect is very evident.

5 Conclusions

In this paper, the dynamic time history analysis and the optimal layout strategy of LRB are studied for a four-story and three-span subway station structure using LRB damping, the influence of the number of stories equipped with LRB on the damping effect of the structure is studied respectively. Main conclusions are as follows:

(1) The damping effect of the column equipped with LRB is evident. The column shear force is reduced by 50%–80%. The sidewall with high design security is only increased by 10–15% by contrast.
(2) The number of stories equipped with LRB has obvious influence on story drifts and shear forces. With the increase of the number of stories equipped with LRB, story drifts increased significantly. When the columns of all the four stories are equipped with LRB, the maximum story drifts is about 1/456 under the rare earthquake.
(3) Comprehensively, in order to achieve the best damping effect, central columns of four stories should be all equipped with LRB.

Acknowledgement. This research was supported by the National Natural Science Foundation of China (Grant No. 41472246, 51778464), Key laboratory of Transportation Tunnel Engineering (TTE2014-01), and “Shuguang Program” supported by Shanghai Education Development Foundation and Shanghai Municipal Education Commission. All supports are gratefully acknowledged.

References

1. Iida, H., Hiroto, T., Yoshida, N., Iwafuji, M.: Damage to Daikai subway station. Soils Found. **36**, 283–300 (1996)
2. An, X., Shawky, A.A., Maekawa, K.: The collapse mechanism of a subway station during the Great Hanshin Earthquake. Cement Concr. Compos. **19**(3), 241–257 (1997)
3. Chen, Z.Y., Zhao, H., Lou, M.L.: Seismic performance and optimal design of framed underground structures with lead-rubber bearings. Struct. Eng. Mech. **58**(2), 259–276 (2016)
4. ABAQUS: Users Manual V. 6.10-1. Dassault Systemes Simulia Corp., Providence, RI (2010)
5. Chen, Z.Y., Chen, W., Zhang, W.: Seismic performance evaluation of multi-story subway structure based on pushover analysis. In: Proceedings of the Advances in Soil Dynamics and Foundation Engineering, pp. 444–454. ASCE (2014)
6. Chen, Z.Y., Chen, W., Zhang, W., Lou, M.L.: Effects of axial compression ratio of central columns on seismic performance of a multi-story underground structure. Int. J. Comput. Methods **13**(04), 1641014 (2016)
7. GB50010: Code for Design of Concrete Structure. China Architecture & Building Press, Beijing (2010)
8. GB50011: Code for Seismic Design of Buildings. China Architecture & Building Press, Beijing, China (2010)
9. Providakis, C.P.: Effect of LRB isolators and supplemental viscous dampers on seismic isolated buildings under near-fault excitations. Eng. Struct. **30**(5), 1187–1198 (2008)
10. Hu, J.W.: Response of seismically isolated steel frame buildings with sustainable lead-rubber bearing (LRB) isolator devices subjected to near-fault (NF) ground motions. Sustainability **7** (1), 111–137 (2014)
11. Mkrtychev, O.V., Dzhinchvelashvili, G.A., Bunov, A.A.: Study of lead rubber bearings operation with varying height buildings at earthquake. Procedia Eng. **91**, 48–53 (2014)
12. Islam, A.S., Hussain, R.R., Jumaat, M.Z., Rahman, M.A.: Nonlinear dynamically automated excursions for rubber-steel bearing isolation in multi-storey construction. Autom. Constr. **30**, 265–275 (2013)
13. Kelly, T.E., Robinson, W.H., Skinner, R.I.: Seismic Isolation for Designers and Structural Engineers. Robinson Seismic Ltd., Wellington (2006)
14. Chen, Z., Chen, W., Li, Y., Yuan, Y.: Shaking table test of a multi-story subway station under pulse-like ground motions. Soil Dyn. Earthq. Eng. **82**, 111–122 (2016)

Fuzzy Comprehensive Evaluation System of Tunnel Construction Method

Tianxiang Wu[1], Wenqi Ding[2(✉)], Shiding Cao[3], and Jun Li[4]

[1] College of Civil Engineering, Tongji University, Shanghai, China
[2] Key Laboratory of Geotechnical and Underground Engineering, Shanghai, China
swjtu_wtx@163.com
[3] Shanghai Municipal Engineering Design Institute (Group) Co., Ltd., Shanghai, China
[4] Shenzhen Traffic and Public Facilities Construction Center, Shenzhen, China

Abstract. BM (Bench Method), CDM (Central-Diaphragm Method) and DSDM (Double-Side-Drift Method) are widely used in large cross-section tunnel. It is necessary to select the best construction method. In this paper, the FCES (Fuzzy Comprehensive Evaluation System) shows how to get the score of each construction method. FCES chooses nine specific indicators, such as, project cost. Firstly, indicators are quantified. Data is standardized. Secondly, evaluation matrix of each construction method should be obtained by comment set and membership function. Thirdly, the weight of each indicator should be obtained through EM (Entropy Method). Finally, the evaluation matrix, comment set and weight are multiplied to get the scores of each construction method, then the best construction method is selected according to the scores. FCES is applied in a tunnel project, using the FEM (Finite Element Method) to simulate each construction method respectively to get data. In rocks of grade V, FCES shows that DSDM is the best construction method, and excavation sequences have little influence. Hence, FCES can be used to choose the best construction method.

Keywords: FCES · Evaluation matrix · Comment set · Weight

1 Introduction

In order to meet the increasing traffic flow and conditions, the section size of tunnel is increasing day by day. For the large cross-section rock tunnel, there are several construction methods including BM, CDM, and DSDM [1]. BM has enough work space and faster construction speed. CDM can convert large section excavation into small section excavation and effectively reduce the ground settlement and lining convergence, but the speed of construction is too slow [2, 3]. DSDM which is often adopted in tunnel excavation with bad geological condition can control the deformation of surrounding rock well [4, 5].

Each construction method has its own advantages and disadvantages, so it is a problem to choose the best construction method. In order to solve these problems, the FCES can be used to evaluate each construction method in order to choose the best construction methods.

© Springer Nature Singapore Pte Ltd. 2018
D. Zhang and X. Huang (Eds.): GSIC 2018, *Proceedings of GeoShanghai 2018 International Conference: Tunnelling and Underground Construction*, pp. 728–736, 2018.
https://doi.org/10.1007/978-981-13-0017-2_73

2 Fuzzy Comprehensive Evaluation System

In order to evaluate construction methods, many factors must be taken into consideration as possible, including construction, safety and stability. But it is impossible to evaluate construction methods directly from such factors. So according to three factors, nine specific indicators can be chosen as project cost, construction difficulty, safety factor, maximum lining axial force, maximum lining moment, maximum building inclination, maximum ground settlement, lining convergence, plastic zone of surrounding rock [6, 7]. The FCES is established (see Fig. 1).

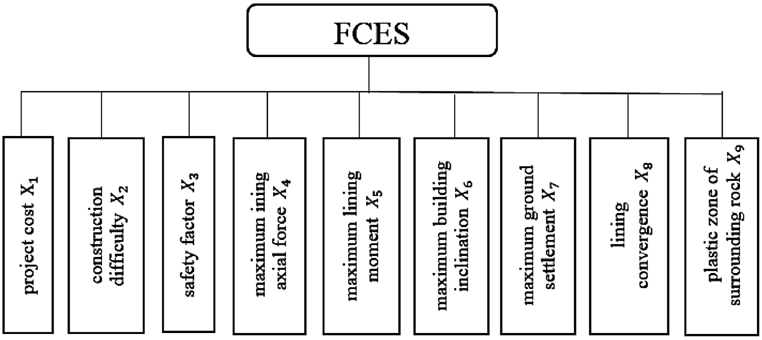
FCES
project cost X_1
construction difficulty X_2
safety factor X_3
maximum ining axial force X_4
maximum lining moment X_5
maximum building inclination X_6
maximum ground settlement X_7
lining convergence X_8
plastic zone of surrounding rock X_9

Fig. 1. FCES (Fuzzy Comprehensive Evaluation System)

The solving processes of FCES are divided into five steps.

Firstly, considering the actual meaning, nine indicators must be quantified to get data. Secondly, the data is standardized to eliminate the influence of units and magnitude. Thirdly, this paper establishes comment set to divide construction methods into five levels when each level has its own membership function. Evaluation matrix of each construction method should be obtained by membership function. Fourthly, the weight of each indicator should be obtained through EM (Entropy Method). Finally, the evaluation matrix, comment set and weight are multiplied to get the score of each construction method.

2.1 Quantification of Indicators

In order to evaluate construction methods, nine specific indicators should be quantified.

This paper considers project cost X_1 including the temporary steel support and RC (Reinforced Concrete). Therefore, the following formula can be used to represent X_1.

$$X_1 = l_{steel} + 0.6 l_{RC}$$

where l_{steel} is the length of temporary steel support; l_{RC} is the length of RC and the coefficient of l_{RC} is 0.6 because RC is cheaper.

The construction difficulty X_2 is linked to the smallest area of excavation, so the following formula can be used to stand for X_2.

$$X_2 = \frac{A_{excavation}}{A_{tunnel}}$$

where $A_{excavation}$ is the smallest area of excavation; A_{tunnel} is the area of total tunnel section. The greater X_2 is, the easier the construction method is.

Safety factor X_3 can be obtained from strength reduction method. The principle is reducing the cohesion C and internal friction angle of soils φ at the same time until the calculation fails to converge.

$$X_3 = \frac{C_{normal}}{C_{failure}} = \frac{\varphi_{normal}}{\varphi_{failure}}$$

where C_{normal} and φ_{norml} are the values of normal state; C_{failure} and $\varphi_{\mathrm{failure}}$ are the values of failure state.

Maximum building inclination X_6 is calculated as the difference between the settlements at two sides of building.

$$X_6 = \frac{V_1 - V_2}{L_D}$$

where V_1, V_2 is respectively the settlement at two sides of the building; L_{D} is the length of building.

Maximum ground settlement X_7 can be obtained directly through FEM.

Lining convergence X_8 can be calculated through the following formula.

$$X_8 = \frac{A_{tunnel} - A_{after\ excavation}}{A_{tunnel}}$$

where $A_{after\ excavation}$ is the area of total tunnel section after excavation.

Plastic zone of surrounding rock X_9 can be calculated as follow.

$$X_9 = \frac{A_{plastic\ zone}}{A_{tunnel}}$$

where $A_{plastic\ zone}$ is the area of plastic zone of surrounding rock.

2.2 Standardization of Data

Because units and magnitude of these indicators are different, there is no comparability between them. This brings difficulties and problems in determining the comprehensive evaluation indicators. We have to standardize data to eliminate the influence of units and magnitude.

The greater project cost X_1 is, the worse the construction method is. However, the greater safety factor X_3 is, the better the construction method is. The type of data is different, so we have to take two kinds of standardization for this two types.

For the first type, we can use this formula to standardize data X_{ij} (i stands for i$^{\text{th}}$ indicator; $i = 1, 4, 5, 6, 7, 8, 9$; j stands for j$^{\text{th}}$ construction method; $j = 1, 2, 3, 4, 5$).

$$m_{ij} = \frac{\max\{X_{ij}\} - X_{ij}}{\max\{X_{ij}\} - \min\{X_{ij}\}}$$

where X_{ij} is data before standardization; $\min\{X_{ij}\}$ is minimum value of the j$^{\text{th}}$ indicator; $\max\{X_{ij}\}$ is maximum value of the j$^{\text{th}}$ indicator; m_{ij} is data after standardization.

For the second type, we can use this formula to standardize $X_{ij}(i = 2, 3;$ $j = 1, 2, 3, 4, 5)$.

$$m_{ij} = \frac{X_{ij} - \min\{X_{ij}\}}{\max\{X_{ij}\} - \min\{X_{ij}\}}$$

2.3 Establishment of Evaluation Matrix R_j

According to the range of m_{ij}, we can establish the comment set V which is divided into five levels to evaluate the construction method.

Standard magnitude of each level is defined as follow.

$$\{S_1, S_2, S_3, S_4, S_5\}^T = \{1.0, 0.8, 0.6, 0.4, 0.2\}^T$$

In order to evaluate j$^{\text{th}}$ construction method's attachment to each level, we can establish membership function to get membership matrix R_{jk} (j stands for j$^{\text{th}}$ construction method; k stands for k$^{\text{th}}$ level; k = 1, 2, 3, 4, 5). According to its distribution characteristics, "half-trapezoidal" function is chosen as membership function. Based on standard magnitude of each level, we can define different membership functions.

The first level. k = 1.

$$R_{jk} = \begin{cases} 1, & m_{ij} \geq S_k \\ \frac{m_{ij} - S_{k+1}}{S_k - S_{k+1}}, & S_{k+1} \leq m_{ij} \leq S_k \\ 0, & else \end{cases}$$

where R_{jk} is a column vector including nine indicators; i stands for i$^{\text{th}}$ indicator.

The second, third and fourth level. k = 2, 3, 4.

$$R_{jk} = \begin{cases} \frac{S_{k-1} - m_{ij}}{S_{k-1} - S_k}, & S_k \leq m_{ij} \leq S_{k-1} \\ \frac{m_{ij} - S_{k+1}}{S_k - S_{k+1}}, & S_{k+1} \leq m_{ij} \leq S_k \\ 0, & else \end{cases}$$

The fifth level. k = 5.

$$R_{jk} = \begin{cases} 0, & m_{ij} \geq S_{k-1} \\ \frac{S_{k-1}-m_{ij}}{S_{k-1}-S_k}, & S_k \leq m_{ij} \leq S_{k-1} \\ 1, & else \end{cases}$$

Evaluation matrix R_j of j^th^ construction method can be established.

$$R_j = \left(R_{j1}, R_{j2}, R_{j3}, R_{j4}, R_{j5}\right)$$

2.4 Establishment of Weight

Weight is a measurement of different indicators' impact on the choice of construction method. The greater weight coefficient means the indicator has a greater impact on the choice of construction method. In order to consider all the values of different indicators and because of obvious variation degree of indicators' values, the EM (Entropy Method) [8] is chosen to calculate weight.

Using the following formula to calculate the entropy of j^th^ indicator E_j.

$$E_j = \frac{-1}{\ln m} * \sum_{i=1}^{m} p_{ij} * \ln p_{ij}$$

where $p_{ij} = \frac{m_{ij}}{\sum_{i=1}^{m} m_{ij}}$; if p_{ij} equals zero, we define that $p_{ij} * \ln p_{ij} = 0$; m is the number of construction methods, and equals 5.

The weight of j^th^ indicator can be calculated as follow.

$$w_j = \frac{1 - E_j}{n - \sum_{j=1}^{n} E_j}$$

where j is the number of indicators, and equals 9.

2.5 Establishment of Fuzzy Comprehensive Evaluation System

We must obtian evaluation matrix R_j, comment set V and weight w, so we can establish FCES to evaluate different construction methods.

$$P_j = R_j * V * w$$

where P_j is the score of j^th^ construction method.

Hence, we can choose the best construction method through the scores of different construction methods (Table 4).

3 Application of FCES

We apply FCES to a tunnel project, using the FEM to simulate each construction method respectively to get values of 9 indicators.

3.1 Establishment of FEM Models

In order to evaluate different construction methods, five models are presented in this paper. The simulation processes of five models [9, 10] are illustrated in Figs. 2, 3, 4, 5 and 6.

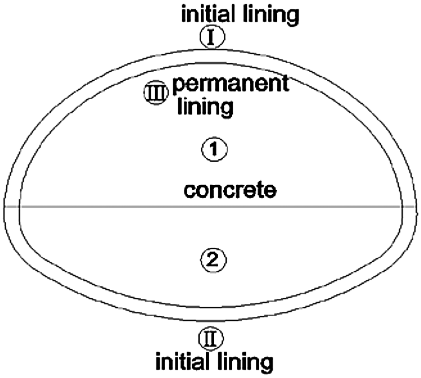
initial lining
Ⅰ
Ⅲ permanent lining
①
concrete
②
Ⅱ
initial lining

Fig. 2. Model-1: BM

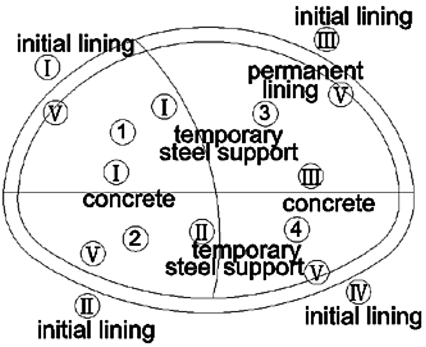
initial lining
Ⅲ
initial lining
Ⅰ
permanent lining Ⅴ
Ⅴ
Ⅰ
③
①
temporary steel support
Ⅰ
Ⅲ
concrete
concrete
②
Ⅱ
④
Ⅴ
temporary steel support Ⅴ
Ⅳ
Ⅱ
initial lining
initial lining

Fig. 3. Model-2: CDM

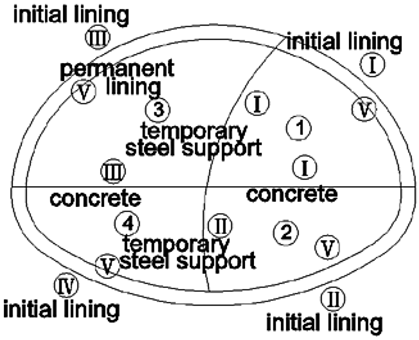
initial lining
Ⅲ
initial lining
Ⅰ
permanent lining
Ⅴ
③
Ⅰ
Ⅴ
temporary steel support
①
Ⅰ
Ⅲ
concrete
concrete
④
Ⅱ
②
temporary
Ⅴ
Ⅴ steel support
Ⅳ
initial lining
Ⅱ
initial lining

Fig. 4. Model-3: CDM (right first)

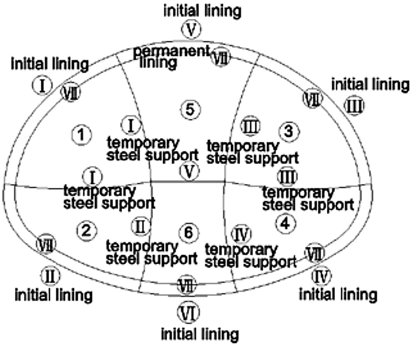
initial lining
Ⅴ
permanent lining Ⅶ
initial lining
Ⅰ
Ⅶ
initial lining
Ⅶ
Ⅲ
⑤
①
Ⅰ
Ⅲ
③
temporary steel support
temporary steel support
Ⅴ
Ⅰ
Ⅲ
temporary steel support
temporary steel support
②
Ⅱ
⑥
Ⅳ
④
Ⅶ
temporary steel support
temporary steel support
Ⅶ
Ⅱ
Ⅶ
Ⅳ
initial lining
initial lining
Ⅵ
initial lining

Fig. 5. Model-4: DSDM

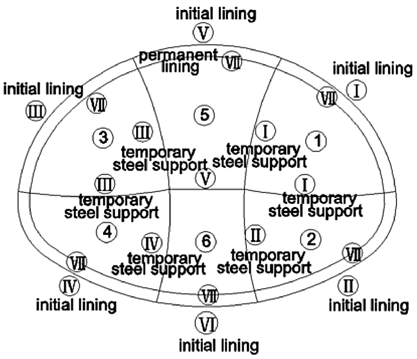
initial lining
V
permanent lining
VII
initial lining
I
VII
initial lining
III
VII
5
3
III
I
1
temporary steel support
temporary steel support
V
III
I
temporary steel support
temporary steel support
4
IV
6
II
2
temporary steel support
temporary steel support
VII
VII
IV
II
initial lining
VII
initial lining
VI
initial lining

Fig. 6. Model-5: DSDM (right first)

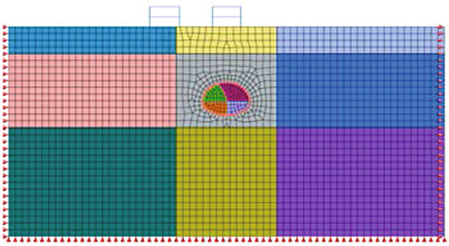

Fig. 7. FEM Model-2

3.2 Solving Process of FCES

Using FEM, we can get data before standardization. See Fig. 7 and Table 1.

Table 1. Data before standardization

Indicators	Model-1	Model-2	Model-3	Model-4	Model-5
X_1	8.40	18.40	18.40	33.00	33.00
X_2	0.43	0.23	0.23	0.16	0.16
X_3	1.30	2.10	2.13	2.30	2.32
X_4	1870.00	1880.30	1860.00	1659.50	1671.20
X_5	150.00	130.60	140.00	154.50	150.60
X_6	2.01	1.80	1.72	1.62	1.61
X_7	8.52	7.02	6.65	6.20	6.13
X_8	23.00	21.60	21.90	19.00	19.00
X_9	0.70	0.27	0.27	0.25	0.22

We can get data after standardization as stated in Sect. 2.2 (see Table 2).

Table 2. Data after standardization

Indicators	Model-1	Model-2	Model-3	Model-4	Model-5
X_1	1.00	0.59	0.59	0.00	0.00
X_2	1.00	0.26	0.26	0.00	0.00
X_3	0.00	0.78	0.81	0.98	1.00
X_4	0.05	0.00	0.09	1.00	0.95
X_5	0.19	1.00	0.61	0.00	0.16
X_6	0.00	0.53	0.73	0.98	1.00
X_7	0.00	0.63	0.78	0.97	1.00
X_8	0.00	0.35	0.28	1.00	1.00
X_9	0.00	0.90	0.90	0.94	1.00

We can get evaluation matrix as stated in Sect. 2.3 (see Table 3).

Table 3. Evaluation matrix of CD method R_2

Indicators	S_1	S_2	S_3	S_4	S_5
X_1	0.000	0.000	0.967	0.033	0.000
X_2	0.000	0.000	0.000	0.296	0.704
X_3	0.000	0.922	0.078	0.000	0.000
X_4	0.000	0.000	0.000	0.000	1.000
X_5	1.000	0.000	0.000	0.000	0.000
X_6	0.000	0.000	0.625	0.375	0.000
X_7	0.000	0.138	0.862	0.000	0.000
X_8	0.000	0.000	0.000	0.750	0.250
X_9	0.493	0.507	0.000	0.000	0.000

We can get the weight of nine indicators as stated in Sect. 2.4.

$$w = (0.125, 0.146, 0.090, 0.140, 0.117, 0.093, 0.092, 0.106, 0.090)^T$$

The scores of different construction methods can be obtained.

Table 4. The scores of different construction methods

Construction methods	BM	CDM	CDM (right first)	DSDM	DSDM (right first)
Scores	0.417	0.553	0.534	0.677	0.682

The best construction method is DSDM (right first).

4 Conclusion

Using FCES, the present paper analyses the rationality of BM, CDM, DSDM and the impact of excavation sequences of CDM and DSDM. The following conclusions can be drawn.

1. In rocks of grade V, DSDM is the best excavation method.
2. Excavation sequences of different methods (left or right first) have little impact on rationality of construction methods.
3. The establishment of FCES which can be applied to other situations is of broad interest.

Acknowledgments. The work presented in this paper is part of a study conducted under the National Natural Science Fund of China (Grant No. 5157840), Researched on Key Technologies of Shallow Buried Large Section Interchange Tunnel in Complicated Environment (Grant No. 20133139), and Research on Key Technology of Highway Tunnel Safety Construction Based on Deformation Control Method of Weak Surrounding Rock (Grant No. 201611).

References

1. Shi, T., Wenqi, D.: Analysis of deformation of yezhushan highway tunnel construction based on analysis of controlled deformation in rocks and soils. Tunn. Constr. **37**(5), May 2017
2. Wang, M.: Shallow Excavation Technology of Underground Engineering Theory, pp. 307–309. Hefei Anhui Education Press Agency (2004)
3. Wang, X.: Analysis of the influences of construction steps of CD method on construction security. Municipal Eng. Technol. **27**(6), October 2009
4. Gao, F., Tan, X.: Stability on large tunnel with double-side-drift method. J. Chongqing Jiaotong Univ. **29**(03), June 2010
5. Li, L.: Research on the influence for stability of surrounding rock between three-step method and CRD method. Highway Eng. **37**(6), December 2012
6. Peng, L.: Traffic tunnel engineering. Central South Univ. **35**(7) (2003)
7. Zhang, X.: Research on the stress behavior of surrounding rock during construction adopting CD method of large cross-section tunnel. Southwest Jiaotong Univ. **17**(6) (2014)
8. Guo, X.: Evaluation of public transit service satisfaction based on entropy weight method and cloud model. J. Chongqing Jiaotong Univ., 1–7 (2017)
9. Wang, H.: Numerical Analysis and Design of Geotechnical Engineering, pp. 199–214. Dalian University of Technology Press (2013)
10. Huang, L.: Comparative analysis and application of the construction method in shallow large span tunnel. Highway Eng. **36**(5), October 2011

Multi-time-Scale Analysis of Tunnel Temperature Field Based on Big Data

Zhiguo Yan[1,2(✉)], Jiangtao Liu[1,2], Hehua Zhu[1,2], and Jingtao Dong[1,2]

[1] Key Laboratory of Geotechnical and Underground Engineering
of Ministry of Education, Tongji University, Shanghai 200092, China
`yanzguo@tongji.edu.cn`
[2] Department of Geotechnical Engineering, College of Civil Engineering,
Tongji University, Shanghai 200092, China

Abstract. It is crucial to alarm people immediately and accurately when fire occurs in a tunnel. There are some uncertainty of fire alarm when responding to temperature of tunnels which may result in false alarms and omissions. Based on the significant amount of temperature data collected from the optical fiber grating temperature system, the multi-time-scale analysis method is used to study the characteristics of temperature field in tunnels in different sizes. According to the research results, some reasonable proposals on how to set the temperature threshold in alarm system and temperature changing rate threshold are given to improve the performance of fire alarm system. Meanwhile, temperature field model under different scales are determined which may be conducive to obtain the preliminary theory of the temperature field of tunnel based on the temperature characteristics. Those conclusions of research are applied to the Dalian Road Tunnel project. It provides not only reliable supports to the subsequent flue gas and temperature field reconstruction, but also reliable theoretical supports to the evacuation of Dalian Road tunnel.

Keywords: Big data · Multi-time-scale analysis · Temperature field
Fire alarm

1 Preface

Fire safety of tunnels are extremely severe during the tunnel operation. The tunnel is long and narrow in space. It is difficult for natural smoke to exhaust in enclosed space. Temperature will heat up rapidly after fire, the flue gas will spread rapidly, and the escape time for people is urgent. Once the fire breaks out, the tunnel will be clogged with traffic, and there are few escape routes for people. Thus, heavy casualties and significant economic losses often occur [1]. On the other hand, fire fighters often lack of attack routes because of congestion. The evacuation and rescue will be very tough.

The earlier detection of tunnel fires, the greater certainty they will be put out. It is key to alarm quick and accurately in the event of a tunnel fire, which can provide valuable time for people to evacuate and rescue.

The accurate acquisition of temperature field information in the tunnel is the first step to realize the rapid and accurate fire alarm. Then the temperature field distribution

© Springer Nature Singapore Pte Ltd. 2018
D. Zhang and X. Huang (Eds.): GSIC 2018, *Proceedings of GeoShanghai 2018 International Conference: Tunnelling and Underground Construction*, pp. 737–748, 2018.
https://doi.org/10.1007/978-981-13-0017-2_74

graph and temperature rise curve should be correctly established, and the temperature field information should be accurately determined to determine whether the temperature field is the fire temperature field after obtaining the information of the tunnel temperature field. Furthermore, the fire type, heat release rate, gas diffusion rate, smoke diffusion range and other fire alarm important information should be acquired to provide theoretical guidance and support for evacuation rescue. Automatic fire alarm systems have been set in the cross-river tunnels of shanghai [2, 3]. Many scholars have carried out research on tunnel fire and tunnel evacuation rescue [4–6]. But a perfect theory of tunnel temperature field has not been set up which leads to an insufficient understanding of the temperature field and results in false alarm and no alarm in automatic fire alarm system when fire.

The multi-time-scale analyses has been used to study the rule of conventional temperature field in tunnel based on a large number of long-term observation data of Dalian Road tunnel and East Yan An Road tunnel in this paper [7]. The temperature field distribution in normal situation can provide valid supports for the subsequent fire alarm.

2 Multi-time-Scale Analysis of Temperature Field in the Middle Part of Tunnel

Temperature data in normal working situation are obtained from Dalian Road Tunnel and East Yan An Road Tunnel in Shanghai. The lengths of Dalian Road tunnel are 1275 m and 1253 m in east and west, respectively. The four-lane tunnel is located between Yangpu Bridge and East Yan An Road Tunnel. The design speed is 40 km/h, and the clear height of passage is 4.5 m. The length of East Yan An Road tunnel is 2261 m with four-lane which is similar with Dalian Road tunnel. Fiber Bragg Grating systems are used in those tunnels to deal with fire [8–10]. The precision of Fiber Bragg Grating system is 0.1 °C

In order to eliminate the influence of the tunnel and cover sufficient temperature variation scale, the measurement point temperature of the fiber grating in the middle of the tunnel is selected in space. Temperature data of 30 days continuously collected in seconds are used to analyze. The analysis with such large amount of data of 2592000 can reflect the change and fluctuation of temperature over time, while excluding the accidental error of data.

2.1 Analysis at Per Second Scale

Temperature data of a fiber Bragg grating point of 30 days are selected to study the characteristics of normal temperature field inside the tunnel, based on four scales from small to large of time scale, from per second scale, per minute scale, per hour scale to per day scale. The quantity of temperature data of 30 days is 2592000 at per second scale.

Figure 1(a) shows that the highest temperature is 36.6 °C while the minimum is 24.6 °C within 30 days. The biggest difference of temperature in 30 days is 12.0 °C. It can be interpreted that the temperature difference will be greater in the summer than in winter. The tunnel temperature could be higher than 45.0 °C in summer time. So a fixed lower temperature threshold such as 40.0 °C should not be taken as the fire alarm judgment. The temperature curve in a day reflect the law that the temperature is lower in the morning compared to the noon, and the temperature fall back at night. It reflect tunnel temperature change tendency in day, and temperature fluctuation in a month under normal condition. And it can be clearly seen from temperature curves that the fluctuation of temperature data can be clearly reflected in small scale of per second.

The temperature data is analyzed by first derivative in per second scale. The database has 25921999 records. From Fig. 1(b) and (c), the absolute value of first derivative of temperature distributes from 0 °C/s to 0.2 °C/s significantly with minute quantity of 0.3 °C/s, whether in a single day or night, whether hot or cold. The first derivative of absolute value maximum temperature is 0.3 °C/s, and the minimum is 0 °C/s. Temperature changing rate per second shows some of regularity and more than 99.9% of the temperature data of first derivative distribute from –0.2 °C/s to 0.2 °C/s. In order to avoid false alarm, temperature changing rate threshold should be set wider than 0.3 °C/s in the fire alarm system per second. Meanwhile, the distribution characteristics of second derivative of temperature are roughly same as the first, and the distribution ranges mostly from –0.15 °C/s^2 to 0.15 °C/s^2.

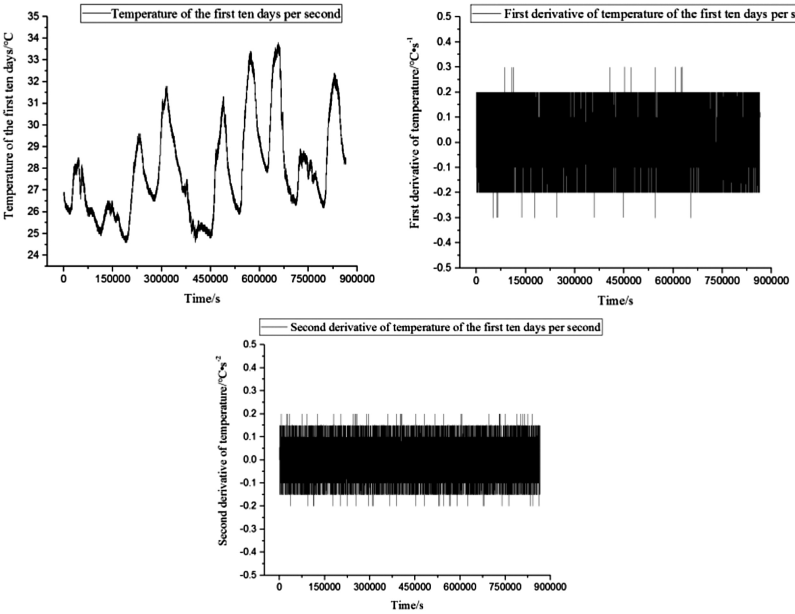

Fig. 1. (a) Temperature of the first ten days per second; (b) First derivative of temperature in the first ten days per second; (c) Second derivative of temperature in the first ten days per second

2.2 Analysis at Every Five Seconds Scale

For every 5 s scale, the quantity of temperature data in 30 days is 518,400. Figure 2(a) shows that the highest temperature is 36.58 °C while the minimum is 24.68 °C within 30 days. The biggest difference of temperature in 30 days is 11.9 °C. The precision of temperature data at every 5 s scale is very high, compared with the actual temperature. At the same time, the information of temperature can be retained. It is easy to see from the curve of temperature that the characteristics of slight fluctuation can be clearly reflected at 5 s scale of tunnel temperature.

There is a first derivative analysis of temperature with the quantity of 518400 at every 5 s scale. The value of first derivative of temperature distributes significantly from –0.13 °C/s to 0.13 °C/s from Fig. 2(b) and (c). The maximum value of temperature changing rate is 0.16 °C/s while the minimum is –0.16 °C/s. Temperature changing rate of every five seconds shows some of regularity and more than 99.9% of the temperature data of first derivative distribute from –0.15 °C/s to 0.15 °C/s. The maximum gradient descends 0.14 °C/s compared with the value of per second scale. This is a corollary of averaging the temperature at every 5 s. The characteristics of second derivative is roughly same as and the first. But the distribution range is bigger and the most distribute from –0.18 °C/s2 to 0.18 °C/s2. The maximum value of Second derivative is 0.26 °C/s2 while the minimum is 0.24 °C/s2.

There are two abnormal data jump at least with one year sequential observation of Dalian Road Tunnel. First jump is located in the tunnel entrance. The value of temperature suddenly fell to 25.4 °C from 26.6 °C, returned to normal after mutation

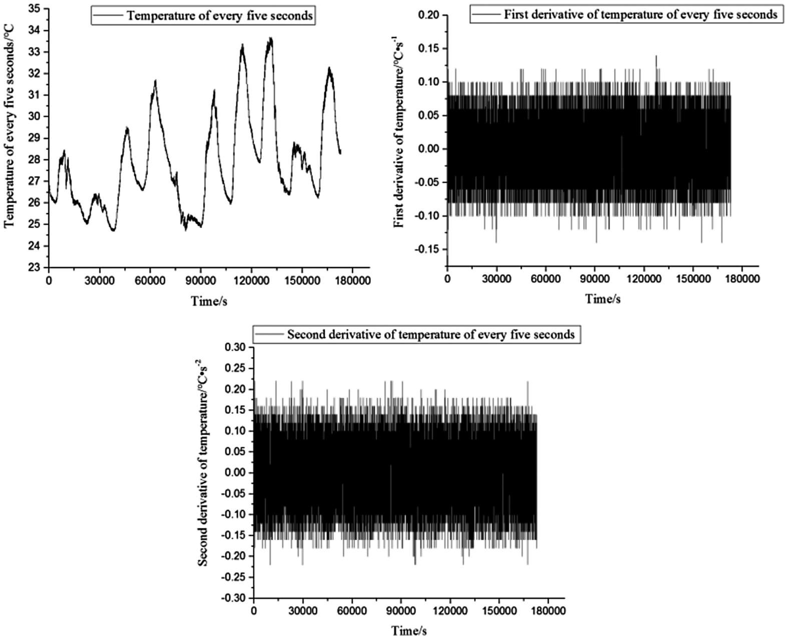

Fig. 2. (a) Temperature of every five seconds; (b) First derivative of temperature of every five seconds; (c) Second derivative of temperature of every five seconds

immediately, stabilized 25.4 °C at last. The second data jump was from 28.5 to 26.2, then returned to normal, fluctuated slowly on the 26.2 basis at last. Fiber Bragg grating is used to collect temperature data. There may be some data jumps because of the instability of instrument in a long time of data collection. This is one of the main sources of false alarming. This situation should be excluded in the case of fire detection.

The temperature change caused by the fluctuation of the instrument can be effectively reduced or eliminated by adopting the temperature data of every 5 s scale. The temperature information can be preserved at the same time. In the fire alarm system, the threshold of temperature changing rate must be greater than 0.2 °C/s of every 5 s. At last, the temperature effect caused by abnormal instrument fluctuation can be effectively eliminated by using the combination of temperature multi-time-scale rule.

2.3 Analysis at Every Ten Seconds Scale

For every 10 s scale, the quantity of temperature data in 30 days is 259200. Figure 3(a) shows that the highest temperature is 36.54 °C while the minimum is 24.7 °C within 30 days. The biggest difference of temperature in 30 days is 11.84 °C. The precision of temperature data at every 10 s scale is acceptable, compared with the actual temperature. At the same time, the information of temperature can be retained. The curve of temperature shows that the characteristics of fluctuation can be clearly reflected at 10 s scale of tunnel temperature.

The quantity of temperature data is 259199 when analyzed by first derivative at every 10 s scale. The value of first derivative of temperature distributes significantly from –0.10 °C/s to 0.10 °C/s from Fig. 3(b) and (c). The maximum value of temperature changing rate is 0.24 °C/s while the minimum is –0.19 °C/s. The maximum gradient descends 0.06 °C/s compared with the value of per second scale. This is a corollary of averaging temperature at every 10 s. The characteristics of second derivative is roughly same as and the first. But the distribution range is bigger and the most distribute from –0.15 °C/s^2 to 0.15 °C/s^2. The maximum value of Second derivative is 0.18 °C/s^2 while the minimum is 0.18 °C/s^2.

The temperature change caused by the fluctuation of the instrument can be effectively eliminated by adopting the temperature data of every 10 s scale. The temperature information can be preserved at the same time. In the fire alarm system, the threshold of temperature changing rate must be greater than 0.2 °C/s of every 10 s.

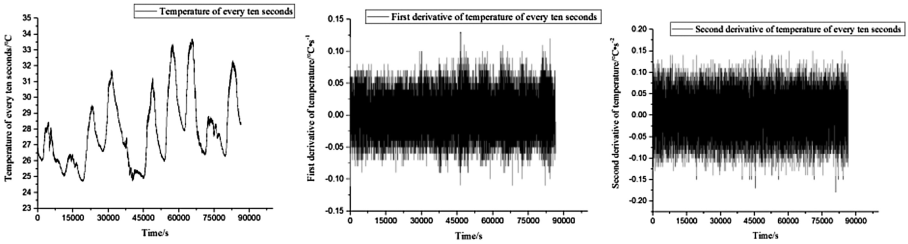

Fig. 3. (a) Temperature of every ten seconds; (b) First derivative of temperature of every ten seconds; (c) Second derivative of temperature of every ten seconds

2.4 Analysis at Every Thirty Seconds Scale

For every 30 s scale, the quantity of temperature data in 30 days is 86400. Figure 4(a) shows that the highest temperature is 36.54 °C while the minimum is 24.71 °C within 30 days. The biggest difference of temperature in 30 days is 11.83 °C. The precision of temperature data at every 30 s scale is acceptable, compared with the actual temperature. The curve of temperature shows that the characteristics of fluctuation can be clearly reflected at 30 s scale of tunnel temperature.

The quantity of temperature data is 86399 when analyzed by first derivative at every 30 s scale. The maximum value of temperature changing rate is 0.35 °C/s while the minimum is –0.46 °C/s. The maximum gradient increases 0.06 °C/s compared with the value of per second scale. Such characteristics are different from the 5 s scale and 10 s scale. The effect of temperature time effect is stronger than averaging. The maximum value of Second derivative is 0.28 °C/s^2 while the minimum is 0.39 °C/s^2. The distribution range is bigger of second derivative and the most distribute from –0.15 °C/s^2 to 0.15 °C/s^2.

The temperature change caused by the fluctuation of the instrument can be effectively eliminated by adopting the temperature data of every 30 s scale, but it will lose a lot of temperature information. The temperature information can be preserved at the same time. In a fire alarm system, the information of every 30 s can be used to help exclude temperature anomalies to avoid false alarming.

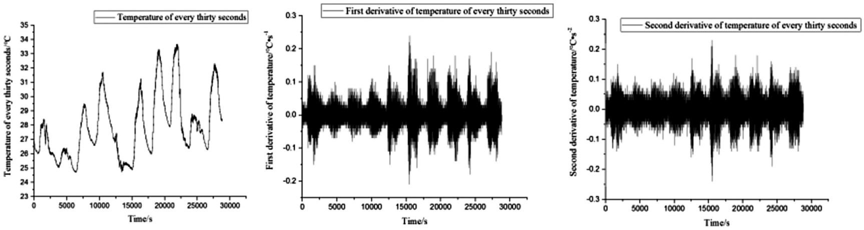

Fig. 4. (a) Temperature of every thirty seconds; (b) First derivative of temperature of every thirty seconds; (c) Second derivative of temperature of every thirty seconds

2.5 Analysis at Per Minute Scale

The average value of tunnel temperature per minute is taken as a data point, there are 43200 records in 30 days. It can be seen from Fig. 5(a) that the highest temperature is 36.5 °C and the minimum lowest is 24.7 °C in the analysis in per minute scale within a month. The greatest difference is 11.8 °C. The feature of temperature field analysis in per minute scale is similar to the noise reduction of temperature records measured in second. The tendency of change of temperature measured in minutes can be reflected. The volatility has shrunk compared with the volatility per second. The average temperature is not as clear as the temperature fluctuation per second, but it can also reflect the fluctuation of normal temperature.

The temperature data is analyzed by first derivative at per minute scale, and the data volume is 43199. It is can be showed from Fig. 5(b) and (c) that the temperature characteristics of per minute scale have presented a similar rule as per second scale. The value of the first derivative of temperature distributes from –0.2 °C/s to 0.2 °C/min significantly with minute quantity of 0.3 °C/min, but there is an individual data which is 0.8 °C/min. It remains to be further studied whether the temperature changing rate of each minute can be used to be judgment value of fire alarming, although temperature changing rate per minute shows some of regularity. The first derivative of temperature per minute can fluctuate greatly, which will affect the accuracy of the alarm. The second derivative of temperature per minute is similar to the first.

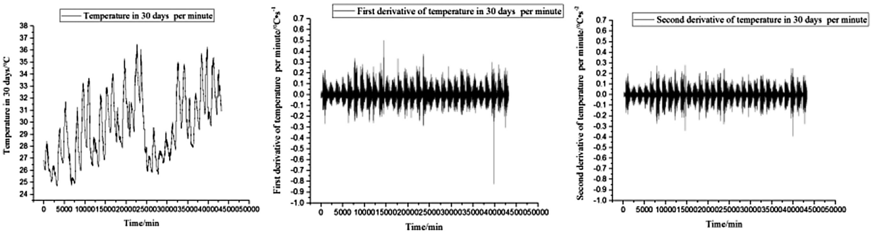

Fig. 5. (a) Temperature in 30 days per minute; (b) First derivative of temperature in 30 days per minute; (c) Second derivative of temperature in 30 days per minute

2.6 Analysis at Per Hour Scale

At per hour scale, the average value of tunnel temperature per hour was taken as a data point, and the temperature data volume is 24 of one day and 720 of one month. It can be gotten from Fig. 6(a) that the highest temperature is 36.0 °C and the minimum is 24.8 °C in the analysis of per hour scale within a month. The biggest difference in temperature is 11.2 °C, which reduces 0.8 °C compared with per minute scale. It is inevitable to get a lower temperature difference when temperature data are averaged per hour.

It can be gotten from data analyses that the change trend of temperature data can roughly reflect normal temperature, and relative error is only 0.8 °C, temperature data in the acceptable range. The downside is that temperature volatility cannot be reflected in large scales. The average value of tunnel temperature can roughly reflect the change trend of conventional temperature per hour and the relative error is only 0.8 °C in an acceptable range. The deficiency is that the temperature fluctuation cannot be reflected at per hour scale. The temperature changing rate per hour is different from per second and per minute significantly. The change interval is from –1.5 to 1.5 °C/h about seven times to second scale. Abnormal huge fluctuation which can reach –4 °C/h may exist. Such a large amount of change cannot be the judgment value for alarm. The second derivative is similar to the first derivative.

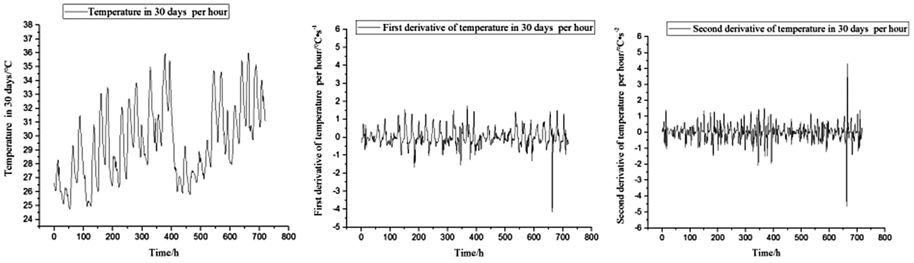

Fig. 6. (a) Temperature in 30 days per hour; (b) First derivative of temperature in 30 days per hour; (c) Second derivative of temperature in 30 days per hour

2.7 Analysis at Per Day Scale

At per day scale, the average value of tunnel temperature per day was taken as a data point, and the temperature data volume is 30 of one month. It can be gotten from Fig. 8 (a) that the highest temperature is 32.9 °C and the minimum is 25.7 °C in the analysis of per day scale within a month. The biggest difference in temperature is 7.2 °C. The errors of the maximum and minimum temperature are 3.7 °C and 1.1 °C, compared with the accurate data per second, respectively. The errors are too large to accurately reflect the temperature change in a day, which can only indicate the daily temperature change roughly. The value of temperature changing rate is bigger and distributes from –5.0 °C/d to 4.0 °C/d (Fig. 7).

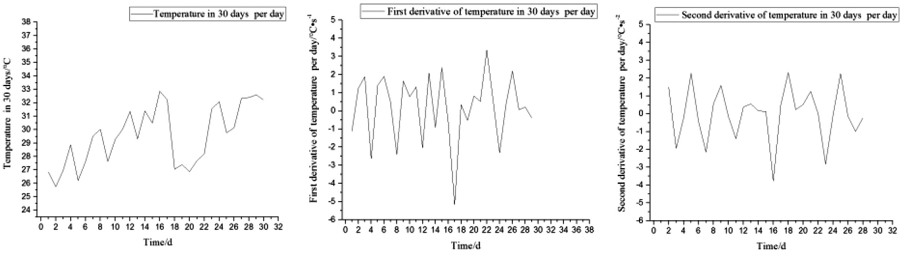

Fig. 7. (a) Temperature in 30 days per day; (b) First derivative of temperature in 30 days per day; (c) Second derivative of temperature in 30 days per day

3 Multi-time-Scale Analysis of Temperature at the Same Time

3.1 Temperature Characteristics of Dalian Road Tunnel Based on Multi-time-Scale Analysis

The observation starts at 12:00 pm in Day 3 and end at 12:00 pm Day 4. The characteristics of temperature at the moment are studied under the large scale measured by months and weeks. The mesoscale is measured by days, while small scale is measured by hours and minutes. The average daily temperature is calculated based on records every second in a week and in a month. A simple linear interpolation is adopted on a daily basis. Temperature varies from 25.7 °C to 32.9 °C in a month. The difference of temperature in a month is 7.2 °C. It is shown in Fig. 8(a) that temperature fluctuation in a week is similar to temperature fluctuation in a month. The lowest value of temperature is 25.7 °C while the highest value is 30.3 °C. The difference of temperature is 4.6 °C within seven days. It can be observed from the temperature curves that the temperature fluctuation are wider under larger scale. The rough daily temperature variation can be observed.

There are 86400 s in a day, and the system record data in every second. Temperature varies from 24.6 °C to 29.6 °C. The difference of temperature is 5.0 °C. As shown in Fig. 8(b), temperature data can reflect the temperature change tendency in a day, and can reflect the fluctuation of temperature. There are 3600 pieces of data per second for small scales within an hour. As shown in Fig. 8(c), temperature varies from 27.8 °C to 28.4 °C. The difference of temperature is 0.6 °C. The temperature variation is relatively small, which can reflect the fluctuation of temperature. There is a record every second of one minute in Fig. 8(d). Temperature varies from 28.0 °C to 28.2 °C.

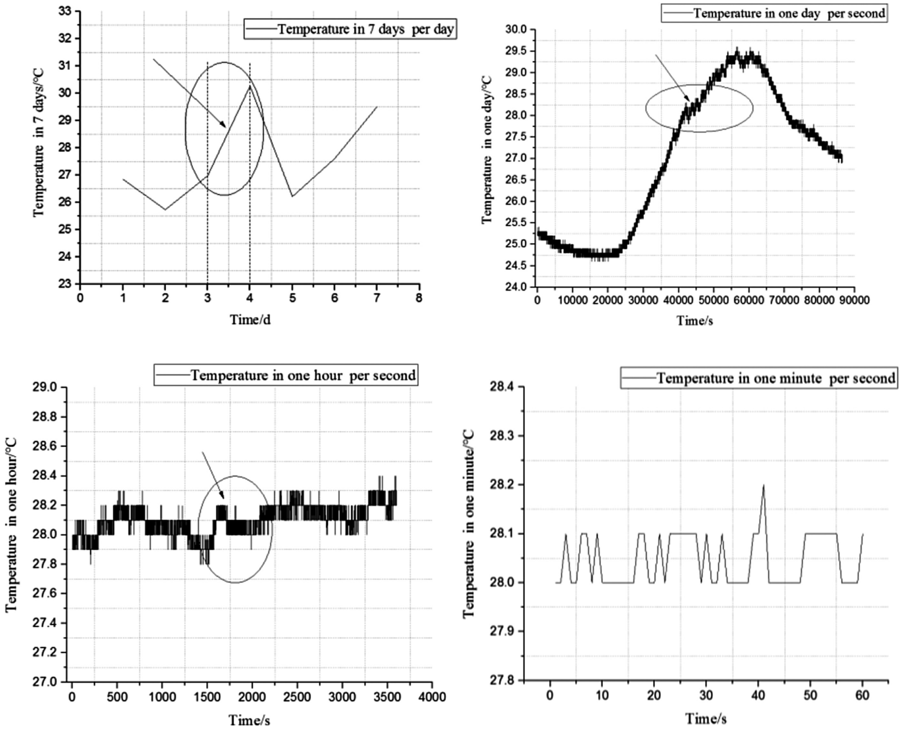

Fig. 8. (a) Temperature in 7 days per day; (b) Temperature in one day per second; (c) Temperature in one hour per second; (d) Temperature in one minute per second

The difference of temperature is only 0.2 °C. The temperature variation is very small. It can be clearly seen that the temperature in tunnels fluctuates slightly between the constant under normal situations.

3.2 Temperature Characteristics of East Yan an Road Tunnel Based on Multi-time-Scale Analysis

The characteristics of temperature of East Yan An Road Tunnel are also researched. Data are recorded in per second. Temperature varies from 30.4 °C to 45.9 °C in a day. The difference of temperature is 15.5 °C. The temperature of the tunnel varies greatly in a day. The maximum temperature is 45 °C. It is not appropriate to take a fixed low fire alarm threshold. As shown in Fig. 9(a), temperature data can reflect the temperature change tendency in a day.

3600 pieces of data are extracted and analyzed at noon. As shown in Fig. 9(b), temperature varies from 39.6 °C to 42.6 °C. The difference of temperature is 3.0 °C. The traffic is about 78,000 and those heavy traffic generated a lot of thermal shock at noon which increases the temperature of the sensor. There is a record every second of one minute in Fig. 9(c). Temperature varies from 41.9 °C to 42.1 °C. The difference of temperature is only 0.3 °C. The temperature variation is small in one minute.

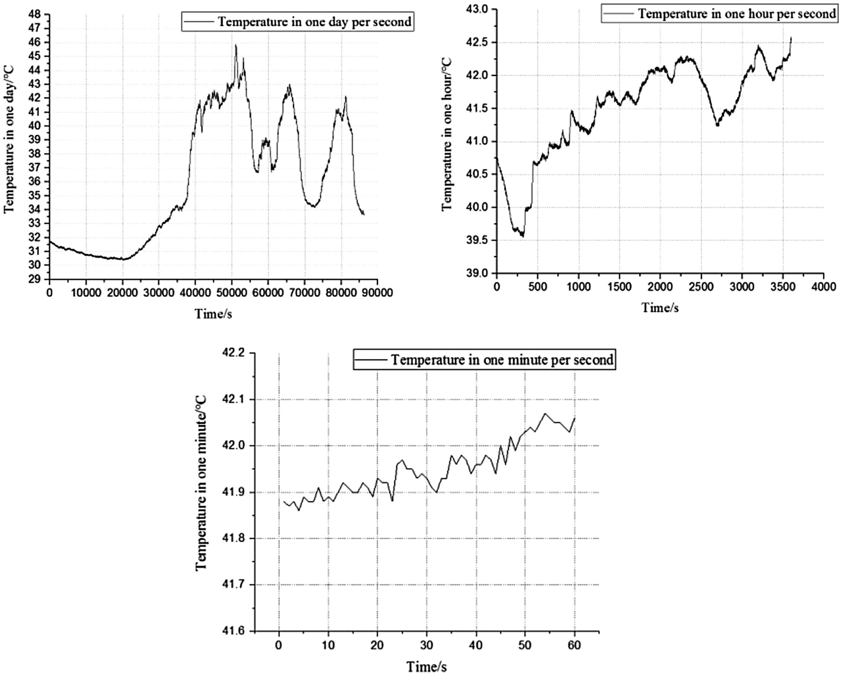

Fig. 9. (a) Temperature in one day per second; (b) Temperature in one hour per second; (c) Temperature in one minute per second

Each tunnel has its own uniqueness, although temperature characteristics of the two tunnels have similarity in one minute at per second scale. Temperature of Dalian Road tunnel change more gradually one day, and the difference of temperature is 5.0 °C of one day contrast with 15.5 °C. The main reason for the difference is traffic. And the traffic of East Yan An Road Tunnel is about three times of Dalian Road tunnel. The difference of temperature is 0.2 °C per minute of Dalian Road tunnel contrast with 0.3 °C. They are both very small. Temperature of every minute is relatively stable under normal conditions.

4 Conclusion

The characteristics and laws of tunnel temperature field are analyzed with the help of multi-time-scale method which is based on tremendous amount of conventional temperature field data. The following conclusions are obtained.

(a) The conventional temperature field of tunnels is dynamic. The temperature difference can reach 12.0 °C in a month of Dalian Road tunnel, and the temperature difference is as high as 15.5 °C in one day of East Yan An Road Tunnel. It is not appropriate to take a fixed lower temperature threshold (e.g. 45.0 °C) as the fire alarm judgment. Threshold should be dynamic over time, and threshold should be diverse with different tunnels.

(b) Temperature difference per second distributes significantly from –0.2 °C/s to 0.2 °C/s of Dalian road tunnel. And the data which is 0.3 °C/s at conventional temperature field has been tested on the rare occasions. The maximum absolute value of temperature changing rate is 0.3 °C/s. In order to avoid false alarm, the temperature changing rate threshold per second in fire alarm system should be set to be greater than 0.3 °C/s of Dalian road tunnel.

(c) Temperature changing rate per minute distributes significantly from –0.2 °C/min to 0.2 °C/min, only a few data can reach 0.3 °C/min in conventional temperature field of Dalian road tunnel. But there are exceptions that temperature changing rate per minute reach 0.8 °C/min. Therefore, further study should be conducted to figure out whether it is appropriate to select the temperature changing rate per minute as the alarm threshold of tunnel fire or not.

(d) It can be clearly proved that tunnel temperature fluctuates slightly in a minute in conventional temperature field of both tunnels. Fluctuation ranges mainly from –0.2 °C/s to 0.2 °C/s. It can be concluded that tunnel temperature at conventional temperature field can be approximately expressed by temperature per minute.

(e) In the fire alarm system, the threshold of temperature changing rate must be greater than 0.3 °C/s of every minute. At last, the temperature effect caused by abnormal instrument fluctuation can be effectively eliminated by using the combination of temperature multi-time-scale rule.

References

1. Yan, Z.: The Study of Long Road Tunnels Fire. Southwest Jiao tong University, Chengdu (2002)
2. Kurioka, H., Oka, Y., Satoh, H., et al.: Fire properties in near field of square fire source with longitudinal ventilation in tunnels. Fire Saf. J. **38**(4), 319–340 (2003)
3. Rogner, A.: Safety and reliability of fire detection systems in road tunnels. In: Fourth International Symposium on Tunnel Safety and Security, Frankfurt am Main, Germany, 17–19 March, p. 561 (2010)
4. Yan, Z., Tian, Y., Zhu, H., et al.: Tunnel fire dynamic early-warning, evacuation and rescue system and its application. Mod. Tunn. Technol. **53**(6), 31–35 (2016)
5. Shen, Y., Yan, Z., Zhu, H.: Full-scale experimental research on the development of the initial stage of fire in a large cross-section road tunnel. Chin. J. Undergr. Space Eng. **11**(4), 1080–1087 (2015)
6. Yan, Z., Guo, Q., Zhu, H.: Full-scale experiments on fire characteristics of road tunnel at high altitude. Tunn. Undergr. Space Technol. **66**, 134–146 (2017). Incorporating Trenchless Technology Research
7. Zhang, X., Ren, Z., Mei, F.: Heat Transfer Theory, 5th edn. China Architecture & Building Press, Beijing (2007)
8. Mashimo, H.: State of the road tunnel safety technology in Japan. Tunn. Undergr. Space Technol. **17**(2), 145–152 (2002)
9. Jun, Z.H.U., Dian, F.A.N.: Design of fiber bragg grating detector in tunnel fire. J. Wuhan Univ. Technol. **29**(4), 107–110 (2007)
10. Feng, W., Zhou, C.: The study and application of fire detected technology based on fiber bragg grating. Fire Sci. Technol. **26**(2), 174–177 (2007)

A Summary of Precast Technology Application in Tunneling

Hong Jiang(✉)

Shanghai Urban Construction Design and Research
Institute (Group) Co., Ltd., Shanghai 200125, China
jianghong@sucdri.com

Abstract. Through discussion on present precast tunnel technology home and abroad, an advanced concept is put forward on intelligent construction for precast tunnel. A series of technical solutions are proposed for different tunnel sections, including precast cut and cover tunnel, monolithic precast cut and cover tunnel, GPST method for shield tunnel etc. A complete construction for tunnel could be realized by applying precast technology in open cut section, expanding the shield section application and adopting the precast components in pit, which indicates a new direction to the whole precast technology application in tunneling. This paper provides a technical guidance and theoretical basis for precast technology in tunnel engineering.

Keywords: Tunneling · Precast · Tunnel construction

1 Introduction

There are various methods: drilling and blasting, TBM, open and cut, pipe-jacking, immersed tube and shallow burial subsurface excavation methods, in tunnel construction. And shield TBM, pipe jacking and immersed tube methods are typical precast technologies. It demonstrates the tunnel precast technology is at the forefront in civil engineering. Usually these methods are widely used in urban and coastal areas, so this paper focuses mainly on construction of precast tunnel in urban area.

Cut and cover method and shield TBM method, are often adopted in urban tunnel construction. Taking Shanghai for example, more than 10 cross-river tunnels and nearly 600 km subway tunnels were constructed by shield method except that the Outer Ring Tunnel was immersed tube. However, there is still room for improvement in tunnel precast technology, for now the working shaft, buried or open section and subway station are still being built by cut and cover method. And the statistical information of some cross-river tunnels in Shanghai is listed in Table 1.

The cast-in-situ process is very complicated with large material consumption and longtime construction but poor quality. Therefore it is necessary to develop a reliable and energy-saving technology to carry out a friendly environmental and highly economical tunnel construction in the urban area.

Some precast tunnel cases have been reported abroad. The Dutch Rotterdam subway adopts precast roof and side walls while the floor was constructed on site. It seems like “shell tunnel” and maintains a good waterproof effect after years of operation [1].

© Springer Nature Singapore Pte Ltd. 2018
D. Zhang and X. Huang (Eds.): GSIC 2018, *Proceedings of GeoShanghai 2018 International Conference: Tunnelling and Underground Construction*, pp. 749–756, 2018.
https://doi.org/10.1007/978-981-13-0017-2_75

Table 1. Statistical information of some cross-river tunnels in Shanghai

Tunnel name	Total length (km)	Shield sections (km)	Proportion (%)	Remark
South Xizang Road Tunnel	2.20	1.18	54%	Completed
South Hongmei Road Tunnel	5.02	3.39	68%	Completed
The Cross-River Channel	6.47	5.09	79%	Under construction
West Xianxia Road Tunnel	1.73	1.04	60%	Completed
North Cross Channel Tunnel	12.4	6.2	50%	Under construction

Precast double cross-box structure, 11.092 m in length and 7.440 m in breadth, is adopted in Sendai subway, Japan. The whole structure is divided into five components: roof, floor, side wall, middle column and bottom [2]. The former Soviet Union once used the assembled and standardized reinforced concrete structure in subway stations, interval tunnels and station affiliated structures. In the late 1980 s, the former Soviet Union began to use the integral pipe lining in interval tunnels built by open and cut method [3]. There are also some applications of precast cut and cover tunnel in China. For example, the double-hole frame structure with 19.9 m × 7.5 m in outer dimension is adopted in the underpass project of Shugang Road, Xiamen, China. In the longitudinal direction the structure is divided into parts per 2 meters and in the horizontal direction the structure is divided into two "E" blocks [4]. The Yuanjiadian station of Changchun Metro Line 2 completed 48 m test section of assembled underground station and used the prefabricated assembly technology for the first time in the subway project in China. The cross-river tunnel in Weisan Road, Nanjing, China uses the beam-plate-column structure system combined with precast and cast-in-situ structure. It explores the construction technology of the internal precast components in overlong shield TBM tunnel [5].

As the demographic dividend disappears, construction cost increases. The advantage of industrialization construction has come into view for its green effect. The government has released the policy guidance: the new residences should mainly adopt the precast technology for the full coverage of green building. Shanghai Traffic Committee issued "*Shanghai traffic construction assembly technology application promotion program (2016–2018)*" in May 2016 and clearly stated that the precast rate in shield section should reach 75% to 90% after using precast "rectangular-shaped components, lane plate, anti-collision wall". Therefore it is important to carry out the research and application of precast tunnel technology; and it is time to replace the traditional manual production mode with large industrial production mode for the green industrialized construction of urban tunnel project.

2 Construction Technology of Precast Tunnel

The construction technology of precast tunnel includes several aspects. Firstly it should use precast technology in open and cut section of tunnel to facilitate the large-scale components' assembly on site; and it also should ensure the structures' impermeability and waterproof performance. Then the precast technology should be expanded to internal lane plate, flue plate, contact channels and other accessory structures in shield tunnels. Finally, the support structure of the foundation pit uses prefabricated components that are recyclable and reusable. If the above points could be achieved, the tunnel can be identified as whole precast tunnel.

2.1 Precast Cut and Cover Tunnel

Based on the characteristics of tunnel and assembly structure, and learning from the precast concept and technology of shield tunnel, prefabricated bridge and precast concrete building, there will be two kinds of precast technology for cut and cover tunnel: precast and monolithic precast.

As most of the tunnels are long and narrow, with uniform cross section, it makes the application of standardized precast component suitable (Fig. 1). There is no ‘wet working’ on site, for the structures are prefabricated in factory. The notion of manufacturing standardization is also realized by adopting this precast technology.

Taking the two-lane traffic tunnel for example, the net height of a single hole is about 5–6 m, the width about 8–9 m and wall thickness 700–1100 mm. The precast components could use the rectangular type or double-hole rectangle when the height limit is allowable in transportation. If the height of component is over clearance limit, the component must be divided into the “U” or “E” types. The conjunction of the components can be bolts, longitudinal pre-stressed cables, embedded reinforced joints and so on. The key technology of this scheme is the waterproofing ability of the gasket, and the relevant seismic design is required too. The construction focuses on the assembly of large-scale precast components. It could be carried out by the ground large gantry crane and jacking assembly in the pit (Fig. 2).

In summary, there is no wet operation on site and the longitudinal pre-stressed tensioning measure is taken when using this method. But the components are often very large in volume. The assembling or joint treating needs stricter quality control during construction.

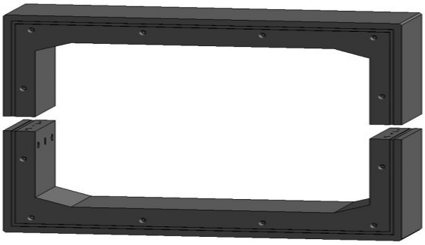

Fig. 1. Illustration of precast components

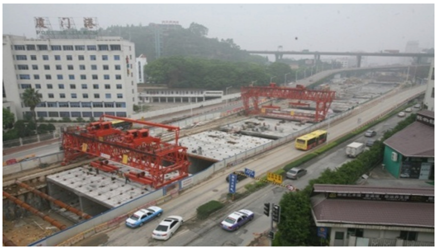

Fig. 2. Site assembly of precast tunnel

2.2 Monolithic Precast Cut and Cover Tunnel

For the monolithic precast cut and cover tunnel (Fig. 3), part of the components have already been manufactured and the rest need concrete casting on site. The idea uses the precast concrete concept in building. The plates and walls are mainly made in the form of single-sided laminated plates with steel truss. The side walls could use single-sided laminated plates, while the enclosure structures are underground diaphragm walls for permanent use. The other walls, including the middle partition walls could adopt the double-sided laminated plates. The laminated plates could reduce site operation and shorten construction period. This technology has been widely used in the underground utility tunnel (Fig. 4).

The thickness of precast plates could be different from those of buildings. This would increase the difficulty of their moving and locating on site. However, the quality could be similar to the cast-in-situ concrete when proper measures are taken, such as enhancing the joint connection and its waterproof. The technology could be used in the working shafts or varying cross sections in tunnel engineering. The advantage of this scheme is that all components are light enough to be lifted and assembled. Although some ‘wet working’ is needed on site, the integrity and the waterproof are quite good in the structures.

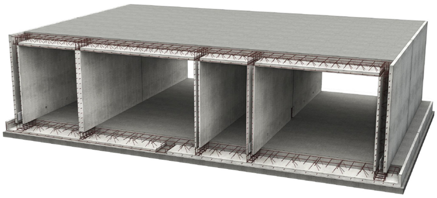

Fig. 3. Illustration of monolithic precast tunnel

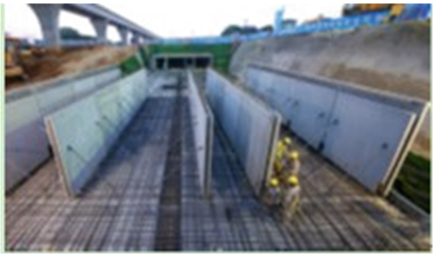

Fig. 4. The construction scene of utility tunnel

2.3 GPST Method in Shield Section

Ground Penetrated Shield Technology (GPST) strives to replace the working shaft with the relatively shallow pit to launch and receive the machine in ultra-shallow covering soil region [6, 7]. Then the conventional open and cut section could be completed by shield TBM method. This technology has been successfully used in a 200 m long section of the subway tunnel from Jiangjun Road to Moling Road in Nanjing, China. The rapid driving technique (URUP) (Fig. 5) was also adopted in an urban expressway of the Shinagawa line in Tokyo, Japan. The shield machine launched and received on ground surface for the first time in the world [8].

Taking a cross-river tunnel in Shanghai for example, the main tunnel will be a double-tube tunnel with a diameter of 11.36 m. It has two ways with four lanes. The shield section will increase about 270 m and the open and cut section will decrease when GPST method is applied. Then the impact on surrounding environment will be greatly reduced or even vanish. The shield machine could directly traverse the main trunk road and the rain pipes below without affecting the current pipeline and road (Fig. 6). The overall cost of this tunnel will be reduced greatly, as the working shaft and shallow buried section are no more needed.

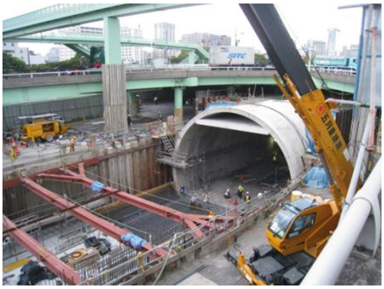

Fig. 5. Japanese UPUP method

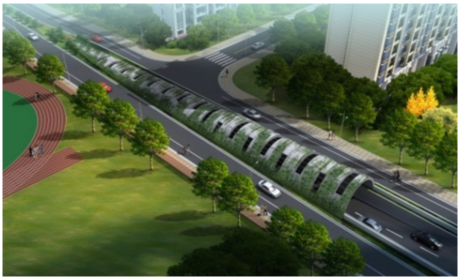

Fig. 6. Effect drawing of GPST tunnel

2.4 Precast Accessory Component in Shield Tunnel

At present the precast “rectangle” member is widely used inside the segment section, synchronously with the driving of the tunnel. But the lane plates at two sides are casted on site now. It delays the construction progress.

The technologies of “precast plate + casted beam-plate joints” and “precast plate + support” are studied in Weisan Road Tunnel, Nanjing, China. Similar studies and practice are also conducted in Zhuguang Road Tunnel in Shanghai too. The precast lane plate is also studied on two sides of the “rectangle” member in a single-layer shield tunnel in Hengqin Tunnel in Zhuhai, China. The laminated plate with steel and truss scheme is adopted to replace the template on curved surface and the assembly of rebars. It would speed up the construction in tunnel engineering. Particularly, the precast flue plates have been successfully used in cross-river tunnel of South Hongmei Road, Shanghai (Figs. 7 and 8). The precast ratio of main structure in shield tunnel could reach 100%. The precast accessory would ensure the structure quality and shorten the construction period in a shield tunnel.

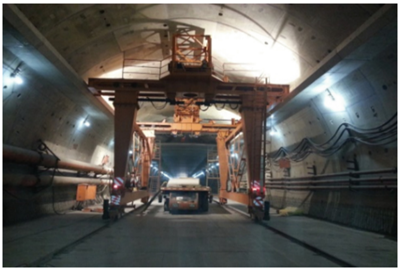

Fig. 7. Flue plate installment

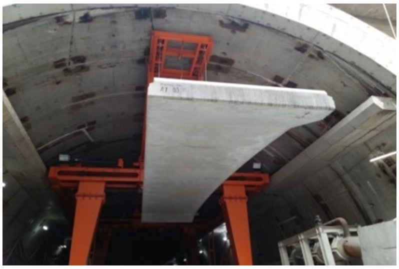

Fig. 8. Fully precast flue plate

2.5 Precast Bypass Channel

Bypass channels are often set in a long tunnel for the safe evacuation from fire. It is done by digging and casting on site after freezing (Fig. 9). But the construction risk is very high with low efficiency.

The link project From Tunmen to Chilie Corner Island, Hong Kong is 4.2 km long with double-line highway tunnel. This tunnel is designed with 44 bypass channels. The German Herrenknecht Ag has invented the bypass boring machine with pipe jacking method, and this machine has successfully completed many bypass channels (Fig. 10). At the same time, Shanghai Tunnel Engineering Co., Ltd and Ningbo Metro Company have also developed similar equipments. The shield method could be used in bypass project too. With these innovations, the prefabrication and mechanization in bypass project would be in practice soon.

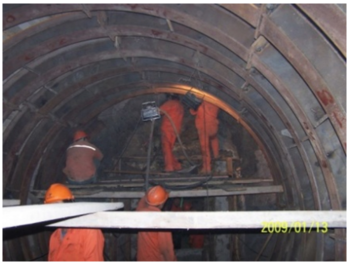

Fig. 9. Bypass construction by freezing method

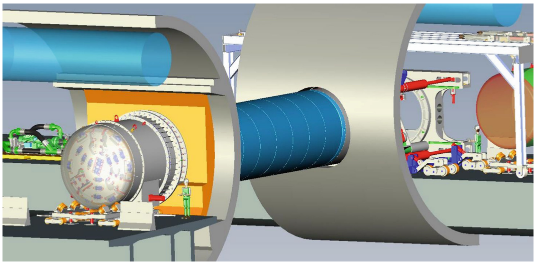

Fig. 10. Bypass construction by tunnel boring machine

2.6 Precast of Foundation Pit Engineering

The precast and recyclable structure and supporting components could be adopted in foundation pit too. Usually the concrete or steel retaining structure has great impact on the surroundings environment. Some precast underground diaphragm wall has been applied in Shanghai, but the technology still needs further improvement. Now ultra-high frequency non-resonance hydraulic vibration hammer has been invented to construct steel pipe pile. It is an eco-friendly alternative method to the bored piles and SMW. This technology could also be used to pull out recycled steel pipes (Figs. 11 and 12).

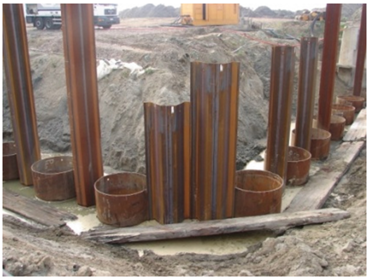

Fig. 11. Steel-tube composite wall in construction

Fig. 12. The precast pavement in construction

2.7 Precast Segment Vertical Shaft Technology

The vertical shaft structure is mainly used in underwater tunnels and deep tunnels. The construction method includes traditional caisson method, cut and cover method and vertical sinking machine (VSM) method (Figs. 13 and 14). VSM excavation is gradually used in the underground shaft, garage, the subway tunnel ventilation shaft and other engineering [9]. It has the advantage of high automation and fast construction with only small construction site.

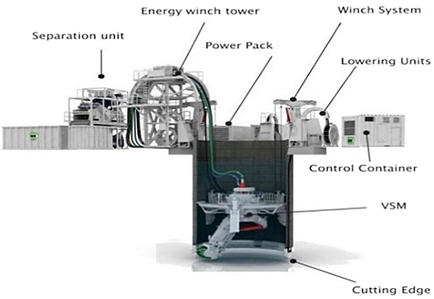

Fig. 13. The structure diagram of VSM

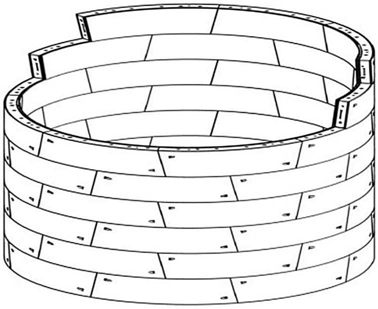

Fig. 14. The assembly of segments

It is a new construction method, using the vertical shaft excavator created by the German Herrenknecht Ag. The VSM is composed of subsidence unit, telescopic milling arm and slurry separation system. The sinking of VSM is carried out by settling unit. The rotary grinding head with special cutting tools is installed on the telescopic milling cupping arm. The milling arm can be used to loosen the soil at the bottom of the shaft. When the shaft is difficult to sink, the milling arm could conduct some super-digs at the bottom of the blade to ensure the structure's sinking. Vertical shafts could be assembled by precast reinforced concrete segments.

This technology has already been used in the United States, Europe and Russia. More than 50 vertical shafts have been successfully built in Naples, Girona, Petersburg, Seattle, Hawaii and other cities. And the total excavation depth has reached 3,000 m. The maximum diameter is 10 m and the maximum excavation depth could reach 85 m.

3 Conclusion

The above discussion shows the precast technology in the whole tunnel construction is practicable. The main solutions include precast cut and cover tunnel, monolithic precast cut and cover tunnel and GPST in shield section. It should also adopt precast accessory component and bypass channel, precast component in foundation pit and precast Segment Vertical Shaft Technology etc.

By these innovations, precast technology could be widely applied to tunnel structure. If information technology, intelligent construction and other means are supplemented, the intelligent construction of precast tunnel could be achieved. The application of intelligent construction of precast tunnel would greatly raise the quality of structure, and the construction period would be shortened in great extent. In the meantime, the impact on the traffic and the surrounding environment could be certainly reduced. It would finally lead the tunneling to a eco-friendly and highly industrialized construction.

Acknowledgements. This paper is supported by the following projects: “Key Technical Research on Deep Underground Space Development between the Existing Dense Buildings (15DZ1204003)”, “Key Technical Research on Industrial Construction of Cut and Cover Tunnel (17DZ1203402)” and “Shanghai Engineering Research Center of Industrialized and Prefabricated Municipal Civil Engineering (17DZ2251900)” which is funded by the Shanghai Science and Technology Commission.

References

1. Liu, H.: Study on Mechanical Properties of Assembled Lining for Open Trench Subway Tunnels. Southwest Jiaotong University, Chengdu (2003)
2. Wang, M., Li, Z., Guan, B.: Study on prefab concrete lining technology for open trench subway tunnels. Journal of the China Railway Society **26**(3), 88–92 (2004)
3. Chen, J.: Study on Mechanical Properties of Assembled Lining for Mining Railway Tunnels. Southwest Jiaotong University, Chengdu (2005)
4. Huang, W., Lin, S.: The application of the prefabricated frame culvert block and multi-directional assembly construction technology in the tunnel under the urban road. In: 2014 On-site Technical Exchange Meeting. China Traffic Construction Co., Ltd. (2014)
5. Guo, X., Dai, H.: Research and Practice on the Construction Technology of Oversize Mud and Water Shield - Nanjing Yangtze River Tunnel. China Building Industry Press, Beijing (2013)
6. Zhao, W., Ding, W., Jiang, H., et al.: Research on internal forces computational methods for ground penetration shield tunnel. In: Seminar on the Academic and Technical Research of the 12th Cross-strait Tunnel and Underground Engineering (2013)
7. Wu, H., Zhou, W., Teng, L.: Case study on ground penetrating shield technology (GPST). Tunn. Constr. **34**(1), 67–72 (2014)
8. Beijer, A.J.: Ultra rapid under pass: the adaptation of the URUP method for the Netherlands Ph.D. thesis. Delft University of Technology, Netherlands (2010)
9. Bao, H.: Research on parking efficiency of mechanical three-dimensional garage. Chin. Municipal Eng. **190**(1), 52, 53, 56 (2014)

Discussions About Key Problems in the Research and Development of Technology System for Rectangular Shield Tunnel

Yaohong Zhu[1], Zibo Dong[2(✉)], Peinan Li[3], and Junfu Lu[4]

[1] Faculty of Architectural, Civil Engineering and Environment,
Ningbo University, Ningbo 315211, Zhejiang, China
[2] Ningbo Rail Transit Group Co. Ltd., Ningbo 315101, China
`lshopingk@126.com`
[3] Shanghai Tunnel Engineering Co. Ltd., Shanghai 200232, China
[4] State Key Laboratory of Geohazard Prevention and Geoenvironment
Protection, Chengdu University of Technology,
Chengdu 610059, Sichuan, China

Abstract. Rectangular shield tunnel has advantages over round shield tunnel of space utility and through capacity in a confined area. However, it has not been effectively developed because of such problems as structural force and deformation, shield tunneling machine advancement control and the installation of rectangular segments. This paper intends to solve spatial arrangement problems in central urban area and old urban area based on entry and exit section of Ningbo rail transit line 3 by taking advantages of rectangular shield tunnel. Supply reasonable research programs and technology routes of rectangular shield tunnel system through systematic analyses on key and difficult points including structural design, equipment manufacturing and construction technology and summarize current scientific research achievements in China. Finally, form rectangular shield tunnel technology system characterized by independent and integrated which includes such aspects as design, equipment and construction and supply specific thoughts and suggestions for the further construction of rectangular shield tunnel.

Keywords: Rectangular shield · Technology system · Lining structure design
Shield equipment · Construction technology

1 Introduction

With the gradual development of underground space in urban area, applicable underground space is becoming less in the central and old urban area especially in large cities. The effect of tunnel construction on surrounding environment has become a social problem required to be resolved urgently [1]. Compared with round section, the effective utility of area of rectangular section is larger by over 20%. The technology mentioned above can make a full use of structural section, and thus save underground resources and it can also form double-track tunnel for one time through single

© Springer Nature Singapore Pte Ltd. 2018
D. Zhang and X. Huang (Eds.): GSIC 2018, *Proceedings of GeoShanghai 2018 International Conference: Tunnelling and Underground Construction*, pp. 757–765, 2018.
https://doi.org/10.1007/978-981-13-0017-2_76

excavation, thus reducing the amount of lands expropriated and obviously increasing the capacity of tunnel in passing through narrow roads or high-rise buildings.

As for former rectangular shield tunnel, Japan undoubtedly is in the leading position. In Japan, thanks to the occurrence of DPLEX eccentric multi-spindal cutter-head rectangular earth pressure balance shield manufactured by Ishikawajima-Harima Heavy Industries (IHI) [1]. DPLEX rectangular shielding machine with a size of 3.98 m 4.38 m was applied in the works constructed within the district of Jutianchuan No. 2 trunk line in Narashino City in 1995 [1]. The rectangular shielding machine with a size of 6.87 m × 10.24 m was applied in Liudizangbei Work Area at the east and west lines of underground road in Kyoto [2]. At present, the researches on rectangular tunnel construction technology have acquired certain achievements in China. However, most of them are limited to the field of pipe jacking method technology and have differences from rectangular shield tunnel in such aspects as segment erection and tunnel stability [4].

Rectangular shield tunnel may meet many difficulties in actual design and construction, such as irregular lining structure design, special shield equipment, segment erection in irregular sections and high-precision axial control. This paper systematically expounds the overall program and technology routes for rectangular shield tunnel technology system and summarizes the primary progresses of large-section rectangular shield tunnel designed for urban rail transportation in such aspects as structural design, equipment research and development and refinement construction.

2 Research and Development Program for Rectangular Shield Technology System

2.1 Technological Program for the Design Tunnel Lining Structure

To determine the construction clearance of rectangular shield tunnel, such principles as applicability, spacial optimization and inclusive design must be considered and force conditions, section utility rates and economical performances of different section programs must be compared in a coordinated way, so as to determine the best rectangular shield section size.

To determine the form of lining joint, full-scale tests aimed at simulating segment structure under designed load and construction condition and ultimate condition must also be conducted through segment structure test (as is shown in Fig. 1), so as to grasp different force mechanisms and corresponding ultimate bearing capacities of rectangular segment structure under different working conditions and define the full-process development of the performances of rectangular shield segment structures under different working conditions, and thus acquire the force and deformation characteristics of segments under designed loading condition, verify the reliability of quasi-rectangular segments and supply basis for optimizing the design of rectangular shield segments.

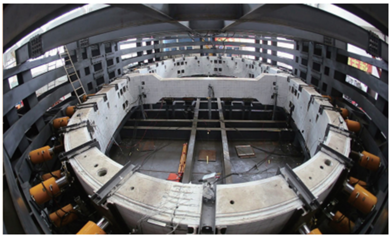

Fig. 1. Load test of segment structure

2.2 Technological Program for the Research and Manufacturing of Shield Equipment

During the advancement of tunnel with quasi-rectangular section, realizing the full-section cutting function of rectangular shield is of vital importance to the balance of soil body in the excavated surface, the axis control of tunnel and the disturbance control surrounding soil layers. Therefore, the internal contents of researches on full-section cutting include in-depth searches on the structure of cutter head, cutting mode and driving technology, especially the form of cutter head, the selection and arrangement of cutting tool, driver integrated technology and the adaptability of support device.

Large-section rectangular shield erector must satisfy the technical requirements of quasi-rectangular segment for erection accuracy and operation, and thus must realize the moving function with multiple degree of freedom [4]. For large-section irregular segment, such issues as researching the structure, system and integration of applicable erector, defining the functional parameters of such erector, complete the refining of structural calculation and the improvement of system for the erector, realizing all the erection movements of the erector for irregular segment and implementing in-depth research on erection process must be conducted. Therefore, erector researches include the mechanism and performance parameters as well as refined calculation of its structure, so as to realize the erection movements with multiple degree of freedom of the erector.

2.3 Technical Program for Shield Construction

Cutting and Dumping Improvement. The excavation surface of rectangular shield is generally large, the bottom of soil chamber is relatively flat and the liquidity of muck is poor, all of which may easily result in concretion or slurry cake, thus influencing the stability of excavation surface and aggravating the disturbance of soil layer. Besides, improvement materials, supporting equipment and construction parameters of rectangular shield are all different from traditional soil body improvement process of round shield ideally. Therefore, pertinent researches must be conducted for soil body improvement in coordination with shield cutter head cutting mode and new type of improvement additives and technologies [5]. Researches and analyses on the improvement mechanism, improvement additives and their mixing ratio, reform process, soil body fluidity situations in the soil chamber and soil excavation performance in rectangular shield soil body improvement process should be implemented through numerical analog simulation (see Fig. 2).

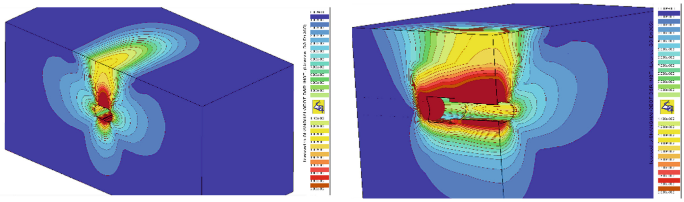

Fig. 2. Numerical simulation

Synchronous Grouting at Shield Tail. Limited by its geometrical shape, rectangular shield tunnel may easily result in the sedimentation of slurry, which is not good for the filling of gaps and is likely to produce the phenomenon of uneven filling of slurry. Therefore, the research on rectangular shield should focus on such issues as grouting hole positioning, slurry materials, supporting equipment and pressure filling process [6].

Large-scale simulation experiment on synchronous grouting should be carried out through the comprehensive simulation experiment platform for sunk shield tunneling machine in Shanghai Shield Experiment Center (see Fig. 3); So as to explore slurry filling situations and mechanisms in the process of synchronous grouting of rectangular shield and compare the grouting effects of different grouting positions, thus acquiring the best grouting construction parameters.

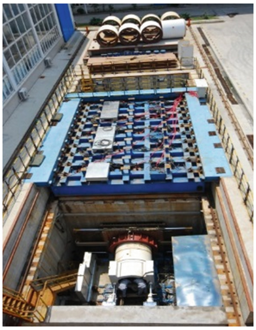

Fig. 3. Experimental platform of large-sized sunk shield tunneling machine

There are totally 8 grouting holes at the rear of shieldtail symmetrically distributed in the lower and upper parts as well as sides of shield shell. Considering that the fluidity of rectangular route is not good enough, 8 spare grouting holes are arranged in the same position, as is shown in Fig. 4. Boundary model is composed of tail shell, rear boundary as well as internal and external boundaries of rectangular shield machine.

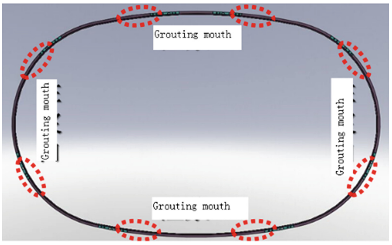

Fig. 4. Grouting system of quasi-rectangular shield machine

The modeling of geometrical model adopted is implemented in full scale by 1:1 based on experiment model, and boundary model adopted is composed of tail shell, rear boundary as well as internal and external boundaries of rectangular shield machine. The experiment of accurate synchronous grouting of rectangular shield can be simulated through accelerating the longitudinal movement speed of the model by 2 cm/min. As the external boundary is the interface between surrounding soil body and slurry, SPH particles should be deposited before simulating the synchronous grouting experiment of rectangular shield to simulate the loading of soil body in the experiment just mentioned, as is shown in Fig. 5.

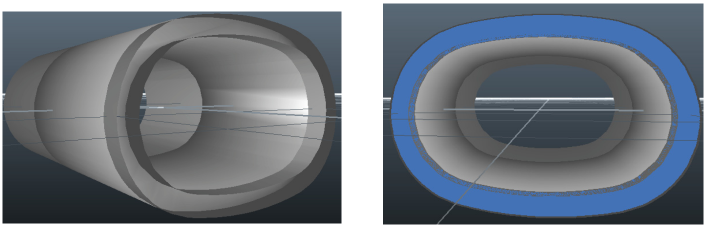

(a) Simulation model (b) Accumulation of SPH particles

Fig. 5. Simulation of shield synchronous grouting experiment

3 Research Achievements Regarding Rectangular Shield Tunnel

3.1 Tunnel Structural Design

The design of construction crosssection and clearance should satisfy the functions of the shield zone tunnel constructed in Ningbo No. 3 urban rail transportation line.

The clearance should be made by means of B2 type vehicle powered by national standard overhead line system, longitudinal evacuation platform should be arranged in main-track zone, and the main principles for the arrangement of cable and equipment pipelines should be consistent with existing lines. Construction clearance should be designed in an inclusive way, and according to clearance requirements, the size of the tunnel's construction clearance is determined as 10300 × 5200 mm. Considering existing design and construction experience, construction error (±100 mm, including measurement error) and later uneven sedimentation (±50 mm), the clearance size within the tunnel is determined as 10600 × 6037 mm. Lining ring segments are erected by means of break joint. Each ring is composed of 11 segments with a width of 1,200 mm and a thickness of 450 mm, as is shown in Fig. 6.

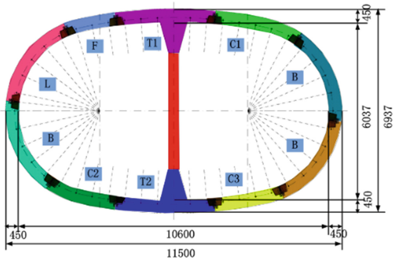

Fig. 6. Quasi-rectangular shield segments

3.2 Tunnel Equipment Research and Manufacturing

The external diameter of shield is determined as 11.83 m × 7.27 m according to the appearance of segment (11.83 m × 7.27 m). It can be seen from Fig. 7 that rectangular shield machine is mainly composed of mainframe and auxiliary structures, including: (1) cutter head system; (2) cutter head drive; (3) shield shell system; (4) promotion system; (5) hinge joint system; (6) screw conveyor system; (7): erection system; (8) man lock; (9) hydraulic system; (10) intensified lubrication system; (11) synchronous grouting system; (12) soil body improvement system; (13) shield tail sealing system; (14) electrical system; (15) automatic orientation measurement system.

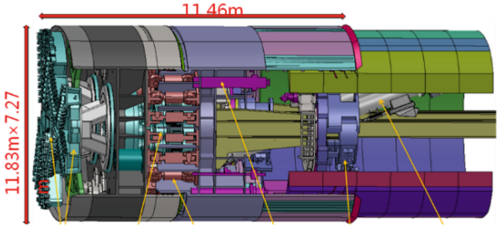

Fig. 7. Quasi-rectangular shield machine

As the cutting section of rectangular is in the shape of ellipse, just like that of quasi-rectangular shield. The cutting form combining large cutter head and eccentric small cutter head is adopted to ensure full-section cutting, as is shown in Fig. 8.

As is shown in Fig. 9, shield propulsion system adopted is inverted ballhead propulsion system that can reconstitute 8 zones. The propulsion system can be divided into 8 zones, with each zone containing 4 jacks. The zones can be adjusted in accordance with axial requirements. The following zoning method can be adopted for

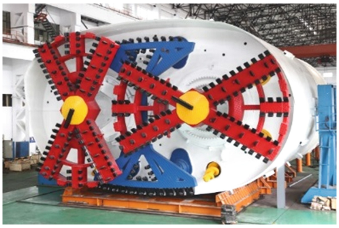

Fig. 8. Cutter head system

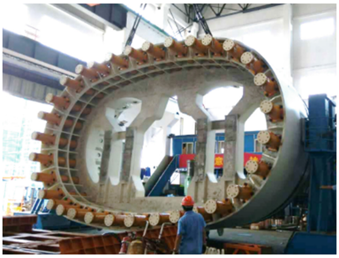

Fig. 9. Thrust system on shield machine

leftward or rightward deviation rectification, so as to form a proper difference between left and right jacking force.

Considering the advantages of the erector mentioned above and the characteristics and form (with stand column) of rectangular shield segment, we think that a kind of erection mechanism with relatively long force arm that can grasp heavy single segments is necessary, therefore, we finally select the erector with ringed arm and the function of automatic track control (Fig. 10). Such a kind of erector can easily realize erection without the support of any other auxiliary mechanism, and it can complete the installation of center pillar simply in its rotation track without occupying too much space or interfering the erection of other mechanisms. Finally, relying on the shield erector system, we can comprehensively grasp the intelligent core and key technologies of rectangular shield erection robot for urban rail transportation (Fig. 17).

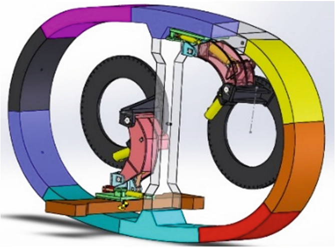

Fig. 10. Automatic track control erector with ring arm pattern

3.3 Tunnel Construction Technology

Through a large quantity of indoor experiments and the experiment aimed at simulating injection improvement, we have got the mixing ratio and performance parameter indexes of corresponding improvement additive materials, and the mixing ratio of the ameliorant adopted as follows: the concentration of foam ameliorant is 3%, and its foaming rate of 12–20 times; the amount of polymer mixed in the polymer slurry is 0.1 kg/m^3.

Based on the construction characteristics of rectangular shield, rectangular shield machine should be equipped with complete soil body improvement system, including

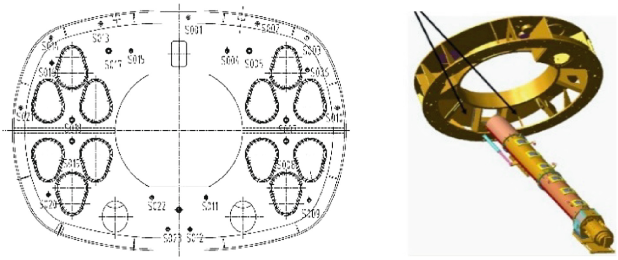

(a) Cutter head and soil improvement region (b) Screw injection region

Fig. 11. Soil improvement system of shield machine

foam system and bentonite slurry system in the rear frame and cutter head and soil chamber injection system. See Fig. 11 for soil body improvement system of shield machine.

For the rectangular segments adopted for the subway tunnel constructed at Ningbo No. 3 subway line, 11 ones are arranged within a single ring, as is shown in Fig. 12. The ring is 1.2 m wide and 45 cm thick, erected by means of break joint. 40 M36 screws and 8 M27 screws are adopted for circumferential connection, and 30 M30 screws are adopted for longitudinal connection. Meanwhile, 10 shear pins are arranged longitudinally.

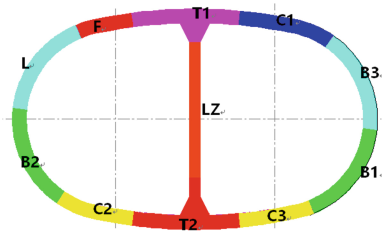

Fig. 12. Quasi-rectangular segment

Through comparing Segment F - Segment LZ and Segment LZ - Segment F erection sequences after corresponding geometrical simulation calculation on the erection of segments within a single ring, it can be concluded that: (1) LZ - F erection sequence can effectively control the insertion space of Segment LZ and ensure its erection quality without too much influence on Segment F, in other words, the sequence incurs little influence on Segment F for the insertion of Segment LZ in advance; (2) as for erection error control, LZ - F erection sequence is better than the other one.

Segment erection mode is determined based on primary achievements of segment erection technologies, as is shown in Fig. 12. According to the erection mode, Segments T2 and C3 are erected firstly, followed by the erection of Segments C2, B1, B2, B3, L and C1, and finally Segments T1, LZ and F are erected.

4 Conclusions and Discussions

After a systematic and effective development lasting for over a year, although trial project is still under implementation, the following primary effects have been acquired, based on which we may embrace a good expectation for its further promotion:

(1) As for structural design, quasi-rectangular tunnel section form that can satisfy the requirements for train operation as well as pipeline and equipment installation clearance in terms of Ningbo rail transportation and such major sizes as lining structure thickness and ring width have been determined according to structural design;

(2) As for equipment research and manufacturing, the erector characterized by six degree of freedom and the function of automatic track control has been developed. Enhanced by the overall design technology and systematic integration technology of quasi-rectangular full-section cutting shield advancement machine, the erector supports the propulsion system that can realize zone reconstitution and satisfy the demand on active hinge joint technology in case of large section and sharp curve and the function of stand column erection;

(3) As for construction, a complete set of soil body improvement technology system applicable to the construction of rectangular shield tunnel has been figured out, and the technology system on such construction items as tunneling, erection and grouting has been established.

References

1. Kashima, Y., Kondo, N., Inoue, M.: Development and application of the DPLEX shield method: results of experiments using shield and segment models and application of the method in tunnel construction. Tunn. Undergr. Space Technol. **11**(1), 45–50 (1996)
2. China Association of Metros: Statistic Report of Urban Rail Transit in 2014, Beijing, China (2015)
3. Zhang, G., Wang, Q.: Synchronous construction technology of large section rectangular shield and cast in place lining. In: Shanghai International Symposium on Tunnel Engineering, Shanghai (2005)
4. Bai, Y., Zhang, G.: Study on Tunneling Construction Equipment and Technology for Large Section and Rectangular Underground Passageway. Shanghai Tunnel Engineering Co., Ltd., Shanghai (2006)
5. Huang, D.: Research of soil improvement during super-large diameter earth pressure balanced shield. Mod. Tunn. Technol. (4), 65–71 (2011)
6. Zhang, H.: Shield Tunnel Theoretical Research and Construction Practice. China Building Industry Press, Beijing (2010)

Research on Field Acquisition Geological Data Application in the Rock Tunnel Construction Phase Based on iS3

Chao Chen[1(✉)], Ziyang Chen[1], and Jin Lei[2]

[1] Tongji University, Shanghai 200092, China
chenchao19921224@126.com
[2] Anhui Transportation Holding Group Co. Ltd., Hefei 230088, China

Abstract. The Complicated-long Tunnel, with high uncertainty of factors such as geological and environment conditions, may cause major challenges in the design and construction process. Specifically the static data of geological exploration based on traditional design and construction can't meet the requirements of refined structure design and construction control. Aimed at more refinement services for rock tunnel construction, this paper, describes the whole process application of the dynamical geological information based on the core concept of infrastructure smart service system (iS3). The platform, covers the essential information flow of geology such as data acquisition, processing, expression, analysis and finally helps to offer integrated decision making services for engineer construction.

Keywords: Infrastructure smart service system (iS3)
Dynamical geological information · Hoek Brown's strength criterion
Refined application

1 Introduction

With the development of highway construction in China, the scale of the long and large tunnel projects is increasing day by day. As a fact, the geological survey results are relatively rough due to the complexity and high costs of geological exploration in the design phase of tunnel. However, the designer usually carry out tunnel route and structure design based on limited geological exploration data, which may lead to the missing calculation parameters and inaccuracy in the design process. Fortunately, during the construction of rock tunnel, more accurate dynamical geological information can be revealed by the tunnel surface and refined field test, which can help to guide the design and construction better [1]. For instance, more refined parameters of rock mass can be analyzed and obtained from field test and joint statistical data. Furthermore, by adopting the modified generalized three dimensional H-B strength criterion, updated refined parameters will help to serve for subsequent structural analysis and engineering decision.

When it comes to the application of engineering information, digital technology is power tool to change and improve the efficiency of traditional management and decision, and a lot of research has been carried out in the application of digital

© Springer Nature Singapore Pte Ltd. 2018
D. Zhang and X. Huang (Eds.): GSIC 2018, *Proceedings of GeoShanghai 2018 International Conference: Tunnelling and Underground Construction*, pp. 766–774, 2018.
https://doi.org/10.1007/978-981-13-0017-2_77

technology of infrastructure both at home and abroad. In 1998, vice President Gore first proposed the idea of digital earth. In 2005, the European Union launched the research program of the technology in underground construction. In 2005, the university of Cambridge and imperial college jointly launched the Smart Infrastructure research program [1]. However, since 1998, Professor Zhu's research group have devoted to research on digital underground space, and became the first in China to build an integrated digital platform for both construction and maintenance period, and in 2017 officially launched infrastructure smart service system (iS3), in other words, the integrated intelligent decision-making system of data acquisition, processing, expression, analysis and service of the whole life of infrastructure [2, 3].

Above all, this paper will carry on the elaboration from field data acquisition, refined rock parameters updating by using modified generalized three dimensional H-B strength criterion, structure analysis of rock mass to final integrated decision making services. Though the whole process, more refine and quantitative analysis result will efficiently guide the construction decision, and thus further the step to refine and remote engineer decision-making and service.

2 Overview of the Infrastructure Smart Service System (iS3)

The infrastructure smart service system (iS3), specifically means the integrated decision-making smart service system served for the full life cycle of infrastructure in the terms of data acquisition, processing, expression and analysis. Mainly it will be applied to the infrastructure objects such as roads, bridges, tunnels, utility tunnels, and cover the whole life cycle from planning, survey, design, construction and maintenance [4, 5]. This system covers the whole information flow, as shown in Fig. 1

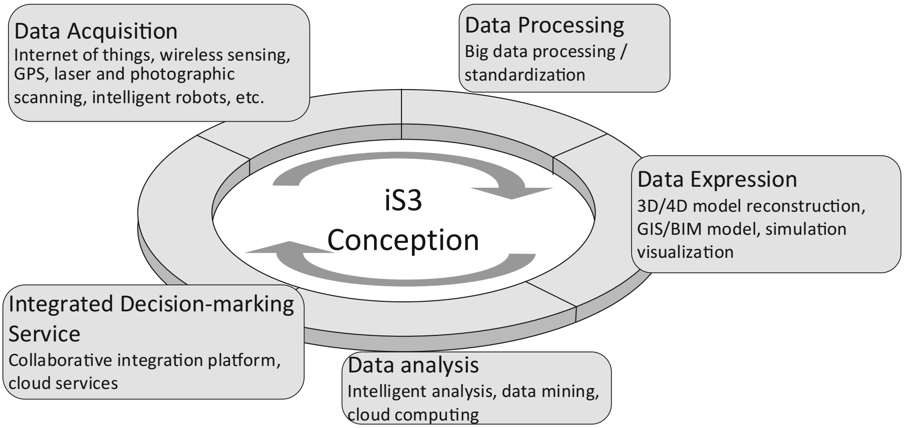
Data Acquisition
Internet of things, wireless sensing, GPS, laser and photographic scanning, intelligent robots, etc.
Data Processing
Big data processing / standardization
iS3
Conception
Data Expression
3D/4D model reconstruction, GIS/BIM model, simulation visualization
Integrated Decision-marking Service
Collaborative integration platform, cloud services
Data analysis
Intelligent analysis, data mining, cloud computing

Fig. 1. Conception of infrastructure smart service system (iS3)

3 The Application of Geological Information in the Construction Phase of Rock Tunnel Based on iS3

3.1 The Framework Outlines

Based on the core concept of iS3, the geological information in construction phase can be organized in the way of information flow and can be particularized as follows:

(1) Data acquisition: according to the standard process, geologic information in spot can be collected through the tunnel surface sketch and point load test and other methods;
(2) Data processing: the parameters of rock strength of tunnel excavation are obtained through the processing of sketch and test data;
(3) Data expression: combined with the BIM model and geological model, the exposed geological information can be displayed in the way of both 2D and 3D;
(4) Data analysis: combining with the existing investigation data and the new added geological information, which provides parameters selection basis for the generalized Hoek Brown's strength criterion, then the finite element calculation can be carried out;
(5) Integrated decision making: combining with field geological gathering information and finite element calculation results, effective decision-making services can be provided for design and construction.

And Fig. 2 shows the whole process of the application of geological information in the construction phrase.

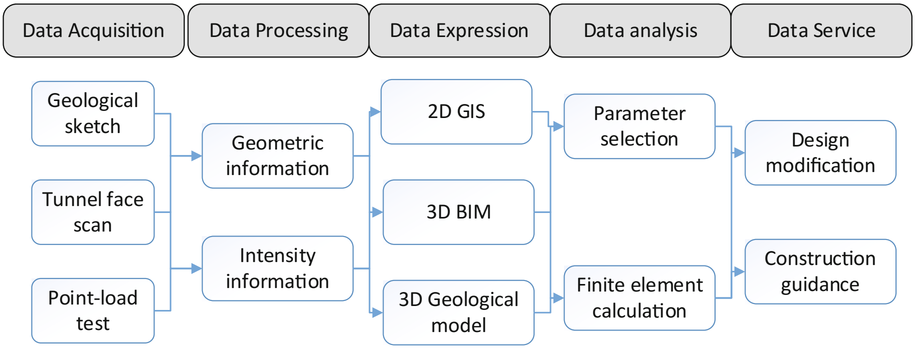
Data Acquisition
Data Processing
Data Expression
Data analysis
Data Service
Geological sketch
Tunnel face scan
Point-load test
Geometric information
Intensity information
2D GIS
3D BIM
3D Geological model
Parameter selection
Finite element calculation
Design modification
Construction guidance

Fig. 2. The whole process of the application of geological information in construction phrase

3.2 Geological Data Acquisition and Processing

The geological data acquisition of rock mass is the basis of the fine analysis and service of rock mass. By using 3D binocular digital photography or 3D laser scanning technology, we can automatically collect rock surface information automatically, and get high-precision information of rock geometry structure effectively, as shown in Fig. 3a.

For instance, through the use of 3D laser automatic scanning equipment, we can directly obtain the 3D point cloud information of the rock mass surface which will help to reconstruct the triangular mesh surface model. And in iS3, based on the data sources mentioned above, more detailed rock parameters can be analyzed, as shown in Table 1 [6].

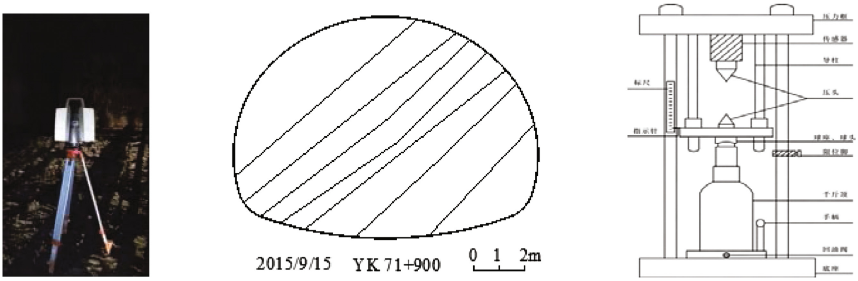

(a) 3D laser scanning (b) Geological sketch (c) Point-load test

Fig. 3. Means of geological data acquisition

Table 1. Information obtained from rock surface

Type	Description
Occurrence statistic	Reflecting the direction of the main structure, it is helpful to analyze the regional structure
Interfacial spacing	It's an important measure of structural surface development, and can be expressed by the structural plane density that the linear density refers to the number of the same set of structures within the unit length
Trace length	The trace length of the structure surface is the length of the outlet surface of the structure surface, reflecting the development scale of the structure

However, in some situation, we may not have the conditions to use the method above. Thus, some traditional method can also be carried out. For instance, geological sketch is an effective means to master tunnel vision and regional geological conditions. During the excavation of excavation, geological sketch of tunnel face can timely, intuitive, and effectively grasp the formation lithology, geological structure, the degree of weathering, rock mass structure, development degree of structure surface, such as geological information, constraints on it and the geological condition in front of the overall qualitative judgment, as shown in Fig. 3b. And also, the test of point load, which is small, lightweight, and easy to carry, easy to operate and good for field test can help to the acquisition of rock mass mechanical parameters easily, making us more quickly solve the problem of engineering practice, as shown in Fig. 3c.

3.3 Geological Data Expression

With the help of emerging technologies such as Geographic Information System (GIS), Building Information Modeling (BIM) and so on, geological information can be well presented in various forms. However, the most important thing is to build a digital model to realize the correspondence between spatial entities and attribute information.

In the terms of 2D visualization, by using GIS technology, data acquired from both survey and test can be expressed by graphics and attribute descriptions; in the terms of 3D visualization, both structure model and geological model can be expressed in the same way, as shown in Fig. 4.

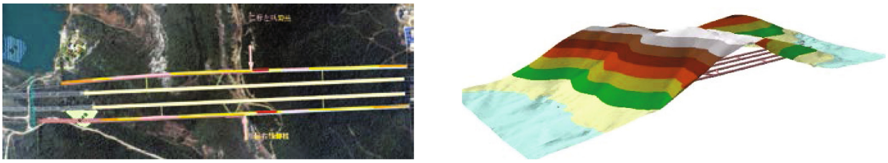

(a) 2D GIS (b) 3D BIM

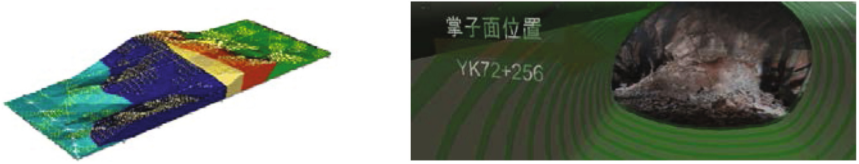

(c) Geological modeling (d) Tunnel face photo

Fig. 4. 3D expression of both geological model and structure model

3.4 Geological Data Analysis

As for the analysis of acquired geological data, iS3 provides various software interface for developing extension tools. In the terms of continuous numerical analysis of rock mass, the iS3 finite element calculation module adopt the 3D nonlinear failure criterion in the rock mass failure calculation. Three types of Lode angle functions are used to modify the yield surface of generalized three-dimensional H-B strength criterion (see Fig. 5, TC is three axial compressive stress and TE is three axis tensile stress), which will take discontinuous parameters of rock mass, such as more finer field test and joint statistical data into consideration. In this way, the information acquired from field is more fully utilized, with higher accuracy compared with other traditional rock failure criteria [7].

3.5 Integrated Decision-Making Service

On the basis of refine collection and analysis of rock mass, iS3 can be used to carry out various engineering services, such as engineering information visualization and project management based on 2D/3D information model and the integrated platform covering data collection, analysis and service, the analysis of geological parameters of the difference and so on.

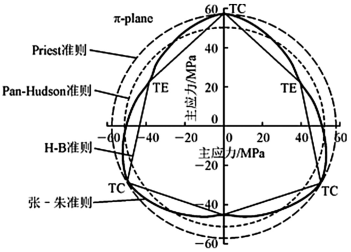

Fig. 5. 3D nonlinear failure criteria for rock mass

In the case of geological information application in the construction phrase, the integrated decision-making serves can be explained as follows:

(1) Providing data management and visualization of geological information during tunnel construction process.
(2) Combined with survey and data acquired on the spot, updating the key analyzing parameters of rock mass and carrying out the refine finite element analysis later.
(3) Guiding the design and construction using the displacement and stress results obtained by the finite element analysis.

4 Examples of Project Application

Shidao mountain tunnel, a separated tunnel of the Hefei-Wuhu Highway, also faces the complex geological conditions such as the broken fault zone. However, both survey and construction data are well managed under the framework of iS3, and geological information is well utilized to aid decision making and construction, as shown in Fig. 6.

Along with the construction of the tunnel, the data of the tunnel surface sketch and point-load test are collected and integrated in the platform, as shown in Fig. 7a and b, and geological data is used to update geological models, as shown in Fig. 7c and d.

Also, combined with survey and data acquired on the spot, the refine rock parameters can be analyzed through modified generalized three dimensional H-B strength criterion, the result can be seen in Table 2

By using the parameters analyzing above, the finite element analysis can be carried out to make sure safety of tunnel excavation and support, as shown in Fig. 8.

Finally, the analysis result by iS3 can help to construction decision. Take the finite element analysis as an example, by using the updated parameters, we can obtain the influence of dynamic construction on the horizontal convergence of the surrounding rock of the target section. However, as shown in Fig. 9a, the horizontal convergence changed slowly as the tunnel excavation face is far, and in the construction step 83, its displacement changed rapidly and finally moves to −2.5 cm. And in the Fig. 9b, the horizontal displacement of the arch waist is divided into 3 stages with the change of the construction step, and most of it happens during the construction stage. In this way, the final result analyzing from geological will help to construction control.

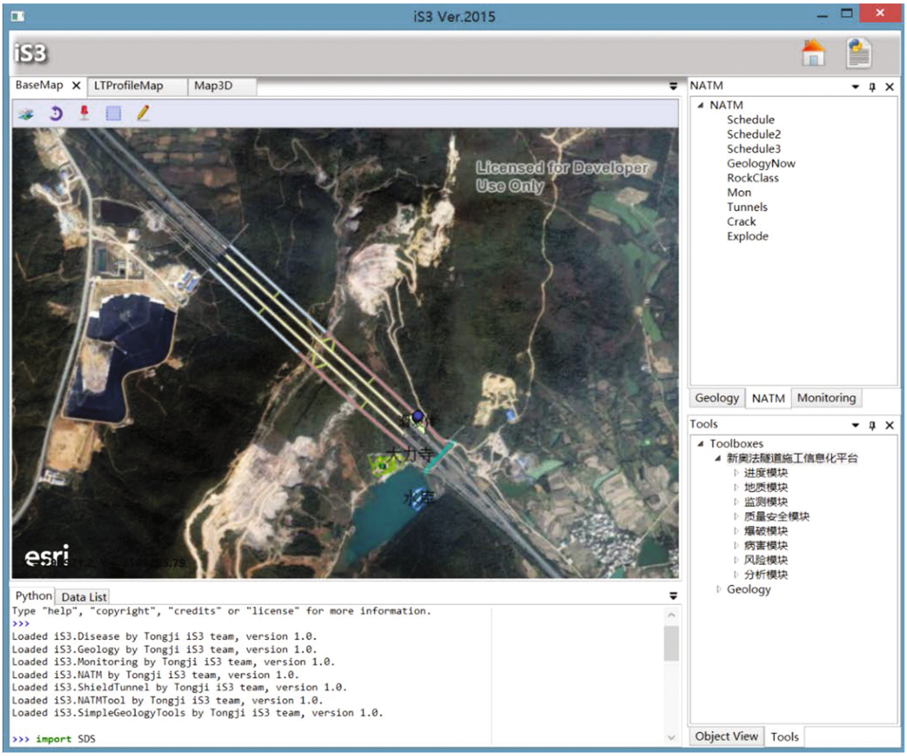
iS3 Ver.2015
iS3
BaseMap
LTProfileMap
Map3D
Licensed for Developer Use Only
esri
NATM
NATM
Schedule
Schedule2
Schedule3
GeologyNow
RockClass
Mon
Tunnels
Crack
Explode
Geology
NATM
Monitoring
Tools
Toolboxes
新奥法隧道施工信息化平台
进度模块
地质模块
监测模块
质量安全模块
爆破模块
病害模块
风险模块
分析模块
Geology
Object View
Tools
Python
Data List

```
Type "help", "copyright", "credits" or "license" for more information.
>>>
Loaded iS3.Disease by Tongji iS3 team, version 1.0.
Loaded iS3.Geology by Tongji iS3 team, version 1.0.
Loaded iS3.Monitoring by Tongji iS3 team, version 1.0.
Loaded iS3.NATM by Tongji iS3 team, version 1.0.
Loaded iS3.ShieldTunnel by Tongji iS3 team, version 1.0.
Loaded iS3.NATMTool by Tongji iS3 team, version 1.0.
Loaded iS3.SimpleGeologyTools by Tongji iS3 team, version 1.0.

>>> import SDS
```

Fig. 6. Management platform for Shidao mountain tunnel in the construction phrase

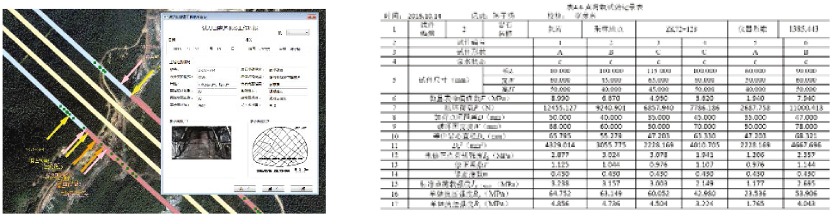

(a) Geological sketch data (b) Point-load test data

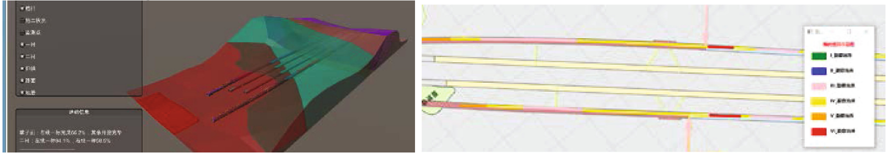

(c) Geological 3d model (d) Updated geological information

Fig. 7. Geological data acquired on the spot in the construction phrase and its expression

Table 2. The refine rock parameters of YK72+600

YK72+600	m_i	GSI	m_b	s	a	D
	7	23	0.447495	0.0001925	0.5357571	0
	E (GPa)	μ	γ	H	C(MPa)	∅(°)
	1.409873039	0.4	22	164 m	0.3503393	32.85153

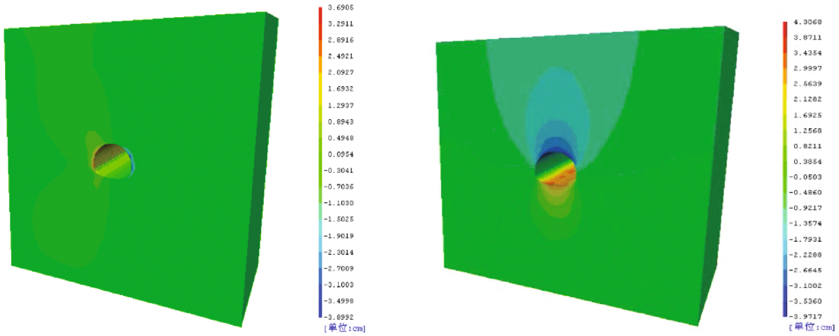

(a) Horizontal displacement nephogram (b) vertical displacement nephogram

Fig. 8. The finite element analysis carried out using the updated rock mass parameters

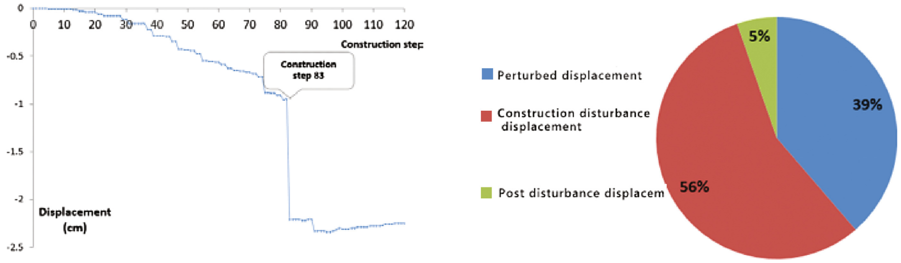

(a) The horizontal convergence (b) The statistics of convergence

Fig. 9. The influence of dynamic construction on the horizontal convergence of the surrounding rock of the target section

5 Conclusions and Discussion

Based on iS3 platform, this paper mainly describes the whole process of geological information application. And by organized the geologized information in the way of data collection, processing, expression, analysis and final decision-making service, the information can be well managed, visualized and utilized.

However, there exist many things which need improving, such as the means of data collection, data analysis and so on. Later we can use 3D laser scanning or digital photography to quickly collecting geological information that we need. Also we can image recognition and 3D reconstruction techniques to process the data we have collected. Finally, the updated geological information can be used in various way such as Construction safety risk forecast and so on.

References

1. Zhu, H.: From digital earth to digital stratum—a new idea in the development of geotechnical engineering. Geotech. Eng. World **1**(12), 15–17 (1998). (in Chinese)
2. Zhu, H., Wei, W., Li, X., Chen, J., Huang, X.: Fine collection, analysis and service of rock tunnel information based on iS3 platform. Chin. J. Rock Mech. Eng. **36**(10), 2350–2364 (2017)
3. Zhu, H., Li, X.: Digital underground space and engineering. J. Rock Mech. Geotech. Eng. **190** (11), 2277–2288 (2007)
4. Zhu, H., Li, X., Chen, X.: Digitization techniques for integrated construction and maintenance of infrastructure—Part 1: theory and methodology. China Civil Eng. J. **48**(4), 99–110, 123 (2015)
5. Zhu, H., Li, X., Chen, X.: Digitization techniques for integrated construction and maintenance of infrastructure—Part 2: engineering application. China Civil Eng. J. **48**(6), 114–121 (2015)
6. Jin, H.: Study on the extraction and extraction of rock mass based on three laser scanning. Northeastern University, China (2013)
7. Zhu, H., Zhang, Q., Zhang, L.: Research on the progress and application of Hoek-Brown strength criterion. Chin. J. Rock Mech. Eng. **32**(1), 1945–1963 (2013)

Author Index

A
An, Cong, 112

B
Bai, Mei-yan, 207
Bai, Yun, 103, 442, 528
Bao, Ting, 685
Bao, X. H., 696
Bi, Jing, 605
Bloodworth, Alan, 250
Bouazza, Abdelmalek, 710

C
Cai, Y. Q., 496
Cao, Shiding, 728
Chai, Jin-Chun, 674
Chen, Ang, 103
Chen, Chao, 766
Chen, Cheng, 112
Chen, Guoxing, 241
Chen, Jianbin, 652
Chen, Jing, 339
Chen, Jixiang, 103
Chen, Luhai, 612
Chen, Nan, 112
Chen, Weiyun, 241
Chen, Weizhong, 369, 376
Chen, Xiao-Liang, 198
Chen, Yifan, 112
Chen, Zhiyi, 718
Chen, Ziyang, 766
Cheng, Wen-chieh, 224
Cheng, Xiaohu, 164
Cui, H. Z., 696
Cui, Lan, 121

D
Diaz, Diana, 528
Ding, Hao, 605
Ding, Wenqi, 23, 32, 292, 432, 728
Ding, Zhi, 136
Dong, Jingtao, 666, 737
Dong, Zibo, 757
Du, Shou-Ji, 559
Du, Yan-Jun, 84

F
Fang, Di, 241
Fang, Pengfei, 710
Feng, Shi-Jin, 319

G
Ge, Louis, 224
Gong, Chenjie, 292
Gong, Xiao-Nan, 198
Gong, Yifan, 292
Green, Christopher, 685
Guo, Qinghua, 612
Guo, Shu-xun, 309

H
Han, Changling, 517
Han, Dong, 190
Hicher, Pierre-Yves, 506
Hong, Bichen, 329
Hu, Biao, 486
Hu, Jun, 477
Hu, Shufan, 112
Huang, Dezhong, 232
Huang, Hong-hao, 402
Huang, Hongwei, 392, 451

© Springer Nature Singapore Pte Ltd. 2018
D. Zhang and X. Huang (Eds.): GSIC 2018, *Proceedings of GeoShanghai 2018 International Conference: Tunnelling and Underground Construction*, pp. 775–777, 2018.
https://doi.org/10.1007/978-981-13-0017-2

Huang, Maosong, 1
Huang, X., 468
Huang, Xin, 384
Huang, Zhong-Kai, 300, 422

J
Ji, Shan, 477
Jia, Jian, 548
Jiang, An-nan, 63, 309
Jiang, Hong, 749
Jiang, Xi, 103, 528
Jin, Junwei, 93
Jin, Yuelang, 292

K
Kang, Zhijun, 74
Kou, Xiaoyong, 232

L
Lang, Rui-qing, 339
Laouafa, Farid, 506
Lee, Y. L., 54
Lei, Jin, 766
Leung, C. F., 1
Li, Jinlong, 74
Li, Jun, 728
Li, Ke, 605
Li, Mingyu, 93, 536
Li, Ning, 40
Li, Peinan, 232, 432, 757
Li, Peng, 559
Li, Xiaojun, 190, 329
Li, Xiongwei, 633, 652
Lin, Gao, 63
Ling, Shenlin, 215
Liu, Chuanping, 548
Liu, F. Y., 496
Liu, G. B., 696
Liu, Jiangtao, 737
Liu, Jie, 351
Liu, Jun, 232, 432
Liu, Junyan, 567
Liu, Naifei, 40
Liu, Ting-jin, 402
Liu, W., 468
Liu, Xiao-Guang, 559
Liu, Yan, 567
Liu, Zhen, 685
Liu, Zhiqian, 718
Lu, Junfu, 215, 757
Luo, Zhe, 486
Lv, Zhitao, 517

M
Ma, Shaosen, 369, 376
Meldrum, Jay, 685
Michalowski, Radoslaw L., 361
Mingi, H. Y., 696
Mu, Linlong, 1

N
Ni, James C., 224

P
Pan, Yu, 121
Park, Dowon, 361
Peng, Fang-Le, 587
Peng, Jian, 587
Peng, Mao-Zhu, 300, 319, 422

Q
Qiao, Yafei, 23, 32
Qin, Tan, 112
Qin, Yu, 633

R
Ren, Dong-Jie, 674
Ren, Yuanyang, 40

S
Shen, Chuan, 207
Shen, Shui-Long, 674
Shen, Yi, 273, 282, 625
Shi, Jingkang, 451
Si, Chen, 642
Song, Weikang, 93
Sun, Li-qiang, 339

T
Tan, Yong, 74
Tang, Xin-wei, 402
Tian, Longgang, 263

W
Wang, Changhong, 181
Wang, Fei, 84
Wang, Hong-wei, 207
Wang, Jin-man, 309
Wang, Min, 652
Wang, Shan-yong, 402

Wang, X., 496
Wang, Xiao, 263
Wang, Yahui, 567
Wang, Yanli, 652
Wang, Yong, 633, 652
Wang, You-fu, 63
Wang, Youwen, 486
Wang, Yuesong, 517
Wang, Zhongjin, 710
Wei, Gang, 136
Wei, Lixin, 32
Wei, Xinjiang, 136
Wu, Di, 576
Wu, Lin, 156
Wu, Tianxiang, 728
Wu, Weifeng, 32
Wu, Yangchun, 612

X
Xi, Baoping, 612
Xia, Caichu, 517
Xiayang, Yuyu, 605
Xie, Kai-zhong, 207
Xie, Wei-Ping, 477
Xie, Xin, 392
Xie, Xinyu, 710
Xin, Y. X., 54
Xiong, Y. L., 696
Xu, C. J., 496
Xu, Meng-fei, 63
Xu, Rao, 402
Xue-liang, Zhang, 63

Y
Yan, Shu-wang, 339
Yan, Zhi-guo, 273, 282
Yan, Zhiguo, 597, 625, 666, 737
Yang, Bowen, 250
Yang, Jie, 506
Yang, Min, 40
Yang, Rui, 309
Yifeng, Lin, 460
Yin, Xinsheng, 136
Yin, Zhen-Yu, 506
Yu, Jian, 1
Yuan, Da-Jun, 674

Z
Zhai, Yixin, 432
Zhan, Jingyuan, 93
Zhang, Chenrong, 1
Zhang, Dong-Mei, 300, 319, 351, 422, 506
Zhang, Dongming, 392, 451
Zhang, Feng-rui, 309
Zhang, Guangchao, 263
Zhang, Hang, 156
Zhang, Liangliang, 567
Zhang, Qi, 263
Zhang, Rong-Jun, 121
Zhang, Xiao-lei, 319
Zhang, Xiao-Lei, 422
Zhang, Xiedong, 156
Zhang, Xuehui, 103, 442, 528
Zhang, Yao, 273
Zhang, Yiming, 131
Zhang, Yuxin, 597, 625, 666
Zhang, Z. X., 468
Zhang, Zhao, 215
Zhang, Zhihua, 156
Zhang, Zhu, 40
Zhang, ZhuanZhuan, 528
Zhang, Zixin, 384
Zhao, Jibin, 536
Zhao, Tianchi, 23, 32
Zhao, Yong, 319, 422
Zhao, Yonghui, 112
Zheng, Jun-Jie, 121
Zheng, R. Y., 696
Zheng, Shi-jie, 309
Zhi, Lin, 642
Zhou, Chen, 442
Zhou, Long, 282
Zhou, Min, 84
Zhou, Xiaozhou, 329
Zhou, Yu, 517
Zhu, Hehua, 273
Zhu, He-hua, 282
Zhu, Hehua, 329, 597, 612, 625, 666, 737
Zhu, Yanfei, 384
Zhu, Yaohong, 757
Zhu, Yeting, 384
Zhuang, Q. W., 468
Zhuang, Xiaoying, 131
Zong, Xiang, 300